



## **9. EUROPEAN CONFERENCE ON RENEWABLE ENERGY SYSTEMS**

**ECRES 2021  
21-23 April 2021  
Istanbul / TURKEY**

**[www.ecres.net](http://www.ecres.net)**

# **PROCEEDINGS**

**Edited by**

**Prof. Dr. Erol Kurt**

**ISBN: 978-605-86911-9-3**

## Organizing Institutions

---



Electrical and Computer Engineering Research Group - [ecerg.com](http://ecerg.com)



Projenia R&D Consultancy Service Limited Company - [projenia.net](http://projenia.net)

*Published by*  
**Erol Kurt**  
on 6<sup>th</sup> May 2021  
(Ankara/Turkey)

©All rights of the abstract book of European Conference on Renewable Energy Systems (ECRES) are preserved. No part of this publication may be produced, stored in retrieval system, or transmitted in any form of electronic, mechanical and photocopying or reproduction technique without the prior permission of the publisher. The responsibility for the ingredients covering information and opinion rests exclusively with the authors and independent from the organizers and publisher.

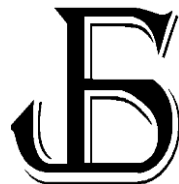
---

*Book typesetted and designed by*  
Assoc. Prof. Dr.Yunus Uzun and Bekir Dursun

## Cooperative Institutions



## Supporting Institutions



JOURNAL OF ENERGY SYSTEMS  
[dergipark.org.tr/jes](http://dergipark.org.tr/jes)

## **Committees**

---

### **Conference Founder & Chairman**

Prof. Dr. Erol KURT, Gazi University, Turkey

### **Local Organizing Committee**

Prof. Dr. Erol Kurt, Gazi University, Turkey

Assoc. Prof. Dr. Yunus Uzun, Aksaray University, Turkey

### **International Organizing Committee**

Prof. Dr. Adnan Sozen, Gazi University, Turkey

Prof. Dr. Alfredo Vaccaro, Sannio University, Italy

Prof. Dr. Carlos Rubio-Maya, Univ. Michoacana de San Nicolás de Hidalgo, Mexico

Assoc. Prof. Dr. Fontina Petrakopoulou-Robinson, Universidad Carlos III de Madrid, Spain

Prof. Dr. Ian Hunter, University of Leeds, UK

Prof. Dr. Jose Manuel Lopez Guede, University of Basque Country, Spain

Prof. Dr. Mehmet Tekerek, Kahramanmaraş Sutcu Imam University, Turkey

Prof. Dr. Murat Kunalbayev, Inst. of Information and Computational Technologies, Kazakhstan

Prof. Dr. Nicu Bizon, Pitesti University, Romania

Prof. Dr. Peter Childs, Imperial College London, UK

Prof. Dr. Poul Alberg Østergaard, Aalborg University, Denmark

Prof. Dr. Raoul Rashid Nigmatullin, Kazan National Research Tech. Univ., Tatarstan, Russia

Prof. Dr. Saad Mekhilef, University of Malaya, Malaysia

Prof. Dr. Saeed Badshah, Int. Islam. Uni. Islamabad, Pakistan

Prof. Dr. Sagdulla L. Lutpullaev, Uzbekistan Academy of Sciences, Uzbekistan

Prof. Dr. Serguei Martemianov, University of Poitiers, France

Prof. Dr. Shadi Shahedipour-Sandvik, University at Albany, USA

Prof. Dr. Shadia J. Ikhmayies, Al Isra University, Jordan

Prof. Dr. Waqar Mahmood, University of Engineering and Technology, Pakistan

Assoc. Prof. Dr. Yussupova Gulbakhar, Turan University, Kazakhstan

### **International Scientific Committee**

Prof. Dr. Alessandro Zanarini, University of Bologna, Italy

Assoc. Prof. Dr. Ali Jazie, University of Al-Qadisiyah, Iraq

Dr. Angeliki Chatzidimitriou, Aristotle University of Thessaloniki, Greece

Prof. Dr. Antonio Soria Verdugo, Universidad Carlos III de Madrid, Spain

Dr. Athar Waseem, International Islamic University, Pakistan

Prof. Dr. Aybaba Hançerlioğulları, Kastamonu University, Turkey

Prof. Dr. Ayman El-Hag, American University of Sharjah, UAE

Prof. Dr. Bernabé Marí Soucase, Polytechnical University of Valencia, Spain

Assist. Prof. Dr. Burak Akin, Yildiz Technical University, Turkey

Assoc. Prof. Dr. Bünyamin Tamyürek, Eskisehir Osmangazi University, Turkey

Prof. Dr. Carolina Marugan Cruz, Universidad Carlos III de Madrid, Spain

Assoc. Prof. Dr. Christiane Hennig, German Biomass Research Center, Germany

Prof. Dr. Corneliu Marinescu, Transilvania University of Brasov, Romania

Assoc. Prof. Coşku Kasnakoğlu, TOBB Ekonomy and Technology University, Turkey

Assoc. Prof. Dr. Çigdem Yangın Gömeç, Istanbul Technical University, Turkey

Dr. Danny Müller, Technische Universität Wien, Austria

Assoc. Prof. Dr. Diana Zalostiba, Riga Technical University, Latvia

Dr. Eduar Eduardo Zarza, CIEMAT Solar Platform of Almeria, Spain

Prof. Dr. Eleonora Guseinoviene, Klaipeda University, Lithuania  
Prof. Dr. Farqad Al-Hadeethi, Royal Scientific Society of Jordan, Jordan  
Assoc. Prof. Dr. Fontina Petrakopoulou-Robinson, Universidad Carlos III de Madrid, Spain  
Prof. Dr. Francesco Calise, University of Naples Federico II, Italy  
Assoc. Prof. Dr. Francesco Cottone, University of Perugia, Italy  
Prof. Dr. Guang-Bin Huang, Nanyang Technological University, Singapore  
Prof. Dr. Guido Van Oost, University of Gent, Belgium  
Prof. Dr. Güngör Bal, Gazi University, Turkey  
Prof. Dr. H. Hilal Kurt, Gazi University, Turkey  
Prof. Dr. H. Mehmet Şahin, Karabük University, Turkey  
Prof. Dr. Haitham Abu-Rub, Texas A&M University at Qatar, Qatar  
Assoc. Prof Dr. Hasan Köten, Medeniyet University, Turkey  
Prof. Dr. Herman Vermaak, Central University of Technology, Free State, South Africa  
Prof. Dr. Ibrahim Dincer, University of Ontario, Canada  
Prof. Dr. Ibrahim Sefa, Gazi University, Turkey  
Prof. Dr. Ilya Galkin, Riga Technical University, Latvia  
Assoc. Prof. Dr. Ilona Sárvári Horváth, University of Borås, Sweden  
Prof. Dr. Jongho Yoon, Hanbat National University, S. Korea  
Prof. Dr. Jongsoon Song, Chosun University, S. Korea  
Prof. Dr. Jorge R. Frade, University of Aveiro, Portugal  
Prof. Dr. Jose A. Aguado, University of Malaga, Spain  
Prof. Dr. Jose A. Ramos Hernanz, Universidad del Pais Vasco, Spain  
Prof. Dr. Jose M. Lopez Gude, Universidad del Pais Vasco, Spain  
Prof. Dr. Josep Guerrero, Aalborg University, Denmark  
Assoc. Prof. Dr. K.Premkumar, Rajalakshmi Engineering College, Chennai, India  
Prof. Dr. Kozo Taguchi, Ritsumeikan University, Japan  
Prof. Dr. Leijun Xu, Jiangsu University, China  
Prof. Dr. Jun Yang, Huazhong University of Science and Technology, China  
Dr. Loreto V. Gutierrez, CIEMAT Solar Platform of Almeria, Spain  
Prof. Dr. Mahmood Ghoranneviss, Islamic Azad University, Iran  
Prof. Dr. Maria Venegas, Universidad Carlos III de Madrid, Spain  
Assoc. Prof. Dr. Mario E. Magana, Oregon state University, USA  
Prof. Dr. Maris Klavins, University of Latvia, Latvia  
Prof. Dr. Mehmet Önder Efe, Hacettepe University, Turkey  
Prof. Dr. Mehmet Tekerek, Kahramanmaraş Sutcu Imam University, Turkey  
Assoc. Prof. Dr. Merih Palandöken, İzmir Katip Çelebi University, Turkey  
Prof. Dr. Metin Gürü, Gazi University, Turkey  
Prof. Dr. Milan Stork, University of West Bohemia, Czech Republic  
Prof. Dr. Mohammad N. A. Hawlader, International Islamic University, Malaysia  
Prof. Dr. Munir Nayfeh, University of Illinois at Urbana-Champaign, USA  
Prof. Dr. Muris Torlak, Sarajevo University, Bosnia and Herzegovina  
Prof. Dr. Mustafa İlbas, Gazi University, Turkey  
Prof. Dr. Mykola Radchenko, Admiral Makarov National University of Shipbuilding, Ukraine  
Prof. Dr. N. Nasimuddin, Institute for Infocomm Research, Singapore  
Dr. Nam Choon Baek, Korea Institute of Energy Research, S. Korea  
Prof. Dr. Namazov Subhan Nadiroglu, Azerbaijan Technical University, Azerbaijan  
Prof. Dr. Narasimha G. Reddy, Lamar University, USA  
Assoc. Prof Dr. Natalia Tintaru, Vilnius University, Lithuania  
Prof. Dr. Nicolae Paraschiv, Petroleum - Gas University of Ploiesti, Romania  
Prof. Dr. Nicu Bizon, Pitesti University, Romania  
Prof. Dr. Nikolay Djagarov, Nikola Vaptsarov Naval Academy, Bulgaria  
Dr. Nilufar R. Avezova, Uzbekistan Academy of Sciences, Uzbekistan  
Prof. Dr. Pedro Juan Roig, Universidad Miguel Hernández, Spain  
Prof. Dr. Peter Lund, Aalto University, Finland  
Prof. Dr. Poul Alberg Østergaard, Aalborg University, Denmark  
Prof. Dr. Rachid Chenni, University Mentouri of Constantine, Algeria  
Prof. Dr. Rafael K. Jardan, Budapest Univ. of Technology and Economics, Hungary

Prof. Dr. Rafaela Hillerbrand, RWTH Aachen University, Germany  
Prof. Dr. Ramazan Bayindir, Gazi University, Turkey  
Prof. Dr. Raoul Rashid Nigmatullin, Kazan National Research Technical University, Russia  
Dr. Rosaria Villari, Italian National Agency for New Technologies, Italy  
Prof. Dr. Saffa Riffat, Nottingham University, UK  
Assist. Prof. Dr. Sertac Bayhan, Texas A&M University at Qatar, Qatar  
Prof. Dr. Shadia J. Ikhmayies, Al Isra University, Jordan  
Prof. Dr. Sing Lee, Institute for Plasma Focus Studies, Australia  
Prof. Dr. Sor Saw Heoh, Nilai University, Malaysia  
Prof. Dr. Souad A.M. Albathi, Int. Islamic Uni. Malaysia, Malaysia  
Prof. Dr. Sujit Barhate, Savitribai Phule Pune University, India  
Assoc. Prof. Dr. T.Thamizhselvan, Rajalakshmi Engineering College, Chennai, India  
Prof. Dr. Tae Hee Lee, Hanyang University, S. Korea  
Prof. Dr. V. Jagannathan, Bhabha Atomic Research Center, India  
Prof. Dr. Wail N. Al-Rifaie, Philadelphia University, Jordan  
Prof. Dr. Wang Ru-Zhu, Shanghai Jiao Tong University, China  
Assoc. Prof. Dr. Yong Song, Institute of Nuclear Energy Safety Technology, China  
Prof. Dr. Zhiqiang Zhu, Institute of Nuclear Energy Safety Technology, China



## **FOREWORD**

***Dear Colleagues,***

We are glad to see you and your contribution for the 9<sup>th</sup> European Conference on Renewable Energy Systems (ECRES 2021). The event has been organized in Istanbul/Turkey on 21-23 April 2021 by the local organizers ECERG – Electrical and Computer Engineering Research Group at Gazi University and PROJENIA in the virtual format. Besides, many institutions world-wide took a part as the cooperating institutions including many international refereed academic journals.

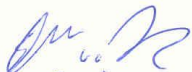
Historically, the first, second, third, fourth, fifth, sixth, seventh and eighth conferences were completed very successfully in Alanya/Antalya (2012), Antalya (2013), Kemer/Antalya (2015), Istanbul (2016), Sarajevo / Bosnia and Herzegovina (2017), Istanbul (2018), Madrid (2019), Istanbul-remote (2020), respectively.

Many of the extended forms of selected papers were published in SCI, E-SCI and SCOPUS indexed reputable journals following the previous events. This year, 225 papers have been received world-wide. Among them, 146 papers from 40 countries have been accepted by the scientific committee. Following the virtual presentation of the authors, these papers are put into the proceedings. We gratitute all authors, keynote speakers, special session organizers, reviewers, session chairmen and scientific board for their precisious contribution aand hope to extend these cooperation for the next events, too.

The purpose of the ECRES is to bring together researchers, engineers and natural scientists from all over the world, interested in the advances of all branches of renewable energy systems such as wind, solar, hydrogen, hydro-, geothermal, solar concentrating, fuel-cell. It aims to present and disseminate the cutting-edge results to the international community of energy in the form of research, development, applications, design and technology. It is thereby expected that it can assist researchers, scientists, manufacturers, companies, communities, agencies, associations and societies to keep abreast of new developments in their specialist fields and to find innovative solutions in their problems.

This proceeedings have been delivered to the participants via the conference website link. In addition, high amount of selected papers will be considered for the publication in reputable journals indexed in Science Citation Index (SCI-indexed), Emerging SCI-indexed, SCOPUS-indexed and EBSCO-indexed journals after the standard peer-review processes of the journals.

We would like to send our warmest greetings to all of you and looking forward to having your future contribution to the future events for a much green, pandemy-free and peaceful word. (1<sup>st</sup> May 2021, Ankara)



**Prof. Dr. Erol KURT**

Chairman of ECRES Series  
Gazi University, Technology Faculty  
Department of Electrical and Electronics Engineering  
06500 Besevler ANKARA TURKEY  
E-mail: ekurt52tr@yahoo.com



## CONTENTS

### KEYNOTES

Title	Presenter	Page
Is exergy destruction minimization the same thing with energy efficiency maximization?	Birol Kılıç	3
A state-of-the-art: DC-to-DC converters for fuel cell vehicular power train – power electronics in fuel cell technology	Sanjeevikumar Padmanaban	14
Next-generation smart grids: Power electronics dominated power systems	Sertaç Bayhan	15
The co-simulation studies of the power electronic circuits with FEA software	Selami Balci	16
IoT with green energy	Sudan Jha	17

## REGULAR ABSTRACTS

Paper ID	Title	Authors	Page
2	Towards integration of carbon capture and storage approaches in waste processing technologies	Maris Klavins, Dmitry Porshnov	20
23	Renewable energy supply chain network design	Bader A. Al-Abiani, Marwa Mekky M, Noura A. Al-Ghimplas	21
41	Deep-learning approach to the iron concentration evaluation in silicon solar cell	Olikh Oleg, Lozitsky Oleg, Zavhorodnii Oleksii	22
45	Energy harvesting through landscape design	İşıl Kaymaz, Ecem Hoşgör	23
54	Design of 2S2L based buck - boost converter with wide conversion range	Nagi Reddy Bandi, Prasanna Chunduru, Neelima Kalahasti, Surya Prakash Jalli, Akshay Reddy Bobbala, Dinesh Goud Kotha	24
61	Technological forecasting for electric battery technology in the electric vehicle industry	Koten Hasan	25
63	Analysis of positive output buck-boost topology with extended conversion ratio	Nagi Reddy Bandi, Sahithi Priya Kosika, Manish Patel Gadam, Jagadishwar Banoth, Ashok Banoth, Srikanth Koundinya	26
74	Data extraction of perovskite solar cells materials by using natural language processing tools	Mary Zuleika Jiménez Díaz, Cristian David Camacho Parra, Mónica Andrea Botero Londoño, Alexander Sepúlveda Sepúlveda, Camilo Andres Otáloa Bastidas	27
87	Upscaling of perovskite solar cell technology by a semi-automatic blade-coating technique at ambient condition	Luigi Vesce, Maurizio Stefanelli, Luigi Angelo Castriotta, Jan Philipp Herterich, Markus Kohlstädts, Uli Würfel, Aldo Di Carlo	28
133	Electric energy load forecasting with ARIMA vs XGBoost for Australia VIC state	Muhammed Can Özdemir, Hasan Köten, Nejat Yumuşak	29
146	ESS influence investigation on the operation of critical network nodes	Virginijus Vasylius	30
153	Application of PEMFC electrical fluctuation for in-situ diagnostics	Evguenii Denisov	31
155	High strength and lightweight steel profiles used in the installation of photovoltaic systems	Hakan Erçay, Celal Erkal Kahraman, Tuncay Dikici	32
157	Assessment of energy saving possibilities in construction with the use of solutions based on renewable energy sources	Elżbieta Szafranko	33
158	An attempt to assess the correctness of assembly and geometry of solar panels using laser scanning	Elżbieta Szafranko, Joanna A. Pawłowicz	34
166	Bioinspired polymer materials for thermal management of heating and cooling in buildings	Stiubianu George, Bargan Alexandra, Dascalu Mihaela, Racles Carmen, Bele Adrian, Tugui Codrin, Ursu Cristian, Cazacu Maria	35
183	The impact of the external environment on energy consumption in residential ventilation and air-conditioning systems on the example of north-eastern Poland	Aldona Skotnicka-Siepsiak	36
185	Analysis of the actual and standard consumption of thermal energy in buildings	Bogacz Piotr	37
186	Differential settlement of pile foundation for wind turbine tower on multilayered subsoil	Dyka Ireneusz, Jolanta Harasymiu	38

## FULL PAPERS

Paper ID	Title	Authors	Page
5	Establishing reduced thermal mathematical model (RTMM) for a space equipment	Mustafa Akbulut, Zafer Karadayi, Ahmet H. Ertaş	40
12	Design the superconducting magnet power supply for medical proton accelerator	Shengmin Pan	46
24	Power loss calculation of photovoltaics using python	Kerry Sado, Ismail Ali, Lokman Hadi, Shivan Sado	53
29	Techno-economic feasibility analysis of PV potential with passive cooling in the desert climate	AlAmri Fahad, AlZohbi Gaydaa	59
30	Promissing HDR project in the North Caucasus	Alan Lolaev, Anatoly Gurbanov, Victor Gazeev, Aleksey Lexin, Aleksan Oganesyan	69
31	Application of power spectral density and the support vector machine to fault diagnosis for permanent magnet synchronous motor	Zerdani Sara, Larbi Elhafyani Mohamed, Zouggar Smail,	74
32	The impact of radiant heating on the performance of sustainable constructional component under elevated temperature: Part 2	Wail N. Al-Rifaie, Talal Al-Hajri, Waleed K. Ahmed	83

34	System integration and data models to support smart grids energy trading	Silva Fábio, O'Leidhin Eoin, Tahir Farah, Mould Karen, O'Regan Brian	89
35	Power control strategy of a photovoltaic system	Bedoud Khouloud, Bahi Tahar, Merabet Hichem	96
36	Artificial neural network forecasting models for wind and photovoltaic energy prediction utilizing time-series input data with different resolutions	Mutaz AlShafeey, Csaba Csáki	103
37	Performance assessment of the windows glazing system for the office building	Pinar Usta, Basak Zengin	109
39	Wireless charging systems for electric vehicles: Review article	Kerry Sado, Lokman Hadi	115
40	Exergy assessment of the energy efficiency of the clean room air treatment system	Andrei Sergeevich Riabyshenkov, Valery Ivanovich Karakeyan, Nikolay Romanovich Kharlamov, Mikhail Aleksandrovich Gundartsev, Valeria Pavlovna Sharaeva	121
42	Determining of optimal tilt angle of solar panels in three cities in Albania	Buzra Urim, Mitrushi Driada, Serdari Eduart, Topciu Daniela, Muda Valbona	129
43	Effect of Estonian woody biomass gasification temperature on the composition of the producer gas	Alejandro Lyons Cerón, Alar Konist, Heidi Lees, Oliver Järvik	135
44	The increasing importance of smart home applications as a major trend for the future value creation of German energy companies	Andreas Ensinger, Max-Robert Salzer, Karlheinz Bozem, Anna Nagl, David K. Harrison, Bruce M. Wood	140
46	Thermal energy grid simulation (TEGSim) for smart urban regions	David Huber, Viktoria Illyés, Veronika Turewicz, Stefan Hoyer, Gregor Götzl, Karl Ponweiser	146
47	A two-step metal-assisted chemical etching process for formation of silicon nanowires based black silicon	Hazem ElGhoniemy, Talal Albuqami, Ahmed ElNaggar, Mohamed Abdel-Rahman	153
48	Performance investigation of an integrated solar-powered RO/Adsorption cooling trigeneration system	Ahmed A. Hassan, Ahmed E. Elwardany, Ibrahim I. El-Sharkawy	159
50	Development of energy saving system based on microcontroller for boiler manufacturer	Ibrahim Cetiner, Halit Cetiner	165
51	Energetic analysis of a PVT-based solar-driven hybrid adsorption-compression refrigeration system	Mohamed G. Gado, Tamer F. Megahed, Shinichi Ookawara, Sameh Nada, Ibrahim I. El-Sharkawy	171
52	Testing the Abrasion resistance of broadband anti-reflection coatings for solar modules	Sibel Yilmaz, Adam Michael Law, John Michael Walls	177
55	Hybrid dedicated outdoor air system in buildings	Dararat Tongdee, Somchai Maneewan, Chantana Punlek	183
56	Energy analysis of vapor compression refrigeration cycle using a new generation refrigerants with low global warming	Rabah Touaibi, Koten Hasan	188
59	Estimating of the output voltage parameters for T-type Inverter with ANN	Tugba Atar, Selami Balci, Ahmet Kayabasi	194
60	Estimating of the leakage inductance value for single-phase isolation transformer with ANFIS	Busra Aslan, Selami Balci, Ahmet Kayabasi,	202
62	New concepts and technologies for electrical machines and mechanical engineering	Aldan A. Sapargaliyev, Amangeldy M. Zhunusbekov, Nurlan Ungarov	206
65	Recycling of waste tires by thermal dissolution (pyrolysis) and thermochemical degradation (gasification)	Yayalik İbrahim, Koten Hasan	213
66	Review of Thomson heat	Yuri G. Gurevich, Igor Lashkevych, Viktor Matsyuk	220
70	Development of an adaptive control system for a hot water supply using solar power plant	Vasily Stan, Yury Koshlich, Aleksandr Belousov, Nadezhda Koshlich	224
71	Comparison of different regression algorithms for estimating energy consumption	Halit Cetiner, Ibrahim Cetiner	230
76	Performance of a combined power and cooling system under solar, solar storage and storage mode of operations	Tapan Kumar Gogoi, Utpal Kumar Dutta	236
77	Enhancing the flexibility of electricity generation and heating for Kızıldere II geothermal power plant by demonstrating heat storage systems	Hakan Alp Sahiller, Ural Halaçoglu, Raziye Şengün, İsmail Pekdüz, Sylvie Rougé, Elie Ghanatos, Jérôme Pouvreau, Pall Valdimarsson, Sebastian Gamish, Mayra Paulina Alferez Luna, Shiladitya Paul, Alexandre Sabard, Francesco Fanicchia, Volkan Ediger, Gokhan Kirkil, Emilien Baudouin	243
80	Selection of the suitable greenhouse orientation on the basis of energy saving	Ouazzani Chahidi Laila, Mechaqrane Abdellah	251
83	Supercritical CO <sub>2</sub> binary mixtures for brayton power cycles complex configurations coupled to solar thermal energy plants	Paul Tafur-Escanta, Robert Valencia-Chapi, Luis Coco-Enríquez, Javier Muñoz-Antón	256
84	A Review of the life cycle assessments of Brazilian biodiesel	Costa Marina W., Oliveira Amir A. M.	262
86	Ageing effect evaluation of PV installation after 10 years continuous operation	Nikolay Tyutyundzhiev, Plamen Tsankov, Konstantin Lovchinov, Gergana Alexieva	268
88	Clean power generation: environmentally friendly lubrication products and pollution prevention	Helena M. Wilhelm, Paulo O. Fernandes, Laís Pastre Dill, Camila Steffens, Kethlyn G. Moscon, Sergio M. Peres, Luana Moreira, Thiago L. Zanin	274
89	Distance protection based on the synchrophasor data in control room	Igor Ivanković, Dalibor Brnobić	279
92	Torrefaction and carbonization of water hyacinth stems and leaves: impact on energy	Amr Moataz Sanad, Hamdy Hassan, Hassan Shokry, Shinichi Okawara, Ahmed Elwardany	286

93	Energetic and financial evaluation of a solar-powered absorption chiller integration into a CO <sub>2</sub> commercial refrigeration system	Evangelos Sygounas, Dimitrios Tsimpoukis, Stavros D. Anagnostatos, Maria K. Koukou, Michail Gr. Vrachopoulos	292
94	Determination of wind energy potential and evaluation of the feasibility analysis of a wind turbine via RETScreen for Çerkezköy, Turkey	Ahmet Erhan Akan, Aytac Perihan Akan	299
95	Technological ecovillages: auto sustainable urban pilots in the community of Llucanayacu in Chazuta, San Martin, Peru	Bartra Gardini Gumerindo, Pastrana Diaz Nerida del Carmen, Fu Pastrana Enzo Yen Gen	305
96	Computational thermal-fluid coupling analysis of a variable nozzle turbine for solar power generation	Abdelmadjid Chehhat, Arrif Toufik, Mouna Maache	311
97	Optimization of an offshore wind jackets manufacturing project through an investment analysis using 3D discrete-event simulation	Adolfo Lamas Rodriguez, Santiago José Tutor Roca, Inés Taracido López	317
99	On Minimization of the group variability of intermittent renewable generators	Dubravko Sabolić, Roman Malarić	324
103	Assessments of global warming potential of Brazilian biodiesel	Costa Marina W., Oliveira Amir A. M.	330
104	Solar collector with increased heat transfer efficiency	Andrey Batukhtin, Sergey Batukhtin, Marina Baranovskaya, Pavel Safronov	335
105	Effect of position of heat flux profile on the absorber surface of parabolic trough solar collector for direct steam generation	Ram Kumar Pal, K. Ravi Kumar	341
113	Mode excitation energy	Tarik Tufan, Hasan Köten	346
114	Economic aspects of market formation reactive power in electric power industry	Vladimir Kolibaba, Konstantin ZHabin, Vladimir Velikorossov, Sergey Filin, Ona Rakauskiene, Alexey Yakushev	351
116	A innovative methodology for visual impact assessment of wind power plants	Blois Luciano	356
119	Characteristics of beach erosion at Kkotji Beach in Korea	Hyun Dong Kim, Jinwoo Jeong, Kyu Han Kim	362
121	Issues of renewable energy sources with grid-tied inverter connected to an off-grid system	Mantas Zelba, Tomas Deveikis, Justinas Barakauskas	369
122	Improving the fatigue of newly designed mechanical system subjected to repeated food loading	Seongwoo Woo	375
123	Geothermal projections in Colombia from oil & gas industry	López-Ramos Eduardo, Patiño-Suarez Cesar, A., Alvarez - Gutierrez Angela, P., López-Pulido Albeiro, Gonzalez-Penagos Penagos, Pinilla - Granados Daniela, M.	381
124	Hybrid state of charge estimation of lithium-ion batteries; improvements on electric vehicle battery management system	Odera Ohazurike	386
126	Energy efficiency improvement for the mobile air conditioning systems	Cenk Onan, Serkan Erdem	391
128	The magnetic saturation effect on fault diagnosis in squirrel cage induction motor using current park's vector pattern	Chaouch Abdellah, Belaid Mohamed, Meflah Abderrahmane Mohamed Reda,	396
129	Effect of the three main directions of an external magnetic field on the free convection in Fe <sub>3</sub> O <sub>4</sub> -water nanofluid filled cubic enclosure	Maache Mouna Battira, Chehhat Abdelmadjid, Noui Samira, Bessaïh Rachid	402
131	Bio-energy characteristics of black pine ( <i>Pinus nigra</i> Arn.) hydrodistillation waste products	Hafize Fidan, Stanko Stankov, Nadezhda Petkova, Bozhidar Bozadziev, Milen Dimov, Lazar Lazarov, Apostol Simitchiev, Albena Stoyanova	408
136	Predicting cost of farm-based biogas plants	Arash Samizadeh Mashhadi, Noori M. Cata Saady, Carlos Bazan	414
137	Use of synthesis gas as fuel for a solid oxide fuel cell	Jesus Antonio. Álvarez-Cedillo, Teodoro Álvarez-Sánchez, Mario Aguilar-Fernández	420
138	An averaged large-signal model method of DC-DC isolated forward resonant reset converter based on solar cells battery charger for IoT application	Pattarapongsathit Wachiravit, Bilsalam Anusak	426
142	The importance of natural insulation building materials in sustainable energy efficient buildings	Filiz Bal Koçyiğit, Hatice Mehtap Öz, Gülsen Bilge Ülkü, Elmas Pak, Cahit Canberk, Ece Dinç, Barış Koçyiğit, Ercan Köse, Oğuz Emrah Turgut	433
144	The place of biopolymer-based composites in energy-efficiency architectural design	Filiz Bal Koçyiğit, Elmas Pak, Cahit Canberk, Gülsen Bilge Ülkü, Ece Dinç, Barış Koçyiğit, Hatice Mehtap Öz, Oğuz Emrah Turgut, Ercan Köse	439
148	Smart grid simulation based on high level architecture	Abdul Razaq, Muhammad Majid Hussain, Muhammad Siddique	445
149	Contribution to the study of a DFIG wind energy generation system based on a quasi Z inverter	Larafa Ahcene, Oudina Sofiane, Bahi Tahar	451
151	Numerical investigation of energy desorption from magnesium nickel hydride based thermal energy storage	Sumeet Kumar Dubey, K. Ravi Kumar	457
152	A comparative study of melting performance for ultra-high temperature latent storage system	Alok Kumar Ray, Dibakar Rakshit, K. Ravi Kumar, Hal Gurgenci	463
154	Single-phase grid-connected inverter with high frequency isolation for DC nano-grids	Ruiz Caldera Luis Jorge, Beristáin Jiménez José Antonio, Mendivil Cuadras Hiram, Pérez Ramírez Javier	470
156	The use of ZnO thin films as a friction layer in energy harvesting	Yüzük Durak Gizem, Özkan Seray, Yüzük Ercüment	476
162	TCAD-model of betavoltaic battery structure with vertical micro trenches	Konstantin Petrosyants, Andrey Pugachev, Igor Kharitonov, Dmytry Dymov	481

164	Towards high crystallinity and stable MASnI <sub>3</sub> Perovskite films treated with different antisolvents	Amal Bouich, Shafi Ullah, Julia Mari, Asmaa Bouich, Bernabé Mari, Mohamed Ebn Touhami	484
167	Evaluation of the temperature impact on the production of photovoltaic energy in the Brazilian national scene	Gustavo Neves Margarido, Federico Bernardino Morante Trigoso, Renato Chaves Souza, Wilson Carlos da Silva Junior, Roberto Nunes Duarte, Fabio da Silva Bortoli, Carlos Frajua	489
168	Analysis and optimization of hybrid wind and solar PV Generation system for off-grid small village	Nabaz Mohammedali Rasool, Serkan Abbasoglu, Mehrshad Radmehr Hashemipour	495
169	The possibility of integrating electricity through renewable sources in Sazani Island	Driada Mitrushi, Urim Buzra, Daniela Topciu, Eduart Serdari, Valbona Muda	502
170	Advanced exergoeconomic evaluation of a cogeneration system combined with a drying unit of fertilizers	Asmae Echeeri, Mostafa Maalmi	507
171	Kriging surrogate models for optimization in energy-efficient building design	Salma Lahmar, Rachida Idchabani, Mostafa Maalmi	513
172	Developing a real-time power price algorithm for an autonomous demand side management in solar community-grids with battery storage	Sebastian Finke, Michele Velenderic, Semih Severengiz	519
173	Investigation of geometries for increasing the energy density in electromechanical battery flywheels	Daniel Coppede, Marco Antonio de Souza, Renato Chaves Souza, Wilson Carlos da Silva Junior, Roberto Nunes Duarte, Fabio da Silva Bortoli, Carlos Frajua	525
175	Modelling and control of a hybrid wind solar system optimized by fuzzy based MPPT controller	Mennad Mebrouk, Bentaallah Abderrahim, Djeriri Yousef, AmeurAissa, Bessas Aicha	531
176	Energy production using water collectors subjected to solar radiation to improve building indoor thermal conditions	Eusébio Conceição, João Gomes, Mª Manuela Lúcio, André Ramos, Hazim Awbi	538
177	Evaluation of mechanical and thermodynamic properties of BaZn compound by DFT	İlknur Kars Durukan, Yasemin Oztekin Ciftci	544
178	Ab initio calculations of the mechanical, vibration and bond nature of the CdSr compound	İlknur Kars Durukan, Yasemin Oztekin Ciftci	549
179	Analysis of optical properties of the CeTl intermetallic structure	İlknur Kars Durukan, Yasemin Oztekin Ciftci	553
180	The physical properties of newly synthesized superconductor compound LaNiGe via Ab-initio calculatios	Yasemin Oztekin Ciftci, İlknur Kars Durukan	556
181	A theoretical study of pressure-induced effects on CeAs compound	Yasemin Oztekin Ciftci, İlknur Kars Durukan	559
182	Optoelectronic properties of Zn doped Lead free photovoltaic CsSnI <sub>3</sub> compound	Yasemin Oztekin Ciftci	562
184	Innovative activity of integrated business structures	Vladimir Velikorossov, Yury Korechkov, Maksim Maksimov, Ona Grazyna Rakauskiene, Anatoliy Kolesnikov, Evgeniy Genkin	565
189	Level of meeting the needs for solar energy for hot water production in the Ionian coast of Albania	Halili Daniela, Serdari Eduart, Mitrushi Driada, Buzra Urim	570
192	Morphological properties of low temperature hydrothermally grown TiO <sub>2</sub> films for DSSCs devices	Atli Aycan, Yildiz Abdullah	576
193	Molarity of precursor dependent morphological properties hydrothermally grown TiO <sub>2</sub> films	Atli Aycan, Yildiz Abdullah	579
195	The fabrication of SnO <sub>2</sub> /Si heterojunction diode	Ozel Kenan, Yildiz Abdullah	582
196	The investigation of UV detection performance of SnO <sub>2</sub> /p-Si heterojunction	Ozel Kenan, Yildiz Abdullah	585
197	Thermal analysis and parametric study on the influence of thermo-physical properties on droplet condensation heat transfer	Mete Budakli	587
198	Iterative ekf-based parameter estimation algorithm for a nonlinear PMSM model	Artun Sel, Cosku Kasnakoglu	593
199	Algorithms for ESS reinforced RES portfolio bidding in Turkish energy markets	Abdülhadi Çiftçi, Abdulkadir Balıkçı	598
200	p-n heterojunction diode based on TiO <sub>2</sub> /p-Si	Sekertekin Betül, Ozel Kenan, Yildiz Abdullah	611
201	Various receipts TiO <sub>2</sub> based pastes for semi-flexible DSSCs	Abdullah Atılgan, İrem Sütçü, Abdullah Yıldız	614
202	Effect of substrate rotation speed on the optical, and electrical properties of TiO <sub>2</sub> /FTO blocking layer fabricated by Spin-Coating	Abdullah Atılgan, Abdullah Yıldız	618
203	Continuous ocean data analysis using artificial intelligence	Kisu Kwak, Kyu Han Kim, Chi-ok An, Byung-sun Cho, Young-eun An	621
204	Stability analysis of sunken vessel for artificial reef use	Hyun Dong Kim, Kyu Han Kim, Hyumin Oh	628
205	High performance ion-exchange microporous zeolite material for application in the cold plasma device	B.G. Salamov, H. Hilal Kurt	635
206	Filamentation in a plasma cell with GaP wafer	H. Hilal Kurt, B.G. Salamov	641
207	Mean electron energy distribution in a plasma system with ZnSe	H. Hilal Kurt	644
209	Gas discharge systems with CdSe electrode	Selçuk Utaş, H. Hilal Kurt	647
210	Theoretical plasma simulation results of the microdischarge cell with GaSb cathode	Selçuk Utaş, H. Hilal Kurt	650
211	The Features of the InGaAs/InP detectors in plasma systems	Selçuk Utaş, H. Hilal Kurt	653
212	Dependence of solution molarity on structural, optical, and electrical properties of spin coated TiO <sub>2</sub> /FTO films	Abdullah Atılgan, Abdullah Yıldız	657
213	Electric vehicle energy efficiency contribution through laboratory implementation	Felipe A. Núñez-Donoso, Jose Manuel Lopez-Guede, Ekaitz Zulueta, Unai	660

		Fernandez-Gamiz, Jose Antonio Ramoz-Hernanz	
214	Computational modeling of a 2D Vanadium redox flow battery cell	Iñigo Aramendia, Joseba Martinez-Lopez, Unai Fernandez-Gamiz, Mirko Messaggi, Matteo Zago, Ekaitz Zulueta, Jose Manuel Lopez-Gude	664
215	Automatic identification algorithm of equivalent electrochemical circuit based on electroscopic impedance data for a lead acid battery	Javier Olarte, Jaione Martínez de Ilarduya , Ekaitz Zulueta, Raquel Ferret, Unai Fernández-Gámiz, Jose Manuel Lopez-Gude	669
216	Multipurpose sensor designed to monitor electrochemical parameters of 12 V lead acid battery blocks	Javier Olarte, Jaione Martínez de Ilarduya, Ekaitz Zulueta, Raquel Ferret, Unai Fernández-Gámiz, Jose Manuel Lopez-Gude	676
217	Cell-set modelling of an active rotating microtab on a DU91W(2)250 airfoil	Alejandro Ballesteros-Coll, Koldo Portal-Porras, Unai Fernandez-Gamiz, Iñigo Aramendia, Ekaitz Zulueta, Jose Manuel Lopez-Gude	682
218	Automatic optimization algorithm for electrical energy contracts in Spanish market	Decebal Aitor Ispas-Gil, Asier Zulueta, Ekaitz Zulueta, Unai Fernández-Gámiz, Jose Manuel Lopez-Gude	687
219	Ciphering and deciphering technique on the images of energy plants and networks	Erol Kurt, Batuhan Arpacı	692
220	Comparison of the efficiency values of the rectifiers used in the RF energy harvesting systems	Kayhan Çelik, Erol Kurt	701
221	MPPT system implementation for a piezoelectric energy harvester	Erol Kurt, Davut Özhan	706
222	Analysis of atmospheric transported particulate matter and investigation of its effects on solar panel	Murat Altıntaş, Serdal Arslan	712
228	Developing a LoRa based IoT application for outdoor street lighting fault detection in smart cities	Ezgim Çelik, Mehmet Tekerek	719
229	Sodium doped cadmium telluride (CdTe:Na) thin films prepared by the Spray pyrolysis method	Shadia J. Ikhmayies	725
Countries and presenters list			731



# **KEYNOTES**



# IS EXERGY DESTRUCTION MINIMIZATION THE SAME THING WITH ENERGY EFFICIENCY MAXIMIZATION?

Birol Kilkis

EU Renewable Heating and Cooling (RHC)

OSTIM Technical University and Polar Teknoloji, Ankara Turkey

Cite this paper as:

Kilkis, B. Is exergy destruction minimization the same thing with energy efficiency maximization?.  
9th Eur. Conf. Ren. Energy Sys. 21-23 April 2021 Istanbul, Turkey

**Abstract:** This paper discusses whether the exergy destruction minimization or energy efficiency maximization comes first in resolving the climate emergency issue and shows that there are sustainable solution options in terms of the 2nd Law of thermodynamics. It has been shown that low-temperature district energy systems with renewable energy sources and waste heat are effective in minimizing exergy destructions, while energy efficiency has a secondary impact.

**Keywords:** Exergy destruction, exergy efficiency, low-temperature applications, energy efficiency

© 2021 Published by ECRES

## Nomenclature

$c, c'$	Nearly-avoidable unit CO <sub>2</sub> responsibility of exergy destruction, kg/kW-h
$c_E, c_H$	Nearly-avoidable unit CO <sub>2</sub> responsibility of exergy destruction, kg/kW-h
$c_K$	Unit emission coefficient, kg CO <sub>2</sub> /kW-h
$E$	Electric power, kW
$PEF$	Primary energy factor (2.5 in Europe)
$Q$	The amount of energy or power transformed to the useful application(s)
$R$	Ratio of destroyed exergy to the supply exergy
$R_{EX}$	Exergy-based renewables mix in the energy supply stock
$T$	Temperature, K
CO <sub>2</sub>	Direct emission, kg CO <sub>2</sub> /kW-h
$\Delta CO_2$	Nearly-avoidable emission, kg CO <sub>2</sub> /kW-h
$\Sigma CO_2$	Total emission, kg CO <sub>2</sub> /kW-h
$\epsilon$	Unit exergy, W/W or kW-h/kW-h
$\eta_I$	First-Law efficiency
$\eta_{II}$	Second-Law efficiency
$\psi_R$	Rational Exergy Management Model (REMM) Efficiency

## Subscripts

$dem$	Demand
$des$	Destroyed
$f$	Fuel, energy source
$FPC$	Flat-Plate Collector
$PV$	Photo-voltaic (Cell)
$ref$	Environment reference
$sup$	Supply

## 1. INTRODUCTION

As of November 19, 2020, UN Secretary-General's remarks on Climate Action to European Council on Foreign Relations officially elevated the global warming issue to the global emergency status, of which 38 countries have already ratified [1].

*"It is essential that the European Union commits to reducing emissions by at least 55 percent by 2030. The Climate Ambition Summit on the fifth anniversary of the Paris Agreement represents a clear opportunity for the EU to present its more ambitious climate plan."*

UN Secretary-General Antonio Guterres told at the Climate Ambition Summit that more must be done to hit net-zero emissions [2]. The expression 'something must be done' in his speech is very important in the sense that the global warming and CO<sub>2</sub> content in the atmosphere are well measured and documented yet today's decarbonization measures fall short because the 1<sup>st</sup> Law of Thermodynamics limits the ability to see the entirety of solution in terms of the quality of energy. A much more sustainable set of potentially effective measures are hidden in the 2<sup>nd</sup> Law of Thermodynamics, which directly fits into that expression that *more has to be done*. In other words, more has to be done initiative may take action if and only if the technical, scientific, political, and intergovernmental awareness is raised in terms of the 2<sup>nd</sup> Law, which deals with the quality of energy rather than the quantity of energy that the 1<sup>st</sup> Law deals with. If the qualities of energy supply and demand are not properly matched, some of the quality of energy (exergy) will be irreversibly destroyed causing additional CO<sub>2</sub> emissions, which we kept ignoring or dismissing so far.

We are dealing only with half of the global warming problem,

Birol Kilkis, 2020

The goals and methods for achieving 100% renewable energy cities and communities, mainly in terms of renewable heating and cooling [3] involve innovative solutions with a better understanding of the fundamental theory, which covers a broad chain of low-enthalpy renewable and waste energy sources, distribution technologies, and rational utilization of energy and power at the final consumption points. Solar energy is not an exception and is indeed a very important component of holistic circularity provided that it is not limited to economics and quantity of energy [4]. To realize the EU 2050 decarbonization roadmap EC has identified four implementation fields. One of them is solar. The other three are geothermal, biomass, and cross-cutting fields [5]. According to the European Council [6], sector integration for a circularity offers significant opportunities for wider utilization of renewables and decarbonization along with the new *Circular Economy Action Plan* [7].

Such a goal may be realized by establishing strong synergies between electricity power, gas, heat, and cold networks. However, this brings a new problem that has been ignored before. This problem is the need for a new balancing format among various qualities of different forms of energy supplies and demand, all of which have different unit exergy. In other words, such a circularity elevates the importance of the quality management of energy above quantity management. EC reports only address the economy in energy quantity format and ignore the energy quality [8]. For example, EU strategists offer the option of decarbonization by total electrification by using heat pumps, which operate on green electricity [9]. According to many strategists, total electrification may seem to be a perfect solution for the quantity management of energy (1<sup>st</sup> Law of Thermodynamics). One of the four key cross-cutting energy technologies identified by Science Europe or applications is heat pumps with green electricity [5]. However, even if a 100% renewable energy system generates the power to operate the vapor compression heat pumps, the exergy (Quality) of electricity is higher than the quality of thermal energy generated by pumps (Heating or cooling). This difference renders an exergy deficit, which causes additional CO<sub>2</sub> emissions, even though the electricity is generated by renewables. This shows that 100% renewables on the energy generation side do not guarantee nearly zero carbon applications in the global energy and environment stock. In this respect, green solar energy must stay green by utilizing it in the least exergy-destroying applications in a good balance between the supply and demand exergy. Figure 1 shows a projection about consumption scenarios until 2040 [10]. There are two alternative predictions for 2040, namely 50% RHC and 100% RHC. According to this scenario, the major component of heating and cooling by non-RES energy sources will diminish to zero in the 100% RHC scenario in 2040, by definition. All these predictions are based on the 1<sup>st</sup> Law of thermodynamics. Consider a house with PV panels, which contributes to the 100% RHC target. Yet PV panels miss the opportunity of generating collocated heat that a PVT system could do. Therefore, an additional roof area is needed for installing flat plate solar hot water collectors. This time they will miss the opportunity of generating solar power. According to the 2<sup>nd</sup> Law, missed opportunities mean irreversible destructions of the quality of solar energy (Exergy). These destructions are responsible for indirect CO<sub>2</sub> emissions. Although a PVT array seems to largely solve the problem, it was shown by Kilkis, B. [11] that there will always be exergy destructions, and mathematically speaking, an absolute 100% renewable RHC target will not be possible due to the diminishing nature of solar equipment embodiments with traces of fossil fuels to be spent for the next steps for achieving 100% RHC [4, 12]. E-gas and hydrogen shown in Figure 2, are derivatives of solar and wind energy sources. Therefore, they may be included in a broader solar and wind energy spectrum. E-gas will not be a complete solution either [13]. Kilkis [12] has further shown that without the 2<sup>nd</sup> Law, despite seeing and measuring global warming, almost half of the fundamental and sustainable decarbonization

opportunities will remain missing because exergy destructions causing additional CO<sub>2</sub> emission responsibilities are not recognized. In other words, we are aware of the global warming problem but we are aware of only half of the potential solutions. Yet many scientists and engineers insist that the 1<sup>st</sup> Law is sufficient for solving the entire problem because the 2<sup>nd</sup> Law gives similar solutions. The following section is an answer to such statements.

According to Tanay, S. U. [14] the cause of the coronavirus epidemic cannot be disassociated from the consequences of the climate crisis. Activities to revert the climate crisis, however, seem to be insufficient, and atmospheric CO<sub>2</sub> concentration seems to increase despite the introduction of new and widely implemented green systems, carbon capture, and storage (CCS) (Figure 3). The best measure against climate emergency that has been conceived so far, which is Greener Growth +CCS might only stabilize the CO<sub>2</sub> content to 450 ppm by 2050, which is far beyond the target of the Paris Agreement. Figure 3 is a revelation that the previous work that has been carried out and the future attempts on green transition for achieving the targets of the Paris Agreement have been and will be necessary but not sufficient measures, like in terms of EU 20-20-20 strategy (20% Energy Savings, 20% Use of Renewables, and 20% Increase in Energy Efficiency), and despite great interest in solar energy, wind, and geothermal. Yet the fundamentally missing point in these efforts has been the ignorance of the 2<sup>nd</sup> Law of Thermodynamics, which deals with the quality of energy sources and demand.

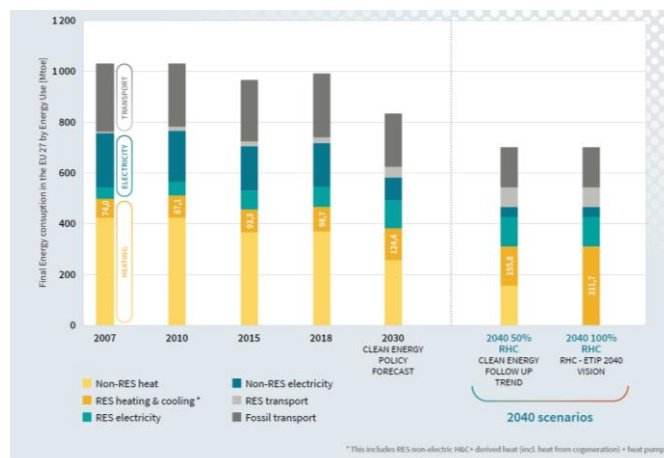


Figure 1. 2007-2040 Final Energy Consumption Scenarios in the EU 27 Countries and Their Origin. RES Included [10].

In this respect, all energy sources are not created equal. Each of them has different useful work potential (exergy) and they must be matched with demands with similar exergy. Otherwise, exergy mismatches result in nearly-avoidable CO<sub>2</sub> emissions (by minimizing exergy mismatches). There are few studies about exergy analysis like in low-temperature, renewable district energy systems. Falk, P. M. [15], a member of Annex 64 has focused on exergy principles of district energy optimization. The EU parliament has already been alerted about the immediate essence of the 2<sup>nd</sup> Law.

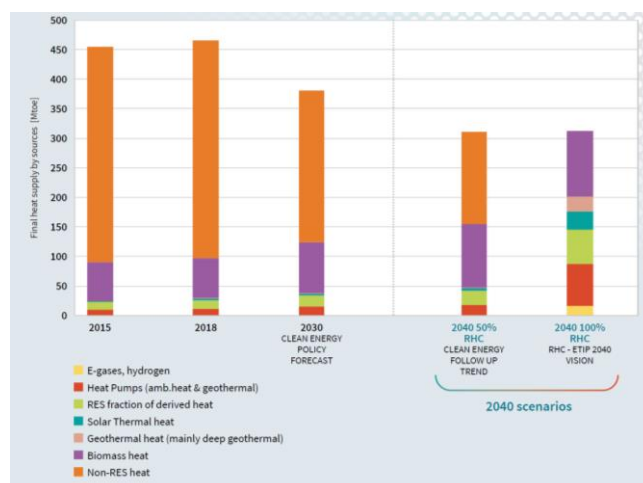


Figure 2. Thermal Power Generation by Sources and Uses.

Data extracted on 20/06/2020 21:29:37 from (ESTAT) Dataset: Final energy consumption by-product [TEN00123] Last updated: 06/06/2020 23:00. RES fraction of derived heat refers to heat by cogeneration from renewable electricity (e.g., bioenergy electricity plant that cogenerates heat for a DHC network)

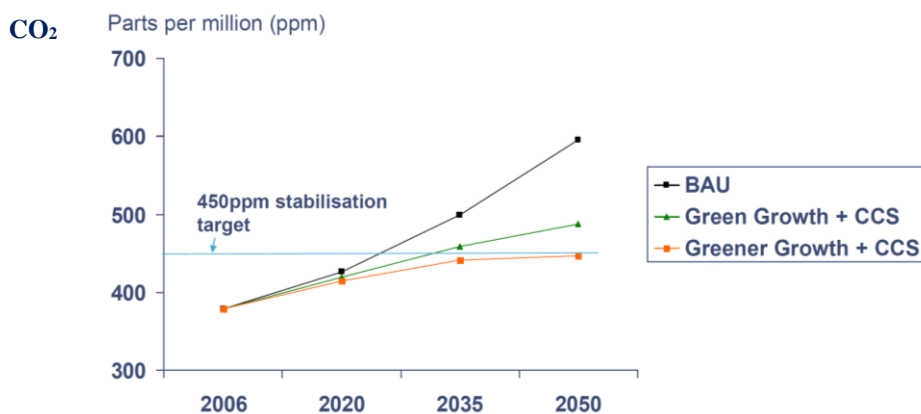


Figure 3. Atmospheric CO<sub>2</sub> Content and Green Growth Trends (PwC, 2008), Source: WMO for 2006, PwC Model Projections for Later Years)

Kilkis [16] has proposed transformation tools to facilitate the transformation of several EU guides and directives from the 1<sup>st</sup> Law to the 2<sup>nd</sup> Law. Science Europe Scientists have also issued a brochure on the critical contribution potential of exergy analysis [8]. Solar heating and cooling call for low-temperature (LT) district energy systems. This requirement for 5DE systems amplifies the current problem of the total energy and primary energy ratio of the building sector, which is 2.3, second in a row, following the commercial sector (2.7) in the USA. This means that buildings consume much more than what they spend in-house [17, Table 2.1]. Therefore, district energy systems must minimize this ratio in heat and cold distribution/collection.

The most common argument made by the exergy-skeptics and opponents is the following claim.

Claim: Because the exergy destruction minimization is the same as energy efficiency maximization; exergy analysis is not necessary but redundant.

Response: Assume that *energy supply* (In this case solar energy) with an identical amount of  $Q_{sup}$  is utilized in two different applications at the same reference temperature,  $T_{ref}$ , 283 K, or 287 K (Williams, M., 2015: Average surface temperature of the world).

**Case 1** generates only electrical energy at an efficiency of  $\eta_{PV}$ , by using part of the solar energy input, in an amount of  $Q_E$ . The remaining energy ( $Q_{sup}-Q_E$ ) in the form of heat is rejected at a temperature of  $T_E$ . This case destroys exergy downstream by a unit amount of  $\varepsilon_{des1}$ , in terms of useful thermal energy potential. This case is typical for solar photovoltaic applications.

**Case 2** generates only thermal energy at an efficiency of  $\eta_{FPC}$ , by using the same amount of solar energy,  $Q_E$ , starting this time from  $T_E$  down towards  $T_{ref}$ . Different unit exergy in an amount of  $\varepsilon_{des2}$  is destroyed in terms of potentially useful electrical energy upstream the thermal energy generation.  $T_f$  is the energy source temperature (or Carnot cycle-equivalent). This case is typical for solar flat-plate collector (FPC) for hot domestic hot water (DHW) generation.

Everything looks the same in terms of energy quantity utilized,  $Q_E$ , as long as it remains the same in any process or design. Let the classical objective be to maximize the efficiency,  $\eta_I$  according to the 1<sup>st</sup> Law of Thermodynamics:

$$\eta_I = \frac{Q_E}{Q_{sup}} \quad \{\text{Maximize}\} \quad (1)$$

As a solar energy system, the 1<sup>st</sup> Law energy efficiencies,  $\eta_I$  in Equation 1 are identical for both cases, irrespective of whether heat or power is generated and heat, power, or both opportunities are destroyed upstream or downstream. Furthermore, if the power conversion efficiencies of both power conversions are considered, the PV efficiency (about 0.20) is much lower than the FPC efficiency (about 70%). This is a dilemma of system efficiency and conversion efficiency, which cannot be resolved by the 1<sup>st</sup> Law. Figure 4 shows this dilemma. In other words, two solar power conversion applications have different efficiency but the solar system efficiency (Equation 1) is the same. Furthermore, FPC may be preferred because it has higher efficiency.

Such a preference of course does not consider that electricity has much higher unit exergy,  $\varepsilon$ , meaning more useful work and value-adding potential in the energy and economy domain.

The only step that 1<sup>st</sup> Law can proceed with about the environment is the usual practice of predicting the CO<sub>2</sub> emissions reduction potential from the carbon stock in proportion to  $Q_E$  in both cases.

In Equation 2,  $R_{EX}$  is the exergy-based mix of renewable energy in the energy stock of a given region concerning  $Q_{sup}$ .  $R_{EX}$  is equal to one in solar PV or FPC cases (neglecting different embodiments). In fossil fuel cases  $R_{EX}$  is zero. PEF in EU countries is around 2.5, and  $c_K$  for both cases may be taken equal to 0.2 kg CO<sub>2</sub>/kW·h of  $Q_E$  (Equivalent to natural gas). Beyond this point of environmental concerns, the 1<sup>st</sup> Law, for a given energy supply ( $Q_{sup}$ ), does not differentiate between whether electric power, steam, heat, or cold, at any temperature, are generated as long as  $Q_E$  is the same, although each of them represents different forms of energy with different qualities (Exergy). For example, electric power has unit exergy,  $\varepsilon_E$  of 0.95 kW/kW, which means that 95% of electrical energy may be utilized in value-adding useful work(s). According to the ideal Carnot cycle, thermal power has a much lower,  $\varepsilon_H$  in heating or cooling (See Equation 4). Exergy-based Equation 5, which at this point the 1<sup>st</sup> Law stops working, shows that exergy destructions for Cases 1 and 2,  $\Delta E_{X1}$  and  $\Delta E_{X2}$ , respectively are not equal with different minimum points regarding  $T_E$  and  $T_f$ . Only the 2<sup>nd</sup> Law can show such differences on both sides of Equation 5.

$$-\text{CO}_2 = c_K \text{PEF} \cdot Q_E \cdot (1 - R_{EX}) \quad \{\text{Case 1}\}; \quad -\text{CO}_2 = c_K / \eta_B Q_E \cdot (1 - R_{EX}) \quad \{\text{Case 2}\} \quad (2)$$

Because these destructions must be offset by the corresponding type of exergies by someone, somewhere, with some technology and sources, CO<sub>2</sub> emission responsibilities are also unequal.

$$\varepsilon_H = \left( 1 - \frac{T_{ref}}{T_E} \right) \ll \varepsilon_E \quad \{\text{Ideal Carnot Cycle}\} \quad (4)$$

$$\cancel{\left( 1 - \frac{T_{ref}}{T_E} \right)} \neq \cancel{\left( 1 - \frac{T_E}{T_f} \right)} \quad \{\text{Minimize}\} \quad (5)$$

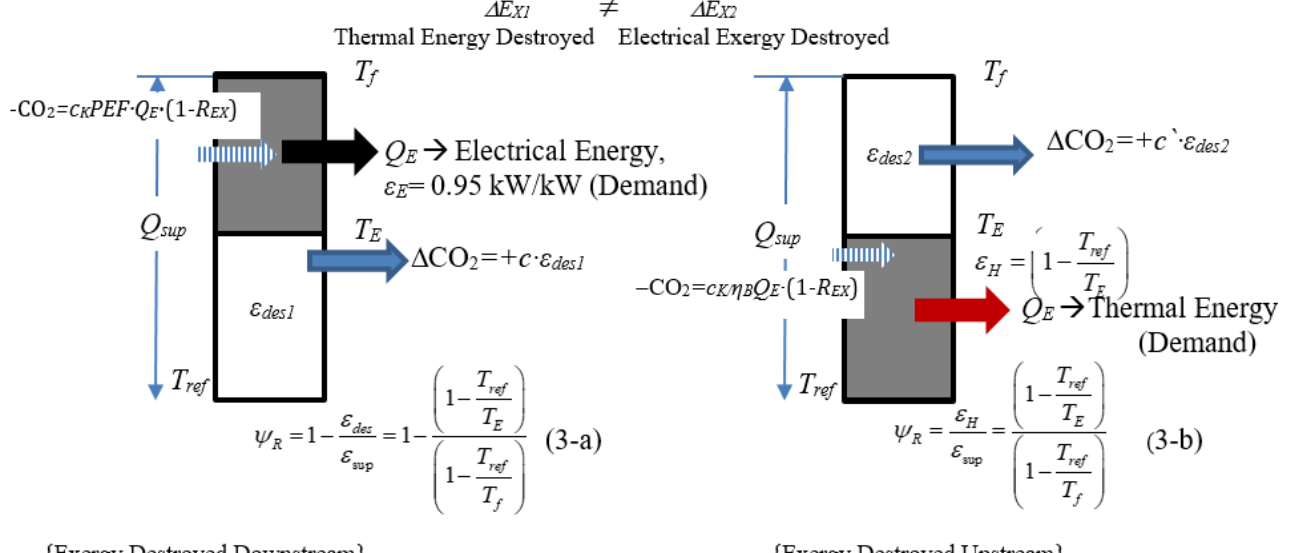


Figure 4. Two Different Power Conversions with The Same Solar Energy Utilization but Different Exergy Destructions.

**Case 1:**  $\Delta \text{CO}_2 = c \cdot \varepsilon_{des1}$  {Thermal power opportunity is destroyed,  $c_H = 0.27$ } (6-a)

**Case 2:**  $\Delta \text{CO}_2 = c' \cdot \varepsilon_{des2}$  {Electrical power opportunity is destroyed,  $c_E = 0.63$ } (6-b)

Clearly:

$$0.27 \left( 1 - \frac{T_{ref}}{T_E} \right) \neq 0.63 \left( 1 - \frac{T_E}{T_f} \right) \quad . \quad (7)$$

The above-mentioned ΔCO<sub>2</sub> terms are nearly avoidable and additional CO<sub>2</sub> emissions. The 1<sup>st</sup> Law cannot predict ΔCO<sub>2</sub> emissions responsibility at all. Because ΔCO<sub>2</sub> term is generally in the same order as CO<sub>2</sub> emissions, only about half of the global warming sources will remain visible as long as the 2<sup>nd</sup> Law is not recognized. Factors  $c_H$

and  $c_E$  are the exergy-based unit  $\Delta CO_2$  emissions, depending upon the resource mix (Including renewables) for heat and power sectors, respectively. At a reference temperature,  $T_{ref}$  of 283 K, if  $T_E$  and  $T_f$  are 400 K and 620 K, respectively, the left-hand side of Equation 7, which may correspond to PV will be 0.079 kg CO<sub>2</sub>/kW·h of heat destroyed ( $\varepsilon_{des1}$ : 0.295 kW/kW) and the right-hand side, which may correspond to an FPC will be 0.223 kg CO<sub>2</sub>/kW·h of power generation opportunity destroyed ( $\varepsilon_{des2}$ : 0.355 kW/kW). The inequality ratio is 2.7.

This example gives a definite answer to the claim: according to Equations 5 and 7, any pair of optimum solutions regarding the 1<sup>st</sup> and the 2<sup>nd</sup> Laws for the same problem, and their derivatives give different results for minimum exergy destructions-including now  $\Delta CO_2$  emissions responsibilities- versus energy efficiency maximizations. If it is insisted that there is a feasible  $T_E$  value, at which equal solutions are possible, then, a simultaneous solution of Equation 7 gives a positive  $T_E$  root of 503.6 K (230.5°C). In practice, a PV panel frame may not be as hot as that temperature and an FPC panel may not be as hot as 503.6 K. So, such practical limits in the field impose additional constraints for equal exergy values for two different systems. The rationality of utilizing solar energy, as defined by Kilkis, S., and Kilkis, B. [18], namely the REMM efficiency,  $\psi_R$  are also different as given in Equations 3-a and 3-b:

$$\psi_{RPV} = 1 - \frac{\varepsilon_{des}}{\varepsilon_{sup}} = 1 - \varepsilon_{des} / \left( 1 - \frac{T_{ref}}{T_f} \right) = 1 - \frac{0.355}{0.543} = 0.346 \quad \text{Case 1, major exergy is destroyed downstream}$$

If thermal energy is utilized further down to the reference temperature, which is not possible:

$$\psi_{RFPC} < \frac{\varepsilon_{dem}}{\varepsilon_{sup}} = \frac{0.292}{0.543} = 0.537 \quad \text{Case 2, major exergy is destroyed upstream}$$

If thermal energy is utilized for DHW use only down to 65°C (338 K) against the Legionella risk in open-water circuits, then, the solar PV system becomes relatively more rational ( $\psi_{RPV} = 0.346$ ):

$$\psi_{RFPC} = \frac{\varepsilon_{dem}}{\varepsilon_{sup}} = \frac{\left( 1 - \frac{338 \text{ K}}{400 \text{ K}} \right)}{0.543} = \frac{0.155}{0.543} = 0.285$$

These results show that even in a simple solar flat plate collector case, the number and type of useful applications in tandem, like further using the remaining heat in preheating the municipal water is important for exergy-based higher rationality in a holistic view, which may also be related to  $\Delta CO_2$ :

$$\Delta CO_2 ; \varepsilon_{sup} c_E (1 - \psi_R) \text{ or } \varepsilon_{sup} c_H (1 - \psi_R) \quad (8)$$

It must be also noted that the PV system generates electric power with unit exergy of 0.95 kW/kW, while FPC generates only heat by an amount of about 0.155 kW/kW, meaning that the value-adding potential in the energy budget is comparably small. With the less value-adding potential of FPC systems, more responsibility for  $\Delta CO_2$  emissions exists. Such realities may only be revealed by the 2<sup>nd</sup> Law, such as dedicating available solar surfaces to solar photo-voltaic-heat (PVT) panels, which occupy practically the same solar area but simultaneously generate power and heat, which is a renewable form of cogeneration systems, with less exergy destruction.

All the above discussions and sample calculations show that a new exergy-based, holistic optimization model is necessary to cover a multitude of solar systems, equipment, solar-energy derivatives, and exergy-based constraints.

## 2. THEORY

To bring a resolution platform for the dilemma about energy and exergy, especially from the global climate emergency point of view, the total CO<sub>2</sub> emissions, which is simply the algebraic sum of the direct and nearly-avoidable emissions,  $\Delta CO_2$  due to exergy destructions a combined emissions equation was derived (Kilkis, S., and Kilkis, B., 2019).

$$\sum CO_2 = \frac{c_K}{\eta_I} [1 + (1 - \psi_R)] \sum Q + \frac{c_K}{\eta_I \eta_T} \sum E \quad (9)$$

$\Sigma Q$  is the heat consumption worldwide and  $\Sigma E$  is the electrical energy consumption, worldwide. According to IEA Statistics reproduced in Figure 5, only 18% of that total *world energy* was in the form of *electricity*. Most of the

other 82% was used as *heat in districts, in the industry, and in mobility*. Assume that transport is a heat engine (except electric mobility) with an efficiency of 35% on average

<[https://en.wikipedia.org/wiki/World\\_energy\\_consumption](https://en.wikipedia.org/wiki/World_energy_consumption)>

$\Sigma E = 21\%$ . Assume transport in the form of heat engines, out of which 63% is from fossil fuels. Assume transport in the form of heat engines. Based on fossil fuels the emissions are:

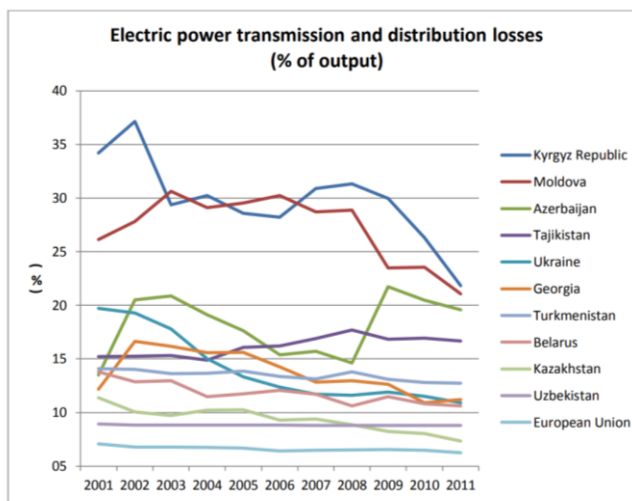
$$\sum CO_2 = \frac{c_K}{\bar{\eta}_I} \left[ \{1 + (1 - \psi_R)\} 0.79 + \frac{1 \times 0.21 \times 0.63}{0.85} \right] \sum Q \quad (10)$$

$$\sum CO_2 = \frac{c_K}{\bar{\eta}_I} [0.79 + (0.79 - 0.79\psi_R) + 0.156] \sum Q \quad (11)$$

After further simplification,

$$\sum CO_2 = \frac{c_K}{\bar{\eta}_I} [1.74 - 0.79\psi_R] \sum Q \quad (12)$$

$\eta_T = 0.9$ , T&D losses is about 10% today. Furthermore, assume that 15% of  $Q$  is from renewables.



Source: IEA Statistics – Electricity Information (transmission and distribution losses, includes pilferage)

Figure 5. Electric Power T&D Losses. <<https://www.worldenergydata.org/world-total-final-consumption/>>

$$\frac{\sum CO_2}{\sum Q} = \frac{c_K}{\bar{\eta}_I} [1.74 - 0.79\psi_R] \times 0.85 \quad \text{kgCO}_2/\text{kW-h of heat} \quad (13)$$

For unit CO<sub>2</sub> emissions, worldwide, excluding embodied emissions and ΔCO<sub>2</sub> taking place in renewables, as shown in Figure 4.

$$\frac{\sum CO_2}{\sum Q} = \frac{c_K}{\bar{\eta}_I} [1.48 - 0.67\psi_R] \quad (14)$$

$$\text{Let } R = \frac{\varepsilon_{des}}{\varepsilon_{sup}} , \text{ by definition, then:} \quad (15)$$

$$\psi_R = (1 - \frac{\varepsilon_{des}}{\varepsilon_{sup}}) = (1 - R) \quad . \quad (16)$$

$$\psi_R = \left[ 1 - \frac{\varepsilon_{des}}{\left| 1 - \frac{T_{ref}}{T_{sup}} \right|} \right] = 1 - \varepsilon_{des} \times \left| 1 - \frac{T_{ref}}{T_{sup}} \right|^{-1} \quad (17)$$

$$\sum CO_2 = \frac{c_K}{\bar{\eta}_I} \left[ 0.48 + \varepsilon_{des} \times \left| 1 - \frac{T_{ref}}{T_{sup}} \right|^{-1} \right] \quad (18)$$

Today,  $R$  is about 0.8. For green applications,  $R$ -value must be approximately less than 0.3(1-0.7). Now, equation 18 shows the second dilemma about whether maximization of energy or minimization of exergy destructions come first for achieving a sustainable set of measures against climate emergency. In this equation, in a single pass-through transfer of energy, like shown in Figure 4, the global average 1<sup>st</sup> Law efficiency may be replaced by the 2<sup>nd</sup> Law efficiency given in Equation 19. Furthermore,  $\varepsilon_{des}$  is indexed to the unit supply exergy of natural gas (Heat-based Analysis) with 0.87 W/W (Equation 20).

$$\eta_{II} = \frac{0.06T_{sup}}{(T_{sup} - T_{ref})} \quad \{T_{ref} = 283 \text{ K}\} \quad (19)$$

$$\varepsilon_{des} = 1 - \eta_{II} \quad (20)$$

$$\sum CO_2 = \frac{c_K}{\bar{\eta}_{II}} \left[ 0.48 + 0.87R \times \left| 1 - \frac{T_{ref}}{T_{sup}} \right|^{-1} \right] \quad \{T_{sup} > T_{ref} \text{ in heating}\} \quad (21)$$

Efficiency must be maximized but, in many sectors, it is already high. The function is inverse hyperbolic. Destruction must be minimized. Min Max Problem. More room exists for solutions. Linear relation in terms of  $\varepsilon_{des}$ . A minimum point may be searched for  $T_{sup}$ , which in fact, is not available from the following simple differentiation of Equation 21.

$$\frac{d \sum CO_2}{dT_{sup}} = 0 = \left[ -0.87R \times \left| 1 - \frac{T_{ref}}{T_{sup}} \right|^{-2} \times \left( \frac{T_{ref}}{T_{sup}^2} \right) \right] \quad \{\text{No minimum}\} \quad (21)$$

### 3. RESULTS

The equations derived above were used to determine the relationship between the operating (supply) temperatures in the built environment and the CO<sub>2</sub> emissions, including the embodied emissions in district energy piping, which is gaining more popularity in Europe for achieving the targets of decarbonization with total electrification.

Figure 6 shows the variation of total CO<sub>2</sub> emissions concerning the supply temperature in the built environment, by assuming a constant 1<sup>st</sup> Law efficiency in all sectors, namely 0.8 on average. Because only the 1<sup>st</sup> Law efficiency is used in the calculations, Figure 6 shows that the energy maximization base gives a misleading result, such that emissions decrease with higher temperatures at high-temperature sources (HT), which generally mean fossil fuels. In fact, from an exergy point of view, exergy destructions are higher and exergy destructions are lower in low-temperature (LT) applications with better exergy match with renewable and waste energy sources. Therefore, Figure 6 misses the exergy point and opposes the utilization of renewables and waste heat, which is a wrong indication. Therefore, the exergy efficiency-modified Figure 7 was drawn. Figure 8 shows the corresponding exergy destructions that may be minimized only at lower temperatures.

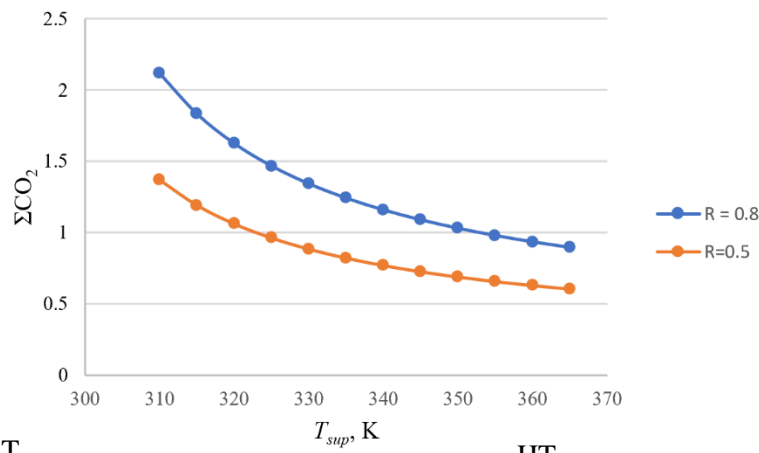


Figure 6. Total  $CO_2$  Emissions with Supply Temperatures. Constant 1<sup>st</sup> Law efficiency of 0.8

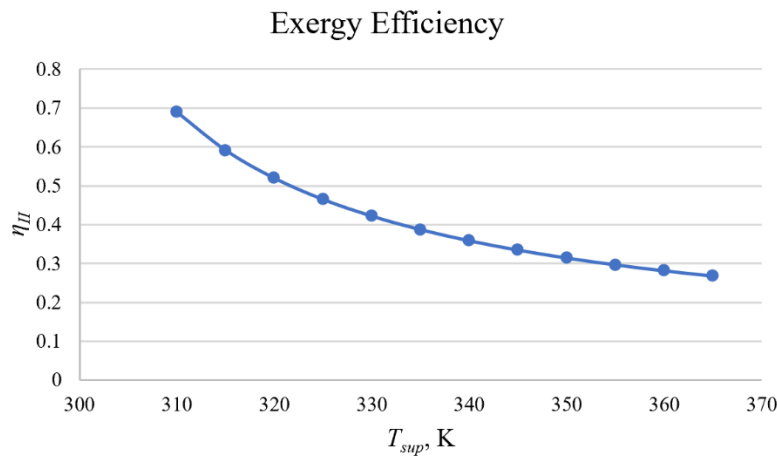


Figure 7. Exergy Efficiency Decrease with Supply Temperature

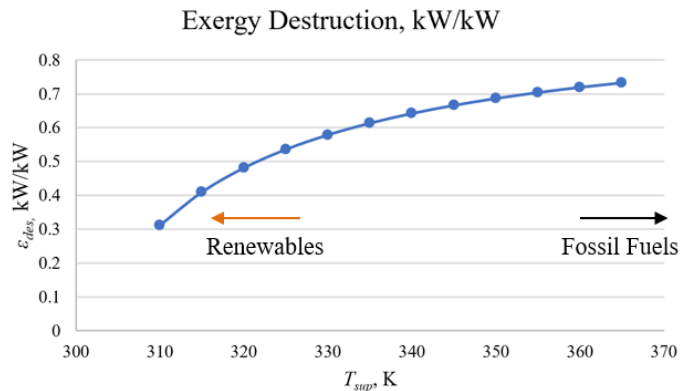


Figure 8. Exergy Destructions Increase with Supply Temperature

When Figure 7 is imposed to Figure 6, the correct solution, which acknowledges that exergy destructions come first in solutions for sustainable measures for climate emergency. By increasing the main loop pipe diameter, the pumping power (Thus running costs) are fixed, but the lower the supply temperature is, the higher the  $CO_2$  embodiments in a district energy system. Therefore, Low and Ultra-Low temperature applications are realistically justified with this graph in typical thermal applications.

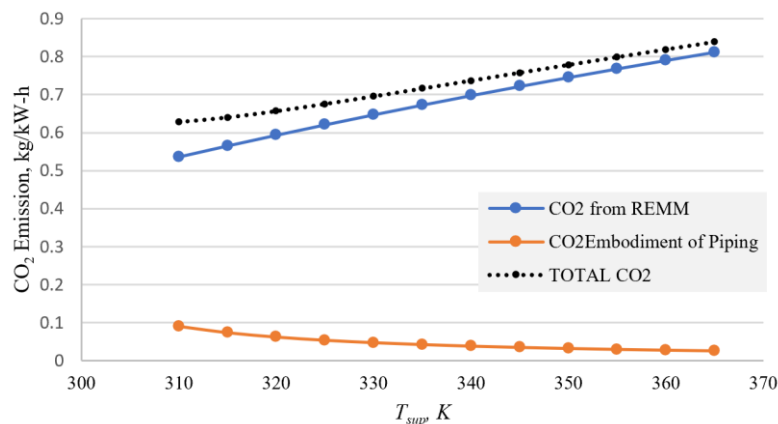


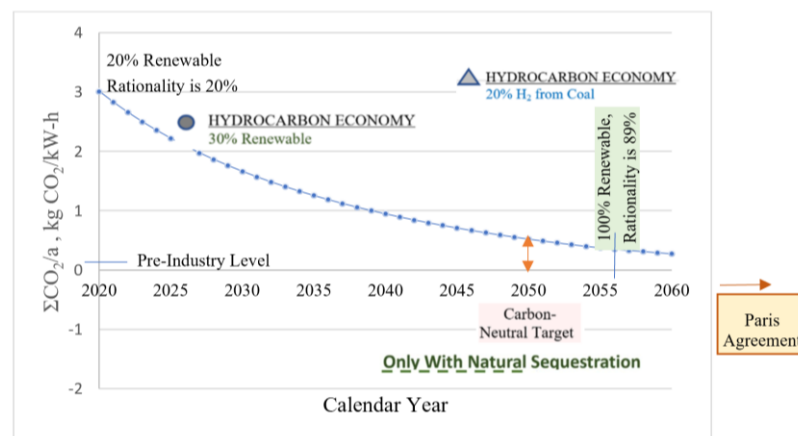
Figure 9. Exergy-Based Sustainable Environment Conditions

Even when embodiments are considered, Figure 9 shows that total emissions responsibility decreases at low application temperatures. Therefore, Low and Ultra-Low temperature applications are realistically justified with this graph in typical thermal applications.

#### 4. CONCLUSIONS

This paper has answered the question about whether energy efficiency comes first or the exergy destructions issue comes first, in implementing a complete set of measures for reducing global warming in the context of climate emergency. Figure 10 shows that the Paris Agreement goal may be reached only with exergy-based solutions as well as increasing the *R* (Renewable mix) of the energy mix, low-temperature harvesting of solar, low-enthalpy geothermal, and waste heat which are abundantly available all over the world. But until now their positive impact was not recognized, which are only visible with the exergy destruction minimization.

It is understood that when we recognize the importance of the rationality factor, which is the missing link so far, the targets of the Paris agreement will not be reached. Now, this link is included in Figure 10. According to Figure 10, the carbon-neutral target for 2050, based on simple emission calculations will be missed by about 0.6 kg CO<sub>2</sub>/kW-h in the best scenario of today's strategies. In 2060, the Paris Agreement goal will also be missed by about 0.3 kg CO<sub>2</sub>/kW-h. Even worse, a 30% renewable target of around 2025 will stay above the requirements for reducing climate crisis and remain there unless the recent natural gas craze and insistence of coal is abandoned by all nations. Generating hydrogen from coal will not a solution either and it will stay at a high emissions point if the hydrocarbon economy continues. Figure 10 further shows that whatever measures are taken, we will not be able to reach a negative carbon state unless we embrace nature and incorporate it with rational carbon capture methodologies. As a result, all strategists and energy policymakers need to recognize the importance of the rationality factor in all applications. Then new methodologies, new equipment, buildings, machinery, and performance metrics need to be developed to rate these applications towards truly minimum CO<sub>2</sub> emissions responsibilities, which have a definite effect on global warming. In this quest, the goal must be to minimize useful work potential (exergy) destructions.

Figure 10. Total Global CO<sub>2</sub> Emissions per Year, kg CO<sub>2</sub>/kW-h ©2020 B. Kılıç

## REFERENCES

- [1] UNIS. 2020. The Secretary-General Remarks on Climate Action to European Council on Foreign Relations, UNIS/SGSM/1084, 19 November 2020.
- [2] The Guardian. 2020. Climate Change, UN Secretary-General Urges All Countries to Declare Climate Emergencies, December 12, 2020. <<https://www.theguardian.com/environment/2020/dec/12/un-secretary-general-all-countries-declare-climate-emergencies-antonio-guterres-climate-ambition-summit>>
- [3] RHC-SRIA. 2020. Strategic Research and Innovation Agenda for Climate-Neutral Heating and Cooling in Europe, Sria For the Renewable Heating And Cooling Sector, European Technology and Innovation Platform. <<https://www.rhc-platform.org/content/uploads/2020/10/RHC-ETIP-SRIA-2020-WEB.pdf>>
- [4] Kilkis, B. Accelerating the Transition to 100% Renewable Era. But How? Exergy Rationality in the Built Environment (Ed. Uyar, T. S.), Lecture Notes Energy, Vol. 74, Chapter 1, Springer Nature.
- [5] EC. 2014. Common Implementation Roadmap for Renewable Heating and Cooling Technologies European Technology Platform on Renewable Heating and Cooling, RHC Platform, Brussels. <[https://www.rhc-platform.org/content/uploads/2019/04/RHC\\_Common\\_Roadmap.pdf](https://www.rhc-platform.org/content/uploads/2019/04/RHC_Common_Roadmap.pdf)>
- [6] EC. 2020. Powering a climate-neutral economy: An EU Strategy for Energy System Integration, Brussels, 8.7.2020 COM(2020) 299 final.<[https://ec.europa.eu/energy/sites/ener/files/energy\\_system\\_integration\\_strategy\\_.pdf](https://ec.europa.eu/energy/sites/ener/files/energy_system_integration_strategy_.pdf)>
- [7] EC. 2020. Communication From The Commission To The European Parliament, The Council, The European Economic and Social Committee and The Committee of The Regions, A New Circular Economy Action Plan for a Cleaner and More Competitive Europe, Brussels, 11.3.2020, COM (2020). 98 final.
- [8] SE, Science Europe. 2016. In a Resource-Constrained World: Think Exergy, not Energy, Published June 2016. Science Europe, Brussels. <[https://www.scienceeurope.org/media/0vxhcyhu/se\\_exergy\\_brochure.pdf](https://www.scienceeurope.org/media/0vxhcyhu/se_exergy_brochure.pdf)>
- [9] Thomassen, G., Konstantinos Kavvadias, K., Navarro, J. P., 2021. The Decarbonization Of The EU Heating Sector Through Electrification: A Parametric Analysis, Energy Policy, Vol. 148, Part A, January 2021, 111929. <<https://doi.org/10.1016/j.enpol.2020.111929>>
- [10] Caviedes, L. L. 2020. (Ed.), Strategic Research and Innovation Agenda for Climate-Neutral Heating and Cooling in Europe, <[www.rhc-platform.org](http://www.rhc-platform.org)>
- [11] Kilkis, B. 2020. Development of a Composite PV Panel with PCM Embodiment, TEG Modules, Flat-Plate Solar Collector, and Thermally Pulsing Heat Pipes, *Solar Energy*, 200 2020 (89-107).
- [12] Kilkis, B. 2020. Exergy-Based Hydrogen Economy With 100% On-Board Renewables, H<sub>2</sub>S Reserves, and Coastal Hydrogen Cities in the Black Sea Region, Special Report to Turkish Ministry of Energy and Resources (MENR), 79 Pages, August 30, 2020, Ankara, Turkey.
- [13] ICCT. 2020. E-fuels Won't Save The Internal Combustion Engine, Posted on Tuesday, 23 June 2020. <<https://theicct.org/blog/staff/e-fuels-will-not-save-ice>>
- [14] Tanay, S. U. (Ed.). 2020. Accelerating the Transition to a 100% Renewable Energy Era, Lecture Notes on Energy, Vol. 74, Springer. <<https://doi.org/10.1007/978-3-030-40738-4>>
- [15] Falk, P. M., 2017. Evaluation Of District Heating Systems Based On Exergy Analysis, Ph. D. Thesis, Technical University Darmstadt (TTD), 115 pages, <URL: <https://tuprints.ulb.tu-darmstadt.de/7372>> <[http://tuprints.ulb.tu-darmstadt.de/7372/1/2018\\_04\\_24\\_Dissertation\\_Falk.pdf](http://tuprints.ulb.tu-darmstadt.de/7372/1/2018_04_24_Dissertation_Falk.pdf)>
- [16] Kilkis, B. 2017. Sustainability and Decarbonization Efforts of the EU: Potential Benefits of Joining Energy Quality (Exergy) and Energy Quantity (Energy) in EU Directives, Exclusive Position Report Submitted to EU Presidency (Malta), 25.0.6.2017, 19 pages and three-paper appendix, TTMD Report: 2017-1, Ankara. ISBN-e: 978-975-6263-48-8
- [17] EIA, 2018. Total Energy, US Energy Information Administration, *Monthly Energy Review*, Table 2.1, April 2018. <<https://www.eia.gov/totalenergy/data/monthly/archive/00351804.pdf>>
- [18] Kılıkış, Şıir, and Kılıkış, B. 2019. An Urbanization Algorithm for Districts with Minimized Emissions, Based on Urban Planning and Embodied Energy Towards Net-Zero Exergy Targets, *Energy*, 179 (2019) 392-406.

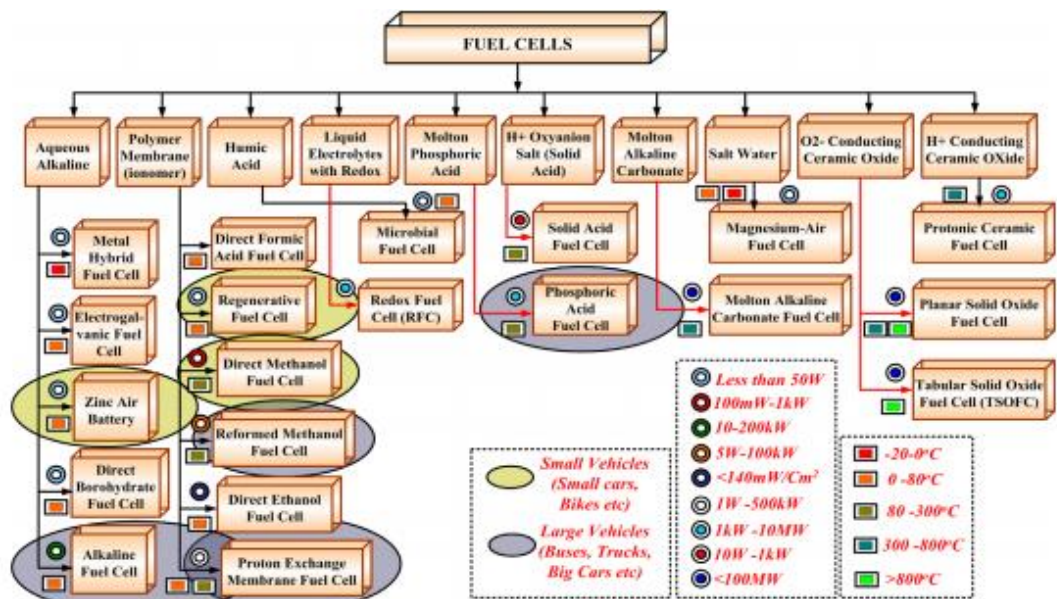
# A STATE-OF-THE-ART: DC-TO-DC CONVERTERS FOR FUEL CELL VEHICULAR POWER TRAIN – POWER ELECTRONICS IN FUEL CELL TECHNOLOGY

Sanjeevikumar Padmanaban

Department of Energy Technology, Aalborg University, Denmark, san@et.aau.dk

*Cite this paper as:* **Padmanaban, S. A State-of-The-Art: DC-to-DC Converters for Fuel Cell Vehicular Power Train – Power Electronics in Fuel Cell Technology. 9th Eur. Conf. Ren. Energy Sys. 21-23 April 2021 Istanbul, Turkey**

**Abstract:** The automobile companies in the global market focused on the recent technologies towards the Hydrogen (H<sub>2</sub>) and FC-VPT, to improve the Tank-To-Wheel (TTW) efficiency. Cost-effective solution for 'Eco' friendly, free of emission and high-power capacity are the inherent benefits. The DC-DC power converters play a crucial influence in boosting the fuel cell stack power through voltage conversion. Therefore, ensure the demand of the motor and transmission in the vehicles. Several DC converter topologies proposed for various vehicular applications. State-of-the-art technology, newly developed families of the unidirectional non-isolated DC-DC Multistage Power Converter (MPC) configuration for Fuel Cell – Vehicular Power Train (FC-VPT), Renewables and Microgrids application will be discussed with the presentation. DC-DC power converters with the new modified version are viable and cost-effective solutions with reduced size and increased efficiency. The comprehensive review, comparison of different topologies and suitability for various applications will be discussed in the presentation, correctly applied to the power train of a small vehicle to large vehicles (bus, trucks etc.). Finally, the advantages/disadvantages will be pointed out in the presentation for the prominent features of each converter, its challenges, and application for fuel cell (FC) technology, EVs, Microgrids and Renewables.



**Keywords:**

© 2021 Published by ECRES

# NEXT-GENERATION SMART GRIDS: POWER ELECTRONICS DOMINATED POWER SYSTEMS

Sertaç Bayhan

College of Science and Engineering, Hamad Bin Khalifa University, Doha, Qatar

*Cite this paper as:*

*Bayhan, S. Next-Generation Smart Grids: Power Electronics Dominated Power Systems. 9th Eur. Conf. Ren. Energy Sys. 21-23 April 2021 Istanbul, Turkey*

---

**Abstract:**

Over the last few decades, electrical energy systems have become overstrained and faced various stressed conditions more often because of increased electricity demand and the adaptation of various fluctuating renewable energy resources. Undoubtedly, at some point within the next decade, intensive electricity demand will exceed total electricity generation and transmission capacity, which will force decision-makers to build new plants and put major changes in the whole grid infrastructure. Building new bulk power plants will not be practical considering economic, safety, and environmental concerns. Therefore, the traditional utility grid has to experience an inclusive transformation to avoid a prospective crisis with existing power plants and available infrastructure. To ensure power continuity and minimize the difference between the supply and demand energy, the smart grid paradigm has to be introduced with solutions that include demand response, energy efficiency improvement, and renewable energy sources (RES) integration. RES-based generators are often connected to the grid via power electronics converter (PEC). The massive deployment of PECs leads to a hybrid ac/dc transmission system and bring challenges in operation and planning of power system, especially in the transient time frame. The high penetration level of PECs reduces the inertial response capability and the short circuit power of the grid and consequently reduces the level of transient stability of the power system. This talk primarily focuses on design consideration of next-generation smart grids, including the PEC-interfaced generators, energy storage systems, their grid connection requirements, current status, and also future opportunities.

---

**Keywords:**

© 2021 Published by ECRES

# THE CO-SIMULATION STUDIES OF THE POWER ELECTRONIC CIRCUITS WITH FEA SOFTWARE

Selami Balci

Department of Electrical Electronics Engineering, Karamanoglu Mehmetbey University, Turkey

Cite this paper as:

*Balci, S.. The Co-Simulation Studies of the Power Electronic Circuits with FEA Software. 9th Eur. Conf. Ren. Energy Sys. 21-23 April 2021 Istanbul, Turkey*

---

**Abstract:**

Among the power switches used in the past, the conduction losses of silicon-based MOSFETs increase after a certain voltage, and the switching losses increase when the IGBTs are operated at high switching frequency values. This increase in power losses was the factor that prevented designs from reaching high power values with higher power density. Depending on the developments in semiconductor power switches technology, SiC / Gan power switches have been developed, and accordingly, the possibility of switching at much higher frequency values has emerged for designs with higher power values. Thus, an important step was taken in reducing the size of power electronic circuits and improving their performance. However, extraordinary developments in switches are not enough to achieve the smallest dimensions. Inductors and transformers, which are the basic energy-storing elements used in a converter design, must also be in a structure that can operate in accordance with the current high frequency values. These developments can be stated mainly as changes in core materials and design details in windings. These changes can be seen in many areas such as electric vehicles, uninterrupted power supplies, grid-scale energy storage systems, renewable energy sources, and telecommunication power supply systems.

---

**Keywords:**

© 2021 Published by ECRES

## IoT WITH GREEN ENERGY

Sudan Jha

Department of Computer Science and Engineering, Chandigarh University, India

*Cite this paper as:* [\*Jha, S. IoT with Green Energy. 9th Eur. Conf. Ren. Energy Sys. 21-23 April 2021 Istanbul, Turkey\*](#)

---

**Abstract:**

Internet of things (IoT) has been a noteworthy zone of research for empowering interconnection and joining the physical world through the Internet. At the beginning, it was used for single things but later advancements in different computing devices resulted in a new terminology called the internet of computing (IoC). The recent advancements on IoT with IoC has yielded out (1) devices connected via various communication modes and (2) deterministic communication in IoT. The talk will focus on how the data stored in the cloud needs to be mapped with geographic information system in order to fit with IoT and IoC. Besides, it will also focus on how the reliable connection plays a vital role in collaborated IoT and IoC towards green energy environment; especially, "free" green energy to power IoT devices and revolutionarily enable wireless charging of these devices. Green IoT can be introduced in three ways (ambience, harvesting and wireless charging), in which the latter step reinforces the former step to ensure the availability of green energy. With the ongoing worldwide development of IoT, an unprecedented number of IoT devices imperatively consume a substantial amount of energy. IoT devices have been predicted to be the leading energy guzzler in Information and Communications Technology by 2021.

---

**Keywords:**

© 2021 Published by ECRES



# **REGULAR ABSTRACTS**



# TOWARDS INTEGRATION OF CARBON CAPTURE AND STORAGE APPROACHES IN WASTE PROCESSING TECHNOLOGIES

Maris Klavins

Department of Environmental Science, University of Latvia, Riga, Latvia, maris.klavins@lu.lv, ORCID: 0000-0002-4088-9348

Dmitry Porshnov

Department of Environmental Science, University of Latvia, Riga, Latvia, maris.klavins@lu.lv, ORCID: 0000-0002-2512-3782:

*Cite this paper as:* Klavins, M, Porshnov, D. Towards integration of carbon capture and storage approaches in waste processing technologies. 9th Eur. Conf. Ren. Energy Sys. 21-23 April 2021, Istanbul, Turkey

**Abstract:** Waste processing according to waste-to-energy concept remains a major challenge to deal with growing amounts of different waste types. The aim of the study is to expand the knowledge base of Carbon Capture and Storage (CCS) technology for municipal solid waste as well as biomass waste treatment in an approach that integrates the CCS within the waste-to-energy concept. In accordance to this concept, waste thermochemical processing (torrefaction and gasification) technology is further advanced by evaluating, studying and adapting the most technologically and economically feasible approach of pre-combustion carbon capture; and by developing a pilot scale facility with the aim to demonstrate its potential to offer the industry an innovative solution for solid waste processing. Pre-combustion carbon capture involves CO<sub>2</sub> sequestration from fossil fuel or biomass after gasification of CO<sub>2</sub> and H<sub>2</sub> enriched syngas. This approach allows flexible performance at different scales and achieves high thermal efficiency. Several different systems have been studied, including, sorption by amines and ethanolamines in a liquid phase, sorbed on solid matrixes or hydrogels, activated carbon and others. Use of absorbents is superior in terms of high loading capacity at ambient conditions, low energy consumption, economical regeneration process, mechanical and chemical stability, simple operation and maintenance..

**Keywords:** Refuse derived fuels; gasification; biomass waste, sorbents, carbon capture

© 2021 Published by ECRES

## Acknowledgements

Research is supported by ERDF project Nr.1.1.1/19/A/013 “Innovation of the waste-to-energy concept for the low-carbon economy: Development of novel carbon capture technology for thermochemical processing of municipal solid waste (Carbon Capture and Storage from Waste - CCSW)”

# RENEWABLE ENERGY SUPPLY CHAIN NETWORK DESIGN

Bader A. Al-Ablani

Mechanical Engineering Department, Faculty of Engineering at Shoubra, Benha University, Cairo, Egypt  
alablani@hotmail.com, ORCID: <https://orcid.org/0000-0002-4731-9778>

Marwa Mekky M.

Department of Mechanical Design and Production Engineering, Cairo University, Giza, Egypt  
marwa\_mekky\_m@yahoo.com, ORCID: <https://orcid.org/0000-0001-7377-0186>

Noura A. Al-Ghimlas

Department of Quantitative Methods and Information Systems, College of Business Administration, Kuwait University,  
Kuwait, noura.alghimlas@ku.edu.kw, ORCID: <https://orcid.org/0000-0001-8053-9644>

*Cite this paper as:* **Al-Ablani, BA, Marwa Mekky MA, Al-Ghimlas, NA. Renewable energy supply chain network design. 9th Eur. Conf. Ren. Energy Sys. 21-23 April 2021, Istanbul, Turkey**

---

**Abstract:**

In this study a renewable energy supply chain network is designed with the goal of wider coverage by using advanced storage and delivery technique. The decision of using advanced storage and delivery techniques, such as hydrogen electrolysis, was prioritized in a previous study in order to build a robust supply chain network. The goal was wider use of renewable energy by overcoming the challenges faced in the supply chain. This study uses recommendation from the previous study and data from literature to formulate the model for the supply chain network. Thus, solar-hydrogen energy supply chain network is designed with the objective of wider coverage of the supply chain to include rural and distant areas that are hard to be fully provided with electrical power.

Accordingly, a mixed integer programming model is formulated with the objective of maximization of demand fulfilment. The study uses the common structure of conventional products or service supply chains with multi layers. The renewable energy supply chain network consists of plants, storage points, distribution grids, transportation routes, and demand points. The model is solved using optimization software and a previously developed algorithm based on shortest path (SSP) approach. The optimization software is able to solve small and medium sized network problems, however large problems cannot be solved using the software. Thus, the SSP algorithm was successful on solving large real-world size of problems.

The resultant designed network is efficient in fulfilling the objective of maximizing power delivered to demand points, including ones in distance areas. Distance demand points simulate rural areas that are usually deprived of energy provision due to complications of power supply. The study emphasizes the importance of robust supply chain network designs to increase the dependability and reliability of renewables to provide required power by different communities

---

**Keywords:**

*Renewable energy supply chain, supply chain network design, energy network optimization, solar-hydrogen network*

# DEEP-LEARNING APPROACH TO THE IRON CONCENTRATION EVALUATION IN SILICON SOLAR CELL

Olikh Oleg

Taras Shevchenko National University of Kyiv, Kyiv, Ukraine, olegolikh@knu.ua, ORCID: 0000-0003-0633-5429

Lozitsky Oleg

Taras Shevchenko National University of Kyiv, Kyiv, Ukraine, olozitsky@gmail.com, ORCID: 0000-0002-6872-6655

Zavhorodnii Oleksii

Taras Shevchenko National University of Kyiv, Kyiv, Ukraine, nevermor464@gmail.com, ORCID: 0000-0001-8080-766

*Cite this paper as:* Olikh, O, Lozitsky, O, Zavhorodnii, O. Deep-learning approach to the iron concentration evaluation in silicon solar cell. 9<sup>th</sup> Eur. Conf. Ren. Energy Sys. 21-23 April 2021, Istanbul, Turkey

---

**Abstract:**

Impurities are crucial for solar cell (SC) performance. The aim of our work is to show the possibility of fast and easy evaluation of iron concentration in silicon SC by using current-voltage characteristics (IVC). For this purpose, SCAPS was used to simulate the IVCs for  $n^+$ - $p$ - $p^+$ -Si structures with various both base thickness (150-240  $\mu\text{m}$ ) and boron doping level ( $10^{15}$ - $10^{17}$   $\text{cm}^{-3}$ ) in range 290-340 K. The recombination was considered to be associated with iron atoms with concentration  $10^{10}$ - $10^{13}$   $\text{cm}^{-3}$  and two cases (the coexistence of interstitial atoms  $\text{Fe}_i$  and pairs  $\text{Fe}_i\text{B}_s$  as well as the presence of  $\text{Fe}_i$  only) were under investigation. The IVC ideality factors were calculated in these cases ( $n_{\text{Fe-FeB}}$  and  $n_{\text{Fe}}$  respectively).  $n$  values and SC parameters for more than 10,000 structures were used for neural network learning. Keras was used to construct the network with up to 4 hidden dense layers (up to 300 neuron, relu activation) and iron concentration as output. It was shown that mean squared relative error for test data prediction was up to 0.28 in case of network, which trained by  $n_{\text{Fe-FeB}}$  value and up to 0.06 in case of both  $n_{\text{Fe-FeB}}$  and  $n_{\text{Fe}}$  using. The work was supported by NRFU (project 2020.02/0036).

---

**Keywords:**

Silicon solar cell, iron concentration, neural network, ideality factor

---

© 2021 Published by ECRES

# ENERGY HARVESTING THROUGH LANDSCAPE DESIGN

Işıl Kaymaz

Ankara University, Ankara, Turkey, cakci@agri.ankara.edu.tr, ORCID: 0000-0002-2659-4965

Ecem Hoşgör

Ankara University, Ankara, Turkey, ecembaki@gmail.com, ORCID: 0000-0001-7175-2785

*Cite this paper as:*

*Kaymaz, I., Hoşgör, E. Energy Harvesting Through Landscape Design. 9th Eur. Conf. Ren. Energy Sys. 21-23 April 2021, Istanbul, Turkey*

---

**Abstract:**

Spatial planning, design and management of urban landscapes should be seen as a priority for resilience and smart development in this age of global environmental crisis. This paper aims to address the potential of urban landscape design practices for harvesting renewable energy via selected examples throughout the world. The resource and technology used in the examples vary from generating electricity from wind (Windbelts™) to kinetic tech paving slabs that create electricity (Pavegen). It is also aimed to draw attention of related actors to promote the idea of everyday urban public space as a medium for sustainable energy practices. On the other hand, findings show that high cost of supply and installation is the major setback for adapting these examples in spatial design and management. Furthermore, relatively low energy output might be discouraging to investors. Still, these tools are inspiring and innovative, especially when spatial limitations seem intimidating for energy harvesting. Therefore, collaboration between different disciplines to ensure aesthetic and functional quality while developing more effective energy harvesting solutions in urban environments is crucial. When such examples are visible in everyday urban life, it would certainly increase public awareness and willingness to support sustainable energy systems.

---

**Keywords:**

*Landscape design, smart city, energy harvesting, sustainable design*

© 2021 Published by ECRES

## **DESIGN OF 2S2L BASED BUCK - BOOST CONVERTER WITH WIDE CONVERSION RANGE**

Nagi Reddy Bandi

Vignana Bharathi Institute of Technology, Hyderabad, India, nagireddy208@gmail.com, ORCID:0000-0002-9202-1153

Prasanna Chunduru

Vignana Bharathi Institute of Technology, Hyderabad, India, prasannachunduru2k@gmail.com,  
ORCID:0000-0002-6437-0735

Neelima Kalahasti

Vignana Bharathi Institute of Technology, Hyderabad, India, prasannachunduru2k@gmail.com,  
ORCID:0000-0001-9627-5620

Surya Prakash Jalli

Vignana Bharathi Institute of Technology, Hyderabad, India, suryaprakash4501@gmail.com, ORCID: 0000-0001-8887-579X

Akshay Reddy Bobbala

Vignana Bharathi Institute of Technology, Hyderabad, India, bobbala.akshay.reddy@gmail.com ORCID:  
0000-0002-3959-7081

Dinesh Goud Kotha

Vignana Bharathi Institute of Technology, Hyderabad, India, dineshgoud.kotha@gmail.com, ORCID: 0000-0002-9639-7932

*Cite this paper  
as:*

*Bandi, NR, Chunduru, P, Kalahasti, N, Jalli, SP, Bobbala, AR, Kotha, DG. Design of 2S2L  
based buck-boost converter with wide conversion range. 9<sup>th</sup> Eur. Conf. Ren. Energy Sys. 21-  
23 April 2021, Istanbul, Turkey*

---

**Abstract:**

A new non-isolated negative output buck- boost type configuration is proposed for the wide voltage conversion applications. This converter is derived by considering the conventional buck-boost converter configuration. The active switch in the conventional buck-boost converter is replaced by two switch - two inductor (2S2L) cell. This cell uses an energy storage capacitor for transferring the energy. The continuous conduction mode (CCM) operation of this converter is briefly analyzed under steady state conditions, along with the necessary designed equations. The proposed converter has less component count and low voltage stresses on the switches. The major advantage of this buck boost converter is that the wide range of step down and step-up voltage conversions can be achieved. To validate the performance, this converter is designed and simulated in the MATLAB/simulink software. For most of the operating conditions, the proposed configuration gives the efficiency around 94-96%. A few comparisons are also presented to demonstrate the competitiveness of proposed buck-boost type configuration.

---

**Keywords:**

*Buck-boost, wide conversion range, two switch- two inductor(2S2L), continuous conduction mode (CCM), DC-DC converter.*

# TECHNOLOGICAL FORECASTING FOR ELECTRIC BATTERY TECHNOLOGY IN THE ELECTRIC VEHICLE INDUSTRY

Hasan Koten

Istanbul Medeniyet University, Mechanical Engineering Department, Istanbul, 34700, Turkey, ORCID: 0000-0002-1907-9420

Cite this paper as:

Köten, H. *Technological Forecasting for Electric Battery Technology in the Electric Vehicle Industry 9th Eur. Conf. Ren. Energy Sys. 21-23 April 2021, Istanbul, Turkey*

---

**Abstract:**

Technology forecasting is a useful tool for the technology level analyzing and it shows the technological effects for the long term on the new products. Quantitative and qualitative methods are the two main parts of the technology forecasting but they are further divided into several subgroups. The goal of this study is to get the forecasting of electric vehicle batteries technology that would help the automotive industry. They can estimate the future of the electric vehicle batteries technology that they are planning to design on their vehicles and govern their resources and investments properly. In this research, technology forecasting methods are explained compared with each other in detail and new electric source technologies for the automotive industry is analyzed. Different types of electric batteries in the automotive industry are analyzed using forecasting methods. In the forecasting methods, patent analysis is used and the forecasts are performed using pearl curve. Lastly, technology substitution model created from this patent analysis is employed

---

**Keywords:**

*Energy density; electric car; technological forecasting.*

---

© 2021 Published by ECRES

# ANALYSIS OF POSITIVE OUTPUT BUCK-BOOST TOPOLOGY WITH EXTENDED CONVERSION RATIO

Nagi Reddy Bandi

Vignana Bharathi Institute of Technology, Hyderabad, India, nagireddy208@gmail.com, ORCID:0000-0002-9202-1153

Sahithi Priya Kosika

Vignana Bharathi Institute of Technology, Hyderabad, India, kosikapriya05@gmail.com, ORCID:0000-0002-2841-346X

Manish Patel Gadam

Vignana Bharathi Institute of Technology, Hyderabad, India, gmpatel9703@gmail.com, ORCID: 0000-0003-0905-2280

Jagadhiswar Banoth

Vignana Bharathi Institute of Technology, Hyderabad, India, jagadhiswarbanoth@gmail.com, ORCID: 0000-0002-9202-8937

Ashok Banoth

Vignana Bharathi Institute of Technology, Hyderabad, India, banothashok823@gmail.com, ORCID:0000-0002-1085-104X

Srikanth Koundinya

Anurag College of Engineering, Hyderabad, India, srikanth.b@anuraghyd.ac.in, ORCID:0000-0002-5107-9738

Cite this paper as:

*Bandi, NR, Kosika, SP, Gadam, MP, Banoth, J, Banoth, A, Koundinya, S. Analysis of positive output buck-boost topology with extended conversion ratio. 9th Eur. Conf. Ren. Energy Sys. 21-23 April 2021, Istanbul, Turkey*

---

**Abstract:**

In this paper, a new non-isolated buck-boost converter with positive output is designed. This buck-boost converter contains two active switches which operates synchronously. Hence, the control circuit for the given converter is simple. Compared with the conventional buck-boost converter, the newly designed topology has few advantages such as positive output voltage and quadratic voltage gain. Due to the quadratic voltage gain, this converter can achieve wide voltage conversion ratios without the use of extreme (very low or high) duty ratios. The output voltage of this proposed converter is common ground with the input voltage and its polarity is positive. The continuous conduction mode operation (CCM) of the converter is deeply analyzed in steady state conditions. The necessary component design equations are also obtained along with the switching stresses. The MATLAB/Simulink software is used to design and simulate the proposed converter. The simulated results as well as the comparisons are provided to evaluate the effectiveness of the proposed buck-boost converter.

---

**Keywords:**

*Buck-Boost, quadratic voltage gain, continuous conduction mode (CCM), positive output voltage.*

© 2021 Published by ECRES

# DATA EXTRACTION OF PEROVSKITE SOLAR CELLS MATERIALS BY USING NATURAL LANGUAGE PROCESSING TOOLS

Mary Zuleika Jiménez Díaz

Universidad Industrial de Santander, Bucaramanga, Colombia, mary.jimenez@correo.uis.edu.co, ORCID: 0000-0001-8981-5211

Cristian David Camacho Parra

Universidad Industrial de Santander, Bucaramanga, Colombia, cristian.camacho2@correo.uis.edu.co, ORCID: 0000-0001-5470-700X

Mónica Andrea Botero Londoño

Universidad Industrial de Santander, Bucaramanga, Colombia, mabotero@uis.edu.co, ORCID: 0000-0003-1706-3182

Alexander Sepúlveda Sepúlveda

Universidad Industrial de Santander, Bucaramanga, Colombia, alexander.sepulveda@saber.uis.edu.co, ORCID: 0000-0002-9643 -5193

Camilo Andres Otálora Bastidas

Universidad Industrial de Santander, Bucaramanga, Colombia, camilo.otalora@correo.uis.edu.co, ORCID: 0000-0002-5330-0408

*Jiménez-Diaz, M, Camacho-Parra C, Botero-Londoño, M, Sepúlveda-Sepúlveda A, Otálora-Bastidas C. Data Extraction of Perovskite Solar Cells materials by using Natural Language Processing tools. 9th Eur. Conf. Ren. Energy Sys. 21-23 April 2021, Istanbul, Turkey*

---

**Abstract:**

Recently, the interest in photovoltaic Perovskite technologies has increased significantly. The data resulting from experiments, reported by researchers in their scientific articles, is producing an important amount of valuable information that makes possible the use of machine learning methods to materials science. This information can be used to automate the discovery of new materials, providing efficient solutions to material problems in a way that human researchers might be unable. However, manual data extraction, as developed in [1], is expensive and labor-intensive; thus, the ability to automatically extract and codify the relevant information reported in scientific literature has an immense potential to generate enough data required in machine learning related applications. This paper presents a method for the automatic extraction of Perovskite solar cell materials from research articles by using natural language processing (NLP) and text mining tools. For this purpose, 584 items of conventional Perovskite solar cells consigned in the dataset reported in [1] are used. In particular, the "Spacy" NLP tool was used to develop a Named Entity Recognition procedure. As a result, values of 0.87 and 0.93 were obtained for recall and precision, respectively. Moreover, when comparing the predicted and reference values, an accuracy of 88.10% was obtained.

---

**Keywords:**

*Data mining, natural language processing, perovskites, solar cells, intelligent artificial*

---

© 2021 Published by ECRES

---

**REFERENCE**

- [1] Ç. Odabaşı Özer and R. Yıldırım, “Performance analysis of perovskite solar cells in 2013–2018 using machine-learning tools,” *Nano Energy*, vol. 56, pp. 770–791, 2019, doi: 10.1016/j.nanoen.2018.11.069.

# UPSCALING OF PEROVSKITE SOLAR CELL TECHNOLOGY BY A SEMI-AUTOMATIC BLADE-COATING TECHNIQUE AT AMBIENT CONDITION

Luigi Vesce

CHOSE – Centre for Hybrid and Organic Solar Energy, Department of Electronic Engineering, University of Rome “Tor Vergata”, Rome, Italy, vesce@ing.uniroma2.it, ORCID: 0000-0003-3322-8688

Maurizio Stefanelli

CHOSE – Centre for Hybrid and Organic Solar Energy, Department of Electronic Engineering, University of Rome “Tor Vergata”, Rome, Italy, maurizio.stefanelli@uniroma2.it, ORCID: 0000-0002-1197-1246

Luigi Angelo Castriotta

CHOSE – Centre for Hybrid and Organic Solar Energy, Department of Electronic Engineering, University of Rome “Tor Vergata”, Rome, Italy, luigi.angelo.castriotta@uniroma2.it, ORCID: 0000-0003-2525-8852

Jan Philipp Herterich

Fraunhofer Institute for Solar Energy Systems ISE, Freiburg, Germany, jan.philipp.herterich@ise.fraunhofer.de, ORCID: 0000-0001-9436-200X

Markus Kohlstaedt

Fraunhofer Institute for Solar Energy Systems ISE, Freiburg, Germany, markus.kohlstaedt@ise.fraunhofer.de, ORCID: 0000-0002-9399-466X

Uli Würfel

Fraunhofer Institute for Solar Energy Systems ISE, Freiburg, Germany, uli.wuerfel@ise.fraunhofer.de, ORCID: 0000-0003-4151-8538

Aldo Di Carlo

CHOSE – Centre for Hybrid and Organic Solar Energy, Department of Electronic Engineering, University of Rome “Tor Vergata”, Rome, Italy, aldo.dicarlo@uniroma2.it, ORCID: 0000-0001-6828-2380

Cite this paper as:

*Vesce, L., Stefanelli, M., Castriotta, L.A., Herterich, J., Kohlstaedt, M., Würfel, U., Di Carlo, A. Upscaling of perovskite solar cell technology by a semi-automatic blade-coating technique at ambient condition. 9th Eur. Conf. Ren. Energy Sys. 21-23 April 2021, Istanbul, Turkey*

---

**Abstract:**

In the last decade, perovskite solar cell technology showed an efficiency improvement approaching the Si record. The low-cost perspective of PSCs is achievable only if scalable processes in manufacturing conditions are designed and optimized for the full device stack. Here, a full semi-automatic scalable process based on the blade-coating technique is demonstrated to fabricate efficient and stable perovskite solar modules in ambient conditions. The CsMAFA perovskite is deposited with a double step process assisted by green anti-solvent air quenching. The developed coating procedure permits the fabrication of several highly reproducible small area cells on module size substrate with an efficiency exceeding 17%. Corresponding reproducible modules with a 90% geometrical fill factor achieved a champion efficiency of 16.1% and a T80=750 h in light soaking condition at MPP and RT/ambient. The properties of the film depositions are assessed by different characterization techniques such as Scanning Electron Microscopy, profilometry, UV-vis and Photo-luminescence spectroscopy, Photo- and Electro-luminescence imaging. The last two techniques confirmed less defects and local coating variations of the ambient air/bladed devices respect to the reference procedure based on the spin-coating technique at nitrogen air. Finally, this work provides a scalable procedure to realize large area modules at real ambient conditions

---

**Keywords:**

*Perovskite solar cells, blade-coating, module up-scaling, ambient air, stability.*

# ELECTRIC ENERGY LOAD FORECASTING WITH ARIMA VS XGBOOST FOR AUSTRALIA VIC STATE

Muhammed Can Özdemir

Sakarya University, Sakarya, Turkey, mcan.ozdemir@gmail.com, ORCID: 0000-0002-4002-7967

Hasan Köten

İstanbul Medeniyet Üniversitesi, İstanbul, Turkey, hkoten@gmail.com, ORCID: 0000-0002-1907-9420

Nejat Yumuşak

Sakarya University, Sakarya, Turkey, nyumusak@sakarya.edu.tr, ORCID: 0000-0001-5005-8604

Cite this paper as:

Ozdemir, MC, Koten, H, Yumusak, N. Electric Energy Load Forecasting with ARIMA vs XGBoost for Australia VIC State. 9th Eur. Conf. Ren. Energy Sys. 21-23 April 2021, Istanbul, Turkey

---

**Abstract:** In this study, It is investigated on electrical power demand data from 1999 to 2019 of Australia VIC state. This work focuses on short term load forecasting with two different forecasting methods. Two models ARIMA and XGBoost were used to estimate the energy demand to predict future electrical demands. While building models it is used only the first week of October for every year to predict the first week of October for future years. Our focus is to compare the ARIMA and XGBoost to forecasting on time series. The importance of short term load forecasting is rising with the rise of using the smart grids. This paper shows the accuracy of XGBoost and ARIMA models for short term load forecasting

---

**Keywords:** ARIMA, XGBoost, short term load forecasting

---

© 2021 Published by ECRES

# ESS INFLUENCE INVESTIGATION ON THE OPERATION OF CRITICAL NETWORK NODES

Virginijus Vasylius

Kaunas University of Technology, Kaunas, virginijus.vasylius@ktu.edu, ORCID: 0000-0002-6734-505X

*Cite this paper as:*

*Vasylius, V. ESS influence investigation on the operation of critical network nodes. 9th Eur. Conf. Ren. Energy Sys. 21-23 April 2021, Istanbul, Turkey*

---

**Abstract:**

The growing number of renewable energy sources is causing various difficulties for the operation of the electricity transmission network, its security and reliability. As a result, there is a growing perception that energy storage systems (ESS) can be one of the tools to address these challenges. This investigation focuses on the application of optimization methodology for energy storage systems influence on the operation of critical transmission network elements. The investigation presents a methodological approach and application to the IEEE 24-bus system. Using the above-mentioned simplified power system, the principle based on optimal power flow modeling and nonlinear programming to find critical elements are analyzed and critical elements for a selected period are indicated. After selecting the optimal location of the ESS in the transmission network, the influence of ESS on the operation of the mentioned critical elements is also investigated. The results of the analysis show that proper site selection in the ESS can significantly facilitate the operation of the system and enhance its security and reliability

---

**Keywords:**

*Optimal power flow, energy storage system, critical elements protection*

---

© 2021 Published by ECRES

# APPLICATION OF PEMFC ELECTRICAL FLUCTUATION FOR IN-SITU DIAGNOSTICS

Evgenii Denisov

Kazan National Research Technical University named after A.N. Tupolev-KAI, Kazan, Russia, genia-denisov@yandex.ru,  
ORCID: 0000-0001-9677-8375.

*Cite this paper as:*

*Denisov, E. Application of PEMFC electrical fluctuation for in situ diagnostics. 9th Eur. Conf. Ren. Energy Sys. 21-23 April 2021, Istanbul, Turkey*

---

**Abstract:**

PEMFC stays one of the most perspective power sources for wide range of applications from small portable electronics to power plants. Due to principles of operation, they need complex control and diagnostic systems. The technical difficulties here is related with the fact that the information difficult to measure (MEA humidification, current distribution, etc.) is required for correct and reliable operation. Furthermore, the most of existing methods require interruption or perturbation of operating modes. Last years, new method based on electrical fluctuation analysis are developing. The existing works shows possibilities to detect excess and insufficient humidification, nonhomogeneous current distribution for single cells and stacks. Most of the experiments were carried in laboratory environment and question concerning in-situ diagnostics for real application are still open. The work considers effective adaptation of such approaches for real applications. It was found that the main obstacle is related with interferences generated by power supply networks, variative load and PWM-controllers. It has been established, that in case of small impact, the influence of the mentioned could be reduced by means of correct tuning of frequency ranges of measuring channels, while in case of large impact, the original methods based on relaxation processes analysis are more preferable.

---

**Keywords:**

*PEMFC, fuel cells, electrical fluctuation, noise, technical diagnostics*

---

© 2021 Published by ECRES

# HIGH STRENGTH AND LIGHTWEIGHT STEEL PROFILES USED IN THE INSTALLATION OF PHOTOVOLTAIC SYSTEMS

Hakan Erçay

Özkan Iron and Steel Industry, Izmir, Turkey, hakan.ercay@ozkansteel.com, ORCID: 0000-0002-3858-4246

Celal Erkal Kahraman

Özkan Iron and Steel Industry, Izmir, Turkey, celal.kahraman@ozkansteel.com, ORCID: 0000-0003-0291-6971

Tuncay Dikici

Dokuz Eylul University, Torbali Vocational School, Izmir, Turkey, tuncay.dikici@deu.edu.tr, ORCID: 0000-0002-7004-9788

*Cite this paper as:* Erçay, H, Kahraman, CE, Dikici, T. High Strength and Lightweight Steel Profiles Used in the Installation of Photovoltaic Systems, 9th Eur. Conf. Ren. Energy Sys. 21-23 April 2021, Istanbul, Turkey

**Abstract:** The sun is a renewable clean energy source alternative to fossil fuels, being one of the most important energy sources in the world. Solar energy has a very strategic importance in combating global climate change due to its high potential, ease of use and environmental friendliness. Photovoltaic energy continues to be a constantly growing market that is predicted to have significant impacts on global trade. Installation of such photovoltaic power systems requires expertise. Steel is the most important material used as a building material in the construction of solar energy systems. As it is known, these materials are used as carrier systems (construction) thanks to the advantages of steel such as high strength, rigidity, ductility, usability, elasticity and recyclability. Steel construction structures provide economical sizing with their behavior against dynamic loading, stability, vibrations and their performance in deflections. The structural element mainly used in such systems is steel profiles with different cross-sections. Wide flange profiles (I and H types) have been used extensively in the installation of solar energy systems until recent years. The profiles called W profiles in the American ASTM A6 standard have become one of the advantageous materials in the installation of solar energy systems in terms of strength and cost, since they are relatively lighter and stronger. In the way of reducing the installation cost of solar energy systems, the use of lighter and durable materials is also a reason for investors to choose. Our company has the production capability of light and high strength W profiles..

**Keywords:** Renewable energy, steel construction, w shape profiles

© 2021 Published by ECRES

# ASSESSMENT OF ENERGY SAVING POSSIBILITIES IN CONSTRUCTION WITH THE USE OF SOLUTIONS BASED ON RENEWABLE ENERGY SOURCES

Elżbieta Szafranko

Institute of Geodesy and Civil Engineering, Faculty of Geoengineering, University of Warmia and Mazury in Olsztyn,  
Poland, e-mail: elasz@uwm.edu.pl, ORCID: 0000-0003-1074-9317

*Cite this paper as:* Szafranko, E. *Assessment of energy saving possibilities in construction with the use of solutions based on renewable energy sources.*, 9th Eur. Conf. Ren. Energy Sys. 21-23 April 2021, Istanbul, Turkey

---

**Abstract:** Construction is a branch of the economy with one of the highest energy consumption rates. Energy is needed at all stages of the life cycle of construction projects. Both the production of building materials at the investment preparation stage and the execution of most processes at the implementation stage require the supply of electricity and heat. However, the biggest problem is the service life - the longest stage in the life cycle of buildings. In the European Union, about 50% of the energy consumed is spent on heating or cooling, and no major changes are forecast in this respect. However, due to the obligations resulting from the ratification of the Paris Agreement by the European Union, conventional fuels may be replaced with energy obtained from renewable sources. The use of devices that allow the use of solar, wind or earth energy can improve this situation. The article will analyze the possibility of reducing energy demand from traditional suppliers through the use of alternative renewable energy sources. Examples will show savings when using solar panels and a heat pump for a residential house and a public facility. The results of the analysis show that the use of renewable energy sources allows for a significant reduction in the demand for traditionally produced energy, and the processes themselves allow for organically harmful emissions, including CO<sub>2</sub>.

---

**Keywords:** Efficiency assessment, energy saving, methodology of assessment

---

© 2021 Published by ECRES

# AN ATTEMPT TO ASSESS THE CORRECTNESS OF ASSEMBLY AND GEOMETRY OF SOLAR PANELS USING LASER SCANNING

Elżbieta Szafranko

Institute of Geodesy and Civil Engineering, Faculty of Geoengineering, University of Warmia and Mazury in Olsztyn,  
Poland, e-mail: elasz@uwm.edu.pl, ORCID: 0000-0003-1074-9317

Joanna A. Pawłowicz

Institute of Geodesy and Civil Engineering, Faculty of Geoengineering, University of Warmia and Mazury in Olsztyn,  
Poland, e-mail: jopaw@uwm.edu.pl, ORCID: 0000-0002-1334-5361

*Cite this paper as:* Szafranko, E. Pawłowicz, JA. An attempt to assess the correctness of assembly and geometry of solar panels using laser scanning. 9th Eur. Conf. Ren. Energy Sys. 21-23 April 2021, Istanbul, Turkey

**Abstract:** Energy is an essential condition for the economic development of any society. Its use may be different, but most of all it is needed for industrial production, in transport, heating or lighting. A large part of it is used in households. Primary energy production methods are based on the use of resources such as wood, lignite and coal, oil and gas. However, the ever-increasing demand for energy and the simultaneous shrinking of fossil resources, ecological and economic considerations led to interest in other energy sources. Ecological and economic considerations indicate that an alternative solution may be the use of renewable energy sources. One of the most popular in recent years is the use of solar energy. Solar panels are the element used to use solar energy. Research shows that their proper installation, and especially maintaining the correct direction and angle of inclination, determines the achievement of the assumed parameters and optimal use of the installation. The article shows how 3D laser scanning can be used to diagnose the correct installation of panels. The results of the measurements illustrate the possibility of measuring, comparing the existing state with that assumed in the project

**Keywords:** Solar panels, 3D laser scanning, deviations from the project

© 2021 Published by ECRES

# BIOINSPIRED POLYMER MATERIALS FOR THERMAL MANAGEMENT OF HEATING AND COOLING IN BUILDINGS

Stiubianu George

Petru Poni Institute of Macromolecular Chemistry, Iasi, Romania, george.stiubianu@icmpp.ro, ORCID: 0000-0002-8439-7089

Bargan Alexandra

Petru Poni Institute of Macromolecular Chemistry, Iasi, Romania, anistor@icmpp.ro, ORCID: 0000-0002-9433-9595

Dascalu Mihaela

Petru Poni Institute of Macromolecular Chemistry, Iasi, Romania, amihaela@icmpp.ro, ORCID: 0000-0002-0278-8124

Racles Carmen

Petru Poni Institute of Macromolecular Chemistry, Iasi, Romania, raclesc@icmpp.ro, ORCID: 0000-0003-3343-9389

Bele Adrian

Petru Poni Institute of Macromolecular Chemistry, Iasi, Romania, bele.adrian@icmpp.ro, ORCID: 0000-0001-8602-5273

Tugui Codrin

Petru Poni Institute of Macromolecular Chemistry, Iasi, Romania, tugui.codrin@icmpp.ro, ORCID: 0000-0003-3680-3174

Ursu Cristian

Petru Poni Institute of Macromolecular Chemistry, Iasi, Romania, cristian.ursu@icmpp.ro, ORCID: 0000-0003-3568-920X

Cazacu Maria

Petru Poni Institute of Macromolecular Chemistry, Iasi, Romania, mcazacu@icmpp.ro, ORCID: 0000-0003-4952-5548

*Cite this paper as:* Stiubianu, G, Bargan, A, Dascalu, M, Racles, C, Bele, A, Tugui, C, Ursu, C, Cazacu, M. *Bioinspired polymer materials for thermal management of heating and cooling in buildings. 9th Eur. Conf. Ren. Energy Sys. 21-23 April 2021, Istanbul, Turkey*

---

**Abstract:**

We prepared polymer materials for dynamic thermal management by using as inspiration the fast dynamic optical color changing capabilities of the mirror comb-footed spider, replicating the capability of spiders to change the reflectance and transmittance of light in the infrared wavelength range.

The new polymer films, prepared by spin coating or doctor blading, have low cost, easily scalable implementation, and provide on-demand control of temperature. The procedure can be scaled up by using polymer spraying and metal layer deposition.

The polymer films use the versatile chemistry of silicone and styrene polymers and can actively modulate heat flux of 50 W/m<sup>2</sup> and thus lower the energy load for cooling and heating in buildings, as determined from measurements with infrared video camera. Under mechanical or electrical actuation, the polymer films can dynamically modulate 70% of the heat flux emitted by the human body, with possible integration in clothing. With global use in buildings, it would provide significant energy savings amounting to ~3% of worldwide energy consumption. The new materials developed by our team are safe for human use, can be prepared without use of volatile organic solvents, and are scalable for commercial-scale application

---

**Keywords:**

*Bioinspired, heating/cooling systems, polymer nanocomposite, thermal management, heat flux control*

© 2021 Published by ECRES

---

**Acknowledgements:**

This work was supported by a grant of the Romanian Ministry of Education and Research, CCCDI - UEFISCDI, project number PN-III-P2-2.1-PED-2019-1885, within PNCDI III (Contract 463PED/2020).

# THE IMPACT OF THE EXTERNAL ENVIRONMENT ON ENERGY CONSUMPTION IN RESIDENTIAL VENTILATION AND AIR-CONDITIONING SYSTEMS ON THE EXAMPLE OF NORTH-EASTERN POLAND

Aldona Skotnicka-Siepsiak

University of Warmia and Mazury in Olsztyn, Faculty of Geoengineering, 10-724 Olsztyn, Heweliusza 4, Poland;  
aldona.skotnicka-siepsiak@uwm.edu.pl, ORCID: 0000-0002-8576-1954

*Cite this paper as:* Skotnicka-Siepsiak, A. *The impact of the external environment on energy consumption in residential ventilation and air-conditioning systems on the example of north-eastern Poland. 9th Eur. Conf. Ren. Energy Sys. 21-23 April 2021, Istanbul, Turkey*

**Abstract:** The aim of this study was to determine the impact of the external environment on energy consumption in ventilation and air-conditioning systems. Meteorological data for 2017-2019 were analyzed and compared with typical meteorological year (TMY) data. The analysis was conducted on the example of a single-family home with a usable floor area of approximately 118 m<sup>2</sup>. Three types of ventilation and air-conditioning systems were analyzed. In the first scenario, the demand for thermal energy in the building was determined for a natural ventilation system. The second scenario involved a mechanical ventilation system coupled with a ground heat exchanger. In the third scenario, the energy demand for cooling was determined for different building orientation variants. The study revealed differences between the theoretical energy demand of HVAC systems calculated based on TMY data and real-world meteorological conditions in the three examined years. Weather conditions are beyond human control, but analyses of energy loss in natural ventilation systems support rational decisions concerning the choice of VAC systems that guarantee a healthy and comfortable indoor environment. The study demonstrated that a building's external environment, such as a ground heat exchanger, can generate significant energy savings in residential ventilation systems.

**Keywords:** Energy consumption, ventilation and air-conditioning, ground-to-air heat exchanger  
© 2021 Published by ECRES

# ANALYSIS OF THE ACTUAL AND STANDARD CONSUMPTION OF THERMAL ENERGY IN BUILDINGS

Bogacz Piotr

University of Warmia and Mazury in Olsztyn, Poland, Piotr.bogacz@uwm.edu.pl, ORCID: 0000-0003-0011-676X

*Cite this paper as:*

*Piotr, B. Analysis of the actual standard consumption of thermal energy in buildings. 9th Eur. Conf. Ren. Energy Sys. 21-23 April 2021, Istanbul, Turkey.*

---

**Abstract:**

The analyzes of the actual energy consumption in buildings have shown that they are lower than the values given in the standards. Research was carried out in 3 buildings - single-family and two multi-family buildings, heated with coal, gas and district heat. The values of the consumption of thermal energy for heating on the basis of measurement systems were recorded. The amount of heat necessary to heat the building was calculated based on the standards. The results were mixed, but in all cases showed that the amount of real energy for heating is lower than the value resulting from the standard calculations, even at higher temperatures inside the building. The values of the energy consumed were strictly dependent on the atmospheric factors, the basic parameters of which were recorded. The results indicate that the updating of the standard standards should be considered in order to better adapt them to the actual conditions. This will allow for more real consumption of thermal energy in buildings in Poland.

---

**Keywords:**

*Thermal energy, buildings, heating, standards*

---

© 2021 Published by ECRES

# DIFFERENTIAL SETTLEMENT OF PILE FOUNDATION FOR WIND TURBINE TOWER ON MULTILAYERED SUBSOIL

Dyka Ireneusz

University of Warmia and Mazury, Olsztyn, Poland, i.dyka@uwm.edu.pl, ORCID: 0000-0002-0996-264X

Jolanta Harasymiuk

University of Warmia and Mazury, Olsztyn, Poland, jolanta.harasymiuk@uwm.edu.pl, ORCID: 0000-0002-1239-0646

Cite this paper as:

*Dyka, I, Harasymiuk, J. Differential settlement of pile foundation for wind turbine tower on multilayered subsoil. 9th Eur. Conf. Ren. Energy Sys. 21-23 April 2021, Istanbul, Turkey*

---

**Abstract:**

Wind farms are a present symbol of development. They also support both climate and environmental protection. According to Wind Europe data, in 2021-25, Europe should install 105 GW of new wind farms. It is estimated that over 70% of them will come from onshore wind farms. There are many engineering issues which are important for ensuring a safe operation of a wind farm. The most difficult is the design of the foundation. Wind turbines are supported by tall tower structures that transmit loads to the ground via the foundation. The areas of wind farms location are often characterized by geotechnical conditions with a stratified profile, with soils of different geotechnical characteristics. These conditions cause the foundation on pile foundations are preferred, which transfer the load to the successive layers of soil. Our paper shows the analytical method which takes into account the interaction between pile groups in the process of transferring the loads from the structure to the soil. The paper also presents the geotechnical parameters responsible for the calculation results, the theoretical basis of the method of analyzing the settlement curve of a single pile and the calculation of the settlement of working piles in a group connected with a reinforced concrete cap. Moreover, the impact of pile arrangement on the size and load distribution of individual piles, settlement and tilting of the wind turbine tower foundation is showed in the paper. The presented method allows for a more precise, safe and optimal design of wind turbine foundation.

---

**Keywords:**

*Wind energy, pile foundation, pile arrangement, settlement.*

---

© 2021 Published by ECRES

# **FULL PAPERS**

# ESTABLISHING REDUCED THERMAL MATHEMATICAL MODEL (RTMM) FOR A SPACE EQUIPMENT

Mustafa Akbulut

TÜBİTAK Marmara Araştırma Merkezi, 41470, Gebze, Kocaeli, Turkey, mustafa.akbulut@tubitak.gov.tr, ORCID: 0000-0003-4820-7601

Zafer Karadayı

RUTE, TUBITAK, Kocaeli 41470, Gebze, Kocaeli, Turkey, zafer.karadayi@tubitak.gov.tr, ORCID: 0000-0002-7612-6860

Ahmet H. Ertaş

Department of Mechanical Engineering, Faculty of Engineering & Natural Sciences, Bursa Technical University, Bursa 16330, Turkey, ahmeth.ertas@btu.edu.tr, ORCID: 0000-0002-6253-7597

*Akbulut, M, Karadayı, Z, Ertaş, HA. Establishing Reduced Thermal Mathematical Model (RTMM) For A Space Equipment. 9<sup>th</sup> Eur. Conf. Ren. Energy Sys. 21-23 April 2021, Istanbul, Turkey*

**Abstract:** In thermal design process of many space equipment, instead of a full FEM model, a reduced thermal mathematical model (RTMM) is devised in order to save computational time and CPU usage. In this method, an attempt is made to find out the interface temperatures instead of fully determining the temperature distribution of the whole body or the complete structure. In this Study, A reduced thermal mathematical model was established for a lithium -Ion battery package. In four node RTMM, The distribution of heat flux among the nodes were computed by means of an iterative procedure in which an optimization algorithm known as Particle Swarm Optimization (PSO) was employed. In the RTMM, experimental temperature distributions achieved through Thermal Vacuum Test were used.

**Keywords:** *Reduced thermal mathematical model (RTMM), lithium-ion battery, optimization, particle swarm optimization (PSO).*

© 2021 Published by ECRES

## 1. INTRODUCTION

In Many space equipment consists of various sub components that dissipate or absorb heat to and from surrounding environment. In all these equipment, there are various sorts of sensitive devices, which can be affected negatively. In this respect, a need arises to find out the temperature of certain locations in the space structure as a whole or within an individual equipment. In this study, the interface temperatures of a satellite battery are computed through a reduced thermal mathematical model (RTMM).

Satellite batteries like many other lithium based counterparts are equipped with battery management systems (BMS) which include electronic components inevitably inducing high rate of heat dissipation. In a battery cell, heat is also generated by two other ways; i.e. entropy change from electrochemical reactions and secondly Joule's effect (or ohmic heating) caused by current transfer across internal resistances [1]. The rate at which heat is generated in a cell can be calculated from [2]: At this point a need arises to take the temperature of the components under control. In thermal analysis [3] of battery packs, conduction and convection are mainly taken into consideration. However in space equipment, except for closed loop cooling, convection does not exist. When excessive temperatures occur in undesired locations, necessary precautions are taken to remove heat through conduction and radiation heat transfer [4]. There are various approaches and commercial packages in literature such as MCRT (Monte Carlo Ray Tracing) method [5] Thermica by Jacquiqau and Noel [6] to analyze the heat transfer phenomenon in similar systems. This software are handy tools to precisely calculate the thermal radiative heat transfer conductances in the space applications.

A simplification approach is taken for the thermal model, if the equipment has a small number of components. In this case, it can be directly used the RTMM (Reduced Thermal Mathematical Model), however, in cases of a multi component equipment it is difficult to establish the RTMM directly.

Since the equipment involved in this study is a simple device consisting of battery cells and BMS, the RTMM is achieved with the help of only four nodes without resorting to a commercial package of any kind. All the calculations are carried out by a specially prepared Matlab script file.

## 2. PROCEDURE FOR THERMAL REDUCTION:

In Figure 1, the solid modeling of the lithium-ion battery pack considered is given. In this model, there are a battery management unit at the top, the cells area and the base structure. In the early steady-state thermal analysis, it was found that very high temperature gradients occur around the PCB cards of the Battery Management System (BMS) and the cells area. Another important location in the Battery pack is the contact area between satellite base and the bottom of the pack, therefore the four node interface temperature locations were selected as illustrated in Figure 2.

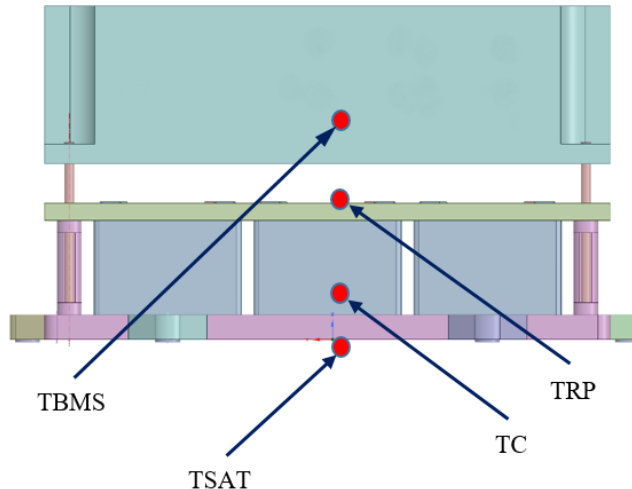


Figure 1. Solid model representation of the battery and RTMM nodes

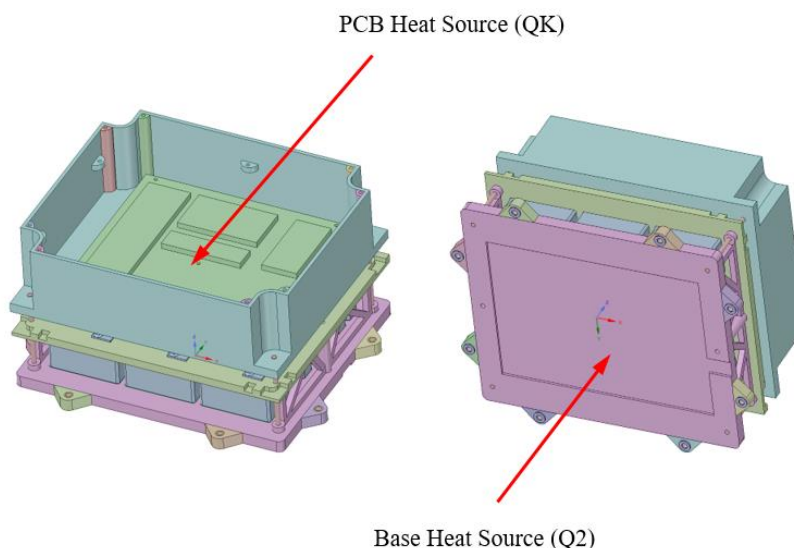


Figure 2. Heat Source Application Areas

The symbolic representation of the four-node RTMM is presented in Figure 3. In the representation, TK is a location right on the bottom PCB card, TRP is a reference point at the cells top, and TH2 is another reference point at the cells bottom.

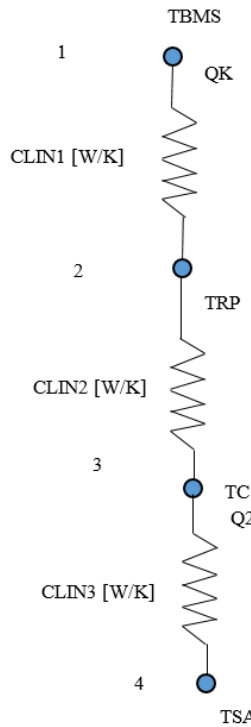


Figure 3. The symbolic representation the four-node RTMM

In Figure 3, CLIN1 [W/K]  $\Rightarrow$  K12A1/L1, CLIN2 [W/K]  $\Rightarrow$  K23A2/L2, CLIN3 [W/K]  $\Rightarrow$  K34A3/L3 represent conduction between node 1 and node 2, node 2 and node 3, and node 3 and node 4, respectively. The corresponding conservation of energy equations for nodes 1, 2, and 3 can be given as the following:

$$m_1 c_1 \frac{\Delta T}{dt} = Q_K * \eta + \frac{k_{12} A_1}{L_1} (T_{RP} - T_{BMS}) \quad (1)$$

$$m_2 c_2 \frac{\Delta T}{dt} = Q_2 * \lambda + Q_K * (1 - \eta) - \frac{k_{12} A_1}{L_1} (T_{RP} - T_{BMS}) + \frac{k_{23} A_2}{L_2} (T_C - T_{RP}) \quad (2)$$

$$m_3 c_3 \frac{\Delta T}{dt} = Q_2 * (1 - \lambda) - \frac{k_{23} A_2}{L_2} (T_C - T_{RP}) - \frac{k_{34} A_3}{L_3} (T_C - T_{SAT}) \quad (3)$$

In the steady-state case, the time-dependent terms are taken zero and the equations are reconfigured in the matrix form as follows;

$$\begin{bmatrix} T_{RP} - T_{BMS} & 0 & 0 \\ -(T_{RP} - T_{BMS}) & T_C - T_{RP} & 0 \\ 0 & -(T_C - T_{RP}) & -(T_C - T_{SAT}) \end{bmatrix} * \begin{bmatrix} \frac{k_{12} A_1}{L_1} \\ \frac{k_{23} A_2}{L_2} \\ \frac{k_{34} A_3}{L_3} \end{bmatrix} = \begin{bmatrix} -Q_K * \eta \\ -Q_2 * \lambda - Q_K * (1 - \eta) \\ -Q_2 * (1 - \lambda) \end{bmatrix} \quad (4)$$

$$[T] * [K] = [Q] \quad (5)$$

$$[K] = [T]^{-1} * [Q] \quad (6)$$

### 3. THERMAL VACUUM TEST AND EXPERIMENTAL SET UP

#### 3.1 Test Description and Approach

The thermal balance test aims to provide a time-independent temperature distribution under certain boundary conditions, the heat emitted by the Li-Ion battery, and operating conditions to match the distribution with the analysis results. The test procedure here has been prepared based on the thermal balance test procedures [7].

#### 3.2 Test Set-Up

In the experiments, the same test setup is used for the cases given in Table 1. Test setup for thermal balance is given in Figure 4. First, after the heaters is placed on the Li-Ion battery, thermocouples are attached to the specified places.

After the equipment is placed in the thermal vacuum cabinet, it is closed and vacuumed. Scenarios for Steady-State Balance for Li-Ion Battery Pack is given in Table 1

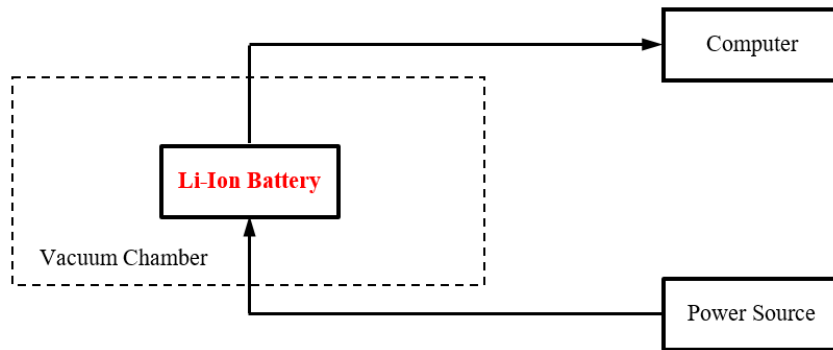


Figure 4. Schematic Illustration of Li-Ion battery thermal stability test setup

Table 1: Scenarios for Steady-State Balance for Li-Ion Battery Pack

Scenario #	Initial Temperature (°C)	1 <sup>st</sup> Heater Power (W)	2 <sup>nd</sup> Heater Power (W)	3 <sup>rd</sup> Heater Power (W)
TB1	-10	15	4	2
TB2	-10	8	4	2
TB3	-10	0	4	2
TB4	0	15	4	2
TB5	0	8	4	2
TB6	0	0	4	2
TB7	30	0	4	2
TB8	40	0	4	2

In each scenario case, initial temperatures and heat fluxes applied to the pack are different. Apart from this, the thermal load sharing coefficients  $\eta$  and  $\lambda$  are not known. An optimization procedure has been developed using the particle swarm optimization (PSO) algorithm for their determination. PSO algorithm is a kind of swarm intelligence techniques, which are inspired by the social behavior of flocking animals such as swarms of birds or fish school. This population based stochastic optimization algorithm was first developed by Eberhart and Kennedy [8]. The approach can be considered as a distributed behavioral algorithm that operates as a multi-dimensional search. Flow Chart of the developed Algorithm is given in Figure 5.

Heat Load Distribution are given in the following equations:

$$Q_1 = -Q_K * \eta \quad (7)$$

$$Q_2 = -Q_2 * (1 - \lambda) - Q_K * (1 - \eta) \quad (8)$$

$$Q_3 = -Q_2 * \lambda \quad (9)$$

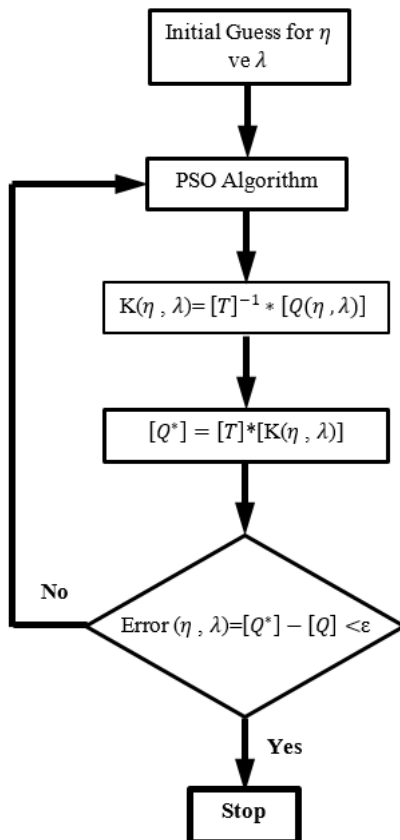


Figure 1. Optimization Procedure Developed to Find Heat Load Distribution over Nodes

#### 4. RESULTS

In order to determine conductance values, the steady-state balance scenarios given in Table-1 were used. As can be seen from the developed code, in each run, a couple of two scenarios were employed to minimize the error calculated between the heat source distributions. The results are presented in Table 2.

Table 2: The Calculated Conductance Values between Nodes

# of employed Scenarios	K12A1/L1	K23A2/L2	K34A3/L3	$\eta$	$\lambda$	Error
TB5-TB7	0.04414	11.8624	2.6105	0.9999	0.0886	4.164
TB2-TB8	0.04413	10.2843	2.6107	0.9996	0.05698	5.28
TB3-TB6	0.03162	10.9980	2.7726	0.7162	0.000002	3.20
TB1-TB4	0.03985	8.6543	2.6661	0.9027	0.000003	1.21

In each run, close values for conductance were obtained. Heat power distribution coefficient  $\eta$  gets closer to unity, which means there is almost no heat power sharing between node 1 and node 2. The lowest error value attained during the runs was 1.21 at which conductance values are 0.03985, 8.6543, and 2.6661 for K12A1/L1, K23A2/L2 and K34A3/L3, respectively.

In real conditions, the conductance values are temperature dependent but for simplicity here, an assumption was made and they were assumed as constant. Therefore, each scenario resulted in slightly different values. It should be also pointed out that thermocouple reading errors could contribute to conductance value differences as well.

## **5. CONCLUSIONS**

In this study a four node RTMM was established in order to find out the thermal conductance values pertaining to interface locations of a lithium Ion Battery. Since the whole equipment were shrouded by Multi-Layer Insulation (MLI), heat transfer through radiation was neglected. Various thermal balance scenarios were employed to find the conductance values. The computed conductance values were very close to each other for each case, which shows the accuracy of the procedure applied. Small deviations occur because of temperature independent conductivity assumption and thermocouple reading errors.

## **REFERENCES**

- [1]. Billy Wu, Vladimir Yufit, Monica Marinescu, Gregory J. Offer, Ricardo F. Martinez-Botas, Nigel P. Brandon, “Coupled thermal electrochemical modelling of uneven heat generation in lithium-ion battery packs” Journal of Power Sources; 2013;243: 544-554
- [2]. Yufei Chen, James W.Evans, “Thermal analysis of lithium polymer electrolyte batteries by a two dimensional model—thermal behaviour and design optimization” Electrochimica Acta,1994; 39;517-526.
- [3]. S.C. Chen, C.C. Wan, Y.Y. Wang, “Thermal analysis of lithium-ion batteries” Journal of Power Sources; 2005;140; 111-124.
- [4]. W.Walker H.Ardebili, “Thermo-electrochemical analysis of lithium ion batteries for space applications using Thermal Desktop”, Journal of Power Sources, 2014;269; 486-497.
- [5]. Howell JR. The monte-carlo method in radiative heat transfer. J. Heat Transfer 1998;120:547–60.
- [6]. acquiqau M, Noel P. Thermica user’s manual v3.2. EADS Astrium. Toulouse 2003.
- [7]. ECSS-E-ST-10-03
- [8]. Kennedy J., Eberhart RC. Particle swarm optimization. In: Proceedings of the fourth IEEE international conference on neural networks,1995. p. 1942–1948.



# DESIGN THE SUPERCONDUCTING MAGNET POWER SUPPLY FOR MEDICAL PROTON ACCELERATOR

Shengmin Pan

Institute of Plasma Physics Chinese Academy of Sciences, Hefei, China, 230031, ORCID: 0000-0003-2694-4782

Cite this paper as: Pan, SM. Design the Superconducting Magnet Power Supply for Medical Proton Accelerator. 9<sup>th</sup> Eur. Conf. Ren. Energy Sys. 21-23 April 2021, Istanbul, Turkey

**Abstract:** Proton has outstanding therapeutic advantage in the field of cancer radiation therapy because of its excellent Bragg Peak characteristics. For medical proton accelerator superconducting magnet power supply requirements, the topology is proposed based on phase-controlled rectifier and PWM active filter. By this way, low-frequency harmonics absorbed by passive filtering, and PWM active filtering device through frequency ripple to eliminate non-characteristic harmonics. Finally, MATABLE simulation proved the feasibility of the program, which provides a theoretical guidance for the power supply design. At last, the feasibility of the scheme is verified by experiments.

**Keywords:** Magnet power supply, high precision, low ripple, active filter

© 2021 Published by ECRES

## 1. INTRODUCTION

Proton therapy is a complex process of control, from the generation of protons to the arrival of beams to the tumor area for radiotherapy, which requires a series of precise fitting and control of components.

Foundation projects: HT7U superconducting tokamak nuclear fusion experimental device funding project of national “ninth five-year plan” major scientific project (ji investment (1998) no.1303); National “973” project(2008GB104000); key technical personnel of Chinese academy of sciences in 2017, document no: ren zi [2018] no.5

Shengmin Pan, nan, 1979-, Ph.D., associate research, research direction is high power pulse power technology These components form a proton therapy device. Superconducting magnet power supply is an indispensable part of medical accelerator.

With the enhancement of China’s comprehensive strength and the improvement of superconducting materials and technology, superconducting magnets have been widely used in accelerators. The proton accelerator mentioned in this paper uses superconducting coil with excellent performance as the superconducting coil to control the track of proton motion. The superconducting magnet is very sensitivity to the fluctuation of current. Excessive fluctuation of current will cause the loss of superconducting coil, which will seriously affect the normal work of the superconducting magnet and even damage the superconducting magnet.

This puts forward strict requirements on ripple, stability, precision and dynamic response ability of the output current of the superconducting magnet power supply. According to these parameters, the output current of the power supply is required to have a higher stability ( $10^{-5}$ - $10^{-4}$ ) and lower current ripple( $10^{-5}$ - $10^{-4}$ ), and should be able to quickly respond to the Quench protection. Therefore, the research of superconducting magnet power supply has important practical significance.

Taking the superconducting magnet power supply of medical proton accelerator as an example, this paper proposes the H bridge active filter circuit in parallel based on the thyristor phase-controlled rectifier and IGBT to form a high-precision DC power supply current. The thyristor phase-controlled rectifier circuit is used to realize rough current adjustment of the power supply, and the load current is adjusted with high precision by the active filter circuit. When the load is quenched, the energy stored in the superconducting magnet is fed back to the power grid through the phase-controlled rectifier circuit to ensure the safety of the load. The simulation results of MATABLE show that the system design is reasonable, the stability and precision reach the design indexes, and meet the requirements of superconducting magnet on the load power

supply. Finally, through the performance test of the power supply, the feasibility and correctness of the scheme are proved.

## 2. POWER SUPPLY TOPOLOGY

According to the parameter requirements of loaded superconducting coil:

- a)The load is large inductance:390H, Parasitic resistance:0.033ohm, maximum load current:175A, ripple is less than  $10^{-5}$ ;
- b)The tracking error is less than  $10^{-4}$ , the dynamic response is more than 0.1A/s;
- c)Stability: $10^{-5}/8h(10^{-4}/24h)$ , the accuracy is higher than  $10^{-5}$ ;

According to the above parameters, considering all kinds of power supply topology, finally put forward based on phase-controlled rectifier+ Voltage topology of parallel active filter dual structure, the scheme has fast response, small volume, the current precision and stability can be achieved by adjusting the system, the main point is that when the load is quenched, phased rectifier can be used for Quench protection.

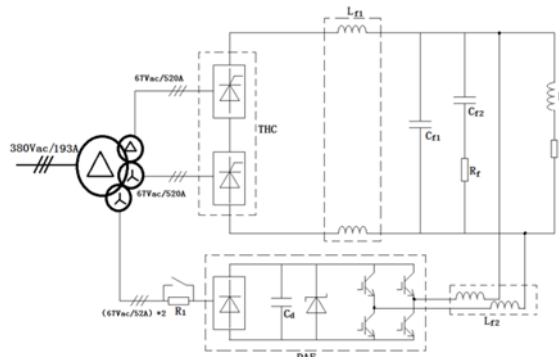


Figure 1. Power supply topology

The circuit structure of power supply topology is shown in figure 1. The whole system consists of 12 pulse phase-controlled rectifier (THC), LCR passive filter and parallel active filter (DAF). Active filter adopts H-bridge PWM circuit composed of high frequency switching device IGBT, with switching frequency of 10kHz and output carrier frequency of 20kHz.  $C_{f1}$  is to filter out the high frequency harmonics generated by PWM switching devices, and to prevent the switching devices from producing higher  $dv/dt$  added to the load to damage the superconducting coils.

Parallel damped branch is used to eliminate resonance. The power system is composed of active filter and passive filter, and the best filtering effect is achieved by using the advantages of active filter to suppress harmonic current efficiently. Meanwhile, active filter improves a fast regulating channel for current regulation. As H-bridge switching frequency is 10kHz, the lag time is about 0.05ms, which is much less than the lag time of phased-controlled rectifier (about 1.7ms), greatly shortening the system regulation time, making the actual current of the system approximate to track the given current without lag.

## 3. TRANSFER FUNCTION

The active filter is a bridge converter composed of IGBT, switching frequency  $f_s$  is 10kHz, as the system frequency is far less than  $3.14f_s$ . Therefore, the power variation cycle can be regarded as a proportional link, its adjustment time is less than that of the rectifier part, so during the dynamic adjustment process of PWM converter, it can be approximately considered that the phase-controlled rectifier part is basically unchanged. Therefore, PWM convert、passive filtering and load constitute a fast regulating system. The adjustment loop block diagram is shown in FIG.2.

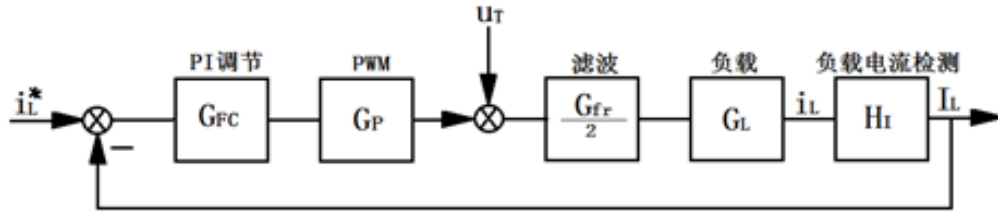


Figure 2. Active filter adjustment loop block diagram

The transfer function of this part is expressed as:

$$G_{of} = \frac{1}{2} G_p * G_{fr} * G_L H_I \quad (1)$$

PWM convert in the passband can be considered as a proportional link, taking the proportional amplification factor is 20, so

$$G_L = 1/400 s. \quad (2)$$

Load transfer function: since the load time constant is large, large inertia is approximately regarded as integral link:

$$G_L = 1/(L_L s + R_L) \approx 1/L_L s \quad (3)$$

the load inductance is 400H, therefore

$$G_L = 1/400 s \quad (4)$$

Load transfer feedback coefficient: rated maximum load current is 175A, and the detection signal at 1000A is 10V, so

$$H_I = 10/1000 = 0.01 \quad (5)$$

Determination of transfer function of passive filter link:

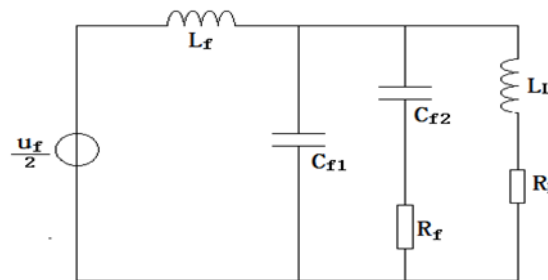


Figure 3. Passive filtering link equivalent circuit

Passive filtering link transfer function  $G_{fr}$  is a four-order link, which can be approximated to a second-order link through simulation analysis:

$$G_{fr} = \frac{\omega_2^2}{s^2 + 2\xi\omega_2 s + \omega_2^2} \quad (6)$$

Among them:  $\omega_2 = \frac{1}{[L_f C_f]^{\frac{1}{2}}}$ ;  $R_f = \frac{2}{\xi} \left[ \frac{L_f}{C_f} \right]^{\frac{1}{2}}$ ;  $L_f = L_{f1}/L_{f2}$ ;  $C_f = C_{f2}$

Bring the transfer function of each link obtained above into the formula (1), we can get:

$$G_{of} = \frac{\frac{20 \times 1}{2} \times 1 \times 10 \times 0.01}{S(T_2^2 S^2 + 2\xi T_2 S + 1)} = \frac{1}{S(T_2^2 S^2 + 2\xi T_2 S + 1)} \quad (7)$$

It can be seen from formula (7) that the amplitude-frequency characteristic of the transfer function is type of -1/-3. For such an adjustment object, the switching frequency characteristic of the system can be corrected to the typical type of -2/-1/-3 by mean of the proportion integral regulator. At this time, the open-loop transfer function of the system can be expressed as:

$$G = \frac{K(\tau_2 S + 1)}{S^2(\tau_1 S + 1)} \quad (8)$$

$K$  is the open loop gain of the system,  $\tau_1$  is the inertia link time constant, and  $\tau_2$  is the integral time constant. The transfer function of regulator is:

$$G_{FC} = K_1 \left( 1 + \frac{1}{T_1 S} \right) = K_1 \left( \frac{1 + T_1 S}{T_1 S} \right) \quad (9)$$

According to the above formula, the open-loop transfer function of the system is:

$$W_o = G_{FC} * G_P * \frac{1}{2} * G_{fr} * G_L * U_I = \frac{K_1(1 + \tau_1 S)}{T_1 S^2(T_2^2 S^2 + 2\xi T_2 S + 1)} \quad (10)$$

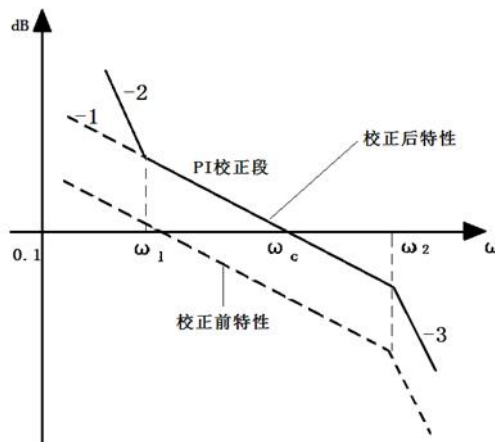


Figure 4. Open-loop amplitude-frequency characteristics of the system before and after calibration

The open-loop amplitude-frequency characteristics are shown in Fig.4, where  $\omega_2$  is the turning frequency of passive filtering environment,  $\omega_2 = \frac{1}{T_2}$ ,  $\omega_1$  is the turning frequency of PI calibration link,  $T_1 = \frac{1}{\omega_1}$ ,  $\omega_c$  is the transit frequency of the system. For a system like is, its medium bandwidth  $n = \frac{\omega_2}{\omega_1}$  has a fixed relation curve with the phase margin.  $n = 8$ , the phase margin is about  $35^\circ$ . At the same time, the system response overshoot is small, so the final choice is  $n = 8$ . Under this condition, different values of passive filter capacitor are simulated to make the current error meet the design requirements. Through simulation,  $C_{f2} = 5\mu F$ , the error satisfies this requirement. In order to prevent the filter link oscillation, we select the optimal parameters of the second-order  $\xi = 0.7$ , selected  $C_{f1} = 1600\mu F$  by simulation, so the damping branch resistance is:

$$R_f = \frac{2}{\xi} \sqrt{\frac{L_f}{C_f}} \approx 2 \quad (11)$$

So let's take  $R_f = 2$ .

The turning frequency of passive filter is:

$$\omega_L = \frac{1}{\sqrt{L_f C_f}} = \frac{1}{\sqrt{1600 \times 0.5 \times 10^{-9}}} \approx 1118(\text{rad/s}) \quad (12)$$

$$T_2 = \frac{1}{\omega_2} \approx 0.001(\text{s}) \quad (13)$$

$$G_{fr} = \frac{\omega_2^2}{s^2 + 2\xi\omega_2 s + \omega_2^2} = \frac{1}{10^{-6}s^2 + 1.4 \times 10^{-3} + 1} \approx 0.7 \quad (14)$$

The current regulating link of active filter is proportional integral (PI) regulator, and the transfer function is:

$$G_{FC} = K_1 \left( 1 + \frac{1}{T_1 s} \right) = K_1 \left( \frac{1+T_1 s}{T_1 s} \right) \quad (15)$$

For the typical -2/-1-3/ system, the open-loop gain is:

$$K = \omega_c * \omega_1 \quad (16)$$

$$\omega_1 = \frac{\omega_2}{n} = 140(\text{rad/s}) \quad (17)$$

$$T_1 = \frac{1}{\omega_1} = 0.007(\text{s}) \quad (18)$$

$$\omega_C = \sqrt{\frac{n(n-2)}{2n-1}} * \omega_1 = 250(\text{rad/s}) \quad (19)$$

So, the open-loop gain is:

$$K = \omega_C * \omega_1 = \frac{0.688K_1}{T_1} = 35000 \quad (20)$$

$K_1$  can be obtained from the above equation  $K_1 = 356(\text{rad/s})$

$$\text{So, } G_{FC} = 356 \left( 1 + \frac{1}{0.007s} \right) \quad (21)$$

### 3 MATLAB SIMULATION

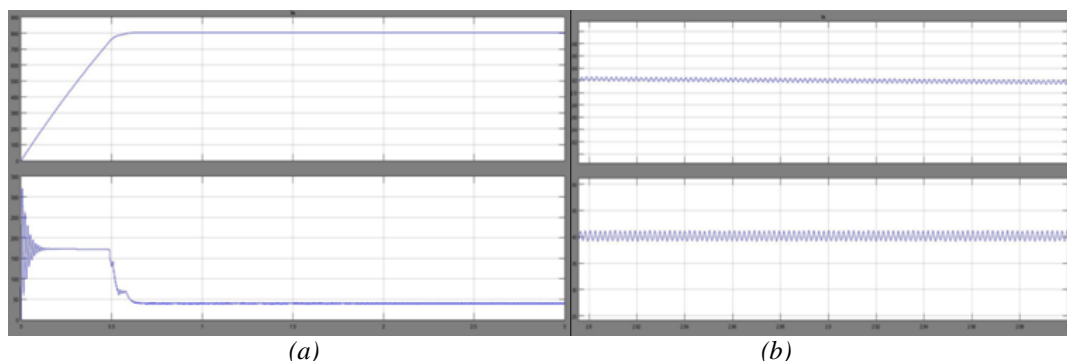


Figure 5.(a) load voltage and current waveform(b) load voltage current harmonic component

In order to develop the feasibility of the scheme, a simulation system is built by MATLAB simulation software, which measures the harmonic component of load current, voltage harmonic component and output voltage and current ripple of active filter.

FIG.5(a) shows the load voltage and current waveform when the load current ranges from 0 to 200A. It can be seen from figure that the establishment time of the current ranges from 0 to 200A is about 0.5h, meeting the design requirements of 0.1A/s.

FIG.5(b) shows the voltage waveform on the rectifier side and the voltage AC component waveform measured by the active filter. It can be seen from the figure that the ripple on the rectifier side has the same amplitude in opposite direction as the ripple on the active filter.

#### 4 EXPERIMENTAL VERIFICATION

Connect the power supply with the load so that the output current of the power supply runs in the working range. FIG.6 shows the current ripple pattern when the output current of the power supply is 175A. It can be seen from the figure that the peak value of the current ripple is less than 20mV(100mV=1mA), so the accuracy is required to meet the load design requirements. Figure.7 shows the waveform of steady-state voltage broiler. The fluctuation range of steady-state voltage and current is about 5mA, which meets the design requirements.

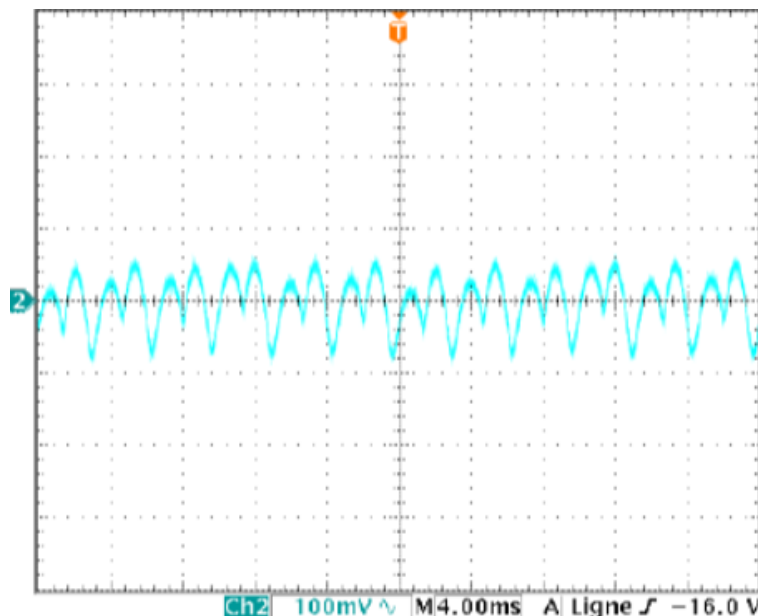


Figure 6. Current ripple waveform

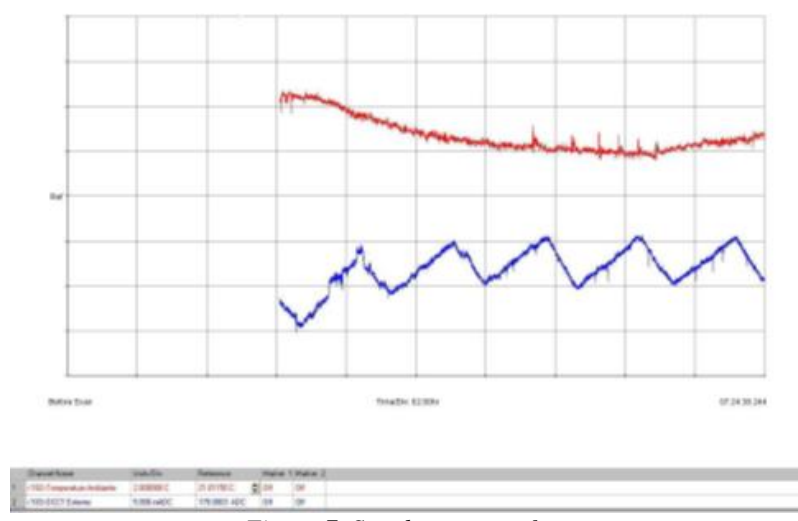


Figure 7. Steady test waveform

#### 5 CONCLUSION

In the paper, the magnet power supply for medical proton accelerator is designed, and the open-loop transfer function and closed-loop transfer function of the topological structure of the power supply are given through theoretical analysis, and the PID feedback adjustment parameters are given through theoretical analysis. Finally, through the experimental verification, the experimental test results are the same as the simulation

results. The design of the power supply completely meets the design requirements, providing a strong support for the construction of medical proton accelerator.

## **REFERENCES**

- [1]X Zhang, Y Wang, H Dang. Research on High-precision Power Supply with Synchrotron Superconducting Magnet[J]. Electric Drive, 2010,40(10):49-53.
- [2]Z Xu, F Wang, X Qi. Experimental Studies on Sub-Harmonic Suppression of Magnet Power Supply[J]. High Energy Physics and Nuclear Physics, 2003, 27(7): 637-640.
- [3]EL Refaie AM. Fractional-slot concentrated-windings synchronous permanent magnet machines: opportunities and challenges[J]. IEEE Transactions on Industrial Electronics, 2010, 57(1): 107-121.
- [4]Y Deng. Research on Suppression of Magnet Power Supply[J]. Shipboard Electronic Warfare, 2003, 26(4): 46-48.
- [5]W Wu, Y Wang, J Wang. Study of the power supply topology with high stability for accelerator[J]. Nuclear Electronics and Detection Technolgy, 2005,25(3):296-301.
- [6]J Li, X Ruan. Hybrid Control Strategy of Full Bridge LLC Converters[J]. Transactions of China Electrotechnical Society,2013,28(4):72-78.
- [7]X Jiao, L Jing, etc. Design of digital adjustor applied to power supply system for HIRFL-CSR[J]. High Power Laser and Particle Beams, 2011,23(1):185-189.
- [8]B Bai, D Chen, X Wang. Loss Calculation of Inverter IGBT and Design of Cooling Device[J]. Transactions of China Electrotechnical Society, 2013,28 (8) :97-106.
- [9]X Tao, H Li. Theoretical Calculation of a Long Pulse Power Supply for Linac[J]. Acta Electronica Sinica, 2006,34(12) :2319-2321.
- [10] X Qi etc. Magnet Power Supply System for China Spallation Neutron Source[J]. Power Electronics, 2014,48(12): 8-10.
- [11]Z Lv, A Luo, W Jiang, X Xu. New Circulation Control Method for Micro-Grid with Multi-Inverter Micro-Sources[J]. Transactions of China Electrotechnical Society, 2012,27 (1) : 40-47.
- [12]W Liu,W Qiao etc. Development of Magnet Power Supply Control System for Heavy Ion Accelerator[J]. Atomic Energy Science and Technology, 2015,49(2):362-365.



# POWER LOSS CALCULATION OF PHOTOVOLTAICS USING PYTHON

Kerry Sado

University of Duhok, Duhok, Iraq, kherysado@yahoo.com/ kerry.sado@uod.ac, ORCID: 0000-0002-5565-4795

Ismail Ali

University of Duhok, Duhok, Iraq, ismail@uod.ac, ORCID: 0000-0001-6684-2399

Lokman Hadi

University of Duhok, Duhok, Iraq, lokman.hadi@uod.ac. email address, ORCID: 0000-0001-8982-7482

Shivan Sado

University of Nebraska-Lincoln Lincoln, NE, USA shivansado@yahoo.com/ssado2@unl.edu, ORCID: 0000-0003-2403-8647

Cite this paper as:

Sado, K, Ali, I, Hadi, L, Sado,S. Power loss calculation of photovoltaics using Python. 9th Eur. Conf. Ren. Energy Sys. 21-23 April 2021

---

**Abstract:**

In this report, a PV system modeling software package, PVLib, is used to calculate the power loss of PV modules from partial shading. In-order to calculate the power loss of modules from partial shading, the IV curves for individual cells should be calculated, by solving the single diode IV curve. Different Python libraries are used and imported in this report. Brief introduction to the background of each library is introduced, steps of adding an external package to Python are also mentioned.

---

**Keywords:**

Python, PV cell, Solar Panel, renewable energy

---

© 2021 Published by ECRES

## 1. INTRODUCTION

Although the PV cell is the primary power generation unit, since module-level parameters are much more accessible and it greatly decreases the computational scope of the simulation, PV modeling is mostly performed for convenience at the module level. Module-level simulations, though, are too coarse to be able to simulate results such as mismatch of cell to cell or partial shading. This example measures IV curves at cell level and combines them to recreate the IV curve at module level. It uses this approach to find the maximum power under various shading and irradiance conditions. Flexibility of modeling is useful in designing, organizing, the performance of photovoltaic panels and predicting them. Currently, A range of software packages are available that can be used to model PV Systems' performance, for both commercial and educational purposes. However, most of these simulation programs have limitations. For starters, users often have limited access to algorithms and assumptions used in simulation programs such as PVSyst and PVSol [1]. Users often find it difficult to simulate more sophisticated systems than what the developers originally allowed. Examples of such complex systems range from multiple array orientations, differing PV panels and inverters and varied PV system designs. Some packages use default input limitations such as DC to AC power ratios and they are often not easy to modify. Bug fixing is often time-consuming in those systems, as it has to be performed by the innovative authors and then rearranged. PVLib has the ability to bridge this gap in PV system modelling. The rest of this report is organized as follows: the following section gives account of the theoretical framework of PVLib. The analyses of the results of the simulations and the conclusions will be given in the following pages.

## 2. HISTORY OF PVLIB

The PVLib toolbox is a common repository for algorithms for high-quality modeling and study of PV structures. The toolbox has the privilege of being developed and tested continually and collaboratively. This not only makes for better accuracy, but also for easier bug fixing. The code is open-source; therefore, users can freely view, easily modify and redistribute the original source code. `pvlb python` is developed on GitHub by contributors from academia, national laboratories, and private industry [2]. In this examples different Python libraries are imported, libraries like Panda, NumPy, SciPy and Matplotlib. A brief introduction to each library will be given in the following:

### Panda

The panda package is the most powerful platform accessible to today's Python-based data scientists and analysts. All of the focus can be paid to powerful machine learning and stylish visualization methods, but pandas are the foundation of most data projects. Pandas is built on top of the NumPy package, which means that Pandas uses or reproduces a lot of the NumPy structure [3]. Panda data is also used to feed SciPy statistical analysis, Matplotlib plotting functions, and Scikit-learn machine learning algorithms.

### Numpy

NumPy is a package for Python. It stands for 'Python Numeric'. It is a library consisting of objects in a multidimensional array and a set of array processing routines [4]. Using NumPy, following operations can be performed by developers:

- Mathematical and/or logical operations on arrays.
- Fourier transforms and routines for shape manipulation.
- Operations related to linear algebra. NumPy has built in functions for linear algebra and random number generation.

### Scipy

SciPy is a series of mathematical algorithms based on Python's NumPy extension and convenience functions [5]. By providing the user with high-level commands and classes to manipulate and visualize data, it adds important power to the interactive Python session. With SciPy, an interactive Python session becomes a data-processing and system-prototyping environment rivaling systems, such as MATLAB, IDL, Octave, R-Lab, and SciLab.

### Matplotlib

It is one of the most popular Python packages used for data visualization. Matplotlib provides an object-oriented API that helps in embedding plots in applications using Python GUI toolkits such as PyQt, WxPython or Tkinter [6]. It can be used in Python and IPython shells, Jupyter notebook and web application servers also

## 3. SINGLE DIODE EQUATION

In this section the solutions of single diode equation used in `pvlb-python` to generate an IV curve of a PV module will be reviewed.

`pvlb-python` supports two ways to solve the single diode equation:

1. Lambert W-Function
2. Bishop's Algorithm

### Lambert W-Function

According to Lambert algorithm, the single diode model equation can be given as [7]:

$$I = I_L - I_0 \left( \exp\left(\frac{V+IR_s}{nN_S V_{th}}\right) - 1 \right) - \frac{V+IR_s}{R_s h} \quad (1)$$

Lambert W-function is the inverse of the function

$$f(w) = w \exp(w)$$

Defining the following parameter, z, is necessary to transform the single diode equation into a form that can be expressed as a Lambert W-function

$$z = \frac{R_s I_0}{n N s V_{th} \left( 1 + \frac{R_s}{R_{sh}} \right)} \exp \left( \frac{R_s (I_L + I_0) + V}{n N s V_{th} \left( 1 + \frac{R_s}{R_{sh}} \right)} \right) \quad (2)$$

where,

$I_L$ : Is the light current (A)

$I_D$ : reverse saturation current of the diode (A)

$R_s$ : series resistance ( $\Omega$ )

$R_{sh}$ : shunt resistance ( $\Omega$ )

$n$  : ideality factor of the diode (unitless)

Then Lambert W-function,  $W(z)$  can be used to solve the current.

$$I = \frac{\frac{I_L + I_0 - V}{R_{sh}}}{1 + \frac{R_s}{R_{sh}}} - \frac{n N s V_{th}}{R_s} W(z) \quad (3)$$

### Bishop's Algorithm

This algorithm uses an explicit solution that finds points on the IV curve by first solving for  $(V_d, I)$  where  $V_d$  is the diode voltage  $V_d = V + I * R_s$ . Then the voltage is backed out from  $V_d$ . Points with specific voltage [8][9], such as open circuit, can be given by:

$$V_{oc,est} = n N s V_{th} \log \left( \frac{I_L}{I_0} + 1 \right) \quad (4)$$

It's known that  $V_d=0$  corresponds to a voltage less than zero, and we can also show that when  $V_d=V_{oc,est}$ , the resulting current is also negative, meaning that the corresponding voltage must be in the 4th quadrant and therefore greater than the open circuit voltage (proof below) [10]. Therefore, the entire forward-bias 1st quadrant IV-curve is bounded because  $V_{oc} < V_{oc,est}$ .

$$\begin{aligned} I &= I_L - I_0 \left( \exp \left( \frac{V_{oc,est}}{n N s V_{th}} \right) - 1 \right) - \frac{V_{oc,est}}{R_{sh}} \\ I &= I_L - I_0 \left( \exp \left( \frac{n N s V_{th} \log \left( \frac{I_L}{I_0} + 1 \right)}{n N s V_{th}} \right) - 1 \right) - \frac{n N s V_{th} \log \left( \frac{I_L}{I_0} + 1 \right)}{R_{sh}} \\ I &= I_L - I_0 \left( \exp \left( \log \left( \frac{I_L}{I_0} + 1 \right) \right) - 1 \right) - \frac{n N s V_{th} \log \left( \frac{I_L}{I_0} + 1 \right)}{R_{sh}} \\ I &= I_L - I_L - \frac{n N s V_{th} \log \left( \frac{I_L}{I_0} + 1 \right)}{R_{sh}} \\ I &= I_L - I_0 \left( \frac{I_L}{I_0} \right) - \frac{n N s V_{th} \log \left( \frac{I_L}{I_0} + 1 \right)}{R_{sh}} \\ I &= - \frac{n N s V_{th} \log \left( \frac{I_L}{I_0} + 1 \right)}{R_{sh}} \end{aligned} \quad (5)$$

## 4. CALCULATING A MODULE'S IV CURVES

Multiple methods are used to calculate the electrical parameters for an IV curve of a solar PV cell at a certain irradiance and temperature by using the module's base characteristics at standard test conditions (STC) conditions. Afterwards those electrical parameters are used to calculate the module's IV curve by solving the single-diode equation using the Lambert W method.

The single-diode equation is an equivalent electrical circuit (see Figure 1 ) model of a PV cell with five electrical parameters that depend on the operating conditions[11][12].

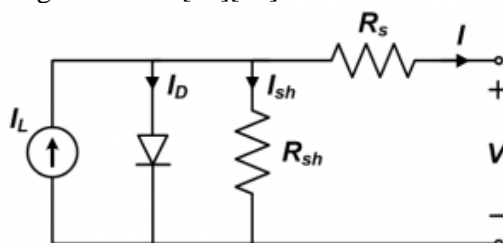


Figure 1 Equivalent circuit for a single solar cell [13]

To calculate the five electrical parameters of a single diode model we will use `pvlib.pvsystem.calcpars_desoto()` which is imported from Pvlib package, then we use `pvlib.pvsystem.singlediode()` to generate the IV curves. Modules reference parameters used i.e., the parameters at STC, these parameters are:

#### Parameters:

- **effective\_irradiance** (numeric) – The irradiance ( $\text{W/m}^2$ ) that is converted to photocurrent.
- **temp\_cell** (numeric) – The average temperature of a cells within a module, measured in C.
- **alpha\_sc** (float) – The temperature coefficient of short-circuit current of the module in units of A/C.
- **a\_ref** (float) – The product of the normal diode ideality factor (n, unitless), quantity of cells in series (Ns), and cell thermal voltage at STC, in units of V.
- **I\_L\_ref** (float) – The light-generated current (or photocurrent) at STC, measured in amperes.
- **I\_o\_ref** (float) – The dark or diodes reverse saturation current at STC, measured in amperes.
- **R\_sh\_ref** (float) – The value of shunt resistance at STC, in ohms.
- **R\_s** (float) – The value of series resistance of the cell at STC, in ohms.
- **EgRef** (float) – Energy bandgap at reference temperature in units of eV. 1.121 Ev.
- **dEgdT** (float) – Temperature dependence of the energy bandgap at stc in units of 1/K.
- **irrad\_ref** (float (optional, default=1000)) – Reference solar irradiance in  $\text{W/m}^2$ .
- **temp\_ref** (float (optional, default at STC=25)) – Reference temperature of the cell measured in C.

Then the function returns Tuple of the following results:

- **photocurrent** (numeric) – Light-generated current measured in amperes
- **saturation\_current** (numeric) – Diode saturation current in amperes
- **resistance\_series** (float) – Series resistance in ohms
- **resistance\_shunt** (numeric) – Shunt resistance in ohms
- **nNsVth** (numeric) – The product of the usual diode ideality factor (n, unitless), number of cells in series (Ns), and cell thermal voltage at specified effective irradiance and cell temperature.

Parameters for a PV module available in the lab are used, Python codes for adjusting the reference parameters according to STC are used. The IV curve is shown in Figure 2 below:

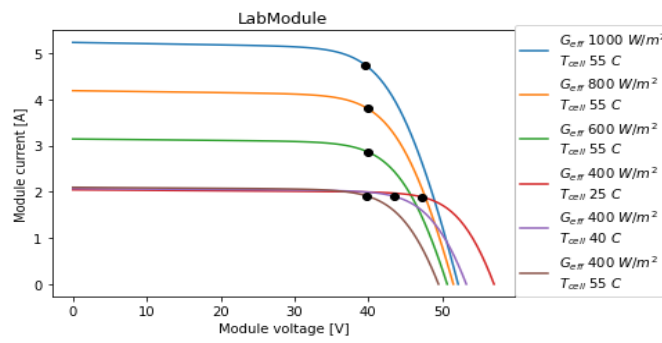


Figure 2 SD IV curve

The above figure shows the effect of both Irradiance and cell temperature on the current and voltage of the cell, the dotted points at the knee of the curve are the values of current and voltage at maximum power point (MPP).

## 5. PARTIAL MODULE SHADING

For simplicity PV modelling is often done at the module level because it reduces the computational scope of the simulation. However, these types of simulations are poor to be able to module cell to cell partial shading. In this report cell-level IV curves are calculated and then combined to reconstruct the module-level IV curves. The module-level IV curves are used to find the maximum power of each cells combined under different shading and irradiance conditions. During the simulation we assume that shading only applies to beam irradiance (i.e., the same amount of diffuse irradiance is received by all cells) and the temperature of a cell is uniform and not affected by cell-level irradiance variation. The same parameters of the PV cell used previously in this report are assumed for calculating the shading effects on the module. First, IV curves for individual cells are calculated, the process is as follows:

- A single-diode model with given set of cell parameters at STC is used to calculate the single diode equation parameters for the cell at the operating conditions. De Soto model is used via `pvlib.pvsystem.calcpars_desoto()`.
- In order to calculate reverse bias characteristic in addition to the forward characteristic of a single diode module Bishop '88 method (`pvlib.singlediode.bishop88()`) is used from Pvlib, this method This gives us a set of (V, I) points on the cell's IV curve.

- After calculating cell-level IV curves, then we compare a fully-irradiated cell's curve to a shaded cell's curve. One important points should be noted that shading typically does not reduce a cell's irradiation to zero – tree shading and row-to-row shading block the beam portion of irradiance but leave the diffuse portion largely intact. In this simulation plot, we assume that the shaded cell receives 350W/m<sup>2</sup> as the amount of irradiance.

Figure 3 shows the IV curve for both forward and reverse biased cell with Full-sun (i.e., Irradiation is 1000W/m<sup>2</sup>) cell and for shaded cell (i.e., Irradiation is 350W/m<sup>2</sup>)

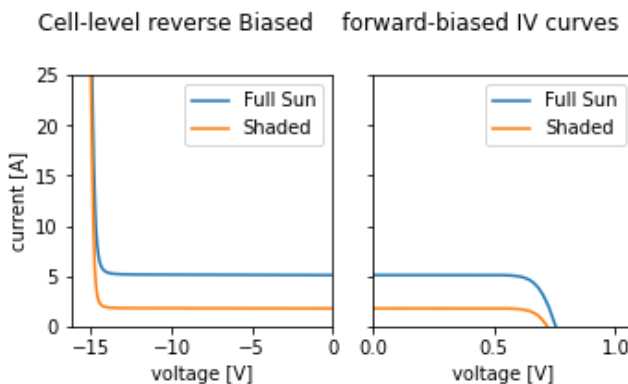


Figure 3 IV curve of Full-Sun and Shaded cell

The above figure shows that a cell's current decreases roughly in proportion to the reduction in irradiance from shading, but voltage changes much less, comparing to Figure 2, the voltage changes proportionally with the temperature of the cell. It concluded from the above figure that the effect of shading is shifting the I-V current down to lower currents rather than change the curve's shape. I-V curves from Cell-Level simulation are combined to create a module I-V curve, cells in each substring are added in series, and the substrings are also connected in series and have a parallel bypass diode to protect from reverse biased voltages. Each module has 72 cells connected in series and normal crystalline silicon cell reaches only ~0.6V in forward bias, for convenience we will only assume that there are three types of cells (fully irradiated, fully shaded, and partially shaded), also it is assumed that the rest of the cells will behave identically within each of the three mentioned cell types. For simulation purpose we assume that the bottom 10% of the module is shaded. Assuming 12 cells per column, that means one row of cells is fully shaded and another row is partially shaded. Even though only 10% of the module is shaded, the maximum power is decreased by roughly 80%. Without using bypass diodes, operating the shaded module at the same current as the fully irradiated module would create a reverse-bias voltage of several hundred volts. Yet, the diodes prevent the reverse voltage from exceeding 1.5V (three diodes at 0.5V each). Module-Level IV curves are shown in Figure 4.

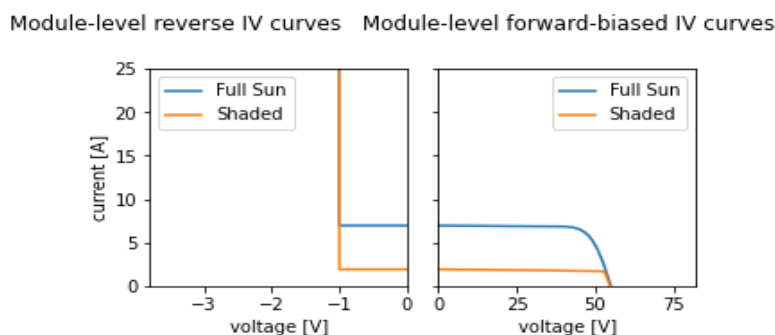


Figure 4 Module-Level IV curves

## 6. CONCLUSION

In this report, a PV system modeling software package, PVLib, is used to calculate the power loss of PV modules from partial shading. In order to calculate the power loss of modules from partial shading, the IV curves for individual cells are calculated, by solving the single diode IV curve, then combined to create the IV curve of module-based system. It is concluded that using Python to investigate the performance of Photovoltaic cells is efficient in terms of time consuming when comparing with other simulation programs.

## **REFERENCES**

- [1] S. Ransome, J. Stein, W. Holmgren, J. Sutterlueti, T. Pvpmc, and P. V Performance, "PV PERFORMANCE MODELLING WITH PVPMC / PVLIB Introduction to PVPMC / PVLIB Why do we need the PVPMC ? Introduction to Python PVLIB - Open Source Toolbox Contributing to PVLIB PVPMC Website contents : PV performance Modelling steps Running PVLIB Python scri," pp. 2–5.
- [2] W. F. Holmgren, C. W. Hansen, and M. A. Mikofski, "Pvlib Python: a Python Package for Modeling Solar Energy Systems," *J. Open Source Softw.*, vol. 3, no. 29, p. 884, 2018, doi: 10.21105/joss.00884.
- [3] W. McKinney and P. D. Team, "Pandas - Powerful Python Data Analysis Toolkit," *Pandas - Powerful Python Data Anal. Toolkit*, p. 1625, 2015.
- [4] N. Community, "NumPy User Guide 1.19," p. 214, 2020.
- [5] SciPy Community, "SciPy Reference Guide 0.7," p. 1229, 2013.
- [6] L. Wall *et al.*, "About the Tutorial Copyright & Disclaimer," p. 2, 2015, doi: 10.1017/CBO9781107415324.004.
- [7] R. M. Corless, G. H. Gonnet, D. E. G. Hare, D. J. Jeffrey, and D. E. Knuth, "On the Lambert W function," *Adv. Comput. Math.*, vol. 5, no. 1, pp. 329–359, 1996, doi: 10.1007/bf02124750.
- [8] J. W. Bishop, "Computer simulation of the effects of electrical mismatches in photovoltaic cell interconnection circuits," *Sol. Cells*, vol. 25, no. 1, pp. 73–89, 1988, doi: [https://doi.org/10.1016/0379-6787\(88\)90059-2](https://doi.org/10.1016/0379-6787(88)90059-2).
- [9] A. Izadian, A. Pourtaherian, and S. Motahari, *Basic model and governing equation of solar cells used in power and control applications*. 2012.
- [10] C. Hansen, *Parameter Estimation for Single Diode Models of Photovoltaic Modules*. 2015.
- [11] K. A. Sado, L. H. Hassan, and M. Moghavvemi, "Design of a PV-powered DC water pump system for irrigation: a case study," in *2018 53rd International Universities Power Engineering Conference (UPEC)*, 2018, pp. 1–6, doi: 10.1109/UPEC.2018.8542072.
- [12] K. A. Sado and L. H. Hassan, "Modeling and Implementation of a PV-powered DC Water Pump System for Irrigation in Duhok City," *Acad. J. Nawroz Univ. Vol 7 No 4 (2018)DO - 10.25007/ajnu.v7n4a294*, Dec. 2018, [Online]. Available: <http://journals.nawroz.edu.krd/index.php/ajnu/article/view/294>.
- [13] V. Tamrakar, S. C. Gupta, and Y. Sawle, "Single-Diode Pv Cell Modeling And Study Of Characteristics Of Single And Two-Diode Equivalent Circuit," *Electr. Electron. Eng. An Int. J.*, vol. 4, pp. 13–24, Aug. 2015, doi: 10.14810/elelij.2015.4302.



# TECHNO-ECONOMIC FEASIBILITY ANALYSIS OF PV POTENTIAL WITH PASSIVE COOLING IN THE DESERT CLIMATE

AlAmri Fahad

Department of Mechanical and Energy Engineering, College of Engineering, Imam Abdulrahman Bin Faisal University, P.O. Box 1982, Dammam, KSA; fgalamri@iau.edu.sa, ORCID:000-0001-6132-9043

AlZohbi Gaydaa

Department of Mathematical and Natural Sciences, Prince Mohammad Bin Fahd University, P.O. Box 1664, Al Khobar, Kingdom of Saudi Arabia; ghizoh\_m@htmail.com, ORCID: 0000-0002-0697-993X

*Cite this paper as:* AlAmri, F, AlZohbi, G. 'Techno-economic feasibility analysis of PV potential with passive cooling in the desert climate' 9th Eur. Conf. Ren. Energy Sys. 21-23 April 2021, Istanbul, Turkey.

**Abstract:** Solar energy can be an efficient energy source in the Kingdom of Saudi Arabia (KSA) owing to its location on the sun-belt. However, the harsh desert climate of the Kingdom rises the temperature of the solar photovoltaic (PV) panel, which affects its efficiency. This issue can be solved by using a cooling system. This article evaluates the impact of passive cooling system on the PV panel power output in Dammam and Riyadh cities of KSA by considering an 80 kW solar panel system. Besides, techno-economic feasibility and estimation of CO<sub>2</sub> emission reduction of PV panel with and without a cooling system were carried out. The findings showed that Riyadh registered the highest energy generated by the PV panel and more efficient use of the cooling system. In addition, the use of a cooling system in the two studied cities increased the output energy of PV, decreased the payback period of the PV system, and reduced the annual CO<sub>2</sub> emission by 20.8 tons/year in Dammam and 21.73 tons/year in Riyadh.

**Keywords:** PV system; passive cooling; technical feasibility; economic feasibility.

© 2021 Published by ECRES

I.			
r	The resistance		
$\alpha$	The thermal conductivity	$\delta$	Transmissivity
$\eta_{Tref}$	Efficiency at reference test temperature	$\gamma$	Absorptivity of solar cell
A	Area	$\theta$	Angle of wind speed
$T_{ref}$	Temperature at reference test temperature	N	Number of fins
$\omega_{rf}$	Temperature coefficient at reference test temperature	$\sigma$	Stefan-Boltzmann constant
t	The thickness		<b>Subscripts</b>
L	Length	EVA	Ethylene vinyl acetate
W	Width	Ad	Adhesive material
I	Irradiance	F	Front side
Qt	Total heat flow.	B	Back side
Q2	Heat flow at the back side.	G	Glass
Q1	Heat flow at the front side.	MBC	Metal back-sheet
Ta	Ambient temperature	ARC	Anti-reflective layer
$\varepsilon_{si}$	Emissivity of silicon.	tdl	Tedlat polymer
$\beta$	Tilt angle of solar panel.	rad	Radiation
V	Wind velocity	conv	Convection
Prl	Prandtl number of air	Bs	Base of fin
Lct	Characteristic length	Hb	Heat sink base

$Nu_{fn}$	Nusselt number
$T_{\text{solar}}$	The solar panel temperature
$G_{\text{cn}}$	Critical Grashof Number
$\text{Ra}$	Rayleigh number

## 1. INTRODUCTION

The electricity in the Kingdom of Saudi Arabia (KSA) is mainly generated from fossil fuels, which causes greenhouse gas emissions. Meanwhile, the electricity consumption raised from 39,487 ktoe in 1990 to 140,709 ktoe in 2017 [2]. Moreover, It has been predicted that, between 2010 and 2028, the electricity demand in the Kingdom will increase from 40 GW up to 120 GW [3]. This increase of electricity consumption has been driven by many factors such as population and economic growth, industrialization, urban development, and desert climate. According to [4], the photovoltaic and the concentrated solar power (CSP) technologies are among the most efficient renewable energy technologies for KSA since the country is located on the Sun-belt makes it a very suitable place to use solar energy for electricity production.

The solar photovoltaic (PV) is a rapidly growing technology, which is favorable to achieve environmental and economic sustainability. Besides being clean, abundant, and cheap, the power generation is silent and requires only minimal maintenance. The transmission losses can be avoided by onsite power generation and utilization. Many environmental and installation factors such as operating temperature, irradiance, humidity, wind velocity, dust, precipitation, and tilt angle affect the efficiency and the lifespan of the PV panel. Hence, the extremely high temperature recorded in the country affects the efficiency of the PV panel. Many active and passive cooling mechanisms using air, water, and phase change materials (PCM) have been proposed to minimize the influence of high temperature on the performance of the PV system. A comparative study [8] of the different cooling techniques has found that the active techniques can achieve higher efficiency but are costlier than passive techniques. Zubeer et al. [9] showed that water spray cooling technique had a significant impact on improving the efficiency of the PV panel.

The PV potential in different cities of KSA has been studied by many researchers. Awan et al. [11] assessed the solar radiation and the efficiency of the PV system in 44 cities of KSA based on data collected over one year. They found that Tabuk province and Riyadh province were the most appropriate locations to implement solar PV.

The present paper endeavors to study the effectiveness of the PV system with and without passive cooling system to generate electricity in two different cities (Dammam and Riyadh) of KSA by using real data collected during a period of three years from 2015 to 2017. In each case, the PV power output was estimated by using the analytical model developed. In addition, a techno-economic analysis was performed to assess the profitability of the PV system to produce electricity in the two considered cities. Also, the amount of CO<sub>2</sub> emissions that can be reduced by using a PV panel with and without using a cooling system in the two studied cities was estimated. The novelty of this paper is to explore the technical, environmental, and economic aspects of using a cooling system with a PV system in harsh climates as prevailing in KSA.

## 2. MATERIALS AND METHODS

### 2.1 The study locations

The two cities considered in the present study are Riyadh and Dammam. Riyadh is the capital and the biggest city of KSA, located at the center of the Arabian Peninsula on a height of 600 m above sea level. Dammam, the third biggest city of KSA, is located in the Eastern province of KSA on the Arabian Gulf with an altitude of 10 m above sea level. Saudi Arabia is characterized by a desert climate with extremely high temperatures in summer, mild winter, and a very low annual precipitation. However, the relative humidity varies from one city to another; it is very low in Riyadh while it is very high in Dammam.

### 2.2 System description

A hybrid system of PV panels with a passive cooling system by using heat sink is considered in the current study. Figure 1 shows the layout of the PV panel with the considered cooling system. In the present study, 200 PV modules are used, and the specifications are presented in Table 1.

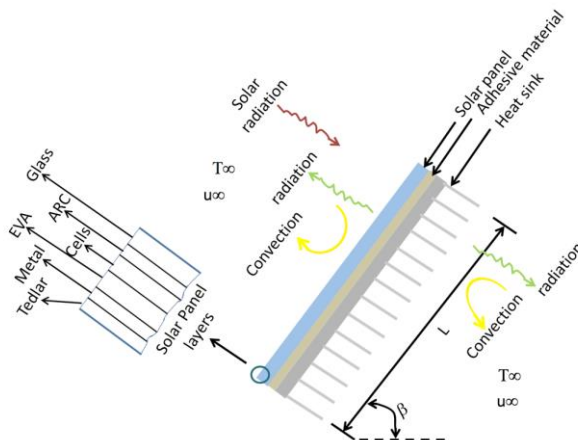


Figure 1. Configuration of the PV panel with the considered cooling system

Table 1. Modelled PV system specifications

PV module	Inverter
PV Rated Maximum Power (W)	400
Open Circuit Voltage (V)	49.58
Maximum Power Voltage (V)	41.33
Short Circuit Current (A)	10.33
Maximum Power Current (A)	9.68
Module Efficiency (%)	20
Temperature Coefficient of Isc	0.044%/°C
Temperature Coefficient of Voc	-0.272%/°C

The thermal and electrical calculations of the solar panels have been performed based on the following assumptions to simplify the analysis of the system: The solar irradiance on the solar panel is uniform, the heat transfer is steady, and the heat transfer is one-dimensional as the total thickness is small compared to its length and width.

### 2.3 Analytical model for estimating PV power

The evaluation of power output of the PV system requires an estimation of the solar panel temperature that is a function of irradiation, wind velocity, ambient temperature, tilt angle, thermos-physical properties of the components of the solar panel, and the heat sink geometry. Such a complicated problem (see the problem geometry in Figure 1) can be simplified by applying Ohm's and Kirchhoff's laws to evaluate the heat flows inside the thermal circuit of the solar panel system as shown in Figure 2, and deducing a closed-form equation for solar panel temperature [15].

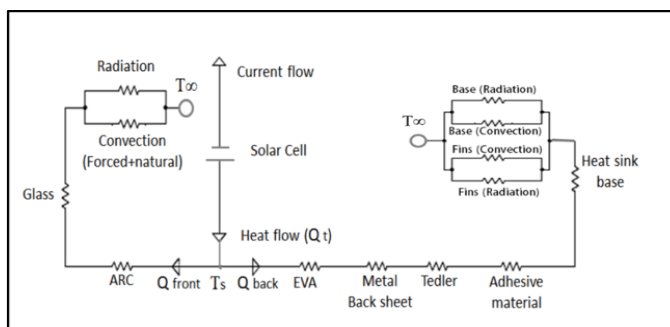


Figure 2. Thermal resistance circuit of the system.

The analytical approach and the deduced equations for solar cell temperature and output power were experimentally validated [15]. After deriving the heat flows of the front and back sides of the solar panel, the solar panel temperature can be estimated by using Eq. (1)[15].

$$T_{solar} = \frac{(I \times A \times \gamma_s \times \delta_g \times \Sigma r_f \times \Sigma r_b) \times (1 - \eta)}{(\Sigma r_f + \Sigma r_b)} + T_a \quad (1)$$

where  $r_f$  and  $r_b$  are the total resistance on the front and backside on the PV panel respectively,  $T_a$  is the ambient temperature,  $I$  is the incident light ( $\text{W/m}^2$ ),  $A$  is the solar panel area ( $\text{m}^2$ ),  $\delta_g$  is the transmissivity of the glass cover,  $\gamma_s$  is the absorptivity of the solar cell and  $\eta$  is the performance of the solar panel and it can be estimated by Eq. (2).

$$\eta = \eta_{T,\text{ref}} [1 - \omega_{rf}(T_{rf} - T_{\text{solar}})] \quad (2)$$

where  $\eta_{\text{ref}}$  is the efficiency of the solar panel at reference test temperature,  $\omega_{rf}$  is the temperature coefficient at reference test temperature and  $T_{\text{ref}}$  is the reference test temperature.

The expression of total front resistance is given by Eq. (3).

$$\Sigma r_f = r_g + r_{AR} + \frac{r_{rad(f)} \times r_{conv(f)}}{r_{rad(f)} + r_{conv(f)}} \quad (3)$$

where  $r_g$  is the resistance of the glass cover ( $\Omega$ ),  $r_{AR}$  is the anti-reflective layer resistance,  $r_{\text{rad}(f)}$  is the radiation resistance on the front surface,  $r_{\text{conv}(f)}$  is the resistance of combined (forced and natural) convection on the front surface.

The total resistance of the backside is expressed by Eq. (4).

$$\Sigma r_{th(b)} = r_{EVA} + r_{MBC} + r_{Tr} + r_{ad} + r_{hb} + \frac{r_{bs} \times r_{fs}}{r_{bs} + r_{fs}} \quad (4)$$

where  $r_{MBC}$  is the sheet back metal resistance on the solar panel resistance ( $\Omega$ ),  $r_{EVA}$  is the ethylene-vinyl acetate resistance ( $\Omega$ ),  $r_{bs}$  is the base resistance of fin for convection and radiation,  $r_{Tr}$  is the Tedlar polymer resistance on the solar panel ( $\Omega$ ),  $r_{ad}$  is the adhesive material resistance ( $\Omega$ ),  $r_{hb}$  is the conductive resistance of the heat sink base ( $\Omega$ ) and  $r_{fs}$  is the base resistance of fin for radiation and convection.

## 2.4 Techno-economic analysis

The technical feasibility and economic viability of the PV system were studied with and without the proposed cooling system in the two cities. The technical and economic indicators used in the present study are:

Capacity factor

The annual is calculated by dividing the energy generated over a year by the installed power at STC for 24 hours per day for a year (Eq. 5).

$$PR = \frac{E_{PV,\text{annual}}(\text{kWh/year})}{P_R * 8760} \quad (5)$$

Performance Ratio

Performance Ratio (PR) is expressed as the ratio of the actual to the theoretical energy of the PV system (Eq. 6).

$$CP = \frac{\text{Actual energy output}(\text{kWh/year})}{\text{Theoretical plant output}} \quad (6)$$

Levelized cost of electricity of PV

The levelized cost determines the amount of money that should be obtained per unit of electricity to recover the lifecycle cost of the system. It can be estimated by Eqs. (7) .

$$LCOE (\$/\text{kWh}) = \frac{C_i + \sum_{n=1}^N \frac{C_{O\&M}}{(1+r)^n} - \sum_{n=1}^N \frac{INT_n}{(1+r)^n} (\text{tax rate})}{\sum_{n=1}^N \frac{E_{out,n}}{(1+r)^n}} \quad (7)$$

where  $C_i$  is the initial investment cost,  $C_{O\&M}$  is the maintenance and operation costs,  $INT_n$  is the interest payment in period n,  $E_{out,n}$  is the energy generated by PV system in period n,  $r$  is the discount rate.

Net present Value (NPV)

The net present value is used to estimate the net profit of the investment, as expressed in Eq. (8) [18].

$$NPV (\$/\text{KWP}) = \sum_{n=1}^N \frac{Q_n}{(1+r)^n} - C_i \quad (8)$$

where  $C_i$  is the initial cost,  $Q_n$  is the net cash flow for a year, and  $r$  is the discount rate.

Simple Payback Period (SPP)

Simple payback period (SPP) is expressed by Eq. (9).

$$SPP = \frac{\text{Initial investment}}{\text{Annual Saving}} \quad (9)$$

Profitability Index (PI)

The profitability index is a relation between the costs and the profits of an investment project, as expressed by Eq. (10).

$$\text{Profitability Index} = 1 + \frac{NPV}{\text{Initial investment}} \quad (10)$$

The cost analysis of the PV system is presented in Table 2. The cost of a cooling system is estimated as 40% of the PV panel cost and the cost of the adhesive material is considered as 10% of the cost of the cooling system.

Table 2. Cost analysis of PV system

Item	Cost (SAR)
Discount rate ( $r$ )	0.025
Cost of PV panels	106,400
Cost of Inverter	30,222
Cost of Installation	40,000
Cost of AC wiring &AC backers	4000
Cost of DC wiring &DC backers	4000
Structure cost	40,000
Cost of cooling system	53,200

### 3- RESULTS AND DISCUSSION

#### 3.1 Solar panel temperature

The monthly variation of solar panel temperature with and without cooling system registered during 2015, 2016, and 2017 in Riyadh and Dammam are shown in Figures 3 and 4 respectively. It can be seen from Figure 18 that the obtained values of monthly solar panel temperature in 2015, 2016, and 2017 with and without cooling systems are similar for all months in Riyadh. However, the solar panel temperatures in 2015 and 2016 with and without a cooling system are similar for all months in Dammam, whereas the values obtained in 2017 are unpaired with those in 2015 and 2016 for the months January, February, and March. The highest solar panel temperature, with and without a cooling system, is recorded in June and July in Riyadh and Dammam. However, the lowest solar panel temperature was observed in December and January in both cities.

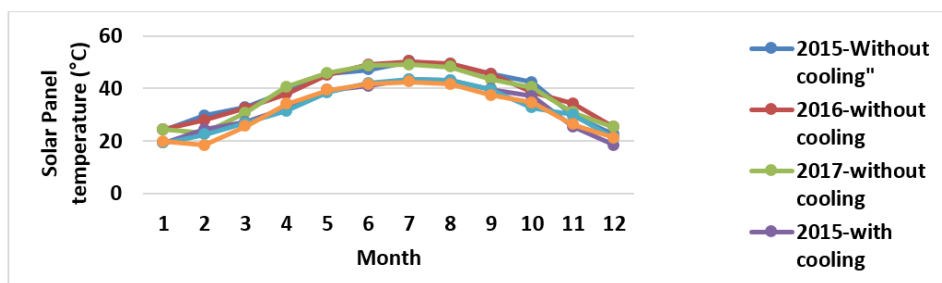


Figure 3. Mean monthly solar panel temperature obtained with and without cooling system in Riyadh

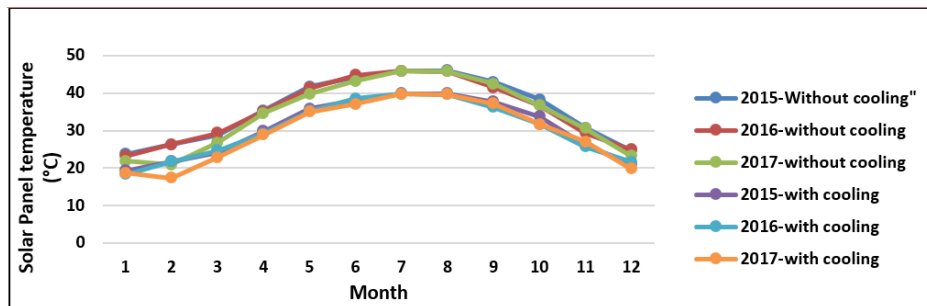


Figure 4. Mean solar panel temperature obtained with and without a cooling system in Dammam

Figure 5 displays the mean hourly solar panel temperature in Dammam and Riyadh with and without a cooling system. The solar panel temperatures recorded in Riyadh are higher than those in Dammam except for December and January (where the temperatures are similar). The highest and the lowest solar panel temperatures obtained in Riyadh without a cooling system were 49.08°C in July and 24.3°C in December and January, respectively. However, by using a cooling system, the highest and lowest solar panel temperatures decreased to 43°C and 19.4°C respectively. In Dammam, the highest and the lowest solar panel temperatures without a cooling system reached 45.8°C (in July and August) and 22.9°C (in January), respectively, which were reduced to 39.7°C and 18.76°C, respectively by using the cooling system. This observation testifies the potential of the proposed passive cooling in reducing the solar panel temperature, which eventually improves panel efficiency and life.

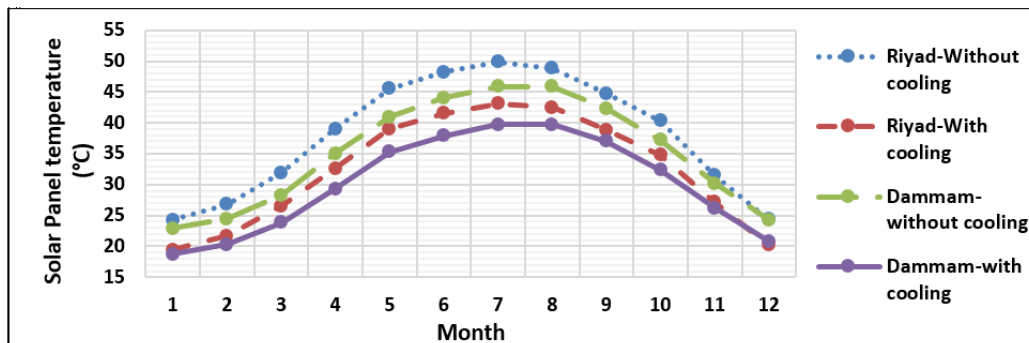


Figure 5. Mean monthly solar panel temperature with and without a cooling system in Riyadh and Dammam

### 3.2 The output energy of the solar panel

The monthly energy produced by a solar panel with and without using a cooling system in Riyadh and Dammam is presented in Figure 6. It can be observed that the highest energy is generated with the cooling system in Riyadh for all months except June. This can be explained by the highest GHI and the lowest relative humidity recorded in Riyadh city. The energy produced in Dammam without cooling ranged from 21,005 W/m² in December to 39,163 W/m² in June, which were increased to 21,938 W/m² in December and 41,773 W/m² in June respectively, by the use of cooling system. For Riyadh, the energy produced without cooling were between 21,895 W/m² in December and 37,291 W/m² in July, and with cooling were 23,091 W/m² in December and 40,203 W/m² in July.

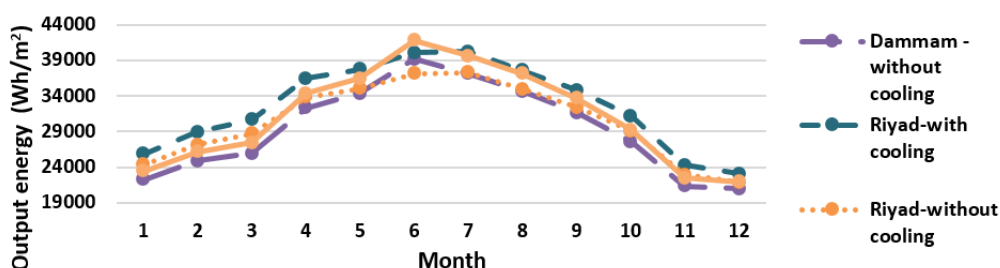


Figure 6 Monthly energy produced by a solar panel with and without a cooling system in Riyadh and Dammam

### 3.3 Enhancement in efficiency by using a cooling system

The enhancement in the efficiency of the solar panel by the proposed cooling system in Dammam and Riyadh is shown in Figure 7. It is obvious that the cooling system is more efficient in Riyadh. The efficiency of the cooling system varies between 5.18% in December and 7.24% in July and August in Riyadh city. However, it varies between 4.25% in December and 6.57% in July in Dammam.

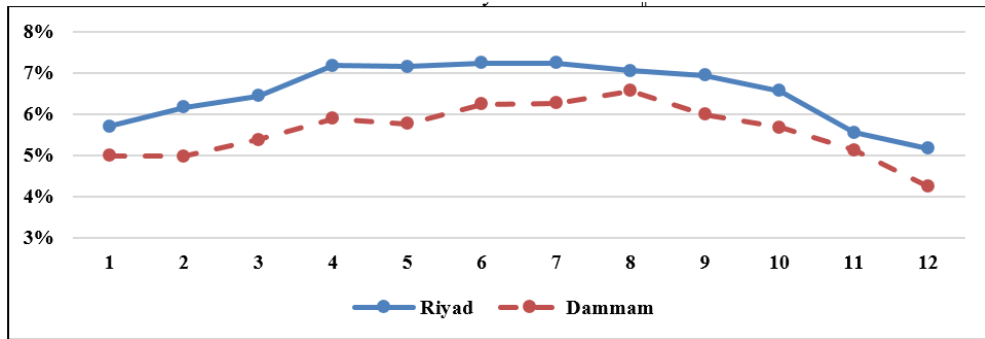


Figure 7. Enhancement in efficiency by using a cooling system in Dammam and Riyadh.

### 3.4 Technical analysis

#### Capacity factor

The capacity factor in Riyadh and Dammam for a PV system with and without a cooling system are shown in Figures 8 and 9. The capacity factor for a PV system with a cooling system in Riyadh city ranges between 15.07% and 26.24%, with the highest values around June and July. However, for a PV system without a cooling system, it ranges between 14.29% and 24.44%. The average annual CF without a cooling system 20.83% while it is 22.32% with a cooling system. The obtained values of the annual CF with and without the cooling system are higher than the typical CF (21%).

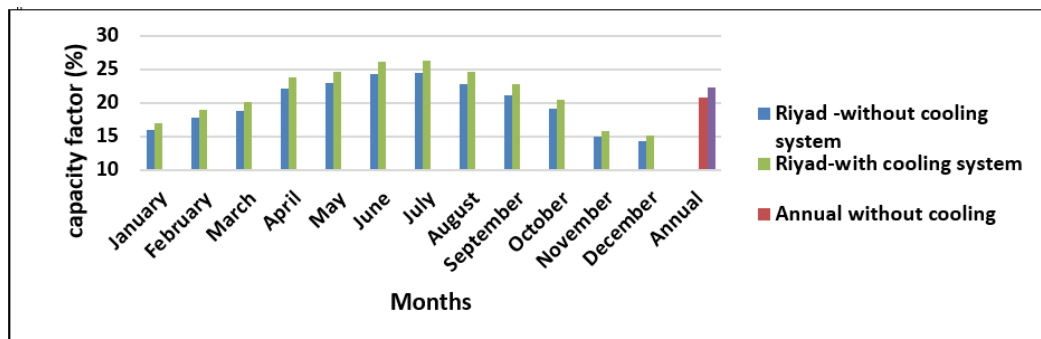


Figure 8. Monthly and yearly mean of the capacity factor in Riyadh city.

The capacity factor for a PV system without a cooling system in Dammam city ranges between 13.71% in December and 25.56% in June, whereas it ranges between 14.32% and 27.26% with cooling system. The average annual CF without a cooling system is 20.11%, while it is 21.34% with a cooling system. The obtained values of the annual CF with and without the cooling system are close to the typical CF (21%).

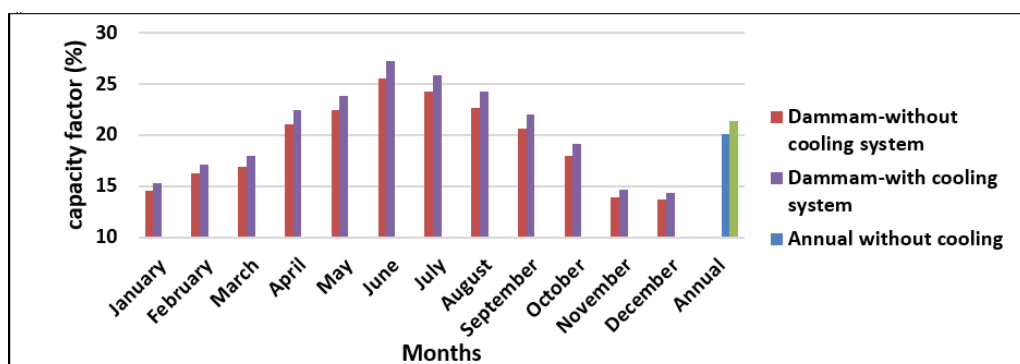


Figure 9. Monthly and the yearly mean of the capacity factor in Dammam city

The comparison between the annual CF with and without cooling system shows that the considered PV system with and without cooling is more efficient in Riyadh city.

#### Performance ratio

The performance ratio for the considered PV system with and without the cooling system in Riyadh and Dammam city is displayed in Figures 10 and 11. It can be seen that the performance factor in Riyadh city ranges between 77.14% in July and 87% in December and January for a PV system without a cooling system and it ranges between 83.15% in July and 92.38% in January for a PV system with the cooling system. The annual performance ratio is 80.75% and 86.6% for a PV system without and with a cooling system respectively. The annual PR for PV system with and without cooling system shows the high performance of the PV system, especially with the use of a cooling system.

The performance factor in Dammam city ranges between 79.1% in August and 88.75% in January for a PV system without a cooling system and it ranges between 84.66% in August and 93.5% in January for a PV system with the cooling system. The annual performance ratio is 83.94% and 89.05% for a PV system without and with a cooling system respectively. The annual PR for PV system with and without a cooling system shows the reliability of the PV system, especially with the use of a cooling system.

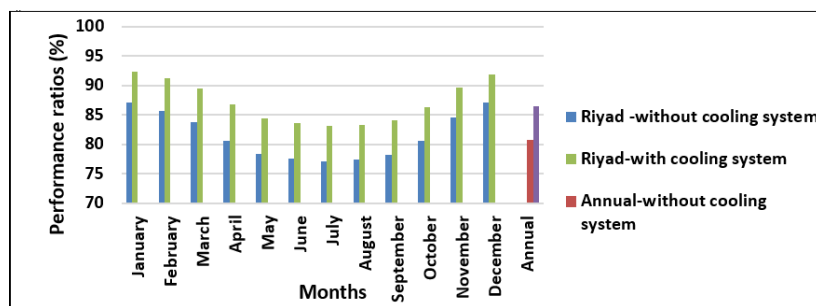


Figure 10. Monthly and a yearly mean of the performance ratio in Riyad city

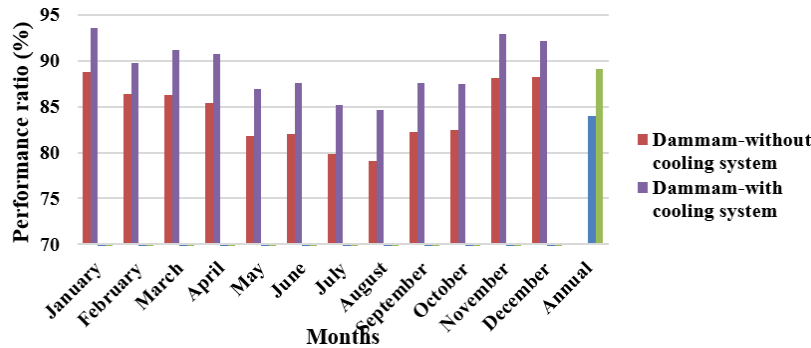


Figure 11. Monthly and a yearly mean of the performance ratio in Dammam city

#### 3.5. Economic analysis

The results of net present values, levelized cost of energy, payback period, and profitability index of the energy produced by the considered PV system in Dammam and Riyad with and without cooling system are presented in Table 4. The results show that:

The proposed solar PV power plant without a cooling system has a positive net present value NPV of 2592952.29 SAR and 2496267.27 SAR in Riyad and Dammam, respectively. Meanwhile, the NPV recorded for the solar PV system 2591197 SAR in Riyad and Dammam, respectively.

The values of LCOE for a PV system without a cooling system in Riyad and Dammam are 5.66 Hallalah /kWh and 5.86 Hallalah /kWh, respectively. Whereas, the LCOE for a PV system with a cooling system is 6.3 Hallalah /kWh and 6.6 Hallalah /kWh in Riyad and Dammam, respectively. The values of LCOE recorded in the two studied cities for a PV system with and without a cooling system is lower than the price of electricity provided by the government. The lowest LCOE is recorded in Riyad for a PV system without a cooling system, while the highest is registered in Dammam for a PV system with a cooling system.

The values of PI in the two studied cities for a PV system with and without cooling are more than one, which evinces, the profitability, and the acceptability of the project. The highest value of PI of 13.54 is recorded in Riyad for a PV panel without a cooling system while the lowest of 11.32 is recorded in Dammam for a PV system with a cooling system. The initial investment for a PV system without a cooling system will have been paid back in 6.1 years in Riyad and in 6.8 years in Dammam. However, for a PV system with a cooling system, the initial investment will be paid back in 6 years in Riyad and in 6.7 years in Dammam.

Table 2. NPV, LCOE, PI and PP in Dammam and Riyadh

	Without cooling system		With cooling system	
	Riyad	Dammam	Riyad	Dammam
NPV	2592952.29	2496267.27	2718710	2591197
LCOE (SAR/kWh)	0.0566	0.0586	0.063	0.066
PI	13.54	13.11	11.78	11.32
Payback Period	6.1	6.8	6	6.7

It can be concluded that the use of a cooling system can reduce the payback period and the LCOE of the PV project. Moreover, it can improve the profitability of the PV project, as evident from the increase of PI and the NPV.

### 3.8 Environmental effect

Since the PV systems do not need fossil fuel to produce energy, the CO<sub>2</sub> emissions are hugely small compared to energy produced using conventional power plants. Thus, a reduction of CO<sub>2</sub> emissions can be obtained using solar PV. The CO<sub>2</sub> emission saved by using a solar PV system can be estimated based on the CO<sub>2</sub> emission from the conventional electricity generation in the Kingdom, which is 0.28 kg CO<sub>2</sub>/kWh. The annual equivalent saved CO<sub>2</sub> from the considered PV system with and without a cooling system is Dammam and Riyad is displayed in Figure 12. It ranges from 19.7 tons/year in Dammam without a cooling system to 21.73 tons/year in Riyad with a cooling system.

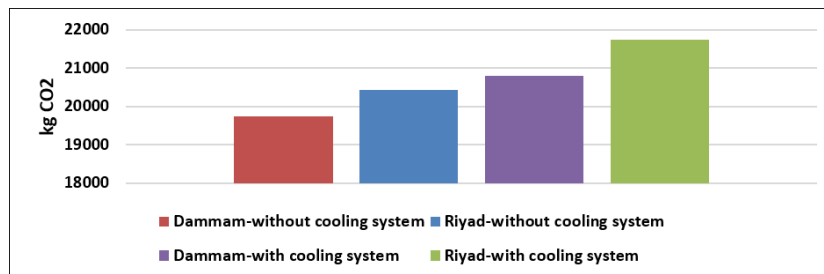


Figure 12. The annual equivalent saved CO<sub>2</sub> emissions from the PV system with and without a cooling system in Dammam and Riyadh

## 4. CONCLUSIONS

The potential of solar energy in Dammam and Riyadh cities of Saudi Arabia has been evaluated by considering 80 kW of solar panel system with and without a passive cooling system. Besides, techno-economic feasibility study has been performed by estimating the capacity factor, performance ratio, NPV, discounted payback, levelized cost of energy, and profitability index. Subsequently, the benefit of using solar PV with and without a cooling system in reducing the quantity of CO<sub>2</sub> emissions was estimated. The following findings are obtained:

The annual generated energy by using PV panel in Riyad is 362254 W/m<sup>2</sup> and 388121 W/m<sup>2</sup> without and with using a cooling system respectively, while the corresponding values for Dammam city are 350561 W/m<sup>2</sup> and 371605 W/m<sup>2</sup>.

The considered cooling system in the present study is more effective and functional in Riyad. Moreover, the use of a cooling system with a solar PV panel increases the efficiency and the lifetime of the solar PV panel by decreasing its temperature.

The PV system with and without cooling system is lucrative and prolific in the two studied cities since the cost of electricity generation is lower than that the electricity price in KSA (13-18 Hallalah/kWh). Also, the PV panel with a cooling system can attain an NPV of 2718710 SAR in Riyad and 2591197 SAR in Dammam and a discounted payback period of 6 years in Riyad and 6.7 years in Dammam.

The PV panel without a cooling system can reduce the annual equivalent saved CO<sub>2</sub> to 19.7 tons/year in Dammam and to 20.436 tons/year in Riyadh. However, the use of a PV panel with a passive cooling system can reduce it by 20.8 tons/year in Dammam and 21.73 tons/year in Riyadh.

The current study proved the feasibility of using a PV system in Dammam and Riyadh, and demonstrated the benefits of using a cooling system in increasing the output energy and profitability of PV panel.

#### **ACKNOWLEDGMENTS:**

The authors would like to thank King Abdullah City for Atomic and Renewable Energy (KACARE) for providing the data and for their support.

#### **REFERENCES**

1. McCarthy, N., <https://www.statista.com/chart/4887/the-20-worst-cities-worldwide-for-air-pollution/>, in Statista. 2016.
2. Al Zohbi, G. and F.G. AlAmri, Current Situation of Renewable Energy in Saudi Arabia: Opportunities and Challenges. Journal of Sustainable Development, 2020. **13**(2).
3. Faruqui, A., et al., Bringing demand-side management to the kingdom of Saudi Arabia. The Brattle Group, 2011.
4. Al Garni, H., et al., A multicriteria decision making approach for evaluating renewable power generation sources in Saudi Arabia. Sustainable Energy Technologies and Assessments, 2016. **16**: p. 137-150.
5. Khan, M.M.A., M. Asif, and E. Stach, Rooftop PV potential in the residential sector of the Kingdom of Saudi Arabia. Buildings, 2017. **7**(2): p. 46.
6. Almarshoud, A., Performance of solar resources in Saudi Arabia. Renewable and Sustainable Energy Reviews, 2016. **66**: p. 694-701.
7. Almasoud, A. and H.M. Gandayh, Future of solar energy in Saudi Arabia. Journal of King Saud University-Engineering Sciences, 2015. **27**(2): p. 153-157.
8. Grubišić-Čabo, F., S. Nižetić, and T. Giuseppe Marco, Photovoltaic panels: A review of the cooling techniques. Transactions of FAMENA, 2016. **40**(SI-1): p. 63-74.
9. Zubeer, S.A., H. Mohammed, and M. Ilkan. A review of photovoltaic cells cooling techniques. in E3S Web of Conferences. 2017. EDP Sciences.
10. Muhsen, A. and A. Elshurafa, The Potential of Distributed Solar PV Capacity in Riyadh: A GIS-Assisted Study. 2019.
11. Awan, A.B., M. Zubair, and A.G. Abokhalil, Solar energy resource analysis and evaluation of photovoltaic system performance in various regions of Saudi Arabia. Sustainability, 2018. **10**(4): p. 1129.
12. Rehman, S. and L.M. Al-Hadhrami, Study of a solar PV–diesel–battery hybrid power system for a remotely located population near Rafha, Saudi Arabia. Energy, 2010. **35**(12): p. 4986-4995.
13. Aldossary, A., S. Mahmoud, and R. Al-Dadah, Technical feasibility study of passive and active cooling for concentrator PV in harsh environment. Applied thermal engineering, 2016. **100**: p. 490-500.
14. Popovici, C.G., et al., Efficiency improvement of photovoltaic panels by using air cooled heat sinks. Energy Procedia, 2016. **85**(2016): p. 425-432.
15. AlAmri, F., Al Zohbi, G., AlZahrani, M., Aboulebdah, M., Analytical modeling and optimal design of a heat sink for cooling PV panel below the safe temperature. Submitted paper to the journal of Sustainability, 2020.
16. Incropera, F.P., et al., Fundamentals of heat and mass transfer. 2007: Wiley.
17. Company, S.E. Tariffs and connections fees. 2018 [cited 2020].
18. Bernal-Agustín, J.L. and R. Dufo-López, Economical and environmental analysis of grid connected photovoltaic systems in Spain. Renewable energy, 2006. **31**(8): p. 1107-1128.
19. Fesharaki, V.J., et al. The effect of temperature on photovoltaic cell efficiency. in Proceedings of the 1st International Conference on Emerging Trends in Energy Conservation–ETEC, Tehran, Iran. 2011.
20. Aish, Q.M., Temperature effect on photovoltaic modules power drop. Al-Khwarizmi Engineering Journal, 2015. **11**(2): p. 62-73.
21. Kawajiri, K., T. Oozeki, and Y. Genchi, Effect of temperature on PV potential in the world. Environmental Science & Technology, 2011. **45**(20): p. 9030-9035.
22. Panjwani, M.K. and G.B. Narejo, Effect of humidity on the efficiency of solar cell (photovoltaic). International Journal of Engineering Research and General Science, 2014. **2**(4): p. 499-503.
23. Koehl, M., et al., Modeling of the nominal operating cell temperature based on outdoor weathering. Solar Energy Materials and Solar Cells, 2011. **95**(7): p. 1638-1646.



# PROMISING HDR PROJECT IN THE NORTH CAUCASUS

Alan Lolaev

VSC RAS, NOSU, Vladikavkaz, Russia, proflolam@gmail.com, ORCID: 0000-0003-0943-6807

Anatoly Gurbanov

IGEM, VSC RAS, Moscow, Russia, gurbanov@yandex.ru, ORCID: 0000-0001-7143-8817

Victor Gazeev

IGEM, VSC RAS, Moscow, Russia, gazeev@igem.ru, ORCID: 0000-0003-1950-1297

Aleksey Lexin

IGEM RAS, Moscow, Russia, lexin@igem.ru, ORCID: 0000-0001-6308-7551

Aleksan Oganesyan

VSC RAS, NCIMM, Vladikavkaz, Russia, alexoganesyan1984@mail.ru, ORCID: 0000-0001-6292-037X

Cite this paper as:

Lolaev, A., Gurbanov, A., Gazeev, V., Leksin, A., Oganesyan, A. Promissing HDR project in the North Caucasus. 9<sup>th</sup> Eur. Conf. Ren. Energy Sys. 21-23 April 2021, Istanbul, Turkey

---

**Abstract:**

There are many geothermal areas in Russia. These areas are located tectonically active regions. In these areas, we can access hot rock at relatively shallow depth. Positive thermal anomalies in the area of the Kazbek volcanic center, revealed according to the data of remote thermal sensing from the NOAA satellite system, in combination with the results of geophysical studies, indicate the connection of these anomalies with the subsurface magma chambers located under them with the melt. The studies performed allow us to consider it possible to build geothermal power plant in the Genaldon river valley, using the endogenous replenished (due to a deep feeding chamber) thermal energy of the Kazbek magma chambers.

---

**Keywords:**

Hot dry rock, geothermal areas, volcano, temperature

---

© 2021 Published by ECRES

## 1. INTRODUCTION

The rapid development of scientific and technological progress and the world energy potential is accompanied by an ever-increasing impact on nature. This poses a vital task for humanity to reduce the technogenic impact on the environment, primarily from the side of energy-generating technologies. In the last decades of the last century, interest in renewable (non-traditional) energy sources and, in particular, in geothermal resources has sharply increased. This is due to both the limited nature of traditional energy sources and noticeable climate change and global warming caused by anthropogenic greenhouse gas emissions.

The problem of the integrated use of endogenous heat sources all over the world is urgent, and for volcanically active regions, which include the North Caucasus, this problem is doubly urgent. Positive examples of using the endogenous heat of active volcanoes with heating small towns and generating electricity have long been available: in Los Alamos (USA, Iceland and New Zealand, France, etc.) and at Mutnovskaya TPP (Russia, Kamchatka). These studies began and were implemented earlier than in the USSR and Russia and have been intensively developing in recent years [1-6].

## 2. CASE HISTORY

The assessment of thermal reserves in the area of the Kazbek volcanic center is also of great economic importance for the Republics of the North Caucasus, since the near-surface magma chambers identified here, the deep hearth

feeding them, and geothermal systems, having a huge energy potential, can ensure the widespread development of power plants and geothermal heat supply systems.

The aim of the study is to discuss the regional potential of geothermal energy of hot dry rocks in the North Caucasus and to identify what geological, technological and economic obstacles need to be overcome in order to make the use of hot dry rock energy possible.

Positive thermal anomalies in the area of the Kazbek volcanic Center (KVC), identified by remote thermal sensing data from the NOAA satellite system [7], combined with the results of geophysical studies [8-9], indicate the connection of these anomalies with the near-surface magma chambers with melt located below them. These data, together with radiocarbon dating of one of the young lava flows of the Kazbek volcano [10] (Fig.1), allow us to classify it as an active but currently dormant volcano. As a result of research in the Genaldon river valley (Fig. 2), a near – surface magma chamber was identified-the roof at a depth of 1-2 km, and the sole-no more than 5-7 km below sea level.

The identified thermal anomalies formed over near-surface magma chambers had to be verified by geophysical methods (gravimetry and audio-magnetotelluric sounding) and the dynamics of their thermal fields deciphered by reliable ground-based methods, for example, using automatic thermal sensors. To this end, in 2011, studies of the dynamics of the thermal field in the positive circuit for 1990-2010 were started and continue to this day. a stable anomaly elongated in the meridional direction, located in the valley of the Genaldon River on a stretch of 1.0 km south of the "Lower Karmadon" thermal springs (in the south) and almost to the village. Tmenikau, Kony (in the north) (Fig. 2).



Figure 1. Volcano Kazbek



Figure 2. The Genaldon river valley

### 3 METHODS AND RESULTS

In the valley of the Genaldon River, 6 thermal sensors were installed along the meridional profile. They were placed in pits with a depth of 0.9-1.0 m, covered with earth. The sensors began to record the endogenous temperature (with an accuracy of 0.001 °C) after 15-17 hours, which is necessary for the sensors to enter a stable measurement mode. The coordinates and elevation of the installation site of each sensor were recorded using a GPS receiver and are presented in Table 1. Temperature sensors recorded the temperature around the clock every hour [11].

Table 1. Data on observation points (places of installation of thermal sensors)

Point No	Sensor No	Latitude	Longitude	Height, m
1/11	7	42°50'29,3"	44°30'49,9"	1386
2/11	9	42°49'57,3"	44°30'27"	1406
3/11	10	42°49'04,3"	44°29'53,9"	1462
4/11	14	42°48'46,5"	44°29'47,6"	1529
5/11	15	42°48'39,4"	44°29'47,1"	1463
6/11	16	42°48'18,3"	44°29'32,4"	1596

As a result of our studies, in combination with those previously performed [11], we obtained:

- a) If there is a peripheral near-surface magma chamber with a melt that has not yet cooled down, then theoretically it should warm up the host rocks, including those lying in its roof, at least by the first degrees or tens of degrees, depending on their power and heat capacity. This theoretical premise is confirmed by the data of thermal remote sensing from the NOAA satellite in the form of positive thermal anomalies of various intensities (in degrees of radiation temperature) [7].
- b) The presence of a positive thermal anomaly planned for research in the upper reaches of the Genaldon River (the area of the Lower Karmadon thermal mineral springs) is confirmed by the results of temperature measurement by ground-based automatic thermal sensors [11]. In the contour of this anomaly at a depth of 0.8-1.0 m, the temperature varied from 23 °C to 31 °C, and outside the anomaly (background temperature) it varied from 14 °C to 17 °C, which clearly indicates the presence of an independent endogenous heat source under the positive anomaly, which is a magma chamber with a melt.
- c) According to the data of gravimetric [8] and audio-magnetotelluric [9] studies, it was found that the positive thermal anomaly is caused by a magma chamber with a melt located at a depth: the roof is 1-2 km, and the sole is 5-7 km below sea level.
- d) The almost simultaneous appearance of peaks of maximum temperature values according to the readings of thermal sensors located at different observation points in the contour of the thermal anomaly in the Genaldon River valley can be explained, for example, by the entry of small portions of magmatic melt into the peripheral magma chamber.
- e) To calculate the heat flux density and calculate the reserves of thermal energy accumulated in the magma chamber and in the rocks containing it, temperature measurements in the faces of 10 wells with a depth of 30-40 m (with entry into the bedrock) will be used, which will exclude the influence of daily, seasonal and annual temperature fluctuations on the true value of endogenous temperature.
- e) Taking into account the geothermal gradient for the neointrusive regions of the Caucasus [12] of the order of 44-46 °C / km and the maximum temperature on the earth's surface (22-23 °C and 30-31 °C) in the contour of the positive thermal anomaly in the Genaldon River valley, it can be assumed that here at a depth of ~ 2.0-2.5 km from the earth's surface, the temperature of dry rocks should reach a temperature of 270-300 °C. In this case, it is quite possible to use the endogenous heat accumulated in the magma chamber and in the rocks containing it for the construction of an environmentally friendly geothermal power plant.

The performed studies allow us to consider it possible to build a geothermal circulating geothermal power plant in the Genaldon River valley, using the endogenous heat energy of the magmatic chambers of Kazbek, which is replenished (due to a deep feeding source). Such a geothermal power plant will become the basis of energy and heat supply in the region, will contribute to the development of tourist and hotel complexes, will give new jobs in conditions of total unemployment

The preliminary calculations of the parameters of the power plant operating on the basis of renewable energy showed that the natural and territorial characteristics of the mountainous territories of the Republic of North Ossetia-Alania allow implementing projects for the construction of small-scale energy facilities without large preliminary material costs.

#### **4. CONCLUSIONS AND RECOMMENDATIONS**

To prepare a justification for the construction of a geothermal power plant on an endogenous renewable heat source on the northern spurs of the Kazbek volcano in the upper reaches of the Genaldon River, the following main stages of work and planned results are envisaged:

1. Continued monitoring of the dynamics of the thermal field in the contours of the positive thermal anomaly in the upper reaches of the Genaldon River using automatic thermal sensors installed at a depth of 0.9-1.0 m and measuring the temperature of mineral water at self-discharge in the area of the Lower and Upper Karmadon thermal springs and air temperature.
2. Drilling in 2021-22 of 10 wells with a depth of 30-40 m, in the faces of which temperatures will be measured for several days with high-precision thermometers. This will help to exclude the influence of daily, seasonal and annual temperature fluctuations on the true value of endogenous temperature. These data will be necessary for calculating the heat flux density and calculating the reserves of thermal energy accumulated in the magma chamber and in the rocks containing it, and for selecting the locations of injection and production wells.
3. For the final assessment of the possibility of using the endogenous heat accumulated by the magma chamber and its host rocks, and the implementation of a new project in the contours of the thermal anomaly in the upper reaches of the Genaldon River, it is necessary to drill one injection well with a depth of 2-2.5 km in 2023. If the temperature

required for the construction of a geothermal power plant is set in this well, then micro-explosions or hydraulic fracturing are made in the bottom of the well to form the necessary volume of a fractured heat exchanger (strongly fractured rocks). Then, next to this well, 2 or 3 more production wells are drilled into the formed zone of the crack heat exchanger (their number will depend on the capacity of the projected geothermal power plant and the calculated reserves of thermal energy) with casing pipes to the same depth as the injection well. The injection well will pump water filtered from the sand from the Genaldon River, and at the mouths of 2 or 3 production wells, it will flow in the form of superheated steam to a generator that converts thermal energy into electrical energy.

4. When the planned Geothermal "waste" steam, after passing through the generator, mining well condenseries in the form of hot water will flow in a looped pipe system used for heating, and then re-injected to the injection well. After several cycles, the water in the system will become highly mineralized, and carbonates will begin to deposit intensively on the walls of the pipeline, gradually clogging the pipeline system and quickly reducing the efficiency of the heat supply system. Therefore, there will be an urgent and expensive problem of replacing heavily clogged sections of pipes in the heat supply system. To solve this problem, a theoretical development of the system (removable and replaceable modules) is provided) to clean the water coming after the generator installed on the production well, in the heat supply system; creating a model of a removable mobile module for water purification and conducting its laboratory tests.

5. The concept of development of the economic complex of North Ossetia provides for the development of sparsely populated and poorly economically developed mountain areas. Low-voltage distribution networks for power supply of these areas are in poor technical condition, run in difficult terrain and climatic conditions, have a significant length, which complicates the conditions of their operation and leads to inevitable power outages of consumers. It should be noted that many small villages in mountainous areas are often left without power due to the low reliability of distribution networks in the mountains and the lack of electricity.

6. Removing heat and power generation using hot dry rocks surrounding the magmatic chamber on the Northern spurs of "sleeping" volcano Kazbek (headwaters of Genaldon, the lower-Karmadon thermal mineral springs) may be one of the foundations of energy this mountainous part of the Republic of North Ossetia-Alania. Moreover, it will serve the development of economy and tourism, will help the construction of settlements in the valleys of the rivers Genaldon, Midagrabindon and Fiagdon. Hot water, after generating electricity, can be used to heat the houses of the village. Kani, Tmenikau, the buildings of the sanatorium and the Border Detachment, as well as the creation of a greenhouse farm for year-round vegetable production.

7. The experience of this project will be useful for the further development of geothermal energy in the Republic of North Ossetia-Alania and the Kabardino-Balkar Republic (on the "sleeping" volcano Elbrus).

## **ACKNOWLEDGMENT**

The work was carried out according to the plan of the research work of the Vladikavkaz Scientific Center of the Russian Academy of Sciences – registration number: AAAA-A19 119040190054-8.

## **REFERENCES**

- [1] Rummel F., Baumgartner J. Hydraulic Fracturation measurements in the GPK1 borehole, Soultz-sous-Forets. In: Geothermal Energy in Europe. The Soultz Hot Dry Rock Project / Ed.J. C. Brezee. 1991. Gordon and Breach Publishers. V.3.
- [2] Baumgartner J., Jung R. Gerard A. et al. The European HDR project at Soultz-sous-Forets: stimulation of the second deer well and first circulation experiments. In: 21st Workshop on Geothermal Reservoir Engineering, Stanford University. Stanford. California. January 22-24, 1996. pp.267-274
- [3] Baumgartner J., Teza D., Hettkamp T. et al. Production from Hot Rocks. In: Proceeding of Word Geothermal Congress Antalya, Turkey. 24-29 April, 2005.
- [4] Dezavas C., Genter A., Gentier S. Fracture network of the EGS geothermal reservoir at Soultz-sous-Forets (Rhine Graben, France). In: Geothermal Resources Council 28 GRC Transection, Palm Spring, California, USA. 2004. pp. 213-218.
- [5] Dezayes C., Genter A., Hooijkaas G.R. Deep-Seated Geology and Fracture System of the EGS Soultz Reservoir (France) Based on Recent 5-km Depth Boreholes. In: Proceeding of Word Geothermal Congress Antalya, Turkey. 24-29 April, 2005.
- [6] Kaieda H., Ito H., Kiho K. et al. Review of the Ogahri HDR Project in Japan. In: Proceeding of Word Geothermal Congress Antalya, Turkey. 24-29 April, 2005.
- [7] Kornienko S. G., Lyashenko O. V., Gurbanov A. G. Identification of signs of focal magmatism within the Kazbek volcanic center according to thermal space survey data. Bulletin of the Vladikavkaz scientific Center of the Russian Academy of Sciences and the Government of the RSO-A. 2004. Vol. 4. No. 3. pp. 25-32
- [8] Kopaev A.V., Gurbanov A. G. Gravimetric studies in the Genaldon gorge: first results. Bulletin of the Vladikavkaz scientific. center of RAS and government of RNO-A. 2004. Vol. 4. No. 3. pp. 9-11.

- [9] Arbuskin V. N., Feldman I. S., Trofimenko E. A. Results of the first stage of electrical exploration works of AMTZ and MTZ in Genaldon gorge. Vestnik VSC RAS. 2004, V4, No. 3, pp. 12-24.
- [10] Burchuladze A.A., Dzhanelidze Ch. G., Togonidze G. I. Application of the radiocarbon method for solving some issues of paleogeography of the Pleistocene and Holocene of Georgia. Actual issues of modern geochronology. Moscow. Nauka. 1976. pp. 238-243.
- [11] Gurbanov A. G., Gazeev V. M., Leksin A. B., Dokuchaev A. Ya., Tsukanova L. E. Dynamics of the thermal field in the contours of an anomaly in the upper reaches of the Genaldon River valley according to ground-based thermal sensors. center of RAS and government of RNO-A. 2012. Vol. 12. No. 3. Pp. 13-19.
- [12] Hess J.C., Lippolt H.J., Gurbanov A.G, Michaloski I. The cooling history of the late Pliocene Eldzhurtinskiy granite (Caucasus, Russia) and the thermochronological potential of grain-size/age relationships. Earth Planet. Sci. Lett. 1993. V.117. pp. 393–406.



# APPLICATION OF POWER SPECTRAL DENSITY AND THE SUPPORT VECTOR MACHINE TO FAULT DIAGNOSIS FOR PERMANENT MAGNET SYNCHRONOUS MOTOR

Zerdani Sara

Laboratory of Electrical Engineering and Maintenance (LGEM), Higher School of Technology, University Med First Oujda, Morocco, zerdanisara9@gmail.com, ORCID: 0000-0002-7624-1316

Larbi Elhafyani Mohamed

Laboratory of Electrical Engineering and Maintenance (LGEM), Higher School of Technology, University Med First Oujda, Morocco, elhafyani77@gmail.com, ORCID: 0000-0003-1931-0079

Zouggar Smail

Laboratory of Electrical Engineering and Maintenance (LGEM), Higher School of Technology, University Med First Oujda, Morocco, szouggar@gmail.com, ORCID: 0000-0002-4653-4847

*Cite this paper as:* Zerdani, S., Elhafyani, M.L., Zouggar, S., "Application of power spectral density and the support vector machine to fault diagnosis for permanent magnet synchronous motor". 9<sup>th</sup> Eur. Conf. Ren. Energy Sys. 21-23 April 2021, Istanbul, Turkey.

---

**Abstract:**

The present study proposes a new technique for diagnosing the Inter-Turn Stator-Winding fault in Permanent Magnet Synchronous Motors. Under faulty operating conditions, the system's model is built while considering specific parameters linked to fault location and sharpness. The proposed fault-detection method is principally based on the Power Spectral Density estimator's association with the Support Vector Machine. We used this classifier to separate different regions of system performance. It has been trained to associate the Power Spectral Density current's magnitude and the stator's current negative sequence with the fault severity. This method has shown exceptional performance as long as it achieves a fault detection rate of 98.5% for different fault severities. A comparative study was developed between two Power Spectral Density estimators, the Welch method and the Burg approach. We analyzed these techniques in terms of their frequency resolution and their effect on determining the defect's spectral components. The results obtained show that the Welch with the classifier performs the extraction of fault characteristics better than the Support Vector Machine-Burg estimator.

---

**Keywords:** *Inter-Turn Stator-winding fault, Fault detection, Welch, Support Vector Machine, Burg.*

---

© 2021 Published by ECRES

---

**Nomenclature**

PSD	Power Spectral Density
SVM	Support Vector Machine
ITSWF	Inter-Turn Stator Winding Fault
AR	Autoregressive
PMSM	Permanent Magnet Synchronous Motor

---

## 1. INTRODUCTION

Reliability, safety, and service continuity are prerequisites in current electrical systems. Occasionally, these devices may come to a complete or partial shutdown due to the actuating or conversion devices' failure, thereby jeopardizing the system's operation continuity. In such systems, a diagnostic tool capable of detecting and identifying the fault in question is indispensable to ensure the system properly functioning.

Permanent Magnet Synchronous Motors (PMSM) find their place in various applications due to their increased reliability and efficiency. They are often deployed in critical systems such as automotive and aerospace. However,

these machines are prone to short circuits, usually caused by the rotor magnets' permanent excitation. Reliable detection with an acceptable confidence margin is therefore required to prevent the rapid fault's propagation outside the system.

To design powerful diagnostic tools in advance while avoiding machine damage, precise modeling of the machine, taking into account the severity of the fault and its nature, is compulsory. In this context, two approaches are often considered to model the ITSWF. The first way concerns the connection between the electrical circuit and the equivalent magnetic circuit. This model considers the slots' real current distribution and even the magnetic circuits' saturation [2]. However, its implementation is relatively complicated and time-consuming in defining the variables, which invalidates the faulty motor's simulation with the diagnostic unit in question.

Differently, the circuit design can be built in different reference frames, such as the static reference frame ( $\alpha\beta 0$ ) or the rotating reference frame ( $dq0$ ). [3] [4]. This mode also allows easy access to the motor parameters that determine the faulty winding's severity and location.

As the stator-winding fault causes a change in machine output sizes, such as stator current and torque signal, they were usually employed to extract the fault imprint. In reference [5], the current negative sequence component is taken as the fault signature signal to distinguish the sound state from the machine's faulty state. However, it does not indicate the winding under consideration.

On the other hand, current frequency analysis, such as the Fast Fourier Transform, has been widely deployed to identify the fault's characteristics and even locate the fault from the three-current phase. However, the FFT is significantly destabilized by the load variation and the winding motor's asymmetry. Besides, it exhibits low-frequency resolution and poor performance for non-stationary signals [6]. Some of these weaknesses can be solved using Time-Frequency (TF) analysis algorithms such as the empirical mode decomposition or the Wigner Ville distribution [7] [8].

The first one allows reaching a balance between the suppression of cross-terms and TF resolution loss. In comparison, the second method does not require an adaptive filter to track motor frequencies, thereby making it insensitive to load variations. Both approaches impose lengthy calculations and are subject to complex interpretation.

Another way to detect the fault under study is via the machine-learning algorithm. The latter has come up to overcome the shortcomings as mentioned earlier related to fault diagnosis methods. Against this background, a variety of learning methods can be found in the literature and include the following features: the dispersed auto-encoder [9], the deep belief network (DBN) [10], and dispersed filtering [11].

In this paper, a conventional machine-learning method, namely the Support Vector Machine (SVM), was used. Extracting the signal characteristics was carried out using an advanced Power Spectral Density (PSD) calculation technique. Two distinct defect characteristic estimators have been studied: the Welch method, which belongs to non-parametric analyses. This method determines the spectrum of the signal without being dependent on the system model. Besides, it allows the reduction of spectral losses, and it is known to have a high-frequency resolution. On the other hand, the parametric method, such as Burg's method, focuses on autoregression, which also takes some parameters of the model into account for spectrum estimation [12].

The mechanism of the exposed fault diagnosis method is briefly described in section 2. Moreover, the SVM was adopted to separate and classify different system performance regions in the function of fault severity ratio [11].

## 2. PMSM'S DYNAMIC MODEL IN $(\alpha\beta)$ REFERENCE FRAME WITH ITSF

Typically, the Inter-Turn Stator Winding Fault is caused by an insulation problem between adjacent windings in the same phase. The winding in question is divided into two parts, one sound and the other defective. As depicted in the figure 1, this anomaly involves a parallel resistance between the winding extremes (a2) through which the current  $i_f$  flows. The ratio between the short-circuited turns  $N_f$  and the total number of turns  $N_s$  was designed by  $\mu$ .

The following formula can define the equation of the PMSM stator voltage in terms of fault severity and the resistance associated with the defective winding in the (ABC) stationary reference frame:

$$[v(t)]^{abcf} = [R_s]^f [i_s]^{abcf} + [L_s]^f \frac{d}{dt} [i_s]^{abcf} + [e_s]^{abcf} \quad (1)$$

With:

$$[v]^{abcf} = [v_a \ v_b \ v_c \ 0]^T, \quad [i]^{abcf} = [i_a \ i_b \ i_c \ i_f]^T, \quad [e_s]^{abcf} = [e_a \ e_b \ e_c \ e_f]^T$$

$$\text{Where: } [R_s]^f = \begin{bmatrix} R_s & 0 & 0 & \mu R_s \\ 0 & R_s & 0 & 0 \\ 0 & 0 & R_s & 0 \\ -\mu R_s & 0 & 0 & \mu R_s + r_f \end{bmatrix} \text{ and } [L_s]^f = \begin{bmatrix} L_s & 0 & 0 & \mu L_s - M_{a1a2} \\ 0 & L_s & 0 & -M_{a2b} \\ 0 & 0 & L_s & -M_{a2b} \\ -\mu L_s - M_{a1a2} + M_{a2b} & 0 & 0 & \mu L_s \end{bmatrix}$$

The following parameters ( $M_{a1a2}$  and  $M_{a2b}$ ) are respectively the mutual inductances between the windings (as2, as1) and the windings (as2, bs) resulting from the new stationary magnetic field, which can be identified based on the Finite Element Method (FEM) [13].

For a machine having one notch per pole and per phase, the axes of the sub-coils as1 and as2 are aligned and are not shifted concerning the coil axis. In this case, one can presume that:

$$M_{a2c} = M_{a2b}.$$

Thus, it is necessary to include the electromagnetic torque-mechanical in the system's state-space model to complete the machine model. The following formula can express this:

$$T_{em} = \frac{i_a e_a + i_b e_b + i_c e_c - i_f e_f}{\Omega} \quad (2)$$

Due to the conceptual clarity obtained with a single set of two windings on the stator, it was necessary to apply the Clarke transformation to the electrical equation (1). The matrix model of the PMSM in case of malfunction is shown below:

$$\begin{bmatrix} V_\alpha \\ V_\beta \\ 0 \end{bmatrix} = \begin{bmatrix} R_s & 0 & -R'_{a2} \\ 0 & R_s & 0 \\ R'_{a2} & 0 & R'_f \end{bmatrix} \begin{bmatrix} i_\alpha \\ i_\beta \\ i_f \end{bmatrix} + \begin{bmatrix} L_s & 0 & M_{f\alpha} \\ 0 & L_s & 0 \\ M_{f\alpha} & 0 & L_{a2} \end{bmatrix} \frac{d}{dt} \begin{bmatrix} i_\alpha \\ i_\beta \\ i_f \end{bmatrix} + \begin{bmatrix} e_\alpha \\ e_\beta \\ -e_f \end{bmatrix}$$

Where:

$$R'_{a2} = \sqrt{\frac{2}{3}} R_{a2}, R'_f = R_{a2} + r_f; \text{ and } M_{f\alpha} = -\sqrt{\frac{2}{3}} (L_{a2} + M_{a1a2} + M_{a2b}).$$

Based on this reductive model in terms of equations, the electromagnetic torque can then be defined in ( $\alpha\beta$ ) reference frame by this equation:

$$T_{em} = \frac{i_\alpha e_\alpha + i_\beta e_\beta + -i_f e_f}{\Omega} \quad (3)$$

This model is implemented within the Matlab Simulink environment to analyze the machine's behavior in ITS fault's presence. The values of the mutual inductances are listed in Table 5. Therefore, the simulation is carried out under normal and faulty operating conditions. Figure 1.a represents the three current phases when the machine is run at healthy mode, while figure 1.b showed the stator currents when the fault occurs in phase A.

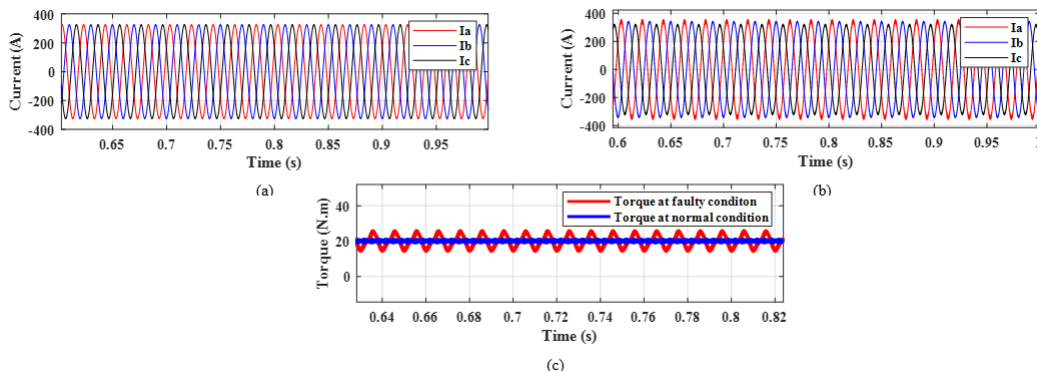


Figure 1 : The output Motor size under regular and faulty operating conditions (a) stator currents at healthy mode (b) stator currents under  $r_f = 10 \Omega$ ,  $\mu = 50\%$  (c) condition The electromagnetic torque with  $r_f = 10 \Omega$ ,  $\mu = 50\%$

Because of winding asymmetry, an unbalance appears in the three currents phase, leading to harmonics, which heightens with fault severity and for small fault resistance value. These harmonics intensify specifically in the current phase, as depicted in figure 1.b.

From these results, it is notable for fragmenting fault sharpness in four regions. In the first one, the system stay works around nominal condition with small torque oscillation; however, in the rest regions, the fault current  $i_f$  arise inducing a braking torque that hinders the electromagnetic torque. In this circumstance, the use of a fault detector becomes irreplaceable.

### 3. FAULT DIAGNOSIS METHODOLOGY

The fault diagnosis approach is presented with the entire system through Figure 2. This method's main advantage resides in the fact that it references different areas of system performance. The boundary between distinct operating regions is thus established while calculating the current negative sequence, which is expressed as follows:

$$i_- = \frac{1}{3}(i_a + a^2 \cdot i_b + a \cdot i_c) \quad (5)$$

With:  $a = e^{j2\pi/3}$

The current negative sequence and the stator current pre-processing data are inputs to the SVM, which essentially aims to classify the fault in the function of its severity. More explicitly, the SVM builds a model that assigns new samples to either class.

Typically, the classification is not efficient without pre-processing the input signal. This step makes the classifier easier to learn by converging to the most appropriate data for accurate and consistent classification results [14]. There are many recommended means for signal pre-processing, among which the PSD estimation method has been chosen. The input data size is then considerably reduced by a so-called Findpeak function, which returns a vector with the current PSD signal's peaks. Another standard solution for data reduction includes Principal Component Analysis (PCA)[15].

After performing all of the above processes, the classifier provides a binary vector in its output with the form [x y]. The [00] corresponds to the normal state, the [01], [10], and [11] are respectively referred to as zone 1, zone 2, and zone 3.

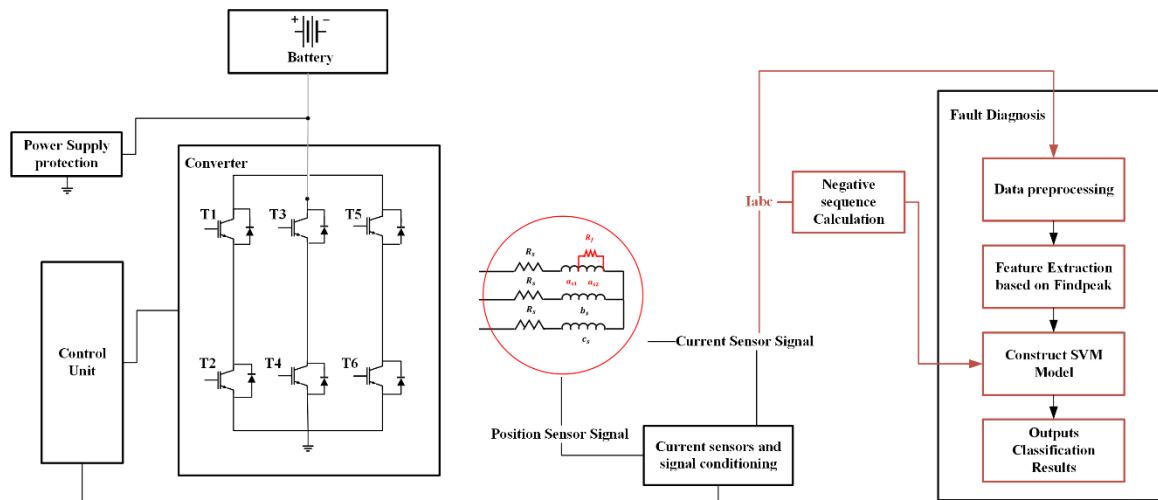


Figure 2: Inter-Turn Stator Winding Fault diagnosis methodology

#### Current pre-processing:

To extract the ITSF characteristics, we calculated the current PSD of the three-stator currents. Two separate PSD estimators have been employed, namely the Welch and the autoregressive method. In this context, the Burg technique was applied to estimate the autoregressive parameters. For more details on the theory behind the Welch method and the Burg autoregressive method, it is recommended to refer to [16].

In this section, these techniques are compared in terms of their frequency resolution and ability to track the defect frequency using the simulation tool. The current was sampled at the 4 kHz frequency, and for each condition, we recorded 131,072 current samples. The result reported here refers to 0% and 50% of fault severity and 0, 1, and 10 Ω. For the Welch method, the current segments can be distributed in different window types, such as the Bartlett method. Nevertheless, the latter has shown a poor result in magnitude detection, which corresponds to the fault frequency. For this reason, the Hanning window was chosen to ensure the windowing of the segments.

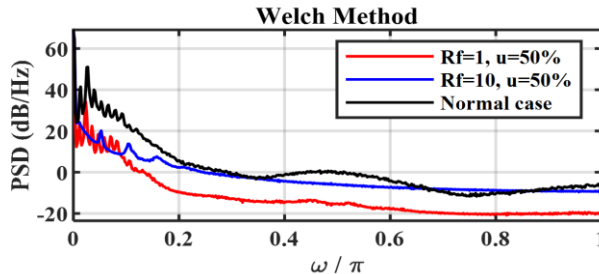


Figure 3: The current's PSD estimation based on WELCH at different operating conditions

The Welch method has shown that the most critical fault components have been recognizable from the result obtained. Therefore, even for a low fault severity, an acceptable amplitude that identifies the defect has appeared. Because of the winding's asymmetry, the PSD displays a displacement of the fault frequencies, which arise significantly with fault severity.

For the same condition as Welch, the current's PSD was plotted based on the Burg method. Using the Akaike Criterion, the model order is set up to 200 so that the entire fault features could correctly be estimated.

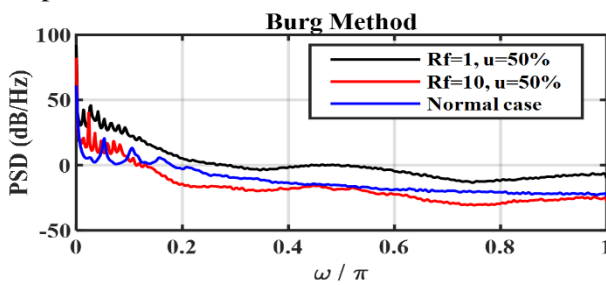


Figure 3: The current's PSD estimation based on Burg at different operating conditions

It has been proven that it is nearly unattainable to properly quantify fault frequencies when the model order is less than or greatly exceeding 200. In the first case, only the fundamental component is recognized, whereas if the model order is higher than 200, there are some other components in the frequency spectrum that are not forcefully included. By analyzing both figures 3 and 4, it can be deduced that these methods can separate the three areas of system performance previously mentioned. Each region has its proper feature signature. Furthermore, it is quite understandable that nearly all the fault frequency components are more evident using the Welch except the second one. The peak at this frequency is precisely identified using Burg when the machine runs under the following condition  $\mu = 0.5$ , and  $r_f = 10\Omega$ .

### Fault classification detection based Support Vector Machine

Once the fault feature is extracted from the current signal, the classifier is then used to distinguish different system performance regions. This section will closely explain the selected classifier, the Support Vector (SVM) Machine algorithm.

The SVM is a linear non-probabilistic classification method. It was first initially introduced to deal with binary classes and then extended to multi-class problems. With SVM, one class's data points are separated from those of the other class by finding the optimized hyperplane. Reasonable choice means the best fitting hyperplane, i.e., the one with the most significant margin between the two classes. The hyperplane can be expressed as follows:

$$d(x, w, b) = w^T x + b = \sum_{i=0}^l w_i x_i + b \quad (16)$$

Where:  $w$  is the vector of weights,  $x$  is an input vector, and  $b$  represents bias.

When the training data is linearly divisible, two parallel hyperplanes that assign the two data categories are determined so that the distance between them is the most comprehensive attainable size. The following equations can express these hyperplanes:

$$w^T x + b = 1 \quad \text{for the class labeled } 1$$

$$w^T x + b = -1 \quad \text{for the class labeled } -1$$

Geometrically, the distance between these two hyperplanes is  $\frac{2}{\|\vec{w}\|}$ , in order to maximize the distance between the planes, it is necessary to minimize  $\|\vec{w}\|$ , besides, it is recommended to check data points from falling into the margin, which can be translated as it follows:

$$y_i(w^T x_i + b) \text{ for all } 1 \leq i \leq n$$

With:  $y_i = \pm 1$

Mutually, these constraints are established to get the optimization problem:

$$\text{Min } \|w\|^2 \quad \text{and} \quad y_i(w^T x_i + b) \geq 1 \quad \forall i \in [1, n]$$

Classically, the current quadratic optimization problem with inequality constraints can be solved by the saddle point of the Lagrange functional [17]:

$$L(w, b, \alpha) = \frac{1}{2} w^T w - \sum_{i=1}^l \alpha_i \{y_i [w^T x_i + b] - 1\}, \quad (17)$$

Where the size ( $\alpha_i$ ) are Lagrange multipliers. The solutions  $\alpha_i$  of the dual optimization problem determine the parameters  $w_0$  and  $b_0$  of the optimal hyperplane as it follows:

$$w_0 = \sum_{i=0}^l \alpha_i y_i x_i \quad (18)$$

$$b_0 = \frac{1}{N_{sv}} \sum_{s=1}^{N_{sv}} (y_s - x_s^T w_0) = \frac{1}{N_{sv}} \sum_{s=1}^{N_{sv}} \left( \frac{1}{y_s} - x_s^T w_0 \right) \quad (19)$$

$N_{sv}$ : Denotes the number of support vectors.

Once the parameters ( $w_0$  and  $b_0$ ) are determined, the final decision hyperplane and the indicator function  $i_F$  are then obtained as given below:

$$d(x) = \sum_{i=0}^l w_{0i} x_i + b_0 \quad (20)$$

$$i_F = \text{sgn}(d(x)) \quad (21)$$

Separating more than two classes involves reducing the single problem of multi-class to a binary classification problem. The one-versus-rest and the one-versus-one are two ways to make this reduction [18].

#### 4. FAULT DIAGNOSIS METHODOLOGY

To verify the proposed fault diagnosis method's efficiency and, therefore, choose the most appropriate PSD technique for the feature extraction process, the classification model is built with SVM aid. The one-vs-one method relying on SVM multi-class with a linear kernel function is employed in the current work. The classifier's input data set has been prepared first by estimating the current PSD based on both methods: the Welch and Burg estimator. Simultaneously, the current's negative sequence is calculated under various scenarios; at normal and faulty operating conditions. Four labels have been assigned to each operating state, as shown in the following table:

Table 1: The label corresponding to each faulty operating condition

State	Label
$\mu=0\% , r_f = 0$	00
$\mu=20\% , r_f = 10$	01
$\mu=50\% , r_f = 10$	10
$\mu=50\% , r_f = 1$	11

Before the learning phase, the stator current signals are analyzed under the following conditions: the measurement time is 0.6 s; the sampling frequency f is 10 kHz. As a result, the number of samples is set at 6000. A low-pass filter is used to cut off the fundamental frequency at 50Hz because some fault characteristics will have a small amplitude and could be neglected in the presence of the current's fundamental component.

To keep a limited number of SVM training data and thus identify the amplitude and location of spectral peaks, the function findpeaks located in the signal-processing tool have been deployed.

Using this function and setting the minimum distance between each peak at 100 Hz, the data is reduced from 4100 samples to 250 main elements.

Nearly 250 data are collected from different operating conditions (healthy and defective) under various fault severity and resistance value. One hundred fifty data are used for training and the rest for testing.

Two analyses are performed in this study. The first aims to evaluate the accuracy of the ITS diagnostic method, including all the data. While the second is done to compare the PSD method's impact on classification results.

#### ■ Analyze 1:

According to the parallel coordinate plot, it is evident that the negative sequence predictor separates the preference classes from each other. These results have been achieved under static condition; which means that the speed and the load torque are considered constant.

It is also visibly illustrated that in the interval corresponding to the peak frequency [1 kHz, 1.5 kHz] and [2.6 kHz, 3.6 kHz], the data can be entirely separated using the SVM with a linear kernel. It is then conceivable to eliminate the negative sequence to predict the severity of the fault in this interval. However, it is still necessary to rely on the peaks in low frequency to avoid the noise effect caused by external conditions.

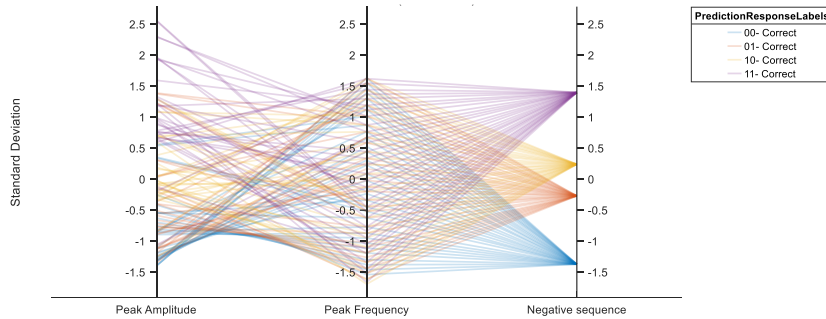


Figure 5: The parallel coordinate plot of the standard deviation between different predictors

In order to assess the learner's effectiveness, we are calculated the accuracy of the classification based on the ratio between the number of correctly classified samples and the total number of classified samples under dynamic condition. According to the confusion matrix, the 5-fold classification error is 1.5 %, which means that all the remains records were classified correctly.

#### ■ Analyze 2

In this analysis, we restricted the frequency interval at [2640 Hz, 3650 Hz] using a bandpass filter, and the minimum distance between each peak is set up to 50 Hz so that the number of a dataset will be significant. Moreover, to compare the AR-based Burg and the Welch performance, we eliminate the current negative sequence and the data corresponding to zone 2 in the training phase.

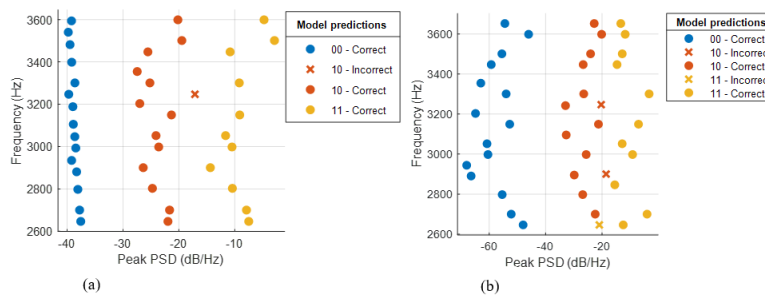


Figure 4: the classification of stator current's PSD (a) AR based Burg (b) Welch

Using the Welch method, the fivefold classification error is 2.5%. One of the defective samples corresponding to the “10” class is misclassified as a sample belonging to the “11” class. On the other hand, it can be observed that the samples corresponding to the normal state are entirely separated since all the peaks are aligned.

Table 2. Confusion Table for testing dataset based Welch method

00	100%	0%	0%
10	0%	92.9%	0%
11	0%	7.1%	100%
Positive Predictive	100%	92.9%	100%
False Discovery	0%	7.1%	0%
	00	01	10

By contrast, when using the AR model-based Burg, the misclassification rate increase to 7.3%. On all samples, 14.3 % from the class ‘10’ was misclassified as ‘11’ and, 8.3% from the class ‘11’ was misclassified as ‘10’. We concluded from these results that the classifier has benefited from a careful selection of feature extraction methods from this analysis. The Welch analysis demonstrates more adequate results in extracting fault features at the high frequencies range.

*Table 3: Confusion Table for testing dataset based Burg estimator*

00	100%	0%	0%
10	0%	85.7%	8.3%
11	0%	14.3%	91.7%
Positive Value	100%	85.7%	91.7%
False Discovery	0%	14.3%	0%
	00	01	10

## 5. CONCLUSION

In this paper, a new method of detecting an Inter-Turn Stator Winding fault for Permanent Magnet Synchronous Motor is considered. This technique uses the Power Spectral Density estimator to extract the fault characteristic from the motor’s three phases’ stator current and then explores these characteristics to classify the system’s normal and faulty states. It has the advantage of separating the different performance regions according to the fault severity ratio of the fault being studied. The simulation results demonstrated that different system performance areas are easily identified and classified at a rate of 98.5% if the machine is subjected to dynamic conditions such as load or speed variation. Furthermore, this can be explained by using the current negative sequence component as an SVM predictor. In addition to exposing the fault diagnosis methodology, this study highlighted the Autoregressive Model estimators’ difference based on Burg and the Welch method in extracting fault characteristics. Simulation results showed that the Welch method combined with linear SVM offers relatively optimizable performance compared to the Burg method for ITS Winding Fault detection.

It should be noted that the autoregressive method based on the Burg parameter estimator also allows adequate monitoring of the frequencies characterizing the fault and therefore it detects the ITSW fault; however, it is dependent on the model order; thus, the wrong choice of the model order would automatically lead to erroneous results. By way of perspective, this method could be applied to diagnose various PM Synchronous Motor’s powertrains defects of the electric vehicles in which the engine occupies a primordial place.

## REFERENCES

- [1] D. Grenier, L. A. Dessaint, O. Akhrif, Y. Bonnassieux, and B. Le Pioufle, “Experimental nonlinear torque control of a permanent-magnet synchronous motor using saliency,” *IEEE Trans. Ind. Electron.*, vol. 44, no. 5, pp. 680–687, 1997.
- [2] B. Vaseghi and N. Takorabet, “Experimentally Validated Dynamic Fault Model for PMSM with Stator Winding Inter-turn Fault,” no. Umr 7037, pp. 1–5, 2008.
- [3] J. Choi, B. Gu, and C. Won, “Modeling and Analysis of PMSMs under Inter Turn Short Faults,” vol. 8, no. 5, pp. 1243–1250, 2013.
- [4] K. Ludwinek, “Influence of DC voltage and current of field winding on induced stator voltages of a salient pole synchronous generator,” no. January 2014, 2016.
- [5] R. M. Tallam, T. G. Habetler, and R. G. Harley, “Transient model for induction machines with stator winding turn faults,” *IEEE Trans. Ind. Appl.*, vol. 38, no. 3, pp. 632–637, 2002.
- [6] Z. Wang, J. Yang, H. Ye, and W. Zhou, “A review of permanent magnet synchronous motor fault diagnosis,” *IEEE Transp. Electrif. Conf. Expo, ITEC Asia-Pacific 2014 - Conf. Proc.*, 2014.
- [7] J. Rosero, A. Garcia, J. Cusido, L. Romeral, J.A. Ortega. Fault Detection by means of Hilbert Huang Transform of the stator current in a PMSM with Demagnetization- Conf. Proc., 2007.
- [8] J. A. Rosero, L. Romeral, J. A. Ortega, and E. Rosero, “Short-circuit detection by means of empirical mode decomposition and Wigner-Ville distribution for PMSM running under dynamic condition,” *IEEE Trans. Ind. Electron.*, vol. 56, no. 11, pp. 4534–4547, 2009.
- [9] SZ. Su, Z.H. Liu, S.P. Xu, S.Z. Li, Sparse auto-encoder based feature learning for human body detection in depth image, *Signal Process.* 112 (2015) 43–52.
- [10] H.D. Shao, H.K. Jiang, X. Zhang, M.G. Niu, Rolling bearing fault diagnosis using an optimization deep belief network, *Meas. Sci. Technol.* 26 (2015) 115002.
- [11] X. Jia, M. Zhao, Y. Di, P. Li, and J. Lee, “Sparse filtering with the generalized  $l_p/l_q$  norm and its applications to the condition monitoring of rotating machinery,” *Mech. Syst. Signal Process.*, vol. 102, no. March 2020, pp. 198–213, 2018.

- [12] S. Zerdani, M. L. Elhafyani, and S. Zouggar, "Inter-Turn Stator Winding fault Diagnosis for PMSM based Power Spectral Density Estimators," 2020 In press.
- [13] Y. Chen, L. Wang, Z. Wang, and A. U. Rehman, "Inter-turn Fault in DFIG," no. 1, pp. 244–247, 2015.
- [14] S. Zerdani, M. L. Elhafyani, and S. Zouggar " Traction Inverter fault detection method based on Welch and K-Nearest Neighbor algorithm," Proc. Springer LNEE, volume 681, pp. 411–419, 2020.
- [15] T. Wang, J. Qi, H. Xu, Y. Wang, L. Liu, and D. Gao, "Fault diagnosis method based on FFT-RPCA-SVM for Cascaded-Multilevel Inverter," ISA Trans., pp. 1–8, 2015.
- [16] Silvia Maria Alessio, "Digital Signal Processing and Spectral Analysis Processing for Scientists," Springer, 2016
- [17] Y. Lu, V. Roychowdhury, L. Vandenberghe, Distributed parallel support vector machines in strongly connected networks, IEEE Trans. Neural Netw. 19 (7) (2008) 1167–1178.
- [18] C.-W. Hsu, C.-J. Lin, A comparison of methods for multi-class support vector machines, IEEE Trans. Neural Netw. 13 (2) (2002) 415–425.

## Appendix

*Table 4: PMSM Parameters*

PARAMETERS	QUANTITIES
<i>Winding resistance (<math>R_s</math>)</i>	$0.6 \Omega$
<i>Winding inductance (<math>L_s</math>)</i>	$2.1 \text{ mH}$
<i>Moment of inertia (<math>J</math>)</i>	$0.0011 \text{ g.m}^2$
<i>Number of pole pair (<math>p</math>)</i>	4
<i>DC bus Voltage</i>	$330 \text{ V}$
<i>Mutual inductance (<math>M_{a1a2}</math>)</i>	$0.52 \text{ mH}$
<i>Mutual inductance (<math>M_{a2b}</math>)</i>	$-0.35 \text{ mH}$



# THE IMPACT OF RADIANT HEATING ON THE PERFORMANCE OF SUSTAINABLE CONSTRUCTIONAL COMPONENT UNDER ELEVATED TEMPERATURE: PART 2

Wail N. Al-Rifaie

Philadelphia University, Amman, Jordan, wnrifaie@yahoo.com, ORCID: 0000-0003-1426-4130

Talal Al-Hajri

Gulf University, Manama, Bahrain, talalalhajri2020@outlook.com, ORCID: 0000-0001-8430-1713

Waleed K. Ahmed

UAE University, Al Ain, UAE, w.ahmed@uaeu.ac.ae, ORCID: 0000-0002-8294-0981

Cite this paper as:

*Al-Rifaie, W., Al-Hajri, T., K.Ahmed, W. The impact of radiant heating on the performance of sustainable constructional component under elevated temperature: Part 2. 9<sup>th</sup> Eur. Conf. Ren. Energy Sys. 21-23 April 2021, Istanbul, Turkey*

## Abstract:

The present paper reports the results concerning the effect of radiant heating on the strength of ferrocement slabs. One hundred and twenty-six (126) ferrocement slab specimen's 500x500 mm were cast and tested under central patch loads. The main parameters that are considered in the present work are temperature: 23, 100, 200, 300, 400, 500, and 600 oC, mixture (cement: sand ratio = 1:1, 1:2), thickness: 20, 30, 40 mm and number of layer of wire mesh reinforcement: 2, 4 and 6. All slab specimens were prepared with 28 curing days, then heated up to specified temperatures and then tested under the central patch load. The specimens were heated under the above temperatures for one hour, then the specimens were left to cool prior to testing. The behavior of the specimen was observed by reading the central deflections of the specimens and observing the crack patterns. It is concluded that increasing the number of wire mesh, and specimen thickness will lead to an increase in the initial cracking and ultimate loads of the slab specimens.

## Keywords:

*Ferrocement; radiant heating; compressive strength; modulus of elasticity; elevated temperature*

© 2021 Published by ECRES

## INTRODUCTION

Producing sustainable material is one of the most attractive fields to researchers nowadays trying to find a powerful solution to the thermal pollution caused by the massive construction building using concrete<sup>(1-12)</sup>. As it has been mentioned that, the present paper entitled "*The Impact of Radiant Heating on the Performance of Sustainable Constructional Component under Elevated Temperature*" is the continuity of the works submitted to 2021 6th International Conference on Renewable Energy: Generation and Applications (ICREA) – Renewable Energy Technologies, Applications and Materials. So that, the experimental work using ferrocement (micro reinforced concrete) which is defined as a thin-wall reinforced concrete was carried out and empirical expressions are proposed for estimating the cube compressive strength, modulus of elasticity, and yield stress and ultimate stress of wire mesh used through the investigation in terms of temperature.

## EXPERIMENTAL WORK

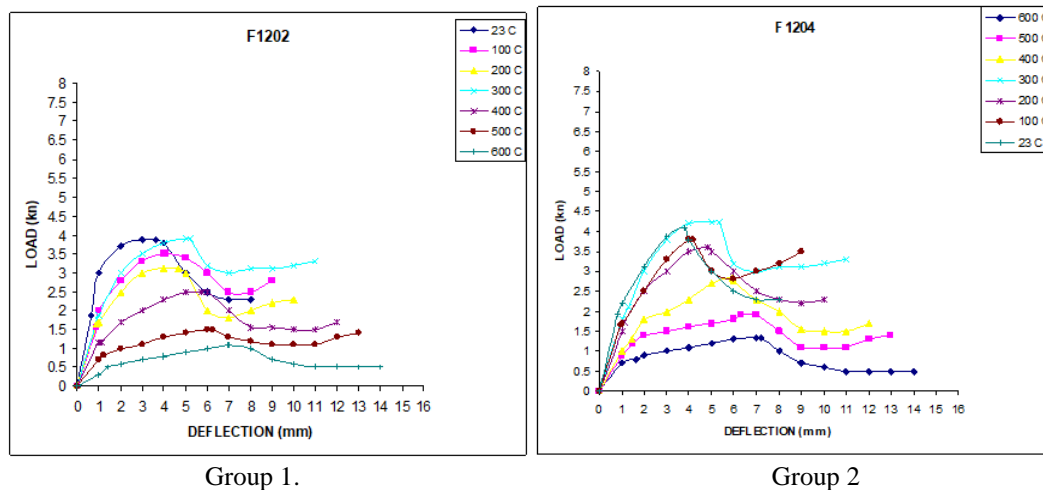
A total of one hundred and twenty-six (126) ferrocement slab specimens (500x500 mm), were cast<sup>(13)</sup> to satisfy the structural behavior of 1-18 groups of ferrocement slab specimens as given in reference<sup>(13)</sup>. These slab specimens were then, heated and tested under central patch load. The present study investigates the impact of the heat treatment on the mechanical properties of the ferrocement element especially the flexural characteristics. The specimens were subjected to heating for one hour, then the specimens were left to cool prior to testing. 1-18 main groups were

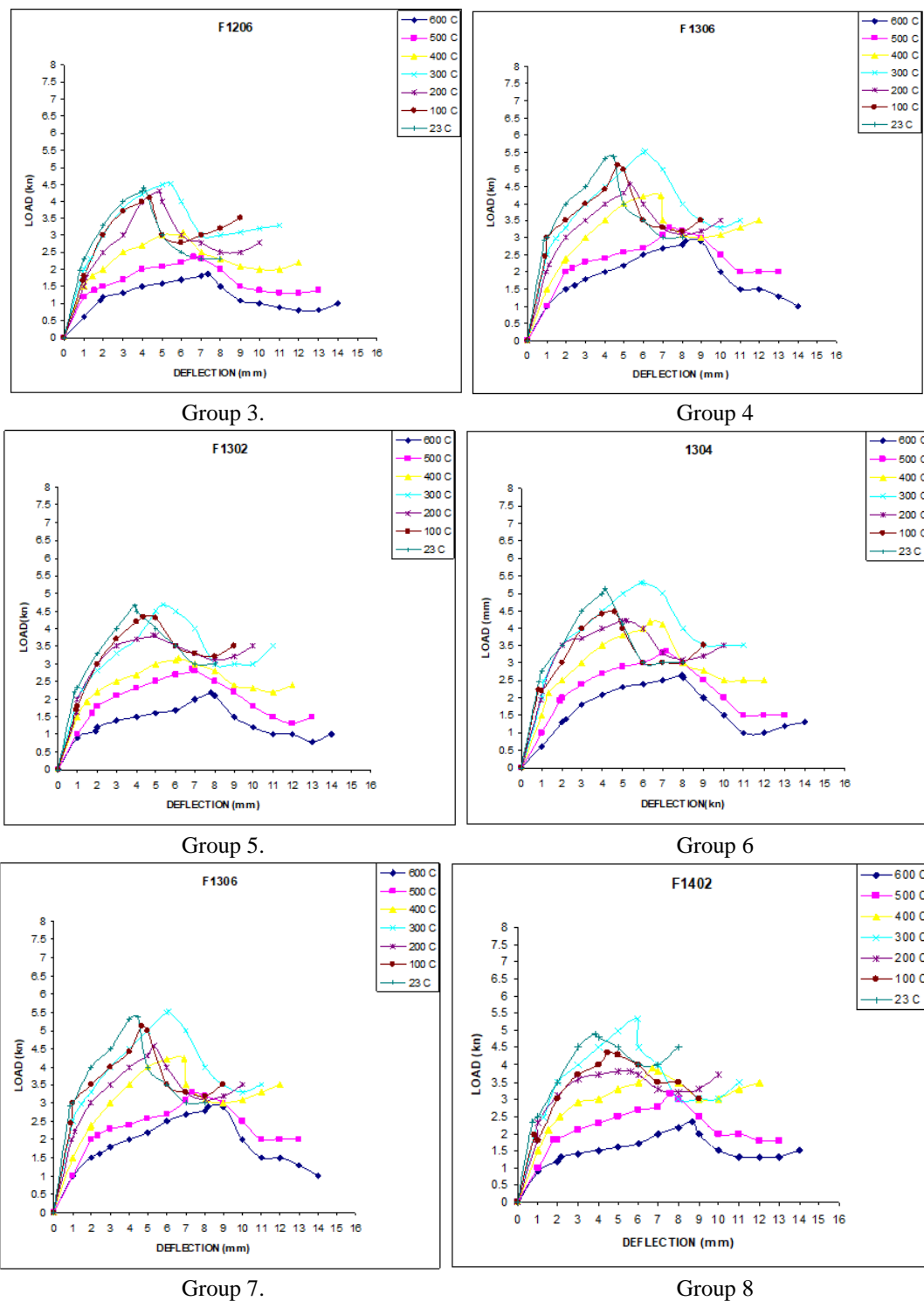
chosen in the present investigation, to study the structural behavior and ultimate strength of ferrocement slabs under different of temperatures. More details may be found in reference (13).

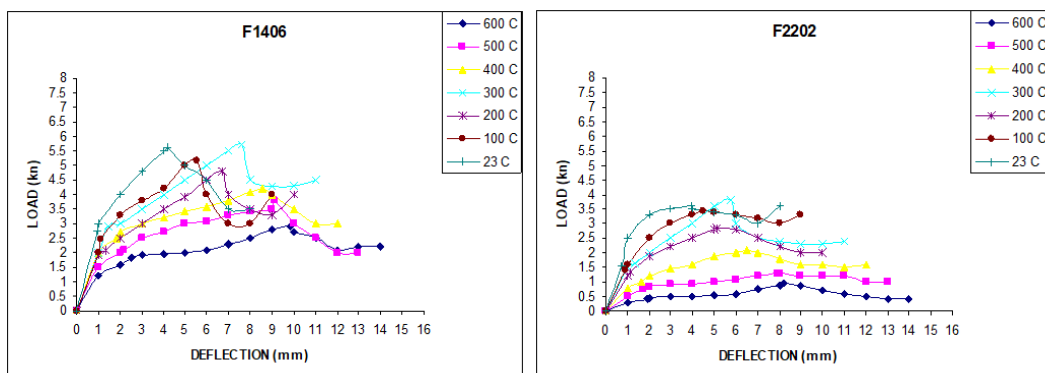
### Behavior of Ferrocement Specimens under Central Patch Load

As it was stated earlier, point loads were applied at the center of the specimens through 75x75 mm steel plate, and the proving ring reading were recorded, using the dial gauge with increment of the loading was continued until ultimate load was reached and failure of the slab occurred. Failure was defined by the sudden release of loading indicated on the dial gauge of the proving ring during the period of measuring deflections.

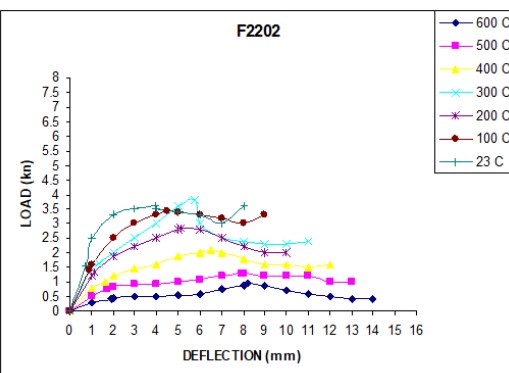
In Table 1, the initial cracking deflection, initial cracking load, ultimate deflection, ultimate load, ductility factor and residual strength for the specimens are given. All the specimens were cracked first at lower surface of the specimen were the cracks growth at center toward the sides of the specimen when the load is increased. At last the specimens were failed by punching under point load. It was noted that when the number of wire mesh is increased the ultimate load is increased by 10-30 %. This is may be attributed to the increase in the yield stress ( $f_y$ ). Similarly, when the thickness is increased while the number of wire mesh is fixed, the ultimate load is increased by 10-30 %, because of the increase in the moment of inertia of the specimen section. It may also be, noted that by increasing the sand ratio in mixture, at temperature (400) °C and above, the ultimate load will be increased by 10- 20 %. It was observed that at temperature (300) °C and below, with the increase the sand ratio in the mixture the ultimate load will be decreased by 5-10 %. That behavior of the ultimate load for the slab owing behavior of the compressive strength ( $fcu$ ) MPa at any temperature. Figures 1 (group's 1-18) show the load-central deflection curves for groups 1-18. In general, the load-deflection curve that is linear up to first cracking load. In cracked stage, the slope of the load-deflection curve was decreased where its approach to zero at temperature (600) °C. It may be attribute to the decrease in modulus of elasticity of mortar ( $Em$ ).Table 3 gives the ductility factor (the ratio of the ultimate deflection to the initial cracking deflection ( $\Delta u / \Delta cr$ ) for the ferrocement slab specimens. Increase the temperature tend to increase the ductility ratio by 5-18 % because the elevated temperature due to micro cracks in mortar that lead to increase in deflection and consequently increase the ductility. Further, increase the number of layers tend to increase the ductility by 4-12 % because of increasing in the steel area and increase the volume of fraction. While increase the thickness tend to decrease the ductility ratio by 3-15 %.Commonly, increase the mixture ratio (increase sand ratio) tend to increase the ductility by 2-17 %. Where the number voids or capillary pores increased with the increase in sand ratio (increase the water/cement ratio), the propagation of cracks yet increase. The first crack was observed in the lower surface of the specimen, it may be due to the effect of the maximum positive moment developed at mid surface of the slab due to increasing the load. It may be observed that the cracks were noticed at the upper surface of the specimen. It may be due to the maximum negative moments, which are developed at these positions. It may be stated that increase number of mesh layers tends to increase the number of cracks and decrease cracks spacing at ultimate load stage. It may be observed that, increase specimen thickness tend to decrease the number of cracks due to the increase in the moment of inertia. At temperature between 300 °C and 600 °C, the failure was more controlled and the specimens were able to undergo large strain. At higher temperature, the material softened and the descending branches had definitely negative slop, with more ductile failures. Most of the specimens were failed by shear (punching shear) in particular if the specimen thickness was small. Views of failure mode for specimens were given in Figure 2.



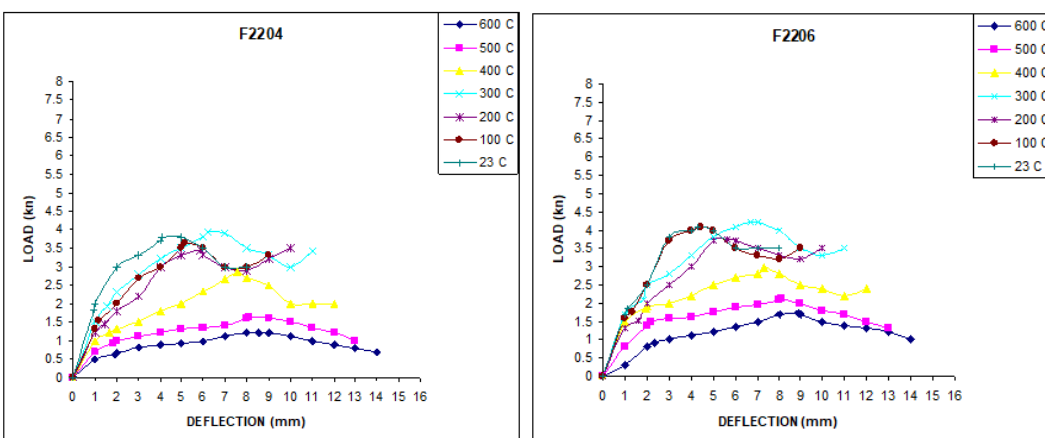




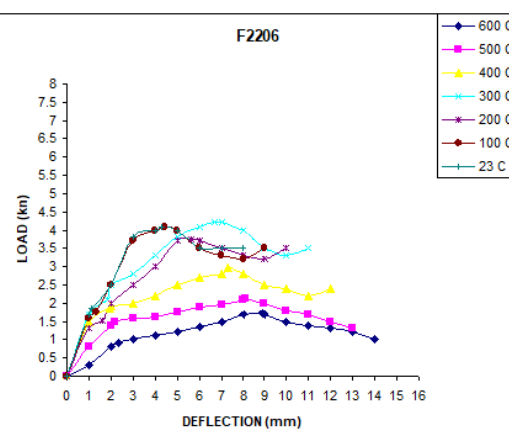
Group 9.



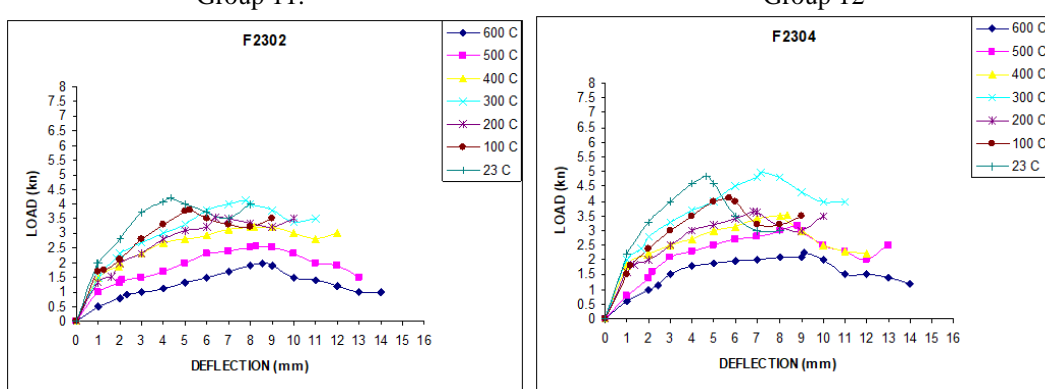
Group 10



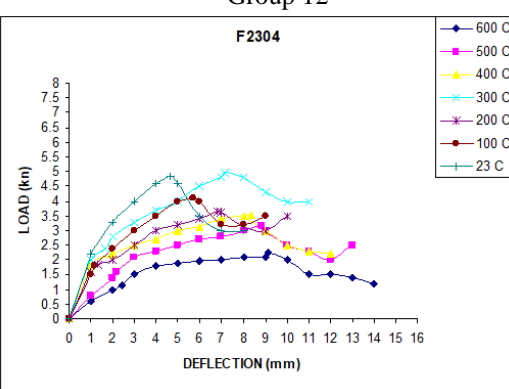
Group 11.



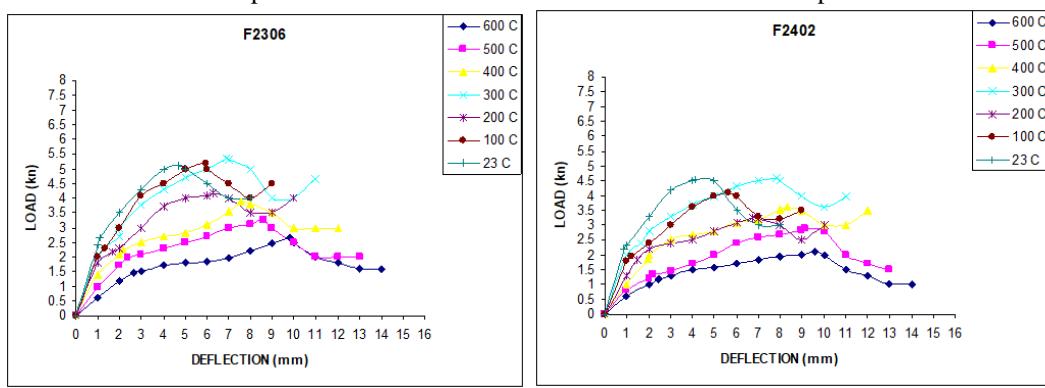
Group 12



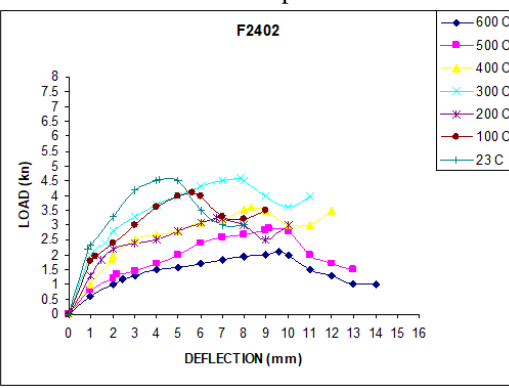
Group 13.



Group 14



Group 15.



Group 16

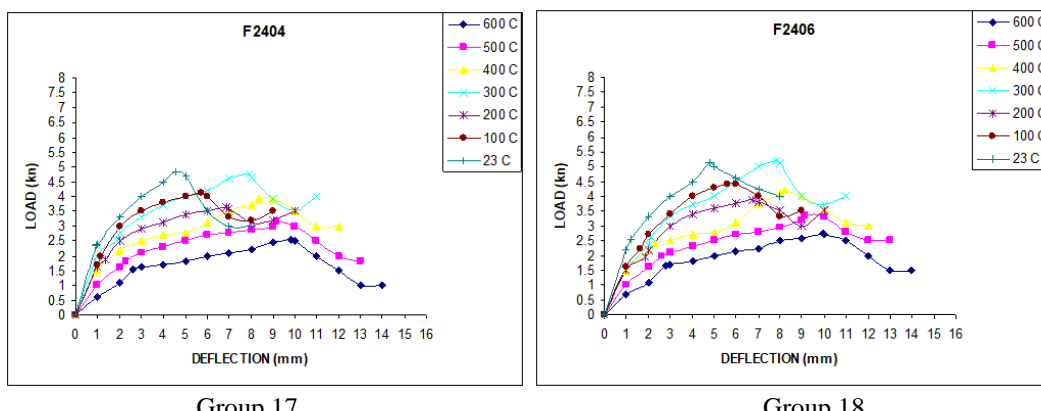


Figure 1. Load-Deflection Relationships

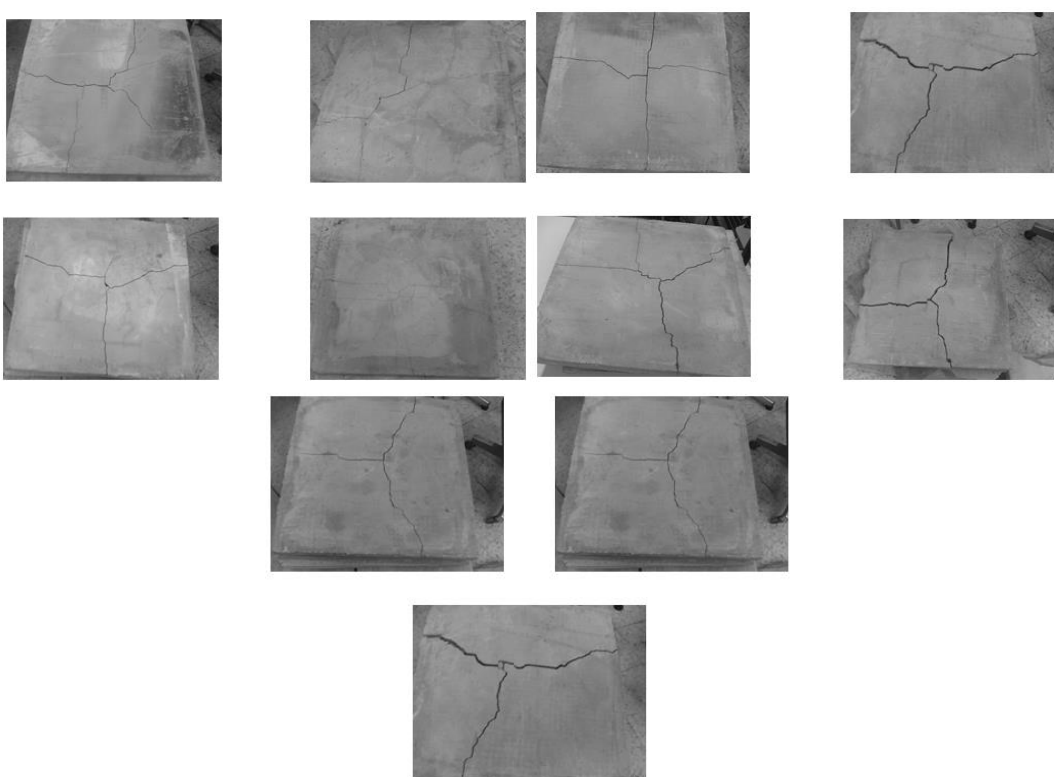


Figure 2 Failure Mode of Ferrocement Slab Specimens: (S1202, 1204, 1206, 1302, 1304, 1306, 1402, 1404, 1406) at temperature 600 °C.

## CONCLUSION

Based upon the experimental investigation on ferrocement slabs, the following conclusions may be drawn which are valid within the range of parameter considered in this investigation:

1. Increase temperature to (100) °C, the strength decreased compared to room temperature for both mixture (1:1, 1:2) by (21, 24) % under room temperature strength respectively.
2. Strength in each mixture dropped sharply, at temperature range of (400 to 600) °C.
3. At temperature (100) °C the residual modulus of elasticity were (89, 87) % for both mixtures (1:1, 1:2) respectively.
4. The yield stress and ultimate tensile strength are not affected at temperature (300) °C.
5. By increasing temperature to (400) °C the residual yield stress and residual ultimate tensile strength will be decreased to (72, 68) %, respectively in comparison with room temperature.
6. At temperature (600) °C the residual yield stress and residual ultimate tensile strength are decreased to (59, 64) % respectively.
7. The behavior of ferrocement slabs are linear up to first cracking load.

8. In crack stage, the slope of the load-deflection curve was decreased where its approach to zero at temperature (600) °C.
9. Increase thickness (10 mm), the ultimate load (Pu) and initial cracking load (Pcr) will be increased by (10-30) %.
10. By increasing sand ratio the value of ultimate load and initial cracking load increased by (5-20) % at temperature (400) °C.
11. By increasing sand ratio the value of ultimate load and initial cracking load decreased by (2-18) % at temperature (300) °C and down.
12. Increase the layers from 2, 4 to 6 the initial cracking load increase by (5-25) % and ultimate load increase by (10-40) %.
13. Increase the temperature tend to increase the ductility by (5- 18) %.
14. Increase the number of layer tend to increase the ductility by (4- 12) %.
15. Increase the thickness tend to decrease the ductility by (3-15) %.
16. Increase the mixture ratio, increase sand ratio tend to increase the ductility 2-17%.
17. Increase number of mesh layer tends to increase the number of cracks and decrease cracks spacing at ultimate load stage.
18. Increase slab thickness tends to decrease the number of cracks.

## **REFERENCES**

1. Al-sulaimani, G. J. and, S. F., "Deflection and Flexural Rigidity of Ferrocement I- and Box Beam", Journal of Ferrocement, Vol. 18, No.1, January 1988, pp. 1-12.
2. Al-Salihi, M. and Al-Rifaie, W, N,"Design of Ferrocement in Flexural", Journal of Engineering and Technology, Vol. 18, No. 4, 1999, pp. 3 15-325.
3. ACI Committee 549 (1999) "Guide for the Design, construction, and Repair of Ferrocement", ACI structural Journal).
4. Dias, W. P. S., Khaury, G. A. and Sullivan, P. J. E., "Mechanical Properties of Hardened Cement Paste Exposed to Temperatures up to 700c" (1292 F)", ACI Material Journal, Vol. 89, No. 2, March- April 1990, pp. 160- 166.
5. Abrams, M. S., "Compressive Strength of Concrete at Temperature to 1600 F (871 C)," ACI Special Publication, SP 25-2, 1971, pp 33- 58. Cite from, 29.
6. Fahmi, H. M. and Nuri, D., "Influence of High Temperature on Compressive and Tensile Strength of Concrete", Journal of Building Research, Vol. 5, No. 2, November 1986, pp.85- 102.
7. Elizzi, M. A., Al-Haddad, I H., Yousif, S. H. and Ali, F. A., " Influence of Different Temperature on Compressive Strength and Density of Concrete", Journal of Building Research, Vol.6, No.2, NOV. 1987, pp. 1-23.
8. Consolazio, G. R., Mcvay, M. C. and Rish, J. W., "Measurment and Prediction of Pore Pressures in Saturated Cement Mortar Subjected to Radiant Heating", ACI Material Journal, September- October 1998, Vol. 95, No. 5, pp. 535-535.
9. ASTM Standards C 469-87a, "Static Modulus of Elasticity and Poisson's Ratio of Concrete in Compression" Vol. 04.02.
10. ACI Committee 549, "State-of-the-Art Report on Ferrocement", Concrete International: Design and Construction. Vol. 4, No. 8, August 1999. pp 13-38.
11. Hawlader, M. N, Mansur, M. A. and Rahman, M., "Thermal Behavior of Ferrocement ", Journal of Ferrocement, Vol. 20, No. 3, 1990, pp. 33 1-239
12. Mathews, M. s, Sudhakumer, J. and Thomas, A. V., "Behavior of Ferrocement Roofing Panels under Periodic heat Flow Condition", Journal of Ferrocement, Vo1. 22, No. 2, April 1992, pp. 125-134.
13. Wail N. Al-Rifaie, Talal Al-Hajri, Waleed K. Ahmed. Private communication: wnrifaie@yahoo.com.



# SYSTEM INTEGRATION AND DATA MODELS TO SUPPORT SMART GRIDS ENERGY TRADING

Silva Fábio

International Energy Research Centre, Tyndall National Institute, Cork, Ireland, fabio.silva@ierc.ie, ORCID: 0000-0001-6019-372X

O'Leidhin Eoin\*

International Energy Research Centre, Tyndall National Institute, Cork, Ireland, eoin.oleidhin@ierc.ie, ORCID: 0000-0002-7443-1431

Tahir Farah

International Energy Research Centre, Tyndall National Institute, Cork, Ireland, farah.tahir@ierc.ie, ORCID: 0000-0002-1696-7828

Mould Karen

International Energy Research Centre, Tyndall National Institute, Cork, Ireland, karen.mould@ierc.ie, ORCID: 0000-0001-9692-4790

O'Regan Brian

International Energy Research Centre, Tyndall National Institute, Cork, Ireland, brian.oregan@ierc.ie, ORCID: 0000-0002-3627-2353

*Silva, F, O'Leidhin, E, Tahir, F, Mould, K, O'Regan, B. "System integration and data models to support smart grids energy trading.", 9th Eur. Conf. Ren. Energy Sys. 21-23 April 2021, Istanbul, Turkey.*

**Abstract:** As smart grids gained relevance in the renewable energy landscape, the demand for new data management models became evident. Independently, whether emerging models are centralised on the Transmission System Operators (TSO), Distribution System Operators (DSO), or even on a third-party entity/aggregator (under proper regulatory supervision), the complexity of integration and interoperability of heterogeneous systems are worsened by the increase of renewable energy sources - given its potential reach and the diversity of solution providers. This work provides a detailed study of the main systems concerns present on TSO and DSO platforms alike, and main concerns in relation to renewable energy sources, sensor devices (e.g., smart meters and Internet of Things (IoT) devices) and processes. Furthermore, this work also carries out an analysis of the available integration studies - including a study case. Finally, this work proposes a top-level ontology-based standardisation for smart grid integration to support energy trading initiatives.

**Keywords:** Smart grid, sustainable energy, renewable energy, energy trading, energy informatics

© 2021 Published by ECRES

## 1. INTRODUCTION

Apart the current COVID-19 pandemic, climate change has been the top agenda item for governments globally for the last decade. Increased CO<sub>2</sub> emissions, dependence on fossil fuels and their impact on the environment, have seen the rise in demand for renewable and more sustainable options, primarily driven by public opinion. Most electricity grids in the world have needed to adapt in order improve grid stability, reliability and resilience and meet growing electricity demand.

In 2007, European Union (EU) leaders [1] agreed a set of targets which they aimed to meet by 2020. When these targets were brought into legislation, they were considered highly ambitious, they included a 20% cut in greenhouse gas emissions (from 1990 levels), a 20% of EU energy from renewables and a 20% improvement in energy

efficiency. More recently, an even more ambitious targets at least 32% renewables by 2030 is bound at EU level [2]. The term Smart Grid (SG) came to prominence in 2007, when it was defined in the Energy Independence and Security Act (EISA) of 2007 [3]. The intention was to clearly provide guidance for the evolution of the grid, from digital information and removing of barriers.

SG have had to transform quickly, technology adoption has significantly increased over the last decade, enormous integration of renewable energy options, such as wind and solar have put serious strain on the grid operators and introduced a great deal of issues [4], [5]. For some grid operators this is proving to be a real challenge [6]. A topology that was already complex to monitor and react accordingly has become even more convoluted [7]. The traditional power plants, the distribution systems (for industrial plants, building offices, community houses and more) and all the monitoring subsystem (e.g., PMUs and electronic relays) have been overloaded with the new complexities brought by SGs [8].

All sorts of renewable energy sources added to the grid (e.g., Photovoltaic (PV)/solar, wind, biomass) and demands of Household Energy Storage (HES) and/or Community Energy Storage (CES), create a scenario where the problems of integration - both the energy itself and the information necessary to support such complex new scenarios - are more urgent and demand new approaches and solutions.

The rest of this paper is organised as follows. Section 2 surveys some related work covering the main topics explored in this paper. Section 3 describes the TSO/DSO landscape concerning data integration. Section 4 explores the challenges and opportunities of the SGs. Section 5 presents a high-level ontology-based standardisation proposal. Section 6 concludes the paper and suggests future work. Finally, a list of the abbreviations and acronyms used in this paper can be found as an appendix at the end of the paper.

## **2. RELATED WORKS**

In the next subsections, we explore a few the state-of-the-art publications on SGs and the complexities involving their integration on the traditional energy grid. Also, we explore references of ontology in the energy sector that supported our ontology-based standardisation proposal.

### **Integration concerns**

The work of [9] approaches the Smart Grid (SG) integration as an evolution of power networks due to the ubiquitous presence of new sensors or IoT in general – with all the heterogeneous protocols and sensor devices that integrate them. What once was considered as isolated systems, now must be integrated to deliver new energy management resources. The authors propose a “Web of Energy” with guidelines to tackle performance, accessibility, and availability. The Actor Model paradigm presented in the paper brings insightful considerations on modelling of the systems involved. However, as a proposal of an overall development model it can face limitations as the subsystem are becoming increasingly specific.

In the work [10], the authors highlight the importance of energy management to reduce the overall expenditure on electricity and the need of flexible systems to encompass a broad range of consumers, IoT, data storage and analytics. They proposed a hardware implementation capable of gathering the necessary info and algorithms to develop cost optimisation. However, the “local” operation of such devices can be tricky and face problems related to users’ interaction, they have also implemented a web solution associated with the IoT implementation where it is possible for the user to check its consumption behaviour. Although the implementation covers a broad range of important points related to energy consumption, its scope falls short of a more generic approach to integrate diverse IoT devices.

The Data and Citizen-centric Approach (DCA) discussed in the work of [11], introduces a model to support SG and, in a broader aspect, Smart City (SC) governance. In this model, the biggest challenges are customer engagement, legal framework and technology and system integration – especially in what concerns sensing, e.g., Radio-frequency Identification (RFID), actuators, smart meters (new and legacy) combined with sensitive citizen data, and standardisation in the smart power sector. Several approaches are discussed, such as a “mediator” software that could translate the data to keep uniformity amongst systems, or a Service-oriented Architecture (SOA) implementation with data integration functionalities. However, the standardisation concerning data integration is still the best long-term alternative.

### **Ontology in energy**

Ontology is a branch of philosophy that studies the kind of structures of objects, their properties, events, processes where they interact and their relation in all areas of reality [12], [13]. However, the use of ontology is flexible, and the levels of detailing vary significantly depending on its usage.

The ontologies can be interpreted in levels, a proposed by [14] when lists three levels of ontologies in energy: upper ontology (referenced by other ontologies), domain ontology (defining concepts using classes, entities and relationships) and application ontology (which extends domain ontologies for applications). In [15], there is also references to ontologies for SG divided in layers, such as: field layer, knowledge layer and management layer.

In a less generic approach, the Common Information Model (CIM) describes a well-established International Electrotechnical Commission (IEC) standard 61970/61968/62325 [16] expressed in Unified Modelling Language (UML) notation. CIM can address the complexity of data but has obstacles within its standards. As the standard has developed confusions – not in compatibility between versions, but as the standard is in the English language – non-English-speaking vendors must develop translations for their users of the system [17]. Also, as in general systems do not have a native use of UML format for data, real system then ultimately has to convert the data structure to support the data management [17]. As a result, ontologies offer a better data integration with interoperability [18] and offers a powerful tool in direction to a standardised model.

### **3. TSO AND DSO SYSTEMS LANDSCAPE**

TSOs and DSOs have always shared common challenges on what concerns the integration of their distribution system and the recurring need to renewal ageing grids. More recently, the overgrowing need for data and new demands for flexible services require coordinated efforts and constant investments [19] in communication hardware and software - especially when faced with the integration of large number of renewable energy sources. One of the main priorities is to achieve such a level of integration that would connect dispersedly distributed resources and/or new service providers into the market and the electricity system as a whole and, at the same time, ensure security and value for customers [20].

The importance of cooperation in the energy sector [2], [4] (transmission, distribution, micro-generation and so on) in all administrative levels is mandatory in face of the challenges of combining distributed flexible resources into an innovative environment. Examples of that are initiatives such as [21] where TSOs and DSOs create a cooperation for the creation of efficient network codes, the Network Code Implementation and Monitoring Group (NCIMG) bringing together experts from both TSO and DSO in 2018.

With the increasing number of Distributed Energy Resource (DER) on the grids, DSOs will need to have a more effective role while guaranteeing the integrity its network and, at the same time, fomenting DER services – and a satisfactory coordination between TSOs, DSOs and DERs will be compulsory [22].

In areas where a decentralised data exchange is the current model – most common model around the world and especially in Europe – it is noticeable a trend to involve TSOs, DSOs and all sorts of third-party participants. These Data Exchange Platforms (DEPs) motivations are efficiency in data management, flexibilization for new market entrants and, most importantly, empowerment of customers. A few implementations of such collaboration are already in course.

For example, the Datahub is a central IT platform jointly developed by Eandis [23], Elia [24], Infrax [23], Ores [25], Resa [26] and Sibela [27]. It aggregates the data necessary to evaluate the flexibility services used (e.g., the users' consumption profile) and estimates the amount of energy generate (or simply not consumed) in a given period of time. This way, the Datahub has the fundamental information to guarantee an uneventful operation in the controlled flexibility market.

The growing share of DER in the distribution grid offer possibilities for both the TSO and the DSO to use resources for the mutual benefit [28]. These integration initiatives foment innovation, such as The International Renewable Energy Agency (IRENA) reports in [29] identifying 30 innovative solutions to enabling technologies, new market and business models, and operation. From that, as suggested by [30] in Table 1, the innovation landscape for renewable energies expanded significantly.

### **4. SMART GRID LANDSCAPE**

SGs can principally be defined as the use of technology across the energy grid, but differing research centres and agencies have differing ideas on what a smart grid can offer, and thus how it can be defined.

The United States (US) research agency, Electric Power Research Institute (EPRI), has worldwide hubs specialising research in smart grids and utilities, resulting in contribution to the definition of standards as set by the Institute for Electrical and Electronic Engineers (IEEE) [31]. The EPRI states that its concept of a smart grid is that the use of information and communications technology through the generation of electricity can help minimise environmental impacts, improve reliability, enhance markets, and aid customers with reduced costs and improved efficiency.

The ABB Asea Brown Boveri (ABB) is a global technology company that is focusing on a more productive and sustainable future [32], and defines a smart grid as a bidirectional flow of power and digital information, by modernisation of the utility infrastructure, through improved efficiency, enabling new applications, lowered costs, conservation of power, and improved quality to the customer [33]. In July 2009 a smart grid assessment released by the US Department of Energy (DOE) described a smart grid as not a 'thing' but could be described as a vision, with a role as a transactive agent, and that would enable financial, informational, and electrical transactions among consumers, grid assets, and other authorized users [34], [35].

This assessment was characterised by performance goals, including to involve customers participation, and provide better services, and to make the grid more resilient to disturbances, such as natural disasters [36], as well as concepts for operation efficiency and the enablement of new products and services [34], [20].

*Table 1. Enabling solutions for flexibility in the power system [32]*

○ Enabling technologies	○ Business Models	○ Market Design	○ System Operation
1 Utility-scale batteries	12 Aggregators	17 Increasing time granularity in electricity markets	25 Future role of distribution system operators
2 Behind-the-meter batteries	13 Peer-to-peer electricity trading	18 Increasing space granularity in electricity markets	26 Co-operation between transmission and distribution system operators
3 Electric-vehicle smart charging	14 Energy-as-a-service	19 Innovative ancillary services	
4 Renewable power-to-heat	15 Community-ownership models	20 Re-designing capacity markets	27 Advance forecasting of variable renewable power generation
5 Renewable power-to-hydrogen	16 Pay-as-you-go models	21 Regional markets	
6 Internet of things		22 Time-of-use tariffs	28 Innovative operation of pumped hydropower storage
7 Artificial intelligence		23 Market integration of distributed energy resources	
8 Blockchain		24 Net billing schemes	29 Virtual power lines
9 Renewable mini-grids			30 Dynamic line rating
10 Supergrids			
11 Flexibility in conventional power plants			

The EU states that a smart grid is defined in the Trans-European Networks for Energy (TEN-E) regulation as one of the twelve trans-European energy infrastructure priority corridors and areas. It explains that an electricity network should integrate, in a cost-efficient manner, to ensure a power system, with high level of quality and low losses, with generators and consumers that can also generate (prosumers) [37].

The European Commission (EC) in 2006 published a booklet defining a SG as not a technical venture, but that it would address commercial and regularity issues as well [38]. To achieve that, SG should provide solutions to allow power injections from distinct energy resources (rapidly and cost effectively), be based open technical standards and protocols, facilitate cross border trading (through regulatory and/or commercial agreements), develop Information and Communication Technology (ICT) to enable efficiency and support backward compatibility and interoperability amongst old and new equipment in the grid.

Finally, the United Kingdom (UK) Department of Energy & Climate Change (DECC) defines the SG as an electricity network capable of integrating all participants (e.g., generators, consumers and prosumers) to efficiently deliver sustainable, economic and secure electricity supplies [39]. It also highlights the importance of developing innovative services and products to improve monitoring, control, and communication.

## 5. HIGH-LEVEL ONTOLOGY-BASED STANDARDISATION

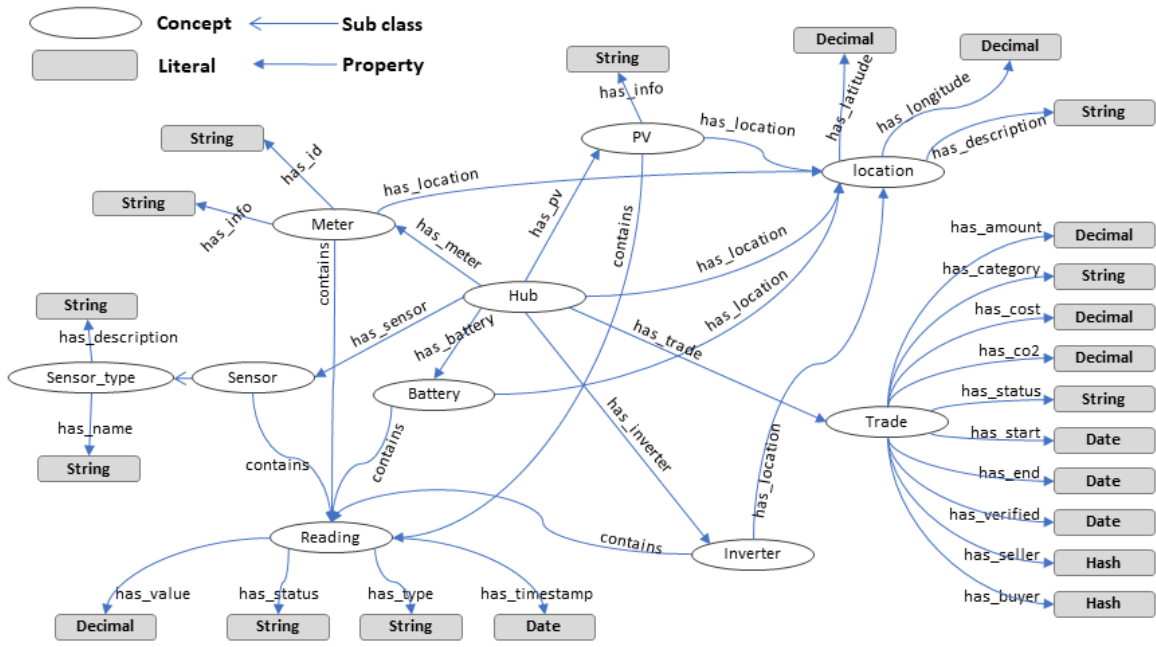
As distinct as the very definition of a SG can become around the globe [18] (concerning diverse technologies, regulations, standardisation efforts and so on), the underlying concept of efficiency achieved through the establishment of bi-directional communication is a constant [4] to achieve interoperability. All devices participating

in a SG would need a common structure of data communication that would allow users and systems to share information across the energy network. To achieve that, an Ontology (a method for sharing knowledge through a formal representation of real-world domains) is a powerful tool [18]. As such, and for the scope of this project, our Ontology offers a framework for typology of distinct SG system components, defines the key concepts connection these systems and suggests a neutral language to integrate its components [40].

The ontology described in Figure 1 is part of the Cooperative ENergy Trading System (CENTS) project. This project is a project coordinated by the International Energy Research Centre (IERC) and will rely on the industry experience from mSemicon [41] and Community Power [42], and the research capabilities of University College Cork (UCC) [43], National University of Ireland Galway (NUIG) [44], and Dublin Institute of Technology (DIT) [45]. CENTS is a disruptive technology platform for the electricity sector where consumers, producers, prosumers (simultaneously production and consumption) and communities will be empowered with the infrastructure to generate their own electricity, earn from the electricity generation, and finally, to be an integral part of decarbonising their homes and communities for sustainable living.

This ontology helped to define how the sensors and IoT devices – energy storage (battery status), PV readings, temperature, transactions (blockchain-based), and any other meters and sensors in general – would be integrated to the CENTS platform and be the base for the energy trading and user empowerment.

In this use case, the class Hub represents a local hardware device responsible for collecting all relevant data and transmitting it a central platform and integrating also the trading data structure.



## 6. CONCLUSIONS

The high-level ontology described in this work is intended to pave the way for the standardisation of data integration in what concerns Smart Grid integration. A formal way to describe the information to be shared between the systems and subsystem present on a TSO/DSO and Smart Grid will facilitate commercialisation, operation and control of energy trading and empowering the customer.

## ACKNOWLEDGEMENTS

The authors acknowledge the support of the Department of Business, Enterprise, and Innovation, who generously funded the CENTS project under the Government of Ireland's Project 2040 Plan.

## REFERENCES

- [1] E. C. EU Comission, “Commission proposes an integrated energy and climate change package to cut emissions for the 21st Century,” [https://ec.europa.eu/commission/presscorner/detail/en/IP\\_07\\_29](https://ec.europa.eu/commission/presscorner/detail/en/IP_07_29), Jan. 2007.
- [2] P. O. o. t. E. Union, “Clean energy for all Europeans.” <http://op.europa.eu/en/publication-detail/-/publication/b4e46873-7528-11e9-9f05-01aa75ed71a1/language-en>, Jul. 2019.
- [3] O. US EPA, “Summary of the Energy Independence and Security Act,” <https://www.epa.gov/laws-regulations/summary-energy-independence-and-securityact>, Feb. 2013.
- [4] K. Ouahada and O. Longe, Eds., smart energy management for smart grids. Switzerland: MDPI AG, 2020.
- [5] M. L. Tuballa and M. L. Abundo, “A review of the development of Smart Grid technologies,” Renewable and Sustainable Energy Reviews, vol. 59, pp. 710–725, Jun. 2016.
- [6] E. Espe, V. Potdar, and E. Chang, “Prosumer Communities and Relationships in Smart Grids: A Literature Review, Evolution and Future Directions,” Energies, vol. 11, no. 10, p. 2528, Sep. 2018.
- [7] I. Colak, S. Sagiroglu, G. Fulli, M. Yesilbudak, and C.-F. Covrig, “A survey on the critical issues in smart grid technologies,” Renewable and Sustainable Energy Reviews, vol. 54, pp. 396–405, Feb. 2016.
- [8] G. Dileep, “A survey on smart grid technologies and applications,” Renewable Energy, vol. 146, pp. 2589–2625, Feb. 2020.
- [9] V. Caballero, D. Vernet, A. Zaballos, and G. Corral, “Prototyping a Web-of-Energy Architecture for Smart Integration of Sensor Networks in Smart Grids Domain,” Sensors, vol. 18, no. 2, p. 400, Jan. 2018.
- [10] P. Pawar and P. Vittal K, “Design and development of advanced smart energy management system integrated with IoT framework in smart grid environment,” Journal of Energy Storage, vol. 25, p. 100846, Oct. 2019.
- [11] Z. Mahmood, Ed., Smart Cities, ser. Computer Communications and Networks. Cham: Springer International Publishing, 2018.
- [12] L. Floridi, “Blackwell Guide to the Philosophy of Computing and Information,” Ontology and Geographic Categories, vol. 1, pp. 155–166, 2003.
- [13] E. P. B. Simperl and C. Tempich, “Ontology Engineering: A Reality Check,” in On the Move to Meaningful Internet Systems 2006: CoopIS, DOA, GADA, and ODBASE, D. Hutchison, T. Kanade, J. Kittler, J. M. Kleinberg, F. Mattern, J. C. Mitchell, M. Naor, O. Nierstrasz, C. Pandu Rangan, B. Steffen, M. Sudan, D. Terzopoulos, D. Tygar, M. Y. Vardi, G. Weikum, R. Meersman, and Z. Tari, Eds. Berlin, Heidelberg: Springer Berlin Heidelberg, 2006, vol. 4275, pp. 836–854.
- [14] M. Haghgoo, I. Sychev, A. Monti, and F. H. Fitzek, “SARGON – Smart energy domain ontology,” IET Smart Cities, vol. 2, no. 4, pp. 191–198, Dec. 2020.
- [15] A. Hameurlain, R. Wagner, F. Morvan, and L. Tamine, Eds., Transactions on Large-Scale Data- and Knowledge-Centered Systems XL, ser. Lecture Notes in Computer Science. Berlin, Heidelberg: Springer Berlin Heidelberg, 2019, vol. 11360.
- [16] M. Uslar, M. Specht, S. Rohjans, J. Trefke, and J. M. González, The Common Information Model CIM: IEC 61968/61970 and 62325 - A Practical Introduction to the CIM, ser. Power Systems. Berlin Heidelberg: Springer-Verlag, 2012.
- [17] L. Wang and H. Murayama, “A multi-version CIM-based database platform for smart grid,” IEEJ Trans Elec Electron Eng, vol. 10, no. 3, pp. 330–339, May 2015.
- [18] A. T. Yee Chong, M. A. Mahmoud, F.-C. Lim, and H. Kasim, “Description for Smart Grid: Towards the Ontological Approach,” in 2020 8th International Conference on Information Technology and Multimedia (ICIMU). Selangor, Malaysia: IEEE, Aug. 2020, pp. 218–222.
- [19] “TSOs-DSOs to continue cooperation for smarter electricity grids — E.DSO,” <https://www.edsoforsmartgrids.eu/tsos-dsos-to-continue-cooperation-for-smarter-electricity-grids/>.
- [20] P. Verma, B. O'Regan, B. Hayes, S. Thakur, and J. G. Breslin, “EnerPort: Irish Blockchain project for peer- to-peer energy trading: An overview of the project and expected contributions,” Energy Inform, vol. 1, no. 1, p. 14, Dec. 2018.
- [21] E. , A. , and E. , “Network Code Implementation and Monitoring Group,” [https://ec.europa.eu/energy/topics/markets-and-consumers/wholesale-market/network-code-implementation-and-monitoring-group\\_en](https://ec.europa.eu/energy/topics/markets-and-consumers/wholesale-market/network-code-implementation-and-monitoring-group_en), Oct. 2017.
- [22] T. Borsche and J. Wolst, “Study: data exchange in electric power systems: European State of Play and Perspectives,” <https://www.entsoe.eu/news/2017/06/26/study-data-exchange-in-electric-power-systems-european-state-of-play-and-perspectives/>.
- [23] “Fluvius,” <https://www.fluvius.be/nl>.
- [24] Elia, “Elia Group is one of Europe’s five leading transmission system operators,” Feb. 2021.
- [25] “Bienvenue - Particuliers & Professionnels — ORES,” <https://www.ores.be/>.
- [26] “Resa,” <https://www.resa.be/fr/homepage/>.
- [27] “Sibelga,” <http://www.sibelga.be/fr/>.
- [28] H. Gerard, E. I. Rivero Puente, and D. Six, “Coordination between transmission and distribution system operators in the electricity sector: A conceptual framework,” Utilities Policy, vol. 50, pp. 40–48, Feb. 2018.
- [29] “IRENA – International Renewable Energy Agency,” <https://www.irena.org/>.
- [30] IRENA, “Innovation landscape for a renewable-powered future: Solutions to integrate variable renewables. Summary for policy makers.” 2019.
- [31] C. Sweet, “A New Template for the Integrated Grid,” <https://eprijournal.com/a-new-template-for-the-integrated-grid/>, Apr. 2019.
- [32] “ABB Group,” <https://global.abb/group/en/about>.

- [33] W. ABB, “Solution Overflow - Smart Grids,” Jan. 2016.
- [34] “A VISION FOR THE SMART GRID,” Jun. 2009.
- [35] W. Feng, M. Jin, X. Liu, Y. Bao, C. Marnay, C. Yao, and J. Yu, “A review of microgrid development in the United States – A decade of progress on policies, demonstrations, controls, and software tools,” *Applied Energy*, vol. 228, pp. 1656–1668, Oct. 2018.
- [36] Q. Sun, X. Ge, L. Liu, X. Xu, Y. Zhang, R. Niu, and Y. Zeng, “Review of Smart Grid Comprehensive Assessment Systems,” *Energy Procedia*, vol. 12, pp. 219–229, 2011.
- [37] E. Commission, “Smart grid regional group,” [https://ec.europa.eu/energy/topics/infrastructure/projects-common-interest/regional-groups-and-theirrole/smart-grid-regional-group\\_en](https://ec.europa.eu/energy/topics/infrastructure/projects-common-interest/regional-groups-and-theirrole/smart-grid-regional-group_en), Oct. 2016.
- [38] E. Kommission, Ed., European Technology Platform SmartGrids: Vision and Strategy for Europe’s Electricity Networks of the Future, ser. EUR. Luxembourg: Office for Official Publications of the European Communities, 2006, no. 22040.
- [39] N. Jenkins, C. Long, and J. Wu, “An Overview of the Smart Grid in Great Britain,” *Engineering*, vol. 1, no. 4, pp. 413–421, Dec. 2015.
- [40] D. Dori and H. Sillitto, “What is a System? An Ontological Framework,” Wiley Online Library, pp. 207–219, Apr. 2017.
- [41] “mSemicon — Custom Product Development,” <https://www.msemicon.com/en-GB/>.
- [42] “Community Power,” <https://communitypower.ie/our-story/>.
- [43] “World-class Undergraduate and Postgraduate Education in Ireland,” <https://www.ucc.ie/en/>.
- [44] “NUI Galway - NUI Galway,” <http://www.nuigalway.ie/>.
- [45] “TU Dublin - City Campus — Technological University Dublin,” <https://www.dit.ie/>.



# POWER CONTROL STRATEGY OF A PHOTOVOLTAIC SYSTEM

Bedoud Khouloud

Research Center in Industrial Technologies CRTI, BP 64 Cheraga, Algeria, k.bedoud@crti.dz & khouloud1981@yahoo.fr,  
ORCID: <https://orcid.org/0000-0003-1290-0041>

Bahi Tahar

Automatic Laboratory and Signals, Badji Mokhtar University, Annaba, Algeria, tbahi@hotmail.fr, ORCID:  
<https://orcid.org/0000-0001-6822-2492>

Merabet Hichem

Research Center in Industrial Technologies CRTI, BP 64 Cheraga, Algeria, h.merabet@crti.dz, ORCID:  
<https://orcid.org/0000-0001-7479-3195>

Cite this paper as:

*Bedoud, K, Bahi, T, Merabet, H. Power Control Strategy of a Photovoltaic System. 9<sup>th</sup> Eur. Conf. Ren. Energy Sys. 21-23 April 2021, Istanbul, Turkey*

---

**Abstract:**

The development of voltaic production systems is undoubtedly accompanied by the development of efficient and reliable control strategies. These systems require the use of static converters on the one hand for amplifying the voltages at the output of the solar panels (chopper) and on the other hand inverters to be able to synchronize and adapt with the power supply network. Therefore, in this work the so-called maximum power point tracking technique is considered to extract the maximum power produced by the solar panels, whatever the climatic conditions. Moreover, the use of static converters in the conversion chain which are nature nonlinear systems inevitably cause distortion of currents and consequently consumption of reactive energy. Indeed, a separate control of the active and reactive powers is planned to improve the energy quality. After developing models of each part of the photovoltaic system, a performances analysis is presented thanks to the simulation under the Matlab / Simulink software. The analysis reveals a good quality of the produced energy.

---

**Keywords:**

*Photovoltaic system, performance, MPPT control, simulation*

---

© 2021 Published by ECRES

## 1. INTRODUCTION

In the last decades, renewable energy conversion systems for the production of electrical energy such as wind or photovoltaic energy have seen a great deal of attention from governments both in the industrial and research fields. Because of its several advantages such as: less maintenance requirement with a maintenance costs relatively low, non-polluting, minimum power losses on the transmission line and easy to implement, photovoltaic panels installation for the exploitation of solar energy around the world has increased considerably [1-4]. In Algérie, a special attention has been noticed for the development of renewable energy, notably, solar energy for reducing the dependence and the use of fossil fuels. The Algerian government provides to highlight the inexhaustible renewable resources such as solar and wind energy. For this, at 03 February 2011, the Algerian government has adopted an ambitious program for the development of Renewable Energies (RE) and energy efficiency. Where, the electricity production from renewable energy will be increased to 40% of total energy consumption by 2030 and 37% will be assured by photovoltaic systems [5, 6]. In order to reduce the load on the electricity network and relieve generation, transmission and distribution systems, such a production system is usually placed near the points where the consumption of electric power is high [1]. Knowing that the power produced by photovoltaic generator (GPV) always depends on cell temperature and irradiation, then, the variation of these two parameters also influences on its maximum power value. Indeed, the remedy for control techniques to extract maximum power has become a necessity. Several control techniques have been developed for the extraction of maximum power from photovoltaic systems [4, 7-11]. The work presented in this paper is organized as follows: in section 2 the system description and

modeling are exposed. Section 3 presents the control strategies. Simulation results are analyzed and discussed in section 4. Finally, the 5th section is devoted to the conclusion and the work perspectives.

## 2. DESCRIPTION AND MODELING OF THE STUDIED SYSTEM

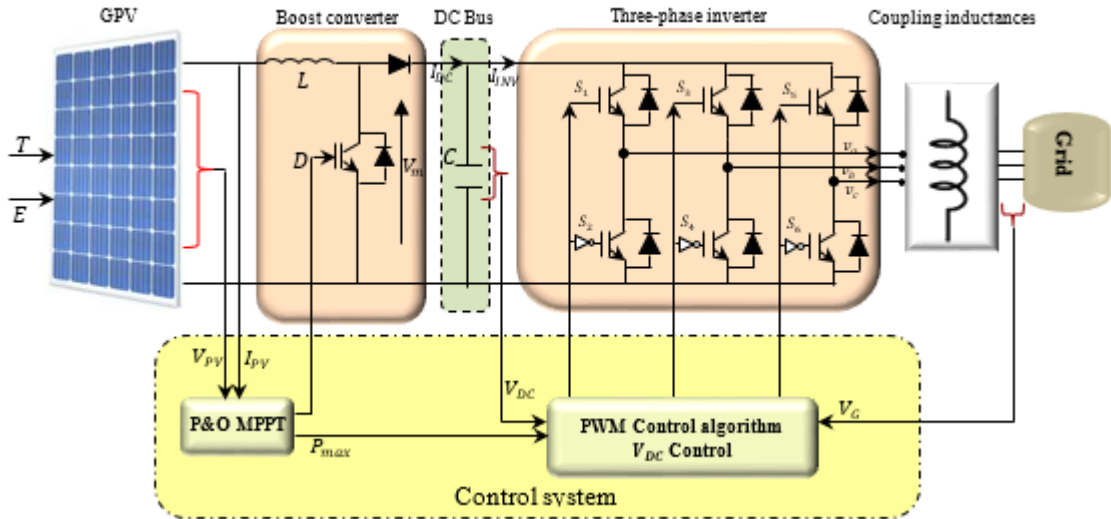


Figure 1. Block diagram of a photovoltaic conversion chain

The structure of the studied photovoltaic chain connected to the network is essentially composed of a: photovoltaic generator, boost converter, DC bus stage, three-phase inverter followed by coupling inductances and connected to the electrical network. The three-phase inverter allows to converts a DC to AC current. The structure is shown by figure 1.

### 2.1. PHOTOVOLTAIC GENERATOR MODELING

As shown in figure 2 an equivalent circuit named one diode model is given to represent the PV equivalent model. It is composed of: two resistors (series and shunt) and a single diode. The photo current ( $I_{ph}$ ) can be written according to solar radiation (E) and temperature (T) as follows [7]:

$$I_{ph} = I_{ph}(T_{ref}) \cdot (1 + K_0 \cdot (T - T_{ref})) \quad (1)$$

$$I_{ph}(T_{ref}) = \frac{E}{E_{ref}} \cdot I_{sc}(T_{ref}) \quad (2)$$

$$K_0 = \frac{I_{sc}(T) - I_{sc}(T_{ref})}{T - T_{ref}} \quad (3)$$

Where;  $K_0$  is a constant,  $I_{ph}$  is the photo current at a nominal temperature and  $I_{sc}$  is the short circuit current.

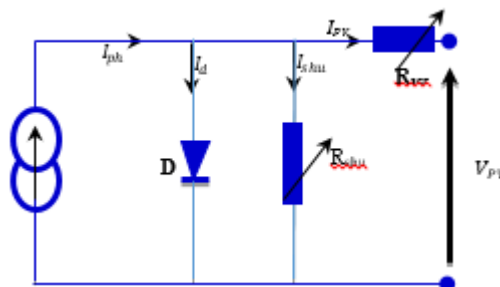


Figure 2. Equivalent circuit of photovoltaic cell

In the case where environmental temperature is equal to the nominal one, we can write:

$$I_{ph} = \frac{E}{E_{ref}} \cdot I_{sc}(T_{ref}) \quad (4)$$

Applying Kirchoff's current law we can write [3, 4, 7]:

$$I_{pv} = I_{ph} - I_{sat} \left[ \exp \left( \frac{q(v_{pv} + (I_{pv} * R_{Ser}))}{nkt} \right) - 1 \right] - \frac{V_{pv} + (I_{pv} * R_{Ser})}{R_{shu}} \quad (5)$$

With:  $I_d = I_{sat} \left[ \exp \left( \frac{q(v_{pv} + (I_{pv} * R_{Ser}))}{nkt} \right) - 1 \right]$  (6)

$$I_{shu} = \frac{V_{pv} + (I_{pv} * R_{Ser})}{R_{shu}} \quad (7)$$

We can write:  $I_{pv} = I_{ph} - I_{sat} \left[ \exp \left( \frac{q(v_{pv} + (I_{pv} * R_{Ser}))}{nkt} \right) - 1 \right] - \frac{V_{pv} + (I_{pv} * R_{Ser})}{R_{shu}}$  (8)

## 2.1. BOOST CONVERTER AND DC LINK MODELING

The boost converter can be described by its mathematical model as follows:

$$\begin{bmatrix} V_m \\ I_{DC} \end{bmatrix} = m. \begin{bmatrix} V_{DC} \\ I_L \end{bmatrix} \quad (9)$$

$$\frac{dV_{PV}}{dt} = \frac{1}{C} (I_L - I_{PV}) \quad (10)$$

$$\frac{di_L}{dt} = \frac{1}{L} (V_m - V_{PV}) - \frac{R_{Ser}}{L} I_L \quad (11)$$

Equation (12) presents the DC link model:

$$\frac{dV_{DC}}{dt} = \frac{1}{C} (I_{DC} - I_{INV}) \quad (12)$$

## 2.2. INVERTER MODELING

The use of inverters for the connection of a GPV to the grid, allows to generate an alternating voltage adjustable in frequency and amplitude from a DC voltage received from the generator. From figure 1 we can write  $V_{an}$ ,  $V_{bn}$  and  $V_{cn}$  as follow :

$$\begin{cases} V_{an} = (S_1 - S_2)V_{DC} \\ V_{bn} = (S_2 - S_3)V_{DC} \\ V_{cn} = (S_3 - S_1)V_{DC} \end{cases} \quad (13)$$

The quantities to be checked are the phase-to-neutral voltages on the load side ( $V_a$ ,  $V_b$  and  $V_c$ ). For a balanced three-phase load  $V_a + V_b + V_c = 0$ , the Phase-to-phase voltages can be calculated by:

$$\begin{bmatrix} V_a \\ V_b \\ V_c \end{bmatrix} = \frac{V_{DC}}{\sqrt{3}} \begin{bmatrix} 2 & -1 & -1 \\ -1 & 2 & -1 \\ -1 & -1 & 2 \end{bmatrix} \begin{bmatrix} S_1 \\ S_2 \\ S_3 \end{bmatrix} \quad (14)$$

## 3. CONTROL STRATEGY

The block diagram of figure 3-a represents the adopted control chain. The P&O control strategy defined by the algorithm in Figure 3-b allows generating the duty cycle ( $\alpha$  daty cycle). The P&O algorithm is developed so that the system instantly tracks the maximum power point (MPPT).

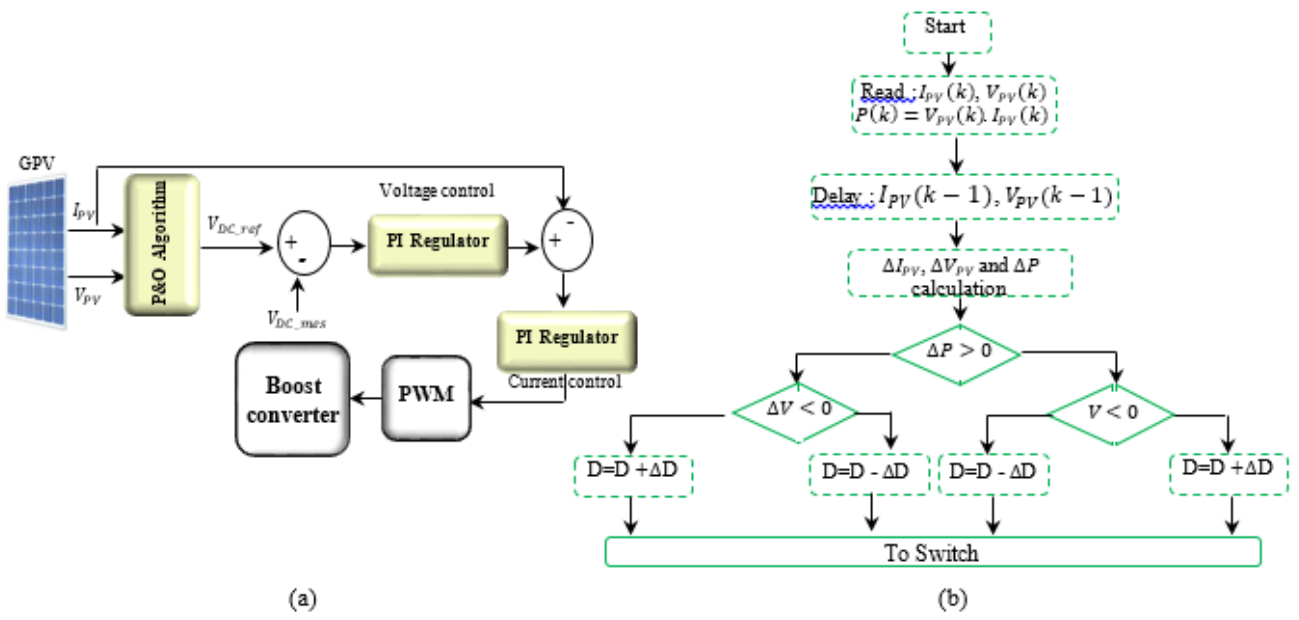


Figure 3. (a) Structure of boost converter control, (b) P&O algorithm

In addition, the proposed power system consists of controlling the active and reactive powers from the grid side inverter, designated by  $P_{gd}$  and  $Q_{gd}$ , respectively. Where:

$$\begin{cases} P_{gd} = \frac{3}{2}(V_{gd\_d}I_{gd\_d} + V_{gd\_q}I_{gd\_q}) \\ Q_{gd} = \frac{3}{2}(V_{gd\_q}I_{gd\_d} - V_{gd\_d}I_{gd\_q}) \end{cases} \quad (15)$$

With:  $V_{gd\_d}$ ,  $V_{gd\_q}$  are d-q components of grid voltage and  $I_{gd\_d}$ ,  $I_{gd\_q}$  are the d-q components of grid current. Considering that the reference frame synchronized with the grid voltage, the equation system (15) can be written as:

$$\begin{cases} P_{gd} = \frac{3}{2}V_{gd\_d}I_{gd\_d} \\ Q_{gd} = -\frac{3}{2}V_{gd\_d}I_{gd\_q} \end{cases} \quad (16)$$

#### 4. SIMULATION RESULTS AND ANALYSIS

In order to analyze the operation of this installation, a simulation program was developed under Matlab/Simulink environment. Then, considering that the irradiation and the temperature vary under the profiles shown in the figure 4 (a) and (b), respectively. We notice that during a simulation period of three (03) seconds the chain of conversion is requested under standard conditions ( $E = 1000 \text{ W/m}^2$  and  $T = 25^\circ \text{C}$ ) during periods  $(0 \leq t \leq 0.75)$  and  $(2 \leq t \leq 3)$ .

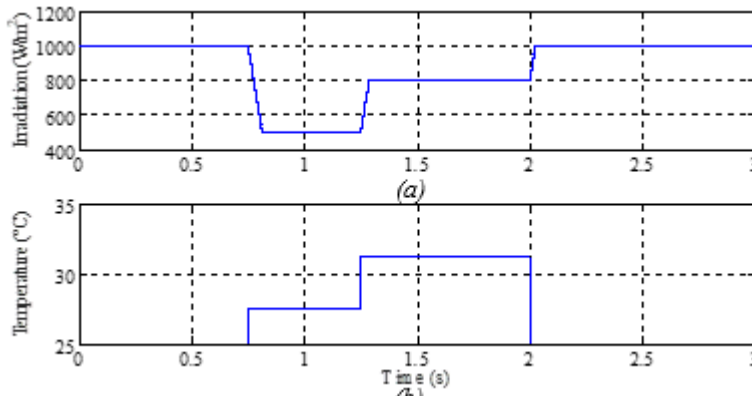


Figure 4. (a) Irradiation, (b) Temperature

Considering these conditions, the voltage and current of the PV generator are measured instantaneously and used for the P&O algorithm to impose the duty cycle value, shown in figure 5.

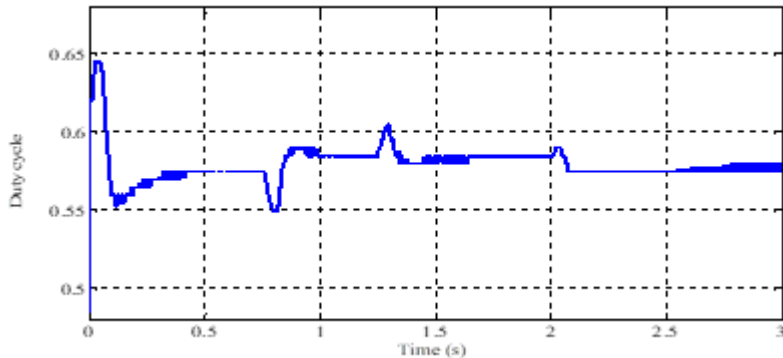


Figure 5. Duty cycle

Furthermore, to ensure the adjustment of the DC voltage at the output of the chopper, a reference of 700V has been imposed. From figure 6 we clearly note that the output voltage follows its reference perfectly despite the inevitable changes irradiation and temperature, previously shown in figure 4.

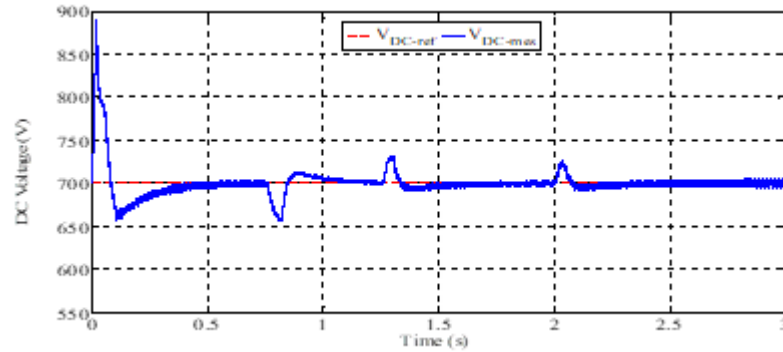


Figure 6. DC Voltage

Indeed, this voltage obtained and applied to the input of the three-phase inverter and which in turn has a command of its six (06) semiconductors. Then, the active and reactive powers injected into the network are illustrated by figure 7. An active power which evolves according to the climatic conditions reaching at each moment the maximum power (see the dotted line which represents the reference to be reached). Also, it is interesting to notice that the reactive power ( $Q$ ) is kept at zero ( $Q = 0$ ). All this, under the voltage and current shown respectively by the figure 8 (a) and (b).

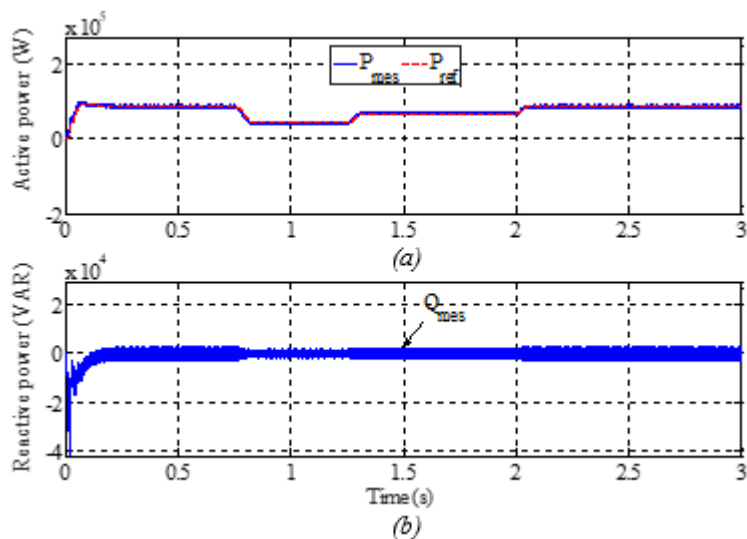


Figure 7. (a) Active power, (b) Reactive power

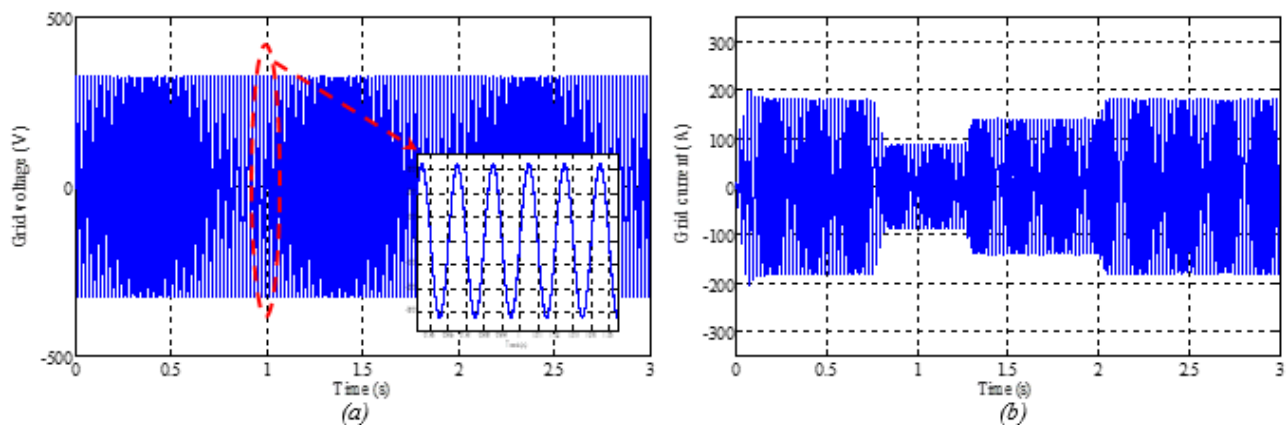


Figure 8. (a) Grid voltage, (b) Grid current

## 5. CONCLUSION

The duplication of photovoltaic systems associated with energy distribution networks contributes significantly to energy balance across the world. However, for a good efficiency of these systems, the development of consistent control strategies must accompany the installation. The commands in question are generally intended to control the boost converter and the DC voltage at its output. The latter is regulated at a voltage level imposed by the reference value in a way that it ensures a voltage injected into the network of the required amplitude and frequency. Moreover, it has been shown that the reactive power is kept equal to zero whatever the metrological changes. In addition, at the end of the work presented in this paper which therefore only concerns an analysis for operation over the sun, we count for the extension of this work, in the near future, to develop it by considering a storage system equipped with a power management control.

## REFERENCES

- [1] Fabio, LA, Adélio, JM, Geraldo, CG, Sérgio, MRS, Alexandre, R. Photovoltaic solar system connected to the electric power grid operating as active power generator and reactive power compensator, *Solar Energy* 2010; 84:1310–1317 <<https://doi.org/10.1016/j.solener.2010.04.011>>
- [2] Herman, B, Antti, P, Antti, A, Tero, M, Mikko, RAP, Anders, VL. Photovoltaic system modeling: A validation study at high latitudes with implementation of a novel DNI quality control method, *Solar Energy* 2020; 204:316–329 <<https://doi.org/10.1016/j.solener.2020.04.068>>
- [3] Aissou, S, Rekioua, D, Mezzai, N, Rekioua, T, Bacha, S. Modeling and control of hybrid photovoltaic wind power system with battery storage, *Energy Conversion and Management* 2015; 89:615–625 <https://doi.org/10.1016/j.enconman.2014.10.034>

- [4] Bedoud, K, Bahi, T, Merabet, M. Modeling and Characteristics Study of Photovoltaic Generator. In: ICSRESA 2019. 1<sup>st</sup> International Conference on Sustainable Renewable Energy Systems and Applications (IC; 4-5 December 2019: Tebessa, Algeria, IEEEExplore, <10.1109/ICSRESA49121.2019.9182545>
- [5] Program for renewable energy and energy efficiency. Ministry of energy and mines, Sonelgaz Group Company <<http://www.mem-algeria.org>>
- [6] Diaf, S, Notton, G. Evaluation of electricity generation and energy cost of wind energy conversion systems in southern Algeria, *Renew Sustain Energy Rev* 2013; 23:379–90 <<https://doi.org/10.1016/j.rser.2013.03.002>>
- [7] Georgio, T, Georgio, A. Investigation of the behavior of a three phase grid-connected photovoltaic system to control active and reactive power, *Electric Power Systems Research* 2011; 81:177–184 <<https://doi.org/10.1016/j.epsr.2010.08.008>>
- [8] Vishnu, P, Jayasree, PR, Sruthy, V. Active Power Sharing and Reactive Power Compensation in a Grid-tied Photovoltaic System, *Materials Today: Proceedings* 2018; 5:1537–1544 <<https://doi.org/10.1016/j.matpr.2017.11.243>>
- [9] Sonam, D, Dekar, W, Tshering, C, Tandin, T. Maximum Power Point Tracking of solar photovoltaic cell using Perturb & Observe and fuzzy logic controller algorithm for boost converter and quadratic boost converter, *Materials Today: Proceedings* 2020; 27:1224–1229 <<https://doi.org/10.1016/j.matpr.2020.02.144>>
- [10] José, AC, Oscar, B, Patxi, A, Jon C. Sliding mode control of an active power filter with photovoltaic maximum power tracking, *Electrical Journal of Power and Energy Systems* 2019; 110:747–758 <<https://doi.org/10.1016/j.ijepes.2019.03.070>>
- [11] Ahmad, D, Gholamreza, F, Hani, V, Kamal, AH. Model predictive control design for DC-DC converters applied to a photovoltaic system, *Electrical Power and Energy Systems* 2018; 103:537–544 <<https://doi.org/10.1016/j.ijepes.2018.05.004>>



# ARTIFICIAL NEURAL NETWORK FORECASTING MODELS FOR WIND AND PHOTOVOLTAIC ENERGY PREDICTION UTILIZING TIME-SERIES INPUT DATA WITH DIFFERENT RESOLUTIONS

Mutaz AlShafeey

Corvinus University of Budapest, Budapest, Hungary, mutaz.alshafeey@uni-corvinus.hu, ORCID: 0000-0002-0935-226X

Csaba Csáki

Corvinus University of Budapest, Budapest, Hungary, casaki.csaba@uni-corvinus.hu, ORCID: 0000-0002-8245-1002

*Cite this paper as:* AlShafeey, M, Csáki, C. "Artificial neural network forecasting models for wind and photovoltaic energy prediction utilizing time-series input data with different resolutions" 9<sup>th</sup> Eur. Conf. Ren. Energy Sys. 21-23 April 2021, Istanbul, Turkey

**Abstract:** Accurate photovoltaic (PV) and wind energy forecasting play a major role in energy security, economic performance, and grid stability. There are various modeling techniques and methods available to design forecasting models. Each of those techniques and methods leads to different forecasting accuracy. In this article, Artificial Neural Network forecasting models were designed and tested to forecast day-ahead PV and wind energy utilizing time-series input data with different resolutions. Input data of 15, 30, and 60 minutes resolutions were applied to forecast the energy of a 546 kWp grid-connected PV farm and a 2 mW wind turbine. The time-series energy data were collected from the above-mentioned wind and solar farms for one full year. The results show a huge variance between wind and PV forecasting accuracies. The models were able to forecast the PV energy accurately, while same models show a bad performance in predicting wind energy. It was also found that the input data resolutions have very small effects on the models' accuracy in the PV case, yet higher resolution leads to better forecasting performance. While in wind energy prediction the input data resolution has minor effects on the accuracy of the model.

**Keywords:** PV energy forecasting, wind energy forecasting, ANN forecasting model, input data resolution

© 2021 Published by ECRES

Nomenclature	
$n$	Number of observations
$yt$	Observed (real) output power at time t.
$pt$	Forecasted output power at time t.
$\hat{y}$	The average of the observed values
$ws$	Weighted sum
$w_1, w_2, \dots, w_n$	Weights of each neuron inputs
$v_1, v_2, \dots, v_n$	Neurons inputs
$b$	Bias
$X$	Neurons output

## 1. INTRODUCTION

Several widely used methods of energy generation rely on fossil fuel (coal, oil, natural gas) and its derivatives. They produce different types of pollution- air, noise, and environmental pollution, which have negative impacts on humans and nature (climate change, greenhouse effect, deforestation, etc.) [1]. Moreover, the depletion of fossil fuel reserves and inequality in the distribution of energy consumption and reserves causes serious problems for the current energy systems [2]. Renewable resources can offer a reliable solution for the energy demand problem. Green sources such as solar, wind, tidal wave, or biomass are among the main sustainable technologies that may offer competitive advantages and their use has been accelerated over the last decade [3]. Since photovoltaic (PV)

equipment can be easily installed almost everywhere and operates efficiently in different geographical regions with low maintenance required, thus solar energy is considered to be an effective environmentally friendly technology for energy production [1]. Another growing trend in renewable energy generation is wind resources. Wind technologies offer reliable, eco-friendly, simple, and low maintenance methods for energy generation. Despite all the attractive advantages of utilizing solar and wind technologies, some major challenges limit their wider applicability. The fluctuations in wind and solar resources create ambiguities in the produced energy. Uncertainties in energy production affect energy security, economic performance, and most importantly, grid stability (in case of grid-connected solutions). Hence, effective ways of integrating these intermittent resources with electricity grids are needed. Some of the integrating methods use energy storage systems to stabilize the power. Yet, using storage units are impractical for large applications. In addition, storage units like batteries have limited usage cycles and it has to be replaced after a certain time adding extra costs [4]. Another method for better integration is forecasting energy production. Accurate energy forecasting models provide value through reduced imbalance penalties, but they also lead to increased competitiveness by providing advanced knowledge in real-time energy market trading. Low error production predictions improve the construction, operations, and maintenance planning of energy projects [5]. This means that good forecasting tools would positively impact both the cost and integration of wind and solar farms.

Different techniques are currently used to forecast renewable energy production, especially for wind and solar. Physical models based on numerical weather predictions (NWPs), statistical and probabilistic models, and Artificial intelligence (AI) models based on Machine Learning (ML) are among the main utilized techniques [6]. Machine learning has several modeling algorithms like supervised, unsupervised, and meta-learning algorithms, each used for specific learning tasks [7]. Artificial Neural Networks (ANN) is one of the supervised ML algorithms which can be used to solve complex nonstationary and nonlinear problems [8]. Some ANN forecasting models show very good abilities in predicting the power with minimum errors and lowered uncertainties compared to other ML algorithms [6]. Forecasting the potential wind and solar power is not an easy task, many factors impact performance and forecasting accuracy. Besides the modeling techniques and algorithms used in the forecasting process, the input data utilized by the forecasting models as well as the forecasting horizon and resolution might also affect the performance of these models [9]. Depending on the input data (i.e. explanatory variables) utilized by the forecasting models (including ANN), there are three main methods for building the forecasting models [10]: 1) in the structural method the forecasting models utilize geographical and meteorological parameters (such as wind speed, ambient temperature, humidity, and so on); 2) in the time-series method only past power values are utilized by the models as inputs; 3) in the hybrid method meteorological variables as well as past power values are utilized by the forecasting models. Generally, regardless of the modeling technique or data utilization method used, forecasting accuracy is expected to decrease for longer horizons [11]. Moreover, the input data resolution (frequency of the input variables per time unit) is also affecting the accuracy of the forecast [12]. The goal of the research reported here was to investigate and compare the performance of ANN-based time-series forecasting models of both PV and wind energy for 24-hour (day-ahead) horizons under different input data resolutions. This testing aimed to find the input data resolution that leads to the best accuracy for a 24-hours forecasting horizon. Input data resolutions of 15, 30, and 60 minutes were utilized.

## **2. DESIGN OF THE EXPERIMENT, DATA COLLECTION AND METHODS**

As discussed earlier, different forecasting horizons lead to different forecasting accuracies. Moreover, the resolution of the input data might also affect accuracy. Thus, the objective of the research reported here was to find the input data resolution that leads to the best accuracy. Consequently, two sets of ANN time series forecasting models were designed, built (i.e. trained), and tested to forecast wind and PV out power respectively for 24 hours ahead, each set utilizing input data with three different resolutions (of 15, 30, and 60 minutes).

The input to the time-series ANN models are past power values, therefore, to train the ANN models, past energy values of both PV and wind were required. Hence, actual PV and solar energy values were collected covering one full year. Data collection started on May 1, 2019 and lasted till June 13, 2020. PV data collected from a 546 kW<sub>p</sub> grid-connected solar farm located in Hungary. While wind data collected from a 2 mW wind turbine located also in Hungary. All data were collected in 15, 30, and 60 minutes resolutions.

Once the models were trained, the accuracy of all six resulting models was then calculated. Subsequently, a comparative analysis was conducted to determine the best settings leading to the best performance. To calculate the performance of the forecasting models, an evaluation method is needed. Evaluation methods such as Mean Absolute Error (MAE), Mean Square Error (MSE), Coefficient of Determination (COD) can be used to evaluate the

forecasting models' performance [9], as can be seen in Eqs. [1-3]. Better modeling accuracy means MAE, and MSE measures should be closer to zero, while the COD value should be closer to 1.

$$\text{Mean Absolute Error (MAE)} = \frac{1}{n} * \sum_{i=1}^n |yt - pt| \quad (1)$$

$$\text{Mean Square Error (MSE)} = \frac{1}{n} * \sum_{i=1}^n (yt - pt)^2 \quad (2)$$

$$\text{Coefficient of Determination (COD)} = \frac{\sum_{i=1}^n (yt - pt)^2}{\sum_{i=1}^n (yt - \hat{y})^2} \quad (3)$$

Generally, ANN is composed of layers of neurons. The bottom layer is called the input layer, followed by hidden layer(s), and finally the top layer is the output layer. To that end, Multi-Layer Feed-Forward Neural Network (MLFFNN) was designed. Additionally, the error of the output is utilized to tune the network. In MLFFNN, the outputs of each layer are the inputs to the succeeding one. In any MLFFNN given layer, each neuron combines its inputs using a weighted linear combination as shown in Eq. [4] (i.e. each neuron in the hidden or output layers has dedicated weights for the output value of each neuron in the preceding layer):

$$ws = w_1 \times v_1 + w_2 \times v_2 + \dots + w_n \times v_n + b \quad (4)$$

Then, a nonlinear transfer function modifies the results as in the following equation:

$$X = \varphi(ws) \quad (5)$$

There are different transfer function might be used, yet, the sigmoid transfer function is among the most used [13]. Eq. [6] shows the sigmoid transfer function.

$$\varphi(ws) = \frac{1}{1 + e^{-ws}} \quad (6)$$

Tansig transfer function was used instead of the sigmoid in case of negative values are found as can be seen in Eq. [7].

$$\varphi(ws) = \frac{1 - e^{-2ws}}{1 + e^{-2ws}} \quad (7)$$

### 3. RESULTS AND DISCUSSION

Once the ANN time-series forecasting models were trained using real past power values in different resolutions, the measures (mentioned above) were applied to calculate and then compare the performance of each forecasting model. The performance was calculated during the train and test period (one full year). Additionally, the performance of each forecasting model was visualized for the last week of the testing which covers the period 7<sup>th</sup> to 13<sup>th</sup> of June 2020 as can be seen in Figures 1 and 2. In Figure 1 (a) it can be seen that the PV forecasting model utilizing 15 minutes of input data resolution has good prediction abilities, yet some errors can be observed especially on the 8<sup>th</sup> of June where the model failed in predicting the sudden dip that happened in the afternoon. Figure 1 (b) and (c) show the performance of the PV forecasting model utilizing 30 and 60 minutes of input data respectively. In both cases the model shows good prediction abilities as well. Yet, the 60 minutes resolution model in Figure 1 (c) has higher forecasting errors for the 12<sup>th</sup> of June 2020. Figure 2 shows the performance of the wind energy forecasting models utilizing different input data resolutions. Generally, it can be noticed that the ANN time-series forecasting model used is not good enough in predicting wind energy. Figure 2 (a) shows the performance utilizing input data of 15 minutes resolutions and this wind model was not able to predict the energy accurately especially in the last few days of testing (9<sup>th</sup> till 13<sup>th</sup> of June) when the produced energy was zero most of the time. Utilizing input data of 30 and 60 minutes didn't improve the forecasting performance much as can be seen in Figure 2 (b) and (c).

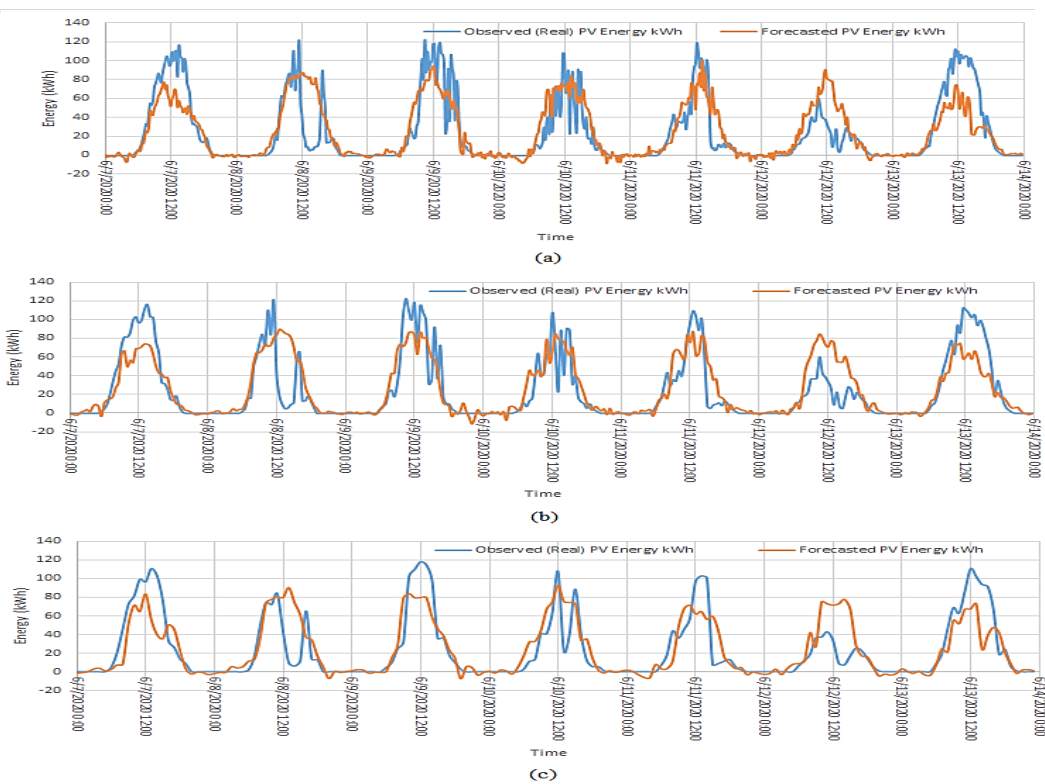


Figure 1 PV energy forecasting model performance utilizing (a) 15; (b) 30; and (c) 60 minutes input data resolution

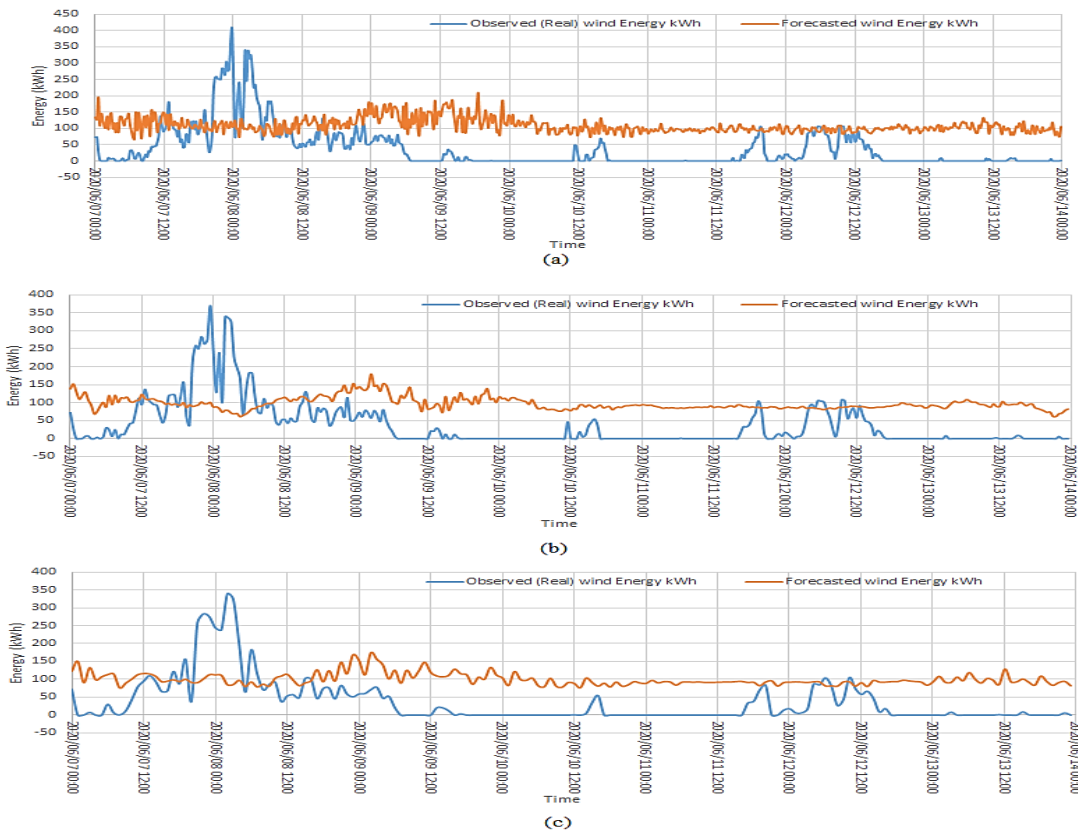


Figure 2 Wind energy forecasting model performance utilizing (a) 15; (b) 30; and (c) 60 minutes input data resolution

The results show a big variance in the performance between PV and wind forecasting performance as can be seen in Table 1. ANN time-series method was efficient in predicting the PV energy output with average COD of 0.75. Also, the average MAE and MSE are 9.95 and 303.55 respectively. Same method shows very poor abilities in forecasting wind energy with a 0.064 COD, 117.59 MAE, and 20870.79 MSE.

Table 1 Performance measures comparison

Model	Performance measures		
	COD ( $R^2$ )	MAE	MSE
PV forecasting	15 min. resolution	0.75	9.72
	30 min. resolution	0.76	10.00
	60 min. resolution	0.74	10.13
	Average	0.75	9.95
Wind forecasting	15 min. resolution	0.058	119.69
	30 min. resolution	0.076	116.29
	60 min. resolution	0.058	116.80
	Average	0.064	117.59

ANN time-series method shows similar abilities in forecasting the PV output energy regardless of the input data resolutions as can be seen in Figure 3. Although all performance measures are very close and comparable, yet the 60 minutes resolution shows higher values of MAE and MSE, yet slightly lower COD. This indicates higher input data resolutions lead to slightly better accuracy – and, interestingly, 30 minutes performs slightly better than 15 minutes in some performance measures.

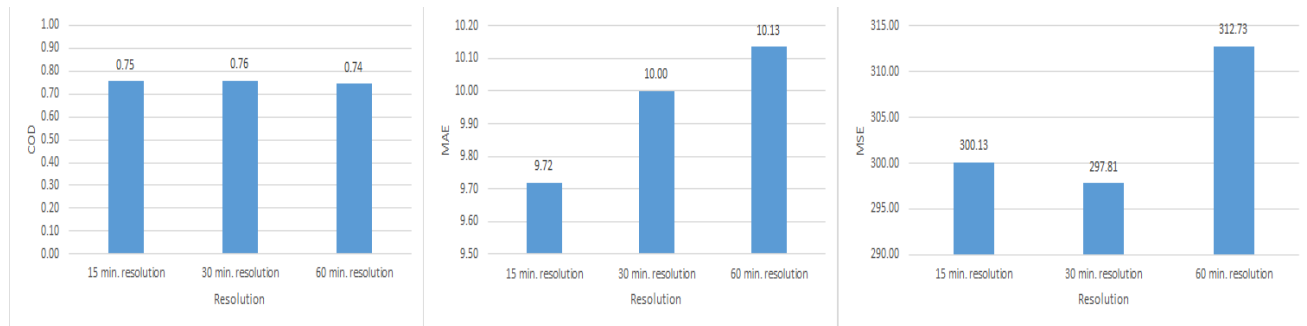


Figure 3 Performance measures of PV energy forecasting utilizing different input data resolutions

For wind energy forecasting, different input data resolutions show some effects on the forecasting performance. The 30 mins resolutions show the lowest MAE and MSE. While higher values of MAE and MSE were observed utilizing 15 mins of input data resolution as can be seen in Figure 4. Interestingly, here 60 minutes performs better, than 15 mins.

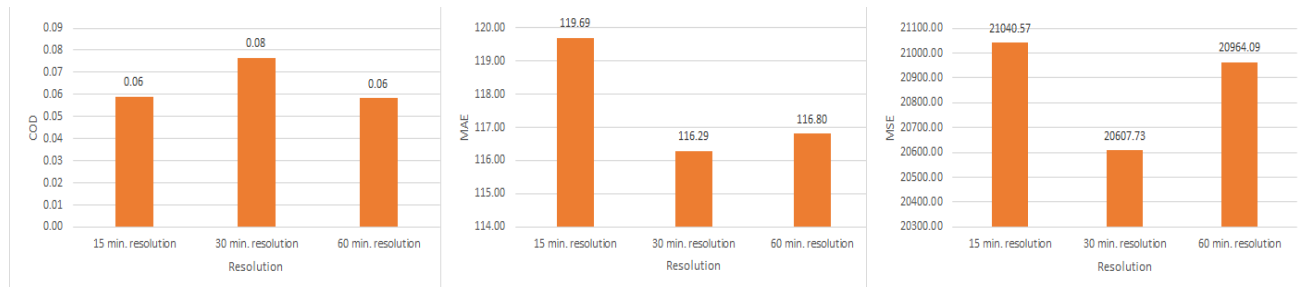


Figure 4 Performance measures of wind energy forecasting utilizing different input data resolutions

#### 4. CONCLUSION

This article reported a research of building and testing PV and wind energy forecasting models. ANN modeling technique was used utilizing time-series past energy values as input data. The time-series energy values were collected from a 546 kWh grid-connected solar farm and a 2 mW wind turbine, both located in Hungary. All energy values were collected in different resolutions (i.e. 15, 30, and 60 minutes). Then, the forecasting models were trained and tested to predict the output energy of both PV and wind farms for a 24-hour ahead horizon, utilizing the above input data resolutions. It was found that ANN time-series model was efficient in predicting the PV energy regardless of the input data resolution. In fact, input data resolutions have only a small effect on the accuracy of the ANN time-series PV forecasting model as forecasting measures are fairly close when utilizing 15, 30, or 60 minutes input

data resolution. Yet, the 15 minutes resolution shows slightly better forecasting performance. The same model shows poor performance in predicting wind energy. ANN time-series wind forecasting model has huge errors in forecasting wind energy regardless of the input data resolution. Yet, the 30 minutes input data resolution shows a slightly better performance.

All in all, it can be concluded that ANN time-series forecasting models are suitable for predicting PV output energy, while these models (at least in this form) might not be the best choice for predicting wind energy. Furthermore, utilizing different input data resolutions might not help in improving wind energy forecasting accuracy. Future research should investigate ANN model variants and other data input methods for better wind energy prediction performance.

## ACKNOWLEDGMENTS

This research has been supported by the European Union and Hungary and co-financed by the European Social Fund through project EFOP-3.6.2-16-2017-00007, titled "Aspects of developing an intelligent, sustainable and inclusive society: social, technological, innovation networks in employment and digital economy". Solar power plant operation data is provided by 3Comm Hungary (3comm.hu/). Wind turbine data is supplied by E.on Hungary (eon.hu/).

## REFERENCES

- [1] M. Alshafeey and C. Csaki, "A Case Study of Grid-Connected Solar Farm Control Using Artificial Intelligence Genetic Algorithm to Accommodate Peak Demand," in *Journal of Physics: Conference Series*, 2019, p. 012017.
- [2] M.-A. Perea-Moreno, Q. Hernandez-Escobedo, and A.-J. Perea-Moreno, "Renewable energy in urban areas: Worldwide research trends," *Energies*, vol. 11, p. 577, 2018.
- [3] A. Juaidi, F. G. Montoya, I. H. Ibrik, and F. Manzano-Agugliaro, "An overview of renewable energy potential in Palestine," *Renewable and Sustainable Energy Reviews*, vol. 65, pp. 943-960, 2016.
- [4] X. Wang, P. Adelmann, and T. Reindl, "Use of LiFePO<sub>4</sub> batteries in stand-alone solar system," *Energy Procedia*, vol. 25, pp. 135-140, 2012.
- [5] J. Lerner, M. Grundmeyer, and M. Garvert, "The importance of wind forecasting," *Renewable Energy Focus*, vol. 10, pp. 64-66, 2009.
- [6] A. Ahmed and M. Khalid, "A review on the selected applications of forecasting models in renewable power systems," *Renewable and Sustainable Energy Reviews*, vol. 100, pp. 9-21, 2019.
- [7] B. Lantz, *Machine learning with R: expert techniques for predictive modeling*: Packt Publishing Ltd, 2019.
- [8] R. H. Inman, H. T. Pedro, and C. F. Coimbra, "Solar forecasting methods for renewable energy integration," *Progress in energy and combustion science*, vol. 39, pp. 535-576, 2013.
- [9] R. Ahmed, V. Sreeram, Y. Mishra, and M. Arif, "A review and evaluation of the state-of-the-art in PV solar power forecasting: Techniques and optimization," *Renewable and Sustainable Energy Reviews*, vol. 124, p. 109792, 2020.
- [10] S. Aggarwal and L. Saini, "Solar energy prediction using linear and non-linear regularization models: A study on AMS (American Meteorological Society) 2013–14 Solar Energy Prediction Contest," *Energy*, vol. 78, pp. 247-256, 2014.
- [11] H. Liu, J. Shi, and E. Erdem, "An integrated wind power forecasting methodology: interval estimation of wind speed, operation probability of wind turbine, and conditional expected wind power output of a wind farm," *International Journal of Green Energy*, vol. 10, pp. 151-176, 2013.
- [12] Y.-K. Wu and J.-S. Hong, "A literature review of wind forecasting technology in the world," in *2007 IEEE Lausanne Power Tech*, 2007, pp. 504-509.
- [13] H. K. Ghritlahre and R. K. Prasad, "Application of ANN technique to predict the performance of solar collector systems- A review," *Renewable and Sustainable Energy Reviews*, vol. 84, pp. 75-88, 2018.



# PERFORMANCE ASSESSMENT OF THE WINDOWS GLAZING SYSTEM FOR THE OFFICE BUILDING

Pinar Usta

Isparta University of Applied Science, Isparta , Turkey, [pinarusta@isparta.edu.tr](mailto:pinarusta@isparta.edu.tr), ORCID: 0000-0001-9809-3855

Basak Zengin

Nisantasi University, Istanbul, Turkey, [zenginbasak@gmail.com](mailto:zenginbasak@gmail.com), ORCID: 0000-0003-3719-9423

*Cite this paper as:* Usta, P, Zengin, B. Performance assessment of the windows glazing system for the office building. 9<sup>th</sup> Eur. Conf. Ren. Energy Sys. 21-23 April 2021, Istanbul, Turkey

**Abstract:** Building energy requirement in Europe is around 40% of total energy needs. To achieve significant energy savings in this sector, the European Energy Performance Building Directive (EPBD) promotes the use of passive strategies that improve thermal conditions in buildings, especially in summer, thereby allowing the energy requirements of air conditioning systems to be reduced. In addition to the proper selection of windows glazing and their design is also one of the effective strategies to minimize the energy consumption level. In this paper, an office building was chosen to assess energy efficiency using Openstudio and Energyplus software. Energy modeling of the office building was conducted by using VRF systems for air-conditioning and a dedicated outdoor air system for ventilation. The effect of different windows glazing system properties on the energy performance and total energy need was calculated by considering the fixed indoor thermal and visual comfort conditions were evaluated. The study results indicated that energy consumption can reduce about 24.88 kBtu/ft<sup>2</sup> (25%) using suitable glazing material.

**Keywords:** Energy, energy efficiency, energy demand, window glazing, energy saving

© 2021 Published by ECRES

## 1. INTRODUCTION

Nowadays, climate change is a huge long-term problem facing the world. [1]. Energy and thermal performance in buildings have gained global importance in recent years due to the goal of maintaining thermal comfort with a more efficient approach. As energy efficiency gained importance, the construction industry had to analyze the capacity of buildings to save energy. An adequate energy efficiency study is required for heating, ventilation, air conditioning (HVAC) systems, building materials, architectural design, etc. [2]. Many researchers have stated that there is enormous energy conservation potential on the exterior of the building, especially in the exterior windows. Most undesirable heat gains occur through sunlight radiation and air infiltration in windows, which are the most vulnerable area of buildings in terms of heat gain. Therefore, windows always play an important role in reducing energy consumption for a room area.[3]. Recently, the use of glass facades in buildings has become widespread and buildings have begun to be characterized in this way. The large efficacy of solar gains on the thermal energy performance of the building in both summer and winter seasons, lighting energy demand thermal and visual ease [4]. One of the most common causes of overheating in buildings is excessive solar gain from windows. This is the key to controlling solar gains and maintaining indoor comfort to implement low-energy building design. Sun gains can be limited by effective shading design. Overheating in buildings can be reduced, and the cooling loads of the building can be deductible by regulating temperature surges. In buildings, by paying attention to window and glass details, it is possible to save energy compared to mechanical cooling by shading. This is a more cost-effective way to control overheating in buildings [5]. Direct radiation falling on the transparent surfaces of buildings adds a significant amount of energy to the energy use of the building. Clear Glass transmits more than 80% of incoming solar radiation and more than 75% of visible light. The penetration of solar radiation into indoor spaces may be positive and healthy in some cases, but it can be also extremely unfavorable depending on the climate, season, building function, and occupant activity [6,7].

Various types of heat-blocking glass have been enhanced to improve the thermal performance of external windows and to reduce incoming solar heat recovery. The most used heat barrier glasses for buildings are low-emission (low-E) glass and heat-absorbing-colored glasses. Allowing visible (VIR) light to pass through windows, Low-E glass has a microscopically transparent coating that can reflect mainly of the near-infrared light. The light which is desired for the building is provided by filtering the sunlight. Though, the energy-saving potential of general residential buildings is normally enormous. Particularly in high-density cities, energy-saving design and not applying energy-saving material is the biggest reason for this. Clear Glass has a high transmittance, but also a low reflection of solar radiation. this makes windows the biggest source of involuntary heat gain. [3,8]. Typically, a window with Low-E coating saves roughly 40% of the energy consumption. Low-E coating also reduces the U-factor while keeps high levels of visible transmittance. Thermal performance significantly determines solar heat gain for the minimum or maximum amount to be involved is based on weather conditions as well as the building orientation. Thus, different glazing materials might be designed to prevent unwanted heat gain in a warm climate or give permission to it for transmitting the solar radiation to the interior space in a cold climate [9, 11]. Performing a time-dependent heat transfer analysis requires complex numerical calculations. Recently, it has become a standard feature of worldwide use of computational numerical tools such as energy thermal simulation software in building design to easily perform these operations [11].

## Energy Use In Office Buildings

Especially, in buildings in regions with significant thermal emission and solar radiation; In terms of minimum energy consumption in buildings, it is extremely important to decide on the building system that contributes the most to the thermal comfort conditions of the building and to make time-dependent heat transfer analysis before using the heating or air conditioning systems[12]. The methodology of this study consists of four steps. In the first step, it was formed with a 4 mm thick flat glass. Then, the base model was changed in the second step to account for how much the glass properties affected the energy factors of the structure. In step three, the total and hourly energy requirements of the space were extracted from the simulation to study the effect of glazing window material. Finally, the effect of glazing material on energy-saving was categorized according to its applicability for the suggested suitable glazing window factors for different orientations. SketchUp software was used to draw and create the model geometry. Next, OpenStudio is used to change model properties including construction, materials, usage, internal loads, and charts. EnergyPlus is used to perform an annual energy simulation for case the study with different parameters. Eventually, the results obtained are presented in OpenStudio and prepared in a suitable format. To determine the cooling and heating schedule for each unit in the office and office, the necessary definitions were made from the Openstudio "schedule" tab, and the "heating" and "cooling" program for the working office was created for the whole measurement year. With the introduction of dynamic windows, the energy demand requirements of existing sources such as sunbathing and daylight are met and the comfort of the building residents is contributed. In the previous years, research on dynamic window technologies have been carried out to determine the energy consumption and the comfort of the building occupants. The results from these studies shows the potential of dynamic fenestration ingredients, ranging from a reduce in cooling and lighting demand [13, 14].

## 2. CASE STUDY

### Description of the Building and Climate Data

In this study, a typical office building has been selected as the case study for evaluating the energy performance of windows Glazing parameters.The office basement plane is shown in Fig.2, It can be seen that the house has breakroom, offices, vending, conference, Elec/ Mech room, IT room, Lobby, corridor, storage WC and toilet. The area of conditioned space is 118.64 m<sup>2</sup>. The Electrical equipment consists of printers, computers, microwave, etc., they are normal equipment for such an office. The use of this equipment is adjusted to the needs of an office throughout the year, depending on the season and time of day.

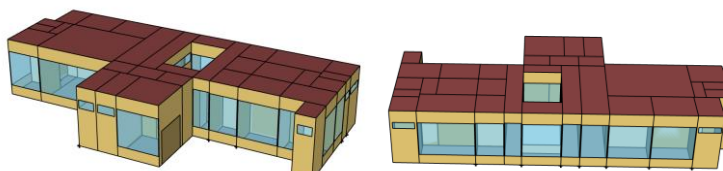


Figure 1. The simulated office building

The office is engaged from 8:00 to 18:00, Monday through Friday. Employees (people) are sitting at their desk, which is with the side towards the windowed wall. Internal loads associated with electrical equipment are measured considering personal computers, monitors, a laser printer and a copier with constant average power over the career period. The office building has a chiller, which works in conjunction with a variable volume cooling system and has an external ventilation unit for the building floor as well as heat recovery. For this reason, there is a heat pump system in the building with VRF and an outdoor ventilation unit in total. In OpenStudio modeling, electrical equipment, lighting, cooling, and heating of office spaces, the people schedule in the office also were taken into account. The office building using VRF systems for air-conditioning and a special outdoor air system for ventilation. To determine the energy performance of such study of office buildings on the number of office buildings in Turkey and which has the highest number of figures from the study of pain has been chosen Istanbul. In Istanbul, summers are warm, humid, dry, and clear, winters are long, cold, windy, and partly cloudy. Throughout the year, the temperature typically ranges from 3 °C to 30 °C and is infrequently below -1 °C or above 32 °C [15]. Wet and Dry bulb temperature and Monthly Average Temperature of Istanbul are shown in Fig 3. respectively. Climates city of Istanbul and a the office building with Typical air-conditioned has been analyzed all year round.

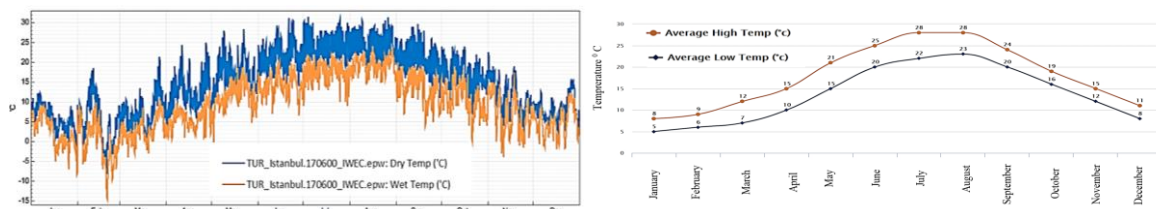


Figure 2. Wet and Dry temperature for Istanbul (°C) Monthly Average Temperature graph for Istanbul (°C) [16].

The energy requirements of the main technical systems (heating, cooling, and lighting) have been evaluated. Large windows are often used in office buildings to make more use of daylight. Table1 shows the case studies implemented in the sample office. The results of its energy performance were compared for different glazing window and air materials.

Table 1. Combination for Case study

Climate/ City	Code	Glazing Windows Material	Gas Window Material	Wall Composition	Roof Composition	Floor Composition
<b>Istanbul</b>	Glazing-A	4mm Glass	Air 6mm	Building Mat.	Roof Mat.	Floor Mat.
	Glazing-B	6mm Glass		Building Mat.	Roof Mat.	Floor Mat.
	Glazing-C	4 mm LE Glass		Building Mat.	Roof Mat.	Floor Mat.
	Glazing-D	6 mm LE Glass		Building Mat.	Roof Mat.	Floor Mat.

### Material Properties

It is expectative to develop a design that increases thermal comfort in buildings by using a specific combination of materials and passive systems. Computer simulation techniques stand out as effective tools for accurately evaluating the thermal performance of buildings and predicting the current and future behavior of the project. To make a dynamic simulation of a building, information about the building, such as the building's geometry, weather data, and thermal and optical properties of materials, is needed. Because the properties of building materials and their effects on the energy balance of the building represent critical information [2, 17]. The physical properties of the floor as well as the materials and constructions used in the model, walls, ceiling, windows, doors.

### 3. ANALYSIS RESULTS

Computer simulation results for each configuration were compared considering windows glazing with different material characteristics. Below are the results of the simulation in terms of energy consumption according to four different window combinations of the entire building, as well as the results under categories for the entire simulation period. If offices are compared; it can be seen that Offices, has Glazing-D window material, are using less energy than others. It can be seen in Figures 6 and Figures 7. The figures show monthly energy consumption and load category in bar graph form.

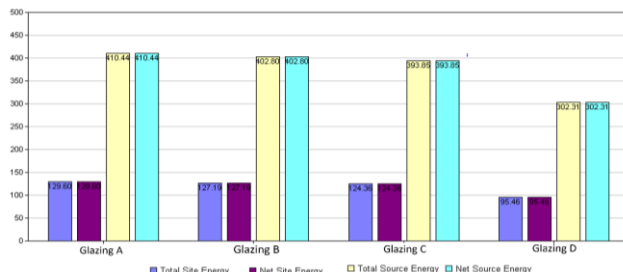


Figure 3. Annual Energy performance summary

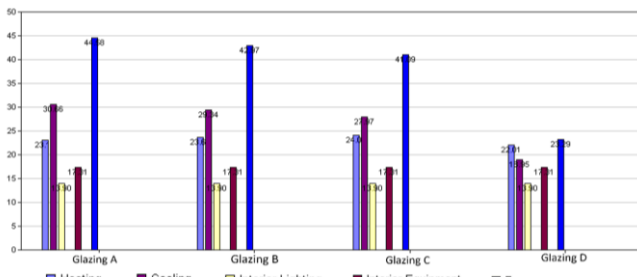


Figure 4. The annual Electricity performance summary

When offices with Glazing-A are compared it can be seen offices with Glazing-B is using 0.52 GJ more energy for heating. If Glazing-C is compared with Glazing-D; Glazing-D needs 2.08 GJ more energy for heating. Considering the energy requirement for cooling and fan in 4mm thick windows A and B, window B with emission feature requires less energy, the same applies to C and D windows of 6 mm thickness.

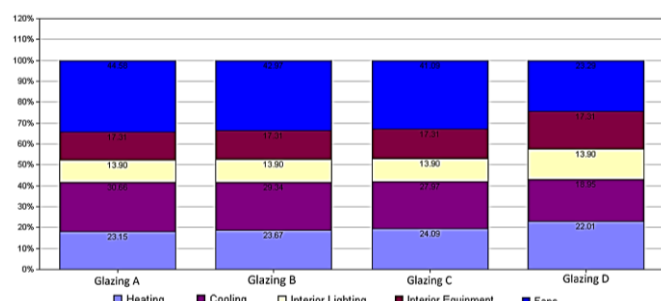


Figure 5. Electricity performance summary

Considering the energy requirement for HVAC in 4 mm thick Glazing-A and Glazing-B; Glazing-B with emission feature requires less energy in the same square meter. The same applies to Glazing-C and Glazing-D of 6 mm thickness. It is observed that Glazing-D with emission feature, especially among the Glazing with 6 mm thickness, provides energy saving at a significant amount of energy. The Building heating and cooling electricity peak demand performance according to the months is shown in Figure. 9, Figure. 10.

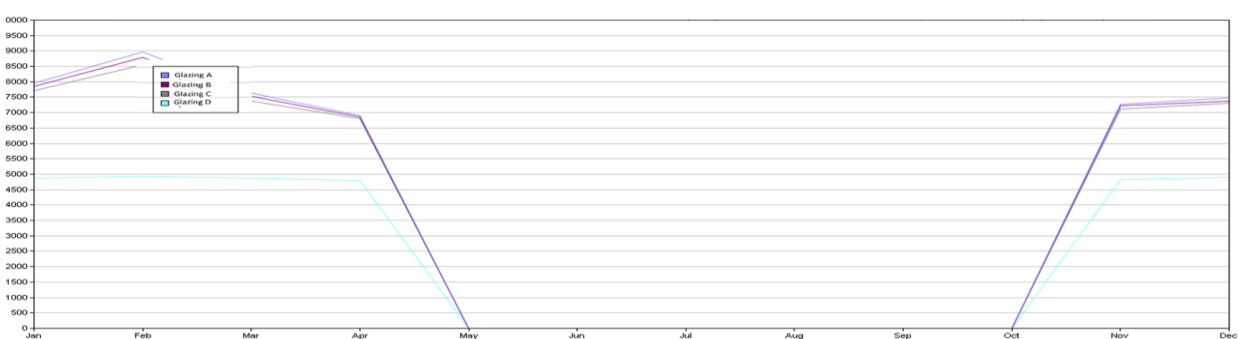


Figure 6. Heating Electricity peak demand (W)

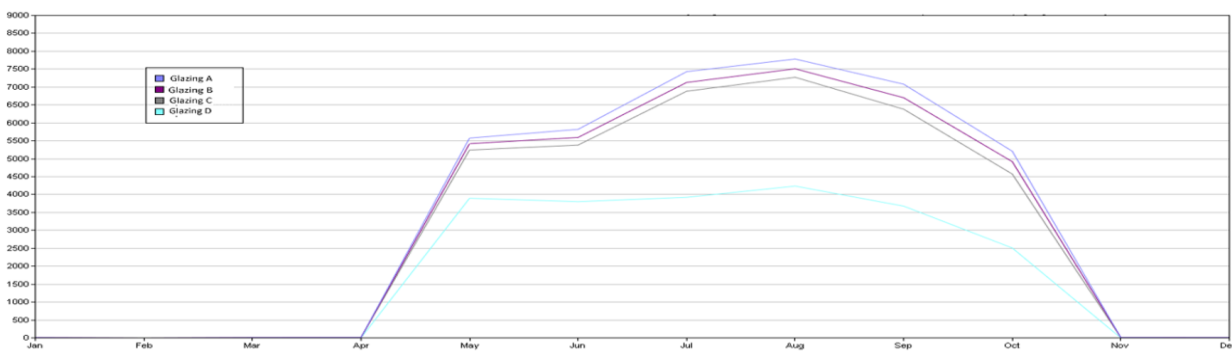


Figure 7. Cooling Electricity peak demand (W)

The results show that the total cooling peak demand load was around 6500-8000 W for Glazing-A, B and D. As shown in Figure 8, the minimum cooling load value in August was around 4000 W for all Glazing-D. The graph becomes a parabola with its maximum at the ends and the minimum in the middle in winter, however, the cooling power is decreased. By contrast, the highest heating power points are in January and February, specifically in February with a value of 9000 W for Glazing A, B, and D. Glazing-D was not visible in a sudden increase and growth. There is peak cooling load demand in August, and peak heating load demand in January and February. Glazing-A, Glazing-C (clear glass glazing), and Glazing-B (In Low emissivity Glazing with 4 mm thickness) have more cooling and heating load according to the Glazing-D (In Low emissivity Glazing). In Glazing-D which is Low emissivity When the simulation consequences of glazing are evaluated, it is seen that cooling energy with low emission glass decreases as a result of the higher overall reflectance of solar energy. Due to the low heat transfer coefficient, there is a decrease in the heating energy need. By changing the glass types, it is possible to achieve a significant reduction in sensitive heat gains and associated cooling loads. This reduction is due to a decrease in solar radiation and heat gain from conduction.

#### 4. CONCLUSIONS

The following is a comparison of the results of the office building conditions and the results of the four architectural improvements relating to Glazing-A, Glazing-B, Glazing-C, and Glazing-D types. Once the office model was analyzed the simulation results were created to compare the difference between the various cases. As shown in study results, the office is heating dominated during November-April months, the cooling energy use was significant during April-October months. Peak points of heating were observed in February for four glazing combinations. In cases where emission glass was used in February, the need for a fan decreased compared to other situations. The least need was observed in Glazing-D. If the glazing cases are compared in terms of heating load, Glazing-D has less heating and cooling load demand than Glazing-A, B, and C, especially due to its emission and thickness properties.

Nowadays, energy modeling can be done, and the loads, consumption, and energy behavior of buildings can be calculated, and the energy use density of buildings can be calculated by combining all the resulting results. Energy Use Intensity (EUI) is defined as energy consumption per unit area, especially in the field of building technologies, and is used in energy measurement. By looking at this value, the energy efficiency of the building can be evaluated. Considering the energy consumption density in our models, it was found to be 95.73 kBtu / ft<sup>2</sup>, 94.40 kBtu / ft<sup>2</sup>, 92.30 kBtu / ft<sup>2</sup> 70.85 kBtu / ft<sup>2</sup> for Glazing-A, Glazing-B, Glazing-C, and Glazing-D, respectively. These values are considerably higher than the article and Miliopoulos R. [19] undergraduate thesis, "Use of Energy in Office Buildings". While designing buildings, attention should be paid to energy efficiency, in this process architects and engineers have a great job. Incorrectly designed structures can be strengthened later. In other words, the energy efficiency of buildings can be increased by many methods such as thermal insulation of buildings, strengthening them with materials with low thermal conductivity, using more efficient doors and frames in terms of energy consumption, and adopting some renewable energy systems. However, this is a negative situation when the unnecessary use of resources and financial aspects are considered.

#### REFERENCES

- [1] Rezvani, F. Energy modelling and u-value calculation of scottish house elements: assessment of thermal performance improvement (Doctoral dissertation, Universidad de Zaragoza), 2019.

- [2] Borbon-Almada, A. C., Rodriguez-Muñoz, N. A.; Najera-Trejo, M. Energy and economic impact on the application of low-cost lightweight materials in economic housing located in dry climates. *Sustainability* 2019; 11(6), 1586.
- [3] Wang, D., Lu, L., Zhang, W., Overall energy performance assessment of a new heat blocking coating. *Journal of Sustainable Development of Energy, Water and Environment Systems*, 2019; 7(1), 1-12.
- [4] Atzeri, A., Cappelletti, F., Gasparella, A. Internal versus external shading devices performance in office buildings. *Energy Procedia* 2014; 45, 463-472.
- [5] Littlefair, P. Design for Improved Solar Shading Control, 2006.
- [6] American Society of Heating Refrigerating Air-Conditioning Engineers, ASHRAE handbook : Fundamentals. Atlanta, GA: ASHRAE, 1997.
- [7] Samah K., Alghoul, Hassan G., Alrijabo, The impact of external window shading on energy requirements of office buildings, *Journal of Multidisciplinary Engineering Science and Technology (JMEST)* 2016; ISSN: 2458-9403 Vol. 3 Issue 11.
- [8] Zhang, W., Lu, L., Peng, J., Song, A., Comparison of the overall Energy Performance of semi-transparent Photovoltaic Windows and common Energy-efficient Windows in Hong Kong, *Energy and Buildings* 2016; Vol. 128, pp 511-518, <https://doi.org/10.1016/j.enbuild.2016.07.016>.
- [9] Tahouri, A. Evaluation of Windows and Energy Performance Case-Study: Colored Building, Faculty of Architecture (EMU) (Doctoral dissertation, Eastern Mediterranean University (EMU), 2015.
- [10] Gueymard, C., A., DuPont, W., C., Spectral effects on the transmittance, solar heat gain, and performance rating of glazing systems. *Solar Energy* 2009; 83(6), 940- 953.
- [11] Mateus, N.M., Pinto, A., Graça, G.C. da, Validation of EnergyPlus thermal simulation of a double skin naturally and mechanically ventilated test cell. *Energy Build.* 2014; 75, 511–522. doi:10.1016/j.enbuild.2014.02.043.
- [12] Barrios, G., Huelsz, G., Rojas, J., Ener-Habitat: a cloud computing numerical tool to evaluate the thermal performance of Walls/Roofs. *Energy Procedia* 2014; 57, 2042–2051. doi:10.1016/j.egypro.2014.10.169
- [13] Lee, E.S., DiBartolomeo, D.L., Selkowitz, S.E., Thermal and daylighting performance of an automated venetian blind and lighting system in a full-scale private office. *Energy and Buildings* 1998; 29 (1), 47–63.
- [14] Nielsen, M. V., Svendsen, S., Jensen, L. B. (2011). Quantifying the potential of automated dynamic solar shading in office buildings through integrated simulations of energy and daylight. *Solar Energy* 2011; 85(5), 757-768.
- [15] <https://weatherspark.com/y/95434/Average-Weather-in-%C4%B0stanbul-Turkey-Year-Round>
- [16] <https://www.worldweatheronline.com/istanbul-weather-averages/istanbul/tr.aspx>
- [17] International Energy Agency. WEO-2015 Special Report: Energy and Climate Change; IEA: Paris, France, 2015.
- [18] Miliopoulos R., Building Energy Modeling using EnergyPlus and OpenStudio Building Energy Modeling using EnergyPlus and OpenStudio. University of Thessaly Polytechnic School Department of Electrical Engineering and Computer Engineering, 2017.



# WIRELESS CHARGING SYSTEMS FOR ELECTRIC VEHICLES: REVIEW ARTICLE

Kerry Sado

University of Duhok, Duhok, Iraq, kherysado@yahoo.com/ kerry.sado@uod.ac/khery88@gmail.com, ORCID: 0000-0002-5565-4795

Lokman Hadi

University of Duhok, Duhok, Iraq, lokman.hadi@uod.ac, email address, ORCID: 0000-0001-8982-7482

Cite this paper as:

*Sado, K, Hadi, L, Wireless charging systems for electric vehicles: Review article. 9th Eur. Conf. Ren. Energy Sys. 21-23 April 2021, Istanbul, Turkey*

---

**Abstract:**

Wireless Power Transfer (WPT) methods used in electrical vehicles (EVs) battery charging transfers electric power from an electrical power source to an EV without the use of any wired connection. Beside of their usage in EV's, WPTs are significant for numerous industrial applications for their advantages over the wired power transfer systems, advantages like no exposed cables, ease of charge, and fearless delivery under unfavorable environmental conditions. Some industries and researchers are paying attention to the implementation of wireless power transfer for charging the on-board batteries of an electrical vehicle (EV), and attempts are being made to create and enhance the various related topologies. The wireless power transfer technology is achieved through using the coupling between two affordable inductive coupling between two coils named as transmitter and receiver. In applications with EV charging, the transmitter coils are buried under the road and the vehicle is equipped with receiver coils. Inductive-based WPT of resonant type is commonly used for applications of medium to high power transfer such as EV charging because greater efficiency is observed. Generally, two types of WPT are used in EV charging applications, Dynamic and Static WPT. In this report the focus is on Dynamic WPT, investigating the type of power electronics circuits used, also the impact of WPT on the environment and health is investigated. Finally, future application of power transfer for electrical vehicles is discussed.

---

**Keywords:**

*EV, Power Electronics, EV charging, Wireless power transfer.*

---

© 2021 Published by ECRES

## 1. INTRODUCTION

Due to several issues such as environmental effects, global warming, oil resources limitations, and energy security, the attentions to the investment, production, and usage of renewable energy and other energy sources as a replacement to the currently used fossil energies are increasing. In private EVs, vehicles are plugged into the grid and the battery is charged using electricity. Furthermore, by managing the charging process, the charging of EV could be done during the low demand periods such as at night when the stress on the grid is less and the grid has enough capacity for the EV charging. Different chargers have been proposed for the charging of the EVs at different power levels. According to the power level, the chargers are classified into three levels [1]. As revealed in Table 1, the level-1 charger is a slow charger that is suitable for EV charging at home during the night. This charger is compatible with the home electrical plug. The level-2 charger is a semi-fast charger which is considered as the main technique for both private and public cars. Nowadays, the most attention is on level-2 chargers which can provide sufficient power and can be realized in most locations. Usually, level-1 and level-2 chargers are single phase chargers. The level-3 charger is a high-power fast charger and is used for massive charging of the EVs. Usually, these types of chargers are three phase chargers and the main purpose for implementation of them is for applications in public and commercial sectors. The level 3 chargers are able to charge the EV battery to 80% in only thirty minutes however

they are not compatible in all EVs. At present, there is not any standard for level 3 chargers but this kind of chargers are available commercially. The electric vehicles such as Mitsubishi I and Nissan LEAF can be charged with level 3 charger [2].

*Table 1: EV charger type classifications [1].*

Charger type	Supply voltage	Phase	Usage type	Power-supply interface	Level of Power	Charging-time
Level 1	120 V	single phase	home or office charging	Conventional outlet	1.4-1.9 kW	17 Hours
Level 2	240 V	1 or 3 phases	private or public outlets charging	Dedicated chargers	3.1-19.2 kW	8 Hours
Level 3	300-600 V	3 phases	Charging at station	Dedicated chargers	50-240 kW	30 minutes

## 2. CLASSIFICATION OF EVS CHARGING SYSTEMS

The original WPT technology to be used was a static system, with the device configured to charge electrical vehicles in charging stations or public parking places when the EV has not been used for a significant period of time. In WPT charging, since a physical connection is not needed during the charging, the potential of charging electrical vehicles while they are in motion has been of major interest. Charging an electrical vehicle while in move is called dynamic wireless charging (DWC). A traditional DWC electrical vehicle is a pure rechargeable battery-only EV that remotely takes its electrical charge from a wireless charger buried under the road surface while the vehicle is in move. Electrified highways or charging lanes are named roads capable of providing wireless charging EVs with electrical power. Quasi-dynamic wireless charging is the other category, in this type of system the charging happens when the electrical vehicle brakes or accelerates from a reference spot. When it comes to safety, Stationary wireless charging is safer and more convenient than Dynamic charging method [3]. Though, static-charging is not much different than the conventional plug-in charging methods when it comes to charging time, the vehicle's operation and the site of the charging station. In response, dynamic wireless charging method enables EV's battery to be charged while the vehicle is in motion.

## 3. COMPONENTS OF DWC ELECTRICAL VEHICLES

General configuration of the DWC electrical vehicles system (Figure 1) consist of the followings:

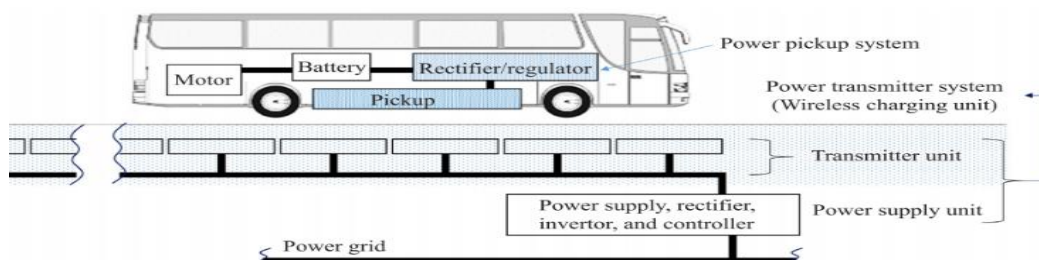


*Figure 1. general configuration of wireless charging electrical vehicle system[4]*

- Power Supply: Through the power supply, the system is connected to electric grid which can be either from conventional or renewable energy sources to receive power.
- Charging facility, also named power track or the transmitter, it is an extended path driven by the power-supply.
- the pickup or the receiver, which captures some amount of the magnetic field and then convert it into a controlled electrical energy.
- The load or the receiver, which is the unit being charged by the electrical power.

It is important here to classify the types of EV charging based on the operating technique, generally there are four types of wireless EV charging techniques [5].

#### 4. DYNAMIC WPT CHARGING

The battery problems are the most significant obstacle to the commercialization and widespread distribution of electric vehicles. Batteries are bulky, expensive and with limited life span, size of the batteries consume most of the EV space. In dynamic WPT charging method, the problem of batteries can be solved by charging while the vehicle is on move. The structure of dynamic systems is similar to the static. The basic circuit of dynamic WPT is revealed in Figure 2. The primary benefit of this topology is that the coefficient of coupling is constant along the road and not reliant on the vehicle's location. In this topology just one H-bridge converter is required to energize the entire pathway, which makes control much easier. However, there are several disadvantages to long path topology, because of the long size of the transmitter coil and therefore, the coupling factor between the coils of transmitter and receiver is very low. Hence, the high stray magnetic field is introduced, also this leads to low power transfer efficiency. Moreover, because the receiver coil size is small when compared with transmitter coil some part of the energy from the transmitter is not covered by the EV, therefore the generated magnetic field becomes dangerous for the nearby environment and population. Because one H-bridge converter is used for supplying the whole road, the used H-bridge should have a very high VA rating. A substantial compensation capacitor must be added because of the high current of the road. In order to limit the amount of compensation capacitor voltage stress, the switching frequency should be in the range of 20-40 kHz.

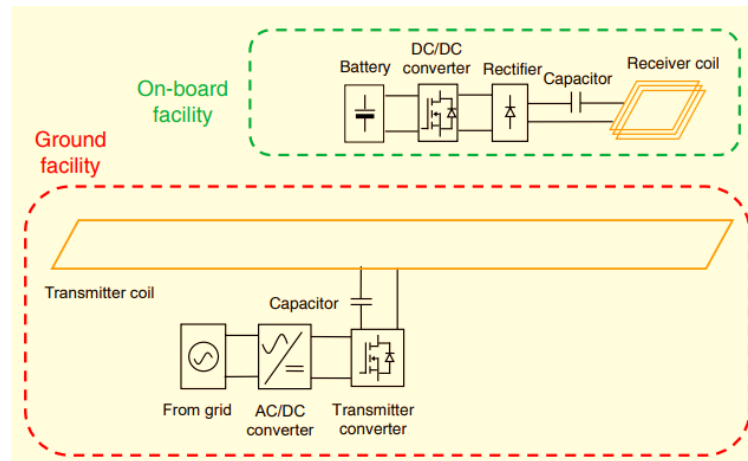


Figure 2 The basic diagram of dynamic WPT

Another dynamic WPT solution is segmented track topology. The basic diagram of dynamic WPT with segmented track topology is illustrated in Figure 3. In this topology, the transmitter coil length is smaller than the vehicle's size. For energizing each transmitter coil, an independent low VA H-bridge converter is employed. In this solution, several transmitter coils are embedded into the ground. But instead of supplying the transmitter coils with independent H-bridge converters, they are all connected to a common H-bridge converter and energizing the coils are managed by a switching device. Each transmitter coil is energized when the presence of the vehicle is identified and EV is exactly on the top of that. Thus, the magnetic field is shielded by the vehicle and problems related to the magnetic field and safety are recovered. In this topology, the value of the coupling topology is higher and for this reason, higher efficiency can be achieved [6]. One of the biggest challenges of this solution is that the presence of the vehicle must be identified and then the transmitter coil which is covered by the vehicle becomes turned on. The presence of the vehicle can be identified with different solutions such as sensors, communication devices or other auxiliary circuits, however this system must be fast enough in order to be able to charge the vehicle even in fast speed of the vehicle.

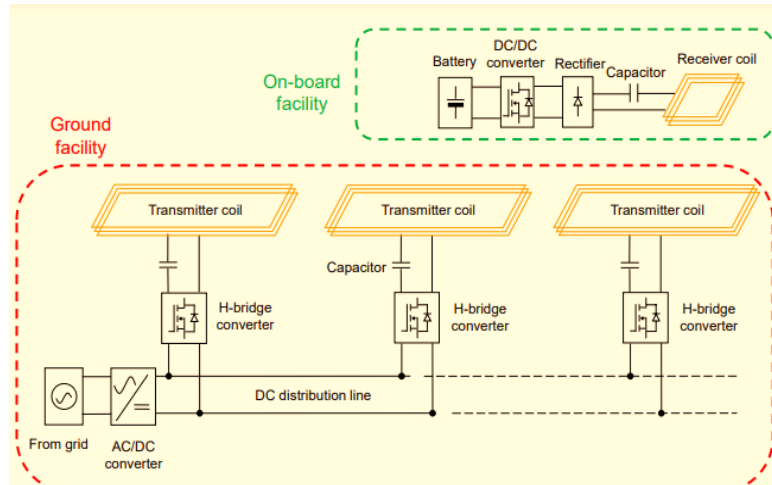


Figure 3 Diagram of dynamic WPT with segmented track topology [6]

The whole structure of a WPT charging system can be expressed as presented in Figure 4. The transmitter converter is a high frequency H-bridge converter composed of switches S1, S2, S3 and S4. The H-bridge converter provides the excitation current to the transmitter coil. Then, the power is transferred to the receiver across a gap. Then, an AC voltage induces to the receiver coil. The induced AC voltage is rectified by a passive rectifier composed of diodes D1, D2, D3 and D4 and then the DC power is transferred to the load RL. In this figure, the battery is modeled with a resistance RL.

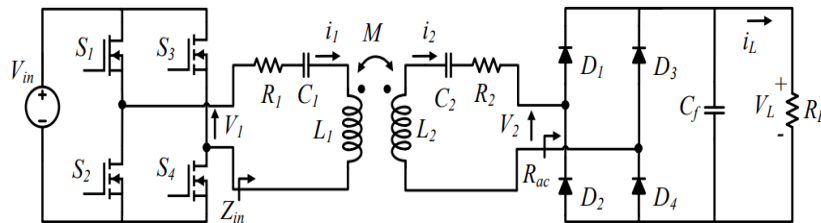


Figure 4 Complete power circuit of a WPT system [7].

The relation between the equivalent model and the complete model can be expressed according to the First Harmonic Approximation analysis (FOA). The waveform of the DC-AC converter output voltage is a square wave. The Fourier series of the converter output voltage is equal to:

$$V_1(t) = \frac{4V_{in}}{\pi} \sum_{n=1}^{\infty} \frac{1-(-1)^n}{2n} \sin(n\omega t) \quad (1)$$

By neglecting higher order harmonics, the Fourier series of the inverter output voltage can be simplified and the first harmonic equation can be determined by

$$V_1 = \frac{2\sqrt{2}}{\pi} V_{in} \quad (2)$$

Now, the H-bridge output voltage can be modeled as an AC voltage source with the RMS value of the first harmonic equation as follows:

$$V_1 = \frac{2\sqrt{2}}{\pi} V_{in} \quad (3)$$

The waveform of the voltage at the output of the receiver coil is a square wave and the FOA analysis can be extended to it as well. Therefore, the first-order harmonic of the receiver voltage can be expressed as

$$i_2 = \frac{\pi\sqrt{2}}{4} i_L \quad (4)$$

Furthermore, the relation between  $i_L$  and the receiver current can be written according to the following equation:

$$i_2 = \frac{\pi\sqrt{2}}{4} i_L \quad (5)$$

Based on (4) and (5), the relation between the load resistance ( $R_L$ ) and the equivalent resistance seen from the input of the rectifier ( $R_{ac}$ ) can be determined by:

$$R_{ac} = \frac{8}{\pi^2} R_L \quad (6)$$

## 5. HEALTH AND SAFETY ISSUES

Along with the bonuses of wireless charging systems there comes important possible health and safety issues specifically electrical, magnetic and fire hazards. Since WPT electric vehicle charging systems works in high voltage and high current levels, safety concerns become most important. Occasionally it can also produce electrical shocks due to the breakdown of devices or physical damage or by environmental conditions [8]. Moreover, there are two levels of wireless electric vehicle charging systems which are frequently adapted in small places such as houses, dorms, parking lots, etc., where the charging pads are installed underneath the road. Such arrangements demand some additional safety rules and regulations in order to avoid any possible accidents. While working at high power levels it is possible for magnetic flux to exceed the minimum value given by the standard authority, in such cases the surrounded area of plants and wild life becomes vulnerable and are exposed to a probable danger. To safeguard them, electromagnetic compatibility and electromagnetic interference must be inquired which can resolve the difficulty of the safety attributes. Since there is a high-power transfer from the transmitter side to the receiver charging pads at significantly big air gap of about 150-300 mm, the range of high frequency leakage flux produced increases. There is a pre-defined allowable flux value which must not be exceeded considering human body [9]. Exposure of these leakage fluxes may harm a person while sitting inside the vehicle or even walking near a charging pad. The consequence of electromagnetic compatibility and electromagnetic interference problems had to be verified; to achieve the solution setting a variety of different shapes of magnetic ferrite are propounded with finite element method (FEM) simulation [10]. Furthermore, numerous research and development projects are in progress to achieve a user friendly Wireless electric vehicle charging systems. In conclusion, while defining safety and health standards one must consider construction, electronic design, manufacturing and installation for to produce user friendly harmless wireless EV charging system.

## 6. FUTURE APPLICATIONS

### **Vehicle to grid wireless systems (W-V2G)**

The increasing adaptation of plug-in electric vehicles has increased the energy requirement. for demand compensation, auxiliary power supply is required which is fulfilled by renewable energy sources (RES) but they have short support facilities. Rapidly with the improved scheduling for charging and discharging the distribution network, the vehicle to grid abstract can provide a spontaneous outcome demonstrating the bi-directional power transfer application for plug-in electric vehicles comprehensive of both plug-in mode and wireless mode [11]. Plug-in V2G involves electric vehicles with bi-directional charger on-board to permit the EV user to switch between home and grid network throughout the peak hours. The EV is charged using an AC socket when used during the non-rush hours. To produce the DC source, the AC is converted to DC and is given to a DC converter unit so as to ensure safety of the user. The converted direct current is supplied to a battery via battery management system, protection and control and a multi directional DC converter. When the battery bank needs to be charged, this bi-directional DC converter operates in step down mode and in the process to increase the power level while discharging, it boosts up to ensure optimum power supply. The drawback involving in this process is that it demands a direct contact and physical handling to ensure that charging and discharging takes place in the electric vehicles [12]. The manual and physical contact demands additional safety measures to be taken to avoid accidents involving electric shocks and trip risk. To avoid these situations, a wireless V2G network is being processed.

### **In wheel wireless charging system**

Both the static and dynamic wireless charging systems are facing challenges; the most crucial challenge is the power transfer efficiency, affected due to air gap. Air gap here is the gap between the coils of transmitter and receiver which can vary according to the type of vehicle, larger for heavy vehicles smaller for light duty passenger vehicles [13]. Another important factor on which the power transfer efficiency depends is the alignment of coils which can be improved by using the parking assistance to find the center of the coil. Further to ameliorate the air gap issues in electric vehicles, in wheel wireless charging system has been introduced for both static and dynamic applications [14]. The future technologies in wireless charging are inclusive of static and dynamic WCS in both electric and

hybrid electric vehicles. The transmitter is located similarly as in the other WEVCS, but the receiver coil is placed into the Tyre structure which eventually reduces the air-gap and increases coupling efficiency for more effective power transfer [15]. To obtain an efficient static and dynamic wireless charging systems, three components must be designed carefully namely power source, wireless transformer, and Tire's internal structure.

## 7. CONCLUSION

In conclusion, this article review contains a fundamental review of the wireless electric vehicle charging systems for static and dynamic applications with present day technologies. Besides, it also discusses the components of a Dynamic wireless charging system for electrical vehicles, and discuss the types of wireless electric vehicle charging systems. Moreover, health issues and safety problems have been addressed in order to avoid accidents and hazards which are important for the evolution of WEVCS in EVs. Lastly, it contains the detailed description of the future technologies. Overall, the evolution in the field of wireless electric vehicle charging systems is illustrated in this study.

## REFERENCES

- [1] A. Ahmad, M. S. Alam, and R. Chabaan, "A Comprehensive Review of Wireless Charging Technologies for Electric Vehicles," *IEEE Trans. Transp. Electrif.*, vol. 4, no. 1, pp. 38–63, 2018, doi: 10.1109/TTE.2017.2771619.
- [2] M. Yilmaz and P. T. Krein, "Review of Battery Charger Topologies, Charging Power Levels, and Infrastructure for Plug-In Electric and Hybrid Vehicles," *IEEE Trans. Power Electron.*, vol. 28, no. 5, pp. 2151–2169, 2013, doi: 10.1109/TPEL.2012.2212917.
- [3] V. Cirimele, M. Diana, F. Freschi, and M. Mitolo, "Inductive Power Transfer for Automotive Applications: State-of-the-Art and Future Trends," *IEEE Trans. Ind. Appl.*, vol. 54, no. 5, pp. 4069–4079, 2018, doi: 10.1109/TIA.2018.2836098.
- [4] Y. J. Jang, "Survey of the operation and system study on wireless charging electric vehicle systems," *Transp. Res. Part C Emerg. Technol.*, vol. 95, pp. 844–866, 2018, doi: <https://doi.org/10.1016/j.trc.2018.04.006>.
- [5] D. Abinand, M. Deepak, M. Ahmed, and P. R. Parimi, "WIRELESS CHARGING OF ELECTRIC VEHICLE : A REVIEW," no. June, pp. 6182–6189, 2020.
- [6] N. Korakianitis, G. Vokas, and G. Ioannides, *Review of wireless power transfer (WPT) on electric vehicles (EVs) charging Review of Wireless Power Transfer (WPT) on Electric Vehicles (EVs) Charging*. 2019.
- [7] Z. Li, C. Zhu, J. Jiang, K. Song, and G. Wei, "A 3-kW Wireless Power Transfer System for Sightseeing Car Supercapacitor Charge," *IEEE Trans. Power Electron.*, vol. 32, no. 5, pp. 3301–3316, 2017, doi: 10.1109/TPEL.2016.2584701.
- [8] Y. Gao, K. B. Farley, A. Ginart, and Z. T. H. Tse, "Safety and efficiency of the wireless charging of electric vehicles," *Proc. Inst. Mech. Eng. Part D J. Automob. Eng.*, vol. 230, no. 9, pp. 1196–1207, Sep. 2015, doi: 10.1177/0954407015603863.
- [9] R. Bashirullah, "Wireless Implants," *IEEE Microw. Mag.*, vol. 11, no. 7, pp. S14–S23, 2010, doi: 10.1109/MMM.2010.938579.
- [10] H. Hou *et al.*, "Electrical Vehicle Wireless Charging Technology Based on Energy Internet Application in China," *Procedia Comput. Sci.*, vol. 83, pp. 1332–1337, 2016, doi: <https://doi.org/10.1016/j.procs.2016.04.278>.
- [11] S. BHATNAGAR, S. Parihar, R. NATHIYA, and N. MUNDRA, "CHARGING SYSTEM ANALYSIS IN STATIC AND DYNAMIC WIRELESS ELECTRIC VEHICLE," *Int. J. Adv. Res. Eng. Technol.*, vol. 10, Jan. 2019, doi: 10.34218/IJARET.10.1.2019.011.
- [12] O. Nezamuddin and E. C. dos Santos, "Vehicle-to-Vehicle In-Route Wireless Charging System," in *2020 IEEE Transportation Electrification Conference & Expo (ITEC)*, 2020, pp. 371–376, doi: 10.1109/ITEC48692.2020.9161472.
- [13] W. Zhou, Y. Su, L. Huang, X. Qing, and A. P. Hu, "Wireless Power Transfer Across a Metal Barrier by Combined Capacitive and Inductive Coupling," *IEEE Trans. Ind. Electron.*, vol. 66, no. 5, pp. 4031–4041, 2019, doi: 10.1109/TIE.2018.2849991.
- [14] R. Wireless and E. Energy, "© i a e m e," vol. 6545, pp. 43–51, 2012.
- [15] C. Panchal, J. Lu, and S. Stegen, "Static In-wheel Wireless Charging Systems for Electric Vehicles," *Int. J. Sci. Technol. Res.*, vol. 06, no. 09, pp. 280–284, 2017.



# EXERGY ASSESSMENT OF THE ENERGY EFFICIENCY OF THE CLEAN ROOM AIR TREATMENT SYSTEM

Andrei Sergeevich Riabyshenkov

National Research University of Electronic Technology, Moscow, Russia, ryabyshenkov@mail.ru, ORCID: 0000-0001-8723-953X

Valery Ivanovich Karakeyan

National Research University of Electronic Technology, Moscow, Russia, zelikar@mail.ru, ORCID: 0000-0002-6200-4053

Nikolay Romanovich Kharlamov

National Research University of Electronic Technology, Moscow, Russia, kolya.kharlamov2017@yandex.ru, ORCID: 0000-0001-6346-7407

Mikhail Aleksandrovich Gundartsev

National Research University of Electronic Technology, Moscow, Russia, gundartcev.m@yandex.ru, ORCID: 0000-0002-2020-5973

Valeria Pavlovna Sharaeva

National Research University of Electronic Technology, Moscow, Russia, sharaevalera@mail.ru, ORCID: 0000-0003-3137-8412

*Cite this paper as:* Riabyshenkov, AS., Karakeyan, VI., Kharlamov, NR., Gundartsev, MA., Sharaeva, VP. "Exergy assessment of the energy efficiency of the clean room air treatment system" 9<sup>th</sup> Eur. Conf. Ren. Energy Sys. 21-23 April 2021, Istanbul, Turkey

## Abstract:

The energy efficiency of the clean room air conditioning system is investigated as a thermodynamic technical system, to the analysis of energy transformations in which an exergy approach is applied. Based on this approach, the main factors affecting the losses of exergy in the apparatuses and devices that determine the energy efficiency of the system are established. The theoretical basis of the analysis is the exergy balance of the system, compiled on the basis of its structural diagram, and a visual representation of the distribution of exergy losses is illustrated by Grassmann diagrams for various periods of the year. The interrelationships of exergy losses in the main elements of the system of different layout decision and the air velocity in a clean room are established, which allow identifying ineffective air treatment processes and take timely and appropriate measures to adjust the technological process of air preparation. A criterion for the efficiency of the functioning of the air conditioning and filtration system of clean rooms is proposed, which based on the determination of exergy losses in its elements, which enable optimizing the system configuration. It has been found that improved air treatment efficiency can be achieved by reducing exergy losses in the processes of heating and humidifying the air.

## Keywords:

Exergy analysis, air treatment system, efficiency criterion, clean rooms, Grassmann diagrams.

© 2021 Published by ECRES

## 1. INTRODUCTION

The air conditioning and filtration system (ACFS) of clean rooms (CR) is a complex of technical devices that convert atmospheric air into a technological environment of a specific quality. Such a combination of instruments and devices can be considered as a thermodynamic technical system, to the analysis of energy efficiency of which

the exergy approach is fully applicable [1-4]. It consists in analyzing the all sequence of energy transformations occurring in the air flow, accounting for energy losses, which associated with the irreversibility of thermodynamic processes in the ACFS of the CR, and is based on the exergy balance equation, which reflects the ratio of exergies and its losses at different steps of air treatment in the warm (WPY) and cold (CPY) periods of the year.

Research methodology.

The exergy balance of the system is based on the structural diagram shown in Figure 1.

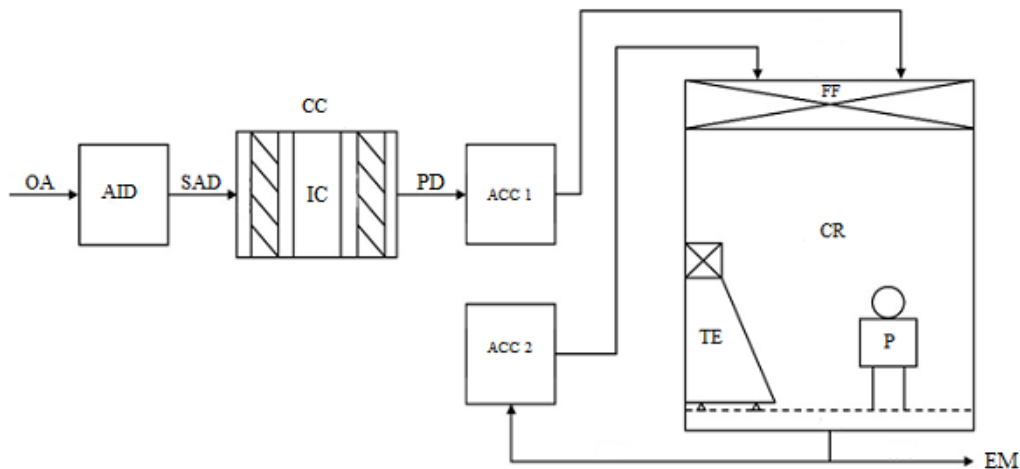


Figure 1 - Structural diagram of ACFS of CR: OA – outside air; AID - air intake device; SAD - suction air duct; CC- central air conditioner; CAL1 and CAL2 - calorifiers of the 1st and 2nd heating; IC - irrigation chamber; PD - pressure air duct; ACC1 and ACC2 - air conditioners - closers; FF - finishing filters; FP - falspol; EM - environment; TE - technological equipment; P - personnel.

OA through AID enters the central air conditioner, where preliminary processes of its heating and cooling in CAL1 and CAL2, drying and humidification in IC take place. The air is brought up to the values required by the technology in the ACC1, from where it is supplied directly to the clean room itself through the FF. Passing along the whole height of clean room from FF to FP, spent air is supplied to EM. As a rule, 10% of the exhaust air is removed to the EM, and 90% goes to the ACC2 for recirculation. Taking into account the fact that the air temperature in the CR increases approximately, by 0,5-1°C due to heat emissions from energy-intensive technological equipment and personnel, the ACC2 in the ACFS of the CR is used primarily for cooling and re-cleaning of exhaust air from the CR.

## 2. THE MATHEMATICAL APPARATUS

The exergy balance equation of the technical system has the form [5]:

$$E_{en} = E_{ex} + \sum_{i=1}^n \Delta E_i \quad (1)$$

where:

$E_{en}$  – exergy of air at the entrance to the system, kJ;

$E_{ex}$  – exergy of the air at the exit from the system, kJ;

$\sum_{i=1}^n \Delta E_i$  – sum of exergy losses of the system, kJ.

For the structural diagram of Figure 1, equation (1) is specified as follows:

$$E_{en} = \Delta E_{IC} + \Delta E_{CAL2} + \Delta E_{ACC1} + \Delta E_{CR} + \Delta E_{FP} + \Delta E_{ACC2} = 100\%, \quad (2)$$

where  $\Delta E_{IC}, \Delta E_{CAL2}, \Delta E_{ACC1}, \Delta E_{CR}, \Delta E_{FP}, \Delta E_{ACC2}$  - losses of an exergy in system elements. Kilojoule.

Air exergy is determined by the maximum useful work of its interaction with the environment before establishing the balance with it in terms of temperature, moisture content and pressure.

The specific exergy of air in the individual elements of the system ( $e_i$ ) is determined by the formula:

$$e_i = T_{OA} \left\{ \frac{\left( C_{p,d} + d_i C_{p,v} \right) \left( \frac{T_i}{T_{OA}} - 1 - \ln \frac{T_i}{T_{OA}} \right) +}{R_v \left[ (0,622 + d_i) \ln \frac{p_i (0,622 + d_{OA})}{p_{OA} (0,622 + d_i)} + d_i \ln \frac{d_i}{d_{OA}} \right]} \right\} \quad (2)$$

where:

$T_{OA}$  and  $d_{OA}$  – temperature and moisture OA, K and kg/kg, accordingly;

$C_{p,d}$ ,  $C_{p,v}$  – specific heat capacity of dry air and water vapor, kJ/kg\*K, accordingly;

$p_i$ ,  $p_{OA}$  – partial air pressure in the  $i$ -element of the system in OA, Pa, accordingly;

$R_v$  – gas constant of water vapor, kJ/(kg\*K);

$T_i$ ,  $d_i$  – temperature and moisture content of the air in the  $i$ -th element of system, K and kg/kg, respectively.

A visual representation of the distribution of exergy losses in the system is provided by Grassmann diagrams constructed at an air velocity of 0.5 m / s in WPY and CPY (tables 1-6 and figures 2-7).

### 3. CALCULATIONS

Table 1 - Specific exergy in the main elements of the ACFS at the maximum air temperature in the WPY

Line segment on the diagram	$T, ^\circ C$	$\varphi, \%$	$d, g/kg$	$I, kJ/kg$	$e_i, kJ/kg$
OA	30	56	15,1	69	0
CAL1	-				
IC - cooling	15	87	9,4	39	-79,13
CAL2 - heating	18	72	9,4	42	-62,60
ACC - moistening	9	92	6,6	25,8	-112,52
ACC1 - heating	21,5	41	6,6	38,5	-43,31
CR - heating	22	40	6,6	39,1	-40,67
FP - heating	22,5	38,6	6,6	39,6	-38,04
ACC2 – cooling and moistening	21,5	41	6,6	38,5	-43,31

The loss of exergy in its main elements (as a percentage) is determined as follows:

- in IC:  $\Delta E_{IC} = \frac{e_{IC}}{e_{en}} \times 100 = 18,86\%$ ;

- in CAL2:  $\Delta E_{CAL2} = \frac{e_{CAL2}}{e_{en}} \times 100 = 14,92\%$ ;

- in ACC1:  $\Delta E_{ACC1} = \frac{e_{ACC1}}{e_{en}} \times 100 = 37,14\%$ ;

- in CR:  $\Delta E_{CR} = \frac{e_{CR}}{e_{en}} \times 100 = 9,69\%$ ;

- in FP:  $\Delta E_{FP} = \frac{e_{FP}}{e_{en}} \times 100 = 9,07\%$ ;

- in ACC2:  $\Delta E_{ACC2} = \frac{e_{ACC2}}{e_{en}} \times 100 = 10,32\%$ .

Similarly, the loss of exergy is determined and Grassman diagrams are plotted in the main elements of the system for the minimum air temperature in the WPY and CPY over a specified period of time.

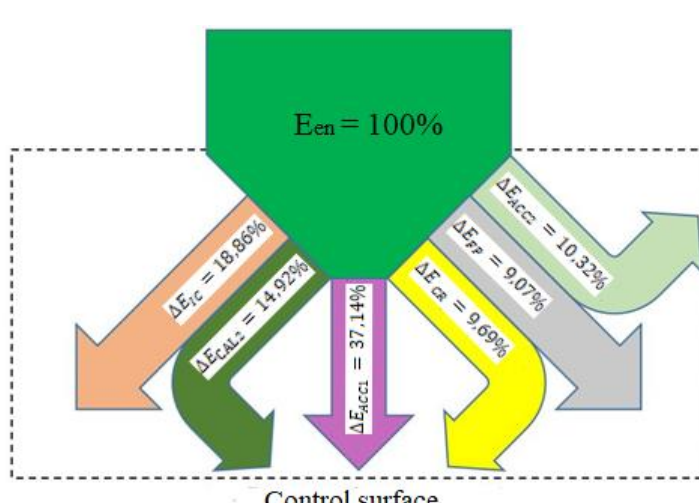


Figure 2 - Grassmann diagram at maximum air temperature for WPY

Table 2 - Specific exergy in the main elements of ACFS at the average air temperature in the WPY

Line segment on the diagram	$T, ^\circ\text{C}$	$\varphi, \%$	$d, \text{g/kg}$	$I, \text{kJ/kg}$	$e_b, \text{kJ/kg}$
OA	15,7	67	7,5	34,9	0
CAL1	-				
IC	11,5	78	6,6	28,3	-22,59
CAL2	19	48	6,6	35,9	17,30
ACC1	21,5	41	6,6	38,5	30,13
CR	22	40	6,6	39	32,67
FP	22,5	38,5	6,6	39,5	35,20
ACC2	21,5	41	6,6	38,5	30,13

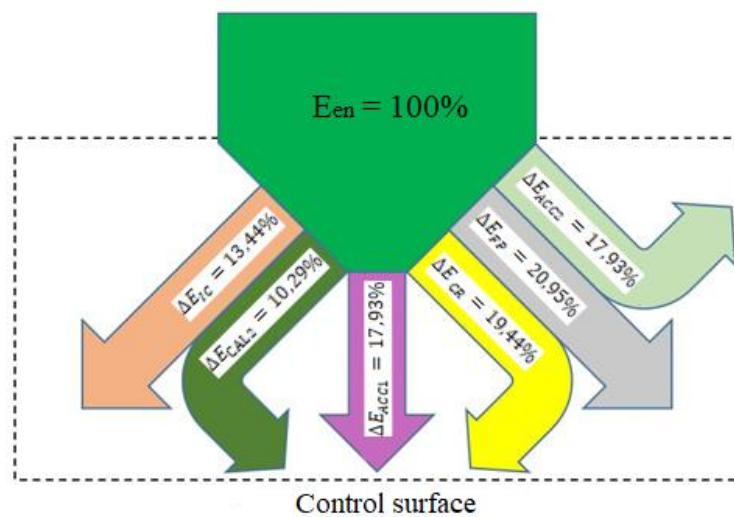


Figure 3 - Grassmann diagram at the average air temperature for WPY

Table 3 - Specific exergy in the main elements of the ACFS at the minimum air temperature in the WPY

Line segment on the diagram	$T, ^\circ\text{C}$	$\varphi, \%$	$d, \text{g/kg}$	$I, \text{kJ/kg}$	$e_b, \text{kJ/kg}$
OA	-3,1	73	2,2	2,2	0
CAL1	10	28	2,2	15,5	71,33
IC	10	86	6,6	26,7	72,18
CAL2	17	54	6,6	33,9	107,85
ACC1	21,5	41	6,6	38,5	129,87
CR	22	40	6,6	39	132,28
FP	22,5	38	6,6	39,5	134,68
ACC2	21,5	41	6,6	38,5	129,87

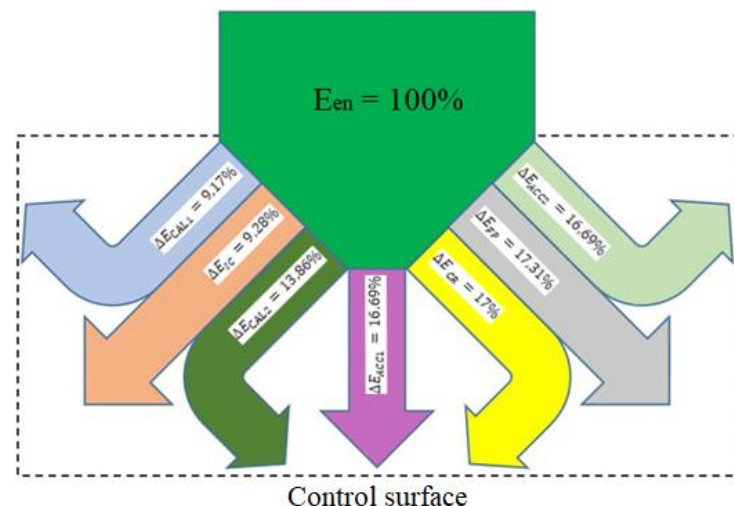


Figure 4 - Grassmann diagram at the minimum air temperature for WPY

Table 4 - Specific exergy in the main elements of ACFS at the maximum air temperature in CPY

Line segment on the diagram	$T, ^\circ\text{C}$	$\varphi, \%$	$d, \text{g/kg}$	$I, \text{kJ/kg}$	$e_b, \text{kJ/kg}$
OA	18	52	6,7	35,3	0
CAL1	-				
IC	17	54	6,6	33,9	-5,27
CAL2	20	45	6,6	37	10,43
ACC1	21,5	41	6,6	38,5	18,15
CR	22	40	6,6	39	20,71
FP	22,5	38,6	6,6	39,5	23,26
ACC2	21,5	41	6,6	38,5	18,15

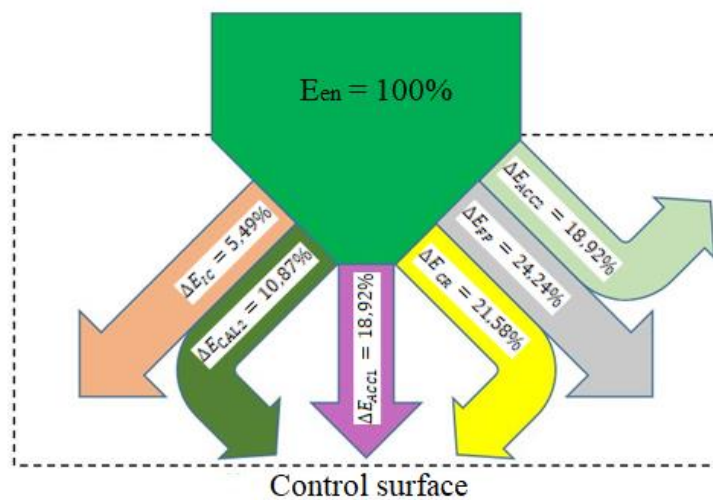


Figure 5 - Grassmann diagram at maximum air temperature for CPY

Table 5 - Specific exergy in the main elements of ACFS at the average air temperature in CPY

Line segment on the diagram	$T, ^\circ\text{C}$	$\varphi, \%$	$d, \text{g/kg}$	$I, \text{kJ/kg}$	$e_b, \text{kJ/kg}$
OA	-3	87	2,6	3,4	0
CAL1	9	36	2,6	15,6	65,61
IC	9	92	6,6	25,8	66,29
CAL2	17	54	6,6	34	107,22
ACC1	21,5	41	6,6	38,6	129,25
CR	22	40	6,6	39,1	131,66
FP	22,5	38,7	6,6	39,6	134,06
ACC2	21,5	41	6,6	38,5	129,25

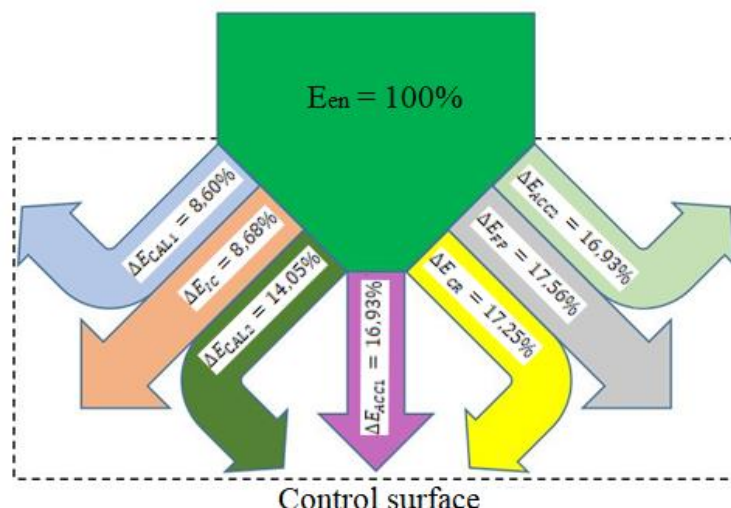


Figure 6 - Grassmann diagram at average air temperature for CPY

Table 6 - Specific exergy in the main elements of ACFS at the minimum temperature in CPY

Line segment on the diagram	$T, ^\circ C$	$\varphi, \%$	$d, g/kg$	$I, kJ/kg$	$e_b, kJ/kg$
OA	-19	92	0,7	-17,6	0
CAL1	9	9	0,7	10,7	154,58
IC	9	92	6,6	25,8	157,04
CAL2	17	54	6,6	34	195,98
ACC1	21,5	41	6,6	38,6	216,97
CR	22	40	6,6	39,1	219,26
FP	22,5	38,7	6,6	39,6	221,54
ACC2	21,5	41	6,6	38,5	216,97

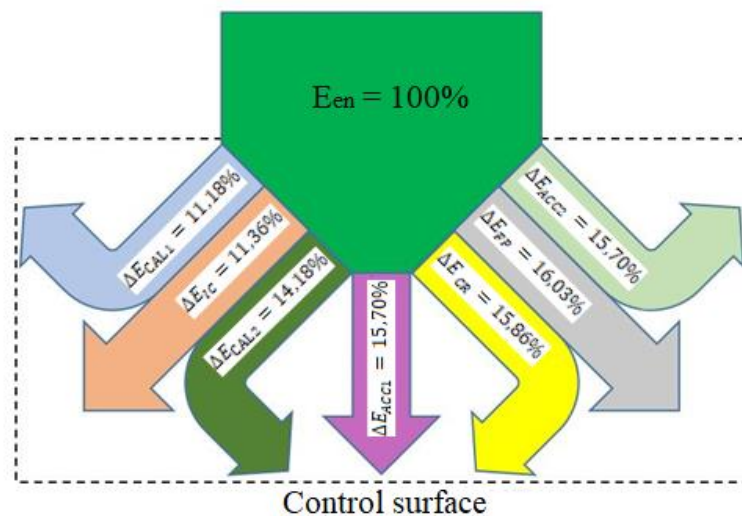


Figure 7 - Grassmann diagram at minimum air temperature for CPY

Analysis of the Grossman diagrams showed that increasing the exergy efficiency of the system for TPG need to reduce the exergy losses in the processes of moistening and heating of air, and for CPY - in the processes of heating in CAL2, as well as in humidification of air in IC.

From the operating experience of the ACFS CR, it implies that the change in the speed of air directly in the CR has an impact on the parameters of the air leaving from the air conditioner-closer. The dependence of the exergy losses in the air conditioner-closer on the air velocity in the CR at the maximum and minimum values of the air temperature in the WPY and CPY are shown in Figures 9-12.

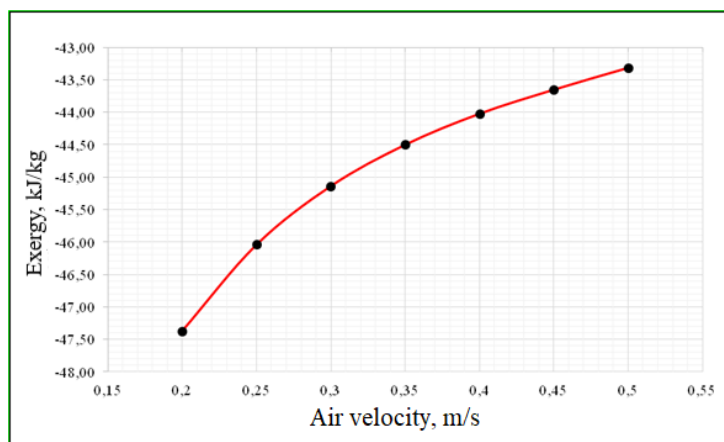


Figure 9 - Dependence of exergy losses in ACC on the air velocity in the CR at the maximum air temperature in the WPY

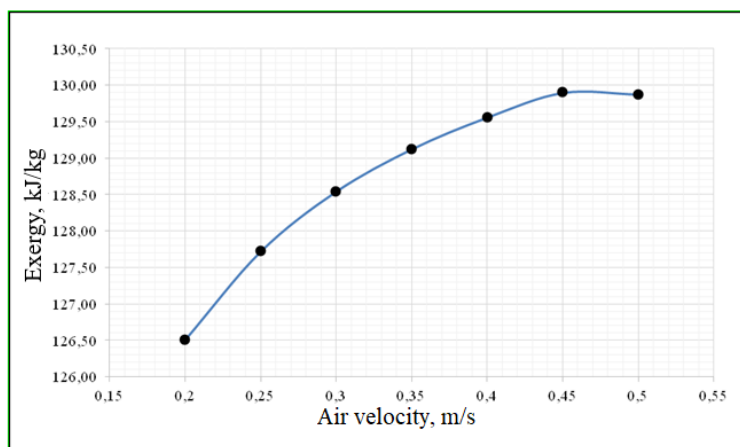


Figure 10 - Dependence of exergy losses in ACC on the air velocity in the CR at the minimum air temperature in the WPY

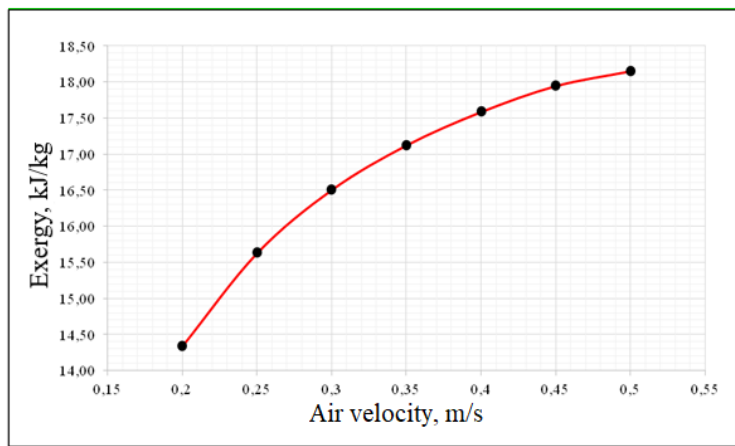


Figure 11 - Dependence of exergy losses in ACC on the air velocity in the CR at the maximum air temperature in the CPY

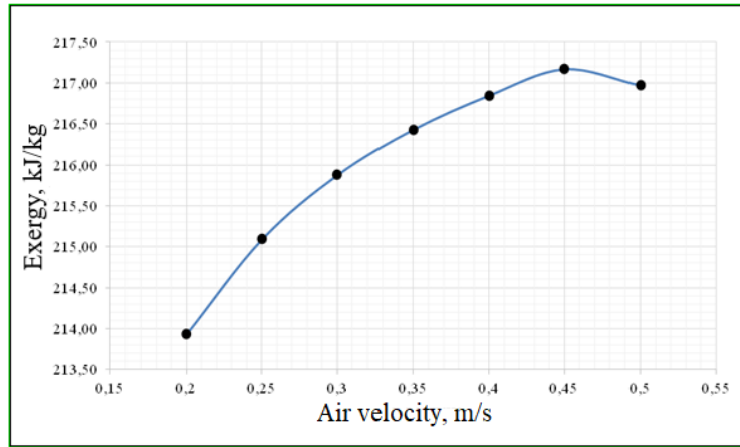


Figure 12 - Dependence of exergy losses in ACC on the air velocity in the CR at the minimum air temperature in the CPY

Analysis of the obtained dependencies made it possible to establish that in CPY there are more losses of exergy than in WPY. It should also be noted that in WPY, the loss of exergy decreases with increasing air velocity in CR, and in CPY, the exergy losses increases with increasing air velocity in CR. Therefore, from the point of view of exergy analysis, it is most rational to choose the air velocities in CR for WPY - 0.2 m/s, and for CPY - 0.5 m/s, which fits well into the given range of air flow velocities from 0.2 to 0.5 m/s.

#### **4. MAIN CONCLUSIONS**

The constructed Grassman diagrams for WPY and CPY make it possible to estimate the relative losses of exergy in individual elements and the system at all. Improvement of efficiency of air treatment in CR can be achieved due to reduction of coolant consumption, optimization of energy consumption at heating in calorifier and humidification in irrigation chamber.

The analysis of the regularities of exergy losses, depending on the air speed in CR showed that the value of the losses of exergy as changes in air velocity from 0.2 to 0.5 m/s: in the WPY for the maximum temperature is 9% and the minimum temperature is 3%; in the CPY for the maximum air temperature is 27% and minimum temperatures of 1%, which allows to identify inefficient processes of air treatment in the system taking into account the studied layout of its elements.

The use of an exergy approach to the evaluation of the effectiveness of the functioning of the ACFS has been established and a criterion in the form of a minimum of exergy losses in its individual elements has been proposed.

#### **REFERENCES**

- [1] Kazakov V. G. Exergy methods for evaluating the effectiveness of heat settings: tutorial. Kazakov V. G., Lukanin P. V., Smirnova O. S., St. Petersburg 2013. pp. 93.
- [2] Arkharov A.M. Entropy-statistical analysis of distribution of energy costs for compensation of irreversibility of working processes of air conditioning systems. Arkharov A.M., Shishov V.V. Bulletin of Moscow State Technical University named after N.E.Baumana. Series Engineering, 2013. pp. 84-93.
- [3] Karakeyan V. I. Methodology of system analysis in the study of energy-ecological characteristics of clean rooms. Karakeyan V. I., Larionov N. M. Vectors of development of modern science: collection of materials of the III International Scientific and practical Conference, Ufa 2016. pp. 83-89.
- [4] Thein Htut Oo. Exergetic analysis air preparation system with heat exchanger for clean room. Thein Htut Oo, Phyto Thu and other. Young Researchers in Electrical and Electronic Engineering (EICoRus), 2019 IEEE Conference of Russian, 2019. pp. 2333-2336.
- [5] Riabyshenkov A. S. Exergy Analysis of the Recirculation Scheme for Air Preparation of Clean Rooms Based on a System Approach. Karakeyan Valery, Zaharov Artem, Larionnov Nikolay. International Seminar on Electron Devices Design and Production, SED 2019 – Proceedings. IEEE, 2019. – pp. 8798384-1–8798384-4.



# DETERMINING OF OPTIMAL TILT ANGLE OF SOLAR PANELS IN THREE CITIES IN ALBANIA

Buzra Urim

Polytechnic University of Tirana, Tirana, Albania, u.buzra@fimif.edu.al, ORCID: 0000-0002-9240-8825

Mitrushi Driada

Polytechnic University of Tirana, Tirana, Albania, d.mitrushi@fimif.edu.al, ORCID: 0000-0001-8722-4231

Serdari Eduart

University of Vlora, Vlora, Albania, eduard.serdari@univlora.edu.al, ORCID: 0000-0001-7784-7398

Topciu Daniela

University of Elbasan, Elbasan, Albania, halili@uniel.edu.al, ORCID: 0000-0002-5740-8993

Muda Valbona

Polytechnic University of Tirana, Tirana, Albania, v.muda@fimif.edu.al, ORCID: 0000-0001-7535-4856

*Cite this paper as:* Urim, B, Driada, M, Eduart, S, Daniela, T, Valbona, M. "Determining of optimum tilt angle of solar panels in three cities in Albania" 9<sup>th</sup> Eur. Conf. Ren. Energy Sys. 21-23 April 2021, Istanbul, Turkey

---

**Abstract:**

The performance of solar energy systems is strongly correlated with tilt angle of solar panels installation, because the angle of inclination of solar panels influenced the amount of solar radiation reaching the tilted surface. Due to rotation of the Earth around the Sun in elliptical orbit, and its own axis, the angle of incidence of sunlight reaching the Earth varies during the year. For this reason, the tilt angle of the solar panels should be changed monthly or seasonally to maximize the solar energy capture by the solar panels. In this study, the BMS Model is used to determine the yearly and seasonally optimum tilt angle of the solar panels in three cities in Albania. Based on the above mathematical model, the yearly and seasonally optimum tilt angle of the solar panels for three different cities is calculated. The evaluation of the optimal tilt angle is made considering the fact that the solar energy reaching the solar panels has maximum value for optimal tilt angle. The yearly optimum angle of inclination of the solar panels for the cities: Tirana (41.3275° N, 19.8187° E), Kukes (42.0807° N, 20.4143° E) and Vlora (40.4661° N, 19.4914° E) are respectively 38°, 39° and 37°. It should be noted that, the yearly optimal tilt angle of solar panels based on the above mathematical model is nearly equal to the latitude of the location. The energy received per square meter at optimal tilt angle of the panels is approximately 22 % more than energy received on a horizontal panel and is approximately 2 % less than energy received per square meter yearly for adjusted tilt angle of the panels.

---

**Keywords:**

*Bernard-Menguy-Schwartz (BMS) Model, Solar energy, optimum tilt angle, solar panels (solar water heating SWH, or PV panels)*

---

© 2021 Published by ECRES

---

**Nomenclature**

$\beta$	Tilt angle
$\delta$	Solar declination
$\alpha_s$	The height of the sun at solar noon
$\omega$	Hour angle
$\theta$	Incidence angle.
$I_D$	The direct beam radiation
$D_H$	The sky- diffused radiation
$G_H$	The overall radiation

---

$D_i$	Diffuse radiations
$G_i$	Overall radiations on tilted plane
$\alpha$	Albedo
$\varphi$	latitude of the location

## 1. INTRODUCTION

The fact that economic growth and living standards of a country is strongly related with energy consumption has imposed the rise of energy generated from different sources. Renewable energy and particularly solar energy plays a critical role in the future sustainable energy in terms of capacity to meet the energy demand and ecological aspects as a source of energy environmentally friendly [1]. Solar energy is abundant and combined with economic feasibility and the fact that solar energy is clean, the solar energy harnessed in both systems (solar water heating, solar photovoltaic) has attracted more attention [2]. With an average of sunny days from 240-300 days per year, combined with favorable conditions of temperature and relative humidity, Albania is considered a country with good potential for the use of solar energy [3]. The exploit of solar energy by solar systems depends on several geometrical parameters. The angle of incidence is defined as the angle between solar rays and the perpendicular line on the surface, and the amount of the solar radiation incident on a surface is inversely proportional to the value of incidence angle. The incidence angle can be calculated using a long equation which depends on several angles. To maximize the employ of solar energy by solar systems (solar water heating, solar photovoltaic), these geometrical parameters must be determined [4]. The tilt angle of solar panels is an important factor for each location, which affects the annual energy the solar system yields, to capture the maximum solar energy, we must optimize it. There are many factors that influence the optimum tilt angle such as latitude of location, air pollution, clearness index which has local character, and sunny days of the year which represent the climatic condition of the location [5]. In this study we have determined the optimal tilt angle of the solar panels based on the BMS model for three cities in Albania.

## 2. METHODOLOGY AND COMPUTATIONAL MODEL

To appraise the solar energy received on a tilted surface, we have used the BMS model, the mathematics of the model is given from equation [1–11]. The solar declination angle changes daily and monthly throughout the year, the expression for solar declination is given in Equation 1. From the Equation 1, we can determine the solar altitude angle at true midday, refer to Equation 2. The angle  $\theta$  formed between the normal of the collector and the solar rays at solar midday is given in Equation 3, which contain the tilt angle  $\beta$  of the solar panels, the angle which must optimized. It can vary from  $-90^\circ$  to  $90^\circ$ . In our case the tilt angle varies from 0 (horizontal) to  $90^\circ$  [6]. The hour angle  $\omega$  is negative for period in the morning time, positive afternoon time, and zero at solar noon, the angle  $\omega$  changes  $15^\circ$  per hour [7].

The solar declination angle is given by:

$$\delta = \frac{23.45 \pi}{180} \sin\left(\frac{2\pi(284 + n)}{365}\right) \quad (1)$$

n stands for the days of the year, n=1 for 1st January [2].

- The height of the sun at true midday

-

$$\alpha_s = 90 - \varphi + \delta(t) \quad (2)$$

In our case of study is use the characteristic declinations

Table 1 Characteristic declination [7]

Month	Date	$\delta$ (degrees)	Day number
January	17	-20.84	17
February	14	-13.32	45
March	15	-2.40	74
April	15	+9.46	105
May	15	+18.78	135
June	10	+23.04	161
July	18	+21.11	199
August	18	+13.28	230
September	18	+1.97	261
October	19	-9.84	292
November	18	-19.02	322
December	13	-23.12	347

The angle  $\theta$  at solar noon:

$$\theta = 90 - (\beta + \alpha_s) \quad (3)$$

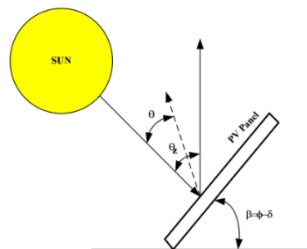


Figure 5. Incidence and tilt angels

In solar energy applications it is necessary to evaluate all components direct radiation, diffuse radiation, and ground reflected of solar radiation surviving the atmosphere and reaching the earth's surface. In this study the components are determined according to BMS Model, from equation (4) – (8). The direct radiation under of clear sky condition is given:

$$I_D = 1230e^{\left(\frac{-1}{3.8\sin(\alpha_s+1.6)}\right)} \quad (4)$$

The sky- diffused radiation received on the horizontal plane in clear sky condition is:

$$D_H = 125(\sin(\alpha_s))^{0.4} \quad (5)$$

The overall radiation falling in a horizontal plane is given by.

$$G_H = D_H + I_D \sin(\alpha_s) \quad (6)$$

Diffuse and overall radiations in tilted solar collector plane:

$$D_i = \frac{1 + \cos(\beta)}{2} D_H + \frac{1 - \cos(\beta)}{2} G_H \alpha \quad (7)$$

$$G_i = I_D \cos(\theta) + D_i \quad (8)$$

$\alpha$  is the albedo coefficient of the surface usually takes 0.2.

Duration of the day:

$$\Delta T = \frac{2}{15} \operatorname{arccosh}(-\tan(\varphi) \tan(\delta)) \quad (9)$$

$\varphi$  is latitude of the location.

For period between March 21 and September 23 the duration of the day is given by:

$$\Delta T' = 12 + \frac{\Delta T - 12}{7} \quad (10)$$

The energy received is given: [8]

$$E = \frac{2}{\pi} G_i \Delta T \quad (11)$$

### 3. RESULTS AND DISCUSSION

#### The determination of the ideal tilt angle of the solar collectors

For most systems in solar energy, knowing the variations of optimal tilt angle of the solar panels is of a particular importance. The optimal tilt angle varies daily, monthly, seasonally, so it is very important to take into account monthly or seasonally collector tilt adjustment. Another angle to consider is the azimuth angle, or the angle of the solar panels facing the equator, in our case this angle is set to be zero.

As a rule of thumb, the angle of inclination of the solar collector is the difference between the latitude of the location and the characteristics solar declination, in absolute value.

$$\beta = |\varphi - \delta| \quad (12)$$

Figure 2 shows that monthly optimal tilt angle for Tirana city varies between  $18^\circ$  and  $64^\circ$  according to the date. Also, the calculations demonstrate that in Kukes and Vlora city, the monthly tilt angle of solar panels varies between  $19^\circ$  and  $65^\circ$  and  $17^\circ$  and  $63^\circ$  respectively. Figure 2 is divided in to three zones according to the variation of the optimal tilt angle of the collector. Zone 1 ranges from  $48^\circ$  to  $64^\circ$ , Zone 2 ranges from  $30^\circ$  to  $48^\circ$ , and Zone 3 from  $18^\circ$  to  $30^\circ$ . We suggest changing the tilt angel of the collector according to zones in figure 2. The tilt angle according to the zones is found to be in average as  $\beta_{opt} = \varphi + 15$  in zone 1,  $\beta_{opt} = \varphi$  in zone 2, and  $\beta_{opt} = \varphi - 17$  zone 3.

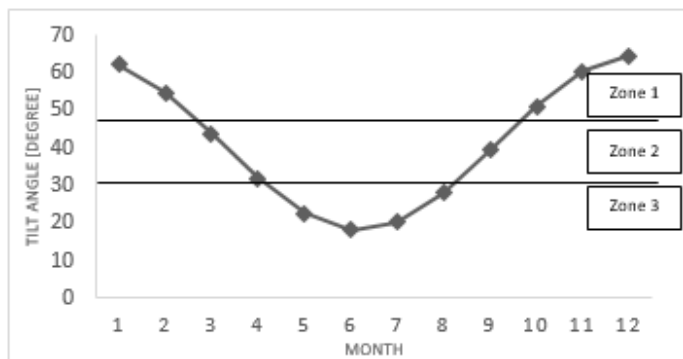


Figure 2. Monthly variation of tilt angle of the collector, Tirana city

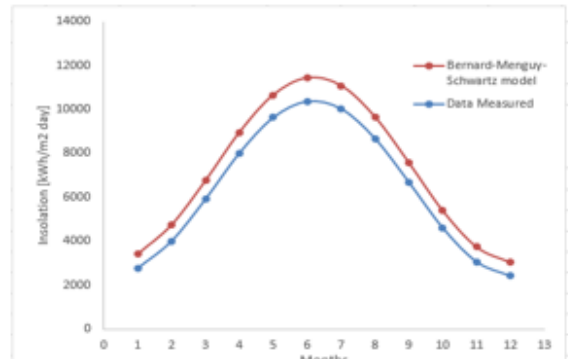


Figure 3. The comparison between data measured and Bernard-Menguy-Schwartz model

#### Energy received on the tilted solar panels

The yearly optimum tilt angle for our cities study is calculated using Equations [1–11]. Figure 4 show the influence of the tilt angle on energy received on solar panels for 12 months of the year for Tirana city. From figure 4 it seems that in summer months, the optimal tilt angle of solar panels is between  $19^\circ$  and  $29^\circ$ , and in the winter months, the optimal tilt angle is between  $55^\circ$  and  $64^\circ$ . For Kukes city the optimal tilt angle of the solar panels during the summer months is between  $20^\circ$  and  $30^\circ$  and during winter months is between  $53^\circ$  and  $63^\circ$ , and for Vlora city the results show that during summer months, the optimum tilt angle is between  $19^\circ$  and  $29^\circ$ , and during the winter months, the optimum tilt angle is between  $54^\circ$  and  $63^\circ$ .

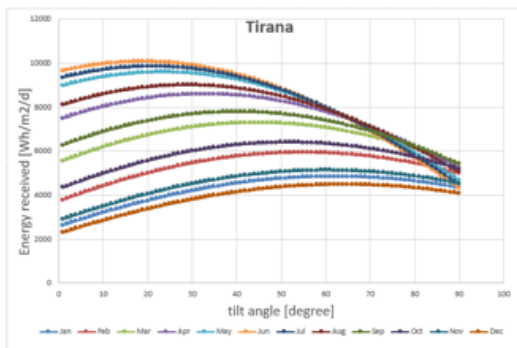


Figure 4. Energy received per square meter per day in Tirana city

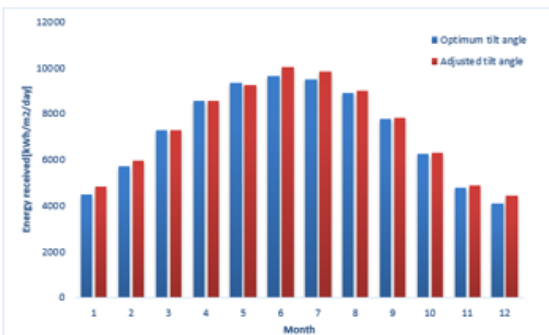


Figure 5. The daily energy received in Tirana city for optimum tilt angles and adjusted tilt angle

Based on BMS mathematical model, the optimal tilt angle of the solar panels for three different cities is calculated. The determination of the optimum angle is made taking into account the fact that the solar energy reaching the solar panels has maximum value for optimum tilt angle. From the BMS model the yearly optimal tilt angle of the solar panels for the cities of Tirana, Kukes and Vlora are respectively  $38^\circ$ ,  $39^\circ$  and  $37^\circ$ . It should be noted that, the yearly optimum tilt angle of solar panels based on the above mathematical model is almost equal to the latitude of the location. We compared the above results with PVGIS network data. Based on PVGIS data for our cities in study the yearly optimum tilt angle is  $38^\circ$ ,  $36^\circ$  and  $34^\circ$  for Tirana, Vlora and Kukes city.

Figure 5, 6 and 7 shows the energy received per square meter per day, for fixed optimum tilt angle and seasonally adjusted tilt angle of the solar panels in Tirana, Kukes and Vlora City. From the calculation, the energy received yearly per square meter on a horizontal surface for cities in our study is  $70501.73 \text{ kWh/m}^2 \text{ year}$  for Tirana city,  $69604.7 \text{ kWh/m}^2$  for Kukes city, and  $71501.6 \text{ kWh/m}^2$  for Vlora city. The energy received per square meter in fixed optimum tilt angle is 22.2% more than energy received on a horizontal surface and 2 % less than energy received per square meter yearly for seasonally adjusted tilt angle of the solar panels for Tirana City. The energy received per square meter in fixed optimum tilt angle is 23.2% more than energy received on a horizontal surface and 2 % less than energy received per square meter yearly for seasonally adjusted tilt angle of the solar panels for Kukes City. The energy received per square meter in fixed optimum tilt angle is 21.2% more than energy received on a horizontal surface and 1.9 % less than energy received per square meter yearly for seasonally adjusted tilt angle of the collector for Vlora City.

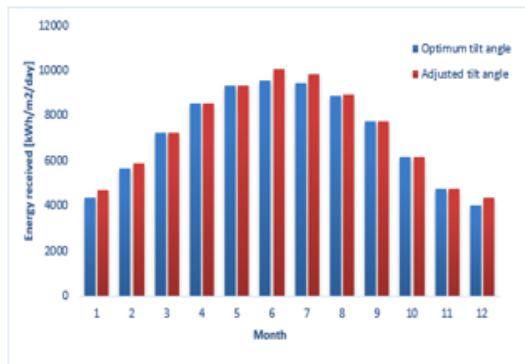


Figure 6. The daily energy received in Kukes city for optimum tilt angles and adjusted tilt angle

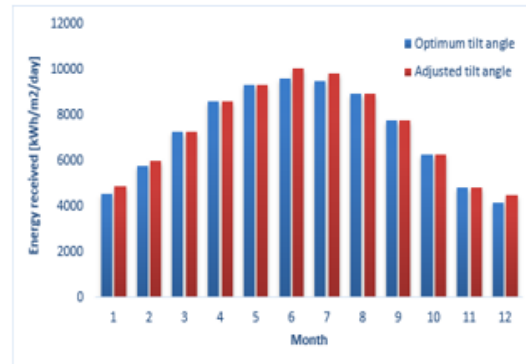


Figure 7. The daily energy received in Vlora city for optimum tilt angles and adjusted tilt angle

### Comparison data measured and BMS model.

The solar energy per unit area per day was measured in the city of Tirana using meteorological station Davis instrument, situated at high 20 m above the ground on the upper building near to the FEM&EP (Faculty of Engineering Mathematics and Engineering Physics). The data was analyzed for a one year period. The instrument of meteorological station, measure the solar energy reaching in a horizontal surface. From the data measured, the solar energy in yearly optimal tilt angle of solar panels was calculated for Tirana city determined by the BMS model, and the data was corrected considered the incidence angle of solar radiation on solar panels during the day. Figure 3 show the comparison between data measured from the meteorological station and the BMS model. From

the figure 3 we can say that the biggest relative deviation of measured data with the model is during months from May-August 16.6 % to 21.5 %, while in other months this deviation lies between 9-13 %. [8]

#### **4. CONCLUSIONS**

In this study, BMS Model is used to determine the optimum tilt angle of the solar panels in three cities in Albania. The tilt optimum angle of the solar panels for the cities of Tirana, Kukes and Vlora are respectively  $38^\circ$ ,  $39^\circ$  and  $37^\circ$ . The calculations of optimal tilt angle are done for two scenarios: annual fixed tilt angle of the panels and monthly adjustable tilt angle according to figure 2.

For summer months the optimum tilt angle is found to be  $\beta_{\text{opt}} = \varphi - 17$ , for winter months the optimum tilt angle is found to be  $\beta_{\text{opt}} = \varphi + 15$ , and for spring and autumn months is  $\beta_{\text{opt}} = \varphi$ . To increase the harness of solar radiation, the optimum tilt angle of solar panels should be adjusted monthly, but this has additional cost to operate. From the calculation, the energy received yearly per square meter on a horizontal surface for cities in our study is 70501.73 kWh/m<sup>2</sup> year for Tirana city, 69604.7 kWh/m<sup>2</sup> for Kukes city, and 71501.6 kWh/m<sup>2</sup> for Vlora city. The energy received per square meter in optimum tilt angle is approximately 22 % more than energy received on a horizontal surface and is approximately 2 % less than energy received per square meter yearly for adjusted tilt angle of the panels. From comparison the data measured and the BMS model the biggest relative deviation of measured data with the model is during months from May-August 16.6 % to 21.5 %, while in other months this deviation lies between 9-13 %.

#### **REFERENCES**

- [1] Danny H.W. Li and Tony N. T. Lam, "Determining the Optimum Tilt Angle and Orientation for Solar Energy Collection Based on Measured Solar Radiance Data," *International Journal of Photoenergy*, 2007.
- [2] Asad Ullah, Hassan Imran, Zaki Maqsood, Nauman Zafar Butt, "Investigation of optimal tilt angels and effects of soiling on PV energy production in Paksitan," *Elsevier, Renewable Energy*, pp. 830-843, 2019.
- [3] N. A. o. N. Resources, "Renewable energy," Tirana, 2019.
- [4] Abbas sari Shareef Mohammed Hassan Abood, "Experimental investigation on a flat plate solar collector using Al<sub>2</sub>O<sub>3</sub> Nanofluid as a heat transfer agent," *INTERNATIONAL JOURNAL OF ENERGY AND ENVIRONMENT*, 2015/1.
- [5] Arbi Gharakhani Siraki, Pragases Pillay, "Study of optimum tilt angles for solar panels in different latitudes," *Solar Energy*, pp. 1920-1928, 2012.
- [6] S. Bhatia, Advanced Renewable Energy Systems, India: Woodhead Publishing India, 2014.
- [7] M. Iqbal, An Introduction to Solar Radiation, Canada: Academic Press, 1983.
- [8] R. B. Slama, "Incidental Solar Radiation to the Solar collector slope-Horizontal Measurements Conversion on an Inclined Panel Laws," *The Open Renewable Energy Journal*, vol. 2, pp. 52-58, 2009.



# EFFECT OF ESTONIAN WOODY BIOMASS GASIFICATION TEMPERATURE ON THE COMPOSITION OF THE PRODUCER GAS

Alejandro Lyons Cerón

Tallinn University of Technology, Tallinn, Estonia, allyon@taltech.ee, ORCID: 0000-0002-2800-851X

Alar Konist

Tallinn University of Technology, Tallinn, Estonia, alar.konist@taltech.ee, ORCID: 0000-0001-5492-248X

Heidi Lees

Tallinn University of Technology, Tallinn, Estonia, heidi.lees@taltech.ee, ORCID: 0000-0002-1395-9822

Oliver Järvik

Tallinn University of Technology, Tallinn, Estonia, oliver.jarvik@taltech.ee, ORCID: 0000-0001-8530-2582

*Cite this paper as:* Lyons Cerón, A, Konist, A, Lees, H, Järvik, O. Effect of Estonian woody biomass gasification process conditions on the composition of the producer gas. 9th Eur. Conf. Ren. Energy Sys. 21-23 April 2021, Istanbul, Turkey

**Abstract:** The use of biomass in thermochemical gasification is a potential alternative to produce renewable energy. The type of biomass and operational parameters directly affect the composition and quality of the producer gas. This paper studies the composition of the producer gas from the gasification of three Estonian woody biomass species: alder, spruce, and pine. The experiments were carried out in a drop-tube reactor at 750, 850, and 950 °C, using air as a gasifying agent, with an equivalence ratio of 0.39. The composition of the producer gas was measured using gas chromatography with a thermal conductivity detector. The measurements demonstrated a very similar producer gas composition for the three wood species. The highest concentration of combustible gases was obtained at 950 °C, with an average of 4.1, 20.5, and 4.6 vol% for H<sub>2</sub>, CO, and CH<sub>4</sub>, respectively. The results were in accordance with other gasification studies of woody species. Higher temperatures improved the producer gas composition by promoting endothermic and exothermic gasification reactions, increasing the gas yield, and decreasing the solids and tar.

**Keywords:** Alder, gasification, pine, spruce, temperature, woody biomass

© 2021 Published by ECRES

## Nomenclature

ER	Equivalence ratio
GC-TCD	Gas-chromatography-thermal conductivity detector
HHV	Higher heating value
LHV	Lower heating value
WB	Woody biomass

## 1. INTRODUCTION

Biomass is one of the most promising renewable resources of Estonia, providing over 50% and 7% of the heat and electricity, respectively, using wood residues and woody resources from forests [1]. Forests in Estonia cover around 50% of the country's territory, of which around 32% are pine, 18% spruce, and 13% alder [2]. Estonia has advanced technical expertise in thermochemical conversion processes from the conversion of oil shale for electricity and the conversion of biomass for heat supply through district heating [3]. This expertise allows the potential implementation of thermochemical processes, such as gasification or co-processing of biomass and oil shale, to produce energy and high-quality products. Woody biomass (WB) resources can be converted into fuels and chemicals through biochemical, mechanical, and thermochemical conversion processes [4]. From the

thermochemical conversion processes, gasification is used for the production of syngas or producer gas, rich in H<sub>2</sub> (5–20 vol%), CO (17–22 vol%), CH<sub>4</sub> (2–3 vol%), and CO<sub>2</sub> (9–15 vol%) [5]. The yields and composition of the gasification products depend on the operational parameters used. The selection of the gasification parameters dramatically affects the gasification process performance and products, determining the temperature, availability of oxygen, gas, and tar yields [6]. The gasification temperature influences the yield of products, duration, and efficiency of the process [7].

This paper studied the composition of the producer gas obtained from the gasification of Estonian WB at different temperatures. Samples of spruce, alder, and pine were gasified in a laboratory-scale batch reactor at 750, 850, and 950 °C using a blend of N<sub>2</sub> and O<sub>2</sub> as the gasifying agent. The producer gas composition was measured using gas-chromatography with a thermal conductivity detector (GC-TCD). The results obtained contribute to identifying and characterizing the gaseous products from the gasification of WB species, as well as setting the grounds for further studies on using local Estonian WB resources in thermochemical gasification processes.

## **2. MATERIALS AND METHODS**

Three of the most common species of WB from Estonian forest were used as feedstock: Norway spruce, Grey alder, and Scots pine. The feedstocks were collected, separated into bark and wood, ground, and homogenized to a particle size of less than 1 mm. The WB samples were previously characterized in terms of proximate analysis (moisture, ash, volatile and fixed carbon content), ultimate analysis (C, H, N, S, and O), and calorimetry [8]. The ultimate analysis was carried out with a Vario MACRO CHNS elemental analyzer according to ISO 16948 and with a Dionex ICS-1000 Ion Chromatography according to ISO 16994. The proximate analysis was carried out with Memmert and Nabertherm RT120 drying ovens according to ISO 18134-2 and a Nabertherm L9 Muffle furnace according to ISO 18122. The calorific values were measured using bomb calorimeters IKA 2000C and IKA 5000C Calorimetric systems according to ISO 18125.

## **EXPERIMENT SET UP**

Gasification experiments of alder, spruce, and pine were conducted in a prototype batch drop-tube reactor at 750, 850, and 950 °C in isothermal conditions. The total mass used for each experiment was approximately 1.5 g of WB. Each experiment condition was carried out three times to ensure reproducibility. The gasifying agent used was a mixture of N<sub>2</sub> and O<sub>2</sub> at a flow rate of 0.3 l/min with an Equivalence Ratio (ER) of 0.39. Each experiment was carried out for around 8 min. After the producer gas was cleaned and cooled, it was measured with a GC-TCD Gazohrom 3101 gas analyzer. The GC-TCD measured H<sub>2</sub>, CO, CH<sub>4</sub>, and CO<sub>2</sub>. Two packed columns with a total length of 2.5 m long and 3.6 mm in diameter were used for the separation of these gases at room temperature. Air (70 ml/min) was used as the gas carrier to detect H<sub>2</sub>, CO, and CH<sub>4</sub>, while Argon (40 ml/min) was used to detect CO<sub>2</sub>. Three replicates were made for GC-TCD measurements.

## **3. RESULTS AND DISCUSSION**

### **Woody Biomass Composition**

The composition of the studied samples of Norway spruce, Grey alder, and Scots pine are provided in Table 1, including ultimate analysis, proximate analysis, and calorific values. Besides, results from other studies are provided for comparison. The composition obtained from local WB samples is comparable and similar to samples of the same species characterized in other studies. Moreover, the composition of the three studied samples is within the same range of elemental composition, as well as ash content, moisture, fixed carbon, and heating values.

*Table 1. Ultimate, proximate analysis and calorific value for spruce, alder, and pine*

Composition	Feedstock used [8]			Literature	
	Norway spruce	Grey alder	Scots pine	Spruce [9–11]	Alder [12,13]
Ultimate analysis [wt%]	C	50.3	49.9	50.1	49.5–51.7
	H	6.6	6.6	6.1–6.2	5.1
	N	0.1	0.2	0.1–1.0	0.5
	S	n.d.	n.d.	<0.1	0.3
	O*	42.7	43.0	41.2–43.2	43.4
Proximate analysis [wt%]	Ash content	0.3	0.3	0.2–0.6	0.7
	Moisture	6.9	7.6	7.6	7.3
	Fixed carbon	14.2	14.0	12.8–28.3	12.5
	Volatile matter	85.5	85.7	70.2–87.0	87.4
Calorific value [MJ/kg]	LHV	18.6	18.5	19.0	19.0
	HHV	20.0	19.9	19.7–20.3	19.0

\* Calculated, n.d. – Not detected.

## PRODUCER GAS COMPOSITION

The H<sub>2</sub>, CO, CH<sub>4</sub>, and CO<sub>2</sub> concentrations in the producer gas obtained at 750, 850, and 950 °C are shown in Table 2. As observed in the composition of the samples, the producer gas from individual gasification of each biomass species had very slight differences in the concentration of measured gases. CO was the main constituent of the combustible gases, with a concentration from 9.3–10.4 vol% at 750 °C, 14.7–15.9 vol% at 850 °C, and 19.9–21.4 vol% at 950 °C. The H<sub>2</sub> concentration varied from 0.7–1.3 vol% at 750 °C, 2.4–2.5 vol% at 850 °C, and 4.0–4.3 vol% at 950 °C. The concentration of CH<sub>4</sub> was 2.5–3.1 vol% at 750 °C, 3.4–3.9 vol% at 850 °C, and 4.1–5.2 vol% at 950 °C. The CO<sub>2</sub> concentration varied from 1.9–7.5 vol%. The similarities in the composition of the producer gas for all three wood species were due to the similarities in their elemental composition and other properties (moisture, fixed carbon, ash content, heating values).

*Table 2. Producer gas composition from the gasification of spruce, alder, and pine*

Biomass	Gas concentration [vol%]	Temperature [°C]		
		750	850	950
Spruce	H <sub>2</sub>	1.3	2.5	4.3
	CO	10.4	14.7	19.9
	CH <sub>4</sub>	2.7	3.4	4.1
	CO <sub>2</sub>	3.7	3.0	2.8
Alder	H <sub>2</sub>	1.4	2.4	4.0
	CO	9.7	15.4	20.2
	CH <sub>4</sub>	3.1	3.8	4.7
	CO <sub>2</sub>	3.3	3.2	1.9
Pine	H <sub>2</sub>	0.7	2.4	4.0
	CO	9.3	15.9	21.4
	CH <sub>4</sub>	2.5	3.9	5.2
	CO <sub>2</sub>	5.8	5.3	3.9

The results obtained at 950 °C had the highest concentration of combustible gases (H<sub>2</sub>, CO, CH<sub>4</sub>, and CO<sub>2</sub>) and were compared to the results of other studies on gasification of WB and other biomass in an air atmosphere at temperatures from 700 to 1100 °C. These studies used WB [17,18], pine pellets [19,20], pine sawdust [20], woodchips [21] and rice husks [22] as feedstocks. The comparison of the average composition is shown in Figure 1. It can be observed that CO is the main combustible gas in all cases, with concentrations ranging from 9–35 vol%. The combustible gases concentrations from this work are comparable and within the same range as results obtained in other works [17–19,21,23–25]. The H<sub>2</sub> from the current study had a concentration from 4.0 to 4.3 vol%, similar to the results of Joka et al., Inayat et al., and Poskrobo et al. [18–20].

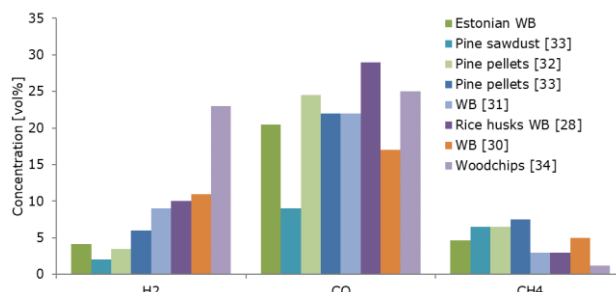


Figure 1. Comparison of the producer gas composition of Estonian WB with other studies found in the literature

## EFFECT OF TEMPERATURE

The effect of the gasification temperature on the main combustible gases (H<sub>2</sub>, CO, and CH<sub>4</sub>) and CO<sub>2</sub> in the producer gas is shown in Table 2. The concentrations of H<sub>2</sub>, CO, and CH<sub>4</sub> clearly increased as the gasification temperature increased from 750 to 850 and 950 °C. The CO<sub>2</sub> concentration decreased as the temperature increased. At 950 °C, H<sub>2</sub>, CO, and CH<sub>4</sub> increased 3.6, 2.1, and 1.7-fold, respectively, compared to those in gasification at 750 °C. This behavior agrees with gasification experiments conducted by Almeida et al. [26] at 700–950 °C who observed that up to 850 °C, the H<sub>2</sub>, and CO concentration increased, CH<sub>4</sub> slightly raised, and CO<sub>2</sub> decreased. The present results also agree with the gasification of palm fiber by Halim et al. [27] at 650–900 °C, where the concentration of H<sub>2</sub> significantly increased with temperature, CO increased, but CH<sub>4</sub> decreased. Results by Yahaya et al. [28] also agree with the current results, in which the gasification showed a drastic increase in the CO and H<sub>2</sub> when increasing the temperature from 700 to 900 °C. The yield of gas species also depended on the chemical reactions, that occur in the reduction zone during gasification. The main gasification reactions analyzed are indicated below.

(R <sub>1</sub> )	Methane formation	C + 2H <sub>2</sub> → CH <sub>4</sub>	(-75.0 kJ/mol)
(R <sub>2</sub> )	Boudouard	C + CO <sub>2</sub> ↔ 2CO	(+172.0 kJ/mol)
(R <sub>3</sub> )	Water-gas	C + H <sub>2</sub> O → CO + H <sub>2</sub>	(+131.0 kJ/mol)
(R <sub>4</sub> )	Water-gas shift	CO + H <sub>2</sub> O ↔ CO <sub>2</sub> + H <sub>2</sub>	(-41.0 kJ/mol)
(R <sub>5</sub> )	CH <sub>4</sub> dry reforming	CH <sub>4</sub> + CO <sub>2</sub> ↔ 2CO + 2H <sub>2</sub>	(+247.0 kJ/mol)
(R <sub>6</sub> )	CH <sub>4</sub> steam reforming	CH <sub>4</sub> + H <sub>2</sub> O ↔ CO + 3H <sub>2</sub>	(+206.0 kJ/mol)

The gasification process improved at temperatures 850 and 950°C, resulting in an overall increase in H<sub>2</sub>, CO, and CH<sub>4</sub> concentrations. The concentrations of gases increased at higher temperatures as the products of endothermic reactions (R<sub>2</sub>, R<sub>3</sub>, R<sub>5</sub>, and R<sub>6</sub>) were favored, and the reactants of the exothermic reactions (R<sub>1</sub>, R<sub>4</sub>) were favored, according to Le Chatelier's principle [29]. The higher yield of combustible gases was due to an increase in the rate of all reactions, especially R<sub>1</sub>-R<sub>4</sub>, and due to a more complete thermal cracking at higher temperatures. The water-gas reactions (R<sub>3</sub> and R<sub>4</sub>), the Boudouard (R<sub>2</sub>), and the steam reforming reactions (R<sub>6</sub>) played an essential role at temperatures above 850 °C, producing higher yields of CO and H<sub>2</sub>.

## 4. CONCLUSIONS

- The present work studied the effect of temperature in the composition of the producer gas (H<sub>2</sub>, CO, CH<sub>4</sub>, and CO<sub>2</sub>) from the gasification of Estonian woody biomass (WB). The obtained results demonstrate that Estonian WB resources are suitable for gasification, as the producer gas has a composition comparable to results obtained by other studies.
- There were no significant differences in the composition and properties of the studied WB samples. Besides, the producer gas obtained from each woody species had a comparable concentration of combustible gases, which demonstrates the potential of using mixtures and residues of these local wood species to produce high-quality producer gas through gasification. The results of the producer gas composition agreed with the results from other studies.
- The gasification temperature significantly affected the composition of producer gas. Higher temperatures, such as 850 and 950 °C, resulted in gas with higher concentrations of H<sub>2</sub>, CO, and CH<sub>4</sub>, while CO<sub>2</sub> content decreased. The optimal temperature for obtaining the highest concentration of combustible gases was 950 °C.

## ACKNOWLEDGMENTS

This work was supported by the European Regional Development Fund and the Estonian Research Council Grant (PSG266).

## REFERENCES

- [1] Republic of Estonia Ministry of Economic Affairs and Communications, National Development Plan of the Energy Sector until 2030, (2017).
- [2] Statistics Estonia, Eesti Statistika Kvartalikiri. 2/18. Quarterly Bulletin of Statistics Estonia - Statistics Estonia, (2018).
- [3] International Renewable Energy Agency, National Renewable Energy Action Plan (NREAP) 2020, 2020.
- [4] W. Lan, G. Chen, X. Zhu, X. Wang, B. Xu, Progress in techniques of biomass conversion into syngas, *J. Energy Inst.* (2015) 151–156.
- [5] V. Strezov, T.J. Evans, Biomass Processing Technologies, CRC Press, Boca Raton, 2014. <https://doi.org/10.1201/b17093>.
- [6] A.A. Ahmad, N.A. Zawawi, F.H. Kasim, A. Inayat, A. Khasri, Assessing the gasification performance of biomass: A review on biomass gasification process conditions, optimization and economic evaluation, *Renew. Sustain. Energy Rev.* 53 (2016) 1333–1347. <https://doi.org/10.1016/j.rser.2015.09.030>.
- [7] M. La Villeta, M. Costa, N. Massarotti, Modelling approaches to biomass gasification-review, *Renew. Sustain. Energy Rev.* (2017) 71–88.
- [8] M. Sulg, A. Konist, O. Järvik, Characterization of different wood species as potential feedstocks for gasification, *Agron. Res.* 19 (2021) 2021. <https://doi.org/10.15159/AR.21.005>.
- [9] M.F. Demirbas, Characterization of bio-oils from spruce wood (*Picea orientalis* L.) via pyrolysis, *Energy Sources, Part A Recover. Util. Environ. Eff.* 32 (2010) 909–916. <https://doi.org/10.1080/15567030903059970>.
- [10] C. Branca, C. Di Blasi, A. Galgano, M. Broström, Effects of the torrefaction conditions on the fixed-bed pyrolysis of Norway spruce, *Energy and Fuels.* 28 (2014) 5882–5891. <https://doi.org/10.1021/ef501395b>.
- [11] J. Rath, G. Staudinger, Cracking reactions of tar from pyrolysis of spruce wood, *Fuel.* 80 (2001) 1379–1389. [https://doi.org/10.1016/S0016-2361\(01\)00016-3](https://doi.org/10.1016/S0016-2361(01)00016-3).
- [12] M. Balat, M.F. Demirbas, Bio-oil from pyrolysis of black alder wood, *Energy Sources, Part A Recover. Util. Environ. Eff.* 31 (2009) 1719–1727. <https://doi.org/10.1080/15567030802459685>.
- [13] B. Formowitz, Pyrolysis behavior of modified grey alder wood samples by TG-MS and TGA techniques, in: 18th Eur. Biomass Conf. Exhib., 2010: pp. 3–7.
- [14] S. Sutibak, K. Sriprateep, A. Pattiya, Production of Bio-oil from Pine Sawdust by Rapid Pyrolysis in a Fluidized-bed Reactor, *Energy Sources, Part A Recover. Util. Environ. Eff.* 37 (2015) 1440–1446. <https://doi.org/10.1080/15567036.2011.631091>.
- [15] B. Purevsuren, O. Dashzeveg, A. Alyeksandr, N. Janchig, J. Soninkhuu, Pyrolysis of pine wood and characterisation of solid and liquid products, *Mong. J. Chem.* 19 (2018) 24–31. <https://doi.org/10.5564/mjc.v19i45.1086>.
- [16] A. Pistis, C. Tugulu, F. Floris, C. Asquer, E.A. Scano, Fast pyrolysis of pine wood at pre-industrial scale: Yields and products chemicalphysical characterisation, *Eur. Biomass Conf. Exhib. Proc.* 2017 (2017) 1198–1204.
- [17] S. Sethuraman, C. Van Huynh, S.C. Kong, Producer gas composition and NO<sub>x</sub> emissions from a pilot-scale biomass gasification and combustion system using feedstock with controlled nitrogen content, *Energy and Fuels.* 25 (2011) 813–822. <https://doi.org/10.1021/ef101352j>.
- [18] M. Inayat, S.A. Sulaiman, Effect of Blending Ratio on Quality of Producer Gas from Co-Gasification of Wood and Coconut Residual, *MATEC Web Conf.* 225 (2018) 1–6. <https://doi.org/10.1051/matecconf/201822505005>.
- [19] M. Joka, S. Poskrobko, Methane rich gasification of wood pellets, *E3S Web Conf.* 10 (2016) 1–6. <https://doi.org/10.1051/e3sconf/20161000031>.
- [20] S. Poskrobko, D. Król, A. Borsukiewicz Gozdur, Gasification of waste wood biomass, *Drewno.* 59 (2016) 241–248. <https://doi.org/10.12841/wood.1644-3985.C25.21>.
- [21] J. Brynda, S. Skoblia, M. Pohorelý, Z. Beňo, K. Soukup, M. Jeremiáš, J. Moško, B. Zach, L. Trakal, M. Šyc, K. Svoboda, Wood chips gasification in a fixed-bed multi-stage gasifier for decentralized high-efficiency CHP and biochar production: Long-term commercial operation, *Fuel.* 281 (2020) 118637. <https://doi.org/10.1016/j.fuel.2020.118637>.
- [22] A. Chaurasia, Modeling simulation and optimization of downdraft gasifier: Studies on chemical kinetics and operating conditions on the performance of the biomass gasification process, *Energy.* (2016) 1065–1076.
- [23] M.A.A. Mohammed, A. Salmiaton, W.A.K.G. Wan Azlina, M.S. Mohammad Amran, A. Fakhru'L-Razi, Air gasification of empty fruit bunch for hydrogen-rich gas production in a fluidized-bed reactor, *Energy Convers. Manag.* 52 (2011) 1555–1561. <https://doi.org/10.1016/j.enconman.2010.10.023>.
- [24] S. Bhatia, Biomass Gasification, in: *Adv. Renew. Energy Syst.*, Woodhead Publishing India PVT, 2014: pp. 474–490. <https://doi.org/10.1016/b978-1-78242-269-3.5.0018-8>.
- [25] F. Huang, S. Jin, Investigation of biomass (pine wood) gasification: Experiments and Aspen Plus simulation, *Energy Sci. Eng.* 7 (2019) 1178–1187. <https://doi.org/10.1002/ese3.338>.
- [26] A. Almeida, P. Neto, I. Pereira, A. Ribeiro, R. Pilão, Effect of temperature on the gasification of olive bagasse particles, *J. Energy Inst.* 92 (2019) 153–160. <https://doi.org/10.1016/j.joei.2017.10.012>.
- [27] N.H.A. Halim, S. Saleh, N.A.F.A. Samad, Effect of gasification temperature on synthesis gas production and gasification performance for raw and torrefied palm mesocarp fibre, *ASEAN J. Chem. Eng.* 19 (2019) 120–129. <https://doi.org/10.22146/ajche.51873>.
- [28] A.Z. Yahaya, M.R. Somalu, A. Muchtar, S.A. Sulaiman, W.R. Wan Daud, Effect of particle size and temperature on gasification performance of coconut and palm kernel shells in downdraft fixed-bed reactor, *Energy.* 175 (2019) 931–940. <https://doi.org/10.1016/j.energy.2019.03.138>.
- [29] B. Lau Sze Yii, W. Muhammad Syafiq Wan Ismail, F. Nasuha Yahya, R. Abdul Rasid, The Effect of Operating Temperature and Equivalence Ratio in an Entrained Flow Gasification of EFB, *Mater. Today Proc.* 19 (2019) 1373–1381. <https://doi.org/10.1016/j.matpr.2019.11.155>.



# THE INCREASING IMPORTANCE OF SMART HOME APPLICATIONS AS A MAJOR TREND FOR THE FUTURE VALUE CREATION OF GERMAN ENERGY COMPANIES

Andreas Ensinger

Ueberlandzentrale Woerth/I.-Altheim Netz AG, Landshut, Germany, Andreas.Ensinger@web.de, ORCID: 0000-0003-3965-0935

Max-Robert Salzer

Aalen University, Aalen, Germany, Max-Robert.Salzer@hs-aalen.de, ORCID: 0000-0002-8140-4749

*Cite this paper as:* Ensinger, A., Salzer, M.R. *The increasing importance of smart home applications as a major trend for the future value creation of German energy companies. 9<sup>th</sup> Eur. Conf. Ren. Energy Sys. 21-23 April 2021, Istanbul, Turkey*

**Abstract:** The aim of this study is to analyze the added value of smart home applications for customer loyalty of energy companies and electricity customers. In particular, this study will define smart home-applications and the intelligent control and integration of PV systems. Above all, the avoiding of peak loads will play an increasingly important role in the energy grids of the future. The research methodology investigates the factors that lead to increased customer loyalty through value-added services. As a result of this research, it was found that value-added services can offer increased customer loyalty to the energy company. Smart home-based services are highly relevant in a rapidly growing target market. However, there will only be a broad acceptance of these smart home-applications for load control if the user is offered added value, for example by load-variable electricity tariffs. Energy companies that want to position themselves as digital service providers in the future need to enable smart home-based services, such as intelligent load control, load-dependent tariff models, that enable the user to have financial added value.

**Keywords:** Digitization, Germany, Renewables, Smart home, Smartgrid

© 2021 Published by ECRES

## 1. INTRODUCTION

Under the supervision of Dr. Karlheinz Bozem from bozem | consulting associates | munich and Prof. Dr. Anna Nagl, Director of the Competence Center for Innovative Business Models, Aalen University, the future importance of smart home applications as an important trend for the future value creation of German energy companies has been examined. Why are smart home applications necessary and how do they affect customer loyalty? These research questions were pursued in cooperation with the consulting firm of the energy expert Karlheinz Bozem, who supports the research projects with expertise in both the renewable energy and the competitive strategy.

In the evolution of Germany's energy industry, which has lasted well over 100 years now, production has always been adapted to consumption. The demand for electricity in the individual grid levels could be predicted precisely enough, so that the demand could be met by a large number of power plants, which provided the electricity in sufficient quantities at any time. [1] The use of different energy sources has enabled dependencies to be identified. The use of mostly fossil fuels led to significantly different electricity production costs, which, in turn, had an impact on the operating time of these power plants. At the same time, however, this energy mix guaranteed a high level of security of supply. This power plant deployment planning is called Merit Order Effect. The model describes the power plant deployment planning on the basis of the variable costs in the energy industry. The aim of this model is purely the most economically sensible power plant deployment planning. The cheapest type of electricity generation is intended to provide the most energy, thereby making energy production as cost-effective as possible. Other factors, such as ecological or social ones, are not considered in this model. [2] The power plants are sorted according

to their variable costs in ascending order. The power plants with the lowest variable costs are called up first, then, the ones with the second lowest variable costs, and so on. The following Figure 1 shows the Merit Order Effect.

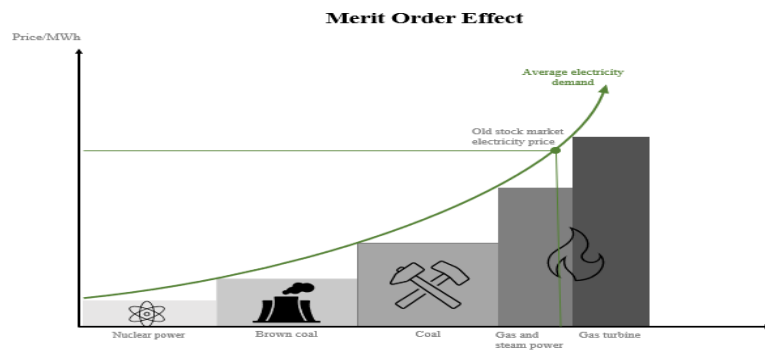


Figure 1 Merit Order Effect

The great advantage of this system is the high level of resilience, which cannot be guaranteed by producing purely on volatile energy sources. If the balance between supply and demand of electricity was disturbed due to a surprising unplanned event, this imbalance could always be compensated by activating sufficient control power.

However, this system, which has been in place for decades, has now become unbalanced. The share of electrical energy generated in Germany by the use of renewable, volatile energy sources is steadily increasing. Due to the necessary decarbonisation, as well as the resulting shift away from fossil fuels in energy production, this development will gain momentum in the future. In order to be able to ensure the energy supply with renewable energy plants in the future, significant construction of renewable energies plants is required. In order to be able to absorb this electrical energy, the grids have to be expanded and part of the infrastructure has to be extensively modernized, so in addition to the investments in renewable energies, there is a requirement for investments in the distribution networks. [3]

Despite the need to build up production output, the volatility of production will make it no longer possible to fully adjust production to consumption. However, since there must be no imbalance between production and consumption, the result would be a deviation of the network frequency, which can lead to a blackout event. [4] In this case, there are only two solutions.

On the one hand, there is the basic possibility to store surplus energy and to make it available in load-intensive times, on the other hand, consumption can be made more flexible and adapted to production. Since sufficient storage capacities will not be available throughout Germany for the foreseeable future, there is an increasing need for a more flexible load in customer plants, which would also reduce the network expansion requirements and save costs economically.

While in industrial plants it has long been common practice to monitor the demand for services wherever possible and to control them over time, there is no need or technical possibility to control the load for household customers, except for manual interventions. The smart home applications, as they are already available on the market, are mainly systems that serve to increase comfort, whereas the load control in the home is not the focus. In addition to influencing performance requirements, innovative smart home applications can strengthen customer loyalty to the energy company, enabling energy companies to tap into new parts of the value chain. As a classic commodity product, electricity essentially only offers the differentiating feature of the electricity price level. These intelligent business models in conjunction with smart home applications could create a real differentiation opportunity, which would also significantly increase customer loyalty.

## 2. STATE OF THE ART

As already pointed out at the beginning, there will be an increasing need to intelligently manage the burdens of household customers and thereby bring consumption behaviour into line with production, especially as the demand for electricity among traditional household customers will increase sharply in the coming years. As expected, heat and mobility applications are particularly crucial for this. Around two-thirds of the energy needed in a private home is used to generate heat. Heat pumps offer a great potential for CO<sub>2</sub> savings, which is why their distribution will continue to increase in the future. In order to be able to estimate the added value of smart home applications in conjunction with a PV system and heat or mobility applications, it is first of all necessary to determine the average energy consumption of a heat pump. In order to be able to quantify this average electricity requirement of a heat

pump in a medium-sized energy company, consumption data from 179 heat pumps of different sizes were evaluated. The data source was the anonymised billing data of the “Überlandzentrale Wörth/I-Altheim Netz AG”, a regional energy company. The analysis of the data provided showed that in 2019 1,121,730 kWh of electrical energy was taken from these 179 consumption points. The consumption distribution can be taken from Figure 2 Heat Pump evaluation Database. The average consumption in 2019 was 6,266.6 kWh.

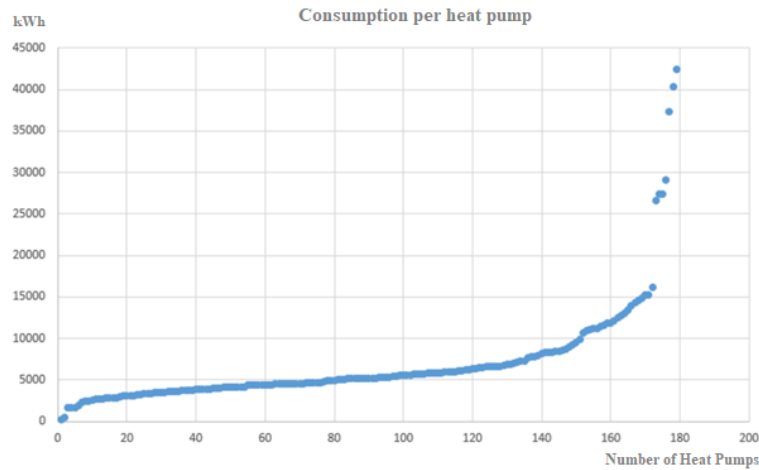


Figure 2 Heat Pump evaluation Database

For 2018 and 2017, an identical evaluation was carried out with the same customer group, so that the different lengths of heating periods could be taken into account. In 2018, the average consumption was 5,248.2 kWh, in 2017 5,787.7 kWh. The three-year average was 5,757.5 kWh.

The second trend mentioned in the energy sector is the use of electrical energy for mobility applications, which will also lead to an increase in electricity demand. Here, too, the expected additional demand was determined. With an average annual mileage of 13,727 km [5], the additional consumption per electric car is 2,289 kWh. By way of comparison, according to an evaluation by the statistics portal Statista, a two-person household without electric hot water heating required an average of 2,100 kWh of electrical energy in 2019. This electricity requirement will thus more than double if a car, belonging to the household is exchanged for an electric car. [6] If the heat demand is additionally covered by a heat pump, the electricity requirement would more than quadruple which underlines the need for intelligent smart home applications for load control in the customer's system and thus to relieve the burden on the network infrastructure. A study by the Karlsruhe Institute of Technology (KIT), which was presented at the edna conference of the Federal Association of Energy Market & Communication e.V. on 21 November 2019, found that even with a market penetration of 15% in 2030, the additional amount of energy required by electromobility for the distribution networks is not a problem. [7] However, the additional performance can become a challenge for the distribution networks, especially in the case of uncontrolled loading. [8] This was also recognized on the part of the standardisation bodies. In order to meet this challenge, standard VDE-AR-N 4100 stipulated that charging devices with a power between 4.6 kW and 11 kW must be registered with the network operator, whereas charging devices with a power >11 kW require the approval of the network operator. Without smart home systems that are able to flexibly regulate the charging processes in the customer system, this normative regulation will miss its target. For electricity supply customers, flexibility in their electrical system should not be associated with a loss of comfort. The original purpose of the smart home application is to increase the comfort of customers. If burdens are shifted over time, this must offer added value to the user, otherwise the customer will not accept such a smart home application. If the necessary added value can be achieved, this will also strengthen customer loyalty.

Due to the lack of communication technology, the electrotechnical measuring devices installed up to now do not support intelligent load control. It is true that the Federal Office for Security in Information Technology (BSI) has now issued the market declaration in accordance with Section 30 of the Measuring Point Operations Act on 24 February 2020, [9] and thus the basic possibility has been created to install intelligent measuring systems, which can be integrated communicatively, with household customers. These offer the possibility to record and transfer consumption, delivery and load flows to and from the network, which is a necessary basis for the smart home application. However, as these systems are still too expensive and not yet available to the mass market, they have not yet facilitated any control interference in the customer system.

The need to manage loads more flexibly will create an important market for energy companies in the future. With this context, incentives must be created for the customer to avoid peak loads during peak periods and to shift the demand for power in times of low load.

One provider that offers a feasible solution for such a load-variable pricing is the company Tibber Deutschland GmbH, [10] in the form of a flexible electricity tariff in conjunction with an intelligent measuring system. Tibber's load variable electricity tariff is based on stock market prices, which at a certain point reflecting the relationship between electricity supply and demand. In times of electricity shortages, the price of electricity can be up to four times the average price, whereas in times of low load, the customer benefits from extremely low prices. The customer only pays the purchase price of the electrical energy plus a monthly basic amount. However, if a customer wants to make use of the benefit of this tariff model, they are dependent on a controllable, flexible infrastructure in the customer's system, precisely the already mentioned smart home applications. Tibber offers value-added services around the topic of electricity in order to cover the costs of business operations and generate profit. In this way, a much greater customer loyalty can be achieved than would be possible with the pure supply of electricity.

For several years now, more and more new companies have been pushing into the market for smart home applications. One of the most popular examples of a smart home device is probably Amazon's Alexa, which enables simple control tasks such as music playback, lighting controls, online services, etc. Until now, these smart home applications have only added value through increased comfort, although load control is possible, too, which is however, currently not the prioritized purpose. For this reason, the interaction of different smart home components had to be tested in a pilot application.

### **3. APPROACH**

Prior to practical implementations in the pilot application, a market analysis of the available load variable tariffs was carried out, i.e., which additional components are required, how they need to be installed and what control options exist. The scope of the pilot plant had to be determined and a suitable pilot user had to be found.

An essential criterion for customer benefit lies in the customer-friendly setup: especially for less IT-savvy users, a "plug and play" solution is necessary.

Different expansion stages were planned for the pilot application. The pilot plant was built in the self-occupied residence of an electrician who is familiar with up-to-date control systems due to his professional background. The converted residential building is heated by means of a heat pump with an additional heating rod and suitable arrangements were made for a later PV installation.

### **4. PILOT APPLICATION**

As a first step, the basic functions were implemented in the smart home system, so that the heating control as well as the control of the lighting and the shading were carried out from the very beginning by the smart home user-oriented system. Access control was one of the first building blocks, a sensor bar, which is firmly installed in the masonry near the access door, detects the smartphone of the user and the authorized persons and the front door is automatically unlocked. These first functions were only used to increase comfort. This would not allow for a shift in load or increased customer loyalty.

The subsequent expansion of the smart home system enabled the first efficiency improvements and load shifts to be realized. For example, a 10 kWp PV system and a 3.15 kWh storage system were installed, which made it possible to shift part of the load, for example that of the heat source, into the low load time.

In the last expansion stage, the performance of the PV system was increased to 15.28 kWp and the storage capacity doubled to 6.3 kWh. The purchase of intelligent household appliances, an air conditioning system coupled to the smart home system, as well as an electric vehicle with a communication-capable charging infrastructure have created great potential for load shifting. The multimedia system has also been fully integrated into the smart home system, which significantly increases the control comfort due to the possibility of voice control. Figure 3 shows the schematic structure.

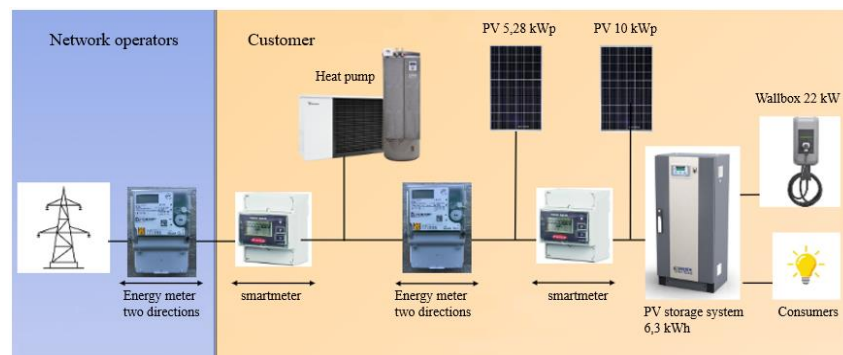


Figure 3 Schematic structure of the pilot plant installation

The controller provides for the following prioritization for the use of the self-generated electrical energy:

- 1.) Dishwasher, washing machine and dryer
- 2.) Water heating
- 3.) Storage of overproduction in the storage system
- 4.) Passive cooling by means of shading
- 5.) If this is not sufficient, active cooling via air conditioning
- 6.) Charging of the electric vehicle

Smart home applications have achieved a degree of self-sufficiency of around 60 % despite mobility and heat applications, with 7,500 kWh of the 10,000 kWh produced annually, which corresponds to a self-consumption rate of 75 %. In order to increase the economic efficiency, the regional energy company offered a power to heat electricity tariff, which enables the use of the self-generated energy for household electricity demand and heat generation thanks to the special measurement concept. In accordance with § 14a of the EnWG (Energy Economics Act), a reduced grid charge and thus a lower electricity price are offered for the electricity used for heat generation. Unfortunately, during the pilot project, it turned out that the installed smart home components are not interoperable. The individual system components had to be purchased by different manufacturers and a plug and play solution was not possible. Due to the high effort of system integration, the installation takes a lot time, which is usually to be provided by a specialist company. Even after commissioning, regular adjustments and software updates provide ongoing maintenance. Which are, however, not feasible in this complexity of the smart home solution for laymen at this time.

Despite the huge savings, the high investments in technology, installation, commissioning and maintenance do not enable any economic operation at this stage. The offer of the power to heat tariff model has enabled customer loyalty to be achieved, a load shift in load-free times is possible within the frame, but the limiting factor here is the available storage capacity.

## 5. CONCLUSION

In summary, the implementation of the pilot application shows that the appropriate investment in the smart home infrastructure can enable the shifting of the customer's peak load. In this way, the control of the electric vehicle could be coupled to the generation of the PV system, which significantly reduced the electricity demand in the summer months. It was also possible to operate the heat pump in connection with PV generation, but due to the often missing generation current in the dark months, this measure alone has only little influence on the electricity demand. If a significant reduction in performance is to be achieved, significantly more consumables must be flexibly controlled. In the absence of a load-variable tariff, the controllability in the customer system currently refers exclusively to the needs of the user or to the optimization of the self-consumption rate of the PV system. The grid operation of the smart home components requires control by the energy company.

The use of smart home components in combination with a power to heat electricity tariff, which enables the use of the self-generated electrical energy for both home and heat demand while maintaining the lower heat flow tariff, has significantly increased customer loyalty.

Investments in plant technology are taken into account, and no financial added value can be created for the user at present. Although the self-consumption rate and thus the necessary electricity supply from the public grid can be significantly reduced, this is far from sufficient to cover the cost of the investments. In particular, the high installation effort has a negative impact on the business case. If a positive business case is to be created for the user, the smart home components must be standardized, which reduces on the one hand the purchase price and installation

costs, and on the other hand, a load-variable tariff would be required that harnesses the potential for fluctuating electricity procurement costs.

## REFERENCES

- [1] Rath V , Bozem K , Nagl A . 20 Jahre Liberalisierung, Energiewende und Digitalisierung am Strommarkt - Von der vertikalen Wertschöpfungskette zur ‘smarten Plattform’. Energiewirtschaftliche Tagesfragen 2020, pp. 10–13.
- [2] Next Kraftwerke GmbH. Das Merit Order Modell: Eine Theorie mit Fragezeichen. Online available <<https://www.next-kraftwerke.de/wissen/merit-order>>
- [3] Ensinger A . Standortidentischer Neubau einer Ortsnetztrafostation. ew Magazin für Energiewirtschaft. 1/2021. pp. 36-39.
- [4] Gobmaier T . Netzfrequenz als Indikator für die Stabilität des Verbundnetzes. In: IEWT 2017 10. Internationale Energiewirtschaftstagung; 17 February 2017.
- [5] Kraftfahrt Bundesamt – Verkehr in Kilometern. Online available <[https://www.kba.de/DE/Statistik/Kraftverkehr/VerkehrKilometer/pseudo\\_verkehr\\_in\\_kilometern\\_node.html](https://www.kba.de/DE/Statistik/Kraftverkehr/VerkehrKilometer/pseudo_verkehr_in_kilometern_node.html)>
- [6] Statista . Stromverbrauch eines 2-Personen Haushaltes. Online available <https://de.statista.com/statistik/daten/studie/558277/umfrage/stromverbrauch-einen-2-personen-haushalts-in-deutschland/>
- [7] Karlsruher Institut für Technologie (KIT) . Einfluss der Elektromobilität auf die Verteilnetze. In: edna Fachkonferenz 2019; 21 November 2019.
- [8] BDEW Anwendung der repräsentativen VDEW-Lastprofile step-by-step. Online available [https://www.bdew.de/media/documents/2000131\\_Anwendung-repraesentativen\\_Lastprofile-Step-by-step.pdf](https://www.bdew.de/media/documents/2000131_Anwendung-repraesentativen_Lastprofile-Step-by-step.pdf)
- [9] BSI . Allgemeinverfügung zur Feststellung der technischen Möglichkeit zum Einbau intelligenter Messsysteme. Online available [https://www.bsi.bund.de/SharedDocs/Downloads/DE/BSI/SmartMeter/Marktanalysen/Allgemeinverfuegung\\_Feststellung\\_Einbau\\_01\\_2020.pdf?\\_\\_blob=publicationFile&v=4](https://www.bsi.bund.de/SharedDocs/Downloads/DE/BSI/SmartMeter/Marktanalysen/Allgemeinverfuegung_Feststellung_Einbau_01_2020.pdf?__blob=publicationFile&v=4)
- [10] Business Insider . Ökostrom zum Selbstkostenpreis: Das norwegische Startup Tibber greift deutsche Energiekonzerne mit neuen Tarifen an. Online available <https://www.businessinsider.de/wirtschaft/startups/oekostrom-zum-selbstkostenpreis-das-norwegische-startup-tibber-greift-deutsche-energiekonzerne-mit-neuen-tarifen-an/>



# THERMAL ENERGY GRID SIMULATION (TEGSIM) FOR SMART URBAN REGIONS

David Huber

TU Wien, Institute for Energy Systems and Thermodynamics, Vienna, Austria, david.huber@tuwien.ac.at, ORCID: 0000-0001-7164-8275

Viktoria Illyés

TU Wien, Institute for Energy Systems and Thermodynamics, Vienna, Austria, viktoria.illyes@tuwien.ac.at, ORCID: 0000-0002-4030-6958

Veronika Turewicz

Geological Survey of Austria, Hydrogeology and Geothermal Energy, Vienna, Austria, veronika.turewicz@geologie.ac.at, ORCID: 0000-0002-8936-7719

Stefan Hoyer

Geological Survey of Austria, Hydrogeology and Geothermal Energy, Vienna, Austria, stefan.hoyer@geologie.ac.at, ORCID: 0000-0002-3753-1505

Gregor Götzl

Geological Survey of Austria, Hydrogeology and Geothermal Energy, Vienna, Austria, gregor.goetzl@geologie.ac.at, ORCID: 0000-0001-7361-7085

Karl Ponweiser

TU Wien, Institute for Energy Systems and Thermodynamics, Vienna, Austria, karl.ponweiser@tuwien.ac.at, ORCID: 0000-0003-0838-8778

*Huber D, Illyés V, Turewicz V, Hoyer S, Götzl G, Ponweiser K. Thermal energy grid simulation (TEGSim) for smart urban regions. 9<sup>th</sup> Eur. Conf. Ren. Energy Sys. 21-23 April 2021, Istanbul, Turkey*

---

**Abstract:**

Fifth-generation district heating and cooling (5<sup>th</sup> DHC) systems are promising concepts for decarbonizing space heating, cooling and domestic hot water supply. Due to the low exergy approach, these systems are highly efficient. As part of the Smart Anergy Quarter Baden (SANBA) project, the numerical simulation tool *TEGSim* is further developed and used to design an ultra-low-temperature heating and cooling (ULTHC) network with hydraulic and thermal components fitted to the specific regional characteristics of the investigated case. A borehole thermal energy storage (BTES) used as seasonal storage ensures long-term feasibility. The annual discrepancy of input of thermal energy provided by space cooling and output of energy demanded by space heating and hot water is supplied by an external low-grade industrial waste heat source. This paper presents the functionality of the simulation and shows how to interpret some findings concerning all components' design and their interplay, energy consumption and efficiencies.

---

**Keywords:**

5<sup>th</sup> DHC, ULTHC network, LowEx, BTES, numerical simulation

---

© 2021 Published by ECRES

## 1. INTRODUCTION

In Austria, 27 % (305 PJ) of the final energetic consumption was used for space heating (H), cooling (C) and domestic hot water (DHW) supply in 2019, 198 PJ of that in private households alone. About 40 % (79 PJ) of the energy required for H, C and DHW is supplied by fossil fuels and about 36 % (71 PJ) by CO<sub>2</sub> neutral resources. The remaining 24 % (48 PJ) are provided by electricity or district heating [1]. The Federal Ministry of Austria for Agriculture, Regions and Tourism calls transforming this sector drastically the “*starting shot for the end of the*

*fossil age in Austria*" [2]. The Austrian government's ambitious goal is to free H and DHW supply from coal- and oil-based fuels until 2035 and to eliminate fossil gas-based fuels until 2040 [3].

A promising concept for areas that cannot be supplied with long-distance heating from renewable sources is 5<sup>th</sup> DHC [4]. Despite the complexity of such smart systems, their stage of development is not advanced yet. Most sites in operation can be found in Germany and Switzerland e.g. *ETH Hönggerberg*. Currently, the largest ULTHC network in Austria is the *Viertel Zwei Plus*. The dynamic interaction of all network components, such as heat pumps, BTES, and the ULTHC network, is crucial for the technical design [5]. To further encourage development, thereby making 5<sup>th</sup> DHC systems a competitive technology, design and simulation tools are in great demand.

Commercially available software such as *EED* or *FEFLOW* can usually only simulate individual parts of the energy supply system such as the geothermal energy storage. In contrast to commercial software, *TEGSim* simultaneously solves the entire network. A key advantage of *TEGSim* is that it enables holistic process simulation of all relevant components. Compared to other simulation environments, *TEGSim* can be scaled and extended at any level. The developed simulation tool can perform reliable simulations of any district heating and cooling networks of any size with different discretization, parameters and components.

## 2. METHODOLOGY

In the course of the national project SANBA, the ULTHC network simulation tool from Nagler [6] was further developed and programmed using *MATLAB*. The developed thermal and hydraulic simulation program *TEGSim* is a stand-alone tool that does not require external calculation software for the individual components apart the programming language. The network is modelled as a closed-loop two-pipe system with the possibility of bidirectional volume and energy flow. At the energy transfer stations (ETS) prosumers can be provided with energy for H and DHW via heat pump, free cooling (FC) directly from the grid and active cooling (AC) via the reversible heat pump that otherwise supplies heating energy.

The necessary input is the predefined topology of the pipe network as well as the prosumers' heat load curves. If, as in most cases, additional energy is required to balance the system, the load curve of the heat source must be given. *TEGSim* automatically estimates the pipe diameters in a first step. However, they can later iteratively be adjusted by hand, for example, according to technical-economic criteria (price per diameter, installation costs, efficient flow rate). All parts, property data, performance data of heat pumps, hydraulic pumps and many more can be configured. Also, different geometry and operating modes of the BTES can be picked, e.g. 1U- or 2U-probes with diagonal flow, adjoining flow with or without U-crossing. In a first draft, *TEGSim* estimates the dimension of components such as the seasonal and daily storages. If wanted, the storage sizes can be adapted or further defined by the user.

### Thermohydraulic Simulation

The network simulation calculates the thermal and hydraulic operating conditions at given boundary conditions. Due to the energy distribution grid's complexity, a thermohydraulic calculation method was designed to keep the calculation time and data storage capacity as low as possible. Compared to the transient thermal simulation, the network's hydraulic simulation is carried out quasi-stationary. The variables resulting from the iterative hydraulic simulation, such as pressure and mass flow, serve as boundary conditions for the following transient thermal calculation. For the selected simulation time step of one hour the hydraulic quantities are kept constant. In the transient thermal simulation the main task is to calculate all the temperatures in the network and the BTES. The time step for the thermal simulation is set to 30 minutes per default. After the thermal calculation has been completed, new boundary conditions are set for the hydraulic simulation.

The program was designed to simulate the yearly behavior and to show the long-term suitability of the proposed concept. In order to obtain reliable simulation results, it is necessary to consider the full range of time-dependent load profiles and boundary conditions.

### BTES and Pipe Network

To model the thermal behaviour of the BTES, multiple 2D thermal resistance and capacity models (RCMs) for CX-, 1U- and 2U-probes according to [7] were used. Figure 1 (a) shows the 2D RCM for a 2U-probe. The thermal conductivity and capacity of each of the different layers and materials of the probe are taken into account. Inside the pipes, the heat transfer coefficients are calculated according to the flow regime and the properties of the heat transfer medium, which is assumed incompressible. The calculation of thermal resistances is realized partly with empirical approaches from [7] and using the 1<sup>st</sup> order multipole method from Claesson and Javed, [8, 9]. The

surrounding ground is modelled axially symmetrically and coupled to the borehole wall using thermal resistances and capacities. In the surrounding ground, energy transfer is only possible by conduction but not by convection. By linking the nodes in the vertical direction with transport equations (heat conduction for solid components and heat conduction and convection for the fluid in the pipes), a two-and-a-half-dimensional model of the probe and the surrounding ground is obtained. The thermal model is fully transient by using the implicit formulations of the 1<sup>st</sup> order forward differences in time and the 1<sup>st</sup> order upwind scheme in space. Axial and radial discretization has been evaluated and optimized according to calculation time and accuracy, see [10]. The reciprocal influence of the quadratic probe field is taken into account by a global process with Kelvin's line source theory's help. Thus, the temperature at the lateral boundary layer of the simulated probes is adjusted every 24 hours. The pipe network's thermal behaviour is calculated similarly to the BTES using a horizontal 1U-probe RCM; see Figure 1 (b). Dirichlet boundary conditions for the BTES and the pipe network are considered, taking the geothermal temperature gradient into account. In the near-surface area, down to a depth of 15 m, the temperatures at the lateral boundaries are determined by solving the one-dimensional heat transfer equation and typical ground temperatures from a test reference year.

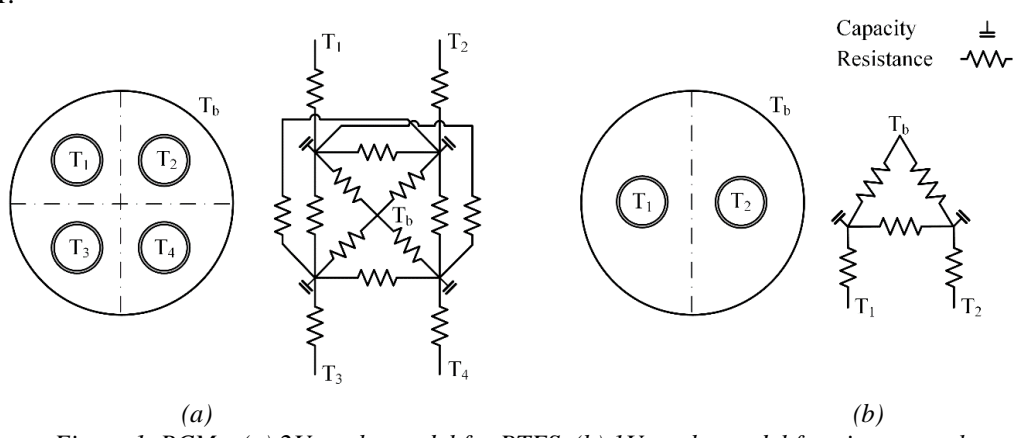


Figure 1. RCMs: (a) 2U-probe model for BTES, (b) 1U-probe model for pipe network

The equations from the BTES, the pipe network and the boundary conditions are formulated as a linear equation system in one matrix that is solved every time step. Therefore, all the BTES and pipe network temperatures of all nodes are known for every simulation time step.

## Validation of the BTES model

In order to verify the reliability of the simulation results of *TEGSim*, the programmed BTES model was validated by using the already well-established software *FEFLOW*. The finite element program is able to simulate heat transport processes in the underground and model geothermal heating systems [11].

For this purpose, numerical simulations were performed with *TEGSim* and *FEFLOW* using identical and simplified initial and boundary conditions. A homogenous subsurface model with a depth-averaged effective thermal conductivity of 1.75 W/m/K and a constant ground temperature of 15 °C were chosen. Furthermore, the same simplified input data, massflow of the fluid and the feed temperature into the BTES, were used.

Throughout the validation process, the resulting outlet temperatures of the BTES were compared for each time step. The values of the thermal resistances of the *FEFLOW* model were adjusted in such a way that a mean annual deviation of less than 0.65 % was achieved. Larger deviations can only be observed when input values change abruptly. The highest resulting local deviations are between 10 and 40 %, but they decrease again to less than 1 % after only a few minutes. A possible reason is the different time discretization for solving the systems of both models. *TEGSim* uses constant time intervals of one hour, whereas *FEFLOW* uses an automatic time-step control scheme which is a *Predictor-corrector* scheme, [12]. Nevertheless, the small overall deviations show a good correspondence of the simulation results and thus the validation's success.

## Energy Transfer Stations

The ETS connect the prosumers to the ULTHC network. Depending on the consumers, their tasks are:

- supply of hot/cold water for floor heating/cooling or radiator heating/cooling
  - supply of hot water for DHW
  - supply of cold water for FC or AC

Furthermore, these components are located in the ETS: valves, circulation pumps, short term water storages and heat exchangers. Since not all prosumers have the same requirements in delivering energy for DHW, H and C, different types of ETS are generally necessary. They all consist of the same kind of components except for different numbers of heat pumps with different sizes and storage sizes. Latter are of the same size class to enable buying them off-the-shelf and to ensure economic feasibility.

The ETS modelling, especially the modelling of grid pumps, heat exchangers, and water storages, was kept simple to reduce complexity and, therefore reduce calculation time. A more detailed model would only affect the simulation results to a minor degree. For example, the water storages are modelled with two temperature levels, a one-dimensional thermocline and a charging level. Evaluating the results, it was found that the storages are frequently charged and discharged and idle charging cycle times are in the range of a few hours what justifies the simple model.

The temperature dependence of the coefficient of performance (COP) values of the heat pumps was taken into account using COP values specified by the manufacturer for two temperature levels (e.g. 35 °C for H and 63 °C for DHW). However, it has been shown that the assumed source temperature for the prosumers (e.g. 15°C) varies only slightly. A more detailed calculation of the COP values requires more computing time, while the influence on results is negligible. Each of the ETS has several circulation pumps depending on its configuration. The pumps are controlled so that a user-defined temperature difference of e.g. 4 K at the heat exchangers can always be ensured.

### 3. USE CASE: THE PROJECT SANBA

In the national project SANBA, a ULTHC grid is investigated to be applied at the former military base *Martinek-Kaserne* using the *TEGSim* program. This real estate with an area of 40 hectares in the city of Baden south of Vienna was abandoned in 2014. The consortium developed different urban mix-use scenarios, including residential houses, an education campus, office buildings, an area for dining, shops, a supermarket and event halls, [13].

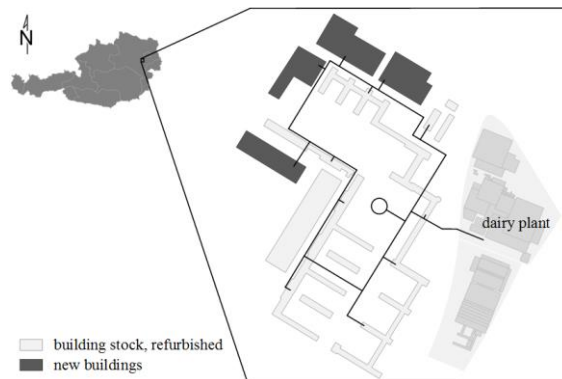


Figure 2. Area of interest in SANBA - scenario MIDI: ground view of buildings, grid network and BTES

In this publication, the use of *TEGSim* based on one of the investigated DHC development scenarios - the so called MIDI scenario, which was estimated to very likely be realized are discussed. The findings of this scenario show the methods and results obtained by *TEGSim*. Figure 2 shows the scenario MIDI from the project SANBA. The black lines represent the annular thermal energy grid itself. The circle represents the location of the BTES. In total, 4458 m of supply and return pipes (3031 m ring line, 1427 m branch line) are considered for the ULTHC network. Due to the high pipe volume of 157 m<sup>3</sup> and moderate minimum temperatures inside the network way above 0°C, water is used as the heat transfer medium. In this scenario, a majority of the existing buildings with 65 590 m<sup>2</sup> gross floor area will be renovated. Besides that, apartments, a school and a supermarket with a total gross floor area of 94 000 m<sup>2</sup> are considered. Overall, there are twelve ETS and more than 30 heat pumps at a cumulative peak load of more than 4.4 MW<sub>th</sub>.

#### Energy Demand

A distinction is made between electrical and thermal energy demand. The thermal energy demand is subdivided according to the use: DHW, H and C. These fluctuating energy demands serve as input for *TEGSim* and can basically be created with any building simulation programme. In this case, the software *EDSL Tas* was used. The thermal energy demand for H is 6224 MWh<sub>th</sub>/a, for DHW it is 1843 MWh<sub>th</sub>/a and for C it is -2814 MWh<sub>th</sub>/a. In contrast to energy for H, energy for C must be provided much faster to achieve the necessary living comfort and

prevent overheating on hot summer days. Therefore, the maximum cooling power is approximately the same as the maximum power needed for H and DHW. Contrary to the other thermal energy demands, energy for C has to be supplied by charging the seasonal storage.

The electricity demand is subdivided into two parts. On the one hand, the electricity demand for users and residents of the buildings was calculated using standard load profiles according to [14] at 9.44 GWh<sub>el</sub>/a. On the other hand, the electricity demand for the operation of the ULTHC network (circulation pumps and heat pumps) results from the simulation of the holistic system. The electricity demand of the circulation pumps is linearly interpolated based on five operating points of the pump maps. The database is made up of discrete operating states of different Grundfos pumps. Based on the maximum pump head and the volume flow, the simulation determines the electrical power demand for each point in time.

## **4. RESULTS AND DISCUSSION**

### **System design and heat input**

For a seasonally balanced system, a couple of parameters play an important role. The most critical parameters are the size of the BTES field, which means the number of probes, and the waste heat supplied from the dairy plant. Optimizing these two values for a balanced BTES is always possible. Finally, it is crucial for energy efficiency to keep temperatures low in summer in order to ensure FC instead of AC via a heat pump. FC is only possible up to 18 °C supply temperature of the heat exchangers. The highest return temperature for FC is set to 23 °C, considering the plate heat exchangers' pinch point between the cooling surfaces in the buildings and the ULTHC network.

After determining the minimal probe number, a parameter study was performed to find the adjustable input parameters' optimal values. In this scenario, 349 probes with a depth of 180 m are required in the probe field. In total, only a fraction of the low-grade waste heat potential is required. In order to enable as much FC as possible in summer, the feed-in of the low-grade waste heat source is significantly reduced during the cooling season. The temperature level of the heat supply fluctuates according to the season between 20 and 40 °C. The lower temperature limit of the fluid in the pipes is set to 1 °C to prevent freezing in the water-filled pipes and the surrounding soil.

### **Dynamic Behavior**

Since the simulation calculates temperatures, pressures and velocities at every node of the grid, much information can be found in the trends apart from highest and lowest values.

For example, Figure 3 (a) shows the feed temperature into the BTES in red and the outlet temperature in black for one year. From hour 1 to 1400 it can be seen that the outlet temperature is higher than the feed temperature which means discharging during winter. The opposite is true in summer when the BTES is charged.

The BTES is charged a few times during the heating (discharging) period at hour 750, 1400, 7200 and 7800, as shown in a positive sign of the massflow in Figure 3 (b). The changing sign of the massflow is due to the complex interplay of low heat demands and high amounts of energy fed into the system by the supplier. The transitional season in spring and autumn is marked by frequent changes in charging/discharging and varying feed temperatures. The highest massflows are needed in summer when cooling demand and grid temperatures are high.

The aggregated energy of the BTES shows a smooth trend near the ideal sinus curve, see Figure 3 (c). The BTES can only be used as seasonal thermal energy storage over a long period if the same amount of energy is discharged during the heating season as is charged during the cooling season which is met well in the use case.

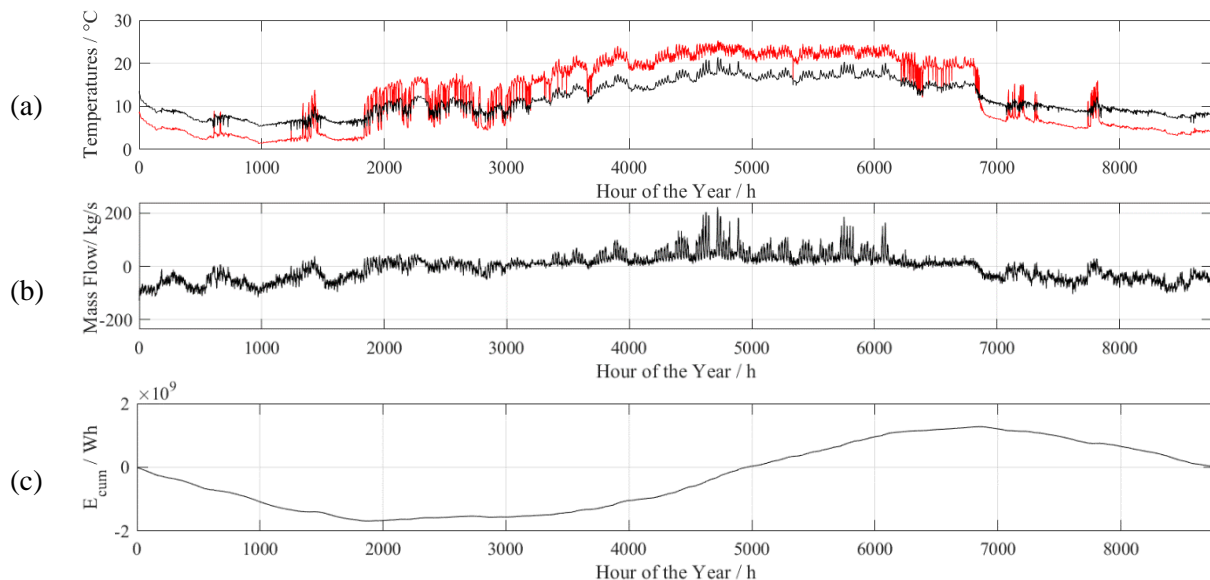


Figure 3. Annual performance of the BTES: (a) feed (red) and outlet (black) temperature, (b) massflow, (c) aggregated energy

### Energy Flows

With the help of *TEGSim*, it is possible to make detailed statements about the energy flows occurring in the investigated system. Together with other parameters, such as configuration and number of ETS, network topology, size of the BTES and waste heat costs, these results enable an economic evaluation of the investigated energy supply system.

Figure 4 shows the yearly thermal and electrical energy flows to operate the case-specific ULTHC network. Around 2796 MWh<sub>th</sub>/a is supplied to the grid by the waste heat producer. 8066 MWh<sub>th</sub>/a are supplied in terms of H and DHW. The thermal energy demand for H and DHW is more than twice the amount of the C demand. This ratio reflects the mixed-use of the investigated area well. The electricity required to operate the case-specific ULTHC comes down to 2508 MWh<sub>el</sub>/a representing 22.5 % of total energy demand. About 3030 MWh<sub>th</sub>/a, which is a share of 27 % of the total 11154 MWh/a, is charged and discharged within the BTES in a yearly cycle. The BTES is not entirely balanced to zero. It is charged more than it is discharged by 6 MWh<sub>th</sub>/a.

Furthermore, it is possible to discuss the calculated heat losses and reduce them by varying pipe parameters, such as the material, diameter, or insulation. Due to the short residual times of the water in the case-specific pipe network, the thermal losses are shallow and about 52 MWh<sub>th</sub>/a, representing a share of 0.5 % of total energy.

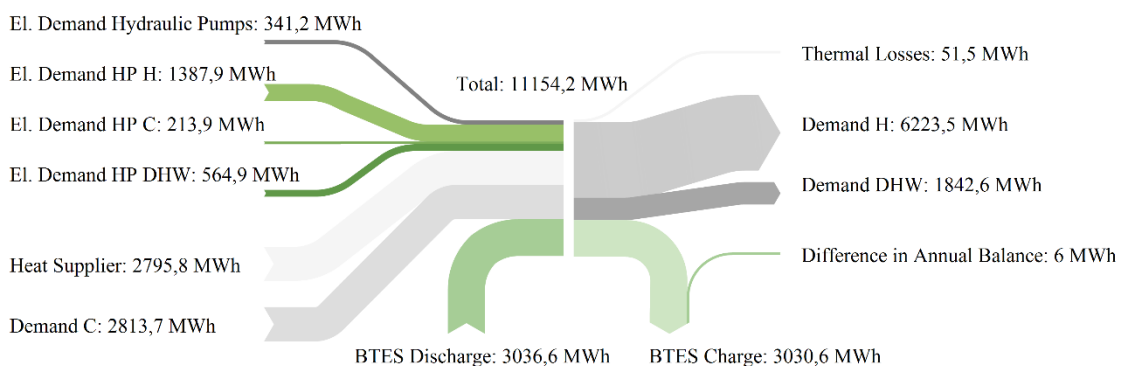


Figure 4. Sankey diagram: yearly energy flows to operate the ULTHC grid

### 5. CONCLUSION

The MATLAB simulation tool *TEGSim* is able to give detailed information about specific use cases of ultra-low-temperature heating and cooling networks. In contrast to other available software, all crucial thermal and hydraulic components of the grid as the BTES field, heat distribution grid and consumer/prosumer energy transfer stations are modelled and calculated simultaneously.

Another factor is the partly holistic approach on components' design. The most crucial model of the simulation, the one of the BTES, was validated with *FEFLOW*. The results of *TEGSim*, exemplarily shown for a use case of the national funded project SANBA, are: design of the grid and its components, necessary auxiliary heat input for a balanced system, dynamic behavior and energy flows for the simulated time period. One major advantage of ULTHC networks could be shown in the results: the use of free cooling lowers the consumption of electrical energy significantly compared to conventional cooling technologies. Hence, the results show that *TEGSim* can be used as a very powerful tool for decarbonizing space heating, cooling and domestic hot water supply.

## **ACKNOWLEDGMENT**

This work was funded and made possible by the Climate and Energy Fund of the Austrian government and the *Austrian Research Promotion Agency (FFG)*, project number 16832905. The authors express their great acknowledgement.

## **REFERENCES**

- [1] Gollner M, Nutzenergieanalyse für Österreich 1993 - 2019. Vienna, Austria: Bundesanstalt öffentlichen Rechts - Direktion Raumwirtschaft, 2020.
- [2] Bundesministerium für Landwirtschaft, Regionen und Tourismus, Mission 2030. 2020. From: <https://www.bmlrt.gv.at/english/environment/Climateprotect/-mission2030.html>, 12.2020.
- [3] Die neue Volkspartei, Die Grünen. Aus Verantwortung für Österreich - Regierungsprogramm 2020 - 2024. Vienna, Austria: Österreichische Bundesregierung, 2020.
- [4] Buffa S, Cozzini M, D'Antoni M, Baratieri M, Fedrizzi R. 5th generation district heating and cooling systems: A review of existing cases in Europe. *Renewable and Sustainable Energy Reviews* 2019, 104:504-522.
- [5] Fuchsluger M, Goetzl G, Steiner C, Weilbold J, Rupprecht D, Kessler T, Heimlich K, Ponweiser K, Nagler J, Bothe D, Biermayr P, Haslinger E, Plank O, Strauß A, Höfer-Öllinger G. DEGENT-NET Dezentrale geothermale Niedertemperatur-Wärmenetze in urbanen Gebieten, 2017.
- [6] Nagler J. Design criteria for GCHP-systems with seasonal storage (Anergienetze). PhD, TU Wien, Vienna, Austria, 2018.
- [7] Bauer D. Zur thermischen Modellierung von Erdwärmesonden und Erdsonden-Wärmespeichern. PhD, Universität Stuttgart, Stuttgart, Germany, 2018.
- [8] Claesson J, Javed S. Explicit Multipole Formulas for Calculating Thermal Resistance of Single U-Tube Ground Heat Exchangers. *Energies* 2019, 11(1):214.
- [9] Claesson J, Javed S. Explicit Multipole Formulas and Thermal Network Models for Calculating Thermal Resistances of Double U-pipe Borehole Heat Exchangers. *Science and Technology for the Built Environment* 2019, 25(8):980-992.
- [10] Huber D. Modellierung, Simulation und Analyse von verschiedenen Rohrsonden-Typen zur Nutzung geothermischer Energie. MSc, TU Wien, Vienna, Austria, 2020.
- [11] DHI-WASY GmbH: Simulation package *FEFLOW*. From: <http://www.feflow.info>, 01.2021.
- [12] Diersch H-J G, Perrochet P. On the primary variable switching technique for simulating unsaturated-saturated flows. *FEFLOW White Papers Vol. I*, DHI-WASY GmbH, 2009.
- [13] Haslinger E, Götzl G, Ponweiser K, Biermayr P, Hammer A, Illyés V, Turewicz V, Huber D, Friedrich R, Stuckey D, Bartak G, Vogl F, Niederbrucker R, Koch G, Bauernfeind D, Kinner P; Holzer P, Kienberger T. Low-temperature heating and cooling grids based on shallow geothermal methods for urban areas. *Proceedings World Geothermal Congress* 2020.
- [14] Fünfgeld C, Tiedemann R. Anwendung der Repräsentativen VDEW-Lastprofile step-by-step. Germany: Brandenburgische Technische Universität Cottbus, 2000.



# A TWO-STEP METAL-ASSISTED CHEMICAL ETCHING PROCESS FOR FORMATION OF SILICON NANOWIRES BASED BLACK SILICON

Hazem Elghonimy

KACST-TIC in Radio Frequency and Photonics for the e-Society (RFTONICS), College of Engineering, King Saud University, Riyadh, 11421, Saudi Arabia, hazemalghonaimy@gmail.com, ORCID: 0000-0003-0833-6329

Talal Albuqami

Electrical Engineering Department, College of Engineering, King Saud University, Riyadh, 11421, Saudi Arabia, talal9902@hotmail.com, ORCID: 0000-0003-3147-149X

Ahmed Elnaggar

Physics and Astronomy Department, College of Science, King Saud University, Riyadh, 11451, Saudi Arabia, elnaggar@ksu.edu.sa, Web of Science Researcher ID: H-9098-2018, ORCID: Will be provided later. Web of Science ID provided instead.

Mohamed Abdel-Rahman

Electrical Engineering Department, College of Engineering, King Saud University, Riyadh, 11421, Saudi Arabia, KACST-TIC in Radio Frequency and Photonics for the e-Society (RFTONICS), College of Engineering, King Saud University, Riyadh, 11421, Saudi Arabia, mabdelrahman@ksu.edu.sa, ORCID: 0000-0001-6132-0575

*Cite this paper as:* Elghonimy, H, Albuqami, T, Elnaggar, A, Abdel-Rahman, M. A two-step metal-assisted chemical etching process for formation of silicon nanowires based black silicon. 9<sup>th</sup> Eur. Conf. Ren. Energy Sys. 21-23 April 2021, Istanbul, Turkey.

---

**Abstract:**

In the present study, Silicon Nanowires (SiNW) based black silicon surfaces were successfully formed on  $1.75 \times 1.75 \text{ cm}^2$  p-type CZ wafers with a bulk resistivity of  $1\text{-}10 \Omega\cdot\text{cm}$  using a two-step Metal-Assisted Chemical Etching (MACE). Fabricated Silicon Nanowires (SiNW) structures were found to have varying lengths ranging between  $(0.69 - 1.89 \mu\text{m})$ , depending on various factors such as deposition times. An optimized SiNWs fabrication process yielded structures with an average length of  $1.74 \mu\text{m}$  and an average pore size of  $319 \text{ nm}$ . Diffuse spectrophotometry measurement shows a reduction in silicon bulk diffuse reflectivity in the visible light wavelength range ( $400 - 800 \text{ nm}$ ) from 37.27% to 12.32%, and 6.73% for deposition times of 30 mins, and 60 mins, respectively. Moreover, PC1D simulations were conducted to estimate the performance of the proposed silicon solar cells. This study shows that SiNWs based black silicon surfaces are a suitable, simple, and low-cost replacement for conventional anti-reflection coatings used in silicon solar cells.

---

**Keywords:**

Black Silicon, Solar Cells, Silicon Nanowires, Metal-Assisted Chemical Etching

© 2021 Published by ECRES

## 1. INTRODUCTION

Black silicon is a micro-textured layer formed by altering the structure of a silicon wafer's surface using chemical [1-11] or plasma etching techniques [12-14]. This layer is called "Black Silicon" in reference to the color that appears on the surface of the silicon wafer. It was first created in 1996, by E. Mazur who developed a black silicon fabrication method [15] using femto-second laser pulses in order to create high detection night vision cameras, due to its high absorptance at near- and shortwave infrared wavelength[16]. However, the potential of black silicon goes far and beyond image detection applications. Black silicon can be used for a plethora of other applications such as ammonia gas sensing [17], lithium-ion batteries[18, 19], micro-electro-mechanical systems (MEMS) [20], and photovoltaics [1-6, 11].

Black silicon can be utilized in solar cells as a replacement for anti-reflection layers, due to its high light absorption and low reflectivity [1,2,4,11]. In addition, the fabrication cost of solar cells is reduced as a result of replacing anti-reflection layers with black silicon, as anti-reflection layers' fabrication in regular c-Si solar cells is performed in a two-step process: texture etching, and anti-reflection coating deposition. The etching is done to form a pyramidal light-trapping surface and then an anti-reflection layer is deposited using plasma deposition techniques. Whilst black silicon is created by etching the surface of the wafer directly.

In this work, we propose a process for manufacturing black silicon surfaces for photovoltaic solar cell applications using a fully chemical black silicon formation process. Black silicon surfaces are formed on the silicon substrate using a two-step Metal-Assisted Chemical Etching (MACE) process. Scanning electron microscopy imaging (SEM) and spectrophotometry techniques are used to study the morphological properties and optical performance of the fabricated structures. The resulting reflectance spectra are visualized and compared with polished silicon performance Furthermore, PC1D simulations are conducted to estimate the performance of the proposed black silicon solar cells.

## 2. BLACK SILICON FORMATION

Recently, different methods of fabricating black silicon have been utilized such as Reactive-ion etching (RIE) [12-14], electrochemical etching [7], stain etching [8, 9], and metal-assisted chemical etching (MACE) [1-6, 10, 11]. Among these methods, MACE has gathered much attention due to its simplicity, low-cost, and ability to control the morphological properties of such structures. It involves the use of noble metal nanoparticles (NPs), etchants, and oxidative agents in a wet chemical solution in order to develop silicon nanostructures, such as Silicon Nanowires (SiNW), on top of silicon substrates. Fig. 1 summarizes the fundamental MACE mechanism. There are two types of MACE: One-Step MACE and Two-Step MACE. In One-Step MACE, noble metal NPs deposition and silicon etching are done simultaneously in a single solution. Whilst in Two-Step MACE, noble metal nanoparticles are separately deposited on the silicon wafer before the etching process, which increases the porosity of the topmost layer of the substrate. In this study, a two-step metal-assisted chemical etching process is developed and utilized to fabricate black silicon.

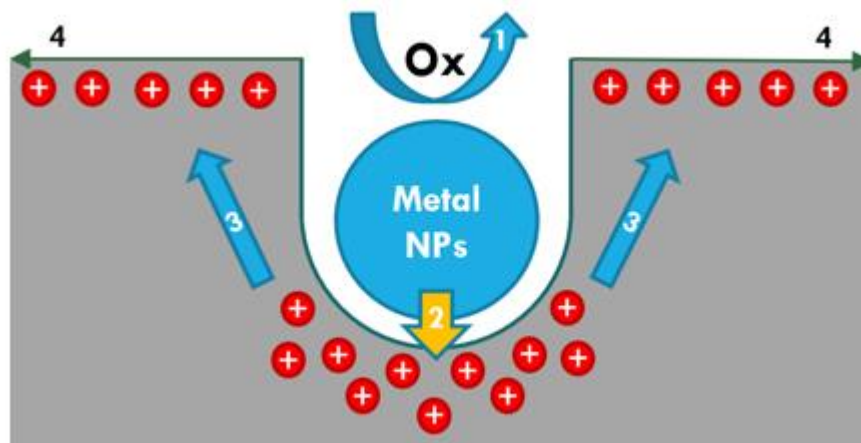


*Figure 6. An illustration of the metal-assisted chemical etching process: (1) Oxidative agent reduction catalyzed by noble metal nanoparticles; (2) holes generated by reduction are injected into the silicon substrate, with the highest hole concentration underneath the metal particle; (3) holes migrate to the silicon surface and sidewalls and (4) SiO<sub>2</sub> is removed by HF. [10]*

## Experimental Details

Silicon Nanowires (SiNWs) were fabricated on a 1.75 cm × 1.75 cm p-type CZ (1-10 Ω.cm, Boron doped, 375 μm ± 20 μm) double-side polished silicon <1 0 0> wafer samples. First, the samples were ultrasonically cleaned in acetone, isopropanol, and DI water for 5 minutes in each cleaning solution. Next, the backside of the samples was covered in Shipley S1813 positive photoresist to protect it during the etching process. Then, the samples were immersed in a 5 vol% HF solution for native oxide removal. After that, Silver (Ag) nanoparticles were deposited in a freshly prepared 9 vol% HF and 0.015 mol/L AgNO<sub>3</sub> aqueous solutions for two different durations: 30, and 60 mins. Following the metal deposition, the samples were immersed in 12.5 vol% HF, 3 vol% H<sub>2</sub>O<sub>2</sub> aqueous solutions for further etching. Finally, the residual silver nanoparticles were dissolved in two consequent 30 wt.% HNO<sub>3</sub>

solutions and the samples were rinsed in H<sub>2</sub>O and dried in N<sub>2</sub>. Fig. 2 shows a block diagram of the black silicon formation process.

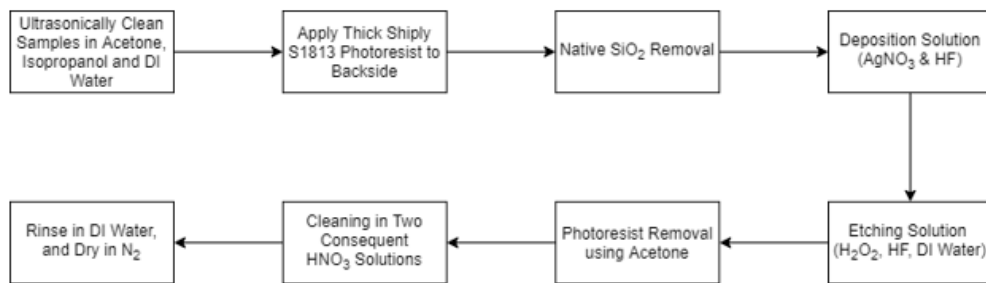


Figure 7. Black Silicon Formation Process

### 3. OPTICAL CHARACTERIZATION

#### Scanning Electron Microscopy (SEM) Imaging

Morphological properties of the resulting black silicon structures were studied using Field Emission SEM (JOEL JSM 7600 F). Fig. 3 shows optical images of the resultant black silicon samples taken by a digital camera. Fig. 4 shows the surface morphologies of the black silicon samples with different deposition time durations. Fig. 4 (a) shows an under-developed SiNWs array due to limited deposition time. As the deposition time increases, SiNWs array appears more vertically aligned and structured, as shown in Fig. 4 (b), (c). Table 1 demonstrates the details of the fabricated black silicon samples. The scattering of AgNPs on the surface of Fig. 4 (a) is due to the insufficient dissolution of AgNPs in HNO<sub>3</sub>, as the sample was only cleaned once in the HNO<sub>3</sub> solution.

Table 1. Black Silicon Samples Details

Sample no	Deposition Time	Etching Time	HNO <sub>3</sub> Time
A	30 mins	15 mins	3 mins
B	60 mins	15 mins	3 mins

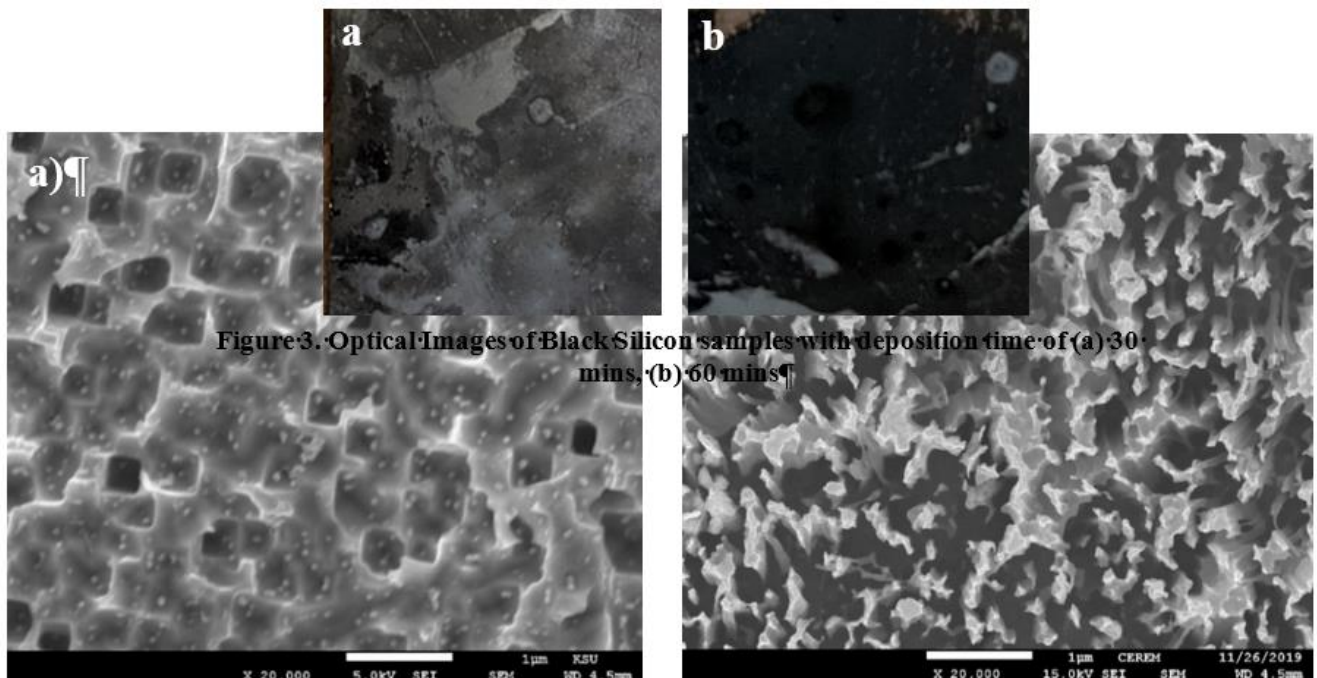


Figure 3. Optical Images of Black Silicon samples with deposition time of (a) 30 mins, (b) 60 mins

Figure 8. Optical Images of Black Silicon samples with deposition time of (a) 30 mins, (b) 60 mins

To measure the effect of deposition time on the length of the SiNWs, cross-sectional imaging of samples A and B was performed, shown in Fig. 5. The length of the SiNWs increases from 0.75  $\mu\text{m}$  to 1.74  $\mu\text{m}$ , whilst pore size reduced from 781 nm to 319 nm. The results further prove the dependency of SiNWs' length and porosity on deposition time, as shown in Table 2, thus indicating that the sinking of AgNPs into the silicon substrate is a continuous operation that stops only if HF is consumed or AgNPs concentration is exhausted.

*Table 2: Dependence of SiNWs Length and Pore Size on Deposition Time*

Sample no.	Deposition Time	Length	Pore size
A	30 mins	0.75 $\mu\text{m}$	781 nm
B	60 mins	1.74 $\mu\text{m}$	319 nm

### Spectrophotometry Analysis

Specular and diffuse spectrophotometry measurements were carried out by UV-Vis Spectrophotometers (Cary 5000 & Shimadzu UV-2550) in the visible light wavelength range (400-800 nm). In specular reflectance, the reflected light is measured with respect to the incidence angle, shown in the law of reflectance in Eq. [1].

$$\theta_i = \theta_r \quad (1)$$

Specular reflectance of the silicon was significantly reduced to an average reflectance of 1.109%, and 0.859% for samples A, and B, respectively, as shown in Fig. 6 (a). Due to the irregularity of the SiNWs surface, lightly scattered of SiNWs must be assessed, thus the diffuse reflectance of the samples was measured. Fig. 6 (b) shows the diffuse reflectance of the fabricated SiNWs black silicon. Diffuse reflectance was reduced from a polished silicon average of 37.27% to 12.32%, and 6.73% for samples A, and B, respectively. These results show that the diffuse and specular reflectance decreases as the length of the SiNWs increases. This can be explained by the increased light trapping attributes long SiNWs possess over shorter lengths of SiNWs. Table. 2 summarizes the results of the spectrophotometry analysis.

*Table 3. Spectrophotometry Results*

Sample no	Deposition Time	Length	Reflectance	
			Specular	Diffuse
A	30 mins	0.75 $\mu\text{m}$	1.109%	12.32%
B	60 mins	1.74 $\mu\text{m}$	0.859%	6.73%

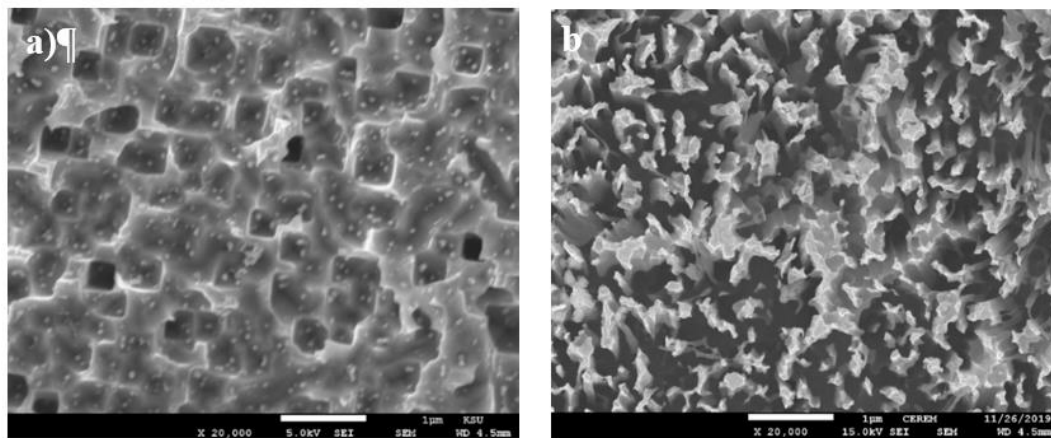


*Figure 9. Surface SiNWs morphologies with deposition times of (a) 30 mins, (b) 60 mins*

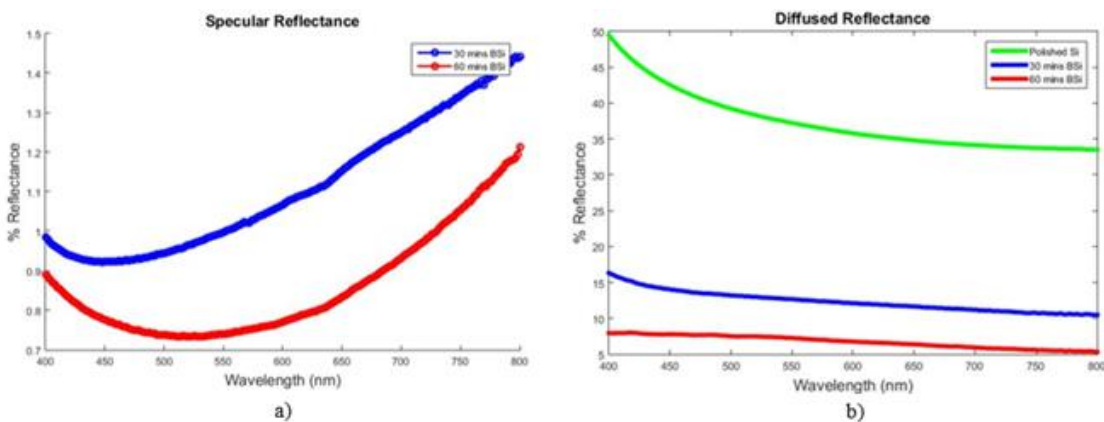


Figure 10. (a) Specular Reflectance, (b) Diffused Reflectance

#### 4. PC1D SIMULATION

An n<sup>+</sup>-p-p<sup>+</sup> solar cell with an exterior reflectance of 6.73% was simulated, based on the results of sample B. To create an emitter, p-type silicon with background doping of  $1 \times 10^6 \text{ cm}^{-3}$  was n-type front doped with a peak concentration of  $2 \times 10^{20} \text{ cm}^{-3}$ . To enhance the solar cell efficiency, a back surface field was created by a p-type back doping with a peak concentration of  $3 \times 10^{18} \text{ cm}^{-3}$ . Front and rear recombination velocities were put in as  $2 \times 10^5 \text{ cm/s}$  and  $2 \times 10^7 \text{ cm/s}$ , respectively. The simulation was conducted at Air Mass 1.5 G (AM1.5G) spectra under the one-sun condition with an intensity of 100 mW/cm<sup>2</sup>. After running the simulation model, it was observed that the fabricated solar had an expected open-circuit voltage ( $V_{oc}$ ) of 598.4 mV, a short circuit current ( $I_{sc}$ ) of 19.63 mA, and a maximum base output power of 9.71 mW. These voltage and current results mean that the fabricated black solar cell has an expected efficiency of 9.71%. The calculation used to determine the expected efficiency is shown in Eq. [2]. The following Fig.7 shows the simulated one-sun I-V and power graph obtained from PC1D.

$$\eta\% = \frac{V_{oc} \times I_{sc} \times FF}{P_{in}} \times 100 \quad (2)$$

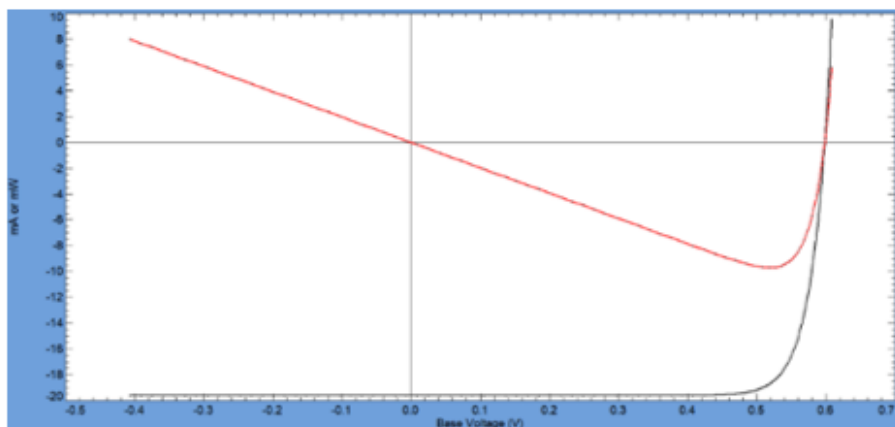


Figure 11: Simulated one-sun I-V and Power curves.

#### 5. SUMMARY

In conclusion, micro-textured black silicon surface samples were fabricated using a two-step MACE process. After optical characterization of the fabricated samples, black silicon samples showed a massive improvement on reflectivity compared to bare polish silicon. This reduction of reflectivity is caused by the fabrication of Nanowires on the silicon wafer's surface. This is verified by SEM imaging which confirmed the presence of silicon nanowires on top of the fabricated samples. We recommend, moving forward, the exploration of optimizing our deposition methods to further improve the distribution and uniformity of the structures fabricated on the silicon. Also, to discover the different applications of black silicon, mainly the fabrication of low cost, low reflectance solar cells.

## ACKNOWLEDGMENT

Our special thanks are extended to Dr. Mohammad Alduraibi, Dr. Najeeb Al-Khali and Dr. Nacer Debbar for their help and support throughout the work. We also like to thank the Center of Excellence for Research of Engineering Materials (CEREM) and King Abdullah Institute of Nanotechnology (KAIN) for allowing us to use their equipment to characterize our results.

## REFERENCES

- [1] Gouda AM, Elsayed M, Allam NK, Swillam MA. Black silicon based on simple fabrication of mesoporous silicon nanowires for solar energy harvesting. In: 2016 IEEE 43rd Photovoltaic Specialists Conference (PVSC). 5-10 June 2016: pp. 2893-5.
- [2] Huang B-R, Yang Y-K, Lin T-C, Yang W-L. A simple and low-cost technique for silicon nanowire arrays based solar cells. *Solar Energy Materials and Solar Cells* 2012;98:357-62.
- [3] Hung Y, Jr., Lee S-L, Wu K-C, Tai Y, Pan Y-T. Antireflective silicon surface with vertical-aligned silicon nanowires realized by simple wet chemical etching processes. *Optics Express* 2011;19:15792-802.
- [4] Jung J-Y, Um H-D, Gee S-W, Park K-T, Bang JH, Lee J-H. Optimal design for antireflective Si nanowire solar cells. *Solar Energy Materials and Solar Cells* 2013;112:84-90.
- [5] Oh J, Yuan H-C, Branz HM. An 18.2%-efficient black-silicon solar cell achieved through control of carrier recombination in nanostructures. *Nature Nanotechnology* 2012;7:743-8.
- [6] Yang L, Liu Y, Wang Y, Chen W, Chen Q, Wu J, et al. 18.87%-efficient inverted pyramid structured silicon solar cell by one-step Cu-assisted texturization technique. *Solar Energy Materials and Solar Cells* 2017;166:121-6.
- [7] Kleimann P, Linnros J, Juhasz R. Formation of three-dimensional microstructures by electrochemical etching of silicon. *Applied Physics Letters* 2001;79:1727-9.
- [8] Dimova-Malinovska D, Sendova-Vassileva M, Tzenov N, Kamenova M. Preparation of thin porous silicon layers by stain etching. *Thin Solid Films* 1997;297:9-12.
- [9] Kolasinski KW. Porous Silicon Formation by Stain Etching. In: Canham L, editor. *Handbook of Porous Silicon*. Cham: Springer International Publishing, 2017. pp. 1-21.
- [10] Huang Z, Geyer N, Werner P, de Boor J, Gösele U. Metal-Assisted Chemical Etching of Silicon: A Review. *Advanced Materials* 2011;23:285-308.
- [11] Scheul T, Emilian, Khorani E, Rahman T, Boden S. Metal-assisted chemically etched black silicon for crystalline silicon solar cells. In: PV-SAT 14 18 - 20 April 2018: pp.
- [12] Chowdhury ZR, Loh JYY, Pishon MNN, Kherani NP. Black silicon morphologies using conventional RIE processing. *AIP Advances* 2017;7:055115.
- [13] Dussart R, Boufnichel M, Marcos G, Lefaucheux P, Basillais A, Benoit R, et al. Passivation mechanisms in cryogenic SF<sub>6</sub>/O<sub>2</sub>etching process. *Journal of Micromechanics and Microengineering* 2003;14:190-6.
- [14] Dussart R, Mellhaoui X, Tillocer T, Lefaucheux P, Boufnichel M, Ranson P. The passivation layer formation in the cryo-etching plasma process. *Microelectronic Engineering* 2007;84:1128-31.
- [15] Her T-H, Finlay RJ, Wu C, Deliwala S, Mazur E. Microstructuring of silicon with femtosecond laser pulses. *Applied Physics Letters* 1998;73:1673-5.
- [16] Lv J, Zhang T, Zhang P, Zhao Y, Li S. Review Application of Nanostructured Black Silicon. *Nanoscale Research Letters* 2018;13:110.
- [17] Liu X-L, Zhu S-W, Sun H-B, Hu Y, Ma S-X, Ning X-J, et al. "Infinite Sensitivity" of Black Silicon Ammonia Sensor Achieved by Optical and Electric Dual Drives. *ACS Applied Materials & Interfaces* 2018;10:5061-71.
- [18] Zhao Y, Liu X, Li H, Zhai T, Zhou H. Hierarchical micro/nano porous silicon Li-ion battery anodes. *Chemical Communications* 2012;48:5079-81.
- [19] Vu A, Qian Y, Stein A. Porous Electrode Materials for Lithium-Ion Batteries – How to Prepare Them and What Makes Them Special. *Advanced Energy Materials* 2012;2:1056-85.
- [20] Barillaro G, Nannini A, Piotto M. Electrochemical etching in HF solution for silicon micromachining. *Sensors and Actuators A: Physical* 2002;102:195-201.



# PERFORMANCE INVESTIGATION OF AN INTEGRATED SOLAR-POWERED RO/ADSORPTION COOLING TRIGENERATION SYSTEM

Ahmed A. Hassan

Egypt-Japan University of Science and Technology (E-JUST), Alexandria, Egypt, ahmed.hassan@ejust.edu.eg,  
ORCID: 0000-0002-8344-0129

Ahmed E. Elwardany

Egypt-Japan University of Science and Technology (E-JUST), Alexandria, Egypt, ahmed.hassan@ejust.edu.eg,  
ORCID: 0000-0002-2536-2089

Ibrahim I. El-Sharkawy

Egypt-Japan University of Science and Technology (E-JUST), Alexandria, Egypt, ahmed.hassan@ejust.edu.eg,  
ORCID: 0000-0003-2690-9661

*Hassan, A., Elwardany, A., El-Sharkawy, I. Performance investigation of an integrated solar-powered RO/Adsorption cooling trigeneration system. 9<sup>th</sup> Eur. Conf. Ren. Energy Sys. 21-23 April 2021, Istanbul, Turkey.*

**Abstract:** In this paper, an integrated solar-powered RO/Adsorption cooling trigeneration system has been investigated theoretically. The system comprises hybrid solar collectors, reverse osmosis (RO) unit and adsorption chiller. The hybrid solar collectors consist of commercial Photovoltaic/thermal (PVT) collectors and flat plate thermal collectors (FPT) for electricity and solar thermal energy capture. Part of the generated electricity is utilized to drive the RO unit, while the rest can be used in the building needs or delivered to the grid. The captured thermal energy is used to drive a double-bed, silica gel/water pair-based adsorption chiller for cooling production. The system is investigated under the climate condition of Alexandria, Egypt. The results show that the maximum cooling capacity of 10.7 kW and COP of 0.46 occurs in the month of August, while the average cooling production is about 6.2, 7.1 and 7.07 kW for the summer months, respectively. The generate electric energy per day during summer months by the PVT collectors are about 52.5, 54.4 and 53.9 kWh/day. The RO unit consume about 1.6 kW or 4.78 kWh/m<sup>3</sup> to produce 3 m<sup>3</sup>/day fresh water between 8 AM to 5 PM.

**Keywords:** Adsorption cooling, RO unit, Trigeneration system, Hybrid solar collectors.

© 2021 Published by ECRES

## 1. INTRODUCTION

Global warming and freshwater scarcity are two major problems that threaten many countries worldwide. Fossil fuel-based systems for the separate production of fresh water, cooling and electricity are of the main top contributors of carbon dioxide emissions that engraves the global warming crisis. Integrated multigeneration systems that are powered with renewable energy are one possible solution to these problems.

Many scholars and companies are investigating PVT solar collectors because it is the only collector type that can generate electricity while capturing solar thermal energy as well [1]. Thermally-activated chillers such as adsorption chillers can be driven by low-grade thermal energy such as solar energy and waste heat, and they employ natural refrigerants with no effect on the environment. The only disadvantage is their relatively low COP and higher cost compared to traditional vapor-compression chillers. That is why researchers heavily investigated experimentally and theoretically how to increase their performance [2], and also investigated different adsorbent/adsorbate pairs to improve their cooling production [3]. Solar-powered multigeneration systems, including adsorption chillers for cooling production, are a very promising solution to mitigate global warming [4].

In this paper, a theoretical study of the performance of a novel integrated solar-powered RO/Adsorption chiller system for simultaneous production of electricity, fresh water and cooling has been performed. The study is performed under the climate conditions of Alexandria, Egypt (31.2°N, 31.23°E) during the three months of summer. Hybrid solar collector system, comprises commercially available FPT and PVT solar collectors, is used to

generate electricity and capture solar thermal energy. RO unit is utilized to produce three m<sup>3</sup> fresh water per day. The RO unit is driven by part of the electricity generated by the PVT collectors. A double-bed, silica gel/water pair-based adsorption chiller driven by the captured solar energy is used for cooling production. Dynamic performance of the solar system and adsorption chiller has been simulated using lumped parameter model, while the power requirement and the water quality of the RO unit has been estimated using ROSA software by Dow industries [5].

## 2. SYSTEM DESCRIPTION

Figure 1 illustrates the main layout of the proposed system.

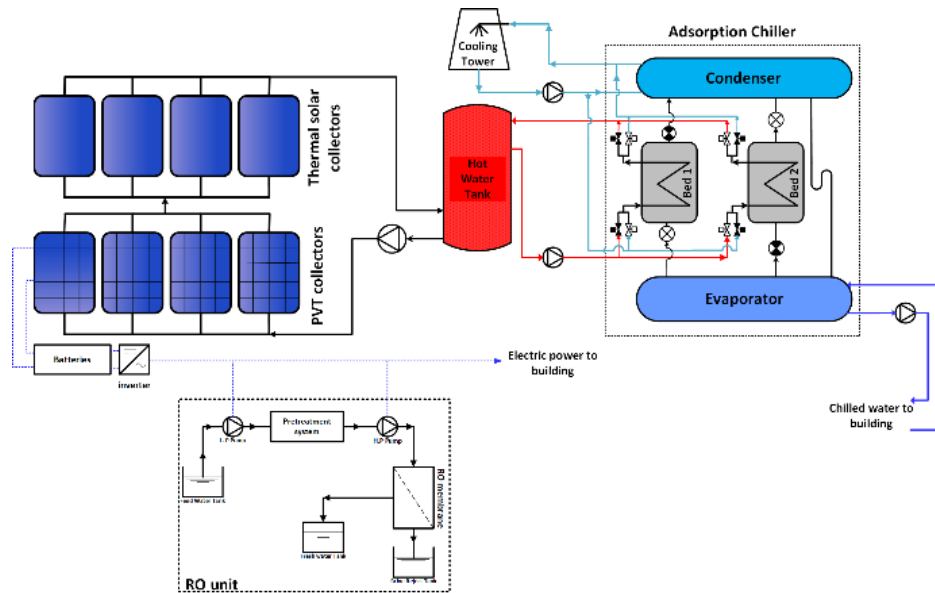


Figure 1. Main layout of the proposed system.

The hybrid solar collector system comprises two groups of commercial collectors available on the market. The first one is the PVT collectors, linked in parallel arrangement, made by DUALSUN company in France, while the other group is flat plate thermal solar collectors FPT made by Apricus Company in USA, also linked in parallel arrangement. The two collector groups are linked together in series arrangement as shown in Fig. 1. The two commercial collectors used in the investigation are certified by European and North American agencies such as Solar Keymark and Solar Rating & Certification Corporation (SRCC). The specifications of both collectors used in the investigation are illustrated in Table 1.

Table 1. Specifications of the solar collectors used in the study.

Criteria	PVT collector	FPT collector
Model	Spring 310M	FPC-A32
Number of collectors used	30	20
Aperture area ( $A_{sc}$ )	1.58 m <sup>2</sup>	2.8 m <sup>2</sup>
Optical efficiency ( $\eta_0$ )	58.2%	75.5%
Heat loss Coefficient ( $a_1$ )	10.8 Wm <sup>-2</sup> k <sup>-1</sup>	3.738 Wm <sup>-2</sup> k <sup>-1</sup>
Heat loss Coefficient ( $a_2$ )	0.0 Wm <sup>-2</sup> k <sup>-2</sup>	0.007 Wm <sup>-2</sup> k <sup>-2</sup>
Nominal electrical efficiency ( $\eta_n$ )	19.1%	---
Power temperature Coefficient ( $\beta$ )	-0.39%	---

The adsorption chiller used for cooling production is a single stage, double-bed chiller, where a silica gel/water pair is utilized. The specifications and the required values regarding the adsorption chiller and silica gel/water pair used in the present study can be found in [6].

The hot water storage tank utilized in the investigation is made by Solarfocus Company in Germany. The capacity of the tank is 1250 liters and it employs a hard polyurethane thermal insulation to reduce the thermal losses to the environment.

The RO unit is used to desalinate 3 m<sup>3</sup> per day of Seabeach well saline water in Alexandria, Egypt for the building fresh water needs. the properties of the saline water is illustrated in Table 2 [7]. The RO membrane chosen for the RO unit is the SW30-4040 made by FilmTec corporation. The maximum allowed feed water flow rate, applied pressure and operating temperature of this membrane are 7.4 m<sup>3</sup> per day, 69 bar and 45°C, respectively. Additionally, the membrane active area and salt rejection are 7.3 m<sup>2</sup> and 99.7%, respectively.

### 3. MATHEMATICAL MODEL

#### Solar collector electrical and thermal performance

Energy balance method is used to model thermal performance of both PVT and FPT solar collectors. The PVT collector can be modeled as a conventional solar thermal collector with its absorber covered by the PV layer. The following assumptions are made for the PVT collectors: I) The absorber surface and the PV layer are at thermal equilibrium, II) one-dimensional heat transfer, III) steady state conditions, IV) Neglect dynamic effects. These assumptions simplify the model and provide sufficiently accurate description of the thermal efficiency of the PVT collectors [8].

The thermal efficiency  $\eta_{th,sc}$  of the FPT and PVT solar collectors can be calculated based on the incident solar radiation ( $G_t$ ), ambient temperature ( $T_{amb}$ ) and the average solar collector heat transfer fluid temperature ( $\bar{T}_{hw}$ ), which here is water, as in Eq. [1].

$$\eta_{th} = \eta_0 - a_1 \left( \frac{\bar{T}_{hw} - T_{amb}}{G_t} \right) - a_2 \left( \frac{(\bar{T}_{hw} - T_{amb})^2}{G_t} \right) \quad (1)$$

The electric performance of the PVT collectors is represented by estimating the electrical efficiency of the PVT solar collector ( $\eta_{elec}$ ) as given by Eq. [2]

$$\eta_{elec} = \frac{P_{elec}}{G_t A_{sc}} \quad (2)$$

where  $P_{elec}$  is the instantaneous generated electrical power by the PVT collectors. The manufacturers of the PVT collectors provide the values of  $\eta_{elec}$  at the standard testing conditions (STC), in which the  $G_t$  is 1000 W/m<sup>2</sup> and  $T_{amb}$  is 25°C. However, these conditions are changing continuously throughout the day. Therefore, to get the value of  $\eta_{elec}$  at different  $G_t$  and  $T_{amb}$ , Eq. [3] is used.

$$\eta_{elec} = \eta_n + \beta(T_{sc} - 25^\circ\text{C}) \quad (3)$$

The energy balance equations of the solar collectors and the hot water storage tank are taken as presented by El-Sharkawy et. al [6].

#### Silica gel/water adsorption equilibrium and kinetics

All the equations in addition to constants required to simulate the dynamic performance the of silica gel/water pair-based adsorption beds are taken as in [6].

#### Evaporator, condenser and adsorption bed energy balance

All the energy balance equations of the evaporator, condenser and the two adsorption beds are taken as in [6].

#### Adsorption chiller performance

Adsorption chiller performance parameters such as the average cyclic cooling capacity ( $\dot{Q}_c$ ) and coefficient of performance ( $COP_c$ ) are calculated by Eqs. [4,5].

$$\dot{Q}_c = \frac{\int_{t_{0,c}}^{t_{f,c}} (\dot{m} C_p (T_{in} - T_{out}) dt)_{chill}}{\int_{t_{0,c}}^{t_{f,c}} dt} \quad (4)$$

$$COP_c = \frac{\int_{t_{0,c}}^{t_{f,c}} (\dot{m} C_p (T_{in} - T_{out}) dt)_{chill}}{\int_{t_{0,c}}^{t_{f,c}} (\dot{m} C_p (T_{in} - T_{out}) dt)_{hw}} \quad (5)$$

Where  $t_0, c$  and  $t_{f,c}$  is cycle starting and finishing times, respectively.

#### RO performance

The required electrical power and energy to desalinate 3 m<sup>3</sup> of saline per day is calculated by ROSA software. Additionally, the permeate and concentrate water properties are also estimated by the software.

## 4. RESULTS AND DISCUSSION

### Climate conditions

The climate conditions at Alexandria (31.2°N, 31.23°E) during the summer months are estimated using Meteonorm software, which has a large up-to-date database composed of data from thousands of weather ground stations worldwide and five satellites. The climate data is provided as discrete data that consists of 24 values of time in hours throughout the day with the corresponding average values of  $G_t$  and  $T_{amb}$  to MATLAB software, and the software interpolate linearly the data for the times that do not have direct values of  $G_t$  or  $T_{amb}$ . Figure 2 shows the total solar radiation on a tilted surface by 30° and the ambient temperature for the three months of summer for the climate conditions of Alexandria.

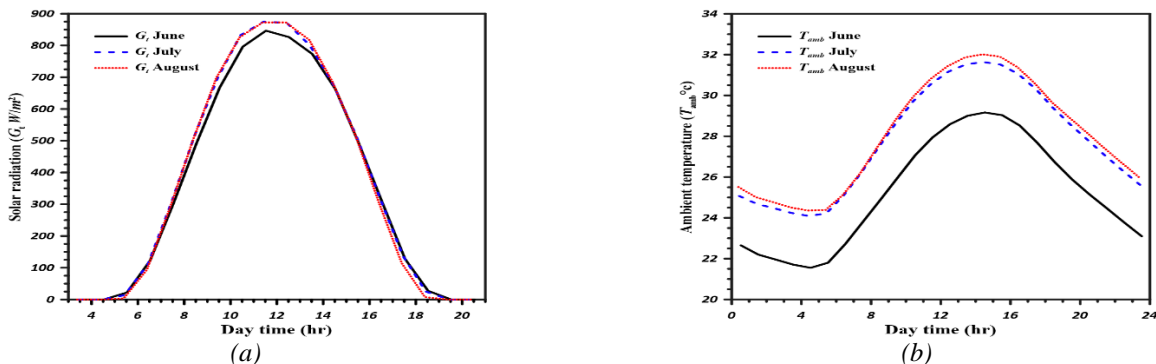


Figure 2. (a) Solar radiation during summer months, (b) Ambient temperature during summer months

### Adsorption chiller performance

Figure 3a shows the  $\dot{Q}_c$  and  $COP_c$  in a typical day during the month of August, while Fig. 3b illustrates the maximum and average values of the  $\dot{Q}_c$  during the three months of summer, and Fig. 3c show the maximum and average values of the  $COP_c$  during summer months.

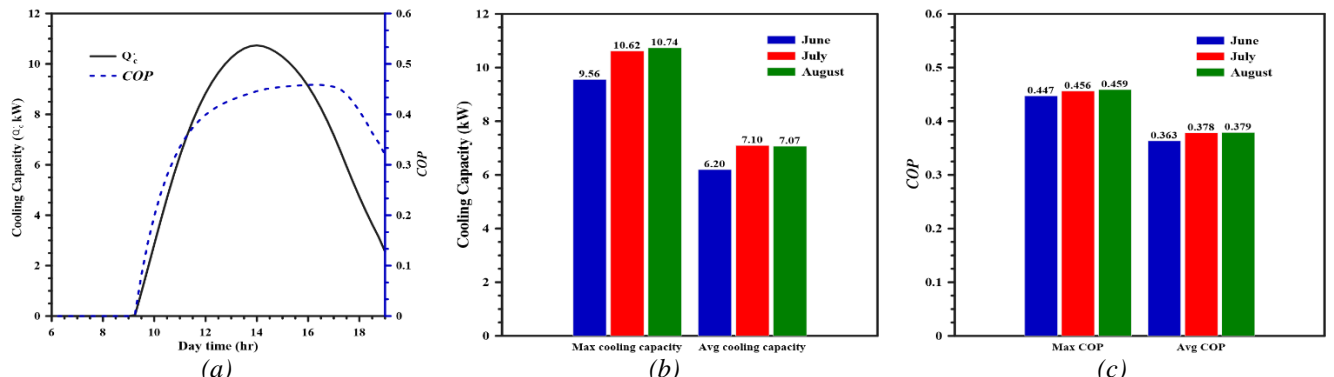


Figure 3. (a)  $\dot{Q}_c$  and  $COP_c$  in a typical day during the month of August, (b) Maximum and Average  $\dot{Q}_c$  during summer months, (c) Maximum and Average  $COP_c$  during summer months.

As shown in Fig. 3a, the cooling production starts at about 9:00 AM when the temperature in the hot water storage tank become high enough to drive the silica gel beds at about 52°C. Then, the cooling capacity starts to increase gradually as the temperature of the hot water increases in the tank, until it reaches its maximum value of 10.74 kW at about 14:00 PM, before it start to decrease due to the decreasing solar radiation and the corresponding hot water temperature in the tank.  $COP_c$  takes the same trend as the  $\dot{Q}_c$  and reaches a maximum value of about 0.46 at about 16:00 PM. The month of August has almost the highest average  $\dot{Q}_c$  and  $COP_c$  of about 7.1 kW and 0.38, respectively because it has the highest solar radiation and ambient temperatures, which helps in decreasing the thermal losses from the hot water tank to the environment and thus increasing the cooling production.

### PVT solar collectors performance

Figure 4a illustrates the electric power generated by PVT collectors and RO required electric power in the month of July, while Fig. 4b shows the electric energy generated in a typical day during the three months of summer.

The month of July has the highest electric power production of 54.43 kWh/day as shown in Fig. 4b. This is because it has almost the same solar radiation as the month of August while having less ambient temperature which help reducing the temperature of the PV modules in the PVT collectors and thus increasing the electric power generation.

### RO unit performance

The RO unit starts working at 8:00 AM for about 9 hours until 5:00 PM and generate about  $0.33 \text{ m}^3$  per hour or  $3 \text{ m}^3$  per day of permeate fresh water. The recovery ratio is taken as 30% and four SW30-4040 membrane is used. The software results show that the required electric power to drive the pump is about 1.6 kW or about 4.78 kWh per  $\text{m}^3$  of fresh water. Table 2 illustrates the properties of the raw, permeate and concentrate water generated in the RO unit.

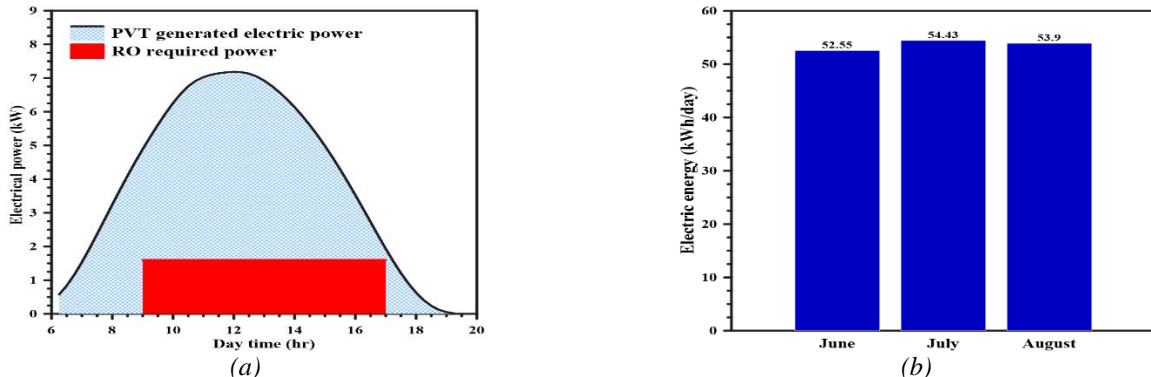


Figure 3. (a) PVT generated power and RO required power in a typical day during the month of July, (b) generated electrical energy during summer months

Table 2. Properties of the raw, concentrate and permeate water of the RO unit.

Property	Raw seawater	Permeate water	Concentrate water
$\text{Na}^+$ (ppm)	10,562	133	15,031
$\text{Cl}^-$ (ppm)	14,079	217	25,551
$\text{Ca}^{++}$ (ppm)	653	2.5	932
$\text{K}^+$ (ppm)	138	4.5	238
$\text{SO}_4^{--}$ (ppm)	2,692	4.1	3844
$\text{Mg}^{++}$ (ppm)	838	133	1,196
Total Dissolved Solids (TDS)	29,157	370	47,024

## 5. CONCLUSIONS

In this paper, a theoretical investigation of a solar-powered trigeneration system for electricity, cooling and fresh water production for a building in Alexandria, Egypt during the summer months, has been performed. Hybrid solar collector configuration from commercial PVT and FPT collectors has been used to generate electricity and capture solar thermal energy. A double-bed, silica gel/water pair-based adsorption chiller is used for cooling production, while an RO unit is utilized for fresh water production. The maximum cooling capacity and COP of 10.7 kW and 0.46 occur in the month of August, while the average cooling capacity generated in the three months of summer are 6.2, 7.1 and 7.07, respectively. The generated electric energy in a typical day during the summer by the PVT collectors are 52.5, 54.4 and 53.6 kWh/day, respectively. The RO unit generate  $3 \text{ m}^3$  of fresh water in 9 hours operation time between 8 AM to 5 PM, and needs an electric power of 1.6 kW or about 4.78 kWh per  $\text{m}^3$ .

## REFERENCES

- [1] Herez A, El Hage H, Lemenand T, Ramadan M, Khaled M. Review on photovoltaic/thermal hybrid solar collectors: Classifications, applications and new systems 2020; 207: 1321–47.
- [2] Saha BB, El-Sharkawy II. Thermally Powered Adsorption Cooling: Recent Trends and Applications. Heat Pipes Solid Sorption Transform. Fundam. Pract. Appl.; CRC Press 2013; p. 29.
- [3] Younes MM, El-Sharkawy II, Kabeel AE, Saha BB. A review on adsorbent-adsorbate pairs for cooling applications 2017; 114: 394–414.
- [4] Hassan AA, Elwardany AE, Ookawara S, Ahmed M, El-Sharkawy II. Integrated adsorption-based multigeneration systems: A critical review and future trends 2020; 116: 129–45.
- [5] ROSA software. Dow DuPont inc. [cited 2020 Dec 20] Available from: ([https://www.desalitech.com/rosa\\_download\\_lp/](https://www.desalitech.com/rosa_download_lp/)).

- [6] El-Sharkawy II, AbdelMeguid H, Saha BB. Potential application of solar powered adsorption cooling systems in the Middle East 2014; 126: 235–45.
- [7] Monjezi AA, Chen Y, Vepa R, Kashyout AE-HB, Hassan G, Fath HE-B, et al. Development of an off-grid solar energy powered reverse osmosis desalination system for continuous production of freshwater with integrated photovoltaic thermal (PVT) cooling 2020; 495: 114679.
- [8] Buonomano A, Calise F, Palombo A. Solar heating and cooling systems by absorption and adsorption chillers driven by stationary and concentrating photovoltaic/thermal solar collectors: Modelling and simulation 2018; 82: 1874–1908.



# DEVELOPMENT OF ENERGY SAVING SYSTEM BASED ON MICROCONTROLLER FOR BOILER MANUFACTURER

Ibrahim Cetiner

Vocational School of Technical Sciences, Mehmet Akif Ersoy University, Burdur, Turkey, [icetiner@mehmetakif.edu.tr](mailto:icetiner@mehmetakif.edu.tr),  
ORCID: 0000-0002-1635-6461

Halit Cetiner

Vocational School of Technical Sciences, Isparta University of Applied Sciences, Isparta, Turkey,  
[halitcetiner@isparta.edu.tr](mailto:halitcetiner@isparta.edu.tr), ORCID: 0000-0001-7794-2555

Cite this paper as:

*Cetiner, I., Cetiner, H., Development of energy saving system based on microcontroller for boiler manufacturer. 9<sup>th</sup> Eur. Conf. Ren. Energy Sys. 21-23 April 2021, Istanbul, Turkey*

---

**Abstract:**

Industrialization, urbanization and technological developments in the digital field in the world have facilitated consumption. In this sense, environmental factors such as the depletion of the ozone layer, global warming and climate change, which make its presence felt more and more every day, have created the need to control the use of energy resources. Heating boilers are used extensively in greenhouses and house heating systems. In these boilers, heat is produced by using all kinds of materials such as wood, sawdust, gasoline, coal, diesel oil and natural gas. It is important in terms of energy saving that these substances regularly generate energy in certain temperature ranges in a controlled manner in the boiler. In the work we do on the requests of boiler manufacturers, the engine that ignites the heat in the boiler stops 45 minutes after the fuel runs out. In experimental studies, the power source size, Darlington transistor providing stronger current than a normal transistor, and microcontrollers, a programmable device to control the strong current, were used. An algorithm development and an integrated heating system have been proposed in order to construct the system that will ensure the most efficient use of energy performance in buildings.

---

**Keywords:**

*Boiler, manufacturers, energy saving, micro controller, programmable device*

---

© 2021 Published by ECRES

## 1. INTRODUCTION

It has become a threat to human life due to rapidly increasing energy use, supply difficulties, depletion of energy resources and environmental effects such as global warming and climate change. Considering the limited energy reserves and resources in this sense, conscious consumption should be expanded. The global contribution to energy consumption from buildings, both residential and commercial, has steadily increased in developed countries, reaching figures between 20% and 40% [1]. These figures even exceed energy consumption in the industry and transportation sectors. The increasing trend in energy demand is expected to continue in the future with the increase in population, the continuous increase in the number of buildings and the continuous increase in the amount of energy consumed due to comfort levels. For these reasons, it is seen that all kinds of work that will reduce or regulate the energy consumption in buildings or industries are necessary. Limited energy resources and the rapid increase in consumption cause energy prices to rise. However, this situation increases energy savings and reduces the occurrence of environmental problems. Although expensive energy consumption limits energy consumption, it is not sustainable. To be sustainable, more effective solutions must be found. Due to the increase in energy demand and global greenhouse gas emissions, we decided to do a study to ensure the correct use of limited energy resources. One of the most popular methods used as a method of heating in buildings in Turkey is to get heat from the solid fuel. The boiling of water is provided by burning solid fuel in heating systems. Afterwards, the boiling water is transported to all areas where it is desired to be heated by means of radiators and pipes. In these ways, it is actively used in rural areas, cities and greenhouses with or without soil. With the development of technology, it has become possible to control all features of solid fuel systems with the help of programmable micro controllers. In this study, we will try to show only some of these features. In solid fuel systems, automatic solid fuel intake can be expanded

to include features such as how long they will be taken, what kind of warning will give the user at the end of fuel. The automatic loader mechanism in the heating systems can be controlled by PLC or micro-controller based electronic cards. PLC-based systems are preferred to be controlled by programmable microcontrollers because they are expensive. It is aimed to optimize energy consumption in solid fuel systems, which are generally used in building automation, depending on where they are used. By optimizing energy consumption, emissions such as CO<sub>2</sub> and NO<sub>x</sub>, which are known to be harmful to the environment, will be reduced. In minimizing the specified emissions, there are studies that reduce emission values by adjusting the travel time of solid fuel in solid fuel grids and height adjustment of the fuel ejection chamber [2]. In minimizing the specified emissions, there are studies that reduce emission values by adjusting the travel time of solid fuel in solid fuel grids and height adjustment of the fuel ejection chamber. Liao and Dexter state in their study that heating systems in buildings built in the UK are responsible for approximately 25% of the total carbon emission. They state that a lot of work has been done to reduce carbon emissions in many European countries. In their study, they investigate the energy saving potential that can be achieved by improving boiler controls in heating systems. They state that as a result of the research, improvement of the boiler controls can provide up to 20% energy savings and a significant improvement in thermal comfort [3].

Junga et al. states that attention should be paid to the fuel used in small-scale boilers. The quality of used the fuel also indicates that it contributes to the efficient use of energy [4]. Carvalho et al. made a study to find the solid fuel with the best efficiency in European standards. In their study, it states that the boilers should be cleaned continuously in order to prevent energy efficiency decreases in boilers operating with agricultural fuels. They have been observed that as the energy efficiency increases, the emission values decrease [5]. In a Slovenian power plant, Strušnik et al. worked on the energy efficiency of boilers. For effective energy efficiency, features of all boilers are modeled with ANN, ensuring that the boilers operate at the highest efficiency [6]. Carpio et al. examined the effects of boilers on carbon emissions in six cities. The study compared the use of natural gas and renewable energy sources in building heating systems. As a result of these studies, the effect of energy rating, economic costs and climate in the reduction of CO<sub>2</sub> emission was underlined. With the use of biomass instead of natural gas fuels, an emission reduction of up to 95% has been achieved. In terms of energy efficiency, it was stated that they reached approximately 88% success rate [7]. Zhou et al. are talking about a software package to monitor emissions from solid fuel boilers. The model developed by using support vector regressions was compared with different back propagation neural networks methods. They state that she uses a lot of NOx emission data from a real power plant to train these models [8].

Jassar et al. have developed an adaptive network-based sensor to provide closed loop control for space heating systems. They aim to improve the overall performance of heating systems in terms of energy efficiency and thermal comfort [9]. Srivastava et al. mention that NOx controls are very common in the United States of electric boilers and coal-fired auxiliary boilers [10]. Zhang et al. state that energy saving and emission reduction in solid fuel boilers are important to reduce climate change and environmental pollution. They conducted an experimental study on a domestic boiler operating with 141 solid fuel boilers located in Liaoning province of China. An analysis model based on thermodynamics has been developed to reduce emissions. In their study, they are stated the necessity of boiler manufacturing so that there is no unburned solid fuel to reduce emissions [11].

Tańczuk et al. mention that solid fuel boilers are very common in some European countries. They state that a large amount of waste material is generated in boilers operating with solid fuel in district heating and power generation plants. They suggested that these waste materials should be used as an energy source due to their high temperature value. They have sought to recover the physical enthalpy of waste materials. states that they achieved energy savings from 58.8% to 88% with heat pump development [12]. In the literature, it is seen that studies are carried out using different methods in terms of energy saving and emission reduction. These studies show that only result in energy savings from all over the country that perform energy production in Turkey is not solid fuels and emission reduction is important. In this context, it can be said that many different parameters such as automatic fuel loading times of the boilers, fuel run-out controls, the height of solid fuel compartments, and the reusability of solid fuel wastes are important in saving and emission reduction. This study will focus on the control of programmable microcontrollers that will work on existing boilers. Other electronic circuit elements with which the specified micro-controller will work together on an electronic card will be introduced.

## **2. MATERIAL AND METHOD**

The studies have been performed to automated fuel supply mechanism. Investigation of solid fuel supply mechanisms which consist of control elements are needed to automate the heating system. The control elements are

composed of electronic based circuit boards. When these systems are examined, electronic circuit boards have been found to work problematic. During real-time operation it is determined experiencing many difficulties. For this reason, in this study, we have developed a circuit that control the fuel level in the boiler.

Table I. Used Materials and Explanations

Circuit Element	Item Description
4060	Time delay
7805	Voltage regulator
Transformer	A transformer transfers electrical energy from one electric circuit to another between two or more circuits without changing the frequency. Winding value changes according to the desired voltage [13]
Bc107	Silicon planar epitaxial NPN transistors
At89c1051	1k Byte of Flash, 64 bytes of RAM, 15 I/O lines, one 16 bit timer/counter [14]
At90s1200	1k byte of system programmable flash, 64 bytes EEPROM, 15 general purpose I/O lines, 32 general working registers [15]
Mpsa13	Darlington transistors with NPN silicon [16]

The AT89C1051 is a low-voltage. It is high performance CMOS 8-bit microcomputer with 1K byte of Flash programmable and erasable read only memory (PEROM). It is manufactured using Atmel and is compatible with MCS-51 instruction set [17].

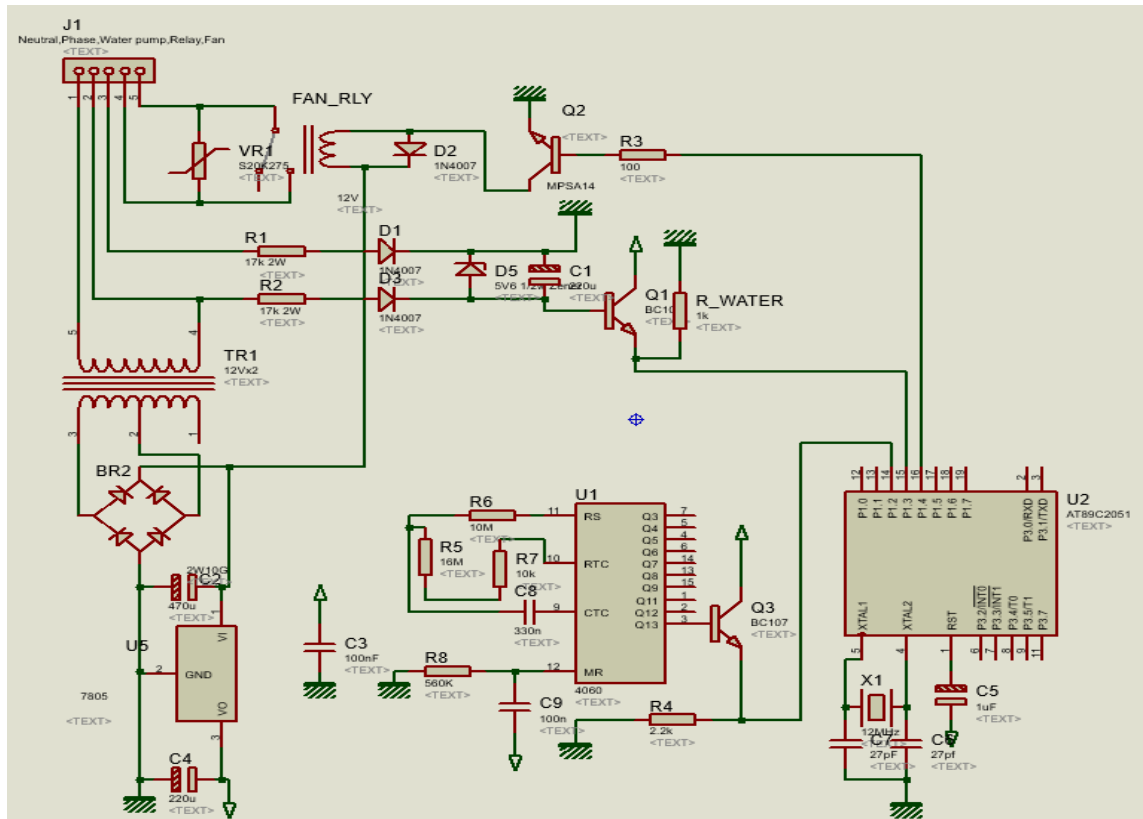


Figure 1 Open wiring diagram of the developed electronic card

Every code byte in Flash array can be written and erased by using the appropriate combination of control signals. Figure 1 shows that write and erase pins [12]. Mpsa13 is preferred due to a high current. Thanks to relay is to provide a comfortable way of working of Mpsa13 with high current.

We wanted to stop the engine after run out of fueling the heat in the boiler. Because boiler manufacturer said that very important to control the temperature of the boiler water. In addition, they don't want to operation of the boiler fan under the desired the temperature value of the boiler water. Also, the proposed building automation system is sending to signal to stop the engine after 45 minutes from the end of boiler fuel. Algorithm developed at this point is shown in Figure 2.

Solid fuel is loaded in heating boiler. After consumption of solid fuel in heating boiler, system starts working. The algorithm is to check the status of the pump. It is necessary to stop the pump when the water temperature drops below adjusted degrees. For this reason, the pump control is the key point of algorithm. In this case, the fan is blowing in the region, which does not fuel. To control the fan, it is has become important. Because this event will help us to reduce energy consumption.

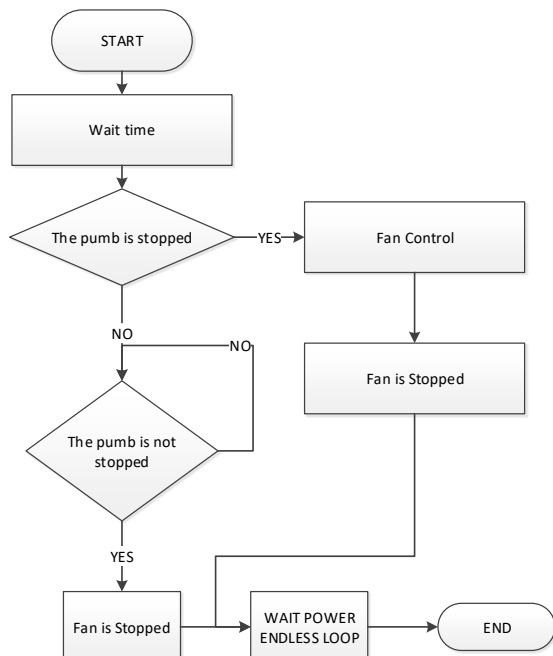


Figure 2. Algorithm of Building Automation System

For example, it is known as the fan runs continuously in vain in public institutions and organizations. In this study, we provide energy saving by its less energy consumption and the reduction of emissions such as CO<sub>2</sub> and NO<sub>x</sub> with pump and fan control. In addition, we reduce the energy consumption with this algorithm. Also, we have provided to extend the life of the materials used. The energy savings alone should not be considered as a money gain. The amount of earth fossil fuels is known to be limited. It is necessary to prevent the unnecessary use of natural resources. In addition, resulting gases such as CO<sub>2</sub> when burned in solid fuel, which lead to global warming due to the greenhouse effect. We should be used efficiently in heating system. Earth is the only habitat of human beings and other living things. This state is extremely important for the atmosphere surrounding it. The proposed building automation system is performed with experiments studies. We exchanged information during experimental studies with boiler manufacturers. Microcontrollers, Darlington transistors, the power supply are used in the experiments. The proposed building automation system controlled by a microcontroller has been achieved successful results. An electronic circuit in the proposed building automation system is designed. This electronic circuit is small size due to limiting control space of heating boilers. Power supply in the proposed building automation system has covered more areas of electronic circuits. In the end, Figure 3 shows that electronic circuit of this developed system.

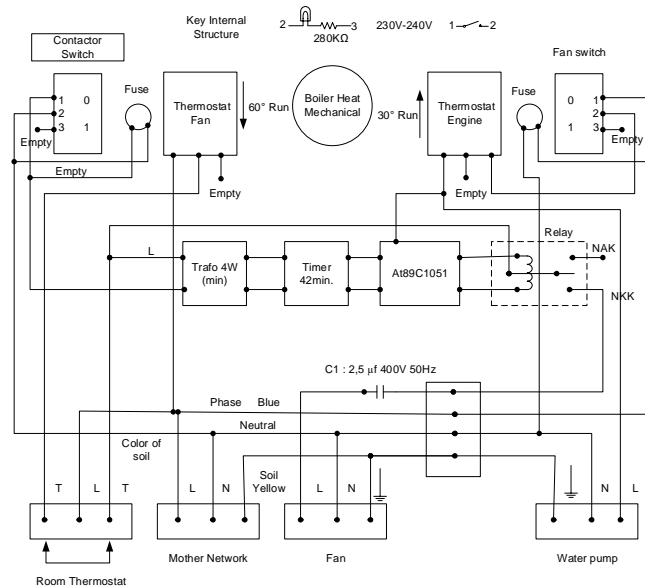


Figure 3 Developed electronic circuit of boiler



Figure 4. Implemented State of the Circuit

The open scheme of the circuit drawn in the proteus program is shared in Figure 1. A detailed diagram about the pin connections of the study was shared in Figure 3. Figure 4 shows the open shape of the printed circuit board connected to the boiler as a result of these studies. In the light of this information, a basic study has been carried out for the control of solid fuel boiler circuits. In order to control this basic work with the help of more advanced menus, it is thought to use interrupts in further studies.

### 3. RESULTS AND DISCUSSION

Conventional energy production and consumption increase due to increase of world's urbanization, industrialization, population, digital technologies. Today's developed energy policies focused on increasing the production of energy. Because over the years, the energy consumption has increased accordingly. Therefore, we think that should be developed of energy saving systems. All kinds of building are heated by using one of the any energy sources using calorific such as coal, wood, sawdust, gasoline, diesel, etc. in the boiler. We proposed a method which is to increase of more efficient and economical use of the nature resources. Today, energy saving, due to the risk of depletion of energy resources has become even more important. The cost of developing the system is satisfied with the energy savings obtained in a very short time. We believe that saving energy is not just consisting of cost. The amount of energy resources on Earth is limited. It is important to avoid from using surplus of energy resources. Also, energy saving will help prevent more spread in environment of harmful gases such as carbon

dioxide. In this study, we aim at provide energy saving by its less energy consumption and the reduction in CO<sub>2</sub> emissions with developed system.

## 5. CONCLUSION

Our proposed building automation system check the fuel level in the boiler. The proposed building automation system is suitable for control of energy management systems. Within energy management systems, simple circuits are preferred because of advantages such as efficiently, sensitivity, low cost. In this study, we aimed to design a simple circuit which is tested within a laboratory established at Isparta, Turkey. Designed electronic circuit is small size due to limiting control space of heating boilers. Power supply in the proposed building automation system has covered more areas of electronic circuits. In the end, this developed system provided study with electronic circuit of boiler.

## REFERENCES

- [1] Pérez-Lombard, L., Ortiz, J., & Pout, C., A review on buildings energy consumption information. *Energy and buildings*, 40(3), 394-398, 2008.
- [2] Rusinowski, H., Szega, M., Szelć, A., & Wilk, R., Methods of choosing the optimal parameters for solid fuel combustion in stoker-fired boilers. *Energy conversion and management*, 43(9-12), 1363-1375, 2002.
- [3] Z. Liao and A. L. Dexter, "The potential for energy saving in heating systems through improving boiler controls," *Energy Build.*, vol. 36, no. 3, pp. 261–271, Mar. 2004.
- [4] Junga, R., Chudy, P., & Pospolita, J., Uncertainty estimation of the efficiency of small-scale boilers. *Measurement*, 97, 186-194, 2017.
- [5] Carvalho, L., Wopienka, E., Pointner, C., Lundgren, J., Verma, V. K., Haslinger, W., & Schmidl, C., Performance of a pellet boiler fired with agricultural fuels. *Applied energy*, 104, 286-296, 2013.
- [6] Strušnik, D., Golob, M., & Avsec, J., Artificial neural networking model for the prediction of high efficiency boiler steam generation and distribution. *Simulation Modelling Practice and Theory*, 57, 58-70, 2015.
- [7] Carpio, M., Zamorano, M., & Costa, M., Impact of using biomass boilers on the energy rating and CO<sub>2</sub> emissions of Iberian Peninsula residential buildings. *Energy and buildings*, 66, 732-744, 2013.
- [8] H. Zhou, J. Pei Zhao, L. Gang Zheng, C. Lin Wang, and K. Fa Cen, "Modeling NOx emissions from coal-fired utility boilers using support vector regression with ant colony optimization," *Eng. Appl. Artif. Intell.*, vol. 25, no. 1, pp. 147–158, Feb. 2012.
- [9] S. Jassar, Z. Liao, and L. Zhao, "Adaptive neuro-fuzzy based inferential sensor model for estimating the average air temperature in space heating systems," *Build. Environ.*, vol. 44, no. 8, pp. 1609–1616, Aug. 2009.
- [10] R. Srivastava and R. Hall, "Nitrogen oxides emission control options for coal-fired electric utility boilers," *J. Air Waste Manage. Assoc.*, vol. 55, pp. 1367–1388, 2005.
- [11] Zhang, Q., Yi, H., Yu, Z., Gao, J., Wang, X., Lin, H., & Shen, B., Energy-exergy analysis and energy efficiency improvement of coal-fired industrial boilers based on thermal test data. *Applied Thermal Engineering*, 144, 614-627, 2018.
- [12] Tańczuk, M., Masiukiewicz, M., Anweiler, S., & Junga, R., Technical aspects and energy effects of waste heat recovery from district heating boiler slag. *Energies*, 11(4), 796, 2018.
- [13] "Transformers | Explaining The Basics of Transformers." [Online]. Available: <https://www.galco.com/comp/prod/trnsfmrs.htm>. [Accessed: 17-Feb-2020].
- [14] "BC107." [Online]. Available: [http://www.uniroma2.it/didattica/le1/deposito/SS\\_BJT\\_NPN\\_BC107\\_ST.pdf](http://www.uniroma2.it/didattica/le1/deposito/SS_BJT_NPN_BC107_ST.pdf). [Accessed: 17-Feb-2020].
- [15] "AT90S1200." [Online]. Available: <http://www.atmel.com/images/doc0838.pdf>. [Accessed: 14-Feb-2020].
- [16] "MPSA13 Darlington Transistors." [Online]. Available: [http://www.onsemi.com/pub\\_link/Collateral/MPSA13-D.PDF](http://www.onsemi.com/pub_link/Collateral/MPSA13-D.PDF). [Accessed: 17-Feb-2020].
- [17] "Atmel AT89C1051 Data Sheet." [Online]. Available: <http://www.keil.com/dd/docs/datashts/atmel/doc0366.pdf>. [Accessed: 14-Feb-2020].



# ENERGETIC ANALYSIS OF A PVT-BASED SOLAR-DRIVEN HYBRID ADSORPTION-COMPRESSION REFRIGERATION SYSTEM

Mohamed G. Gado

Energy Resources Engineering Department, Egypt–Japan University of Science and Technology (E-JUST), New Borg El-Arab City, Alexandria, Egypt, mohamed.gado@ejust.edu.eg, ORCID: 0000-0002-5293-5532

Tamer F. Megahed

Electrical Power Engineering, Egypt–Japan University of Science and Technology (E-JUST), New Borg El-Arab City, Alexandria, Egypt, mohamed.gado@ejust.edu.eg, ORCID: 0000-0003-1411-5602

Shinichi Ookawara

Energy Resources Engineering Department, Egypt–Japan University of Science and Technology (E-JUST), New Borg El-Arab City, Alexandria, Egypt; Department of Chemical Science and Engineering, Tokyo Institute of Technology, Tokyo 152-8552, Japan, email address, ORCID: 0000-0002-7912-3403

Sameh Nada

Energy Resources Engineering Department, Egypt–Japan University of Science and Technology (E-JUST), New Borg El-Arab City, Alexandria, Egypt, email address, ORCID: 0000-0002-1975-7543

Ibrahim I. El-Sharkawy

Energy Resources Engineering Department, Egypt–Japan University of Science and Technology (E-JUST), New Borg El-Arab City, Alexandria, Egypt, email address, ORCID: 0000-0003-2690-9661

*Cite this paper as:* MG. Gado, TF. Megahed, S. Ookawara, S. Nada, II. El- Sharkawy. Energetic analysis of a PVT-based solar-driven hybrid adsorption-compression refrigeration system. 9th Eur. Conf. Ren. Energy Sys. 21-23 April 2021, Istanbul, Turkey

---

**Abstract:**

In the present paper, the system performance of a solar-driven hybrid adsorption-compression refrigeration system has been investigated theoretically using the typical meteorological data of Alexandria, Egypt. The required thermal and electrical energy of the hybrid adsorption-compression refrigeration system is attained using photovoltaic/thermal (PVT) collectors. Employing a system size ratio between the adsorption system and the compression system of 3 can increase the COP from 2.9 to 5 for the compression system. Simulation results reveal that using the optimum size ratio of 7 can dramatically reduce the electricity consumption by 30.8%, as compared to the hybrid system of the size ratio of 3, which attains only energy savings of 22.1%. The utilization of PVT collectors could not only feed the hybrid system by 3.474 kWh but also could supplement the electric grid by ~100 kWh, at an optimum size ratio of 7.

---

**Keywords:**

Adsorption system; Compression system; Hybrid system; PVT

---

© 2021 Published by ECRES

## 1. INTRODUCTION

Nowadays, refrigeration and air conditioning applications are a key contributor to electricity usage, which made up 17% of the global consumed electricity [1]. Thus, enhancing the performance of a vapor compression system could play a role in decreasing the exerted electric power. One way of improving the performance of the compression system is by reducing the heat sink (condensation temperature) of the compression system. Therefore, using hybrid refrigeration systems in an attempt to diminish the intermediate temperature, could ameliorate the performance of a vapor compression refrigeration system and harvest the inherent merits of the adsorption refrigeration systems, such as operation with low driving temperatures and lack corrosion and crystallization [2,3]. Several authors have

been studied the amalgamation of adsorption refrigeration systems with compression systems. For instance, Vasta and co-authors [4] have carried out an experimental study on a hybrid adsorption-compression refrigeration system. It was found that isobutane and propane seemed to be viable alternatives for R717, R744 and R410A. Regarding using different configurations of hybrid adsorption-compression systems, Palomba et al. [5] examined series, parallel and cascade connections. Results showed that the attainable energy savings of a cascade chiller can be ameliorated in the case of the elevated temperature difference between the evaporator and condenser. Kilic and Anjirini [6] investigated the performance of a coupled adsorption-compression system using different types of refrigerants (R410A, R152A, R1234yf, R1270, and R32). It was found that HFO-R1234yf refrigerant can save electricity by about 65% compared with the used refrigerants.

Hybridizing of an adsorption refrigeration system with a vapor compression refrigeration system could share in; (i) operation at low evaporating temperatures as compared to adsorption systems, (ii) running at low heat source temperatures without a considerable performance reduction in comparison to adsorption systems, and (iii) reducing electricity bills by utilizing hybrid systems relatively with electric chillers, especially at higher condensation temperatures. This study focuses on investigating the performance of a hybrid adsorption/vapor compression refrigeration system based on PVT collectors. Herein, PVT collectors are used to covering the required power of the compressor with supplementary electricity production. Also, PVT collectors are utilized to thermally drive the adsorption subsystem.

## 2. SYSTEM DESCRIPTION AND WORKING PRINCIPLES

Fig. 1 shows the main components of the solar-assisted hybrid adsorption-vapor compression refrigeration system, which is composed of a photovoltaic/thermal solar energy subsystem, an adsorption refrigeration subsystem and a vapor compression refrigeration subsystem. Silica gel/water pair is used in the adsorption refrigeration subsystem, while R134a is presented as a working fluid for the vapor compression subsystem. The cooling capacity of an adsorption refrigeration system is about 12 kW, which is evaluated at generating, cooling and chilled water temperatures of 85°C, 30°C and 12°C, as opposed to a cooling capacity of a vapor compression refrigeration system, is about 4 kW, which is evaluated at cooling and chilled water temperatures of 30°C and -18°C. Ethylene glycol/water mixture is employed as a heat transfer fluid (HTF) to cover the product load of different applications, i.e., supermarket and cold stores. The solar energy subsystem is made up of PVT collectors, which are utilized to drive thermally the adsorption refrigeration subsystem and power electrically the vapor compression refrigeration subsystem.

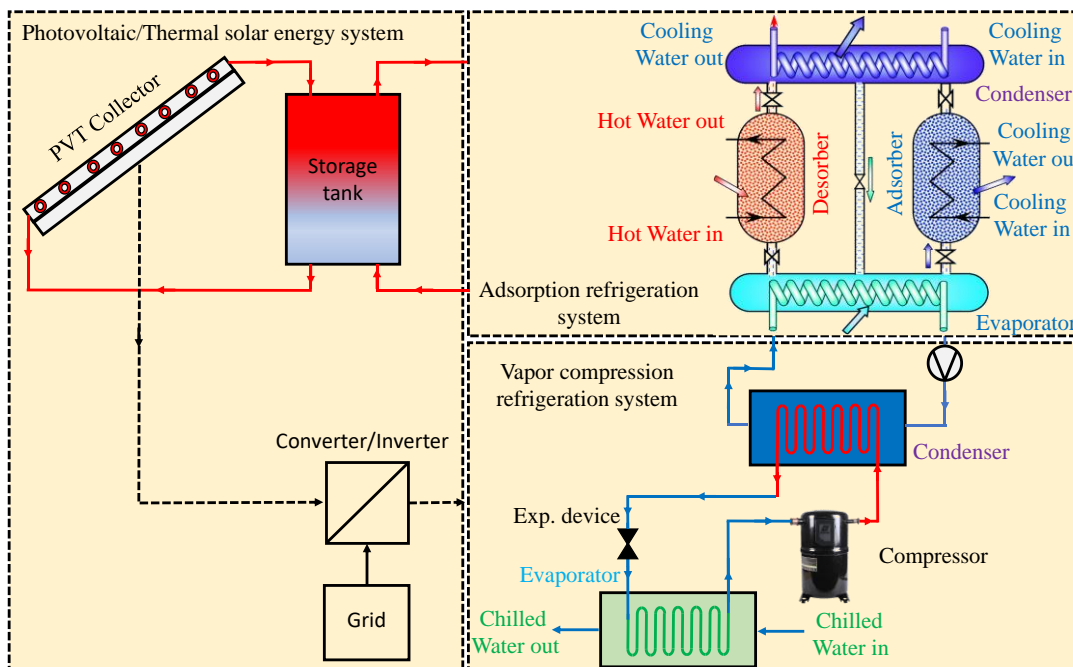


Figure 1. Hybrid adsorption-vapor compression refrigeration system integrated with photovoltaic/thermal collectors.

### 3. MATHEMATICAL MODELING

#### I. SOLAR ENERGY SUBSYSTEM

Based on meteorological data of Alexandria city in Egypt, the daily global horizontal irradiation and the dry bulb (ambient) temperature can be correlated as expressed below [7]:

$$\begin{cases} I(t) = I_{\max} \sin\left(\frac{\pi(t - t_{sr})}{t_{ss} - t_{sr}}\right) \\ T_{dbt} = \left(\frac{T_{\max} + T_{\min}}{2}\right) - \left(\frac{T_{\max} - T_{\min}}{2}\right) \cos\left(\frac{\pi}{12}(t - 1)\right) \end{cases} \quad (1)$$

where sunrise and sunset times ( $t_{sr}$  and  $t_{ss}$ ), the peak and trough temperature ( $T_{\max}$  and  $T_{\min}$ ), and peak irradiation ( $I_{\max}$ ). For photovoltaic/thermal collectors, the electric and thermal characteristics can be estimated as:

$$\begin{cases} (Mc_p)_{PVT} \frac{dT_{PVT}}{dt} = \eta_{PVT,th} I(t) A_{PVT} + \dot{m}_{PVT} c_{PVT} (T_{PVT,in} - T_{PVT,out}) \\ \eta_{PVT,th} = k_0 - k_1 \left( \frac{T_m - T_{dbt}}{I(t)} \right) - k_2 \left( \frac{(T_m - T_{dbt})^2}{I(t)} \right) \\ \eta_{PVT,el} = \eta_r [1 - \beta_r (T_{PVT} - NOCT)] \\ P_{el} = \eta_{sys} \eta_{PVT,el} I(t) A_{PVT} \end{cases} \quad (2)$$

here for monocrystalline silicon PVT collectors, reference efficiency represents  $\eta_r$  while  $\beta_r$  denotes the temperature coefficient for cell efficiency. Specifications of the selected PVT modules are proffered in ref. [8].

#### II. ADSORPTION REFRIGERATION SUBSYSTEM

The mathematical modeling of the silica gel-based adsorption system is based on solving simultaneously the adsorption isotherm, the adsorption kinetics, mass and energy balance of the system's major components, namely, an adsorber, adsorber, a condenser and an evaporator. Main operating parameters and constants are invoked from ref. [7].

#### III. VAPOR COMPRESSION REFRIGERATION SUBSYSTEM

The energy balance of both the condenser and the evaporator can be expressed as follows [9]:

$$\begin{cases} (Mc_p)_{con} \frac{dT_{con}}{dt} = \dot{m}_{ref} (h_{comp,out}^{actual} - h_{exp,in}) + \dot{m}_{cw} c_{cw} (T_{int,in} - T_{int,out}) \\ (Mc_p)_{eva} \frac{dT_{eva}}{dt} = -\dot{m}_{ref} (h_{comp,in} - h_{exp,out}) + \dot{m}_{chw} c_{chw} (T_{chw,in} - T_{chw,out}) \end{cases} \quad (3)$$

The following expressions can be used to compute the compressor power, refrigerant mass flow rate as given below:

$$\begin{cases} P_{el} = \dot{m}_{ref} (h_{comp,in} - h_{comp,out}) \\ \dot{m}_{ref} = V_{st} \eta_v RPM \rho_{comp,in} \\ h_{exp,in} = h_{exp,out} \end{cases} \quad (4)$$

where  $V_{st}$ ,  $\rho_{comp,in}$  and RPM refer to the compressor stroke volume, suction density and the revolution per minute.

#### IV. PERFORMANCE CHARACTERISTICS

Integrating the adsorption refrigeration system with the compression system is executed via energy balance between the evaporator of the adsorption system and the condenser of the compression system [4–6]:

$$Q_{eva}^{ads} = Q_{con}^{comp} \quad (5)$$

$$Size\ Ratio\ (SR) = \frac{Q_{eva,ads}}{Q_{eva,VC}} \quad (6)$$

To conceive to what extent how the used hybrid system is beneficial, the performance of hybrid adsorption-vapor compression refrigeration system in terms of cyclic average COP and the mean energy savings is calculated based on:

$$\left\{ \begin{array}{l} COP_{VC} = \frac{Q_{eva,VC}}{P_{el,VC}} \\ COP_{ads} = \frac{Q_{eva,ads}}{Q_{gen,ads}} \\ ES = \frac{P_{el,VC} - P_{el,hybrid}}{P_{el,VC}} \times 100 \end{array} \right. \quad (7)$$

#### 4. RESULTS AND DISCUSSION

The developed mathematical model for the hybrid adsorption-compression refrigeration system is performed using MATLAB/SIMULINK and REFPROP. Sequential S-functions are employed for invoking the thermodynamic properties of the working fluids. Herein, ODE15s functions are utilized as a solver of the ordinary differential equations. The hybrid system is driven with 60 PVTs (total aperture area of 98 m<sup>2</sup>). The total adsorption cycle time repeats itself each quarter-hour, comprising comprises preheating time (30 s), desorption time (420 s), pre-refrigeration time (30 s) and adsorption time (420 s). The system performance is examined using the meteorological data for Alexandria, Egypt (Latitude of 31.2°N and Longitude of 29.9°E).

#### V. MODEL VALIDATION

Both adsorption and vapor compression subsystems are independently validated to confirm the reliability of the mathematical model. In the case of the adsorption system, the dynamic modeling of the system is validated with experimental data of Saha et al. [10]. Whilst, for the compression system validation, it is clear from Fig. 2 that an adequate consistency between the experimental and simulation results, with an average deviation between the predicted and the experimental data of the coefficient of performance, is about 6.4%.

#### VI. PROPER INTEGRATION AND HEAT BALANCE VERIFICATION

To envisage the thermal balance of the hybrid system operation, which is recognized by the energy balance between the evaporator of the topping cycle (adsorption cycle) and the condenser of the bottoming cycle (compression cycle), Eq. 5 is employed. This dynamic coincidence is exhibited in Fig. 3. by conspicuously revealing not only the discontinuity of the refrigeration capacity of the adsorption refrigeration system (dynamic behavior) compared to the approximately constant value of the condensation power for the compression system (steady-state behavior) but also the equivalence of the average values of this heat rate as recognized by Eq. 5.

#### VII. PERFORMANCE INVESTIGATION OF THE HYBRID SYSTEM

Fig. 4 reveals the temperature histories of the hybrid system chief elements, namely the adsorption system's elements: PVT collector, storage tank, desorber, adsorber, condenser and evaporator; and compression system's elements: condenser and evaporator. The storage tank temperature is given a driving temperature and it is varying according to the daily solar radiation and the thermal inertia of the solar system, while the cooling water inlet temperature is taken as 30°C. The chilled inlet temperature is taken as -18°C for the evaporator of the compression system. It can be observed from Fig. 4 that the storage tank temperature reaches its maximum value (~67°C) at 2 pm, which corresponding to a minimum intermediate temperature of ~13°C. This significantly can result in enhancing the system performance of the compression system. Accordingly, as the intermediate temperature decreases to 13°C as compared to the conventional compression system, in which its intermediate temperature is 30°C, the compressor power drastically reduces. Fig. 5 indicates that the minimum attainable compression power is 1.00 kW as compared to 1.37 kW of the conventional system.

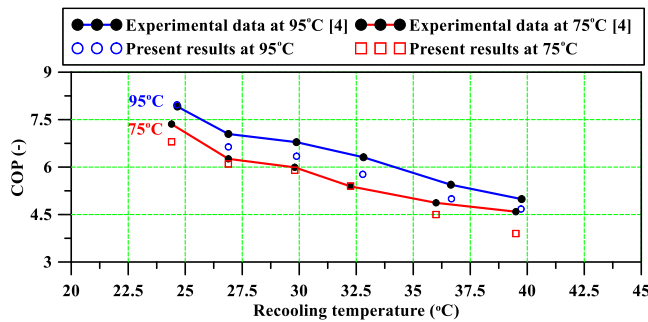


Figure 2. Mathematical model validation against experimental data of Vasta et al. [4] for the compression system.

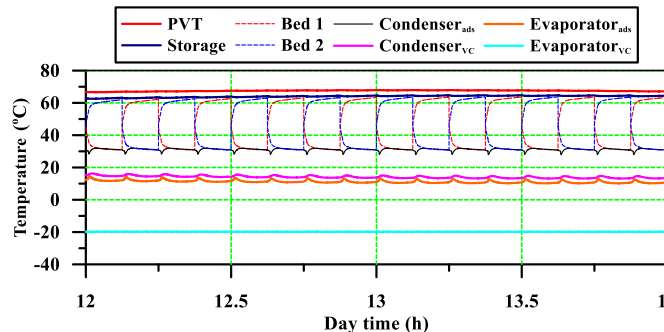


Figure 4. Temperature profiles for the hybrid system major components for Alexandria during July.

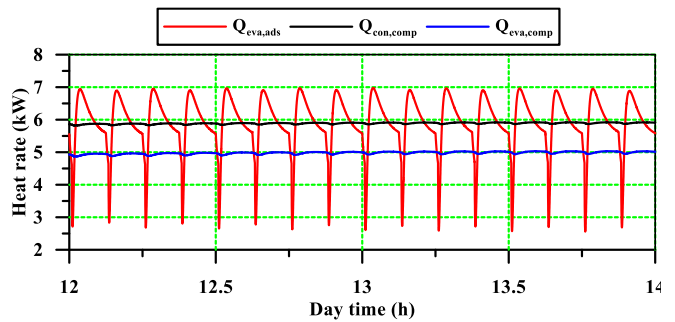


Figure 3. Equivalence of the cooling capacity of the adsorption system with condensation power of the compression system.

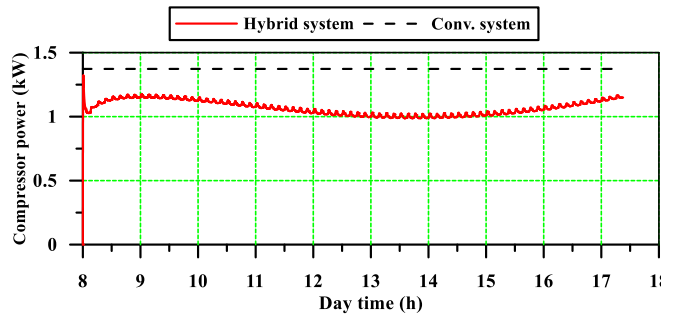


Figure 5. Comparison between the compression power for both the hybrid system and the conventional system.

The coefficient of performance for the conventional compression, the hybrid compression and adsorption system are shown in Fig. 6. The cycle COP of the adsorption system increases to an average cyclic value of  $\sim 0.7$  at the late hours of the day. The higher value of the COP for the adsorption system might be attributed to the higher values of the evaporation temperature of the adsorption system (intermediate temperature  $\sim 13^\circ\text{C}$ ). Whereas, the COP of the hybrid system increases and then decreases, following the solar system radiation and the thermal inertia of the hot storage tank. It achieves a peak COP of 5 as opposed to the COP of 2.9 of the conventional compression systems. Fig. 7 exhibits the daily resulted variation of the energy savings of the hybrid system during July using the meteorological data of Alexandria. It can be seen the hybrid system could attain a maximum energy savings of 27% at 2 pm, which coincides with the peak driving temperature and minimum intermediate temperature. Overall, the hybrid system could achieve a daily averaged energy savings of 22.1%.

## VIII. OPTIMUM MATCHING AND INTEGRATION

To attain the optimum performance of the hybrid system, SR is varied over a wide range (3:7). The size ratio between the adsorption system and the compression system is changed till reach the minimum possible intermediate temperature (the freezing limit of water  $\sim 5^\circ\text{C}$ ) and as a result lead to a profoundly better performance of the compression system. Fig. 8 shows that the maximum attainable energy savings (30.8%) are obtained at SR of 7, while SR of 3 attains minimum energy savings of 22.1%. Therefore, in this study, it is preferable to operate the system beyond SR of 7. Also, Fig. 9 exhibits the daily electricity production of PVT collectors for various size ratios between the adsorption and the compression system, which are used basically to cover the required electricity of the hybrid system and the remainder is fed to the electric grid. It can be observed that the SR of 7 could generate electricity of 103.3 kWh, which is used to cover the requisite electricity of the hybrid system (3.474 kWh). The surplus electricity of 100 kWh is supplied to the grid. It is worth mentioning that the SR of 3 requires 10 kWh to drive the hybrid system and PVT collectors can produce 108 kWh.

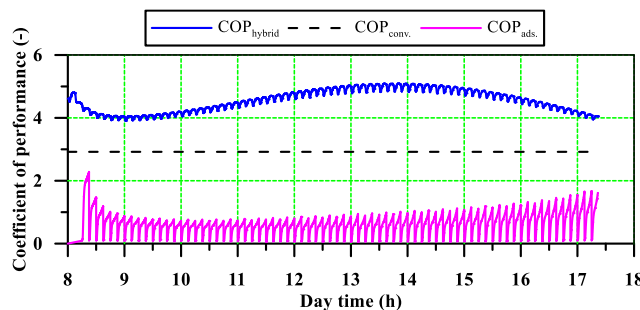


Figure 6. Cyclic variation of the system performance indicators throughout the day for Alexandria during July.

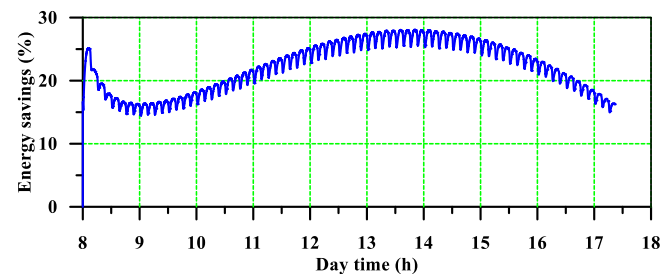


Figure 7. Cyclic variation of the attained energy savings throughout the day for Alexandria during July.

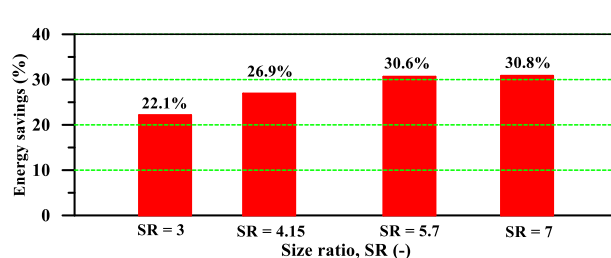


Figure 8. Energy savings for different proposed size ratios.

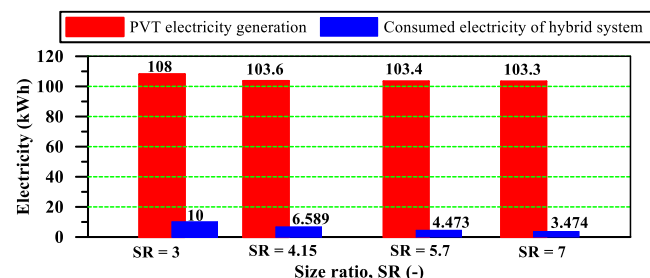


Figure 9. PVT electricity generation and the required electricity for the hybrid system at different size ratios.

## 5. CONCLUSION

In this paper, a simulation program is developed and validated against experimental data. The influence of the system size ratio was investigated to examine the system performance in terms of COP and ES for the hybrid adsorption-compression refrigeration system. Based on the simulation key findings, the following conclusion can be drawn:

- The hybrid system at the size ratio of 3 yields a minimum compression power of 1.0 kW as compared to 1.37 kW for the conventional compression system.
- Simulation results show the maximum COP for the hybrid system is about 5 as compared to 2.9 for a conventional compression system, while maximum adsorption COP is about 0.7 for SR of 3.
- The hybrid system can substantially save electricity by 22.1% at SR of 3 and significantly improves this value to 30.8% at the optimum SR of 7.

## REFERENCES

- [1] Liu X, Qu M, Liu X, Wang L. Membrane-based liquid desiccant air dehumidification: A comprehensive review on materials, components, systems and performances. *Renewable and Sustainable Energy Reviews* 2019;110:444–66.
- [2] Younes MM, El-Sharkawy II, Kabeel AE, Saha BB. A review on adsorbent-adsorbate pairs for cooling applications. *Applied Thermal Engineering* 2017;114:394–414.
- [3] Gado M, Elgendi E, Elsayed K, Fatouh M. Performance enhancement of an adsorption chiller by optimum cycle time allocation at different operating conditions. *Advances in Mechanical Engineering* 2019;11:1–12.
- [4] Vasta S, Palomba V, La Rosa D, Mittelbach W. Adsorption-compression cascade cycles: An experimental study. *Energy Conversion and Management* 2018;156:365–75.
- [5] Palomba V, Dino GE, Fazzica A. Coupling sorption and compression chillers in hybrid cascade layout for efficient exploitation of renewables: Sizing, design and optimization. *Renewable Energy* 2020;154:11–28.
- [6] Kilic M, Anjrini M. Comparative performance analysis of a combined cooling system with mechanical and adsorption cycles. *Energy Conversion and Management* 2020;221:113208.
- [7] El-Sharkawy II, AbdelMeguid H, Saha BB. Potential application of solar powered adsorption cooling systems in the Middle East. *Applied Energy* 2014;126:235–45.
- [8] DualSun - EN - Datasheet DualSun - EN - Datasheet 2019.
- [9] Ali SM, Chakraborty A, Leong KC. CO<sub>2</sub>-assisted compression-adsorption hybrid for cooling and desalination. *Energy Conversion and Management* 2017;143:538–52.
- [10] Saha BB, Boelman EC, Kashiwagi T. Computer simulation of a silica gel-water adsorption refrigeration cycle - the influence of operating conditions on cooling output and COP. *ASHRAE Transactions* 1995;101:348–57.



# TESTING THE ABRASION RESISTANCE OF BROADBAND ANTI-REFLECTION COATINGS FOR SOLAR MODULES

Sibel Yilmaz

Duzce University, Duzce, TURKEY, sibelyilmaz@duzce.edu.tr, ORCID: 0000-0001-5591-7818

Adam Michael Law

Loughborough University, Leicestershire, UK, a.law@lboro.ac.uk, ORCID: 0000-0002-3031-0355

John Michael Walls

Loughborough University, Leicestershire, UK, j.m.walls@lboro.ac.uk, ORCID: 0000-0003-4868-2621

Cite this paper as:

*Yilmaz, S, Law, AM, Walls, JM. Testing the abrasion resistance of broadband anti-reflection coatings for solar modules. 9<sup>th</sup> Eur. Conf. Ren. Energy Sys. 21-23 April 2021, Istanbul, Turkey*

**Abstract:** Reflection from the front glass of solar modules causes over 4% optical loss leading to a significant decrease in module efficiency. Single layer solution gelation (sol-gel) anti-reflective (AR) coatings are effective over a narrow range of wavelengths, whereas reflection losses can be reduced over a broader wavelength when multilayer broadband AR coatings are applied. In this work, three different multilayer AR coatings including 4-layer SiO<sub>2</sub>/ZrO<sub>2</sub>, 4-layer SiO<sub>2</sub>/ITO, and 6-layer SiO<sub>2</sub>/ZrO<sub>2</sub> were deposited using magnetron sputtering. Abrasion resistance is important because the coatings will be subject to regular cleaning cycles. A variety of abraders including Felt pad, CS-10 and CS-8 under different loads are used. The optical performance and durability of these coatings were analysed using a spectrophotometer, Optical Microscope, Scanning Electron Microscope, and Scanning White Light Interferometer. No damage was observed after abrasion of the coatings with a Felt pad under 1 and 2 N loads. However, there was slight increase in Weighted Average Reflection. When coatings were tested with CS-10 and CS-8 abraders, coatings with ZrO<sub>2</sub> resulted in lower scratch resistance in comparison to coating with ITO. It was concluded that all-dielectric broadband AR coatings were more durable and have better optical performance compared to single layer sol-gel coatings.

**Keywords:** Anti-reflection (AR) coating, photovoltaic (PV), abrasion resistance

© 2021 Published by ECRES

## 1. INTRODUCTION

Generating electricity from photovoltaic (PV) systems is becoming a mainstream energy source. As deployment of solar increases, PV asset managers are starting to focus on operation and management (O&M) issues including the long-term durability and costs of maintenance. Losses in efficiency caused by the module cover glass are a major problem in solar utilities. The reflection losses from the front surface due to the refractive index difference between air and the glass substrate is >4% which limits the current generation from PV modules [1]. Single layer anti-reflective (AR) coatings are used in the PV industry and have gained significant market share to mitigate reflection losses [2], [3]. Application of an AR coating can decrease these optical losses and increase the power output. However, the durability of the AR coatings exposed outdoors is a significant issue since PV modules are warranted for between 25 and 30 years [4], [5]. Single layer silica coatings rely on the introduction of voids to achieve a low refractive index. The voids introduce vulnerability to water ingress and also reduce abrasion resistance [6]. Multilayer, all-dielectric, AR coatings have been developed to overcome these limitations [7]. There are several techniques for depositing AR coatings such as solution gelation (sol-gel), thermal evaporation, sputtering, and electron beam [8], [9]. Single layer sol-gel AR coatings are commonly used in the PV industry due to their low cost and fast manufacturing [9]; however, they minimise reflection at a single wavelength [9]. Sol-gel deposition methods require a low refractive index material, which can lead to lower scratch resistance [6]. Improving the scratch resistance of the sol-gel AR coatings may increase the refractive index and reduce the AR effect [6]. The mechanical properties such as hardness of coatings depend on the thickness of the material, where the hardness

decreases with increasing the thickness [10]. Multilayer AR coatings consist of pairs of materials with high and low refractive index. Silicon dioxide ( $\text{SiO}_2$ ) has a refractive index of 1.46 at 550 nm wavelength and it is commonly used as a low refractive index material.  $\text{SiO}_2$  is chemically stable, scratch resistant [11]. There is a variety of high refractive index materials including zirconium dioxide ( $\text{ZrO}_2$ ) or titanium dioxide ( $\text{TiO}_2$ ) [6]. Zr-based materials have high hardness, good wear resistance and improved temperature stability [12]. It is a crucial step to select the proper material for high index optical properties and durability of the coating. Multilayer AR coatings are widely used in the ophthalmic industry to reduce reflection [13], however further investigation is required to adapt these coatings for use on PV modules. Three different coatings were used in this study, designated ‘A’, ‘B’ and ‘C’ (Table 1). Coating A was designed to be deposited onto the superstrate of thin film cadmium telluride ( $\text{CdTe}$ ) solar cells to reduce the reflection losses. It is a 4-layer multilayer AR coating composed of  $\text{SiO}_2$  and  $\text{ZrO}_2$  [6]. Coating B was optimized to be AR within the required wavelength range for silicon (Si) solar cells and this coating also limits the increase in the module temperature via reflecting infra-red (IR) radiation. Lower operating temperatures will lead to an increase in efficiency. The coating has 4-layer structure using  $\text{SiO}_2$  and indium tin oxide (ITO) [14]. In Si solar cells, increased operating temperature is responsible for a significant loss in efficiency [15]. To address this issue, coating B which reflects IR radiation was examined. Coating C is a 6-layer AR coating for use on Si solar cells. It comprises  $\text{SiO}_2$  and  $\text{ZrO}_2$  materials. [16] It is possible to modify these multilayer AR coating designs for other PV absorber materials. The performance and durability of these multilayer AR coatings, deposited using pulsed-DC magnetron sputtering, have been investigated. Pulsed-DC magnetron sputtering deposits hard, dense thin films with excellent uniformity. It is possible to control the thickness of each layer with time only using computer control. Abrasion resistance tests have been conducted to evaluate the durability of these coatings. Abrader materials including Felt pad, CS-10 and CS-8, all of which are used in industrial standard tests to simulate the effects of cleaning processes. The tests with a Felt pad were adapted from BS EN 1096 [17]. A Felt pad abrader is the least aggressive material used in this study. Whereas, a CS-10 abrasive material is a rubber pad which applies a mild to medium abrasion and CS-8 abrader provides a medium abrasion [18]. A spectrophotometer, Optical Microscope, Scanning Electron Microscope (SEM), and Scanning White Light Interferometer (SWLI) were used to investigate the optical and mechanical performance of the coatings.

## 2. EXPERIMENTAL

Multilayer AR coatings were deposited at Loughborough University using pulsed-DC magnetron sputtering. A “PV Solar” system (from PowerVision, Ltd.) was used to deposit AR coatings on 5x5 cm soda lime glass substrates. [19] The substrates were placed on a rotating carrier and then loaded into the deposition chamber via a load lock. Multilayer broadband AR coatings investigated in this study are listed in Table 1.

*Table 1 Multilayer AR Coatings and their applications*

Coating	Description	Application
A	AR 4-layer $\text{SiO}_2/\text{ZrO}_2$	Thin film $\text{CdTe}$ solar cells
B	AR/IR 4-layer $\text{SiO}_2/\text{ITO}$	Si solar cells
C	AR 6-layer $\text{SiO}_2/\text{ZrO}_2$	Si solar cells

A Taber abrader (5900 reciprocating abrader) was used to test the linear abrasion resistance of the multilayer AR coatings. Felt pad, CS-10 and CS-8 were used as abrader materials for simulating the cleaning process. The stroke length was 30 mm, and speed was set as 60 cycles per minute. A range of loads from 1 N to 10 N was applied for 50 cycles. Following the abrasion resistance tests, the coatings were cleaned with de-ionized (DI) water and a brush to remove excess material. A Varian Cary 5000 UV-Vis-NIR spectrophotometer was used to measure the reflectance of the coatings before and after the abrasion resistance tests. The wavelength range was between 200 to 1200 nm. Eq. [1] was used to calculate the WAR from the measured data [20].

$$WAR (\lambda_{min}, \lambda_{max}) = \int_{\lambda_{min}}^{\lambda_{max}} \frac{\phi \cdot R}{R} d\lambda \quad (1)$$

An Olympus CX41 optical microscope was used to observe the surface degradation of the coatings. The magnification of the lenses was x10. An Infinity 2 camera and Infinity Analyse software were used to obtain the images. A Jeol 7100 F and Leo 1530 VP Field Emission Gun (FEG)- SEM were used to analyse the surface damage caused to the coatings. The samples were pasted with silver on metal stubs and then a sputter coater was used to

coat a palladium-gold alloy layer on the coatings prior to SEM measurements. A Bruker NPFlex SWLI was used to characterize the surface roughness of the coatings before and after the scratch resistance tests. Three-dimensional (3D) images were generated, and the roughness profile parameters were calculated.

### 3. RESULTS

In this study, three types of coatings have been investigated. A Felt pad abrader material was applied to the coatings with a force of 1 N for 50 strokes with a speed of 60 cycles per minute and a stroke length of 30 mm. There was no visible damage observed. The WAR measurements showed no serious degradation as shown in Table 2.

*Table 2 WAR measurements of Coating A, B and C after abrasion resistance tests*

Abrader	Load	Increase in WAR (%)		
		Coating A	Coating B	Coating C
Felt pad	1 N	0.07	0	0
CS10	1 N	1.5	0.12	0.14
CS10	2 N	2.26	0.44	0.23
CS8	1 N	3.2	0.7	0.61

A CS-10 abrasive material simulates a mild to medium abrasion. This material was used for the scratch resistance testing under 1 N and 2 N loads. The increase in WAR is due to minor damage to the multilayer AR coating after the testing. The CS-8 medium abrader showed a more serious increase in the WAR measurements. Figure 1 presents the optical microscope images of the surface of Coating C; abraded with a Felt pad, CS-10 and CS-8 respectively under 1 N load.



*Figure 1 Optical Microscope images of Coating C abraded with (a) Felt pad, (b) CS-10, (c) CS-8. 1 N force was applied.*

The images show that coatings were not severely damaged after the abrasion resistance tests. Coating B abraded with Felt pad, CS-10 and CS-8 under 1 N load and the optical microscope images are shown in Figure 2.



*Figure 2 Optical Microscope images of Coating B abraded with (a) Felt pad, (b) CS-10, (c) CS-8. 1 N force was applied.*

It was anticipated that more damage would be observed on Coating B compared to Coating A or C due to the inclusion of ITO layers. ITO is not as hard as ZrO<sub>2</sub>. Coating B was abraded with a Felt pad under 1 N, 10 N load, and CS-8 under 1 N load. SEM images of the abraded surfaces are shown in Figure 3.

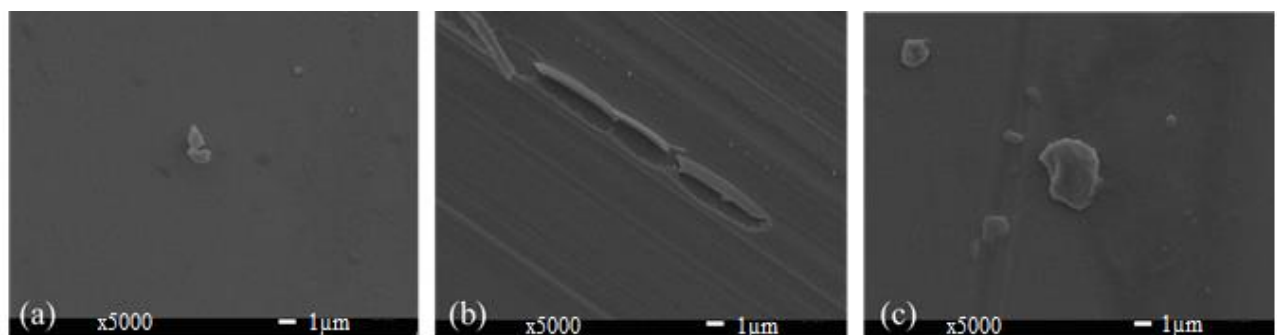


Figure 3 SEM images showing the defects on Coating B after abrasion with (a) Felt pad under 1 N load, (b) Felt pad under 10 N load, (c) CS-8 under 1 N load

When the Felt pad abrader was applied with a force of 1 N, there were no defects observed on Coating B. However, when the force increased to 10 N, the coating peeled. The CS-8 abrader under 1 N load also caused scratches on the coating. A Felt pad and the CS-8 abrader materials were used with the linear abrasion tester to simulate the cleaning effect on Coating C. The Felt pad abrader was applied under 1 N and 10 N loads and CS-8 was tested with a force of 1N. The SEM images are shown in Figure 4 (a), (b), and (c) respectively.

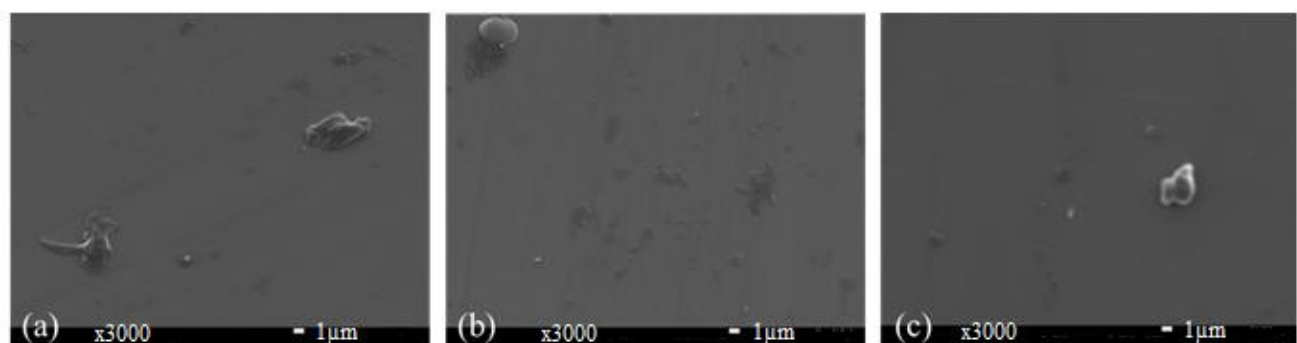


Figure 4 SEM images showing the defects on Coating C after abrasion with (a) Felt pad under 1 N load, (b) Felt pad under 10 N load, (c) CS-8 under 1 N load

The images do not show any scratches or damage to the coatings. It was observed that while Coating B showed severe defects on the coatings, Coating C was more stable after abrasion tests due to its higher scratch resistance. SWLI was used to analyse the surface roughness of Coating A, B and C after abrasion with the linear abrasion tester. The roughness profile parameters were calculated. The width, maximum depth and mean depth parameters of all three coatings abraded with CS-10 under 1 N load are given in Table 4.

Table 4 Profile parameters of the scratches observed with SWLI

Parameters	Coating A	Coating B	Coating C
Width (μm)	5.364	0.612	5.324
Maximum depth (μm)	0.323	0.075	0.445
Mean depth (μm)	0.265	0.071	0.423

The width of the scratches on Coating A and C were over 5 μm, whereas it was only 0.612 μm for Coating B. The maximum depth was higher for Coating C and A compared to Coating B.

3D images were generated to observe the scratches on the coatings. Figure 5 indicates the roughness of Coating B and C after abrasion with the Felt pad and CS-8 under applied force of 1 N.

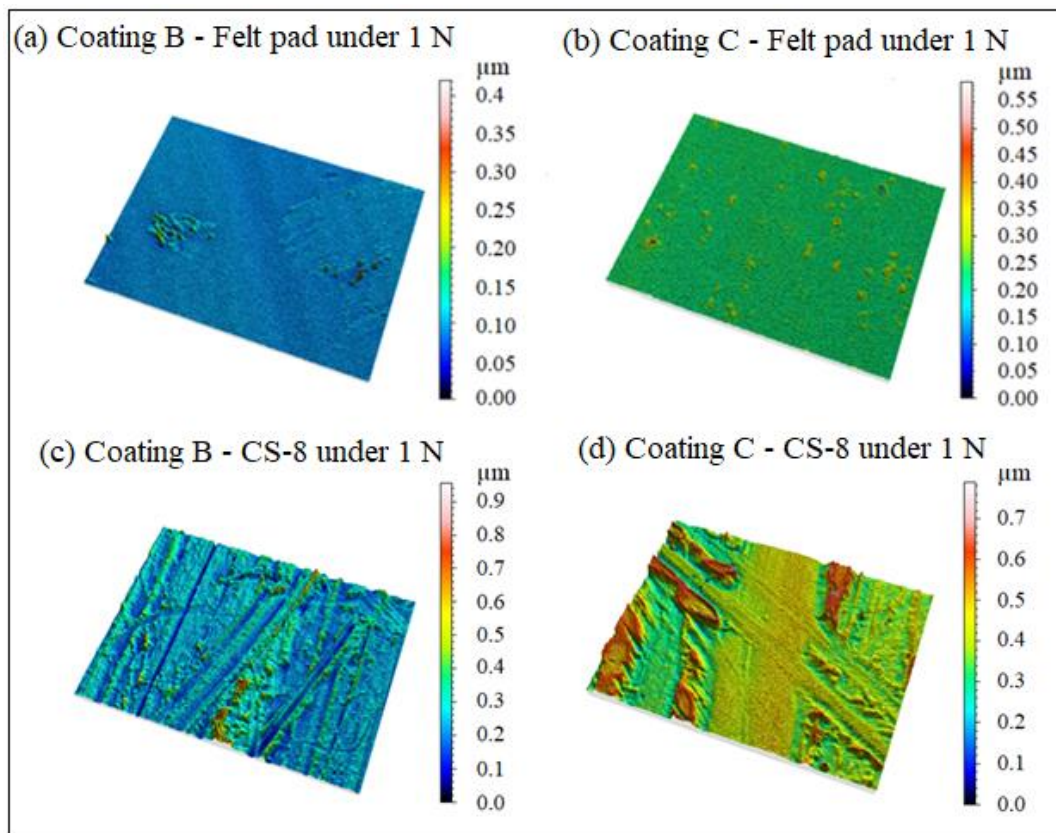


Figure 5 SWLI images showing the scratches after abrasion under 1 N load (a) Coating B with Felt pad, (b) Coating C with Felt pad, (c) Coating B with CS-8, and (d) Coating C with CS-8.

The coatings remained quite smooth under 1 N load with a Felt pad. CS-8 is an aggressive material; therefore, it is not surprising that there were several scratches observed on both coatings. It was found that roughness increases when more aggressive abrader materials are used.

#### 4. CONCLUSIONS

Improving the performance and durability of multilayer AR coatings is potentially important for the PV industry. These coatings can reduce the reflection losses and improve module efficiency. It is important that these coatings withstand environmental stresses and are durable to withstand the cleaning processes applied during maintenance. In this study, three different coatings were examined using a linear abrasion tester with a variety of abraders under different loads to investigate the effect of cleaning processes on multilayer AR coatings. Reflectance was measured with a spectrophotometer and the WAR was calculated. The WAR of coatings abraded with a Felt pad under 1 N load were largely undamaged. However, increasing the applied force during tests does increase the WAR for all coatings. Using CS-10 and CS-8 abraders increases the WAR due to minor defects or scratches caused to the multilayer AR coatings. Optical microscope images show that minor scratches occurred on coating C, whereas there was more severe damage observed on Coating B. This may be due to the inclusion of ITO which has inferior hardness to  $\text{ZrO}_2$ . SEM was used to characterise surface damage occurring on Coating B abraded with a Felt pad under a 1N load. No damage was observed. When a 10 N load was applied, the coating was damaged, and peeling was observed. Scratches were observed after abrasion with CS-8 under 1 N load. Coating A and C did not show significant damage after testing with the abrader. The surface roughness of Coating B and C were smooth after abrasion with a Felt pad under 1N load, however, the roughness and the depth of scratches increased when a CS-8 abrader was used. It was unexpected that the maximum depth of the scratches on Coating A and C was higher compared to Coating B. However, a larger number of scratches were observed on Coating B. Residues from the abrader material or other particles such as dust may be responsible for the higher measurement of the scratches of Coating B. The surface roughness of each coating increased when more aggressive abrader materials used. These results demonstrate that using more aggressive abraders or higher loads caused more surface damage and increased surface roughness. The WAR increased for all coatings after the linear abrasion resistance test. This study shows similar observations with the findings on durability of Coating A, a 4-layer  $\text{SiO}_2/\text{ZrO}_2$  [21]. Moreover, it was

extended to analyse and compare the results with Coating B composed of 4-layer SiO<sub>2</sub>/ITO and with Coating C, a 6-layer SiO<sub>2</sub>/ZrO<sub>2</sub>. The outcomes obtained from this study demonstrate that Coating A and C resulted in lower scratch resistance compared to Coating B. However, multilayer AR coatings are more resilient and scratch resistant than single layer sol-gel AR coatings. Their adoption by glass or module manufacturers would improve the performance and lifetime of PV panels. These coatings will now be tested in outdoor conditions in Turkey to correlate outdoor environmental tests with accelerated laboratory tests.

## REFERENCES

- [1] Gupta, P, Pandey, A, Vairagi, K and Mondal, SK. Solving Fresnel equation for refractive index using reflected optical power obtained from Bessel beam interferometry. *Rev. Sci. Instrum.* 2019; 90:1, pp. 015110. doi: 10.1063/1.5043240.
- [2] Vincent, A, Babu, S, Brinley, E, Karakoti, A, Deshpande, S, Seal, S. Role of Catalyst on Refractive Index Tunability of Porous Silica Antireflective Coatings by Sol-Gel Technique. *J. Phys. Chem. C* 2007; 111:23, pp. 8291–8298. doi: 10.1021/jp0700736.
- [3] Chhajed, S, Schubert, MF, Kim, JK, Schubert, EF. Nanostructured multilayer graded-index antireflection coating for Si solar cells with broadband and omnidirectional characteristics. *Appl. Phys. Lett.* 2008; 93:25, pp. 251108. doi: 10.1063/1.3050463.
- [4] Prieto-Castrillo, F, Núñez, N, Vázquez, M. Warranty assessment of photovoltaic modules based on a degradation probabilistic model. *Prog. Photovoltaics Res. Appl.* 2020; 28:12, pp. 1308–1321. doi: 10.1002/pip.3328.
- [5] Sevinc, PC, Albayrak, FS, Bagriyanik, M, Batman, A. Lifetime and Efficiency Concerns of a Photovoltaic Power. In: ECRES 2015 3. European Conference on Renewable Energy Systems; 07-10 October 2015, pp. 1-6.
- [6] Womack, G, Kaminski, PM, Abbas, A, Isbilir, K, Gottschalg, R, Walls, JM. Performance and durability of broadband antireflection coatings for thin film CdTe solar cells. *J. Vac. Sci. Technol. A Vacuum, Surfaces, and Films.* 2017; 35:2, pp. 021201. doi: 10.1116/1.4973909.
- [7] Phillips, BM, Jiang, P. Biomimetic Antireflection Surfaces., In: Lakhtakia A, Martin-Palma RJ, editors. *Engineered Biomimicry*, MA, USA: Elsevier, 2013. pp. 305–331.
- [8] Mehmood, U, Al-Sulaiman, FA, Yilbas, BS, Salhi, B, Ahmed, SHA, Hossain, MK. Superhydrophobic surfaces with antireflection properties for solar applications: A critical review. *Sol. Energy Mater. Sol. Cells* 2016; 157, pp. 604–623. doi: 10.1016/j.solmat.2016.07.038.
- [9] Shanmugam, N, Pugazhendhi, R, Madurai Elavarasan, R, Kasiviswanathan, P, Das, N. Anti-Reflective Coating Materials: A Holistic Review from PV Perspective. *Energies* 2020; 13:10, pp. 2631. doi: 10.3390/en13102631.
- [10] Chen, D. Anti-reflection (AR) coatings made by sol–gel processes: A review. *Sol. Energy Mater. Sol. Cells* 2001; 68:3–4, pp. 313–336. doi: 10.1016/S0927-0248(00)00365-2.
- [11] Ali, K, A. Khan, S, Jafri, MZM. Effect of Double Layer (SiO<sub>2</sub>/TiO<sub>2</sub>) Anti-reflective Coating on Silicon Solar Cells. *Int. J. Electrochem. Sci.* 2014; 9, pp. 7865–7874.
- [12] Ul-Hamid, A. The effect of deposition conditions on the properties of Zr-carbide, Zr-nitride and Zr-carbonitride coatings – a review. *Mater. Adv.* 2020; 1:5, pp. 988–1011. doi: 10.1039/D0MA00232A.
- [13] Walls, M. Optical coatings for ophthalmic lenses by reactive magnetron sputtering. In: OSA 2001 Opt. Interference Coatings Conference; 15 July 2001: OSA, Washington, D.C.: pp. ThD1.
- [14] Law, AM, Kaminski, PM, Isherwood, PJM, Michael Walls, J. An Infra-red Reflecting Optical Coating for Solar Cover Glass. In: 2019 46<sup>th</sup> Photovoltaic Specialists Conference; 16-21 June 2019: IEEE, OR, Canada, pp. 1913-1918.
- [15] Javed, A. The Effect of Temperatures on the Silicon Solar Cell. *Int. J. Emerg. Technol. Comput. Appl. Sci. ( IJETCAS )* 2014; 3:9, pp. 305–308.
- [16] Law, AM, Wright, LD, Smith, A, Isherwood, PJM, Walls, JM. 2.3% Efficiency Gains for Silicon Solar Modules Using a Durable Broadband Anti-reflection Coating. In: 2020 47<sup>th</sup> Photovoltaic Specialists Conference; 15-21 August 2020; IEEE; pp. 0973-0975.
- [17] BS EN 1096-2:2012. Glass in building - Coated glass Part 2: Requirements and test methods for class A, B and S coatings. 2012.
- [18] ASTM D4060. Standard Test Method for Abrasion Resistance of Organic Coatings by the Taber Abraser. 2014.
- [19] Lisco, F *et al.* High rate deposition of thin film cadmium sulphide by pulsed direct current magnetron sputtering. *Thin Solid Films* 2015; 574, pp. 43–51. doi: 10.1016/j.tsf.2014.11.065.
- [20] Lind, MA, Pettit, RB, Masterson, KD. The Sensitivity of Solar Transmittance, Reflectance and Absorptance to Selected Averaging Procedures and Solar Irradiance Distributions. *J. Sol. Energy Eng.* 1980; 102:1, pp. 34–40. doi: 10.1115/1.3266119.
- [21] Newkirk, JM *et al.* Artificial linear brush abrasion of coatings for photovoltaic module first-surfaces. *Sol. Energy Mater. Sol. Cells* 2021; 219, pp. 110757. doi: 10.1016/j.solmat.2020.110757.



# HYBRID DEDICATED OUTDOOR AIR SYSTEM IN BUILDINGS

Dararat Tongdee

Naresuan University, Phitsanulok, Thailand, dararatt59@nu.ac.th, ORCID: 0000-0003-2357-6857

Somchai Maneewan

Naresuan University, Phitsanulok, Thailand, somchaim@nu.ac.th, ORCID: 0000-0003-4767-2536

Chantana Punlek

Naresuan University, Phitsanulok, Thailand, chantanap@nu.ac.th, ORCID: 0000-0003-4397-1571

*Cite this paper as:* Tongdee, D, Maneewan, S, Punlek, C. *Hybrid dedicated outdoor air system in buildings. 9<sup>th</sup> Eur. Conf. Ren. Energy Sys. 21-23 April 2021, Istanbul, Turkey*

**Abstract:** The dedicated outdoor air system (DOAS) was developed from HVAC technology for improving the indoor air quality and increasing the fresh air in buildings. The various equipment was applied to the DOAS in different method such as heat wheel, thermoelectric, silica gel and water tube. In this paper, we propose data analysis and control performance of a hybrid dedicated outdoor air system in the building. The hybrid dedicated outdoor air system is specifically designed with a composite desiccant unit and thermoelectric module. The designed system is intended to monitor and control indoor environmental factors such as temperature, humidity, and carbon dioxide ( $\text{CO}_2$ ) concentrations. The designed system is trialed under the corresponding ASHREA 62.2 and indoor air quality standard (IAQs) by the set of conditions. The experimental result indicates that the temperature and humidity in the comfort zone, due to the developed system are approximately 27 °C and 57% respectively. Moreover, the  $\text{CO}_2$  level is controlled lower than 1000 ppm accordingly indoor air quality standard by hybrid dedicated outdoor air system. Therefore, the proposed system can effectively work and is suitable for application in buildings.

**Keywords:** Indoor Air Quality, Dedicated Outdoor Air System, Hybrid dedicated Outdoor Air System

© 2021 Published by ECRES

## 1. INTRODUCTION

Recently, the thermal comfort and indoor environment inside buildings are the popular topic in many researches due to their effect that affect human health, comfort and work performance. The Dedicated Outdoor Air System (DOAS) is one of the Heating, Ventilation, and Air Conditioning system (HVAC) that developed for improving the hot air, humidity and other indoor environmental factors. The different technology and equipment are applied to the DOAS to increase the better performance such as application of material for dehumidification in DOAS [1-4], and testing heat wheel and enthalpy wheels [5,6]. Moreover, there are a number of studies that intended to examine DOAS in conception part. For instance, a novel model predictive control for a DOAS-assisted Separated Sensible and Latent Cooling (SSLC) system was developed to optimize energy saving and improve indoor thermal comfort. The experiment in this study evaluates control performance [7]. The DOAS-assisted SSLC system consists of another secondary cooling coil that uses higher-temperature chilled water to deal with the remaining sensible load. It was found that this system could control indoor humidity better than the conventional single coil system [8]. To enhance the system energy efficiencies of the next-generation dedicated outdoor air-cooling systems, Chen *et al.* [9] propose the innovative systems that coupled with energy recovery and renewable energy system. This paper analyzes the equipment performance for selecting the equipment parameter value to boost the system energy performance.

For this research, we proposed the control of a hybrid dedicated outdoor air system. The presented system can control the indoor environmental factors like temperature, humidity, and  $\text{CO}_2$  concentrations for improving indoor thermal comfort and environment by a combination of thermoelectric and composite desiccant units. The collected data is used to analyze and determine the effects of the designed system and control performance.

## 2. HYBRID DEDICATED OUTDOOR AIR SYSTEM FEATURE

The architecture of the hybrid dedicated outdoor air system and its feature are presented in this section. The design, control, operation of hybrid dedicated outdoor air system and results was shown in below respectively.

### Hybrid dedicated outdoor air system design:

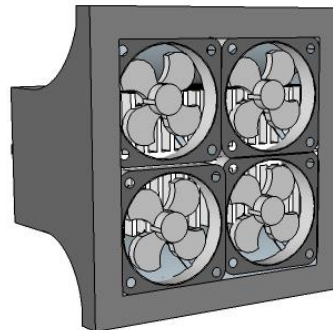


Figure 1. The structure of hybrid dedicated outdoor air system.

Table 1. The specification of thermoelectric module in hybrid dedicated outdoor air system

Material Types	$Q_{max}$ (W)	$V_{max}$ (V)	$\Delta T_{max}$ ( $^{\circ}$ C)	$R(\Omega)$	Number of TEC (n)	Ref.
TEC-Module 12712	120	15.4	75	1.05	12	[10]

The designed system was developed based on the dedicated outdoor air system. This system was 30 cm x 30 cm x 16 cm respectively as shown in figure 10. It was specially designed by using thermoelectric and dehumidification units. The silica + LiCl is coated on heat sink in both sides of the Thermoelectric for air inlet moisture removal. The 12 modules of thermoelectric cooling model 12712 were used to reduce the temperature of the air inlet by the cold side and regenerate the desiccant unit by the hot side. In addition, the fan units and thermoelectric modules can switch mode for the pre-cooling and regeneration process. When the desiccant unit of each side is saturated, the system will switch mode automatically to regenerate the dessicant on the heat sink.

Table I shows the specifications of the thermoelectric modules in the experiment. The power supply of thermoelectric had around 12-15 V and can produce  $\Delta T = 45$   $^{\circ}$ C. The thermoelectric system combined with the dessicant unit to improve indoor surroundings.

### Hybrid dedicated outdoor air system control:

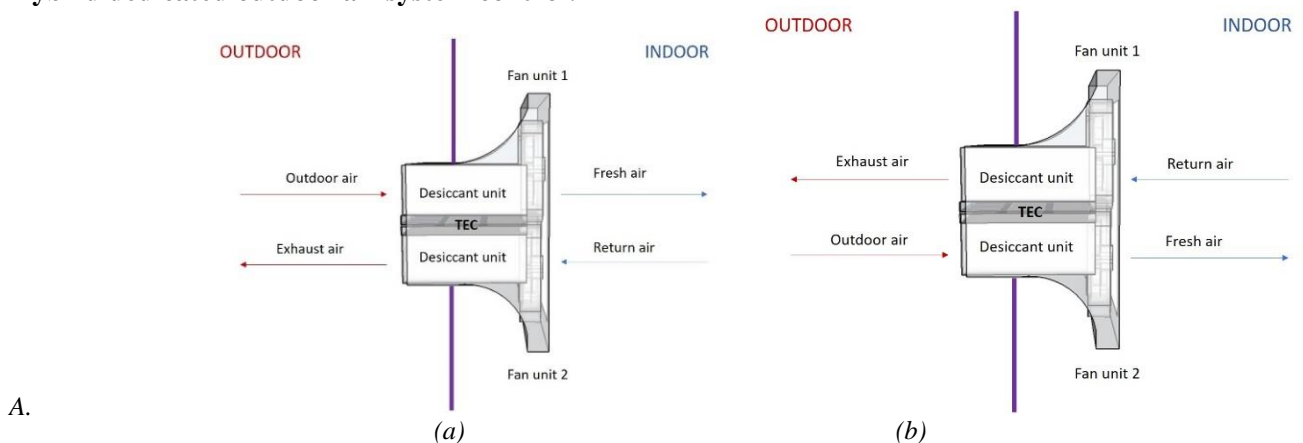


Figure 2. The operation of hybrid dedicated outdoor air system: (a) the hybrid dedicated outdoor air system on. (b) switch mode for regeneration process.

Table 2. The set of experimental condition

Conditions	Description
Fan	12 V/4 modules
Thermoelectric	12 V/12 modules
Composite desiccant	Silica + LiCl
Heat sink	Size 30 cm x 30 cm x 16 cm
Weather location	Phitsanulok, Thailand
Period of experiment	November – December

The operation of hybrid dedicated outdoor air system combined the dedicated outdoor air process to improve the indoor environment and regeneration process to remove moisture out of desiccant. These processes are presented in figure 2 (a) and (b).

The system was controlled under conditions as shown in Table II. Table II shows the set of conditions that used in the experimental study. The hybrid dedicated outdoor air system was run to evaluate the performance of system for 30 days in the Thai winter. The outdoor air temperature and humidity in the period of the experiment ranges from 25 °C to 32 °C and from 60% to 74% respectively. The 12 modules of thermoelectric are designed to be parallel by four sets of eight serialized modules, operated at 12 V, and producing the maximum temperature of the hot side and the cold side around 62 °C and 17 °C respectively. The indoor temperature, humidity, including the CO<sub>2</sub> level are controlled to the thermal comfort zone by depending on the ASHARE standard 62.2 and indoor air quality standard.

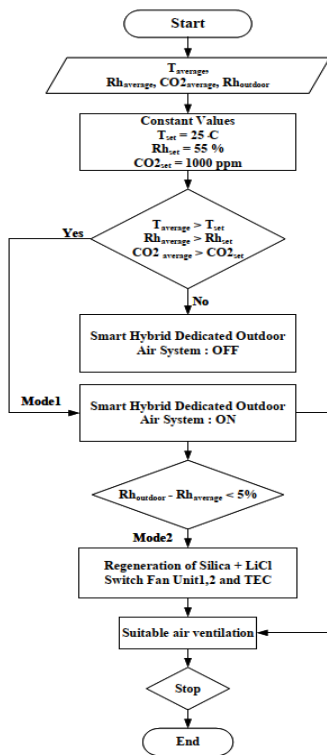


Figure 3. Flowchart of hybrid dedicated outdoor air system work.

The flowchart of hybrid dedicated outdoor air system operation is shown in figure 3. When the average values of indoor environmental factors such as temperature, humidity and CO<sub>2</sub> concentrations increase more than the set point, the hybrid dedicated outdoor air system is operated and controlled by the user. The fan unit 1 and 2 of designed system are working in Mode1. Then the dedicated outdoor air is pre-cooled and dehumidified simultaneously by cold side of thermoelectric and Silica + LiCl composite desiccant on heat sink respectively. Whenever the system is continued working until the dessicant is saturated according to set condition. Then the system operates in Mode2. The fan unit 1,2 and thermoelectric are switched in this mode to regenerate Silica + LiCl composite dessicant. These processes operate until the room is comfortable.

**Results and Analysis:** The experimental results of the hybrid dedicated outdoor air system are separated into two cases such as thermal comfort and indoor air quality evaluation, and dehumidification process.

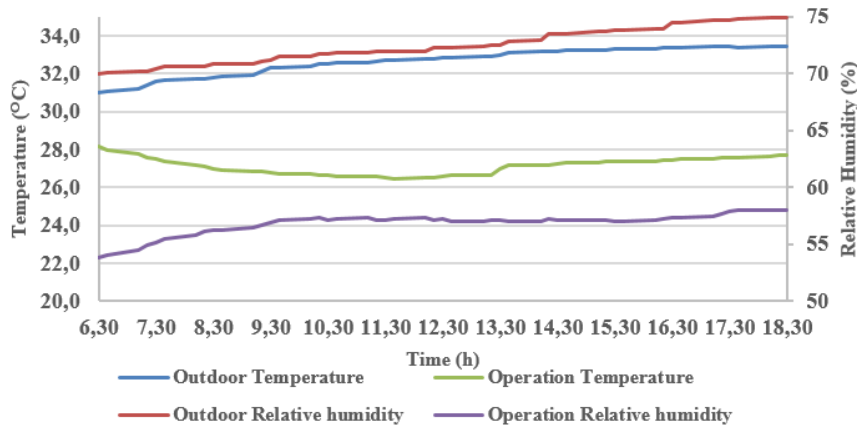


Figure 4. Indoor humidity and temperature controlled by hybrid dedicated outdoor air system.

### 1) Thermal comfort and Indoor Air quality evaluation

In this part, we investigate the thermal comfort and indoor air quality that influences the occupants of the building. The temperature, humidity, and CO<sub>2</sub> concentrations are observed in this experiment. These parameters are measured under the free air flow rate for 12 hours. The hybrid dedicated outdoor air system is run at 12 V. The reduction of the outdoor temperature and humidity is presented in figure 4. The result shows that the proposed system can decrease outdoor temperature and humidity around 5 °C and 15% under the boundary condition. The average of outdoor temperature and humidity during of the 30 days is approximately 32 °C and 72%. Moreover, the average operation temperature and humidity (fresh air) is operated is approximately 27 °C and 57% respectively.

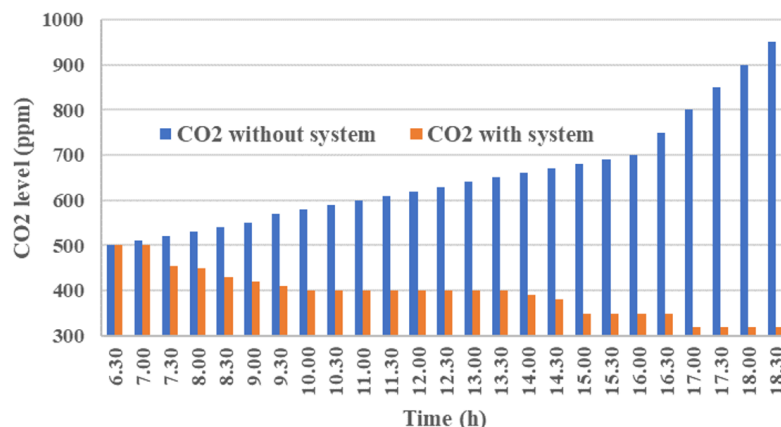


Figure 5. CO<sub>2</sub> concentrations controlled by hybrid dedicated outdoor air system.

Figure 5 shows the performance of the designed system to reduce the CO<sub>2</sub> levels. The capability of average CO<sub>2</sub> reduction is around 270 ppm. In addition, the average CO<sub>2</sub> during the day is approximately 650 ppm. Consequently, we summarize that the performance of hybrid dedicated outdoor air system is quite suitable for decreasing the indoor CO<sub>2</sub> levels due to the CO<sub>2</sub> reducing capability.

### 1)2) Dehumidification Process

In the air dehumidification process, the Silica + LiCl is a composite desiccant for desiccant coated heat sink to remove moisture out of the air inlet. The uptake water of Silica + LiCl composite adsorbent improved by 30-45% [11] compared with pure silica gels. Furthermore, the recovery temperature and ambient relative humidity for Silica + LiCl regeneration range from 52.3-71.3°C and 55-73% [12]. Therefore, the thermoelectric hot side is chosen for the

regeneration of the desiccant in this study. The experimental results show the dehumidification capacity of the system is approximately 20.83%.

$$2) \quad \eta = \frac{Rh_{bf} - Rh_{af}}{Rh_{bf}} \times 100 \quad (1)$$

Eq. [1] describes the efficiency of the dehumidification process of Silica + LiCl composite dessicant. Where  $\eta$  is the efficiency of moisture removal of the composite desiccant unit.  $Rh_{bf}$  and  $Rh_{af}$  represent the relative humidity of before and after operating system.

### 3. CONCLUSION

This study focuses on the development of a hybrid dedicated outdoor air system for the building. The proposed system was specially designed to improve indoor environmental factors by an integration of thermoelectric and dessiccant units. The thermal comfort and indoor air quality were evaluated to estimate the control performance of the system. The result shows that the proposed system can enhance the indoor environment factors of the building. Thus, the hybrid dedicated outdoor air system is suitable for monitoring and control the indoor environment without risk of the sick building syndrome.

### ACKNOWLEDGMENT

The authors would like to thank the International Research Network (IRN5703PHDW02), Thailand Science Research and Innovation for financial support in this research. The authors are also grateful to Physics Department, Faculty of Science, Naresuan University for the use of their laboratory in this experiment.

### REFERENCES

- [1] Yau, Yat H. Application of a heat pipe heat exchanger to dehumidification enhancement in a HVAC system for tropical climates-a baseline performance characteristics study. *International Journal of Thermal Sciences* 2007; 46: 164-171 <<https://doi.org/10.1016/j.ijthermalsci.2006.02.006>>
- [2] Han, Xing, Zhang, Xu, Wang, Lihui, Niu, Runping. A novel system of the isothermal dehumidification in a room air-conditioner. *Energy and Buildings* 2013; 57: 14-19 <<https://doi.org/10.1016/j.enbuild.2012.10.039>>
- [3] X.H. Liu, Y. Jiang, K.Y. Qu. Heat and mass transfer model of cross flow liquid desiccant air dehumidifier/regenerator. *Energy Conversion and Management* 2007; 48(2): 546-554 <<https://doi.org/10.1016/j.enconman.2006.06.002>>
- [4] W. Zhu, et al. In situ performance of independent humidity control air conditioning system driven by heat pumps. *Energy and Buildings* 2010; 42: 1747-1752 <<https://doi.org/10.1016/j.enbuild.2010.05.010>>
- [5] Jia, Jie, Lee, W.L., Chen, Hua. Modeling and Experimental study of performance of a dry cooling and dedicated ventilation (DCDV) system under different space cooling load conditions. *Energy Conversion and Management* 2013; 73: 158-166 <<https://doi.org/10.1016/j.enconman.2013.04.017>>
- [6] Ling, Jiazen, Kuwabara, Osamu, Hwang, Yunho, Radermacher, Reinhard. Enhancement options for separate sensible and latent cooling air-conditioning systems. *International journal of refrigeration* 2013; 36: 45-57 <<https://doi.org/10.1016/j.ijrefrig.2012.09.003>>
- [7] Yang, Shiyu, Wan, Man Pun, Ng, Bing Feng, Dubey, Swapnil, Henze, Gregor P., Chen, Wanyu, Baskaran, Krishnamoorthy .Experiment study of model predictive control for an air-conditioning system with dedicated outdoor air system. *Applied Energy* 2020; 257: 1–15 <<https://doi.org/10.1016/j.apenergy.2019.113920>>
- [8] Gatley DP. Dehumidification enhancements for 100-percent-outside-air AHUs, Part 3. Heating/piping/air Condition. Eng. 2000; 72(11): 31–5.
- [9] Chen, Tianyi, Norford, Leslie. Energy performance of next-generation dedicated outdoor air-cooling systems in low-energy buildings operations. *Energy and Buildings* 2020; 209: 1-17 <<https://doi.org/10.1016/j.enbuild.2019.109677>>
- [10] TEC-12712 Datasheet. Accessed: Jan. 30, 2020. [Online]. Available: <https://datasheet4u.com/datasheet-pdf/HB/TEC1-12712/pdf.php?id=1399931>
- [11] Hu L., Ge T., Jiang Y., et al.. Hygroscopic property of metal matrix composite desiccant. *Journal of Refrigeration* 2014; 35: 69–75 <<http://dx.doi.org/10.3969/j.issn.0253-4339.2014.02.069>>
- [12] Rambhad, K.S. and Walke, P.V.. Regeneration of composite desiccant dehumidifier by parabolic trough solar collector: An experimental investigation. *Materials Today: Proceedings* 2018; 5: 24358-24366 <<https://doi.org/10.1016/j.matpr.2018.10.231>>



# ENERGY ANALYSIS OF VAPOR COMPRESSION REFRIGERATION CYCLE USING A NEW GENERATION REFRIGERANTS WITH LOW GLOBAL WARMING

Rabah Touaibi

Laboratory of Industrial Fluids, Measurements and Applications (FIMA), Djilali Bounaama University, Ain Defla, Algeria, ORCID: 0000-0003-1236-0516

Koten Hasan

Mechanical Engineering Department, Istanbul Medeniyet University, Istanbul, 34700, Turkey, ORCID: 0000-0002-1907-9420

*Rabah, T, Koten, H. Energy analysis of vapor compression refrigeration cycle using a new generation refrigerants with low Global Warming, 9<sup>th</sup> Eur. Conf. Ren. Energy Sys. 21-23 April 2021, Istanbul, Turkey*

**Abstract:** An energy analysis study studied on a vapor compression refrigeration cycle using refrigerants with low GWP of the Hydro-Fluoro-Olefin (HFO) type, in particular R1234yf and R1234ze fluids to replace HFC refrigerants . Computer code was developed using software for solving engineering equations to calculate performance parameters; for this, three HFC type fluids (R134a, R404A and R410A) were selected for a comparative study. The results showed that R1234ze is the best refrigerant among those selected for the mechanical compression refrigeration cycle. The thermodynamic analysis showed the effect of the evaporator temperature (-22 °C to 10 °C) and the condenser temperature (30 °C to 50 °C) on the steam cycle performance. Compression refrigeration, including the coefficient of performance. The results showed that the HFO-R1234ze with low GWP gives the best coefficient of performance of 3.14 close to that of the R134a fluid (3.17). In addition, R1234ze is considered an alternative fluid to R134a for their ecological properties.

**Keywords:** New generation, refrigeration cycle, energy analysis, ecological properties, GWP

© 2021 Published by ECRES

Nomenclature	
$h$	specific enthalpy, kJ/kg
$\dot{m}$	Masse flow rate, kg/s
$\dot{Q}$	Heat rate, kW
$T$	Temperature, °C
$\dot{W}$	Mechanical Power, kW
Subscripts	
$Comp$	Compressor
$Cond$	Condenser
$Evap$	Evaporator
$Ev$	Expansion valve
$in$	Input
$out$	Output
Abbreviations	
ODP	Ozone depletion potential
GWP	Global warming potential
HFC	Hydrofluorocarbon
HFO	Hydrofluoroolefin

## 1. INTRODUCTION

Antunes et al (2016) presented an experimental study of a refrigeration system to replace HCFC-22 with other refrigerants as similar studies [1-9]. Mota-Babiloni et al (2017). Have proposed R32 to replace R410A, especially in residential air conditioning systems; they also showed that R32 has good heat transfer characteristics compared to R410A and other lower GWP alternatives [10]. Fang et al presented a work which presents a thermodynamic cycle studies. Comparisons were made regarding the performance of the ejector under various operating conditions and the proportions of the refrigerant mixture. R1234yf seems to be a good candidate for the immediate replacement of R134a [11]. Belman-Flores et al. modeled a refrigeration system to compare three refrigerants: R134a, R450A and R513A. The results show that R450A has a slightly lower cooling capacity than R134a, which represents a 10% reduction in cooling capacity [12-15]. Following bibliographic research, current research is migrating to natural refrigerants. The objective of this work is to make an energy analysis of a vapor compression refrigeration cycle using two new generation low GWP fluids (R1234yf and R1234ze) by comparing its performance when it works with fluids that are characterized by a high GWP.

## 2. METHODOLOGY

### Description of system

The vapor compression refrigeration system is given in Figure 1.

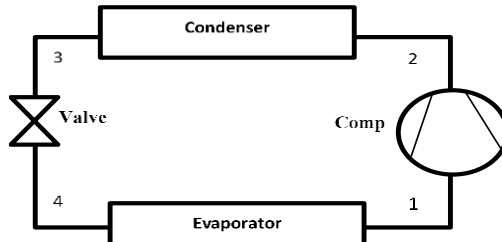


Figure 1. Schematic diagram of vapor compression refrigeration

### Thermodynamic analysis

In this section, governing equations are defined as follows [16-18]:

$$\sum \dot{m}_{in} = \sum \dot{m}_{out} \quad (1)$$

Where,  $\dot{m}$  is in (kg/s),

The energy balance:

$$\sum \dot{m}_{in} h_{in} + \sum \dot{Q}_{in} + \sum \dot{W}_{in} = \sum \dot{m}_{out} h_{out} + \sum \dot{Q}_{out} + \sum \dot{W}_{out} \quad (2)$$

The energy analysis of the Vapor Compression Refrigeration Cycle requires the application of the first law of thermodynamics. The general equations corresponding to this principle are presented below (Table 1):

Table 1. Energy balance of vapor compression refrigeration cycle.

Components	Energy balance equations
Compressor	$\dot{m}_1 h_1 + \dot{W}_{Comp} = \dot{m}_2 h_2$
Condenser	$\dot{m}_2 h_2 = \dot{m}_3 h_3 + \dot{Q}_{Cond}$
Expansion valve	$\dot{m}_3 h_3 = \dot{m}_4 h_4$
Evaporator	$\dot{m}_4 h_4 + \dot{Q}_{Evap} = \dot{m}_1 h_1$
Mass balance	$\dot{m}_1 = \dot{m}_2 = \dot{m}_3 = \dot{m}_4 = \dot{m}$

Cycle performance equations:

$$\sum \dot{m}_{in} h_{in} + \sum \dot{Q}_{in} + \sum \dot{W}_{in} = \sum \dot{m}_{out} h_{out} + \sum \dot{Q}_{out} + \sum \dot{W}_{out} \quad (3)$$

### 3. STUDIES

The result of unit using different refrigerants have been studied in order to see the performance of some new generation low GWP refrigerant (R1234yf, R1234ze) compared to other HFC type fluids (R134a, R404A and R407C), the thermodynamic properties of these refrigerants are listed in Table 2.

Table 2. Thermodynamic properties of the refrigerants

Refrigerants	Type	GWP	ODP
R134a	HFC	1430	0
R404A	HFC	2088	0
R407C	HFC	1774	0
R1234yf	HFO	4	0
R1234ze	HFO	7	0

The study was made on a vapor compression refrigeration cycle with cooling capacity  $\dot{Q}_{\text{Evap}} = 10 \text{ kW}$  and under the following conditions:  $T_{\text{Cond}} = 30^\circ\text{C}$  and  $T_{\text{Evap}} = -20^\circ\text{C}$ . It was found from the calculation results found (Table 3) that the new generation refrigerants with low GWP, in particular R1234yf and R1234ze, give good coefficients of performance compared to those of the HFC type. Subsequently, a parametric study was carried out in order to see the effect of certain parameters on the performance of the steam refrigeration cycle using the various refrigerants in order to see the effect of the use of new generation refrigerants, which have a low GWP compared to other HFC refrigerants.

Table 3. Performance of the vapor refrigeration cycle for different refrigerants.

Fluid	$\dot{m} [\text{kg/s}]$	$\dot{Q}_{\text{Cond}} [\text{kW}]$	$\dot{W}_c [\text{kW}]$	COP [-]
R134a	0.06905	13.15	3.15	3.174
R404A	0.08983	13.50	3.50	2.857
R407C	0.06465	13.68	3.678	2.719
R1234yf	0.09038	13.30	3.304	3.026
R1234ze	0.07765	13.18	3.181	3.143

The importance of the evaporation temperature on the different quantities of the refrigeration cycle has been studied in this section, in particular the coefficient of performance, mass flow of the refrigerant, mechanical power of the compressor and the thermal power of the condenser using the various HFO and HFCs refrigerants. Figure 2 shows the effect of the evaporation temperature on the coefficient of performance using three HFC fluids (R134a, R404A and R407C) and two new generation HFO fluids (R1234yf and R1234ze). The results show that the coefficient of performance of the vapor compression refrigeration cycle increases with the increase in the evaporation temperature of each fluid used, of the HFC or HFO type. An important discovery on the results showed that HFO (R1234yf and R1234ze) gives good performance coefficients like R134a compared to other HFC fluids (R404A and R407C). The results also show that the two HFO fluids give a good coefficient of performance for positive refrigeration (air conditioning). The two fluids R1234yf and R1234ze give a coefficient of performance which approximates the coefficient of performance of the fluid R134a (3.17); R1234ze fluid gives a performance coefficient of 3.14; the advantage of the latter is that this fluid has a low GWP value (7) compared to the R134a fluid (1430). The results also show that the coefficient of performance increases with increasing evaporation temperature over the interval  $[-20^\circ\text{C}; 10^\circ\text{C}]$  for all fluids studied. The coefficient of performance of the R1234ze fluid of low GWP over the temperature range  $[-20^\circ\text{C}; 10^\circ\text{C}]$  increases from 3.14 to 10.2.

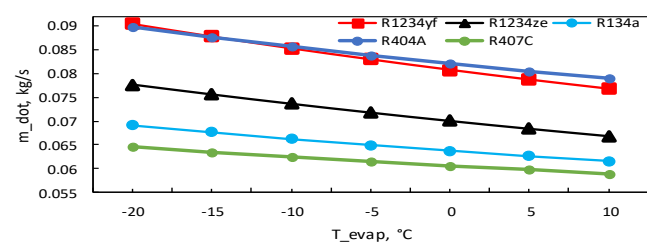
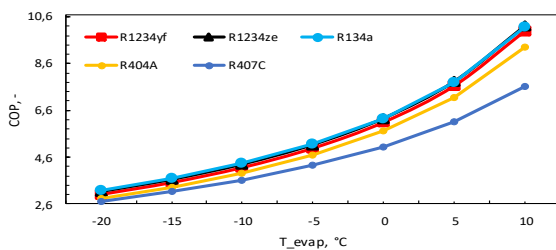


Figure 2. Variation of the coefficient of performance as a function of the evaporation temperature. Figure 3. Variation in mass flow as a function of evaporation temperature.

Figure 3 shows the effect of the evaporation temperature on the mass flow rate using three HFC fluids (R134a, R404A and R407C) and two new generation HFO fluids (R1234yf and R1234ze). The results show that the mass flow rate decreases with the increase in the evaporation temperature of each fluid used, of the HFC or HFO type. It should also be noted that the R1234ze fluid uses a lower mass flow rate compared to the R1234yf and R134a fluids. The mass flow rate required to supply the vapor compression refrigeration cycle decreases from 0.077 kg/s to 0.66 kg/s over the interval of the evaporation temperature [-20 °C; 10 °C]. Figure 4 shows the effect of the evaporation temperature on the mechanical power consumed by the compressor of the vapor compression refrigeration cycle using three HFC fluids (R134a, R404A and R407C) and two fluids of the new generation of types HFO (R1234yf and R1234ze). The results show that the mechanical power consumed by the mechanical compressor decreases with the increase in the evaporation temperature of each fluid used, of the HFC or HFO type. It should also be noted that, when working with the R1234ze fluid, the refrigeration cycle does not consume much energy at the mechanical compressor compared to other fluids of the HFC type and also compared to the R1234yf. The results also show that the vapor compression refrigeration cycle consumes less energy for positive temperatures, which shows that the system consumes less for positive refrigeration. For R1234ze fluid the mechanical power of the compressor decreases from 3.18 kW to 0.98 kW over the evaporative temperature range [-20 °C; 10 °C].

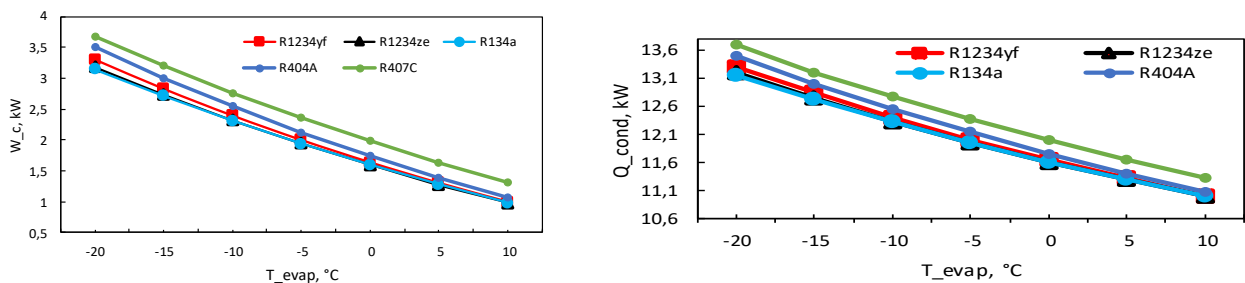


Figure 4. Variation of the mechanical power of the compressor as a function of the evaporation temperature. Figure 5. Variation of the condenser power as a function of the evaporation temperature.

Figure 5 shows the effect of the evaporation temperature on the thermal power transferred to the condenser level of the vapor compression refrigeration cycle using three HFC fluids (R134a, R404A and R407C) and two new generation HFO fluids (R1234yf and R1234ze). The results show that the thermal power transferred by the condenser decreases with the increase in the evaporation temperature of each fluid used, of the HFC or HFO type. It should also be noted that, when working with R1234ze fluid, the refrigeration cycle gives thermal energy to the condenser compared to other HFC type fluids and also compared to R1234yf fluid. For the R1234ze fluid, the results show that the power at the level of the condenser transferred to the external medium decreases from 13.18 to 10.98 over the temperature range [-20 °C, 10 °C]. Figure 6 shows the effect of the condensation temperature on the coefficient of performance using three HFC fluids (R134a, R404A and R407C) and two new generation HFO fluids (R1234yf and R1234ze). The results show that the coefficient of performance of the vapor compression refrigeration cycle decreases with the increase in the condensation temperature of each fluid used, of the HFC or HFO type. An important discovery on the results showed that HFO (R1234yf and R1234ze) gives good performance coefficients like R134a compared to other HFC fluids (R404A and R407C). The results also show that the two HFO fluids give a good coefficient of performance. The R1234ze fluid gives a good coefficient of performance compared to the R1234yf fluid. For R1234ze, the results show that the coefficient of performance decreases from 3.14 to 1.86 over the condensing temperature range [30 °C; 50 °C].

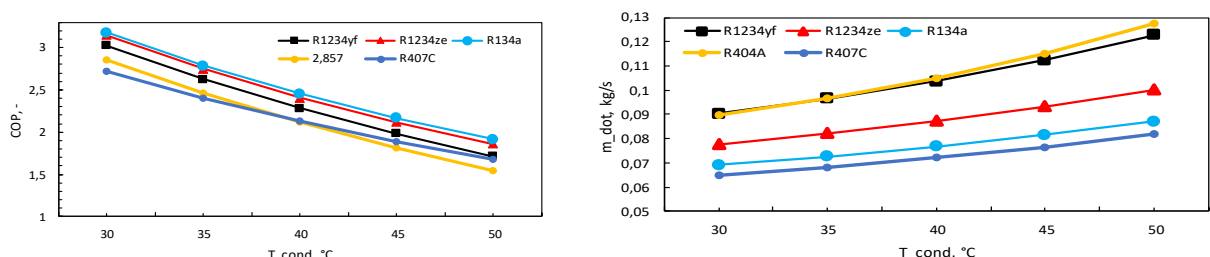


Figure 6. Variation of the coefficient of performance as a function of the condensing temperature. Figure 7. Variation in mass flow as a function of condensing temperature.

Figure 7 shows the effect of the condensing temperature on the mass flow using three HFC fluids (R134a, R404A and R407C) and two new generation HFO fluids (R1234yf and R1234ze). The results show that the mass flow rate increases with the increase in the condensation temperature of each fluid used, of the HFC or HFO type. It should also be noted that the R1234ze fluid uses a mass flow rate lower than that of the R1234yf and R134a fluids. For the R1234ze fluid the mass flow rate required to supply the vapor compression refrigeration cycle increases from 0.077 kg / s up to 0.1 kg / s over the condensing temperature range [30°C, 50 °C]. Figure 8 shows the effect of the condensing temperature on the mechanical power consumed by the compressor of the vapor compression refrigeration cycle using three HFC fluids (R134a, R404A and R407C) and two new generation HFO fluids (R1234yf and R1234ze). The results show that the mechanical power consumed by the mechanical compressor increases with the increase in the condensation temperature of each fluid used, of the HFC or HFO type. It should also be noted that, when working with the R1234ze fluid, the refrigeration cycle does not consume much energy at the mechanical compressor compared to other fluids of the HFC type and also compared to the R1234yf fluid. The results also show that the vapor compression refrigeration cycle consumes less energy for low condensing temperatures, which shows that the system consumes less for one at low condensing temperatures. For the R1234ze fluid, the results show that the mechanical power required to supply the compressor for the refrigeration cycle increases from 3.18 to 5.37.

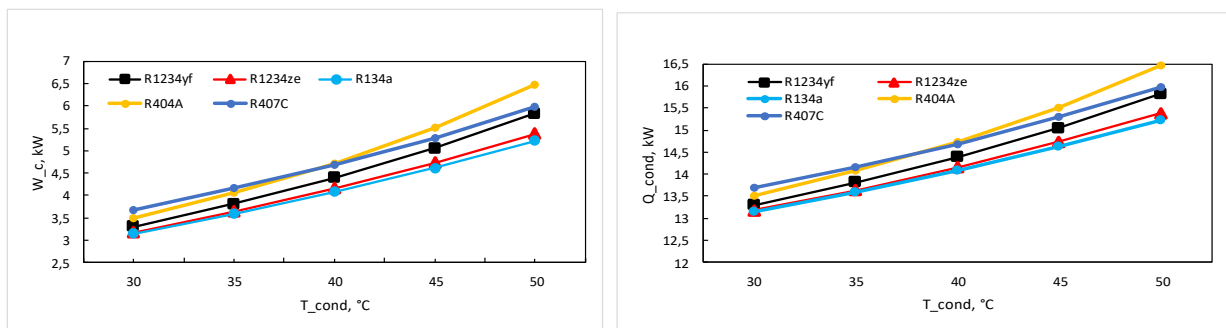


Figure 8. Variation of the mechanical power of the compressor as a function of the condensing temperature. Figure 9 Variation of condenser power as a function of condensing temperature.

Figure 9 shows the effect of the condensation temperature on the thermal power transferred to the condenser of the vapor compression refrigeration cycle using three HFC fluids (R134a, R404A and R407C) and two new generation HFO fluids ( R1234yf and R1234ze). The results show that the thermal power transferred by the condenser increases with the increase in the condensation temperature of each fluid used, of the HFC or HFO type. It should also be noted that, when working with R1234ze fluid, the refrigeration cycle gives thermal energy to the condenser compared to other HFC type fluids and also compared to R1234yf fluid. For the R1234ze fluid, the results show that the power at the condenser level increases from 13.18 kW to 15.38 kW.

#### 4. CONCLUSION

A comparative analysis of the performance of certain refrigerants to see the new generation performance at low GWP of HFO refrigerants (R1234yf and R1234ze) compared to other HFC fluids on the vapor compression refrigeration cycle was carried out, followed a parametric study to see the effect of a few parameters, notably the evaporation temperature and the condensation temperature. This led us to the following conclusions. New generation HFOs fluids (R1234yf and R1234ze) have better performance than R134a fluid compared to that of HFC refrigerants (R404A and R407C); and the HFO-1234ze fluid gives a good coefficient of performance (3.14) compared to that of the HFO-1234yf fluid which gives a coefficient of performance of 3.0. The coefficient of performance of the vapor compression refrigeration cycle increases with the increase in the evaporation temperature for each refrigerant used, either of the HFC or HFO type; or HFO (R1234yf and R1234ze) gives good performance coefficients like R134a compared to other HFC fluids (404A and R407C). The coefficient of performance of the vapor compression refrigeration cycle decreases with the increase in the condensation temperature of each fluid used, of the HFC or HFO type. The mass flow rate decreases with the increase in the evaporation temperature for each refrigerant used, of the HFC or HFO type. It should also be noted that the R1234ze fluid uses a mass flow rate lower than that of the R1234yf and R134a fluids. The R1234ze gives a coefficient of performance that approximates to the R134a fluid or this fluid has a very high GWP. The mass flow of refrigerant required by R1234a is lower compared to R134a. Overall, R1234a may be a better substitute for R134a.

## REFERENCES

- [1]The Cooling Imperative Forecasting the size and source of future cooling demand, A report by The Economist Intelligence Unit, <https://www.eiu.com/n/> (2019).
- [2]Abas N, Kalair A. R, Khan N, HaiderA, Saleem Z, Saleem M. S. Natural and synthetic refrigerants, global warming: A review. *Renewable and Sustainable Energy Reviews*, 90:557-569, 2018.
- [3]CiconkovR. Refrigerants: There is still no vision for sustainable solutions. *International Journal of Refrigeration*, 86: 441-448, 2018.
- [4]Gil B, KasperskiJ. Efficiency evaluation of the ejector cooling cycle using a new generation of HFO/HCF refrigerant as a R134a replacement. *Energies*, 2018; 11(8): 2136.
- [5]Aprea C, Greco A, Maiorino A, MasselliC. The drop-in of HFC134a with HFO1234ze in a household refrigerator. *International Journal of Thermal Sciences*, 127: 117-125, 2018.
- [6]Belman-Flores J. M, Mota-Babiloni A, LedesmaS, Makhnatch P. Using ANNs to approach to the energy performance for a small refrigeration system working with R134a and two alternative lower GWP mixtures. *Applied Thermal Engineering*, 127: 996-1004, 2017.
- [7]Daviran S, Kasaeian A, Golzari S, Mahian O, Nasirivatan S, Wongwises S. A comparative study on the performance of HFO-1234yf and HFC-134a as an alternative in automotive air conditioning systems. *Applied Thermal Engineering*, 110: 1091-1100, 2017.
- [8]Longo G. A, Zilio C, RighettiG. Condensation of the low GWP refrigerant HFC152a inside a Brazed Plate Heat Exchanger. *Experimental Thermal and Fluid Science*, 68: 509-515, 2015.
- [9]Antunes A. H. P, Bandarra Filho E. P. Experimental investigation on the performance and global environmental impact of a refrigeration system retrofitted with alternative refrigerants. *International journal of refrigeration*, 70: 119-127, 2016.
- [10]Mota-Babiloni A, Navarro-Esbri J, Makhnatch P, Molés F. Refrigerant R32 as lower GWP working fluid in residential air conditioning systems in Europe and the USA. *Renewable and Sustainable Energy Reviews*, 80: 1031-1042, 2017.
- [11]Fang Y, Croquer S, Poncet S, Aidoun Z, Bartosiewicz Y. Drop-in replacement in a R134 ejector refrigeration cycle by HFO refrigerants. *International journal of refrigeration*, 77: 87-98, 2017.
- [12]Belman-Flores J. M, Rangel-Hernández V. H, Usón S, Rubio-Maya C. Energy and exergy analysis of R1234yf as drop-in replacement for R134a in a domestic refrigeration system. *Energy*, 132: 116-125, 2017.
- [13]Yataganbaba A, Kilicarslan A, Kurtbaş İ. Exergy analysis of R1234yf and R1234ze as R134a replacements in a two evaporator vapour compression refrigeration system. *International journal of refrigeration*, 60: 26-37, 2015.
- [14]Mendoza-Miranda J. M, Salazar-Hernández C, Carrera-Cerritos R, Ramírez-Minguela J. J, Salazar-Hernández M, Navarro-Esbri J, Mota-Babiloni A. Variable speed liquid chiller drop-in modeling for predicting energy performance of R1234yf as low-GWP refrigerant. *International Journal of Refrigeration*, 93: 144-158, 2018.
- [15]Mota-Babiloni A, Mateu-Royo C, Navarro-Esbri J, Molés F, Amat-Albuixech M, Barragán-Cervera Á. Optimisation of high-temperature heat pump cascades with internal heat exchangers using refrigerants with low global warming potential. *Energy*, 165: 1248-1258, 2018.
- [16]Touaibi R, Feidt M, Vasilescu E. E, Abbes M. T. Parametric study and exergy analysis of solar water-lithium bromide absorption cooling system. *International Journal of Exergy*, 13(3): 409-429, 2013.
- [17]Touaibi R, Köten H, Feidt M, Boydak O. Investigation of three Organic Fluids Effects on Exergy Analysis of a Combined Cycle: Organic Rankine Cycle/Vapor Compression Refrigeration. *Journal of Advanced Research in Fluid Mechanics and Thermal Sciences*, 52(2): 232-245, 2018.
- [18]Touaibi R, Feidt M, Vasilescu E. E, Abbes M. T. Modelling and Optimization Study of an Absorption Cooling Machine using Lagrange Method to Minimize the Thermal Energy Consumption. *Journal of Advanced Research in Fluid Mechanics and Thermal Sciences*, 58 (2): 207-218, 2019.



# ESTIMATING OF THE OUTPUT VOLTAGE PARAMETERS FOR T-TYPE INVERTER WITH ANN

Tugba Atar

Karamanoglu Mehmetbey University, Graduate School of Natural and Applied Sciences, Department of Electrical and Electronic Engineering, Karaman, Turkey, tugbaatar7@yandex.com, ORCID: 0000-0002-2818-3422

Selami Balci

Karamanoglu Mehmetbey University, Faculty of Engineering, Department of Electrical and Electronic Engineering, Karaman, Turkey, sbalci@kmu.edu.tr, ORCID: 0000-0002-3922-4824

Ahmet Kayabasi

Karamanoglu Mehmetbey University, Faculty of Engineering, Department of Electrical and Electronic Engineering, Karaman, Turkey, ahmetkayabasi@kmu.edu.tr, ORCID: 0000-0002-9756-8756

Cite this paper as:

Atar, T., Balci, S., Kayabasi, A. *Estimating of the output voltage parameters for T-type inverter with ANN*. 9th Eur. Conf. Ren. Energy Sys. 21-23 April 2021, Istanbul, Turkey

**Abstract:**

Inverters are frequently used in power electronics applications in the industrial area. Research on multi-level inverter circuit designs in power systems interfaces has intensified in recent years. The design type and quality of the inverter circuit topology is important for the output voltage to be closer to the sinusoidal waveform. In addition, artificial intelligence techniques for the control algorithms of the power switches of the inverter circuit provide useful information in terms of monitoring the estimated voltage conditions of the inverter output parameters. In this study, an artificial neural network (ANN) model is proposed to estimate the output root mean square (RMS) value of a T-type DC-AC inverter circuit. By changing the operating frequency and PWM pulse number in the control circuit of the inverter, a data set is obtained for the inverter output voltage through parametric simulation studies with ANSYS-SIMPLORER. This data set is used for the training and testing of ANN model based on feed forward back propagation multilayer perception (FFBP-MLP). Thus, the Mean Absolute Error (MAE) value of the FF\_MLP model is determined as 0.1693.

**Keywords:**

T type inverter, parametric simulation, estimating with artificial neural network

© 2021 Published by ECRES

Nomenclature	
ANN	Artificial Neural Networks
PWM	Pulse Width Modulation
FFBP-MLP	Feed Forward Back Propagation Multilayer Perception
MAE	Mean Absolute Error
RMS	Root Mean Square

## 1. INTRODUCTION

Inverters are widely used for many industrial applications such as induction motor drives, uninterrupted power supplies, electric vehicle power systems, renewable energy sources, in general in power electronics application areas. Designs can be made in different topologies such as single phase and multiphase designs. For this reason, studies on inverters are increasing gradually and accordingly, inverter technology is developing rapidly. The main goal in all studies is to keep the number of switches at a minimum and to obtain a better quality of output voltage and load current [1]. Inverters have applications in the literature as two-level with square wave inverter structure in classical designs or as multi-level circuit topologies with increasing the number of switching elements. In addition, designs can be made with diode or capacitor clamping circuits in neutral clamping inverters. On the other hand,

with cascaded inverter circuits, circuit structures that have been frequently studied in recent years are also used, especially in renewable energy systems such as piecewise Fuel Cell and solar energy. In this context, in a study on multi-level inverter circuits, a 5-level cascade connected inverter design for asynchronous motor drives has been implemented. From the experimental results and harmonic analysis obtained in such a setup, it has been determined that the system operates stable, is not affected by electrical noise, protection circuits work, and the inverter gives the desired response [2].

In a study on the optimization of switching angles in multi-level inverters, by using the selective harmonics elimination pulse width modulation technique (SHEPWM), certain harmonics in the output waveforms of inverters at different levels were eliminated. Thus, the nonlinear equation sets that are obtained by SHEPWM technique to find the switching angles to eliminate the dominant harmonics have been optimized by particle swarm optimization (PSO) and genetic algorithms (GA) methods. The total harmonic distortion amount of the output waveform has been reduced. According to the data obtained, it has been observed that it is better than the optimization results made with the genetic algorithm [3]. On the other hand, carrier phase-shifted PWM has been proposed in the past literature to reduce the Common Mode Voltage (CMV) for three-level T-type NPC inverters. Consequently, phase regulation can reduce the peak value of CMV by 50% compared to pulse width modulation (PWM) method. With this method, lower root mean square value can be obtained. It has been observed that the proposed carrier phase shifted PWM method has good output waveform performance and lowers CMV [4].

In addition, selective harmonic reduction of inverter circuits using bio-inspired intelligent algorithms (BIA) for renewable energy sources was examined and the working principles of nine well-known BIAs were explained in detail. A few factors such as inverter control parameters of the best five BIAs were evaluated and it was found that PSO performance was superior to control algorithms in terms of performance parameters. It can be said that all BIAs are easy to realize and apply and show a good potential to solve the specific reason in inverter circuits, especially in voltage source inverters [5]. In a study in which multi-level T-type inverter circuits performance analysis based on modified hysteresis current controller was conducted, and this control system was operated and performed for a multi-level T-type inverter circuits. Thus, the feedback control system was tested according to the switching control signals for the operating frequency values (at kHz levels) according to different hysteresis bands. Compared with the traditional SPWM technique applied of the multi-level T type inverters, it can be said that the THD of this type of controller usage is lower than the SPWM controlled inverters [6].

In another study where a 3-level T-type inverter high efficiency drive system is examined, a variable speed drive was presented. The efficiency of the system, which consists of a proposed 3-level T-type converter topology and a standard induction machine, which is very efficient for low switching frequencies, is optimized in terms of fundamental and harmonic induction machine losses as well as converter losses [7]. Blaabjerg and Lee examined the quality performance of the three-level T-type inverter with the new control strategy and operated of the inverter circuit under the fault conditions. Thus, it was performed a fault-tolerant control system with the sinusoidal waveforms and explained the fault by dividing it into two states. Generally, open circuit faults occur at half bridge switches or neutral point switches. The applicability and validity of the error-resistant control methods proposed from simulation and experimental results have been verified [8]. It covers gate control requirements, switching capability, inverter performance, cooling system volume, output filter, and dead time of the switching signals with compared to single-phase inverters using Si IGBTs, SiC (or GaN) Mosfets. Considering the switching ability, GaN has the much more performance among these developments at 350V, 16A and provides much more efficiency at the higher operational frequency for the power electronics circuits [9].

Wang et al. proposed a multi-scale fault diagnosis technique based on signal symmetry reconstruction pretreatment to perform diagnostics for any power switch of the inverter circuits under the load condition. This method consists of multi-scale features and artificial neural network (ANN). Thus, the performance of this diagnostic method was confirmed with simulation and experimental studies [10]. When the advantages of SiC switches for the grid interactive T-type inverters were investigated. Thus, SiC type switching devices significantly reduces semiconductor power losses and allows the much more power capacity level at the more switching frequency values for the same switching power losses. It can be said that the use of SiC type power switches for inverter circuits is a potentially useful alternative [11].

Nonlinear condition effects of three-level T-type inverters can be analyzed and the main reasons for nonlinearity are switching pulse conditions such as dead time esitmation and voltage value on the switches. Thus, in the past literature, improvement methods with the pulse width modulation (PWM) of T-type inverter were suggested from the research results to alleviate the nonlinearity of the inverter [12]. Samadai et al. introduced a new module for asymmetric multi-level inverters with few components, and proposed a new combination module of two cascaded T-type inverters and a few other switch elements. The lower total harmonic distortion (THD) value of the output

voltage or current and the fewer semiconductor devices were the best advantages for this proposed module. Thus, this method was used as the new switching control system to improve the best quality output voltage with the lower THD value, and, it was shown to perform well in both simulation and experimental results [13]. In a study for solar photovoltaic (PV) inverters, an intelligent-based fault tolerance system was examined. The control system based on ANN was used in solar PV panels, battery banks, power switches of the inverter circuits. Thus the significant advantage of this inverter topology can be powered from input to output even under the fault conditions, and it was proven that the system can provide power despite faulty environments [14]. A comprehensive review of different T-type multi-level inverter topologies and the circuits performance were conducted by Salem and Abido. Thus, 3-Level, dual 3-Level and 5-Level T-type inverter topologies were presented and it was observed that the performance of T-type inverters was superior to conventional 2-level and NPC converters [15]. In a study where a multi-dimensional comparison of two common topologies for a 120 kW permanent magnet synchronous motor drive circuit to be used in electric vehicles was carried out, two-level topology and three-level neutral point clamp type voltage supply inverter output voltage and current quality, thermal performance, efficiency and switching frequency limitation, and, compared in terms of semiconductor thermal reliability [16].

In this study, ANN model is used to estimating the output RMS value in the T-type inverter circuit. Simulation studies have been carried out in order to obtain parametric data with the inverter circuit ANSYS-ELECTRONICS software. Using the data set obtained here, the parameters were calculated with a very high accuracy with ANN. Thus, a lot of useful information is presented in the development of the control algorithms of the inverter circuit.

## 2. T-TYPE INVERTER CIRCUIT TOPOLOGY AND MATHEMATICAL EXPRESSIONS

T-Type inverter circuits, defined as Neutral Point-Clamping inverter, are a subgroup of the multi-level inverter circuits for output in multi-level output voltage waveforms. It is one of the very useful circuit for single or multi-phase multi-level power electronics circuits (three or five level circuits are widely used) and is extremely suitable for a special area of the power electronics application. In this context, the scheme of the T-type inverter circuit and the switching gate control waveforms are presented in Figure 1 (a) and (b), respectively. In this circuit, the power switches that make up the S1 and S4 half-bridge are powered from a DC source marked as  $V_{dc}$ , and the two-way operated power switches S2 and S3 are divided symmetrically through the capacitors as  $V_{dc} / 2$ . Thus, the conversion of the output current occurs between the power switches S1 and S2 in the positive half, and current flows between S3 and S4 in the negative half-wave according to the switching signals. Then on the contrary, S3 is fully open in the positive cycle and S2 is fully open at the negative half cycle of the inverter output current to use the reverse conduction capacity of the power devices. The dead time of the power switch conditions S1, S2 and S3, S4 should be as small as possible for SiC and GaN devices to minimize transmission power losses across the bidirectional switches. On the other hand, one of the bidirectional devices will be in reverse transmission mode at any zero state switching moment [9].

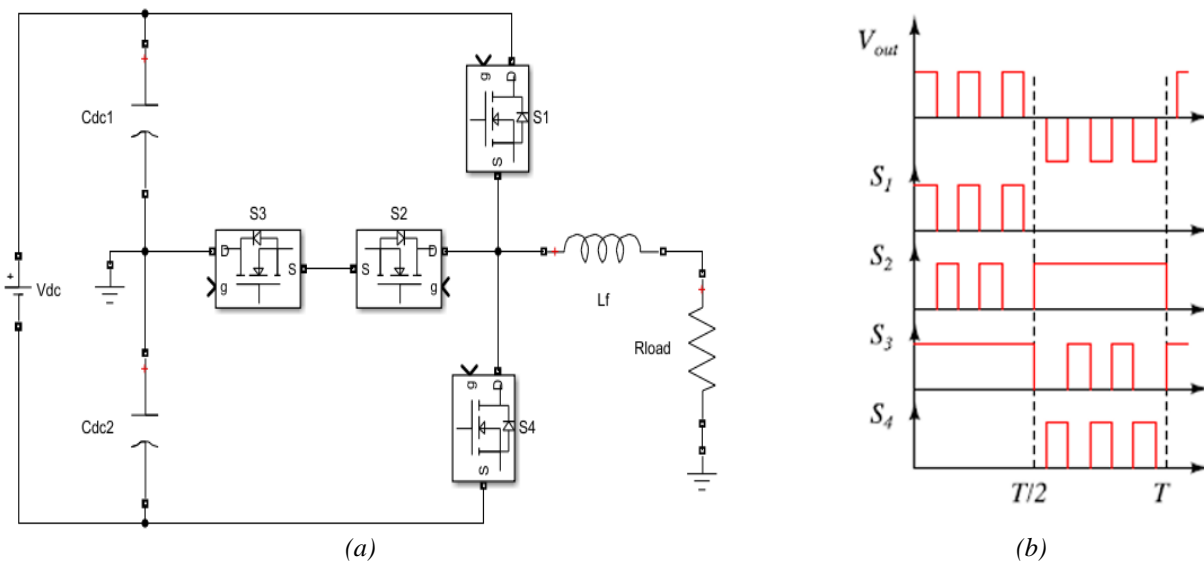


Figure 1. The basic circuit of a three level T-type inverter, (a) topology, (b) gate control signals [9, 19].

Thus, according to the inverter circuit topology of a 3-level T-type inverter, it consists of four uni-directional switches ( $S_1$ ,  $S_2$ ,  $S_3$  and  $S_4$ ), a bidirectional power switches and two symmetrical DC sources with capacitor clamped for each phase [18]. The bi-directional power switches offered includes two back-to-back one-way switches and can be operated simultaneously. For a higher voltage levels, the inverter circuit consists much more bidirectional power switches and a few dc voltage supplies such as Fuel Cell or PV renewable energy sources [19-22].

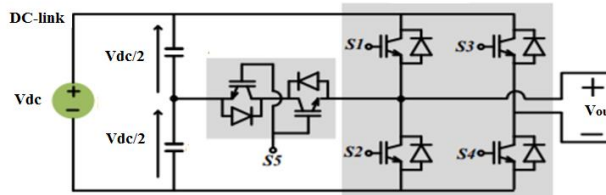


Figure 2. The circuit topology of five level T-type inverter [6].

Table 1. The Power Switching Conditions of a Five-Level T-Type Inverter [6].

<b>S1</b>	<b>S2</b>	<b>S3</b>	<b>S4</b>	<b>S5</b>	<b>Vout</b>
1	0	0	1	0	+Vdc
0	0	0	1	1	+Vdc/2
0	0	1	0	1	-Vdc/2
0	1	1	0	0	-Vdc
0	1	0	1	0	0
1	0	1	0	0	0

Generally, T-type inverter circuits are connected to a serial impedance ( $R-L$ ) load such as induction motor or isolation transformer, the voltage and current relationship on the load side is given by Eq.1: [6, 23]:

$$V_{out} = R i_{load} + L \frac{di_{load}}{dt} \quad (1)$$

This equation can be rearranged and written in new forms as seen in Eqs.2 and 3, respectively [6].

$$\Delta i_{load} = i_{load}^* - i_{load} \quad (2)$$

$$V_{out} = R i_{load} + L \frac{\Delta i_{load}}{dt} \quad (3)$$

Assuming that the resistor value is too small, the resistor value is thus neglected and the reference voltage can be given with Eq.4 [6].

$$V_{ref} = L \frac{\Delta i_{load}}{dt} \quad (4)$$

With these last changes, it is clear that, as indicated in Eqs.5 and 6, the output voltage is controlled with the simple revision in the load current condition [6, 23].

$$L \frac{\Delta i_{load}}{dt} = L \frac{di_{load}^*}{dt} - V_{out} \quad (5)$$

$$L \frac{\Delta i_{load}}{dt} = V_{ref} - V_{out} \quad (6)$$

### 3. PARAMETRIC SIMULATION STUDIES WITH POWER ELECTRONICS CIRCUIT

In this section, simulation studies with ansys-electronics will be briefly explained. Also, parametric simulation will be emphasized and the data obtained will be emphasized. T-type DC-AC inverter circuit modeling has been carried out in the Finite Element Method (FEM) program. Circuit modeling is simulated by changing the modulation ratio (MR) of the PWM switching circuit, the PWM frequency (fPWM), the R and L values of the RL serial impedance load at the inverter output using the parametric analysis method in ansys-electronics software. In the simulation

studies, the simulation circuit shown in Figure 2 was used to determine the performance of the inverter circuit under more realistic conditions.

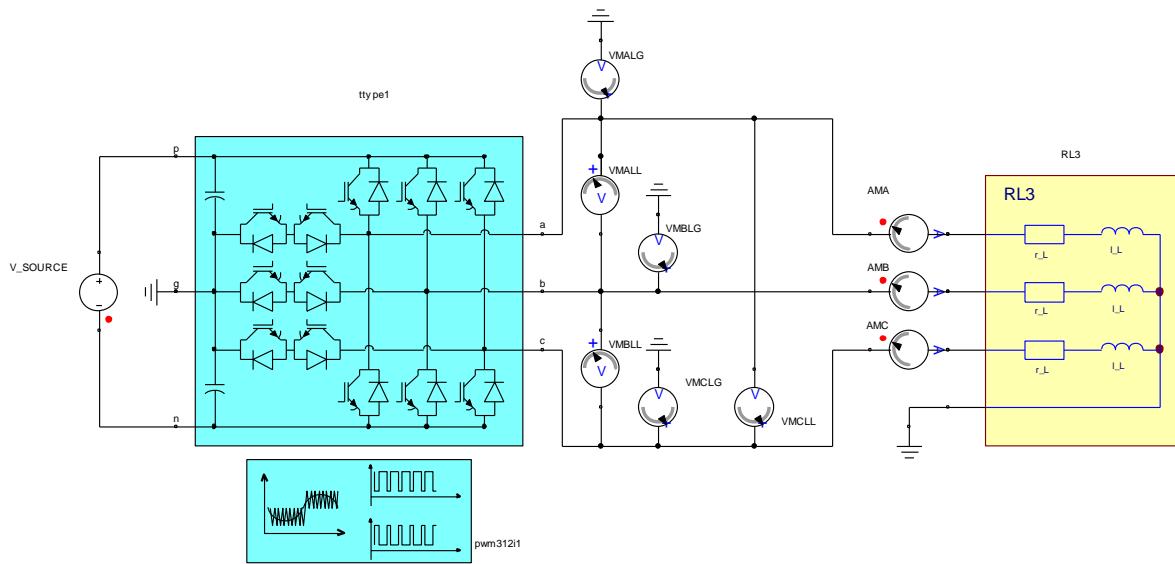


Figure 2. The circuit scheme of parametric simulation studies with ANSYS-SIMPLORER.

The inverter circuit is performed with power electronics software regard to the simulation parameters given in Table 2, and this data are carried-out with the ANN training interface. Regard to the reports obtained from this parametric study, a total of 288 data are verified the output voltage according to the PWM switching parameters and the R-L load conditions. Thus, the data set is used in the training of 230 of the ANN models and 58 in the classification of the test process [24].

Table 2. The Range Value of the Parametric Simulation Studies

Parameters	Value	Parametric Step
Vi	400 V	constant
fs	50 Hz	constant
mr	0.60-0.86	0.04
f <sub>PWM</sub>	5-20 kHz	2.5 kHz
R	1-4 Ω	1 Ω
L	1-3 mH	1 mH

In parametric simulation studies, the modulation ratio (MR) of the PWM switching circuit in the range of 0.60-0.86 with 0.04 steps; PWM frequency is changed in 2.5 kHz steps for the 5-20 kHz range. Simulation studies of the R and L values of the RL serial impedance load at the inverter output are also carried out with different parameters in the values given in the table. Thus, a data set is created for different input variables and inverter output voltage RMS values with the parametric simulations.

#### 4. PARAMETER ESTIMATION WITH ARTIFICIAL NEURAL NETWORKS

Artificial Neural Networks are computing systems that are inspired by the learning function, which is the best basic feature of the human brain behavior, and contributing the learning process with the help of examples. These networks consist of artificial nerve cells (neurons) connected to each other. As seen in Figure 3, each connection has a weight value and the information of ANN is hidden in these weight values [25]. ANN has a structure that imitates biological neural networks with its structural features.

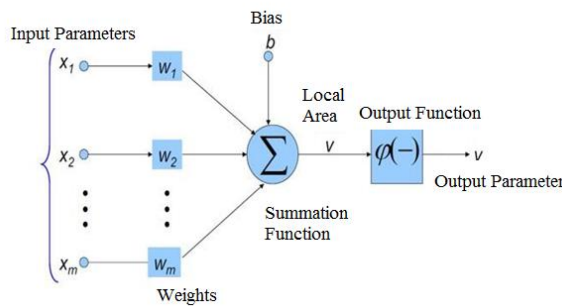


Figure 3. The block diagram of ANN

A very important artificial intelligence technique (such as ANN) in scientific studies basically consists of 3 main layers. These main layers are input, hidden and output layers. In this regard, the input parameter data is directly applied to the input layer, so the number of neurons in the input layer is also treated as equal to the number of each of the different input parameters. Then, this data is passed through a series of mathematical operations such as addition, multiplication and activation until it reaches the output layer, and this data is finally transferred to the output layer. Also, depending on the complexity of the process, ANN may have multiple hidden layers, gather information about samples for this purpose, make generalizations, and make decisions about these variables using the learned information compared to examples they have never seen before. Thus, because of its learning and generalizations, ANN has wide application areas in many scientific fields and has proven its ability to successfully solve complex problems [26]. In general, the data set obtained from various simulated or experimental studies is randomly divided into two groups as 80% and 20%. In this study, ANN models are used to find the model that can best estimate the output RMS value of the T-type inverter circuit obtained from parametric simulation studies. In this context, 288 data were obtained by using ANSYS-SIMPLORER software in order to create a data set. Dha then 80% of this dataset was used for training and the remaining 20% was used to test the performance of the trained model. In addition, Mean Absolute Error (MAE) was chosen as the performance determination criterion.

Table 3. The best test results for different learning methods

ALGORITHM	MAE
CFB	1.0561
FFB	0.9874
FFB_MLP	0.1693

The best test results for different learning methods are given in Table 3. The best results were obtained with FFBP\_MLP. The parameters such as required function, number of neurons and number of layers of the network with four inputs and one output have been selected accordingly. ANN structure, input, output and multi-layer perceptron (MLP) type with two hidden layers are used. The operating frequency and PWM pulse number are changed and then updated and transmitted to the output layer using activation functions. The internal structure of the developed network is given in Figure 4.

$$MAE = \frac{1}{N} \sum_{i=1}^N |output - target| \quad (7)$$

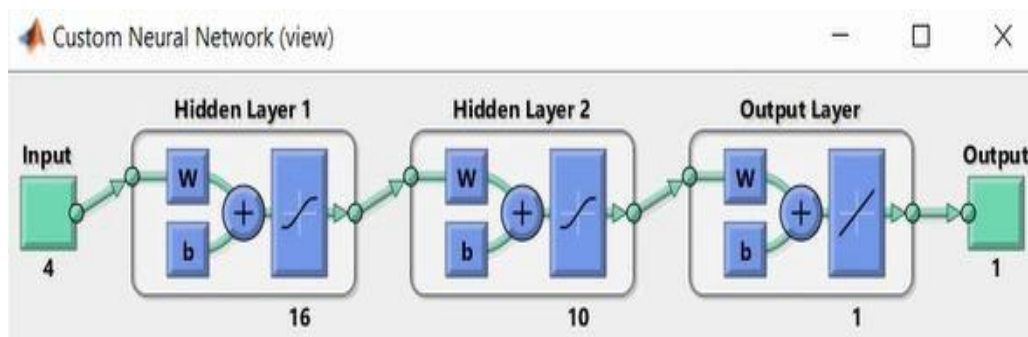


Figure 4. Internal structure of the developed network

## 5. CONCLUSION

In this study, ANN model is used to estimating inverter output RMS voltage of a T-type DC-AC inverter circuit. 288 data are obtained by using power electronics simulation software (ANSYS-SIMPLORER). 230 of these data are performed to train the ANN model and the remaining 58 data were used for the performance testing. More successful results were obtained with FFBP\_MLP compared to other methods. The MAE value of this FFBP\_MLP model is calculated as 0.1693. Thus, the obtained data can be used in the design of the feedback control system in future studies. In addition, this study is thought to be a guide to researchers in creating data meat in parametric simulation studies.

## REFERENCES

- [1] Çamur S., Arifoğlu B., Beşer E. Kandemir and Beşer E., "Design and Application of a Novel Structure and Topology for Single-Phase FiveLevel Inverter", Wseas Transactions on Electronics, 2006.
- [2] Tuncer, S. and Tatar, Y. "Design and Implementation of Three-phase 5-Level Cascade Inverter", Fırat University Journal of Science and Engineering, 16(4), 702-717, 2004.
- [3] Durak E.S. Switching Angles Optimization in Multilevel Inverter, MSc, KTU, Trabzon, Turkey, 2016.
- [4] Tuyen D. Nguyen, Dzung Quoc Phan, Dat Ngoc Dao, and Hong-Hee Lee, Carrier Phase-Shift PWM to Reduce Common-Mode Voltage for Three-Level T-Type NPC Inverters, Journal of Power Electronics, 14(6), pp. 1197-1207, November 2014.
- [5] Mudasir Ahmed Memona, Saad Mekhilefa, Marizan Mubina, Muhammad Aamirb, "Selective harmonic elimination in inverters using bio-inspired intelligent algorithms for renewable energy conversion applications: A review", Renewable and Sustainable Energy Reviews, 82, 2018, pp. 2235–2253.
- [6] İnci M. Performance Analysis of T-type Inverter Based on Improved Hysteresis Current Controller", Balkan Journal of Electrical & Computer Engineering, 7(2), April 2019.
- [7] Mario Schweizer and Johann W. Kolar, "High efficiency drive system with 3-level T-type inverter" Proceedings of the 14th IEEE International Power Electronics and Motion Control Conference (ECCE Europe 2011), Birmingham, UK, August 30 - September 1, 2011.
- [8] Frede Blaabjerg and Kyo-Beum Lee, "Reliability Improvement of a T-Type Three-Level Inverter with Fault-Tolerant Control Strategy", IEEE Transactions on Power Electronics, 30(5), 2015.
- [9] Gurpinar E., Single-Phase T-Type Inverter Performance Benchmark Using Si IGBTs, SiC MOSFETs, and GaN HEMTs", IEEE Transactions on Power Electronics, 31(10), 2016.
- [10] Zhanshan Wang, Zhanjun Huang, Chonghui Song, and Huaguang Zhang, Multiscale Adaptive Fault Diagnosis Based on Signal Symmetry Reconstitution Preprocessing for Microgrid Inverter Under Changing Load Condition, IEEE Transactions on Smart Grid, 9(2), 2018.
- [11] Alexander Anthon, Zhe Zhang, Michael A. E. Andersen, Donald Grahame Holmes, Brendan McGrath, Carlos Alberto Teixeira, "The Benefits of SiC MOSFETs in a T-Type Inverter for Grid-Tie Applications, IEEE Transactions on Power Electronics, 32(4), 2017.
- [12] Hyeon-Sik Kim, Yong-Cheol Kwon, Seung-Jun Chee, Seung-Ki Sul, "Analysis and Compensation of Inverter Nonlinearity for Three-Level T-Type Inverters", IEEE Transactions on Power Electronics, 32(6), 2017.
- [13] Emad Samadai, Abdolreza Sheikholeslami, Sayyed Asghar Gholamian, Jafar Adabi, "A Square T-Type (ST-Type) Module for Asymmetrical Multilevel Inverters", IEEE Transactions on Power Electronics, 33(2), 2018.
- [14] Albert Alexander Stonier and Brad Lehman, "An Intelligent-Based Fault-Tolerant System for Solar-Fed Cascaded Multilevel Inverters", IEEE Transactions on Energy Conversion, 33(3), 2018.
- [15] Salem, A., Abido, M.A. T-Type Multilevel Converter Topologies: A Comprehensive Review. Arab J Sci Eng 44, 1713–1735, 2019, <https://doi.org/10.1007/s13369-018-3506-6>.
- [16] Madan, A. Performance and Thermal Reliability Comparisons of 2-Level and 3-Level Npc Voltage Source Inverters for Electric Vehicle Drive Applications, MSc, METU, Ankara, Turkey, 2019.
- [17] A. Narendrababu, N. Yalla, and P. Agarwal, A modified T-type single phase five-level inverter with reduced switch voltage stress, 2018 International Conference on Power, Instrumentation, Control and Computing (PICC), 2018, pp. 1-5.
- [18] H. P. Vemuganti, D. Sreenivasarao, and G. S. Kumar, "Improved pulselwidth modulation scheme for T-type multilevel inverter," IET Power Electronics, vol. 10, no. 8, pp. 968-976, 2017.
- [19] P. Singh, S. Tiwari, and K. K. Gupta, A new topology of transistor clamped 5-level H-Bridge multilevel inverter with voltage boosting capacity, 2012 IEEE International Conference on Power Electronics, Drives and Energy Systems (PEDES), 2012, pp. 1-5.
- [20] N. Abd Rahim, M. F. M. Elias, and W. P. Hew, "Transistor-Clamped H-Bridge Based Cascaded Multilevel Inverter With New Method of Capacitor Voltage Balancing," IEEE Transactions on Industrial Electronics, vol. 60, no. 8, pp. 2943-2956, Aug 2013.

- [21] G. E. Valderrama, G. V. Guzman, E. I. Pool-Mazun, P. R. MartinezRodriguez, M. J. Lopez-Sanchez, and J. M. S. Zuniga, "A Single-Phase Asymmetrical T-Type Five-Level Transformerless PV Inverter," Ieee Journal of Emerging and Selected Topics in Power Electronics, 6(1), pp. 140-150, 2018.
- [22] M. Anzari, J. Meenakshi, and V. T. Sreedevi, "Simulation of a transistor clamped H-bridge multilevel inverter and its comparison with a conventional H-bridge multilevel inverter," 2014 International Conference on Circuits, Power and Computing Technologies-ICCPCT-2014, 2014, pp. 958-963.
- [23] W. Huaisheng and X. Huifeng, "A Novel Double Hysteresis Current Control Method for Active Power Filter," Physics Procedia, Vol. 24, pp. 572-579, 2012.
- [24] Selami Balci, Ahmet Kayabasi, and Berat Yildiz, Artificial Neural Network Based Estimation of the Output Ripple of the DC DC Boost Battery Charger for EVs, Ecres 2018, 25-27 June 2018, Istanbul, Turkey.
- [25] Öztemel, E. Yapay Sinir Ağları. İstanbul, Türkiye: PapatyaYayincilik. Yapay Sinir Ağları, 2003, <https://ieeeturkiye.files.wordpress.com/2017/10/yapay-sinir-aglariceran-oztemel.pdf>.
- [26] Ergezer, H., Dikmen, M. ve Özdemir, E. Yapay Sinir Ağları Ve Tanıma Sistemleri. PiVOLKA, 2 (6), 14-17, 2003.



# ESTIMATION OF LEAK INDUCTANCE OF A PHASE ISOLATION TRANSFORMER VIA ANFIS

Busra Aslan

Karamanoglu Mehmetbey University, Department of Electrical and Electronics Engineering, Karaman, Turkey,  
busragungorer@gmail.com, ORCID: 0000-0002-0313-0172

Selami Balci

Karamanoglu Mehmetbey University, Department of Electrical and Electronics Engineering, Karaman, Turkey,  
sbalci@kmu.edu.tr, ORCID: 0000-0002-3922-4824

Ahmet Kayabasi

Karamanoglu Mehmetbey University, Department of Electrical and Electronics Engineering, Karaman, Turkey,  
ahmetkayabasi@kmu.edu.tr, ORCID: 0000-0002-9756-8756

Cite this paper as: *Aslan, B., Balci, S., Kayabasi, A. Estimation of Leak Inductance of A Phase Isolation Transformer via ANFIS. 9<sup>th</sup> Eur. Conf. Ren. Energy Sys. 21-23 April 2021, Istanbul, Turkey*

**Abstract:** With the increasing use of renewable energy sources in recent years, the need to isolate power electronics circuits and grid interface from each other has emerged. In this context, the design of an isolation transformer to be designed keeping costs and losses to a minimum is of great importance. In this study, an isolation transformer is designed with a Finite Element Analysis (FEA) analysis. The primary and secondary winding dimensions and number of turns of the designed isolation transformer are changed by linear steps. A dataset is produced with the leakage inductance values of the isolation transformer, which changes depending on the changed parameters. The produced dataset was used in the training and testing phase of Adaptive-Network Based Fuzzy Inference Systems (ANFIS), an artificial intelligence algorithm, and the estimation of the leakage inductance value was successfully performed. At the end of the estimation phase, the error values for training and testing are 0.3470% and 0.4448%, respectively.

**Keywords:** Isolation transformer, Leakage inductance, FEA, ANFIS

© 2021 Published by ECRES

Nomenclature	
ANFIS	Adaptive-Network Based Fuzzy Inference Systems
FEA	Finite Element Analysis
FEM	Finite Element Method

## 1. INTRODUCTION

Transformers have been widely used in daily life and industry since the first day they were invented. They are used to raise or lower the voltage level and to isolate two or more systems from each other. Since transformers do not have moving parts, they operate with a very high efficiency. The transmission and distribution of electrical energy, which is the primary energy source in everyday life and industry, is as important as the production. In this context, transformers play a major role in the transmission and distribution of electrical energy. In power systems, they are generally used for lowering and increasing the voltage level, and sometimes they are frequently used for isolation purposes.

Isolation transformers isolate the secondary output voltage from the primary input voltage and insulate the source and load from each other. In this way, while some sensitive electrical devices (such as uninterruptible power supplies, operating room devices, computerized systems and power electronics giants) operate safely, electrical accidents that may occur in humid environments can be prevented [1]. The basic structure of transformers has not changed since the first production date, but research studies are still active to reduce the new generation core

materials and dimensions. [2]. On the other hand, while designing the transformer, care should be taken to keep losses as low as possible. For this reason, the losses of transformers with ideal windings have been examined many times. Aghaei, et al. [3] investigated the leakage inductance value of transformers with non-ideal windings. In this way, the transformer designer will have an idea about the losses of the transformer before starting the production phase and the critical situations that may be encountered will be prevented. In the related study, FEA and its experimental results were compared.

Medium frequency transformers are widely used in power converter circuits and power distribution networks. Many properties of transformers must be predicted before they are integrated into the circuit in order to adapt to the increasing switching frequency. In this context, Tian, et al. [4] developed a current analytical frequency dependent method to determine the resulting leakage inductance value in the middle frequency range based on the magnetic field density distribution and the stored magnetic energy method of the transformer. In this way, it was ensured that the leakage inductance was determined more accurately. They presented the advantages of different winding models and their effects on losses by comparing the interspersed winding structure to keep the leakage inductance at a minimum. In order to test the accuracy of the proposed new method, they produced the transformer with the characteristics of 10kW, 500 / 5000V, 5 kHz and used it during the test phase. They found that the results obtained during the test phase and the results obtained using FEA coincided. In a different study, Mogorovic and Dujic [5] designed a medium frequency transformer used in the construction of galvanically isolated power electronic converters. Detailed analytical modeling of the stray inductance value, which plays a major role in this design, has been carried out and analyzed using the Finite Element Method (FEM). Prieto, et al. [6] used Finite Element Analysis (FEA) techniques to account for all frequency and geometry effects in order to estimate the leakage inductance and alternating current resistance of the transformer. With this method, the designer can easily use interleaving techniques. In this way, it is aimed to use an efficient strategy in order to determine the best winding shape of the transformer designed with a simple calculation. It has been stated that by using the interleaving technique correctly, the leakage inductance can be reduced by up to nine times.

## 2. PARAMETRIC SIMULATION STUDIES

The isolation transformer designed for the estimation of the leakage inductance value is given in Figure 1. The core material of the isolation transformer modeled in three dimensions is defined as TDK - PC40, 60C in the material library of the software.

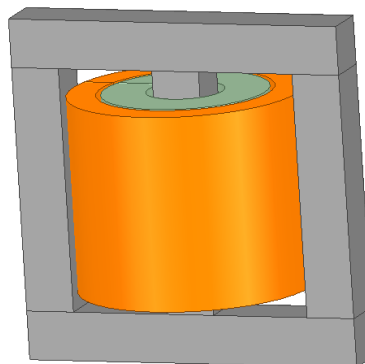


*Figure 1. The isolation transformer with Parametric modeling simulation studies*

For parametric analysis, the winding number (N), primary winding radius ( $L_{pr}$ ) and secondary winding radius ( $L_{sc}$ ) values of the isolation transformer were calculated with the FEA solver with the linear steps determined as given in Table 1. Thus, data can be obtained for the leakage inductance of the isolation transformer, which varies depending on the three input variables.

*Table 1. Parametric analysis values of the isolation transformer*

Parameters	Value	Step
Primary winding radius ( $L_{pr}$ )	10-17 mm	0.5
Secondary winding radius ( $L_{sc}$ )	18.5-24 mm	0.5
Number of turns (N)	20-50	5

### 3. ANFIS-BASED LEAKAGE INDUCTANCE ESTIMATION AND RESULTS

The general problem of many projects is that future uncertainties and risks cannot be predicted. The main reason behind the inability to identify risks and uncertainties is the negative effects of uncontrollable variable factors on the system. There are some estimation methods used in order to save the system from these negative effects or to reduce the system to a level that will affect the system at the minimum level, that is, to predict the uncertainty and risks that may occur in the future. The correct prediction of future events is only possible with the correct analysis of past events. For this purpose, past events should be archived accurately and useful and meaningful information should be produced when necessary [7]. ANFIS, one of the artificial intelligence techniques developed in recent years, is an artificial intelligence technique that uses Artificial Neural Networks to determine fuzzy logic parameters. Due to the fact that fuzzy logic cannot easily adapt to environmental conditions and does not have the ability to learn, ANFIS system has been established by taking advantage of the learning ability of artificial neural networks. ANFIS is used to model nonlinear functions, define nonlinear components linearly and predict a chaotic time series [8]. Accordingly, in this study, the leakage inductance values obtained by parametric simulations based on the radius of the primary winding ( $L_{pr}$ ) at the entrance to the ANFIS model, the radius of the secondary winding ( $L_{sc}$ ) and the number of turns (N) are presented as a target. 1260 data were obtained to be used in the training and testing phase of the ANFIS system. Of these data, 1008 of them were used in the training and 252 of them were used in the test phase. As a result of various preliminary studies, the most efficient membership function in the ANFIS interface has been determined. The training graphic obtained as a result of the studies is given in Figure 2 and the test graphic in Figure 3.

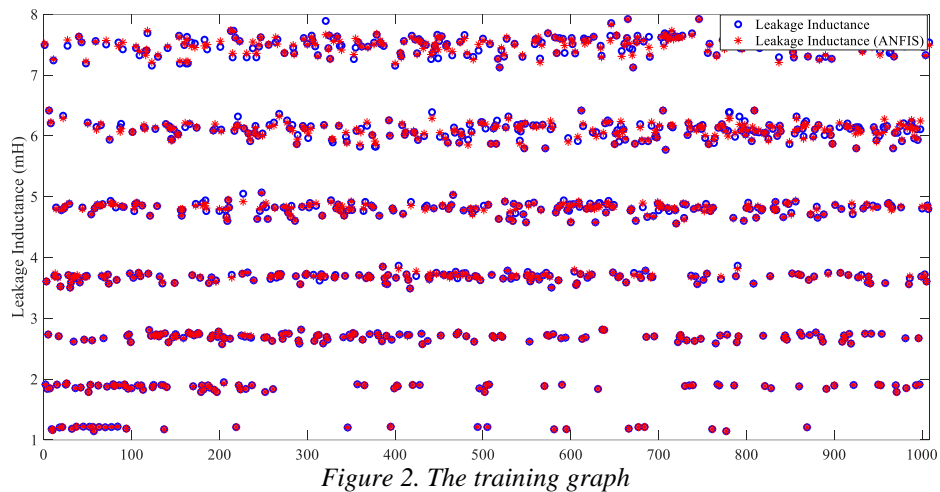


Figure 2. The training graph

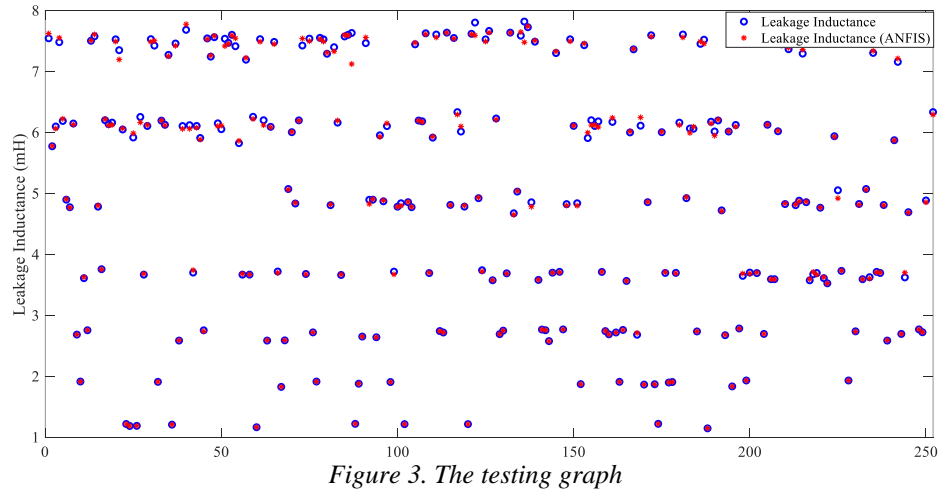


Figure 3. The testing graph

As can be seen from the graphs given and the results obtained with the rule-based viewer given in Figure 4, the average percentage error is less than 1% as a result of the training and testing stages.

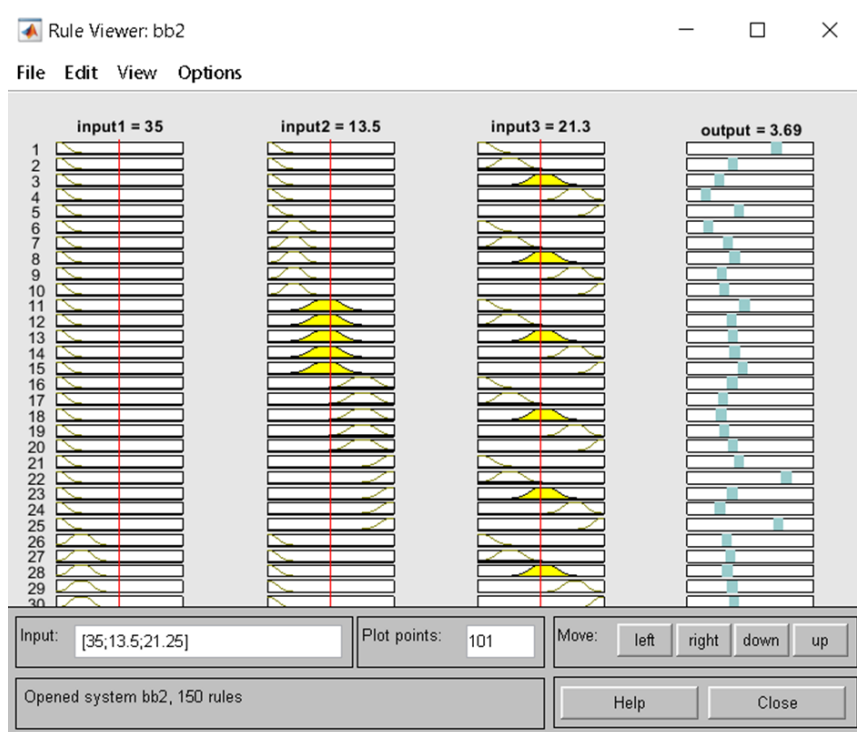


Figure 4. Testing ANFIS Model

## CONCLUSION

In this study, parametric simulations of an isolation transformer were carried out using ANSYS-Maxwell software, whose analysis can be performed efficiently and close to reality with FEM. With the data obtained, the leakage inductance value of the isolation transformer was evaluated depending on different parameters and a dataset was created. These data were processed with ANFIS, an artificial intelligence algorithm, and the error was 0.3470% for training and 0.4448% for testing. The leakage inductance value of the isolation transformer has been successfully estimated. In this way, it is easier to determine the most effectively working isolation transformer that can be determined as a result of long and tiring studies in practice.

## REFERENCES

- [1] X. Li, W. Huang, B. Cui, and X. Jiang, "Inductance Characteristics of the High-Frequency Transformer in Dual Active Bridge Converters," in 2019 22nd International Conference on Electrical Machines and Systems (ICEMS), 2019: IEEE, pp. 1-5.
- [2] S. Balci, I. Sefa, and N. Altin, "An investigation of ferrite and nanocrystalline core materials for medium-frequency power transformers," Journal of Electronic Materials, vol. 45, no. 8, pp. 3811-3821, 2016.
- [3] M. Aghaei, S. Mohsenzade, and S. Kaboli, "On the Calculation of the Leakage Inductance in Transformers With Nonideal Windings," IEEE Transactions on Power Electronics, vol. 35, no. 8, pp. 8460-8471, 2019.
- [4] H. Tian, Z. Wei, S. Vaisambhayana, M. P. Thevar, A. Tripathi, and P. C. Kjær, "Calculation and Experimental Validation on Leakage Inductance of a Medium Frequency Transformer," in 2018 IEEE 4th Southern Power Electronics Conference (SPEC), 2018: IEEE, pp. 1-6.
- [5] M. Mogorovic and D. Dujic, "Medium frequency transformer leakage inductance modeling and experimental verification," in 2017 IEEE Energy Conversion Congress and Exposition (ECCE), 2017: IEEE, pp. 419-424.
- [6] R. Prieto, J. Cobos, O. Garcia, P. Alou, and J. Uceda, "Taking into account all the parasitic effects in the design of magnetic components," in APEC'98 Thirteenth Annual Applied Power Electronics Conference and Exposition, 1998, vol. 1: IEEE, pp. 400-406.
- [7] A. Mellit and S. A. Kalogirou, "ANFIS-based modelling for photovoltaic power supply system: A case study," Renewable energy, vol. 36, no. 1, pp. 250-258, 2011.
- [8] J.-S. Jang, "ANFIS: adaptive-network-based fuzzy inference system," IEEE transactions on systems, man, and cybernetics, vol. 23, no. 3, pp. 665-685, 1993.



# NEW CONCEPTS AND TECHNOLOGIES FOR ELECTRICAL MACHINES AND MECHANICAL ENGINEERING

Aldan A. Sapargaliyev

OiArna LLP, 157 Askarov street, block 9, apartment 571, residential complex «Solar Valley», «Miras» microdistrict, 050043, Almaty, Republic of Kazakhstan, e-mail: oiarna.doc@gmail.com, ORCID: 0000-0003-3408-1235

Amangeldy M. Zhunusbekov

L.N. Gumilyov Eurasian National University, Satpayev Str., 2, Nur-Sultan, Republic of Kazakhstan, 010008. e-mail: zhunusbekov\_am@enu.kz, ORCID: 0000-0003-2052-0065

Nurlan Ungarov

OiArna LLP, 157 Askarov street, block 9, apartment 571, residential complex «Solar Valley», «Miras» microdistrict, 050043, Almaty, Republic of Kazakhstan, e-mail: oiarna.doc@gmail.com, ORCID: 0000-0003-3408-1235

*Sapargaliyev AA, Zhunusbekov AM, Ungarov N. New concepts and technologies for electrical machines and mechanical engineering. 9<sup>th</sup> Eur. Conf. Ren. Energy Sys. 21-23 April 2021, Istanbul, Turkey*

**Abstract:** The production activities of mankind in the power industry, mechanical engineering and their impact on the environment, including climate, strongly depends on the level of development of ES→EE (ES→EE—generation of electrical energy) and EE↔ME (EE↔ME— mutual conversion of electrical and mechanical energy). Currently, the major technological problems of the equipment for ES→EE and EE↔ME are significant harm to the environment, including climate, low energy efficiency, they are heavy and material-intensive.

To address these problems, this article proposes new concepts and technologies. Based on these concepts and technologies in particular, it is possible to create a new types of electric generators (for conversion of energy water, wind, solar energy, etc., into electrical energy), of electric motors (for conversion of electrical energy into mechanical energy, for of power industry and mechanical engineering including the automobile and aerospace industries).

These products have by far surpasses the performance than their known analogues:

- specific output power is up to 4 times higher in terms of volume;
- specific material consumption in terms of power (ratio of material consumption/(output power) from 2 to 3 times lower
- relative COP is up to 30% higher.

**Keywords:** 2VS-shaped curves; multi-vector electrical machines mEMa-jk; mEMa-jk with EEI induction cohesion

© 2021 Published by ECRES

## 1. INTRODUCTION

The production activities of mankind in the power industry, mechanical engineering, and their impact on the environment, including climate, strongly depends on the level of technological development of ES→EE (ES→EE – generation of electrical energy) and EE↔ME (EE↔ME – mutual conversion of electrical and mechanical energy). Currently, the major technological problems of the equipment for ES→EE and EE↔ME are significant harm to the environment, including climate, low energy efficiency, they are heavy and material-intensive.

Important properties of electrical energy – the ability to convert into any other type of energy, storage and transportation makes it the key source of energy. Equipment related to electricity is also very diverse: electric heat generators, generators of electromagnetic waves, including electric light sources, pulsed electromagnetic propulsion systems. The key tools (equipment), used to implement ES→EE and EE↔ME processes are EMa (EMa - electrical machinery, which is the common name of EG - electric generator and EM - electric motor)

First, whatever the original source of energy, renewable or other, normally (except for the direct conversion of solar energy into electrical energy), it is converted into electrical energy using electric generator (EG). Currently, over 90% of electricity is generated by EG.

Secondly, currently about 60% of the electricity produced (from all types of sources) is consumed by EM. It is also worth noting that the mass transition from internal combustion engine (ICE) to EM, especially in vehicles, to which the society rushes, will entail the need to increase the power generation. All this will result in a subsequent additional increase in the number and role of EG and EM in various fields of the mankind activity.

The existing EMa concepts and their implementation technologies have major weaknesses that hinder the wider application of EMa in various industries, in particular, transition from ICE to EM in self-propelling vehicles. The classical concept, which implies a single-vector electromagnetic field and full-tier surface of the induction cohesion [1-4], and its implementation technologies, on which the well-known EMa are based, have remained constant over the past 180 years:

- the electromagnet is two-sided and single-vector - i.e. the averaged flux of the magnetic field vector of the electromagnet coil on one side is directed inside it, and on the other side it is directed outward;
- the stator and rotor are full-tier – i.e. active surfaces that create inductively interacting fields are uniformly distributed over the surface of the stator and rotor.

Therefore, the existing EMa can be called single-vector, full-tier (single-vector, full-tier: oEMa-FF - electrical machine, oEG-FF - electric generator, oEM-FF - electric motor).

In order to develop power industry and preserve the ecology of the planet, the world community is taking measures to raise requirements for the level of technologies involved in EM, and they are focused on increasing their energy efficiency and expanding application in those areas where old technologies harmful to the environment prevailed, for example, ICE. In advanced types of EM, there is a struggle to win tenths of a percent of efficiency. As it is known, the following efficiency classes are adopted in Europe [5]: IE1 (standard efficiency), IE2 (high efficiency), IE3 (Premium Efficiency), IE4 (Super Premium Efficiency) and IE5 (Ultra-Premium Efficiency). Fig. 1 shows the energy efficiency classes of electric motors as the graph of the efficiency (%) of an electric motor depending on its power (kW).

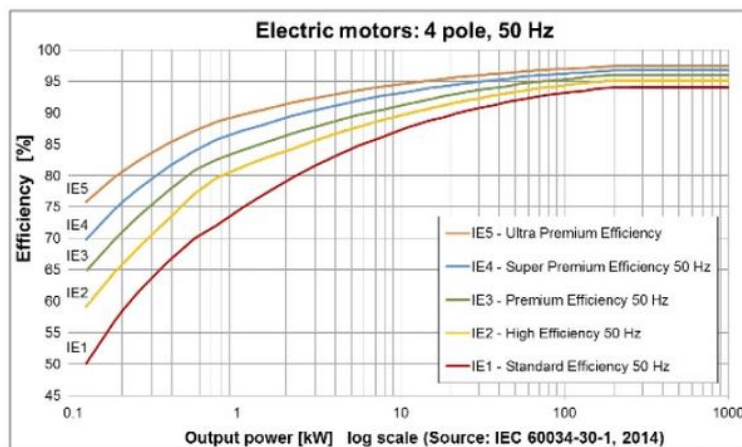


Figure 1. The energy efficiency classes of electric motors.

Note that since January 2017, literally all motors with a power from 0.75 to 375 kW must be of a class not lower than IE3 (restrictions for IE2 remain in effect) [6].

Currently, the existing oEMa-FFs have reached their limit of capabilities in terms of technical implementation, have significant weaknesses and do not meet the modern high standards of mechanical engineering and power industry. In particular, oEMa -FF have a low specific power density in terms of weight-size parameters (output energy values in relation to size and weight are low). As a result of such a high power, oEMa -FF have large weight and size, while with small and medium dimensions, oEMa -FF have relatively low shaft torque and COE (efficiency; coefficient of efficiency) in comparison with generally required in practice.

To increase the shaft torque and COP of small and medium sized oEMa -FF, for example, used in electric vehicles and aircrafts, it is necessary to use permanent magnets with components of rare earth metals and/or very high intensity of electric current  $P_E$  (work per unit time).

The intensity of electric current  $P_E$  is determined by the following expression:

$$P_E = IU \quad (1)$$

where:  $I$  - current intensity;  $U$  - is the electrical voltage.

In the OEM-FF of electric vehicle, the values of  $U$  - electric voltage and  $I$  - current intensity reach 700V and 400A, respectively [5-7]. Such large values of  $I$  and  $U$  are necessary in order to create a significant inductive cohesion force in the limited volume of the OEM-FF.

oEMa -FF with very high intensity of electric current  $P_E$  have a number of significant disadvantages. The amount of heat released during the passage of electric current through the conductor is determined by the Joule-Lenz law.

$$Q=I^2Rt \quad (2)$$

where:  $I$  - current intensity,  $R$  - conductor resistance,  $t$  - time during which the current flows.

Due to the large  $I$  value, a large amount of heat is generated in the electric motors of electric vehicles. This entails a number of problems:

- harmful effect on the climate and the environment (for life on Earth);
- the energy efficiency of the electric motor and batteries decreases – much of electricity is spent on heat generation;
- extreme temperature reduces the service life of the electric motor and batteries;
- complicates the design, increases the weight and production cost of electric vehicle: it is necessary to use an effective cooling system for the electric motor and energy batteries; they are forced to carry a large amount (500 kg or more) of expensive energy batteries.

It is also worth noting that the increase in the weight of electric vehicles due to the large number of batteries further increases the energy consumption of the electric vehicle. According to the National Highway Safety Traffic Administration – NHTSA, decrease in vehicle weight is the most powerful way to improve fuel economy. Decrease in the weight of aircraft vehicle by every 10% reduces fuel consumption by 8% [7].

The use of permanent magnets from expensive rare-earth components also entails a number of negative consequences:

- high load and extreme environmental conditions (high temperature and/or magnetic fields) means weakening of the magnetic properties (demagnetization) of permanent magnets;
- magnets containing rare earth elements have a high initial cost, and their prices depend on production costs, which entail significant fluctuations of exchange prices.

In practice, the construction of aircraft, including VTOA (VTOA - vertical takeoff and landing aircraft), can be used a number of low power EMs instead of one powerful EM - from 4 to 36 [8]-[10]. At the same time, the dependence on magnets containing rare earth elements and high values of electric voltage and current in EM will reduce. This approach of using multiple EMs also has major weaknesses - increased consumption of materials, total weight, and overall dimensions of the propulsive system, consequently, increases energy consumption.

We also note the following factors.

A major weakness of the structure of energy complex in the world is such that 2/3 of electricity is generated at thermal power stations, where the main fuel is gas or coal [11].

The percentage ratio of the number of electric vehicles and cars with internal combustion engine (ICE) is very small - about 1% of the global vehicle pool. Internal Combustion Engines (ICE) counted for over 90% of global car sales in H1 2019 [12]. In 2018, total passenger vehicle sales made up 88.9 million [13]. Whereby, the annual turnover of the automobile industry is about 2 trillion USD. According to a new report by Bloomberg New Energy Finance, 58% of global passenger vehicle sales in 2040 will come from electric vehicles, yet they will make up less than 33% of all cars on the road [14]. The cost of electric motors of electric vehicles is on average about 18% of the cost of electric vehicle.

The need to accelerate the transition from internal combustion engine (ICE) to EM, as well as the transition from fossil fuel to renewable energy, to which the society rushes, are among a number of incentives ensuring the advisability of developing energy efficient, small-size, low-cost new type EMs.

## 2. NEW CONCEPTS AND TECHNOLOGIES

In this article, in order to address technological problems of equipment for ES→EE and EE↔ME, an interconnected chain of new concepts and technologies is proposed [15- 22]:

- the concept of a multi-vector electromagnetic field;
- the concept for a family of 2VS-shaped curves;

- technologies of multi-vector electromagnets and a new type EMa – mEMa type (mEMa – multi-vector electrical machine, which is the general name of mEG – multi-vector electrical generator and mEM – multi-vector electric motor);

- the concept of mEMa-jk with EEI and their implementation technologies (mEMa-jk with EEI – mEMa-jk with energy-efficient sector-type induction cohesion), where the j and k show, respectively, the number of sectors of the active surface of the induction cohesion on the stator and on the rotor;

- technologies of a family of 2VS-shaped rotary EMa (2VS-shaped EMa), including EEI-type mEMa-jk.

Two of the above concepts - the concept of a multi-vector electromagnetic field and the concept for a family of 2VS-shaped curves are related not only to EMa, but allow addressing a wider range of problems and they can be called interdisciplinary.

## 2.1 Interdisciplinary concepts

### 2.1.1 The concept of a multi-vector electromagnetic field.

There are many diverse technologies for the implementation of a multi-vector electromagnetic field (electromagnet). Accordingly, the geometry of electromagnet and the set of directions of the electromagnetic induction vectors also have many aspects. To explain the foundations of the concept of a multi-vector electromagnet (electromagnetic field) and its fundamental difference from the well-known concept of a single-vector electromagnet (electromagnetic field), consider Fig. 4-6b.

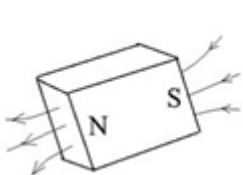


Figure 2.

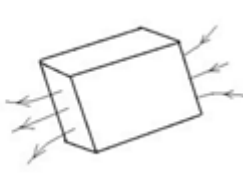


Figure 2-3. Single-vector electromagnet.

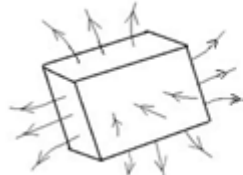


Figure 4a.

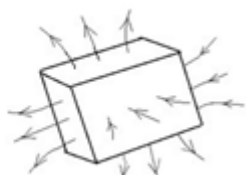


Figure 4a-4b. Multi-vector electromagnet.

From an aggregation of geometries of the multi-vector electromagnet and a set of directions of vectors of the multi-vector electromagnetic induction, Fig. 4-6b shows only two types. The sources of magnetic field and electromagnetic field in Fig. 4-6b are presented as a rectangle (for clarity), and their field vectors are shown as thin lines with arrows indicating their direction.

A permanent magnet has two poles, and the induction vector (averaged induction vector) is single-vector (Fig. 2). The existing electromagnets, in particular electromagnets in EM, are made both as single-vector (Fig. 3), and as a permanent magnet. They repeat the cyclic process: the induction vector enters from one of its small end surface and exits from the other end side, and vice versa. Fig. 4a and Fig. 4b show two options from the family of multi-vector electromagnets. Their cyclical process is as follows:

- induction vectors enter from two lateral sides and can come out of all 4 end sides of the electromagnet (as shown in Fig. 4a) and vice versa - induction vectors enter from all four end sides and come out of two lateral sides of the electromagnet);

- induction vectors enter from two lateral sides and one of the end sides, and can come out of 3 end sides of the electromagnet (Fig.4b) and vice versa - induction vectors enter from 3 end sides and come out of two lateral sides and one of end sides of the electromagnet.

### 2.1.2 The concept for a family of 2VS-shaped curves.

The family of 2VS-shaped curves is a new type of closed curves in general terms that will play an important role in the development of new directions in various disciplines. A representative from the family of 2VS curves is fundamentally different from the closed curves known in mathematics, in that it consists of an adjustable finite number of curve pieces with adjustable specified constant radii of curvature.

Any representative of the family of 2VS-shaped curves is smooth (the tangent changes continuously) and one curvature sign (the curvature does not change sign) of a closed curve, two end sides (vertex sectors of the circle) of which are sectors of circles with radii of curvature and, bounded within

Any representative of the family of 2VS-shaped curves is smooth (the tangent changes continuously) and one curvature sign (the curvature does not change sign) of a closed curve, two end sides (vertex sectors of the circle) of which are sectors of circles with radius of curvature  $R_{01}$  and  $R_{02}$  limited within  $0 < R_{02} \leq R_{01} < \infty$ ,  $R_{01} \leq R_{02} + \ell_0$ , where  $\ell_0$  – the distance between the centers of the vertex sectors of circles is limited within  $0 \leq \ell_0 < \infty$ . The longitudinal axis  $Ax_B$  (in Fig. 5 the axis  $O^I O^{II}$  is bundled with the longitudinal axis) divides the 2VS-shaped curve into two regions, which are generally not symmetrical about

the longitudinal axis  $Ax_B$ . The longitudinal axis  $Ax_B$  divides each of the vertex sector angles  $\vartheta_1$  and  $\vartheta_2$ , with radius of curvature, respectively  $R_{01}$  and  $R_{02}$ , into two parts:  $\vartheta_1 = \sum_{j=1}^2 \vartheta_{1j}$ ;  $\vartheta_2 = \sum_{j=1}^2 \vartheta_{2j}$ . In this case, the parts of the central sector angles  $\vartheta_{1j}$  and  $\vartheta_{2j}$ , where  $j=1, 2$ , are limited within  $0 < \vartheta_{1j} < \pi$  and  $0 < \vartheta_{2j} \leq \frac{\pi}{2}$ . In addition, the 2VS-shaped curve includes two lateral parts, each of which is closed by its two end sides, selected from a row of the circle sector and straight line segments. Fig. 5 shows one of the options of the family of 2VS-shaped curves, in which one lateral side is presented as a segment of length  $L_{Sp1}$ , and the other side is presented as a sector of the circle with the central angle  $\vartheta_{Sp2}$ .

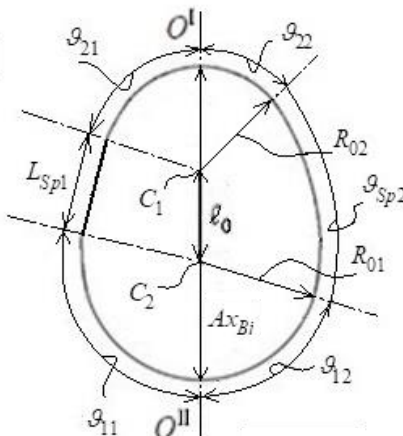


Figure 5. One of the options of the kind of 2VS-shaped curves.

Divided by the longitudinal axis  $Ax_{Bi}$ , any of the sides (longitudinal-axial region) of any representative of the family of 2VS-shaped curves, generally may refer to one of two groups:

- convex group satisfying the equation as follows:

$$R_{Spj} = \frac{\ell_0 + R_{01} \sin \vartheta_{1j} + R_{02} \sin \vartheta_{2j}}{\sin \vartheta_{1j} + \sin \vartheta_{2j}}, \quad (2)$$

where  $R_{Spj}$  – the radius of curvature of one of the lateral sectors of the circle, with  $j = 1$  from one and with  $j = 2$  from the other side, relative to the axis  $Ax_B$ ;

- degenerate group satisfying the equation as follows:

$$R_{02} = R_{01} - \ell_0 \sin \left( \frac{\pi}{2} - \vartheta_{2j} \right) \quad (3)$$

under the condition  $|\vartheta_{1j}| = |\vartheta_{2j} + \frac{\pi}{2}|$ , with  $j = 1$  from one and with  $j = 2$  from the other side, relative to the axis  $Ax_B$ .

For a convex part of the 2VS-shaped curve, the ratio of the length of the longitudinal axis  $Ax_{BR}$  to the width  $h_{Rj}$  is determined using the following expression:

$$\frac{Ax_{BR}}{h_{Rj}} = \frac{(R_{Spj} - R_{01}) \sin \vartheta_{1j} + (R_{Spj} - R_{02}) \sin \vartheta_{2j} + R_{01} + R_{02}}{R_{Spj} - (R_{Spj} - R_{01}) \cos \vartheta_{1j}} \quad (4)$$

Note that as it appears from the expression (3), the degenerate longitudinal-axial part (half) from the group of the family of 2VS-shaped curves consists of several subgroups.

1) When  $R_{02} < R_{01}$  and  $\ell_0 > 0$  conditions are met, the expression (3) will refer to the variant of the curve with lateral part as a straight line segment with an inclination at the angle  $\psi = \frac{\pi}{2} - \vartheta_{2j}$  to the longitudinal axis. The ratio of the length of the longitudinal axis  $Ax_{BL}$  to the width  $h_{Lj}$  of this curve is determined using the following expression:

$$\frac{Ax_{BL}}{h_{Lj}} = 1 + \frac{R_{02}}{R_{01}} + \frac{R_{01} - R_{02}}{R_{01} \sin \left( \frac{\pi}{2} - \vartheta_{2j} \right)}. \quad (5)$$

2) When  $R_{02} = R_{01}$  and  $\ell_0 > 0$ , conditions are met, the expression (3) will refer to the variant of the curve with lateral part as a straight line parallel to the major longitudinal axis. The ratio of the length of the longitudinal axis  $Ax_{BL}$  to the width  $h_{Lj}$  of this curve is determined using the following expression:

$$\frac{Ax_{BL}}{h_{Lj}} = 2 + \frac{\ell_0}{R_{01}}, \quad (6)$$

where  $\ell_0$  value is limited within  $0 < \ell_0 < \infty$ .

3) When  $R_{02} = R_{01}$ ,  $\ell_0 = 0$  and  $\vartheta_{2j} = \frac{\pi}{2}$ , conditions are met, the expression (3) will refer to the variant describing the circle.

Based on the concept of a multi-vector electromagnetic field (electromagnet), it is possible to create multi-vector EMa, that is, in the form of mEMa, which have significantly higher performance than their known analogues in the form of oEMa -FF:

- specific output power is up to 4 times higher in terms of volume;
- specific material consumption in terms of power (ratio of material consumption/(output power) from 2 to 3 times lower
- relative COP from to 30% higher.
- increased service life (from 25% to 40% more) and repair period (from 20% to 35% more)
- low production cost (from 2 to 10 times)

Based on the concept of 2VS-shaped curve family, it is possible to create 2VS-shaped rotational EMa family, including the 2VS-shaped rotational mEMa family. This allows EMa to be designed in a variety of forms, depending on the specific application.

The concept of mEMa-jk with EEI and their implementation technologies implies a special distribution of the active elements of the induction cohesion on the surface of the EMa stator and rotor, in order to achieve maximum energy efficiency. The technology of the mEMa-jk with EEI along with other requirements depending on the specific type and shape (for example, 2VS-shape) of EMa rotation, includes the multi-sector EMa, i.e. in the form of EMa -jk (EM-jk and EG-jk). The technology of implementation of the mEMa-jk with EEI allows to make EMa with a significantly higher torque than existing analogues, with the same overall weight and overall dimensions. Of course, EMa -jk can be designed as multi-vector, i.e. as mEMa -jk (mEM-jk и mEG-jk).

The priority of creating the direction of multi-vector and multi-sector mEMa-jk electric machines, i.e. mEG-jk electric generators and mEM-jk electric motors, refers to the beginning of 2014 (*Sapargaliev A. A., patent KZ 32377 dated 12016, restored: bulletin No. 17, April 26, 2019, priority 14.03.2014*). Over the past 6 years, Kazakhstani scientists have been developing the concept of mEMa-jk and their implementation technologies both in theoretical and practical terms - the performance of the constructed mEMa-jk and the results of various research have been discussed at major international conferences and published in leading scientific journals of the world [15-22]. The concept of a multi-vector clutch in EM and its multiple advantages over a single-vector clutch in EM is currently proven and recognized internationally. In August 2019 (more than 4 years after our patent), Linear Labs (USA) introduced a 4-vector full-row electric motor "HET" ("HET" - Hunstable Electric Turbine), which has twice the torque, 3 times higher output power and 20% higher relative efficiency compared to the known oEM-FF [23]. We have patented technologies of a large family (and not a separate EM) 2VS-form rotational mEMa-jk (2VS-form mEMa-jk), including EEI-form mEMa-jk (2VS-form EEI-form mEMa-jk). Representatives of the 2VS-form family of the EEI-type mEMa-jk have more fundamental possibilities in relation to any known EM, both in terms of functional characteristics and the use of any geometric solutions for objects: (a) can be not only 4-vector, but also 3 or 2 vector; (b) may have higher efficiency, based on multi-sector and EEI-type of implementation with more "goodness"; (c) the shape of rotation can be performed in any of the kinds of 2VS curves.

As discussed above, the performance and consumer benefits of mEMa -jk are significantly higher than those of oEMa -FF. Therefore, in many cases there is no need to use permanent magnets in mEMa-jk with expensive rare earth elements and/or very high electric power  $P_E$  to achieve the required high torque and high efficiency. This will further result in the widespread implementation of electric machines such as mEMa-jk in all areas of power industry and mechanical engineering.

The development of these areas will result in the new type of products that are classified as breakthrough innovation, and radically change the ratio of values in the market and, ultimately, displace previously prevailing products.

**Author Contributions:** Conceptualization, technologies, guidance on the creation of mEMa –jk, A. A. Sapargaliyev writing—review and editing, creating mEMa –jk, A. M. Zhunusbekov, N. Ungarov. All authors have read and agreed to the published version of the manuscript.

## **REFERENCES**

- [1]. Ilyinsky N.F. Fundamentals of Electric Drive: Textbook for Universities.— 2nd ed., M .: Publishing House of MEI, 2003. - P. 220. - ISBN 5-7046-0874-4. (on Russian)
- [2]. Onishchenko G.B. Electric drive. - M .: Academy, 2003. (on Russian)
- [3]. Electronic textbook "Electric machines". - L. Nauka, 1968, 487 p. (on Russian)
- [4]. Usoltsev A.A. Electric machines / Textbook. SPb: NIUITMO, 2013, 416. (on Russian)
- [5]. <https://www.quora.com/What-are-the-differences-between-IE3-and-IE2-motors>
- [6]. <https://avtprom.ru/news/2017/03/27/ie4-ili-ie5-budushchee-v>
- [7]. [https://mgimo.ru/files/120132/polyakova\\_vodorod.pdf](https://mgimo.ru/files/120132/polyakova_vodorod.pdf)
- [8] <https://www.aviationtoday.com/2020/01/02/top-10-air-taxi-stories-2019/>
- [9] <https://vc.ru/transport/90762-aerotaksi-i-transportirovka-gruzov-bespilotnikami-kak-nemeckiy-startap-volocopter-hochet-reshit-problemu-probok>
- [10].<https://ecotechnica.com.ua/transport/4526-elektricheskoe-aerotaksi-lilium-jet-vypolnilo-polnotsennyj-testovyj-polet-video.html>
- [11]. [http://www.ixbt.com/car/general/electric\\_car\\_ecology.shtml/](http://www.ixbt.com/car/general/electric_car_ecology.shtml/)
- [12]. <https://www.jato.com/internal-combustion-engines-ice-counted-for-over-90-of-global-car-sales-in-h1-2019/>
- [13]. <https://www.focus2move.com/world-car-group-ranking-2018/>
- [14]. <https://pv-magazine-usa.com/2020/05/19/the-future-of-cars-is-electric-but-how-soon-is-this-future/>
- [15]. Sapargaliyev A.A., KZ 32377, dated 2016, renewed: newsletter № 17, April 26, 2019 (priority 14.03.2014);
- [16]. WO 2015137790 A3, 12.11.2015, Sapargaliyev A.A.
- [17]. WO 2016153328 A3, 15.12.2016, Sapargaliyev A.A.
- [18]. WO 2016195465 A1, 8.12.2016, Sapargaliyev A.A.
- [19] PCT/KZ2019/000017, filing date 09/11/2019, priority from 09/10/2018
- [20]. Sapargaliyev A.A., Sapargaliyev Y.A. “Volume Density of Power of Multivector Electric Machine”, World Academy of Science, Engineering and Technology International Journal of Electrical, Computer, Energetic, Electronic and Communication Engineering Vol:11, No:6, 2017.
- [21]. Sapargaliyev A.A., «New prospects of science and technology development of energy industry and improvement of conditions for living on the planet Earth» Global Journal of Researches in Engineering ISSN: 2455-3689, Volume 18 Issue 4 Version 1.0, 2018.
- [22]. <https://drive.google.com/file/d/1-rtYeU971cRNtRd39pKqQbNTz4JILqtu/view?usp=sharing> (mSRM-31).
- [23]. <https://hevcars.com.ua/linear-labs-razrabotali-elektromotor-budushhego/>



# RECYCLING OF WASTE TIRES BY THERMAL DISSOLUTION (PYROLYSIS) AND THERMOCHEMICAL DEGRADATION (GASIFICATION)

Yayalik İbrahim

Mechanical Engineering Department, Yıldız Technical University, Yıldız, İstanbul, 34349, Turkey, ORCID: 0000-0001-9438-1040

Koten Hasan

Istanbul Medeniyet University, Mechanical Engineering Department, İstanbul, 34700, Turkey, ORCID: 0000-0002-1907-9420

Cite this paper as:

*Yayalik, I., Köten, H. Recycling of waste tires by thermal dissolution (pyrolysis) and thermochemical degradation (gasification). 9<sup>th</sup> Eur. Conf. Ren. Energy Sys. 21-23 April 2021, İstanbul, Turkey*

**Abstract:**

Billions of Waste Tires are produced every year in the world. It is an important environmental pollutant because it does not dissolve in nature. It has attracted attention because it can be a source of energy with global warming. Many studies have been done for the disposal or recycling of Waste Tires. But still a sustainable and applicable method has not been identified. Direct use of black carbon and pyrolytic liquid (tar) produced as a result of thermal dissolution is not possible. In the normal gasification process (800-900 °C), tar gasification reactor, which cannot be disintegrated, forms accumulations in the installation afterwards. In plasma gasification, on the other hand, heavy Hydrocarbons (Tar) do not decompose sufficiently and pass into the liquid phase since a significant part of the gassing occurs at low temperatures in the reactors with top entry and top gas outlet. In this study, the recovery of Waste Tires by the Full Mass Plasma Gasification method was investigated. In this method, all heavy Hydrocarbons (Tar) are broken down as all material is raised to Reactor temperature (above 1500 °C). As a complete activation is achieved, all particles gasify and a clean gas is obtained. Since the reaction takes place above the melting temperature of the steel, the Waste Tires can be gasified directly and the wires in it can be melted into semi-finished products.

**Keywords:**

*Waste tire, pyrolysis, plasma gasification, energy*

© 2021 Published by ECRES

## 1. INTRODUCTION

The rapidly increasing population and increasing living standards in the world have caused a rapid increase in waste and energy consumed. The primary source of energy needs is fossil fuels. The depletion of fossil resources and its environmental effects have forced researchers to seek sustainable and environmentally friendly energy. One of the wastes that cause environmental problems today is waste vehicle tire. In the USA alone, 300 million tires are discarded annually. More than 1.5 billion waste tires are produced in the world [1]. only the number of highway vehicles in Turkey in 2020. According to Turkstat is over 23 million. Considering that the average vehicle has an average of four tires and the tire life is assumed to be five years, over 18 million tires per year are scrapped [2]. Tires are stored in scrapyards, they contain visual and environmental pollution as well as fire hazard in warehouse areas. Waste tires have high calorific values (38.2 MJ / Kg [3], since they are made up of hydrocarbons. However, the high ratios of heavy hydrocarbons (Tar) limit their use as an energy source by burning [4].

For this reason, many studies have been carried out in order to transform the waste tires into solid, liquid and gas components by pyrolysis, and convert the products into economic products [1-7]. The high ratio of heavy hydrocarbons (tar) formed after the pyrolysis and the fact that it was not in a homogeneous structure, it was not possible to convert it into energy or into high-value products by burning. Due to the inorganic substances contained in the solid product (Char), it made it difficult to turn it into pure Black Carbon. For this reason, at the end of the process, only gaseous products were formed and their disposal studies were carried out by the Gasification process,

where they can easily be converted to energy [8-11]. In the gasification processes performed at 800-1000 °C, the fact that all of the heavy hydrocarbons did not break down, formed in liquid products and blocked the installation. Full Mass Plasma gasification method will ensure that all the materials entering the process are gassed above 1500 °C degrees, and all heavy hydrocarbons will break down [22].

## Structure of tires

Tires consist of different compounds, such as natural and artificial rubbers, Carbon black, Steel, Cloth belt and various fillers. It consists of simply 60-65% Rubber, 25-35% black Carbon, 9-13% steel wire, 5-6% textile yarn, 3% fillers and accelerators [1]. Material quantities vary depending on the area of use and purpose. Rubber is composed of elastomeric polymers characterized by a network structure that can deform in the short term under the influence of external forces. A mixture of natural rubber obtained from rubber tree and synthetic rubber obtained from petroleum-based products is used. Carbon black is used to strengthen the rubber and increase its resistance to wear. Fillers are added to make the rubber softer and more workable (a combination of aromatic, naphthenic and paraffinic organics).

## Thermal Dissolution (Pyrolysis)

It is the process of thermal degradation of polymers with large molecules. Pyrolysis process is carried out in an oxygen-free environment with or without catalyst. During this degradation, bond breaks or chain breaks occur in the structure of the polymer and many reactive radicals are formed. These radicals react in a series to stabilize, forming solid, liquid and gaseous products. Product quantities depend on test parameters such as pressure, temperature, heating rate. [7-11].

*Table 1. Composition of Waste Tires [7].*

<b>Elementary Composition</b>	
Rubber	38%
Fillers (Carbon black, silica, carbon chalk)	30%
Reinforcing material (steel, rayon, nylon)	16%
Plasticizers (oils and resins)	10%
Vulcanisation agents (Sulphur, zinc oxide, various chemicals)	4%
Antioxidants	1%
Miscellaneous	1%
<b>Proximate Analysis</b>	
Carbon	86%
Hydrogen	8%
Nitrogen	1%
Sulphur	2%
Oxygen	3%
Volatiles	62%
Fixed carbon	30%
Ash	7%
Moisture	1%

Thermal cracking (Pyrolysis) of waste tires takes place at approximately 350-600 °C in an inert environment. Thus, waste tires turn into olefins, various chemicals, gases and many useful products such as black carbon. Figure 1 shows the stages of the Pyrolysis process of waste tires. Before pyrolysis, the reinforcement wires in the waste tires are mechanically separated. The remaining part is broken down and made available to the reactors [12-18].

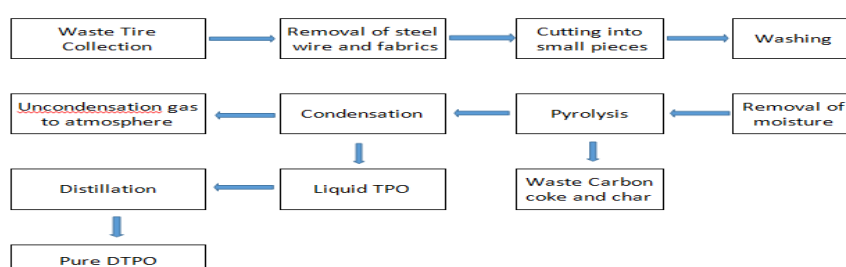


*Figure 1. Production of distilled tire pyrolysis oil from waste tire [11].*

In Table 2, the phases formed in the Pyrolysis process of waste liquids and their approximate amounts are shown. Amounts vary according to the pyrolysis speed and tire type. It is seen that its thermal value is quite high.

*Table 2. Mass balance of tire pyrolysis process [18]*

Source	Percent composition (%)				Elemental composition (%)			
	Volatile	Ash	FC	C	H	N	S	Other
Carbon Black	3.25	9.05	87.7	86.49	1.30	0.51	1.96	9.74
Deviation	0.55	2.05	2.60	2.70	0.01	0.18	0.13	2.38

## 2. METHODOLOGY

### 1. Liquid products from waste tire pyrolysis

It is a product that leaves the pyrolysis reactor as hydrocarbon vapor and condenses under normal conditions and becomes liquid. Approximately 35-45% of Pyrolytic oil is obtained from the waste tire. Pyrolysis oil is a fuel consisting of complex hydrocarbon compounds in the C<sub>6</sub>-C<sub>24</sub> range in content. Valuable light hydrocarbons such as benzene, toluene, xylene, limonene and polycyclic aromatics such as Naphthalene, pentane, fluorine and biphenyl are found in significant amounts in the pyrolytic oil. It has a high calorific value (41-44 MJ / kg). However, it is very difficult to burn heavy oils (tar). In Table 3, the types and quantities of liquid products obtained in Waste Tires pyrolysis are indicated. These amounts and types vary according to the type of Waste Tires and the Pyrolysis rate. However, they break down completely at high temperatures like 1200 °C. Heavy hydrocarbons separated without reacting in combustion and pyrolysis reactors condense and become liquid (tar) and accumulate in the installation, cleaning is very difficult and causes energy loss. They need to be refined [9-18]. Many studies have been done to convert it to energy by burning it in internal combustion engines [16-21].

*Table 3. Chromatographic analysis of liquid fraction (oil) from tire pyrolysis to show its Chemical composition [18].*

Substances	Mass Percent (g/g, %)
Isopentane (C <sub>5</sub> H <sub>12</sub> )	1.78 ± 0.08
1-Pentene (C <sub>5</sub> H <sub>10</sub> )	1.07 ± 0.08
2-Pentene (C <sub>5</sub> H <sub>10</sub> )	7.00 ± 0.12
1,3-Pentadiene (C <sub>5</sub> H <sub>8</sub> )	36.47 ± 0.67
2-Metil-1butene (C <sub>5</sub> H <sub>10</sub> )	0.32 ± 0.08
2-Metil-2butene (C <sub>5</sub> H <sub>10</sub> )	17.84 ± 0.67
n-Pentane (C <sub>5</sub> H <sub>12</sub> )	1.38 ± 0.08
Hexanes(~C <sub>6</sub> )	10.09 ± 4.15
Higher oils	24.05 ± 0.67

## 2. SOLID PRODUCTS FROM PYROLYSIS

The solid product obtained by pyrolysis is called Black Carbon (char). Waste Depending on the type of tire, pyrolysis creates 30-35% Char by mass, but it is not suitable for direct use because it contains 10-15% ash. In addition, if the tire is pyrolysed without disassembled parts, it may be contaminated with char, wire, linen, nylon and fiber rubber material. This situation makes it difficult to use char as carbon black. Some methods such as steam activation, acid treatment, benzene extraction, filtration are applied to bring the char to carbon black quality. The amount and elemental analysis of the solid phase obtained as a result of pyrolysis are given in Table 4. There is a large amount of non-Black Carbon material such as 20%. While the carbon black obtained can be used in the production of rubber, paint, plastic and plastic goods, the surface area is increased by activation with gas or chemicals between 800-1000 °C for its use as activated carbon [8,9,15].

*Table 4. Evaluation of carbon black obtained [18].*

Source	Percent composition (%)				Elemental composition (%)			
	Volatile	Ash	FC	C	H	N	S	Other
Carbon Black	3.25	9.05	87.7	86.49	1.30	0.51	1.96	9.74
Deviation	0.55	2.05	2.60	2.70	0.01	0.18	0.13	2.38

### 3. GAS PRODUCTS FORMED IN PYROLYSIS

It is the product that leaves the reactor as gas in the pyrolysis process but does not condense. Waste is formed by 10-15% by mass, depending on the type of tire. The calorific value of the gas is around 30-40 MJ / m<sup>3</sup>. The gas product obtained from pyrolysis is a medium calorific value gas fuel and can be used in power plants, heating processes and drying of the feed. Gases obtained by pyrolysis of tires are carbon monoxide (CO), carbon dioxide (CO<sub>2</sub>), hydrogen sulphide (H<sub>2</sub>S), methane (CH<sub>4</sub>), ethane. It consists of (C<sub>2</sub>H<sub>6</sub>), propane (C<sub>3</sub>H<sub>8</sub>), butane (C<sub>4</sub>H<sub>8</sub>) and butadiene (C<sub>4</sub>H<sub>6</sub>) [6-15]. Table 5 shows the gases formed as a result of the pyrolysis of waste tires and their amounts. Its calorific value is even higher than natural gas.

*Table 5. Pyrolysis Gas Constituents [18].*

Substances	Mass Composition (g/g, %)
Carbon dioxide (CO <sub>2</sub> )	24.70 ± 0.23
Methane (CH <sub>4</sub> )	36.77 ± 4.15
Ethane (C <sub>2</sub> H <sub>6</sub> )	12.09 ± 1.38
Propane (C <sub>3</sub> H <sub>8</sub> )	9.19 ± 2.05
Isobutene (C <sub>4</sub> H <sub>10</sub> )	1.94 ± 0.20
2-Metilpropane (C <sub>4</sub> H <sub>10</sub> )	6.57 ± 0.67
2-Metilpropene (C <sub>4</sub> H <sub>10</sub> )	6.30 ± 1.38
n-Butane (C <sub>4</sub> H <sub>10</sub> )	2.44 ± 0.20
Natural gas calorific value (kJ/kg)	42,420 ± 3089
GLP calorific value (kJ/kg)	60,128 ± 1256

### Thermochemical Degradation (Gasification)

The process of producing flammable gases such as hydrogen, methane, ethane, carbon monoxide by reacting organic materials with air, steam, oxygen, hydrogen, carbon dioxide or their mixtures at high temperatures to produce gas suitable for the intended use is called gasification. Gas / solid, gas / liquid and gas / gas reactions occur during gassing. Gasification occurs so quickly that liquid / gas reaction is hardly seen with the effect of high temperature. Apart from flammable gases, carbon dioxide, nitrogen, oxygen and water vapor are also formed depending on the nature of the substances entering the gasification. These reactions are often not single-step. Generally, the gas / solid reaction that occurs takes place in the pores in the outer surface area of the layer [22]. In Figure 2, the processes applied to the gasification and post products are seen.

The products formed as a result of gasification vary depending on the gasification temperature. Most of the large molecules (Tar) do not break down between 600 and 1000 °C. Under normal conditions, it becomes liquid. It causes clogging by precipitation in the installation after the reactor. It is also a waste of energy. As the temperature increases, fragmentation increases and liquid product formation decreases. After 1200 °C, all Hydrocarbons are broken down. However, after 1000 °C, the total calorific value of the gas products begins to decrease. For this reason, gasification is generally not done above 1000 °C.

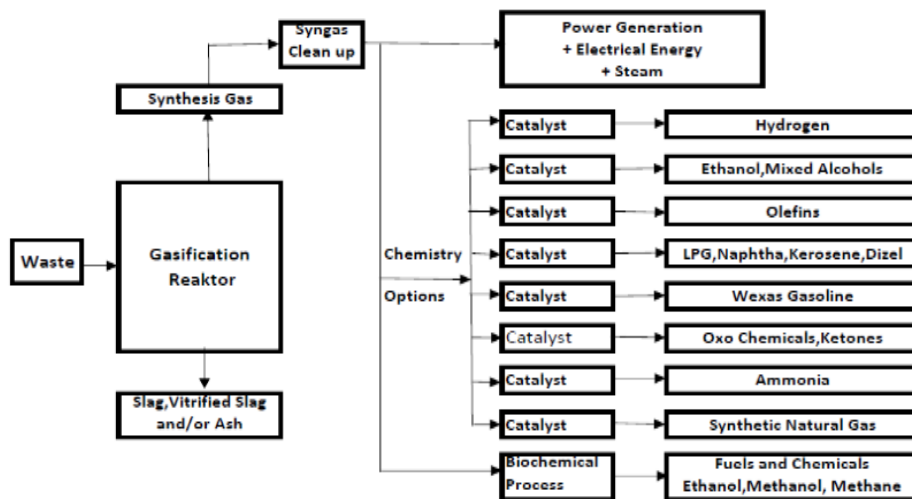
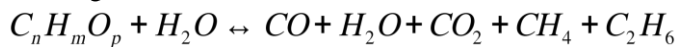


Figure 2. Pathway of waste to energy by gasification [22].

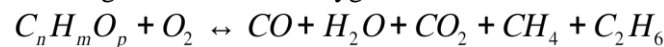
In existing gasification reactors (Fixed Bed, Fluidized Bed, Rotary Furnace, Plasma etc.) Hydrocarbons generally go into gas phase at low temperatures and leave the reactor. Therefore, liquid products (Tar) are formed more since complete decomposition does not occur. For this reason, additional reactors are built to increase the temperature of the gas products after the reactor and to ensure full gasification. However, this only prevents the formation of liquid products by breaking heavy molecules (Tar) and does not make a significant contribution to the energy value.

Plasma gasification method was developed for high efficiency and fast reaction. Three methods are the most prominent, namely Oxygen, steam and direct gasification. Carbon that cannot react in Hydrocarbons with a high rate of carbon, remain as black carbon.

Plasma gasification with steam;



Plasma gasification with oxygen;



Plasma gasification;



Since there are elements such as C, H, O, S, N in the Waste Tire, there will be Nitrogen and Sulfur compounds such as NOx and H2S in the products after gasification. Since the amount of Carbon in Waste Tires is very high, a large amount of black Carbon will remain without gasification as a result of Plasma Pyrolysis.

### 3. RESULTS AND DISCUSSION

#### 1. Gasification of Waste Tires

Waste tires, Fixed bed, fluidized bed, Rotary furnace, Plasma etc. Gasification is possible in all gasification reactors. Most of the incoming material turns into gaseous products. Some of the Heavy Hydrocarbons (Tar) come out without breaking down and turn into liquid products. All of the carbon can be gasified by feeding enough Oxygen or Water vapor. Thus, no black carbon remains in the solid phase. Waste tires can be fed into the reactor after the steel wires are stripped, as in Pyrolysis. Otherwise, it will not be possible to provide material flow. This requires a process and cost to separate the wires before gasification and to separate the tires into small pieces [24-28].

#### 2. Gasification of waste tires in Full Mass Plasma Gasification (FMPG) reactor

In this type of reactor, it is not necessary to remove the steel wires in the gasification process of waste tires. At a temperature above 1500 °C, post-process molten steel can be converted into high-value semi-finished materials with additional processes. All hydrocarbons turn into gases with high calorific value by gasification. A very clean gas is obtained since there is no large molecule Hydrocarbon and solid particles left inside. Since Waste Tires have a high carbon ratio, enough steam or oxygen must be supplied to turn all carbon into gaseous products. This gas is easily converted into electrical energy in the Gas-Steam Turbine cycle.

## 4. CONCLUSION

In the recycling of Waste Tires, it is not possible to directly use the solid, liquid and gas products resulting from the Pyrolysis process. Therefore, it must be converted into usable products with different processes or additives. All hydrocarbon molecules are broken down by plasma gasification at high temperature (above 1500 °C) of all materials subjected to gasification process. CO, CO<sub>2</sub>, CH<sub>4</sub>, C<sub>2</sub>H<sub>6</sub>, CmHn, H<sub>2</sub> etc. turns into flammable gases. Harmful gases such as NOx and H<sub>2</sub>S are also produced in Waste Tires. It is converted into electrical energy as a clean fuel in combined gas-steam turbine systems. Waste tire is easily cleaned with the Sulfur flue gas cleaning. Melting steel wires are transformed into semi-finished steel products as desired.

## REFERENCES

- [1] Alsaleh A. & Sattler M L. Waste Tire Pyrolysis: Influential Parameters and Product Properties Curr Sustainable Renewable Energy Rep (2014) 1:129–135.
- [2] Karagöz M., Yanbuloğlu B. Pirolitik Yakıt-Dizel-Alkol Karışımı ile Çalışan Bir Dizel Motorun HC ve NO Emisyonlarının Araştırılması Düzce Üniversitesi Bilim ve Teknoloji Dergisi, 8 (2020) 2183-2192
- [3] Lopez g., Alvarez j., Amutio m., Mkhize N.M., Danon B., Van der Gryp P., Görgens J.F., Bilbao J. and Olazar M. Waste truck-tyre processing by flash pyrolysis in a conical spouted bed reactor Pyrolysis Process Optimisation to Maximise Limonene Production from Waste Tyres, Energy Conversion and Management Volume 142, 15 June 2017, Pages 523-532.
- [4] Ouyang S., Xiong D., Li Y., Chen L.Z.J., Pyrolysis of scrap tyres pretreated by waste coal tar, Carbon Resources Conversion 1 (2018) 218–227.
- [5] Xua S., Laia D., Zenga X., Zhang L., Hanb Z., Chengb J., Wua R., Mašekd O., Xub G., Pyrolysis characteristics of waste tire particles in fixed-bed reactor with Internals, Carbon Resources Conversion 1 (2018) 228–237.
- [6] Mahapatra S.S., Experimentation and Evaluation of Tyre Pyrolysis Oil, Department of Mechanical Engineering National Institute of Technology, Rourkela 2013–2014.
- [7] Nkosi N. and Muzenda E., A Review and Discussion of Waste Tyre Pyrolysis and Derived Products, Proceedings of the World Congress on Engineering 2014 Vol II, WCE 2014, July 2 - 4, 2014, London, U.K.
- [8] Zhang X., Li H., Cao Q., Jin L. and Wang F., Upgrading pyrolytic residue from waste tires to commercial carbon black, Waste Management & Research 2018, Vol. 36(5) 436–444.
- [9] González-González R.B., González L.T., Iglesias-González S., González-González E., Martínez-Chapa S.O., Madou M., Alvarez M.M. and Mendoza A., Characterization of Chemically Activated Pyrolytic Carbon Black Derived from Waste Tires as a Candidate for Nanomaterial Precursor, Nanomaterials 2020, 10, 2213.
- [10] Čížková A., Juchelková D., Comparison Of Yield Of Tires Pyrolysis In Laboratory And Pilot Scales, GeoScience Engineering Volume LV(2009), No.4 p. 60-65.
- [11] Khan M.Z.H. and Hossain M.I., Fuel properties of pyrolytic tyre oil and its blends with diesel fuel – towards waste management, Int. J. Environment and Waste Management, Vol. 18, No. 4, 2016.
- [12] Šuhaj P., Husář J. and Haydary J., Gasification of RDF and Its Components with Tire Pyrolysis Char as Tar-Cracking Catalyst, Sustainability 2020, 12, 6647.
- [13] Zhang Y., Wu C., Nahil M.A., and Williams P., Pyrolysis–Catalytic Reforming/Gasification of Waste Tires for Production of Carbon Nanotubes and Hydrogen, Energy & Fuels, April 2015.
- [14] Wang C., Tian X., Zhao B., Zhu L. and Li S., Experimental Study on Spent FCC Catalysts for the Catalytic Cracking Process of Waste Tires, Processes 2019, 7, 335.
- [15] Nkosi N., Muzenda E., Mamvura T.A., Belaid M. and Patel B., The Development of a Waste Tyre Pyrolysis Production Plant Business Model for the Gauteng Region, South Africa, Processes 2020, 8, 766
- [16] C. Wongkhorsub, N. Chindaprasert, A Comparison of the Use of Pyrolysis Oils in Diesel Engine, Energy and Power Engineering, 2013, 5, 350-355
- [17] Bašković U.Z., Vihar R., Seljak T., Dimitriadis A., Bezergianni S., Katrašnik T., Combustion and emission characterisation of innovative fuels in compression ignition engine: Tire Pyrolysis Oil and Hydrotreated Vegetable Oil, Digital proceedings of the 8th European Combustion Meeting, 18-21 April 2017, Dubrovnik, Croatia.
- [18] Cardoso de Oliveira Neto G., Carvalho Chaves L.E., Rodrigues Pinto L.F., Curvelo Santana J.C., Castro Amorim M.P., and Ferreira Rodrigues M.J., Economic, Environmental and Social Benefits of Adoption of Pyrolysis Process of Tires: A Feasible and Ecofriendly Mode to Reduce the Impacts of Scrap Tires in Brazil, Sustainability 2019, 11, 2076.
- [19] Islam M. N. and Nahian M. R., Improvement of Waste Tire Pyrolysis Oil and Performance Test with Diesel in CI Engine, Journal of Renewable Energy Volume 2016, Article ID 5137247, 8 pages.
- [20] Towski A., Tyre Pyrolysis Oil As An Engine Fuel, Journal of KONES Powertrain and Transport, Vol. 21, No. 1 2014.
- [21] Soni T. & Gaikwad A., Waste Pyrolysis Tire Oil As Alternative Fuel For Diesel Engines, International Journal of Mechanical and Production Engineering Research and Development (IJMPERD) Vol. 7, Issue 6, Dec 2017, 271-278.
- [22] Seo Y.C., Alam T., Yang W.S., Gasification of Municipal Solid Waste. Gasification for Low-grade Feedstock Chapter: 7 Publisher: Intech Open 2018.
- [23] Yayałık I., Koyun A., Akgün M., Gasification of Municipal Solid Wastes in Plasma arc medium, Plasma Chemistry and Plasma Processing, (2020) 40:1401–1416.
- [24] Betancura M., Arenasa C.N., Martíneza J.D., Navarro M.V., Murillo R., CO<sub>2</sub> gasification of char derived from waste tire pyrolysis: Kinetic models comparison. Fuel 273 (2020) 117745.
- [25] Šuhaj P., Husář J. and Haydary J., Gasification of RDF and Its Components with Tire Pyrolysis Char as Tar-Cracking Catalyst. Sustainability 2020, 12, 6647.

- [26] James G., Nema S.K,Singh A.,Murugan V., A comparative analysis of pyrolysis and gasification of tyre waste by thermal plasma technology for environmentally sound waste disposal. Institute of Plasma Research, Gujarat, India.
- [27] Ongen A.,Ozcan H.O.,Elmaslar Ozbas E. & Pangaliyev Y., Gasification of waste tires in a circulating fixed-bed reactor within the scope of waste to energy. Clean Technologies and Environmental Policy volume 21, pages1281–1291(2019).
- [28] Zhang Y., Chunfei Wu ,Nahil M.A.,Williams P., Pyrolysis-Catalytic Steam Reforming/Gasification of Waste Tires for Production of Carbon Nanotubes and Hydrogen. Energy & Fuels, 29 (5). pp. 3328-3334.



## REVIEW OF THOMSON HEAT

Yuri G. Gurevich

CINVESTAV-IPN, Mexico City, Mexico, gurevich@fis.cinvestav.mx, ORCID: 0000-0001-9057-7425

Igor Lashkevych

Instituto Politécnico Nacional, México City, Mexico (Sabatica in Ternopil Volodymyr Hnatiuk National Pedagogical University, Ternopil, Ukraine), i32555@gmail.com, ilashkevych@ipn.mx, ORCID: 0000-0002-1816-7787

Viktor Matsyuk

Ternopil Volodymyr Hnatiuk National Pedagogical University, Ternopil, Ukraine, mvm279@i.ua, ORCID: 0000-0002-8710-3082

*Cite this paper as:* Gurevich Yu G, Lashkevych I, Matsyuk V, Review of Thomson heat. 9th Eur. Conf. Ren. Energy Sys. 21-23 April 2021, Istanbul, Turkey

**Abstract:** The review of Thomson heat is presented: the traditional and modern descriptions. It is emphasized that the value of Thomson heat in the newest and traditional descriptions are different. It is presented explanation that the Thomson heat is equal to the product of the Seebeck coefficient, the temperature gradient, and the current density. This is result of the newest theory.

**Keywords:** Thomson effect, Thomson heat, Thomson coefficient, seebeck coefficient

© 2021 Published by ECRES

### 1. INTRODUCTION

In 1854, Thomson (Lord Kelvin) rationalized that the Peltier voltage has to be equal to the Seebeck voltage. Moreover, these two voltages must be proportional to the temperature in a linear manner [1]. This conclusion he made from the assumption that the electrical current produces only the Peltier heat, when it passes through two junctions. Nevertheless, the experiment did not prove it. Therefore, Thomson deduced that another reversible thermoelectric process must exist. This process consists in the evolution or absorption of heat, if the electrical current passes through a conductor with a temperature gradient. Mathematically,

$$Q_\tau = \tau \vec{j} \nabla T \quad (1)$$

where  $Q_\tau$  is the heat source density of a conductor,  $\tau$  is the Thomson coefficient,  $\vec{j}$  is the electric current density, and  $\nabla T$  is the temperature gradient. In addition, Thomson has found the relationship between the Thomson, Peltier, and Seebeck coefficients, so cold Kelvin relationships:  $\Pi = ST$  and  $\tau = -T \frac{dS}{dT}$ , where  $S$  is the Seebeck coefficient,  $\Pi$  is the Peltier coefficient.

### 2. TRADITIONAL THEORY OF THE THOMSON HEAT

The rate of heat absorbed or liberated in a unit volume of a conductor,  $Q$ , by Seeger is [2]:

$$Q = \vec{j} \vec{E} - \nabla \cdot (\Pi \vec{j} - \kappa \nabla T - \frac{\mu}{e} \vec{j}) \quad (2)$$

where

$$\vec{q} = \Pi \vec{j} - \kappa \nabla T \quad (3)$$

is the thermal (heat) flux density [2-7],  $\kappa$  is the thermal conductivity coefficient,  $\mu$  is the chemical potential,  $e$  is the magnitude of an electron charge,  $\vec{E}$  is the electric field strength.

Excluding  $\vec{E}$  from Eq. [2] using the electrical current density expression [3,8],

$$\vec{j} = -\sigma(\nabla\psi + S\nabla T) = \sigma\left(\vec{E} + \frac{1}{e}\nabla\mu - S\nabla T\right) \quad (4)$$

we obtain the following

$$Q = \frac{j^2}{\sigma} - T \frac{dS}{dT} \vec{j} \nabla T + \nabla(\kappa \nabla T) \quad (5)$$

Here  $\psi = \varphi - \frac{1}{e}\mu$  is the electrochemical potential of electrons [9],  $\varphi$  is the electrical potential. From Eq. [5], Seeger [2] and traditional theory makes decision that the second term,  $-T \frac{dS}{dT} \vec{j} \nabla T$ , is the Thomson heat and the Thomson coefficient is equal to  $-T \frac{dS}{dT}$ . In Eqs. [4,5]  $\sigma$  is the electrical conductivity coefficient. The first term in Eq. [5] corresponds to the Joule heat and the third term corresponds to heat transport due to the thermal conductivity transport process.

Let us use the equation from mathematical physics. Let  $\vec{p}$  is the flux of a physical quantity  $P$ . In this case, in the following equation

$$\nabla \cdot \vec{p} = D \quad (6)$$

$D$  plays a role of a source of the physical quantity  $P$  under stationary conditions [10,11]. The last means that, according to the traditional theory of the rate of heat absorbed or liberated in a unit volume, the stationary heat balance equation must be the following (considering the sample does not absorb nor radiate light) [12]

$$\nabla \cdot \vec{q} = -T \frac{dS}{dT} \vec{j} \nabla T + \frac{j^2}{\sigma} \quad (7)$$

Equation [7] must be correct because, according to the traditional theory, the Joule heat is  $\frac{j^2}{\sigma}$ , and the Thomson heat is  $-T \frac{dS}{dT} \vec{j} \nabla T$ .

*Consequence of a traditional theory:* There are two heat sources: the Thomson heat,  $-T \frac{dS}{dT} \vec{j} \nabla T$ , and the Joule heat,  $\frac{j^2}{\sigma}$ . Nevertheless, as follows from the modern theory of heat absorbed or liberated in a unit volume of a conductor, Eq. [7] is wrong.

### 3. MODERN THEORY OF THE THOMSON HEAT

The energy flux density,  $\vec{w}_n$ , in an electron subsystem in a monopolar conductor is  $\vec{w}_n = -\kappa_n \nabla T + \Pi \vec{j} + \psi \vec{j}$  [13], where  $\kappa_n$  is the heat conductivity coefficient of electrons. If we add the phonon thermal flux density,  $-\kappa_{ph} \nabla T$ , we obtain the expression for the total energy flux density in a conductor,  $\vec{w}$ :

$$\vec{w} = \vec{q} + \psi \vec{j} \quad (8)$$

Here,  $\kappa = \kappa_n + \kappa_{ph}$ ,  $\kappa_{ph}$  is the phonon thermal conductivity coefficient.

Let us use the energy conservation law. Using this law we can write the following equation,  $\frac{\partial u}{\partial t} = -\nabla \cdot \vec{w}$ . This equation is correct, when radiation or absorption of light is absent. Here  $u$  is the energy density. The term,  $-\nabla \cdot \vec{w}$ , describes energy transport. Let us consider the stationary process. In this case,  $\frac{\partial u}{\partial t} = 0$ . Therefore, we obtain the following equation under stationary conditions:

$$\nabla \cdot \vec{w} = 0 \quad (9)$$

This is the stationary energy balance equation, when light radiation or absorption is absent. It follows from comparison of Eq. [9] with Eq. [6] that the energy sources are absent.

Using the expression for the energy flux density,  $\vec{w}$ , Eq. [8], the equation [9] transforms to:

$$\nabla \cdot \vec{q} = -\vec{j} \nabla \psi \quad (10)$$

Obtaining this equation, we have used  $\nabla \cdot \vec{j} = 0$  [13]. This is the consequence of the charge conservation law under stationary conditions [13].

Expressing  $\nabla \psi$ , using Eq. 4, Eq. 10 can be rewritten as follows [14]:

$$\nabla \cdot \vec{q} = \frac{j^2}{\sigma} + S \vec{j} \nabla T \quad (11)$$

This is the *stationary heat balance equation, when light radiation or absorption is absent*. Comparing Eq. [11] with Eq. [6], we can conclude that there are only two heat sources: the Joule heat,  $\frac{j^2}{\sigma}$ , and the Thomson heat [14]:

$$Q_\tau = S \vec{j} \nabla T \quad (12)$$

It follows from Eq. [1] and Eq. [12] that the Thomson coefficient,  $\tau$ , is equal to the Seebeck coefficient,  $S$ :

$$\tau = S \quad (13)$$

*Important.* The equation [11] is the consequence of the energy conservation law. Therefore, we can trust this equation more, than Eq. [7]. Thus, we must conclude that Eq. [7] is wrong. Hence, as Eq. [11] is correct, whereas, Eq. [7] is wrong, we must conclude that the correct Thomson heat is  $S \vec{j} \nabla T$ , but not  $-T \frac{dS}{dT} \vec{j} \nabla T$  [12, 14] and we must accept that the Thomson coefficient,  $\tau$ , is equal to the Seebeck coefficient,  $S$ :  $\tau = S$ .

#### 4. COMPARISON OF THE TRADITIONAL THEORY WITH THE MODERN ONE

Substituting expression for the heat flux, Eq. [3], into the stationary heat balance equation, Eq. [11], we obtain the following:

$$\frac{j^2}{\sigma} - T \frac{dS}{dT} \vec{j} \nabla T + \nabla \cdot (\kappa \nabla T) = 0 \quad (14)$$

Comparing this equation with Eq. [5] we deduce that the value of the rate of heat absorbed or liberated in a unit volume of a conductor,  $Q$ , by Seeger is always equal to zero. This is the consequence of the energy conservation law. This means that the definition, Eq. [2] of the rate of heat absorbed or liberated in a unit volume of a conductor,  $Q$ , by Seeger, that is used by traditional theory, is wrong. Moreover, the following equation must be accepted as the correct definition of the rate of heat absorbed or liberated in a unit volume of a conductor,  $Q$ , under stationary conditions:

$$\nabla \cdot \vec{q} = Q \quad (15)$$

Thus, comparing this equation with Eq. [11] we obtain for  $Q$ :

$$Q = \frac{j^2}{\sigma} + S \vec{j} \nabla T \quad (16)$$

It means that only two heat sources for the heat flux,  $\vec{q}$ , exist: the Joule heat,  $\frac{j^2}{\sigma}$ , and the Thomson heat,  $S \vec{j} \nabla T$ .

#### 5. THOMSON HEAT IN A BIPOLAR SEMICONDUCTOR

The expression for the energy flux density,  $\vec{w}_b$ , in a bipolar semiconductor can be written as follows [15]

$$\vec{w}_b = \vec{q}_b + \psi_n \vec{J}_n + \psi_p \vec{J}_p \quad (17)$$

where

$$\vec{q}_b = \Pi_n \vec{j}_n + \Pi_p \vec{j}_p - \kappa_b \nabla T \quad (18)$$

is the thermal (heat) flux density in a bipolar semiconductor;  $\Pi_n$  ( $\Pi_p$ ) is the Peltier coefficient of conduction electrons (holes);  $\vec{j}_n$  ( $\vec{j}_p$ ) is the electrical current density of conduction electrons (holes);  $\kappa_b = \kappa_n + \kappa_p + \kappa_{ph}$  is the thermal conductivity coefficient of a bipolar semiconductor;  $\kappa_p$  is the thermal conductivity coefficient of holes;  $\psi_n = \varphi - \frac{1}{e}\mu_n$  is the electrochemical potential of conduction electrons;  $\psi_n = \varphi + \frac{1}{e}\mu_p$  is the electrochemical potential of holes [9];  $\mu_n$  ( $\mu_p$ ) is the chemical potential of conduction electrons (holes).

Substituting the expression for the energy flux density in a bipolar semiconductor, Eq. [17], into the stationary energy balance, Eq. [9], we obtain [15]

$$\nabla \cdot \vec{q}_b = (\mu_n + \mu_p)R + \frac{j_n^2}{\sigma_n} + \frac{j_p^2}{\sigma_p} + S_n \vec{j}_n \nabla T + S_p \vec{j}_p \nabla T \quad (19)$$

According to Eq. 15 it follows from Eq. 19 that there are two Thomson heat sources in a bipolar semiconductor: Thomson heat of conduction electrons,  $S_n \vec{j}_n \nabla T$ , and Thomson heat of holes,  $S_p \vec{j}_p \nabla T$ . Here  $S_n$  ( $S_p$ ) is the Seebeck coefficient of conduction electrons (holes),  $R$  is the recombination rate.

## ACKNOWLEDGMENT

The authors, Yu.G. Gurevich and I. Lashkevych, thank CONACYT-IPN, Mexico for partial financial support.

## REFERENCES

- [1] Thomson W. Account of researchers in thermo-electricity, Philos. Mag. [5] 1854; 8: 62-69
- [2] Seeger K. Semiconductor Physics. Berlin: Springer, 1985.
- [3] Honig JM. Irreversible Thermodynamics and Basic Transport Theory in Solids. In: Bassani F, Liedl GL, Wyder P, editors. Encyclopedia of Condensed Matter Physics. Amsterdam: Elsevier, 2005.
- [4] Gurevich YuG, Logvinov GN. Thermolectric and electrothermic heating and cooling in semiconductors and semiconductor structures. „J.Thermoelectr. 2008; 1: 13-30 <<https://www.dropbox.com/s/bvjlyjqh768en7x/g.pdf?dl=0>>
- [5] Sellmyer DJ, Hurd CM. Galvanomagnetic and Related Effects. In: Lerner RG, Trigg GL, editors. Encyclopedia of Physics, 2<sup>nd</sup> edn. New York: VCH, 1991, pp. 421-423.
- [6] Samoilovitsch AG, Korenblit LL. The current state of the theory of thermoelectric and thermomagnetic phenomena in semiconductors. Usp. Fiz. Nauk 1953; 49(2): 243-272 <<https://ufn.ru/ru/articles/1953/2/c/>> (in Russian)
- [7] Samoilovitsch AG, Korenblit LL. The current state of the theory of thermoelectric and thermomagnetic phenomena in semiconductors. Fortschritte der Physik 1953; 1(9-10): 486-554 <<https://doi.org/10.1002/prop.19530010903>> (in German)
- [8] Anselm A. Introduction to Semiconductor Theory. Moscow: Mir / Englewood Cliffs: Prentice-Hall, 1981.
- [9] Shockley, W. The Theory of p-n Junctions in Semiconductors and p-n Junction Transistors. Bell Syst. Tech. J. 1949; 28: 435-489 <<https://doi.org/10.1002/j.1538-7305.1949.tb03645.x>>
- [10] Labrosse G, Kasperski G. Newtonian Fluids and Thermohydraulics. In: Francoise JP, Naber GL, Tsun TS, editors. Encyclopedia of Mathematical Physics, vol. 3. Amsterdam: Elsevier, 2006, pp. 492-502.
- [11] Woodhouse NMJ. Introductory Article: Electromagnetism. In: Francoise JP, Naber GL, Tsun TS, editors. Encyclopedia of Mathematical Physics, vol. 1. Amsterdam: Elsevier, 2006, pp. 40-51.
- [12] Lashkevych I, Gurevich YuG. Correct Thomson Heat. In: International Science-Practice Conference "Preparation of Future Teachers of Physics, Chemistry, Biology and Natural Sciences in the Context of the Requirement of a New Ukrainian School" Original name in Ukrainian: "Підготовка майбутніх учителів фізики, хімії, біології та природничих наук у контексті вимог нової української школи"; 20-21 May 2019: Ternopil Volodymyr Hnatiuk National Pedagogical University, Ternopil, Ukraine: pp. 18-19. <[https://www.researchgate.net/publication/333882081\\_Correct\\_Thomson\\_Heat](https://www.researchgate.net/publication/333882081_Correct_Thomson_Heat)>
- [13] Landau L, Lifshitz E. Electrodynamics of Continuous Media, Course of Theoretical Physics. New York: Pergamon, 1984.
- [14] Lashkevych I, Velazquez JE, Titov OYu, Gurevich YuG. Special important aspects of the Thomson effect. Journal of Electronic Materials 2018; 47(6): 3189-3192 <<https://doi.org/10.1007/s11664-018-6205-x>>
- [15] Gurevich YuG, Lashkevych I. Sources of fluxes of energy, heat, and diffusion heat in a bipolar semiconductor: Influence of nonequilibrium charge carriers. Int. J. Thermophys. 2013; 34: 341-349 <<https://doi.org/10.1007/s10765-013-1416-0>>



# DEVELOPMENT OF AN ADAPTIVE CONTROL SYSTEM FOR A HOT WATER SUPPLY USING SOLAR POWER PLANT

Vasily Stan

Belgorod State Technological University after V.G.Shukhov, Belgorod, Russia, madseal@yandex.ru, ORCID 0000-0002-0609-7013

Yury Koshlich

Belgorod State Technological University after V.G.Shukhov, Belgorod, Russia Belgorod, Russia, koshlich@yandex.ru, ORCID: 0000-0002-6905-5275

Aleksandr Belousov

Belgorod State Technological University after V.G.Shukhov, Belgorod, Russia Belgorod, Russia, ntk@intbel.ru, ORCID: 0000-0002-6905-5275

Nadezhda Koshlich

Belgorod State Agricultural University Named after V. Gorin, Belgorod, Russia Belgorod, Russia, ORCID: 0000-0002-6905-5275

*Cite this paper as:* Stan, V., Koshlich, Yu., Belousov, A., Koshlich, N. *Development of an adaptive control system for a hot water supply using solar power plant.* 9<sup>th</sup> Eur. Conf. Ren. Energy Sys. 21-23 April 2021, Istanbul, Turkey

---

**Abstract:**

The article is devoted to the development of a comprehensive solution aimed at improving the efficiency of solar water heating installations. In the process, a number of issues were considered, one way or another related to the development process, in particular, the reasons that are the motivation for its implementation. Using the methods of regression analysis, models of heat and mass transfer processes between solar collectors and a storage tank were built, on the basis of which an algorithm was developed for determining the optimal initial speed of movement of the adaptive regulator coolant. The structure of the control system is developed on the basis of the developed regulator using wireless information interaction between its elements, the scheme of interaction between them is described. A control device has been developed and the effectiveness of the developed solution has been assessed and conclusions have been drawn about the feasibility of further development with the subsequent massive introduction of the device into local water heating systems.

---

**Keywords:**

solar plant, wireless communications, automatic control, adaptive regulation

---

© 2021 Published by ECRES

## 1. INTRODUCTION

The speed of human development is growing every year, and the modern world can no longer be imagined without its technological equipment. However, the rapid development of technologies is accompanied by an increase in the demand for energy resources that ensure their normal functioning.

Traditional energy sources, which are hydrocarbons, the energy of the flow of rivers and the energy of the decay of atomic nuclei, carry with them both real and potential danger of environmental pollution. In view of these circumstances, modern energy is placing increasing emphasis on alternative or renewable energy sources that are safe enough for the environment, and, at the same time, are able to meet energy needs [1, 2].

Among all the variety, due to the simplicity and ease of operation, the most common are sources that use the energy of solar radiation, which, in turn, are subdivided into installations that generate electric current and installations that heat a liquid or gaseous heat carrier. As a rule, the greatest interest is shown precisely in the first type of solar installations, because electricity is much easier to accumulate, transport and convert into other types of energy,

however, they have one significant drawback - a relatively low efficiency, which, at the moment, is no more than 10% [3].

The highest level of interest in alternative energy is observed in developed countries, especially where energy carriers are imported, such as in Germany, Great Britain and a number of Scandinavian countries. An equally important factor that has a stimulating effect on the development of this industry is active support at the legislative level. So for the integration of alternative energy in an enterprise or household, subsidies are allocated to cover part of the cost of implementation. Moreover, the active introduction of smart grids (Smart Grid) allows the owners of such stations to sell electricity, which reduces the average cost of energy on the market and the payback period of the equipment [4].

In the Russian Federation, the share of alternative energy is no more than 1%, which indicates a low level of interest. This situation, for the most part, is due to the low level of solar radiation per unit area (with the exception of the southern regions and the Far East), unsuitable landscape and severe climatic conditions. In addition, unlike the previously mentioned developed countries, the introduction of renewable energy sources is not subsidized in the Russian Federation, which, coupled with the high cost of the necessary equipment, has put the Russian alternative energy into stagnation.

Thus, the main reasons for the low level of development of alternative energy in Russia are low energy efficiency and high cost of equipment, as well as the high availability of traditional fossil energy resources.

## 2. CONTROL PRINCIPLES DEVELOPMENT

Among the tasks set, the most important is to increase the efficiency of the installation, which is achieved by developing appropriate control algorithms, the most significant of which is the algorithm for regulating heat and mass transfer processes between the main elements of the solar plant [5].

For this, an adaptive step-by-step algorithm for regulating the process of charging a heat accumulator was developed [6]. A graphic illustration of the algorithm's operation is shown in Fig. 1.

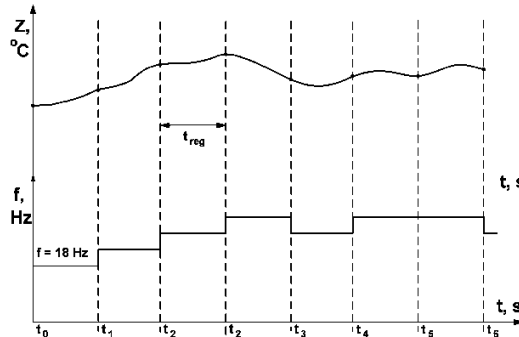


Figure 1. Demonstration of the regulation algorithm

The principle of this algorithm is as follows:

1. During the operation of the installation, the temperature indicators at the inlet and outlet to the storage tank are measured, and their difference  $z$  is calculated, ie:

$$z = T_{in}^{st} - T_{out}^{st}. \quad (1)$$

2. Further, after a time interval  $\tau_{reg}$ , the temperature is measured again and the value  $z$  is calculated, which is subsequently compared with the previous one:

$$\Delta z = z_i - z_{i-1}. \quad (2)$$

3. After that, on the basis of condition (2), the frequency of the supply voltage of the circulation pump was recalculated relative to the "zero frequency", which, according to the calculated data, is equal to 18 Hz [7]:

$$\begin{cases} \Delta z > 0 \rightarrow f_i = f_{i-1} + \Delta f, \\ \Delta z < 0 \rightarrow f_i = f_{i-1} - \Delta f, \\ \Delta z = 0 \rightarrow f_i = f_{i-1}. \end{cases} \quad (3)$$

It should be noted that such a mechanism for circulating the coolant is provided thanks to a frequency-controlled electric drive as soon as it can provide smooth control of the engine speed while maintaining its dynamic properties. Moreover, the use of a frequency drive has less impact on the service life of the motor and the electrical network that supplies it.

During the operation of the solar plant, the following disadvantages of this algorithm were identified:

- "long" reaching the optimal speed: since each time the pump started to work with a fixed frequency value and a sufficiently long control time constant, this was the reason that the regulator found the optimal speed for a long time, up to several hours;

- the influence of external factors: even taking into account the fact that this control algorithm is independent of the influence of weather factors, their influence sufficiently reduced the overall efficiency of the installation.

Thus, in order to eliminate the identified shortcomings, it was decided to supplement the previously used regulation algorithm. For this, it is necessary to reveal the functional relationship between the thermal power  $P$  generated by the installation, the coolant velocity  $v$  and the value of absorbed insolation  $q$  [8], or:

$$P = f(v, q). \quad (4)$$

It was decided to determine this dependence, according to the methodology of S.N. Sautin [12], two-factor analysis by the method of a full factorial experiment. For this it is required to carry out a number of experiments according to the following plan (Table 1) [9].

*Table 1. Key features of the experiment plan*

Characteristics	$v, m/s$	$q, W/m^2$
Main level	0,0017	850
Variation interval	0,0002	100
Upper level	0,002	1000
Lower level	0,0002	100

As a result of the experiment, a matrix of power values in kW was obtained for the corresponding values of the circulation rate (rel. units) and specific insolation ( $W/m^2$ ). After processing the obtained data [10], the response surface was obtained in the factor space (Fig. 2).

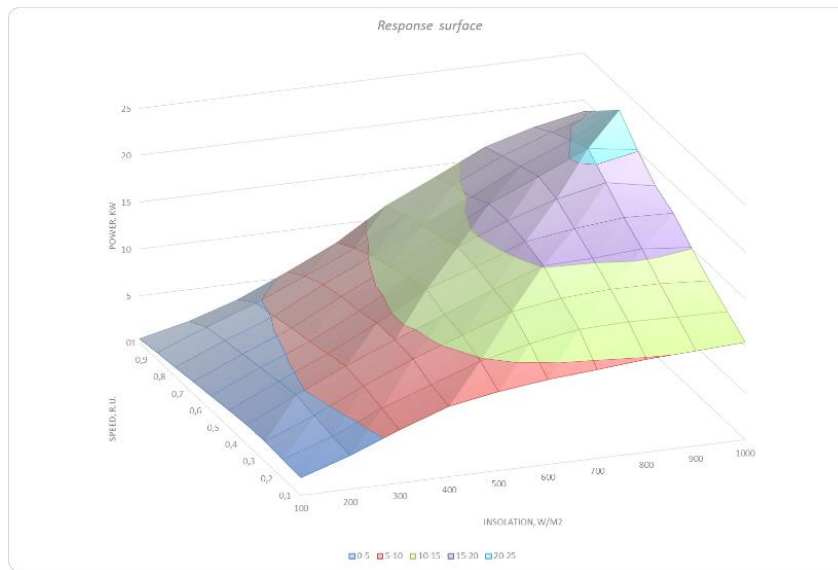


*Figure 2. Response surface*

We will seek a mathematical description of the process under study as a regression equation of the form:

$$P = Av^2 + Bq^2 + Cvq + Dv + Eq + F, \quad (5)$$

where  $A, B, C, D, E, F$  are regression coefficients.

To find the regression coefficients, we will use the least squares method. According to this method, to find a mathematical description of the functional dependence, it is necessary to minimize the value of the variance [11], or:

$$Q = \sum_{i=1}^{10} \sum_{j=1}^{10} (P_{ij} - (Av_i^2 + Bq_j^2 + Cv_i q_j + Dv_i + Eq_j + F))^2 \rightarrow \min. \quad (6)$$

Compose a system of equations for finding the regression coefficients and solve it in the Mathcad 14 software package, the following values of the regression coefficients were obtained:

$$\begin{aligned} A &= -3,196 \cdot 10^8; B = -0,012; C = 121,798; \\ D &= 2,089 \cdot 10^6; E = 30,178; F = -3717. \end{aligned}$$

Substituting the obtained values of the coefficients in (5), we obtain the desired regression equation:

$$P = -3,196 \cdot 10^8 v^2 - 0,012q^2 + 121,798vq + 2,089 \cdot 10^6 v + 30,178q - 3717. \quad (7)$$

Taking this condition into account, we obtain an expression for the partial derivative of equation (7) with respect to velocity:

$$\frac{\partial P}{\partial v} = -6,392 \cdot 10^8 v + 121,798q + 2,089 \cdot 10^6. \quad (8)$$

Hence, the value of the optimal speed can be determined from the expression:

$$v = \frac{121,798q + 2,089 \cdot 10^6}{6,392 \cdot 10^8}. \quad (9)$$

As you can see, there is only one unknown in equation (9) - the value of specific insolation at the current time. To determine it, you can resort to direct measurement or indirectly obtaining the desired values based on other data. In the first case, the maximum reliability of the data obtained takes place, however, the cost of the measuring equipment required for this is several tens of thousands of rubles, which will seriously increase the total cost of the control system.

Thus, the determination of the current level of insolation will be made indirectly according to the empirical models presented in [13]. In this case, to determine insolation, you need to know the date and time; the models are designed for each of the months during which the solar plant is able to generate heat energy. So, to determine the level of insolation in June, the following polynomial is used:

$$\begin{aligned} q_6(\tau) = & 7,693 \cdot 10^{-9} \tau^{11} - 1,025 \cdot 10^{-6} \tau^{10} + 5,872 \cdot 10^{-5} \tau^9 - 1,889 \cdot 10^{-3} \tau^8 + 0,037 \tau^7 - 0,464 \tau^6 + 3,592 \tau^5 \\ & - 16,476 \tau^4 + 41,833 \tau^3 - 51,986 \tau^2 + 23,404 \tau + 0,029, \end{aligned}$$

where  $\tau$  – current time.

### 3. CONTROL DEVICE DEVELOPMENT

In addition to the development of the algorithmic component, in order to create high-quality software, it is necessary to determine all the data that will be processed by it, as well as to determine the delimitation of access to them. To do this, it is necessary to determine between which elements of the controller and external devices the information exchange will take place.

To begin with, let's define all the components included in the control system:

The microcontroller structure includes: heat accumulator charging regulator; water heating regulator; module for determining the date and time; communication module for remote access; indication devices.

The outer periphery includes:

- frequency converter; temperature sensors; additional peripherals.

Further, it is necessary to indicate the direction of movement of information flows, since, for example, in the case of a frequency converter, there is a two-way exchange of information, and with temperature sensors - exclusively one-way.

As a result of this analysis, the structure shown in Fig. 3, regarding which data will be exchanged. It should be noted that it does not contain a time counter and an indication device, since their presence or implementation entirely depends on the selected microcontroller.

The development of this structure is an integral part of the development of both software and hardware of the device, since it provides an opportunity for an approximate estimate of the complexity of the task and the amount of material and human resources required to solve it, which allows you to optimize development costs and reduce the risks of errors and abnormal situations that have a direct impact on the design speed and quality of the final result.

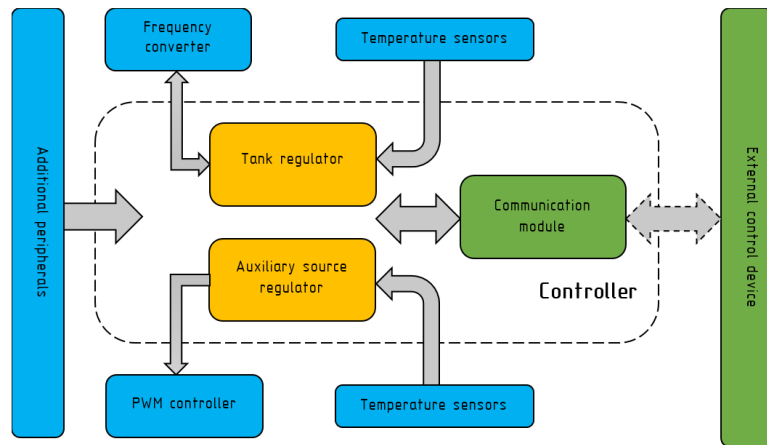


Figure 3. Model of information interaction of the controller

For the manufacture of the device, the ATMega 328P microcontroller was chosen. and the UM801LP network module, since they are simple and convenient to use, and also have high energy efficiency. The device is powered by an 18650 lithium-ion battery with a nominal voltage of 3.7 V. Additionally, LED signaling is used to indicate the operation of the device, to carry out communication exchange via the RX and TX lines of the UART interface. To ensure the required quality of the supply voltage, we use a linear stabilizer LM317, providing 3.3 V. As a result, a device was developed, its diagram (Figure 4 (a)), and its appearance is presented in (Figure 4 (b)).

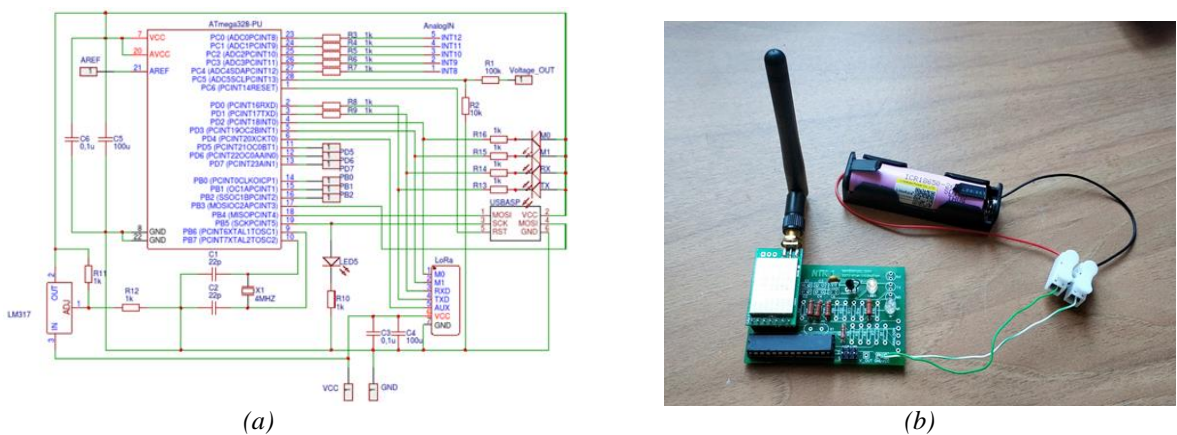


Figure 4. Schematic electrical diagram (a) and appearance (b) of the laboratory sample of the device

#### 4. ANALYSIS OF SYSTEM PERFORMANCE

The second component of the feasibility study is the assessment of energy efficiency, which is determined by the relative performance of the equipment. A comparative analysis of the efficiency of the solar plant under the control of an adaptive and single-position system, carried out earlier, showed that the use of the first one gives an overall increase in productivity equal to 20 - 25% (Fig. 5). In other words, the use of the adaptive regulation mechanism made it possible to accumulate a much larger part of the energy absorbed by the collectors in the storage tank. Elimination of the drawback revealed in the course of the study will presumably increase this indicator by another 5%, which in conditions of a deficit of solar radiation is a rather significant value.

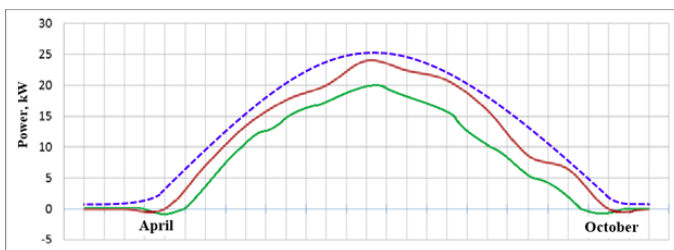


Figure 5. Graph of the instantaneous power of the investigated solar plant

Thus, the result of the completion of the final qualifying work can be considered a decrease in the total cost of the control system, with an increase in its productivity. It should also be remembered that the assessment of economic indicators was made relative to ideal conditions, i.e. all the energy generated by the collectors must be accumulated and then consumed. Otherwise, the calculated values of the payback period and the cost of hot water will inevitably increase, which proves the decisive role of control algorithms in the viability of solar plants.

## 5. CONCLUSION

1. Based on the analysis results, it was revealed that the problems of alternative energy in Russia are complex. The determining factor is the poor performance (and payback) and the low level of government support. It is possible that the data.
2. Thanks to the study of the local climate and adaptive control algorithms, it became possible to achieve the best performance indicators of solar water heating installations by reducing losses arising in the processes of heat and mass transfer between collectors and storage tanks.
3. The implementation of technical solutions for the application of the control system is possible without the use of expensive components and equipment: the most expensive purchase of an electric pump and a frequency converter to control it. Moreover, the current availability of technologies to implement new methods of solving problems of communication interaction.

Thus, the result of the work done is a control device for the forced recirculation system in solar hot water installations, which allows their more efficient operation due to the developed control methods.

## REFERENCES

- [1] Belousov, A. V., Koshlich, Yu. A. Analysis of the operation of a thermal solar plant in a temperate continental climate. International research journal 2013; 12 (19) part.1: 99-101.
- [2] Vagner, V.V., Slesarenko V.V. Research of the structure of automation systems for solar installations. Modern problems of science and education 2012; № 14: 148 – 157.
- [3] Steklenev, A.S., Tolmachev, O. N. Problems and prospects of using alternative energy sources in the Russian Federation. Youth scientific and technical bulletin 2014; 3: 21-26.
- [4] Gibilisco, S. Alternative energy without secrets. Moscow: Eksmo-press, 2010.
- [5] Sanaye, S., Sarrafi A. Optimization of combined cooling, heating and power generation by a solar system. Renewable Energy 2015; 80: 699-712.
- [6] Aleksandrov, A.G. Optimal and adaptive systems. Moscow: Higher School, 1989.
- [7] Beckman U. Calculation of solar heat supply systems. Moscow: Energoizdat, 1982.
- [8] Adler, Yu.P. Planning an experiment to find optimal conditions. Moscow: Science, 1971.
- [9] Belousov, A. V., Glagolev, S. N., Koshlich, Yu. A. Mathematical modeling of a hot water supply system for buildings with a peak heat source based on a solar power plant. Information systems and technologies 2013; 6: 16-23.
- [10] Samarsky, A.A. Mathematical modeling. Ideas. Methods. Examples. Moscow: Fizmatlit, 2002.
- [11] Arkhipov, G.I. Lectures on mathematical analysis. Moscow: Higher School, 2004.
- [12] Koshlich, Yu.A. Control system for a solar hot water supply. PhD, Belgorod State Technological University after V.G.Shukhov, Belgorod, Russia, 2015.
- [13] Sautin, S.N. Planning an experiment in chemistry and chemical technology. Leningrad: Chemistry, 1975.



# COMPARISON OF DIFFERENT REGRESSION ALGORITHMS FOR ESTIMATING ENERGY CONSUMPTION

Halit Cetiner

Vocational School of Technical Sciences, Isparta University of Applied Sciences, Isparta, Turkey,  
halitcetiner@isparta.edu.tr, ORCID: 0000-0001-7794-2555

Ibrahim Cetiner

Vocational School of Technical Sciences, Mehmet Akif Ersoy University, Burdur, Turkey, icetiner@mehmetakif.edu.tr,  
ORCID: 0000-0002-1635-6461

Cite this paper as:

*Cetiner, H., Cetiner, I., Comparison of Different Regression Algorithms for Estimating Energy Consumption. 9<sup>th</sup> Eur. Conf. Ren. Energy Sys. 21-23 April 2021, Istanbul, Turkey*

---

**Abstract:**

Depending on the growth of parameters such as population, economy, industry and consumption centers, the amount of energy needed will increase even more in the coming years. The majority of the energy requirement is used in buildings dominated by overpopulation. As a result, overpopulated residences can be considered as one of the most important objectives in terms of efficient use of energy and global energy sustainability. There seems to be a recent increase in artificial intelligence-supported housing systems consisting of electronic devices to minimize energy consumption in residences. Considering the increase in environmental factors such as global warming, greenhouse gas emissions, carbon dioxide, chemical solvents, and radiation, it is necessary to increase studies for efficient use of energy. For this purpose, the data set showing the hourly data consumption of the Asian region in terms of Mega Watts obtained from the website of PJM Interconnection LLC (PJM), the regional communication organization in the United States, was used. A study was conducted to compare the performances of different regression algorithms on this data set. XGBoost, Ransac (Random Sample Consensus), Linear regression, Long short term memory (LSTM) methods have been experimental studies on both normalized data and without normalization in the same data set.

---

**Keywords:**

*RANSAC, Linear regression, LSTM, normalization, energy consumption*

---

© 2021 Published by ECRES

## 1. INTRODUCTION

The world population is increasing rapidly. According to the researches, the world population is expected to approach 10 billion in 2040 or 2050 [1]. A population growth of this size naturally indicates that energy consumption will increase significantly. In the next 30 years, it is estimated that two-thirds of the world population will live in sites far from rural areas. It is reported that every four months there is an increase in population as much as China's largest city. It becomes more difficult to meet the energy demand by reducing harmful emissions such as CO<sub>2</sub>, NO<sub>x</sub> to meet the specified population increase. The reports that worldwide emission values in the past two years ago exceeded 45% of the values twenty years ago. For the reasons stated, it is obvious that all kinds of energy are needed in the coming years, including clean electricity. electricity demand is predicted to increase more than twice as fast as in previous years [1]. In order to meet the energy demand due to the increasing population and to reduce harmful emissions, clean energy production and energy consumption supported by accurate, conscious and smart systems should be widespread. Increasing energy efficiency in dwellings where the population spends a lot of time is based on reducing energy consumption. Energy must be used consciously in order to minimize energy use. Moreno et al. He mentions the works they developed to save 23% energy. In their study, they conducted experimental studies to determine which parameters should be considered by building designers to reduce energy consumption. As a result of their studies on effective energy use, they determined that human life span is closely related to energy consumption. They tried to identify the most relevant parameters that should be controlled for effective energy use [2]. In a belief that can be regarded as the continuation of the determination of the relationship between the correct and conscious energy use and the time of human energy consumption that substitutes in houses,

environmental changes are directly caused by human activities. It is stated that the global change due to environmental changes is the result of improper unconscious energy use. It is said that global climate changes due to environmental changes have become a global problem [3]. It is stated that global warming due to these environmental changes will disrupt flood, drought and food production. For this reason, it is stated that people can migrate even to safer areas as a temporary solution. However, there is no guarantee that this problem will not occur in the destination region. Exposure to extreme and irregular heat waves different from what is normally expected can impair human health and diseases can spread very easily in many regions [4]. According to [3], energy generation accounts for a quarter of the total worldwide emission value. This ratio shows that the necessity for efficient, conscious, accurate and technology-supported energy consumption to be sustainable becomes more and more important every day.

Studies on energy consumption have recently increased with devices that can be controlled over the internet with electronic devices such as PLC, arduino, atmega, sensors. It is seen that there is a need for studies aiming to prevent the extra energy use of all energy consuming devices. In line with this information, energy consumption data of an eastern region in America will be taken as the basis for these experimental studies. The data between 2002 and 2015, which form part of this consumption energy data, were used as training data. The data of 2015 and after were used as test and verification data. After training data with different regression algorithms, it will be tried to be predicted over test data that has never been seen before. Here, the results of the most popular regression algorithms on energy data commonly used in research will be discussed in a controversial manner.

## 2. RELATED WORKS

[5] sought to find ways to reduce energy consumption in residential buildings in Singapore. [6] analyzed the energy consumption data taken from the house controlled in more than one electronic system by linear regression method. These data include energy consumption data between 2014-2016 within the scope of the housing project controlled by electronic systems. Linear regression model was used to analyze these consumption data. To measure the relationship between energy consumption and outside temperature, the  $R^2$  value is calculated. The estimated energy data is compared with the actual energy consumed. In this comparison, the  $R^2$  value is vital in understanding the relationship between them. It has been reported that  $R^2$  values close to 1 have a better correlation. [7] tries to estimate the energy consumption of different appliances in households. They are talking about a method that tries to know the electricity consumption of the next day through today's electricity consumption. [8] applies seven different machine learning algorithms to hourly energy consumption data collected every fifteen minutes. The most successful of these algorithms in estimating the energy consumed at a future date is tried to be determined. [9] presents a new methodology to solve the problem of inhomogeneity in the energy modeling of houses. This method proposed a physically and statistically based mathematical approach to generate inhomogeneity to increase prediction accuracy.

[10] developed a compartmentalized model to determine residential energy performance. [11] includes an extension of a pre-existing work. This extension includes the time temperature curve prediction model. [12] is trying to estimate the energy consumption of a medical clinic. It models this prediction process using an artificial neural network. They tried to estimate the electricity consumption by using the data in the attribute table created with the definitions of days such as time of day, weekend, and holiday. [13] propose a new artificial neural network-based approach that predicts the relationship between harmful greenhouse gas emissions and energy consumption. [14] developed a least-squares support vector machine to determine the energy consumed on a daily basis. [15] developed a mathematical model for determining future energy consumption based on energy data used in the Republic of Serbia. These developed models are compared with the artificial neural network model. [16] tried to estimate China's energy density using an LSTM-based neural network model.

## 3. MATERIAL AND METHOD

Energy consumption data belonging to an eastern state region in America will be used in this study. The data set consists of two columns: date and time information and energy consumed. The part of this energy data between 2002 and 2015 was used as training data. The year 2015 and later were used as test and verification data. After the training data is trained by different regression algorithms, it will be tried to be predicted over the test data that has never been seen before. Experimental studies were conducted using XGBoost, Ransac (Random Sample Consensus), Linear regression methods without normalization by extracting eight different attributes such as day of the week, day of the month, day of the year from the date data of the first column. Experimental studies have

been carried out using XGBoost, Ransac, Linear regression methods and LSTM time series deep learning algorithm by normalizing the same data set. Only original data were used in the normalized data set. The data set was not expanded by extracting attributes from the original data. The  $R^2$  scoring value is used to compare the results of the algorithms. Experimental studies were carried out in visual studio code environment using python 3.8 version. The Ransac algorithm has been proposed by Fischler and Bolles [17]. The RANSAC algorithm, which is a general estimation approach, is used for accurate estimation of selected model parameters. The number of iterations, N, are chosen high enough to ensure that the probability that at least one of the random sample sets does not contain an outlier is p.  $\mu$  represents the probability that any data point has an initial value.  $v = 1 - \mu$  represents the probability of observing an outlier [18]. XGBoost is a high performance version of the Gradient Boosting algorithm optimized by various arrangements. The algorithm is proposed by Chen and Guestrin [19] in 2016. XGBoost is a machine learning technique with decision tree and inclination increase. XGBoost is a supervised learning algorithm that implements a process called boost to obtain accurate models. XGBoost speeds up the running speed by varying the computing power allocated to the inner and outer loops and greatly reduces the parallelization overhead. This predictive model can then be applied to new unseen samples. XGBoost prioritizes depth, it significantly increases complexity and hence computing performance [20]. The XGBoost algorithm was used for regression. The number of increased trees is usually set to 1000.

Linear correlation and simple linear regression are mathematical methods that investigate the linear connection between two variables. Here correlation shows how connected the two variables are, while linear regression involves creating a mathematical equation that allows one to estimate the value of one from the other based on the connection between the two variables. The relationship between the two variables is decisive if one variable can be correctly expressed by the other. Long short term memory (LSTM) is a specific form of recurrent neural network [16]. Unlike RNN, LSTM has three gates. There is an entrance, exit and forgetting door. Each LSTM layer must be accompanied by a Dropout layer. This layer will help prevent overfitting by ignoring randomly selected neurons during training, thus reducing the sensitivity to specific weights of individual neurons. The settings given in table 1, the lstm algorithm was run on both the training and test data sets on the normalized data.

*Table 1 LSTM setting parameters*

Parameter	Value
Layers	3
Loss	Mean squared error
Optimizer	Adam
Epochs	10
Batch size	28
Activation	Relu

Figure 1 shows the non-normalized data. Normalization is the rescaling of the data in the original range so that all values are in the new range 0 and 1. Normalization allows us to know or accurately predict minimum and maximum observable values. You can estimate these values from your current data. Figure 2 shows the normalized data. Five of the most common measures used to measure the accuracy of continuous variables were used to evaluate results. Mean squared error (MSE), is defined as the mean square of the errors, that is, the mean square difference between the predicted values and the actual values. Root mean square error (RMSE), represents the square root of the second sample moment of the differences between the predicted values and the observed values, or the quadratic mean of these differences. Mean absolute error (MAE), measures the average magnitude of errors in a range of estimates regardless of their direction. It is the mean of the absolute differences on the test sample between the estimate that all individual differences have equal weight and the actual observation. Mean absolute percentage error (MAPE) is frequently used to measure the accuracy of predictions in regression and time series models. If there are zero among the real values, the MAPE cannot be calculated as there will be division by zero.

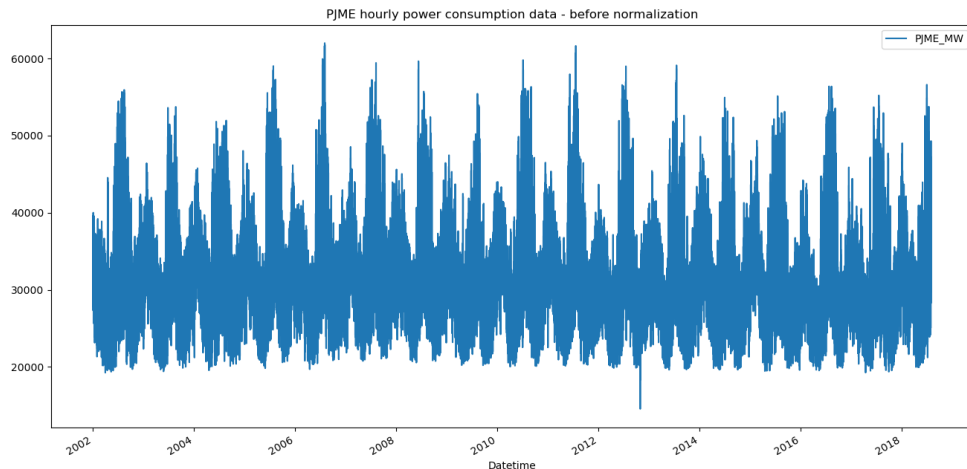


Figure 1. PJME hourly power consumption data - before normalization

For very low predictive values, the percent error cannot exceed 100%, but there is no upper limit for the percent error for very high predictive values.

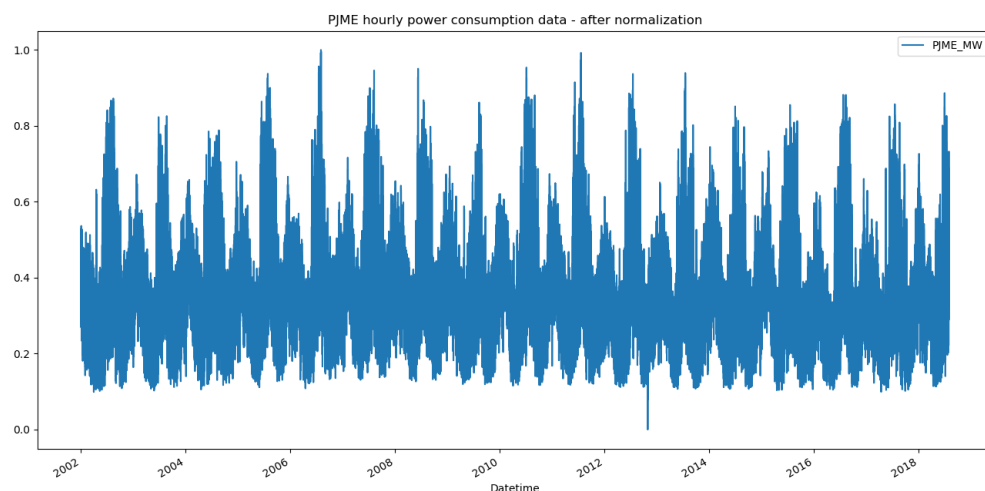


Figure 2. PJME hourly power consumption data - after normalization

When MAPE is used to compare the accuracy of estimators, it is biased as it systematically selects a method that is too low for estimates. This small but serious problem can be overcome with an accuracy criterion that finds the ratio of predicted values to their true values. This approach leads to estimates that can be interpreted in terms of the geometric mean. The results obtained in Table II are the results obtained from the expanded data set by removing the attributes of the hour, day of the week, month, period, year, day of the year, day of the month, week of the year from the time data in the first column of the data set. However, in these results, the values in the input data set are the results obtained from the values that were not normalized by reducing them to the 0-1 interval.

Table 2. Statistical results obtained without normalization

Algorithm	R <sup>2</sup> Score	MSE	RMSE	MAE	MAPE
Linear (Train)	0.2857	29735459.1477	5453.0229	4193.3740	13.0141
Linear (Test)	0.2266	32171295.3672	5671.9746	4588.8227	14.9020
RANSAC (Train)	0.1307	47072270.2538	6860.9234	5301.9489	15.8857
RANSAC (Test)	0.0341	43016642.9497	6558.7074	5188.4813	16.6747
XGBoost (Train)	0.7862	8901379.2930	2983.5179	2124.8559	6.2598
XGBoost (Test)	0.6644	13960913.3057	3736.4306	2757.2169	8.5108

The results obtained in Table III are the results obtained from normalizing the energy data by reducing it to 0-1 interval, except for the time data in the first column of the data set. Only the original data were used in the results in Table III. There is no feature extraction from the original data. By looking at the results in Table II and Table III,

it is concluded that the normalization step must be done in the data set used for estimation. For this purpose, the data set to be used for regression has been brought to the range of 0-1.

*Table 3. Results obtained on the normalized data set*

Algorithm	R <sup>2</sup> Puan	MSE	RMSE	MAE	MAPE
Linear (Train)	0.9810	0.0004	0.0188	0.0125	0
Linear (Test)	0.9799	0.0004	0.0191	0.0120	3.9059
RANSAC (Train)	0.9801	0.0004	0.0192	0.0125	0
RANSAC (Test)	0.9787	0.0004	0.0196	0.0119	3.8903
XGBoost (Train)	0.9975	0	0.0068	0.0047	0
XGBoost (Test)	0.9876	0.0002	0.0150	0.0088	2.8145
LSTM (Train)	0.9725	0.0005	0.0226	0.0158	0
LSTM (Test)	0.9723	0.0005	0.0224	0.0155	3.100

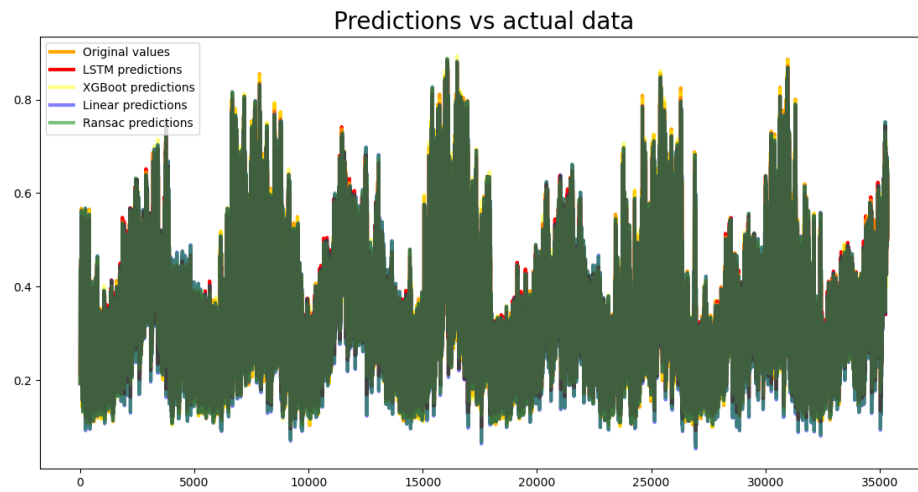


*Figure 3. Prediction results made with LSTM, XGBoost, Linear, Ransac model*

Figure 3 shows the estimation results obtained with the LSTM, XGBoost, Linear, Ransac methods. When we look at the results on table III, the results obtained are satisfactory. The differences between the predictions made with the specified models and the actual values are given in a table. Considering the figure, it is seen that the model estimation values are very close to the real value.

### 3. RESULTS AND DISCUSSION

In regression processes, the data must be normalized. It is seen that the  $R^2$  scoring values of the algorithms used are close to each other. In this study, although other measurement models were given in a table,  $R^2$  scoring was taken as a basis in the evaluation phase. According to the  $R^2$  scoring values, it can be said that the XGBoost algorithm has 1 point higher accuracy than other models. All of the regression algorithms used in this sense can be used in the energy consumption data set. In order to achieve better results, excluding holidays and public holidays will provide better results. LSTM algorithm took more time in the training phase than other algorithms. Here, by expanding the data set over the date column and minimizing irrelevant attributes by attribute selection, faster regression operations can be performed with LSTM. For LSTM, different results were obtained at different parameters. Modeling parameters with the best results were used. Experimental parameters obtained as a result of several experimental studies were used. This study is important in that it forms the basis of the automatic LSTM parameter determination algorithm that will be used to automatically determine the parameters in the future.

### REFERENCES

- [1] Change, G. E. (2020). Meeting the food security challenge for nine billion people in 2050: What impact on forests?. *Global Environmental Change*, 62, 102056.
- [2] Moreno, M., Úbeda, B., Skarmeta, A. F., & Zamora, M. A. How can we tackle energy efficiency in iot based smart buildings?. *Sensors*, 14(6), 9582-9614, 2014.

- [3] Pachauri, R.K., Meyer, L.A., IPCC, Climate Change 2014: Synthesis Report. Contribution of Working Groups I, II and III to the Fifth Assessment Report of the Intergovernmental Panel on Climate Change IPCC, Geneva, Switzerland, 151 pp, 2014.
- [4] Xu, L, Impact of Climate Change and Human Activity on the Eco-environment an Analysis of the Xisha Islands. Springer, 2015.
- [5] Bhati, A., Hansen, M., & Chan, C. M., Energy conservation through smart homes in a smart city: A lesson for Singapore households. *Energy Policy*, 104, 230-239, 2017.
- [6] Moletsane, P. P., Mothamme, T. J., Malekian, R., & Bogatmoska, D. C., Linear regression analysis of energy consumption data for smart homes. In 2018 41st International Convention on Information and Communication Technology, Electronics and Microelectronics (MIPRO) (pp. 0395-0399). IEEE, 2018.
- [7] Arghira, N., Hawarah, L., Ploix, S., & Jacomino, M., Prediction of appliances energy use in smart homes. *Energy*, 48(1), 128-134, 2012.
- [8] Edwards, R. E., New, J., & Parker, L. E., Predicting future hourly residential electrical consumption: A machine learning case study. *Energy and Buildings*, 49, 591-603, 2012.
- [9] Lü, X., Lu, T., Kibert, C. J., & Viljanen, M., Modeling and forecasting energy consumption for heterogeneous buildings using a physical-statistical approach. *Applied Energy*, 144, 261-275, 2015.
- [10] O'Neill, Z., & O'Neill, C., Development of a probabilistic graphical model for predicting building energy performance. *Applied energy*, 164, 650-658, 2016.
- [11] Roldán-Blay, C., Escrivá-Escrivá, G., Álvarez-Bel, C., Roldán-Porta, C., & Rodríguez-García, J., Upgrade of an artificial neural network prediction method for electrical consumption forecasting using an hourly temperature curve model. *Energy and Buildings*, 60, 38-46, 2013.
- [12] Bagnasco, A., Fresi, F., Saviozzi, M., Silvestro, F., & Vinci, A., Electrical consumption forecasting in hospital facilities: An application case. *Energy and Buildings*, 103, 261-270, 2015.
- [13] Antanasićević, D., Pocajt, V., Ristić, M., & Perić-Grujić, A., Modeling of energy consumption and related GHG (greenhouse gas) intensity and emissions in Europe using general regression neural networks. *Energy*, 84, 816-824, 2015.
- [14] Jung, H. C., Kim, J. S., & Heo, H., Prediction of building energy consumption using an improved real coded genetic algorithm based least squares support vector machine approach. *Energy and buildings*, 90, 76-84, 2015.
- [15] Protić, M., Fathurrahman, F., & Raos, M., Modelling energy consumption of the republic of Serbia using linear regression and artificial neural network technique. *Tehnički vjesnik*, 26(1), 135-141, 2019.
- [16] Li, Y., Prediction of energy consumption: Variable regression or time series? A case in China. *Energy Science & Engineering*, 7(6), 2510-2518, 2019.
- [17] Fischler, M. A., & Bolles, R. C., Random sample consensus: a paradigm for model fitting with applications to image analysis and automated cartography. *Communications of the ACM*, 24(6), 381-395, 1981.
- [18] Derpanis, K. G., Overview of the RANSAC Algorithm. *Image Rochester NY*, 4(1), 2-3, 2010.
- [19] Chen, T., & Guestrin, C., Xgboost: A scalable tree boosting system. In Proceedings of the 22nd ACM SIGKDD international conference on knowledge discovery and data mining (pp. 785-794), 2016.
- [20] Mitchell, R., & Frank, E., Accelerating the XGBoost algorithm using GPU computing. *PeerJ Computer Science*, 3, e127, 2017.



# PERFORMANCE OF A COMBINED POWER AND COOLING SYSTEM UNDER SOLAR, SOLAR STORAGE AND STORAGE MODE OF OPERATIONS

Tapan Kumar Gogoi

Tezpur University, Tezpur, India, tapan\_g@tezu.ernet.ac.in, ORCID: <https://orcid.org/0000-0003-3927-5098>

Utpal Kumar Dutta

Tezpur University, Tezpur, India, ukdutta123@gmail.com, ORCID: 0000-0002-4828-2284

*Cite this paper as:* Gogoi, TK, Dutta, UK. Performance of a solar based combined power and cooling system under solar, solar storage and storage mode of operations. 9th Eur. Conf. Ren. Energy Sys. 21-23 April 2021, Istanbul, Turkey

**Abstract:** In this article, the performance of a solar operated power and cooling system is evaluated at solar, solar storage, and storage mode of operations. The solar and solar storage modes refer to the system operation during the daytime of low and high-solar radiation respectively while the storage mode refers to nighttime operation. Water is heated in a parabolic trough solar collector and in the solar mode; the entire hot water is used to drive an organic Rankine cycle first and subsequently an absorption cooling system. In the solar storage mode, a fraction of the hot water is used to heat Therminol VP-1 in a storage heat exchanger for storing the hot oil in a storage tank which is later used to drive only the ACS during the storage mode. From performance evaluation, it was found that during the solar mode, the ORC produced 1.1 MW of net power and the ACS provided 2.45 MW of cooling. In the solar storage mode, due to high turbine inlet temperature, the ORC net power increased to 2.256 MW while the ACS cooling reduced to 2.155 MW. During the storage mode, the hot oil-driven ACS could generate only 0.553 MW of cooling.

**Keywords:** Performance, Solar, Organic Rankine Cycle, Absorption Cooling System

© 2021 Published by ECRES

## 1. INTRODUCTION

Solar is a clean, non-polluting and abundantly available energy source. Solar based technologies are used in many industrial applications. Multi-generation systems are quite promising for solar energy utilization. In this regard, the power, cooling and heating systems are the combined cogeneration systems that can certainly be operated with solar energy. Solar thermal power plants with energy storage provision cater to the variation in energy demand more appropriately and they are also cheap compared to the non-storage type plants. In solar thermal power plants, parabolic trough solar collectors (PTSCs) are used to trap the solar heat. In the PTSC, the heat gained by a heat transfer fluid (HTF) is transferred to water in a heat recovery vapor generator (HRVG) for power generation in a steam turbine. The organic Rankine cycle (ORC) is another technology which can be used for solar power generation. Solar driven ORCs have been proposed in many research studies. Jing et al. [1] evaluated the performance of an ORC, integrated with a low temperature PTSC at six different locations where they found higher efficiency for two-stage solar collectors over single-stage collectors. Prabhu [2] examined the economic feasibility of PTSC combined ORC for power and cooling at different locations. Delgado-Torres and Garcia-Rodriguez [3] analyzed a solar hybrid ORC to minimize the aperture area of four different types of solar collectors with a dozen of organic fluids. Bellos and Tzivanidis [4] examined the working of a solar driven ORC with four organic fluids where they found maximum ORC power with toluene followed by the power obtained from Cyclohexane, MDM and n-pentane as working fluids. Solar cooling is also gaining significant research interest. Assilzadeh et al. [5] simulated a solar ACS, that was designed for Malaysia's climatic conditions. Liu and Wang [6] presented a double effect water-LiBr ACS where they used a storage tank for storing the hot water heated in the PTSC which was later

used as heat source for driving the low pressure generator of the double effect ACS. Li et al. [7] analyzed a solar heat driven double effect ACS to evaluate its performance at various collector temperatures and they used the meteorological data of Guangzhaou province of China in the simulation.

Analysis of solar driven combined ORC and ACS has also been the research subject at recent times. Al-Sulaiman et al. [8] analyzed the performance of a solar PTSC based ORC integrated with a single effect ACS at the solar, solar storage and storage mode of operations. They used Therminol 66 both as HTF and storage fluid while n-octane was the ORC working fluid. Marin et al. [9] analyzed a solar operated ORC combined with a single effect ACS where they considered R245fa and water-LiBr as working fluids in the ORC and ACS respectively. Eisavi et al. [10] evaluated the performance of a solar driven ORC combined with a water-LiBr operated double effect ACS. While using Therminol 66 as HTF, they performed a thermodynamic analysis for all the year months to determine the system efficiency. Zhao et al. [11] investigated performance of three different solar systems combining ORC and ACS in series and parallel configurations. Gogoi and Saikia [12] carried out thermodynamic analysis of a solar system integrated with an ORC and a water-LiCl operated single effect ACS. They considered R245fa, R245ca, Isopentane, Neopentane, and Butane as ORC working fluids for comparison of system performance. In the present study, a solar based CPC system similar to the one presented in [12] is thermodynamically analyzed under the solar, solar storage and storage mode of operations. Unlike in [12], here in the present schematic, two storage tanks are used where Therminol VP-1 is used as the storage fluid.

## 2. SYSTEM DESCRIPTION

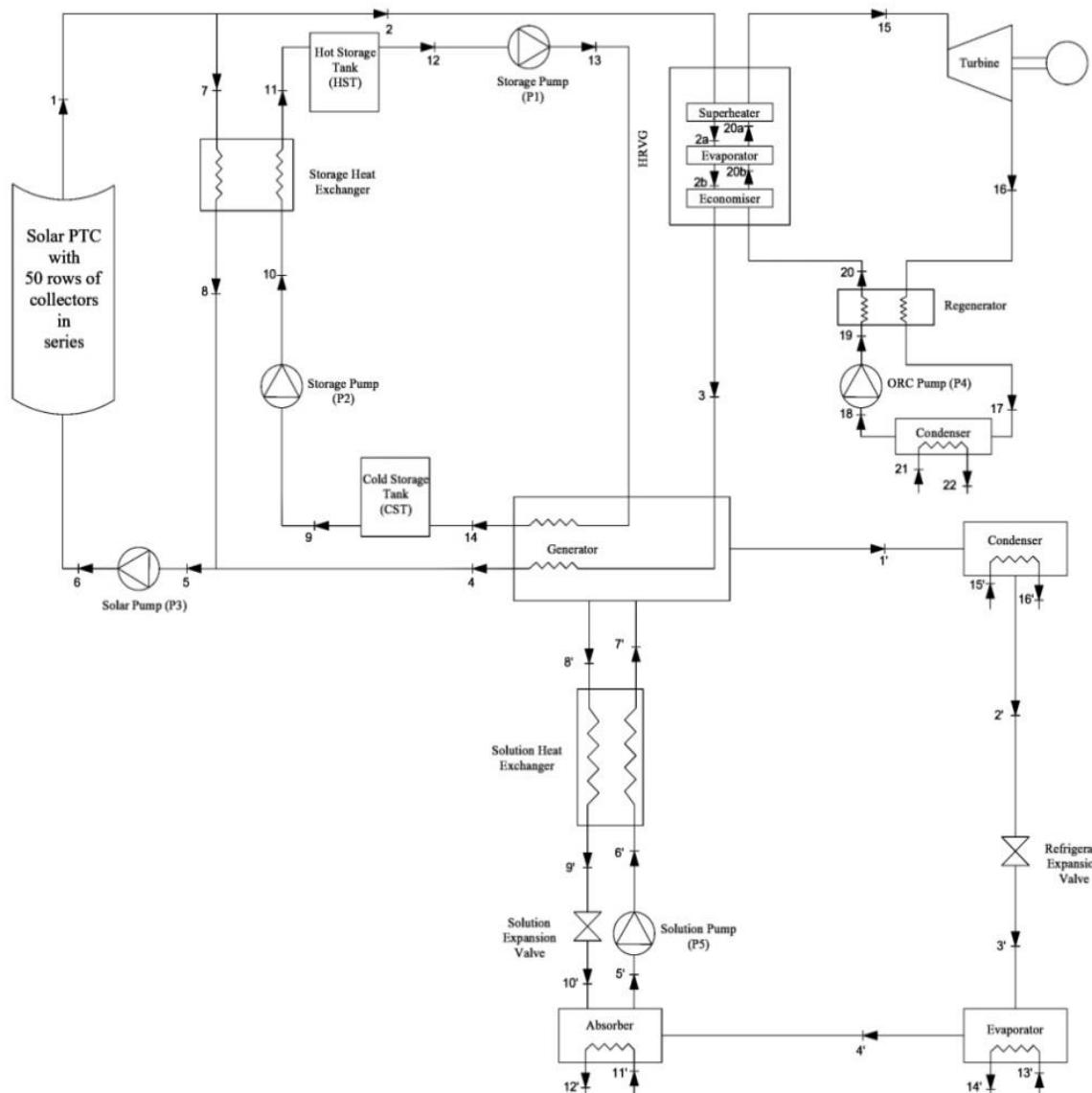


Figure 1. Schematic of the solar heat operated combined cogeneration system.

Fig. 1 shows the solar heat operated cogeneration system that is integrated with the ORC and the ACS. A single PTSC element has a parabolic trough with an absorber tube surrounded by a glass envelope which is supported with a number of brackets. In a single row, ten PTSC elements are used in a series configuration and 50 rows of such collectors are considered. The ORC has its usual components such as heat recovery vapour generator (HRVG), the vapour turbine (VT), condenser and regenerator etc. Similarly, the ACS in the schematic is a single effect one with one generator and other as usual components. The HTF (water) heated in the PTSC is used as heat source for driving the ORC and the ACS. The system operates at three different modes viz. solar, solar storage, and storage modes. During low sunshine period in the morning and late afternoon, the entire HTF is used as heat source for driving the ORC and subsequently the ACS (solar mode). During daytime, when the solar intensity is relatively high, a part of the hot HTF is used to heat the storage fluid in a heat exchanger for harvesting the solar energy in the hot storage tank (HST) while the remaining HTF drives the ORC and the ACS (solar storage mode). After sunset, when no solar radiation is available, the storage fluid from the HST flows to the cold storage tank (CST) for driving the ACS generator (storage mode). As such, in the storage mode, only cooling is produced by operating the ACS with hot Therminol VP-1.

### 3. SYSTEM MODELLING AND ASSUMPTIONS

It is assumed that the system operation is steady. Pressure loss in the pipelines and heat loss between the system and surroundings are neglected. Water is the HTF in the PTSC with 90 °C temperature at PTSC inlet. The solar radiation intensity ( $I_{solar}$ ) for the solar mode of operation during the low sunshine period (say from 6 to 8 am in the morning and 4 to 6 pm in the evening) is taken as 640 W/m<sup>2</sup>. Similarly, the time duration for the solar storage mode of operation is considered from 8 am in the morning to 4 pm in the evening and for this time period, the representative solar radiation is taken as 950 W/m<sup>2</sup>. The assumed geometrical and optical parameters of the PTSC are same with those of Ref. [12]. In the ORC, iso-pentane is considered as the working fluid and other ORC model input parameters are taken from Ref. [12]. In the ACS, as usual assumptions are made as presented in Ref. [13] except the generator temperature which is taken as 75 °C. The PTSC modelling involves calculation of HTF temperature at PTSC outlet against known values of solar radiation intensity, HTF flow rate and temperature at PTSC inlet. This is done with the help of optical and thermal models. The details regarding the PTSC model are available in Ref. [12]. In fact in Ref. [12], the model equations of Forristal [14] were only used and in Ref. [14], all the details regarding PTSC model equations, used optical and geometrical parameters, model verification etc. are described in full. The hot and cold storage tanks are modeled mostly in line with the model equations presented in Ref [8]. The temperature of Therminol VP-1 at state 11 ( $T_{11}$ ) is considered 25 °C less than the hot water temperature at state 7 ( $T_7$ ). The tank heat loss coefficient is taken as 0.1 W/m<sup>2</sup>K for both the HST and CST. The oil temperature in the HST and CST ( $T_{HST}$  and  $T_{CST}$ ) are calculated iteratively. The oil properties at state points 9–14 are calculated. At state 14, the oil temperature is assumed as 92.4 °C. The HST and CST dimensions are calculated assuming equal length and diameter. The temperature at state 8 is assumed 20 °C more than the temperature at state 10 and accordingly, from heat balance in the storage heat exchanger, the mass flow rate of hot water passing through the storage heat exchanger is calculated. The thermodynamic properties of iso-pentane at different state points of the ORC are calculated using the REFPROP 9.0 library. Mass and steady flow energy equations are employed for calculating the energy transfer terms. The temperature difference between hot water at ORC inlet and iso-pentane at VT inlet is assumed 30 °C. Similarly, the saturation temperature of iso-pentane in the ORC is assumed 46 °C less than the VT inlet temperature. A pinch point temperature difference (PPTD) of 20 °C is assumed between hot water at state point 2b and iso-pentane at state 20b. Accordingly, the organic fluid mass flowrate is calculated. Net ORC powers for the solar and solar storage mode of operations are calculated using Eq. (1) and Eq. (2) respectively. The ORC efficiency is calculated using Eq. (3).

$$Power_{net} = \dot{m}_{ORC} \left[ (h_{15} - h_{16})\eta_{VT} - \frac{(h_{19} - h_{18})}{\eta_P} \right] - \dot{W}_{P3} \quad (1)$$

$$Power_{net} = \dot{m}_{ORC} \left[ (h_{15} - h_{16})\eta_{VT} - \frac{(h_{19} - h_{18})}{\eta_P} \right] - (\dot{W}_{P2} + \dot{W}_{P3}) \quad (2)$$

$$\eta_{ORC} = \frac{Power_{net}}{\dot{m}_{ORC}(h_{15} - h_{20})} \quad (3)$$

In Eqs. (1)and (2) $\eta_{VT}$ and  $\eta_P$ are the VT and pump efficiencies. $\dot{W}_{P2}$ and $\dot{W}_{P3}$ are the pumping powers consumed by the pumps P2and P3 respectively. The pumping power required for running the solution pump(SP) of the ACS is very small and can be neglected. Properties of water–LiBr, used in ACS, are determined from the equations given in Ref. [15]. Water and steam properties are computed from IAPWS formulation 1997[16].The procedure described in Refs. [13, 17] is only used for iterative calculation of the ACS cooling capacity ( $\dot{Q}_E$ ). The coefficient of performance (COP) of the ACS is defined as usually.

$$\text{The overall system energy efficiency is: } \eta_{CPC} = \frac{\text{Power}_{\text{net}} + \dot{Q}_E}{I_{\text{solar}} A_a N_{\text{row}}} \quad (4)$$

where,  $A_a$  is the aperture area of the PTSC and  $N_{\text{row}}$ is the number of rows of collectors in the PTSC field.

#### 4. RESULTS AND DISCUSSION

The system performance was evaluated under the solar, solar storage and storage mode of operations.Under the solar mode of operation, the HTF, with a flow rate of 26.542 kg/s could be heated in the PTSC to 184.98 °C while in the solar storage mode, the HTF flow rate is little less (24.512 kg/s) and its temperature at PTSC outlet is 243.93 °C. The state wise thermodynamic properties and mass flow ratethat are crucial for system performance under a given set of operating conditionsfor each operational mode are shown in Table 1 and Table 2.

*Table 1.State properties and mass flow rates at solar and solar storage mode of operations*

States	Solar mode					Solar storage mode				
	P (kPa)	T ( °C)	$m\dot{x}$ (kg/s)	h (kJ/kg)	s (kJ/kgK)	P (kPa)	T ( °C)	$m\dot{x}$ (kg/s)	h (kJ/kg)	s (kJ/kgK)
1	1179.20	184.98	26.542	787.50	2.193	3763.50	243.93	24.51	1083.70	2.793
2	1179.20	184.98	26.542	787.50	2.193	3763.50	243.93	19.91	1083.70	2.793
3	1120.20	119.43	26.542	501.40	1.522	3575.30	127.23	19.91	534.59	1.605
4	1064.20	89.95	26.542	377.59	1.192	3396.50	92.4	19.91	389.69	1.218
5	1064.20	89.95	26.542	377.59	1.192	3396.50	89.95	24.51	379.34	1.190
6	1325.10	90.00	26.542	377.81	1.192	4166.50	90	24.51	379.61	1.191
7	-	-	-	-	-	3763.50	243.93	4.60	1083.70	2.793
8	-	-	-	-	-	3575.30	79.21	4.60	334.52	1.064
9	-	-	-	-	-	52.45	59.21	6.00	650.630	0.401
10	-	-	-	-	-	55.08	59.21	6.00	650.633	0.401
11	-	-	-	-	-	52.32	218.93	6.00	1224.80	2.254
15	872.18	154.98	17.56	576.89	1.554	3363.95	213.92	22.941	660.789	1.6183
16	109.16	113.15	17.56	504.45	1.601	109.17	130.37	22.941	540.859	1.694
17	872.18	51.10	17.56	383.89	1.262	3363.95	56.41	22.941	393.580	1.292
18	109.16	30	17.56	4.99	0.017	109.16	30	22.941	4.993	0.0165
19	872.18	30.42	17.56	6.55	0.175	3363.95	31.75	22.941	11.665	0.021
20	872.18	86.46	17.56	144.44	0.434	3363.95	101.10	22.941	184.112	0.530
20a	872.18	108.98	17.56	205.88	0.599	3363.95	186.93	22.941	487.10	1.2471
20b	872.18	108.98	17.56	469.44	1.289	3363.95	186.93	22.941	520.36	1.319
1'	0.0563	75	1.04	2640.81	8.584	0.0563	75	0.91	2640.81	8.584
2'	0.0563	35	1.04	146.65	0.505	0.0563	35	0.91	146.65	0.505
3'	0.0087	5	1.04	146.65	0.528	0.0087	5	0.91	146.65	0.528
4'	0.0087	5	1.04	2510.07	9.025	0.0087	5	0.91	2510.07	9.025
5'	0.0087	35	22.30	85.37	0.211	0.0087	35	19.58	85.37	0.211
6'	0.0563	35	22.30	85.37	0.211	0.0563	35	19.58	85.37	0.211
7'	0.0563	63.49	22.30	143.40	0.391	0.0563	63.49	19.58	143.40	0.391
8'	0.0563	75	21.26	175.96	0.439	0.0563	75	18.66	175.96	0.439
9'	0.0563	45	21.26	116.71	0.261	0.0563	45	18.66	116.71	0.261
10'	0.0087	45	21.26	116.71	0.261	0.0087	45.00	18.66	116.71	0.261

As can be seen, with the change in HTF flow rate and solar radiation in the solar and solar storage mode of operations, the HTF temperature at PTSC outlet were changing and higher temperature was obtained in the solar storage mode of operations. In the solar mode, with the chosen operating parameters listed in Table 1, 1.1 MW of net power and 2.45 MW of cooling could be obtained respectively from the ORC and the ACS (refer to Table 3). Thus, the total energy output is 3.55 MW and an overall system efficiency of 16.2 % is found in the solar mode. In the solar storage mode, since the hot water temperature is more at PTSC outlet (refer to Table 1), therefore, more vapour could be generated in the ORC (22.941 kg/s) against 17.56 kg/s associated with the solar mode of operation. Although, less amount of hot water was passing through the HRVG of the ORC in the solar storage mode, but due to increased hot water temperature, it was possible to maintain high VT inlet temperature in the ORC. One can see the change in property values at all salient points of the ORC (15 to 20, 20a, 20b) at the solar and solar storage mode of operations in Table 1. Due to change in the property values and also due to higher mass flow rate, the ORC in the solar storage mode produced a net power of 2.256 MW (almost double) against 1.1 MW associated with the solar mode. Accordingly, the ORC efficiency was also more (20.89 %) at the solar storage mode compared to ORC efficiency of 14.62 % at the solar mode of operation. Similarly, from the ACS, 2.155 MW of cooling was obtained in the solar storage mode, which is however 0.295 MW less than the cooling obtained during the solar mode (refer to Table 3). As compared to the solar mode, the hot water temperature at the ACS generator inlet was 7.8 °C more in the solar storage mode. But since the hot water mass flow rate was less, therefore, less amount of heat was supplied to the generator and this has affected the ACS evaporator cooling output. But overall the total energy output obtained from the CPC system at the solar storage mode of operation is more (4.411 MW) compared to 3.55 MW obtained at the solar mode. Although more (0.861 MW) total energy was obtained, but the overall system efficiency is less (13.45%) at the solar storage mode. This was due to the fact that a certain portion of the hot water at PTSC outlet was used to heat the oil in the storage heat exchanger that could not be utilized for direct energy generation.

*Table 2.State properties and mass flow rates at storage mode of operation*

States	P (kPa)	t ( °C)	$m_k^{\circ}$ (kg/s)	h (kJ/kg)	s (kJ/kgK)
12	49.27	145.9	4.00	946.79	1.298
13	51.74	145.9	4.00	946.80	1.298
14	49.27	92.4	4.00	761.55	0.728

In the storage mode, the temperature range of hot oil in the HST was such that, the ORC operation was not possible and therefore, only the ACS was operated. By operating the ACS with oil from the HST, only 553.49 KW of cooling could be obtained. The property values at various states of the ACS remaininvariant to the mode of operation because same component temperatures were maintained at all the three modes of operation. Only the mass flow rate of the refrigerant, weak and strong solutions are different. Refrigerant mass flow rate was the highest in the solar mode of operation (1.04 kg/s) followed by those of the solar storage (0.91 kg/s) and storage mode (0.234 kg/s). The mass flow rates of the strong and weak solutions at the storage mode are 5.027 and 4.793 kg/s respectively. This was the reason that the highest cooling was obtained during the solar mode and the minimum during the storage mode. The refrigerant mass flow rate in the ACS is subjected to change with cooling load which was calculated iteratively. The maximum 3.286 MW of heat was supplied to the ACS generator by hot water during the solar mode of operation followed by 2.885 MW during solar storage mode. During the storage mode, the hot oil from the HST could provide only 740.98 kW of heat to the ACS generator. Accordingly, the mass flow rates changed in the ACS and different amount of cooling was obtained at the three modes of operations.

Table 3. Comparison of system performance at the solar, solar storage and storage modes of operations

Modes	$I_{solar}$ (W/m <sup>2</sup> )	Net power (MW)	$\eta_{ORC}$ (%)	$\dot{Q}_E$ (MW)	COP	Total output (MW)	$\eta_{CPC}$ (%)
Solar	640	1.1	14.62	2.45	0.747	3.55	16.2
Solar storage	950	2.256	20.89	2.155	0.747	4.411	13.45%
Storage	—	—	—	0.553	0.747	—	—

## 5. CONCLUSION

The performance of a solar based CPC system was evaluated in this study under the solar, solar storage, and storage modes of operation. The following conclusions are made from the main findings of this study.

- In the solar mode, with a solar radiation of 640 W/m<sup>2</sup>, the HTF could be heated from 90 °C to 184.98 °C and using this hot water, 1.1 MW of net power and 2.45 MW of cooling were obtained from the ORC and ACS.
- In the solar storage mode, although less amount of hot water was passing through the ORC, but due to higher hot water temperature at HRVG inlet, the operating conditions in the ORC changed leading to more organic vapour generation and high net power. The ORC efficiency was therefore high at the solar storage mode compared to the solar mode of operation.
- Further in the solar storage mode, although the hot water temperature at the ACS generator inlet was 7.8 °C more, but due to lower mass flow rate, less amount of heat was supplied and accordingly the ACS provided less cooling which was 0.295 MW less compared to that of the solar mode.
- The total energy outputs obtained from the solar based system at the solar and solar storage modes of operations are 3.55 MW and 4.411 MW respectively. Although, the total system energy output was the maximum during the solar storage mode but the overall system efficiency was however more during the solar mode of operation.
- During storage mode, only the ACS could be operated which provided only 0.553 MW of cooling. In order to produce power and cooling simultaneously during the storage mode at night time, system operation in hybrid mode utilizing conventional energy source may be considered.

Thus from this study, important data regarding performance of a solar based CPC system is made available for solar, solar storage and storage modes of operations. The results may be useful for manufacturers dealing with the construction and installation of solar based power and cooling systems.

## REFERENCES

- [1] Jing Li, Gang Pei, Jie Ji. Optimization of low temperature solar thermal electric generation with organic rankine cycle in different areas. *Applied Energy* 2010;87(11):3355e65.
- [2] Prabhu E. Solar trough organic rankine electricity system (stores) stage 1:power plant optimization and economics; 2006. NREL/SR-550-39433.
- [3] A.M. Delgado-Torres, L. García-Rodríguez, Analysis and optimization of the lowtemperature solar organic rankine cycle (ORC), *Energy ConversionandManagement* 2010; 51:2846–2856.
- [4] Bellos, E.,Tzivanidis, C., Investigation of a hybrid ORC driven by waste heat and solar energy, *EnergyConversion Management* 2018; 156: 427–439.
- [5] F. Assilzadeh, S.A. Kalogiro, Y. Ali, K. Sopian, Simulation and optimization of a LiBr solar absorption cooling system with evacuated tube collectors, *Renewable Energy*2005;30:1143–1159.
- [6] Y.L. Liu, R. Wang, Performance prediction of a solar/gas driving double effectLiBr–H<sub>2</sub>O absorption system, *Renewable Energy*2004; 29:1677–1695.
- [7] Z. Li, X. Ye, J. Liu, Performance analysis of solar air cooled double effect LiBr/H<sub>2</sub>Oabsorption cooling system in subtropical city,*Energy Conversion and Management* 2004; 85:302–312.
- [8] Al-Sulaiman, F. A., Hamdullahpur, F., Dincer, I. Performance assessment of a novel system using parabolic trough solar collectors for combined cooling, heating, and power production. *Renewable Energy* 2012; 48:161-172.
- [9] A. Marin, A. Untea, L. Grosu, A. Dobrovicescu, D. Queiros-Conde, Performance evaluation of a combined organic Rankine cycle and an absorption refrigerationsystem 2013;*Termotehnica* 1, 81–90.
- [10] B. Eisavi, S. Khalilarya, A. Chitsaz, M.A. Rosen, Thermodynamic analysis of a novelcombined cooling, heating and power system driven by solar energy, *Applied Thermal Engineering* 2018;129:1219–1229.

- [11] L. Zhao, Y. Zhang, S. Deng, J. Ni, W. Xu, M. Maa, S. Lin, Z. Yu, Solar driven ORCbased CCHP: comparative performance analysis between sequential and parallel system configurations,*Applied Thermal Engineering* 2018; 131:696–706.
- [12] Gogoi, T. K. and Saikia, S. Performance analysis of a solar heat driven organic rankine cycle and absorption cooling system. *Thermal Science and Engineering Process* 2019; 13:100372.
- [13] Nondy, J., Gogoi, T. K., Comparative performance analysis of four different combined power and cooling systems integrated with a topping gas turbine plant, *Energy Conversion and Management* 2020; 223:113242
- [14] R. Forristal, Heat transfer analysis and modelling of a parabolic trough solar receiver implemented in Engineering Solver Equation, No. NREL/TP-550-34169, National Renewable Energy Laboratory, Golden, CO. (US); 2003.
- [15] J. Patek, J. Klomfar, A computationally effective formulation of the thermodynamic properties of LiBr–H<sub>2</sub>O solutions from 273 to 500 K over full composition range., *International Journal of Refrigeration* 2006;29(4):566–78.
- [16] W. Wagner, J.R. Cooper, A. Dittmann, J. Kijima, H.J. Kretzschmar, A. Kruse, I.A.P.W.S. The, Industrial Formulation, for the thermodynamic properties of water and steam, *Journal of Engineering for Gas Turbines and Power* 2000; 122:150–181.
- [17] Gogoi, T. K., Hazarika, P. Comparative assessment of four novel solar based triple effect absorption refrigeration systems integrated with organic Rankine and Kalina cycles 2020, *Energy Conversion and Management*;226:113561.



# **ENHANCING THE FLEXIBILITY OF ELECTRICITY GENERATION AND HEATING FOR KIZILDERE II GEOTHERMAL POWER PLANT BY DEMONSTRATING HEAT STORAGE SYSTEMS**

**Hakan Alp Sahiller**

Zorlu Enerji, İstanbul, Turkey, hakan.sahiller@zorlu.com, ORCID: 0000-0001-5360-8675

**Ural Halaçoğlu**

Zorlu Enerji, İstanbul, Turkey, ural.halacoglu@zorlu.com, ORCID: 0000-0003-4606-124X

**Raziye Şengün**

Zorlu Enerji, İstanbul, Turkey, raziye.sengun@zorlu.com, ORCID: 0000-0002-5692-4355

**İsmail Pekdüz**

Zorlu Enerji, İstanbul, Turkey, ismail.pekduz@zorlu.com, ORCID: 0000-0002-3886-0968

**Sylvie Rougé**

CEA, Grenoble, France, sylvie.rouge@cea.fr, ORCID: 0000-0003-2019-4909

**Elie Ghanatos**

CEA, Grenoble, France, elie.ghanatos@cea.fr, ORCID: 0000-0001-7333-7577

**Jérôme Pouvreau**

CEA, Grenoble, France, jerome.pouvreau@cea.fr, ORCID: 0000-0001-6014-5840

**Pall Valdimarsson**

pvald ehf and Reykjavik University, Reykjavik, Iceland, pall.valdimarsson@pvald.com, ORCID: 0000-0003-2971-3760

**Sebastian Gamish**

Fraunhofer, Institute for Solar Energy Systems ISE, Freiburg, Germany, sebastian.gamisch@ise.fraunhofer.de, ORCID: 0000-0001-5913-8416

**Mayra Paulina Alferez Luna**

Fraunhofer, Institute for Solar Energy Systems ISE, Freiburg, Germany, mayra.alferez.luna@ise.fraunhofer.de, ORCID: 0000-0002-8661-5529

**Shiladitya Paul**

TWI, Cambridge, UK, shiladitya.paul@twi.co.uk, ORCID: 0000-0002-8423-313X

**Alexandre Sabard**

TWI, Cambridge, UK, alexandre.sabard@twi.co.uk, ORCID: 0000000243843054

**Francesco Fanicchia**

TWI, Cambridge, UK, francesco.fanicchia@twi.co.uk, ORCID: 0000000200775469

**Volkan Ediger**

Kadir Has University, İstanbul, Turkey, volkan.ediger@khas.edu.tr, ORCID: 0000-0003-4925-483X

Gokhan Kirkil

Kadir Has University, Istanbul, Turkey, gokhan.kirkil@khas.edu.tr, ORCID: 0000-0001-9213-007X

Emilien Baudouin

Naldeo, Paris, France, emilien.baudouin@naldeo.com, ORCID: 0000-0001-7071-5325

*Sahiller HA., Halaçoğlu U., Şengün R., Pekdüz I., Pekdüz S., Ghanatos E., Pouvreau J., Valdimarsson P., Gamish S., Alferez Luna MP., Paul S., Sabard P., Fanicchia F., Ediger V., Kirkil G., Baudouin E. Enhancing the flexibility of electricity generation and heating for Kizildere II geothermal power plant by demonstrating heat storage systems. 9th Eur. Conf. Ren. Energy Sys. 21-23 April 2021, Istanbul, Turkey*

**Abstract:**

In the geothermal energy field, the main goal is to recover energy from brine, extracted several kilometers deep underground, in the form of heat to heating networks and/or producing electricity. Geothermal is currently engineered as an “always on” baseload supply, due to the limited flexibility to throttle the well without scaling and piping fatigue issues, and it is engineered for maximal efficiency at this output level. This energy source needs more flexibility to function as a fully reliable and controllable energy source. The EU H2020 GEOSMART project, started in June 2019 for a duration of 4 years, has the objective to optimize and demonstrate innovations to improve the flexibility of geothermal heat and power production systems. This article will focus on thermal energy storage demonstrations on the Kizildere II site in Turkey, which is one of the largest power plants in Turkey and in the world with 80 MWe of installed capacity. The main issue is to design a steam accumulator (5MWh) and a PCM storage (2MWh) adapted to the particular conditions of the brine extracted several kilometers underground containing a high proportion of non-condensable gases (mainly CO<sub>2</sub>) and highly mineralized water with a high risk of precipitation/scaling as soon as the temperature drops.

**Keywords:**

*Geothermal, flexibility, thermal energy storage, brine, PCM*

© 2021 Published by ECRES

## 1. INTRODUCTION

Turkey has the fourth largest installed capacity in the world with 1688 MWe as per thinkgeoenergy.com. The geothermal journey of the country started in 1965 by a public institution called the General Directorate of Mineral Research and Exploration (MTA). MTA drilled the first production well in the Kizildere region in 1968 at a depth of 540 m and the temperature was 198°C [1]. This was the first pilot geothermal plant for electricity production with initial installed capacity of 0,5 MWe in Turkey and the produced electricity was used in near fields. 500 kW prototype steam turbine was built in local workshops and provided free electricity to the nearby towns for 4 years [2].

The Kızıldere geothermal field is located on the northern flank of the Büyük Menderes Graben formed between the Babadag and Buldan horsts in the metamorphic rocks of the southern sub-massif which is part of the Menderes Massif in western Turkey. The Sazak Formation, the Igdecik Formation, and the lower layers of the Menderes Metamorphic constitute the reservoir rocks and they are identified as multi-reservoir systems with different temperatures [3]. There is no direct connection between the reservoirs. The Sazak Formation is formed from intercalations of limestone and marl, which became permeable due to tectonic activities [4] [5]. This formation is partly used for reinjection. The Igdecik formation is made up of metamorphic rocks, consisting of marble, mica schist, and quartzite intercalation. The metamorphic formation consist of mica schist, quartzite, calc-schist, sericite-schist, and chlorite-schist. This formation is more permeable than the first reservoir and the temperature is between 155–170°C.

The pilot plant was replaced by a 15 MWe single flash power plant, Kızıldere 1 Geothermal Power Plant (GPP), by Turkish Electricity Generation Company (EÜAŞ) in 1984 [6]. However, geothermal power production did not record a significant increase after Kızıldere 1 GPP as the total installed capacity remained nearly the same until 2005. Intensive research was carried out in 2005 to demonstrate the geothermal potential of Turkey. It was estimated that the country has 31500 MWt geothermal potential. [7] Many campaigns to provide incentives were introduced, but the geothermal investments were boosted only after the introduction of the feed-in tariff mechanism in 2011. Fifty-eight new geothermal power plants were commissioned by January 2020, reaching a total installed capacity of 1688 MWe.

Zorlu Enerji bought the rights of the Kızıldere concession in privatisation auction in 2008 and started to increase production of Kızıldere 1 power plant. The power plant production declined to 6 MWe due to the scaling problem caused by high CO<sub>2</sub> ratio in the geofluid and after the rehabilitation works were completed by Zorlu Enerji capacity increased to 15 MWe production capacity. Following the rehabilitation process, Zorlu Enerji started to make geological and geophysical surveys in the Kızıldere field to evaluate the geothermal resource. In the first development phase, Kızıldere II GPP was commissioned in 2013 with a triple flash and binary combined cycle power plant, and with 80 MWe capacity. In the second development phase, Kızıldere 3 U1 GPP and Kızıldere 3 U2 GPP was commissioned in 2017 and 2018 with the same cycle technology with total installed capacity of 165 MWe. This is the largest geothermal power plant in Turkey. Zorlu Enerji had decided to undertake a detailed maintenance of the Kızıldere 1 power plant in 2020. The reason for the maintenance of the plant was the ageing equipment (e.g. turbine, compressor). The power plant will undergo a major overhaul to ascertain the main issues in order to prevent possible failures. In the meantime, Kızıldere 1 production wells will be directed to the Kızıldere II GPP since it has some surplus capacity.

The 4-year H2020 GeoSmart project started in June 2019 with the main objective to optimise and demonstrate technological innovations at TRL7 that will improve the flexibility and efficiency of geothermal plants producing heat and electricity. Nineteen European partners are involved in the consortium. The two geothermal demonstration sites are located in (i) Germany and (ii) Turkey. This article will focus on the heat storage demonstration program in the Kızıldere II site in Turkey. The GPP commissioned into a feed-in tariff period for 10 years in 2013. The operator, Zorlu Enerji, is seeking ways to increase sales revenue after the incentive period. A total of 7 MWh storage capacity will be introduced to the site in order to help the power plant to operate flexibly and in a smart manner, and become competent in balancing the electricity and heat demand regardless of the time of the day. The main partners involved in this activity are Zorlu (industrial partner, site owner), PVald, KHAS (specialists in geothermal sites), CEA, Naldeo (specialists of heat storage demonstrators), Fraunhofer (PCM characterisation), and TWI (materials and corrosion specialists).

## 2. KIZILDERE II SITE

One of the R&D objectives of the GeoSmart project (there are several and these will not be described in detail in this article) is the design and installation of two demonstration systems of heat storage on Kızıldere II site in order to increase the flexibility and performance of the site. Kızıldere II GPP was designed as a combined heat and power (CHP) production facility. 80 MWe installed electricity capacity corresponds to the consumption of 400,000 households; 20 MWt installed district heating capacity corresponds to the demand of 2500 households, and 30 MWt installed greenhouse heating capacity is able to supply heat to 500 hectares of vegetable greenhouses [8].

Kızıldere II GPP with 80 MWe installed capacity runs with triple flash and binary combined cycle technology which allows to reach high power outputs through advanced steam turbine technology. Kızıldere II GPP has 12 production wells which feed the process via the High Pressure (HP) Separator. The brine which was previously processed in the Kızıldere 1 power plant is now sent to the Low Pressure (LP) Separator to enhance the productivity. Kızıldere 1 and Kızıldere 2 power plants share a common re-injection infrastructure via a set of brine injection pumps which increases the brine's pressure to  $\leq 35$  bar(a) to ensure the sustainability of the reservoir. HP, IP and LP turbines are all mounted to the same shaft and transmit the torque to a common generator for 60 MW electricity generation. 20 MWe is generated in bottoming cycle, which gains heat from the HP turbine exhaust.

On the Kızıldere 2 site, the brine is used directly in the topping cycle process, without any intermediate brine/water heat exchanger. Therefore, a main issue for this site is to design thermal storage systems: a steam accumulator and Phase Change Material (PCM) heat storage, adapted to the particular conditions of the brine extracted several kilometers underground containing a high level of non-condensable gases (mainly CO<sub>2</sub>, 99.52%) and highly mineralized water (Table 1) with risks of precipitation/scaling as soon as the temperature drops.

Table 1. Kızıldere 2 Brine Composition (mg/L) @1000 kJ/kg enthalpy

K	Na	Ca	Mg	Li	PO <sub>4</sub>	Hg	Sr	Zn	Ba	Al
196,00	1538,00	3,87	0,23	5,40	<0,05	<0,005	0,10	<0,05	<0,05	1,30
Fe	B	SiO <sub>2</sub>	NH <sub>4+</sub>	CO <sub>3</sub> 2-	HCO <sub>3</sub> -	Cl-	SO <sub>4</sub> 2-	F -	Br -	As
<0,05	24,00	460,00	8,00	127,00	2390,00	175,00	937,00	28,00	0,50	0,97

The main storage system is the steam accumulator on the steam line going to the turbine. The process is convenient because there are three levels of pressure which allows storing and discharging steam with a reasonable gradient of

pressure. Unfortunately, the steam at the outlet of the HP Separator has a very high content of non-condensable gases. This fraction of 10% would result in a decrease of the storage capacity by 64% as depicted in the Figure 1. Some modifications of the Kızıldere 2 process had to be proposed to integrate the steam accumulator, mainly a new IP Separator with a design pressure of 5 bar.

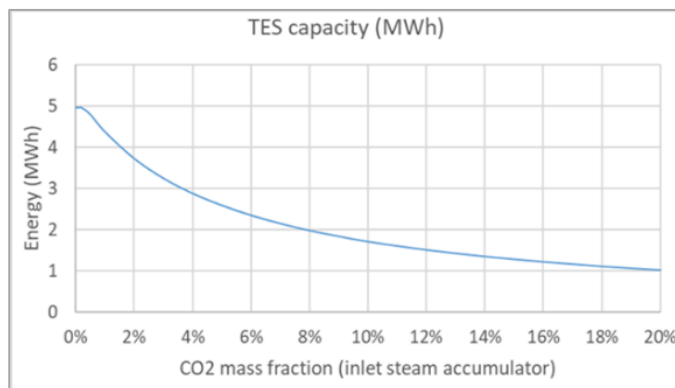


Figure 1. Thermal Energy Storage Capacity of the steam accumulator versus CO<sub>2</sub> mass fraction

The second storage demonstrator is a PCM module storing heat from the brine flow directly. Similar to the steam accumulator, it is important to have the maximal variation of temperature between heat charge and discharge, therefore the PCM module is directly connected to the outlet of the HP separator during charge, and to the LP separator during discharge. For this module, the main issue is to avoid scaling inside the tubes. Therefore, the brine is maintained in the liquid phase throughout the charging and discharging process in the module specifically designed for this purpose. Figure 2 shows a simplified process flow diagram (PFD) of the Kızıldere 2 site after integration of the new IP Separator and the two heat storage demonstrators.

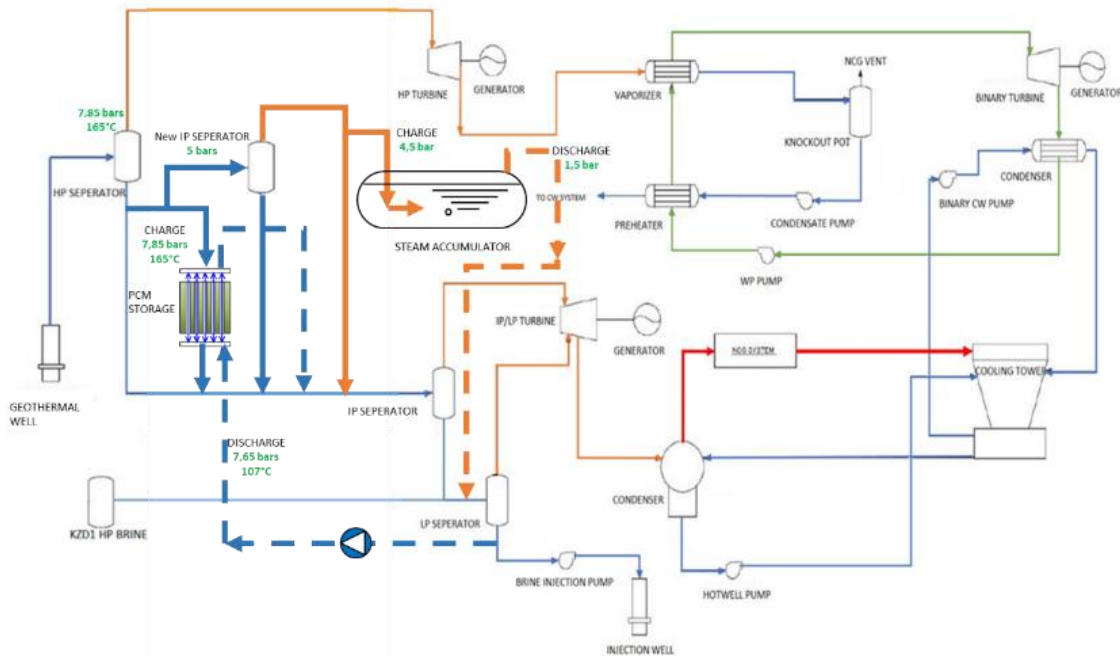


Figure 2. Simplified PFD for Kizildere 2 site with the addition of the thermal energy storage demonstrators and the new IP separator

### 3. STEAM ACCUMULATOR DESIGN

For the steam accumulator on Kızıldere 2 site, the target energy is 5MWh. This storage technology is industrially mature, the principle is to store the latent heat of steam condensation in the liquid water. At the beginning of the charging phase, the tank contains liquid water at saturation and a saturated steam sky at the minimum operating

pressure. Steam (at a higher pressure than the vessel's pressure) is injected through the injection line submerged in water. The steam bubbles condense on contact with the cold water and release energy which increases the temperature and level of the liquid. During this phase, the pressure in the tank increases continuously, and storage stops when the pressure is close to the pressure of the injection line. During the discharge, the injection line is closed and the discharge valve is open. The pressure in the vessel decreases resulting in the vaporization of the liquid water. This vaporization requires energy (latent heat of vaporization) which is provided by the liquid water. The temperature decreases continuously during discharge. This phase stops when the accumulator reaches its minimum pressure.

The addition of the new IP Separator in the process reduces the proportion of CO<sub>2</sub> in the steam from 10 to 2.8%, but the storage capacity is also reduced by 33% compared to pure steam (Figure 1). CEA has developed steam accumulator and PCM storage models using DYMOLA, a multi-physics simulation software used for system modeling.

Figure 3 shows the difference between the pressure evolution in a steam accumulator (345 m<sup>3</sup>) without (A) and with (B) non-condensable gases in the steam, with a charge flowrate of 0.58 kg/s. In both cases, the charging phase stops when the maximal total pressure (7.5 bar) is reached. With a mass fraction of 2.8% of non-condensable gases in the inlet steam, the charge is shorter (2h and 40 minutes instead of 4h in case A) and the final steam pressure is lower (6.3 bar instead of 7.5 bar in case A). This is due to the increasing presence of non-condensable gases (CO<sub>2</sub>) in the tank sky.

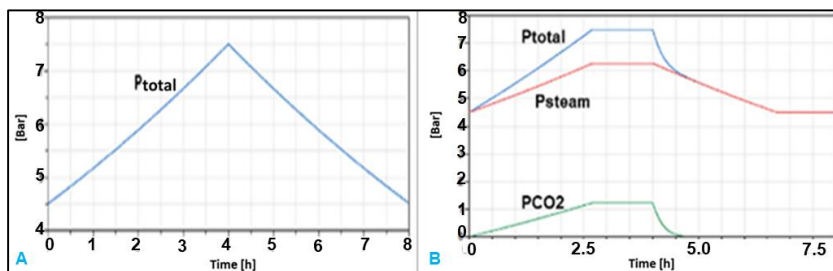


Figure 3. Evolution of the total pressure in steam accumulator versus time without (A) and with (B) a mass fraction of 2.8% of non-condensable gases in the steam input

These results are obtained by assuming a thermodynamic equilibrium between the phases. In case of a slight thermodynamic non-equilibrium, the effect of the presence of non-condensable gases will be more important. Several operating strategies have then been proposed and modeled to limit the effect of non-condensable gases in the input steam on the storage capacity of the steam accumulator.

#### 4. PCM STORAGE DESIGN

For the PCM storage on Kızıldere 2 site, the target energy is 2MWh. The heat transfer fluid is the brine in liquid phase, which transfers heat between 165°C and 107°C to the PCM. The PCM stores heat mainly in a solid –liquid latent form. During charge, the PCM melts and during discharge, it solidifies. A fraction of heat is also stored in a sensible form in this kind of storage systems.

The first design step involves the selection of a suitable PCM. In the case of Kızıldere 2, the PCM should melt in the range 107 to 165°C. Considering this temperature range, four PCMs were selected due to their reported melting temperatures between 152 and 161°C. The selected PCMs are organic compounds, namely, adipic acid, salicylic acid and Benzanilide, and an inorganic eutectic salt mixture- LiNO<sub>3</sub>-NaNO<sub>2</sub>.

To identify the thermal storage capacity, the phase change temperature range and the cycle stability the materials were characterized and cycled with differential scanning calorimeter (DSC). Organic compounds were cycled in air while LiNO<sub>3</sub>-NaNO<sub>2</sub>, due to its hygroscopic nature, was cycled under nitrogen atmosphere. Different DSC's are used as the first three material tend to sub-cool for smaller sample mass. A Q2500 DSC from TA Instruments and a SensysEvo DSC. The latter allows a sample mass about five times larger. Materials were cycled 100 times, except adipic acid, which was cycled 70 times.

Table 3 summarizes the results of the experimental characterization. As melting and crystallization point, the peak temperature of the DSC characterization was selected. It provides information of a possible shift of the phase change behavior during cycling. All materials except salicylic acid offer a high cycle stability with respect to the melting enthalpy, melting point and crystallization point. For salicylic acid, the melting and crystallization point is

significantly shifting during cycling towards lower temperatures. Thus, the material is not suitable for the application.

Table 3. Material properties determined by DSC

PCM	Melting enthalpy	Melting point / °C	Crystallization point / °C
Adipic acid	239.4- 252.0	151.6-152.0	147.1-148.31
Salicylic acid	-	60.3-161.1	49.7-165.0
Benzanilide	154.2-161.3	164.4-168.9	133.2-157.8
$\text{LiNO}_3\text{-NaNO}_2$	101.5-110.2	137.8-139.6	131.8-133.5

In Figure 4, the melting enthalpy is shown over the cycle number for adipic acid, benzanilide and  $\text{LiNO}_3\text{-NaNO}_2$ . For adipic acid, a slight decrease of the phase change enthalpy with increasing cycle number is visible. For heating and cooling, a reduction of about 5.5 J/g from maximum value to last cycle is determined. This indicates a degradation in air atmosphere. Nonetheless, the highest melting enthalpy of the materials is reached by adipic acid followed by Benzanilide and  $\text{LiNO}_3\text{-NaNO}_2$ .

The most suitable melting temperature is provided by adipic acid. Benzanilide needs to be heated up above the maximum temperature of the wellhead of 164 °C to enable full phase change enthalpy. For  $\text{LiNO}_3\text{-NaNO}_2$  the crystallization temperature is about 15 K lower compared to adipic acid, what would lead to a reduced performance of the plant during discharge.

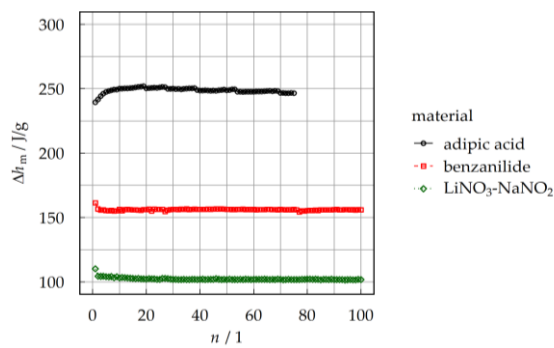


Figure 4. Melting enthalpy  $\Delta h_m$  versus the cycle number  $n$ .

Due to the suitable temperature and high melting enthalpy, **adipic acid** has been chosen as final material. For the application of the material in service, other properties, especially the degradation in the PCM at working conditions needs to be investigated. In addition to the PCM selection, there are several key points that need to be taken into account when designing a PCM storage module. One such parameter is the control of the melting front and the ease of expansion as the liquid has a lower density than the solid phase. A vertical position is often selected for this purpose, even if it is less convenient for installation. The second one is the very low conductivity of the PCM (<1W/m/K) which is enhanced by using finned tubes (fins increase the conductivity of the PCM). In the case of the present PCM module, the preselected tubes are made of commercial carbon steel with aluminum circular fins, the external diameter of tubes and fins are 25.4 mm and 57.4 mm, respectively. The third point is the flow regime inside the tubes when the heat transfer fluid is in single phase. As the velocity is very small, the flow regime is often in a transition zone between natural convection and forced convection, which is unsteady and hardly predictable [9]. Reducing the hydraulic section of the tubes is a way to resolve this issue. For the present module, we could add inserts in the tubes with a diameter of 13.5 mm, moving from the transition zone between natural and forced convection to laminar forced convection. This solution is convenient from a hydraulic point of view, but may bring other difficulties due to the high salinity of the brine. This high salinity is the last key design point. In order to avoid deposits inside the tubes and ease cleaning, the tubes bundle is straight and single pass. The general features of the PCM module are: (i) a shell and tube heat-exchanger, (ii) finned tubes with hydraulic inserts, (iii) single pass on HTF side, and (iv) vertical position.

For the requested energy of 2MWh, the PCM module will have a volume of 30 m<sup>3</sup>. It contains 954 tubes and 30 tons of Adipic acid. The energy is stored mainly as latent heat (70%) but also as sensible heat.

Figure 5A represents the energy evolution versus time in the storage during one charge. This energy reaches the target value of 2MWh after three hours of charge. The water inlet and outlet temperatures of storage during one charge are plotted in Figure 5B. During a short initial time, the water flows out very cold as it recovers the sensible cold stored in the PCM and the metal structures during the previous discharge, then it presents a plateau around

150°C symptomatic of the progressive melting of the PCM, and finally gradually rises towards the inlet temperature. The charge stops before the end of this final rise during which the stored power tends towards zero.

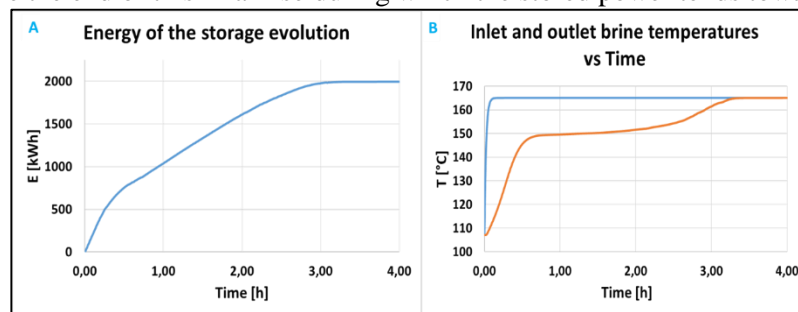


Figure 5. Evolution of the module stored energy (A), and inlet (blue) and outlet (orange) temperatures (B)

## 5. COATINGS AND MATERIALS

Through design and development of innovative material/coating systems, the life of heat exchangers can be enhanced to satisfy the plant requirements. When exposed to geothermal brine between 50 and 146°C, the effect of corrosion and scaling can impact the heat conduction and the efficiency of the system. For multi-material heat exchanger systems, galvanic corrosion of the less noble component can be an issue. In addition to the brine, the liquid PCM has the potential to corrode the materials of construction. Even if we mitigate corrosion by prudent selection of the materials, the scaling issues will still remain. By modifying the surface properties of the substrate, such as the steel-Al system or steel tubes, by the application of coatings such as fluoropolymers or sol-gel SiO<sub>2</sub>/TiO<sub>2</sub> systems, the electrolytic contact could be eliminated or decreased and the degradation and/or fouling of the heat exchanger can be reduced. Due to a lower surface free energy, materials such as polyphenylenesulfide (PPS) [10] [11] and sol-gel SiO<sub>2</sub> and TiO<sub>2</sub> [12] can provide corrosion and fouling protection, as well as enhance thermal conductivity via the use of appropriate fillers such as Multiwalled Carbon Nanotubes (MWCNT) [13].

Several coating systems were investigated to optimise the heat exchanger efficiency and reduce the degradation due to the exposure to aggressive environment. Based on criteria such as applicability to the system geometry, but also market readiness level and durability, three coating systems were down selected- (i) commercially available phenolic epoxy, (ii) fluoropolymers with carbon nanotubes fillers and (iii) amorphous SiO<sub>2</sub> sol-gel coatings.

## 6. CONCLUSION

Kızıldere II GPP is one of the largest power plants in Turkey and in the world with 80 MWe of installed capacity. The uniqueness of the Kızıldere 2 GPP is the use of brine directly in the process, without an intermediate brine/water heat exchanger. The GeoSmart project's main goal is to introduce a set of new equipment, adapted to the particular conditions of the brine, to Kızıldere 2 in order to enhance its flexibility and efficiency. This article is focused on the thermal design of the energy storage systems that will be installed on site, a steam accumulator (5MWh) module and a PCM heat storage (2MWh) module. These two modules will be intermediate size demonstrators which will validate the technology of thermal energy storage for geothermal applications, but larger capacity storage units would be needed to make the entire site's production more flexible. This preliminary design study will be followed by the detailed study, manufacture, installation on site and commissioning. The first demonstration tests are expected to start in 2023.

## ACKNOWLEDGMENT

The authors thank the European Commission that funded the H2020 GeoSmart project under GA 818576.

## REFERENCES

- [1] S. Yamanlar, E. D. Korkmaz Başel et U. Serpen, «Assessment of geothermal power potential in Buyuk Menderes Basin, Turkey. Geothermics , vol.88.,» 2020.
- [2] Çetin et al, «Denizli ili Elektrik Enerjisi Üretim Tesislerinin incelenmesi, Ege Bölgesi Enerji Forumu 12-13.10.2009,» 2009.

- [3] S. Simsek, «Hydrogeological and isotopic survey of geothermal fields in the Buyuk Menderes graben, Turkey. *Geothermics*, 32(4–6), 669-678.,» 2003.
- [4] S. Simsek, «Aydin-Germencik-Omerbeyli Geothermal Field of Turkey. Utilization of Geothermal Energy for Electric Power Production Space Heating (pp. 1-30). Florence: United Nations Economic Commission for Europe.,» 1984.
- [5] İ. Karamenderesi et M. Özgüler, «Mendere ve Gediz Graben sahalarında jeotermal enerji alanlarının oluşum mekanizması. Akdeniz Üniversitesi Isparta Mühendislik Fakültesi, 4, 196-229.,» 1988.
- [6] A. Kindap, T. Kaya et F. Haklidir, «Privatization of Kizildere geothermal plant and current approaches for the field and plant. GRC Transactions, Vol. 33, 2009,» 2009.
- [7] A. Satman, «Türkiye'de Jeotermal-Güncel Bakış, TESKON 2019, İzmir,» 2019.
- [8] U. Halaçoğlu et al, «Four Decades of Service – Kızıldere Reservoir, Units and Management, GRC Transactions vol. 42,» 2018.
- [9] M Martinelli et al, «Experimental study of an externally finned tube with internal heat transfer enhancement for phase change thermal energy storage. *J. Phys.: Conf. Ser.* 745 032029,» 2016.
- [10] T. Sugama et K. Gawlik, «Poly(tetrafluoroethylene)/(hexafluoropropylene) coatings for mitigating the corrosion of steel in a simulated geothermal environment,» *Progress in Organic Coatings*, vol. 42, n° % 13-4, pp. 202-208, 2001.
- [11] T. Sugama, «Anti-silica fouling coatings in geothermal environments,» *Materials Letters*, pp. 666-673, 2002.
- [12] J. Song, M. Liu, X. Sun,, J. Wang et J. Zhu, «Antifouling and anticorrosion behaviors of modified heat transfer surfaces with coatings in simulated hot-dry-rock geothermal water,» *Applied Thermal Engineering*, vol. 132, pp. 740-759, 2018.
- [13] E. Yang, T. Hwang, A. Kumar et K. Kim, «Anti-Biofouling, Thermal, and Electrical Performance of Nanocomposite Coating with Multiwall Carbon Nanotube and PTFE-blended PPS,» *Polymer Technology*, vol. 37, n° % 13, pp. 1-7, 2018.



# SELECTION OF THE SUITABLE GREENHOUSE ORIENTATION ON THE BASIS OF ENERGY SAVING

Ouazzani Chahidi Laila

SIGER, Intelligent Systems, Georesources and Renewable Energies Laboratory, Faculty of Sciences and Techniques of Fez, Sidi Mohamed Ben Abdellah University, PO. Box 2202, Fez, Morocco, laila.ouazzanichahidi@usmba.ac.ma, ORCID: 0000-0001-9490-8658

Mechaqrane Abdellah

SIGER, Intelligent Systems, Georesources and Renewable Energies Laboratory, Faculty of Sciences and Techniques of Fez, Sidi Mohamed Ben Abdellah University, PO. Box 2202, Fez, Morocco, ORCID: 0000-0002-3362-4608

Cite this paper as:

*Chahidi, OL, Mechaqrane, A. Selection of the suitable greenhouse orientation on the basis of energy saving. 9<sup>th</sup> Eur. Conf. Ren. Energy Sys. 21-23 April 2021, Istanbul, Turkey*

**Abstract:** Protected agriculture is one of the prominent agricultural techniques that allows for creating an adapted microclimate for the plant growth which leads to high quality and off season production. Instead, a significant amount of energy is required. This study aims to provide the potential of energy saving based on the optimal selection of the greenhouse orientation under Fez city's climatic conditions (Morocco). For this purpose, a dynamic model of a gothic arch shaped greenhouse is created in EnergyPlus environment. To define the prospect of the energy-saving, two variables were first evaluated: the greenhouse inside air temperature variation and thermal loads prompted by creating the optimum microclimate for tomato plant, in four different orientations ( $0^\circ$ ,  $90^\circ$ ,  $45^\circ$  and  $-45^\circ$ ). Finally, an economic analysis is performed. The results show that  $0^\circ$  relative north (longer axis) is the optimal orientation for a gothic arch greenhouse under the climate condition of Fez.

**Keywords:** agricultural greenhouse - energy modeling – orientation- EnergyPlus

© 2021 Published by ECRES

## 1. INTRODUCTION

Currently, climate change, disappearance of fossil fuels, population growth, constant increase of energy needs and other numerous constraints are facing the world. Therefore, opting for energy efficient systems has become an unavoidable necessity. Being one of the energy-intensive systems agricultural greenhouse ought to be a part of this strategy. Therefore, energy optimization must be considered at the earliest stages of the greenhouses construction. The greenhouse heating and cooling energy needs undoubtedly depend on its design and geographic localization. Thus, in specific climatic conditions and for a particular type of cultivation, the greenhouses design should be chosen to maintain, as much as possible, adequate microclimate parameters.

The greenhouse orientation significantly influences the solar heat gains and thus the microclimate of the greenhouse. To evaluate energy comportment of greenhouse with different orientations, researches are conducted. Gupta et al. [1] studied the effect of the greenhouse orientation ( $0^\circ$  /  $30^\circ$  /  $45^\circ$  /  $60^\circ$  /  $90^\circ$ ) and area ( $4 \times 6$  /  $4 \times 12$  /  $12 \times 18$ ) on the total solar fraction transmitted based on a 3D shadow analysis in Auto-Cad software. The comparison was done based on a typical clear day of winter and summer, under the climatic condition of New Delhi, India, considering only the beam solar radiation. Their results show that the greenhouse oriented  $45^\circ$ clock-wise (Relative East-West orientation) resulted in lowest radiation loss during winter and maximum one during summer. In another work, Dragićević [2] analyzed the total solar radiation availability in an uneven span greenhouse located in Belgrade, Serbia in EW and NS orientation (longer axis). Based on the measured global solar radiation on a horizontal surface, the total incident solar radiation was calculated. The model adopted in their study was experimentally validated by comparing the predicted and measured daily average of incident solar radiation on a horizontal surface and on the south wall. According to them, an EW oriented uneven span greenhouse is the best one. Exhaustive reviews on this field have been presented. Odesola and Ezekwem [3] Reviewed the effect of greenhouses shape and orientation studies. Choab et al. [4] presented a comprehensive review on the developments

and researches conducted on greenhouses from different point of view; greenhouse design, thermal modeling and simulation, and climate controlling technologies.

Several thermal modeling and simulation methods was used to study the agricultural greenhouse behavior. Sethi [5] modeled different greenhouse shapes and orientation by developing a C++ program to compute the hourly incident total solar radiation on different inclined and vertical surfaces for all studied greenhouses. Using the object-oriented modelling, Rodríguez et al. [6] modeled a typical Mediterranean greenhouse located in Almería, South-East Spain, based on mass and energy balances. Ouazzani Chahidi et al. [7] modeled in EnergyPlus environment a high efficiency greenhouse located in the Northwest of Italy considering the interaction between all greenhouse's components including plants, soil and internal masses in order to assess the contribution of different energy saving strategies.

The optimal selection of greenhouse orientation helps maintaining an adequate microclimate and leads to decrease the heating and cooling loads, thereby the operating cost. The aim of this study is to evaluate different greenhouse orientation ( $0^\circ$ ,  $90^\circ$ ,  $45^\circ$  and  $-45^\circ$ ), in order to select the most suitable one in term of energy optimization. For this purpose, a dynamic energy model is created in EnergyPlus environment of a gothic arch greenhouse at the Mproccan city of Fez ( $33.93^\circ\text{N}$ ,  $4.98^\circ\text{W}$ , 579 m). To assess the potential of energy-saving, two variables were first evaluated: the inside air temperature variation and thermal loads in tomato greenhouse. Finally, an economic analysis is performed.

## 2. MODELING

The aim of this study is to assess the energy-saving potential generated from the optimal selection of a tomato greenhouse orientation under the climatic condition of Fez, Morocco. Gothic arch and bubbled polyethylene (BPE) plastic have been chosen as greenhouse shape and covering material, respectively. On a previous author' investigation [8] this combination represents the optimal design in protected agriculture under the climatic conditions of Fez, Morocco. The greenhouse is of an area of  $220 \text{ m}^2$  ( $20\text{m} \times 11 \text{ m}$ ) with a height of 6 m. Figure 1 represents the greenhouse 3D model created in SketchUp graphical interface. Four greenhouse orientations are considered in this study;  $0^\circ$ ,  $90^\circ$ ,  $45^\circ$  and  $-45^\circ$  relatively to the north direction (longer axis).

The modeling and simulation are carried out in EnergyPlus software. The greenhouse is modeled as a single zone interacting with its outside environment as well as with its interior components (plants and soil). The loads calculation is based on the air heat balance of the zone and the different greenhouse components. The heat balance equation is solved in the time domain based on a third order backward approximation of the zone temperature derivative with a time step calculation of 6 times per hour. Moreover, the vegetation is defined in EnergyPlus as a layer of the floor material and their effect were considered based on the FASST model [9] developed for the US Army Corps of Engineers by Frankenstein and Koenig. Moreover, the climate data are obtained from Meteonorm software and the simulation is conducted over a year. Table 1 represents the greenhouse parameters used for modeling.

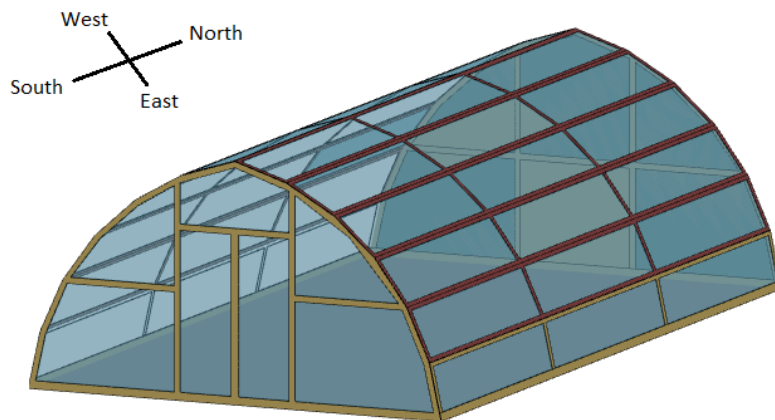


Figure 12. Greenhouse 3D model (orientation  $0^\circ$ )

Table 1. Greenhouse parameters.

Site localization							
City	Longitude	Latitude	Altitude				
Fez	4.98°W	33.93°N	579 m				
Dimension							
Shape	Length	Width	Roof-top height				
Gothic arch	20 m	11 m	6 m				
Covering material [10]							
Material	$\tau_{PAR}$	$\rho_{PAR}$	$\alpha_{PAR}$	$\tau_{NIR}$	$\rho_{NIR}$	$\alpha_{NIR}$	$Q$
BPE	63%	14%	23%	68%	14%	18%	63%
Plant							
Height	Leaf area index			Minimum stomatal resistance			
1 m	4			120 s/m			
Soil							
Conductivity of dry soil	Density of dry soil			Specific heat of dry soil			
0.35 W/m.K	1100 kg/m³			600 J/kg.K			

### 3. RESULTS AND DISCUSSIONS

Simulations are performed separately for the four greenhouse orientations. Thereafter, the analysis of the greenhouse thermal behavior is conducted to investigate the impact of its orientation; first on the inside air temperature without an air conditioning system, then on the thermal loads for heating and cooling by considering the adapted microclimate for tomato plant (mean daily value of 21°C and relative humidity of 75% [11]). Finally, the annual energy cost of the air conditioning system is estimated and the operational cost reduction generated from the right selection of the greenhouse orientation is evaluated.

#### Inside temperature

In order to clearly assess the greenhouse inside air temperature variability depending on the greenhouse orientation, January 15<sup>th</sup> (winter) and July 15<sup>th</sup> (summer) are represented in Figure 2. As a general observation of the graphs, the effect of the orientation on the greenhouse inside air temperature is clear during winter comparing to summer, especially in the hours when the sun is height in the sky. Since the sun is the major source of thermal loads in agricultural greenhouses and since the system is transparent from the four sides, it is obvious that the temperature effect seems more noticeable during winter when solar altitude is lower than that of summer.

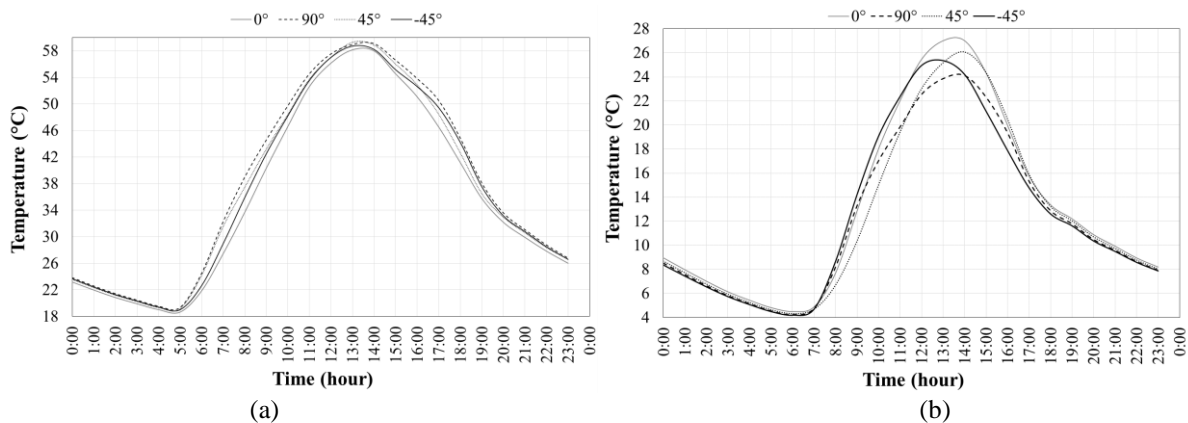


Figure 13. Inside air temperature for different orientation (a) winter, January 15<sup>th</sup> (b) summer, July 15<sup>th</sup>.

During winter, the temperature does not exceed 28°C. The maximal temperature is obtained when the orientation is 0° relative north while orientations 90°, 45° and -45° provide smaller air inside temperature with a maximal difference of about 3°C at 13h00, 10h00 and 15h00 respectively. In summer, the higher temperature during the day reaches 59°C. The orientation 0° provides the minimal temperature during the whole day. The maximal difference is about 5°C, 4°C and 3°C for 90°, 45° and -45° orientations respectively.

## Heating and cooling requirements

This section presents the effects of orientation on reducing heating and cooling requirement. The comparison is based on the monthly thermal loads of the greenhouse. 21°C is assigned as a mean daily set point temperature. Figure 3 shows the greenhouse monthly heating and cooling loads. Based on the graphs, the maximal heating and cooling requirements occurs during the month of January and July respectively. In January, the heating loads of the greenhouse oriented 0°, 90°, 45° and -45° are about 23.96, 24.13, 25.36 and 24.36 kWh/m<sup>2</sup>, respectively. For the cooling loads, amounts of about 75.84, 85.36, 81.85 and 81.84 kWh/m<sup>2</sup> are observed during the month of July. Finally, on an annual basis, the minimal heating loads (around 102.05 kWh/m<sup>2</sup>) are observed in greenhouse oriented 90° relatively to the north direction. For the other orientations, the heating loads are about 104.28 kWh/m<sup>2</sup>, 106.13 kWh/m<sup>2</sup> and 107.26 kWh/m<sup>2</sup> (+2%, +4% and 5% comparing to 90°) for -45°, 0° and 45° respectively. Although, the minimal cooling loads occur when the greenhouse is oriented 0° with a value around 427.20 kWh/m<sup>2</sup>. For the other orientations, cooling loads of about 448.86 kWh/m<sup>2</sup>, 450.42 kWh/m<sup>2</sup> and 463.24 kWh/m<sup>2</sup> (+5%, +5.5% and +8.4 comparing to 0°) are obtained in -45°, 45°, and 90° respectively.

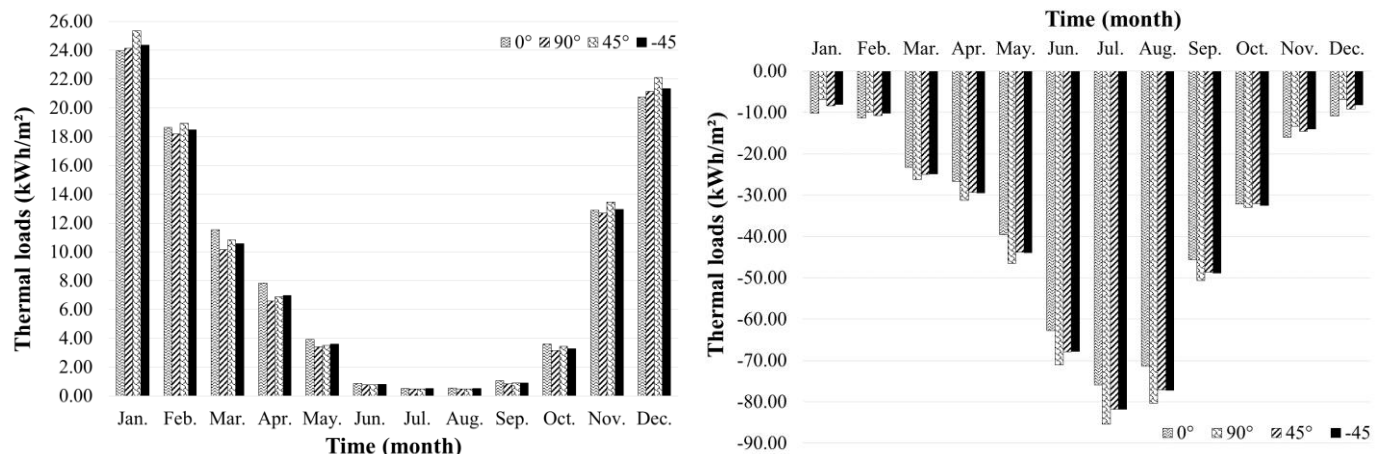


Figure 14. Greenhouse monthly heating and cooling loads.

## Economic analysis

To evaluate the economic gain obtained from the optimal selection of the greenhouse orientation, a comparison on the annual basis is conducted. The annual energy operating cost is calculated for each orientation and considered as the main indicator to select the optimal one. In this study, a standard conventional system for the greenhouse air conditioning is selected. This system is composed by of a boiler with a top efficiency  $\eta = 0.96$  and a chiller for cooling purpose with  $EER = 3.5$ . In Morocco, electricity consumers associated to the agricultural sector benefits from a special pricing “green tariff”. In this pricing mode, the electrical kWh price depends on several parameters; season, time of the day...etc. [12]. The electrical kWh price considered in this study is 0.9 MAD/kWh.

Figure 4 represents the annual energy cost (MAD/m<sup>2</sup>) variation depending on the greenhouse orientation. It can be observed from the graph, that the orientation of 0° relatively to the north direction is the optimal one with an annual energy cost of about 209.60 MAD/m<sup>2</sup>. For the other orientations; -45°, 90° and 45°, the annual energy cost is around 213.42 MAD/m<sup>2</sup>, 215.03 MAD/m<sup>2</sup> and 216.62 MAD/m<sup>2</sup> (+1.80%, +2.54% and +3.25% comparing the 0°) respectively.

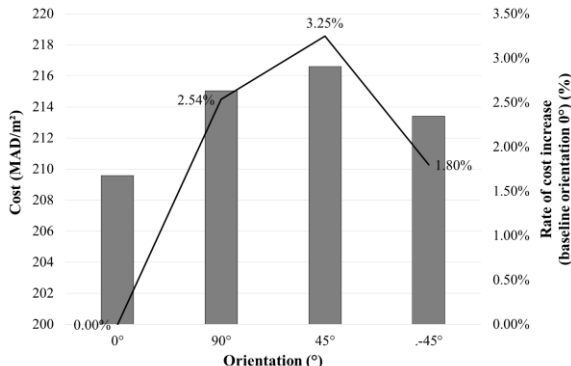


Figure 15. Annual energy cost for the greenhouse air conditioning

## 4. CONCLUSIONS

In this study, different greenhouse orientations are evaluated, namely; 0°, 90°, 45° and -45° relatively to the north direction (longer axis). For this aim, a dynamic model of a gothic arch shaped greenhouse is created in EnergyPlus environment. To determine the potential of energy-saving, two variables were first examined: the greenhouse inside air temperature variation during winter day (15<sup>th</sup> January) and summer day (15<sup>th</sup> July), and, thermal loads resulted from ensuring the adapted microclimate for tomato plant. Finally, an economic analysis is performed by calculating the annual energy cost of the greenhouse with the different studied orientations. The annual energy cost is considered as the main indicator to select the optimal orientation.

The results show that a gothic arch shaped greenhouse with Bubbled polyethylene (BPE) plastic covering and oriented 0° relatively to the north direction (longer axis) are recommended for an optimal design of protected agriculture. This conclusion is obtained by considering the yearly energy cost of the air conditioning system for tomato plants greenhouse in the climatic conditions of Fez, Morocco. The annual energy cost for the selected design is estimated around 209.60 MAD/m<sup>2</sup>, lower than the one of -45°, 90° and 45° orientations by about 1.80%, 2.54% and 3.25%, respectively.

## REFERENCES

- [1] Gupta R, Tiwari G. N, Kumar A, and Gupta Y, "Calculation of total solar fraction for different orientation of greenhouse using 3D-shadow analysis in Auto-CAD," *Energy Build.*, vol. 47, pp. 27–34, 2012, doi: 10.1016/j.enbuild.2011.11.010.
- [2] Dragićević S. M, "Determining the optimum orientation of a greenhouse on the basis of the total solar radiation availability," *Therm. Sci.*, vol. 15, no. 1, pp. 215–221, 2011, doi: 10.2298/TSCI100220057D.
- [3] Odesola I. F and Ezekwem C, "The Effect of Shape and Orientation on a Greenhouse: A Review," *An Int. J. Sci. Technol.*, vol. 1, no. 1.
- [4] Choab N, Allouhi A, El Maakoul A, Kousksou T, Saadeddine S, and Jamil A, "Review on greenhouse microclimate and application: Design parameters, thermal modeling and simulation, climate controlling technologies," *Solar Energy*, vol. 191. Elsevier Ltd, pp. 109–137, 01-Oct-2019, doi: 10.1016/j.solener.2019.08.042.
- [5] Sethi V. P, "On the selection of shape and orientation of a greenhouse: Thermal modeling and experimental validation," *Sol. Energy*, vol. 83, no. 1, pp. 21–38, Jan. 2009, doi: 10.1016/j.solener.2008.05.018.
- [6] Rodríguez F, Yebra L.J, Berenguel M, and Dormido S, "Modelling and simulation of greenhouse climate using dymola," in *IFAC Proceedings Volumes (IFAC-PapersOnline)*, 2002, vol. 35, no. 1, pp. 79–84, doi: 10.3182/20020721-6-es-1901.01322.
- [7] Ouazzani Chahidi L, Fossa M, Priarone A, and Mechaqrane A, "Energy saving strategies in sustainable greenhouse cultivation in the mediterranean climate – A case study," *Appl. Energy*, vol. 282, p. 116156, Jan. 2021, doi: 10.1016/j.apenergy.2020.116156.
- [8] Ouazzani Chahidi L and Mechaqrane A, "Greenhouse Design Selection under the Climatic Conditions of Fez, Morocco," in *Proceeding of the 6th International Conference on Wireless Technologies, Embedded and Intelligent Systems*. October 14-16, 2020, Fez, Morocco.(in press).
- [9] Frankenstein S and Koenig G, "FASST Vegetation Models," *Cold Reg. Res. Eng. Lab.*, no. December, p. 56, 2004.
- [10] Kittas C and Bailie A, "Determination of the spectral properties of several greenhouse cover materials and evaluation of specific parameters related to plant response," *J. Agric. Eng. Res.*, vol. 71, no. 2, pp. 193–202, Oct. 1998, doi: 10.1006/jaer.1998.0310.
- [11] Baudoin W, Nono-Womdim R, Lutaladio N, Hodder A, Castilla N, Leonardi C, et al. , *Good Agricultural Practices for greenhouse vegetable crops: principles for mediterranean climate areas*. FAO. 2013.
- [12]"Site web officiel de l'ONEE - Branche Electricité." [Online]. Available: <http://www.one.org.ma/FR/pages/interne.asp?esp=1&id1=2&id2=35&id3=11&t2=1&t3=1>. [Accessed: 12-Feb-2021].



# SUPERCRITICAL CO<sub>2</sub> BINARY MIXTURES FOR BRAYTON POWER CYCLES COMPLEX CONFIGURATIONS COUPLED TO SOLAR THERMAL ENERGY PLANTS

Paul Tafur-Escanta

Universidad Politécnica de Madrid, Madrid, Spain, pm.tafur@alumnos.upm.es, ORCID: 0000-0002-0760-6350

Robert Valencia-Chapi

Universidad Politécnica de Madrid, Madrid, Spain, robert.valencia.chapi@upm.es, Universidad Técnica del Norte, Ibarra, Ecuador, rmvalencia@utn.edu.ec  
Investigación, Desarrollo e Innovación Energética, Madrid, Spain, robert.valencia@idie.es, ORCID: 0000-0003-1977-2118

Luis Coco-Enríquez

Universidad Politécnica de Madrid, Madrid, Spain, luiscocoenriquez@hotmail.com, ORCID: 0000-0002-3655-2654

Javier Muñoz-Antón

Universidad Politécnica de Madrid, Madrid, Spain, jamunoz@etsii.upm.es, ORCID: 0000-0002-1980-0863

*Tafur-Escanta, P., Valencia-Chapi, R., Coco-Enríquez, L., Muñoz-Antón, J. Supercritical CO<sub>2</sub> Binary Mixtures for Brayton Power Cycles Complex Configurations Coupled to Solar Thermal Energy Plants. 9<sup>th</sup> Eur. Conf. Ren. Energy Sys. 21-23 April 2021, Istanbul, Turkey.*

**Abstract:** In this work, Brayton cycles analysis operating with mixtures based on supercritical carbon dioxide (s-CO<sub>2</sub>/COS, s-CO<sub>2</sub>/H<sub>2</sub>S, s-CO<sub>2</sub>/NH<sub>3</sub>, and s-CO<sub>2</sub>/SO<sub>2</sub>) as a working fluid is carried out. Four complex configurations were studied: recompression with double and triple reheating (RCC-2RH), (RCC-3RH); recompression with main compressor intercooling with double and triple reheating (RCMCI-2RH), (RCMCI-3RH). Design parameters such as the aperture area of the solar field and the performance of the cycle at the design point are evaluated. The methodology used in calculating the plant performance is to establish total conductance values of the heat recuperator ( $UA_{total}$ ) between 5 and 25 MW/K. This work's main conclusion is that the cycle efficiency has improved due to s-CO<sub>2</sub> mixtures as a working fluid; this is significant compared to that obtained using pure s-CO<sub>2</sub>. The mixture of s-CO<sub>2</sub>/COS with a 70/30 molar fraction is considered the best in efficiency since it increases between 3 and 4 percentage points compared to pure s-CO<sub>2</sub>. This mixture has the lowest cost of the solar field for the RCC configuration. It is closely followed by the mixture of s-CO<sub>2</sub>/H<sub>2</sub>S with a 60/40 molar fraction with very similar efficiency and the lowest solar field cost for the RCMCI configurations.

**Keywords:** Brayton cycle; supercritical CO<sub>2</sub>; fluid mixture; solar thermal plant.

© 2021 Published by ECRES

Nomenclature	
CIP	Compressor inlet pressure
CIT	Compressor inlet temperature
COS	Carbonyl Sulfide
CSP	Concentrated solar power
H <sub>2</sub> S	Hydrogen Sulfide
NH <sub>3</sub>	Ammonia
PTC	Parabolic trough solar collector
RCC-2RH	Recompression with double reheating
RCC -3RH	Recompression with triple reheating
RCMCI-2RH	Recompression with main compressor intercooling with double reheating
RCMCI-3RH	Recompression with main compressor intercooling with triple reheating

REFPROP	Reference fluid properties
SO <sub>2</sub>	Sulfur Dioxide
s-CO <sub>2</sub>	Supercritical Carbon Dioxide
SCSP	Supercritical concentrated solar power plant
TIT	Turbine inlet temperature
UA	Heat exchanger conductance

## 1. INTRODUCTION

The global energy market has been changing progressively in recent years. These changes can be explained with different facts, being the most outstanding ones the growing concern for the environment and climate change, the increase of fossil fuel cost and their depletion, and the development of new renewable technologies that are increasingly competitive. From a statistical analysis point of view, in the 2010-2020 period, there has been a massive revolution in renewable technologies. There have been more installations of this kind than non-renewable since 2013, reaching one-third of the total installed capacity worldwide [1].

Supercritical carbon dioxide power cycles are emerging as one of the promising alternative energy conversion systems for next-generation concentrated solar power plant technologies (CSP-Gen3) [2], nuclear [3], and geothermal energy [4]. In some cases of residual heat recuperation from internal combustion engines (ICE) [5]. The high density, nearly two times the steam's and volumetric heat capacity of s-CO<sub>2</sub> regarding other working fluids, makes it more energy-dense. These characteristics mean that the size of most of the system components, such as the compressor, the turbine, and the heat exchangers, can be considerably reduced. Therefore, the plant's size is small, which can be reflected in possibly lower capital costs. Recent research has been based on improving the efficiency of the s-CO<sub>2</sub> cycle trying to get a working fluid, including fluid mixtures, that adapt to the variable input conditions of temperature and pressure in thermal power plants [6].

Improving the Brayton s-CO<sub>2</sub> cycle performance has become a fundamental challenge in areas with high ambient temperatures; this can be achieved by relocating the critical point of the working fluid to higher temperatures using CO<sub>2</sub> mixtures [6 – 8]. The design of a binary mixture based on s-CO<sub>2</sub> is carried out by adding one or more inorganic / organic compounds that allow increasing the critical temperature and pressure by relocating its critical point. Then, by increasing the temperature of the mixture, the initial operating temperature of the cycle will increase, thus coinciding with hot and desert climates with a high ambient temperature. This factor has been of great importance and has contributed to the emergence of research on different configurations of the Brayton s-CO<sub>2</sub> cycle with CSP technologies in terms of costs and thermal efficiency [8]. Various configurations this cycle are currently being studied, focusing on their design, performance and cost to achieve greater efficiency [9 – 11]. Valencia et al. [6] studied the influence of fluid mixtures (binary mixtures decreasing and increasing the critical temperature) on an s-CO<sub>2</sub> Brayton cycle with recompression. The conclusions research indicate that the s-CO<sub>2</sub> mixtures increase the cycle thermal efficiency by 3 and 4%.

The primary purpose of this study is to evaluate the benefits of s-CO<sub>2</sub> binary mixtures with substances that increase the mixture's critical temperature (s-CO<sub>2</sub>/COS, s-CO<sub>2</sub>/H<sub>2</sub>S, s-CO<sub>2</sub>/NH<sub>3</sub>, s-CO<sub>2</sub>/SO<sub>2</sub>) in complex Brayton s-CO<sub>2</sub> cycle configurations coupled to Concentrated Solar Power.

## 2. MATERIALS AND METHODS

The plant performance calculation assumes a constant heat recuperator total conductance (UA) [12]. A compressor inlet temperature of 51 °C is established, and also the pressure drops in the heat exchanger (PHX and RHX), precooler (PC), and heat recuperators (LTR and HTR). Four complex configurations were studied: recompression with double

reheating (RCC – 2RH) and with triple reheating (RCC – 3RH); recompression with main compressor intercooling and double reheating (RCMCI – 2 RH) and with triple reheating (RCMCI – 3RH) [13]. The components of the cycles are: MC: main compressor; RC: recompressor; C: compressor; G: generator; T: turbine; PC: precooler; LTR: low-temperature recuperator; HTR: high-temperature recuperator; PHX: primary heat exchanger; RHX: reheating heat exchanger; SF: solar field; FS: fluid split; FM: fluid mixture, (Figure 1 and Figure 2).

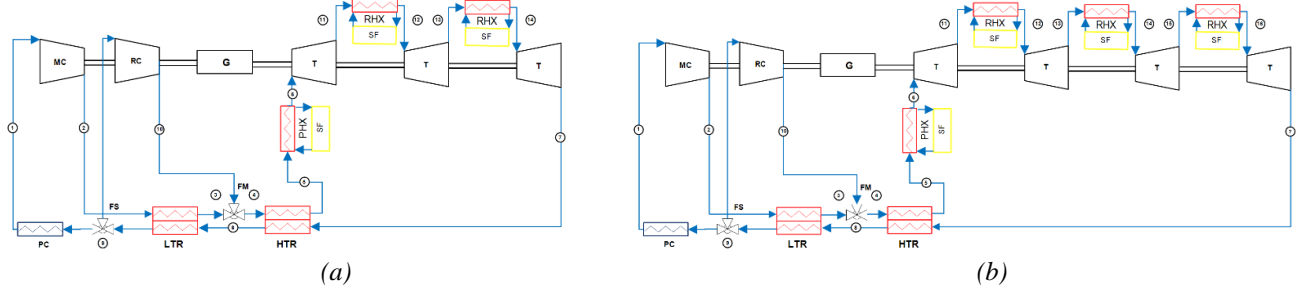


Figure 1. Recompression Brayton cycle. (a) Double reheating, (b) Triple reheating layout.

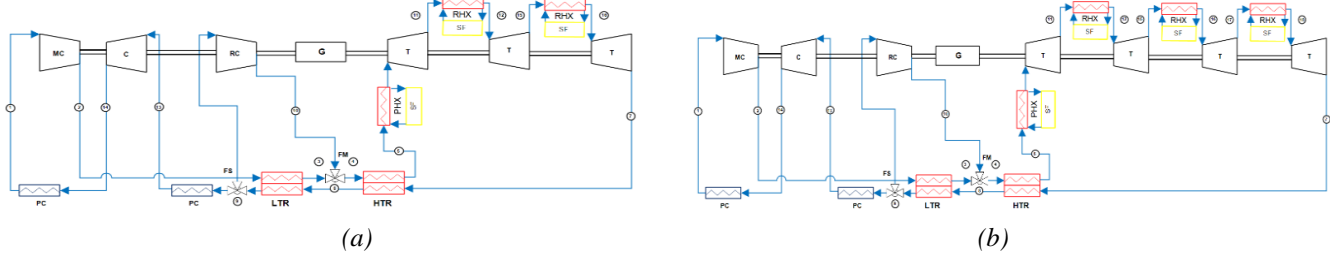


Figure 2. Recompression with main compressor intercooling Brayton cycle (a) Double reheating, (b) Triple reheating layout.

The Software SCSP (Supercritical Concentrated Solar Power Plant) [13] has been used for simulating the performance of the complex configuration at design-point, using pure s-CO<sub>2</sub> and s-CO<sub>2</sub> mixtures as power cycle working fluid. The fluids properties (Figure 3) have been obtained from the REFPROP database developed by NIST in the USA [14]. This figure shows the critical temperature distribution (a) and the critical pressure (b) of the mixtures while varying the mole fraction of the added fluid.

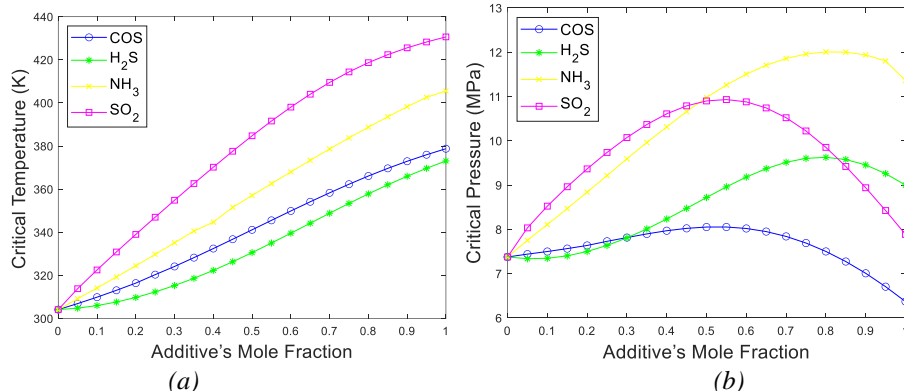


Figure 3. Fluids properties vs. vs. additive's mole fraction. (a) Critical temperature, (b) Critical pressure.

The main assumptions considered are summarized in Table 1. The compressor inlet pressure and the split fraction are optimized with the mathematical algorithms SUBPLEX, UOBYQA and NEWOUA.

Table 1. Input parameters for mixtures that increase the critical temperature.

	Nomenclature	Value	Units
Net power output	$W$	50	MW
Compressor inlet temperature	$CIT$	51	°C
Turbine inlet temperature	$TIT$	550	°C
Compressor efficiency [6]	$\eta_{mc}$	0.89	-
Turbine efficiency [6]	$\eta_t$	0.93	-
UA for the low-temperature recuperator	$UA_{LT}$	2.5 → 12.5	MW/K
UA for the high-temperature recuperator	$UA_{HT}$	2.5 → 12.5	MW/K
Pressure drops for LTR and HTR	$\Delta P/P_{LTR} // \Delta P/P_{HTR}$	1.5 // 1.0	%
Pressure drop Precooler	$\Delta P/P_{PR}$	2.0	%
Pressure drops for PHX and RHX	$\Delta P/P_{PHX} // \Delta P/P_{RHX}$	1.5 // 1.5	%

The thermal efficiency of the cycles studied vs. recuperator total conductance, using pure s-CO<sub>2</sub> as the working fluid without and with pressure drop in the components, is shown in Figure 4. Figure 4b, can be observed the cycle efficiency is worst when the cycle has more reheating because of the pressure drop in the heat exchangers.

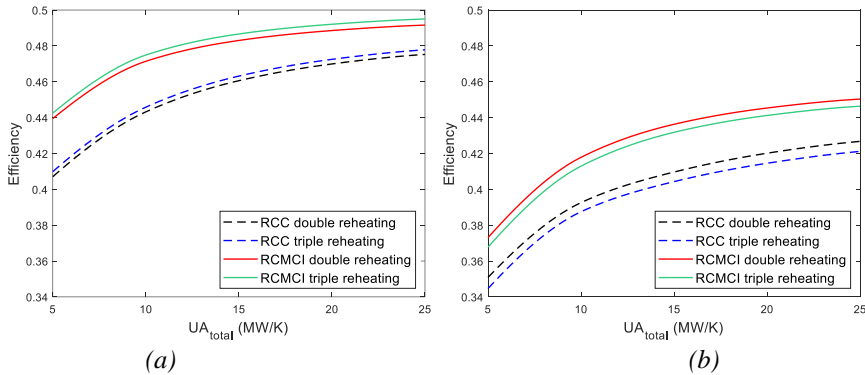


Figure 4. Cycle efficiency vs.  $UA_{total}$ . RCC with double and triple reheating; and RCMCI with double and triple reheating Brayton cycles using pure s-CO<sub>2</sub>. (a) Without pressure drop, (b) With pressure drop

### 3. RESULTS AND DISCUSSION

In most cases, the optimal efficiency is obtained when the working fluid's critical point is close to the compressor inlet temperature (CIT). Figure 5 can be observed that the mixtures that imply the best cycle efficiency are s-CO<sub>2</sub>/COS (70/30) and s-CO<sub>2</sub>/H<sub>2</sub>S (60/40). These mixtures increase the cycle efficiency between 3 and 4 points, While the mixtures of s-CO<sub>2</sub>/NH<sub>3</sub> and s-CO<sub>2</sub>/SO<sub>2</sub> with molar fractions of (81/19) and (90/10) respectively increase their efficiency between 2 and 3 points.

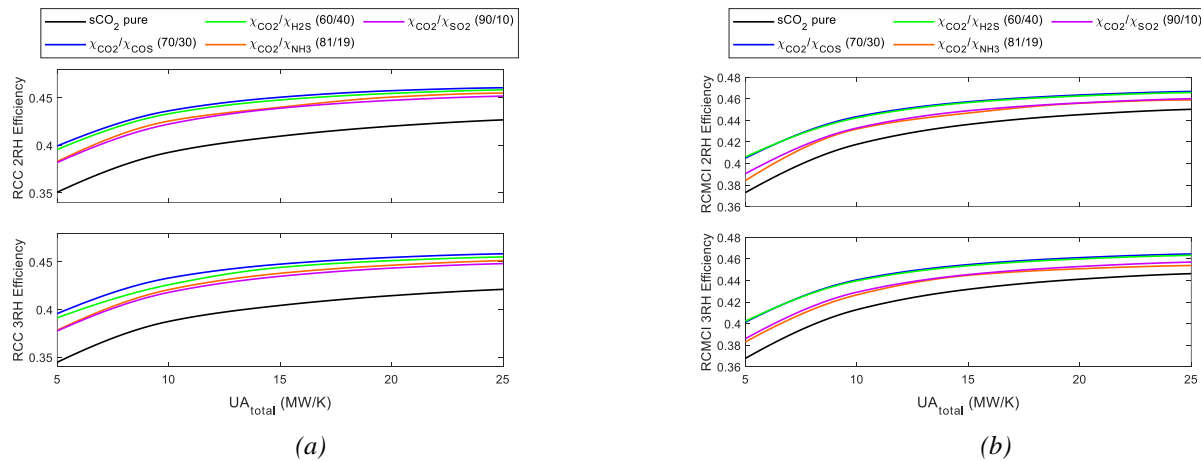


Figure 5. Cycle efficiency vs.  $UA_{total}$ , with pressure drop and using s-CO<sub>2</sub> mixtures. (a) RCC with double reheating and RCC with triple reheating, (b) RCMCI with double reheating and RCMCI with triple reheating

The total recuperator conductance is directly related to the increase in cycle efficiency. This increase is limited by the decrease of the "pinch point", which can be defined as the minimum temperature difference between the hot and cold streams in each heat recuperator (LTR and HTR). The recuperators' characteristic operating values are considered pinch point temperatures between 5 – 10 °C; however, these temperatures can be reduced to a range of 2 – 5 °C in the studied configurations [13]. The results showed that for all study configurations the pinch point decreases by increasing the  $UA_{total}$ .

When it comes to estimating a concentrated solar power plant's costs, it can become a hugely complicated task if considered the required detail level. The main problem is the lack of data, especially when there is a relatively new technology, such as the Brayton s-CO<sub>2</sub> power cycle. Therefore, in this work, cost estimates will be made for the solar field (SF – PTC). The following equation gives the estimated cost of the solar field:

$$SF_{cost} = SF_{EA} * C_{UC} * CF \quad (1)$$

Where  $SF_{cost}$  is the cost of the solar field,  $SF_{EA}$  is the effective area of the solar field,  $C_{UC}$  is the unit cost of the collector with a cost of 432 \$/m<sup>2</sup>, and  $CF$  is the construction factor of the solar field with a value of 1.16. [6]. The solar field estimated cost of the cycles under study is compared to their total recuperator conductance, using pure s-CO<sub>2</sub> and s-CO<sub>2</sub> mixtures as a cycle working fluid (Figures 6).

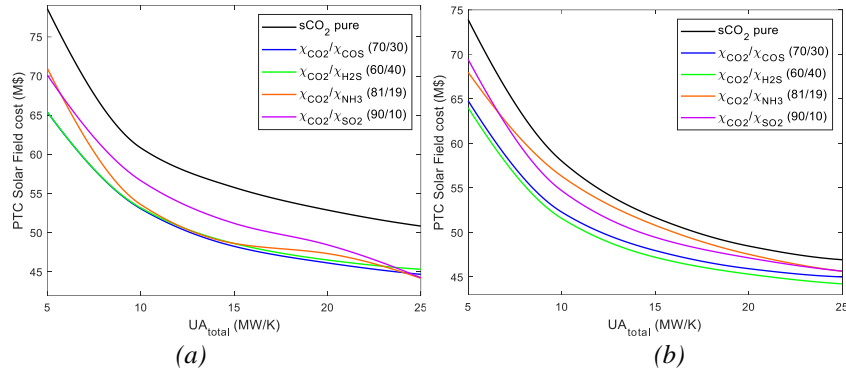


Figure 6. PTC solar field cost vs.  $UA_{total}$ , using s-CO<sub>2</sub> mixtures. (a) RCC – 2RH Brayton cycle. (b) RCMCI – 2RH Brayton cycle.

Figures 7 show the heat exchanger's pressure drop negatively impacts the cycle thermal efficiency. For this reason, the research community focuses on the study and design of heat exchangers used in the Brayton s-CO<sub>2</sub> power cycles. Furthermore, show the pressure drop in the primary heat exchanger (PHX) has a more significant impact on the decrease in cycle efficiency than the pressure drops in each solar field reheating heat exchanger (RHX). An increase in pressure drop has a detrimental effect on the thermal efficiency of the Brayton s-CO<sub>2</sub> cycle by reducing the gap between reheat and no-reheat configurations.

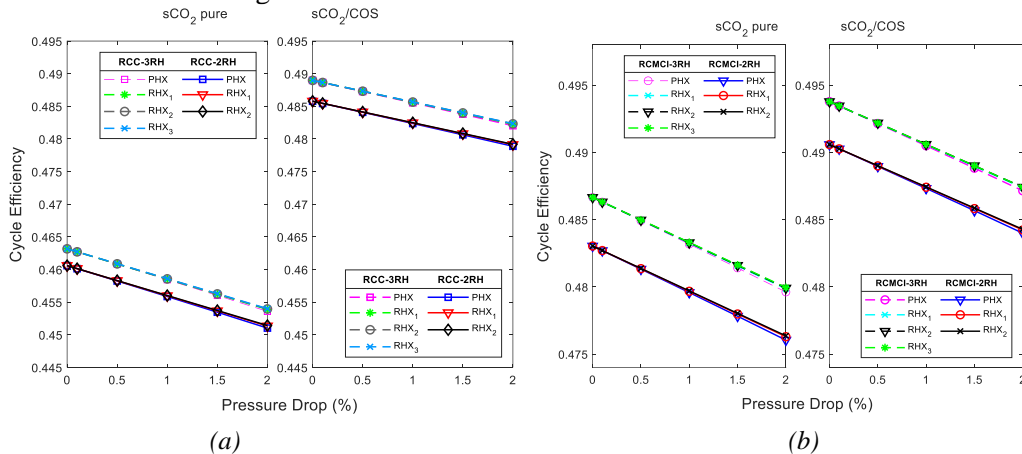


Figure 7. Cycle efficiency vs. pressure drop, using mixtures s-CO<sub>2</sub>/COS and  $UA_{total}=15$  MW/K. (a) RCC-2RH and RCC-3RH Brayton s-CO<sub>2</sub> cycle. (b) RCMCI-2RH and RCMCI-3RH Brayton s-CO<sub>2</sub> cycle.

#### 4. CONCLUSIONS

This work's main conclusion is that the s-CO<sub>2</sub> mixture directly impacts Brayton power cycles thermal efficiency, as previously proposed [6, 7, and 8]. This study shows the need to investigate supercritical fluid mixtures as working fluid in different Brayton s-CO<sub>2</sub> power cycles. In this case, the pressure drops in the heat exchangers (PHXs and RHXs), low and high-temperature heat recuperators (LTR and HTR), and precoolers (PC) were considered. The irreversibilities caused by these components reduce the work done on the turbines and increase the work done by the compressor. Therefore, the cycle efficiency also tends to decrease. So, it is obtained that the cycle efficiency with double reheating is better than with triple reheating, both in the RCC and in the RCMCI configurations when pure s-CO<sub>2</sub> is used as the working fluid.

It is possible to differentiate groups of mixtures that behave similarly in terms of the increasing trend of their efficiency, depending on the recuperator's total conductance. The first group, composed of s-CO<sub>2</sub>/COS (70/30) and s-CO<sub>2</sub>/H<sub>2</sub>S (60/40), have the most significant increase in the cycle efficiency. The mixture with carbonyl sulfide, the best in efficiency terms, ranges from 39% to 46%, depending on the RCC configurations' thermal size. While

in RCMCI configurations, it goes from 40% to 46%. The second group comprises s-CO<sub>2</sub>/NH<sub>3</sub> (81/19) and s-CO<sub>2</sub>/SO<sub>2</sub> (90/10) that behave differently depending on the power cycle configuration. In the RCC configuration with double and triple reheat, the most representative mixture with the highest efficiency is the mixture containing ammonia. While in the RCMCI cycles with double and triple reheat, the mixture with the sulfur dioxide is the one that gains the highest efficiency; however, their margins of difference are minimal.

Regarding the solar field costs using a PTC technology, it can be specified that if the cycle operates with the mixture of carbon dioxide and carbonyl sulfide presents a lower cost in recompression configurations with double and triple reheating. For recompression with main compressor intercooling configurations with double and triple reheating, the mixture with hydrogen sulfide is the one that generally presents the lowest cost of the solar field.

Future work should focus on obtaining a chemical composition of the working fluid (s-CO<sub>2</sub> mixtures) that is friendly to the environment and operates in the environmental conditions where the solar power plant is located. Therefore, it is necessary to study the impact of s-CO<sub>2</sub> binary mixtures that decrease the critical temperature in the thermal efficiency of the recompression Brayton s-CO<sub>2</sub> cycles considering pressure drop. Furthermore, it is proposed to study different Brayton power cycle configurations that include more reheating and recuperator, and even add a preheating in the heat recuperators to achieve an evaluation and quantification of the impact of using s-CO<sub>2</sub> mixtures in the cycle efficiency.

## ACKNOWLEDGMENT

This work was supported by the Community of Madrid's Industrial Doctorates program (IND2018/IND-9952).

## REFERENCES

- [1] Euroheat & Power. 2020. Share of Renewables in EU Energy Consumption Reached 17% In 2016 | Euroheat & Power. [online] Available at: <<https://www.euroheat.org/news/share-renewables-energy-consumption-eu-reached-17-2016/>>.
- [2] Yin, J. M., Zheng, Q. Y., Peng, Z. R., & Zhang, X. R. (2020). Review of supercritical CO<sub>2</sub> power cycles integrated with CSP. *International Journal of Energy Research*, 44(3), 1337-1369. Available from: <https://onlinelibrary.wiley.com/doi/abs/10.1002/er.4909>
- [3] Stepanek, J., Entler, S., Syblik, J., Vesely, L., Dostal, V., & Zacha, P. (2020). Parametric study of S-CO<sub>2</sub> cycles for the DEMO fusion reactor. *Fusion Engineering and Design*, 160, 111992.
- [4] Ahmadi, M. H., Mehrpooya, M., & Pourfayaz, F. (2016). Exergoeconomic analysis and multi objective optimization of performance of a Carbon dioxide power cycle driven by geothermal energy with liquefied natural gas as its heat sink. *Energy conversion and management*, 119, 422-434.
- [5] Song, J., Li, X. S., Ren, X. D., & Gu, C. W. (2018). Performance improvement of a preheating supercritical CO<sub>2</sub> (S-CO<sub>2</sub>) cycle based system for engine waste heat recovery. *Energy Conversion and Management*, 161, 225-233.
- [6] Valencia-Chapi, R., Coco-Enríquez, L., & Muñoz-Antón, J. (2020). Supercritical CO<sub>2</sub> Mixtures for Advanced Brayton Power Cycles in Line-Focusing Solar Power Plants. *Applied Sciences*, 10(1), 55. Available from <https://doi.org/10.3390/app10010055>
- [7] Haroon, M., Sheikh, N. A., Ayub, A., Tariq, R., Sher, F., Baheta, A. T., & Imran, M. (2020). Exergetic, economic and exergo-environmental analysis of bottoming power cycles operating with CO<sub>2</sub>-based binary mixture. *Energies*, 13(19), 5080.
- [8] Manzolini, G., Binotti, M., Bonalumi, D., Invernizzi, C., & Iora, P. (2019). CO<sub>2</sub> mixtures as innovative working fluid in power cycles applied to solar plants. Techno-economic assessment. *Solar Energy*, 181, 530-544. Available from <https://doi.org/10.1016/j.solener.2019.01.015>
- [9] Marchionni, M., Bianchi, G., & Tassou, S. A. (2018). Techno-economic assessment of Joule-Brayton cycle architectures for heat to power conversion from high-grade heat sources using CO<sub>2</sub> in the supercritical state. *Energy*, 148, 1140-1152. Available from: <https://doi.org/10.1016/j.energy.2018.02.005>
- [10] Neises, T., & Turchi, C. (2019). Supercritical carbon dioxide power cycle design and configuration optimization to minimize levelized cost of energy of molten salt power towers operating at 650° C. *Solar Energy*, 181, 27-36. Available from: <https://doi.org/10.1016/j.solener.2019.01.078>
- [11] Linares, J. I., Montes, M. J., Cantizano, A., & Sánchez, C. (2020). A novel supercritical CO<sub>2</sub> recompression Brayton power cycle for power tower concentrating solar plants. *Applied Energy*, 263, 114644. Available from: <https://doi.org/10.1016/j.apenergy.2020.114644>.
- [12] Dyreby, J. J. (2014). *Modeling the supercritical carbon dioxide Brayton cycle with recompression* (Doctoral dissertation, The University of Wisconsin-Madison). Available from: <https://sel.me.wisc.edu/publications/theses/dyreby14.zip>
- [13] Enriquez, L. C. (2017). *Nueva generación de centrales termosolares con colectores solares lineales acoplados a ciclos supercríticos de potencia* (Doctoral dissertation, Universidad Politécnica de Madrid). Available from: <https://doi.org/10.20868/UPM.thesis.44002>
- [14] Lemmon, E. W., Bell, I. H., Huber, M. L., & McLinden, M. O. (2018). NIST standard reference database 23: Reference fluid thermodynamic and transport Properties-REFPROP, Version 10.0, national institute of standards and technology. *Standard Reference Data Program, Gaithersburg*. Available from: <https://www.nist.gov/srd>



# A REVIEW OF THE LIFE CYCLE ASSESSMENTS OF BRAZILIAN BIODIESEL

Costa Marina W.

Federal University of Santa Catarina, Florianópolis, mweylc@gmail.com, ORCID: 0000-0001-9813-3095

Oliveira Amir A. M.

Federal University of Santa Catarina, Florianópolis, Brazil, amir.oliveira@ufsc.br, ORCID: 0000-0002-2826-5778

Cite this paper as:

*Costa, M.W, Oliveira, A.A.M. A Review of the life cycle assessments of Brazilian biodiesel. 9<sup>th</sup> Eur. Conf. Ren. Energy Sys. 21-23 April 2021, Istanbul, Turkey*

**Abstract:** Securing a sustainable biofuel chain is one strategy to reduce the impact of transportation on the global climate. Brazil is the second-largest biodiesel producer, and although soybean oil is the most used feedstock, several other fatty materials are also used. Life Cycle Assessment (LCA) is a convenient tool to evaluate Global Warming Potential and many other impacts. The objective of this study is to compare the existent LCA-studies of Brazilian biodiesel published from 2015 to 2020, aiming at identifying methods and knowledge gaps. Two LCA phases were evaluated: Goal and Scope Definition, and Inventory Analysis. The selected studies were categorized according to feedstock, place, functional unit, system boundaries, processes, and inventory data source. It was found that, despite the relatively large number of available studies, the different functional units, processes, and impacts evaluated hinder the comparison among the LCA results. Also, there is an absence of information on biodiesel production in the North and Northeast regions as well as production of biodiesel from beef tallow in the South region.

**Keywords:** *Biodiesel, Life cycle analysis, Greenhouse gas emissions, Global warming potential*

© 2021 Published by ECRES

Nomenclature	
GHG	Greenhouse gas
LCA	Life Cycle Assessment
LUC	Land Use Change

## 1. INTRODUCTION

Diesel is the most used oil derivative in Brazil. Biodiesel consumption has been stimulated with a mandatory addition in highway diesel since 2002 [1], and currently the country is the second larger biodiesel producer [2]. The most common fatty material is soybean oil, followed by beef tallow, and most of the Brazilian biodiesel is produced in the regions Midwest and South [3]. Despite their intentions to be ecologically friendly, biofuels can cause several ecological impacts during their production chain [4]. A Life Cycle Assessment (LCA) is a tool used to evaluate the impacts of a product during all its life cycle, from the extraction of resources to its production until its final disposal [5]. An LCA consists of four phases: the Goal and scope definitions, where the exact question to be answered is delimited; the Inventory Analysis, where the system studied is delimited and data is collected to produce the inventory (a table containing all the inputs and outputs of all the evaluated phases of the product life); the Impact Assessment, where the inventory is processed to evaluate the impacts generated during the product life cycle; and the Interpretation, where the results of the study are analyzed and recommendations are made [5].

This study aims to compare the existent LCA-studies of Brazilian biodiesel published from 2015 to 2020, focusing on phases 1) Goal and Scope Definitions; and 2) Inventory Analysis; and on the Impact Categories evaluated.

## 2. METHODS

The words "life cycle biodiesel Brazil" were searched in all the fields of Scopus [6] and Web of Science [7]. The period evaluated was from 2015 to 2020. The titles and abstracts of the articles were read. Articles that did not present environmental data of Brazilian biodiesel or its feedstocks were discarded. The remaining articles were evaluated, and the papers that presented data about Brazilian biodiesel were selected and categorized according to: 1) Feedstock evaluated; 2) Place where the search was developed; 3) Functional unit; 4) System boundaries; 5) Processes considered; 6) Source of inventory data; 7) Allocation method; 8) Impacts evaluated.

## 3. REVIEW ARTICLES

Five review articles were found [4; 14-17]. Two of them evaluated Brazilian LCA studies' availability and did not compare biodiesel studies [15,16]. [16] focused on bibliometric analyses and did not present a list of articles evaluated. [16] reports the existence of 3 LCA articles about Brazilian biodiesel published after 2015. One of them [18] has not been found in the previous search in Scopus and Web of Science and was added to the selected articles' list. [14,17] compared LCA studies about algae. [17] evaluated algae biofuels. No Brazilian study about algae biodiesel published after 2015 was mentioned. Finally, [4] compared the LCA of biofuels in America. All studies evaluated were published before 2014; therefore, they are out of this work scope.

## 4. GOAL AND SCOPE DEFINITION

36 case studies of Brazilian biodiesel were found [8-13; 15-50]. Soybean, the most used feedstock for biodiesel production in Brazil, was also the most common feedstock evaluated. Even though algae are not used on an industrial scale to produce biodiesel in Brazil, it was the second most studied feedstock. Different streams and culture conditions were evaluated. Beef tallow follows, and then other crops and residues responsible for a small share of the biodiesel production (palm, macauba, cotton, waste cooking oil) or are not commercially used (residues from palm refineries). LCA of other minorities fatty materials, such as pig tallow and chicken fat, were not localized. Most of the LCA studies are localized in the Midwest region. The South region is the second major Brazilian biodiesel producer and the one with the largest gross consumption of beef tallow [3]. However, no LCA study about biodiesel produced from this feedstock in this region was localized. Southeast and Northeast produce similar shares of Brazilian biodiesel, but only one LCA about biodiesel produced in the Northeast region was found, while six results focused on the Southeast.

Different soybean crop systems and transesterification methods were evaluated: [8] compared traditional cropping with an integrated crop-livestock method, and [18] evaluated the impacts of alternate the soybean culture with sunflower culture. [19-21] compared transesterification using the methylic and ethylic routes. [22] evaluated only the ethylic route, and [23] proposed a double step transesterification.

Figure 1a presents the type of functional unit used. Mass of biodiesel is the most common choice, which differs from the review of [4], that found energy content to be the most used functional unit in LCA of biofuels made in America before 2015. The functional unit must describe the studied product's primary function and delimit its quantity as a reference in the LCA [5]. Several different functional units were used, which makes the comparison between different studies less accurate.

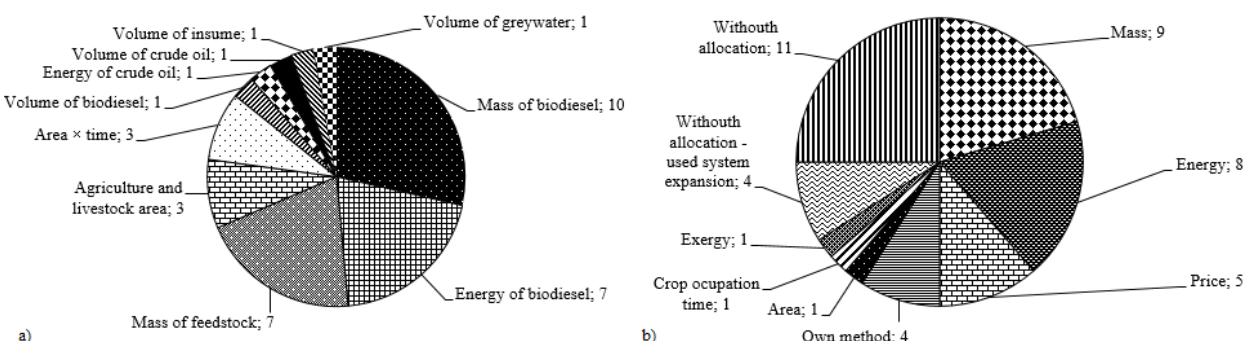


Figure 1.a) Functional units, and b) Allocation methods used by evaluated LCA articles.

## 5. INVENTORY ANALYSIS

Figures 2 and 3 present the boundaries of the studies and the evaluated processes. Most of the LCA of soybean biodiesel evaluated the processes between soybean agriculture and biodiesel transesterification. Biodiesel transport and use are not commonly evaluated. Only four soybean studies evaluated the effects of land use change (LUC) [24-27]. The exclusion of this process is justified due to difficulty in obtaining LUC data but may result in underestimating GHG emissions. [24] reports that LUC is the process with the highest GHG intensity, independent of the allocation method used (mass, energy, or price). [26] also reinforces the extensive influence of LUC in the GHG emissions. A later study of the same group found that LUC was responsible for 97% of biodiesel production GHG emissions [26]. The exclusion of LUC is also observed in the LCA of cotton biodiesel [38], in the studies about residues of the palm industry [39,40], and in some studies about beef tallow biodiesel [11,12], and palm [37].



Figure 2. Processes evaluated by the LCA of soybean biodiesel. Processes are merged in some cases.

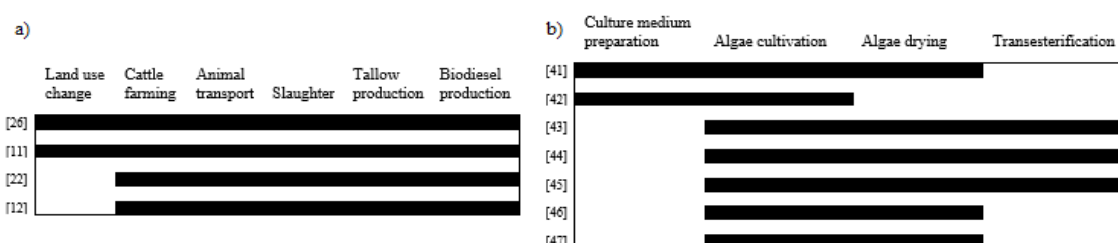


Figure 3. Processes evaluated by the LCA of a) beef tallow biodiesel and b) algae biodiesel.

Both studies about wasted oil evaluated the collecting stage and the transesterification stage [30,50]. The LCA of biodiesel made of residues from the palm industry covers the processes from agriculture to biodiesel transesterification [39,40]. Those are also the processes accessed by the LCA of cotton biodiesel [38]. Four of the seven LCA of algae do not explore the transesterification process [41,42,46,47], nor do the LCA of macauba [48,49]. It can be justified because those studies are exploratory, and those feedstocks are not commercially used in Brazil [3].

Twenty two of the selected research articles presented primary data, completed by secondary data on its inventory table, while 14 used only secondary data from databases, previous studies, or public governmental data. The most used database is Ecoinvent, cited by 16 studies [8,22,23,26,30,34,38-41,44-47,49], while the most used software is Simapro®, referenced by [8,11,18,22,23,25,26,29,34,38,40,41,46,47,49,50]. GaBi® was mentioned by [12,30], and spreadsheets were used by [35].

Figure 1b shows the allocation method used by the evaluated articles. Some studies used more than one allocation method to compare the pathway's impact on the LCA result [8,11,24,28,31,44,45]. Mass and energy are the most used allocation methods. This result is also different from the one found by [4], where system expansion (market analysis for co-products [5]) was the most common method. Other allocation methods used are price [12]; area occupied by the crop [33]; crop occupation time (for crop cultivars that alternate in the same area) [18]; exergy [39]; and methods elaborated by the authors, that are averages of more than one allocation methods [11,25,26,49]. A significant number of studies did not use any type of allocation [20,23,27,32,34,35,37,40,47,41,48].

## 5. IMPACT CATEGORIES

Global warming potential was the most evaluated impact. The same was observed by [4], which was presumably because biofuels aim to reduce GHG emissions [4]. The impact categories assessed were: Abiotic Depletion Potential [22,30,38,41]; Acidification Potential [12,21,22,24,29,30,34,38,39,40,41,46,49]; Biotic Depletion [46]; Biodiversity impact (BIA+) [35]; Carcinogens [29,40,49]; CO<sub>2</sub> emissions [19,21]; Damage to human health [42,49]; Damage to ecosystem quality [42,49]; Damage to resources [42,49]; Ecotoxicity [18,22,29,30,40,41,47,49]; Energy Balance [19-21,44,45,48]; Energy Consumption [37,49]; Eutrophication Potential [12,18,21,22,24,29-31,34,38-41, 46,47,49]; Fossil Energy Use [18,21,29,40,43,45,47,49]; Global Warming Potential [8,11,12,18,21-26,28-34,37-41,43,46-50]; Human Toxicity Potential [18,21,22,30,41,46,47]; Ionizing radiation [40,47]; Land Use [18,19,22,29,39,40,47,49]; LUC [18,21,27,32,36,47]; Mineral Use [18,29,40,47,49]; N<sub>2</sub>O Emissions [32,37]; Ozone Layer Depletion [18,22,24, 30,40,41,46,47,49]; Photochemical Ozone Formation [18,24,29,30,39,41,46,47]; Particulate Matter Emissions [18,47]; Respiratory Inorganics [29,40,49]; Respiratory Organics [40,49]; Terrestrial Acidification [18,40,47]; Terrestrial Ecotoxicity Potential [18,22,30,40,41,47], and Water use [12,18-21,31,47].

## 4. CONCLUSION

The search for LCA articles of Brazilian biodiesel in scientific databases revealed 41 articles of interest published between 2015 and 2020, of which 5 are reviews and 36 are case studies. No previous review of Brazilian biodiesel in the period covered by this paper was found. The most studied feedstock is soybean, which is the most used feedstock for biodiesel production in Brazil. The second most common feedstock in the LCA studies localized was algae, which is not used to produce biodiesel on an industrial scale in the country. Most of the LCA was made in the South and Midwest regions, the largest biodiesel producers in Brazil.

The analysis of the available studies revealed that several functional units, such as mass, volume and energy of biodiesel produced, mass of feedstock, area used to produce the feedstock, volume of inputs, volume and energy of crude oil, and volume of greywater, are used, which makes the comparison of the LCA results less accurate. Therefore, despite the relatively large number of available studies, the different functional units, processes, and impacts evaluated hinder the comparison between the LCA results. Using a standard form of reporting the final LCA results is recommended to facilitate comparison and calculation of country averages.

Besides, the search localized little information about biodiesel production in the regions North and Northeast. No LCA study about beef tallow biodiesel produced in the South region, and Brazilian LCA studies about some minor feedstocks, such as pig tallow and chicken fat, were found.

## ACKNOWLEDGMENT

This work was supported by the Conselho Nacional de Desenvolvimento Científico e Tecnológico (CNPq-Brazil) and the Graduate Program in Mechanical Engineering at UFSC.

## REFERENCES

- [1] Empresa de Pesquisa Energética (Brasil). Brazilian Energy Balance 2020 Year 2019. Rio de Janeiro: Empresa de Pesquisa Energética - EPE, 2020.
- [2] REN21. Renewables 2019 Global Status Report. Paris: REN21 Secretariat, 2021.
- [3] Agência Nacional de Petróleo, Gás e Biocombustíveis. Informações de mercado – 2019. Available online at <<http://www.anp.gov.br/producao-de-biocombustiveis/biodiesel/informacoes-de-mercado>>. Last accessed on 12.08.2020.
- [4] Shonnard, D.R., Klemetsrud, B., Sacramento-Rivero, J., Navarro-Pineda, F., Hilbert, J., Handler, R., SUPPEN, N., Donovan, R.P. A review of environmental life cycle assessments of liquid transportation biofuels in the Pan American region. *Environmental management* 2015, 56:1356-1376. <<https://doi.org/10.1007/s00267-015-0543-8>>

- [5] Guinée, J.B.; Gorrée, M.; Heijungs, R.; Huppes, G.; Kleijn, R.; Koning, A. de; Oers, L. van; Wegener Sleeswijk, A.; Suh, S.; Udo de Haes, H.A.; Bruijn, H. de; Duin, R. van; Huijbregts, M.A.J. Handbook on life cycle assessment. Operational guide to the ISO standards. I: LCA in perspective. IIa: Guide. IIb: Operational annex. III: Scientific background. Dordrecht: Kluwer Academic Publishers, 2002.
- [6] Scopus. Available online at <<https://www.scopus.com>>. Last accessed on 07.31.2020.
- [7] Web of science. Available online at <<https://www.webofknowledge.com>>. Last accessed on 08.12.2020.
- [8] Esteves, E. M. M., Esteves, V. P. P., Bungenstab, D. J., Araújo, O. D. Q. F., & Morgado, C. D. R. V. Greenhouse gas emissions related to biodiesel from traditional soybean farming compared to integrated crop-livestock systems. *Journal of Cleaner Production*. 2018, 179: 81-92. <<https://doi.org/10.1016/j.jclepro.2017.12.262>>
- [9] Instituto Brasileiro de Pesquisa e Estatística. Tabela 1612 - Área plantada, área colhida, quantidade produzida, rendimento médio e valor da produção das lavouras temporárias. Available online at <<https://sidra.ibge.gov.br/Tabela/1612>>. Last accessed on 12.09.2020.
- [10] Instituto Brasileiro de Geografia e Estatística. Tabela 6783 - Número de estabelecimentos agropecuários com bovinos, Efetivos, Venda e Produção de leite, por grupos de área de pastagem e grupos de área total. Available online at <<https://sidra.ibge.gov.br/tabela/6783>>. Last accessed on 11.20.2020.
- [11] Esteves, V. P. P., Esteves, E. M. M., Bungenstab, D. J., Feijó, G. L. D., Araújo, O. D. Q. F., Morgado, C. D. R. V. Assessment of greenhouse gases (GHG) emissions from the tallow biodiesel production chain including land use change (LUC). *Journal of cleaner production*. 2017, 151: 578-591. <<https://doi.org/10.1016/j.jclepro.2017.03.063>>
- [12] Sousa, V. M., Luz, S. M., Caldeira-Pires, A., Machado, F. S., Silveira, C. M. Life cycle assessment of biodiesel production from beef tallow in Brazil. *The International Journal of Life Cycle Assessment*. 2017, 22.11: 1837-1850. <<https://doi.org/10.1007/s11367-017-1396-6>>
- [13] Atabani, A. E., Silitonga, A. S., Badruddin, I. A., Mahlia, T. M. I., Masjuki, H. H., & Mekhilef, S. A comprehensive review on biodiesel as an alternative energy resource and its characteristics. *Renewable and sustainable energy reviews*. 2012, 16.4: 2070-2093. <<https://doi.org/10.1016/j.rser.2012.01.003>>
- [14] Medeiros, D. L., Sales, E. A., Kiperstok, A. Energy production from microalgae biomass: carbon footprint and energy balance. *Journal of Cleaner Production*. 2015, 96: 493-500. <<https://doi.org/10.1016/j.jclepro.2014.07.038>>
- [15] Zanghelini, G. M., de Souza Junior, H. R., Kulay, L., Cherubini, E., Ribeiro, P. T., Soares, S. R. A bibliometric overview of Brazilian LCA research. *The International Journal of Life Cycle Assessment*. 2016, 21.12: 1759-1775. <<https://doi.org/10.1007/s11367-016-1132-7>>
- [16] Bodunrin, M. O., Burman, N. W., Croft, J., Engelbrecht, S., Goga, T., Ladenika, A. O., MacGregor, O.S., Maepa, M., Harding, K. G. The availability of life-cycle assessment, water footprinting, and carbon footprinting studies in Brazil. *The International Journal of Life Cycle Assessment* 2018, 23.8: 1701-1707. <<https://doi.org/10.1007/s11367-018-1484-2>>
- [17] Carneiro, M. L. N., Pradelle, F., Braga, S. L., Gomes, M. S. P., Martins, A. R. F., Turkovics, F., Pradelle, R. N. Potential of biofuels from algae: Comparison with fossil fuels, ethanol and biodiesel in Europe and Brazil through life cycle assessment (LCA). *Renewable and Sustainable Energy Reviews*. 2017, 73: 632-653. <<https://doi.org/10.1016/j.rser.2017.01.152>>
- [18] Matsuura, M. I. F., Dias, F. R., Picoli, J. F., Lucas, K. R. G., de Castro, C., & Hirakuri, M. H. Life-cycle assessment of the soybean-sunflower production system in the brazilian Cerrado. *The International Journal of Life Cycle Assessment*. 2017, 22.4: 492-501. <<https://doi.org/10.1007/s11367-016-1089-6>>
- [19] Interlenghi, S. F., de Almeida Bruno, P., Araujo, O. D. Q. F., de Medeiros, J. L. Social and environmental impacts of replacing transesterification agent in soybean biodiesel production: Multi-criteria and principal component analyses. *Journal of Cleaner Production*. 2017, 168: 149-162. <<https://doi.org/10.1016/j.jclepro.2017.08.222>>
- [20] de Mello, M. C. S., Villardi, H. G. D. A., Young, A. F., Pessoa, F. L. P., Salgado, A. M. Life cycle assessment of biodiesel produced by the methylic-alkaline and ethylic-enzymatic routes. *Fuel*. 2017, 208: 329-336. <<https://doi.org/10.1016/j.fuel.2017.07.014>>
- [21] Altamirano, C. A. A., Yokoyama, L., de Medeiros, J. L., & Araújo, O. D. Q. F. Ethylic or methylic route to soybean biodiesel? Tracking environmental answers through life cycle assessment. *Applied Energy*. 2016, 184: 1246-1263. <<https://doi.org/10.1016/j.apenergy.2016.05.017>>
- [22] Esteves, R. A., Pereira, R. G. Comparing the environmental impacts of ethyl biodiesel production from soybean oil and beef tallow through lca for brazilian conditions. *Independent Journal of Management & Production*. 2017, 8.4: 1285-1308. <<https://doi.org/10.14807/ijmp.v8i4.644>>
- [23] Carvalho, M., Da Silva, E. S., Andersen, S. L., Abrahão, R. Life cycle assessment of the transesterification double step process for biodiesel production from refined soybean oil in Brazil. *Environmental Science and Pollution Research*. 2016, 23.11: 11025-11033. <<https://doi.org/10.1007/s11356-016-6295-z>>
- [24] Castanheira, É. G., Grisolí, R., Coelho, S., da Silva, G. A., Freire, F. Life-cycle assessment of soybean-based biodiesel in Europe: comparing grain, oil and biodiesel import from Brazil. *Journal of Cleaner Production*. 2015, 102: 188-201. <<https://doi.org/10.1016/j.jclepro.2015.04.036>>
- [25] Esteves, V. P. P., Esteves, E. M. M., Bungenstab, D. J., Loebmann, D. G. D. S. W., de Castro Victoria, D., Vicente, L. E., Araújo, O.Q.F., Morgado, C. D. R. V. Land use change (LUC) analysis and life cycle assessment (LCA) of Brazilian soybean biodiesel." *Clean Technologies and Environmental Policy*. 2016, 18.6: 1655-1673. <<https://doi.org/10.1007/s10098-016-1161-8>>
- [26] Esteves, V. P. P., Morgado, C. D. R. V., Araújo, O. D. Q. F. Regional and temporal sustainability assessment of agricultural-based biodiesel." *Clean Technologies and Environmental Policy*. 2020, 22.4: 965-978. <<https://doi.org/10.1007/s10098-020-01842-x>>
- [27] Zortea, R. B., Maciel, V. G., Menezes, W., Cybis, L. F. D. A., Seferin, M. Cálculo de emissões de CO<sub>2</sub> provenientes da mudança do uso da terra para produção de soja no estado do Rio Grande do Sul. *Engenharia Sanitária e Ambiental*. 2019, 24.4: 727-735. <<https://doi.org/10.1590/S1413-41522019127909>>
- [28] Cerri, C. E. P., You, X., Cherubin, M. R., Moreira, C. S., Raucci, G. S., Castigioni, B. D. A., Alves, P.A., Cerri, D.G.P., Mello,F.F.C., Cerri, C. C. Assessing the greenhouse gas emissions of Brazilian soybean biodiesel production. *PloS one*. 2017, 12.5: e0176948. <<https://doi.org/10.1371/journal.pone.0176948>>
- [29] Brondani, M., Hoffmann, R., Mayer, F. D., Kleinert, J. S. Environmental and energy analysis of biodiesel production in Rio Grande do Sul, Brazil. *Clean Technologies and Environmental Policy*. 2015, 17.1: 129-143. <<https://doi.org/10.1007/s10098-014-0768-x>>
- [30] Fernandez, I. A. P., Liu, D. H., Zhao, J. LCA studies comparing alkaline and immobilized enzyme catalyst processes for biodiesel production under Brazilian conditions." *Resources, Conservation and Recycling*. 2017, 119:117-127. <<https://doi.org/10.1016/j.resconrec.2016.05.009>>

- [31] Knoope, M. M., Balzer, C. H., Worrell, E. Analysing the water and greenhouse gas effects of soya bean-based biodiesel in five different regions." *Gcb Bioenergy*. 2019, 11.2: 381-399. <<https://doi.org/10.1111/gcbb.12558>>
- [32] Maciel, V. G., Zortea, R. B., da Silva, W. M., de Abreu Cybis, L. F., Einloft, S., Seferin, M. Life Cycle Inventory for the agricultural stages of soybean production in the state of Rio Grande do Sul, Brazil." *Journal of Cleaner Production*. 2015, 93: 65-74. <<https://doi.org/10.1016/j.jclepro.2015.01.016>>
- [33] Raucci, G. S., Moreira, C. S., Alves, P. A., Mello, F. F., de Almeida Frazão, L., Cerri, C. E. P., & Cerri, C. C. Greenhouse gas assessment of Brazilian soybean production: a case study of Mato Grosso State. *Journal of Cleaner Production*. 2015, 96: 418-425. <<https://doi.org/10.1016/j.jclepro.2014.02.064>>
- [34] Zortea, R. B., Maciel, V. G., & Passuello, A. Sustainability assessment of soybean production in Southern Brazil: A life cycle approach. *Sustainable Production and Consumption*. 2018, 13: 102-112. <<https://doi.org/10.1016/j.spc.2017.11.002>>
- [35] Winter, L., Pflugmacher, S., Berger, M., Finkbeiner, M. Feasibility of applying the biodiversity impact assessment method BIA+: A case study on freshwater biodiversity impacts resulting from phosphorus and 1, 4-DCB emitted during the biodiesel production. *Ecological Indicators*. 2019, 102: 666-672. <<https://doi.org/10.1016/j.ecolind.2019.03.020>>
- [36] Bicalho, T., Bessou, C., Pacca, S. A. Land use change within EU sustainability criteria for biofuels: The case of oil palm expansion in the Brazilian Amazon." *Renewable energy*. 2016, 89: 588-597. <<https://doi.org/10.1016/j.renene.2015.12.017>>
- [37] Munasinghe, M., Jayasinghe, P., Deraniyagala, Y., Matlaba, V. J., dos Santos, J. F., Maneschy, M. C., Mota, J. A. Value-Supply Chain Analysis (VSCA) of crude palm oil production in Brazil, focusing on economic, environmental and social sustainability." *Sustainable Production and Consumption*. 2019, 17: 161-175. <<https://doi.org/10.1016/j.spc.2018.10.001>>
- [38] Lima, Â. M. F., Torres, E. A., Kiperstok, A., Santos, G. D. F. M. Environmental impacts of the biodiesel production chain of cotton seed in Bahia, Brazil." *Clean Technologies and Environmental Policy*. 2917, 19.5: 1523-1534. <<https://doi.org/10.1007/s10098-017-1347-8>>
- [39] Kermani, M., Celebi, A. D., Wallerand, A. S., Ensinas, A. V., Kantor, I. D., Maréchal, F. Techno-Economic and Environmental Optimization of Palm-based Biorefineries in the Brazilian Context." *Computer Aided Chemical Engineering*. 2017, 40:2611-2616. <<http://dx.doi.org/10.1016/B978-0-444-63965-3.50437-2>>
- [40] Batlle, E. A. O., Santiago, Y. C., Venturini, O. J., Palacio, J. C. E., Lora, E. E. S., Maya, D. M. Y., Arrieta, A. R. A. Thermodynamic and environmental assessment of different scenarios for the insertion of pyrolysis technology in palm oil biorefineries. *Journal of Cleaner Production*. 2050, 250: 119544. <<https://doi.org/10.1016/j.jclepro.2019.119544>>
- [41] Scherer, M. D., de Oliveira, A. C., Magalhães Filho, F. J. C., Ugaya, C. M. L., Mariano, A. B., Vargas, J. V. C. Environmental study of producing microalgal biomass and bioremediation of cattle manure effluents by microalgae cultivation. *Clean Technologies and Environmental Policy*. 2017, 19.6: 1745-1759. <<http://dx.doi.org/10.1007/s10098-017-1361-x>>
- [42] Diniz, G. S., Tourinho, T. C., Silva, A. F., Chaloub, R. M. Environmental impact of microalgal biomass production using wastewater resources." *Clean Technologies and Environmental Policy*. 2017, 19.10: 2521-2529. <<http://dx.doi.org/10.1007/s10098-017-1433-y>>
- [43] Souza, S. P., Gopal, A. R., Seabra, J. E. Life cycle assessment of biofuels from an integrated Brazilian algae-sugarcane biorefinery. *Energy*. 2015, 81: 373-381. <<https://doi.org/10.1016/j.energy.2014.12.050>>
- [44] Maranduba, H. L., Robra, S., Nascimento, I. A., da Cruz, R. S., Rodrigues, L. B., de Almeida Neto, J. A. Reducing the life cycle GHG emissions of microalgal biodiesel through integration with ethanol production system." *Bioresource technology*. 2015, 194: 21-27. <<https://doi.org/10.1016/j.biortech.2015.06.113>>
- [45] Maranduba, H. L., Robra, S., Nascimento, I. A., da Cruz, R. S., Rodrigues, L. B., de Almeida Neto, J. A. Improving the energy balance of microalgae biodiesel: Synergy with an autonomous sugarcane ethanol distillery. *Energy*. 2016, 115: 888-895. <<https://doi.org/10.1016/j.energy.2016.09.061>>
- [46] Patel, B., Guo, M., Shah, N., Hellgardt, K. Environmental profile of algal Hydrothermal Liquefaction—A country specific case study. *Algal Research*. 2016, 16: 127-140. <<https://doi.org/10.1016/j.algal.2015.12.017>>
- [47] de Souza Schneider, R. D. C., de Moura Lima, M., Hoeltz, M., de Farias Neves, F., John, D. K., de Azevedo, A. Life cycle assessment of microalgae production in a raceway pond with alternative culture media. *Algal research*. 2018, 32: 280-292. <<https://doi.org/10.1016/j.algal.2018.04.012>>
- [48] Barbosa-Evaristo, A., Fernández-Coppel, I. A., Corrêa-Guimarães, A., Martín-Gil, J., Duarte-Pimentel, L., Saraiva-Grossi, J. A., Navas-Gracia, L.M., Martín-Ramos, P. Simulation of macauba palm cultivation: an energy-balance and greenhouse gas emissions analysis." *Carbon Management*. 2018, 9.3: 243-254. <<https://doi.org/10.1080/17583004.2018.1463783>>
- [49] Fernández-Coppel, I. A., Barbosa-Evaristo, A., Corrêa-Guimarães, A., Martín-Gil, J., Navas-Gracia, L. M., Martín-Ramos, P. Life cycle analysis of macauba palm cultivation: A promising crop for biofuel production." *Industrial Crops and Products*. 2018, 125: 556-566. <<https://doi.org/10.1016/j.indcrop.2018.09.036>>
- [50] Moecke, E. H. S., Feller, R., dos Santos, H. A., de Medeiros Machado, M., Cubas, A. L. V., de Aguiar Dutra, A. R., Santos, L.L.V., Soares, S. R. Biodiesel production from waste cooking oil for use as fuel in artisanal fishing boats: Integrating environmental, economic and social aspects. *Journal of Cleaner Production*. 2016, 135: 679-688. <<https://doi.org/10.1016/j.jclepro.2016.05.167>>



# AGEING EFFECT EVALUATION OF PV INSTALLATION AFTER 10 YEARS CONTINUOUS OPERATION

Nikolay Tyutyundzhiev

Institute of Electronics, Bulgarian Academy of Sciences Sofia, Bulgaria, n\_tyut@ie.bas.bg, Central laboratory of Solar Energy and New Energy Sources, Bulgarian Academy of Sciences, ORCID: 0000-0001-6080-1182

Plamen Tsankov

Faculty of Electrical Engineering and Electronics, Technical University of Gabrovo, Gabrovo, Bulgaria,  
plamen@tugab.bg, ORCID: 0000-0003-1942-608X

Konstantin Lovchinov

Institute of Optical Materials and Technologies "Acad. J. Malinowski", Bulgarian Academy of Sciences, Sofia, Bulgaria,  
lovchinov@iomt.bas.bg, ORCID: 0000-0001-7586-1620

Gergana Alexieva

Sofia University, Faculty of Physics, Sofia, Bulgaria, gerry@phys.uni-sofia.bg, ORCID: 0000-0002-3089-9008

*Tyutyundzhiev N, Tsankov P, Lovchinov K, Alexieva G, Ageing effect evaluation of PV installation after 10 years continuous operation. 9<sup>th</sup> Eur. Conf. Ren. Energy Sys. 21-23 April 2021, Istanbul, Turkey*

**Abstract:** This article describes the research on the aging of solar photovoltaic cells in a solar power plant that has been in operation for more than 10 years. The studied solar power plant is a roof structure with a power of 10kWp, and consists of three 3 sub-systems (PV strings). Two of them are based on polycrystalline-Si modules and the third one – based on thin-film amorphous - Si:H modules (location of this power plant is Tech University of Gabrovo). The available database is constituted by data collected in the period of 10 years with a sampling period of 10 minutes. The basic algorithm, we have followed, was to extract 3 representative days from every month. These days should be as sunny as possible (bottom threshold value of solar irradiance > 500W/m<sup>2</sup> and intra-hour fluctuations to be minimal) in order to compare correctly the PV performance year after year in similar weather conditions.

**Keywords:** Solar irradiation, PV aging, solar plant

© 2021 Published by ECRES

## 1. INTRODUCTION

The boom of PV installations after 2000 has led to an improvement of quality and extension of lifetime of PV modules. Typically, the manufacturers have declared 25 years lifetime and initial tolerances of  $\pm 5\%$  DC nominal power. During the last decade in addition to the tolerance of nominal power another performance metrics parameter has been introduced – annual degradation in PV modules. If we apply this metrics to 20th century PV modules the warranty of 10% decreases in performance in the first 10 years of operation means -1% linear decrease per year. However, these figures have not been frequently checked by on-field measurements. Only approximations have been done on the basis of studies on degradation phenomena in solar cells. Some studies [1-4] have investigated individual PV module defects and extrapolate the results on system level. In fact, the first investigations [5] of SCADA monitoring data from more than 10 years old PV plants in worldwide reveal that the real PV system performance is underestimated. Investors are mainly interested in those results. They require the most precise estimations of PV system performance during the lifetime in order to prepare in advance a bankable project with precise calculation of the payback period.

This paper focuses attention on the PV performance decrease which happens in PV systems because of phenomena as aging of components and aging of the whole system for a period of 10 years. The PV installation is located in

the center of Bulgaria on the roof of main building of Technical University of Gabrovo (TU-Gabrovo), as can be seen at Figure1. The performance analysis was conducted following a detailed procedure of visual inspection of PV strings, infrared thermography of defects and evaluation of aging effects based on 10 years-old monitoring database.

## 2. PV SYSTEM UNDER INVESTIGATION

### *PV system description*

First, the 10 kWp PV installation in TU-Gabrovo has been built during the period of 2003-2006 as part of the European project “PV Enlargement”. It was one of the first PV installations in Bulgaria connected to low-voltage power grid. It consists of 3 sub-systems (PV strings) – two of them are based on polycrystalline-Si modules (250Wp) and the third one – based on thin-film amorphous - Si:H modules (32Wp). The inverter unit consists of 3 x 3.1 kW identical mono-phase inverters. Each of them connected to a single PV string. The PV installation is operating continuously without major interruptions including UDAS monitoring system for more than 10 years period which makes it attractive for evaluation of PV aging.



Figure 1. PV rooftop installation at TU-Gabrovo

### *Proposed methodology*

The available database is constituted by data collected in the period between August 2008 and December 2017 with a sampling period of 10 minutes. The real PV monitoring database after 10 years of continuous operation is full with imperfections – negative numbers, ascii symbols, empty spaces due to monitoring interrupts, grid power interrupts, components failures. Therefore, a preliminary analysis of data and preprocessing of database is needed. Due to the huge amount of data the preprocessing could not be performed manually and an execution of a series of programming scripts over the raw database could be a solution for PV performance evaluation.

It seems reasonable PV performance to be compared month by month every year only in days with optimal efficiencies.

The basic algorithm, we have followed, was to extract 3 representative days from every month. These days should be as sunny as possible (bottom threshold value of solar irradiance  $> 500\text{W/m}^2$  and intra-hour fluctuations to be minimal) in order to compare correctly the PV performance year after year in similar weather conditions.

### *Preliminary analysis of database*

The typical defects which occurred in PV systems during a long-term operation can be divided into 3 main groups. The first group is connected with PV technology: “hotspots”, PID, insulation leakage, bypass diodes failures, etc. The second group is connected with power electronics: MPPT failures, IGBT failures, thermal management degradation. The third one are defects connected with the utility grid events: grid interruptions, transient overvoltage pulses, reactive power fluctuations. In order to evaluate only degradation of the PV technology the DC values of the PV strings are separated from the AC values of inverters.

Since the output performance of the PV strings strictly depend on the input energy- the solar irradiation, particular attention in the analysis of database has been given to the accurate measurement of solar irradiation values in the active plane of PV modules. It has been reported from other research groups [6], that the standard solar pyranometers, thermal detectors or small-area Si photodiodes are not suitable due to differences in thermal

coefficients, spectral mismatches or event dust accumulation compared to PV modules. It was found that the most accurate solar power sensors are small PV modules based on the same PV technology, mounted in the same plane as PV modules in the PV array. If global horizontal irradiance (GHI) solar sensor or solar GHI maps are used for evaluation of long-term stability, then additional recalculation of the tilted Plane-of-Array (POA) irradiation is needed [7].

#### *Database preprocessing*

Recently Python language has been introduced as a useful tool for data processing of big databases. In this paper several scripts based on Python 3.6, Plotly Lib and Pandas Lib are used. Using this programming environment the monitoring data can be compared and represented graphically in any browser and any computer - Win, Linux, iOS, Android machine.

The data format used in the monitoring system is described in the standard CEI EN 61724. All daily monitoring files are prepared in txt format with specific delimiters and data structure.

The first script, named multiopening.py, combines individual daily monitoring files in single file per month. Next step is cleaning of negative values and unification of daily monitoring period from 06:00h to 22:00h.

The second script, named best3days.py, selects “the best 3 days” per month following a defined criterion for a maximum solar irradiation and minimum intra-hour fluctuation. Next step is separation and recording of all monitoring data of “the best3days” in new files suitable for visual interpretation and comparisons.

The third script, named plotting.py, opens the best3days files and plots the graphs in 2D format in any browser.

The last script, named PVyield.py, calculates DC energy in [W.h], AC energy [W.h] and the resultant PV performance efficiency = AC/DC energy.

The above mentioned sequence of Python scripts execution accelerates significantly the PV aging evaluation process.

A slow linear decrease of performance is expected which could be presented in a graph. The ratio of Output DC energy / Input solar energy is calculated for every “best day”. The calculated values are divided in 4 groups depending on the season (Spring values, Summer values, Autumn values and Winter values). Finally, data points are presented in a history graph and linear fits are constructed.

During the process of analysis of collected databases from various PV plants in Bulgaria it was found that correct measurement of input power (solar irradiation in the plane of PV module) is important factor. It depends on the type of solar irradiance sensor (thermal behavior, active sensor area, orientation, spectral responsivity, etc.). In Southern Europe, the large area sensors based on silicon photodiodes or small solar cells have more similar behavior to PV module. This conclusion is related to atmospheric factors as air pollution due to aerosol, solid particles and consequent dust coverage of front glass. Frequent sand storms from Sahara desert and urban pollution with anthropogenic origin seems to affect the air transparency. In dirty environment, non-flat sensors and pyranometers exhibit wrong values of incident solar radiation. In long-term evaluation of PV aging the level of uncertainty of measurement from irradiance sensors, current and voltage sensors, A/D conversion should be reduced as low as possible because it is comparable with the percentage of degradation. That is why regular cleaning and sensor calibration should be performed.

### **3. RESULTS AND DISCUSSIONS**

The output PV power of PV installation is influenced by many optical and environmental factors. Random effects as partial shading of PV modules due to surroundings (buildings, trees, low-passing clouds, etc.) could reduce PV performance for minutes or several hours. Other spectral effect as increased UV-A, UV-B irradiation, solar magnetic storms could increase the PV output power. Low outdoor temperature in sunny days is also a favorable factor for increased PV performance. These random events are presented by dispersion of data points.

#### *Linear fits of PV aging*

Next graphs present first approximation of linear decrease of PV aging. It is constructed by comparing the data from the first full data year (2009) and the last two years (2016, 2017) for poly-Si (Figure 2) and a-Si:H (Figure 3) modules.

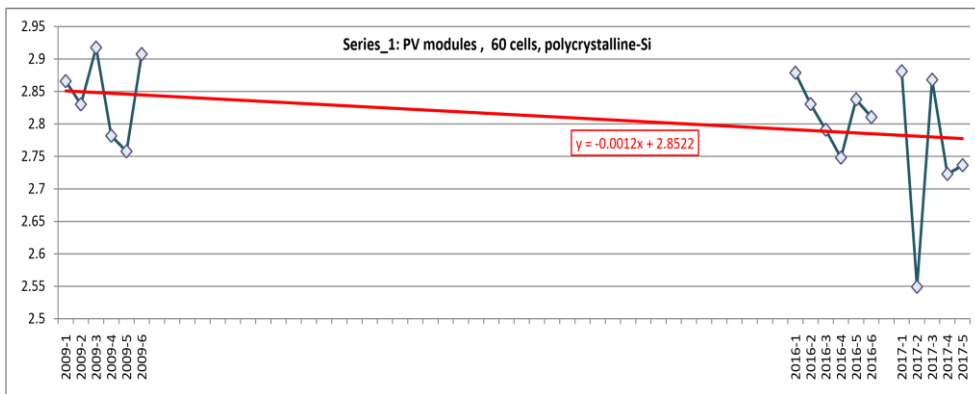


Figure 2. Preliminary linear fit of aging of PV string\_1 consisting of poly-Si modules.

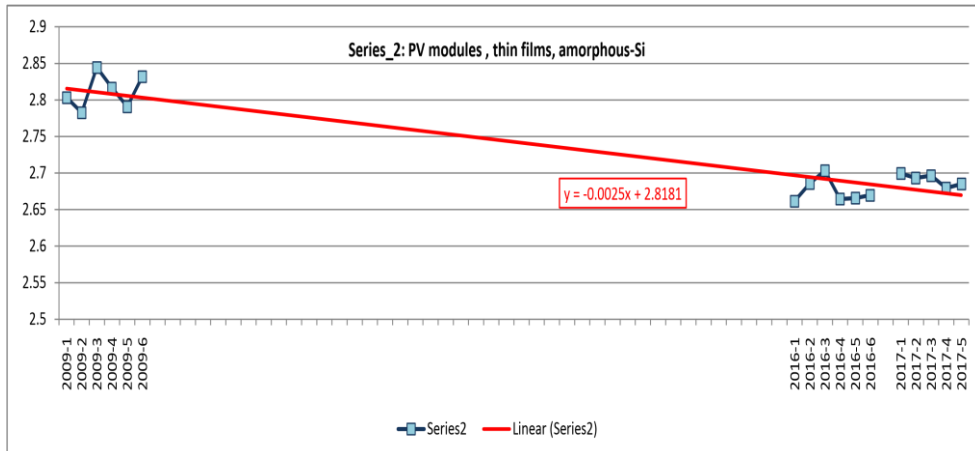


Figure 3. Preliminary linear fit of aging of PV string\_2 consisting of a-Si:H modules.

As can be concluded from data graphs presented at Figure 2 and Figure 3, in real-time equivalent operating conditions a-Si:H modules tends to degrade 2 times faster than polycrystalline-Si modules.

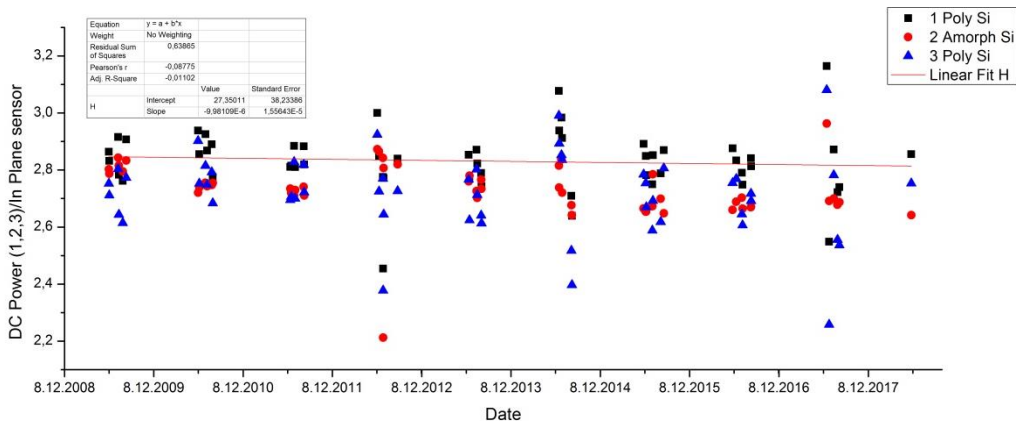


Figure 4. Linear fit of PV aging calculated for all data from 3 PV substrings.

On Figure 4 full data for the whole 10 years' period is shown. As can be seen on that Figure the dispersion of data points in the intermediate years is high but the linear decrease in performance is evident.

If we consider the variation of data points in accordance with the technology of PV modules (Figure 5) it can be distinguished the difference in aging between poly-Si modules (black and blue lines) and thin film amorphous - Si:H modules (red line). The PV aging effect in a-Si:H modules is more than 2 times higher than Series\_1 PV modules.

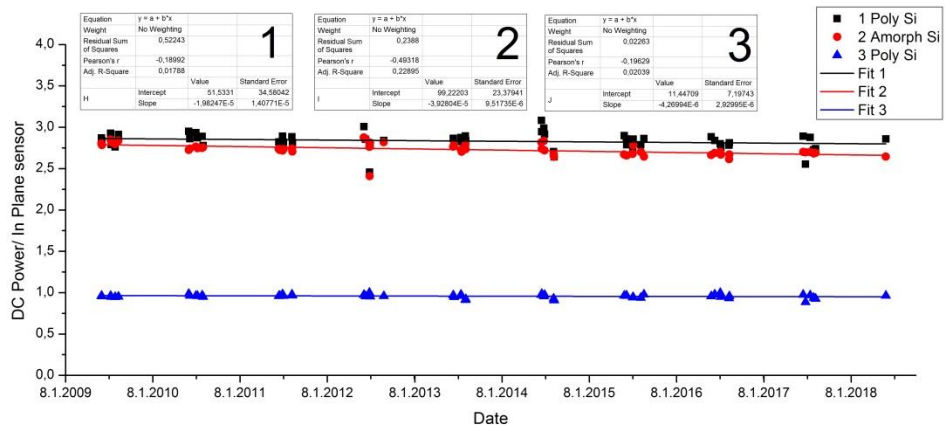


Figure 5. Linear fits of PV aging separated in accordance with PV technology used in PV modules

This could be a confirmation of well-known effect of accelerated degradation of a-Si: films due to Staebller-Wronski effect of hydrogen atoms migration.

#### *Correlation of PV aging with visual defects*

The defects identified are colorization of EVA film, loss of adhesion strength at the cell-encapsulate interface, degradation of AR coating layer, irreversible ‘hot spots’ etc. Accelerated degradation of a-Si: modules have been confirmed by visual inspection of these PV modules. Cell structure defects were detected: “hotspot” in thin films, as can be seen at Figure 5.

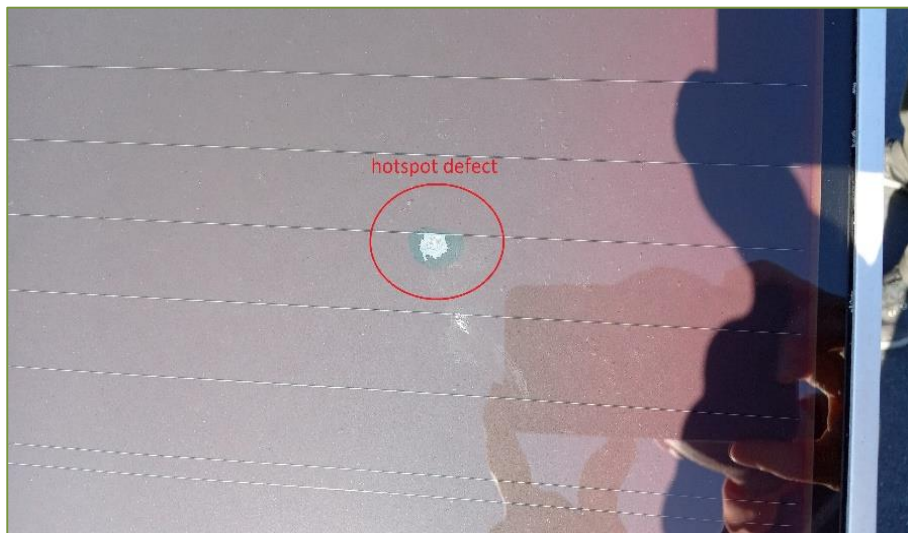


Figure 6. “Hotspot” defect in thin-film a-Si:H module – front side

## 4. CONCLUSIONS

In this paper a computerized approach for evaluation of long-term aging in PV rooftop installation has been presented. The algorithm is based on annual PV performance comparisons only in similar days with optimal efficiencies. Preprocessing of the raw database significantly reduce the time for evaluation.

Correct results on PV aging can be obtained if solar irradiation is measured by in-plane sensors with the similar thermal coefficients and similar active surface soiling as the PV modules.

PV aging effect is overestimated in datasheets. It is below 0.6% per year for most PV technologies.

#### Series 1 (poly-Si modules)

$P_{out}/P_{in}$  ratio per best day -> (2009) = 2.86361 ;  
(2017) = 2.79854

2.3 % degradation (9 years) -> 0.255 % per year

Series 2 (amorphous-Si modules)

$P_{out}/P_{in}$  ratio per best day -> (2009) = 2.78918 ;  
(2017) = 2.66027

4.6 % degradation (9 years) -> 0.511 % per year

Series 3 (poly-Si modules)

$P_{out}/P_{in}$  ratio per best day -> (2009) = 2.75105 ;  
(2017) = 2.67390

2.8 % degradation (9 years) -> 0.311 % per year

PV aging effect of linear decrease starts immediately after start of operation. This study evaluates PV aging of PV systems as energy generation systems not only aging of PV components and materials.

#### **ACKNOWLEDGMENT**

This work is partially supported by the EU "Horizon 2020" program; project GRECO, No.787289, "Fostering a next generation of European Photovoltaic Society through Open Science."

#### **REFERENCES**

- [1] Naciri, M , Aggour, M , Ait Ahmed, W . Wind energy storage by pumped hydro station. *Journal of Energy Systems* 2017; 1: 32-42 <http://dergipark.gov.tr/jes/issue/30882/329315>
- [1] Sanchez-Friera, P, Piliougue, M, Pelaez, J, Carretero, J, Sidrach de Cardona, M, "Analysis of degradation mechanisms of crystalline silicon PV modules after 12 years of operation in Southern Europe", *Prog. Photovolt: Res. Appl.*, 2011, vol. 19, pp. 658–666
- [2] Dunlop, ED, Halton, D, "The performance of crystalline silicon photovoltaic solar modules after 22 years of continuous outdoor exposure", *Progress in Photovoltaics: Research and Applications* 2005, vol.14(1),pp.53–64, DOI: 10.1002/pip.627
- [3] Jordan, D, Sekulic, B, Marion, B, Kurtz, S, "Performance and aging of a 20-year-old silicon PV system." *Journal of Photovoltaics*, 2015, vol.5(3), pp. 744–751
- [4] Reis, A, Coleman, N, Marshal, M, Lehman, P, Chamberlain, C, "Comparison of PV module performance before and after 11-years of field exposure", *Proceedings of the 29th IEEE Photovoltaic Specialists Conference*, 2002, pp. 1432–1435, DOI: 10.1109/PVSC.2002.1190878
- [5] Jordan, D, Kurtz, S, Van Sant, K, Newmiller, J, "Compendium of photovoltaic degradation rates", *Prog. Photovolt: Res. Appl.* 2016, vol.24, pp.978–989,
- [6] Reda, I, "Method to Calculate Uncertainties in Measuring Shortwave Solar Irradiance Using Thermopile and Semiconductor Solar Radiometers," *National Renewable Energy Laboratory, Technical Report NREL/TP-3B10-52194*, 2011
- [7] Dunn, L, Gostein, M, Emery, K, "Comparison of Pyranometers vs. Reference Cells for Evaluation of PV Array Performance," *Proceedings of the 38th IEEE Photovoltaic Specialists Conference (PVSC)*, Austin, TX, 2012.



# CLEAN POWER GENERATION: ENVIRONMENTALLY FRIENDLY LUBRICATION PRODUCTS AND POLLUTION PREVENTION

Helena M. Wilhelm

Vegoor Tecnologia Aplicada, Colombo, Brazil, helena@vegoor.com.br, ORCID: 0000-0002-7749-0701

Paulo O. Fernandes

Vegoor Tecnologia Aplicada, Colombo, Brazil, paulo@vegoor.com.br, ORCID: 0000-0002-2083-9028

Laís Pastre Dill

Vegoor Tecnologia Aplicada, Colombo, Brazil, lais@vegoor.com.br, ORCID: 0000-0003-0987-4612

Camila Steffens

Vegoor Tecnologia Aplicada, Colombo, Brazil, camila@vegoor.com.br, ORCID: 0000-0003-2646-0753

Kethlyn G. Moscon

Vegoor Tecnologia Aplicada, Colombo, Brazil, kethlyn@vegoor.com.br, ORCID: 0000-0002-2040-2635

Sergio M. Peres

Vegoor Tecnologia Aplicada, Colombo, Brazil, sergio@vegoor.com.br, ORCID: 0000-0001-8494-9472

Luana Moreira

Vegoor Tecnologia Aplicada, Colombo, Brazil, luana@vegoor.com.br, ORCID: 0000-0001-6417-4614

Thiago L. Zanin

COPEL, Curitiba, Brazil, thiago.zanin@copel.com, ORCID: 0000-0003-4383-6994

Cite this paper as:

Wilhelm, H.M., Fernandes, P.O., Dill, L.P., Steffens, C., Moscon, K.G., Peres, S.M., Moreira, L., Zanin, T.L. Clean power generation: environmentally friendly lubrication products and pollution prevention. 9<sup>th</sup> Eur. Conf. Ren. Energy Sys. 21-23 April 2021, Istanbul, Turkey

---

**Abstract:**

Hydroelectric energy is considered renewable, since no pollutants are generated during its production, however, several electromechanical equipment of this sector use mineral lubricant oils, which produce wastes that may contaminate surround environment. In order to have environmentally sustainable energy generation, the use of biodegradable lubricants (biolubricants) when combined with its proper bioremediation, using microorganisms, can be a striking alternative. The aim of this study is to evaluate the performance of biolubricant in auxiliary power generation plant equipment and the efficiency of its bioremediation. For this purpose, metallographic, tribologic and ferrographic analyzes were performed for the biolubricant and equipment. Bioremediation is assessed in laboratory scale in a system containing microorganisms in contact with the oil, followed by treated material analysis by an internally developed analysis method for oil and greases, using infrared spectroscopy (FTIR). Biolubricant performance in tested equipment was found adequate. Bioremediation was considered efficient in a continuous flow system, achieving the parameters required by current Brazilian legislation in 4 h of remediation. Therefore, viability of simple exchange of mineral for biolubricant in tested equipment is confirmed and an efficient system for biolubricant oil remediation was developed, which enables clean energy generation. This work is part of the R&D research project ANEEL PD-6491-0365/2015.

---

**Keywords:**

Clean energy generation, renewable lubricant, biolubricant, bioremediation.

---

© 2021 Published by ECRES

## 1. INTRODUCTION

Hydroelectric energy is the main source of electric energy in Brazil, it is considered a green renewable energy, since no pollutants are generated, such as greenhouse gases, during its production. However, several electromechanical equipment in this sector use mineral insulating and lubricant oils, which produce wastes that may damage animal health and the environment. In recent years, environmental preservation concern has been increasing worldwide and waste treatment before disposal is highlighted. Therefore, biodegradable lubricants (biolubricants) have been developed and interest in their application in energy industry and their correct disposal is growing [1].

Despite environmental advantages, simple exchange of mineral lubricant for biolubricant is a process that requires ensuring proper equipment performance. Using biolubricants with adequate performance when combined with their correct remediation, contribute to the development of cleaner energy generation. One of the most recommended techniques to remediate this type of waste is biological remediation (or bioremediation). Bioremediation is a methodology that uses natural microorganisms to consume organic matter. Microorganisms used are usually bacteria specific to tested lubricant oil, which provides efficiency and good environmental acceptance [2-4].

In this study, mineral lubricant and synthetic biolubricant performance in power generation plant auxiliary equipment, in addition to their bioremediation efficiency in a continuous flow system, are investigated.

## 2. METHODOLOGY

### Mineral lubricant and synthetic biolubricant performance in auxiliary equipment

Two auxiliary equipment (SCHULZ-CSL20BR/200L® compressors), one with mineral lubricant and other with biolubricant (synthetic oil), ISO 100, operated for determined time (~669 h) under similar conditions.

Samples of both lubricants were analyzed for total acid number (ASTM D664), water content (ASTM D95), particle counting (ISO 4406:2017), viscosity at 40 °C (ASTM D7945), rotatory pump oxidation induction time (ASTM D2272), elemental determination (ASTM D6595) by SpectrOil Rotating Disk Electrode Optical Emission Spectroscopy (RDE-AES), particle morphology, color and size by ferrography (ASTM D7690) and magnetic particle index using Particle Quantification Instrument (PQI Index) (ASTM D8184).

Auxiliary equipment materials were analyzed by metallography, in which images are obtained by optical microscopy, using Olympus BX51M microscope.

Lubricant oils tribology analyzes were performed in auxiliary equipment material specimens (cylinders), using CETR-UMT tribometer, with a 200 N load cell and results are expressed as friction coefficient. The parameters used in the tests were 25 N normal load, 10 Hz frequency, 10 mm track length, at 55 °C for 4 h. Surface topography evaluations were carried out with 3D roughness measurements, using Taylor Hobson optical interferometer, model CCI Talysurf Lite, before and after tribological assays. Prior to analysis, samples were cleaned using acetone under ultrasonically for 10 minutes.

### Mineral lubricant and biolubricant bioremediation

Bioremediation system under controlled temperature (23 °C) consists of a mixing tank (70 L) with mechanical stirring, oil water coalescence separation system, bioremediation tank (70 L), UV cell to reduce bacteria in final mixture before disposal, and a tank to collect final effluent (Figure 1). In mixing tank water flows at a 7 L/h, in the same tank oil is added at 1% of the water flow. After flowing thru oil water separation system, bioremediator (autochthonous bacteria specific to each oil) is added at ~50 mL/h in the bioremediation tank. After bioremediation tank water flows thru a UV sterilizer device before entering effluent collection tank. Water flow was determined to assure effluent residence time of ~8.5 h. Samples were collected in bioremediation tank immediately after addition of all components (0 h) and at 2, 4, 6 and 8 h of experiment. A test, denominated blank, was performed without bacteria addition, only with water-mineral oil mixture and samples were collected in same time periods (0, 2, 4, 6 and 8 h). Collected samples were analyzed according to an internally developed analysis method for oil and grease, using Fourier transform infrared spectroscopy (FTIR) from Agilent, model Cary 630 FTIR.

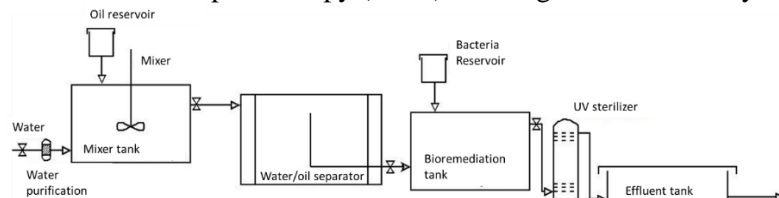


Figure 1: Bioremediation system diagram.

### 3. RESULTS AND DISCUSSION

#### Mineral lubricant and synthetic biolubricant performance in auxiliary equipment

Physical-chemical analyzes (Table 1) of samples collected in auxiliary equipment at 0 h and ~669 h operation showed water content increase over time, mainly for synthetic biolubricant, since it has higher water affinity than mineral lubricant. Biolubricant oxidation induction time showed a growth after 669 h operation, which means better oxidation stability due to some effect of oil modification over time that is still under investigation. Other physical-chemical parameters did not change significantly under experimental conditions.

*Table 1 – Physical-chemical analyzes of mineral lubricant and synthetic lubricant samples collected in auxiliary equipment.*

Parameter	Cycles			
	Mineral oil	Synthetic biolubricant	Mineral oil	Synthetic biolubricant
	0 h	0 h	669 h	669 h
Acidity (mg KOH/g)	0.03	0.05	0.02	0.06
Water content (ppm)	21	282	51	633
Viscosity at 40 °C (cSt)	93.3	103.1	106.8	129.6
Oxidation induction time (min)	325	393	154	655

Metallographic analyzes (Figures 2 e 3 - Appendix) showed that materials from both auxiliary equipment, operating with mineral lubricant and synthetic biolubricant are similar, since they are composed of cast iron with lamellar graphite. Elementary determination was important to confirm equipment iron, which was released at similar contents for both lubricant oils operation (~25 ppm). Ferrographic analysis (data not shown) presented no variation among both lubricants operation over time.

Table 2 shows particle counting analysis and PQI Index revealing slightly variation over time for both lubricant oils, confirming they operated at similar conditions. Synthetic biolubricant total particle count is higher than mineral oil due to 4 and 6 µm particle contents since before operation.

*Table 2 – Particle analyzes of mineral lubricant and synthetic lubricant samples collected in auxiliary equipment.*

Sample	Particle analysis		
	Particle count ISO (4µm/6µm/14µm)	Total particle count (Particle/100 mL)	PQI Index
Mineral oil (0 h)	19/17/14	502	8
Synthetic biolubricant (0 h)	22/21/18	1531	8
Mineral oil (669 h)	20/18/15	594	27
Synthetic biolubricant (669 h)	20/18/15	1309	7

After elemental analysis, tribological tests were performed to determine average friction coefficient in 4 h test (Table 3). In addition, superficial changes were evaluated through roughness heights distribution for cylinder specimens. Table 4 shows 3D roughness (S) before and after tribological tests. Results pointed that there is no significant difference between mineral lubricant oil and synthetic biolubricant since no clear signs of stress, wear or failure were detected for analyzed systems.

*Table 3 - Average friction coefficient of mineral lubricant and synthetic biolubricant.*

Lubricant	Average friction coefficient
Synthetic biolubricant	0.08 ± 0.05
Mineral oil	0.11 ± 0.07

*Table 4 - Roughness of mineral lubricant and synthetic biolubricant before and after tribological tests.*

Sample	Period	Sq	Ssk	Spk	Sk	Svk	Variation					
		µm					%	µm	%	µm	%	
Synthetic biolubricant	Before	1.206	-0.491	1.032	2.895	1.481						
	After	1.096	-0.418	0.936	2.550	1.384	-9.1	14.9	0.345	12.0	0.442	11.2
Mineral Oil	Before	0.993	-0.603	0.707	2.216	1.457						
	After	0.932	-0.983	0.654	1.889	1.479	-6.1	-63.0	0.327	14.8	0.380	13.0

Sq: Average square roughness; Ssk: skewness parameter; Spk: peaks representative parameter; Sk: central region parameter; Svk: valleys contribution parameter.

### Bioremediation

Biolubricant bioremediation results based on oil and grease determination and bioremediation efficiency are presented at Table 5. Parameters required in Brazilian environmental legislation ( $> 20$  ppm) for the disposal of this type of effluent were reached in 4 h for biolubricant and in 6 h for mineral oil (12.2 ppm). Biolubricant bioremediation efficiency of ~80% was achieved in 4 h, which was maintained until the end of the experiment (8 h). On the other hand, in blank test oil and grease reduction was only 23% after 8 h, confirming bioremediation feasibility to reduce oil and grease content.

*Table 5. Oil and Grease determination in bioremediation system of synthetic biolubricant.*

Time (h)	Oil and grease* (g)	Oil and grease (ppm)	Bioremediation efficiency
0	0.047	51.8	0
2	0.055	61.0	0
4	0.010	11.4	79
6	0.009	10.1	81
8	0.011	12.6	76

\*In collected sample (900 mL)

### CONCLUSION

No differences were observed for biolubricant and mineral lubricant in tested auxiliary equipment, which shows feasibility of simple exchange of mineral for biolubricant for tested conditions. Proposed bioremediation set up was able to reduce effluent's oils and greases content in only 4 h (biolubricant) and 6 h (mineral oil). Therefore, an efficient system for biolubricant remediation was developed, helping to increase environmental performance of hydroelectrical energy generating plants.

### ACKNOWLEDGMENT

ANEEL and COPEL (Companhia Paranaense de Energia Elétrica) thanks for their support in the execution of the R&D project PD 6491-0365/2015.

### REFERENCES

- [1] Nagendramma, P, Kaul, S. Development of ecofriendly/biodegradable lubricants: an overview. *Renewable and Sustainable Energy Reviews* 2012, 16: 764- 774. DOI: <https://doi.org/10.1016/j.rser.2011.09.002>.
- [2] Adams, GO, Fufeyin, PT, Okoro, SE, Ehinomen, I. Bioremediation, biostimulation and bioaugmentation: a review. *International Journal of Environmental Bioremediation and Biodegradation* 2015, 3: 28-39. DOI: <https://doi.org/10.12691/ijebb-3-1-5>.
- [3] Bhattacharya, M, Biswas, D, Sana, S, Datta, S. Biodegradation of waste lubricants by a newly isolated *Ochrobactrum sp.* C1. *3 Biotech* 2015, 5: 807-817. DOI: <https://doi.org/10.1007/s13205-015-0282-9>.
- [4] Gopinath, S, Shareef, MI, Ashalatha, Aravind, G. Bioremediation of lubricant oil pollution in water by *Bacillus megaterium*. *International Journal of Innovative Research in Science* 2015, 4: 6773- 6780. DOI: <https://doi.org/10.15680/IJIRSET.2015.0408010>.

## Appendix



Figure 2: Micrograph of Cyllinder A (Mineral oil).



Figure 3: Micrograph of Cyllinder B (Synthetic biolubricant).



# DISTANCE PROTECTION BASED ON THE SYNCHROPHASOR DATA IN CONTROL ROOM

Igor Ivanković

HOPS, Croatian Transmission System Operator, Zagreb, Croatia, igor.ivankovic@hops.hr, ORCID: 0000-0002-7305-6123

Dalibor Brnobić

STER, Rijeka, Croatia, dalibor.bnobic@ster.hr, ORCID: 0000-0003-4496-7742

Cite this paper as:

*Ivanković, I., Brnobić, D. Distance protection based on the synchrophasor data in control room. 9<sup>th</sup> Eur. Conf. Ren. Energy Sys. 21-23 April 2021, Istanbul, Turkey*

**Abstract:** Distance protection function which is based on synchrophasor data and run as a part of Wide Area Monitoring System (WAMS) in control room, will be presented in paper. It is the latest in a series of classical relay protection features developed within WAMS. Synchrophasor measurement units generate estimated phasors value for all phases and symmetrical components of voltage and current, which is in total 12 phasors. Paper will deal with phasors estimation process which can be used for impedance calculation in real time. Analyses were done for voltage and current amplitude estimation for one and two window estimation process. Novel distance protection were compared with real faults in transmission network and recorded responses of relay protection. Newly developed function operated properly and thus could be implemented in WAMS.

**Keywords:** line distance protection, synchrophasor data, WAMS, PMU, control room

© 2021 Published by ECRES

Nomenclature	
WAMS	Wide Area Monitoring System
PMU	Phasor Measurement Unit
WAMPAC	Wide Area Monitoring Protection And Control
PDC	Phasor Data Concentrator
SS	High voltage Substation in transmission network
HOPS	Croatian Transmission System Operator
21	Distance protection according to ANSI
87	Line differential protection according to ANSI
TPP	Thermal Power Plant
OHL	Overhead line

## 1. INTRODUCTION

The PDC (Phasor Data Concentrator) server application in WAMS, located in the control room, is planned to be expanded with a new distance line protection function (ANSI: 21) based on the principle of measuring voltage and current at one end of a high voltage line. For this task, the algorithm is using the available synchronized data from the transmission network line. The distance protection algorithm has the following basic functional parts:

- Module for calculating the impedance on the transmission line using synchrophasors of currents and voltages,
- Distance protection must work for all types of faults,
- Calculation of transmission line impedance and fault location.

Like any function inside WAMS, this distance protection works in real time with continuous monitoring and recording of the distance protection data set, like impedance values, tracing the impedance trajectory, time and others. This function in the next stage should be able to adapt to the existing polygonal characteristics of distance protection in relays together with the event list signals.

## 2. TRANSMISSION SYSTEM MONITORING AND PROTECTION IN THE CONTROL CENTER

In the control center, WAMS will be expanding with certain steps in direction of the WAMPAC system with new protection and control functions. [1], [2], [3], [4].

Based on that plan a new synchrophasor measuring device was designed and built, which has the following characteristics and is connected to the existing [5], [6], WAM system:

- A data stream of synchrophasors and statuses are transmitted in 20 ms resolution,
- The device must enable connection to both measuring and protective cores of current metering transformers,
- The device must receive the commands from WAMPAC system,
- The device has the smallest standardized housing to make its installation in the existing cabinets of secondary equipment as simple as possible and without the need to reconfigure the existing secondary equipment.

The new synchrophasor measuring device meets the requirements of HOPS in terms of migrating the existing WAM system to the WAMPAC system. Using this PMU device [5], all three phase quantities of voltage and current are transmitted, as well as all components, direct, inverse and zero component of voltage and current, i.e. a total of 12 measured quantities [7]. The device also has special communication channels, GPRS, Figure 1.

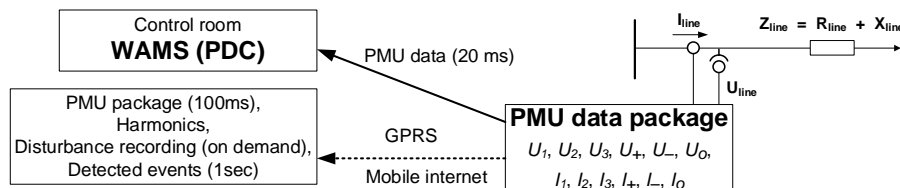


Figure 1. Block scheme of new PMU device with connections towards WAMS, to metering transformers, and GPRS.

Several transmission line protection functions have already been developed and implemented in the WAMPAC system. The development of these functions emerged from simpler overcurrent and voltage functions, then a longitudinal differential protection was developed [8]. Now the first pilot project for the possibility of applying distance protection of a transmission line that uses synchronized measured data has been made.

## 3. DISTANT PROTECTION ALGORITHM

PMUs installed on transmission lines also use the same voltages and currents like relay protection, Figure 1. Distance protection uses the basic principle of measuring the impedance of a transmission line by measuring the voltages and currents at the line end. Relays in their calculations use complex values of current and voltage according to:

$$U_{line}(t) = U_{line} \cdot e^{j(\omega t + \varphi_U)} = U_{line} \cdot [\cos(\omega t + \varphi_U) + j \cdot \sin(\omega t + \varphi_U)] \quad (1)$$

$$I_{line}(t) = I_{line} \cdot e^{j(\omega t + \varphi_I)} = I_{line} \cdot [\cos(\omega t + \varphi_I) + j \cdot \sin(\omega t + \varphi_I)] \quad (2)$$

That is, written in another form:

$$\bar{U}_{line} = Re\{\bar{U}_{line}\} + j \cdot Im\{\bar{U}_{line}\} \quad (3)$$

$$\bar{I}_{line} = Re\{\bar{I}_{line}\} + j \cdot Im\{\bar{I}_{line}\} \quad (4)$$

The voltage measured by the relay at the beginning of the line can be expressed as follows:

$$\bar{U}_{line} = R_{line} \cdot \bar{I}_{line} + j X_{line} \cdot \bar{I}_{line} \quad (5)$$

The most important calculation in a relay is the calculation of impedance in real time. This is the impedance that the relay measures on the protected transmission line, i.e. that the relay "sees" on the transmission line, the apparent impedance, and it is calculated every millisecond and compared with the set values in the relay, inclusion (3) and (4) in (5) we get,

$$Re\{\bar{U}_{line}\} + j Im\{\bar{U}_{line}\} = (R_{line} + j X_{line}) \cdot (Re\{\bar{I}_{line}\} + j Im\{\bar{I}_{line}\}) \quad (6)$$

That is, the real and imaginary component of voltage is:

$$Re\{\bar{U}_{line}\} = R_{line} \cdot Re\{\bar{I}_{line}\} - j X_{line} \cdot Im\{\bar{I}_{line}\} \quad (7)$$

$$Im\{\bar{U}_{line}\} = X_{line} \cdot Re\{\bar{I}_{line}\} + R_{line} \cdot Im\{\bar{I}_{line}\} \quad (8)$$

The impedance calculated by the relay is from (5) and (6),

$$X_{line} = \frac{Im\{\bar{U}_{line}\} \cdot Re\{\bar{I}_{line}\} - Re\{\bar{U}_{line}\} \cdot Im\{\bar{I}_{line}\}}{Re\{\bar{I}_{line}\}^2 + Im\{\bar{I}_{line}\}^2} \quad (9)$$

$$R_{line} = \frac{Re\{\bar{U}_{line}\} \cdot Re\{\bar{I}_{line}\} + Im\{\bar{U}_{line}\} \cdot Im\{\bar{I}_{line}\}}{Re\{\bar{I}_{line}\}^2 + Im\{\bar{I}_{line}\}^2} \quad (10)$$

Pilot project has those algorithms for distance protection and is using synchrophasor data.

#### 4. ESTIMATION OF SYNCHRONIZED MEASUREMENT DATA FOR DISTANCE PROTECTION

The distance protection algorithm running at the WAMS level, compared to the algorithm in relay protection, is executing with a substantially reduced input data set.

Unlike distance protection algorithms in which the impedance calculation is performed after each step of analog-to-digital conversion, typically with a step of one millisecond, the distance protection algorithm in WAMS processes the synchrophasor data stream sent to the PDC server in 20 ms resolution. Therefore, the impedance trajectory at the fault is characterized by a 20-100 times higher time increment, and thus the fault detection itself is slower. Also, in addition to significantly slower sampling, there are two other limiting factors that need to be considered when designing the distance protection function in WAMS.

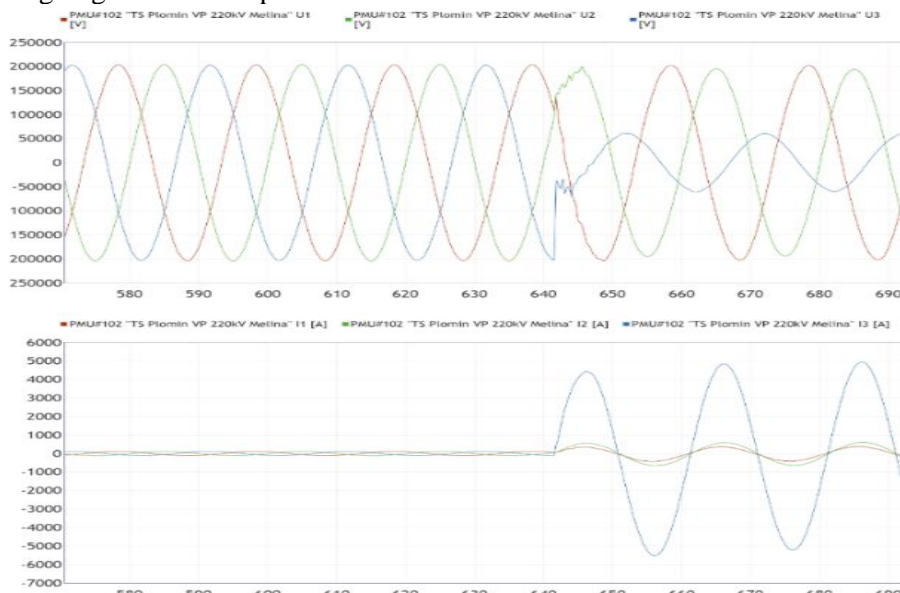


Figure 2. Synchrophasor recording of voltage and current in TPP Plomin on double OHL 220 kV Melina, for 25.5.2020. at 05:19:59.

The synchrophasor data measured by the PMU device and sent to the PDC server is generated by an estimation procedure [9] which determines the amplitude and phase of the sinusoidal signal in the from the time-limited input data window. It is assumed that the frequency of the sine signal corresponds to the nominal frequency of the network, and that the amplitude of the sine signal is constant. Under slowly changing conditions, the negative impact of these assumptions can be ignored. However, when a fault occurs, there is a jump in the amplitude and phase of the signal, which can, depending on the type, size and moment of the jump in the estimation window, result in a vector that significantly reduces or misrepresents the actual amount of current at the observed time. This shortcoming in distance protection relays is eliminated by matching the beginning of the measuring window with the occurrence of a fault, which cannot be done with synchrophasor measurement, because the beginning and end of the estimation window are uniquely determined for all devices in global time, most often synchronized by GNSS (Global Navigation Satellite System) receiver.

Another limitation arises from the width of the window taken to calculate the phasor. The estimation procedure for class P synchrophasor, which is used in protection algorithms, is 2 periods wide, i.e. 40 ms, which at a reporting speed of 20 ms gives a 50% overlap of the input data window. Taking into account that the activation time of the

distance protection algorithm in the relay is of the order of one period, and that the switch time is 40 ms, it can be estimated that the fault current will be eliminated in less than 60 ms. This means that at least one reading of class P synchrophasors should capture the voltages and currents required to calculate the fault impedance.

In order to illustrate the influence of estimation on the calculation of the impedance amount, a post-mortem analysis of data recorded in TPP Plomin on line 220 kV Melina during a single-pole failure on double OHL 220 kV Plomin-Melina was recorded on 25.5.2020. at 05:19:59. At the time of the failure, generator 2 in TPP Plomin was not working.

Figure 2 shows the waveforms of voltage and current at the time of failure. Waveforms collected from the PMU device memory were recorded with a resolution of 64 samples per period, or with a sampling frequency of 3200 samples per second. The fault in phase L3 occurred at 05:19:59.642. The fault current supplied from the observed node was interrupted at 05:19:59.711. The power supply of the fault from SS Melina was interrupted at 05:19:59.701.

Estimation of the magnitude and phase of the vector was made by applying a discrete Fourier transform to the input data bounded by 20 ms and 40 ms wide windows. An estimation procedure was performed for each sample by extending the processing window for 10 ms and 20 ms around that sample to give 3200 vectors per second per channel. The vectors are marked with the timestamp of the sample for which the processing window was created. Figure 3 shows the magnitude of the estimated synchrophasors for the three phase voltages and currents for a 20 ms window on the left and a 40 ms processing window on the right side of the image.

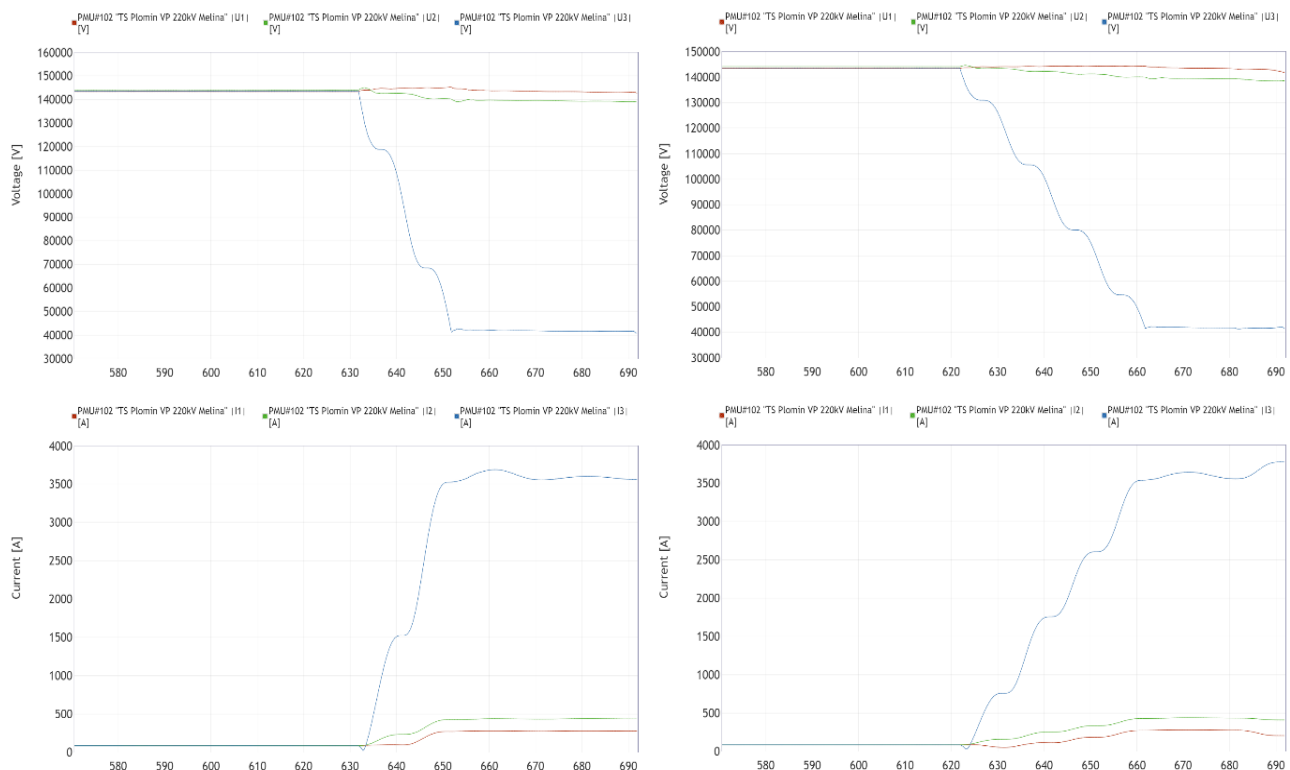


Figure 3. Comparison of the estimation of the synchrophasor values calculated on the 20 and 40 ms window.

The abrupt change that occurred in 642 milliseconds affects the 20 ms calculation procedure in the period 632...652 ms, i.e. for calculations in which the abrupt change is part of the processing window. According to the same principle, in the 40 ms calculation, the transition process between two quasi-stationary states takes 40 ms. The amounts and impedance angles of individual phases were calculated from the obtained vectors. The results are shown in the diagrams, Figure 4 in which the circles indicate the values that can be calculated from the synchrophasor flow sent to the PDC server in real time.

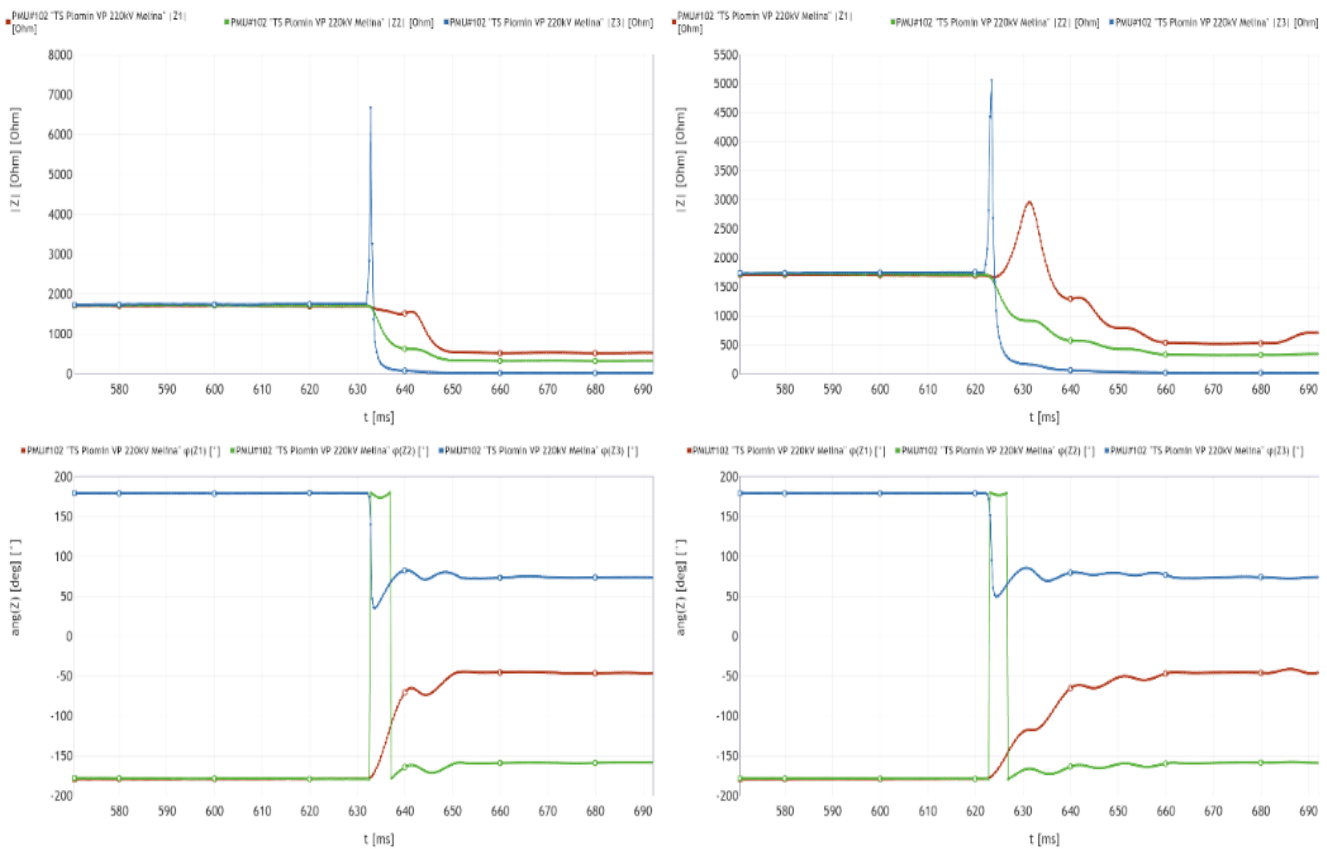


Figure 4. Impedance comparisons calculated using 20 and 40 ms wide estimation windows.

Figure 5. shows the impedance trajectories for the same observation period in the R-X diagram. From the diagram it can be read that the fault occurred at the L3 phase of the protected object. An impedance jump to the amount of a few kOhms confirms the presented thesis that the phase jump within the estimation window will significantly impair the quality of the vector estimation.

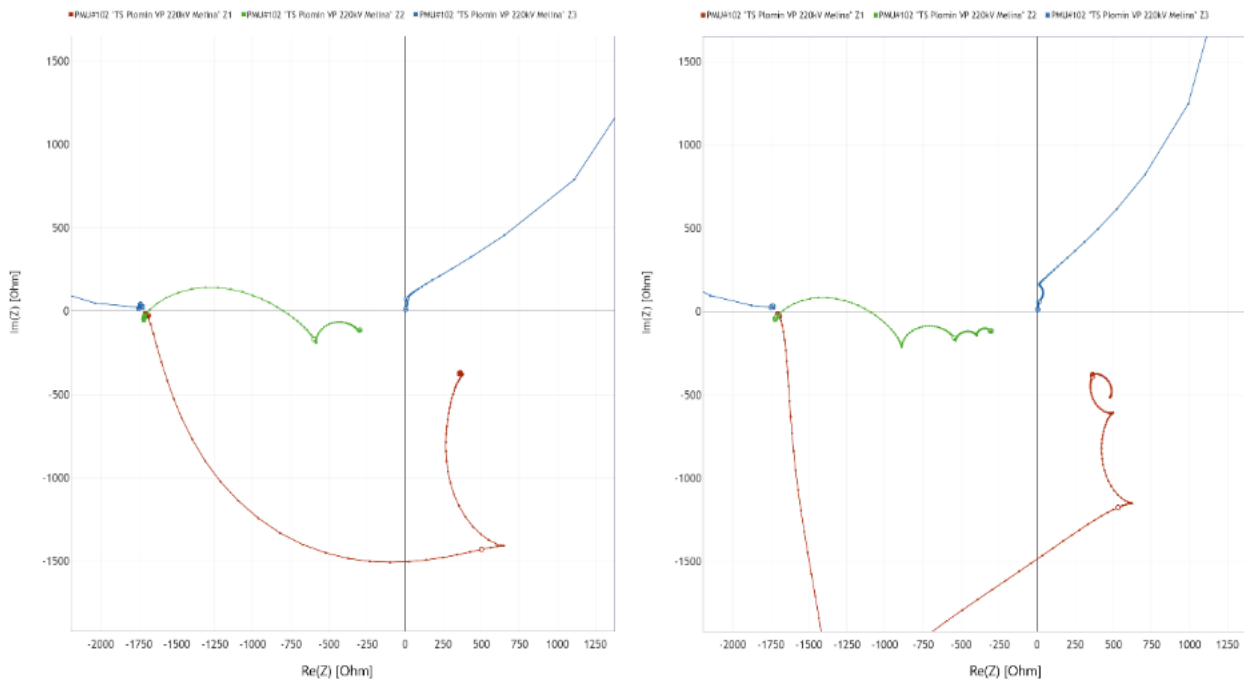


Figure 5. Impedance trajectories comparison on 20 ms and 40 ms estimation windows.

Finally, the detail of the L3 phase fault impedance trajectory for the estimation windows 20 and 40 ms are shown in Figure 6. with specially indicated impedances for moments 660, 680 and 700 ms for both observed synchrophasor estimation modes.

These impedances, including that for the 640 ms synchrophasor reading step, are shown in Table 1.

*Table I. Fault impedance for selected steps of synchrophasor readings*

Width estimation window	Synchrophasor values in time 25.5.2020. 05:19:59							
	.640 ms	.660 ms	.680 ms	.700 ms	Z[Ohm]	Z[°]	Z[Ohm]	Z[°]
20 ms	72.32	82.26	11.43	72.98	11.58	73.25	10.59	73.24
40 ms	57.96	79.28	14.18	76.60	11.71	73.74	11.90	76.67

By a detailed trajectory analysis of the 20 ms procedure, it can be determined that the fault impedance is  $11.6 \pm 0.2$  Ohms when the fault is supplied on both sides. The value of the fault impedance decreases with the power failure on the part of TPP Plomin, but due to the short duration of the condition, a stable reading was not obtained. The trajectory obtained by the 40 ms wide estimation window confirms that the abrupt changes have a greater impact, both at the occurrence and at the end of the failure.

From the presented trajectories, it can be concluded that the norm [8] prescribed by the estimation window of 40 ms and 20 ms resolution of data transmission occurrence of a fault and its characterization can be safely detected. In contrast to the 20 ms estimation, the change in impedance trajectory between the two reading steps is relatively large and it is necessary to increase the reporting speed to 2 or even 4 readings per period in order to increase the probability of steady state synchrophasor capture. On the other hand, reducing the estimation window to 20 ms will give satisfactory readings even at a standard 20 ms reading resolution.

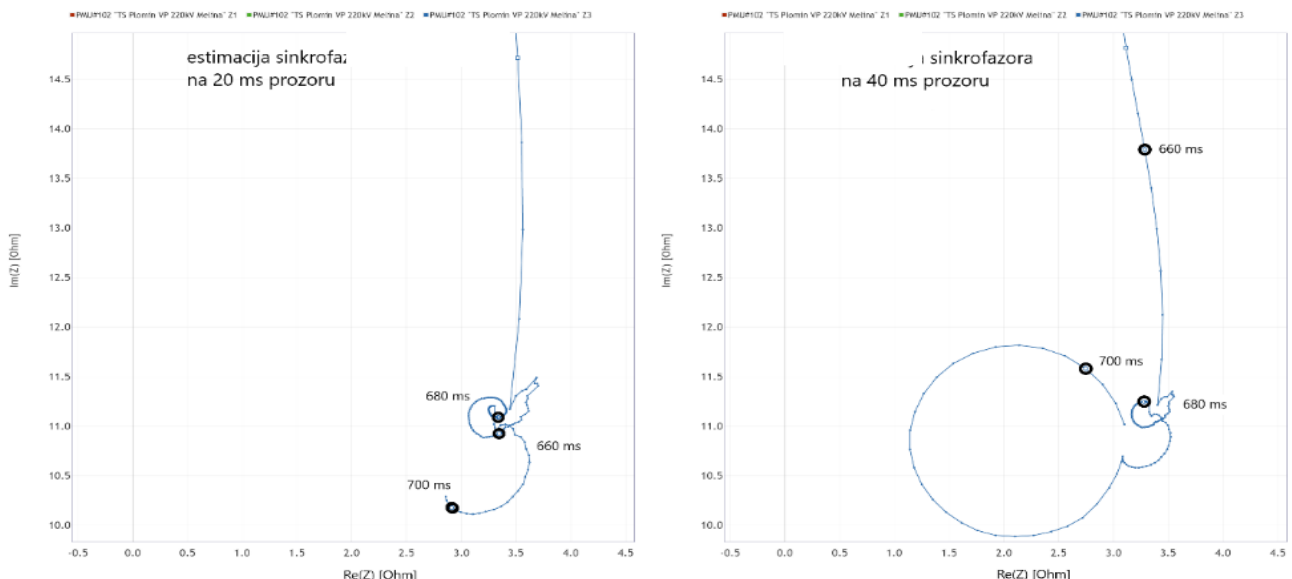


*Figure 6. Synchrophasor readings for impedance trajectory during failure, with estimation window 20 and 40 ms.*

## 6. CONCLUSION

Research in the pilot project showed that results of the distance function (21) that uses synchronized measurement data are satisfactory and adequate for the function to be used in real time on the WAMPAC platform in the control center. The distance protection function developed in this way provides new possibilities for connecting with other functions in the control center, thus improving the monitoring and protection of the transmission network. The input measuring parameters of the function are sampled every 20 ms, which is an order of magnitude smaller than the function in the relay itself. In this regard, a pilot project was made to examine the possibility of using such a data sequence. Also, the longitudinal differential protection function of the transmission line (87) has already been realized [9], with the same set of data with success.

## **REFERENCES**

- [1] I. Ivanković, I. Kuzle, R. Sirovina, "Multifunctional system protection for transmission lines based on phasor data", 16th IEEE International Conference on Environment and Electrical Engineering – EEEIC 2016, 7 – 10 June 2016, Florence, Italy, paper number 233, pp 1-6 (A3-TS4)
- [2] A. Esmailian, T. Popovic, M. Kezunovic, "Transmission line relay mis-operation detection based on time-synchronized field data", Electric Power Systems Research 125 (2015) 174–183, <http://dx.doi.org/10.1016/j.epsr.2015.04.008>
- [3] I. Ivanković, I. Kuzle, N. Holjevac, "Algorithm for Fast and Efficient Detection and Reaction to Angle Instability Conditions Using Phasor Measurement Unit Data", Energies 2018, 11(3), 681; doi:10.3390/en11030681
- [4] I. Ivanković, I. Kuzle, N. Holjevac, "Key Performance Indices for Angle Stability Protection Function in WAMPAC System", 2018 IEEE Power & Energy Society, General Meeting, 5-9 August 2018, Portland, OR, USA, paper 18PESGM0656
- [5] I. Ivanković, R. Rubeša, I. Kuzle, M. Rekić, "Real Time Operation of Synchrophasor Data Functions in Transmission System Control Room", MEDPOWER 2018, Mediterranean Conference on Power Generation, Transmission, Distribution and Energy Conversion, IET and IEEE PES, Dubrovnik, Hrvatska, 12.-15. studeni 2018., pp.1-6, (SES-19), ISBN Print 978-953-184-247-1
- [6] Novosel, D., Bartok, G., Hennerberg, G., et al. (2010). IEEE PSRC report on performance of relaying during wide-area stressed conditions. IEEE Transactions on Power Delivery, 25(1), 3–17
- [7] "IEEE Standard for Synchrophasors for Power Systems", IEEE Standard C37.118.1-2011
- [8] I. Ivanković, D. Brnobić, R. Rubeša, M. Rekić, "Line Differential Protection with Synchrophasor Data in WAMPAC System in Control Room", Proceedings of Third International Colloquium on Intelligent/Smart Grid Metrology 2020 (SMAGRIMET 2020), online event, Croatia, October 20-23 2020, paper No.126
- [9] I. Ivanković, D. Brnobić, R. Rubeša, Z. Zbunjak, V. Grudenić, "Analyses of Phasor Measurement Unit Estimation Algorithms for Protection Functions inside WAMPAC System", Proceedings of First International Colloquium on Smart Grid Metrology 2018 (SMAGRIMET 2018), Split, Hrvatska, 24.-27. travanj 2018., referat br.103, pp 5-9, ISBN: 978-953-184-234-1



## TORREFACTION AND CARBONIZATION OF WATER HYACINTH STEMS AND LEAVES: IMPACT ON ENERGY

Amr Moataz Sanad

Fuels and Combustion Engines Laboratory, Energy Resources Department, Egypt-Japan University of Science and technology, Alexandria, Egypt, amr.sanad@ejust.edu.eg, ORCID: 0000-0003-2903-8486

Hamdy Hassan

Energy Resources Department, Egypt-Japan University of Science and technology, Alexandria, Egypt, hamdy.aboali@ejust.edu.eg, ORCID: 0000-0002-0156-7186

Hassan Shokry

Environmental Engineering Department, Egypt-Japan University of Science and technology, Alexandria, Egypt, hassan.shokry@ejust.edu.eg, ORCID: 0000-0003-2712-2035

Shinichi Okawara

Department of Chemical Science and Engineering, Tokyo institute of Technology, Tokyo, Japan, ookawara.s.aa@m.titech.ac.jp, ORCID: 0000-0002-7912-3403

Ahmed Elwardany

Fuels and Combustion Engines Laboratory, Energy Resources Department, Egypt-Japan University of Science and technology, Alexandria, Egypt, ahmed.elwardany@ejust.edu.eg, ORCID: 0000-0002-2536-2089

Cite this paper as:

*Sanad, A.M., Hassan, H., Shokry, H., Okawara, S., Elwardany, A. Torrefaction and carbonization of water hyacinth stems and leaves: Impact on Energy. 9<sup>th</sup> Eur. Conf. Ren. Energy Sys. 21-23 April 2021, Istanbul, Turkey*

**Abstract:**

This study considers the inclusion of water hyacinth stem and leave in the energy sector by comparing their characteristics. This was done via high temperature pyrolysis, ranging 200-1100°C in an electric muffle in an inert environment utilizing nitrogen. The comparison lead to conclude that the water hyacinth leaves (WHL) had a higher heating value but lower mass yield than that of water hyacinth stem (WHS). The mass yield of WHS at 1100°C was found to be 32.22%, while that of WHL was 23.43%. The overall energy yield reached its maximum for both WHS and WHL at the temperature of 200°C, due to the high mass yield of samples treated at this temperature. Although the energy yield at the highest temperature was found to be 25.49% for WHS and 21.56% for WHL, it should be kept in mind that this contribution is of that biochar solely, further studies on the liquid and gaseous products under the same conditions will assess the overall energy yield of water hyacinth parts. This study would also help researchers finding the optimum part of the water hyacinth for the various applications depending on the required parameters.

**Keywords:**

*Water hyacinth, Biomass, Biochar, Carbonization, Carbon*

© 2021 Published by ECRES

**Nomenclature**

EY	Energy Yield
EF	Enhancement Factor
MY	Mass yield
WHS	Water Hyacinth Stem
WHL	Water Hyacinth Leaves

## **1. INTRODUCTION**

Increasing world population comes with the cost of an increase in energy demand. Despite all efforts to switch to renewable energy resources, the highest contribution is still that of fossil fuel [1]. Consequently, environmental problems keep arising due to the utilization of fossil fuels in different energy sectors and its contribution to the production of greenhouse gases.

Biomass has the advantage of being a renewable energy resource, with net zero carbon emissions as well as its low sulphur and nitrogen content, it can potentially be a replacement for conventional fossil fuel with no or little change in the already adapted systems. This led many researchers to investigate the different types of biomass and their characteristics, this includes but is not limited to, Corn cob, Wheat straw, rice straw, rice husk, sugarcane bagasse and microalgae [1]–[3]. Additionally, Water hyacinth has been investigated as source of bioenergy by several researchers [4]–[7] and it has shown to have a good potential in the energy sector.

Thermochemical conversion, and particularly pyrolysis process is the most commonly used method for biomass conversion to bioenergy [3]. Pyrolysis is the process of heating the biomass samples at elevated temperatures in an inert atmosphere through the usage of gases like Nitrogen or Argon, and is used to produce liquid, solid and gaseous products that could be later used as fuel directly or after some further treatments [8].

On the other hand, water hyacinth (*Eichhornia crassipes*) has been considered a concern to several other environmental problems.[9] It is a highly invasive non-edible aquatic plant that grows in low salinity water and favors high temperature air and water. Its environmental impact on damaging marine life and its high consumption of fresh water as well as its impact on jamming water transportation have driven researchers, concerned organizations and governments to spend their efforts in finding an effective way to eliminate, or at least control the spread of water hyacinth using different methodologies [9].

So far, although there was an advancement in the chemical and biological treatments, their negative impact on environment as well as their high cost and lower durability makes them a less attractive option [5], this is due to the fact that water hyacinth seedbank is able to germinate even after such treatments for a period that could be as long as 28 years, and its invasive nature allows it to spread again easily [10].

Alternatively, mechanical harvesting is an expensive yet efficient methodology. Although in-situ mechanical harvesting, where the removed plants are just left to sink in water, can be cheaper, it has the drawback of lowering oxygen dissolvability and increases Sulphur concentration in water, that in return negatively affects marine life and promotes germination and further growth of water hyacinth. Therefore, mechanical harvesting with harvested plant removal away from source is left as best environmental option, but with the obstacle of being expensive due to logistical conditions as well as proper disposal method, especially for large areas of interest. [5]

The aim of this study is to increase water hyacinth contribution into the Energy sector, making it an added value product, contributing to matching the continuously increasing energy demand. In addition, this will decrease environmental impact of both water hyacinth and fossil fuel, as well as helping the socio-economical impact of water hyacinth removal for the aforementioned reasons. This is done via studying the effect of a wider range of dry pyrolysis treatment temperatures (200 to 1100°C). In addition to that, water hyacinth leaves and stem are for the first time to be treated separately and the effect of each pyrolysis temperature on the properties of biochar produced from each, such as its mass yield, carbon content, calorific value as well as energy yield. With this in hand, proper utilization of each can be achieved by researchers in different fields.

## **2. MATERIALS AND METHODOLOGY**

### **Materials:**

Water hyacinth was collected from a stream near lake Mariout, Alexandria, Egypt. It was sundried for 14 days then stored in the laboratory. Leaves and stem were separated to study the difference in their individual properties. All sample were then water washed and dried in a drying oven (Binder ED 53) at 105 °C until no further mass reduction was noticed, then sieved at a maximum size of 300 µm before pyrolysis.

### **Pyrolysis:**

Pyrolysis was held in an electrical muffle (ASH – AMF 20N) with nitrogen gas flow to ensure inert ambient. The pyrolysis range was 200-1100°C with a residence time of one hour and a heating rate of 40°C/min and left to cool down to room temperature without a cooling control system.

### **Characterization:**

The resulted Biochar was carefully weighted using sensitive balance (Axis-ATE210), then characterized using ultimate (EuroVector EA3000 CHNSO elemental analyzer) and proximate analysis to determine its composition.

### **Calorific value, enhancement factor and energy yield calculations:**

In order to evaluate the characteristics of the biochar produced in each case, the higher heating value was calculated empirically [11] using equation:

$$HHV = 0.2949 C + 0.8250 H \quad [MJ/kg] \quad (1)$$

Where, C and H are the Carbon and Hydrogen weight percentages in sample, respectively.

With this in hand, enhancement factor (EF) and energy yield (EY) were possible to be calculated from the equations:

$$EF_{pyr} = \frac{HHV_{pyr}}{HHV_{100}} \quad (2)$$

$$EY_{pyr} = MY_{pyr} EF_{pyr} \quad (3)$$

Where, MY is the mass yield percentage, and the subscript ‘pyr’ represents pyrolysis temperature.

### 3. RESULTS AND DISCUSSION

#### Mass yield:

The resulting mass yield of both Water Hyacinth Leaves (WHL) and Water Hyacinth Stem (WHS) for different treatment temperatures are shown in figure 1. It is noted that the total mass yield of WHS was more than that of the WHL, with the former being 32.2% and the latter 23.4% both at 1100°C.

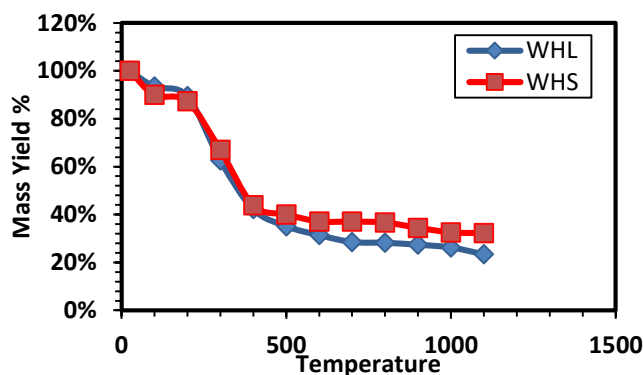


Figure 1. mass yield of WHL and WHS over temperature range 25 to 1100 °C

The highest degradation of hemicellulose and cellulose happens in the temperature range of 220-315°C and 315-400°C, respectively, while Lignin loses mass on a wide range of temperature ranging 160-900°C [12]. Comparing the results from the current work, it is noticeable that the mass loss in the range 200-300°C is sharper in the case of WHL, suggesting a higher content of Hemicellulose, while the opposite is evident in the range of 300-400°C, suggesting a higher content of Cellulose in WHS. The sharper degradation of mass at higher temperature of WHL also suggests the higher content of Lignin in WHL over that of WHS.

#### Proximate and ultimate analysis:

The results of proximate and ultimate analyses of the samples are shown in table 1. It is worth mentioning that although the WHL showed lower mass yield, it did have higher carbon content and lower ash content as well as a higher heating value, compared to that of WHS. On the other hand, the WHS had the advantage of having much lower Nitrogen and Sulphur content.

#### Effect of pyrolysis on calorific values

In Order to better understand the effect of pyrolysis on water hyacinth at various temperature, Elemental analysis (CHNS) has been performed on the treated samples and the results are tabulated in table 2. Which in turn allowed to the calculation of their heating values from equation [1].

Table 1. Proximate and ultimate analyses

Samples	WHS	WHL
Picture		

## Ultimate analysis (wt%)

C	33.8	39.98
H	4.95	5.703
N	1.48	4.24
S	0.205	0.419
O	34.78	33.00
Proximate analysis dry basis (wt%)		
Moisture	10.04	6.54
Volatile matter	56.46	66.60
Ash	14.75	10.11
Fixed Carbon	18.76	16.75
HHV (MJ/kg)	14.05	16.50

Table 2. CHNS results for WHS and WHL samples treated different temperatures.

WHS				WHL				
Temp	N (wt%)	C (wt%)	H (wt%)	S (wt%)	N (wt%)	C (wt%)	H (wt%)	S (wt%)
100	1.48	33.8	4.948	0.205	4.24	39.98	5.703	0.419
200	1.7	35.69	4.811	0.192	4.85	43.62	5.837	0.331
300	2.12	39.8	3.84	0.217	5.96	50.5	4.439	0.381
400	2.57	42.21	2.723	0.269	6.07	50.71	4.71	0.267
500	1.87	37.11	1.831	0.306	5.16	49.17	2.407	0.355
600	1.68	38.66	1.042	0.258	4.33	49.24	1.682	0.38
700	1.51	38.33	0.932	0.25	3.48	47.8	1.363	0.204
800	1.22	37.47	1.076	0.405	2.96	47.84	1.243	0.473
900	0.6	36.28	0.971	0.729	1.74	46.99	1.154	0.473
1000	0.23	35.6	1.015	0.527	0.65	44.86	1.162	0.437
1100	0.05	35.67	0.719	0.784	0.38	48.74	0.975	0.635

The calculated HHV, EF and EY from Eqs. [1-3], respectively, are represented graphically in figure 2 to give a better idea on the general trend in each of them.

As can be seen from the data, as pyrolysis temperature increase, hydrogen content tends to have a generally decreasing trend, while carbon reaches a maximum in both WHS and WHL at the pyrolysis temperature of 400 and then starts decreasing again. This hence leads to a similar trend for the HHV, and therefore the EF. The EY, however, reaches a maximum at the pyrolysis temperature of only 200. This is due to the much higher mass yield in comparison to subsequent pyrolysis temperature.

It can be clearly noted that WHL had a higher heating value across all pyrolysis temperatures compared to that of WHS. Nevertheless, the total energy yield was in favor of WHS after the pyrolysis temperature of 400°C, which is due to its notably higher mass yield.

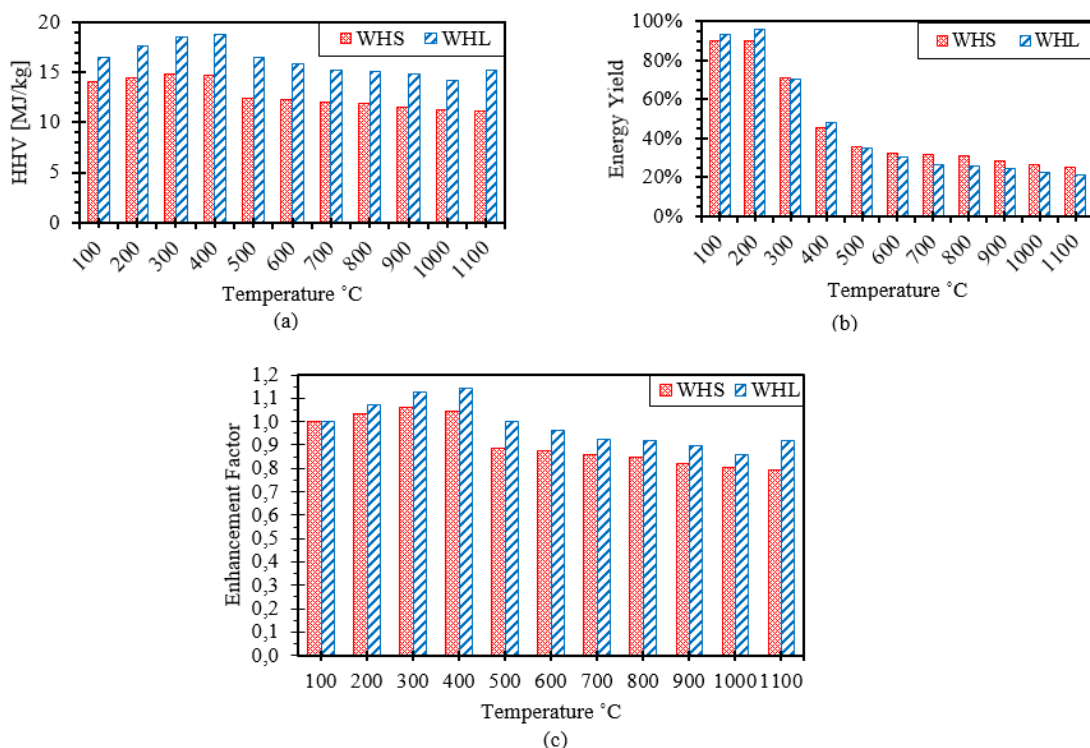


Figure 2. results of comparison between WHS and WHL in (a) HHV (b) EY (c) EF versus pyrolysis temperatures.

### Effect on Nitrogen, Hydrogen and Sulphur content

It is worth mentioning that although the general trends of variation of the weight percentage content with temperature of N, H and S was similar in both WHS and WHL, there was a very clear difference in the percentage itself. WHL, had a much higher N across all temperature range and a slightly higher hydrogen content, but the Sulphur content was higher than that of WHS until high temperatures was reached, namely 900°C, at which it became lower than that of WHS.

### 4. CONCLUSION

WHL have higher HHV than that of WHS across all pyrolysis temperature, this is due to its higher Carbon and hydrogen content. HHV of reaches its maximum at 300°C for WHS and 400°C for WHL. MY of WHS is higher than that of WHL across all pyrolysis temperatures, namely being 32.22% for WHS and 23.43% in WHL. EY is at its maximum at 200°C for both samples, this is due to the relatively high HHV as well as the notably higher value of MY WHL in general has a higher percentage of Nitrogen, Hydrogen and Sulphur than that of WHS, except at temperature range 900-1100 where the Sulphur content in WHS gets slightly higher.

### REFERENCES

- [1] W. H. Chen, B. J. Lin, M. Y. Huang, and J. S. Chang, "Thermochemical conversion of microalgal biomass into biofuels: A review," *Bioresource Technology*, 2015; 184:314-327, doi: 10.1016/j.biortech.2014.11.050.
- [2] B. Debalina, R. B. Reddy, and R. Vinu, "Production of carbon nanostructures in biochar, bio-oil and gases from bagasse via microwave assisted pyrolysis using Fe and Co as susceptors," *Journal of Analytical and Applied Pyrolysis*, 2017; 124:310-318, doi: 10.1016/j.jaat.2017.01.018.
- [3] B. Biswas, N. Pandey, Y. Bisht, R. Singh, J. Kumar, and T. Bhaskar, "Pyrolysis of agricultural biomass residues: Comparative study of corn cob, wheat straw, rice straw and rice husk," *Bioresource Technology*, 2017;237:57-63, doi: 10.1016/j.biortech.2017.02.046.
- [4] K. Alagu *et al.*, "Novel water hyacinth biodiesel as a potential alternative fuel for existing unmodified diesel engine: Performance, combustion and emission characteristics," *Energy*, 2019; 179:295-305, doi: 10.1016/j.energy.2019.04.207.
- [5] S. Román, B. Ledesma, A. Álvarez, C. Coronella, and S. V. Qaramaleki, "Suitability of hydrothermal carbonization to convert water hyacinth to added-value products," *Renewable Energy*, 2020; 146: 1649-1658, doi: 10.1016/j.renene.2019.07.157.
- [6] H. Huang, J. Liu, H. Liu, F. Evrendilek, and M. Buyukada, "Pyrolysis of water hyacinth biomass parts: Bioenergy, gas

- emissions, and by-products using TG-FTIR and Py-GC/MS analyses,” *Energy Conversion and Management*, 2020; 207:112552, doi: 10.1016/j.enconman.2020.112552.
- [7] X. Jin *et al.*, “Co-pyrolysis of rice straw and water hyacinth: Characterization of products, yields and biomass interaction effect,” *Biomass and Bioenergy*, 2019; 127:105281, doi: 10.1016/j.biombioe.2019.105281.
- [8] P. McKendry, “Energy production from biomass (part 2): Conversion technologies,” *Bioresource Technology*, 2002; 83, 1:47-54, doi: 10.1016/S0960-8524(01)00119-5.
- [9] A. M. Villamagna and B. R. Murphy, “Ecological and socio-economic impacts of invasive water hyacinth (*Eichhornia crassipes*): A review,” *Freshwater Biology*. 2010; 55, 2:282-298, doi: 10.1111/j.1365-2427.2009.02294.x.
- [10] P. R. Sullivan and R. Wodd, “Water hyacinth (*Eichhornia crassipes* (Mart.) Solms) seed longevity and the implications for management,” *Eighteenth Australasian Weeds Conference*, 8-11 October 2012, Weed Science Society of Victoria Inc. Frankston Australia. pp. 37-40.
- [11] C. Y. Yin, “Prediction of higher heating values of biomass from proximate and ultimate analyses,” *Fuel*, 2011; 90, 3: 1128-1132, doi: 10.1016/j.fuel.2010.11.031.
- [12] M. Amer, M. Nour, M. Ahmed, S. Ookawara, S. Nada, and A. Elwardany, “The effect of microwave drying pretreatment on dry torrefaction of agricultural biomasses,” *Bioresource Technology*, 2019; 286:121400, doi: 10.1016/j.biortech.2019.121400.



# ENERGETIC AND FINANCIAL EVALUATION OF A SOLAR-POWERED ABSORPTION CHILLER INTEGRATION INTO A CO<sub>2</sub> COMMERCIAL REFRIGERATION SYSTEM

Evangelos Syngounas

National and Kapodistrian University of Athens, Psachna, Greece, esyngounas@uoa.gr, ORCID: 0000-0001-7384-7040

Dimitrios Tsimpoukis

National and Kapodistrian University of Athens, Psachna, Greece, dimtsimp@uoa.gr, ORCID: 0000-0003-3536-5782

Stavros D. Anagnostatos

METRO S.A, Athens, Greece, S.Anagnostatos@metro.com.gr, ORCID: 0000-0002-4860-8862

Maria K. Koukou

National and Kapodistrian University of Athens, Psachna, Greece, mkoukou@uoa.gr, ORCID: 0000-0003-3089-8467

Michail Gr. Vrachopoulos

National and Kapodistrian University of Athens, Psachna, Greece, mgrvrachop@uoa.gr, ORCID: 0000-0001-7558-4491

Cite this paper as:

Syngounas E., Tsimpoukis D., Anagnostatos S.D., Koukou M.K., Vrachopoulos M.Gr. Energetic and financial evaluation of the integration of a solar-powered absorption chiller into a CO<sub>2</sub> commercial refrigeration system. 9<sup>th</sup> Eur. Conf. Ren. Energy Sys. 21-23 April 2021, Istanbul, Turkey

---

**Abstract:**

This study investigates the integration of a solar absorption chiller by means of subcooling to a CO<sub>2</sub> booster system that serves the refrigeration needs of a supermarket refrigeration plant with an installed capacity of 80 kW and 20 kW for medium and low-temperature regimes respectively. The examined configuration is projected to the real refrigeration plant of a METRO S.A supermarket which lies in the region of Athens, Greece. The proposed solution includes the employment of a single-stage absorption chiller operating with LiBr-H<sub>2</sub>O working pair, which is driven by heat produced in evacuated tube collectors installed in the store's rooftop. The energy analysis is conducted with validated numerical models that are developed in MATLAB using the CoolProp library. The collecting area and the corresponding chiller capacity of the proposed configuration are selected through financial evaluation. More specifically, the collecting area is analyzed parametrically from 25 m<sup>2</sup> to 200 m<sup>2</sup>. Finally, 100 m<sup>2</sup> of collecting area with 60 kW of chiller capacity are proved to be the optimum solution financially with 8.4 years payback period and 44.57 k€ net present value. This optimum solution results in an annual power consumption decrease of 8.12% which leads to energy savings of 27.45 MWh/year.

---

**Keywords:** CO<sub>2</sub> refrigeration system, absorption chiller, solar energy, energy efficiency, supermarket

---

© 2021 Published by ECRES

## 1. INTRODUCTION

The biggest share of the energy demand in supermarkets corresponds to the refrigeration needs (60-70%), which are used to reserve the perishable products under cooling or freezing conditions [1]. The recent “F-gas regulation” of the European Commission introduced the gradual phase-out of the widely used hydrofluorocarbon refrigerants (HFCs) in the commercial refrigeration plants [2]. The latter leads to the promotion of carbon dioxide - CO<sub>2</sub> as the only viable and long-term solution for the commercial refrigeration sector. Carbon dioxide (R744) is a natural refrigerant with zero ozone layer depletion potential (ODP=0) and negligible global warming potential (GWP=1). Additionally, it shows better thermophysical properties from the synthetic refrigerants, having lower viscosity and higher thermal conductivity, density, and volumetric cooling efficiency from the HFCs [3]. However, the biggest

drawback of CO<sub>2</sub> employment in refrigeration systems is related to its low critical point (~31°C). More precisely, for ambient temperature around 27°C CO<sub>2</sub> refrigeration systems turn into the so-called transcritical operation. The latter results to lower energy efficiency figures for the CO<sub>2</sub> refrigeration systems in comparison with the conventional direct expansion HFC systems, especially for the warm climates of South Europe which show high ambient temperature levels during the longest time of the year. The solution to the described problem seems to be the exploitation of renewable energy sources (RES) and more precisely of the solar energy, in order to increase the energy efficiency of CO<sub>2</sub> refrigeration systems. Last years, many researchers have been proposed innovative CO<sub>2</sub> refrigeration configurations that integrate RES such as solar energy [4], [5]. The results are very ambitious since they show an increment of the coefficient of performance (COP) up to 50%. The most common way to integrate the heat produced by solar exploitation arrangement into a refrigeration system is through the employment of absorption or adsorption chillers for the subcooling of the working in the main cycle refrigerant.

The aim of this study is the further investigation of solar energy exploitation for the CO<sub>2</sub> refrigeration systems energy efficiency increment, through the theoretical analysis of a solar-powered absorption chiller integration into a real commercial refrigeration plant. More precisely, the cooling produced in the evaporator of the absorption configuration is employed by means of subcooling, in a CO<sub>2</sub> booster refrigeration system which serves the refrigeration needs of display cabinets and coldrooms of a supermarket. The energetic evaluation of the proposed topology leads to the estimation of the annual reduction in electricity consumption for a real supermarket refrigeration plant, due to the corresponding energy benefit achieved. Additionally, collectors area installed in the store's rooftop is parametrically investigated, in order to find the best case scenario in terms of financial profitability of the proposed investment. The latter has been in depth analyzed in conventional solar-powered absorption chiller configurations but never to the authors' knowledge in this specific integration with a CO<sub>2</sub> booster refrigeration system [6], [7]. Finally, a life-cycle cost analysis for the optimum scenario of the proposed configuration leads to the estimation of the future cash flows for the proposed investment for the entire life expectancy of the project. The current approach is the theoretical part of the potential exploitation of its results for the actual implementation of the proposed energy saving configuration in the near future.

## 2. THE EXAMINED CONFIGURATION

This study investigates an innovative CO<sub>2</sub> refrigeration system that serves the cooling and freezing needs of a supermarket refrigeration plant, with an installed capacity of 80kW and 20kW for the medium and low-temperature regimes respectively. The described topology is depicted in Figure 1.

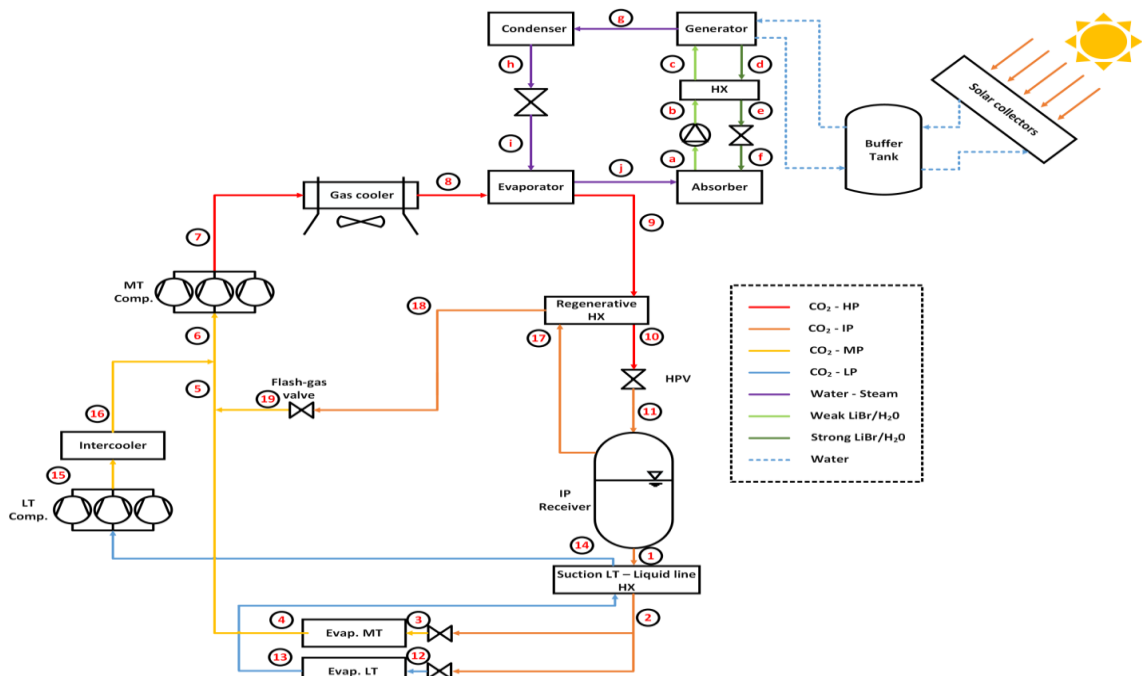


Figure 1. The examined refrigeration system with solar-cooling integration

The proposed energy saving solution includes the integration in the main system of one solar-powered absorption chiller (ACH), which produces subcooling of the CO<sub>2</sub> to improve the efficiency of the total arrangement. The absorption chiller works with LiBr-H<sub>2</sub>O as working pair and consists of the Generator in which is driven the produced solar-heat through water circulation, the Evaporator which is placed at Gas-cooler exit, in which the required CO<sub>2</sub> subcooling is achieved, as well as of the Condenser and Absorber which are used to reject heat to the ambient. Condenser and Absorber are water-cooled devices which are fed by water cooled inside a cooling tower. Evaporation temperature in the ACH Evaporator is selected at  $t_{\text{evap}}^{\text{ach}}=5^\circ\text{C}$ , which is an acceptable value being in the temperature range of 5–15°C that is usually used in the absorption chiller applications [8]. The promising benefit is based on the exploitation of solar-thermal heat for the production of refrigeration effect in the absorption chiller evaporation used for the subcooling of the CO<sub>2</sub> at the exit of gas-cooler module, in order to increase the volumetric refrigeration capacity of the booster system. **Figure 2.** depicts the pressure-enthalpy diagram of the CO<sub>2</sub> refrigeration cycle of the subcritical and transcritical operation, for the case with and without solar-absorption chiller respectively.

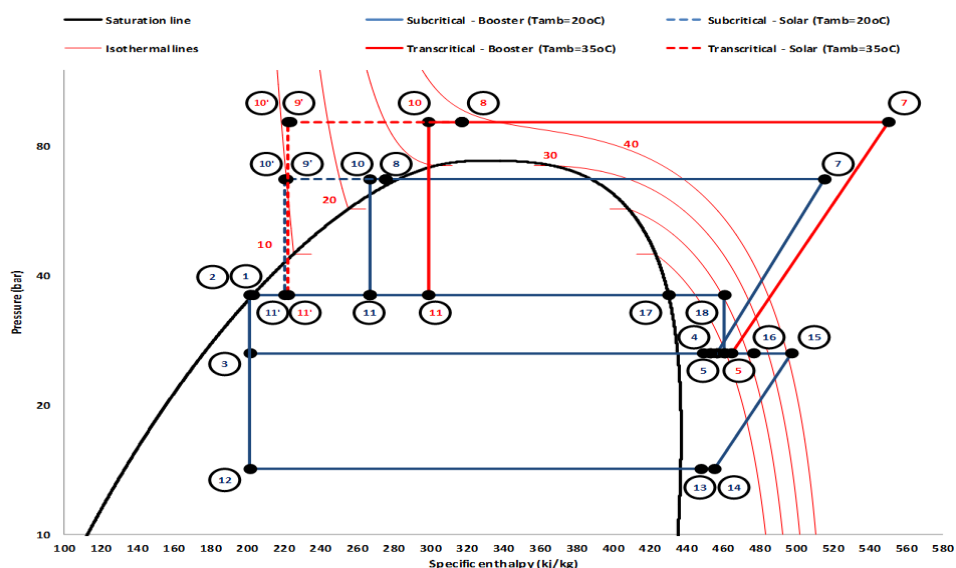


Figure 2.  $\log(p)$ - $h$  diagram of the proposed  $CO_2$  refrigeration cycle

### **3. MATERIALS AND METHODS**

The basic thermodynamic equations used for the energy simulation of the proposed system are presented in this section. These equations solved in a program developed in MATLAB, in which thermodynamic properties were derived from CoolProp library. The main thermodynamic equations used for the energetic evaluation of the described configurations are the following:

Coefficient of performance of the CO<sub>2</sub> booster system (COP<sub>booster</sub>) is calculated as:

$$COP_{booster} = \frac{Q_{evap}^{MT} + Q_{evap}^{LT}}{W_{comp}^{MT} + W_{comp}^{LT} + W_{fans}^{GC}} \quad (1)$$

The absorption chiller coefficient of performance (COP<sub>ach</sub>) is calculated as:

$$COP_{ach} = \frac{Q_{sc}}{Q_a} \quad (2)$$

The total power consumption ( $W_{\text{total}}$ ) sums all the different individual power consumptions of both subsystems and can be written as below:

$$W_{total} = W_{comp}^{MT} + W_{comp}^{LT} + W_{fans}^{GC} + W_{fans}^{IC} + W_{c,tower} \quad (3)$$

Finally, the energetic evaluation of the system proposed and its comparison with the conventional one, is enabled using total coefficient of performance (COP), which is calculated as:

$$COP = \frac{Q_{evap}^{MT} + Q_{evap}^{LT}}{W_{comp}^{MT} + W_{comp}^{LT} + W_{fans}^{GC} + W_{fans}^{IC} + W_{c.tower}} \quad (4)$$

Financial analysis is used for evaluating the best combination of the collector area and the corresponding absorption chiller capacity will be used. The investment examined includes only the additional equipment needed for the implementation of the proposed energy saving configuration, i.e. the solar-powered absorption chiller and the corresponding equipment for its coupling with the CO<sub>2</sub> booster system. The most important parameter examined is

the net present value (NPV) which gives the today value of the investment by considering the potential gains and discount of the future cash flows. NPV is calculated as below, while Table 1 presents all the financial data used in the examined financial analysis.

$$NPV = -C_0 + \sum_{j=1}^M \frac{CF_{net}}{(1+r)^j} \quad (5)$$

Table 1. Data for the financial analysis

Parameter	Symbol	Value	References	Parameter	Symbol	Value	References
ACH specific cost	K <sub>ACH</sub>	300	[9]	Electricity cost	K <sub>el,0</sub>	0.2	[10]
ETC specific cost	K <sub>ETC</sub>	250	[11]	Energy inflation	IR <sub>el</sub>	2%	[12]
Plumbing specific cost	K <sub>plumb</sub>	43.2	[13]	Discount factor	r	3.5%	[14]
Operation and maintenance	K <sub>O&amp;M</sub>	0.5	[15]	Project lifetime	M	20	[16]

The simulation data used in the current study derived from actual environmental data of the region in which the examined supermarket lies (Athens). More precisely, the fluctuation of ambient temperature is taken from the local monitoring system of the refrigeration plant, which refers to the real temperature levels with the examined CO<sub>2</sub> booster systems operates during the last year. Refrigeration loads in medium (Q<sub>evap</sub><sup>MT</sup>) and low-temperature regimes (Q<sub>evap</sub><sup>LT</sup>) are mainly dependent to the fluctuation of ambient temperature [17]. The estimation of mean hourly solar radiation is calculated for inclination angle of β=23° according to the Technical Chamber of Greece Guidelines. The main assumptions made in this study are summarized below, while the basic parameters used in simulation model are presented in Table 2.

- The analysis uses steady-state conditions.
- The expansion inside the throttling devices is ideal without heat losses.
- External SH in MT και LT suction are negligible.
- There is zero SC in CO<sub>2</sub> and ACH condensers.
- Devices/components cells are considered as adiabatic without heat losses outside.

Table 2. Data for the financial analysis

Parameter	Symbol	Value	Parameter	Symbol	Value
Installed refrigeration capacity MT	Q <sup>MT</sup>	80 kW	Approach temperature in condenser (subcritical)	ΔT <sub>apr</sub> <sup>cond</sup>	8 K
Installed refrigeration capacity LT	Q <sup>LT</sup>	20 kW	Approach temperature in gas-cooler (transcritical)	ΔT <sub>apr</sub> <sup>GC</sup>	3 K
Evaporation temperature MT	t <sub>evap</sub> <sup>MT</sup>	-10 °C	Approach temperature in intercooler	ΔT <sub>apr</sub> <sup>IC</sup>	3 K
Evaporation temperature LT	t <sub>evap</sub> <sup>LT</sup>	-30 °C	Water temperature at collectors inlet	T <sub>col</sub> <sup>in</sup>	80 °C
Evaporation temperature ACH	t <sub>evap</sub> <sup>ACH</sup>	5 °C	Water temperature at collectors outlet	T <sub>col</sub> <sup>out</sup>	95 °C
Superheat (internal)	SH	10 K	Heat exchangers effectiveness	η <sub>eff</sub> <sup>hex</sup>	70%

#### 4. RESULTS AND DISCUSSION

The first step of this analysis includes the energy simulation of the proposed solar-powered ACH employment into a conventional CO<sub>2</sub> booster refrigeration system. Solar collector area is analyzed parametrically from 25 to 200 m<sup>2</sup>. The results show as expected that the bigger the collector area is, the highest the energy saving is leading to lower monthly electricity consumption rates for the cases having more collectors installed in the rooftop. **Figure 3.** presents the monthly electricity consumption for each case. It is clear that in summer months the energy saving potential of the proposed configuration is higher. This happens because during summer temperature levels are higher leading to higher power consumption due to transcritical operation, plus radiation levels are also higher meaning higher amounts of solar-heat available to be exploited in the ACH. The greatest collector area of 200 m<sup>2</sup> corresponds to annual power consumption reduction up to 9.5% and maximum monthly energy saving of 13.8% for July, which is the warmest month of the year, in comparison to the conventional booster system. Moreover, an interesting result is that the energy benefit has a declining rate from one case to the other, moving to higher collector areas. This is mainly caused due to the fact that available heat produced has an exploitation limit in the ACH system,

linked to the subcooling minimum down to 10°C degrees in the CO<sub>2</sub> side. The latter makes it clear that since the energy benefit is not increasing a lot moving to higher collector areas, there is an optimum collector area which gives the best combination of energy saving and financial profitability.

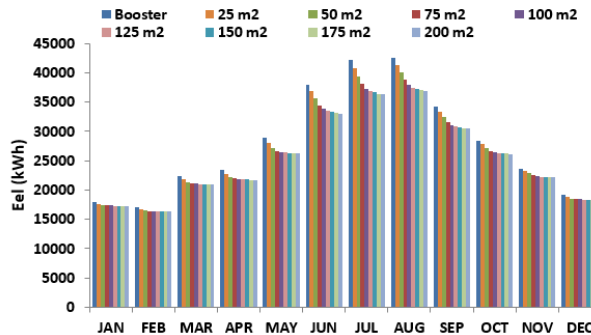


Figure 3. Annual distribution of monthly electricity consumption for the different collector areas

Following energy saving comparison of the examined cases, the next step in order to determine the optimum case of collector area is to evaluate also financially each case. **Figures 7.** presents the calculated NPV for the examined cases. Comparing the eight cases, the highest NPV of 44.75 k€ corresponds to 100 m<sup>2</sup> which is proven the optimum case of collector area, being the most suitable parameter for this investment for the lifetime expectancy of 20 years. The payback of 8.4 years can be achieved for the optimum case, which is a long period but accepted for solar cooling technologies. Finally, the optimum case of 100m<sup>2</sup> collector area leads to maximum evaporation cooling capacity in the ACH up to 55.7kW, so the nominal capacity of the ACH will be used is selected to be 60kW. Moreover, 100m<sup>2</sup> of collector area corresponds to 50 pieces of evacuated tube collectors of 2m<sup>2</sup> each

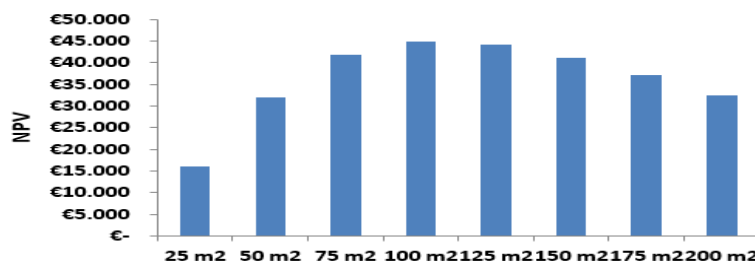


Figure 7. Net present value for the different collector areas

For the optimum case of 100 m<sup>2</sup> energy efficiency analysis is conducted. More specifically, the COP of the proposed configuration is calculated and compared to the conventional case for the mean hour of each month. **Figure 4.** depicts the average daily COP fluctuation for three representative months of the year: January, April and July. Amelioration of COP takes place for each month during the sunshine hours of the day. During the rest hours of the day when there is zero solar radiation, COP is equal to the case of the conventional booster system. Another interesting result is that for summer months which have higher ambient temperature levels, energy efficiency of both examined topologies is lower, while at the same time.

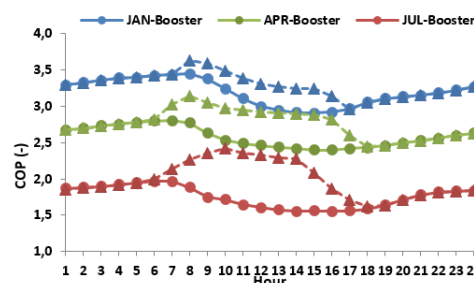


Figure 4. Mean daily COP fluctuation of the examined configuration for three representative months

Finally, for each month of the year the total electricity consumption of the examined configurations is calculated. The results which are illustrated in **Figure 5** confirm that the proposed energy saving topology is more efficient, since it has by 8.12% lower power consumption in comparison to the basic system. The latter percentage

corresponds to annual energy savings of 27.45 MWh/year. The highest energy saving rate of 11.56%<sup>b</sup> is achieved in July which is the warmest month of the year.

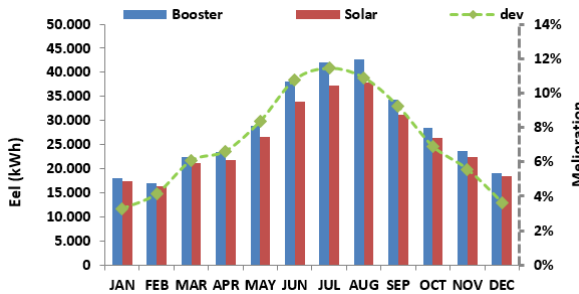


Figure 5. Annual distribution of monthly electricity consumption for the examined configurations

## 5. CONCLUSIONS

The objective of this study is the energy and financial investigation of a solar-powered absorption chiller integration into a CO<sub>2</sub> commercial refrigeration system, by means of subcooling in the main CO<sub>2</sub> cycle. Current analysis consists the theoretical approach of the actual implementation of the proposed energy saving configuration in the real refrigeration plant of the examined supermarket in the near future. The most important conclusions of this work are summarized below:

- Greater collector areas leads to higher energy saving rates, which can results up to 9.5% lower annual power consumption for the case of 200 m<sup>2</sup>. However, financial evaluation 100 m<sup>2</sup> with 60kW of absorption chiller capacity is the optimum case, which corresponds to net present value of 44.75 k€ and approximately 8.4 years payback period.
- The proposed topology for the optimum case is more efficient compared to the conventional booster system. Using real climatic data for the examined region, annual electricity savings are estimated at 8.12% which correspond to 27.45 MWh/year.
- The optimum case is also parametrically investigated in correlation to the ambient temperature in the range of 1-40°C. Results show that the proposed solution leads to maximum COP increment by 26.44% and 47.34% for the cases of low and high solar radiation respectively.
- Higher energy saving rates are achieved during the summer period, since during the warmest months of the year both ambient temperature and solar radiation levels are higher. At the same time during that period solar produced heat exploitation in the absorption chiller is also higher.
- 

## ACKNOWLEDGMENTS

Authors would like to thank the Greek supermarket chain METRO S.A. for enabling access to its measuring configurations installed in its premises, as well as for the support to their research activity in general.

## REFERENCES

- [1] S. A. Tassou, Y. Ge, A. Hadaway, and D. Marriott, "Energy consumption and conservation in food retailing," *Appl. Therm. Eng.*, vol. 31, no. 2–3, pp. 147–156, 2011.
- [2] "European Commission. Regulation (EU) No 517/2014 of the European Parliament and of the Council of 16th April 2014 on fluorinated greenhouse gases and repealing Regulation (EC) No 842/2006," 2014.
- [3] D. Tsimpoukis *et al.*, "Energy and environmental investigation of R744 all-in-one configurations for refrigeration and heating / air conditioning needs of a supermarket," *J. Clean. Prod.*, vol. 279, p. 123234, 2021.
- [4] Z. Sun, C. Wang, Y. Liang, H. Sun, S. Liu, and B. Dai, "Theoretical study on a novel CO<sub>2</sub> Two-stage compression refrigeration system with parallel compression and solar absorption partial cascade refrigeration system," *Energy Convers. Manag.*, vol. 204, no. August, p. 112278, 2020.
- [5] M. Song, L. Wang, J. Yuan, Z. Wang, X. Li, and K. Liang, "Proposal and parametric study of solar absorption/dual compression hybrid refrigeration system for temperature and humidity independent control application," *Energy Convers. Manag.*, vol. 220, no. April, p. 113107, 2020.
- [6] E. Bellos, C. Tzivanidis, and K. Torosian, "Energetic, exergetic and financial evaluation of a solar driven trigeneration system," *Therm. Sci. Eng. Prog.*, vol. 7, pp. 99–106, 2018.
- [7] K. Mohammadi and J. G. McGowan, "A thermo-economic analysis of a combined cooling system for air conditioning and low to medium temperature refrigeration," *J. Clean. Prod.*, vol. 206, pp. 580–597, 2019.
- [8] E. Bellos and C. Tzivanidis, "Enhancing the performance of a CO<sub>2</sub> refrigeration system with the use of an absorption chiller," *Int. J. Refrig.*, vol. 108, pp. 37–52, 2019.
- [9] T. M. Mróz, "Thermodynamic and economic performance of the LiBr-H<sub>2</sub>O single stage absorption water chiller," *Appl.*

*Therm. Eng.*, vol. 26, no. 17–18, pp. 2103–2109, 2006.

- [10] S. Kalogirou, “The potential of solar industrial process heat applications,” *Appl. Energy*, vol. 76, no. 4, pp. 337–361, 2003.
- [11] E. Bellos, C. Tzivanidis, and K. A. Antonopoulos, “Exergetic, energetic and financial evaluation of a solar driven absorption cooling system with various collector types,” *Appl. Therm. Eng.*, vol. 102, pp. 749–759, 2016.
- [12] M. D. Chatzisideris, A. Laurent, G. C. Christoforidis, and F. C. Krebs, “Cost-competitiveness of organic photovoltaics for electricity self-consumption at residential buildings: A comparative study of Denmark and Greece under real market conditions,” *Appl. Energy*, vol. 208, no. September, pp. 471–479, 2017.
- [13] E. Bellos, M. G. Vrachopoulos, and C. Tzivanidis, “Energetic and exergetic investigation of a novel solar assisted mechanical compression refrigeration system,” *Energy Convers. Manag.*, vol. 147, pp. 1–18, 2017.
- [14] E. Bellos, C. Tzivanidis, K. Moschos, and K. A. Antonopoulos, “Energetic and financial evaluation of solar assisted heat pump space heating systems,” *Energy Convers. Manag.*, vol. 120, pp. 306–319, 2016.
- [15] T. Tsoutsos, J. Anagnostou, C. Pritchard, M. Karagiorgas, and D. Agoris, “Solar cooling technologies in Greece. An economic viability analysis,” *Appl. Therm. Eng.*, vol. 23, no. 11, pp. 1427–1439, 2003.
- [16] J. Bukoski, S. H. Gheewala, A. Mui, M. Smead, and S. Chirarattananon, “The life cycle assessment of a solar-assisted absorption chilling system in Bangkok, Thailand,” *Energy Build.*, vol. 72, pp. 150–156, 2014.
- [17] G. Mitsopoulos, E. Syngounas, D. Tsimpoukis, E. Bellos, C. Tzivanidis, and S. Anagnostatos, “Annual performance of a supermarket refrigeration system using different configurations with CO<sub>2</sub> refrigerant,” *Energy Convers. Manag. X*, vol. 1, no. January, p. 100006, 2019.



# DETERMINATION OF WIND ENERGY POTENTIAL AND EVALUATION OF THE FEASIBILITY ANALYSIS OF A WIND TURBINE VIA RETSCREEN FOR ÇERKEZKÖY, TURKEY

Ahmet Erhan AKAN

Namik Kemal University, Tekirdağ, Turkey, aeakan@nku.edu.tr, ORCID: 0000-0003-1806-7943

Aytac Perihan AKAN

Hacettepe University, Ankara, Turkey, apakan@hacettepe.edu.tr, ORCID: 0000-0003-4626-4741

*Cite this paper as:* Akan, AE, Akan, AP. Determination of wind energy potential and evaluation of the feasibility analysis of a wind turbine via RETScreen for Çerkezköy, Turkey. 9<sup>th</sup> Eur. Conf. Ren. Energy Sys. 21-23 April 2021, Istanbul, Turkey.

**Abstract:** In this study, the wind energy potential of Çerkezköy district of Tekirdağ province was investigated and the feasibility analysis of a 1.5 MW capacity wind turbine suitable for installation in the region was carried out with the RETScreen energy analysis program. According to the analysis of hourly wind data recorded by a meteorology station established in Çerkezköy, it was determined that the annual average wind speed for 10m altitude is 5.305 m/s and the dominant wind direction is between NE (45°) and ENE (67.5°). In addition, it has been determined that a 1.5 MW wind turbine would produce 4354 MWh of electrical energy annually, and this energy would contribute to 2012.1 tCO<sub>2</sub> equivalent greenhouse gas reduction annually. It has been determined that the investment to be made would pay for itself in 3.4 years and the energy production cost is 0.399 \$/kWh. This study is expected to give an idea considered for wind power plants to be built in Çerkezköy that is one of Turkey's largest industrial zone.

**Keywords:** Wind power, RETScreen, Weibull distribution, Moment method, Feasibility analysis.

© 2021 Published by ECRES

## 1. INTRODUCTION

Due to the continually increasing world population and developing technology, the demand for energy is of an increasing trend every passing day in order to meet needs of human beings. If the requirement of this energy continues to be met from fossil-based fuels, it is estimated that irreversible ecological effects would occur. For this reason, usage of renewable energy sources instead of fossil fuels to produce the energy has receiving intense attention in the recent decades. Correspondingly, wind has an important share among the frequently preferred renewable energy sources in the world. Although Turkey is among the countries with high wind energy potential, its usable wind energy potential is so low owing to the high cost of wind energy systems [1]. In the literature, there are some studies related to determination of wind energy potential in Turkey and investigation of usage of this potential more effectively. In a study conducted by Yiğit and Kabul (2014) the cost analysis of meeting the electrical energy need of a house in Isparta with a 5 kW wind turbine was made and the payback period of the investment was determined as 11 years [2]. Öner and coworkers (2013) investigated the wind energy potential of İntepe region of Çanakkale, Turkey. They found that the annual average wind speed in the region studied was 4.26 m/s and power density was 115.5 W/m<sup>2</sup> [3]. In a study conducted by Aslan (2018), the wind energy potential of Balıkesir province was investigated and a comparison was economically made between the turbines that could be used in the region. In his study, He used Weibull and Rayleigh probability density functions to obtain wind velocity distribution curves. He stated that the best performance was obtained with Vestas V90 turbine in Akçalde location [4]. In a study conducted by Bayramoğlu (2018), the renewable energy potential and its effects for Bayburt province were investigated. As a result of the study, it has been determined that the total theoretical potential of the studied region is 115281 MW, but only a small part of the total theoretical potential, such as 11%, is usable [5]. Mamur and Karayel (2018) investigated the wind energy potential of Havza district of Samsun province. According to the

results obtained from the study, it was determined that the average wind speed at 80 m tower height is 4.9 m/s. Accordingly the results, it has been concluded that the region examined is not suitable for large wind turbine investments [6]. As it can be understood from the existing studies in the literature, a few of which are mentioned here, investigations on this subject focus on the determination of the wind energy potentials of the studied regions. The wind energy potential of Çerkezköy district of Tekirdağ province that has a key role in the industrialization of Turkey was investigated and also feasibility analyses including energy, economic and environmental factors of a wind turbine selected as a suitable for the energy potential were carried out in the present work. In this respect, it is thought that this study would guide the investments to be made in the region studied and would also provide complementary benefits for the literature.

## 2. MATERIAL AND METHOD

### Çerkezköy, studied region

Çerkezköy district of Tekirdağ province is one of Turkey's largest industrial district. Especially in the occurrence of its east and south districts, Çatalca and Silivri districts of Istanbul, is among the factors accelerating the industrialization of this district. In the district, electrical energies of 340 million kWh for industry and 102 million kWh for cities and residences were consumed [7]. Considering the amount of electrical energy consumed in terms of energy efficiency and environmental health, it is clearly seen that this district should be supported by renewable energy resources. As of now, there are two wind power plants constructed in Çerkezköy district. The first of these is Saray RES with a capacity of 4 MW and the second is Derby wind power plant with a capacity of 0.8 MW [8].

### Wind data

The wind data used in the study consists of the data recorded by the meteorology station established and working actively in Çerkezköy district. The coordinates of the meteorology station are E-279196, N-412607 and its altitude is 160m. Data including years between 2015 and 2018 as hourly were obtained from Turkish State Meteorological Service for 10m altitude.

### Weibull and Rayleigh distribution functions

Probability density functions are used to determine the wind potential in a region. Because, when it is desired to determine the wind potential of the region to be examined, it requires at least ten-year wind data of that region [9]. Especially for regions where long-term wind data are not available, wind potential can be determined using one-year wind data and various statistical methods. The most frequently used statistical methods in wind potential research are Weibull and Rayleigh distributions. The Weibull distribution is a two-parameter distribution, namely scale and shape parameters. Rayleigh parameter is a special example of the Weibull distribution where the shape parameter (k) is 2 [4, 10]. The general expression of the two-parameter Weibull distribution is given in Eq. [1] [11-13].

$$f_w(v) = \frac{k}{c} \left(\frac{v}{c}\right)^{k-1} \exp\left[-\left(\frac{v}{c}\right)^k\right] \quad (1)$$

In Eq. [1], v is the wind speed, c is the Weibull scale parameter, and k is the Weibull shape parameter. For the determination of Weibull parameters, the moment method using average wind speed and standard deviation values was used [14]. Accordingly, the equations giving Weibull parameters k and c are given in Eqs. [2-3].

$$k = \left(\frac{\sigma}{v_m}\right)^{-1.086} \quad 1 \leq k \leq 10 \quad (2)$$

$$c = \frac{v_m}{\Gamma(1 + 1/k)} \quad (3)$$

In the equations, mean velocity refers to the standard deviation. Mean speed and standard deviation are found with the help of Eqs. [4-5].

$$v_m = \frac{1}{n} \left[ \sum_{i=1}^n v_i \right] \quad (4)$$

$$\sigma = \left[ \frac{1}{n-1} \sum_{i=1}^n (v_i - v_m)^2 \right]^{1/2} \quad (5)$$

In the equations, n represents the number of wind measurements. Also, the term  $\Gamma$  given in Eq. [3] is the gamma function. The approximate value of the gamma function is calculated with the help of Eq. [6] or Eq. [7] if the terms k and c are known [9].

$$v_m \cong 0.886 c \Rightarrow \Gamma = \frac{v_m}{c(1 + 1/k)} \quad (6)$$

or

$$c = \frac{2}{\sqrt{\pi}} v_m \cong 1.128 v_m \Rightarrow \Gamma = \frac{v_m}{c(1 + 1/k)} \quad (7)$$

Rayleigh distribution can be calculated using Eq. [8] [4].

$$f_R(v) = \frac{\pi v}{2v_m^2} \exp \left[ -\left(\frac{\pi}{4}\right) \left(\frac{v}{v_m}\right)^2 \right] \quad (8)$$

### Energy analysis

One of the important features affecting the performance of wind turbines is the power values generated by the turbine at different wind speeds [9]. When the wind turbine power curve and the blowing times of wind speeds are grouped and combined, the total amount of electrical energy that can be produced by the wind turbine can be found [9]. The wind power potential of a wind turbine with wing sweep area A at velocity v is given in Eq. [9].

$$P_{(v)} = \frac{1}{2} \rho A v^3 \quad (9)$$

Mean power density for Weibull distribution can be calculated using Eq. [10] [4].

$$\frac{P_w}{A} = \frac{1}{2} \rho c^3 \Gamma \left( 1 + \frac{3}{k} \right) \quad (10)$$

In Eqs. [9-10],  $\rho$  is the density of air. In the current study, the density of air was taken as  $1.225 \text{ kg/m}^3$ .

### Feasibility analysis with RETScreen

The energy capacity, cost, emission reduction and financial values of a wind turbine that would be installed in Çerkezköy have been evaluated through the RETScreen program. Technical characteristics of the turbine are given in Table 1.

Table 1. Technical characteristics of selected wind turbine

Brand	Sinovel		
Model	SL 1500 / 77 - 100m		
Capacity(kW)	1500	Wind shear force	0.14
Height of connection point (m)	100	Sequence losses	2%
Rotor diameter (m)	77.4	Wing losses	5%
Area screening by wings ( $\text{m}^2$ )	4705	Various losses	4%
Global wind atlas 100 m (wind speed, m)	7.17	Usability	95%
Average ambient temperature and pressure ( $^{\circ}\text{C}$ , bar)	14.1, 1	Capacity factor	32.2%

### 3. FINDINGS AND DISCUSSION

According to the findings obtained from analyses, the graph created by the mean monthly data of wind speed between 2015-2018 is presented in Figure 1.

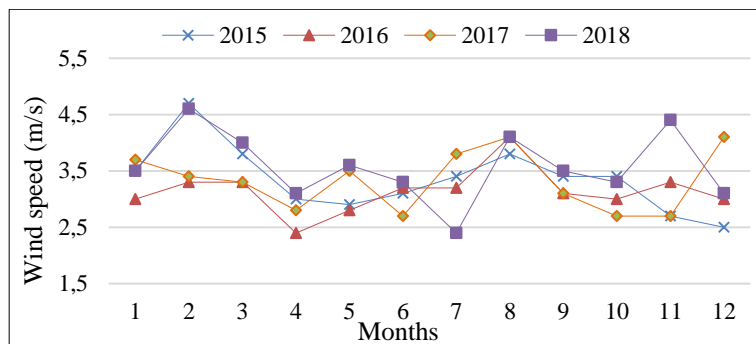


Figure 16. Monthly distribution of average wind in year of 2015-2018

When Figure 1 is examined, it is seen that the month with the highest monthly average wind speed is February and the month with the lowest one is April. When it is seasonally evaluated, it has been determined that wind speeds in spring are lower than those in summer and winter.

With the help of hourly wind data obtained and the relevant formulas given in Section 2, the average wind speed and Weibull parameters of Çerkezköy were calculated and these are presented in Table 2.

Table 2. Estimations for parameter, speed and power between 2015 and 2018

k	c	v <sub>m</sub> (m/s)	σ (m/s)	V <sub>mod</sub> (m/s)	V <sub>max</sub> (m/s)
2.482	5.984	5.305	2.297	4.861	7.592

Table 2 shows that the average wind speed of Çerkezköy is 5.305 m/s, the Weibull shape parameter is 2.482, the scale parameter is 5.984 and the standard deviation is 2.297 m/s. The fact that the standard deviation value is in the range of 0-3 m/s indicates that the wind regime in the studied region is regular.

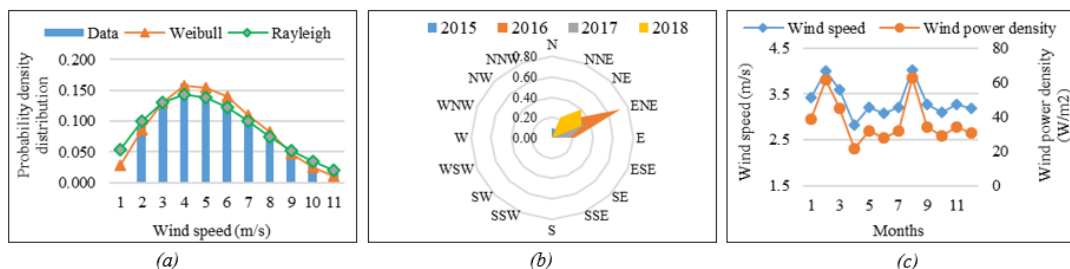


Figure 2. (a) Comparison of Weibull, Rayleigh and Measurement data, (b) 4-year dominant wind directions and their ratio to all blow numbers, (c) Monthly variation in wind speed and wind power density.

In Figure 2 (a), the frequency distributions of hourly wind speed data between 2015-2018 obtained from Turkish State Meteorological Service are compared with the Weibull and Rayleigh probability distributions. When the Weibull and Rayleigh probability distributions are compared, it can be seen that the Weibull distribution shows results more suitable for the frequency distribution of the real data. In addition, it can be seen that the wind velocity in the studied area mainly blows at speeds between 4-5 m/s. Figure 2 (b) shows the wind rose drawn by using the data generated by the monthly prevailing winds between 2015 and 2018 and the rates of all blow numbers for Çerkezköy. It can be seen from the Figure that the dominant wind direction is between NE ( $45^0$ ) and ENE ( $67.5^0$ ). In Figure 2 (c), the graph of wind speed and wind power density is given. The highest wind power density was reached in February and August with values of 61.56 and 62.73 W/m<sup>2</sup>, respectively. The lowest power potential was realized in April with a value of 21.68 W/m<sup>2</sup>.

### RETScreen feasibility analysis

In the choice of wind turbine that would be installed in Çerkezköy, most preferably wind turbine of Sinovel brand, one of the brand in Turkey, SL 1500/77 - 100 model was chosen and the specifications of the wind turbine are given in Table 1. The technical and financial information required for the wind turbine was obtained from the RETScreen software.

## Energy analysis

As a result of the energy analysis, it was determined that the wind turbine with a capacity of 1500 kW can produce 4354 MWh of electricity annually.

## Cost analysis

Findings from cost analysis are given in Table 3.

*Table 3. Costs and savings*

Initial costs (\$)		Annual savings and revenue (\$)		
Feasibility study and development	80000+80000=160,000	Electricity revenue	export	486,787
Engineering services	150,000	Greenhouse reduction revenue	gas	803
Electrical system	164,000	Clean energy generation revenue		194,715
System balance and others	361,575	Other revenues		23,200
Total initial costs	2,311,575	Total		705,505
Annual costs and debts	241,500	Greenhouse reduction cost	gas	0.70 \$/tCO <sub>2</sub>
Total for the first year	2,553,075	Clean energy generation cost		0.08 \$/kWh

## Emission analysis

The greenhouse gas equivalent reduction amounts to be obtained by operating the wind turbine are given in Table 4 by comparing them with different elements.

*Table 4. Emission reduction potentials*

GHG Emission reduction (tCO <sub>2</sub> )	Unconsumed benzine (lt)	Unconsumed raw petrol (barrel)	Recovered waste (tonne)	Unused and cars (number)	tracks
2,012.1	864,560.1	4,679.4	693.8	368.5	

## Financial sustainability

Financial sustainability analysis results of the wind turbine are given in Table 5.

*Table 5. Financial sustainability analyses*

Simple payback period (year)	3.3	Cost benefit ratio	4.5
Equity payback period (year)	3.4	Debt payback ratio	28.2
Net Present Value(\$)	12,057,789	Greenhouse gas reduction cost (\$/tCO <sub>2</sub> )	-643
Annual life cycle savings (\$/year)	1,320,888	Energy generation cost (\$/kWh)	0.399

## 4. CONCLUSIONS

In this study, the wind energy potential of Çerkezköy district of Tekirdağ province was investigated and the feasibility analysis of a wind turbine that would be installed in the region was carried out. The results obtained are as follows:

1- The monthly average wind speed of Çerkezköy is 5.305 m/s. The highest wind speeds are seen in February, and the lowest ones are in April. In general, it has been determined that wind speeds decrease in Spring.

2- As a result of the analysis, it was determined that the Weibull shape parameter, the scale parameter and standard deviation were 2.482, 5.984 and 2.297, respectively.

3- It has been determined that the dominant wind direction for Çerkezköy is between NE (45°) and ENE (67.5°). In addition, it has been found that the most common wind speed in the region varies between 4 and 5 m/s. This phenomenon is proved by the V<sub>mod</sub> value of 4.861 obtained from calculations.

4- According to the feasibility analysis for a 1.5 MW turbine with 100m connection height, it was found that an initial investment cost of \$ 2,311,575 was required, and the annual maintenance and other costs were \$ 241,500. In

addition, it has been determined that if the wind turbine is installed, it would pay for itself within 3.4 years thanks to revenue it would provide.

5- In case of the operation of the wind turbine, it has been determined that 2012.1 tCO<sub>2</sub> equivalent greenhouse gas reduction would be realized annually, and 40242 tCO<sub>2</sub> equivalent greenhouse gas emission reduction would be achieved when the 20-year lifetime for the enterprise is considered.

6- It has been determined that the wind turbine will generate 4354 MWh of electricity annually, resulting in an annual electricity export revenue of \$ 579,076.

## REFERENCES

- [1] Şanlı, BG, Günöz A. Feasibility analyses and comparisons of wind power plants located in different regions of Mersin by using RETScreen program. Erzincan University, Journal of Science and Technology, 2018, 11(3), 478-487. DOI: 10.18185/erzifbed.420365.
- [2] Yiğit, F, Kabul, A. Economic analysis of utilizing wind energy to supply electricity demand of a domicile in Isparta region. Electronic Journal of Machine Technologies, 2014, 11(2), 1-9.  
<<https://app.trdizin.gov.tr/makale/TVRReU1UWTFOUT09/isparta-yoresinde-bir-evin-elektrik-ihitiyacinin-ruzgar-enerjisi-ile-karsilanmasinin-ekonomik-analizi->>
- [3] Öner, Y, Özçira, S, Bekiroğlu, N, Şenol İ. A comparative analysis of wind power density prediction methods for Çanakkale, Intepe region, Turkey, Renewable and Sustainable Energy Reviews, 2013, 23, 491-502.  
DOI: <https://doi.org/10.1016/j.rser.2013.01.052>
- [4] Aslan, A. Investigation of Balikesir wind energy potential and comparison of the turbines based on the economical analysis, Journal of Thermal Science and Technology, 2018, 38(1), 25-41 <<https://dergipark.org.tr/tr/download/article-file/1247213>>
- [5] Bayramoğlu, T. Renewable energy potential and effects: Bayburt sample, Journal of Business Economics and Management Research, 2018, 1, 1, 1-16 <<https://dergipark.org.tr/tr/pub/baybem/issue/32845/377870>>
- [6] Mamur, H, Karayel, M. Evaluation of wind energy potential in Havza-Samsun, Turkey. Omer Halisdemir University Journal of Engineering Sciences, 2018, 7 (1), 316-323 <<https://dergipark.org.tr/tr/download/article-file/414999>>
- [7] Çerkezköy, <http://www.cerkezkoy.bel.tr/cerkezkoy/ekonomi/>, erişim 11.02.2021
- [8] Çerkezköy'deki rüzgar enerjisi santralleri, <https://www.enerjiatlasi.com/ruzgar-enerjisi-haritasi/tekirdag>, erişim 11.02.2021
- [9] Arıkan, Y, Çam, E. Implementation of feasibility analysis of wind and solar energy on the web base, International Journal of Engineering Research and Development, 2017, 9 (1), 1-10, <<https://doi.org/10.29137/umagd.346161>>
- [10] Johnson GL. Wind energy systems. Manhattan, KS. Electronic edition, 2001.
- [11] Haralambopoulos, DA. Analysis of wind characteristics and potential in the east Mediterranean-the Lesvos Case. Renewable Energy, 1995, 6, 445-454, <[https://doi.org/10.1016/0960-1481\(94\)00073-F](https://doi.org/10.1016/0960-1481(94)00073-F)>
- [12] Akpinar, EK, Akpinar, S. Determination of the wind energy potential for Maden-Elazığ, Turkey, Energy Conversion and Management, 2004, 45, 2901-2914, <<https://doi.org/10.1016/j.enconman.2003.12.016>>
- [13] Ülgen, K, Hepbasli, A. Determination of Weibull parameters for wind energy analysis of İzmir, Turkey, International Journal of Energy Research, 2002, 26, 495-506, <<https://doi.org/10.1002/er.798>>
- [14] Mohammadi, K, Mostafaeipour, A. Using different methods for comprehensive study of wind turbine utilization in Zarrineh, Iran, Energy Conversion and Management, 2013a, 65, 463-470, <<https://doi.org/10.1016/>



# TECHNOLOGICAL ECOVILLAGES: AUTO SUSTAINABLE URBAN PILOTS IN THE COMMUNITY OF LLUCANAYACU IN CHAZUTA, SAN MARTIN, PERU.

Bartra Gardini Gumercindo

Pontifical Catholic University of Peru, Lima, Peru, gbartra@pucp.edu.pe, ORCID: 0000-0002-4307-1285

Pastrana Diaz Nerida del Carmen

National University Hermilio Valdizan, Huanuco, Peru, ncpastranad@unheval.edu.pe, ORCID: 0000-0001-8357-3012

Fu Pastrana Enzo Yen Gen

Ricardo Palma University, Lima, Peru, enzofu@hotmail.com, ORCID: 0000-0002-7799-6315

Cite this paper as:

*Gumercindo, BG, Pastrana Diaz, NC, Enzo Yen Gen, FP. Technological ecovillages: Auto sustainable urban pilots in the community of Llucanayacu in Chazuta, San Martin, Peru. 9<sup>th</sup> Eur. Conf. Ren. Energy Sys. 21-23 April 2021, Istanbul, Turkey*

---

**Abstract:**

This work aims to propose the design of a technological ecovillage, as a self-sustainable architectural urban pilot in the Community of Llucanayacu. The methodology was divided into three parts: the political, social, cultural and economic situation of the Chazuta district was analyzed at a macro level, including the urban situation and its chronological evolution [1], the design principles were established: strategies, energy efficiency, materiality, maintenance and reuse, bioclimatic challenges of the tropical rainforest, incidence of the sun, air speed and water flow, main sources of renewable energy [2] and the Urban Master Plan [3] was drawn up. The results indicate that the growth of the community occurs without professional guidance, causing an uncontrolled urban expansion without planning. The self-sustainable urban pilot was designed, bioclimatic housing for residence, tourist accommodation and agrotourism, a telecentre, to connect the community with the world through technology, drinking water systems, photovoltaic solar energy, complementary educational, health and vernacular medicine, common areas and recreation. It is concluded that the prototype of a sustainable architectural urban pilot will improve living conditions, promote tourism and community activities as means of economic development. A design guide is proposed for the future sustainable urban and architectural expansion of the community.

---

**Keywords:**

*Ecovillages, Urban pilots, Renewable Energy, Design principles, Sustainability*

---

© 2021 Published by ECRES

## 1. INTRODUCTION

This research proposes a self-sustaining urban pilot in Llucanayacu. A prototype of a technological and ecological nature, with social, cultural and economic skills, which will generate sustainable development. This community is suspended in time and space as an anachronism in the face of the new challenges that urban cities present today [4]. The lack of interest of the government, the lack of knowledge of the residents and authorities, the disinterest of society, the lack of urban planning that generates a negative growth expansion, the lack of project proposals for the development of the area, the lack of a professional technical guide, basic services like water, sewage, health equipment, education, housing, access roads and economic infrastructure, is an epithet of these communities. Without planning they will continue to expand chaotically, without intervention, these communities limit their personal, professional, and technical aspirations, for not having development opportunities to improve their living conditions. We are not looking to bring the "big cities", we are looking to take this community to them through new urban methods and planned infrastructure technologies [5]. This project proposes a manual for self-sustaining urban pilots, a guide for future growth and progress in social, economic, cultural and infrastructure fields towards small villages [2] [6]. We focus on a prototype of urban planning, considering key elements and instruments to form an

image of a city in a rural area, to be remembered and cause delight, becoming a priority when projecting it, "a construction in space, but one in a large scale, something perceived over long periods. Urbanism is, therefore, a temporary art" [7] and a pilot of "the garden city" designed for a healthy life, with limited growth and surrounded by green areas and rural communities [8], in Peru, the ecovillage approach is non-existent, in other countries they incorporate them as an alternative solution in the urban part, considering their economic and social cultural activities, the research work provides a bioclimatic design adapted in a low tropical rainforest area with high cultural diversity (medicinal plants, fauna, flora, customs, superstitions, crafts, among others). The research proposes a sustainable urban and architectural pilot, which will help to improve the living conditions of the community, promoting various activities that generate growth, for this purpose, the design deficiencies from urban planning to architectural planning are identified, sociocultural factors of the community are recognized and applied to the proposal. [9] It's applied, as the basis of design criteria, renewable energy, digital and ecological designs and prioritizing the self-sustainability of the project. The lack of community equipment is planned and designed, and, in the housing modules, the existing tourism theme is promoted, making this a design criterion when proposing housing prototypes and public equipment. Similarly, a design guide for the community and its future expansion is proposed. The research was structured as follows: abstract, introduction, methodology, Results and Conclusion. It concludes in the self-sustainable proposal of a sustainable urban and architectural pilot in Llucanayacu considering the socio-cultural factors of the community, the same ones that were used as the basis of the design principles: design strategies, energy efficiency, materiality, maintenance, and reuse, prioritizing the self-sustainability of the project. Llucanayacu, chosen to implement this urban prototype and its subsequent articulation with nearby communities, chosen to be a pioneer in this "Copernican Revolution" and change the idea of centralized urban progress, to be an agent of change, a rural pilot to replicate in tropical rainforest areas and anywhere in Peru that has similar conditions. The methodology that was followed for the development of the research was based on the choice of a case study: Llucanayacu Community. The applied methodology was divided into three parts. The first part focused on analyzing the social, cultural, and economic situation of the district Chazuta as a macro level, ergo, the community as a more detailed factor. The second one was to set design principles according to the bioclimate challenges of the region, as well as its methods of construction and its way to an auto sustainable urban pilot) [6]. The third one was the elaboration of the urban Master Plan [7]. The prototype of a sustainable architectural urban pilot was carried out taking into consideration criteria of bioclimatic design, sociocultural factors, lacks and needs of the community, promoting tourism and communal activities as means of economic development [10]. With all this in mind, we can say that the lack of bioclimatic design in homes was identified, lack of planning, development, and equipment services to meet the basic needs of the community. In order to vertebrate this project, five design criteria were defined: design strategies, energy efficiency, materiality, maintenance and reuse. The design guide for the future expansion of the community from the sustainable urban and architectural point of view was developed.

## **2. METHODOLOGY**

In order to plan a technological ecovillage as an auto sustainable urban pilot in this community, we had to divide the process in three parts. Taking in the fact that the project has the urban planning and the architectural design, but this will be detailed and included in the three sections: The first one is to analyze the political, social, cultural and economic situation of the district Chazuta as a macro level, ergo, the community as a more detailed factor. This includes the current urban situations and its chronological evolution [1]. The architectural analysis will be in the studies to the different urban equipment (education, health, commerce, residence, etc.). The second one is to set design principles according to the bioclimate challenges of the region, as well as its methods of construction and its way to an auto sustainable urban pilot [6]. The third one will be the elaboration of the urban Master Plan [3]. This will have the elaboration of the equipment and its architectural prototypes.

The type of research is descriptive; the approach is qualitative.

## **3. RESULTS**

Currently, the town of Llucanayacu, has the system of water supply treated by gravity, captured from one of the streams that runs near the town. However, the indiscriminate felling of the forests has caused a drastic decrease in the flow of water from the streams, which causes discomfort in the population due to the appearance of parasitic and gastrointestinal and dermal diseases, being the most affected, children under Age and pregnant mothers. To solve the problem, the design of a potable water and drainage system for the town of Llucanayacu is proposed, as well as the installation of basic sanitation units (BSU), for a population of 178 people.

The drinking water system includes collection elements, by means of a pump submerged in the bed of the Llucanayacu stream, activated with solar energy, with a barking system to facilitate the collection at times of dryness and keep it at 0.61 lt / sec. Enough to supply the entire population in times of maximum daily consumption. A reinforced concrete reservoir of 15 m<sup>3</sup> capacity, for collection, then the adduction line, another 20m<sup>3</sup> reservoir for water treatment and the piping system for the distribution network of drinking water to each of the local homes. A settler with reinforced concrete structure will be used, whose purpose is to separate the sediments and prevent entry into the conduction line. Slow filter to eliminate water turbidity, but if it is designed and operated conveniently it can be considered as a water disinfection system. Slow filtration consists of a set of physical and biological processes that destroy pathogenic microorganisms in water. This constitutes a clean technology that purifies water without creating an additional source of pollution for the environment. The structure will have a waterproof inner lining, both on walls and floors. The shape will be cylindrical and will allow to store 15 m<sup>3</sup> of water. For household connections, it has been considered to provide water directly to each of the houses in the town of Llucanayacu, with the installation of 35 household connections with PVC-1/2 pipes.

BSU System (Basic Sanitation Unit), 35 systems of basic sanitation units (latrines with urine separators and 2 composting chambers) will be installed.

The water and drainage system are complemented, through health education workshops to improve and greatly reduce the different diseases that have arisen from consuming water without being treated.

Solar energy is one of the sources of life and the origin of most other known forms of energy. By using solar collectors, solar energy can be transformed into thermal energy. In turn, with the use of photovoltaic panels, light energy can be transformed into electrical energy. An important advantage of solar energy is that it allows the generation of energy in the same place of consumption through architectural integration. Within the components of a solar energy system, the solar panel is the main component of all types of photovoltaic systems, responsible for transforming solar radiation into electrical energy through the photoelectric effect. They are made mainly by semiconductors (silicon) mono-crystalline or poly-crystalline. These are characterized by their nominal power or maximum power that this panel can generate under ideal conditions (radiation of 1kW / m<sup>2</sup> and temperature of 25°C). The other component is the Charge Regulator, which efficiently manages the energy to the batteries, prolonging its useful life, protecting the system from overload and over-discharges. The battery or accumulator receives the regulated electrical energy of the panels. The battery stores the electricity to be able to use it at another time, the capacity to store energy is measured in Amps hour (Ah). The inverter converts the direct current and low voltage (12v or 24v typically) from the batteries or controller into alternating current, in the case of Peru 220 Volts, in a simplified way it can be said that it transforms the direct current into an outlet conventional. Its capacity is measured in power (Watts), which is calculated as the voltage per current ( $P = VI$ ). It corresponds to the maximum demand of power of the equipment to be connected. This component can be dispensed with when the equipment to be connected can be powered by direct current. As is the case with some types of lighting, spotlights, television, radio and other equipment such as cell phone chargers, thanks to the energy stored in the panels during the day. A photovoltaic solar energy system must be designed to withstand constant weather, thermal expansions for at least 25 years.

For the community of Llucanayacu, it is proposed to implement a Telecentre, in the community center, which will serve as a meeting place for the inhabitants, and it is also the training center for teaching various workshops on the environment, agriculture, ecology, enterprises; and it has Internet booths composed of 10 computers to search for information related to the activities they carry out in the community and place their products in the globalized world [11] [12] [13] [14].

The Telecentre, as a proposal, is a conic structure made of a thatched roof (made of Yarina palms) called "maloca"; a place to share with the community. In it, social issues are exposed and managed, to face them and learn to handle them. It has circular stands for communal meetings. The maloca has a circular plan design with conic roof structure with big gaps, allowing the indirect entry of sun light and the circulation of the indoor air to keep it cool. An omnidirectional antenna is installed on the top of the roof, which allows access to the Internet through a wireless Wi-Fi network, to all residents from their homes and surroundings to the community, using mobile devices.

The main antenna of the maloca is connected to the fiber optic network point to the Chazuta district, through a point-to-point wireless link.



Figure 1: Telecentre in the Community of Llucanayacu

The inclination of the roof ( $45^\circ$ ) allows the water to slide quickly through it in the rainy season and does not penetrate inside.

For the community of Llucanayacu, it is proposed to implement an agricultural technical education, from the initial and primary levels, so that children recognize the true value of living in harmony with nature and the environment. The technical workshops range from planting a seed, to planting trees and vegetables, as well as raising domestic animals. For the complementary education, the percentage of content appropriate to the socio-cultural reality of each community is used and respecting its high diversity [15].

For the community of Llucanayacu, it is proposed to implement a medical post, for health care, which are strongly linked to the use of vernacular medicinal plants. In Llucanayacu, there is presence of healers, who are highly valued in the region and abroad, people with knowledge of herbal remedies, which indicates a vital connection with the land and natural resources.

In the community of Llucanayacu, it is proposed to prepare and implement 35 homes, in addition to recreation areas and community areas. According to the principles of Permaculture there will be an area equal to that destined for housing, for the cultivation of food and another third for recreation areas and forests. The proposed community facilities include: Natural amusement park for children, sports courts, communal bakery, communal shop, communal fair for agricultural products and handicrafts, fish farms, cabins for tourist accommodation, area of technical workshops, agricultural and crafts.

In Llucanayacu is an ideal prototype. Adjusted to coexistence factors, resource utilization and its economic potential. The design strategies will be detailed in the next graphics and explanations.

We can appreciate, in the image above, the prototype of the house. An SE-NW aerial view. Taking in fact the cover of it: a roof with an interwoven of Yarina palm leaves over a wood beam structure. On the top goes the solar panels, to be precise, over the theatine meant for ventilation and heat control. We can see how the solar geometry shows how it will hit over the prototype surfaces, in this case, we used a specific day and hour, being September 20th at 12:30 p.m. The cover works in a passive solar architecture design as a method of design and the airflow from the predominant winds coming from the north help to cool down the house.

Using the nature as a friendly constructive method and design fundament helps a lot. Protecting the house from direct solar incidence and, in case there is a lot of dirt going with the wind, they purify it.

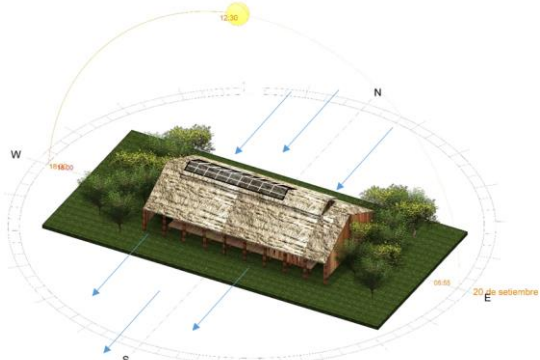


Figure 2: Residential Prototype

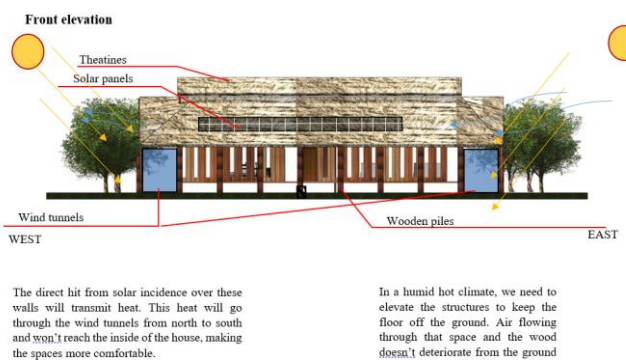


Figure 3. Frontal Elevation

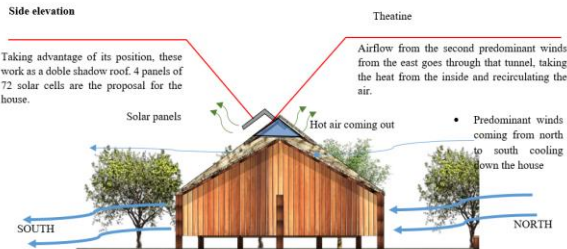


Figure 4. Side l Elevation

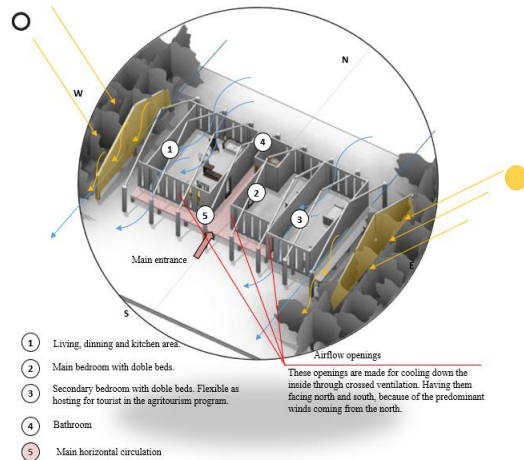


Figure 5: Aerial Distribution View

## CONCLUSIONS

It is concluded that the growth of the community occurs without professional or technical guidance, causing an uncontrolled urban expansion without planning. The proposal of the efficient urban prototype will allow a self-sustainable operation of the community, the same that can be articulated with all the surrounding communities, with the purpose of helping to reduce entropy in Llucanayacu and extend to other similar places where this pilot can be adapted to the different realities that regions may have.

The design principles of the sustainable architectural urban pilot prototype incorporate design strategies, energy efficiency, materiality, maintenance and reuse, bioclimatic challenges of the tropical forest, incidence of sun, air velocity and water flow, as main sources of renewable energy, which allows improving living conditions, promoting tourism and community activities as a means of economic development.

The Urban Master Plan was designed, a self-sustainable urban pilot, which incorporates: bioclimatic housing for residential use, tourist accommodation and agrotourism; a telecentre, to connect the community with the world through Internet technology, drinking water, photovoltaic solar energy system, educational system complementary to the Plan of the Ministry of Education, related to agricultural activities, health system with vernacular medicine, common areas for community fairs and recreation areas.

## ACKNOWLEDGMENTS

The design guide will allow the future expansion of the community in a planned manner from an urban and architectural sustainable point of view, for which its implementation is recommended.

## REFERENCES

- [1] PCM, «distrito.pe,» 10 December 2019. [En línea]. Available: <https://www.distrito.pe/distrito-chazuta.html>. [Último acceso: 10 December 2019].

- [2] Wieser, M. Cuadernos 14. Arquitectura y ciudad. Consideraciones Bioclimáticas en el diseño arquitectónico: El caso peruano. Cuadernos de Arquitectura (Edición digital N°10), Lima, 2011. (<http://departamento.pucp.edu.pe/arquitectura/files/2012/06/CUADERNOS-14-digi.pdf>)
- [3] Lynch, K. *The Image of the City*, Massachusetts: MIT Press, 1960.
- [4] Pérez, A. M. Chazuta y sus Saberes Maravillosos (Recopilación de testimonios). Gobierno Regional de San Martín, San Martín, Lima: Ministerio de Cultura, 2012.
- [5] Gobierno Regional de San Martín, «Mejoramiento y construcción de la carretera departamental SM-106; tramo Chazuta – Curiyacu. En el distrito de Chazuta, provincia de San Martín – San Martín (Estudio de factibilidad del proyecto),» Tarapoto, 2014.
- [6] Wieser, M. Arquitectura y ciudad. Consideraciones Bioclimáticas en el diseño arquitectónico: El caso peruano. Lima, 2011. <http://repositorio.pucp.edu.pe/index/handle/123456789/28699>
- [7] Lynch, K. *La Imagen de la Ciudad*, vol. 3ra. Edición, Barcelona: GG, 2015.
- [8] Ebenezer, H. *Ciudades Jardín del Mañana*. Madrid: Círculo de Bellas Artes, 2018.
- [9] Abdollah, B. D. Seyed R. E. y Elham, M. K. Bioclimatic design strategies: A guideline to enhance human thermal comfort in Cfa climate zones, Journal 1, 2019. <https://doi.org/10.1016/j.jobe.2019.100758>
- [10] González de Olarte, E. *Una economía incompleta. Perú 1950-2007: Análisis estructural*, Lima: Fondo editorial PUCP, 2016.
- [11] OSIPTEL. Memoria institucional de OSIPTEL. Lima: 2019. <https://www.osiptel.gob.pe/media/4xnp0pho/memoria-institucional-de-osiptel-2019-web.pdf>
- [12] ITU. Consideraciones sobre el FMPT: Banda ancha, Ginebra: Foro Mundial de Política de las Telecomunicaciones, 2013.
- [13] MTC. Base de datos sobre infraestructura de fibra óptica regional, Lima: Ministerio de Transportes y Comunicaciones, 2016.
- [14] MTC. Red Dorsal Nacional de Fibra Óptica. 2016. [En línea]. Available: [https://www.mtc.gob.pe/comunicaciones/concesiones/proyectos/red\\_dorsal.html](https://www.mtc.gob.pe/comunicaciones/concesiones/proyectos/red_dorsal.html).
- [15] Hargreaves, A. *Teaching in the Knowledge Society: Education in the age of insecurity*, United Kingdom: Open University Press, 2003.



# COMPUTATIONAL THERMAL-FLUID COUPLING ANALYSIS OF A VARIABLE NOZZLE TURBINE FOR SOLAR POWER GENERATION

Abdelmadjid Chehhat

Abbes Laghrour University, Science and Technology Faculty, Department of Mechanical Engineering, Khencela, 40000, Algeria, E-mail: [achehhat@gmail.com](mailto:achehhat@gmail.com), ORCID: 0000-0003-1088-253X

Arrif Toufik

Unité de Recherche Appliquée en Energies Renouvelables, URAER, Centre de Développement des Energies Renouvelables, CDER, 47133, Ghardaïa, Algérie, E-mail: [arrif.toufik@gmail.com](mailto:arrif.toufik@gmail.com), ORCID: 0000-0002-7113-3332

Mouna Maache

Abbes Laghrour University, Science and Technology Faculty, Department of Mechanical Engineering, Khencela, 40000, Algeria, E-mail: [mounamaache2019@gmail.com](mailto:mounamaache2019@gmail.com), ORCID: 0000-0002-6466-1719

Cite this paper as:

*Chehhat A., Arrif T. and Maache M. Computational thermal-fluid coupling analysis of a variable nozzle turbine for solar power generation. 9<sup>th</sup> Eur. Conf. Ren. Energy Sys. 21-23 April 2021, Istanbul, Turkey*

---

**Abstract:**

The high-speed flow inside turbo-compressor used in solar power generation is still complicated currently; thus accurate calculation of turbine inner flow profiles and prediction of performance characteristics has been of great importance. In this paper, a coupled simulation of turbulent flow and temperature field is performed on a typical variable nozzle radial turbine using computational fluid dynamics. The heat and flow field of turbine under two different inlet temperatures: 600, 800 K and different expansion ratio (ER): 3.1, 3.4, 3.7, 4, 4.2 and 4.5 are analyzed and the turbine performances are compared for different rotational speed: 50, 70 and 80 krpm. The CFD results show that these key parameters have significant influence on the turbine performances when varying the nozzle vane position. It could provide references for adapting the diesel engine turbocharger to mini solar power generation power plant as a turbo-expander.

---

**Keywords:**

*variable nozzle, radial turbine, fluid-heat coupling, expansion ratio*

---

© 2021 Published by ECRES

## 1. INTRODUCTION

Turbochargers represent an important technology for vehicles, and especially for diesel engines, for an internal combustion engine (ICE), the energy of the exhaust gas is almost 30-40% of the energy produced by the combustion in the cylinder, these exhaust gases are relax in the turbocharger turbine, turning the compressor mounted on the same shaft. This leads to increase the density of the intake air; the use of turbochargers allows downsizing the ICE in order to obtain a complete combustion, keeping the generated power unchanged, this technology minimizes the fuel consumption and reduces emissions production to comply with laws imposed by the ecological regulations [1]. For solar power generation needs, the turbocharger is used as a turbo-expander using high temperature fluid discharged from the solar receiver to drive the turbine to rotate at a high speed and drive the coaxial electric generator and the compressor [2] (figure 1). The significant use of the turbocharger in solar power generation will lead to the development of its components technology, indeed, this technology has been evolved enormously in recent years, from flat blades to blades with an aerodynamic geometry used in recent turbomachines, and another development of the turbine is the variable geometries VGT designed to increase boost pressure at low speeds, reduce response times, increase available torque, decrease the boost at high engine speeds to prevent over-boosting, reduce engine emissions, improve fuel economy and increase the overall turbocharger operating range [3], [4]. The use of variable nozzle turbocharger turbine for solar power generation was a subject of several research works.

Yixiong Liu et al. [5] investigated a detailed unsteady flow in a variable turbine nozzle for various opening position. It shown that several complex phenomenon such as shock wave in channel, leakage and mean stream appear in different regions at different positions. A.T. Simpson et al. [6] studied the effect of varying vanless space and vane solidity stator on the performance of radial turbine. CFD simulations are carried out and measurements of static pressure at stator inlet are achieved to optimize the solidity. Christos Kalathakis et al. [2] investigated a solar hybrid MGT based on turbocharger. Turbine inlet temperature and heliostat field size as a key parameters and their influence on the cycle performance is studied. It found that augmentation of the maximum temperature leads to better performance. The study on the complexity of heat, convection-heat coupling and the mechanism of thermal power conversion is far from mature [7-10], so the flow field and temperature is of great significance, and the analysis of rotation of high-speed rotor also helps to enhance the service life of the turbocharger. Based on the CFD software, the flow field and temperature field distribution through a typical 1.4L diesel turbocharger (figure 2) were studied under two different inlet temperatures: 600, 800 K and different expansion ratio (ER): 3.1, 3.4, 3.7, 4, 4.2 and 4.5, the turbine performances are compared for different rotational speed: 50, 70 and 80 krpm.

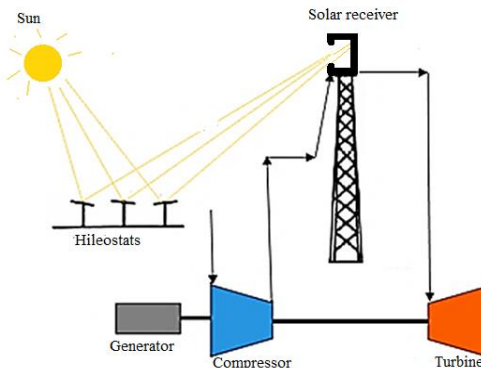


Figure 1: Electric power generation using turbocharger as a solar turbo-expander

## 2. RADIAL TURBINE GEOMETRIC MODEL

This model is a typical vehicle (1.4l engine) variable nozzle turbocharger, the geometry model and the main geometric parameters are shown in Figure 2. The turbine geometric data used in this work are grouped in table 1.

Table 1. Turbine Geometric data

Volute Geometric data	Dimension
Inlet diameter	$D_I = 100 \text{ mm}$
Inlet surface area	$S_I = 1782,8 \text{ mm}^2$
Outlet surface area	$S_2 = 1041,1 \text{ mm}^2$
<i>Stator geometric data</i>	
Stator vane length	24 mm
Cross area at stator outlet	$429,36 \text{ mm}^2$
Inlet angle	$0^\circ$
Outlet angle	$-50^\circ$
Stator vane number	9
<i>rotor geometric data</i>	
Shroud outlet diameter	0,015mm
Hub outlet diameter	0,005mm
Inlet blade angle	$0^\circ$
Outlet blade angle	$70^\circ$
Blades number	11

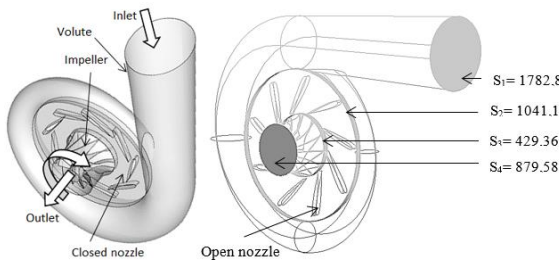


Figure 2. Variable nozzle turbine model and geometric data

### 3. COMPUTATIONAL DOMAIN AND GRID

In this paper, the calculation domain consists of three parts: the volute, the variable nozzle stator and the impeller (rotor). The grid is generated in GAMBIT as a tetrahedron grid then it is imported to Fluent solver and converted to a polyhedral grid as shown in (figure.3) when the volute, the impeller and the distributor (nozzle) were discretized by polyhedral control volumes regarding the complex geometry found in current studied turbine stage [7]. The calculation of the overall grid quality is good, 1516501 elements is the global computational domain grid element number and the grid number has no significant effect on the calculation results.

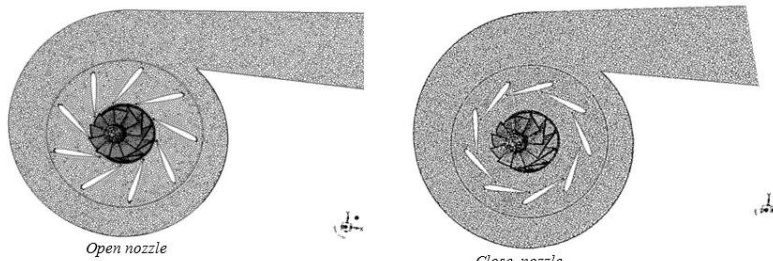


Figure 3. Grid of computational domain

### 5. BOUNDARY CONDITIONS AND SOLUTION CONTROL

The working fluid volume is selected as ideal gas close to the exhaust gas of diesel engine, the cell zone condition for the impeller is a rotating coordinate system adopting the MRF technic, and the other computational domain parts are a fixed coordinate system. The convergence criteria of  $10^{-4}$  are used for all the governing equations. The minimum number of iterations is estimated so that the mass flow rate computed for the outlet cross section become unchanged at about 2000 iterations the convergence can be observed, but the mass flow rate become unchanged since about 200 iterations for each case of simulation. Set to the inlet temperature of 600 K and 800 K. In order to solve the relationship between expansion ratio and mass flow rate, by changing the inlet static pressure, six typical conditions point are considered, the inlet static pressure was 110, 120, 130, 140, 150 and 160 kPa with keeping pressure outlet as 35 kPa. The correspondent expansion ratios (ER) are: 3.1, 3.4, 3.7, 4, 4.2 and 4.5, by setting three conditions of the rotational speed: 50000, 70000 and 80000 r/min.

### 6. RESULTS AND DISCUSIONS

#### Turbine performances

The expansion ratio (figure 4), isentropic efficiency (figure 5) and power recovered by the turbine (figure 6) are studied for two nozzle vane positions (open and closed) and for two inlet temperatures 600 K and 800 K.

Isentropic efficiency of turbine  $\eta$  is given as:

$$\eta_{is} = \frac{1 - \frac{T_{02}}{T_{01}}}{1 - \left( \frac{P_{2s}}{P_{01}} \right)^{\frac{\gamma-1}{\gamma}}} \quad (1)$$

Where:  $T_{02}$  is the total temperature at the outlet;  $T_{01}$  is the total temperature at the inlet;  $P_{2s}$  is the outlet static pressure;  $P_{01}$  is the total pressure at the inlet.

Closing the nozzle vane decreases the cross section at the throttle and increases the ejection angle at the distributor outlet. In other words, it increases the circumferential velocity at the impeller inlet, and therefore for the same flow rate, the power supplied to the turbine. First, it can be observed that the closed position of the nozzle van allows the turbine to operate at very low mass flow rate.

From figure 4, we see that for the same mass flowrate, the turbine recovers more power with the closed position than with the open position. Also to recover a given power, the turbine requires less mass flowrate by having the distributor vane closed. Nevertheless, it is clear that with the closing of the vanes, the isentropic efficiency suffers a considerable drop.

The increase in recovered power and the drop in efficiency with the closed vanes position may appear to be an inconsistent result. However, this result explains that closing the fins provides the turbine with a large amount of energy which is not sufficiently exploited due to secondary flows caused by a large relative flow incidence at the impeller inlet.

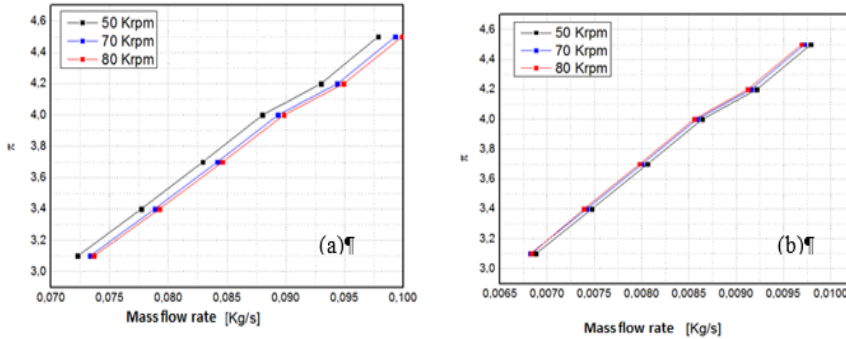


Figure 4. Expansion ratio vs mass flow rate (a) : open position, (b) : close position

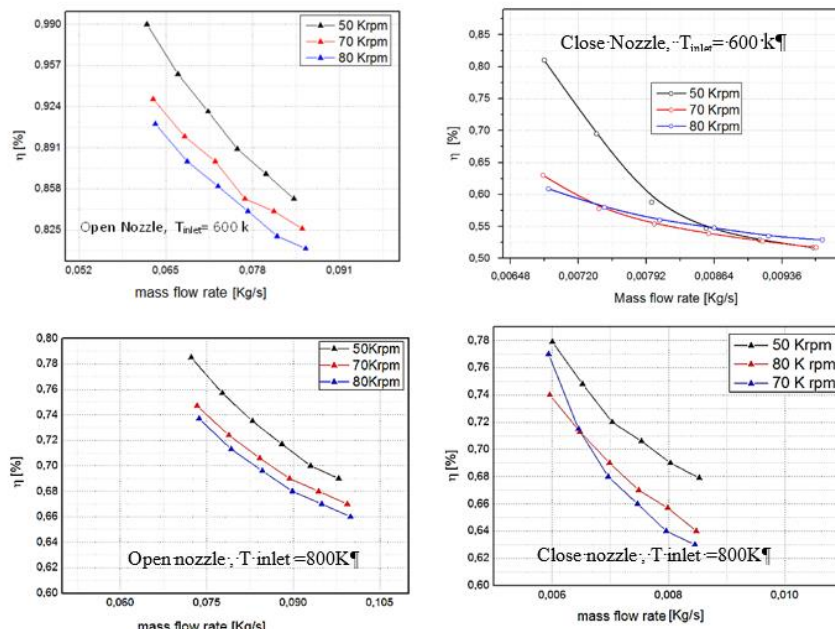


Figure 5. isentropic efficiency vs mass flow rate

## Recovered power

Turbine recovered power can be expressed as:  $P_{rec} = \dot{m}(h_{t1} - h_{t2})$

Where  $h_{t1}$  and  $h_{t2}$  are: the total enthalpy at turbine inlet and turbine outlet respectively.

(11)

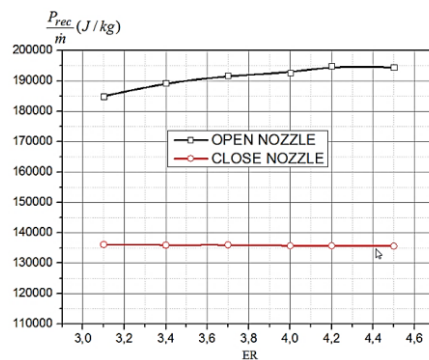


Figure 6. Recovered power reported to mass flow rate vs expansion ratio at 50 krpm

Taking inlet temperature 600 K,  $P_{rec}$  is calculated for different ER and mass flowrates setting a rotational speeds 50 krpm as in the table 2 and 70 krpm as in the table 3. In selected operating range for the two nozzle vane positions, the recovered power increase with increasing expansion ratio and mass flowrate, but by reporting  $P_{rec}$  to the correspondent mass flowrate ( $P_{rec}/\dot{m}$ ) regarding ER , the specific recovered power increase significantly for the open position and decrease slightly in the case of close nozzle vane position figure 6.

Table 2. Recovered power for  $T_{inlet}=600$  K and 50 krpm at different ER

ER	Open nozzle				Close nozzle			
	$\dot{m}_s$ [kg/s]	$h_{t1}$ [J/kg]	$h_{t2}$ [J/kg]	$P_{rec}$ [W]	$\dot{m}_s$ [kg/s]	$h_{t1}$ [J/kg]	$h_{t2}$ [J/kg]	$P_{rec}$ [W]
3.1	0.062	467954.4	283088.8	11461.66	0.0060	466483.5	330393.7	816.53
3.4	0.066	465244.2	278195.1	12494.88	0.0065	462500.9	326654.9	882.99
3.7	0.07	462872.9	273947.9	13413.67	0.0070	458724.1	322741.4	951.87
4	0.075	460784	269934.3	14447.32	0.0075	455068.5	319395.5	1017.55
4.2	0.079	458963.5	266355.2	15389.4	0.0080	451589.2	315910.4	1085.43
4.5	0.084	457360.7	262965.6	16329.18	0.0085	448238.2	312670.4	1152.32

Table 3. Recovered power for  $T_{inlet}=600$  K and 70 krpm at different ER

ER	Open nozzle				Close nozzle			
	$\dot{m}_s$ [kg/s]	$h_{t1}$ [J/kg]	$h_{t2}$ [J/kg]	$P_{rec}$ [W]	$\dot{m}_s$ [kg/s]	$h_{t1}$ [J/kg]	$h_{t2}$ [J/kg]	$P_{rec}$ [W]
3.1	0.063	466821.8	299250.9	10556.96	0.0059	464216.1	330415.4	789.42
3.4	0.068	463899.5	293563.1	11572.87	0.0064	459918.2	334622.8	801.89
3.7	0.072	461358.4	288476.8	12447.47	0.0069	455806.9	333253.7	852.97
4	0.077	459119.1	283638.9	13511.97	0.0074	451905.8	330618.5	897.52
4.2	0.081	457172.8	279072.8	14409.95	0.0079	448249.1	327919.4	957.82
4.5	0.0856	455462.2	274930.3	15345.21	0.0084	444697.8	325198.9	1003.79

## CONCLUSION

In this paper, the calculation and analysis of a typical 1.4L diesel turbocharger turbine are carried out with Fluent CFD software by means of flow-heat coupling calculation. The obtained results of the expansion ratio, isentropic efficiency and power recovered by the turbine for two nozzle vane positions (open and closed) and for two inlet temperatures 600 K and 800 K, under three rotational regimes, show that:

- Expansion ratio obtained for 50, 70, and 80 krpm increase following the increasing of mass flow rate, it seen that the effect of rotational speed on ER changing with mass flow rate is more significant for the open nozzle position.
- The best isentropic efficiency is obtained for the open nozzle position with inlet temperature of 600 K and 50 krpm rotational speed.
- The closed nozzle position show a significant turbine recovered power despite the very low mas flow rate
- The turbine recovered power reported to the mass flow rate which denote the drop of total enthalpy, increase significantly for the open position and decrease slightly in the case of close nozzle vane position.

## **REFERENCES**

- [1] N. Watson, M. Janota Turbocharging the internal combustion engine, Palgrave Macmillan, Basingstoke (1982)
- [2] Christos Kalathakis , Nikolaos Aretakis and Konstantinos Mathioudakis, Solar Hybrid Micro Gas Turbine Based on Turbocharger, *Appl. Syst. Innov.* 2018, 1, 27; doi:10.3390/asi1030027
- [3] H. Aghaali, H.-E. Ångström, A review of turbocompounding as a waste heat recovery system for internal combustion engines, *Renew Sustain Energy Rev.*, 49 (2015), pp. 813-824, 10.1016/j.rser.2015.04.144
- [4] M. Hatami, D.D. Ganji, M. Gorji-Bandpy, A review of different heat exchangers designs for increasing the diesel exhaust waste heat recovery *Renew Sustain Energy Rev.*, 37 (2014), pp. 168-181, 10.1016/j.rser.2014.05.004
- [5] Yixiong Liu, Dazhong Lao and Ce Yang, Investigation of Detailed Flow in a Variable Turbine Nozzle, *Int J Turbo Jet Eng* 2016; 33(4): 329–340, DOI 10.1515/tjj-2015-0034
- [6] A. T. Simpson, S. W. T. Spence, J. K. Watterson, Numerical and Experimental Study of the Performance Effects of Varying Vaneless Space and Vane Solidity in Radial Turbine Stators, *Journal of Turbomachinery*, 2013, Vol. 135, DOI: 10.1115/1.4007525
- [7] Shyang Maw Lim, Anders Dahlkild and Mihai Mihaescu, Aerothermodynamics and exergy analysis in radial turbine with heat transfer, *Journal of Turbomachinery*, J. Turbomach. Sep 2018, 140(9)
- [8] Ababacar Thiam, Elhadji Ibrahima Cissé, Baye Alioune Ndiogou, Kory Faye, and Mactar Faye, Design and CFD modeling of a solar microgas turbine for rural zones in Sahel, *AIP Conference Proceedings* 2126, 140006 (2019); <https://doi.org/10.1063/1.5117654>
- [9] M. Odabaee, M. Modir Shanechi and K. Hooman, CFD Simulation and FE Analysis of a High Pressure Ratio Radial Inflow Turbine, 19th Australasian Fluid Mechanics Conference Melbourne, Australia, 8-11 December 2014
- [10] Nicolas Binder, Sébastien Le Guyader and Xavier Carboneau, Analysis of the Variable Geometry Effect in Radial Turbines, *Transactions of the ASME*, Vol. 134, 2012



# OPTIMIZATION OF AN OFFSHORE WIND JACKETS MANUFACTURING PROJECT THROUGH AN INVESTMENT ANALYSIS USING 3D DISCRETE-EVENT SIMULATION

Adolfo Lamas Rodríguez

Navantia, Ferrol, Spain, alamasr@navantia.es, ORCID: 0000-0002-2405-2513

Santiago José Tutor Roca

UMI Navantia-UDC, Ferrol, Spain, santiago.tutor@udc.es, ORCID: 0000-0002-3071-4202

Inés Taracido López

Navantia, Ferrol, Spain, itaracido@navantia.es, ORCID: 0000-0002-3078-4411

Cite this paper as:

*Lamas Rodríguez, A, Tutor Roca, S, Taracido López, I. Optimisation of an offshore wind jackets manufacturing project through an investment analysis using 3D discrete-event simulation. 9<sup>th</sup> Eur. Conf. Ren. Energy Sys. 21-23 April 2021, Istanbul, Turkey*

---

**Abstract:**

Nowadays, the increasing global demand for renewable energy has led to an interest in the construction of offshore wind farms. However, offshore wind energy is currently facing important challenges due to its high costs compared to other renewable sources. Thereby, being competitive in this market is critical in a world where energy demand is increasing and most of it still comes from fossils fuels. In this context, we present a case study where 3D discrete-event simulator (DES) FlexSim has been used with the aim of optimizing the jackets manufacturing process in a shipyard. To accomplish so, a digital model was developed to represent in a virtual environment this fabrication process. In this way, different scenarios were formulated in FlexSim to size the workstations and the storage space required. Then, an investment analysis has been performed in order to get a better configuration that maximize the throughput and reduce costs even more. Therefore, this paper is an evidence how DES provide us with a parametric decision-support to implement changes in the manufacturing process thanks to its great flexibility and 3D interface. Overall, this case study allow us to enhance shipyard's efficiency and make more profits in the field of offshore wind.

---

**Keywords:**

*offshore wind project, discrete-event simulation, jackets manufacturing process, investment analysis, decision-support tool*

---

© 2021 Published by ECRES

## 1. INTRODUCTION

Currently, offshore wind energy is consolidating its position in the global generation mix as an alternative to fossil fuels and a solution to worsening of climate change effects. Although this form of renewable energy holds very high expectations regarding both installed capacity and planned investment, its elevated costs lead to a high degree of uncertainty. Most governments around the world are more concerned than ever and continue its efforts trying to align their new environmental regulations with economic growth.

Nevertheless and according to [1], wind energy sector is continuing to see consistent development, after having unequivocally established itself as a cost-competitive energy source worldwide. In this way, in Europe, eight new offshore wind projects reached Final Investment Decision (FID) during 2020, with construction due to start in the coming years [2]. Therefore, long terms vision regulations, efficient supply chains and remarkable technology improvements will be essential for the success of offshore wind energy [3].

In this context, Industry 4.0 is conceived as a totally transformation in all productive systems through an increasing of digitalization and cooperative coordination. As part of this revolution, Discrete-Event Simulation (DES) is becoming more popular to modelling the current manufacturing process, allow us to forecast the demand of each stages in any fabrication process.

Over the last few years the use of DES to optimize some manufacturing processes and evaluate the impact of an improvement has witnessed an outstanding evolution. Thus, [4] has used DES to make decisions on investment analysis in advanced manufacturing process and study the effects of adding new equipment. They claim that the traditional methodology to study investments ignores non-financial factors. In this sense, they highlight the potential of DES to carry out faster and better evaluations.

On the other hand, [5] analyze several types of crude oil transfer operations using DES in order to evaluate some project key performance indicators. Results allowed stakeholders to identify the benefits and disadvantages of investing in different kinds of infrastructure, as well as, pinpointing the port's competitiveness.

Likewise, [6] propose a case where simulation-based optimization supports in search of the lowest cost of a specific operation attending to possible unexpected events. They examine the Transportation and Installation (T&I) planning of offshore energy platforms evaluating different solutions by setting either time or cost minimization as main objective.

Furthermore [7], affirms that simulation should be closely interconnected with cost modelling system so that results are nimbly passed between all the systems. Therefore, the propose a solution composed of a cost model, a DES model and an integration tool to integrate both systems by means of Microsoft Excel.

In line with it, this paper presents a case study where 3D DES tool FlexSim have been used to optimize a manufacturing process of jackets. To do so, we implement a digital model in this software to represent in a virtual environment each stage of the fabrication process. In close proximity, [8] performs several DES models to minimize flowtime per jacket through the identification of process bottlenecks and the adjustment of manufacturing time to agreed-upon due dates. Moreover, it highlights how useful DES becomes to study the effect of changing certain parameters in processes, which allow companies to increase their profitability without involving too much investment.

Finally, [9] assesses the internal logistics of a shipyard by means of DES considering cost and resources. Besides, they make an accurate estimation of most adequate dates regarding the entry and exit operations of jackets in each buffer, implementing new storage and assembly strategies.

## 2. CASE DESCRIPTION

In this paper we presented a simulation-based optimization of an offshore wind project, which consist in the manufacturing process of 62 jackets in a shipyard. In this way, our overall objective is to optimize this fabrication increasing the throughput and minimizing the costs of the project. This analysis is very important in a market where the delivery dates are very tight and a delay of a single component may lead to substantial economic losses. For this purpose we have developed a digital model that allow us to represent each fabrication stage in order to resize the number of necessary workstations in our layout (Figure 1). Particularly, the main existing bottlenecks were identified, suggesting feasible solutions to reduce wait times, improving the use of storage spaces as well.

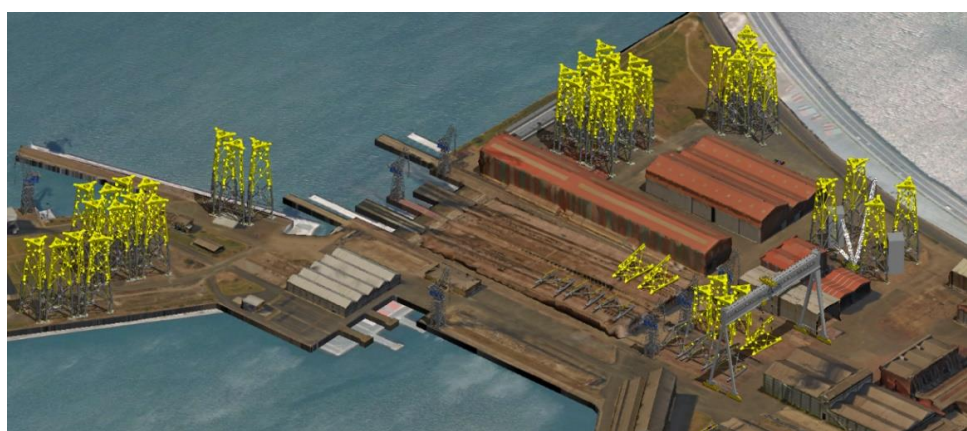


*Figure 1. General view of the shipyard.*

### Jacket Model

Jackets can be mostly divided into three parts (Figure 2): Lower Block (LB) and Upper Block (UB), which make up the main body of the structure, and the Transition Piece (TP) between the jacket body and the wind turbine tower. More specifically, the UB and LB are in turn made up of a series of arms (X-Bracings) that will be in charge

of joining the different legs (Legs) which consist of tubular elements connected by transition nodes on which the jacket is supported.

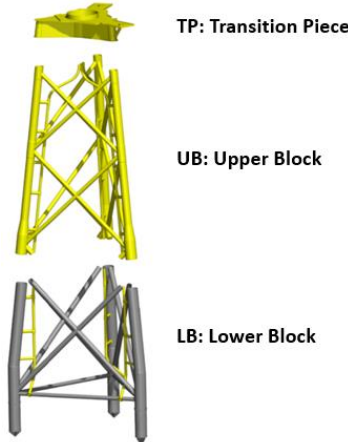


Figure 2. Main components of the jackets.

In this wind energy order, the jackets to be assembled are split into four types of clusters, as to their characteristics and dimensions.

### Jackets Manufacturing Process

The first step in the manufacturing process is painting all the components of the part of the jacket that protudes from the surface of the water for aesthetic reasons. Afterwards, components will be assembled at the existing workstations in slipways depending on the section of the structure to which each one belongs of them.

Once the LB and UB are completed, they are loaded and moved into berth workstations to perform the Assembly 1 and 2 with the aid of a gantry crane. However, due to their dimensions, only jackets of one of the four clusters can be assembled under the gantry crane, so it is necessary to rent an auxiliary crane during the project execution time to complete this last operation on the jackets of the remaining three clusters, which significantly increases project expenses. To accomplish all of this, the strategy shown in Figure 3 below is followed.

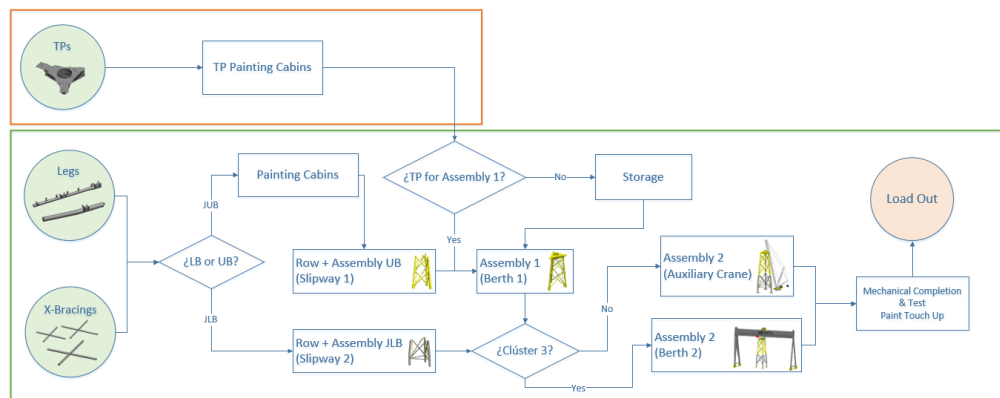


Figure 3. Process flow.

## 3. METHODOLOGY

### Data collection

First of all, several parameters have been collected to carry out the design of the process. For that purpose, information from previous projects together with Personnel of the Production and Engineering Division (PED) have served as data source either during the model conceptualization and validation phases.

### Model Validation

When all data has been obtained and manufacturing process was defined, we create a preliminary model in FlexSim to serve as a representation of the physical system. Then, to validate the model and deemed it as a devoted pattern

of our fabrication process, a simulation was run checking and comparing if the lead times and delivery dates of the components outputted by the model matched with the schedule baseline data included in a Microsoft Project file.

### Model Optimization

Subsequently, one time we have validated our model (Figure 4), we formulated different scenarios during the optimization phase, in which we rethought the manufacturing strategy and resized the number of workstations and storage space required.

In this way, although the project is on schedule to be completed within the deadlines established, we have optimized it identifying possible bottlenecks throughout the process in order to look into likely delays with the aim of fulfill agreed-upon milestones and the project completion in both schedule and budget. In addition, we reached slightly earlier completion dates compare to the current ones through reduced fabrication times and a more efficient use of resources. These little slacks could eventually aid the company in the development of future mitigation plans against unexpected events.

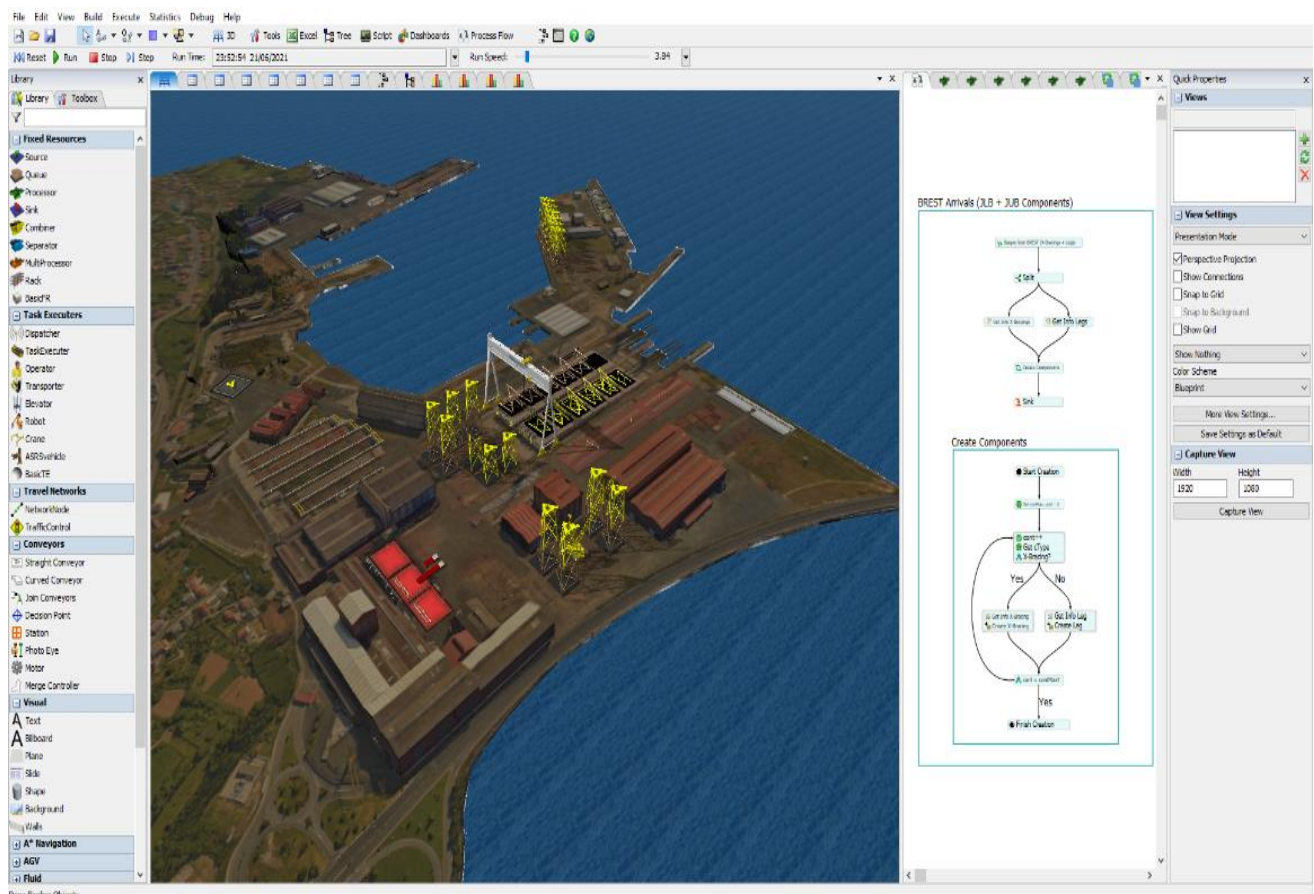


Figure 4. Simulation model in FlexSim.

## 4. EXPERIMENTAL RESULTS

Thus, in order to minimize cycle times, we performed several simulations by modifying the number of workstations on each of them. It should be added that, originally, there were 4 stations of each type of assembly, LB, UB, 1 and 2.

- **Option 1.** With the objective of facing possible delays, we have implemented a mitigation plan in which we carry out a first experiment (Figure 5) where we have varied the number of stations in slipways from 4 to 6 while keeping the number of Assemblies 1 and 2 constant, (since there is not more space in berths), with the aim of knowing what is the optimal distribution of stations in the shipyard that maximizes the throughput.

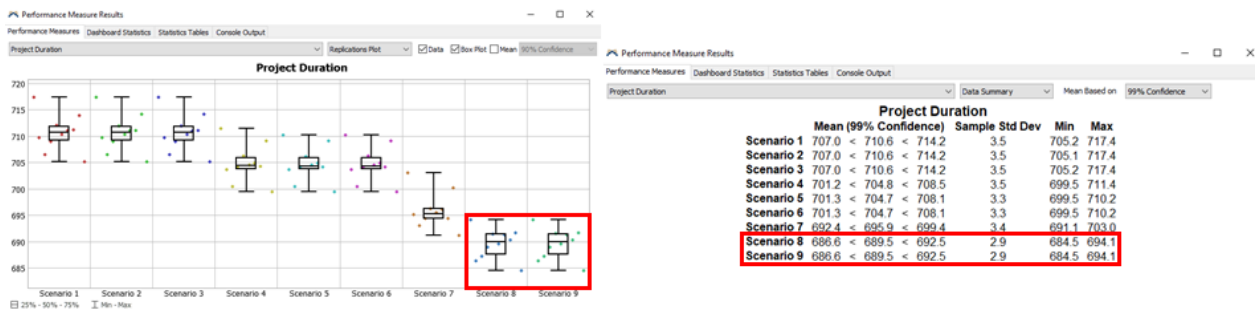


Figure 5. Optimization scenarios varying the number of workstations.

As seen in the previous picture, scenarios 8 and 9 are the ones that mostly reduce the assembly makespan. However, as scenario 8 also minimizes the average fabrication time, it will be the best configuration till the moment, made up of 6 workstations for UB assembly and 5 for LB.

- **Option 2.** Nevertheless it's a fact that we can not reduce manufacturing times to a greater extent because Assembly 2 stations come to be a marked bottleneck. Therefore, we proposed to study an investment analysis that considers the lifting of the gantry crane at the same time one of the slipways is removed, as shown in the Figure 6. This way we have room for increasing the number of Assembly 1 and 2 stations there up to maximum of 8.



Figure 6. View of Assemblies 2 in slipway 1.

For the investment analysis, we considered the cost of removing the slipway 2 to be worth 9 million euros and the process of lifting the gantry crane to be worth 6 million euros, based on data provided by the company. In addition, we valued each LB and UB new workstation at 75.000 € and each Assembly 1 and Assembly 2 new workstation at 100.000 €. As for the savings, it has been considered the cost of the auxiliary crane (1,2 million euros per year), and the profit per any extra jacket manufactured with the new layout, which is valued at 300.000 €.

- **Options 3 & 4.** Finally, although it was not our main objective at first, we have created the last two models, one increasing the number of cabins by 5 and other optimizing the painting logic to alleviate the other bottleneck, the painting process. With both of them, we were able to increase the throughput of the UB components and reduce lead times even more. Anyway, it must be considered that adding more workstations or cabins carries an associated cost. Therefore, its economic impact should be studied, although, due to the high penalty of making a late delivery, the cost of upgrade the number of resources usually pays off (Figure 7).

### INVESTMENT PAYBACK

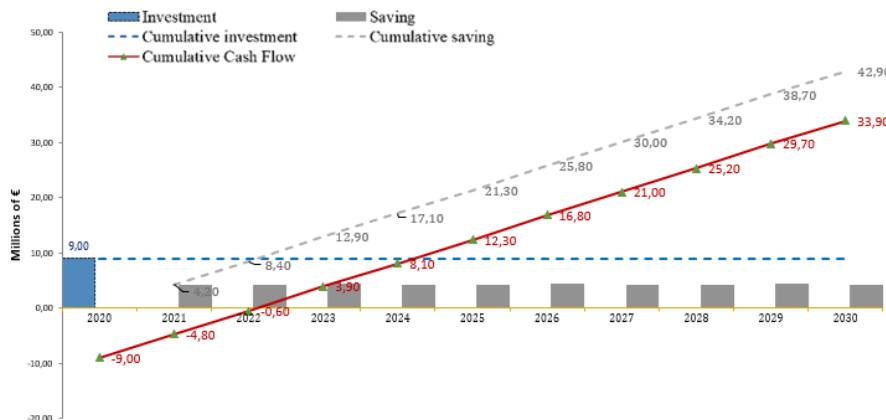


Figure 7. Investment payback with Option 4

## 5. CONCLUSIONS

In this paper, we have been able to develop different scenarios (Figure 8) to increase shipyard's production and identify processes that can be improved. Particularly, the main existing bottlenecks have been detected, proposing feasible solutions in order to minimize lead times, optimizing the use of workstations and storage spaces as well.

MODEL SUMMARY				
PARAMETER	Schedule Base Line	Option 1	Option 2	Option 4
Makespan (days)	713,52	694,1	459,66	427,76
Cycle time (days)	11,57	11,2	7,41	6,90
Average fabrication time (days)	100,51	109,93	90,43	87,55
UB Stations	4	6	5	5
LB Stations	4	5	4	4
Assembly 1 Stations	4	4	4	4
Assembly 2 Gantry Crane Stations	4	4	7	7
Assembly 2 Auxiliary Crane Stations	4	4	-	-
Investment (M€)	-	-	9	9
NPV (M€)	-	-	21,16	29,53
IRR (%)	-	-	35,19	46,33
Result	Model Validation	Mitigation Plan	Investment	Best Layout

Figure 8. Main simulation models implemented in this paper

Therefore, with the best scenario proposed in this project, we were able to decrease the makespan more than 28 weeks. This supposes an increase in the average throughput of jackets more than 30%, in addition to translating into a quantitative improvement in terms of reducing blockages of components in the stations by 80%.

Likewise, we have implemented a detailed economic analysis in Excel totally viable, based on an expected commercial scenario of 10 years of jackets fabrication projects awarded. In the best scenario we achieved a Net Present Value (NPV) of 29.53 million euros and an Internal Rate of Return (IRR) of 46.33% (higher than the 30% that is required by the company), so that we could get our investment back in just 3 years and 2 months. These results allow us to affirm that, if the manufacturing process were carried out in reality, we would meet our expectations by significantly improving project planning, construction strategy and logistics, adding value in the future for other possible offshore wind projects.

All in all, this work is an evidence of how DES gives us an unprecedented advantage, providing a parametric decision-support tool to study changes in any manufacturing process and define feasible mitigation plans to tackle such as late reception of material or engineering variation orders impact caused by prevention protocols designed to avoid COVID-19 pandemic effects.

## REFERENCES

- [1] Lee, J., & Zhao, F. (Global Wind Energy Council, 2019). Global Wind Report 2019.
- [2] Ramírez, L., Fraile, D., & Brindley, G. (Wind Europe, 2021). Offshore Wind in Europe - Key trends and statistics 2020.

- [3] Lamas Rodríguez, A., Pernas Álvarez, J., Taracido López, I. Design of a Visual Testing System in a Robotised Welding Workshop of Jacket Nodes by means of DES and Ergonomic Software. 8th Eur. Conf. Ren. Energy Sys. 24-25 August 2020, Istanbul, Turkey.
- [4] Freiberg, F., & Scholz, P. (2015). Evaluation of Investment in Modern Manufacturing Equipment Using Discrete Event Simulation. *Procedia Economics and Finance*, 34, 217–224.
- [5] Widjaja, L., & Tsai, C.-F. (2019). Discrete Event Simulation for Oil Transshipment Facility. In *Ports 2019: Port Planning and Development* (pp. 489–499).
- [6] Kim, B., & Kim, T. wan. (2017). Scheduling and cost estimation simulation for transport and installation of floating hybrid generator platform. *Renewable Energy*, 111, 131–146.
- [7] Marsh, R., Jonik, M., Lanham, J., Cheung, W. M., Newnes, L. B., & Mileham, A. R. (2010). Modelling an assembly process using a close coupled generative cost model and a discrete event simulation. *International Journal of Computer Integrated Manufacturing*, 23(3), 257–269.
- [8] Lamas-Rodríguez, A., Crespo-Pereira, D., & Sánchez-Tutor, R. (2016). Discrete Events Simulation to improve manufacturing process of jackets offshore structures. 15th International Conference on Modeling and Applied Simulation, MAS 2016, 85–94.
- [9] Lamas Rodríguez, A., Chas Álvarez, D., & Muiña Dono, J. A. (2019). 3D Discrete Events Simulation to Evaluate the Internal Logistic Strategies in a Shipyard. Springer International Publishing.



# ON MINIMIZATION OF THE GROUP VARIABILITY OF INTERMITTENT RENEWABLE GENERATORS

Dubravko Sabolić

Croatian Transmission Operator, Ltd., Zagreb, and the University of Zagreb, Croatia, [dubravko.sabolic@hops.hr](mailto:dubravko.sabolic@hops.hr), ORCID: 0000-0002-7892-8701

Roman Malarić

University of Zagreb, Croatia, [roman.malaric@fer.hr](mailto:roman.malaric@fer.hr), ORCID: 0000-0003-3097-2217

*Cite this paper as:* [\*Sabolić, D, Malarić, R. On Minimization of variability of a group of variable renewable generators. 9<sup>th</sup> Eur. Conf. Ren. Energy Sys. 21-23 April 2021, Istanbul, Turkey\*](#)

**Abstract:** We discuss an approach in minimization of the group variability of generation in a system of intermittent renewable sources using the portfolio theory, whereby the total variability of a system, that can be modeled using various parameters as goal functions, is minimized given any desired level of expected long-term generation. An extensive analysis was carried out on a set of time series of measured generation data obtained from twenty wind plants in Croatia over a five-year period in one hour, and fifteen minute, time resolutions. The choice of the goal function most relevant for the operational (and economic) consequences of short-term variability is discussed.

**Keywords:** *Intermittent renewable sources, Minimization of variability, Goal function*

© 2021 Published by ECRES

Nomenclature	
$C$	Total production capacity intended for installation, that should be distributed among the sites,
$r_i$	The weight factor of total capacity $C$ intended for installation that is allocated to the site $i$ ,
$E_i$	Expected hourly production normalized to the production capacity allocated to the site $i$ ,
$\sigma_i$	The standard deviation of normalized production at the site $i$ ,
$\rho_{ij}$	The correlation coefficient between time series of normalized production at locations $i$ and $j$ ,
$E$	Expected hourly production of the portfolio of wind plants normalized to the total capacity $C$ ,
$\sigma$	The standard deviation of normalized production of the portfolio of wind plants
MPT	Modern portfolio theory

## 1. INTRODUCTION

One of the main tasks of transmission system operators is to keep the balance between total generation plus net imports (or minus net exports) on the one hand, and the total consumption on the other. Technologically, the biggest challenge is to maintain it in the near-real-time, after the last market before physical delivery is closed and thus the last opportunity to adjust market positions by trading individual residual imbalances is gone. To achieve that, the transmission system operator must hire a sufficient amount of flexible generation reserve, to be able to engage it for non-stop compensation of the remaining system-wide imbalance. The latter occurs because a majority of the load is not coordinated nor planned and thus behaves partially as a random variable. In addition, the production in newly massively introduced variable facilities, such as wind or solar plants, can only be predicted with limited precision, because it depends on current wind velocity or insolation on plants' sites.

The following literature review benefited largely from [1]:

The minimization of the variability of wind generation by utilizing statistical cancellation of instantaneous production variations was already studied before, e.g. [2,3]. The system costs of renewable sources (RES) that incorporates the costs of real-time balancing was presented in [4]. The paper [5] analyzed the impacts and associated costs of intermittent power generation on the British system and concluded that decreased reliability cannot be supported by evidence (available at that time), but that the network operation faces more challenges. The authors of [6] sought to the separation of the economic value of energy and related costs and calculated the wind integration

costs as difference between the cost of energy produced with, and without, wind generation plants. They concluded that the economic value of wind-generated energy is somewhat below the base-load value. In [7] it was concluded that the integration costs of about US\$ 5 to 6 per MWh of wind-generated energy can be expected for capacity penetration rates of 20-30 percent. In [8] it was found that organizing electricity trade at time horizons nearer to the real-time than the day-ahead can improve wind production forecasting, which would normally reduce the demand for ancillary services. In [9] it was found that at a 20 percent penetration rate the wind integration costs are somewhere around a tenth of the wholesale energy value.

The article [10] argues that both the uncertainty and variability of wind puts grid operation under stress. However, specifically, the short-term temporal uncertainty (that is, the inability to predict when exactly the forecasted change will occur) appeared to be more challenging. The authors of [11] found that the possible wholesale value difference between better and poorer correlated wind sites is modest, in the order of 5 to 10 percent. In [12] there is a detailed study of the economic value of variable generation at high penetration levels, concluding, among others, that solar-generated energy has high value at low penetration rates, while the value of wind energy can exceed solar at high penetration rates. The paper [13] stresses that market organization can have a significant impact on the value of electricity generated from variable RES.

One of the possible approaches to the minimization of total variability is making use of the concepts of the so-called “modern portfolio theory” (MPT), formulated first by Markowitz [14]. However, the MPT received a good measure of criticism (see e.g. [15]). One of the big problems with Markowitz’s MPT is the underlying assumption that the future basic statistical properties of the time-series of values of financial instruments would remain stationary, that is, stay the same as observed during the long-term history.

While this admittedly can be a problem in the world of finances, it may not be of so big importance when applied to wind speeds, as one can argue that nature changes much slower than the financial markets. (However, given the up-speeding global warming, such a view can be challenged, as well.) Having the long-term historic records of wind production time series (or just wind speeds) at a set of locations suitable for the installation of wind farms may still be used for optimization.

The second major objection on the MPT pertains to its underlying assumption that the distribution of samples in time series were Gaussian. While that may even be close to the truth in the realm of financial markets, there is a lot of evidence that neither wind speeds (e.g. [16]), nor the actual electricity generation (e.g. [17]), are Gaussian.

As regards the potential for statistical cancellation between wind and load variability, [18] showed, on an example of the Croatian power system, but with an extensive set of measured data, that there is essentially no correlation between the two phenomena in the long run, so that it is not feasible.

## 2. MINIMISATION OF VARIABILITY IN THE GROUP OUTPUT

In [1], a detailed description of an optimization model used for minimization of wind generation variability using MPT is given. It will be repeated here for the reader’s convenience. The standard MPT formulation of the optimization problem to solve is as follows:

$$\begin{aligned} \min \sigma^2 &= \sum_i \sum_j r_i r_j \sigma_i \sigma_j \rho_{ij} && i, j \in [1, N] \\ &\text{subject to constraints:} \\ &\sum_i r_i = 1 && i \in [1, N] \\ &r_i \geq 0 && \forall i \in [1, N] \\ &E = \sum_i r_i E_i && i \in [1, N] \end{aligned} \tag{1}$$

However, as we will discuss later, the goal function does not have to be the portfolio variance (or, in another wording more suitable for our purpose, the group variance). The numerous optimization procedures were done numerically, using the non-linear optimization solver software, over a set of the real-life measured time series data from up to twenty different wind plant sites in Croatia that were available in the time resolutions of 1 hour and  $\frac{1}{4}$  hour. For the sake of brevity, only a part of the information obtained will be presented in this paper. Using the numerical algorithms enables the modeler to optimize for other group parameters than the plain variance, which was used in the past mostly because a need to obtain problem formulations simple enough to for analytical computation. The structure of the data is explained in more detail as follows:

- *Timespan:* 2014-2018 (time series of data measured at each plant in two different temporal resolutions: 1 hour, and 15 minutes).
- *The number of wind plants:* from 9 at the beginning of 2014 to 20 at the end of 2018.

- Number of data samples per year:

- 1-hour resolution: 8760 (normal year); 8784 (leap year);
- 15-min. resolution: 35040 (normal year); 35136 (leap year).

- Type of data:

- Original recordings: average production power in megawatts (MW) during the sample interval (1 hour or 15 minutes).

- Normalized data: each sample is divided by the production capacity (MW) installed at the corresponding plant site.

One should note that the wind plants were used here merely as measurement devices to sample the wind flow and translate it into a quantity proportional to the electricity production per unit of installed production capacity. It is more accurate than using the raw wind speed data and converting it into electricity production using inevitably imperfect theoretical models. All data were measured by the Croatian Transmission System Operator coherently in time, with a high accuracy. Without the coherence, any calculation of statistical correlations between the series would not be possible, as well as the performance of the optimization.

First, let us examine how the realistic space of portfolios, in the  $E - \sigma$  plane, looks like. Figures 1 and 2 were taken from [1]. The former depicts a subset of 20 thousand stochastically generated portfolios, out of one million actually calculated. The larger white dots stand for the individual sites, whereas the smaller blue ones belong to the randomly generated portfolios that were computed simply by a random assignment<sup>1</sup> of the  $r$  figures to the nine individual plants whose 2014 hourly data were used to create this example, making sure that all  $r$ 's are non-negative and sum up to 1. Note that the simple two-dimensional graph does not allow the cross-correlations between the individual plant time series to be displayed, although in reality they do exist. The magenta-colored line is an “efficient border” as would result from the “classical” MPT without the non-negativity constraint being enforced. Whereas in the financial world (the “normal” area where MPT is usually utilized) it could make sense in the form of “short-sales”, see e.g. [14,15], in the realm of electricity generators it would be physically impossible. However, the unconstrained efficiency border is good to compute for the “sanity check”, because surely every portfolio that can be constructed from the given individual sites must lie to the right of that quadratic hyperbola. Fig 2 compares the efficient borders computed from the full set of one million random portfolios, and from the subset of one tenth of them. The two experimental efficiency borders were obtained by searching for the portfolio with the lowest variance  $\sigma^2$  among all with the expectation in some close pre-determined neighborhood of the observed value  $E$ , and repeating this across the whole range of attainable  $E$ 's.

Figures 3 and 4 give the efficient frontiers (unconstrained and realistic) obtained from 15-minutes data during one full year each (2018 and 2017, respectively). They also display the individual plants, which are not on the exactly same locations because the wind parameters were not exactly the same in the two years. However, one can note one particular characteristic of the nature, at least in Croatian coastal region, where the plants are situated: the larger the wind energy output at a location, the larger its volatility. It closely follows an exponential law.

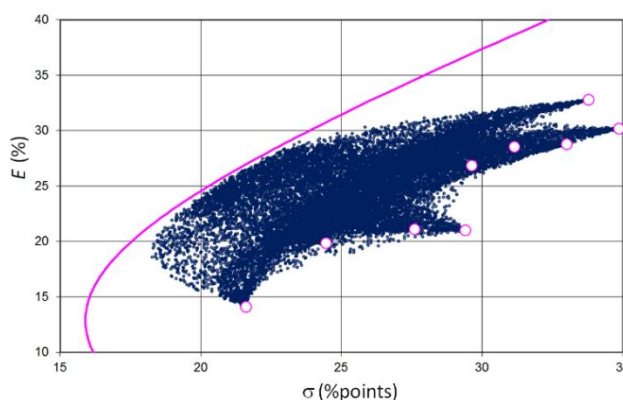


Figure 1. Small dots: 20 thousand random portfolios made with nine then active wind plants, based on 2014 15-minute data. Source: [1].

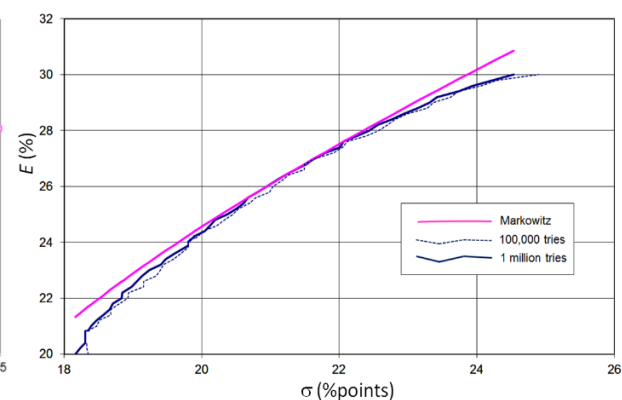


Figure 2. Comparison of experimental efficient frontiers, and the unconstrained (“Markowitz”) one for 2014, obtained from 15-minute data. Source: [1].

A technical note: assigning  $r$ 's using the simplest uniform distributions proved not to be a good strategy because the portfolios tended to massively gather close to the individual plants, so that obtaining the good approximations of actual borders of the feasibility region would require at least hundreds of times more random computations. Therefore, the  $r$ -value drawing procedure that created much more diversity in the final results were created, the description of which is not of the interest here. However, it can be found in [1].

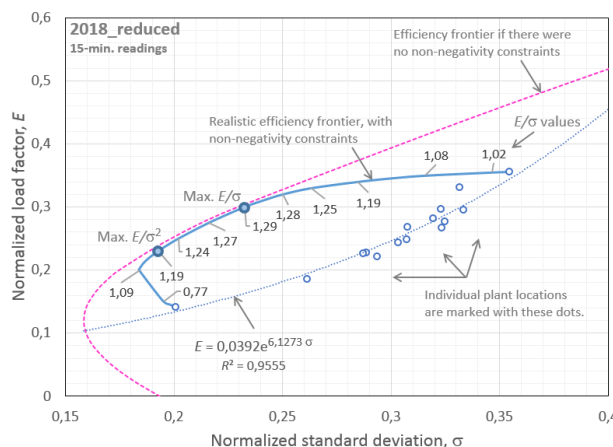


Figure 3. Efficient frontiers derived from the data for 15 Croatian wind plant sites, using the 15-minute readings from the whole of 2018. Source: authors' calculation.

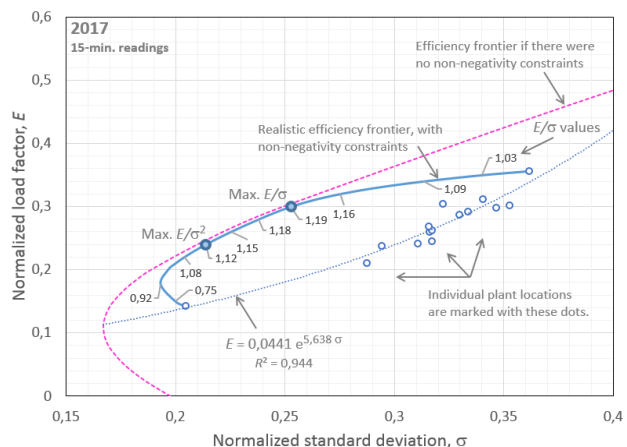


Figure 4. Efficient frontiers derived from the data for 15 Croatian wind plant sites, using the 15-minute readings from the whole of 2017. Source: authors' calculation.

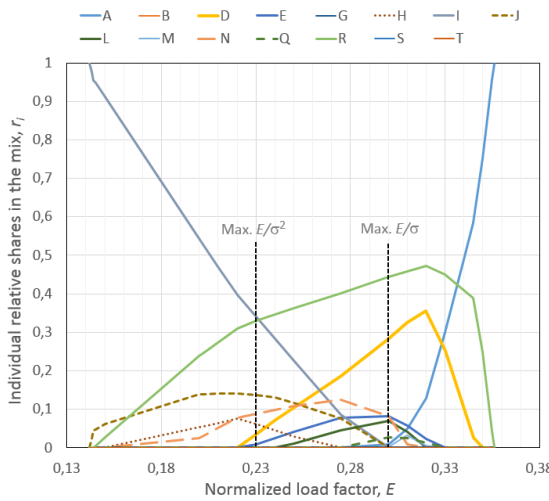


Figure 5. Solutions of the optimization problem for 15 Croatian wind plant sites, using the 15-minute readings during the whole of 2018. Source: authors' calculation.

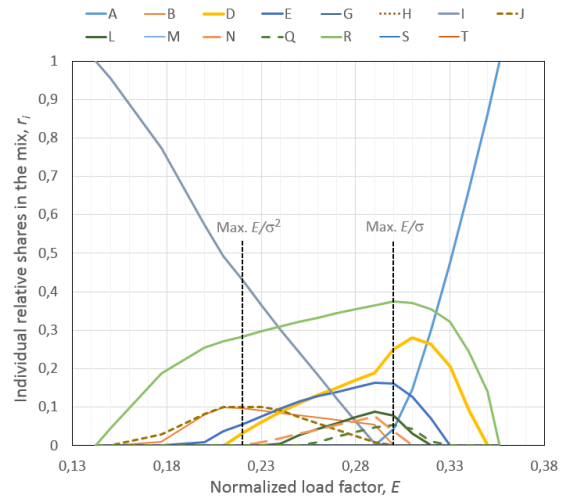


Figure 6. Solutions of the optimization problem for 15 Croatian wind plant sites, using the 15-minute readings during the whole of 2017. Source: authors' calculation.

While the efficient frontiers are a good graphical illustration of what one can achieve with the minimization of variance, the solutions of practical interest are the weight factors assigned to individual sites at the point of optimum achieved concerning a particular goal function that was used. Figs. 5 and 6 present the solutions for 15 locations (marked by capital letters) from Figs. 3 and 4, for the years 2018 and 2017.

Note that at first glance the two graphs look similar. However, paying attention to the details, notable differences are revealed, especially in the region between maximized  $E/\sigma^2$  and  $E/\sigma$ . The solutions seem most stable when only a few of the sites with the highest load factors  $E_i$  are used for planting the windfarms. However, as already commented, they also exhibit the highest volatility. Our results suggest that it would be a good choice to use dominantly the sites more abundant with the wind (for the best stability in time). That would lead to portfolios with still relatively high variability of production, yet considerably lesser than without the optimization. In our present research, it surfaced out as *the most important* point when it comes to optimization of variable energy production. Now that an optimization for total variability in terms of variance is explained, an attention should be put on what really poses a problem in the power system operation. The most critical limited resource relevant for that is the capacity of flexible units that the transmission system operator pays for to be available for fast regulation of the system, to counterweight the swift changes in the intermittent renewable sources output. It is a well-known problem. For example, after studying the seven-year stream of 5-minute readings of the energy output from a large system of wind plants in the north-western USA, the authors of [17] found out that the demand for fast regulation can be expressed as:

$$M_{\text{Reg}} = \frac{\alpha}{\beta} p^\beta + \gamma p, \quad (2)$$

where the Greek letters denote positive real constants.  $M_{\text{Reg}}$  is a quantity that shows by how many times can the total installed power of wind plants exceed the currently available 15-minute flexible regulation reserve, if the system operator deems default risk of  $p$  percent acceptable, nothing else being variable in the power system. Fig. 7, taken from [17], gives the results of the experimentally derived  $M_{\text{Reg}}$  for the above mentioned American wind plant system in the whole of the year 2013, together with the curve (2) fitted to the data using the least squares. Therefore, when contemplating minimization of the short-term variability, it is better to use some parameter that reflects the short-term changes in the total output of a system of wind plants rather than simple variance, or standard deviation.

For example, we carried out an optimization of a probability for a temporal change of total production to exceed a certain pre-defined threshold within one unit of time. For demonstrational purposes, we present the efficient frontier curves in terms of the group load factor  $E$  vs. the above-described probability (see Fig. 8). Fig. 9 shows the problem solutions (the sites' weight factors) for a curve pertaining to the threshold of 20%. Note that the curves from Fig. 8 are all limited to the range of  $0.148 < E < 0.355$ , where the portfolio solutions do not contain negative  $r$ -values. Note also that minimization by that criterion emphasizes the roles of two individual locations (A and I) with the most extreme characteristics (Fig. 9), suggesting (in this particular example) that the system can be optimally arranged by blending merely the two of them.

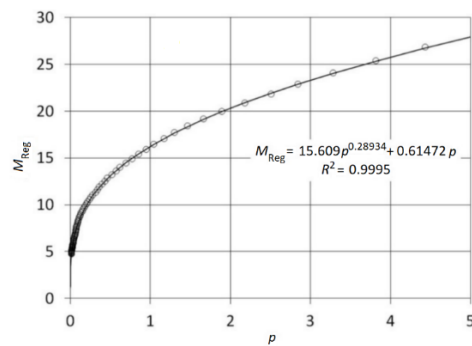


Figure 7. Experimentally obtained demand for fast regulation and the best-fit function (2). Source: [17].

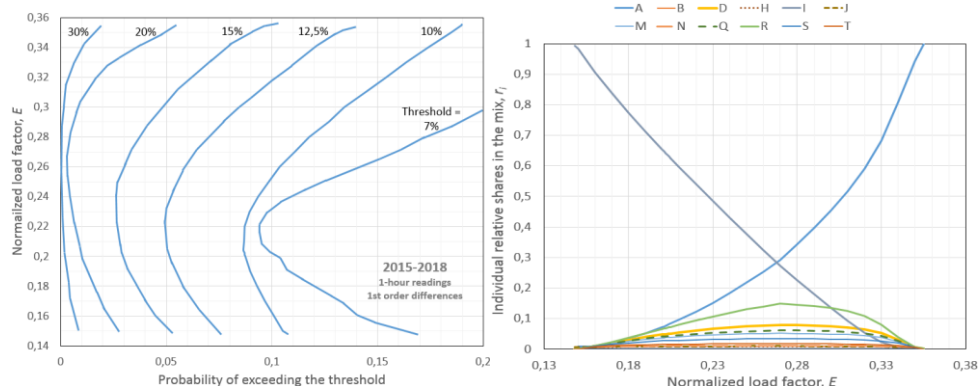


Figure 8. Efficient frontiers where the probability of a one-hour change (1<sup>st</sup> order difference) in total normalized production exceeding the Threshold is minimized for any given  $E$ . Derived from the 4-year time series of 1-hour readings, 2015-2018. Source: authors' calculation.

Figure 9. Solutions of the optimization problem along the curve for the Threshold = 20% from Fig. 8. Source: authors' calculation.

### 3. CONCLUSIONS

The volatility of the energy production from a group of wind plants and/or other intermittent renewable sources is a significant (although perhaps not the most significant) problem in the contemporary power system operation. It can only grow as the share of such generators in the total mix increases. Therefore, it is important to study the possibilities to minimize the short-term variability by organizational measures, such as the coordination of investments of the kind studied here, as well as in earlier literature by the other authors.

Our simulations, carried out on the actual measured production time-series data from a multi-site wind production system suggest that the choice of more windy (and thus, more volatile) sites could prove to be desired regarding the trade-off between the marginal loss of total load factor and decreased total variability expressed through the above described overshooting probability. Furthermore, the results also suggest that this trade-off is harsher when the goal function is the probability of the hourly change in production exceeding a certain level, than when it is the variance. This is essentially a combined consequence of the wind energy production non-normality, with fat-tailed distributions, and temporal volatility. Optimization for this particular parameter, at least in the case of Croatian natural circumstances regarding harvesting the wind energy, seems to prefer the most extreme locations (that is, those with the highest and the lowest output and volatility).

## REFERENCES

- [1] Sabolić, D., Župan, A., Malarić, R. Minimisation of Generation Variability of a Group of Windplants. *Journal of Sustainable Development of Energy, Water and Environment Systems* 2017, 5(3), pp. 466-479. DOI: <http://dx.doi.org/10.13044/j.sdewes.d5.0157>
- [2] Roques, F., Hiroux, C., and Sagan, M. Optimal Wind Power Deployment in Europe—A Portfolio Approach. *Energy Policy* 2010, 38, pp. 3245–3256. DOI: <https://doi.org/10.1016/j.enpol.2009.07.048>
- [3] Katzenstein, W., Fertig, E., and Apt, J. The variability of interconnected wind plants, *Energy Policy* 2010, 38, pp. 4400–4410. DOI: <https://doi.org/10.1016/j.enpol.2010.03.069>
- [4] Ueckerdt, F., Hirth, L., Luderer, G., and Edenhofer, O. System LCOE: What Are the Costs of Variable Renewables? 2013. Available at: [http://papers.ssrn.com/sol3/papers.cfm?abstract\\_id=2200572](http://papers.ssrn.com/sol3/papers.cfm?abstract_id=2200572) (accessed: 16 Feb. 2021)
- [5] Gross, R., Heptonstall, P., Anderson, D., Green, T., Leach, M., Skea, J. The Cost and Impacts of Intermittency: An assessment of the Evidence on the Costs and Impacts of Intermittent Generation on the British Electricity Network. 2006. Available at: <http://www.ukerc.ac.uk/asset/BCD3C9C4-FCC1-4DAD-896A95960CD61D51/> (accessed: 16 Feb. 2021)
- [6] Milligan, M., Kirby, B. Calculating Wind Integration Costs: Separating Wind Energy Value From Integration Cost Impacts, NREL Technical Report TP-550-46275. 2009. Available at: [http://www.consultkirby.com/files/NREL-TP-550-46275\\_Calculating\\_Wind\\_Inegration\\_Costs.pdf](http://www.consultkirby.com/files/NREL-TP-550-46275_Calculating_Wind_Inegration_Costs.pdf) (accessed: 16 Feb. 2021)
- [7] Smith, C., Milligan, M., DeMeo, E., Parsons, B. Utility Wind Integration and Operating Impact State of the Art, *IEEE Trans. Power Syst.* 2007, 22(3), pp. 900-908. DOI: <http://dx.doi.org/10.1109/TPWRS.2007.901598>
- [8] Holttinen, H., Melbom, P., Orths, A., Lange, B., O’Malley, M., Tande, JO., Estanqueiro, A., Gomez, E., Söder, L., Strbac, G., Smith, JC., van Hulle, F. Impacts of Large Amounts of Wind Power on Design and Operation of Power Systems, Results of IEA Collaboration, *Wind Energy* 2011, 14(2), pp 179-192. DOI: <https://doi.org/10.1002/we.410>
- [9] DeCesaro, J., Porter, K. Wind Energy and Power system Operations: A Review of Wind Integration Studies To Date, NREL Subcontract Report SR-550-47256. 2009. Available at: <http://www.nrel.gov/docs/fy10osti/47256.pdf> (accessed: 16 Feb. 2021)
- [10] GE Energy, Western Wind and Solar Integration Study, NREL Subcontract Report SR-550-47434, 2010. Available at: <http://www.nrel.gov/docs/fy10osti/47434.pdf> (accessed: 16 Feb. 2021)
- [11] Fripp, M., Wiser, RH. Effects of Temporal Wind Patterns in the Value of Wind-Generated Electricity in California and the Northwest, *IEEE Trans. Power Syst.* 2008, 23(2), pp 477-485. DOI: <https://doi.org/10.1109/TPWRS.2008.919427>
- [12] Mills, A., Wiser, R. Changes in the Economic Value of Variable Generation at High Penetrations Levels: A Pilot Case Study of California. 2012. Available at: <https://emp.lbl.gov/sites/all/files/lbnl-5445e.pdf> (accessed: 16 Feb. 2021)
- [13] Nicolosi, M. The Economics of Renewable Electricity Market Integration. An empirical and Model-Based Analysis of Regulatory Frameworks and Their Impacts on the Power Market (PhD). Universität zu Köln, Germany, 2011. Available at: <http://kups.ub.uni-koeln.de/4612/> (accessed: 16 Feb. 2021).
- [14] Markowitz, H. Portfolio Selection. *The Journal of Finance* 1952, 7, pp 77-91. DOI: <https://doi.org/10.1111/j.1540-6261.1952.tb01525.x>
- [15] Elton, EJ., and Gruber, MJ. Modern Portfolio Theory, 1950 to Date, New York University, Stern School of Business, Working paper, 1997, pp 2-9. Available at: <http://archive.nyu.edu/bitstream/2451/26674/2/FIN-97-003.pdf> (accessed: 16 Feb. 2021)
- [16] Monahan, AH., He, Y., McFarlane, N., Dai, A. The Probability Distribution of Land Surface Wind Speeds, *Journal of Climate* 2011, Vol. 24, pp. 3892-3909, DOI: <https://doi.org/10.1175/2011JCLI4106.1>
- [17] Sabolić, D., Župan, A., Malarić, R. Statistical Properties of Electricity Generation from a Large System of Wind Plants and Demand for Fast Regulation, *Journal of Sustainable Development of Energy, Water and Environment Systems* 2017, 5(3), pp. 447-465. DOI: <http://dx.doi.org/10.13044/j.sdewes.d5.0156>
- [18] Sabolić, D., Sičaja, I., Ivanković, I. Correlation Between Wind Generation and Load in Croatian Power System. In: Proceedings of the 2019 International Conference on Power Generation Systems and Renewable Energy Technologies (PGSRET), 26-27 Aug. 2019, IEEE, Istanbul, Turkey, pp. 9-12



# ASSESSMENTS OF GLOBAL WARMING POTENTIAL OF BRAZILIAN BIODIESEL

Costa, Marina W.

Federal University of Santa Catarina, Florianópolis, mweylc@gmail.com, ORCID: 0000-0001-9813-3095

Oliveira, Amir A. M.

Federal University of Santa Catarina, Florianópolis, Brazil, amir.oliveira@ufsc.br, ORCID: 0000-0002-2826-5778

Cite this paper as:

*Costa, M.W, Oliveira, A.A.M. Assessments of global warming potential of Brazilian biodiesel. 9<sup>th</sup> Eur. Conf. Ren. Energy Sys. 21-23 April 2021, Istanbul, Turkey*

---

**Abstract:**

Biodiesel has an essential role in the Brazilian energy matrix. Several Life Cycle Assessments of Brazilian biodiesel have been done, but the different functional units and premises hinder the comparison among their results. The objective of this study is to compare global warming potential emissions related to the production of biodiesel from different feedstocks and in different country regions. A literature review was performed to localize the LCAs published between 2015 and 2020, and conversion units were established based on the Brazilian agriculture census and relevant articles. All collected data were converted to  $gCO_2eq/MJ$  of biodiesel. Although only few studies evaluated land use change, it was found that the land use change in the Midwest region due to soybean culture had the higher greenhouse gas intensity of the Brazilian biodiesel production. Cattle farming, agriculture, and wasted oil collecting stage are the processes that emit more GHG gases in the production of beef tallow biodiesel, cotton biodiesel, and wasted oil biodiesel, respectively.

---

**Keywords:**

*Biodiesel, Life cycle analysis, Greenhouse gas emissions, Global warming potential*

---

© 2021 Published by ECRES

---

**Nomenclature**

eq	Equivalent
GHG	Greenhouse gas
GWP	Global Warming Potential
ha	Hectare
IPCC	Intergovernmental Panel on Climate Change
J	Joule
LCA	Life Cycle Assessment
LUC	Land Use Change
MW	Midwest region
N	North region
NE	Northeast region
S	South region
SME	Soy Methyl-Ester
SE	Southeast region
y	Year

---

## 1. INTRODUCTION

The interest in biofuels has grown due to concerns about climate change. Life Cycle Assessment (LCA) can be used to determine the global warming potential (GWP) of biofuels [1]: the impact caused by different greenhouse gases (GHG) converted to kg of equivalent  $CO_2$  in the same period (conventionally 100 years) using the model developed by the Intergovernmental Panel on Climate Change (IPCC) [2]. The diversity of feedstocks used to produce biodiesel in Brazil and the different localizations where the fuel is produced generates the necessity to evaluate and

compare the Brazilian biodiesel production as different system products. Table 1 exhibits the principal fatty materials used to produce biodiesel in Brazil.

*Table 1. Primary fatty materials used to produce biodiesel in Brazil [3].*

	Soybean oil	Beef tallow	Cotton oil	Other fatty materials (a)	Waste cooking oil	Pig tallow	Chicken fat	Palm oil	Corn oil	Rape-seed oil	Total
<b>MW</b>	76.02%	5.29%	1.56%	11.94%	0.06%	0.20%	0.23%	0.89%	3.81%	0.00%	41.36%
<b>NE</b>	34.27%	26.19%	3.37%	17.09%	0.27%	0.00%	0.00%	18.81%	0.00%	0.00%	7.70%
<b>N</b>	74.56%	18.93%	0.83%	3.53%	0.00%	0.00%	0.00%	2.15%	0.00%	0.00%	1.84%
<b>SE</b>	23.02%	30.60%	1.15%	9.35%	16.75%	13.04%	3.64%	2.05%	0.40%	0.00%	8.47%
<b>S</b>	75.61%	10.73%	0.18%	10.68%	0.28%	1.93%	0.44%	0.00%	0.02%	0.13%	40.64%
<b>Brazil</b>	68.12%	11.51%	1.09%	11.45%	1.58%	1.97%	0.58%	2.03%	1.62%	0.05%	

*MW: Midwest region; NE: Northeast region; N: North region; SE: Southeast region; S: South region*

(a)Unidentified blends of fatty materials

This study objective is to compare the available assessments of GWP of Brazilian biodiesel.

## 2. METHODS

A literature review was performed in Scopus [4] and Web of Science [5], searching for the words "life cycle biodiesel Brazil" in all the fields from 2015 to 2020. The Global Warming Potential (GWP) reported for each process of the evaluated articles were compared, divided by feedstock and the Brazilian region where the LCA was done. An energy functional unit was chosen to unify the studies and compare the results of different articles because it represents the studied product's functionality and is the most commonly used in LCA of biofuels in America [1]. The results were converted to  $gCO_2eq/MJ$  of biodiesel using data presented in Table 2. The calorific power of wasted oil biodiesel was assumed to be equal to the calorific power of soybean oil biodiesel because soybean oil is the most used vegetable edible oil in Brazil.

*Table 2. Conversion units.*

<b>Yields</b>		<b>Reference</b>
1 kg of soybean	0.18 kg of soybean oil	[8]
1 kg of soybean oil	0.897 kg of soybean biodiesel	[8]
1 hectare	3018 kg of soybean/year	[9] (data from Mato Grosso, 2017)
1 hectare	1.06 cattle head	[10] (data from Mato Grosso, 2017)
1 cattle head	20.25 kg of beef tallow	[11]
0.0323 kg of tallow	1 MJ of biodiesel	[12]
<b>Calorific power</b>		<b>Reference</b>
1 kg of soybean biodiesel	39.76 MJ	[13]
1 kg of cotton biodiesel	44.43 MJ	[13]
<b>Density</b>		<b>Reference</b>
1 kg of soybean biodiesel	913.8m <sup>3</sup>	[13]

## 3. GLOBAL WARMING POTENTIAL OF BRAZILIAN BIODIESEL

Tables 3 exhibits a comparison between the GWP reported by each studied LCA of soybean biodiesel, divided by processes and Brazilian region. Studies that present results as a percentage of the total impact were not added.

The analysis of Table 3 unveils that LUC is the process responsible for the majority of GHG emissions in the production of soybean biodiesel in most of the studies that considered it. The exception is one of the South states evaluated by [12], where no land use change was reported. [13] evaluated different scenarios of land use change in the South Region and found GHG emissions close to zero. Those studies made the average emissions observed in the Midwest region ( $73.8\text{ g}CO_2eq/MJ$  of biodiesel) be five folds larger than the average emission observed in

the South region ( $14.3 \text{ gCO}_2\text{eq/MJ}$  of biodiesel). The Brazilian average was  $37.5 \text{ gCO}_2\text{eq/MJ}$  of biodiesel. It is essential to highlight that the studies were made using different methodologies. Therefore, the comparison between them must be made carefully – it is possible to affirm that the existent LCA studies of Brazilian biodiesel indicate that soybean expansion in the Midwest region is responsible for most of the GHG emissions of the production of Brazilian biodiesel. However, a comparative study of different regions must be done to determine the values of the emissions. The GHG

Table 3. GWP of soybean biodiesel ( $\text{gCO}_2\text{eq/MJ}$  of biodiesel)

Region	Ref.	Allocation	Land use change	Agriculture	Soy-bean transport	Oil extraction	Oil transport	Oil refining	Trans-esterification	Bio-diesel distribution	Fuel use	Total
MW	[12]	energy	78.00	14.00	N.A.	1.00	N.A.	1.00	4.00	O.E.	N.E.	98.00
		mass	48.00	8.00	N.A.	1.00	N.A.	0.00	4.00	O.E.	N.E.	61.00
		price	87.00	15.00	N.A.	1.00	N.A.	1.00	5.00	O.E.	N.E.	109.00
	[12]	energy	89.00	14.00	N.A.	0.00	N.A.	1.00	5.00	O.E.	N.E.	109.00
		mass	40.00	7.00	N.A.	1.00	N.A.	0.00	4.00	O.E.	N.E.	52.00
		price	101.00	14.00	N.A.	2.00	N.A.	0.00	5.00	O.E.	N.E.	122.00
	[17]	area	N.E.	29.57	N.E.	N.E.	N.E.	N.E.	N.E.	N.E.	N.E.	29.57
	[15]	energy	N.E.	14.00	13.00	4.00	N.A.	N.A.	6.00	N.E.	N.E.	37.00
	[18](a)	mass	N.E.	7.95	N.A.	16.32	N.A.	N.A.	4.23	O.E.	N.E.	24.27
	[18](b)	mass	N.E.	7.95	N.A.	17.83	N.A.	N.A.	12.83	O.E.	N.E.	25.78
	[19](c)	mean value	N.A.	-22.09	19.40	6.46	1.34	N.A.	6.02	N.E.	N.E.	11.13
	[6](c,d)	sub-process division	N.E.	8.00	0.73	1.84	0.00	N.A.	6.39	N.E.	N.E.	16.96
	[6](c,d)	system expansion	N.E.	-14.14	0.73	1.84	0.00	N.A.	6.39	N.E.	N.E.	-5.18
	[20]	mean value	N.A.	-6.16	5.37	1.63	1.26	N.A.	5.06	N.E.	N.E.	7.16
	[14]	mass	N.E.	-67.91	N.A.	5.31	N.A.	N.A.	5.08	1.84	71.93	16.26
	[14](e)	mass	N.E.	-64.89	N.A.	5.08	N.A.	N.A.	11.27	1.84	72.18	25.49
SE	[16]	none	N.E.	N.E.	N.E.	N.E.	N.E.	N.E.	110.37	N.E.	N.E.	110.37
S	[12]	energy	33.00	12.00	N.A.	1.00	N.A.	0.00	5.00	O.E.	N.E.	51.00
		mass	17.00	6.00	N.A.	1.00	N.A.	0.00	4.00	O.E.	N.E.	28.00
		price	36.00	12.00	N.A.	1.00	N.A.	2.00	4.00	O.E.	N.E.	55.00
	[13](f)	none	0.06	N.A.	N.E.	N.E.	N.E.	N.E.	N.E.	N.E.	N.E.	0.06
	[13](g)	none	0.03	N.A.	N.E.	N.E.	N.E.	N.E.	N.E.	N.E.	N.E.	0.03
	[13](h)	none	0.00	N.A.	N.E.	N.E.	N.E.	N.E.	N.E.	N.E.	N.E.	0.00
	[13](i)	none	0.43	N.A.	N.E.	N.E.	N.E.	N.E.	N.E.	N.E.	N.E.	0.43
	[21]	none	71.06	45.62	N.E.	N.E.	N.E.	N.E.	N.E.	N.E.	N.E.	116.68
	[12]	energy	0.00	15.00	N.A.	1.00	N.A.	1.00	5.00	O.E.	N.E.	22.00
		mass	0.00	13.00	N.A.	0.00	N.A.	0.00	5.00	O.E.	N.E.	18.00
		price	0.00	8.00	N.A.	1.00	N.A.	1.00	5.00	O.E.	N.E.	15.00

N.A.: Not available – when data of any stage is presented merged with data of another stage. E.g., [12] merged all transport data inside Brazil with transport; N.E.: Not evaluated; O.E.: Out of the scope – [12] evaluated transport of biodiesel to Europe.

(a) Integrated industrial production chain; (b) Non-integrated industrial production chain; (c) Considered the GWP effects in 20 years; (d) Average; (e) Ethylic route; (f) Soybean area taken from pasts, high carbon stock; (g) Soybean area taken from pasts, intermediate carbon stock; (h) Soybean area taken from pasts, low carbon stock; (i) Soybean area taken from forests.

emissions reported for the agricultural phase vary from  $-67.91 \text{ gCO}_2\text{eq/MJ of biodiesel}$  to  $45.62 \text{ gCO}_2\text{eq/MJ of biodiesel}$ . The negative value reported by [14] is justified by the consideration of the  $\text{CO}_2$  captured by photosynthesis. The soybean transport is evaluated only by [15], being the second process to emit more GHG gases in this study ( $13 \text{ gCO}_2\text{eq/MJ of biodiesel}$ , against  $14 \text{ gCO}_2\text{eq/MJ of biodiesel}$  from agriculture – this study does not evaluate land use change, nor fuel use). [16] presents only the transesterification, but the high emissions of the soybean oil considered in the inventory make this case study have a high GHG intensity. Finally, the fuel use is evaluated only by [14], and this process has a high GHG intensity. The average value,  $72.5 \text{ gCO}_2\text{eq/MJ of biodiesel}$  is close to the average emission observed due to LUC in the region Midwest. A study comparing the same system would be necessary to evaluate which phase is responsible for the most considerable GHG intensity.

The comparison between mass, price, and energy allocation made by [12] unveiled that price allocation results in higher GHG intensity, while mass allocation results in lower GHG intensity. The system expansion adopted by [6] resulted in lower GHG emissions than the sub-process approach, where data is collected exclusively for the studied system processes. [14] compared ethylic and methylic transesterification and found that the GHG intensity of the ethylic route is higher than the methylic route.

Tables 4-6 presents the GWP reported by the LCA of biodiesel made of beef tallow, cotton, and wasted oil. Other feedstocks are not discussed because they do not evaluate the biodiesel production process, so it was not possible to convert their results to the used functional unit. Tables 4-6 evidence the importance of cattle farming, agriculture, and wasted oil collecting stage in the GHG intensity of beef tallow biodiesel, cotton biodiesel, and wasted oil biodiesel, respectively.

Table 4. GWP of beef tallow biodiesel ( $\text{gCO}_2\text{eq/MJ of biodiesel}$ )

Reference	Cattle farming	Animal transport	Slaughter	Tallow transport	Biodiesel production	Total
[19]	87.73	1.47	0.54	0.45	1.37	91.57

Table 5. GWP of cotton biodiesel ( $\text{gCO}_2\text{eq/MJ of biodiesel}$ )

Reference	Agriculture	Oil extraction	Refining	Transesterification	Total
[22]	17.60	1.99	2.32	10.96	33.20

Table 6. GWP of wasted oil biodiesel ( $\text{gCO}_2\text{eq/MJ of biodiesel}$ )

Reference	Collection stage	Production Phase	Total
[23]	51.72	4.46	56.18

## 4. CONCLUSION

A comparison between the GWP of soybean biodiesel indicated that the advance of soy culture in the Midwest region was responsible for most of the GHG emissions in Brazilian biodiesel production. An LCA from land use change to the fuel use would be necessary to compare LUC and combustion GHG emissions. Cattle farming, agriculture, and wasted oil collecting stage are the processes that emit more GHG gases in the production of beef tallow biodiesel, cotton biodiesel, and wasted oil biodiesel, respectively. A comparative study using the same LCA assumptions is necessary to unveil which feedstock of Brazilian biodiesel has the higher GHG intensity.

## ACKNOWLEDGMENT

This work was supported by the Conselho Nacional de Desenvolvimento Científico e Tecnológico (CNPq-Brazil) and the Graduate Program in Mechanical Engineering at UFSC.

## REFERENCES

- [1] Shonnard, D.R., Klemetsrud, B., Sacramento-Rivero, J., Navarro-Pineda, F., Hilbert, J., Handler, R., SUPPEN, N., Donovan, R.P. A review of environmental life cycle assessments of liquid transportation biofuels in the Pan American region. *Environmental management* 2015, 56:1356-1376. <<https://doi.org/10.1007/s00267-015-0543-8>>
- [2] Guinée, J.B.; Gorrée, M.; Heijungs, R.; Huppes, G.; Kleijn, R.; Koning, A. de; Oers, L. van; Wegener Sleeswijk, A.; Suh, S.; Udo de Haes, H.A.; Bruijn, H. de; Duin, R. van; Huijbregts, M.A.J. Handbook on life cycle assessment. Operational guide

- to the ISO standards. I: LCA in perspective. IIa: Guide. IIb: Operational annex. III: Scientific background. Dordrecht: Kluwer Academic Publishers, 2002.
- [3] Agência Nacional de Petróleo, Gás e Biocombustíveis. Informações de mercado – 2019. Available online at <<http://www.anp.gov.br/producao-de-biocombustiveis/biodiesel/informacoes-de-mercado>>. Last accessed on 12.08.2020.
- [4] Scopus. Available online at <<https://www.scopus.com>>. Last accessed on 07.31.2020.
- [5] Web of science. Available online at <<https://www.webofknowledge.com>>. Last accessed on 08.12.2020.
- [6] Esteves, E. M. M., Esteves, V. P. P., Bungenstab, D. J., Araújo, O. D. Q. F., & Morgado, C. D. R. V. Greenhouse gas emissions related to biodiesel from traditional soybean farming compared to integrated crop-livestock systems. *Journal of Cleaner Production*. 2018, 179: 81-92. <<https://doi.org/10.1016/j.jclepro.2017.12.262>>
- [7] Instituto Brasileiro de Pesquisa e Estatística. Tabela 1612 - Área plantada, área colhida, quantidade produzida, rendimento médio e valor da produção das lavouras temporárias. Available online at <<https://sidra.ibge.gov.br/Tabela/1612>>. Last accessed on 12.09.2020.
- [8] Instituto Brasileiro de Geografia e Estatística. Tabela 6783 - Número de estabelecimentos agropecuários com bovinos, Efetivos, Venda e Produção de leite, por grupos de área de pastagem e grupos de área total. Available online at <<https://sidra.ibge.gov.br/tabela/6783>>. Last accessed on 11.20.2020.
- [9] Esteves, V. P. P., Esteves, E. M. M., Bungenstab, D. J., Feijó, G. L. D., Araújo, O. D. Q. F., Morgado, C. D. R. V. Assessment of greenhouse gases (GHG) emissions from the tallow biodiesel production chain including land use change (LUC). *Journal of cleaner production*. 2017, 151: 578-591. <<https://doi.org/10.1016/j.jclepro.2017.03.063>>
- [10] Sousa, V. M., Luz, S. M., Caldeira-Pires, A., Machado, F. S., Silveira, C. M. Life cycle assessment of biodiesel production from beef tallow in Brazil. *The International Journal of Life Cycle Assessment*. 2017, 22.11: 1837-1850. <<https://doi.org/10.1007/s11367-017-1396-6>>
- [11] Atabani, A. E., Silitonga, A. S., Badruddin, I. A., Mahlia, T. M. I., Masjuki, H. H., & Mekhilef, S. A comprehensive review on biodiesel as an alternative energy resource and its characteristics. *Renewable and sustainable energy reviews*. 2012, 16.4: 2070-2093. <<https://doi.org/10.1016/j.rser.2012.01.003>>
- [12] Castanheira, É. G., Grisolí, R., Coelho, S., da Silva, G. A., Freire, F. Life-cycle assessment of soybean-based biodiesel in Europe: comparing grain, oil and biodiesel import from Brazil. *Journal of Cleaner Production*. 2015, 102: 188-201. <<https://doi.org/10.1016/j.jclepro.2015.04.036>>
- [13] Maciel, V. G., Zortea, R. B., da Silva, W. M., de Abreu Cybis, L. F., Einloft, S., Seferin, M. Life Cycle Inventory for the agricultural stages of soybean production in the state of Rio Grande do Sul, Brazil." *Journal of Cleaner Production*. 2015, 93: 65-74. <<https://doi.org/10.1016/j.jclepro.2015.01.016>>
- [14] Altamirano, C. A. A., Yokoyama, L., de Medeiros, J. L., & Araújo, O. D. Q. F. Ethylic or methylic route to soybean biodiesel? Tracking environmental answers through life cycle assessment. *Applied Energy*. 2016, 184: 1246-1263. <<https://doi.org/10.1016/j.apenergy.2016.05.017>>
- [15] Knoope, M. M., Balzer, C. H., Worrell, E. Analysing the water and greenhouse gas effects of soya bean-based biodiesel in five different regions." *Gcb Bioenergy*. 2019, 11.2: 381-399. <<https://doi.org/10.1111/gcbb.12558>>
- [16] Carvalho, M., Da Silva, E. S., Andersen, S. L., Abrahão, R. Life cycle assessment of the transesterification double step process for biodiesel production from refined soybean oil in Brazil. *Environmental Science and Pollution Research*. 2016, 23.11: 11025-11033. <<https://doi.org/10.1007/s11356-016-6295-z>>
- [17] Raucci, G. S., Moreira, C. S., Alves, P. A., Mello, F. F., de Almeida Frazão, L., Cerri, C. E. P., & Cerri, C. C. Greenhouse gas assessment of Brazilian soybean production: a case study of Mato Grosso State. *Journal of Cleaner Production*. 2015, 96: 418-425. <<https://doi.org/10.1016/j.jclepro.2014.02.064>>
- [18] Cerri, C. E. P., You, X., Cherubin, M. R., Moreira, C. S., Raucci, G. S., Castigioni, B. D. A., Alves, P.A., Cerri, D.G.P., Mello,F.F.C., Cerri, C. C. Assessing the greenhouse gas emissions of Brazilian soybean biodiesel production. *PloS one*. 2017, 12.5: e0176948. <<https://doi.org/10.1371/journal.pone.0176948>>
- [19] Esteves, V. P. P., Morgado, C. D. R. V., Araújo, O. D. Q. F. Regional and temporal sustainability assessment of agricultural-based biodiesel." *Clean Technologies and Environmental Policy*. 2020. 22.4: 965-978. <<https://doi.org/10.1007/s10098-020-01842-x>>
- [20] Esteves, V. P. P., Esteves, E. M. M., Bungenstab, D. J., Loebmann, D. G. D. S. W., de Castro Victoria, D., Vicente, L. E., Araújo, O.Q.F., Morgado, C. D. R. V. Land use change (LUC) analysis and life cycle assessment (LCA) of Brazilian soybean biodiesel." *Clean Technologies and Environmental Policy*. 2016, 18.6: 1655-1673. <<https://doi.org/10.1007/s10098-016-1161-8>>
- [21] Zortea, R. B., Maciel, V. G., & Passuello, A. Sustainability assessment of soybean production in Southern Brazil: A life cycle approach. *Sustainable Production and Consumption*. 2018, 13: 102-112. <<https://doi.org/10.1016/j.spc.2017.11.002>>
- [22] Lima, Â. M. F., Torres, E. A., Kiperstok, A., Santos, G. D. F. M. Environmental impacts of the biodiesel production chain of cotton seed in Bahia, Brazil." *Clean Technologies and Environmental Policy*. 2917, 19.5: 1523-1534. <<https://doi.org/10.1007/s10098-017-1347-8>>
- [23] Moecke, E. H. S., Feller, R., dos Santos, H. A., de Medeiros Machado, M., Cubas, A. L. V., de Aguiar Dutra, A. R., Santos, L.L.V., Soares, S. R. Biodiesel production from waste cooking oil for use as fuel in artisanal fishing boats: Integrating environmental, economic and social aspects. *Journal of Cleaner Production*. 2016, 135: 679-688. <<https://doi.org/10.1016/j.jclepro.2016.05.167>>



# SOLAR COLLECTOR WITH INCREASED HEAT TRANSFER EFFICIENCY

Andrey Batukhtin

Transbaikal State University, Chita, Russia, batuhtina\_ir@mail.ru, ORCID: 0000-0002-3798-3675

Sergey Batukhtin

Transbaikal State University, Chita, Russia, batuhtin1@mail.ru, ORCID: 0000-0001-8876-7764

Marina Baranovskaya

Transbaikal State University, Chita, Russia, mak.b192@yandex.ru, email address, ORCID: 0000-0001-8283-9448

Pavel Safronov

Transbaikal State University, Chita, Russia, yakovlevaop1@mail.ru, email address, ORCID: 0000-0002-7554-2774

*Batukhtin A.G., Batukhtin S.G., Baranovskaya M.G., Safronov P.G. Solar collector with increased heat transfer efficiency. 9<sup>th</sup> Eur. Conf. Ren. Energy Sys. 21-23 April 2021, Istanbul, Turkey*

**Abstract:** According to experts' forecasts, renewable energy sources in the next 20 years will become the fastest growing segment of the world energy, their share in the next decade will grow by about one and a half times. Around the world, solar energy is gaining the highest rate of development in comparison with other types of renewable energy sources.

This article provides an overview of many existing and only researched technologies that will help accelerate the implementation of solar energy instead of traditional energy sources, as well as increase productivity and optimize the operation of solar panels, which in turn will increase the amount of energy generated in solar power plants. All presented methods help to improve the efficiency of systems based on the use of solar energy as the main energy resource.

In addition to the description of existing methods, a diagram of a solar-air heating power plant is presented, which allows increasing energy efficiency indicators through the use of a regenerative air solar collector with increased heat transfer efficiency. It is proposed to use hemispherical indentations on the sun-perceiving surface as intensifiers. The principle of operation of this collector is described in detail, as well as a schematic diagram. A comparative calculation of the intensification of the solar collector with and without the use of depressions as modernization was carried out, on the basis of which a conclusion was made about the effectiveness of using this type of solar collector and the economic effect of using this method was indicated. A description of the methodology for calculating the solar collector is presented, thanks to which this development can be used and implemented into existing heating and hot water supply systems.

**Keywords:** Solar energy, collector, intensification, optimization, energy efficiency

© 2021 Published by ECRES

## Nomenclature

WRDC	World Radiation Data Center
RES	Renewable energy sources
HMTI	Heat and mass transfer intensification

## 1. INTRODUCTION

Today, non-traditional and renewable energy sources are very popular all over the world. According to experts' forecasts, renewable energy sources in the next 20 years will become the fastest growing segment of the world energy, their share in the next decade will grow by about one and a half times [1]. Around the world, solar energy is gaining the highest rate of development in comparison with other types of renewable energy sources. This is due

to a number of factors: environmental friendliness of the technology, high reliability of the solar battery, autonomy of power supply to the energy consumer, the presence of an endless source of energy, as well as the absence of noise during operation. Germany leads the world in the use of solar energy, followed by China, Italy, Japan, the USA, Spain, France and other countries. [2]

The policy of countries in which non-traditional energy is actively developing, in particular solar, is aimed at the development and widespread introduction of renewable energy sources into people's lives. For example, China, the United States and the European Union are already actively studying the power of devices and mechanisms from solar energy. This means that in developed countries not only the issue of introducing solar energy instead of traditional energy sources is being studied, but also the issues of modernizing and improving existing methods. Therefore, the scientists of these countries are faced with the question of studying and researching various ways by which it is possible not only to increase the efficiency of solar power plants, but also to increase their power and energy intensity.

There are many possible ways to improve the operation of solar collectors - the use of various kinds of concentrators, optimization of tracking the position of the sun, the choice of the tilt angle and orientation of the solar collector. In addition to optimizing the methods for positioning the solar collector, methods for improving their design are also widely studied. The possibility of using new materials in the production of various elements is being studied; designs of polymer solar collectors, which are twice cheaper than conventional ones, are proposed. A large number of modern developments are devoted to the issue of increasing the efficiency of autonomous heat supply installations based on solar power plants [3-5]. Foreign authors studying solar energy pay attention to the assessment of solar radiation [6-9]. There are several ways to assess data on solar radiation fluxes: analytical; direct measurements on site; long-term measurements using a unified technique at meteorological stations.

One of the most urgent is the issue of researching algorithms based on the analytical interpretation of the sun's motion [10, 11]. Some authors for this method use the function of the average monthly intensity of solar radiation, but this approach is ineffective and is subject to serious criticism from researchers since hourly fluctuations are not taken into account [10-22].

All the necessary parameters of a specific geographic point can be determined by calculation. The general laws considered in [23] determine the parameters of the Sun's motion over the horizon, the energy [24, 25] and spectral characteristics of radiation [26-28]. In [29], the thermodynamic parameters of effective absorption are considered. The Universities of Minnesota and Hanevelt have considered the coefficients of effective absorption of the normal spectrum of solar radiation for the main selective coatings [30-32].

The latter method - direct measurement on site - is the most laborious of all, but it has been used by a number of researchers, both foreign [33-36] and domestic [37]. At present, the World Radiation Data Center (WRDC) has an information retrieval system with an archive and a systematically updated database on the components of the radiation balance of the world actinometric network. [38, 39] The main elements of this network are actinometric installations [40-43], which determine the parameters of direct and scattered solar radiation. In addition, there are private databases of renewable energy resources [44-50]. Much attention is paid to solar installations of a separate type, where the accumulator is located separately from the collector [51, 52], the most common of them are vacuum tubular solar collectors, which occupy more than 60% of the market [53]. One of the main tasks of the development of solar energy is to increase the capacity of solar plants, which will lead to an increase in their economic performance [54-57]. Self-draining solar heat supply systems are also being actively studied, a feature of which is the emptying of solar collectors from the coolant when the solar circuit pump stops in a special tank / storage tank. A significant number of foreign developments are devoted to the development of the "Solar House" system, the essence of which is that electricity, water supply and heating are provided by the energy of the sun. In the United States, a special competition has even been established that brings together 20 international university teams in the fight to create the most attractive and energy efficient solar houses, which also significantly reduce greenhouse gas emissions into the atmosphere [58-62].

All of the above research and development is only a small part devoted to the study of the issue of the development of unconventional and renewable energy sources, namely solar energy. Such a great interest in this problem once again confirms the relevance of the study and use of RES in the modern world.

## **2. MODEL**

This article proposes a method of using a regenerative air solar collector with increased heat transfer efficiency. This heat exchanger (Appendix 1) is designed to improve the efficiency of the implementation of the scheme of an energy-efficient solar-air heating installation. A distinctive feature of this heat exchanger is the ability to

simultaneously heat two types of heat transfer fluids. It is proposed to use hemispherical recesses as intensifiers. A detailed description of this type of intensifier is presented in [64].

The operation of the solar collector with the use of hemispherical depressions is as follows (Appendix 1): the radiation of the Sun, passing through the glass, heats the absorber, which in turn heats the gaseous medium (air) moving in the gas heating cavity 5, while the hemispherical depressions 8 on the sun-perceiving surface 6 will contribute to a significant intensification of heat transfer. The coolant in the collector circulates through a harp-shaped pipe system, and since they are recessed by 50% into the sun-sensing plate, they will heat up, and the hemispherical recesses applied to the inner surface of the tubes will also contribute to the intensification of heat transfer. An increase in the efficiency of heat transfer in the developed collector is determined by a local increase in the heat transfer coefficient and an increase in the area. The growth of the heat transfer coefficient can be determined on the basis of experimental data, or by calculation.

### 3. EXPERIMENTAL RESULTS

To understand how effective intensification is, it is necessary to calculate the daily heat absorption of a flat water-air collector with and without modernization [64]. The calculation was made using [65] under comparable conditions.

Climatological data: Chita: longitude - 113 hours 23 minutes, latitude - 52 hours 6 minutes; date October 1, 2013

Surface direction: tilt angle to the horizon - 45 degrees; azimuth direction 180 deg.

Plate: plate dimensions are taken: 1000 \* 100 \* 10mm, material - copper, wall thickness 2mm.

Tubes: quantity 10 pcs., diameter 25mm, material - copper, wall thickness 1mm; coverage share 50%; thermal interface material - tin, layer thickness 500 microns.

Absorber: coloring - matt black paint (absorption rate 95, blackness 5, selectivity 0.4);

External insulation: glass - two layers, thickness 1 mm, attenuation coefficient 0.4 1 / mm; air passage size 30 mm.

Air parameters: inlet air temperature 0 0C; air consumption - 100.0 m<sup>3</sup> / h.

The results of calculating the daily heat perception of a flat water-air collector are summarized in Table 1.

When calculating the daily heat perception of a regenerative water-air heat exchanger with an increased heat transfer efficiency, the heat transfer coefficients obtained by the standard method increase in proportion to the average (over the hole surface) relative heat transfer coefficients. To take into account the increase in the heat exchange area, it is necessary to estimate its relative increase in K<sub>F</sub> and take it into account in the standard procedure.

For the proposed geometric parameters of hemispherical depressions, K<sub>F</sub> takes values from 1.09 to 1.116, depending on the packing density (for a preliminary estimate, K<sub>F</sub> = 1.1 was taken in the calculations). The calculations showed that the flow regime is turbulent: Re = 69636.4. For such a regime, with intensification on spherical intensifiers, we take [67]  $\alpha$  = 1.25. The results of calculating the daily heat perception of a flat water-air collector with an increased heat transfer efficiency are summarized in Table 2.

The intensification showed a 2.43% increase in efficiency. The annual efficiency of reservoir intensification will be 106 kW / m<sup>2</sup>. At the current tariff for the district heating system in Chita, 1925 rubles / Gcal, the economic effect is 175.5 rubles / m<sup>2</sup>.

Table 1. Results of calculating a flat reservoir without stimulation. Inlet air temperature / ambient temperature 0° C

Nº	The local time	Warmth is beneficially perceived collector, W
1	9:00	0
2	10:00	150
3	11:00	362
4	12:00	550
5	13:00	625
6	14:00	670
7	15:00	655
8	16:00	585
9	17:00	455
10	18:00	260
11	19:00	50
12	20:00	0
13	Total per day	4362

Table 2. Results of calculating a flat reservoir (intensification:  $K_F = 1.1$ ,  $\tilde{\alpha} = 1.25$ ). Inlet air temperature / ambient temperature  $0^\circ C$

Nº	The local time	Warmth is beneficially perceived collector, W:
1	9:00	0
2	10:00	152
3	11:00	377
4	12:00	590
5	13:00	635
6	14:00	675
7	15:00	660
8	16:00	595
9	17:00	465
10	18:00	267
11	19:00	52
12	20:00	0
13	Total per day	4468

#### 4. CALCULATION PROCEDURE

To use the solar air heating installation scheme, it is necessary to calculate the collector. When calculating the solar collector of the solar air heating system, the initial data are: the parameters of the collector, the flow rate of the intermediate heat carrier and air, the characteristic of the time interval, as well as the outside air temperature. From the calculation of the storage tank, the temperature of the intermediate heat carrier at the outlet from it is determined. The result of the calculation is the temperature of the intermediate heat carrier at the inlet to the tank, as well as the air temperature at the outlet.

The basis for calculating the solar collector at a particular moment in time is the characteristic of the intensity of the actual solar radiation incident on the ray-receiving surface, taking into account its installation. A detailed calculation procedure is described in [67]. Knowing the methodology for calculating the solar collector, we can use the scheme of an energy efficient solar air heating installation and implement it in air heating systems, which will significantly increase the efficiency of such systems, and we can also reduce the use of traditional heat sources.

#### 5. FINDINGS

Solar energy is the most affordable and widespread form of all existing energy resources. Many countries are actively pursuing policies to increase the share of solar energy use. However, the installation of conventional solar collectors is no longer so effective, therefore, various methods are being actively studied to improve the characteristics of solar collectors, which in turn leads to an increase in their performance.

Currently, a significant number of different schemes for using solar energy have been developed. The article proposes a method for using a regenerative air solar collector with increased heat transfer efficiency using hemispherical recesses as intensifiers. Testing of this method has shown its high efficiency due to increased intensification, and the economic effect of using this method is also clearly reflected. The use of solar heating with the use of solar collectors of various types in air heating systems will significantly increase the efficiency of such systems, as well as increase the degree of replacement of traditional heat sources.

#### REFERENCES

- [1] The energy of the future becomes the reality of the present. Kommersant Magazine 2019; <<https://www.kommersant.ru/doc/3952751>>
- [2] Top 10 countries for the use of solar energy. Peretok.ru magazine 2014; <https://peretok.ru/articles/freezone/17430/>
- [3] Non-traditional and renewable energy sources: textbook. Manual for UNIVERSITIES / V.A. Ageev - M.: MPEI, 2006 .-- 325 p.
- [4] Vasiliev G.P. Commentary on the article "On the efficiency of using heat pump installations" / G.P. Vasiliev // Energy saving. - 2008. - No. 3. - P. 63–64.
- [5] The choice of a solar heat supply system for individual residential buildings // Materials of the Federal Industrial Association of Germany for household, energy and environmental technologies

- [6] Duncan C.H. "Latest Rocket Measurements of the Solar Constant". *Solar Energy*. 28, 385.
7. Jones R.E. "Effects of Overhand Shading of Windows Having Arbitrary Asimuth". *Solar Energy*. 24, 305.
8. Klein S.A. "Calculation of Monthly Average Insolation on Tilted Surfaces". *Solar Energy*. 19, 325.
9. Dunkle R.V. "Thermal radiation Tables and Applications" Traurs ASME. 76, 549
10. S.A. Klein, W.A. Beckman. Review of Solar Radiation Utilizability // *Journal of Solar Energy Engineering*. 1984. V. 106. P. 1-10.
11. R.K. Aggarwal. Estimation of Total Solar Radiation on Tilted Surface // *Journal of Environmental Engineering and Technology*. 2013. V. 2. P. 4-6.
- [12] Rajesh Kumar, R.A. Gupta, Ajay Kumar Bansal. Economic analysis and power management of a stand-alone wind/photovoltaic hybrid energy system using biogeography based optimization algorithm // *Swarm and Evolutionary Computation*. 2013. V. 8. P. 33-43.
13. Ahmed Said Al Busaidi, Hussein A Kazem, Abdullah H Al-Badi, Mohammad Farooq Khan. A review of optimum sizing of hybrid PV-Wind renewable energy systems in Oman // *Renewable and Sustainable Energy Reviews*. 2015. V. 53. P. 185-193.
14. Arnau Gonzales, Jordi-Roger Riba, Antony Rius, Rita Puig. Optimal sizing of a hybrid grid-connected photovoltaic and wind power system // *Applied Energy*. 2015. V. 154. P. 752-762.
15. Abdolvahad Fetanat, Ehsan Khorasaninejad. Size optimization for hybrid photovoltaic-wind energy system using ant colony optimization for continuous domains based integer programming // *Applied Soft Computing*. 2015. V. 31. P. 196-209.
16. Amit Kumar Yadav, S.S. Chandel. Solar energy potential assessment of western Himalayan Indian state of Himachal Pradesh using J48 algorithm of WEKA in ANN based prediction model // *Applied Soft Computing*. 2015. V. 75. P. 675-693.
17. Giuseppe Marco Tina, Salvina Gagliano. Probabilistic modelling of hybrid solar/wind power system with solar tracking system // *Renewable Energy*. 2011. V. 36. P. 1719-1727.
18. Getachew Bekele, Gelma Boneya. Design of a Photovoltaic-Wind Hybrid Power Generation System for Ethiopian Remote Area // *Energy Procedia*. 2012. V. 14. P. 1760-1765.
19. Orhan Ekren, Banu Yetkin Ekren. Size optimization of a PV/wind hybrid energy conversion system with battery storage using simulated annealing // *Applied Energy*. 2010 V. 87. P. 592-598.
20. Giuseppe Marco Tina, Salvina Gagliano. Probabilistic modelling of hybrid solar/wind power system with solar tracking system // *Renewable Energy*. 2011. V. 36. P. 1719-1727.
21. Karamov D.N. Optimization of the equipment composition of autonomous power complexes using renewable sources and energy storage devices abstract dis. ... Candidate of technical sciences: 05.14.01 Irkutsk, 2016.
22. Manuel Castaneda, Antonio Cano, Francisco Jurado, Higinio Sanchez, Luis M. Fernandez. Sizing optimization, dynamic modeling and energy management strategies of a stand-alone PV/hydrogen/battery-based hybrid system // *International Journal of Hydrogen Energy*. 2013. V. 38. P. 3830-3845.
- [23] Anderson E.E., Fundamentals of Solar Energy Conversion, Addison-Wesley, MA.
- [24] Dunkle R.V. "Randomly Packed Particulate Bed Regenerators and Evaporative Coolers" MCB, 117.
25. Carfers W.W. and L.S. Peterson "Free Convection Suppression Using Honeycomb Cellular Materials". *Solar Energy*. 13, 4.
26. Swinbank W.C., Q.J. Roy "Long Wave Radiation from Clear Skies". *Meteorol Soc*. 89, 339.
27. Sparow E.M., J.W. Ramsey and E.A. Mass "Effect of Finite Width on Heat Transfer and Fluid Flow about an Inclined Rectangular Plate". *Trans. ASME J. Heat Transfer*: 101, 2.
28. Sparow E.M. "Analysis of Laminar Free-Convection Heat Transfer in Enclosed Regions of Flat Rectangular Dunes" NASA Technical Note 3331.
29. University of Minnesota and Honeywell Corp. "Research Applied to Solar Thermal Power Systems". Progress Report No. 2 to National Science Foundation, NSF/RANN/SE/GI-3487/PR/73/2.
30. Edwards D.K., J.T. Gier, K.E. Nelson, R.D. Roddick and J.T. Gier "Basic Studies on the Use and Control of Solar Energy". Report No. 60-93 Department of Engineering, University of California at Los Angeles.
31. Edwards D.K., J.T. Gier, K.E. Nelson and R.D. Roddick "Spectral and Directional Thermal Radiation Characteristic of Selective Surfaces for Solar Collectors". *Solar Energy*. 6, 1.
- [32] Karamov D.N. Optimization of the equipment composition of autonomous power complexes using renewable sources and energy storage devices abstract dis. ... Candidate of technical sciences: 05.14.01 Irkutsk, 2016.
- [33] A. Kaabeche, M. Belhamel, R. Ibtouen. Sizing optimization of grid-independent hybrid photovoltaic/wind power generation system // *Energy*. 2011. V. 36. P. 1214-1222.
34. Wei Wu, Ya-Yan Zhou, Mu-Hsuan Lin, Jenn-Jiang Hwang. Modeling, design and analysis of a stand-alone hybrid power generation system using solar/wind // *Energy Conversion and Management*. 2013. V. 74. P. 344-352.
35. Gilles Notton, Said Diaf, Ludmil Stoyanov. Hybrid Photovoltaic/Wind Energy Systems for Remote Locations // *Energy Procedia*. 2011. V. 6. P. 666-677.
36. V.V. Butuzov. INCREASING THE EFFICIENCY OF SOLAR HEAT SUPPLY SYSTEMS abstract dis. ... candidate of technical sciences: 05.14.08 / All-Russian Scientific Research Institute for Electrification of Agriculture. Moscow 2013.
- [37] World Radiation Data Center URL: [http://wrdc.mgo.rssi.ru/wwwrootnew/wrdc\\_ru\\_new.htm](http://wrdc.mgo.rssi.ru/wwwrootnew/wrdc_ru_new.htm) (date of access: 01.03.2016)
- [38] S. V. Kiseleva. The use of GIS technology for information support of small and distributed energy. Geographic Information System (GIS) "Renewable Energy Sources of Russia".

- [39] Whiller A. "Solar Radiation Graphs". Solar Energy. 9, 164.
40. Norris D.J. "Correlation of Solar Radiation with Clouds". Solar Energy. 12, 107.
- [41] Norris D.J. "Calibration of Pyranometers in Inclined and Inverted Positions". Solar Energy. 16, 53.
42. Meteonorm Software . URL: <http://meteonorm.com> (дата обращения: 01.03.2016)
43. Local base of Europe and North Africa E.S.R.A. 2000. URL: [www.ensmp.fr/Fr/Services/Presses ENS](http://www.ensmp.fr/Fr/Services/Presses/ENS) (date of access: 01.03.2016).
44. Local base of Europe and North Africa S @ tel - Light 2000. URL: [www.satellight.com](http://www.satellight.com) (date of access: 01.03.2016).
45. RetScreen. URL <http://www.retscreen.net/> (дата обращения: 01.03.2016).
46. Climate 1. URL <http://www.climate-one.de/> (дата обращения: 01.03.2016).
47. Fang-Fang Li, Jun Qiu. Multi-objective optimization for integrated hydro–photovoltaic power system // Applied Energy. 2015.
48. Aeidapu Mahesh, Kanwarjit Singh Sandhu. Hybrid wind/photovoltaic energy system developments: Critical review and findings // Renewable and Sustainable Energy Reviews. 2015. V. 52. P. 1135-1147.
49. Surface meteorology and Solar Energy. A renewable energy resource web site URL: <https://eosweb.larc.nasa.gov/sse> (дата обращения: 01.03.2016).
50. V.V.Butuzov. INCREASING THE EFFICIENCY OF SOLAR HEAT SUPPLY SYSTEMS dissertation ... Candidate of Technical Sciences: 05.14.08 / All-Russian Scientific Research Institute of Agricultural Electrification. Krasnodar, 2013.75.
51. Kemp C.M. Apparatus for Utilizing the Sun's rays for heating water // US patent N 451384. 1891.
52. Butuzov V.A. Review of the world market for solar heat supply systems // S.O.K. Journal, №12 / 2013.
53. Banse S. Integrated storage collectors. All inclusive // Sun, Wind & Energy, №2/2012.
54. Tanja Peschel Commercial CSP plant in Saudi Arabia // Sun, Wind & Energy, №13/2016.
55. Butuzov V.A. Plastic solar collectors and solar installations based on them // Journal of SOK, No. 14/2014.
56. Roubcke I. Pool absorbers. Gaujons optimist // Sun, Wind & Energy, №7/2010.
- [57] Butuzov V.A., Bryantseva E.V., Butuzov V.V., Gnatyuk I.S. Self-draining solar plants // Alternative energy and ecology, 2010. №2. S. 10-13.
- [58] Wang, N.; Esram, T.; Martinez, L.A.; McCulley, M.T. A marketable all-electric solar house: A report of a Solar Decathlon project. Renewable Energy 2009, 34 2860–2871.
- [59] Moretti E. Development of Innovative Heating and Cooling Systems Using Renewable Energy Sources for Non-Residential Buildings / Elisa Moretti, Emanuele Bonamente, Cinzia Buratti and Franco Cotana // Energies 2013, 6, 5114-5129.
- [60] Osborne A. Simulation Prototyping of an Experimental / Anna Osborne, Stuart Baur, and Katie Grantham // Solar House Energies 2010, 3, 1251-1262.
- [61] Wermager S. Energy Analysis of a Student-Designed Solar House / Samantha Wermager and Stuart Baur //Energies 2013, 6, 6373-6390.
- [62] Khelifa, A., Touafek, K., Ben Moussa, H., Tabet, I. Modeling and detailed study of hybrid photovoltaic thermal (PV/T) solar collector. SOLAR ENERGY. 135 (2016) pp.: 169-176. DOI: 10.1016/j.solener.2016.05.048.
- [63] Solar energy abroad. Energosovet magazine; <<http://www.energosovet.ru/stat787.html>>
- [64] Dunkle R.V. "Thermal radiation Tables and Applications" Traurs ASME. 76, 549
- [65] Dunkle R.V. "Randomly Packed Particulate Bed Regenerators and Evaporative Coolers" MCB, 117.
- [66] Klein S.A. "Calculation of Monthly Average Insolation on Tilted Surfaces". Solar Energy. 19, 325.
- [67] Batukhtin S.G. Improving the efficiency of energy systems and units of TPPs through the use of non-traditional and renewable energy sources: dis ... cand. tech. Sciences: 05.14.14 / S.G. Batukhtin. - Chita, 2016 .-- 94 p.

## Appendices

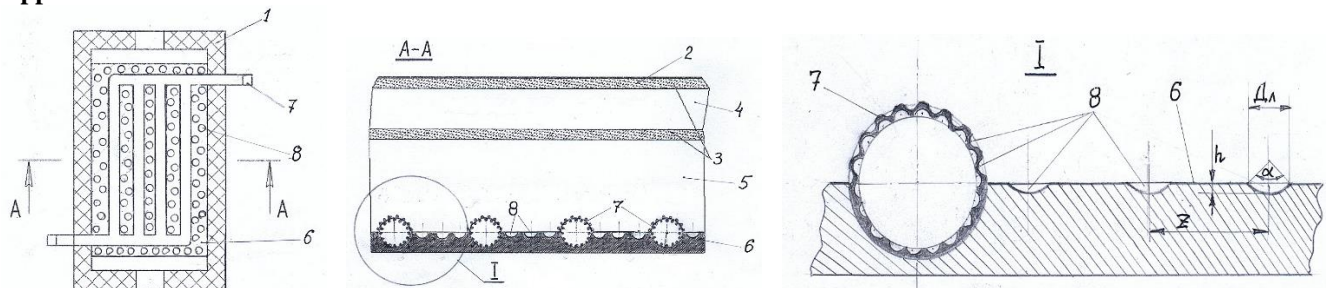


Figure 1. Water-air regenerative heat exchanger with increased heat exchange efficiency:  
1 - insulation; 2, 3 - glass; 4 - vacuum; 5 - air passage; 6 - sun-perceiving surface; 7 - tube; 8 sph



# EFFECT OF POSITION OF HEAT FLUX PROFILE ON THE ABSORBER SURFACE OF PARABOLIC TROUGH SOLAR COLLECTOR FOR DIRECT STEAM GENERATION

Ram Kumar Pal

Centre for Energy Studies, Indian Institute of Technology Delhi, New Delhi – 110016, India, rkpaliitd@gmail.com, ORCID: 0000-0002-8502-4321

K. Ravi Kumar

Centre for Energy Studies, Indian Institute of Technology Delhi, New Delhi – 110016, India, krk@ces.iitd.ac.in, ORCID: 0000-0002-5739-3744

*Cite this paper as:* Pal, RK, Kumar, KR. Effect of transient solar heat flux on direct steam generation in the receiver of parabolic trough solar collector. 9<sup>th</sup> Eur. Conf. Ren. Energy Sys. 21-23 April 2021, Istanbul, Turkey

**Abstract:** Direct steam generation (DSG) is one of the attractive methods to improve the thermal performance of parabolic trough solar collector (PTSC) based solar thermal power plants. However, there is thermal-hydraulic instability due to the phase change in the absorber and the transient solar radiation. In this study, the thermal-hydraulic performance of DSG have been investigated using ANSYS Fluent. The Eulerian two-fluid modeling approach has been used to model the DSG in the solar collector. The numerical modeling has been performed for 12 m length of PTSC, mass flow rate 0.6 kg/s, and operating pressure of 100 bar. The direct normal irradiance (DNI) is considered as 750 W/m<sup>2</sup> and 1000 W/m<sup>2</sup> corresponding to the various times of the day. It has been observed that absorber outer surface temperature varies in the range of 585 K to 643 K. The maximum circumferential temperature difference is observed as 55.5 K. The VVF at the absorber outlet are found as 0.31 and 0.37 respectively for DNI 750 W/m<sup>2</sup> and 1000 W/m<sup>2</sup>. The corresponding pressure losses are 316 Pa and 350 Pa, respectively. The obtained results could be used to characterize the thermal performance of the DSG collectors.

**Keywords:** Concentrated solar power, Parabolic trough solar collector, Two-fluid modeling, Thermal-hydraulic modeling, Direct steam generation

© 2021 Published by ECRES

Nomenclature	
<b>Acronyms</b>	
CFD	Computational Fluid Dynamics
CSHF	Concentrated Solar Heat Flux (W/m <sup>2</sup> )
DNI	Direct Normal Irradiance (W/m <sup>2</sup> )
HT	Heat Transfer
VOF	Volume of Fluid
EMM	Eulerian Multiphase Model
PRESTO	PREssure STaggering Option
PTSC	Parabolic Trough Solar Collector
VVF	Vapor Volume Fraction
<b>Symbol</b>	
$C_p$	Specific heat capacity (J/kg-K)
$LH$	Latent heat (J/kg)
$\dot{q}$	Heat flux (W/m <sup>2</sup> )
<b>Greek Letters</b>	
$\alpha$	Phase volume fraction
$\mu$	Dynamic viscosity (N-s/m <sup>2</sup> )
$\rho$	Density (kg/m <sup>3</sup> )

## 1. INTRODUCTION

Solar energy could be considered as the most emerging green energy source and have the potential to substitute fossil fuels in conventional thermal power generation. The synthetic oil is being used to extract heat from solar collectors in existing PTSC power plants. The heat from the oil is transferred to the water to generate steam using heat exchanger to drive the power block [1]. Whereas, in DSG process, the water/steam is used to extract heat from the solar field and steam is generated in the absorber tube. [2]. This enhances the overall thermal performance of the solar power generation and reduce the investment as well as operational and maintenance cost. The current DSG technology could generate steam around 500-550°C [3]. The benefits of DSG in terms of technology and capital cost have been proved in the European DISS project [4]. TSE-1 is the first commercial DSG solar power plant of capacity 5 MWe installed in Thailand [5].

The various types of two-phase flow patterns may exist in the absorber of the PTSC. Hence, the thermal-hydraulic instability induces in the absorber is the critical issue in terms of the stability and commercialization of the technology. Most of the thermal-hydraulic studies reported in the existing literature are based on the homogeneous modeling approach [1, 6]. Only a few studies have considered the real non-uniform concentrated solar heat flux (CSHF) profile around the absorber surface [7]. In most of the reported studies, the heat flux profile corresponding to solar noon was considered on the absorber outer surface. However, the position of the CSHF profile changes with the time of the day. In this study, the thermal-hydraulic investigation of DSG has been performed considering the CSHF profile on the absorber surface corresponding to the various times of the day. The numerical study is performed by two-fluid modeling technique outlined in next section.

## 2. NUMERICAL MODELING OF DSG

### Governing Equations

The conservation equations for mass, momentum, and energy need to be solved to study the DSG process in the absorber of the PTSC. In this study, the Eulerian multiphase model (EMM) is used to model the DSG process. This model solves separate conservation equations for all phases. The governing equations solved for liquid and vapor phases are given below.

The continuity equation for the liquid phase [8]:

$$\frac{\partial}{\partial t}(\alpha_l \rho_l) + \nabla \cdot (\alpha_l \rho_l \vec{v}_l) = (\dot{m}_{vl} - \dot{m}_{lv}) \quad ((i)$$

Here, the subscripts  $l$  and  $v$  represent the liquid and vapor phase, respectively. The terms  $\rho$  and  $\vec{v}$  are the density and velocity of the fluid.  $\dot{m}$  is the mass transfer rate from one phase to another phase.

The momentum conservation for the liquid phase [8]:

$$\begin{aligned} \frac{\partial}{\partial t}(\alpha_l \rho_l \vec{v}_l) + \nabla \cdot (\alpha_l \rho_l \vec{v}_l \vec{v}_l) = & -\alpha_l \nabla p + \nabla \cdot \bar{\tau}_l + \left( \vec{R}_{vl} + \dot{m}_{vl} \vec{v}_{vl} - \dot{m}_{lv} \vec{v}_{lv} \right) + \alpha_l \rho_l \vec{g} \\ & + \left( \vec{F}_{drag,l} + \vec{F}_{vm,l} + \vec{F}_{lift,l} + \vec{F}_{td,l} + \vec{F}_{wl,l} \right) \end{aligned} \quad ((ii)$$

Here,  $p$  is the pressure shared by both phases;  $\vec{R}_{vl}$ ,  $\vec{v}_{vl}$ ,  $\vec{F}_{drag,l}$ ,  $\vec{F}_{vm,l}$ ,  $\vec{F}_{lift,l}$ ,  $\vec{F}_{wl,l}$  and  $\vec{F}_{td,l}$  are interaction force, interphase velocity, drag force, virtual mass force, lift force, wall lubrication force, and turbulent dispersion force respectively. In Eq. [2] the term  $\bar{\tau}_l$  represents the stress-strain tensor.

The energy conservation equation for the liquid phase [8]:

$$\frac{\partial}{\partial t}(\alpha_l \rho_l H_l) + \nabla \cdot (\alpha_l \rho_l \vec{u}_l H_l) = \alpha_l \frac{\partial p_l}{\partial t} + \bar{\tau}_l : \nabla \vec{u}_l - \nabla \cdot \vec{q}_l + (Q_{vl} + \dot{m}_{vl} H_{vl} - \dot{m}_{lv} H_{lv}) + S_l \quad ((iii)$$

Here, the term  $H_l$ ,  $\vec{q}_l$ ,  $Q_{vl}$ , and  $S_l$  represents specific enthalpy, heat flux vector, interphase heat transfer, and energy source, respectively. The conservation equations for the vapor phase could be defined in a similar way as Eqs. [1-3].

The boiling and mass transfer model is implemented to simulate the DSG.

### Geometry and Boundary Conditions

In this study, the LS-3 PTSC has been considered for simulation. The receiver is incorporated with stainless steel absorber tube enclosed in a glass cover to minimize the thermal losses from the absorber. The 12 m length of absorber tube has been considered as computational domain to investigate the DSG under the variable solar heat flux around the absorber surface. The inner and outer diameters of the stainless-steel absorber tube are 50 mm and

70 mm, respectively. The inlet mass flow rate and operating pressure are 0.6 kg/s, and 100 bar respectively. Fluid is considered as saturated liquid at the absorber inlet. The DNI considered are DNI 750 W/m<sup>2</sup> and 1000 W/m<sup>2</sup>, and optical efficiency as 0.8. The equation of solar heat flux profile developed by Malan et al. [9] is used in this study. To ensure the simulation results to be independent from the cell size variation, the grid-independent study has been performed.

In this work, the thermal-hydraulic simulations are performed for steady-state conditions. The conservation of mass and energy has been established for all simulations. The realizable k-ε turbulence model has been implemented to model the effect of turbulence on fluid flow and HT.

### 3. RESULTS AND DISCUSSION

This study focused on the thermal-hydraulic investigation of the DSG in the absorber tube of PTSC using the two-fluid modeling approach. The effects of variable solar heat flux profile on the thermal-hydraulic parameters have been investigated for DNI 750 W/m<sup>2</sup> and 1000 W/m<sup>2</sup>. It has been observed that the variable CSHF profile at the absorber outer surface and non-uniform heat transfer coefficient (HTC) at the absorber inner surface has a major impact on the absorber temperature distribution.

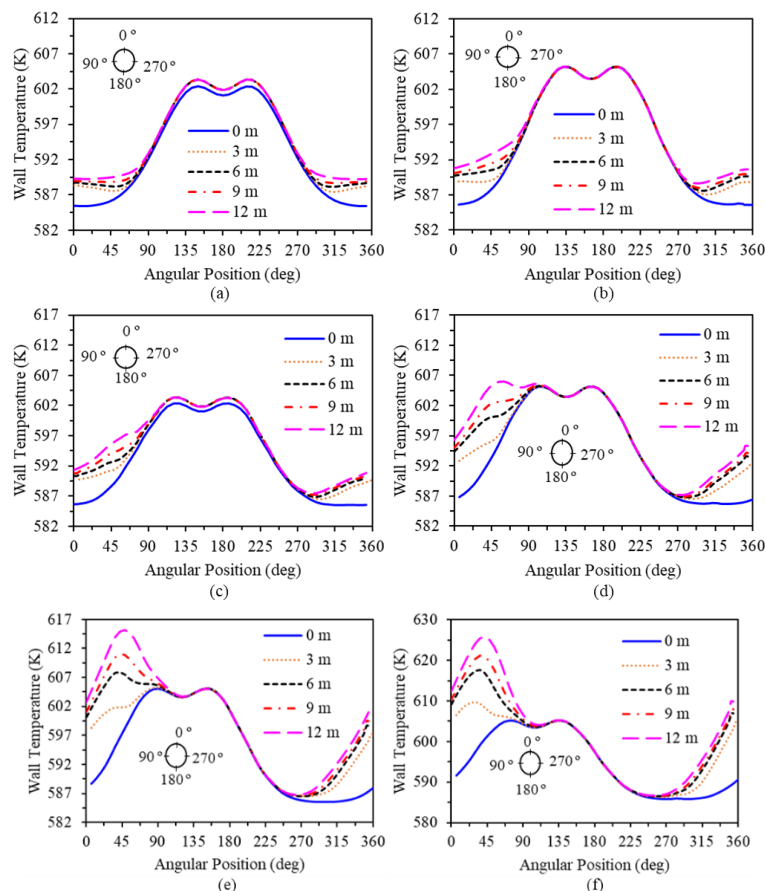


*Figure 1. Variation of absorber outer surface temperature around the circumference for DNI = 750 W/m<sup>2</sup> and heat flux profile corresponding to solar time of: (a) 12:00 h, (b) 13:00 h, (c) 14:00h, (d) 15:00 h, (e) 16:00 h, and (f) 17: 00 h.*

The absorber outer surface temperature distribution around the circumferential surface at five axial positions are shown in Figure 1 and 2. The minimum and maximum absorber outer surface temperature are observed as 585 K to 627 K respectively from solar time of 12:00 h (solar noon) to 17:00 h for DNI of 750 W/m<sup>2</sup>. The maximum absorber circumferential temperature difference ( $\Delta T = T_{\max} - T_{\min}$ ) increases from 17 K to 39 K from 12:00 h to 17:00 h. Similarly, the minimum and maximum absorber outer surface temperature are observed as 586 K to 643 K respectively from solar time of 12:00 h (solar noon) to 17:00 h for DNI 1000 of W/m<sup>2</sup>. The maximum circumferential temperature difference  $\Delta T$  ( $\Delta T=T_{\max}-T_{\min}$ ) increases from 25 K to 55.5 K from 12:00 h to 17:00 h.

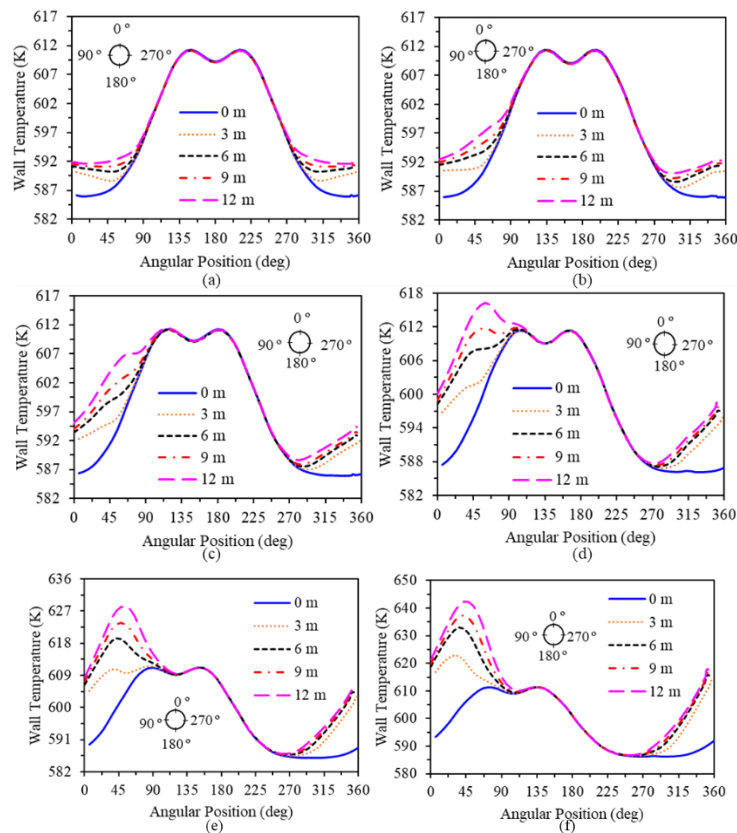


Figure 2. Variation of absorber outer surface temperature around the circumference for  $DNI = 1000 \text{ W/m}^2$  and heat flux profile corresponding to solar time of: (a) 12:00 h, (b) 13:00 h, (c) 14:00 h, (d) 15:00 h, (e) 16:00 h, and (f) 17:00 h.

The absorber inner surface temperature depends on the fluid (liquid or vapor) in contact with the absorber surface. The portion of the surface wetted with the liquid has a very high boiling HTC, however there is low convective HTC at the inner surface in contact with the vapor phase. The portion of the inner surface wetted by the liquid is at a lower temperature even there is high CSHF at the outer surface temperature. The highest heated region at the absorber outer surface shifts with time.

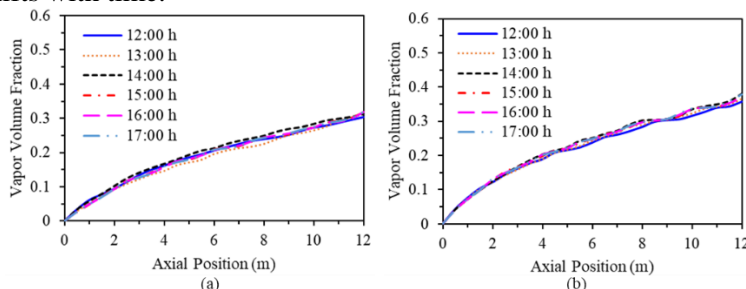


Figure 3. Variation of VVF along the absorber length for (a)  $DNI = 750 \text{ W/m}^2$  and (b)  $DNI = 1000 \text{ W/m}^2$ .

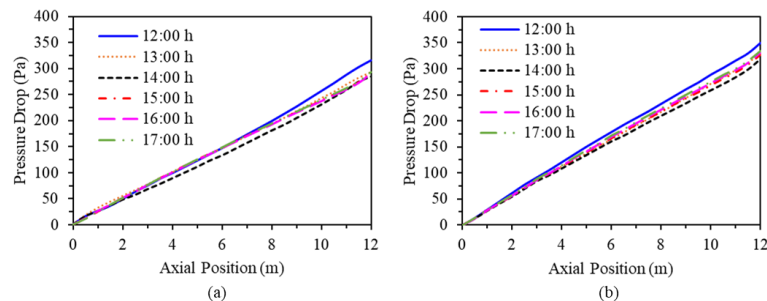


Figure 4. Pressure loss along the absorber length for (a)  $DNI = 750 \text{ W/m}^2$ , and (b)  $DNI = 1000 \text{ W/m}^2$ .

Figure 3 shows the distribution of vapor volume fraction (VVF) along the absorber length. In this study, the DNI is considered constant and only the characteristic of solar flux profile around the absorber outer surface is changing due to the tracking of the PTSC. The total heat input to the absorber remains constant. Hence, the VVFs are not changing from 12:00 h (solar noon) to 17:00 h. However, the variation of VVFs at the absorber outlet are observed as 0.31 and 0.37 respectively, for DNI 750 W/m<sup>2</sup> and 1000 W/m<sup>2</sup>.

As the VVF increases in the axial direction, the fluid mixture velocity increases. There is pressure loss due to an increment in the fluid velocity. The pressure loss also happens due to the boiling of the liquid. The pressure loss along the absorber length is presented in Figure 4. The maximum pressure loss is observed at the solar noon. The corresponding pressure losses are 316 Pa and 350 Pa, respectively, for DNI 750 W/m<sup>2</sup> and 1000 W/m<sup>2</sup> in 12 m length of the solar collector.

## SUMMARY AND CONCLUSIONS

In this article, the two-fluid modeling approach is discussed and implemented for modeling of DSG in the absorber tube of PTSC. The EMM coupled with the CHF model is used to model the boiling HT and fluid flow. A numerical study has been performed to study the effects of variation of CSHF profile on the absorber surface with time on the thermal behavior of the absorber of the PTSC. The variation of absorber wall temperature, vapor volume fraction, and pressure drop have been investigated. The following major results have been observed in this study:

- ❖ The absorber outer surface temperature varies between 585 K to 627 K throughout the day for DNI 750 W/m<sup>2</sup>, while for DNI 1000 W/m<sup>2</sup>, it varies between 586 K to 643 K.
- ❖ The  $\Delta T$  is minimum at the solar noon, and it increases for solar heat flux profile before or after the solar noon. This is due to the stratified flow and shifting of non-uniform CSHF profile to the top portion of the absorber. The  $\Delta T$  varies between 17 K to 39 K throughout the day for DNI 750 W/m<sup>2</sup>, while for DNI 1000 W/m<sup>2</sup>, it varies between 25 K to 55.5 K.
- ❖ The VVF increases along the flow direction. The VVFs at the absorber outlet are observed as 0.31 and 0.37, respectively, for DNI 750 W/m<sup>2</sup> and 1000 W/m<sup>2</sup>.
- ❖ The pressure drop increases with an increase in the DNI and vice versa. The maximum pressure loss is observed at the solar noon.

## ACKNOWLEDGMENT

The authors are grateful for the financial support provided by the Science and Engineering Research Board (SERB), Department of Science and Technology (DST), Government of India, New Delhi (Project Number: ECR/2017/000164).

## REFERENCES

- [1] Sandá A, Moya SL, Valenzuela L. Modelling and simulation tools for direct steam generation in parabolic-trough solar collectors: a review. *Renewable and Sustainable Energy Reviews* 2019; 113:109226, DOI: doi:10.1016/j.rser.2019.06.033.
- [2] Pal RK, Ravi Kumar K. Thermo-hydrodynamic modeling of direct steam generation in parabolic trough solar collector. In: 7th International Conference on Advances in Energy Research; December 10-12, 2019, Mumbai, India. Springer Singapore. DOI: [https://doi.org/10.1007/978-981-15-5955-6\\_13](https://doi.org/10.1007/978-981-15-5955-6_13).
- [3] Willwerth, L, Feldhoff, JF, Krüger, D, Keller, L, Eickhoff, M, Krüger, J, Pandian, Y, Tiedemann, J, Succo, M, Khenissi, A. Experience of operating a solar parabolic trough direct steam generation power plant with superheating. *Solar Energy* 2018; 171: 310–319. DOI: <https://doi.org/10.1016/j.solener.2018.06.089>.
- [4] Zarza E, Valenzuela L, León J, Hennecke K, Eck M, Weyers HD, Eickhof M. Direct steam generation in parabolic troughs: Final results and conclusions of the DISS project. *Energy* 2004; 29:635–644. DOI: [https://doi.org/10.1016/S0360-5442\(03\)00172-5](https://doi.org/10.1016/S0360-5442(03)00172-5).
- [5] Khenissi A, Krüger D, Hirsch T, Hennecke K. Return of experience on transient behavior at the DSG solar thermal power plant in Kanchanaburi, Thailand. *Energy Procedia* 2015. 69:1603–1612. DOI: <https://doi.org/10.1016/j.egypro.2015.03.115>.
- [6] Pal RK, Ravi Kumar K. Thermo-hydrodynamic modeling of flow boiling through the horizontal tube using Eulerian two-fluid modeling approach. *Int. J. of Heat and Mass Transfer* 2021. 168:120794. DOI: <https://doi.org/10.1016/j.ijheatmasstransfer.2020.120794>.
- [7] Serrano-Aguilera JJ, Valenzuela L, Parras L. Thermal 3D model for direct solar steam generation under superheated conditions. *Applied Energy* 2014; 132:370–382. DOI: <https://doi.org/10.1016/j.apenergy.2014.07.035>.
- [8] ANSYS I. ANSYS Fluent theory guide. ANSYS 18.1; 2019.
- [9] Malan A, Ravi Kumar K. Investigation of thermal performance of a large aperture parabolic trough solar collector. *Int. J. of Energy Research* 2020. 239-244. DOI: <https://doi.org/10.1002/er.6128>.

# MODE EXCITATION ENERGY

Tarık TUFAN

Istanbul Medeniyet University, Istanbul, Turkiye, tarik.tufan@medeniyet.edu.tr, ORCID: 0000-0001-9324-2401

Hasan KÖTEN

Istanbul Medeniyet University, Istanbul, Turkiye, hasan.koten@medeniyet.edu.tr, ORCID: 0000-0002-1907-9420

*Cite this paper as:*

*Tufan, T, Köten, H. Mode excitation energy. 9th Eur. Conf. Ren. Energy Sys. 21-23 April 2021, Istanbul, Turkey*

**Abstract:** Energy harvesting, which is a popular subject, can be defined as the use of energy released by environmental forces such as earth shaking, wind, etc. Civil engineering structures also harvest energy in a different way. Thanks to this energy harvest, the modal properties of structures such as natural frequency, mode shape can be estimated from the response histories taken from the structure. Modal properties of the structure gives an impression of the health of the building. However, an important question comes to mind: Did the energy harvesting of the structures sufficiently drive the modes used to detect damage? Or in other words, has it exceeded a certain amount of energy to drive the mods? If the mode in question is not sufficiently excited, it can be interpreted as a harbinger of damage for an undamaged structure in the analysis using these modes. For this reason, it is an important issue to determine to what extent the modes are driven. In this study, the aforementioned subject has been explored with the title "Mode Excitation Energy" using the Modal plot method.

**Keywords:** Mode Excitation Energy, Modal Plot, Energy Harvesting,

© 2021 Published by ECRES

Nomenclature	
FFT	Fast Fourier Transform
DOF	Degree of Freedom
SHM	Structural Health Monitoring
FRF	Frequency Response Function

## 1. INTRODUCTION

Monitoring the health and determining the health status of each building in the building stock of a zone is an important issue in order to minimize the vulnerability parameter in the risk definition in the mitigation step of disaster management. The health of a building can be decided according to the change in the modal properties of the building. However, the reason for this change can be both structural damage in the structure or changes in environmental conditions. Theoretically, the change in the natural frequency of structure is defined as the change in the stiffness of the structure or damage to the structure in cases where there is no change in the mass of the structure and in environmental conditions such as temperature, and humidity.

The structures absorb the surrounding energy at any moment and transform it into unique vibrations that express their own characteristics. If environmental energy is not harvested in this way, vibrations that give information about the properties of the structures do not occur. Because, as can be seen from equation 1, if there is no input force or the frequency band of the input force is not proper, there is no response (in that frequency range), and the transfer function, which expresses the properties of the structure, cannot be determined (in that frequency range).

$$Y(jw) = H(jw)U(jw) \quad (1)$$

where  $Y(s)$  is output spectrum or Fourier transforms of the response,  $U(s)$  is frequency response or Fourier transforms of the input force, and  $H(s)$  is the transfer function [1].

It is well-known concept that operational input (external) forces are modeled as a noise exciting ‘uniformly’ all the frequency components[2-4]. The white noise assumption facilitates identifying the parameters related to the dynamic behavior of the structure under environmental or operational forces.

In practice, due to irregularities in the characterization of a structure [5], location of excitation [6], input frequency content, the structure has not received sufficient energy to excite all the modes properly [7-9]. In the literature, it is usually decided whether the modes are driven or not based on the “Frequency Response Function (FRF)” peaks. In this study, as an alternative to FRF, the Modal plot [10] shows whether the defined input force can activate the modes in a sufficient amount. To the best of our knowledge, there has been no such alternative technique to FRF in SHM literature that is used to detect the mode excitation energy. Therefore, the proposed method offers a novel approach to the literature.

## 2. SYSTEM IDENTIFICATION

In the structural health monitoring procedure, after receiving data such as acceleration, velocity, and displacement from the structure, the first step to be taken is to identify the system. In general, it is desired to estimate modal information such as natural frequency and mode shape of the system using frequency or time-domain methods. Many frequencies and mode shape estimates are subjected to screening and it is desired to calculate the closest “true” natural frequency and mode shape of the system. While the stabilization diagrams aim to accomplish this task with various elimination steps, the Modal Plot aims to construct modal points and also new modal regions without an elimination step.

### 2.1 Modal Plot

Modal Plot is the name given to a graph where the frequency and mode shape estimates of a system under an ambient input force are shown simultaneously according to a DOF. The natural frequencies of the system and the mode shape values corresponding to those frequencies appear in the modal plot as a modal point. Generally, damage information is tried to be calculated using only these mode points. Modal Plots additionally show modal zones other than modal points. The modal zone is an important feature that is eliminated as noise in the liter, but shown to be associated with modal points and provides information about the input force. A representative Modal Plot is shown in Figure 1. In Short, the Modal Plot consists of (1) Modal points expressing natural frequencies and mode shape pair of the system and (2) Modal Zones that can be used as damage-sensitive parameters [10]. Even if Modal Points are not included in the modal zone, they remain quite close to it (Figure 2).

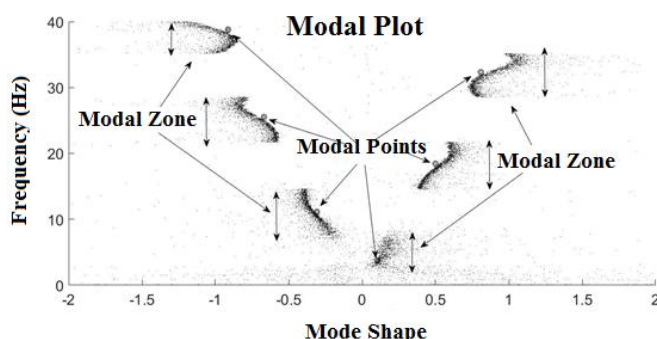


Figure 1. A Representative Modal Plot

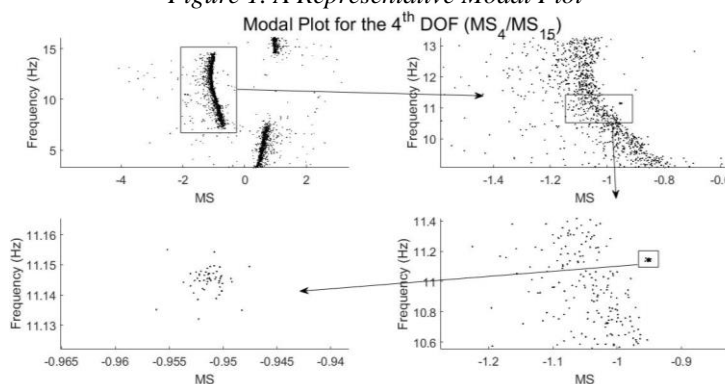


Figure 2. Modal Point

### 3. SIMULATION

The numerical study in this section is aimed at determining modal excitation energy with a Modal Plot. For this purpose, a fixed mass-spring model with 6 translational DOF with one free end and one free end has been investigated. In the piecewise system, all mass values are defined as equal and 1 kg and stiffness values equal and 14000 N / m. Primarily, the free-end, which is the 6th DOF, was chosen as a reference DOF. In the analyzes, the DOF's were examined in pairs together with the reference DOF one by one. Five-minute acceleration data taken from each DOF and sampled at 200 Hz were analyzed into 22-second data segments with 88% overlap. It was observed that the responses did not have a time-dependent slope, and only seven-second data averages were subtracted from it. The data were analyzed with 2933x2933 sized Hankel matrices and modal plots were built with the first 390 mode variable, which was seen to correspond to the 0-40 Hz frequency range that includes all modes. These procedures were repeated six times where force was applied from all DOFs in turn.

Figure 2 consists of 3 sub-graphs. 2 modal plots are showed on top of each other in each subgraph. In the first subgraph, first of all, the ambient force was applied from the 1st DOF and the modal plot was drawn, then the white noise was again applied from only the 4th DOF and again the modal plot was added. Similarly, white noise was applied separately from the 2nd and 5th DOF in the 2nd subgraph, and from the 3rd and 6th DOF in the last subgraph. From the 2nd graph of all sub-figures, we can draw the following 2 conclusions: Modal plots were drawn according to forces exerted by different degrees of freedom 1) pass **quite** close to modal points and 2) modal graphs drawn according to different force action points intersect at modal points. These two features are important for system identification purposes.

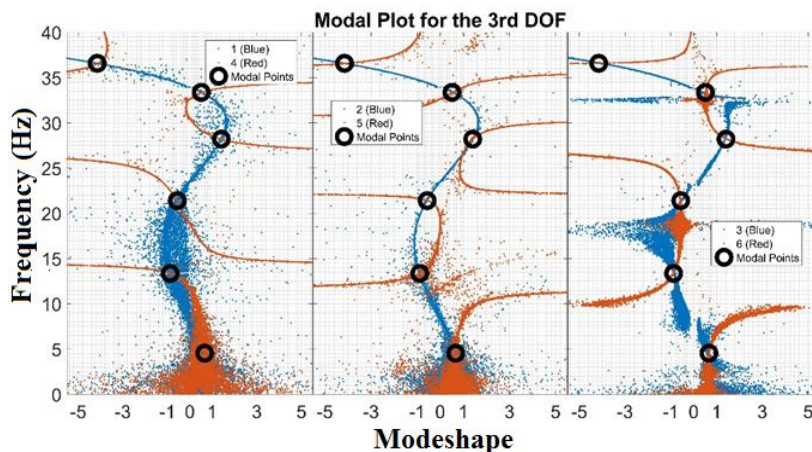


Figure 3. Modal Plot for the 3rd DOF for different input force configuration couples

In this study, it was stated that some modes cannot be driven sufficiently according to the force, and detecting damage with modes that cannot be driven sufficiently will cause the healthy structure to be detected as damaged. To illustrate this phenomenon, an example is shown in Figure 3. In Figure 3, the modal plots are presented in the same way as in Figure 2. Unlike Figure 2, it is aimed to show only the modal zones related to the 2nd modal point of the 5th DOF to better examine the modal plots. As can be seen in Figure 3, when force is applied from all DOF except the 5th DOF, it is seen that the modal zones are very close to the modal points. When force is exerted by the 5th freedom, the 5th degree of freedom 2nd mode shape value will be determined with approximately 5-7% error.

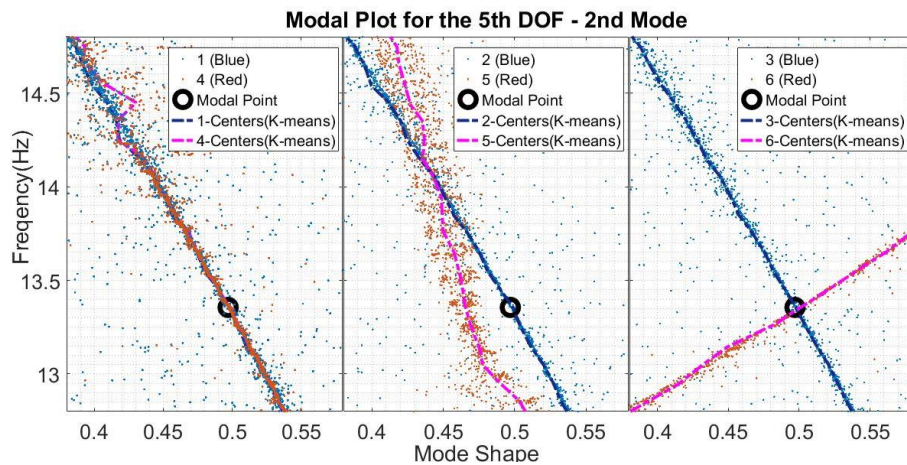


Figure 4. Modal Plot for the 5th DOF and 2nd mode for different input force configuration couples

Let's discuss the determination of modal parameters through a different system whose features are given in Table 1. As it is known, the modal properties of a system with 5% critical damping and an undamped system are expected to be very close to each other

Table 1 Numerical Analysis Specifications

# of DOFs	15
End Conditions	Fixed-Free
Spring Stiffness	2.27E8 N/m
1st-14th DOF mass	4530 kg
15th DOF mass	2265 kg
Input DOF	15th DOF
Input Type	Ambient Vibration

Figure 4 shows the modal plots of the undamped system and systems with 5% critical damping for the 1st DOF when the ambient force is exerted from the 15th DOF. For the undamped system, it is seen that the modal zones pass quite close to the modal points. However, when the damping is introduced to the system, it is seen that the modal zones move away from the modal points, especially from the 3rd Modal point and following modal points. In this case, it is clearly seen that the modal properties of the system to be determined will express the system incorrectly.

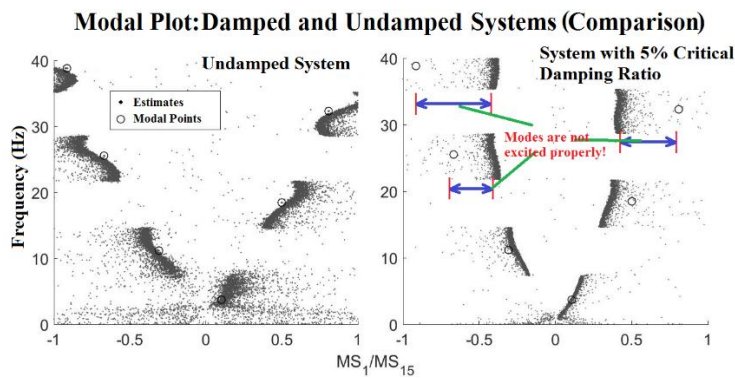


Figure 5. Modal Plot undamped and damped systems

#### 4. CONCLUSION

In this study, an answer to a very important question for structural health monitoring systems was sought. The important question is that "Did the energy harvesting of the structures sufficiently drive the modes used to detect damage?" Or in other words, "has it exceeded a certain amount of energy to drive the mods?" If the mode in question is not sufficiently excited, it can be interpreted as a harbinger of damage for an undamaged structure in the analysis

using these modes. In the content, how important the Modal plan approach can be for this important question is examined and shown over two different examples.

## **REFERENCES**

- [1] Rowell, D. State-space representation of LTI systems, 2002. <<http://web.mit.edu/2.14/www/Handouts/StateSpace.pdf>>
- [2] Yang JN. Application of optimal control theory to civil engineering structures. J Eng Mech Div-ASCE 1975; 101(6), 819-838
- [3] Peeters B. System identification and damage detection in civil engeneering. PhD Thesis, Katholieke Universiteit Leuven, 2000.
- [4] Ren WX and Zong ZH. Output-only modal parameter identification of civil engineering structures, Structural Engineering and Mechanics, 2004, 17(3-4), 429-444.
- [5] Rainieri, C, Fabbrocino, G. Automated output-only dynamic identification of civil engineering structures. Mechanical Systems and Signal Processing, 2010, 24(3), 678-695.<https://doi.org/10.1016/j.ymssp.2009.10.003>
- [6] Alonso, R, Albizuri, J, Esparza, J. Application of model updating techniques to turbomachinery rotor components. Advances in Mechanical Engineering, 2019, 11(7), <https://doi.org/10.1177/1687814019863941>
- [7] Gomes, GF, Mendéz, YAD, da Cunha, SS. A numerical-experimental study for structural damage detection in CFRP plates using remote vibration measurements. Journal of Civil Structural Health Monitoring, 2018 8, 33–47. <https://doi.org/10.1007/s13349-017-0254-3>
- [8] Rao, SS. Mechanical Vibrations, in SI Units, Global Edition, Prentice Hall, 2017.
- [9] Rainieri, C, Fabbrocino, G. Automated output-only dynamic identification of civil engineering structures. Mechanical Systems and Signal Processing, 2010, 24(3), 678-695.
- [10] Tufan, T, Akalp, S. Modal plot—System identification and fault detection. Structural Control and Health Monitoring, 2019, 26(5), e2347.



# ECONOMIC ASPECTS OF MARKET FORMATION REACTIVE POWER IN ELECTRIC POWER INDUSTRY

Vladimir Kolibaba

Ivanovo Power Engineering Institute, Ivanovo, Russian Federation, kolibaba@eiop.ispu.ru, ORCID:  
<https://orcid.org/0000-0001-8577-7326>

Konstantin Zhabin

Branch of JSC "SO UES" ODU Center, Moscow, Russian Federation, zhabin\_kv@icloud.com, ORCID: 0000-0002-2468-2427

Vladimir Velikorossov

Plekhanov Russian University of Economics, Moscow, Russian Federation, corp.innovation@rea.ru, ORCID: 0000-0001-5845-4820

Sergey Filin

Plekhanov Russian University of Economics, Moscow, Russian Federation, Filin.SA@rea.ru, ORCID: 0000-0002-6054-6510

Ona Rakauskiene

Mykolas Romeris University, Vilnius, Lithuania, ona.rakaus@gmail.com, ORCID: 0000-0003-0007-0570

Alexey Yakushev

Plekhanov Russian University of Economics, Moscow, Russian Federation, YAKUSHEV.AZH@rea.ru, ORCID:  
ORCID:0000-0003-0371-0289

Cite this paper as:

*Kolibaba V., Zhabin K., Velikorossov V., Filin S., Rakauskiene O., and Yakushev A. Economic aspects of market formation reactive power in electric power industry. 9<sup>th</sup> Eur. Conf. Ren. Energy Sys. 21-23 April 2021, Istanbul, Turkey*

**Abstract:** This article discusses economic factors of reactive power market formation in relation to wholesale market of electricity and capacity of Russia. The proposed market is based on a reasonable cost structure for reactive power regulation, organization and conduct of qualified selection of reactive power suppliers. The economic agents of the market are generating companies, power grid companies and electricity consumers who can trade.

**Keywords:** reactive power, electric power system

© 2021 Published by ECRES

Nomenclature	
RP1	Reactive power1
EES2	Electric power system2
SCB3	Static capacitor batteries3
CSR4	Control shunt reactors4
STC5	Static thyristor compensators5
SD6	Switching devices6

## 1. INTRODUCTION

Currently, for the effective operation of the subjects of the electricity (power) market of the Russian Federation, the execution of legislative commands by the System Operator is not enough - they must have economic freedom, interest in increasing role in the efficiency and ensuring the safety of the EES as a whole [1]. Obviously, the

expenses of these entities should not only be compensated, but also bring the necessary level of profit. The additional costs of the entities supplying RP may be related to the costs of maintaining reserves, compensating for alternative expenses, operating equipment, etc.

Reactive power is part of the total electrical power spent on electrical magnetic processes in electrical equipment. It is a mandatory part of the process of production, distribution and consumption of active power in the AC system. Reactive power is required to ensure normal operation of most types of electrical equipment: electric motors, welding devices, arc electric furnaces, transformers, etc. [2]. Production of RP is provided by generators (power plants), synchronous compensators, batteries of static capacitors, etc. Reactive power parameters affect the voltage levels in the network nodes, the capacity of power transmission lines, the values of active power losses and electricity during their transmission and distribution.

## 2. METHODOLOGY

In the framework of the presented work, the authors used the following research methods: 1) at the theoretical level: study and generalization, formalization, analysis and synthesis, induction and deduction, axiomatics; 2) at the experimental-theoretical level: experiment, analysis, modeling, synthesis; 3) at an empirical level: observation, measurement, comparison.

## 3. ANALYSIS

Approaches to regulating RP in backbone and distribution networks in Russia differ. The main task of its regulation in backbone networks is to ensure the system reliability of EPS. Figure 1 shows the overall RP control system in EPS and the proposed operating boundary of the RP market.

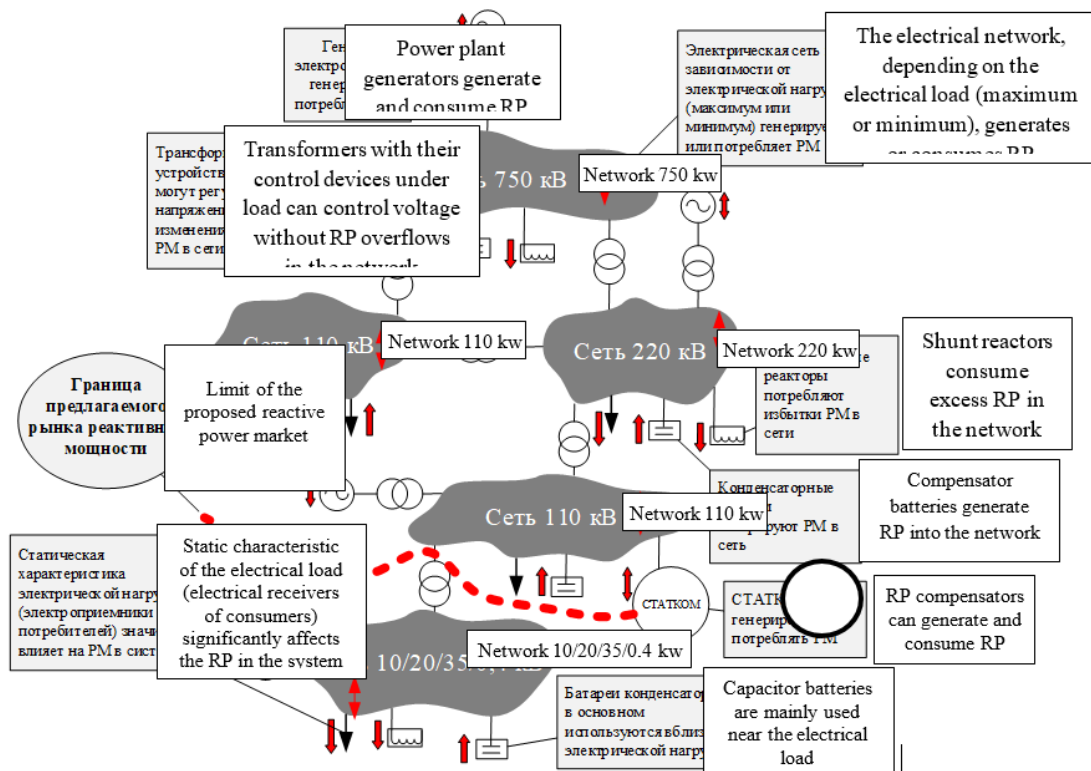


Figure 1. General diagram of reactive power control in electric power systems.

The current regulatory framework (primarily the rules of the wholesale electricity and power market) is not aimed at the effective, interested and coordinated participation of all entities of the electricity market that affect the operating modes of electric networks (PJSC Rosseti, JSC SO UES, generating companies, consumers) in optimizing the modes of generation and consumption of RP. On the contrary, it poses serious barriers to the effective interaction of these actors [3].

Traditionally, in the Russian EPS, the System Operator uses power plants to maintain the required voltage levels at its nodes [4]. All power plants in automatic and real-time modes perform RP balancing and provide it the required reserve to eliminate possible emergency situations. Other devices, such as static capacitor batteries (SCB), control shunt reactors (CSR), static thyristor compensators (STC), etc., are owned and controlled by network companies (consumers). At the same time, these entities are obliged to ensure the operation of these devices at any time without any appropriate economic incentives. Power lines in certain modes of operation of EPS are also considered as a means of regulating RP, since in hours of low load in power lines they can generate RP into the network.

To develop the best market structure, it is necessary to investigate the composition and cost structure of RP production. In this structure, only fuel costs are typical for power plants, and they depend on the production volumes (variable costs). The costs of owners of synchronous compensators (power plants) are the alternative choice of their use (choice of participation in markets (wholesale/system services) and are determined by the cost of the best missed opportunity to use production resources. All other, including renewable, PM sources are independent of electricity generation. Economic analysis shows that they are characterized mainly by the share of constant costs in the cost of production, and costs for a certain period are immediately included in the cost of goods [5]. Variable expenses are negligible and are characterized mainly by active power losses in these RP sources (Table 1).

*Table 1. Analysis of cost structure of various means of reactive power and voltage control*

Item no	Item Description	Percentage
1	<p>1) power plant generators      Variable costs            2) synchronous compensators (power plants)</p> <p>1) costs related to power consumption for generator excitation (for synchronous generator) and for auxiliary equipment;            2) fuel costs (for generators of power plants operating in generator mode) and power losses (mechanical and ventilation);            3) environmental payments;            4) water tax;            5) material expenses;            6) purchase of power of electric power entities in the wholesale electricity market (for synchronous compensator).</p> <p>Fixed costs            1) interest on capital;            2) operating costs;            3) labor costs [6], maintenance, maintenance, other;            4) social deductions.</p>	<p>1) power plant generators. The cost of lost opportunities is related to system requirements, as a result of which the generator is forced to change the supply of active power to the wholesale market in order to increase/decrease the supply of RP;            2) synchronous compensators with the supply of RP are characterized by losses of active power - about 3% of the total generator power;            3) for generators of power plants during the generation of RP, there are losses of electricity in their windings. The latter are usually not measured and are therefore difficult to predict. However, they affect the life of the equipment by exceeding the temperature of the working elements above the permissible values.            -</p>
2	<p>Other RP Compensators      Variable costs</p> <p>1) costs of power losses;            2) the costs associated with the number of switches, which leads to rapid wear of the switching mechanism (for example, devices, DC voltage regulators of transformers, switching devices of BSK);            3) material expenses.</p> <p>Fixed costs            1) interest on capital;            2) operating costs;            3) labor costs, maintenance, maintenance, other;            4) social deductions.</p>	<p>Compared to power plant generators and synchronous compensators, the operating costs of this equipment are quite low. However, it should be borne in mind that some types of equipment, such as transformers with PLC devices, etc., have significant mechanical wear on the switching devices, i.e. there is a limited number of these operations that can be performed during their service life. Thus, each switch operation corresponds to a residual capital value. An important feature of this equipment compared to power plants is that there is no alternative to use for them, since they either supply RP or are in reserve.</p>

Also, investments play a key role in the resumption and increase of production assets, form the material basis for the development of the electric power industry and the involvement of business in the investment process [7]. Figure 2 shows a comparative estimate of the capital intensity of the various RP control technologies currently available.

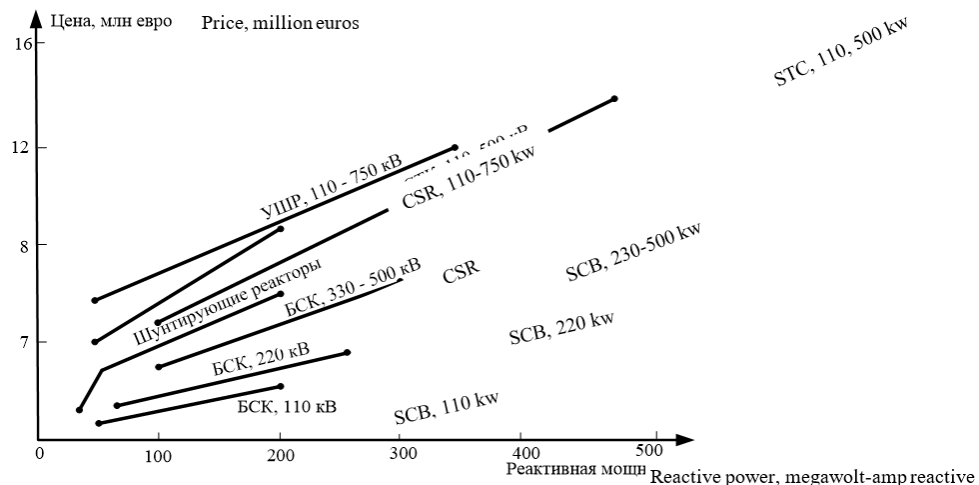


Figure 2. Comparative assessment of capital intensity of various reactive power control technologies.

In this estimate, there are no power plants, since their capital costs are tens of times higher than those of the considered devices for local control of RP. Therefore, such a comparison does not seem correct. Figure 2 shows that the amount of investments depends on the type of PM control technology, its unit power and voltage class [8]. Moreover, the most capital-intensive are the sources of RP of the SCB, CSR of ultra-high voltage.

The economic efficiency of the RP market will greatly depend on the behavior of participants. Theoretically, in the market of perfect competition, all participants show the true value of the product. It is obvious that at the initial start-up stage of the RP market, high concentration and low liquidity will be inherent in this market due to its local nature and the existing low amount of local RP equipment in the EPS.

Also, due to the strong local nature of RP, the market strength of individual suppliers is the main problem in the formation of a competitive RP market. Market power is the ability to change prices from the level of competition and from the magnitude of your own profit. As a rule, only local control of RP can ensure its effective regulation in a certain area of the EPS.

Traditional characteristics, including for measuring market strength, are based on supplier concentration using the following indicators [9]:

- 1) Herfindal-Hirschmann index (in markets with low  $H < 1000$  concentration, and with high  $H > 1800$  concentration):

$$H = 10\ 000 \sum_{i=1}^N s_i^2, \quad (1)$$

where  $s_i$  market shares for  $N$  suppliers;

- 2) entropy coefficient (in the exclusive situation  $E = 0$ , for market equilibrium  $E = \ln(N)$ ):

$$E = - \sum_{i=1}^N s_i \ln(s_i). \quad (2)$$

A high degree of market concentration is often the main reason for the dominance of individual suppliers. Therefore, the absence of competing suppliers leads to an inefficient market. The degree of concentration of the market where a specific product such as RP is traded can be reduced (large suppliers are replaced by many smaller suppliers, given their position in the network) by: (1) taking into account the economic effect of this decentralization, for example, due to reduced power losses (power) and increased reliability; 2) minimizing barriers to entering the market to its participants, for example, the conditions for connecting to the network; initial market participation; 3) formation of a reasonable market price for RP, covering the expenses of its production and giving sellers the necessary profit; 4) ensuring maximum market transparency, access to all necessary information for entrance the market. Currently, in the EPS Russia most of it there is a low market concentration of RP suppliers.

The structure of the EPS is also an important parameter because the dominance of RP suppliers increases with network power limitations [10]. In addition, predictable network events (for example, an increase in the output of a steel mill) can also increase the dominance of participants. Therefore, the System Operator should take actions to mitigate the dominant positions of such suppliers through an appropriate network configuration that promotes optimal competition.

A perfect competitive RP market will be characterized by a large number of sellers and buyers. As a result, a market price will be formed, independent of the behavior of one market participant. Under these conditions, all market participants will have incentives to participate in tenders and declare real costs.

At the same time, the RP market, due to its strong local nature, can be characterized by a lower quantity of participants than is required for the economical, reliable and high-quality functioning of the EPS. This situation may lead to the emergence of suppliers with great market power. The latter can be minimized by concluding long-term contracts with them on a regulated basis, which will allow new participants to enter the market.

#### **4. CONCLUSIONS**

1. RP is an integral and necessary part of the production, transmission and consumption of electrical energy, and it is also necessary to maintain voltage levels in the nodes of the EPS and ensure its stable and economical functioning. This is a specific product, the trade of which requires the formation of special methods and pricing tools.
2. Rational regulation of RP is currently not considered as an economic problem, but it is one of the main tools for managing the efficiency of EPS. In all countries of the world, there are currently no competitive economic mechanisms to stimulate the introduction of RP sources and pricing for RP, which would create a fair price for its suppliers and at the same time, due to its specificity, send appropriate price signals to participants in the electricity market for its rational consumption.
3. The proposed organizational mechanism of pricing for RP and the qualified selection of its suppliers is aimed at determining the range of suppliers of RP capable of meeting the demand for it with the least costs, as well as to stimulate investments in the construction of new sources of RP.

#### **REFERENCES**

- [1] Velikorossov V.V., Genkin E.V., Zakharov A.K., Maksimov M.I., Filin S.A., Khudaibergenov A.K. The Role of Energy Accumulation Systems in Ensuring Energy Security of the State. In: CEED 2019 2nd International Conference on Con-temporary Education and Economic Development. Ser. "Education, Science, Technology, Innovation and Life"; from 2019-10-26 to 2019-10-27: CSP, pp. 141-147. DOI: 10.23977/ceed.2019.023
- [2] Kalinina, I.A., Maslennikov, V.V., Filin S.A. Improvement of the environment through management of waste management of electronic and electrical equipment. Ecology of industrial production 2018; 1: 11-16 <[http://izdat.ntckompas.ru/editions/for\\_readers/archive/article\\_detail.php?SECTION\\_ID=158;&ELEMENT\\_ID=23263](http://izdat.ntckompas.ru/editions/for_readers/archive/article_detail.php?SECTION_ID=158;&ELEMENT_ID=23263)>
- [3] Vorotnitsky, V.E., Rabinovich, M.A., Kakovsky, S.K. Optimization of modes of electric networks 220-750 kV in reactive power and voltage. Energy of a single network 2013; 3: 50-59 <[https://xn----glfcctcdi4bhow0as6psb.xn--p1ai/images/3-8/05\\_Vorotnitskiy\\_3\\_8.pdf](https://xn----glfcctcdi4bhow0as6psb.xn--p1ai/images/3-8/05_Vorotnitskiy_3_8.pdf)>
- [4] Gorozhankin, P.A., Mayorov, A.V., Makarovskiy, S.N., Rubtsov, A.A. Voltage and reactive power control in electric power systems. European experience. Electrical stations 2008; 6: 40-47 <<http://elst.energy-journals.ru/old-site/tocs-ru/2008/06-2008.htm>>
- [5] Velikorossov, V.V., Karyakin, A.M., Tarasova, A.S., Stepanova, K.K., Filin, S.A. Development of The Economic Analysis Method for Wholesale Generating Companies (WGC) In Russia. In: 35th IBIMA 35th international business information management association conference; 1-2 April, 2020: IBIMA Publishing, pp. 10777-10781.
- [6] Kokarevich, V.N., Sidorova, V.N., Zausova, N.V. Features of wage formation at electric power enterprises. Rationing and compensation in industry 2011; 9: 30-36 <<http://elst.energy-journals.ru/old-site/tocs-ru/2008/06-2008.htm>>
- [7] Goncharenko, L.P., Yakushev, A.ZH., Akulinin, F.V., Kuzmishchev, D.A. Realizing the investment potential of the regions by increasing investment attractiveness and involving business in the investment process. Regional economy: theory and practice 2013; 28: 2-11 <<https://www.fin-izdat.ru/journal/detail.php?ID=57810>>
- [8] Ibraimova, S.S., Suleymanova, I.A., Kolibaba, V.I., Filin, S.A., Genkin, E.V. Renewable energy sources: stimulating investments in Russia and abroad. In: International Conference Industrial Technology and Engineering. Proceedings of VI International Conference; from 2019-10-26 to 2019-10-27: M. Auezov Republican State Enterprise on the Right of Economic Management "South Kazakhstan State University", pp. 21-24. <<https://www.elibrary.ru/item.asp?id=44599739>>
- [9] Stoft, S. Economics of Power Systems. Introduction to the design of electricity markets. Moscow, RUSSIA: World, 2006.
- [10] Tarasova, A., Velikorossov, V., Filin, S., Yakushev, A., Ibraimova, S. Development of a set of limits for the main performance indicators of energy-generating companies. In: BTSES 2020 E3S Web of Conferences. 1. Ser. "1st International Conference on Business Technology for a Sustainable Environmental System"; March 19-20: EDP Sciences, p. 07001. DOI: 10.1051/e3sconf/202015907001



# AN INNOVATIVE METHODOLOGY FOR VISUAL IMPACT ASSESSMENT OF WIND POWER PLANTS

Blois Luciano

University "Guglielmo Marconi", Rome, Italy, l.blois@unimarconi.it, ORCID: 0000-0002-0520-6943

Cite this paper as: *Luciano, B. An innovative methodology for visual impact assessment of wind power plants. 9<sup>th</sup> Eur. Conf. Ren. Energy Sys. 21-23 April 2021, Istanbul, Turkey*

**Abstract:** The present paper proposes a methodological procedure aimed at obtaining the best compromise between energy produced and visual impact generated by a wind power plant. To achieve two synergies are needed for this result: a numerical calculation tool, capable of forecasting estimates the energy produced for each solution analyzed; a methodological approach that allows the relative visual impact to be simulated in a realistic way. As regards the numerical calculation tool, recourse was made to a calculation code known (Wasp software). While the codified methodology for the assessment of visual impact is described in this paper.

**Keywords:** Visual impact, wind energy, wind turbine

© 2021 Published by ECRES

## 1. INTRODUCTION

The visual impact assessments (VIAs) generated by a wind power plant on the landscape is based on analysis of two fundamental aspects: visual quality and sensitivity.

Visual quality is understood as the degree or aesthetic value that is given to a specific surrounding area and is characterized by:

- intrinsic quality, consisting of the type of elements they make up the landscape, geomorphology, the set of species plants, land uses, the ecological value of place, as well as the degree of anthropogenic alteration that is present in the district as an attributed semiological value;
- aesthetic quality, determined appearance from subjectivity of the observer and who comes defined, on the one hand, by values aesthetic, cultural, emotional, etc. and on the other by values social, traditional, symbolic, the nature of the prominent signs in the district.

Researchers have demonstrated that by visual quality can predict up to 65 percent of viewers' scenic quality ratings [1].

Visual sensitivity is defined as susceptibility of a landscape to change of its quality due of the presence of a specific construction. Sensitivity depends so much on the type of action that you realize what you give characteristics of the landscape (reliefs, vegetation, uses, etc.) which determine the capacity of insertion in the territory of the designed work. Determining the area with potential visibility of a proposed project of wind turbines is a fundamental component of preparing a VIAs. While this is a simple matter of determining line-of-sight geometry, the results are significantly affected by whether to consider the screening effect of land cover, and if so how. Some authorities recommend using only terrain elevation if long term impacts are being evaluated [2]. Studies of viewsheds included with VIAs have found a wide range of accuracy, but the average seems to be approximately 60 percent [3, 4].

The methodology to analyze the degree of sensitivity of a landscape is based on the following aspects:

- intrinsic sensitivity, defined from the morphology of the visible field, on which the size and compactness;
- acquired sensitivity, determined from the display capacity of the park according to the presence of observers.

Starting with the considerations to which they lead the characteristics of quality and sensitivity yes estimates the value of the landscape impact of the wind farm in study. The problems and the limits main of the classic analyzes of visual impact, they are essentially consisting of impossibility of a translation of the results in quantitative terms, that have a certain value objective and comparable, and the complete split environmental characterization from the technical-design aspects.

This paper proposes a methodological procedure aimed at obtaining the best compromise between energy produced and visual impact generated by a wind power plant.

To achieve two synergies are needed for this result: a numerical calculation tool, capable of forecasting estimates the energy produced for each solution analyzed; a methodological approach that allows the relative visual impact to be simulated in a realistic way.

As regards the numerical calculation tool, recourse was made to a calculation code known [5]. WAsP is a Windows program for predicting energy yields from wind turbines and wind farms. The predictions are based on wind data measured at meteorological stations in the same region, or on generalised wind climates derived from mesoscale model results. The program includes a complex terrain flow model, a roughness change model, a model for sheltering obstacles, a wind turbine wake model and a model for the average atmospheric stability conditions at the site. The software package further contains a Climate Analyst for creating the wind-climatological inputs, a Map Editor for creating and editing the topographical inputs, and a Turbine Editor for creating the wind turbine inputs to WAsP. The fundamentals of WAsP and the wind atlas methodology are described in the European Wind Atlas.[6] While the codified methodology for the assessment of visual impact is described in this paper.

## 2. METHODOLOGY

The application of this methodology is was carried out on projects by wind farms located in potential sites of the Umbrian territory. For each design solution, corresponding to a different plant lay-out, the study is divided into the following stages:

- calculation of the ZVI (Zoning Visual Influence) with mapping of the territory surrounding;
- identification of critical points-sensitive (such as inhabited centers, roads, places of interest historical-cultural, etc.);
- capture frames on three-dimensional model e ‘reference’ frame;
- image processing obtained by vectorization;
- impact assessment and identification of the solution optimal.

The first phase involves the calculation of the ZVI which consists in a mapping of the territory that is classified in areas based on the number of visible wind turbines.

This processing is supported by the use of Digital Elevation Models (DEMs) and specific calculation codes in the CAD environment, and the related result can be presented in the form of second color maps appropriate legends (ad example dark red is equivalent to the maximum number of wind turbines while the green represents the minimum) and also stored in numerical form.

This first step represents in itself a first approach to evaluation of the visual impact although the quantities are reported of the turbines visible regardless of the factor “Distance”: so two sensitive receptors placed at different distance from the system, from which the same number of turbines, they would suffer the same visual impact.

This is why main reason for which the need arises to dedicate a more thorough evaluation of the problem.

Once the map is shown in the GIS environment the second begins phase in which they are detected the critical-sensitive points by superimposition of the ZVI to the information of the territorial planning plans and coordination (eg Territorial Provincial Coordination Plan, Territorial Urban Plan, etc.) that allow to locate the coordinates of such points within a significant distance from the plant, beyond which the turbines become practically indistinguishable e therefore this analysis would not be significant.

In the third phase we proceed with frame detection virtual shots taken from the locations identified in the previous phase, assuming the center of gravity of the plant as a target ed an optical simulation you represent as much as possible the human mean field of view, in in such a way as to represent in the best possible way that an observer can see in reality, both in terms of size absolute and quantity relative field of view.

In the frames like this realized there are three elements essentials: ground, sky (background) and wind turbines, a each of which is attributed a primary color to facilitate some procedures of automatic photo-interpretation by software.

These frames are compared with a frame of reference appropriately defined as that of maximum impact, ie triggered by particular position in which a hypothetical observer would have maximum occupancy possible field of view from part of the wind turbines, ed identified through a procedure geometric.

Graphics processing completed with vectorization of the photos obtained indeed to proceed to the next evaluation phase needs to be calculated the value of the occupied areas from wind turbines in each frame.

As a final passage it is therefore possible to proceed to calculation of the visibility coefficients.

For each observation point that can weigh the importance of sensitive sites through a criticality score scale (defining a parameter i variable between 1 and 4: for churches and abbeys the parameter i will be 4, for newly built towns and with less than a thousand inhabitants i will be equal to 1), and a population scale (defining a parameter A equal to the number of inhabitants of the inhabited center in exam).

The visibility coefficient "v" for a certain vantage point it is defined as:

$$v = i \cdot TO \cdot C/C_0 \quad (1)$$

where C and  $C_0$ , calculated in phases previous, represent respectively the occupied area from the wind turbines in the frame under consideration, and the occupied area from the wind turbines in the frame of reference. In the case of sensitive road sections assumes as an observation point whichever comes closest to the system and the coefficient visibility v is evaluated like:

$$v = i \cdot L \cdot C / C_0 \quad (2)$$

where parameter i is chosen based on the classification of street ( $i = 1$  for urban street,  $i = 2$  for provincial road,  $i = 3$

by state road and  $i = 4$  by sections motorway) and L corresponds to the length of the sensitive section.

The overall visual impact will be given by the sum of all the calculated visibility coefficients for each observation point analyzed. These calculations, applied for each system lay-out solution, allow you to evaluate the visual impact of each design alternative, fit quantitative and therefore comparable, allowing the identification of an optimal solution. To this end, to identify the best compromise between energy produced and visual impact generated, for each proposed solution they go to compare "I" relationships between the value of energy produced and the visibility coefficient global, identifying the value maximum.

This paper reports on a single case study located in potential sites of Italy in Umbrian Apennines, in the municipality of San Giustino (PG).

This case study of the visual impact of the wind farm located in the municipality of San Giustino (PG) was conducted by applying the methodology described in this paper, on an area surrounding the wind farm for a radius of 25 km.

The analysis was carried out by creating a DEM (Digital Elevation Model) with a square mesh of one meter side generated starting from detailed topographic surveys performed on site georeferenced with the Technical Map of the Regions of Umbria, Marche and Tuscany.

Each DEM jersey was then highlighted in proportion to the number of wind turbines visible from that point according to a scale of 12 colors with gradation from yellow (0% visibility) to red (100% visibility).

The wind farm, given the morphology of the surrounding land, is almost invisible from all the inhabited centers of the provinces of Perugia, Arezzo and Pesaro-Urbino located respectively to the west - north west and east of the project area, while is fully visible only from some portions of the territory located to the south-west falling within the province of Perugia. From the analysis described, a map of the intervisibility of wind turbines was generated in which it is highlighted whether the individual wind turbines have a visual impact or not in the surrounding area, but it does not provide information about the visual perception of the individual wind turbines in the perception field of the visual cone of the eye. human. The human visual field, in fact, can be synthetically represented through an ellipse constructed considering as the primary element the distance that divides the observer from the element under study and with the following geometric characteristics:

- semi-major axis "a"
- calculated with the observer-element distance  $\tan(60^\circ)$ .
- semi-minor axis "b"
- calculated with the observer-element distance  $\tan(50^\circ)$

Therefore, the visual field area will be:

$$\text{Area} = a \cdot b \cdot \pi \quad (3)$$

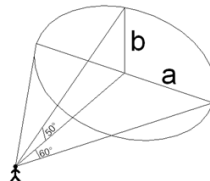


Figure 2 - Visual field area

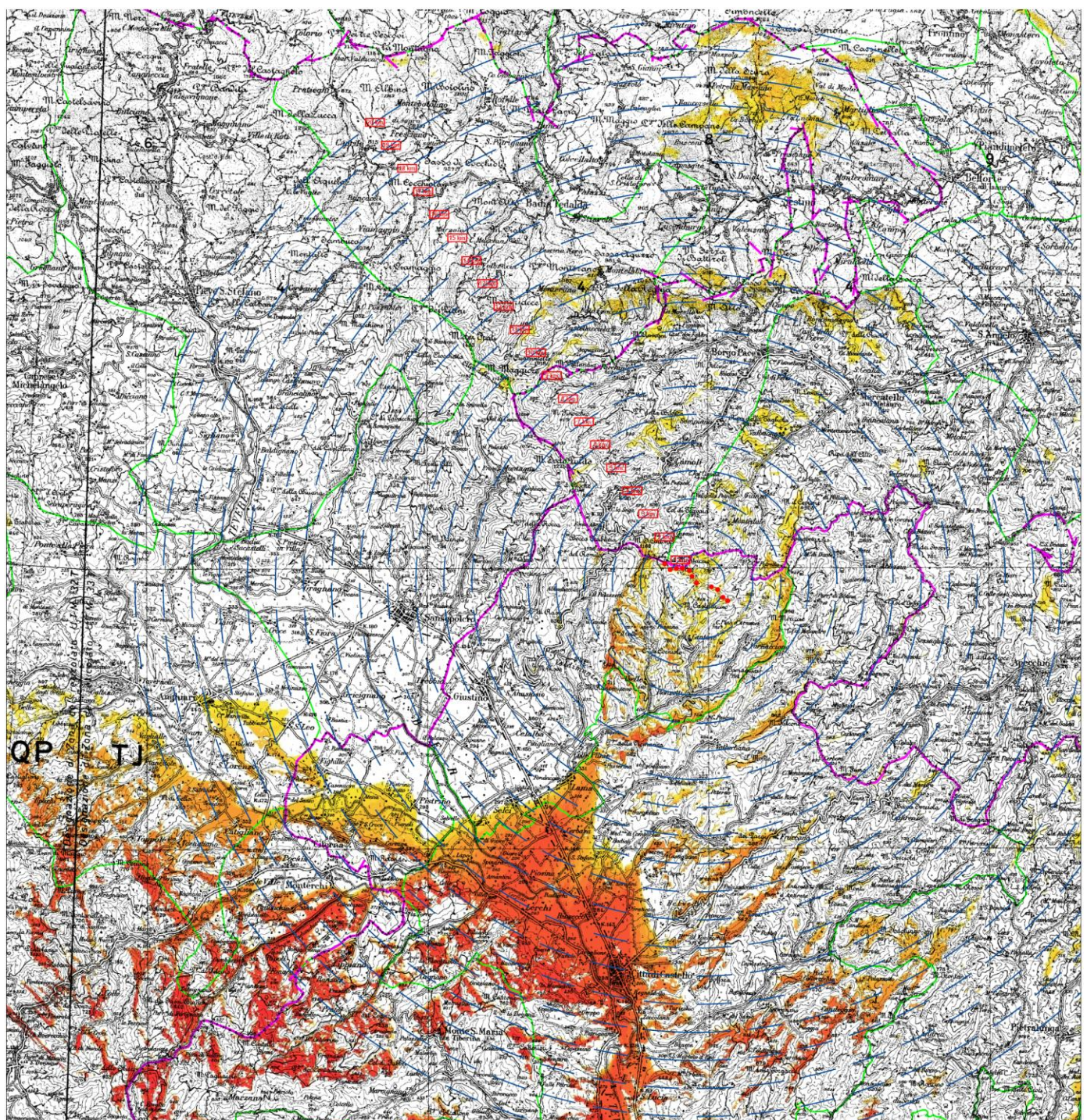


Figure 1 - Map of the intervisibility of visual impact of wind turbines (in red 100% visibility)

In this way, at any distance and angle the observer places himself with respect to the work under study, it is possible to estimate, at least as a first approximation, the percentage of view occupied by the element with respect to the area observed by the human visual field. In the case study, since the wind turbines are objects that have a dimension in height that is much greater than the width, the percentage of visual impact was calculated from the ratio between the height of the wind turbine and the "a" shaft.

For each of the locations shown in the table, three-dimensional views were reproduced into the Appendix I, from which the percentage of visual impact of the wind turbines was calculated in relation to the observation distance, as well as photosimulations made without any effect of scale reduction.

With regard to the observation points 1A, 2A, 3A, 4A and 5A, photorealisms were also carried out into the Appendix II on the basis of photographic images taken in situ.

Table I. Area of visual - Visibility

N	View Point	Coord. East [m]	Coord. North [m]	Altitude [m s.l.m.]	Distance [km]	Half axis (a) [km]	Half axis (b) [km]	Area of visual [km2]	visibility %
		Roma 40 – Fuso est	Roma 40 fuso est						
1	Anghiari	2282137.63	4825039.45	440	16.97	29.40	20.23	1868.22	0.32
2	Sansepolcro	2289288.36	4828242.83	335	9.26	16.04	11.04	556.41	0.58
3	Prato Montagna	2292766.29	4833059.54	682	6.36	11.01	7.58	262.23	0.84
4	Lamoli	2298703.99	4833692.69	600	3.70	6.42	4.41	88.96	1.45
5	Sompiano	2300380.74	4834860.55	528	5.22	9.05	6.23	177.00	1.03
6	Apecchio	2311649.37	4826040.51	493	11.39	19.73	13.58	841.65	0.47
7	Parnacciano	2301393.12	4827139.95	712	1.79	3.10	2.13	20.80	3.00
8	Vallurbana	2300057.42	4823764.18	494	5.00	8.67	5.96	162.39	1.07
9	Lama	2295134.84	4822532.86	331	8.27	14.32	9.85	443.41	0.65
10	Cantone	2299280.50	4827312.43	679	1.94	3.36	2.31	24.41	2.77
11	Uselle	2297692.51	4825755.37	460	4.06	7.04	4.84	106.98	1.32
12	Selci	2292741.59	4821529.85	297	10.66	18.47	12.71	737.02	0.50
13	Celalba	2293825.37	4824304.73	360	7.61	13.19	9.07	375.79	0.71
14	Monterchi	2286435.78	4818815.84	356	16.78	29.07	20.00	1826.64	0.32
15	S. Giustino	2291950.36	4825706.91	336	7.76	13.44	9.24	390.24	0.69
16	Città di Castello	2296581.36	4815144.61	288	14.17	24.54	16.88	1301.67	0.38
17	Riosecco	2295745.41	4817517.81	284	12.22	21.17	14.56	968.42	0.44
18	Monte S.Maria	2290466.96	4813261.71	688	18.45	31.95	21.98	2206.81	0.29
19	Lippiano	2286894.69	4816036.32	423	18.06	31.28	21.52	2115.15	0.30
1A	-	2297265.23	4829334.57	963	1.29	2.24	1.54	10.84	4.15
2A	-	2297337.15	4817054.52	294	12.13	21.00	14.45	953.51	0.44
3A	-	2294578.93	4819231.87	292	11.25	19.48	13.41	820.48	0.48
4A	-	2293852.62	4817264.67	292	13.30	23.04	15.85	1147.60	0.40
5A	-	2296375.07	4827961.91	860	2.86	4.96	3.41	53.22	1.87

## DISCUSSION AND CONCLUSIONS

This case study in applied of new methodology of visual impact, examined the accuracy and adequacy of visual simulations provided for 11 turbines in a wind energy development project. The description of the visual impact and the comparison to simulations is therefore a conservative estimate to the new landscape experience.

Results showed the visual simulations in the environmental screening report and the as-built situation. Locational information was drawn from the environmental screening report and compared to built data provided by the developer. The visual simulations were compared to the experience of viewing the landscape from a fixed position using human field-of-view parameters (for binocular vision) and to the experience of living within the landscape with the freedom to view the horizon in all directions. The simulation frame width was smaller than all human field-of-vision parameters for binocular vision found in the literature (and larger than some focused fields-of-view), yet acceptable for focused vision by a best practices report for wind energy simulations. Future environmental screening reports (particularly the visual impact assessment) should continue to be closely and independently scrutinized prior to being used to inform decision-making or public processes to yield unsurprising landscape changes.

## ACKNOWLEDGMENT

This case study was funded by project of wind farm "Montaccio" in Municipality San Giustino. No limits apply to publication and dissemination of the research results.

The research received support and encouragement from a private research laboratory S.P.R.I.S.S. Lab Ltd and was aided by the accessibility of regional and municipal officials and the transparency with which they discharged their civil service. I thank the editors and anonymous reviewers of this manuscript.

## REFERENCES

- [1] Roth M., Hildebrandt S., Röhner S., Tilk C., Von Raumer H.S., Roser F., Borsdorff M. Landscape as an area as perceived by people: Empirically-based nationwide modelling of scenic landscape quality in Germany. *Journal of Digital Landscape Architecture*, 3–2018, pp. 129-137. <[https://gispoint.de/fileadmin/user\\_upload/paper\\_gis\\_open/DLA\\_2018/537642014.pdf](https://gispoint.de/fileadmin/user_upload/paper_gis_open/DLA_2018/537642014.pdf)>.
- [2] United States Department of Agriculture, Forest Service Landscape aesthetics: A handbook for scenery management USDA FS, Washington, DC (1995) <<https://naldc.nal.usda.gov/download/CAT11132970/PDF>>
- [3] D. Johnson An assessment of the accuracy of the zone of theoretical visibility technique for wind farms. *Unpublished master's thesis University of East Anglia* (2014).
- [4] Wood G. Is what you see what you get? Post-development auditing of methods used for predicting the zone of visual influence in EIA. *Environmental Impact Assessment Review*, 20 (2000), pp. 537-556.

<https://reader.elsevier.com/reader/sd/pii/S019592550000055X?token=44AF96375F573FD8A71A9F1A6D86E84123205A8434160EDDA26CF4633752EF7FC1A4557D80CFB59B308196924EB6A5EE>.

[5] Wind Atlas Analysis and Application Program (Wasp software) DTU Wind Energy Risø Campus Frederiksborgvej 399 Building 118 4000 Roskilde Denmark (2006) <https://www.wasp.dk/>.

[6] Troen, I., & Lundtang Petersen, E. European Wind Atlas. *Risø National Laboratory, Roskilde, Denmark.* 1989. <file:///C:/Users/User/Downloads/European\_Wind\_Atlas.pdf>



# CHARACTERISTICS OF BEACH EROSION AT KKOTJI BEACH IN KOREA

Hyun Dong Kim

The World Association for Waterborne Transport Infrastructure (PIANC), Seoul, Korea, [hdkgm@pianckorea.org](mailto:hdkgm@pianckorea.org), ORCID: 0000-0003-2599-7137

Jinwoo Jeong

Catholic Kwandong University, Gangneung, Korea, [jjw9307@cku.ac.kr](mailto:jjw9307@cku.ac.kr), ORCID: 0000-0002-9238-398X

Kyu Han Kim

Catholic Kwandong University, Gangneung, Korea, [khkim@cku.ac.kr](mailto:khkim@cku.ac.kr), ORCID: 0000-0002-8247-225X

Cite this paper as:

*Kim, H.D., Jeong, J.W., Kim, K.H. Characteristics of beach erosion at Kkotji beach in Korea. 9th Eur. Conf. Ren. Energy Sys. 21-23 April 2021, Istanbul, Turkey*

---

**Abstract:**

The west coast of Korea is shallow and in the form of a bay facing the east coast of China. When a tidal wave enters the bay, there is considerable resonance between the reflected and incident waves, causing substantial tide differences. Among the many beaches on the west coast of Korea, Kkotji beach is a representative coastal tourist location. It has been labeled as a coastal erosion management beach by the Korean government due to continuous severe coastal erosion. The Kkotji beach has been graveled, and the number of tourists has decreased over the years, causing significant economic loss. As a countermeasure to the erosion problem, it is necessary to determine the reason for erosion. Thus, a field survey was conducted from the early 2010s, and by using recent observations, numerical simulations have been conducted using MIKE 21 (powered by DHI). The spectral wave module, hydrodynamic module, and sand transport module were used simultaneously to analyze sediment transport and confirmed the phenomena of erosion and sedimentation by comparing seven years of cross-sectional beach profile evolution data along the coast.

---

**Keywords:**

*Kkotji Beach, Wave Energy Effect, Beach Erosion, Field Observation*

---

© 2021 Published by ECRES

## 1. INTRODUCTION

A beach is a place where land and sea meet and constantly interact with each other. Consequently, it forms an environment in which the phenomena of erosion and sedimentation develop dynamically (Wright and Thom, 1977). The main causes of seabed changes are high waves occurring in certain seasons, rapid seabed changes due to storm waves, and human influences such as the construction of coastal structures or seawalls. Due to the combination of environmental effects of climate change on coasts and artificial changes such as coastal reclamation and structures built for economic development, large-scale erosion of beaches has occurred. Consequently, loss of life, land, recreational areas, and other losses have occurred in many areas. The problem of coastal erosion is recognized as an important social concern. In the case of the west coast of Korea, wide tidal flats are developed as a large island environment and have the characteristic of being connected to the open sea without a barrier island. In particular, the fact that the Kkotji beach is very wide and eroded, with the seabed slope being relatively gentle and the seabed width reaching 300–500 m, was qualitatively confirmed in various field observations conducted for this study over seven years. In this study, based on the basic field survey data, numerical simulations were conducted on Kkotji beach to determine the degree of erosion. Later, using the results obtained from the numerical simulations, seven years of field observation data were used to confirm the tendency of the erosion and sedimentation phenomena in Kkotji beach. For the numerical simulation, MIKE 21, (DHI, Denmark), with modules of spectral wave (SW), hydrodynamic (HD), and sand transport (ST), were simultaneously used for the analysis. SW and HD modules were used to calculate the current field generated on the coast, and the calculation results of these two modules were used as input data to determine the degree of erosion and tendencies by using an ST module.

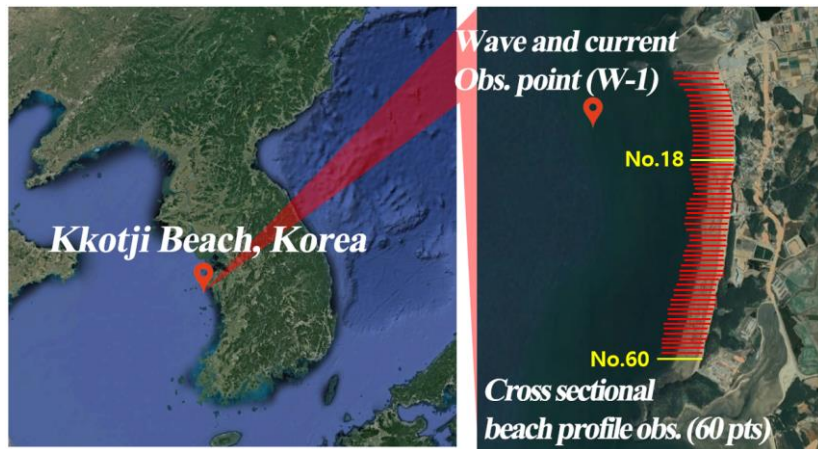


Figure 1. Kkotji Beach with Observation Points.

## 2. METHODS

In this study, field observations were conducted to identify the causes of beach erosion and coastline retreat at Kkotji beach. Wave and tidal current observations were conducted within the target area from February 2020 for the subsequent two months, and a cross-sectional topographic survey was conducted at 60 points, and a bathymetric survey was conducted to use the latest bathymetric data in numerical simulations. With the observed data, the MIKE 21 model was used for SW, HD, and ST module calculations on the phenomenon of beach erosion in Kkotji beach. The past seven years of cross-sectional beach profile data from 60 points at Kkotji beach were compared to confirm the tendency of erosion and sedimentation of Kkotji beach from the numerical simulation results.

## 3. FIELD OBSERVATION

Wave and tidal current observations were carried out for two months and analyzed in this section. Bathymetric surveys were carried out during February and used as input data for the simulations. Cross-sectional beach profile data were used in the results section for comparison with historical data from the past seven years.

### Wave observation

Wave observations were conducted in W-1 (from Figure 1), approximately 2 km from the shoreline in Kkotji beach. As depicted in Figure 2(a), during the winter season, owing to N and NW winds, the W series waves at right angles to the coast are superior, and the significant wave height is 2 m or more.

### Tidal current observation

Tidal current was observed simultaneously with waves and at the same point. The strongest surface currents during flood and ebb were approximately  $0.64 \text{ cm.s}^{-1}$  and  $0.77 \text{ cm.s}^{-1}$ , respectively, with ebb current having the stronger flow. The results are shown in Figure 2(b).

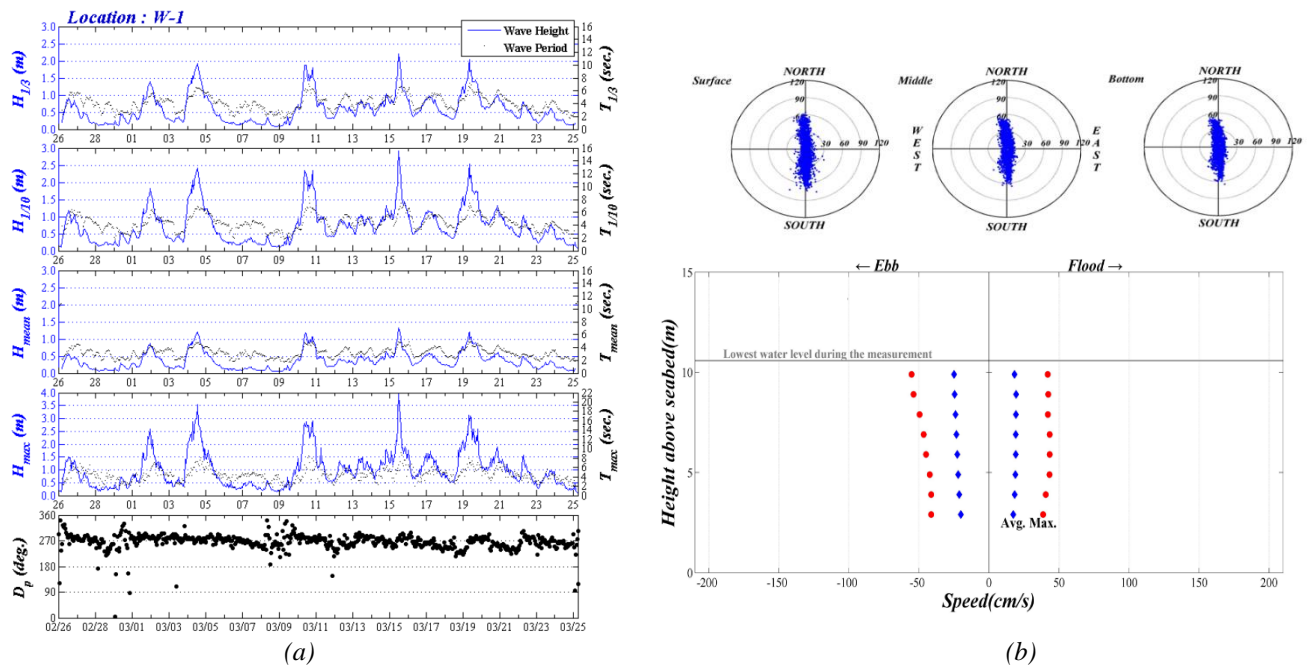


Figure 2. (a) Wave Observation Data of W-1 during Winter, (b) Current Observation Data of W-1 during Winter.

#### 4. NUMERICAL SIMULATION

For the numerical simulations, three modules (SW, HD, and ST) from MIKE 21 were used for the analysis. For the large scale, a total of 10,964 unstructured meshes were used, and for the detailed scale, a total of 17,698 unstructured meshes were used, as illustrated in Figure 3. For the bathymetric data, the latest bathymetric survey data conducted during the month of February, 2020 was used in this study.

##### MIKE 21 – Wave model (SW)

The MIKE 21 SW module is a spectrum wave model that calculates the magnitude of wavelengths generated by wind and can be used for coastal and offshore waves. The input data for calculating the SW model were organized as shown in Table 1. Since the main input of the SW model is wind forecast data, the wind data obtained from the ECMWF ERA 5 and used in this model with u and v components of wind velocity time series data, as illustrated in Figure 3.

Table 1. Conditions for numerical simulation of SW

Input data	Wind data
Basic equation	Fully spectral formulation & Institutionary formulation
Wave breaking	$\gamma=0.75$
Bottom friction	$Kn=0.03$
White capping	$Cdis=4$ , $DELTA dis=0.5$

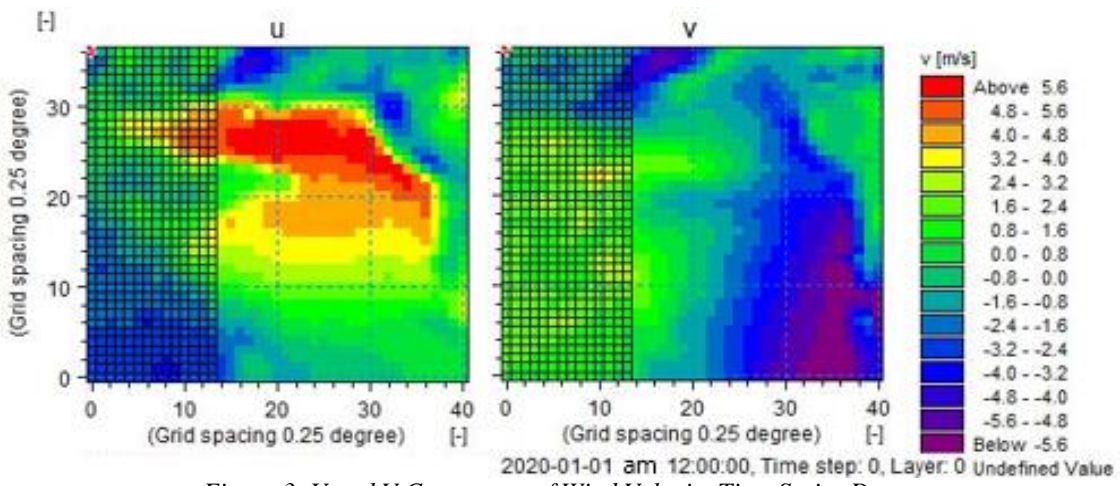


Figure 3. U and V Component of Wind Velocity Time Series Data..

Simulation results obtained for the 42 day period February 20 – April 1, 2020 are presented in Figures 4 and 5.

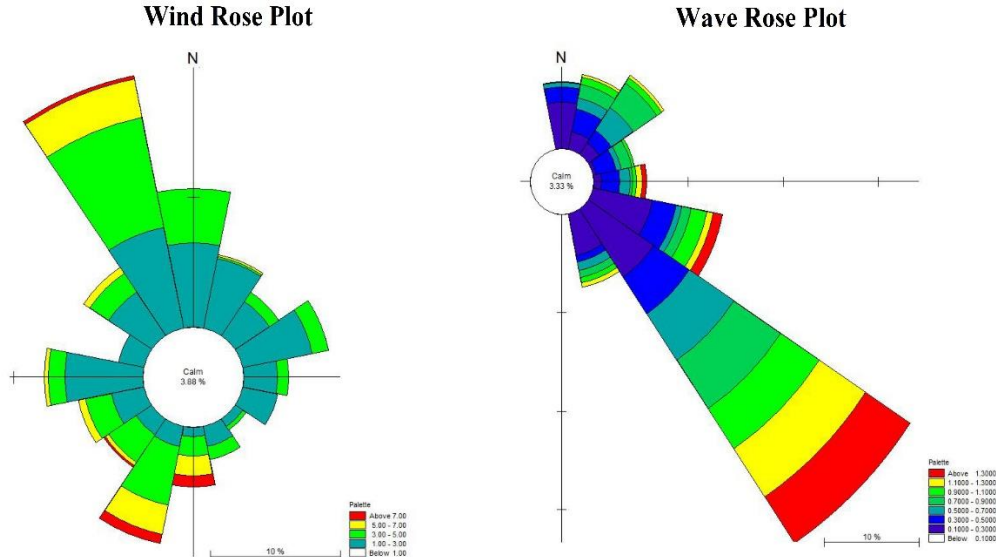


Figure 4. Wind and Wave Rose of Numerical Simulation Results.

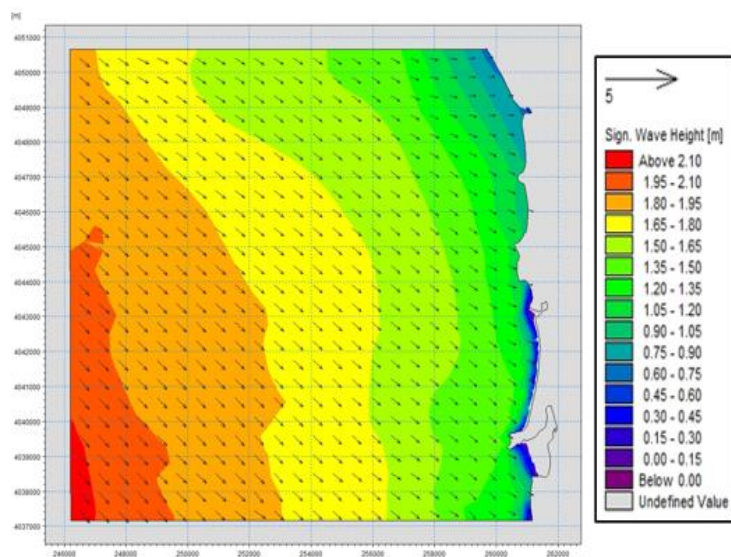


Figure 5. Significant Wave Height and its Vector at Kkotji Beach.

## MIKE 21 – Current model (HD)

The HD module solves the fluid equation for salinity, temperature, mass, and momentum conservation in response to various variables. For the boundary condition, the water level of Kkotji beach, which was obtained during the field observation, was used as the primary input, along with other inputs used in this model, as illustrated in Table 2. A duration of 62 days (February 01 – April 03, 2020) was tested for the model. A time step of 600 s was used throughout the experiment.

*Table 2. Conditions for numerical simulation of HD*

Input data	Wind data
Drying depth	0.005 m
Wetting depth	0.1 m
Eddy viscosity	0.28
Manning number	40 m <sup>-3</sup> / s

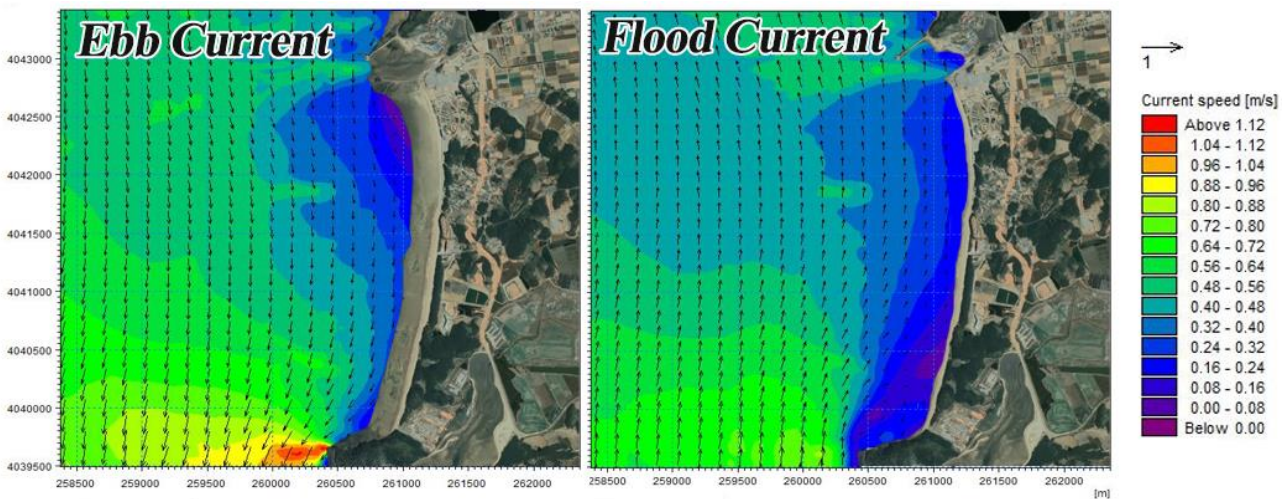


*Figure 6. Ebb and Flood Current Simulation Result from HD model.*

The ST module can simulate sand and non-adhesive sediment. This model is combined with the results of SW and HD modules to calculate sediment transport volume, bed level change, change in sand movement and erosion according to change in current velocity, and morphological changes of non-agglomerated sediment due to waves. The input data used to calculate the ST model are shown in Table 3.

*Table 3. Conditions for numerical simulation of ST*

Input data	Condition
Input model data	HD and SW output
Porosity	0.4
Grain diameter	0.16 mm
Grain coefficient	1.4

Currents flowing in a direction parallel to the coast and high waves of the NW series cause erosion to the coastal line of the beach during winter. Sedimentation occurred at the coastal line of the southern side of the beach, and it seems to be the reason for the dominant ebb currents in this beach; these currents move the sediments along the coast and deposit them on the southern side of the beach. During the flood current, an insufficient amount of sediment moves back to the northern side of the beach, resulting in beach erosion. To confirm these phenomena, seven years of observed cross-sectional beach profile evolution data are analyzed in the results section. The results of the sediment transport and the tendencies of erosion and sedimentation for two months are shown in Figure 7.

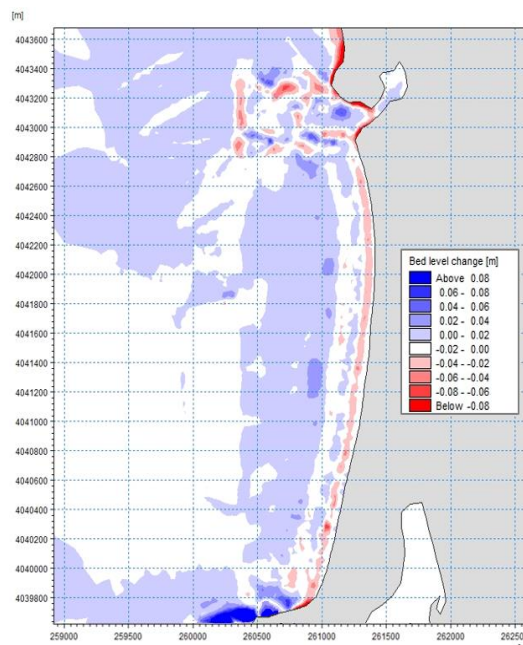


Figure 7. Result of Sediment Transport from ST model.

## 5. RESULTS

After two months of experiments using SW, HD, and ST modules provided by MIKE 21 numerical simulations, results were obtained and compared with the observed data. From the observations, waves of the NW series were dominant, and wave heights higher than 2 m were formed by strong winds during winter. By comparing the observed wave data with the numerical simulation of SW, it can be seen that MIKE 21 resulted in wave heights similar to those of the observed data, as shown in Figure 8(a).

For the current observation, it was found that from February to March, the strongest surface currents during flood and ebb were approximately 0.64 cm.s<sup>-1</sup> and 0.77 cm.s<sup>-1</sup>, respectively, with the ebb current having the stronger flow. By comparing it with the results of the numerical simulation of HD module, flood current shows a reciprocating flow pattern that flows in a direction parallel to the coast and goes to the northern part. Ebb current was observed to be superior, and the strongest flow velocities during flood and ebb were approximately 0.45 m.s<sup>-1</sup> and 0.6 m.s<sup>-1</sup>, respectively, which cause an approximate difference of 15 cm.s<sup>-1</sup>, as illustrated in Figure 8(b).

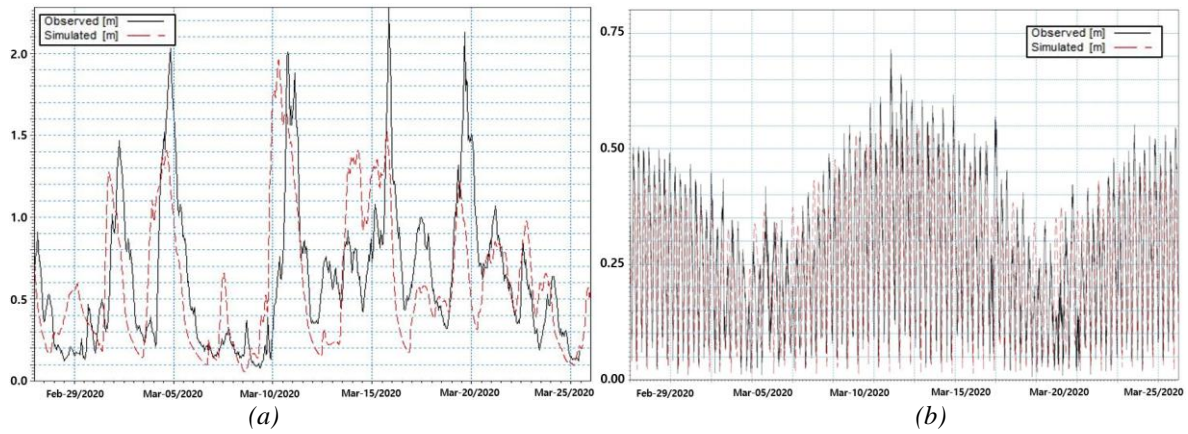


Figure 8. (a) Observed and numerical simulation wave height comparison, (b) Observed and numerical simulation current speed comparison.

Since winter wave heights were higher than the ones in summer, the winter survey was chosen for comparison. Among the survey data for the past seven years, survey data from November 2013, March 2014, December 2014, February 2015, November 2017, October 2018, November 2019, January 2020, and March 2020 were chosen and compared. It was observed from the general cross-sectional beach profile evaluation that erosion persisted and is incremented over time; however, in 2017, continuous nourishment was conducted at this beach, so little erosion was observed. A small amount of erosion was observed

in general from cross-sections No. 1-50 (Figure 1), and sedimentation was observed from cross-sections No. 51-60. Among the data, December 2013, February 2015, November 2019, and March 2020 were chosen to compare the cross-sectional profile evolution where the tendencies of sedimentation and erosion are clear. As shown in Figure 9(a), in cross-section No. 18, continuous erosion can be seen even with some nourishment onshore. From Figure 9(b), in cross-section No. 60, a large amount of deposited sand can be observed onshore of the southern part of the beach.

Despite constant nourishment, continuous erosion can be observed, and the eroded sand seems to be deposited in the southern part due to the dominant ebb current. This causes sediment to be transported to the southern part during ebb, and insufficient sediment had been transported back during the flood. In Figure 9(b), it can be observed that, since 2013, there has been an increase in elevation by approximately 2.5 m. This might have been caused by sediment rich sand moving to the southern part of the beach and being trapped in a vicious circle, unable to return during flood.

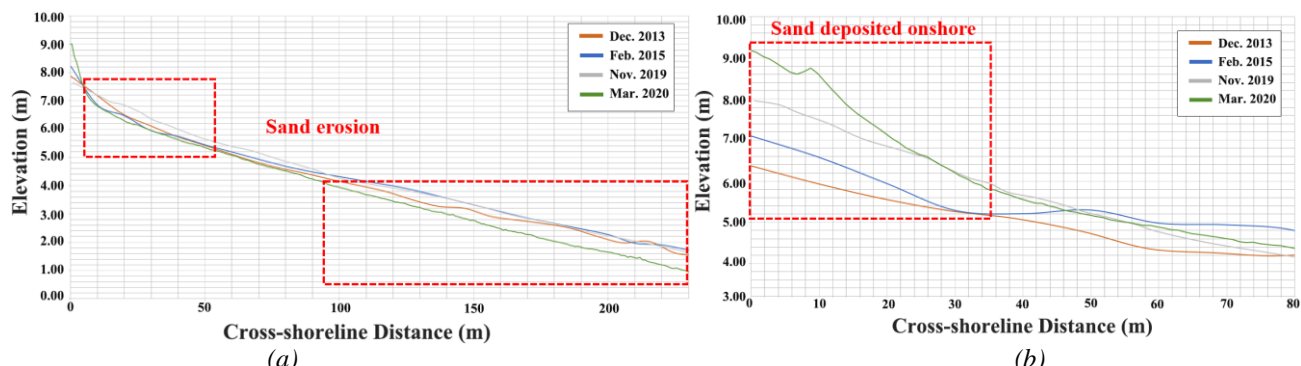


Figure 9. (a) No.18 cross-section where erosion occurs, (b) No.60 cross-section where sedimentation is dominant.

## 6. CONCLUSIONS

A tendency for erosion was found to persist in the coastal line of the beach, and a large amount of nourished sediments were transported to the southern part of the beach and trapped. This was caused by the ebb current being more dominant than the flood current. Therefore, when performing the nourishment, considering the phenomenon of sediment transported to the southern part of the beach, moving the deposited sand to the southern part using sand-by-passing should be considered. Comparing the observed data and numerical simulation results, both the wave and tidal current results seem to be very similar. Additionally, the sediment transport numerical simulation resulted in a similar tendency after comparing the past seven years of sediment transport tendencies from cross-sectional profile evolution. MIKE 21 requires wind data to generate results in the SW, HD, and ST modules; this makes it possible to predict long-term sediment transport on the beach if wind data is available.

## ACKNOWLEDGMENT

This research was a partially supported by the Korean Section of The World Association for Waterborne Transport Infrastructure and The Waterfront and Coastal Research Center, Korea.

## REFERENCES

- [1] Anton, I.A, Rusu, L, and Anton, C. 2019. Nearshore Wave Dynamics at Mangalia Beach Simulated by Spectral Models. *Journal of Marine Science and Engineering*, 7(7), 206
- [2] Kim, C.W, Shin, Y.H, and Yu, K.B. 2015. Changes of beach profiles and sediment properties in Baeksajang sandspit beach, west coast of Korea, during winter season. *The Korean Association of Professional Geographers*, 49(1), pp. 117-131.
- [3] Lee, J.M. 2018. The Study of Hydro-dynamic Sediment Transport in Bottom Boundary Layer of Byeonsan Channel in sub-tidal zone, West Coast, South Korea. Kunsan, South Korea: Kunsan National University, Ph.D. dissertation, 106p.
- [4] Lee, Y.B, Kim, H.D, and Kwak, K. 2018. Verification of Beach Erosion in West Coast of Korea. *Journal of Coastal Research*, 85(sp1), pp.256-260.
- [5] Lim, D.I, Jung, H.S, Chu, Y.S., Park, K.S, and Kang, S.H. 2002. A Study on Shoreline Change in Hampyung Bay, Southwestern Coast of Korea I. Sea-Cliff Erosion and Retreat. *The Korean Society of Oceanography*, 7(3), pp. 148-156.
- [6] Woo, H.B., and Jang, D.H. 2010. A Study on the Erosion and Retreat of Sea-Cliff through the Multi-temporal Aerial Photograph Data and Field Survey: The Case Study of Taean Peninsula, Korea. *Journal of the Korean Geomorphological Association*, 17(4), pp. 71-83.p
- [7] Wright, L., and Thom, B. 1977. Coastal depositional landforms. *Progress in Physical Geography: Earth and Environment*, 1(3), pp. 412-459.



# ISSUES OF RENEWABLE ENERGY SOURCES WITH GRID-TIED INVERTER CONNECTED TO AN OFF-GRID SYSTEM

Mantas Zelba

Kaunas University of Technology, Kaunas, Lithuania, mantas.zelba@ktu.edu, ORCID: 0000-0001-9924-5582

Tomas Deveikis

Kaunas University of Technology, Kaunas, Lithuania, tomas.deveikis@ktu.lt, ORCID: 0000-0002-4319-2554

Justinas Barakauskas

Kaunas University of Technology, Kaunas, Lithuania, justinas.barakauskas@ktu.edu, ORCID: 0000-0002-9840-610X

*Zelba M., Deveikis T., Barakauskas J. Issues of renewable energy sources with grid-tied inverter connected to an off-grid system. 9<sup>th</sup> Eur. Conf. Ren. Energy Sys. 21-23 April 2021, Istanbul, Turkey..*

**Abstract:** Well-known practice is to connect renewable energy sources to a utility grid with grid-tied inverters, but the situation dramatically changes if such a composition is being connected to an off-grid. It is not a common practice, but for the first stage consumers who are minimizing they required peak power with renewables, the next stage will be either complicated or more costly. For the second stage, consumers will think of possibilities becoming independent from utility grid and likely will have an issue of connecting currently owned renewables with grid-tied inverter to an off-grid system. Renewables have an uncertain production, and error-forecast will make an impact to a power balance, resulting either of excess or shortage of power. There are a number of inverter manufacturer, and even a bigger number of different inverter products, where each product is with different parameters and because of excess power, making different affect to an off-grid. The aim of this paper is to identify such a connection possible issues, to look for the feasible alternatives, and the findings could be used further for the arising problems as acceptable solution.

**Keywords:** Renewable energy sources, off-grid, excess energy

© 2021 Published by ECRES

Nomenclature	
RES	Renewable energy sources
VRLA	Valve-Regulated-Lead-Acid
p.u.	Peak units
HAWT	Horizontal-axis wind turbine
SOC	State of charge

## 1. INTRODUCTION

Due to climate changes, and last seen situation with worldwide pandemic, even more attention is being taken to save environment. Going that way, RES are being used in a larger and wider scale, small electricity consumers have a choice to generate electricity by themselves, and it is becoming cost efficient even without subsidies. A grow in RES leads to the second, even more greener way, to become an independent micro energy system owner with a possibility to use the national electricity system just as a reserve generator or to increase reliability of local energy system.

There are increasing number of consumers, who would like to connect their already installed RES plant with grid-tied inverters to a micro grid, or even off-grid. Small power grid-tied inverters up to 10-20 kW of power does not control their power dependently by the frequency or voltage in the most cases. Grid-tied inverters produce as much as they can, until they reach the point, where they switch off because of a faulty grid.

Many other relative publications found with off-grid's and micro-grids are considering of excess power as charging batteries which SOC is never reaching 100% [1], gives excess power to the grid [2, 3], uses off-grid type inverters to implement RES [4, 5], or not dealing with excess power control at all [6]. Moreover none publications were found of using excess energy while not affecting battery SOC level.

The easiest and the most convenient way to connect RES power plant to an off-grid system is via off-grid capable inverter. However, in case then the inverter is not capable to work in an off-grid system conditions, the power balance in such a system becomes an issue. In this paper, such a grid-tied inverter is connected to an off-grid system and achieved problems with possible solutions are analyzed.

## 2. EXPERIMENTAL MODEL

The off-grid system, with its nominal power of 13.8 kW is used in an experimental model. Experimental model is located at Kaunas University of Technology RES laboratory. The model is powerful enough to cover a bigger than annual household power demand. Experimental model consists of:

- 3 x SMA Sunny Island 6.0H. Grid-tied battery inverters, each 4.6 kW of power (or 1/3p.u.), which might work as a bi-directional or an off-grid inverters. Sunny Island units are ensuring demand and supply balance in the off-grid.
- Batteries – 24 pcs, 2V VRLA. In total of 7.3 kWh capacity. If 13.8 kW power (or 1p.u.) were utilized, the batteries would discharge in 0.53 hours.
- Sunny Tripower 6000TL-30 (off-grid type inverter) – three-phase inverter with solar panels, inverter is capable to work in an off-grid system. Inverter got 2.88 kWp (or 0.21p.u.) power solar panels connected in not an optimal orientation.
- GCI-5K-2G-H (grid-tied inverter) – wind and sun grid-tied single-phase inverter. It has a 1 kW power (or 0.07p.u.) HAWT and 2.88 kWp (or 0.21p.u.) power solar panel connected. Solar panels are in an optimal orientation. In total, grid-tied inverter has 3.88 kW (or 0.28p.u.) power.

Experimental model principal scheme is as shown in a fig. 1. Such a configuration of controllable (off-grid type) and non-controllable (grid-tied) RES inverters in an off-grid system are selected to emphasize the problems, which are raised by unpredictable and uncontrollable RES.

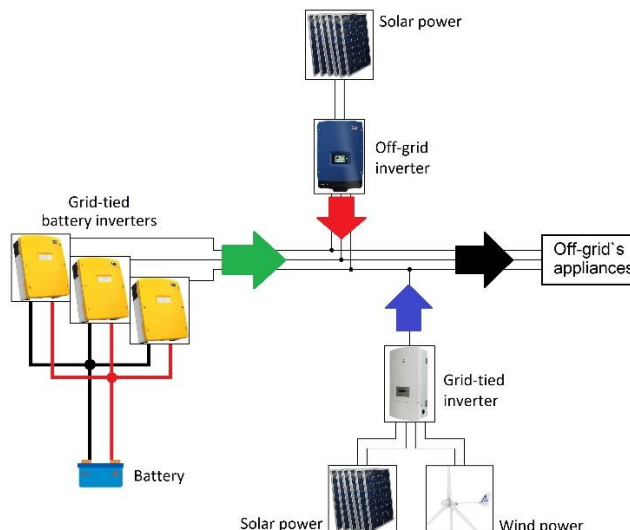


Figure 1. Experimental model principal scheme.

The system is design in such a way, that when the RES power is lower than total demand power (battery charging and load power combined) the system's frequency is set to 48.9 Hz. When the excess power is detected, the frequency rises and might rise up to 55 Hz. Off-grid type RES inverter is set to limit its power if the frequency reaches 50.75 Hz and the grid-tied RES inverter operating frequency is from 48 to 52 Hz. So the designed system status might be indicated while measuring frequency:

- From 48 to 55 Hz systems nominal frequency range.
- 48.9 Hz batteries are discharging and system faces RES deficit power.
- From 48.9 to 50.75 Hz system is in averaged RES and demand power balance.
- At 50.75 Hz off-grid type RES inverter stops generating power.
- From 50.75 to 52 Hz off-grid type RES are not generating and only grid-tied RES inverter is generating power.
- At 52 Hz, grid-tied RES inverter is reaching its upper frequency operating limit and switches off due to the faulty grid.

Solar or wind power usage in the off-grid system is depending on battery capacity. The described off-grid system is supplying electricity for the RES laboratory in Kaunas University of Technology, Department of Electric Power Systems, located in Lithuania. Laboratory's demand from the beginning of June until the end of August, in the sunniest period of time in Lithuania, is at its minimum and during the winter time, when the geographical area is experiencing a dark period of time, the consumption is highest because of electrical heating in a laboratory. Demand and supply periods are in a completely different time of a year, because of this reason, laboratory is experiencing excess power in a summer time and run into shortage of supply in a wintertime.

In a summer time, the demand is at its minimum and the RES supply is at its peak, but considering the battery capacity, micro-grid can be autonomous for 26.5 hours if RES are not supplying any power. In an opposite way – wintertime, during the cold season the heating is in use, so the average power, mostly dependent by the ambient temperature, is 0.08 p.u., and the micro grid is capable to stay autonomous if RES are not producing any power only for 6.5 hours.

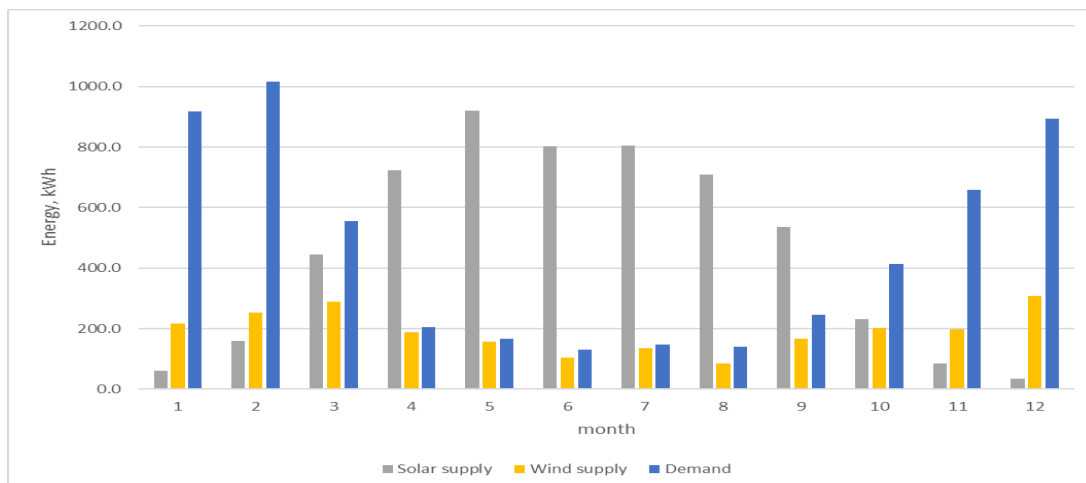


Figure 2. Demand and supply curves of the test system.

Low battery capacity, means that laboratory has more supply power than batteries can handle during summer time and in a wintertime, battery capacity is too low to cover the demand. Considering the winter time, micro-grid's battery capacity is not large enough, if the micro-grid would need to stay autonomous for, as an example, at least three days, battery capacity should be eleven times larger. Besides autonomous time, batteries fully meets the requirements for the power peaks balancing and for the grid-tied inverter to be tested in the off-grid system.

### 3. RESULTS

The tested system consists of two equal parts of solar panels, one part is connected to a power-controlled off-grid type inverter and another part of solar power plant to a grid-tied inverter, which is producing as much as it can without any power control. Solar panels, which are not optimally oriented, are connected to an off-grid type inverter, because of it, the maximum achievable power is not reaching its peak. Grid-tied inverter connected solar power has solar panels oriented optimally and because of it, achieves a higher peak power, combined to off-grid type inverter. During the illustrated timeframe of 2000 seconds, the solar horizontal irradiation varies from 398 to 509 W/sq. m., the variety is not in a large scale, so the RES productions is almost stable. Battery SOC is an average of 80%, because of the beginning of float charging cycle, which reduces the charging current. Average demand is 0.095p.u. in addition, average possible power output of off-grid type RES is slightly lower than demand at 0.086p.u.

According to the results in fig. 3 it is seen that grid-tied RES inverter has switched on and off 5 times in 2000 second period of time and the constant switching is noticed not only in the range of shown timeframe. Constant switching is monitored all the time, with a condition, that RES with grid-tied inverter generating power is higher than total demand (battery charging and loads combined).

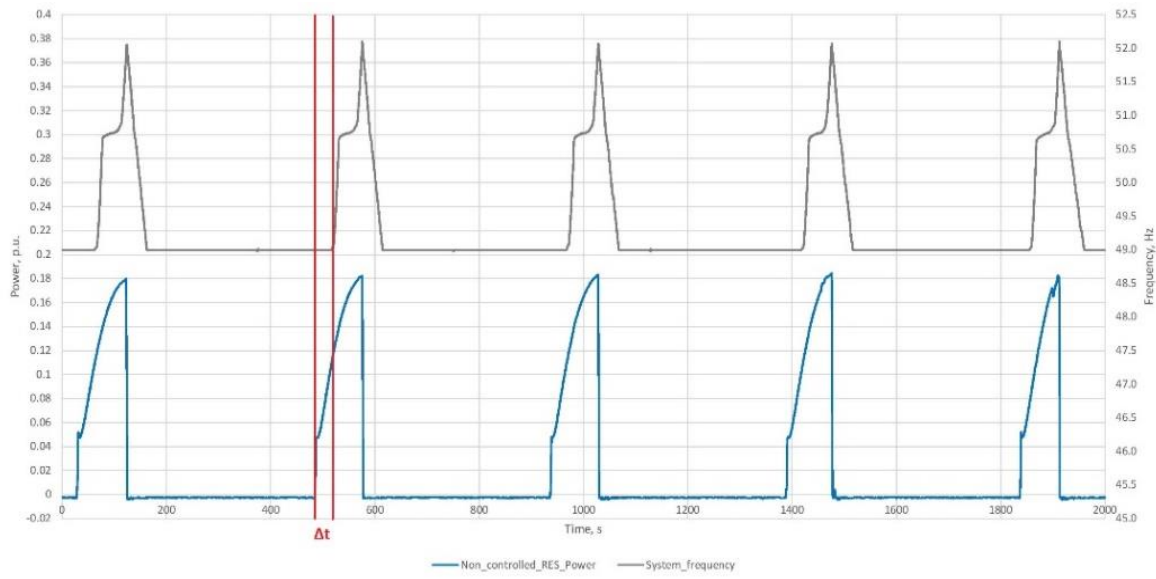


Figure 3. Grid-tied inverter with RES operation during sunny day.

At the scaled transient grid-tied inverter timeframe illustrated in fig. 4, the system operations are explained as follows:

1. First 64 seconds off-grid type inverter with RES connected are generating slightly lower than demand, and the Sunny Island devices are compensating the deficit while discharging batteries. In a mean time, grid-tied inverter is checking grid parameters and synchronizing with an off-grid system. At 65<sup>th</sup> second grid-tied RES inverter is beginning to generate power. Sunny Island devices with excess power from all RES are charging batteries until about 105<sup>th</sup> second, same battery charging time  $\Delta t$  is displayed in fig. 3;
2. At 105<sup>th</sup> second batteries are charged back to 80% SOC, and float charge cycle is switched on. From this point, off-grid type RES inverter is starting to reduce its generating power to keep the supply and demand balance;
3. At 130<sup>th</sup> second, off-grid type RES inverter generating power is nearly equal to zero and the grid frequency is already 50.75 Hz. Besides all the effort of off-grid type RES inverter to keep supply and demand balance, grid-tied inverter is rising its generating power until it reaches a 52 Hz operating range point;
4. Grid-tied inverter is switching off due to faulty (over frequency) grid parameters. At the same time, to keep power balance between production and demand, Sunny Island devices, taking power from batteries, are instantaneous starting to generate power (because grid-tied inverter has switched off), and the frequency in around 10 seconds is slowing down to 50.75 Hz;
5. The frequency goes below 50.75 Hz and the off-grid type RES inverter kicks back to generate power. In parallel grid-tied RES inverter check's the grid's parameters – the frequency is within operating range and it starts a start-up procedure again, which is followed by switching on again.

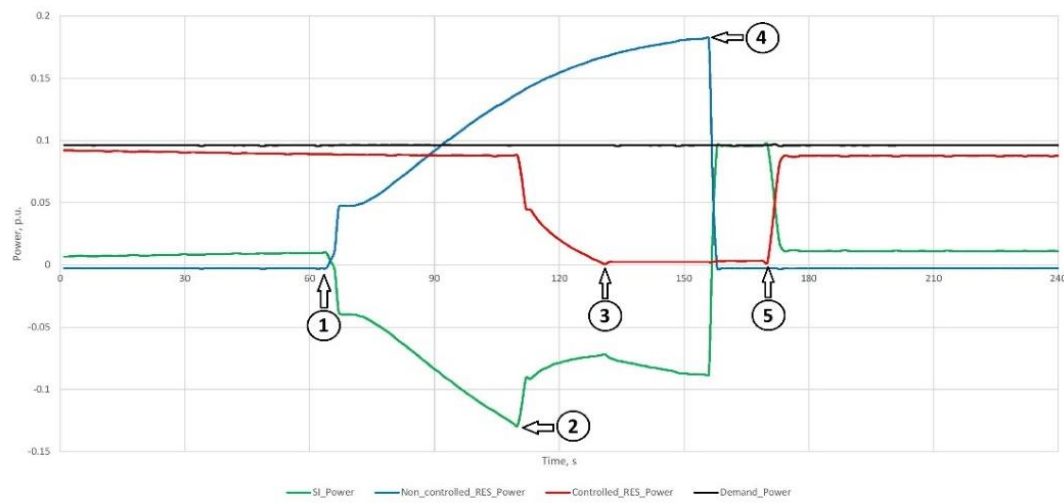


Figure 4. Power supply and demand of system's participants in one scaled transient switch timeframe.

There is a similar project done [7] in which case only off-grid type RES where in use, and destructive grid-tied power excess where not taken into account, in this case authors did not achieve similar issues with excess power. Although, in a paper, it is mentioned that the frequency is varying up to 55 Hz, but the possibility is found to change the frequency ranges in both Sunny Island and Sunny Boy or Tripower devices.

Constant switching illustrated in figures 3 and 4, are happening due to a grid-tied inverter power of RES. The destabilizing error-predictable generating unit is causing an issue and there is a need to find a solution. Possible solution should use the non-controlled excess power in a way that neither battery SOC would be effected neither any other additional issue would arise.

## **4. POSSIBLE SOLUTIONS**

One of the simplest solutions would be to detect the excess power and switch on any load. It is one of easiest solutions to implement, because even Sunny Island devices itself have a dedicated relay for this task, but there is an issue with it. The relay switches an external load for the use of excess energy, but the power of load is fixed. For example, at the experimental model the maximum possible excess power is 0.28p.u. therefore, the load should be at least the size of 0.28p.u. But if the RES are not generating full power in excess, if the excess energy is only 0.1 or even 0.05p.u., the switched on excess power relay will switch more powerful load than needed, because of this battery SOC will be affected. In another hand, if the lower power load will be selected, it will not be powerful enough to use the excess energy, because even a relatively slight excess power is causing the frequency to rise. Another way of excess power control could be achieved with additional control device and Modbus TCP/IP communication [8, 9]. However, this communication option is mostly capable only for commercial scale inverters, small-scale 1-20 kW power inverters often are not capable to control their power via Modbus TCP/IP command. So this option could not be adopted to the described experimental model. Besides that, inverter control via Modbus TCP/IP is individual for all the inverters, because each inverter brand has different protocol control addresses, and this leads, that such a device would be used as individual solution and not a versatile solution.

The achieved situation in results suggests that there is a need for a variable load, which would be dependent by the frequency. If the frequency is below the frequency set value, the variable load should be switched off, if the frequency is above – a calculated part of a load should be switched on. A load power should be limited by the system power and the maximum possible excess power. Besides that, such a variable load would have a little or even no affect to battery SOC level.

## **5. CONCLUSION**

In the real small-scale off-grid system experimental model, integrated RES with off-grid type and grid-tied inverter have led the grid-tied inverter to the constant switching on and off issue, when excess power in a system is detected. Excess power is detected by the frequency rise in a system and the following research is in a process of creating a new device for the efficient use of excess power. The efficient solution for the issue, which would not affect the battery SOC level, were not found, but led to the solution of a variable load power need, dependent by the systems frequency.

## **REFERENCES**

- [1] Huang Youwei, Zhang Xu, He Junping, Qin Yi. The improvement of micro grid hybrid energy storage system operation mode. In: 2014 IEEE PES T&D Conference and Exposition; 14-17 April 2014: IEEE, pp. 1-6.
- [2] Mavrigiannaki A., Kampelis N., Kolokotsa D., Marchegiani D., Standardi L., Isidori D., Christalli C. Development and testing of a micro-grid excess power production forecasting algorithms. Energy Procedia 2017; vol. 134: p. 654-663 <<https://doi.org/10.1016/j.egypro.2017.09.583>>.
- [3] Bastholm C., Fiedler F. Techno-economic study of the impact of blackouts on the viability of connecting an off-grid PV-diesel hybrid system in Tanzania to the national power grid. Energy Conversion and Management 2018; vol. 171: p. 647-658 <<https://doi.org/10.1016/j.enconman.2018.05.107>>.
- [4] Qusay H. Evaluation and optimization of off-grid and grid-tied photovoltaic power system for typical household electrification. Renewable Energy 2021; vol. 164: p. 375-390 <<https://doi.org/10.1016/j.renene.2020.09.008>>.
- [5] Kristiansen A.B., Zhao B.Y., Ma T., Wang R.Z. The viability of solar photovoltaic powered off-grid Zero Energy Buildings based on a container home. Journal of Cleaner Production 2021; vol. 286: article 125312 <<https://doi.org/10.1016/j.jclepro.2020.125312>>.
- [6] Jamiu O. Oladigbolu, Makbul A. M. Ramli, Yusuf A. Al-Turki. Feasibility Study and Comparative Analysis of Hybrid Renewable Power System for off-Grid Rural Electrification in a Typical Remote Village Located in Nigeria. In: IEEE Access (Volume: 8); 18 September 2020: IEEE, pp. 171643 – 171663.

- [7] Kosmak J., Misak S. Power Quality Management in an Off-Grid System. In: 2018 IEEE International Conference on Environment and Electrical Engineering and 2018 IEEE Industrial and Commercial Power Systems Europe (EEEIC / I&CPS Europe); 12-15 June 2018: IEEE, pp. 1-5.
- [8] Faruque R., Scudder M., Ula S. Real-World Implementation of Advanced PV Curtailment and Reactive Power Control Using Non-Smart PV Inverter: A Case Study. In: 2020 IEEE Power & Energy Society General Meeting (PESGM); 2-6 Aug. 2020: IEEE, pp. 1-5.
- [9] Yu-Chun Chou, Pin-Chieh Huang, Yi-Yu Liu. Design and Evaluation of a Bi-directional Data Acquisition and Control System for Small-scale Solar Power Plants. In: 2019 4th International Conference on Intelligent Green Building and Smart Grid (IGBSG); 6-9 Sept. 2019: IEEE, pp. 339-344.



# IMPROVING THE FATIGUE OF NEWLY DESIGNED MECHANICAL SYSTEM SUBJECTED TO REPEATED FOOD LOADING

Seongwoo Woo

Addis Ababa Science & Technology University, PO box 16417, Addis Ababa, Ethiopia, twinwoo@yahoo.com, ORCID: 0000-0001-8216-0558

*Cite this paper as:* Woo, S. *Improving the fatigue of newly designed mechanical system subjected to repeated food loading.* 9<sup>th</sup> Eur. Conf. Ren. Energy Sys. 21-23 April 2021, Istanbul, Turkey

**Abstract:** To enhance the fatigue of new mechanical structure subjected to repetitive food loading, parametric Accelerated Life Testing (ALT) as new systematic reliability method is a proposed procedure to determine and lessen the fatigue disaster due to its design faults. It embraces: (1) ALT scheme found on system BX lifetime, (2) fatigue mechanism and design, (3) tailored ALTs, and (4) estimation of whether the system design(s) accomplishes the BX lifetime. As a test investigation, newly designed mechanical product such as drawer system in a domestic refrigerator subjected to repeated food loading is evaluated. To conduct ALTs, utilizing a force equilibrium, the straightforward food loading of the drawer structure were examined. At first ALT the box cover fractured because of inadequate strength at intersection between its cover and drawer body. As an action plan, we modified the intersection areas by giving rib thickness and corner fillet rounding. At second ALT the sliding rails and the center support in drawer system fractured because of insufficient strength due to no corner rounding and thin rib width. As an action plan, draw structure was altered by magnifying corner rounding and the rib width. After parameter ALTs with these alternations, there is no problem at third ALT. Finally, lifetime of drawer system in a refrigerator is reassured to be B1 life 10 years.

**Keywords:** Fatigue failure, Design flaws, Mechanical system, Parametric ALT, Drawer System

© 2021 Published by ECRES

## 1. INTRODUCTION

The mechanical systems – refrigerator, automobile, and airplane – control (generated) power to attain a work which needs forces and movement, which eventually yield mechanical advantages by modifying system mechanisms. In the process mechanical system will be subjected to repeated loads. Most mechanical products are made of multi-module structures. If the modules are assembled, mechanical system can work properly and perform their own planned functions. For example, as utilizing the vapor-compression refrigeration cycle, a domestic refrigerator is intended to stock natural nourishment. Its evaporator provides cooled air to both the refrigerator and freezer sections. The product lifetime is determined by newly designed module, which has design faults.

To avoid the failure of mechanical system in the field, it should be designed to robustly endure the working conditions exposed by the customers who acquire and utilize. Any design faults therefore should be recognized and altered by statistical method or reliability testing before a commercially manufactured goods is released. However, they requires huge computations for optimum solution but have no results because of not figuring out failure mechanics. That is, if there are design faults that causes an inadequacy of strength (or stiffness) when a system is subjected to repeat loading, the system will fail before its expected lifetime due to fatigue failure.

This paper introduces a parametric ALT as systematic reliability method which might be identified and modified to design faults of newly designed mechanical systems. It embraces: (1) ALT scheme found on system BX lifetime, (2) load examination for ALT, (3) tailored parametric ALTs, and (4) an judgment of whether the system design(s) fulfils the target BX lifetime. As a trial investigation, we will deal with a newly designed drawer system in domestic refrigerator subjected to repeated food loading.

## 2. PARAMETRIC ALT FOR MECHANICAL SYSTEM

### Putting an Whole Parametric ALT Plan

Reliability might be explained as the system capability to work under expressed states for a period of time. Product reliability might be exemplified by an illustration defined a “bathtub curve” that composes as three sections. First of all, there is a lessen failure rate in the earlier product life ( $\beta < 1$ ). Secondly, there is a continual failure rate ( $\beta = 1$ ). Lastly, there is a growing failure rate to the ending of the system life ( $\beta > 1$ ). If a commercially manufactured goods pursues the bathtub curve, it might have problems to achieve success from the marketplace because of the short lifetime and big failure rates due to design faults. Manufactures will emphatically enhance the product design by putting its reliability targets to (1) eliminate untimely failures, (2) lessen random failures for its working period, and (3) lengthen system lifetime. As the design of a mechanical system improves, its failure rate from the marketplace deceases and the product lifetime extends. For such circumstances, the conventional bathtub curve might be changed to a straightforward line.

If product follows exponential distribution, the reliability of a mechanical system could be defined as:

$$R(L_B) = 1 - F(L_B) = e^{-\lambda L_B} \cong 1 - \lambda L_B \quad (1)$$

Equation (1) is relevant less than approximately 20 percent of the cumulative failures. The mechanical system therefore could be attained by putting the objective product lifetime LB and failure rate  $\lambda$  after optimally identifying the market failure by ALT and modifying the design flaws (or material) of structures.

In putting the lifetime target of a mechanical system through a ALT examination, there are trio occasions for various product modules: (1) an altered independent units, (2) a newly designed independent units, and (3) an alike independent units to the previous design on the base of marketplace request. The newly designed drawer system in refrigerator examined here as an instance investigation is a new independent units with design faults that might be rectified because consumers asked to be replaced with a new one if product fails in its lifetime.

The new independent units B from the market data in Table 1 had a failure rate of 0.24% per year and a B1 life 4.2 years. To answer to consumer requests, a new lifetime target for drawer was put to have B1 life 10 years with a cumulative failure rate of one percent.

*Table 1. Whole ALT plan of mechanical system such as modules in a refrigerator.*

Modules	Market Data		Anticipated Reliability				Targeted Reliability	
	Failure Rate per Year, %/year	BX Life, year	Failure Rate per Year, %/year	BX Life, year	Failure Rate per Year, %/year	BX Life, year	Failure Rate per Year, %/year	BX Life, year
A	0.35	2.9	Similar	×1	0.35	2.9	0.10	10(BX = 1.0)
B	0.24	4.2	New	×5	1.20	0.83	0.10	10(BX = 1.0)
C	0.30	3.3	Similar	×1	0.30	3.33	0.10	10(BX = 1.0)
D	0.31	3.2	Modified	×2	0.62	1.61	0.10	10(BX = 1.0)
E	0.15	6.7	Modified	×2	0.30	3.33	0.10	10(BX = 1.0)
Others	0.50	10.0	Similar	×1	0.50	10.0	0.50	10(BX = 5.0)
Product	1.9	2.9	-	-	3.27	0.83	1.00	10(BX = 10)

### Failure Mechanics and Accelerated Testing for Design

Mechanical systems move (generated) power from one location to another through its mechanisms. If there is a design fault in the structure that causes an inadequacy strength (or stiffness) when loads are exerted, the mechanical system may not instantly pass in its lifetime. As reproducing the system disaster by ALT, a designer could be optimally planned to have the product shape and choose a proper material. It sustains repetitive loads in its lifetime so that it can achieve the targeted reliability (Figure 1).

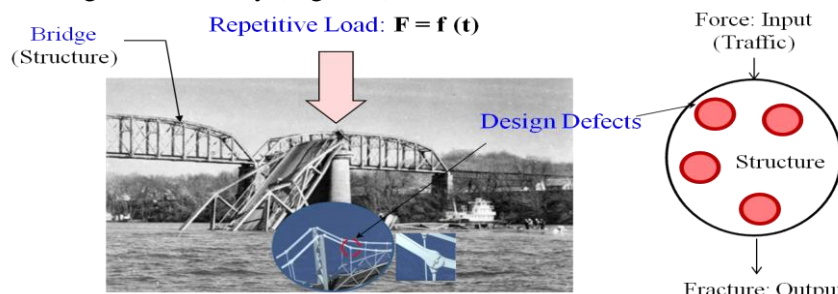


*Figure 1. Fatigue failure on the system generated by repeated loading and design faults.*

The most important issue for a reliability test is how premature the possible failure mode might be obtained. So it is inevitable to derive a failure model and determine the associated coefficients. First of all, we can configure the life-stress (LS) model, which incorporates stresses and reaction parameters. This equation can explain numerous failures such as fatigue on the structure. Because system failure starts from the presence of a material defects formed on a microscopic when repeatedly subjected to a variable tensile and compression loading, we might define the life-stress model from such standpoint. For example, we can figure out the following processes utilized for solid-state diffusion of impurities in silicon that is popularly used as semi-conduct material: 1) electro-migration-induced voiding; 2) build-up of chloride ions; and 3) trapping of electrons or holes.

When electric magneto-motive force,  $\xi$ , is applied, we know that the impurities such as void in material formed by electronic movement is easily migrated because the barrier of junction energy is lowered and distorted/phase-shifted. The generalized life-stress (LS) model could be defined as [1]:

$$TF = A[\sinh(aS)]^{-1} \exp\left(\frac{E_a}{kT}\right) \quad (2)$$

The sine hyperbolic expression  $[\sinh(aS)]^{-1}$  in Equation (5) can be defined as: (1)  $(S)^{-1}$  has a little linear effect at first, (2)  $(S)^{-n}$  has a mean effect, and (3)  $(e^{aS})^{-1}$  has a big in the end. As ALT is normally performed in the medium span, Equation (2) might be defined as

$$TF = A(S)^{-n} \exp\left(\frac{E_a}{kT}\right) \quad (3)$$

Because the stress of mechanical system is not easy to measure the quantity in testing, we have to redefine Equation (9). When the power is defined as the multiplication of flows and effort, stresses may come from effort in a multi-port system [2]. Equation (3) might be redefined as

$$TF = A(S)^{-n} \exp\left(\frac{E_a}{kT}\right) = A(e)^{-\lambda} \exp\left(\frac{E_a}{kT}\right) \quad (4)$$

From Equation (4), the acceleration factor (AF) might be expressed as the proportion between the adequate elevated stress amounts and usual working conditions. AF might be altered to incorporate the effort ideas:

$$AF = \left(\frac{S_1}{S_0}\right)^n \left[ \frac{E_a}{k} \left( \frac{1}{T_0} - \frac{1}{T_1} \right) \right] = \left(\frac{e_1}{e_0}\right)^{\lambda} \left[ \frac{E_a}{k} \left( \frac{1}{T_0} - \frac{1}{T_1} \right) \right] \quad (5)$$

To get the assignment cycle of ALTs from the objective BX lifetime on the experiment scheme, the sample size formulation integrated with the AF should be obtained as follow [3]:

$$n \geq (r+1) \cdot \frac{1}{x} \cdot \left( \frac{L_B^*}{AF \cdot h_a} \right)^{\beta} + r \quad (6)$$

#### *Case Study - Reliability of a Newly Designed Drawer Structure in a Domestic Refrigerator*



Figure 2. French-door refrigerator and drawer system (a) a refrigerator; (b) drawer components: 1) box, 2) the guide rails, and 3) a support center.

As customer want to have food-storing function, manufacturer produces the French door refrigerator with a new drawer system, displayed in Figure 2. It is made up to box, two guide rails, and support center. To stock food fresh in a system lifetime, the drawer structure should be designed to endure the working circumstances subjected to it by the customers who utilize the refrigerator. In the America, the representative customer asserts the refrigerator to

store the food from five and to ten times per day. Stocking food in a refrigerator has some repeated working procedures: 1) open the drawer, 2) put the food into it, and then 3) close it. So the drawer will repeatedly have some different mechanical stored food loading when the customer utilizes it, although relying on the customer working states.

The drawer system from the marketplace had been cracking and fracturing, causing customer to be replaced. As subjected to repeated food stresses in using refrigerator, we knew that the problematic draw system originated from the design defects. Market data also displayed which the products returned from the marketplace had crucial design problems on the structure, including stress raisers - thin ribs and sharp corner angles. The design defects that might not endure the repeated food loadings on the food storing cause a crack to happen and propagate it to the end. Thus, a newly designed drawer structure is designed to robustly endure repeated food loading under customer working conditions.

The drawer mechanically operates like the functional design ideas. That is, when customers touch on the drawer and open it, they can take out the food. Relying on the end-user working conditions, the drawer system experiences repeated food loading in its process. To correctly work the drawer system, many mechanical structural parts in drawer assembly should be designed robustly. Because the concentrated stress in mechanical system reveals at stress raisers such as sharp corner angles, it is crucial to disclose these design flaws experimentally. As a result, engineer can modify them.

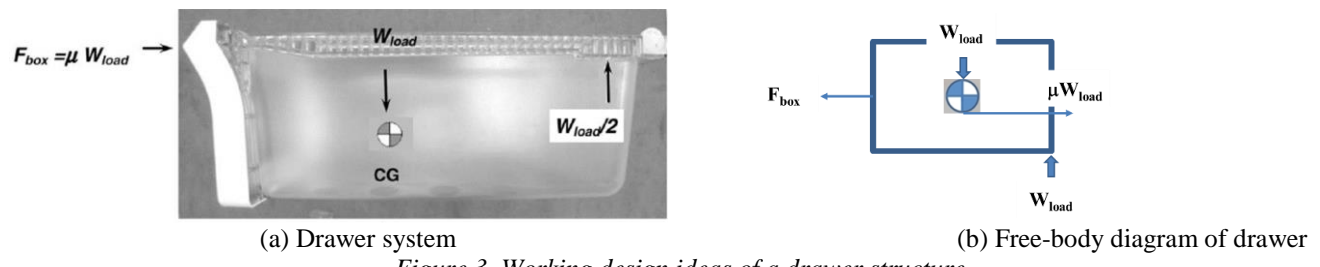


Figure 3. Working design ideas of a drawer structure

As described in Figure 3, from the drawer system and its free-body diagram, we knew that the drawing force came from the food weight. The exerted force in drawer can be defined as

$$F_{box} = \mu W_{load}$$

(8)

As the stress of drawer structure relies on the exerted food weight, Equation (4) could be redefined as

$$TF = A(S)^{-n} = A(F_{box})^{-\lambda} = A(\mu W)^{-\lambda} = B(W)^{-\lambda} \quad (9)$$

where A and B are constants

Therefore, the AF in Equation (11) can be expressed as

$$AF = \left( \frac{S_1}{S_0} \right)^n = \left( \frac{F_1}{F_0} \right)^\lambda = \left( \frac{W_1}{W_0} \right)^\lambda \quad (10)$$

For French-door refrigerator including the drawer system, the environmental (or working) customer conditions are roughly 0 – 43 °C with a humidity varying from 0% to 95%, and 0.2 – 0.24g's of acceleration. As previously mentioned, the drawer structure per day occurs about 5 – 10 times. With design criterion of a product lifetime for 10 years,  $L_B^*$ , drawer structure happens 36,500 usage cycles in worst scenario.

Under lifetime target – B1 life 10 years, if the number of lifetime cycles  $L_B^*$  and AF are computed for assigned sample size, the actual mission cycles,  $h_a$ , might be acquired from Equation (23). Then ALT equipment can be made and performed in accord with the working course of the drawer. Through parameter ALT's we might attain the design flaws for new mechanical system.

The greatest force exerted by the customer in storing food,  $W_1$ , was 0.59 kN (6 kgf). For ALT, the exerted force,  $W_2$ , takes double to 1.17 kN (12 kgf). With a cumulative damage factor,  $\lambda$ , of 2, the AF was 4.0 from Equation (10). To obtain the design defects of a new drawer system, lifetime target might be put to be B1 life 10 years. At first, supposed that the shape parameter,  $\beta$ , was 2.0, the real test cycles computed from Equation (6) were 37,000

cycles for 6 sample units. If ALT is unsuccessful less than once in 37,000 cycles, the lifetime for drawer system will be reassured to be B1 life 10 years (Figure 4).

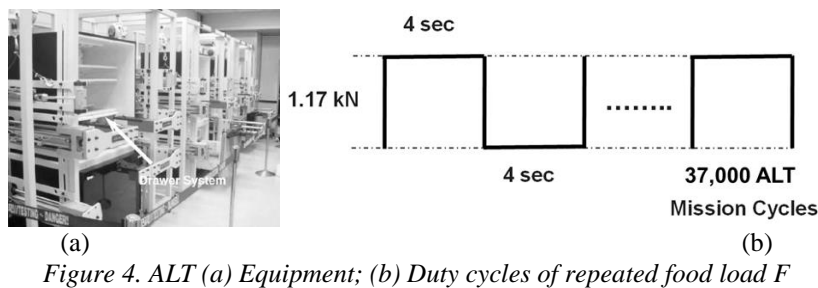


Figure 4. ALT (a) Equipment; (b) Duty cycles of repeated food load F

### 3. RESULTS & DISCUSSION

Initially when 1.17 kN (12 kgf) as the accelerated weight in drawer was loaded, the left/right rollers in the rail structure were left away and the center support rail was bent because of insufficient strength due to design flaws. Because of that the drawer system no longer slid. The rail systems were modified by adding up strengthened ribs on the center support rail as well as extending the roller support to 7 mm (Figure 5).

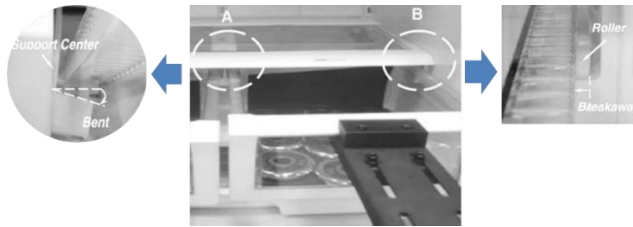


Figure 5. Design issues of drawer system in static loading.

In first ALT, the cover of the drawer cracked and fractured at 3,800 cycles. Figures 6 represents the fractured product in market and the first ALT, respectively. When carefully observing at the failure locations from the marketplace and the first ALT, we found around the junction regions of the drawer cover and its main structure as a consequence of high stress. Figure 13 designates the analysis of a graph when the ALT consequences and market data show in Weibull distribution. As two patterns had similar slopes on its plot, we recognized that each loading of 1<sup>st</sup> ALT and field was alike under the operation condition. For the shape parameter,  $\beta$ , we knew that the final shape parameter from the chart was affirmed to be 3.5, compared with the estimated value – 2.0. Based on both test results and Weibull plot, parametric ALT was effective because it identified the design flaws that were accountable for the field failures. In other words, as substantiated by two discoveries – picture and Weibull pattern, these systematic methods were well-founded in discovering the problematic designs accountable for failures from the marketplace, which decided the product lifetime.

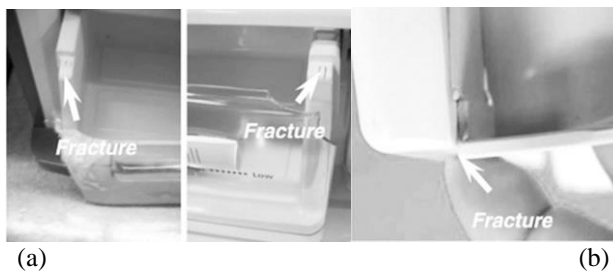


Figure 6. Failed drawer in market and in the first ALT (a) Fractured system structure in market; (b) System structure with crack after first ALT.

Due to design defects such as no corners in the high stress areas of intersection areas (A), the repeated food loading in conjunction with these structural defects may have been fracturing the drawer cover. These design defects can be altered as: (1) making thick the reinforced ribs, Rib1, from T2.0 mm to T3.0 mm; (2) applying the fillets, Fillet1, from R0.0 mm to R1.0 mm (Figure 7).

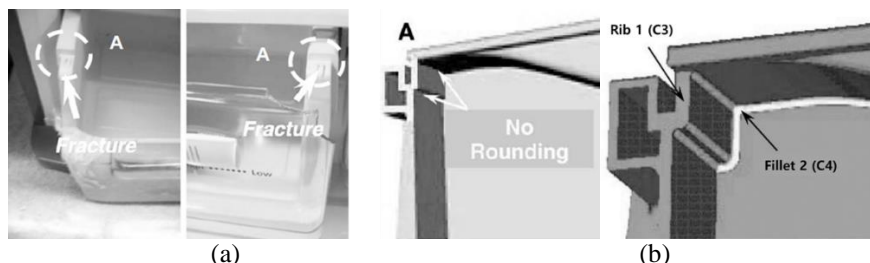


Figure 7. Failed drawer in the first ALT (a) its root cause; (b) design alternations.

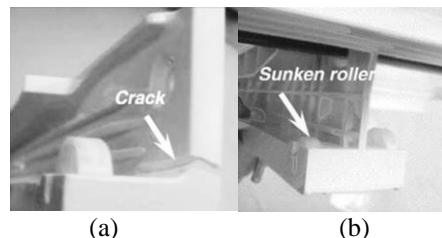


Figure 8. Failed drawer system in the second ALT (a) cracked rail; (b) sunken roller in support rail

With the confirmed shape parameter,  $\beta$ , was 3.5, the real mission cycles computed from Equation (6) were 13,000 cycles for 6 sample units. If drawer structure is unsuccessful less than once for 13,000 cycles, its lifetime might be assured to be B1 life 10 years. As seen in Figure 8, in the second ALT, the fractured guide rail and sunken roller in center support rail happened at 6,000 cycles. When closely examining the product failure in 2<sup>nd</sup> ALT, we recognized that the guide rail in drawer structure had no reinforced rib and insufficient corner rounding to endure the repeated food loads. To improve them, the guide rail also were altered as follows: (1) adding up the reinforced rib; (2) extending the corner rounding from R3 mm to R4 mm. And the center support rail in drawer structure were altered as: (1) extending the roller rib from L0.0mm to L2.0mm.

As the drawer system upgrade, the design basis of new sample pieces was acquired to be more than the lifetime target - B1 life 10 years. To confirm the design of drawer, we carried out 3<sup>rd</sup> ALT. Because the affirmed value,  $\beta$ , on the Weibull plot was 3.5, for the lifetime target – B1 life 10 years, the actual mission cycles in Equation (6) were 13,000 for 6 sample size. In the third ALT, we knew that there were no issues in the drawer structure til the experiment was performed to 22,000 cycles. We thus deduced that the altered designs obtained from first and second ALT were successful.

#### 4. CONCLUSIONS

We proposed a reliability methodology for new mechanical system such as drawer system in French-door refrigerators. It incorporates: (1) an ALT scheme formed on system BX lifetime, (2) a load examination for parametric ALT, (3) a tailored ALTs with the design changes, and (4) an judgment of whether the system design(s) fulfills the objective BX lifetime. As a test investigation, we discussed a new drawer structure in a refrigerator subjected to repeated food loading.

At first when the accelerated load in drawer was loaded, the left/right rollers on the rail were left away and the center support rail was bent. As action plans, these flaws in the drawer system were corrected to thicken the enforced ribs and implement the fillets. In the second ALT, rollers in the center support rail were broken away. To improve them, the guide rail also were altered as: (1) adding up the reinforced rib; (2) enhancing the corner rounding from R3 mm to R4 mm. And the center support rail in drawer structure were altered as: (1) extending the roller rib from L0.0mm to L2.0mm. With these altered design parameters, in the third ALT, there were no issues.

#### REFERENCES

- [1] Grove A. Physics and technology of semiconductor device. 1<sup>st</sup> edition. Wiley International Edition; 1967. p. 37.
- [2] Karnopp DC, Margolis DL, Rosenberg RC. System dynamics: modeling, simulation, and control of mechatronic systems. 5th edition. New York: John Wiley & Sons; 2000.
- [3] Woo S, Pecht M, O'Neal D. 2020. Reliability design and case study of the domestic compressor subjected to repetitive internal stresses, Reliability Engineering and System Safety. 193. 106604.



# GEOTHERMAL PROJECTIONS IN COLOMBIA FROM OIL & GAS INDUSTRY

López-Ramos Eduardo

ECOPETROL, Bogotá, Colombia, Eduardo.lopezra@ecopetrol.com.co, ORCID: <https://orcid.org/0000-0001-7836-470X>

Patiño-Suarez Cesar A.

ECOPETROL, Bogotá, Colombia, cesar.paterno@ecopetrol.com.co, ORCID: <https://orcid.org/0000-0002-5803-1833>

Alvarez - Gutierrez Angela P.

ECOPETROL, Bogotá, Colombia, angela.alvarez@ecopetrol.com.co, email address, ORCID: <https://orcid.org/0000-0002-1604-2745>

López-Pulido Albeiro

ECOPETROL, Bogotá, Colombia, Albeiro.lopez@ecopetrol.com.co, email address, ORCID: <https://orcid.org/0000-0002-1604-2745>

Gonzalez-Penagos Penagos.

ECOPETROL, Bogotá, Colombia, felipe.gonzalez@ecopetrol.com.co, email address, ORCID: <https://orcid.org/0000-0003-1287-1527>

Pinilla - Granados Daniela M.

ECOPETROL, Bogotá, Colombia, daniela.pinilla@ecopetrol.com.co, email address, ORCID: <https://orcid.org/0000-0001-9053-4986>

*López-Ramos, E, Patiño-Suarez, CA, Alvarez – Gutierrez, AP, López-Pulido, A, Gonzalez-Penagos, P, Pinilla – Granados, DM. Geothermal projections in Colombia from oil & gas industry. 9<sup>th</sup> Eur. Conf. Ren. Energy Sys. 21-23 April 2021, Istanbul, Turkey*

**Abstract:** During the last 10 years, O&G companies they have diversified their matrix energy in response to dynamic world energy change. Companies like BP, ENI, Shell, Total and Repsol, among others, have made investments on a large scale aimed at achieving a change in your generation portfolio of energy, the most popular being wind and solar energy. A new concept called Energetic Pivot has taken boom in countries like the United States, Canada, Norway, UK, and recently in Colombia, consists in using the legacy of the industry of hydrocarbons to give rise to a rapid transition to energy approaches (like geothermal E&D) decentralized and sustainable. In this way, experience, research and the large volumes of information acquired around the O&G industry in Colombia during the last 70 years are focused on this purpose.

**Keywords:** *Energetic Pivot, Colombia, O&G industry, geothermal E&D*

© 2021 Published by ECRES

## 1. INTRODUCTION

In light of the current information, one type of energy that lies within the earth's interior has begun to assume an important role in this diversification: **Geothermal energy**. The geothermal energy market is a sector with strong growth worldwide, since in only 5 years its total installed capacity has grown by 52%, with an annual average growth of 8.7%, an increase motivated by the growing popularity of heat pumps that use groundwater or surface water bodies [1]. Colombia is a country with areas of high geothermal potential (Fig. 1), and Ecopetrol has developed its operations in most of these areas. Establishing a methodology, analysis and integration of these basins is a challenge that must be addressed to identify their potential through the incorporation of resources and the value of the subsurface of which there is already abundant information acquired. This is a crucial factor to make use of

the valuable geothermal resource aligned with the energy transition. However, the development of geothermal projects requires studies of the thermal regime of the subsurface, which allow predicting its potential with some degree of confidence [2]. During the last decade there has been an increase in publications showing experiments, modeling, drilling and development of deep reservoir fields in sedimentary basins, characterized by temperature gradients between 30°C/km and 40°C/km, for power generation using heat from water recovered from reservoirs [2]–[4].

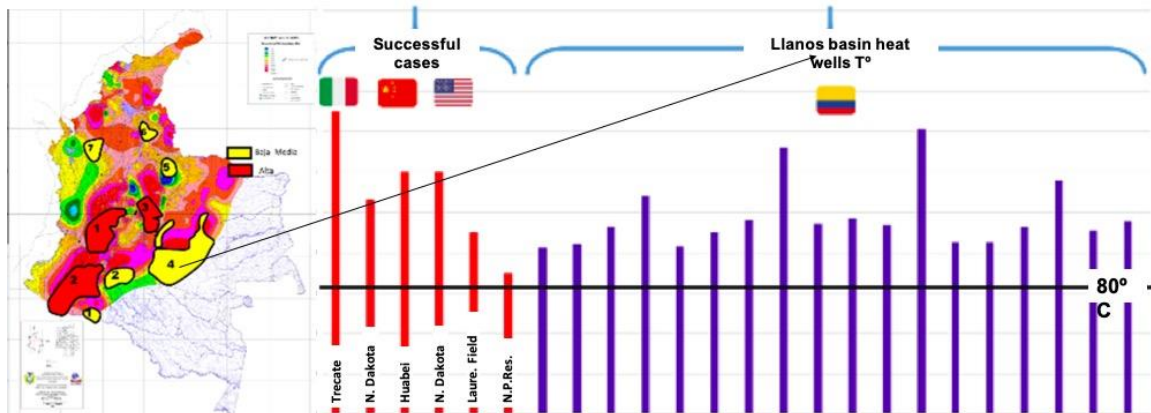


Figure 1. Parts of great Colombian O&G sedimentary basins over areas with temperatures >120°C at 3 km of depth [5]. Wellhead temperatures (right) in medium-enthalpy geothermal world success cases (red color bars) and wellhead temperatures recorded in O&G production wells in the Llanos basin Colombia (blue color bars).

## 2. BACKGROUND

In Colombia, the integration of information from wells, hot springs and fumaroles shows areas with geothermal gradients similar or higher than those analyzed globally (apart from volcanism-active regions) in sedimentary basins such as the Llanos Orientales, Catatumbo and Putumayo [6], [7]. The characterization of the thermal structure in the sedimentary basins of Colombia suggests the presence of a geothermal gradient anomaly in the Eastern Llanos Basin, which is not compatible with the basement constituted by the Precambrian shield [5], [6], [8]. The current geothermal regime in the Llanos basin is characterized by a generalized decrease of the heat flow towards the west and north, from values of 50-60 mW/m<sup>2</sup> to 30-40 mW/m<sup>2</sup>; increasing the depth of the 120°C isograd in the same direction, from less than 3 km below sea level (BSL) to 5 km BSL [9]. These values and temperature behaviors compared with global success cases in hydrocarbon/geothermal co-production systems allow considering a high potential for success in Colombia (Fig. 1). An additional element to temperature is water production, oil wells with high water cuts. (>89% WC), can be used as geothermal wells, generating not only savings in electricity consumption costs, but also recovering large amounts of crude oil. Considering that in Colombia the Oil - Water Ratio varies between 11.6 % and 12.45 % [10], it is possible to estimate a water production between 8'120,000 and 8'715,000 Barrels of Water per Day (BAPD), of which, more than 50% come from the exploitation of fields in the Eastern Plains [10].

This is how anomalous heat flows and large water productivities in operating oil fields (about 4'000,000 BAPD), raise the possibility that deep reservoirs in Colombian basins may present potential for the development of electric power generation projects from low and medium enthalpy sources (<150°C). This has motivated the regional analysis of the geothermal potential in the Colombian basins, considering methodologies of analysis of exploratory hydrocarbon corridors to select the areas with the best potential. Oil and gas exploration and production activities have allowed to identify stratigraphic levels in Colombia, measure water volumes during production stages, geochemically characterize the composition of produced waters, calculate reservoir pressure and measure temperatures along wells. It is important to consider: a) Concepts about the variations of thermal structure in Colombian basins at different depths and more basal stratigraphic intervals (e.g. crystalline basement, Paleozoic and Cretaceous base); b) Perspective of key elements in a geothermal system (temperature, presence and quality of reservoirs, water productivity); c) Map of regional geothermal exploratory corridors, taking into account the processes generating the heat sources and waters found in the reservoirs. These analyses can be developed by E&P teams of oil companies, integrating the compiled information, to evaluate geothermal resources in sedimentary basins and producing assets.

### 3. COLOMBIAN SEDIMENTARY BASIN GEOTHERMAL CONTEXT GEOLOGICAL CONDITIONS OF SEDIMENTARY BASINS

#### High geothermal gradients:

The regional geothermal gradient map prepared by the Colombian Geological Survey [5], was constructed from downhole temperatures and hot springs manifestation, and shows a clear geothermal anomaly in the Central Cordillera (active volcanic centers), Eastern Cordillera (Paipa Zone) and anomalies in basins such as the Eastern Llanos, Putumayo, Catatumbo and Lower Magdalena Valley, proposing geothermal exploratory scenarios in these basins (Fig. 1). These high geothermal gradients allow surface temperatures in some sectors of the basins of more than 120 °C, which are in the range of medium enthalpy geothermal resource exploitation. Downhole temperature and depth data allow locating the large producing fields of these basins in the range defined by [3] within the geothermal systems associated with petroleum reservoirs, where depths of more than 3 km are required (Fig. 2).

#### Well porosities and permeabilities:

The main reservoirs in Colombian basins are siliciclastic units of late Cretaceous to Paleogene age, which overlie Paleozoic and crystalline basement rocks. The trends of porosity values of these formations in basins such as the Llanos are widely distributed reaching values up to 20%. Permeability ranges are between 20 and 300 mD on average[11] (Fig. 2). These values are within the ranges suggested for effective transitivity in a geothermal system at depths greater than 3 km (Fig. 2). These parameters favor such formations to function as corridors for huge volumes of water that are largely meteoric in nature. Additionally, being the most basal stratigraphic units the transfer of high temperatures due to high geothermal gradients is higher, making them the most favorable sequences to prospect for hot fluid extraction.

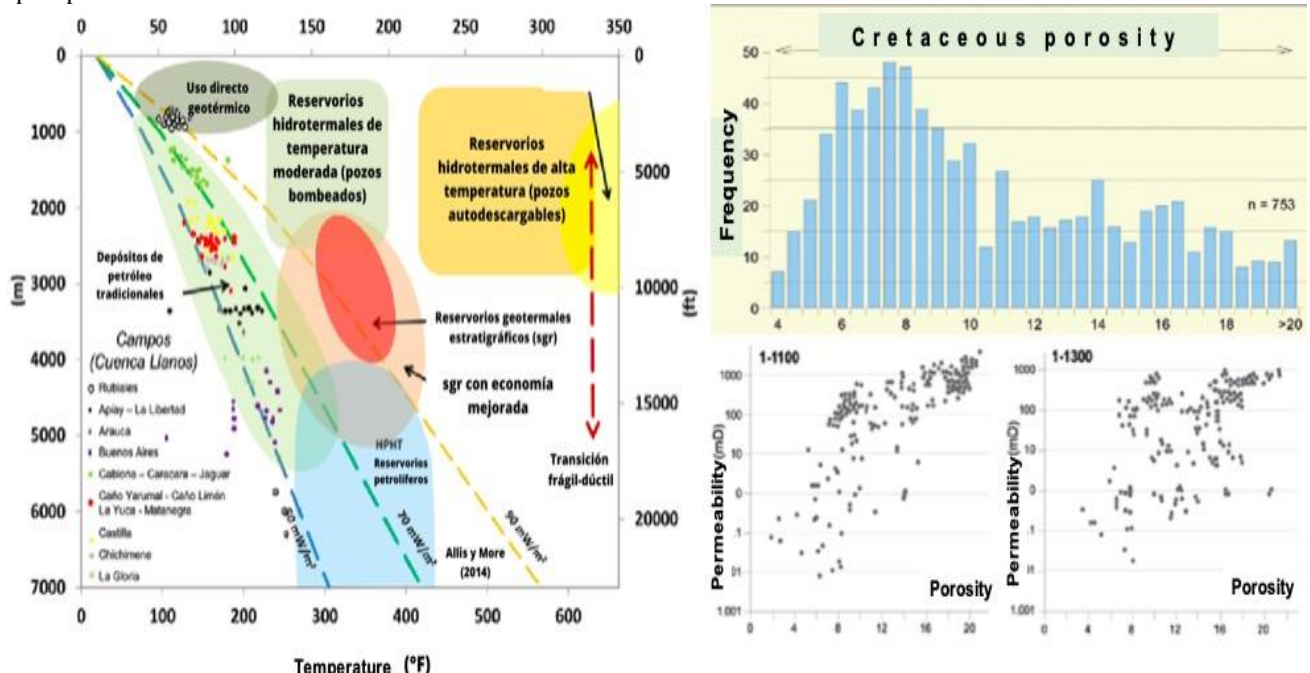


Figure 2. Types of geothermal and petroliferous systems (left) based on their temperature-depth relationship [3]. Petrophysical properties of reservoirs in Cretaceous units (porosity and permeability of the Llanos basin (right)

#### Fluid circulation and heat flow

The fluid circulation system in the reservoirs of Colombia's sedimentary basins is complex. The geochemical markers present in the water have indicators that suggest processes of infiltration and circulation of surface water, which displaces, maintains reservoir pressure, dilutes formation water and influences the thermal system as a boundary condition for modeling. This infinite aquifer condition for reservoirs with a water cut above 80% makes this an abundant source of energy. A hierarchical analysis of these studies allows differentiating water families and trends to sector these processes and associate them to variations in thermal gradients along the basins. The distribution of regional water composition in the basins also shows variations in fluid circulation for each reservoir (Fig. 3). Hydrothermal fluids generally have a high salinity reflecting the mineral interaction of the rock or an eventual deep source of fluids. There are a number of data on the salinity and temperature of these waters in

Colombia, which allow establishing isotopic relationships of these waters and show trends on the influence of meteoric water recharge in deep reservoirs and its impact on the heat flow of the basin (Fig. 3). However, although there are already some indicators that allow zoning areas with potential thermal differences, it is necessary to perform a correct measurement of the surface water temperature and to add new sampling campaigns including metals that allow identifying areas with deep water that possibly suggest thermal sources of higher temperature. The integration and analysis of this information is intended to direct exploratory activities, and the development and production of geothermal projects in the sedimentary basins of Colombia through the construction of analytical methodologies to evaluate geothermal resources and reserves in Ecopetrol's production fields. The studies should help to project the use of candidate abandonment wells, whose water temperatures are recorded in the range of 80 to 120 degrees Celsius, to make use of the heat of the production water by the thermal capacity of the subsoil, which will allow an extension of the life of the production assets of up to 25 years.

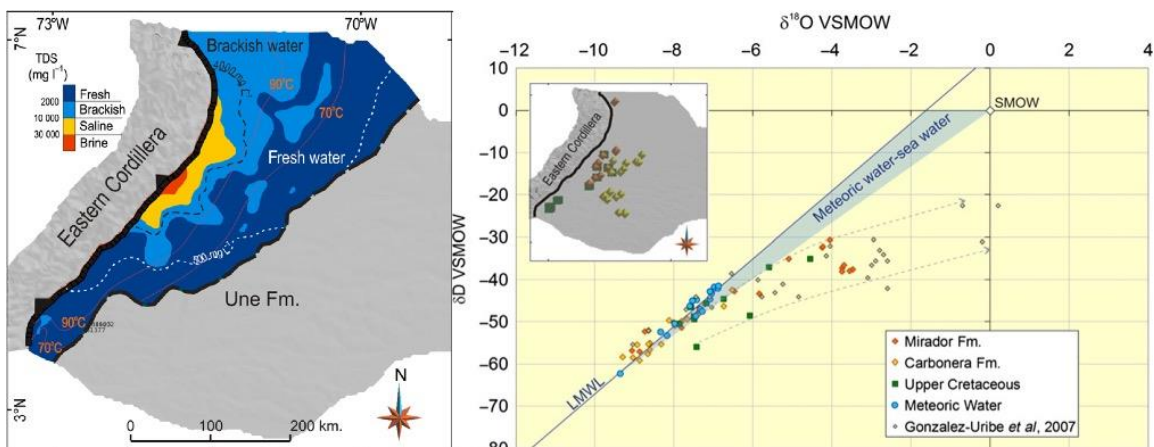


Figure 3. Example of regional salinity distribution for the Une formation (left) [12] and isotopic relationship of waters and their origins (right).

#### FROM APPLIED ENGINEERING

According to the scopes and expected temperatures, the geothermal project is organized as follows: a) Low enthalpy (<90°C): directly use produced water at temperatures below 90°C, or supplement with the use of surface heat sources external to the reservoir to heat produced water and generate electricity. (Fig. 4); b) Medium enthalpy (90°C-150°C): The hot production fluid is used avoiding its mobilization over long distances that can cause temperature loss in the mobilization to the production plant. (Fig. 4); High enthalpy (>150°C): Drilling of a well located in the area with the best identified temperatures of the basins and with the necessary depth to find them. (Fig. 4).

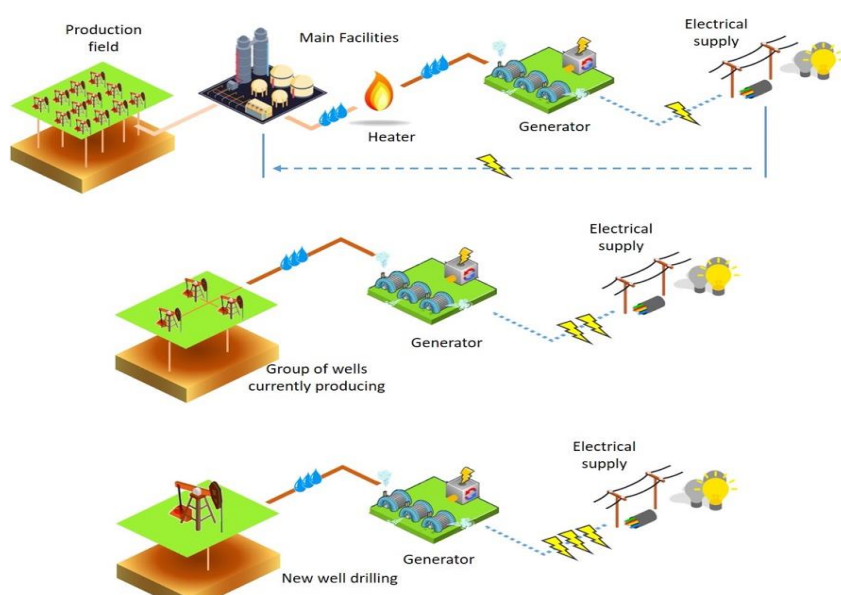


Figure 4. Geothermal resource utilization schemes in oil fields for low enthalpy (upper), medium enthalpy (middle) and high enthalpy (below).

## **ENVIRONMENTAL BACKGROUND**

Considering that the specific activity of energy generation through the use of heat is not approved in the PMA of the oil and gas fields, the diagnosis and environmental feasibility must be carried out in order to proceed with the requests for a pronouncement before the National Agency of Environmental License's (ANLA).

## **REGULATORY FRAMEWORK**

The purpose of Law 1715 of 2014 is to encourage the diffusion, investment, research and in general promote the development and use of non-conventional energy sources, through this it is possible to access tax incentives such as special income tax deduction, accelerated depreciation, VAT exclusion on the acquisition of goods and services, and exclusion of customs duty.

## **4. FUTURE SCOPE OF GEOTHERMAL PROJECTS**

The objective of these projects is to promote the generation of electric energy from the thermal capacity of the subsoil represented at the surface by the high temperatures of the production fluids in the wells of the Colombian Basins. The geothermal evaluation projects in the Colombian Basins should be oriented to: a) Conduct resource and reserve potential evaluation studies; b) Conduct pre-conceptual engineering studies; c) Construct diagnostics and strategies of environmental feasibility; d) Identify opportunities to take advantage of existing resources and extend the useful life of current projects; e) Promote regulation for the development of geothermal projects in Colombia. The development of these projects can leverage benefits such as: a) The use of energy sources, which allows the use of heat from the production water and combustion gas system combustion gases; b) The reduction of CO<sub>2</sub> emissions, which brings as a benefit the mitigation of payments for emissions and the reduction of the carbon footprint; c) The sale of CO<sub>2</sub> - carbon neutral certificates, which contributes to the generation of incremental revenues; d) The release of gas used for electricity generation that can be replaced by steam and allow the commercialization of the gas. NCRE (Non-Conventional Renewable Energies) are an investment attraction for multilateral banks and global organizations, so geothermal projects can be supported and leveraged in these mechanisms. Tax benefits for NCRE, UPME (Mining and Energy Planning Unit), MinCiencias and support from the Ministry of Mines and Energy, are also part of the benefits that can bring to hydrocarbon companies to invest in these projects.

## **ACKNOWLEDGMENT**

Special thanks to ECOPETROL for its support to research in the field of NCRE.

## **REFERENCES**

- [1] J. W. Lund and A. Toth, "Direct utilization of geothermal energy 2020 worldwide review," Proc. World Geotherm. Congr. 2020, 2020.
- [2] V. Gascuel, K. Bédard, F. A. Comeau, J. Raymond, and M. Malo, "Geothermal resource assessment of remote sedimentary basins with sparse data: lessons learned from Anticosti Island, Canada," Geotherm. Energy, vol. 8, no. 3, p. 32, 2020, doi: 10.1186/s40517-020-0156-1.
- [3] R. Allis and J. Moore, "Can deep stratigraphic reservoirs sustain 100 MW power plants?," in Transactions - Geothermal Resources Council, 2014, pp. 1–8.
- [4] M. Babaei and H. M. Nick, "Performance of low-enthalpy geothermal systems: Interplay of spatially correlated heterogeneity and well-doublet spacings," Appl. Energy, vol. 253, p. 19, 2019, doi: 10.1016/j.apenergy.2019.113569.
- [5] C. Alfaro, I. Alvarado, W. Quintero, C. Vargas, and L. A. Briceño, "Mapa preliminar de gradientes geotérmicos de Colombia," Bogotá, 2009.
- [6] P. Aguilera, C. Alfaro, A. Arcila, D. Blessent, J. Rueda, and O. Llamosa, "Colombia - a geothermal opportunity," in 41st New Zealand Geothermal Workshop, 2019, p. 11.
- [7] N. Bernal, G. Ramirez, and C. Alfaro, "Mapa Geotérmico de Colombia, Versión," Bogota, 2000.
- [8] C. Alfaro, I. Alvarado, A. Manrique, and W. Quintero, "Mapa preliminar de flujo de calor terrestre en la cuenca de los Llanos Orientales," Bogotá, 2010.
- [9] S. Bachu, J. C. Ramon, M. E. Villegas, and J. R. Underschultz, "Geothermal regime and thermal history of the Llanos Basin, Colombia," Am. Assoc. Pet. Geol. Bull., vol. 79, no. 1, pp. 116–129, 1995, doi: 10.1306/8d2b14d0-171e-11d7-8645000102c1865d.
- [10] S. L. Mesa, J. M. Orjuela, A. T. Ortega, and J. A. Sandoval, "Revisión del panorama actual del manejo de agua de producción en la industria petrolera colombiana Review of the current state of wastewater management in the Colombian oil industry," Gestión y Ambient., vol. 21, no. 1, pp. 87–98, 2018.
- [11] ANH, "Petroleum Geology of Colombia. Geology and Hydrocarbon Potential Llanos Basin," 2011.
- [12] F. Gonzalez-Penagos, I. Moretti, C. France-Lanord, and X. Guichet, "Origins of formation waters in the Llanos foreland basin of Colombia: Geochemical variation and fluid flow history," Geofluids, 2014, doi: 10.1111/gfl.12086.



# HYBRID STATE OF CHARGE ESTIMATION OF LITHIUM- ION BATTERIES: IMPROVEMENTS ON ELECTRIC VEHICLE BATTERY MANAGEMENT SYSTEM

Odera Ohazurike

Southern University and A&M College, Baton Rouge, USA, Odera.ohazurike@sus.edu, ORCID: 124

Cite this paper as

*Odera, O. Hybrid State of Charge Estimation of Lithium- Ion Batteries: Improvements on Electric Vehicle Battery management system. 9<sup>th</sup> Eur. Conf. Ren. Energy Sys., 21-23 April 2021, Istanbul, Turkey*

**Abstract:** Energy storage system (ESS) technology is still a situation that seems irresolvable for the electric vehicle. Lithium-ion (Li-ion) batteries have attracted good attention in the EV industry because of their high energy density, lifespan, power density, and cost. In Electric vehicles, a Smart battery management system does not only measure the states/condition of the battery correctly and efficiently, but it also guarantees safe operation and keeps the battery life going.

In this research work, the Hybrid method of SOC estimation is explained, introduced and implemented in the form of combining the TVM and Coulomb Counting. Also, the effectiveness and low error rate of the combination in direct measurement and Book keeping methods is well explained in the Literature Review. Thus, an improved model of estimation is introduced and Simulation results are shown to prove the model's performance.

Finally, the design of a unique SOC estimation by programming a Microcontroller and its experimental results are discussed. The possible/likely Improvements is also emphasized .The accurate estimation of the state of charge (SOC) of a Li-ion battery is very tasking because the Li-ion battery is a highly time variant and complex electrochemical system. This research explains the workings of a Li-ion battery and basically implements its SOC hybrid estimation methods. These SOC hybrid estimation method's positive attributes such as reduced error rate and limitations is being shown..

**Keywords:** Bookkeeping, state estimation, coulomb counting, direct measurement

© 2021 Published by ECRES

## 1 INTRODUCTION

Diesel, petroleum, and other non-renewable energy sources saves are diminishing quickly because of their successive use in transport capacities. The generally conveyed utilization of the conventional fuels gives rise of tons of CO<sub>2</sub> yearly, which are perilous to the climate which incorporate; ozone harming substance discharges (Global warming) [1]. Likewise, the expenses of these energies are expanding, so there is a requirement for a subordinate energy source for transport capacities, like electric vehicles (EVs) with Lithium ion Batteries. this energy resource requires an energy conservation system (ESS) for maintaining an excellent and dependable supply to the consumer. Recently, Li- ion batteries are more acknowledged for transportation[2], the Li-ion battery guarantees you of high dependability, long life expectancy and high energy density [3]. The expenses of Li-ion batteries is decreasing, which helps their utilization in the EV business [4]

An effective and precise battery Management system (BMS) is one of that its essential point is to guarantee you a protected and dependable Li-ion battery while managing the power grid and rigorous driving states [5]. The BMS can detect the battery voltage, battery current and furthermore the temperature to abstain from overcharging and its charging times. These deliberate boundaries can be utilized to gauge the state of the Li-ion battery and state of charge (SOC) [6, 7]. The SOC shows the vehicle driving reach of the battery in EVs. furthermore, the Li-ion battery is kept from overcharging or charging states. The Li-ion battery might be an exceptionally perplexing, time fluctuating and nonlinear electrochemical framework; its presentation changes on account of different variables like

the charge-discharge aging and temperature variant. thus, a productive and right SOC assessment of Li-ion battery is a dubious assignment since utilizing an actual sensor wouldn't be conceivable [8].

### **Battery management system**

Rui (2011) discussed how Battery management system monitors, regulate and ensure that batteries operate within levels that are safe. There are different types of battery management systems, in any case, the most well-known is the battery checking framework that records the fundamental operational boundaries like voltage and current course [9]. Yuan, Wu and Yin (2015) research proves that State of charge is a parameter used by BMS to improve battery performance, safety and reliability by controlling the subsystems [11]. Patipati (2011) showed that The Available limit of the battery expressed in a level of the rated capacity the battery has is known as state of charge [12] BMS is able to control the rate of charging and discharging in other to enable the battery to operate in a safe range, the estimation used in this control function of BMS is provided by the state of charge [13]. Juang (2015) explains that State of charge aids in knowing the battery percentage left after use or in use and the extent or length the vehicle can move on the energy left before charge [14]. The direct measurement of SOC cannot be very accurate; rather it can only be estimated [14]. Over the years, varieties of methods have been tried in measuring the SOC and their advantages and disadvantages have been shown. Despite the efforts put into the development of these method factors like battery temperature, ageing effect, varying power request makes it difficult to effectively estimate the state of charge [15].

### **Methods of estimating SOC**

Mohammad (2019) explains the state of charge accurate approximation of a battery as the most analytic and important in an electric vehicle's battery management system. The development of different methods of estimating SOC of batteries accurately has attracted a lot of interest over time. The SOC estimation methods can be expressed int three types which are Book-keeping, Model based with computer intelligence and direct measurement, [10]. We would talk about the hybrid method which is the combination of the direct measurement and the book keeping method. The direct measurement type used is the terminal voltage and Coulomb counting was used from book-keeping.

#### **Direct Measurement**

Direct measurement method of estimating SOC makes use of the actual characteristics of the battery [11].

#### **Terminal Voltage method**

This is formed on a drop from terminal for the reason of internal impedances when the battery is being discharged, here the terminal voltage is correlating with the EMF of the battery considering the EMF of battery and the SOC is in an estimated linear correspondence or in proportion, the terminal voltage of battery is assessed in a linear proportionate to the State of charge. The terminal voltage strategy has been utilized at various temperatures and discharge[16]. Yet, toward the finish of discharging the battery, the assessed mistake of terminal voltage strategy is huge, on the grounds that the terminal voltage of battery abruptly drops towards the finish or climax of discharge [17]

**Book-keeping estimation method;** This makes use of the discharged current data in battery as its input.. It incorporates some internal battery impacts such capacity loss, self-discharge and efficiency of discharge. Coulomb counting method is a model.

#### **Coulomb Counting method:**

Battery charge and discharge values are used as the input for book keeping estimation method. This method makes use of Coulomb counting. Battery Charging and discharging circuit is what this method is based on, which is done over time to estimate SOC [10]. Equation 1 shows the mathematical form of Coulomb counting method.  
This new hybrid method must be able to have an improved accuracy and should not require very high level computing.

### **Methodology and Simulations**

The different parameters of the batteries such as voltage, current, temperature and internal resistance of the battery, the values gotten will be combined with the value gotten through coulomb counting method, the values gotten will be used to train the hybrid method. The hybrid model will learn and map the internal operation of the batteries from

the data from other methods. During charging and discharge of battery, the hybrid method will be able to estimate SOC of battery by being able to use the data sent by the different measuring methods and make a logical decision of the right state of charge according to other parameters.

### SOC Measuring Method.

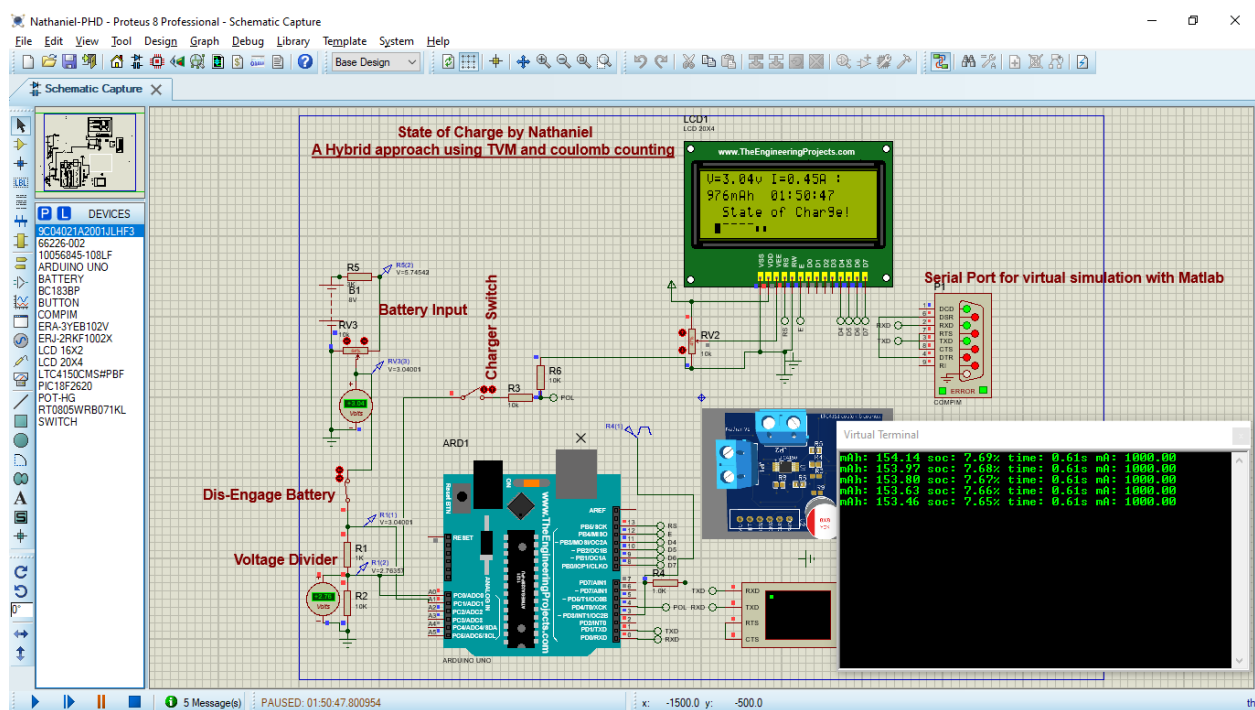
The state of charge of the battery is being decided or dictated using coulomb counting as shown in this equation.

$$SOC(t) = SOC(t_0) - \frac{1}{Q} \int_{t_0}^t (\eta \cdot i_{bat}(t) - S_d) dt \quad (1)$$

Where SOC(t1) tells SOC at its initial times(t) is known as the SOC sampling time,  $\eta$  which is seen as columbic accuracy or efficiency is the nominal capacity,  $S_d$  is the rate which itself discharges.

Open circuit voltage measurement method or TVM which works better with Lithium ion battery of estimating SOC is accurate but requires resting time [10]. This is utilized to decide the underlying or initial SOC of the battery (SOC(t1)) which is used by coulomb counting method. The combination of TVM and Coulomb counting both are employed to receive the data from the measurement method of estimating SOC and different conditions around the battery. Using the data gotten, it gives estimation for SOC that is accurate.

### 1Hour 50 Minutes into Proteus Simulation



## RESULTS

There is a continuous overtime discharge and the state of charge is being approximated or estimated by the discharged current. The initial SOC is determined using TVM while the instantaneous SOC is determined using coulomb count method. constant discharge gave values that corresponds to the discharge value. This is further shown in figure1 where the voltage values do not decrease linearly as that of discharge current over time. This shows that TVM cannot be fully relied on for the estimation of SOC.

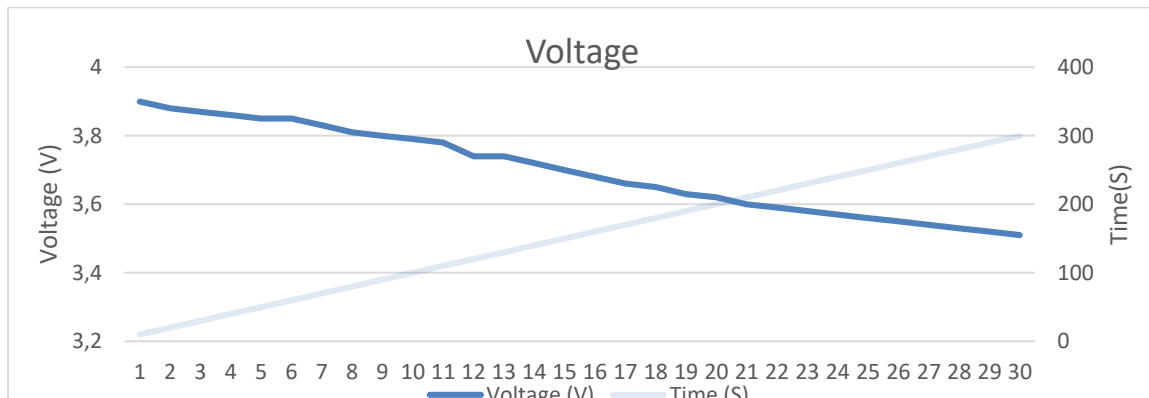


Figure 1. Graph Depicting Terminal Voltage Reading.

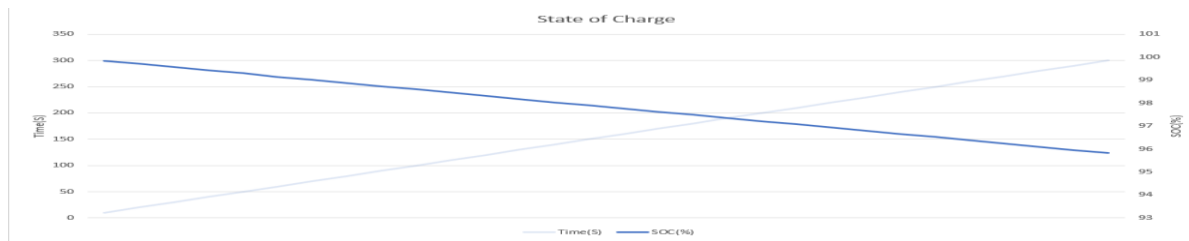


Figure 2. Graph Depicting State of charge

Figure 2 gives the Hybrid values for the SOC when both coulomb count method and TVM are combined together. Going by the nature of the graph and the rate of discharge over time, it can be noticed that the estimated SOC follows the same pattern of discharge. The battery was further discharged to close to 0% SOC, this time around it was discharged constantly for 120minutes. The various values of the battery varied over the course of the two hour mark and it can be seen in Table 2 below. it is shown in figure 3 graph where terminal voltage was constant until 70mins of constant discharge when the terminal voltage drop is no longer linear or constant.

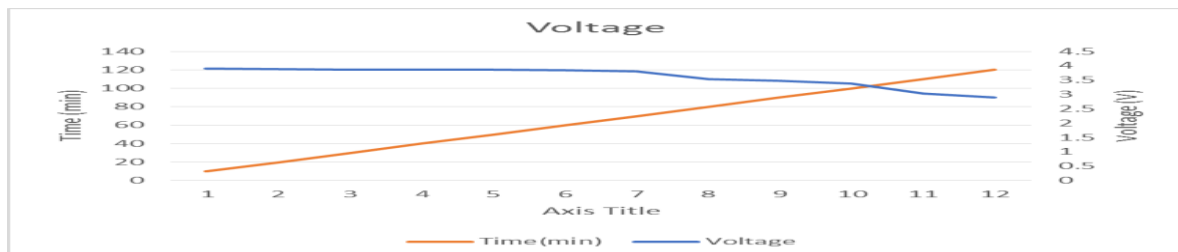


Figure 3. Graph Depicting Terminal Voltage Reading after 120 minutes.



Figure 4. Graph Depicting State of charge of battery after 120 minutes.

The rate at which the Battery SOC dropped over time with constant discharge for 120 minutes as shown in Figure 4 has a linear decrease rate. The nature of results is that both terminal voltage readings and coulomb counts have made it clear that no method can be used alone to be able to approximate or estimate a correct and efficient state of charge of the battery Terminal voltage which is not linear still helps to set the initial state of charge condition of the battery before coulomb count is employed to effectively approximate or estimate the SOC of the battery. TVM cannot be relied on to estimate the SOC of a battery once it has crossed 10% low battery. At that level the TVM of the battery can never be relied on without the help of another method of estimation.

## CONCLUSIONS

A review on estimating SOC battery is shown in this research with different time of discharge and different simulations which have their own characteristic. At fixed discharging condition, This method has a good performance and also in varied discharging current condition. The hybrid State Of Charge estimation or approximation methods which is being developed is anticipated to be worthy in Battery management system applications of electric vehicles.

## REFERENCES

- [1]. K. Jorgensen. Technologies for electric, hybrid and hydrogen vehicles: Electricity from renewable energy sources in transport. *Utili. Policy* 2008, 16, 72–79
- [2] S. Manzetti, F. Mariasiu. Electric vehicle battery technologies: From present state to future systems. *Renew. Sustain. Energy Rev.* 2015, 51, 1004–1012.
- [3] M. Umair Ali, S. Hussain Nengroo, M. Adil Khan, K. Zeb, M. Ahmad Kamran, H. Kim, A real-time simulink interfaced fast-charging methodology of lithium-ion batteries under temperature feedback with fuzzy logic control. *Energies* 2018, 11, 1122
- [4] B. Bilgin, P. Magne, P. Malysz, Y. Yang, V. Pantelic; Preindl, M.; Korobkine, A.; Jiang, W.; Lawford, M.; Emadi, A. Making the case for electrified transportation. *IEEE Trans. Transp. Electrification* 2015, 1, 4–17.
- [5] Y. Xing, E.W Ma, K.L Tsui, M. Pecht, Battery management systems in electric and hybrid vehicles. *Energies* 2011, 4, 1840–1857.
- [6] L. Lu, X. Han, J. Li, J. Hua, M. Ouyang. A review on the key issues for lithium-ion battery management in electric vehicles. *J. Power Sources* 2013, 226, 272–288.
- [7] M.A Hannan, M.H Lipu, A. Hussain, A. Mohamed, A review of lithium-ion battery state of charge estimation and management system in electric vehicle applications: Challenges and recommendations. *Renew. Sustain. Energy Rev.* 2017, 78, 834–854
- [8] P. Adeepa . Electric Vehicle Battery Management System. A thesis at La Trobe University, 2016.
- [9] H.Rui. Battery Management System For Electric Vehicle Applications. A masters Thesis at the University of Windsor Windsor, Ontario, Canada 2011
- [10] U.A Muhammad, Z. Amad , H.N Sarvar , H. Sadam , J.A Muhammad , and K. Hee-Je . Towards a Smarter Battery Management System for Electric Vehicle Applications: A Critical Review of Lithium-Ion Battery State of Charge Estimation. *Energies* 2019, 12, 446; doi:10.3390/en12030446
- [11] K. Young , C.Wang, L.Y Wang, K.Strunz. Electric Vehicle Battery Technologies. In: Garcia-Valle, R., Peças Lopes, J.A. (eds.) *Electric Vehicle Integration into Modern Power Networks*, pp. 15–56. Springer, New York (2013)
- [12] B.Pattipati, C. Sankavaram. And K.Pattipati. (2011) System identification and estimation framework for pivotal automotive battery management system characteristics. *IEEE Transactions on Systems, Man, and Cybernetics, Part C (Applications and Reviews)*, 41(6), pp.869–884.
- [13] K.W.E Cheng, B. Divakar, H. Wu, K.Ding, H.F Ho. Battery-management system (bms) and soc development for electrical vehicles. *IEEE Trans. on Veh. Technol.* 2011, 60, 76–88
- [14] L.W Juang, P. J Kollmeyer, R. Zhao, T.M Jahns and R.D Lorenz. (2015) Coulomb counting state-of-charge algorithm for electric vehicles with a physics-based temperature dependent battery model [online], pp.5052–5059 Available at: <Coulomb counting state-of-charge algorithm for electric vehicles with a physics-based temperature dependent battery model - IEEE Conference Publication
- [15] K. Young, C. Wang, L. Y Wang, K. Strunz, Electric Vehicle Battery Technologies. In: Garcia-Valle, R., Peças Lopes, J.A. (eds.) *Electric Vehicle Integration into Modern Power Networks*, pp. 15–56. Springer, New York (2013)
- [16] A. H. Anbukey and P. E. Pascoe, “VRLA battery state-of charge estimation in telecommunication power systems,” *IEEE Transactions on Industrial Electronics*, vol. 47,no. 3, pp. 565–573, 2000
- [17] S. Sato and A. Kawamura, “A new estimation method of state of charge using terminal voltage and internal resistance for lead acid battery,” in Proceedings of the Power Conversion Conference, pp. 565–570, Osaka, Japan, April 2002. dual-circuit state observer. *J. Power Sources* 2015, 296, 23–29.
- [18] J. Rivera-Barrera, N. Munoz-Galeano, H. Sarmiento-Maldonado. Soc estimation for lithium-ion batteries: Review and future challenges. *Electronics* 2017, 6, 102



# ENERGY EFFICIENCY IMPROVEMENT FOR THE MOBILE AIR CONDITIONING SYSTEMS

Cenk Onan

Yıldız Technical University, Istanbul, Turkey, conan@yildiz.edu.tr, ORCID: 0000-0001-8640-7220

Serkan Erdem

Yıldız Technical University, Istanbul, Turkey, serdem@yildiz.edu.tr, ORCID: 0000-0002-9553-6769

Cite this paper as:

*Onan, C, Erdem, S, Energy efficiency improvement for the mobile air conditioning systems, 9<sup>th</sup> Eur. Conf. Ren. Energy Sys. 21-23 April 2021, Istanbul, Turkey*

**Abstract:** R1234yf is a synthetic HFO refrigerant co-developed as a successor to R134a for automotive air-conditioning applications. So that in this study, alternatives to the R134a refrigerant, that has just been removed from the newly produced devices, have been examined. The performance of the cooling processes of R1234yf and R744 refrigerant gases was compared with that of R134a. R1234yf's global warming potential (GWP) is ultra-low, with a rating of less than 4.4. A refrigeration cycle analysis was performed for a 10 kW cooling load. These analyzes were repeated at different condenser or gas cooler outlet temperatures (30°C, 35°C, 40°C) and constant evaporator temperatures (7.5°C). And then heating mode is calculated for these refrigerants. Cycle's technical specifications are determined as between 0°C - 10°C for the evaporator temperature and 50°C for the condenser or gas cooler outlet temperature.

**Keywords:** Refrigerant, R134a, Air conditioning, COP, Energy efficiency.

© 2021 Published by ECRES

Nomenclature	
comp	Compressor
cond	Condenser
COP	Coefficient of Performance
CFC	Chlorofluorocarbon
evap, e	Evaporator
gc	Gas cooler
gco	Gas cooler outlet
h	Entalphy
HFC	Hydrofluorocarbon
K	Melting
kr	Critical
m	mass
P	Pressure
T	Temperature
Q	Heat
W	Work

## 1. INTRODUCTION

At the beginning of the 20th century, carbon dioxide, the most commonly used refrigerant in combination with ammonia, began to be not preferred in air conditioning applications with the emergence of CFCs. Despite being the most known greenhouse gas, GWP value is much less than CFC and HFC, and due to the increased environmental sensitivity, it has been taken over by the refrigeration industry and viewed as an alternative to R134a. The European Parliament and the Council of Europe's European Union Mobile Climate Regulation of 17 May 2006 entered into

force on 4 July 2006 and were enacted as of 4 July 2008 [1]. R1234yf, which has been developed to take place of R744 ( $\text{CO}_2$ ) as an alternative to R134a and R134a in mobile climate applications, has come to the forefront in vehicle cooling systems.

*Table 1. Thermophysical and environmental specifications of R134a, R1234yf and R744 [2]*

Refrigerants	Weight (kg/kmol)	$T_K$ (°C)	$T_{cr}$ (°C)	$P_{cr}$ (bar)	ODP	GWP	Atmospheric Life (year)
R134a	102.03	-26.1	101.1	40.6	0	1430	14
R1234yf	114.04	-29.5	94.7	33.8	0	<4.4	29
R744	44.01	—	31	73.8	0	1	>50

R1234yf fluid has been developed to replace R134a in mobile climate applications. R1234yf that has very good environmental characteristics, which can be seen in Table 1, shows similar performance characteristics to R134a. Chen et al. (2011) compared the mobile air conditioning (MAC) systems using R134a and R1234yf under different conditions and found that the COP value of R134a was 9% - 12.4% higher [3]. Lee and Jung in their experimental study in 2012 show that, in case of 5°C superheating and subcooling for summer and winter conditions, in comparison with the R134a system, a MAC system with R1234yf will have lower COP of 0.8 - 2.7% and lower cooling capacity of 4% [4]. Sainath et al. (2017) determined the pressure drop across the capillary tube. The optimization was determined by mathematical calculation to evaluate increment length [5]. Zhiyi et al. (2017) used a systematic approach to evaluate the  $\text{CO}_2$ -equivalent emissions when R134a, R152a, R1234yf and R744 ( $\text{CO}_2$ ) are used as refrigerant in MAC systems, integrating a GDP-dependent Gompertz model and  $\text{CO}_2$ -equivalent emissions of each type of refrigerant during MAC systems operate [6]. Devecioğlu et al. (2017) analyzed R1234yf, R444A and R445A refrigerants that can be used in mobile air conditioning systems. In order to evaluate the thermodynamic properties of refrigerants, evaporation temperatures of 5°C and +5°C, condenser temperatures of 30°C and 60°C were taken. According to the calculations, although the cooling capacity of R444A and R445A is higher; COP values were lower compared to R1234yf due to increased electricity consumption. Although the COP value of R444A is smaller than R1234yf, it can be suggested that R444A can be used in air conditioning systems of heavy vehicles such as buses, trucks and trains, due to the reduced risk of burning depending on the mixture content [7]. Wang et al (2019) compared to natural refrigerant  $\text{CO}_2$ , mobile air conditioning and heating performance and superior environment (MAC) it is one of a new generation of refrigerant in the application. To set up this refrigerant-powered MAC, they designed and experimentally studied a new visualized accumulator with five observation mirrors. In addition, the transient migration behavior of the cooler during shutdown and start-up and the flow behavior of lubricating oil with 0.5 mm oil return hole were experimentally investigated. A plateau region with optimum system performance was found to occur between 1100g and 1600g refrigerant charge [8]. Zheng et al. (2020) worked to achieve better scroll compressor performance for  $\text{CO}_2$  in the heat pump air conditioning system. An unsteady Reynolds Average Navier-Stokes run process was performed on a transcritical  $\text{CO}_2$  powered scroll compressor. The effect of  $\text{CO}_2$  properties table resolution on numerical simulation has been studied in detail. Their results provide an instrumental guide for the optimum design of the supercritical  $\text{CO}_2$  scroll compressor [9].

## 2. METHODOLOGY

In this study, the ideal cooling cycle calculations for R134a, R1234yf and R744 were made separately for 10 kW cooling and the findings were compared with each other. In the case of cooling, the condenser or gas cooler outlet temperature is selected as 35°C - 45°C and the evaporator temperature is 7.5°C. Also ideal cooling cycle calculations for these refrigerants were made separately for 13.5 kW heating and the results are shown below. In the case of heating, the evaporator temperature is selected as 0°C - 10°C and the condenser or gas cooler outlet temperature is 50°C.

From the equation [10] proposed by Tillner-Roth and Baehr for the thermodynamic properties of R134a, the equation [11] proposed by Richter et al. For the thermodynamic properties of R1234yf and the thermodynamic properties of R744 proposed by Span and Wagner [12] the equation was used. Also for the cooling cycle the R744 is used, the gas cooler is pressurized by Liao et al. [13] is calculated with the following Eq. [1]:

$$P_{opt} = (2.788 - 0.0157t_e)t_{gc} + (0.381t_e - 9.34) \quad (1)$$

For all cycles, the compressor isentropic efficiency 0.8 and all other efficiencies and activities are assumed as 1. The R134a and R1234yf cycles are single-stage critical sub-cycles, and the R744 cycle is a single-stage transcritical cycle.

1-2: Compressor compression

2-3: Heat transfer in the condenser or in the gas cooler

3-4: Expansion in the TE valve

4-1: Evaporation in the evaporator

In the calculations, heat transfer and compressor work are found as shown below, (Eqs. [2-4])

$$\dot{Q}_{cond} = \dot{m}_{ref} \times (h_3 - h_2) \quad (2)$$

$$\dot{Q}_{evap} = \dot{m}_{ref} \times (h_1 - h_4) \quad (3)$$

$$\dot{W}_{comp} = \dot{m}_{ref} \times (h_1 - h_2) \quad (4)$$

COP is calculated by Eq. [5],

$$COP_R = \frac{\dot{Q}_{evap}}{\dot{W}_{comp}} \quad (5)$$

### 3. RESULTS AND DISCUSSIONS

As a result of calculations made in 2 cycles, compressor power, system efficiency was found. The enthalpy values used in the calculations and these results are shown in Table 2. For R744, the capacity of the gas cooler in the system is given instead of the condenser.

Table 2. Energy and efficiency values calculated for cooling season

Refrigerants (kW or kJ/kg)	R134			R1234yf			R744		
	$T_{cond} = 35^{\circ}\text{C}$	$T_{cond} = 40^{\circ}\text{C}$	$T_{cond} = 45^{\circ}\text{C}$	$T_{cond} = 35^{\circ}\text{C}$	$T_{cond} = 40^{\circ}\text{C}$	$T_{cond} = 45^{\circ}\text{C}$	$T_{gco} = 35^{\circ}\text{C}$	$T_{gco} = 40^{\circ}\text{C}$	$T_{gco} = 45^{\circ}\text{C}$
$h_1$	254.8	254.8	254.8	368.1	368.1	368.1	-81.42	-81.42	-81.42
$h_2$	276.6	280.2	283.6	385.8	388.6kJ	391.3	-60.12	-55.41	-51.13
$h_3 = h_4$	100.9	108.3	115.8	246.5	253.8	261.1	-202.7	-194.2	186.1
$\dot{Q}_{cond} \text{ or } \dot{Q}_{gc}$	11.42	11.74	12.08	11.46	11.02	12.17	11.06	10.56	10.08
$\dot{W}_{comp}$	1.442	1.736	2.077	1.46	1.798	2.172	1.756	2.306	2.896
$COP_R$	7.031	5.759	4.815	6.85	5.563	4.604	5.693	4.337	3.454

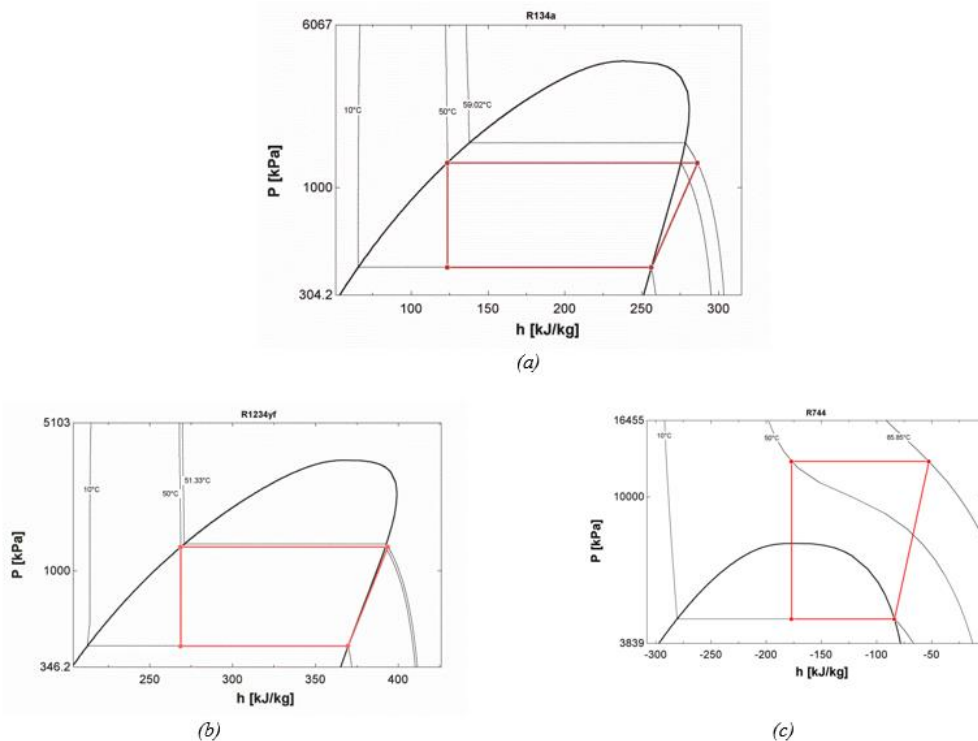


Figure 1. Refrigerant cycles in heating mode at 10°C evaporation temperature (a) R134a (b) R1234yf (c) R744

The cooling cycles for different refrigerants in heating mode at 10°C evaporation temperature are shown in Figure 1. Refrigeration cycle main elements, evaporator and condenser / gas cooler pressures and compressor inlet and outlet conditions are shown in this figure. Also enthalpy change can be seen for each component. The enthalpy values used in the calculations and these results are shown in Table 3.

Table 3. Energy and efficiency values calculated for heating season

Refrigerants (kW or kJ/kg)	R134			R1234yf			R744		
	$T_{eva} = 0^\circ\text{C}$	$T_{eva} = 5^\circ\text{C}$	$T_{eva} = 10^\circ\text{C}$	$T_{eva} = 0^\circ\text{C}$	$T_{eva} = 5^\circ\text{C}$	$T_{eva} = 10^\circ\text{C}$	$T_{eva} = 0^\circ\text{C}$	$T_{eva} = 5^\circ\text{C}$	$T_{eva} = 10^\circ\text{C}$
$h_1$	250.5	253.3	256.2	363.2	366.5	369.6	-75.88	-79.29	-83.9
$h_2$	289.6	287.8	286.1	394.5	394	393.7	-31.97	-41.91	-52.68
$h_3 = h_4$	123.5	123.5	123.5	268.7	268.7	268.7	-180.8	-179.1	-177.2
$\dot{Q}_{eva}$	9.939	10.28	10.61	9.772	10.14	10.5	9.165	9.548	9.741
$\dot{W}_{comp}$	3.061	2.724	2.393	3.304	2.859	2.499	3.835	3.542	3.259
$COP_R$	3.246	3.772	4.433	3.027	3.547	4.201	2.39	2.67	2.989

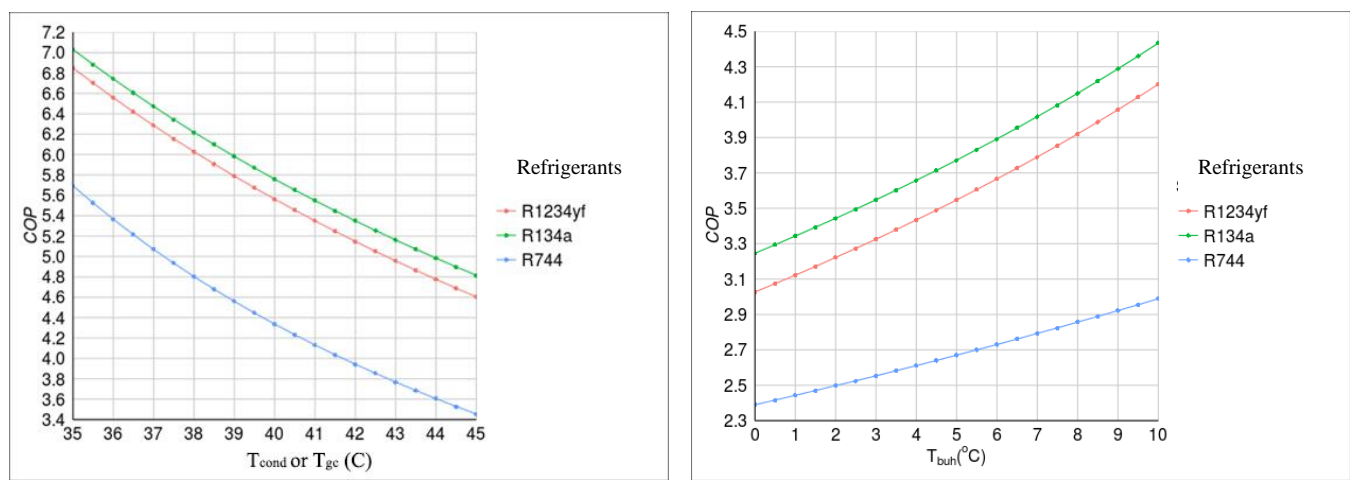


Figure 2. a) System COPs in case of cooling b) System COPs in case of heating

As can be seen from Figure 2a, the COP values of R134a and R1234yf are close to each other in the case of cooling, but the COP of R744 is very low. As the temperature of the condenser increased from 35°C to 45°C, COP values decreased by 31.52% in R134a, 32.79% in R1234yf, and 39.34% in R744. Compared to the R-134a cycle, the COP values are 4.38 - 2.57% for R1234yf and 28.27 - 19.03% for R744. As can be seen from Figure 2b, the COP values of R134a and R1234yf are close to each other in the case of heating, but the COP of the R744 system is very low. By increasing the evaporator temperature from 0°C to 10°C, the COP values increased by 36.57% in R134a, 38.78% in R1234yf, and 25.06% in R744. The COP value of the R1234yf system was 6.75% - 5.23% lower than that of the R134a system, while the COP value of the R744 system was 32.57% - 26.37% lower than that of the R134a system.

#### 4. CONCLUSION

Today, where energy efficiency is important in every field, energy studies are carried out to contribute to the regulations in vehicles. Since the electricity consumption of the compressor will decrease as a result of the correct selection of the refrigerant, more energy-efficient systems can be designed. Different cooling cycles according to refrigerants have been analyzed for different modes, and a system with a high COP value or nearly one's (energy efficient) has been found.

R1234yf refrigerant fluid was found to have a great similarity with R134a. For this reason, mobile heat pump systems using R1234yf can be used instead of R134a with minor modifications.

The R744 refrigerant, on the other hand, gave  $T_{\text{evap}} \text{ (}^{\circ}\text{C)}$  in comparison. Compared to the R134a system, the required compressor powers increased by 2.67% - 4.57% for R1234yf and 23.48% - 39.43% for R744 in the case of cooling. Compared to the R134a system, the COPs are 4.38 - 2.57% lower for R1234yf and 28.27 - 19.03% lower for R744 in the case of cooling. Since the physical properties of the refrigerant and its usability due to environmental effects should also be considered, it is recommended to choose according to the rate of increase in energy consumption for refrigerants with lower COP. Evaluation criteria should be determined according to the advantages and disadvantages of the vehicle. It is recommended that the practitioners choose the refrigerant for the design of energy efficient systems, with the contribution of the results found, in their outdoor conditions.

#### REFERENCES

- [1] Directive 2006/40/EC of the European Parliament and of the Council of 17 May 2006 relating to emissions from air conditioning systems in motor vehicles and amending Council Directive 70/156/EEC. Official Journal of the European Union, 2006, 161, 12–18.
- [2] Calm, JM, Hourahan, GC. Physical, safety, and environmental data for current and alternative refrigerants. In: Proceedings of the 23rd IIR International Congress of Refrigeration, August 21-26, 2011 Prague, Czech Republic.
- [3] Chen, J, Zhao Y, Qi, Z. New developments in mobile air conditioning systems in China, Front. Energy. 2011, 5, 1, 53–58. DOI: <https://doi.org/10.1007/s11708-010-0137-3>
- [4] Lee, Y, Jung, D. A brief performance comparison of R1234yf and R134a in a bench tester for automobile applications. Applied Thermal Engineering, 2012, 35, 240–242. DOI: <https://doi.org/10.1016/j.applthermaleng.2011.09.004>
- [5] Sainath, K, Reddy, TKK, Akella, S. Optimization of capillary tube dimensions using different Refrigerants for 1.5 ton mobile air conditioner. Case Studies in Thermal Engineering, 2019, 16, 100528. DOI: <https://doi.org/10.1016/j.csite.2019.100528>
- [6] Zhiyi, Y, Tianduo, P, Xunmin, O. Scenario Analysis on CO<sub>2</sub>-equivalent Emissions from Alternative Mobile Air Conditioning Refrigerants in China. Energy Procedia, 2017, 142, 2617–2623. DOI: <https://doi.org/10.1016/j.egypro.2017.12.201>
- [7] Devecioğlu, AG, Oruç, V. An analysis on the comparison of low-GWP refrigerants to alternatively use in mobile air-conditioning systems. Thermal Science and Engineering Progress, 2017, 1, 1–5. DOI: <https://doi.org/10.1016/j.tsep.2017.02.002>
- [8] Wang, D, Zhang, Z, Yu, B, Wang, X, Shi, J, Chen, J. Experimental research on charge determination and accumulator behavior in trans-critical CO<sub>2</sub> mobile air-conditioning system. Energy, 2019, 183, 106–115. DOI: <https://doi.org/10.1016/j.energy.2019.06.116>.
- [9] Zheng, S, Wei, M, Song, P, Hu C, Tian, R. Thermodynamics and flow unsteadiness analysis of trans-critical CO<sub>2</sub> in a scroll compressor for mobile heat pump air-conditioning system. Applied Thermal Engineering, 2020, 175, 1153–1168. DOI: <https://doi.org/10.1016/j.applthermaleng.2020.115368>.
- [10] Tillner-Roth, R and Baehr, HD. An International Standard Formulation for the Thermodynamic Properties of 1,1,1,2-Tetrafluoroethane (HFC-134a) for Temperatures from 170 K to 455 K and Pressures up to 70 MPa. Journal of Physical and Chemical Reference Data, 1994, 23, 657. DOI: <https://doi.org/10.1063/1.555958>
- [11] Richter, M, McLinden, MO and Lemmon, EW. “Thermodynamic Properties of 2, 3, 3, 3-Tetrafluoroprop-1-ene (R1234yf): Vapor Pressure and p–p–T Measurements and an Equation of State,” Journal of Chemical & Engineering Data, 2011, 56, 7, 3254–3264. DOI: 10.1021/je200369m
- [12] Span, R and Wagner, W. A new equation of state for carbon dioxide covering the fluid region from the triple-point temperature to 1100 K at pressures up to 800 MPa. Journal of Physical and Chemical Reference Data, 1996, 25, 1509. DOI: <https://doi.org/10.1063/1.555991>
- [13] Liao, S, Zhao, T, Jakobsen, A. A correlation of optimal heat rejection pressures in transcritical carbon dioxide cycles. Applied Thermal Engineering, 2000, 20, 9, 831–841. DOI: <https://doi.org/10.1016/S1>



# THE MAGNETIC SATURATION EFFECT ON FAULT DIAGNOSTICS IN SQUIRREL CAGE INDUCTION MOTOR USING CURRENT PARK'S VECTOR PATTERN

Chaouch Abdellah

Department of Electrical Engineering, Faculty of Sciences and Technology, Mostaganem University, Mostaganem, Algeria, ikchaouchdz@yahoo.fr, ORCID: 0000-0002-2973-6180

Belaid Mohamed

Department of Electrical Engineering, Faculty of Sciences and Technology, Mostaganem University, Mostaganem, Algeria, belmoh33@hotmail.com, ORCID: 0000-0002-5617-4910

Meflah Abderrahmane Mohamed Reda

Department of Electrical Engineering, Faculty of Sciences and Technology, Mostaganem University, Mostaganem, Algeria, meflahreda@yahoo, ORCID: 0000-0003-4420-397X

Cite this paper as:

*Chaouch, A, Belaid, M, Reda Meflah, MAM. The magnetic saturation effect on fault diagnostics in squirrel cage induction motor using current park's vector pattern, 9<sup>th</sup> Eur. Conf. Ren. Energy Sys. 21-23 April 2021, Istanbul, Turkey*

**Abstract:** The magnetic saturation effect on fault diagnosis in squirrel cage induction motor using Current Park's Vector pattern is presented. The aim of this paper is to describe the behaviour of induction motor for healthy and faulty in the presence of saturation. The use of current vector pattern provides that the change of the shape from hexagonal to elliptical and the increasing diameter are indexes in predicting of magnetic saturation. Experimental results demonstrate the effectiveness of the proposed technique for the Discrimination between magnetic saturation in healthy and faulty for squirrel cage induction motor.

**Keywords:** *Squirrel cage induction motor, fault diagnosis, broken bar, Current Park's Vector, magnetic saturation.*

© 2021 Published by ECRES

## 1. INTRODUCTION

In industrial applications, Squirrel cage induction motors (SCIM) are popularly used due to their robustness, reliability and low cost. However, induction machines are often subjected during their operation to several stresses of different kinds (excessive heating, magnetic fatigue caused by electromagnetic forces and environmental stresses that the rotor must undergo during normal use). The accumulation of these stresses causes faults in the various parts of the machine such as winding faults [1, 2, 3], broken rotor bars [4, 5, 6, 7], eccentricity and bearing faults [8, 9, 10]. Several fault diagnosis methods have been developed to detect machine faults using physical parameters, such as current, voltage, speed, efficiency, temperature and vibration. Many techniques for health monitoring and fault diagnosis of induction motors are based on the processing of the stator line currents. Among these, Park's vector approach has been used by different authors for analysing different types of individual faults [11, 12, 13, 14, 15, 16]. Bonett has analysed the winding failures [17] and given the report about that. However, several research in fault diagnosis, the magnetic saturation is not considered in their model.

In our paper [18], the modeling of magnetic saturation for induction motor is presented. Although this phenomenon is secondary in certain applications such as electrical control, but the magnetic saturation is very important because in industrial maintenance, it can put us in the ambiguity between the fault and the saturation of the machine, and consequently it would be very difficult to discriminate the state of the motor. In [18], we have shown by spectral analysis of the stator current on the one hand the saturation harmonic was near that characterizing the properties of the asynchronous motor and on the other hand in the faulty motor.

In this paper, we use the Current Parks Vector Approach (CPVA) to show the effect of this magnetic saturation and its difficulty in discriminating between the healthy, the faulty and the saturate motor.

## 2. MODELING BY CPVA

The method is based on the transformation of a three-phase system to two and simplifies its study, for this reason CPVA [16] is widely used in electrical control and in the study of transient regimes of electrical networks.

In our study, we use CPVA by transforming three-phase currents ( $i_a, i_b, i_c$ ) to two-phase ( $i_d, i_q$ ), these are the Park currents given by the following relations:

$$i_d = \left(\frac{\sqrt{2}}{\sqrt{3}}\right) i_a - \left(\frac{1}{\sqrt{6}}\right) i_b - \left(\frac{1}{\sqrt{6}}\right) i_c \quad (1)$$

$$i_q = \left(\frac{1}{\sqrt{2}}\right) i_b - \left(\frac{1}{\sqrt{2}}\right) i_c \quad (2)$$

With mathematical transformation, we can write:

$$i_d = \left(\frac{\sqrt{6}}{2}\right) i_M \sin(\omega t) \quad (3)$$

$$i_q = \left(\frac{\sqrt{6}}{2}\right) i_M \sin(\omega t - \frac{\pi}{2}) \quad (4)$$

This maps a circle. This geometric shape represents the ideal operation of the machine (figure. 1). This locus is distorted by saturation, broken faults and thus provides easy fault diagnosis.

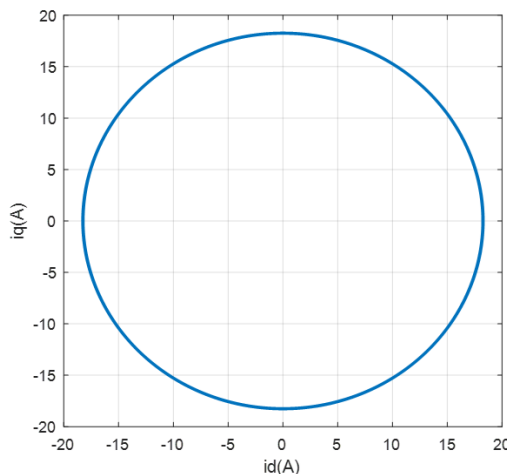


Figure 1. Park's vector pattern for healthy motor and ideal case

## 3. EXPERIMENTAL RESULTS

### Test bench details:

In order to use CPVA in our experimental study, we have mounted a test bench shown in figure 2. The test bench is composed of an asynchronous motor (SCIM) with the following specification 4kW, 1500 rpm, rated supply 380V, the motor drives a permanent magnet synchronous generator (GSAPM) supplying a variable resistive load. For the fault diagnostic test we replace the healthy motor by a faulty in our case a broken bar rotor. Figure 3 shows the different elements of the test bench.

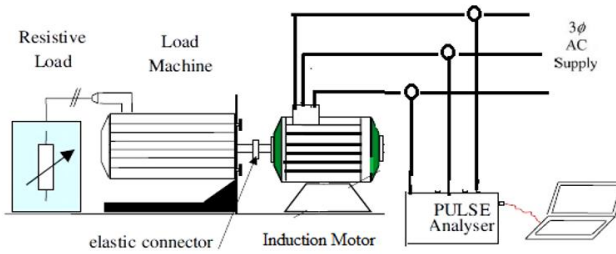


Figure 2. Detection system scheme



Figure 3. Experimental bench test

## RESULTS AND DISCUSSION

To show the effect of saturation in our study, we have tested motor at no load, we noted that the voltage-current characteristic (Figure 4), and we deduced the saturation factor in which the voltage applied to reach the saturation of the machine.

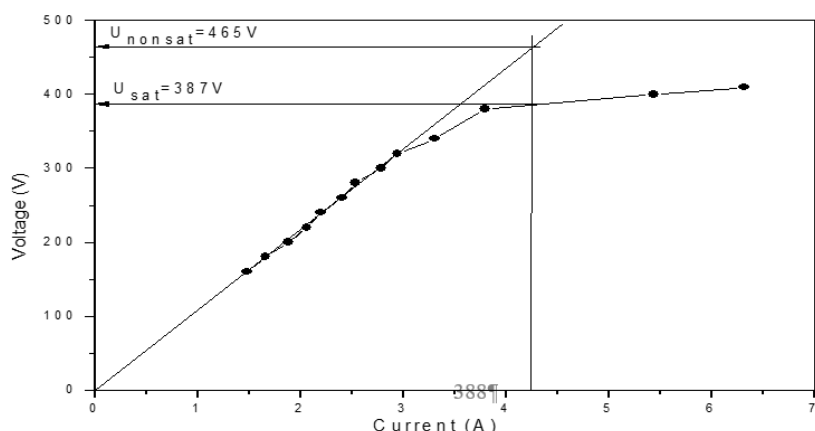


Figure 4. No-load characteristic of the experimental motor

Figures 5 and 6 present the trajectories of Park currents for the healthy motor with and without load for both cases with and without saturation.

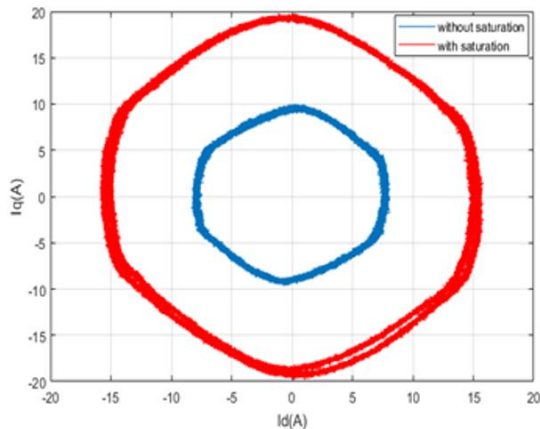


Figure 5. Experimental current Park's vector pattern for healthy motor at no load

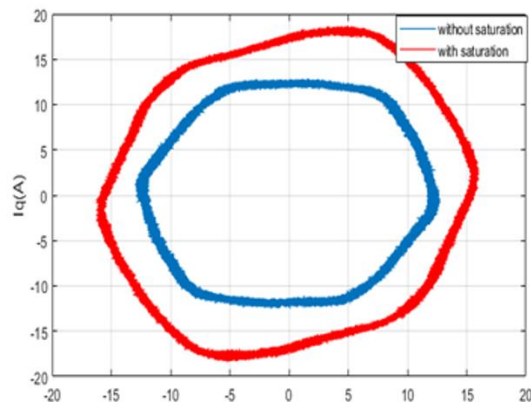


Figure 6 Experimental current Park's vector pattern for healthy motor at full load

The trajectories have a different shape of the circle because of the non-sinusoid of the power source. The saturation effect is marked by the increase of the diameter of the hexagonal shape at no loaded motor (figure.5), in the loaded and without saturation case the current path rotates 90° and when the motor is saturated in addition of increasing the diameter, we notice the change of shape from hexagonal to elliptical (figure.6).

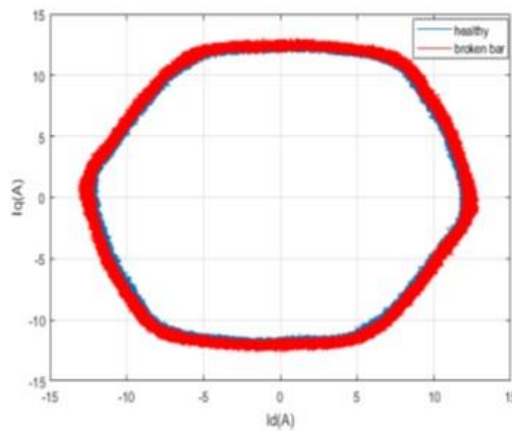


Figure 7. Motor without saturation

Figures 7 and 8 show the motor fault of broken bar at the load and for both cases with and without saturation is detected by the increase of the thickness of the shape (figure.7), however in saturated cases (figure.8), the broken bar becomes difficult to detect, so the saturation effect tends to mask the fault.

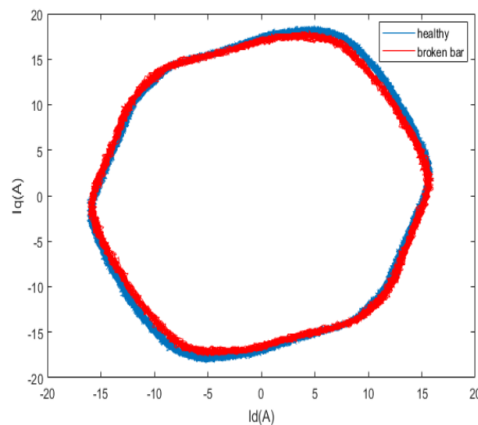


Figure 8. Motor with saturation

#### 4. CONCLUSION

This paper presents the magnetic saturation effect on fault diagnosis in SCIM using CVP Pattern (CVPP) technique. For healthy motor without saturation, the CVPP was hexagonal shape while with saturation CVPP was elliptical. The increasing of the thickness CVP trajectory of broken bar is indexes diagnosis for SCIM without and with saturation. The experimental results prove the effectiveness of this technique in the discrimination between magnetic saturation for healthy and faulty condition. In the next paper, we develop a method to extract different parameters to distinguish saturation from faults.

#### REFERENCES

- [1] Ahmet, K, Mehmet B. Detection of stator winding fault in induction motor using instantaneous power signature analysis”, Turk J Elec Eng & Comp Sci, vol. 23, pp. 1263-1271, 2015.
- [2] Fernão Pires, V, Amaral, Tito, G, J, F, Martins. Stator winding fault diagnosis in induction motors using the dq current trajectory mass center, 2009 35th Annual Conference of IEEE Industrial Electronics, DOI: 10.1109/IECON.2009.5414714.
- [3] Mohammed, S, J, B, Jassim, M, H. Inter-Turn Stator Winding Faults Diagnosis in Three-Phase Induction Motor Fed from Imbalanced Voltage Source, Journal of Engineering and Applied Sciences, 2019, pp.7591-7598. DOI: 10.36478/jeasci.2019.7591.7598.
- [4] Reljic, D, Jerkan, D. Broken Bar Fault Detection in IM Operating Under No-Load Condition, Advances in Electrical and Computer Engineering 16(4):63-70, 2016. DOI: 10.4316/AECE.2016.04010
- [5] Park, Y, S. Investigation on Electromagnetic Performance of Induction Motor with Rotor Bar Faults considering Motor Current Signals, Advances in Electrical and Computer Engineering 20(4), pp.37-40, 2020. DOI: 10.4316/AECE.2020.04005
- [6] Matic, D, Kanovic, Z. Vibration Based Broken Bar Detection in Induction Machine for Low Load Conditions, Advances in Electrical and Computer Engineering, 17 pp.63-70, 2017. DOI: 10.4316/AECE.2017.01007.
- [7] Ojeda-Aguirre, N, A, Garcia-Perez, A, and all. Reassigned Short Time Fourier Transform and K-means Method for Diagnosis of Broken Rotor Bar Detection in VSD-fed Induction Motors, Advances in Electrical and Computer Engineering 19, pp.61-68, 2019. DOI: 10.4316/AECE.2019.02008.
- [8] Metatla, A, Benzahioul, S, Bahi, T, Lefebvre, D. On Line Current Monitoring and Application of a Residual Method for Eccentricity Fault Detection, Advances in Electrical and Computer Engineering 11, pp.69-72, 2011. DOI: 10.4316/AECE.2011.01011
- [9] Guoping An, Qingbin, T, Yanan, Z, and al. An Improved Variational Mode Decomposition and Its Application on Fault Feature Extraction of Rolling Element Bearing, Energies 2021, 14(4), 1079; <https://doi.org/10.3390/en14041079> - 18 Feb 2021
- [10] Wagner, F, G, Daniel, M, Sotelo, Oscar, D, P, and al. Estimation of Bearing Fault Severity in Line-Connected and Inverter-Fed Three-Phase Induction Motors, Energies 2020, 13(13), 3481; <https://doi.org/10.3390/en13133481> - 06 Jul 2020.
- [11] Bonnett, A, H, Soukup, G, C. Cause and Analysis of Stator and Rotor Failures in Three-Phase Squirrel-Cage Induction Motors, IEEE Trans. Ind. Appl., vol. 28, no. 4, pp. 921–937, 1992.
- [12] Braham, A, Lachiri, Z. Diagnosis of Broken Bar Fault in Induction Machines Using Advanced Digital Signal Processing, IREE, vol.5, pp. 1460-1468, July-August.2010 .
- [13] Marques Cardoso, A.J. Inter-turn stator winding fault diagnosis in three-phase induction motors, by Park's vector approach, IEEE Trans.Energy Conversion, Volume: 14, pp. 595 - 598, Sep 1999.
- [14] Nejjari, H, Benbouzid, M.H. Monitoring and diagnosis of induction motor faults using current parks vector approach, IEEE trans. Ind.Applicat.,vol.36,no.3,May/June 2000, pp.730 – 735.

- [15] Izzet Yilmaz, O, N, Mohamed, B. Induction motor bearing failure detection and diagnosis: Park and Concordia Transform Approaches Comparative study, IEEE/ASME Trans. Mechatronics, Vol.13, No.2,pp.257-262, April 2008.
- [16] Cruz, S, M, A. Stator winding fault diagnosis in three-phase synchronous and asynchronous motors, by the extended Park's vector approach, IEEE conf. Ind. Applicat., vol.1, pp. 395 – 401, 2000
- [17] Bonnett, A, H. Analysis of Winding Failures in Three-Phase Squirrel Cage Induction motors, IEEE Trans. Ind. Applicat., Vol: 14 , Issue:3,pp.223 – 226, May 1978.
- [18] Chaouch, A, Bendiabdellah, A. Spectral Analysis to Detect Mixed Eccentricity Fault in Saturated Squirrel Cage Induction Motor, Proc. IEEE, ISPCC' 2013, India.



# EFFECT OF THE THREE MAIN DIRECTIONS OF AN EXTERNAL MAGNETIC FIELD ON THE FREE CONVECTION IN $\text{Fe}_3\text{O}_4$ -WATER NANOFLUID FILLED CUBIC ENCLOSURE

Maache Mouna Battira

Abbes Laghrour University, Science and Technology Faculty, Department of Mechanical Engineering,  
Khenchela, 40000, Algeria, E-mail: mounamaache@yahoo.fr, ORCID: 0000-0002-6466-1719

Chehhat Abdelmadjid

Abbes Laghrour University, Science and Technology Faculty, Department of Mechanical Engineering,  
Khenchela, 40000, Algeria, E-mail: achemhat@gmail.com, ORCID: 0000-0003-1088-253X

Noui Samira

Elhadj Lakhdar University, Sciences of Matter Faculty, Physics Department, Batna, 05000, Algeria  
E-mail: samira.noui@univ-batna.dz, ORCID: 0000-0002-0345-3692

Bessaih Rachid

Mentouri University, Science and Technology Faculty, Department of Mechanical Engineering,  
Constantine, 25000, Algeria, E-mail: bessaih.rachid@gmail.com, ORCID: 0000-0002-0764-7731

Cite this paper as:

*MM Battira, A Chehhat, S Noui, R Bessaih. Effect of the three main directions of an external magnetic field on the free convection in  $\text{Fe}_3\text{O}_4$ - water nanofluid filled cubic enclosure. 9th Eur. Conf. Ren. Energy Sys. 21-23 April 2021, Istanbul, Turkey.*

---

**Abstract:**

The present work studies numerically the influence of the three main directions of an external magnetic field on  $\text{Fe}_3\text{O}_4$ -water nanofluid free convective flow within a cubic enclosure subjected to horizontal temperature gradient. The MHD problem is mathematically modeled, and its dimensionless equations are established. The system of partial differential equations, governing the phenomenon, is resolved by a numerical approach based on the finite volume method using ANSYS Fluent. The impact of Rayleigh number ( $10^3 \leq Ra \leq 10^6$ ), Hartmann number ( $0 \leq Ha \leq 20$ ) and the three principal magnetic field directions on thermo-hydrodynamics behavior of nanofluid is also studied. This study is carried out for pure water ( $\phi = 0$ ) and for a nanofluid with low solid volume fraction ( $\phi = 0.02$ ). The correlations chosen for calculating thermal conductivity and dynamic viscosity are specifically developed for  $\text{Fe}_3\text{O}_4$ -water nanofluid from previous experimental studies. Simulation results reveal that the decrease of Nusselt number with increasing magnetic field strength becomes stronger with increasing the Ra number. Applying magnetic field horizontally i.e. parallel to the temperature gradient, decreases heat transfer greater than in the other two directions. In second position, the most significant reduction in convective heat transfer rate is recorded when magnetic field direction is vertical i.e. parallel to gravity.

---

**Keywords:** Cubical enclosure, Magnetic field direction,  $\text{Fe}_3\text{O}_4$ -water nanofluid, Natural convection.

© 2021 Published by ECRES

## 1. INTRODUCTION

The problem of the influence of an externally applied magnetic field (MF) on free convection in square-shaped closed cavities containing nanofluids (nnfs) has been the focus of numerous numerical and experimental investigations during the last years [1-10]. This is because of its widespread industrial uses, such as crystal growth fluids, electronic equipment cooling, melt casting, geothermal energy extraction, purification of molten metals, nuclear reactors, etc. The nanofluid is produced from the suspension of metallic, oxide metallic or non-metallic nanoparticles (nnps) in the conventional fluid commonly used such as water and oil. The nnf was first proposed by Choi [11]. The relatively high thermal conductivity of nnps increases the nnf thermal conductivity. In some cases,

the use of nnfs as the working medium, greatly enhances the free convection rate; hence, the need to control this improvement. The Lorentz forces developed by the external MF application, slow down the convective currents and thus allow the control of the high heat transfer rate. One of the biggest problems with nnfs substances is the precision of models for calculating their dynamic viscosity and thermal conductivity. While, there are many researches on modeling efficient properties, some scientists show that using certain correlations can perform to false predictions of these properties [12]. D. Toghraie et al. [13] determine experimentally the ( $\text{Fe}_3\text{O}_4$ -water) dynamic viscosity. The viscosity measurements were made between 293 K to 328 K with low volume fraction of nnps ( $\phi \leq 3\%$ ). Results show the significant decrease of the viscosity with the increase of the temperature. In addition, the viscosity augments greatly as the volume fraction of nnps increases. The dynamic viscosity model developed by these researchers [13] is chosen for this work. M. Afrand et al. [14] propose a correlation to estimate the  $\text{Fe}_3\text{O}_4$ -water thermal conductivity. For this study, this correlation is adopted.

This study aims to present a three-dimensional numerical simulation of the convective flow comportment of nnf into a cubical cavity when the base fluid, which is water, is seeded with low volume fraction of  $\text{Fe}_3\text{O}_4$  np. A uniform magnetic field is externally applied on the cavity, each time, in one of the main directions x, y or z. Calculations were made to establish the relation between heat exchange enhancement and magnetic field direction. The models used for calculating thermal conductivity and effective dynamic viscosity are correlations experimentally determined specifically for  $\text{Fe}_3\text{O}_4$ -water nanofluid.

## 2. MATHEMATICAL AND NUMERICAL MODELISATIONS

### 2. 1. Problem geometry

Fig. 1 schematizes the cubical enclosure of side L. The  $\text{Fe}_3\text{O}_4$ -water nnf is enclosed in the cavity and subjected to horizontal temperature gradient. The lateral left wall is kept at a certain temperature  $T_h$ , and the right one is kept at a lower temperature  $T_c$ . The four remaining walls are supposed to be insulating. The direction of a uniform MF externally applied is changed in the three main directions. A Cartesian system (x, y, z) is adopted. Gravity acts along the negative z direction and the temperature difference is imposed in the x direction.

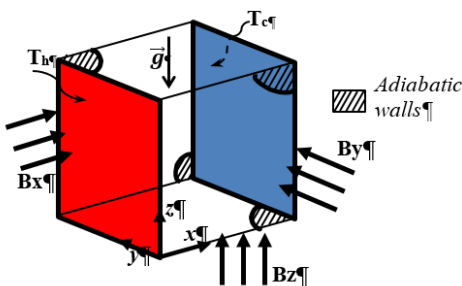


Figure 1. Problem geometry

### 2. 2. Mathematical model

The nnf flow into the cubical cavity, is considered laminar, steady and incompressible. The nnf is Newtonian. It is important to explain here that the Newtonian nnf hypothesis used for this simulation is absolutely valid. Since the base fluid used is the water, which is a Newtonian fluid, and the solid volume fraction considered is relatively low ( $\phi = 0.02$ ), the behaviors of the nnf and the base fluid can be considered as similar. The  $\text{Fe}_3\text{O}_4$  solid particles and the water are supposed in thermal equilibrium, so, the single-phase model is used in this study. According to Boussinesq hypothesis, all the thermo-physical nnf properties are constant, with the exception of the term of density variation. The displacement currents, radiation heat transfer, viscous dissipation, Joule effect and induced magnetic field are neglected. The MF vector of constant magnitude is expressed by:  $\vec{B} = B_0 \vec{e}_B$ . Where  $\vec{e}_B$  represents the unit vector. When MF is applied horizontally parallel to the temperature gradient, the MF vector is expressed by:  $\vec{B} = \vec{B}_x = B_0 \vec{i}$ . If the MF field direction is parallel to gravitational field, its vector is written as :  $\vec{B} = \vec{B}_z = B_0 \vec{k}$ . In the case where the MF is applied perpendicularly to both directions horizontal and vertical, its vector is:  $\vec{B} = \vec{B}_y = B_0 \vec{j}$ . The electromagnetic force  $\vec{F}$  is defined by  $\vec{F} = \vec{j} \times \vec{B}$  where  $\vec{j}$  the electric current is given by:  $\vec{j} = \sigma[-\nabla\Phi + (\vec{V} \times \vec{B})]$ . By using  $(T_h - T_c)$ ,  $L$ ,  $\alpha_f/L$ , and  $\rho_{nf} \alpha_f^2/L^2$  as typical scales for temperature, lengths, velocities, and pressure, respectively, the dimensionless governing equations are:

$$\nabla \cdot \vec{V} = 0 \quad (1)$$

$$(\vec{V} \cdot \nabla) \vec{V} = -\nabla P + \frac{\mu_{nf}}{\alpha_{nf} \rho_{nf}} \nabla^2 \vec{V} - \frac{\rho_f \beta_{nf}}{\rho_{nf} \beta_f} Ra Pr T \vec{k} + \frac{\sigma_{nf} \rho_f}{\sigma_f \rho_{nf}} Ha^2 Pr [(\vec{V} \times \vec{e}_B) \times \vec{e}_B] \quad (2)$$

$$\vec{V} \cdot \nabla \theta = (\alpha_{nf}/\alpha_f) \nabla^2 \theta \quad (3)$$

Where dimensionless numbers are given by: Rayleigh number:  $Ra = \frac{g \beta_f (T_h - T_c) L^3}{\nu_f \alpha_f}$ ; Hartmann number:  $Ha = B_0 L \sqrt{\frac{\sigma_{nf}}{\rho_{nf} \mu_f}}$  and Prandtl number:  $Pr = \frac{\nu_f}{\alpha_f}$ . The other parameters appearing in Eqs. [1]-[3] are explained in the following paragraph. . No slip condition is supposed on all walls.  $T = T_h$  for the left wall,  $T = T_c$  for the right wall and  $\partial T / \partial n = 0$  for the other four walls are the thermal boundary conditions adopted for this problem.

### 2. 3. Nanofluid thermo-physical properties

The  $\text{Fe}_3\text{O}_4$ -water effective density, specific heat, and thermal expansion coefficient [15, 10], are expressed by:

$$\rho_{nf} = (1 - \phi) \rho_f + \phi \rho_s \quad (4)$$

$$(\rho c_p)_{nf} = (1 - \phi) (\rho c_p)_f + \phi (\rho c_p)_s \quad (5)$$

$$(\rho \beta)_{nf} = (1 - \phi) (\rho \beta)_f + \phi (\rho \beta)_s \quad (6)$$

In the above equations,  $f$ ,  $nf$  and  $s$  are indices indicating base fluid, nnf and nnps respectively.

The Maxwell model [16] is used to calculate nanofluid electrical conductivity:

$$\sigma_{nf} = \sigma_f \left[ 1 + \frac{3 \phi (c - 1)}{(c + 2) - \phi(c - 1)} \right] \quad (7)$$

Where  $c = \sigma_s / \sigma_f$ .

For small solid volume fractions of  $\text{Fe}_3\text{O}_4$ -water, correlations have been developed experimentally for computing the dynamic viscosity [13] and thermal conductivity [14]. These correlations are chosen to model these physical properties respectively:

$$\mu_{nf} = \mu_f (1.01 + 0.007165 T^{1.171} \phi^{1.509}) \exp(-0.00719 T) \quad (8)$$

$$k_{nf} = k_f (0.7575 + 0.3 \phi^{0.323} T^{0.245}) \quad (9)$$

Where T is in  $^{\circ}\text{C}$  and  $\phi$  is in %.

At the left hot wall, the local Nu number is calculated by:

$$Nu = -(k_{nf}/k_f)(\partial \theta / \partial X)_{X=0} \quad (10)$$

and the average Nu number is defined by:

$$Nu_{avg} = \int_0^1 \int_0^1 Nu dY dZ \quad (11)$$

### 2. 4. Numerical method

The simulations are made through ANSYS fluent 14.5, based on finite volume method developed by Patankar [17]. For coupling pressure and the velocity field, the SIMPLE algorithm is adopted, and for pressure discretization a PRESTO scheme is applied. The 2-order upwind-scheme is chosen for discretizing the convection-diffusion terms.

## 2. 5. Grid independency

A test of sensibility of five mesh sizes is conducted as shown in Table 2. The  $Nu_{avg}$  is calculated for natural convection of  $\text{Fe}_3\text{O}_4$ -water nnf when  $Ra=10^4$ ,  $\phi = 0.01$ ,  $Ha = 10$  with MF applied in temperature gradient direction (Bx). The code convergence test for this simulation is :  $\max|\Gamma^{n+1} - \Gamma^n| < 10^{-6}$  where  $\Gamma$  replaces the unknown variables (U, V, W, θ) describing the thermos-hydrodynamic behavior in the cavity and n is the number of iterations. A grid size of  $71^3$  is chosen because it ensures the grid independent solution and gives a good agreement between the precision and the calculation time.

Table 2. Grid independency,  $Ra = 10^4$ ,  $\phi = 0.01$ ,  $Ha = 10$  (Bx)

Mesh size	$41^3$	$51^3$	$61^3$	$71^3$	$81^3$
$Nu_{avg}$	1.9998	1.9452	1.9261	1.9266	1.9267

## 2. 6. Validation of the solution

The code used in this simulation is validated by the results found by Al-Rashed study [2]. Fig. 2 shows a good agreement with the  $Nu_{avg}$  values at hot wall for CuO-water nnf filled a cubical cavity for  $Ra = 10^5$  with horizontal external uniform MF (Bx) and for three Ha values (0, 50 and 100).

## 3. RESULTS AND DISCUSSION

This study was realized, first, for pure water ( $\phi = 0$ ) and then for  $\text{Fe}_3\text{O}_4$ -water nnf ( $\phi = 0.02$ ). The simulations are carried out for five values of MF strength, four Rayleigh numbers (Ra), and for three main directions of MF. Fig.3(a) and Fig.3(b) present the variation of the dimensionless number ( $Nu_{avg}$ ), reflecting the rate of convective heat transfer at the left hot wall, depending on Ha number (in each direction separately) for pure water ( $\phi = 0$ ) and for nnf ( $\phi = 0.02$ ) and this, for  $Ra = 10^3$  and  $Ra = 10^6$  respectively. The first thing to notice, that a raise in  $\phi$  conducts to higher heat transfer rate in all MF directions. Also, the diminution in the  $Nu_{avg}$  with the augmentation of Ha, resulting from the development of Lorentz magnetic forces is clearly visible for the three MF directions. It is also interesting to conclude from these two figures, the clear and net effect of varying MF direction on the amount of the convective heat transfer within this studied cavity. The most significant reduction in the heat transfer is recorded when the direction of MF is horizontal, i.e. parallel to the temperature gradient. In second position, for the decrease of heat transfer rate, comes the vertical direction z of the MF, i. e. parallel to the gravitational field. Fig. 4 illustrates the Ra influence on ( $Nu_{avg}$ ) for ( $Ha=20$ ), for  $\phi = 2\%$  and for the MF applied in each of the three directions. The buoyancy forces that increase by raising Ra greatly enhance the rate of thermal transfer for the three MF directions. In this figure, it is noteworthy that the largest decrease in  $Nu_{avg}$  is recorded when MF is directed along the x-axis which is consistent with the above results. Fig. 5 presents the effect of increasing Ha on ( $Nu_{avg}$ ) for four values of Ra, for ( $\phi = 0.02$ ) and when the application of MF is directed horizontally along x axis (Bx). The attenuation effect on heat transfer caused by raising Ha visibly increases with the increase in Ra. This means that the Lorentz forces developed by MF presence, work better at reducing heat transfer when the natural convection regime is dominant.

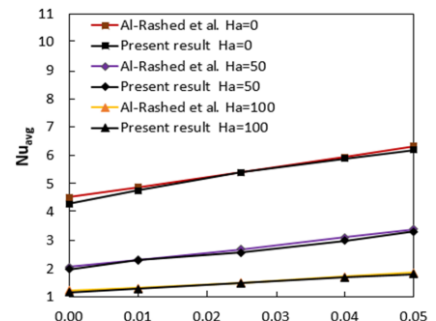


Figure 2. Present code validation with results of Al-Rashed et al. [2]

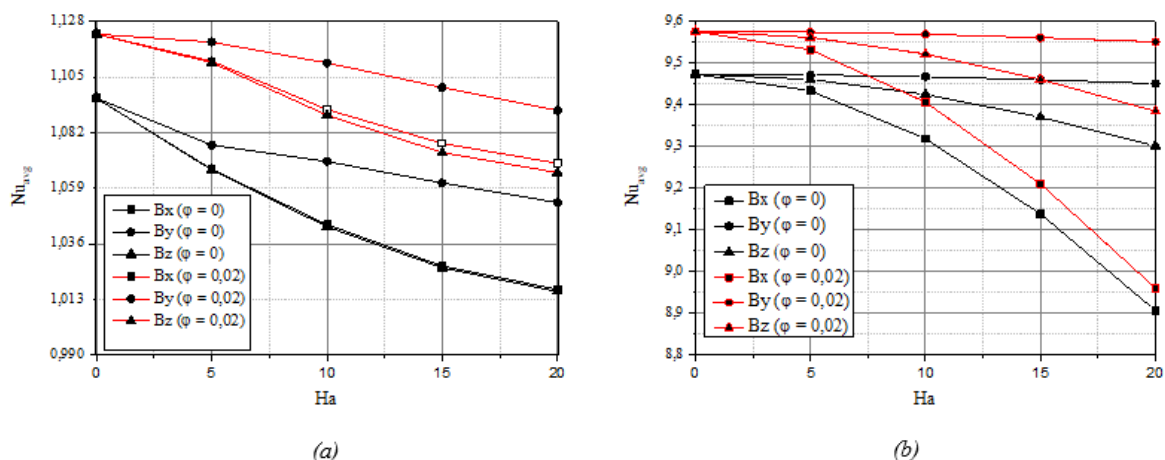


Figure 3.  $Nu_{avg}$  at the hot wall with  $Ha$  for three MF directions. (a)  $Ra=10^3$ , (b)  $Ra=10^6$

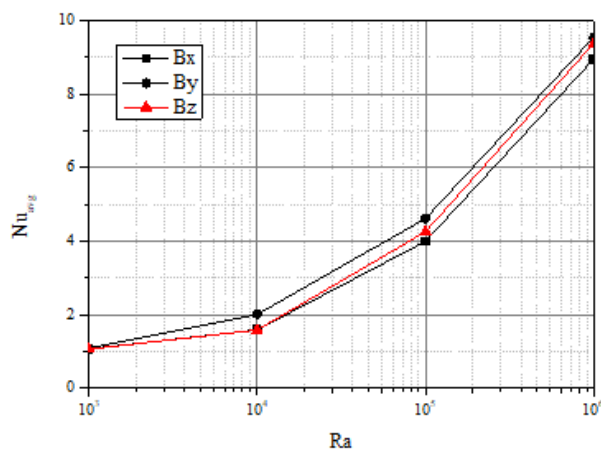


Figure 4.  $Nu_{avg}$  at hot wall with the  $Ra$  for  $Ha=20$ , for three directions of MF and for  $\phi = 0.02$

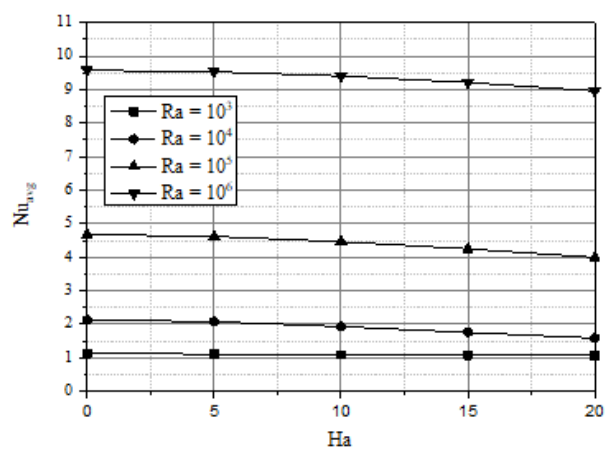


Figure 5.  $Nu_{avg}$  at hot wall with  $Ha$ ,  $Bx$  and  $\phi = 0.02$

#### 4. CONCLUSION

Numerical 3D simulations were carried out in order to shed light on the effect of changing the direction of a MF applied externally to a cubical enclosure on the natural convection of the  $Fe_3O_4$ -water nanofluid which fills it. The direction of MF changes along the three main axis. Results indicate that MF can be used for controlling natural convection in a cubical enclosure. Free convection in the cavity is enhanced with augmentation of buoyancy forces and solid volume fraction but suppressed with rise of Lorentz force resulting from the application of a uniform external MF in one of the three main directions. As the magnetic field magnitude augments, the decrease slope of the Nu number increases with growing Ra number. Applying the magnetic field in the horizontal direction (parallel to temperature gradient) dampens the convection to a greater degree than in the other two directions. In second place, in terms of damping, comes vertical direction of magnetic field (gravity direction).

#### REFERENCES

- [1] M. Sannad, B. Abourida, L. Belarache, H. Doghmi, Numerical Study of Natural Convection in a Three-dimensional Cavity Filled with Nanofluids 2016. Inter. Journal of Computer Science, 13: 51-61. <<https://doi.org/10.20943/01201605.5161>>
- [2] A. A.A.A. Al-Rashed, K. Kalidasan, L. Kolsi, A. Aydi, E. H. Malekshah, A. K. Hussein, P. R. Kanna, Three-dimensional investigation of the effects of external magnetic field inclination on laminar natural convection heat transfer in CNT–water nanofluid filled cavity 2017. Journal of Molecular liquids, 252: 454-468. <<https://doi.org/10.1016/j.molliq.2018.01.006>>
- [3] M. Sheikholeslami, R. Ellahi, Three dimensional mesoscopic simulation of magnetic field effect on natural convection of nanofluid 2015. International Journal of Heat and Mass Transfer, 89: 799-802. <<http://dx.doi.org/10.1016/j.ijheatmasstransfer.2015.05.110>>

- [4] D. D. Dixit and A. Pattamatta, Natural convection heat transfer in a cavity filled with electrically conducting nanoparticle suspension in the presence of magnetic field, Physics of fluids 2019. 31(2): 023302. <<https://doi.org/10.1063/1.5080778>>
- [5] D. D. Dixit and A. Pattamatta, Effect of uniform external magnetic field on natural convection heat transfer in a cubical cavity filled with magnetic nano-dispersion, International Journal of Heat and Mass Transfer 2020: 146, 118828. <<https://doi.org/10.1016/j.ijheatmasstransfer.2019.118828>>
- [6] M. Sheikholeslami, M. Gorji Bandpy, H. R. Ashorynejad, Lattice Boltzmann Method for simulation of magnetic field effect on hydrothermal behavior of nanofluid in a cubic cavity 2015. Physics A, <<https://doi.org/10.1016/j.physa.2015.03.009>>
- [7] M. Sheikholeslami, R. Ellahi, K. Vafai. Study of Fe<sub>3</sub>O<sub>4</sub>-water nanofluid with convective heat transfer in the presence of magnetic source. Alexandria Engineering Journal 2018; 57:565–75. <https://doi.org/10.1016/j.aej.2017.01.027>
- [8] S. O. Giwa, M. Sharifpur, M. H. Ahmadi, J. P. Meyer, A review of magnetic field influence on natural convection heat transfer performance of nanofluids in square cavities. Journal of Thermal Analysis and Calorimetry 2020. <<https://doi.org/10.1007/s10973-020-09832-3>>
- [9] B. Ghasemi, S. M. Aminossadati and A. Raisi, Magnetic Field Effect on Natural Convection in a Nanofluid-filled Square Enclosure 2011. Int. Journal of Thermal Sciences, 50: 1748-1756. <<https://doi.org/10.1016/j.ijthermalsci.2011.04.010>>
- [10] H. F. Oztop, E. Abu-Nada, Numerical study of natural convection in partially heated rectangular enclosure filled with nanofluid 2008. International Journal of Heat and Fluid Flow. 29 : 1326-1336.  
    <<https://doi.org/10.1016/j.ijheatfluidflow.2008.04.009>>
- [11] S. U.S. Choi, Jeffrey A Eastman, Enhancing thermal conductivity of fluids with nanoparticles 1995, ASME International Mechanical Engineering Congress & Exposition, November 12-17, San Francisco, CA. <<https://www.researchgate.net/publication/236353373>>
- [12] C. J. Ho, M. W. Chen, and Z. W. Li, Numerical simulation of natural convection of nanofluid in a square enclosure: effects due to uncertainties of viscosity and thermal conductivity 2008,” International Journal of Heat and Mass Transfer, 51, 17-18, <4506–4516 <https://doi.org/10.1016/j.ijheatmasstransfer.2007.12.019>>
- [13] D. Toghraie, S. Mohammadbagher Alempour, M. Afrand, Experimental determination of viscosity of water based magnetite nanofluid for application in heating and cooling systems 2016. Journal of Magnetism and Magnetic Materials, <<http://dx.doi.org/10.1016/j.jmmm.2016.05.092>>
- [14] M. Afrand a, D. Toghraie, N. Sina, Experimental study on thermal conductivity of water-based Fe<sub>3</sub>O<sub>4</sub> nanofluid: Development of a new correlation and modeled by artificial neural 2016. International Communications in Heat and Mass Transfer 2016, 75: 262-269. <<https://doi.org/10.1016/j.icheatmasstransfer.2016.04.023>>
- [15] K. Khanafaer, K. Vafai, M. Lightstone, Buoyancy-driven heat transfer enhancement in a two-dimensional enclosure utilizing nanofluids. International Journal of Heat and Mass Transfer 2003. 46 : 5181-5188. <[https://doi.org/10.1016/S0017-9310\(03\)00156-X](https://doi.org/10.1016/S0017-9310(03)00156-X)>
- [16] J.C. Maxwell, A Treatise on Electricity and Magnetism, second ed. Oxford University Press, Cambridge, 1904, 435e441.
- [17] S.V. Patankar, Numerical Heat Transfer and Fluid Flow, Hemisphere, McGraw Hill, New Y



## BIO-ENERGY CHARACTERISTICS OF BLACK PINE (*PINUS NIGRA ARN.*) HYDRODISTILLATION WASTE PRODUCTS

Hafize Fidan

University of Food Technologies, Plovdiv, 4002, Bulgaria, hfidan@abv.bg, ORCID: <https://orcid.org/0000-0002-3373-5949>

Stanko Stankov

University of Food Technologies, Plovdiv, 4002, Bulgaria, docstankov@gmail.com ORCID: <https://orcid.org/0000-0003-2332-1782>

Nadezhda Petkova

University of Food Technologies, Plovdiv, 4002, Bulgaria, petkovanadejda@abv.bg, ORCID: <https://orcid.org/0000-0002-5870-9157>

Bozhidar Bozadziev

University of Food Technologies, Plovdiv, 4002, Bulgaria, bbozadjiev@yahoo.de, ORCID: <https://orcid.org/0000-0003-4200-140X>

Milen Dimov

Trakia University, Department of Food Technology, Yambol, 8600, Bulgaria, midimow@abv.bg, ORCID: <https://orcid.org/0000-0002-8339-3932>

Lazar Lazarov

University of Food Technologies, Plovdiv, 4002, Bulgaria, lazarinii@abv.bg, ORCID: <https://orcid.org/0000-0002-6071-7949>

Apostol Simitchiev

University of Food Technologies, Plovdiv, 4002, Bulgaria, asimitchiev@uft-plovdiv.bg, ORCID: <https://orcid.org/0000-0002-2330-8572>

Albena Stoyanova

University of Food Technologies, Plovdiv, 4002, Bulgaria, aastst@abv.bg, ORCID: <https://orcid.org/0000-0001-7140-7826>

*Fidan, H, Stankov, S, Petkova, N, Bozadziev, B, Dimov, M, Lazarov, L, Simitchiev, A, Stoyanova, A. Bio-energy characteristics of black pine hydrodistillation waste products (*Pinus nigra Arn.*). 9<sup>th</sup> Eur. Conf. Ren. Energy Sys. 21-23 April 2021, Istanbul, Turkey*

### Abstract:

The aim of this study was to determine the characteristics of a biomass, obtained after hydrodistillation of different parts of *Pinus nigra Arn.*, growing in Bulgaria, due to revealing potential use in the production of pellets. The biomass, comprised of needles and needles with twigs, was milled and subjected to sieve analysis, thus producing three groups of particle fractions. The results from the study revealed significant differences in the phytochemical composition. Particle fractions were characterized in terms of moisture content (7.10-7.95%), ash (1.96-2.89%), cellulose (21.30-29.20%), total chlorophyll (225.54-896.04 µg/g), total carotenoids (23.52-145.43 µg/g), and polysaccharides (0.14-2.06%). The basic energy indices used in the assessment of biomass potential as conditional fuel were calculated as follows: heating value (16748.79-16877.86 kJ/kg), the density of wood biomass (390.99-421.17 kg/m<sup>3</sup>), and heat equivalent (0.224-0.243 J/m<sup>3</sup>). Our findings revealed that black pine waste products could be used as a potential renewable energy source due to its bio-energy characteristics.

**Keywords:** Bio-energy, renewable, *Pinus nigra*, pellets, waste products

© 2021 Published by ECRES

## 1. INTRODUCTION

The modern world's environmental challenges enhanced the need to look for alternative solutions for renewable energy sources. The biomass generated from forestry and garden, park, food, kitchen, and waste from processing is increasing. Therefore, it is necessary to use biomass' efficiency by increasing its energy consumption and through innovative approaches to its combustion (Bilandzija et al., 2018). Biomass obtained from various plant sources is an inexhaustible energy source during combustion due to its ability to consume as much carbon as it absorbs during its growing season. This ability places biomass in the group of renewable energy sources producing clean or "green" energy. Its main advantage is to lower greenhouse gas emissions compared to conventional fuels (Móricz et al., 2018). Forest waste, part of the timber industry, is a source of biochar, bio-oil, biofuels, energy pellets, and electricity produced by thermochemical conversion methods (Hmaied et al., 2019). In recent years, chips are various raw materials that remain as waste in the agricultural, food, essential oil, timber, and other industries. They are considered and used as a potential source of biomass for the production of pellets, briquettes. The circular economy and its connection to the bio-energy supply are objects at the local level (Sherwood, 2020). The potential of biomass used for extraction of phytochemicals can be cogenerated by the construction of modern combustion plants providing over 60% of the total energy produced in the region, meeting the needs of public buildings or households (Ferreira et al., 2014). Many authors have conducted studies on some physical, chemical, and energy characteristics of biomass. They reported data for pellet characteristics obtained by soybean culture, sugarcane bagasse, eucalyptus wood (Scatolino et al., 2017), waste from agriculture (Holubcik et al., 2015), industrial wood wastes, and peach stone (Rabacal et al., 2013), and waste from woody juniper (Lazarov et al., 2020).

The primary source of wood for energy needs in Bulgaria is forests, that occupy about 34% of the country's territory. About 18% of forest plantations are occupied by conifers - white pine, black pine, spruce, fir, and other species. Apart from being a source of wood, coniferous plants are also processed to obtain essential oils, with the main application in the perfume, cosmetics industry and medicine (Georgiev and Stoyanova, 2006). After the essential oil extraction, which in coniferous plants is mainly consisted in the leaves and thin branches, as well as in the wood. Large amounts of waste remain, which are utilized for the production of various biomass: energy wood chips, tree bark, wood pellets, wood briquettes, etc. (Sabeva et al., 2012; Stoyanova et al., 2014), and for the preparation of other products (Georgiev and Stoyanova, 2006).

In order to appropriately apply bioenergy efficiency in the recovery of biomass from the timber or processing industry, it is necessary to assess its bioenergy potential, both from a consumer point of view and the management of waste products. The characteristics of the input biomass determined the production of pellets, which is a multi-stage process (Pantaleo et al., 2020). To the best of our knowledge, a gap of data concerning biomass characteristics of coniferous and other plants hydrodistillation waste products was observed. Therefore, the aim of the present study was to characterize the biomass from the needles and twigs of black pine growing in Bulgaria obtained after essential oil extraction in order to get raw material for the production of pellets with specific energy potential.

## 2. MATERIAL AND METHODS

*Plant material.* The needles with thin twigs of black pine (*P. nigra* Arn.) growing in Bulgaria were used. The raw material was collected during the spring of 2020. The species has been identified in Agricultural University, Plovdiv. Before processing, the raw material was cut into particle size 1.5-2.5 cm. It was processed by hydrodistillation into a laboratory distillation apparatus according to the British Pharmacopoeia, modified by Balinova and Diakov (1974).

After hydrodistillation, the waste material was subjected to drying by adjusting the humidity (75±2%) and the thickness of the layer of material 2-3 cm. Forced air circulation (0.2 m/s) was provided in the drying rooms (25°C), ensuring even drying and avoiding the development of molds. The biomass was separated on sieve bases and was periodically stirred mechanically during drying process.

*Sieve analysis.* The biomass was grounded (Lazarov et al., 2020).

*Physical and chemical characteristics.* The moisture content of the biomass was determined by drying to constant weight (AOAC, 2005), and the results from the chemical analyses were given on a dry weight basis (dw). The ash content was determined according to AOAC, 2005, by igniting the samples at 550°C for 5 hours. The infrared spectrum was recorded using a Nicolet iS 50 (Thermo Scientific, USA) FT-IR spectrometer in the frequency region of 4000–400  $\text{cm}^{-1}$ , with the samples embedded in KBr matrixes. The total chlorophylls and carotenoid contents were measured, according to the methods described by Lichtenthaler and Buschmann (1983), and Lichtenthaler and Wellburn (2001). The total soluble carbohydrate content was determined according to the method reported by Dubois et al. (1956). Sucrose, glucose, and fructose were analysed by HPLC method (Hadjikinova et al., 2017). The cellulose content was determined following the method of Brendel et al. (2000).

*Energy characteristics.* The heating value (kJ/kg), density of wood biomass ( $\text{kg}/\text{m}^3$ ), and heat equivalent ( $\text{J}/\text{m}^3$ ) were calculated by the methods of Stoyanova et al. (2014).

*Statistical analysis.* The measurements were performed in triplicate and the results were presented as the mean value of the individual measurements with the corresponding standard deviation (SD), using Microsoft Excel.

### 3. RESULTS AND DISCUSSIONS

*Sieve analysis.* The biomass origin and its moisture, temperature, and grinding system influenced the susceptibility to digestion (Jewiarz et al., 2020). The primary fractioned amounts of ground biomass are presented in Table 1. The data showed that the density of distribution of the three samples fractions had similar values in the studied range of size classes. Therefore, the similar average diameters (between 384 and 413 µm) of the particles of the three samples were determined. According to our results, the particle size distribution was uneven. The reason for this could be considered with the different strength in the structure of the vegetative plant parts. The highest distribution density was reported in class size 500/355 µm. Larger particles predominated, mainly from the woody part of the branches, which had higher strength and significantly impact resistance, despite of their low humidity. The finer sieving fractions were composed of ground green needles from pine twigs, and they were easier to grind. The digestion of the biomass and the particle size determined the density of the obtained pellets and, at a later stage, the rate of their combustion (Jewiarz et al., 2020).

Table 1. Fractional characteristic of *P. nigra* biomass

Size class, µm	Needles with twigs		$q_i^*, \text{mm}^{-1}$	Needles (sample 1)		Needles (sample 2)		$q_i, \text{mm}^{-1}$
	m, g	m, %		m, g	m, %	qi, mm <sup>-1</sup>	m, g	
0 – 132	2.0	0.015	0.11	6.8	0.057	0.43	15.6	0.130
132 – 150	0.5	0.004	0.22	0.4	0.003	0.19	0.5	0.004
150 – 180	0.5	0.004	0.13	0.3	0.003	0.08	0.4	0.003
180 – 200	3.0	0.023	1.15	3.3	0.028	1.38	1.7	0.014
200 – 280	5.0	0.038	0.48	3.4	0.028	0.36	1.2	0.010
280 – 355	2.0	0.015	0.20	0.6	0.005	0.07	0.7	0.006
355 – 450	64.0	0.481	5.34	44.5	0.373	4.14	45.4	0.378
450 – 500	56.0	0.421	8.42	60.0	0.503	10.06	54.6	0.455
$\Sigma, \text{g}$	133.0			119.3			120.1	
Medium diameter, µm	413.9			407.4			384.7	

\*Note:  $q_i$ - density of distribution

The particle size distribution of the biomass and the density of distribution of the fractions in the sample needles with twigs are presented in the Table 2. The grinding process and the granulometric evaluation of the biomass provided information on the degree of fragmentation of the particles during the production of the pellets in the presence of pressure. By reducing the volume of the particles, an adequate adhesion between them is ensured without changing the shape of the pellets and forming air pores (Anukam et al., 2020). The size of the biomass digestion corresponds to the digestion rates recommended by other authors (Kruszelnicka et al., 2020) for biomass from plant species used for pellet production.

Table 2. Particle size distribution and distribution density of ground biomass

Nº	Sieve light opening, $x_i, \text{mm}$	Mass part, $\Delta D_i [-]$	Class width, $\Delta x_i, \text{mm}$	Density of distribution, $q_i = \Delta D_i / \Delta x_i, \text{mm}^{-1}$
1	0 – 0.132	0.421	0.132	0.11
2	0.132 – 0.150	0.481	0.018	0.22
3	0.150 – 0.180	0.015	0.030	0.13
4	0.180 – 0.200	0.038	0.020	1.15
5	0.200 – 0.280	0.023	0.080	0.48
6	0.280 – 0.355	0.004	0.075	0.20
7	0.355 – 0.450	0.004	0.090	5.34
8	0.450 – 0.500	0.015	0.050	8.42

*Physical and chemical indices.* The IR spectrum of biomasses is shown in Table 3. All three samples contained OH group, which was confirmed by the absorption bands in the three samples (for needles with twigs ( $3423 \text{ cm}^{-1}$ ), for sample 1 ( $3421 \text{ cm}^{-1}$ ), and for sample 2 ( $3432 \text{ cm}^{-1}$ )), which is further confirmed at the absorption strips for the

sample of needles with twigs ( $2362\text{ cm}^{-1}$ ), sample 1 ( $2360\text{ cm}^{-1}$ ) and sample 2 ( $2361\text{ cm}^{-1}$ ). For the twig needle sample, an absorption band appeared at  $1735\text{ cm}^{-1}$ , a characteristic band for an aldehyde carbonyl group. All three samples have characteristic absorption bands for *cis*- a double bond of the type  $\text{HRC}=\text{CR}'\text{H}$ , respectively at  $1636$ ,  $1637$ , and  $1637\text{ cm}^{-1}$ . The sample of twig needles and sample 1 had absorption bands at  $1517\text{ cm}^{-1}$ , characteristic of an aromatic nucleus band (oscillations for  $\gamma\text{ C=C}$ ). It is noteworthy that in the sample of needles with stems and sample 1 there are characteristic bands of aromatic and vinyl ethers of the type  $=\text{C}-\text{O}-\text{C}$ ,  $\gamma$  as  $\text{C}-\text{O}-\text{C}$ , at a wavelength of  $1262$  and  $1246\text{ cm}^{-1}$ , which is absent in sample 2. Additionally some bands typical for carbohydrates, especially lignin and cellulose were observed (Table 3), that could be explained with high cellulose content in samples. A band around  $1457\text{ cm}^{-1}$  was due to deformation of lignin  $\text{CH}_2$  and  $\text{CH}_3$  and  $1636\text{ cm}^{-1}$  was typical for stretching of the  $\text{C}=\text{C}$  and  $\text{C}=\text{O}$  lignin aromatic ring. A band at  $1735\text{ cm}^{-1}$  was assigned to  $\text{C}=\text{O}$  stretching of unconjugated hemicellulose while the band at  $2925\text{ cm}^{-1}$  was due to asymmetrical stretching of  $\text{CH}_2$  and  $\text{CH}$ . Our observation coincided with the bands reported in literature (Lun et al., 2017) which denoted the characteristics of cellulose. The obtained diffraction peaks corresponded to the previously reported (Paul et al., 2012) showed the difference in the intensities of the peak maxima in the three samples. The obtained carbon bands took into account the carbon fraction obtained in the thermochemical processes. Smaller bands with a visibly smaller volume showed  $\text{C}-\text{C}$  bonds presence and the emergence of additional energy forces forming small volumes, but relatively good conducting electrochemical waves (Paul et al., 2016). The biomass of tree species was composed mainly of cellulose, hemicellulose, and lignin substances. Thus, it was lignocellulose biomass that contained about 50% carbon and 6 to 10% hydrogen (Szufa et al., 2020; Wróbel et al., 2020). The energy characteristics of cellulose and hemicellulose were similar, with about 17.6 and 17.9 MJ/kg, as the energy equivalent of lignin in the biomass composition was decisive in plant species.

Table 3. IR spectrum of *P. nigra* biomass

Characteristic bands ( $\text{cm}^{-1}$ )				Group type
Needles with twigs	Needles (Sample 1)	Needles (Sample 2)	Reference data	
3423	3421	3432	3550 – 3400, 3590 – 3420	vOH intra- and intermolecular H – bond
2925	2925	2924	2940 – 2915	$\nu_{\text{as}}-\text{CH}_2-$
2362	2360	2361	3110 – 2362	vibration of $\gamma(\text{OH})$ bond
1735	1735	1735	1740 – 1720	$\text{R}-\text{CHO}\ \nu_{\text{C=O}}$ ; characteristic band of carbonyl group
1636	1637	1637	1665 – 1635	a characteristic band for <i>cis</i> - $\text{HRC}=\text{CR}'\text{H}$ bond
1517	1517	-	1525 – 1475	a characteristic band of the type $\nu\text{ C=C}$
1458	1449	-	1480 – 1450	linear $-\text{CH}_2-$ bond; $\nu\text{C-Hs(CH}_2\text{)}_2$ in pyranose ring, $\beta\text{o-H(OH)}$ for carbohydrates
1375	1384	1384	1385 – 1370	a characteristic band of the type $\text{C}(\text{CH}_3)_2$
1262	1246	-	1275 – 1200	$=\text{C}-\text{O}-\text{C}$ , $\nu_{\text{as}}\text{C}-\text{O}-\text{C}$ , aromatic and vinyl
1031	1031	1030	1070 – 1000	trisubstituted aromatic ring $\gamma\text{Ar-H}$ in positions 1,2,4; $\nu\text{C-O}$ ( $\text{C}-\text{O}$ ) from pyranose ring for carbohydrates

The physicochemical data obtained for the composition of the biomass are presented in Table 4. The moisture content was in low levels for plant material and did not exceed 8%, while the ash content varies between 1.96 and 2.89. The results in our study showed that values for ash content were higher than those presented for pine (1.21%) by Sabeva et al. (2012) and (1.3%) reported by Rabacal et al. (2015) but were comparable to those determined for pine and eucalyptus (0.59-2.69%) by Nunez et al. (2013). It is known that lignocellulosic biomass has a low ash content (0.2-1.8%), which is considered as a guarantee for the absence of slag, which is formed in biogenic fuels containing more than 4% ash. Compared to other types of biomass (from 38 to 56%), the lower content of cellulose could be explained by the processed raw material, containing mainly leaves with thin branches bearing them, where the essential oil is deposited. The needles had a higher content of chlorophyll and carotenoids, which could be explained by the photosynthesis that takes place during the spring season when the samples were collected. Deligöz et al. (2018) published results for three years investigation of *Pinus nigra* subsp. *pallasiana* (Lamb.) Holmboe about seasonal patterns variations in total soluble carbohydrate chlorophyll, carotenoids in needles. Our data for total soluble sugars were slightly lower than total soluble carbohydrate content in Anatolian black pine, where they varied from 33.60 to 78.26 mg/g (Deligöz et al., 2018) and four times lower than soluble sugar content in Scots pine needles (Mandre et al., 2002). This could be explained with climate conditions, different variety and seasonal changes in carbohydrate accumulation (Deligöz et al., 2018). Extraction of the essential oil during hydrodistillation changed the structure of the cell walls and increased the reactivity of the subsequent heterogeneous reactions related

to combustion (Donohoe et al., 2008). The change in the crystal structure of cellulose during hydrodistillation increased the availability of individual cellulose filaments. It improved the specific contact surface (Yingfu et al., 2013), as a result of which combustion could be regulated and used in automated combustion plants.

*Table 4. Physical and chemical indices of *P. nigra* biomass*

Indices	Needles with twigs	Needles (sample 1)	Needles (sample 2)
Moisture, %	7.10 ± 0.61	7.50 ± 0.71	7.95 ± 0.76
Ash, %	2.66 ± 0.20	1.96 ± 0.10	2.89 ± 0.21
Total carotenoids, µg/g	23.52 ± 2.03	145.43 ± 1.22	80.20 ± 0.52
Total chlorophylls, µg/g	225.54 ± 19.54	896.04 ± 8.82	379.05 ± 6.90
- Chlorophyll a	136.81 ± 29.86	688.04 ± 12.34	218.93 ± 11.52
- Chlorophyll b	88.73 ± 8.64	208.74 ± 5.22	152.57 ± 2.32
Total carbohydrates, %	29.12 ± 1.05	23.43 ± 1.00	31.12 ± 0.85
Cellulose, %	26.10 ± 0.25	21.30 ± 0.20	29.20 ± 0.27
Total sugars, %	2.06 ± 0.2	0.28 ± 0.0	0.14 ± 0.0
- Sucrose	0.70 ± 0.0	Not detected	Not detected
- Glucose	0.45 ± 0.0	0.12 ± 0.0	0.05 ± 0.0
- Fructose	0.91 ± 0.0	0.16 ± 0.0	0.09 ± 0.0

*Energy characteristics.* The calculated energy characteristics are presented in Table 5. The data showed that the calorific values obtained for *P. nigra* biomass in this study were lower than the data in the literature. Sabeva et al. (2012) reported calorific values for pine (16886-17740 kJ/kg) and spruce (18532-19106 kJ/kg) pellets. Our results were comparable to those reported for pine and eucalyptus (16.53-18.13 MJ/kg) pellets by Nunez et al. (2013) and for juniper pellets by Lazarov et al. (2020), understandably with higher ash and moisture content. Biomass density values obtained in this study were lower than that reported in the literature for other biomass (> 650 kg/m<sup>3</sup>) presented by (Nunez et al., 2013; Stoyanova et al., 2014). The differences could be explained by the origin of the raw material, the size of grinding, and moisture content of the plants.

*Table 5. Energy indices of *P. nigra* biomass*

Indices	Calorific value, kJ/kg	Density, kg/m <sup>3</sup>	Heat equivalent, J/m <sup>3</sup>
Needles with twigs	16877.86	421.17	0.243
Needles (sample 1)	16828.26	414.55	0.238
Needles (sample 2)	16748.79	390.99	0.224

#### 4. CONCLUSION

The biomass of *P. nigra* grown in Bulgaria was a residual and waste product obtained during the essential oil production. The biomass, comprised of needles and needles with twigs, was characterized with content of different compounds. The biomass could be considered as a potential source for biofuel production due to the obtained energy indices as the calorific value, biomass density, and heat equivalent. The results from this study may provide an alternative route for residue disposal with the added benefit of energy recovery.

#### ACKNOWLEDGMENT

The authors acknowledge the support by the National Science Fund of Bulgaria, project No KP-06-H36/14.

#### REFERENCES

- [1] Anukam, AI, Berghel, J, Famewo, EB, Frodeson, S. Improving the Understanding of the Bonding Mechanism of Primary Components of Biomass Pellets through the Use of Advanced Analytical Instruments. Journal of Wood Chemical Technology 2020; 40: 15-32.
- [2] AOAC. Method 930.05. Ash of plants. Official Methods of Analysis (Horwitz, W. & Latimer Jr., G.W., Eds.). Gaithersburg, MD, USA: AOAC International, 2005.
- [3] Balinova, A, Diakov, G. On improved apparatus for microdistillation of rose flowers. Plant Science 1974; 11: 77-85.
- [4] Bilandzija, N, Voca, N, Jelcic, B, Jurisic, V, Martin, A, Grubor, M, Kricka, T. Evaluation of Croatian agricultural solid biomass energy potential. Renewable and Sustainable Energy Reviews 2018; 93: 225-230.

- [5] Brendel O, Iannetta, P, Stewart, D. A rapid and simple method to isolate pure  $\alpha$ -cellulose. *Phytochemical Analysis* 2000; *11*: 7-10.
- [6] Deligöz, A, Bayar, E, Genç, M, Karatepe, Y, Kirdar, E, Cankara, FG. Seasonal and needle age-related variations in the biochemical characteristics of *Pinus nigra* subsp. *pallasiana* (Lamb.) Holmboe. *Journal of Forest Science* 2018; *64*: 379-386.
- [7] Donohoe, BS, Decker, SR, Tucker, MP, Himmel, ME, Vinzant, TB. Visualizing lignin coalescence and migration through maize cell walls following thermochemical pretreatment. *Biotechnology and Bioengineering* 2008; *101*: 913-925.
- [8] Dubois, M, Gilles, K, Hamilton, J, Rebers, P, Smith, F. Colorimetric method for determination of sugars and related substances. *Analytical Chemistry* 1956; *28*(3): 350-356.
- [9] Ferreira, PT, Ferreira, ME, Teixeira, JC Analysis of Industrial Waste in Wood Pellets and Co-combustion Products. *Waste and Biomass Valorization* 2014; *5*: 637-650. <https://doi.org/10.1007/s12649-013-9271-6>
- [10] Georgiev, E, Stoyanova, A. A guide for the specialist in the aromatic industry. Plovdiv, 2006.
- [11] Hadjikinova, R, Petkova, N, Hadjikinov, D, Denev, P, Hrusavov, D. Development and validation of hplc-rid method for determination of sugars and polyols. *Journal of Pharmaceutical Sciences and Research*. 2017; *9*: 1263-1269.
- [12] Hmaied, M, Bouafif, H, Magdouli, S, Braghierioli, FL, Koubaa, A. Effect of Forest Biomass Pretreatment on Essential Oil Yield and Properties. *Forests* 2019; *10*: 1042; doi:10.3390/f10111042.
- [13] Holubcik, M, Jachniak, E, Jandacka J. Utilization of materials from agriculture to produce pellets. *Archives of Waste Management and Environmental Protection* 2015; *17*(2): 1-10.
- [14] Jewiartz, M, Wrobel, M, Mudruk, K, Szufa, S. Impact of the Drying Temperature and Grinding Technique on Biomass Grindability. *Energies* 2020; *13*: 3392; doi:10.3390/en1313392.
- [15] Kruszelnicka, W, Kasner, R, Bałdowska-Witos, P, Flizikowski, J, Tomporowski, A. The Integrated Energy Consumption Index for Energy Biomass Grinding Technology Assessment. *Energies* 2020; *13*: 1417.
- [16] Lazarov, L, Bozadzhiev, B, Simitchiev, A, Stoyanova, A. Characteristics of Biomass from Distilled Greek Juniper Needles. *Youth Forum Science, Technology, Innovation, Business – 2020*, Plovdiv, 42-47.
- [17] Lichtenhaler, H, Wellbum, A. Determination of Total Carotenoids and Chlorophylls a and b of Leaf in Different Solvent. *Biochemical Society Transactions* 1983; *11*: 591-592.
- [18] Lichtenhaler, H, Buschmann, C. Extraction of Phytosynthetic Tissues: Chlorophylls and Carotenoids. *Current Protocols in Food Analytical Chemistry* 2001; *1*: F4.2.1-F4.2.6.
- [19] Lun, LW, Gunny, AAN, Kasim, FH, Arbain, D. Fourier Transform Infrared Spectroscopy (FTIR) Analysis of Paddy Straw Pulp Treated using Deep Eutectic Solvent. *AIP Conference Proceedings* 2017; *1835*(1): 020049.
- [20] Mandre, M, Tullus, H, Klöseko, J. Partitioning of carbohydrates and biomass of needles in Scots pine Canopy" *Zeitschrift für Naturforschung C* 2002; *57*(3-4): 296-302.
- [21] Móricz, N, Garamszegi, B, Rasztovits, E, Bidló, A, Horváth, A, Jagicza, A, Illés, G, Vekerdy, Z, Somogyi, Z, Gálos, B. Recent Drought-Induced Vitality Decline of Black Pine (*Pinus nigra* Arn.) in South-West Hungary—Is This Drought-Resistant Species under Threat by Climate Change? *Forests* 2018; *9*: 414; doi:10.3390/f9070414.
- [22] Nunes, L, Maria's, J, Catalao J. Energy Recovery from Cork Industrial Waste: Production and Characterisation of Cork Pellets. *Fuel* 2013; *113*: 24-30.
- [23] Pantaleo, A, Villarini, M, Colantoni, A, Carlini, M, Santoro, F, Hamedani, SR. Techno-Economic Modeling of Biomass Pellet Routes: Feasibility in Italy. *Energies* 2020; *13*: 1636; doi:10.3390/en13071636.
- [24] Paul, R, Etacheri, V, Pol, VG, Hu, J, Fisher, TS. Highly Porous Three-dimensional Carbon Nanotube Foam as a Freestanding Anode for a Lithium-ion Battery. *RSC Advances* 2016; *6*(83): 79734-79744.
- [25] Paul, R, Voevodin, AA, Zemlyanov, D, Roy, AK, Fisher, TS. Microwave-assisted Surface Synthesis of a Boron-carbon-nitrogen Foam and its Desorption Enthalpy. *Advanced Functional Materials* 2012; *22*(17): 3682-3690.
- [26] Rabacal, M, Fernandez, U, Costa, M. Combustion and Emission Characteristics of a Domestic Boiler Fired with Pellets of Pine, Industrial Wood Wastes and Peach Stones. *Renewable Energy* 2013; *51*: 220-226.
- [27] Sabeva, G, Tzvetkov, N, Boycheva, S, Gadzhyanov, P, Stankov, N. Studies to Determine the Fuel and Technical Characteristics of Plant Biomass Products. *Science Conference EFM (Sozopol)* 2012; 63-70. [in Bulgarian].
- [28] Scatolino, M, Neto, L, Protaslo, T, Carneiro, A, Andrade, C, Guimaraes J, Mended, L. Options for Generation of Sustainable Energy: Production of Pellets Based on Combinations between Lignocellulose Biomasses. *Waste and Biomass Valorization* 2017; doi 10.1007/s12649-017-0010-2.
- [29] Sherwood, J. The Significance of Biomass in a Circular Economy. *Bioresource Technology* 2020; *300*, 122755.
- [30] Stoyanova, M, Velichkova, G, Varbanova, M, Stoykov, R. Energy from Lignuous Biomass. *Management and Sustainable Development* 2014; *46*( 3): 76-81.
- [31] Szufa, S, Wielgosinski, G, Piersa, P, Czerwinska, J, Dzikuc, M, Adrian, Ł, Lewandowska, W, Marczak, M. Torrefaction of Straw from Oats and Maize for Use as a Fuel and Additive to Organic Fertilizers—TGA Analysis, Kinetics as Products for Agricultural Purposes. *Energies* 2020; *13*: 2064.
- [32] Wróbel, M, Jewiarz, M, Mudryk, K, Knapczyk, A. Influence of Raw Material Drying Temperature on the Scots Pine (*Pinus sylvestris* L.) Biomass Agglomeration Process—A Preliminary Study. *Energies* 2020; *13*: 1809.
- [33] Yingfu, Z, Songping, Z, Shida, M, Zhiguo, S, Ping, W. Temperature Sensitivity of Cellulase Adsorption on Lignin and its Impact on Enzymatic Hydrolysis of Lignocellulosic Biomass. *Journal of Biotechnology* 2013; *166*: 135-143.



## PREDICTING COST OF FARM-BASED BIOGAS PLANTS

Arash Samizadeh Mashhadi

Civil Engineering Department, Memorial University of Newfoundland, St. John's, NL, Canada, [asamizadehma@mun.ca](mailto:asamizadehma@mun.ca),  
ORCID: 0000-0002-4216-1676

Noori M. Cata Saady

Civil Engineering Department, Memorial University of Newfoundland, St. John's, NL, Canada, [nsaady@mun.ca](mailto:nsaady@mun.ca), ORCID:  
0000-0003-4001-3415

Carlos Bazan

Civil Engineering Department, Memorial University of Newfoundland, St. John's, NL, Canada, [carlos.bazan@mun.ca](mailto:carlos.bazan@mun.ca),  
ORCID: 0000-0001-8920-7486

*Cite this paper as:* Samizadeh MA, Saady, NMC, Bazan, C. Predicting costs of farm-based biogas plants. 9<sup>th</sup> Eur. Conf. Ren. Energy Sys. 21-23 April 2021, Istanbul, Turkey

**Abstract:** Livestock manure and organic agriculture wastes are an environmental challenge because they contribute to climate change by emitting greenhouse gases. Converting these organic wastes to biogas and bioenergy is a sustainable solution. Farmers, investors, and governments' departments involved in developing on-farm biogas projects need an informed decision-making process to fund such projects. Thus, estimating the required initial investment for a farm-based biogas plant is crucial. This study aims to develop models to estimate the cost of farm-based biogas projects and determine their economic viability. A database for farm-based biogas projects in Canada and the USA was established and analyzed before developing the models. Six mathematical models were developed using linear regression to predict the capital cost, engineering and design, operation and maintenance, gross revenue, and net profit. A farm-based biogas plant with 1000 cows requires almost 6 million CAD based on the developed model  $[1203.9 \text{ (number of cows)} + 2 \times 10^6]$  with a marginal error of about 7% in the estimated cost. The economic viability of a biogas plant for a farm housing less than 268 cows is questionable. Future work may investigate determining monetary values for the intangible benefits of such projects and integrate them in the cost estimate and economic evaluation models.

**Keywords:** cost analysis; biogas; on-farm; dairy farms; manure; anaerobic digestion; regression; modeling

© 2021 Published by ECRES

### Nomenclature

AD	Anaerobic digestion
CAD	Canadian dollar
GHG	Greenhouse gases
CHP	Compressed natural gas
CH <sub>4</sub>	Methane
CN	Number of cows
CNG	Combined heat and power
CO <sub>2</sub>	Carbon dioxide
FIT	Feed-in tariff
\$Eng	Cost of engineering and design
\$O&M	Cost of operational and maintenance per year
\$CC	Capital costs
\$R	Annual revenue
\$N	Net profit

## 1. INTRODUCTION

The energy demand is rapidly increasing because of the increasing population and industrial activity. Since the year 2000, the contribution of oil and gas industries has increased by more than 25% globally [1], which increases the impact on the environment and climate. Therefore, countries are willing to increase the contribution of clean and renewable energies to meet their demand.

Biogas is a reliable renewable biofuel that can be used to generate energy. Biogas production can be part of the waste management to produce clean, renewable, and environmentally friendly energy under anaerobic conditions (in the absence of oxygen) in a process called Anaerobic Digestion (AD) [2]. AD is a natural process that can break down organic materials by various bacterial activities in the absence of oxygen to produce biogas. Typically, the biogas produced consists of 60% - 70% of CH<sub>4</sub> and 30 – 40% CO<sub>2</sub>. Typically, methane fermentation occurs in two phases, called the acid phase and the gas phase. It will take four steps to complete the two phases of the AD [3]. The purpose of producing biogas is to produce methane and use it as a source of energy because it is convertible to vehicle fuel, electricity, and heat [4].

The benefits of AD include energy production (electricity and heat), odor reduction, greenhouse gas (GHG) emission reduction, control of pathogens, fertilizers and bedding fiber production, environmental protection, on-farm waste management, and revenue generation [5]. Farmers can benefit from selling the generated electricity to the government for extra income under the “Feed-In Tariff (FIT)” program in Canada while their energy bill is becoming zero. FIT program was developed in 2009 to encourage developers and engineers to use and develop renewable energy sources [6]. By supporting these projects, governments can develop an infrastructure to increase job opportunities and grow their green economy.

The framework of a cost analysis of on-farm biogas production can be divided into three main parts: 1- Input; 2- Biogas plant's components; and 3- Output (Figure 1). The input to the on-farm plant includes different types of waste such as dairy manure and other organic wastes such as food processing wastes. The second part

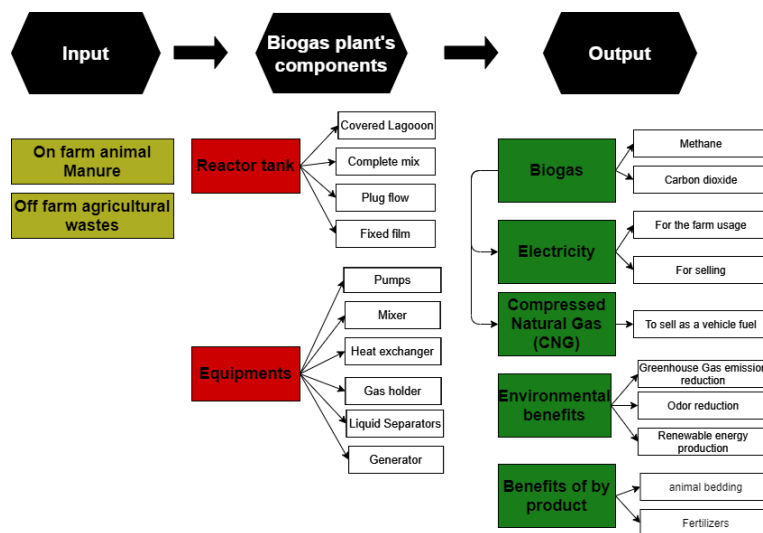


Figure 1 Comprehensive cost analysis and economic viability analysis of on-farm biogas plants

of the framework is the plant's components. Most of the required investments are for installing and constructing the plant. The digester (reactor) tank (i.e., covered lagoon, complete mix, plug flow digester, fixed-film digester) takes about 35% of the capital cost [7]. Also, most of the repair and maintenance costs are toward the digester itself or the ancillary units connected to the digester (e.g., pumps, valves, gas holding tank, connecting pipelines). The last part of the framework is the output and benefits of the plant. These benefits can be in the form of a direct income generated from selling electricity or selling methane gas directly as a Compressed Natural Gas (CNG), or it can be an indirect income for the farm owners like free access to hot water, animal beddings, and fertilizers that will remain at the bottom of the digester [8].

An on-farm biogas plant is a system that is comprised of several components such as a barn, manure collection system (scraping or flushing), manure pumping unit, solid-liquid separation unit, anaerobic digester, digester heating system, digester mixing system, gas storage tank, gas cleaning, and upgrading unit, combined heat & power (CHP) unit, and the digestate dewatering unit, and controlling unit (Figure 2). It is important to recognize each specific component in a biogas plant to: 1) estimate the costs related to the project's design and construction

accurately; 2) understand the environmental and operational factors that affect the performance of each component and decrease the efficiency of the plant. Consequently, they increase the operational and maintenance costs or shut down the entire project [9]. These factors include sudden variation in temperature, pH, the feedstock's moisture, carbon/nitrogen ratio, hydraulic retention time, foam, and scum formation [10].

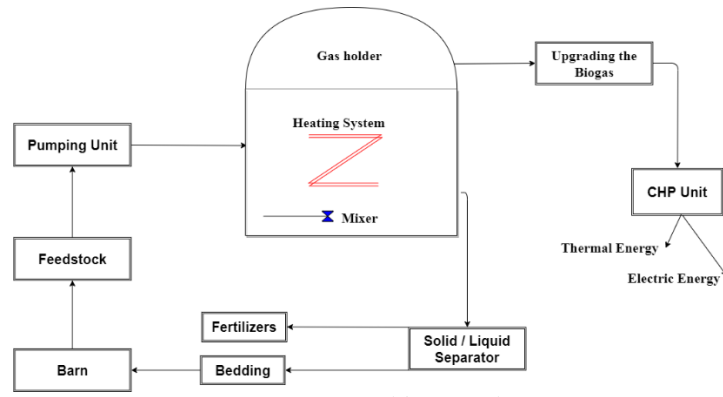


Figure 2 Typical biogas plant

This study analyzes the cost of on-farm biogas plants in North America to develop mathematical models to estimate the cost for dairy farms, particularly in Canada. It also assesses the financial feasibility of such plants. The models would provide investors with informed and better predictions of the required investment to build an on-farm biogas plant.

## 2.METHODOLOGY

The analytical method used in this study is regression modeling which is based on finding a mathematical correlation between the cost and the different components of the biogas plant. The regression modeling can offer both linear and nonlinear equations between variables [11]. The independent variable is the number of cows that implicitly means the volume of generated manure in the farm, and the dependent variable would be the costs (total or capital and the costs of the individual components), with a specific focus on the required capital cost at the beginning of the plant's construction, annual operational costs, and annual revenue.

A database of on-farm biogas plants on dairy farms in North America (Canada and the USA) was developed by retrieving relevant data from the accessible literature. The data points represent the number of dairy cows in each farm, the costs of construction of the plant, cost of each component, revenue from the tipping fees of off-farm organic waste, selling electricity, fertilizer, biofiber, bedding, soil amendment. The dataset was checked for consistency and scope of coverage. Further, the dataset was normalized to the current Canadian Dollar (CAD) value based on the inflation rate data from the Bank of Canada. Similarly, the data of on-farm biogas projects on USA dairy farms have been normalized to the current value [12].

Correlation analysis was conducted on the dataset to identify the relationships between the cost and the various components of the biogas plant. Based on the outcomes of the correlation analysis; regression has been used to develop linear and nonlinear models.

The developed model consists of five major sections. 1) Farm's specification includes the number of cows and the generated wastewater volume per cow per day during the manure collecting process; 2) Biogas yield per day based on the given farm size. This section is a key element in terms of income and financial benefits; 3) Total amount of electricity generated (kWh/day). The main parameters that are involved in the total amount of electricity generated are methane concentration in the collected biogas, and the CHP unit's efficiency during the conversion of CH<sub>4</sub> to energy; 4) Cost prediction for installation and operating the plant; and 5) annual gross income.

To make the model effective and reduce the errors between the actual values (collected from real biogas projects in Canada) and models' estimated (predicted) values, some technical factors were assumed based on the reviewed literature, such as biogas to electricity conversion factor, CHP unit efficiency, average wastewater that generates during the manure collection process.

### 3.RESULTS AND DISCUSSION

The models were developed based on a regression analysis to provide a cost calculator for feasibility studies of on-farm biogas projects. Six models (Table 1) predict the cost of each component of the on-farm biogas plant based on the number of cows (CN) housed in the farm. These models are representing the total capital cost and operational expenses, and the total generated income per year as a function of the number of available cows.

The model of the capital costs estimation is divided into two ranges in terms of the number of cows: 1) Small farms with a herd size of up to 1000 cows. 2) Large farms with a herd size of 1000 cows. The reason for this is that larger farms may require complicated technologies such as biogas purification and upgrading unit that are very expensive and increases the capital and operational costs. Although these technologies would increase the efficiency of the energy conversion from biogas to the electricity of CNG which increase the relevant income, the significant increase in the costs that these technologies add to the project would not be financially feasible for small farms ( CN < 1000 cows).

*Table 1 Cost prediction model based on linear regression analysis*

Model No.	Items	Unit	Cost prediction equations
1	Capital cost (CN<1000)	CAD	$1203.9 \text{ CN}^a + 2 \times 10^6$
2	Capital cost (CN>1000)	CAD	$1442.9 \text{ CN} + 4 \times 10^6$
3	Cost of engineering and design	CAD	$109.44 \text{ CN} + 216361$
4	Operational & maintenance costs	CAD/year	$48.155 \text{ CN} + 95199$
5	Revenue	CAD/year	$376.05 \text{ CN}$
6	Net revenue	CAD/year	$264.26 \text{ CN} - 70786$

a - CN = number of cows.

To validate the models, they were applied to 16 farms with a herd size of 100 cows up to 1600 cows, and the results are shown in Figure 3. To construct an on-farm biogas plant in North America, the minimum required investment (in Canadian Dollars) for a farm that houses 100 dairy cows is about 2 million dollars, and it can increase to about 6.3 million dollars for 1600 cows farm. For the same scope, the change in revenue will start from 37,000 CAD for a farm with 100 cows and it will increase to 600,000 CAD for 1600 cows farm. It should be noticed that this income is the gross income, and the operational and maintenance costs should be deducted from these numbers. The source of this income is selling the electricity produced by the farm's biogas plant or selling the biogas as CNG.

The economic viability of the biogas projects relies on the difference between the annual revenue and the annual operational costs. Based on the results of this study shown in Figure 3, a farm with 500 dairy cows has an annual operational cost of CAD 138,000, and there is a potential of generating CAD 177,000 income which means an annual net income of CAD 40,000. Notice that a biogas project on a farm housing less than 300 cows might not be economically feasible because the operational expenses would be higher than the annual benefit.

However, besides selling electricity, there are some additional benefits for the farmers, such as decreasing the energy bill to zero, availability of free hot water on the farm, and free high-quality fertilizers which could be used by the farm itself for growing crops or be sold. A limitation of the current model is that the intangible environmental benefits of on-farm biogas plants are not factored in the cost analysis; a limitation that is usually observed for most of the cost analysis models probably because of the not so well defined tag value assigned for these intangible benefits.

Errors are inevitable in mathematical modeling, particularly for cost and economic data. Thus, a slight discrepancy exists between the cost predicted by some of the models developed in this study and the real data point. For example, a farm with 1600 cows will need an investment of 6.3 million CAD based on this study's

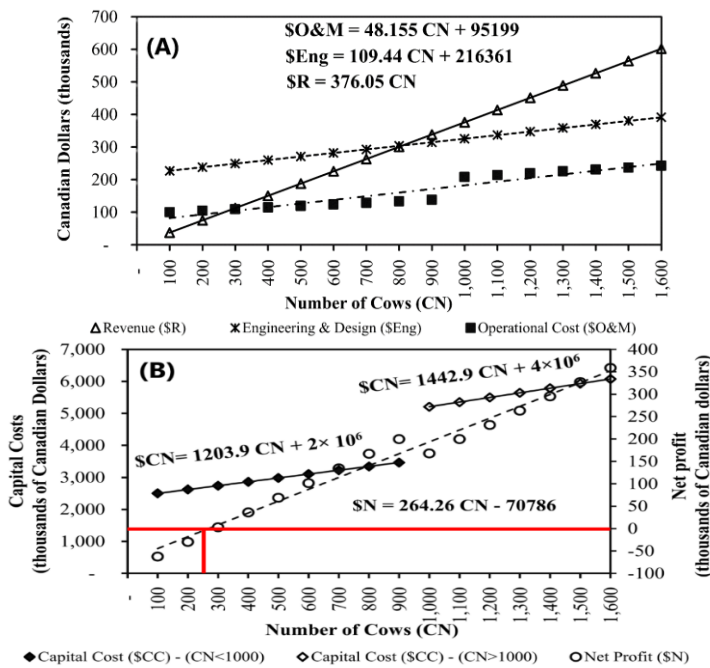


Figure 3 Developed models of costs of biogas plants on Canadian dairy farms; A- Cost of engineering and design, operational and maintenance, and revenue; B- Capital costs and the net profits

results, and the exact data point in the collected database for 1600 cows was 6.8 million CAD. The error in this specific example is 500,000 CAD which is less than 7% of the total capital cost. However, an error at this level is acceptable in this field of work because of the large scale of investment for these types of projects and the wide variability depending on the circumstance of the area, type of farm, relevant regulations, and policies.

The net profit (net revenue) is the difference between the total (gross) revenue and the operational costs. The latter increases with the increase in the herd size; however, for farms with less than 268 cows the operational costs are greater than the gross revenue, only when the herd size exceeds 300 cows the farm starts to make profit. Of course, this scenario is a function of the specific circumstances of the farm. For example, there is a biogas plant at Dawson Creek, British Columbia, that owns 230 cows, but their biogas plant is still economically profitable because 49% of the feedstock is off-farm nonagricultural wastes, which increases the biogas production of the project [13]. The models take into account only the manure and do not consider off-farm waste. The exact farm circumstance should be taken into account carefully on a case-by-case basis, and the results of the models provided in this paper might be used as an approximate estimation only.

#### 4.CONCLUSION

This paper developed six mathematical models to predict the costs of on-farm biogas plants for dairy farms in Canada. The regression models were developed to assist the farmers and project developers in evaluating the economic feasibility of such projects. The models take the herd size (number of cows) housed as input and estimate the capital cost for farms with less than and more than 1000 cows, design and engineering cost, operation and maintenance cost, gross revenue, and net revenue.

The models have three limitations: 1- they are applicable for on-farm biogas projects in Canada only; 2- the marginal error in the predicted capital cost is 7% for farms with around 1600 cows; and 3- the models are applicable for farms with a herd size of up to 1600 cows. The models developed showed that the viability of an on-farm biogas project for farms of less than 300 cows is questionable. Further work could focus on incorporating the intangible benefits (environmental, job creation, improving soil and water quality, control of odors and pathogens, etc.) in the cost analysis and the economic viability evaluation through generating tag values for the intangible benefits of such projects.

#### ACKNOWLEDGMENT

The authors acknowledge the funding received from the Department of Fisheries, Forestry, and Agriculture. Government of Newfoundland and Labrador, through the Canadian Agricultural Partnership Program.

## **REFERENCES**

- [1] Smil, V., *Energy transitions: global and national perspectives*. 2016: ABC-CLIO.
- [2] Mallon, S., *The financial feasibility of anaerobic digestion for Ontario's livestock industries*. 2007, Citeseer.
- [3] Voegeli, Y., *Anaerobic digestion of biowaste in developing countries: practical information and case studies*. 2014, Dübendorf: Eawag-Sandec.
- [4] EBA, *Statistical Report of the European Biogas Association 2018*. 2018: Brussels, Belgium. p. 18.
- [5] Association, C.B., *Biogas and Renewable Natural Gas in Ontario*. 2019. p. 26.
- [6] Yatchew, A. and A. Baziliauskas, *Ontario feed-in-tariff programs*. Energy Policy, 2011. 39(7): p. 3885-3893.
- [7] Amigun, B. and H. Von Blottnitz, *Capital cost prediction for biogas installations in Africa: Lang factor approach*. Environmental Progress & Sustainable Energy: An Official Publication of the American Institute of Chemical Engineers, 2009. 28(1): p. 134-142.
- [8] Möller, K. and T. Müller, *Effects of anaerobic digestion on digestate nutrient availability and crop growth: A review*. Engineering in Life Sciences, 2012. 12(3): p. 242-257.
- [9] Kalra, R., *Anaerobic Digestion of Biodegradable Organics in Municipal Solid Wastes*. 2002: p. 56.
- [10] Chen, Y., J.J. Cheng, and K.S. Creamer, *Inhibition of anaerobic digestion process: a review*. Bioresour Technol, 2008. 99(10): p. 4044-64.
- [11] Montgomery, D.C., E.A. Peck, and G.G. Vining, *Introduction to linear regression analysis*. Vol. 821. 2012: John Wiley & Sons.
- [12] Cowley, C. and B.W. Brorsen, *Anaerobic digester production and cost functions*. Ecological Economics, 2018. 152: p. 347-357.
- [13] Werner, E. and B. Strehler, *British Columbia On-Farm Anaerobic Digestion Benchmark Study*. 2007.



# USE OF SYNTHESIS GAS AS FUEL FOR A SOLID OXIDE FUEL CELL

Jesus Antonio Álvarez-Cedillo

Instituto Politécnico Nacional-UPIICSA, CDMX, MÉXICO, jaalvarez@ipn.mx, ORCID: <https://orcid.org/0000-0003-0823-4621>

Teodoro Álvarez-Sánchez

Instituto Politécnico Nacional-CITEDI, Tijuana, MÉXICO, talvarezs@ipn.mx, ORCID: <https://orcid.org/0000-0002-2975-7125>

Mario Aguilar-Fernández

Instituto Politécnico Nacional-UPIICSA, CDMX, MÉXICO, maguilarfer@ipn.mx, ORCID <https://orcid.org/0000-0003-2621-8692>

*Cite this paper as:* Álvarez-Cedillo, JA, Álvarez-Sánchez, T., Aguilar-Fernández, M. Use of synthesis gas as fuel for a solid oxide fuel cell. 9th Eur. Conf. Ren. Energy Sys. 21-23 April 2021, Istanbul, Turkey

**Abstract:** There is a real need to use various efficient energy supply systems that are not aggressive with the world's environment ambient. Hydrogen has been seen in different research papers presented in the Literature as an essential fuel to generate energy in various energy storage systems. As is well known, using electrolysis, it is possible to generate renewable electricity. The hydrogen produced can be sold as fuel for various systems, most notably its use in solid oxide fuel cells and a host of modern applications today. Current low-temperature fuel cells are ideal for hydrogen operation but are not suitable when hydrogen mixtures are used. In this article, the mathematical analysis was carried out to generate electrical energy in a fuel cell, fed with synthesis gas from the residual biomass gasification process; our primary interest is the generation of electrical energy, we analyze solid oxide fuel cell (SOFC), which operate at the temperature of the gas at the outlet of the gasifier. We show the practical efficiency obtained and the theoretical results of the operation of the SOFC.

**Keywords:** Anode, Cathode, Electrolyte, Biomass, Syngas, Solid Oxide Fuel Cell, Mathematical Model, Steady State.

© 2021 Published by ECRES

## 1. INTRODUCTION

The growth of the world population brings a problem of energy consumption; electric power has presented an increase in its demand in recent years due to the increase in devices connected to the internet and the rise of smart devices. The need to meet this demand has led researchers to seek alternative ways and energy sources to the conventional ones. Fossil resources are not present on earth, and their exploitation generates effects such as acid rain, photochemical smoking and global warming from the release of gases [1]. New energy production alternatives should be less aggressive to the environment. Solid oxide fuel cells have a new boom and a new opportunity to use alternative sources to the conventional ones published in the Literature [2, 3, 4].

Solid oxide fuel cells (SOFC) are devices used to transform renewable energy sources such as biomass into electrical energy [5]. SOFCs have a theoretical efficiency of 100% that favour their operation and application; it works commonly with hydrogen as fuel [6].

In this article, the synthesis gas obtained from the uncooled biomass gasification process is used as fuel because the high temperature is required for its feeding; our proposal avoids the increase in operating costs, our proposal focuses on the analysis of a mathematical model for the design of a fuel cell (SOFC).

It was studied how the production of electrical energy was favoured by the composition, the operating temperature and the reactions that take place inside the anode flow channel to produce hydrogen, resulting from the Nernst

equation that allows calculating the reduction potential of the electrodes, which we compare with results obtained with Literature; we show the convenience of its implementation [7].

## 2. MATERIALS

The materials that are part of our design comprise the following components: Anode, Cathode and Electrolyte. The electrolyte can be made of different ceramic materials. In the Literature, the material used in non-porous solid electrolytes is combinations of oxides, the most widely used material being yttria-stabilized zirconia (YSZ)[8], which is commercially available and inexpensive. Studies have been carried out with other combinations of oxides such as samarium-doped cerium oxide (SCD), bismuth yttrium oxide (BYO) or lanthanum gallate ceramic (LSGM) which have better ionic conduction than YSZ and they work best at the temperature threshold used [9]. As shown in Figure 5.

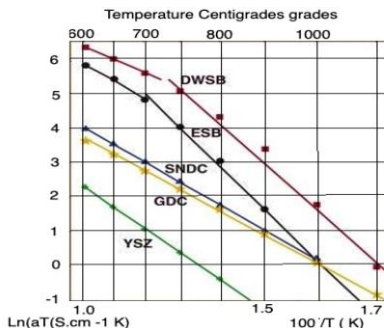


Figure 5. Ionic conductivity of electrolytic materials as a function of temperature.

In the Literature found for the electrical conductivity of YSZ [10], its relationship with the size of the grain is investigated, where it was concluded that the grain sizes of the electrolyte equal to 0.1-0.4, 0.3-1.5, 1-5 and 8-15  $\mu\text{m}$  could be used in the SOFC when the cell operating temperature is high ( $850^\circ\text{C}$ ,  $1000^\circ\text{C}$ ), as the conductivity does not differ between grain sizes. The temperature of  $10250^\circ\text{C}$ , it is appropriate to use a grade size between 8-15  $\mu\text{m}$ . The electrolyte properties, especially that of the intergranular region, affect the general conductivity of this significantly; in some cases, when the electrolyte presents poor conductivity, it is due to the low conductivity of the intergranular region [11,12].

The conductivity of the interior of the grain is usually two or three times greater than that of the grain limit, due to two factors initially, the first the formation of impurity phases near the grain limit, which have a more fantastic appearance when the SOFC operates at low temperature and second, the conduction of oxygen ions is less at the grain boundary due to the decrease in the oxygen vacancy concentration in that same place. The intergranular region's thickness decreases as the grain size YSZ decreases

## CATHODE MATERIAL

The material used was strontium doped lanthanum magnetite (LSM). The SOFC operates at high temperatures; for this reason, the only materials used for the cathode are noble metals or conductive oxide. Noble metals are expensive and do not have long-term stability; for this reason, they do not have a practical application in the cell. Heterometallic oxides are the only options, where it is possible to find several options such as lanthanum magnetite doped with strontium (LSM), perovskite-type lanthanum strontium manganite and lanthanum calcium manganite (LCM). Which have in their properties an adequate thermal expansion when we have a zirconia electrolyte and present good performances when they are operated at temperatures higher than  $800^\circ\text{C}$  156 ANODE [13].

## MATERIAL

The material used was **Ni-ZrO<sub>2</sub>** (Cermet); the anode material is a metal and should not be oxidized due to the fuel composition change during the cell. The anode material is composed of electrolytic material (YSZ, GDC or SDC) and nickel oxide (NiO), reduced to metallic nickel, which currently inhibits metallic particles, providing a coefficient of thermal expansion similar to that of the other cell materials. When using YSZ as the electrolyte material, the suitable material for the anode is NiO / YSZ, but if the electrolyte material is based on ceria, the anode materials are NiO / SCD and NiO / GDC.

## GEOMETRY OF THE CELL

The planar geometric of the Solid Oxide fuel cell is commonly used since its manufacture is not complicated, and it has lower ohmic resistance in the electrolyte, reducing energy losses and being reflected favourably in the potential of the cell [14,17,18]. In Figure 8, It is possible to see the typical configuration of a planar SOFC.

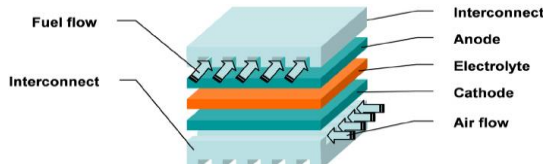


Figure 8. Planar configuration of the SOFC [19].

## CURRENT DENSITY

The current density is given thanks to the transfer of ions or electrons from one side of the cell to the other concerning the flow; it is the partial density obtained by the fuel cell and is measured by the unit of area [20]. See Figure 9.

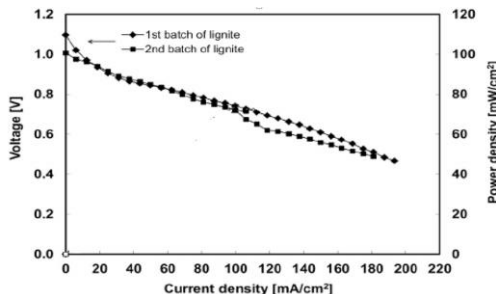


Figure 9. The variation of current density along the axial length of the SOFC at  $y = 0$ ,  $z = 0$  at a voltage of 0.73V.

Table 5 shows the input values of the proposed current density.

Table 5. The input values that are repaired throughout the study.

Input	Value
Output Temperature	850.2 C Cell
Pressure	1 bar
Active surface area	100 cm <sup>2</sup>
Anode current density exchange	0.78 A / cm <sup>2</sup>
Density change cathode current	0.12 A / cm <sup>2</sup>
Anode gaseous diffusivity	0.2 cm <sup>2</sup> / s
Cathode gaseous diffusivity	0.05 cm <sup>2</sup> / s
The temperature difference between outlet and inlet	120 C
Anode	500 μm
Thickness Electrolyte	10 μm
Thickness Cathode thickness	50 μm

## MATHEMATICAL MODEL

The mathematical model is carried out by considering the balance of matter, energy, momentum, and species using the conditions and parameters previously raised. The considerations for the solution of the mathematical model are the following: Steady-state condition; The fuel cell operates at constant pressure and temperature (isothermal); There are no pressure drops in the electrolyte; There is variation in the hydrogen concentration in the anode flux channel and the model; there are no parallel reactions at the limit boundary of the three phases; methane reforming

and water displacement reactions are considered; the velocity is constant in the two flow channels; the momentum balance is not considered and the energy balance is not evaluated because it is an isothermal system [21]. Table 6 shows the values obtained for the solution of the mathematical model.

*Table 6. Parameters for the mathematical model solution.*

Parameters	Value
Operating temperature	850.2 - 1000 ° C
Current density	850 to 3200 A m <sup>-2</sup>
Pressure	1 atm
Flow	104 cm <sup>3</sup> / h
Volumetric Anode material	Ni/ ZrO <sub>2</sub> -Y <sub>2</sub> O <sub>3</sub>
Electrolyte material	0.2 cm <sup>2</sup> / s
Cathode material	0.05 cm <sup>2</sup> / s
The temperature difference between outlet and inlet	120 C
Anode	500 µm
Thickness Electrolyte	10 µm
Thickness Cathode thickness	50 µm

Two types of continuous models apply to Solid Oxide fuel cells: the quasi-homogeneous and the heterogeneous. For this mathematical model's solution, a heterogeneous model with a heterogeneous solid phase was chosen, to which simplifications were made to reach the convergence of the method. It is carried out with a Newton Raphson numerical method, control volumes and finite differences.

When there is a concentration gradient, there is a mass transfer, this being the transport phenomenon that occurs between two analyzed points, and the mass transfer can be classified into two phenomena: Convective phenomenon: The convective mass transfer occurs when the substance that is transported from one point to another is influenced by the components present in the fluid and the medium in which it diffuses and Diffusive phenomenon: Diffusive mass transfer is the step molecule by molecule of a substance neglecting the medium in which it diffuses.

Solid Oxide fuel cells as a whole can be modelled by the diffusive phenomenon by the cell configuration, although the convective phenomenon can be used in the cell for mass transfer of the flow channel and the diffusive one for the porous medium. (electrodes).

## EXPERIMENTAL RESULTS

The following shows the results obtained in the behaviour of the synthesis gas concentration profiles at the anode and interface and the air at the cathode. The synthesis gas concentration profile calculation was performed using Fick's Law for binary diffusion, taking into account the considerations established above for the cell's section corresponding to the synthesis gas. The material balance was carried out for the syngas flow channel and the anode, based on diffusive and convective phenomena. The cell sections' concentration profiles were calculated; the nodal analysis makes it possible to solve the Hydrogen concentration profiles through the length of the electrode. Figure 11 shows the three concentration profiles of node 1, 6 and 11, where the fuel's behaviour during its journey through the cell can be seen.

The hydrogen composition that enters the anode flow channel is 0.2037; this amount of hydrogen is fed to node 1, where a part of it diffuses, and then another goes to the next node. The diffused hydrogen leads to the electrolytic reaction at the interface, and the methane reforming reaction and water shift (toilet gas shift) are generated in the anode flow channel. The change in hydrogen composition at the beginning, middle and end of the cell concerning the thickness of the anode (0.0007m) is demonstrated, where at the end of (node 6) negative composition values begin to be obtained, that is, the hydrogen was wholly consumed before reaching node 7.

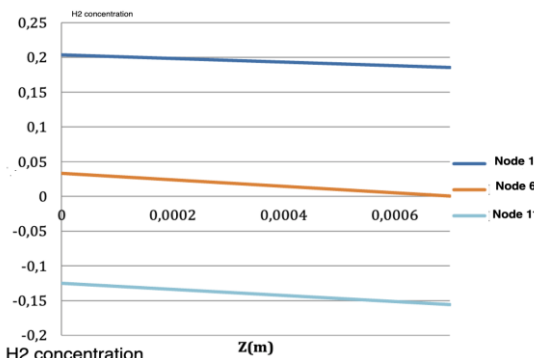


Figure 11. Concentration profiles of node 1, 6 and 11.

This result is attributed to several factors; The first is the Knudsen diffusivity, which makes the amount of hydrogen diffused by each node is more significant, and therefore the concentration at the entrance of the following nodes is drastically reduced; the second is that the reaction rates of methane reforming and displacement of the water (toilet gas shift) considered secondary do not have a significant value compared to the reaction rate of the electrolytic reaction, because of this the amount of hydrogen that is produced by the two secondary reactions does not represent a change that was considered significant.

The current density applied in a cell is lower (1000-3000 A / m<sup>2</sup>) than a Solid Oxide fuel cell (it can reach 11000 A / m<sup>2</sup>). The air that enters the cathode flow channel has a composition of 0.21 for oxygen and 0.79 for nitrogen; as previously said, nitrogen acts as inert in this reaction, so it is not considered. Figure 12 illustrates the behaviour of the composition profile at the cathode.

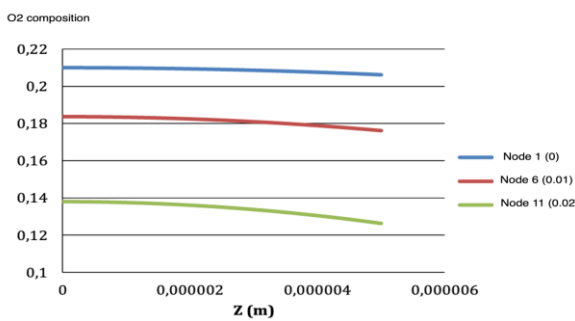


Figure 12. Nodal composition of oxygen.

In Figure 12, it is shown that the behaviour of oxygen during the entire length was 0.02m in the cell, and this decreases; for the concentration profile of the cathode, no negative values are obtained, oxygen is not consumed. It is possible to observe that in the last node, the final oxygen composition is close to 0.12. The composition of oxygen has an adequate decrease due to the constant diffusivity because a binary mixture is not present, the oxygen is pure, and there are no reactions yet.

## CONCLUSION

In this work, little significant changes were obtained in the composition of hydrogen, but an increase in the cell's potential (1.12 V) is observed, compared to some works shown in the Literature [15, 16], which was 0.52 V. From the mathematical model's solution, it was possible to analyze the behaviour of synthesis gas and oxygen, with the diffusive phenomenon in porous media (electrodes) using Fick's Law, where the initial composition of hydrogen in the synthesis gas is 0.2037 (node 0). When reaching node one at an exact length of 0.000362 m, the hydrogen has a composition equal to zero; that is, it was utterly consumed.

The above happened due to the previous general considerations shown for the solution of this mathematical model. However, the model obtained differs from the reality because the proposed model was evaluated in a steady-state, this being one of the main factors by which the cell does not present a possible result for the initiation of tests at the laboratory level, and the cell operates continuously. The current density ranges (700 to 3000) established for this model's solution are a parameter that affects the result obtained since the amount of energy generated by the cell depends on this. In the comparison between the potential generated by a fuel cell at the established conditions and when using a gasifier engine, the power of the 64-cell cell was equal to 3762.6 W, and that of the engine is 15000 W; for This is why the battery is 12.24 times more expensive than the motor. The efficiency of the cell with an

internal combustion engine found in the Literature, where the efficiency of the cell is 65%, and that of the engine did not exceed 32%, however, the results of the obtained model do not make the SOFC A viable device in economic terms, this is due to the considerations that were made in this mathematical model since the energy balance is not assumed. The cell operates continuously, but for this model, it was assumed stationary.

## ACKNOWLEDGMENT

We appreciate the facilities granted to carry out this work to the Instituto Politécnico Nacional through the Secretariat of Research and Postgraduate with the SIP 20180023 project. To the Interdisciplinary Unit of Engineering and Social and Administrative Sciences, Center for Technological Innovation and Development in Computing and Digital Technologies Research and Development Center. Likewise, the Program of Stimulus to the Researchers' Performance (EDI) and the Program of Stimulus COFAA and CONACYT.

## REFERENCES

- [1] Haile, S. M. (2003). Fuel cell materials and components. *Acta Materialia*. <https://doi.org/10.1016/j.actamat.2003.08.000>
- [2] Zhu, W. Z., & Deevi, S. C. (2003). A review on the status of anode materials for solid oxide fuel cells. *Materials Science and Engineering A*. [https://doi.org/10.1016/S0921-5093\(03\)00620-8](https://doi.org/10.1016/S0921-5093(03)00620-8)
- [3] Haile, S. M. (2003). Fuel cell materials and components. *Acta Materialia*. <https://doi.org/10.1016/j.actamat.2003.08.004>
- [4] Evans, A., Bieberle-Hütter, A., Rupp, J. L. M., & Gauckler, L. J. (2009). Review on microfabricated micro-solid oxide fuel cell membranes. In *Journal of Power Sources*. <https://doi.org/10.1016/j.jpowsour.2009.03.048>
- [5] Mahmud, L. S., Muchtar, A., & Somalu, M. R. (2017). Challenges in fabricating planar solid oxide fuel cells: A review. In *Renewable and Sustainable Energy Reviews*. <https://doi.org/10.1016/j.rser.2017.01.019>
- [6] Ivers-Tiffée, E., Weber, A., & Herbstritt, D. (2001). Materials and technologies for SOFC-components. *Journal of the European Ceramic Society*. [https://doi.org/10.1016/S0955-2219\(01\)00120-0](https://doi.org/10.1016/S0955-2219(01)00120-0)
- [7] Buonomano, A., Calise, F., d'Accadia, M. D., Palombo, A., & Vicedomini, M. (2015). Hybrid solid oxide fuel cells-gas turbine systems for combined heat and power: A review. In *Applied Energy*. <https://doi.org/10.1016/j.apenergy.2015.06.027>
- [8] Schlichting, K. W., Padture, N. P., & Klemens, P. G. (2001). Thermal conductivity of dense and porous yttria-stabilized zirconia. *Journal of Materials Science*. <https://doi.org/10.1023/A:1017970924312>
- [9] Hayashi, H., Saitou, T., Maruyama, N., Inaba, H., Kawamura, K., & Mori, M. (2005). Thermal expansion coefficient of yttria stabilized zirconia for various yttria contents. *Solid State Ionics*. <https://doi.org/10.1016/j.ssi.2004.08.021>
- [10] Zhang, Y. (2014). Making yttria-stabilized tetragonal zirconia translucent. *Dental Materials*. <https://doi.org/10.1016/j.dental.2014.08.375>
- [11] Guazzato, M., Albakry, M., Ringer, S. P., & Swain, M. V. (2004). Strength, fracture toughness and microstructure of a selection of all-ceramic materials. Part II. Zirconia-based dental ceramics. *Dental Materials*. <https://doi.org/10.1016/j.dental.2003.05.002>
- [12] Ud Din, Z., & Zainal, Z. A. (2016). Biomass integrated gasification-SOFC systems: Technology overview. In *Renewable and Sustainable Energy Reviews*. <https://doi.org/10.1016/j.rser.2015.09.013>
- [13] Doherty, W., Reynolds, A., & Kennedy, D. (2010). Computer simulation of a biomass gasification-solid oxide fuel cell power system using Aspen Plus. *Energy*. <https://doi.org/10.1016/j.energy.2010.04.051>
- [14] Fryda, L., Panopoulos, K. D., & Kakaras, E. (2008). Integrated CHP with autothermal biomass gasification and SOFC-MGT. *Energy Conversion and Management*. <https://doi.org/10.1016/j.enconman.2007.06.013>
- [15] Bang-Møller, C., & Rokni, M. (2010). Thermodynamic performance study of biomass gasification, solid oxide fuel cell and micro gas turbine hybrid systems. *Energy Conversion and Management*. <https://doi.org/10.1016/j.enconman.2010.04.006>
- [16] Lim, T. H., Song, R. H., Shin, D. R., Yang, J. Il, Jung, H., Vinke, I. C., & Yang, S. S. (2008). Operating characteristics of a 5 kW class anode-supported planar SOFC stack for a fuel cell/gas turbine hybrid system. *International Journal of Hydrogen Energy*. <https://doi.org/10.1016/j.ijhydene.2007.11.017>
- [17] Burt, A. C., Celik, I. B., Gemmen, R. S., & Smirnov, A. V. (2004). A numerical study of cell-to-cell variations in a SOFC stack. *Journal of Power Sources*. <https://doi.org/10.1016/j.jpowsour.2003.08.034>
- [18] Bove, R., & Ubertini, S. (2006). Modeling solid oxide fuel cell operation: Approaches, techniques and results. *Journal of Power Sources*. <https://doi.org/10.1016/j.jpowsour.2005.11.045>
- [19] Buonomano, A., Calise, F., d'Accadia, M. D., Palombo, A., & Vicedomini, M. (2015). Hybrid solid oxide fuel cells-gas turbine systems for combined heat and power: A review. In *Applied Energy*. <https://doi.org/10.1016/j.apenergy.2015.06.027>
- [20] Panopoulos, K. D., Fryda, L., Karl, J., Poulou, S., & Kakaras, E. (2006). High temperature solid oxide fuel cell integrated with novel autothermal biomass gasification. Part II: Exergy analysis. *Journal of Power Sources*. <https://doi.org/10.1016/j.jpowsour.2005.11.040>
- [21] Doherty, W., Reynolds, A., & Kennedy, D. (2015). Process simulation of biomass gasification integrated with a solid oxide fuel cell stack. *Journal of Power Sources*. <https://doi.org/10.1016/j.jpowsour.2014.11.125>



# AN AVERAGED LARGE-SIGNAL MODEL METHOD OF DC-DC ISOLATED FORWARD RESONANT RESET CONVERTER BASED ON SOLAR CELLS BATTERY CHARGER FOR IOT APPLICATION

Pattarapongsathit Wachiravit

Division of Applied Electrical Engineering Technology, Department of Electrical Engineering Technology, College of Industrial Technology (CIT), King Mongkut's University of Technology North Bangkok, Bangkok, 10800, Thailand,  
ORCID No, 0000-0002-6540-7632, wachiravit.pongsa@gmail.com,

Bilsalam Anusak

Division of Applied Electrical Engineering Technology, Department of Electrical Engineering Technology, College of Industrial Technology (CIT), King Mongkut's University of Technology North Bangkok, Bangkok, 10800, Thailand

<sup>2</sup>ORCID No, 0000-0003-4364-2962, anusak.b@cit.kmutnb.ac.th

Cite this paper as:

*Pattarapongsathit, W., Bilsalam, A., An averaged large-signal model method of DC-DC isolated forward resonant reset converter based on solar cells battery charger for IoT application. 9th Eur. Conf. Ren. Energy Sys. 21-23 April 2021, Istanbul, Turkey*

---

**Abstract:**

This paper proposed has analysis and modeling circuits for control battery charge solar cell based on data management through IoT by using DC-DC forward resonant reset converter. Which can be charged in a constant current constant voltage. There are data management of various parameter with IoT technology and can send notifications to the application. The proposed converter can provide output voltage 14.4 Vdc for a minimum to maximum voltage 9-18 VDC solar cell using an isolated transformer and a half wave rectifier circuit. The main switch of the forward resonant reset converter can be operated under a zero-turn on condition. The advantages of this technique are that it uses a leakage inductance  $L_{kp}$  and resonant capacitor  $C_r$  to achieve the reset of remain flux saturation on the high frequency transformer. A prototype simulation model was built and operated at 50 kHz fixed switching frequency, 14.4 VDC constant output voltage, and about 28 W output power. at efficiency is equal to 96 % at the maximum full load. The proposed analysis techniques and math model was verified via simulation results, which were found to be in agreement with the theoretical analysis.

---

**Keywords:**

*Large-signal, Forward, Resonant, Converter, Battery charger, IoT*

---

© 2021 Published by ECRES

## 1. INTRODUCTION

In recent years, high-efficiency and dc-dc converter has been investigating research areas in using distributed photovoltaic cells power energy source. In the renewable energy standalone, grid tie, hybrid and large and very small ac/dc micro grid system until battery charge application. There are many requests such as low-voltage power sources, high-efficiency, high-power density circuit and regulation output side. Converter topologies are classified into operation pulse width modulation (PWM) and semi/full resonant modes (S/FRM). The pulse width modulation is very simple basic technique. But the has important issue high losses/low efficiency of main power state can be occur turn on/off switching time and high electromagnetic interference (EMI) problem. In the order to many solutions at rising efficiency, density with the smaller compact size can be editable major is operation semi/full resonant modes owing to current and voltage across out of phase [1-4]. In the practical, in a control resonant converter can be occur movement of resonant point because of changing input/output voltage or load in the output side unable regulated output voltage their drawbacks [5-8]. The main objective depends on emphasis in the analysis and many parameters on distributed system such as voltage, current, power or observer each state element. Among control those can be classifier are linearization and nonlinear technique. In the section of non-linear control has been widely used in complicated distributed and many controllable of state observer are recognized as the possible

receive good precise and response at the incomprehensive characteristic identity parameter of plane. There are many requests high performance microprocessor for a calculate multi variable state or most sequence process results and eliminates their drawbacks [9-10]. In the fact that, state-of-the-art converter those are typical non-linear system in analysis requires complex techniques and expertise to simplify add ease designer system. In some solution, anyway is transformed into a linear system. Generally, averaged model methods (AMM) are used to estimate significance the elements variable parameter in a circuit as close to reality as possible. Because they are easy to control and still deliver accurate results and appropriate that applies to converter [11]. AMM are used in conjunction with a sub solution of a State-Space Averaging (SSA) metrology and explain convert functionality general uses technique with math model. The small-signal technique (SSt) a some of part in AMM methods are employ investigation impedance-based stability has provide that stability and reliability for the evaluation of converter. It has been applied to single end and multi-switches consist of many passive components as excellent results for the extremely accurate analysis results. Decrease little discrepancy, are inevitable know-how and high expertise require a signal flow graph technique (SFG) method was used to make it easier to analyze large numbers of high orders and maintain accuracy. However, large signal (LSt) technique has been widely because of very easier for find math model because include or neglect impedance-based stability analysis. Which these circuits, mostly was used with single or multi switches dc converters application such as fly-back, forward and push-pull circuit and consist of isolated high frequency transformer, fast recovery diode, inductors and capacitor to simplify circuit analysis. Besides this technical term can be bode plots and used to controller design and math modeling suitable analysis time variant system since quick, easy, accurate, and it also corresponds to the switching model [12-14].

This paper presents the performance analysis of proposed circuit in section 2, circuit description in part A of section 2, analysis large-signal of operation principles in part B of section 2, mathematical analytical in section 3, simulation results in section 4 and conclusion in section 5.

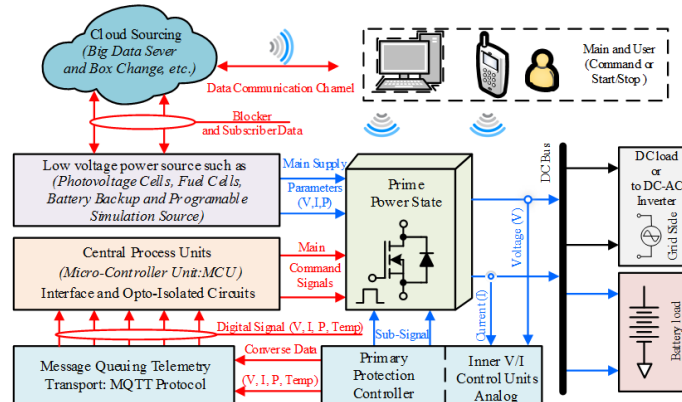


Figure 1 Concept protocol communication of Internet of Thing (IoT) to each power units

## 2. PERFORMANCE ANALYSIS OF PROPOSED CIRCUIT

### A. CIRCUIT DESCRIPTION

The proposed analysis an averaged large-signal model method of dc-dc isolated forward resonant reset converter (FR-RC) based on solar cells battery charger for IoT application as shown Figure 1. The power MOSFET  $M_1$  denote the main switch,  $C_r$  is resonant reset capacitor, high frequency transformer consists of two winding  $L_p$  and  $L_s$ ; sum value of magnetizing and leakage inductance are named as  $L_m$ ,  $L_{lkp}$  built-in primary winding. Leakage inductance secondary side is less value, it can be ignored. In both component of  $N_p$  and  $N_s$  are number of winding primary and secondary high frequency.  $D_1$ ,  $D_2$ , and  $L_x$  are the converter output and current choke inductor respectively;  $C_o$  is the output large capacitor;  $V_{in}$  and  $V_{out}$  represent the input and output voltages, respectively; and  $R_o$  the resistance is seem battery load. The suggestion FR-RC has 3 state time operation in the analysis of the circuit begins with these following assumptions.

- 1) The main power switch and active/passive elements in the on and off state are equal to zero, thus useful will be idea elements.
- 2) The input and output voltage are a dc source and current output constant.
- 3) All capacitors/inductors are large enough with no alteration in the voltage of capacitors and the current inductors.
- 4) The output capacitor is sufficiently bulky for the output voltage to be constant.
- 5) For dc conversion ratio and turn ratio of high frequency transformer are equal as  $n=N_s/N_p$  and  $a=N_p/N_s$

## B. ANALYSIS LARGE-SIGNAL OF OPERATION PRINCIPLES

DC-DC isolated forward resonant reset converters have three stages of conversion dc to ac (inversion: state 1), ac/dc (reset and rectification: state 2) and ac/dc (release energy rectification). Hence, mathematical model in a analyze A-LS have significant of state variable exist:  $[i_{Lm}, i_{Lx}, v_{Cr}, v_{Co}]$ . The precision of the modeling can be improved by including the are leakage inductance  $L_{lkp}$  and parasitic resistance  $r_{Lx}$  of choke output inductor. By applying Kirchhoff's voltage and current laws (KVL, KCL) to input and output power converter circuit depicted in Fig.2(h), It can divide into three stages

**In states 1:** Interval, the power switch MOSFET is turn on, current flow from input voltage source  $V_{in}$  to dot terminal of high frequency transformer and drain-source of power switch MOSFET, when the switch  $M_1$  is turned on and operated under the zero turn on condition. Then, energy primary winding is transferred to secondary side, and diode  $D_1$  is turn on by the flow of current  $i_{D1}$ ,  $i_{Lx}$  through the choke inductor and capacitor output as shown Figure 2(b) This state variables exist  $i'_{Lm}$ ,  $i'_{Lx}$ ,  $v'_{Cr}$  and  $v'_{Co}$ , KVL and KCL on input side, define ( $v_{Lm} = v_p$ ,  $v_{r_{Lk}} = r_{Lk} i_m$ )

Define ( $i_{Lk} = i_{r_{Lk}}$ );

$$i'_{Lm} = \frac{-v_{Cr} - v_{Lk} - r_{Lk} i_{Lk} + v_{in}}{L_m}, v'_{Cr} = \frac{-i_{Lk}}{C_r} \quad (1)$$

KVL and KCL on output side, define ( $v_s = nv_{in}$ ,  $v_{Ro} = v_{Co}$ ,  $v_{r_{Lx}} = r_{Lx} i_{Lx}$ )

$$\text{Define } (i_{Ro} = \frac{v_{Co}}{R_o}, i_{Lx} = i_m a); \quad i'_{Lx} = \frac{nv_{in} - v_{Co} - r_{Lx} i_{Lx}}{L_x}, v'_{Co} = \frac{1}{C_o} \left( ai_{Lm} - \frac{v_{Co}}{R_o} \right) \quad (2)$$

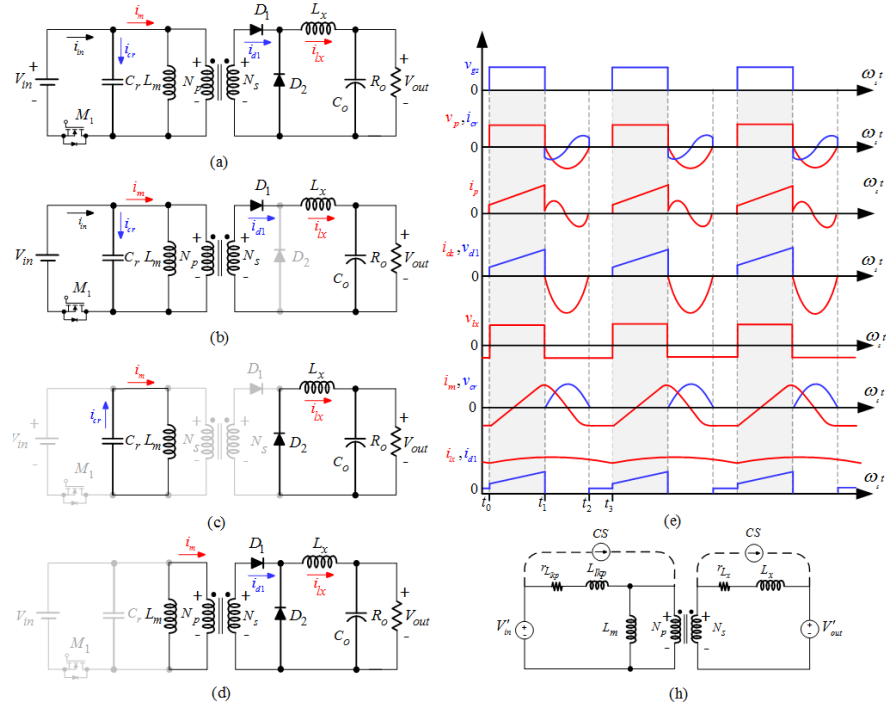


Figure 2 (a) Proposed Dc-Dc Isolate Forward Resonant Reset Converter (b) Equivalent circuit of state 1 (c) Equivalent circuit of state 2 (d) Equivalent circuit of state 3 (e) Key waveform of Dc-Dc Isolate Forward Resonant Reset Converter (h) simplify circuit with Dc-Dc Isolate Forward Resonant Reset Converter

**In states 2:** At the beginning of this state, the power switch MOSFET is turn off as shown Figure 2(c). At time magnetizing inductance  $L_m$  release the energy and commutation energy reset flux saturation between  $L_m$  and reset capacitance  $C_r$  on the high frequency transformer. At the moment time  $t_1-t_2$  and waveforms reset are approximate is two thirds of the half period switching time  $T_s$  and can be seen sinusoidal waveform. [(3) to (4)]. KVL and KCL on input side, define ( $v_{r_{Lk}} = r_i L_m$ ) and Output side, define ( $v_s = nv_{in}$ ,  $v_{co} = v_{Ro}$ ,  $v_{r_{Lx}} = r_{Lx} i_{Lx}$ )

$$i'_m = \frac{-v_{Cr}}{L_m} - \frac{ri_m}{L_m}, v'_{Cr} = \frac{i_m}{C_r} \quad (3)$$

$$\text{Define } \left( i_{R_o} = \frac{v_{C_o}}{R_o} \right); \quad i'_{L_x} = \frac{-v_{C_o} - ri_{L_x}}{L_x}, \quad v'_{C_o} = \frac{1}{C_o} \left( i_{L_x} - \frac{v_{C_o}}{R_o} \right) \quad (4)$$

**In states 3:** At the time, when reset capacitance  $C_r$  is contain full energy receive flow back of current magnetizing inductance  $L_m$  from last time  $t_1-t_2$ . A during completed time, are diode  $D_1, D_2$  turn on remain current continuous through to all component output dc side ( $L_x, C_o, R_o$ ). KVL on input side

$$i'_{L_m} = \frac{v_p}{L_m} \quad (5)$$

$$\text{KCL on output side, define } \left( i_{R_o} = \frac{v_{C_o}}{R_o}, i_{L_x} = ai_{L_m} \right) v'_{C_o} = \frac{1}{C_o} \left( ai_{L_m} - \frac{v_{C_o}}{R_o} \right) \quad (6)$$

### 3. MATHEMATICAL ANALYTICAL

The mathematical simulation of the system by state space averaging (SSA). From relation differential equation are state 1 by using eq (1-2), state 2 can be used eq (3-4) and state 3 following eq (5-6). Three state operation of the state variable parameters are rewrite main general format are expressed as

$$\dot{x} = Ax + Bu \quad (7)$$

Therefore, in the average system solution are combined subsystem  $A_1, A_2, A_3$  and sub-input  $B_1, B_2, B_3$ . Where, are  $(d)$ ,  $(1-d)$  during time power switch turn on  $(d)$  in state 1 and turn off  $(1-d)$  time in both 2, 3 state, combinant parameters are expressed as

$$A = A_1 + A_2 + A_3 = \begin{bmatrix} -\frac{r_{ik}}{L_m} & 0 & -\frac{1}{L_m} & 0 \\ -\frac{r_{L_x}}{L_x} & 0 & 0 & -\frac{1}{L_x} \\ 0 & 0 & 0 & 0 \\ \frac{a}{C_o} & 0 & 0 & -\frac{1}{C_o R_o} \end{bmatrix} [d] + \begin{bmatrix} -\frac{r_{ik}}{L_m} & 0 & -\frac{1}{L_m} & 0 \\ -\frac{r_{L_x}}{L_x} & 0 & 0 & -\frac{1}{L_x} \\ \frac{1}{C_r} & 0 & 0 & 0 \\ 0 & \frac{1}{C_o} & 0 & -\frac{1}{C_o R_o} \end{bmatrix} [1-d] + \begin{bmatrix} 0 & 0 & 0 & 0 \\ 0 & 0 & 0 & 0 \\ 0 & 0 & 0 & 0 \\ \frac{a}{C_o} & 0 & 0 & -\frac{1}{C_o R_o} \end{bmatrix} [1-d] \quad (8)$$

$$B = B_1 + B_2 + B_3 = \begin{bmatrix} 1 \\ L_m \\ \frac{n}{L_x} \\ 0 \\ 0 \\ 0 \end{bmatrix} [d] + \begin{bmatrix} 0 \\ 0 \\ 0 \\ 0 \\ 0 \\ 0 \end{bmatrix} [1-d] + \begin{bmatrix} 0 \\ 0 \\ 0 \\ 0 \\ 0 \\ 0 \end{bmatrix} [1-d] \quad (9)$$

Simplifying, eq (8) and eq (9) into eq (14). Finally, are math model and SSA matrix format result, from eq (14) can be written derived relationship of state variable are defined by

$$x' = \begin{bmatrix} i'_{L_m} \\ i'_{L_x} \\ v'_{C_r} \\ v'_{C_o} \end{bmatrix} = \begin{bmatrix} -\frac{r_{ik}}{L_m} & 0 & -\frac{1}{L_m} & 0 \\ -\frac{r_{L_x}}{L_x} & 0 & 0 & -\frac{1}{L_x} \\ \frac{1-d}{C_r} & 0 & 0 & 0 \\ \frac{a}{C_o} & \frac{1-d}{C_o} & 0 & \frac{d-2}{C_o R_o} \end{bmatrix} \begin{bmatrix} i_{L_m} \\ i_{L_x} \\ v_{C_r} \\ v_{C_o} \end{bmatrix} + \begin{bmatrix} \frac{d}{L_m} \\ \frac{nd}{L_x} \\ 0 \\ 0 \end{bmatrix} [v_{in}] \quad (10)$$

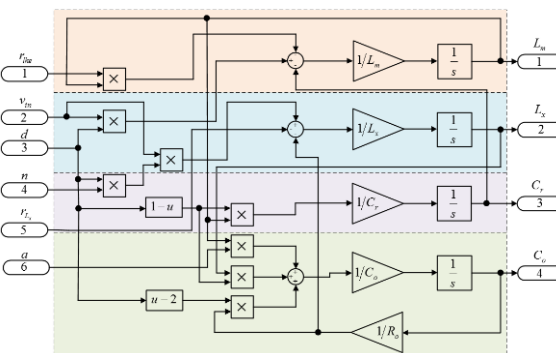


Figure 3 Simplify math modeling by using averaged large-signal technique

## 4. SIMULATION RESULTS

A prototype of the proposed circuit was simulated math model by using parameters listed in Table 1, was used in the simulation results. In the section, state variable of an averaged large-signal model method of dc-dc isolated forward resonant reset converter based on solar cells battery charger response are discussed. The configuration of the proposed technique is simulated math model by using SIMULINK program. The purpose math model of this simulation is to verify the analysis methods and study the static state variable and dynamic performances of the system. The converter under focus is capable of: 1) correctness of state variable [ $i'_{lm}$ ,  $i'_{Lx}$ ,  $v'_{cr}$ ,  $v'o$ ] waveform by using averaged large-signal model 2) dynamic response of output voltage charger. An assumed rated operation of, 14.4 Vdc, 2 A and about 29 W output power at full-load condition.

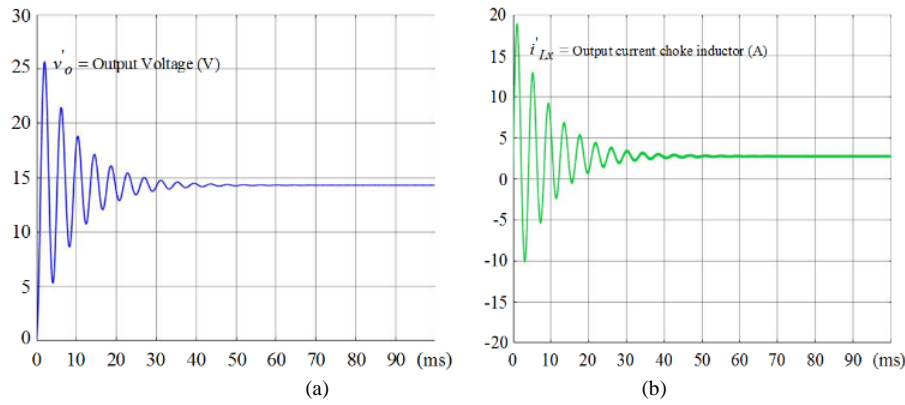


Figure 4 Simulation results for state variable of (a) output voltage  $v'o$  and (b) output current  $i'Lx$  waveform.

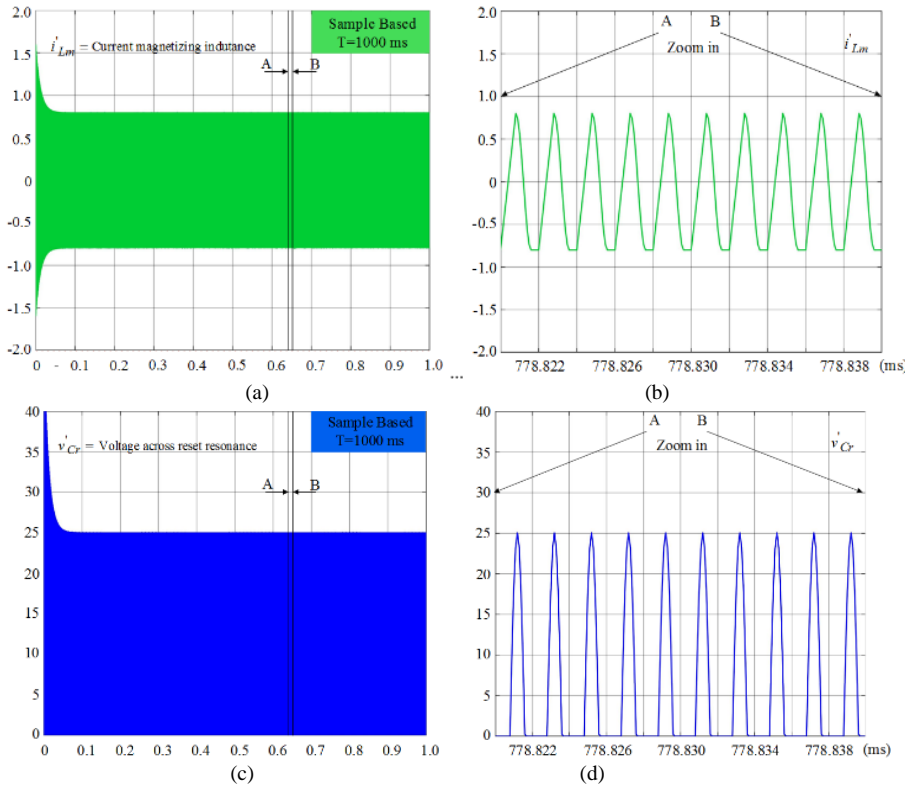


Figure 5 Simulation results state variable of current magnetizing inductance (a) transient time and (b) zoom in waveform and state variable of voltage across reset resonance (c) transient time and (d) zoom in waveform.

The static overall simulation results are shown in Figure 4 (a) – (b). The simulated waveforms of the output voltage  $v'o$  and output current  $i'Lx$  waveform were simulation output voltage 14.4 Vdc and output current about 2 A at an output power of ~29 W. The waveform in Figure 5 (a) and (b) shows the results state variable of current magnetizing inductance were results, it can be seen is similarity sinusoidal waveform. The voltage across reset

resonance, which was operated under reset to achieve the reset of remain flux saturation on the high frequency transformer are shown in Figure 5 (c)-(d). The simulation does analyze the following configuration math model and load conditions: 0.2– 0.325 s: constant operated at load and 0.325-0.649 s: based on step load condition and before 0.649 s: return to first condition. The simulation results of the proposed system are shown in Figure 6 (a)–(f), it can be seen output voltage return to set point are achieved. The first results of transient response of output voltage at step load half-load to no-load were overshoot 14.45 V and setting time to set point 24 ms and return load recover time to set point is 33 ms, undershoot 14.35 V as shown in Figure 6 (a-b). The second results of transient response of output voltage at step load full-load to no-load were overshoot 14.47 V and setting time to set point 34 ms and return load recover time to set point is 44 ms, undershoot 14.32 V as shown in Figure 6 (c-d). The finally results of transient response of output voltage at step full-load load to half-load were less overshoot 14.42 V and setting time to set point 27 ms and when return load recover time to set point is 14 ms, undershoot less than 14.35 V as shown in Figure 6 (e-f).

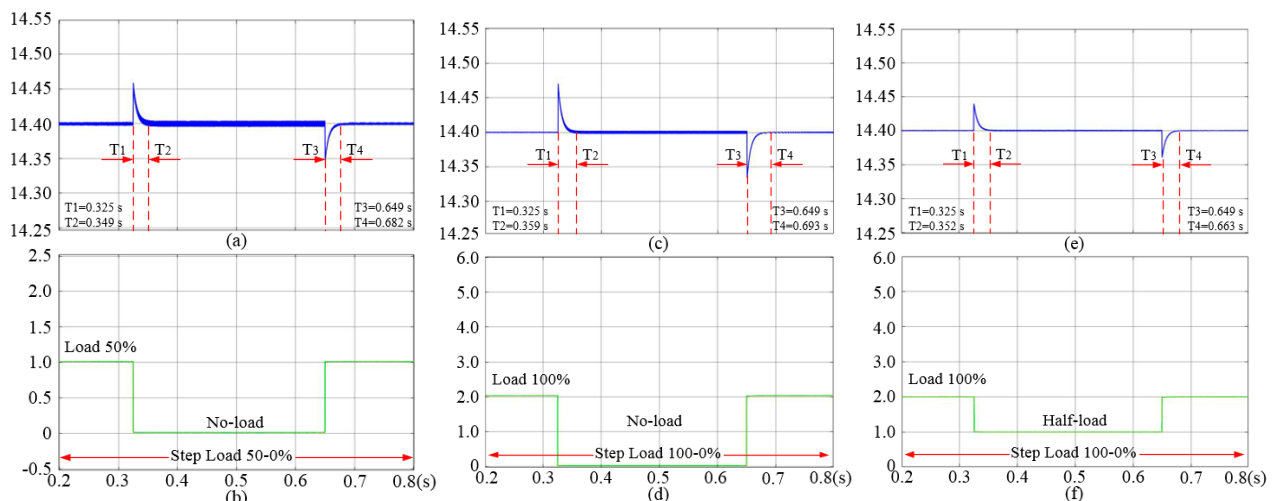


Figure 6 Simulation results of dynamic response of output voltage charger (a) response voltage at step load half-load to no-load (b) current step load half-load to no-load condition, (c) response voltage at step load ful-load to no-load condition(d) current step load full-load to no-load condition, (e) response voltage at step load full-load to half -load (f) current step load full-load to half -load condition.

## 5. CONCLUSION

An analysis and modeling circuits for control battery charge solar cell based on data management through IoT by using DC-DC forward resonant reset converter. has been investigated in this paper. The simulation math model of interest and regard are capable of: 1) correctness of state variable waveform by using averaged large-signal model 2) dynamic response of output voltage charger, when change 50% to 0%, 100% to 0% and 100% to 50% level load output. An averaged large-signal model method derivation has been presented. The main advantages of the proposed system are to observe state variable for built in math model by averaged large-signal model of front-end DC-DC forward resonant reset converter and controllable main power stages and proposed basic simple control unit and improve dynamic response. The simulation results have confirmed that at heavy step load change, desirable setting and recover time to set point output voltage charge under based on assumption regulative condition.

## ACKNOWLEDGMENT

This author would like to thank King Mongkut's University of Technology North Bangkok )KMUTNB(, Thailand, for financially supporting this research under Contract No. KMUTNB-60-GOV-010.

## REFERENCES

- [1] P. Cossoli, M. Cáceres, L. Vera, A. Firman and A. Busso, "Proportional-Resonant Controller And LCL Filter Design For Single-Phase Grid-Connected PV Micro-Inverters," *2018 IEEE PES Transmission & Distribution Conference and Exhibition - Latin America (T&D-LA)*, Lima, Peru, 2018, pp. 1-5, doi: 10.1109/TDC-LA.2018.8511669.
- [2] Ying-Chun Chuang, Hung-Shiang Chuang and Yu-Lung Ke, "Design and Implementation of Battery Charger with Zero-Voltage-Switching Resonant Converter for Photovoltaic Arrays," *2006 IEEE Industrial and Commercial Power Systems Technical Conference - Conference Record*, Detroit, MI, USA, 2006, pp. 1-6, doi: 10.1109/ICPS.2006.1677296.

- [3] Pajer R, Chowdhury A, Rodić M. "Control of a Multiphase Buck Converter, Based on Sliding Mode and Disturbance Estimation, Capable of Linear Large Signal Operation," *Energies* **2019**, 12, 2790; doi:10.3390/en12142790.
- [4] Rodríguez-Licea M-A, Perez-Pinal F-J, Barranco-Gutiérrez A-I, Nuñez-Perez J-C, "Switched Polytopic Controller Applied on a Positive Reconfigurable Power Electronic Converter," *Energies* 2018, 11, 116; doi:10.3390/en11010116.
- [5] Chaohui Liu, Jiabin Wang, K. Colombe, C. Gould and B. Sen, "A CLLC resonant converter based bidirectional EV charger with maximum efficiency tracking," *8th IET International Conference on Power Electronics, Machines and Drives (PEMD 2016)*, Glasgow, UK, 2016, pp. 1-6, doi: 10.1049/cp.2016.0152.
- [6] S. Bolte, F. Schafmeister and J. Böcker, "Bidirectional Resonant Converter with Integrated Magnetics for On-Board Chargers," *2019 IEEE 28th International Symposium on Industrial Electronics (ISIE)*, Vancouver, BC, Canada, 2019, pp. 770-774, doi: 10.1109/ISIE.2019.8781295.
- [7] Fang Z, Wang J, Duan S, Xiao L, Hu G, Liu Q, "Rectifier Current Control for an LLC Resonant Converter Based on a Simplified Linearized Model," *Energies* 2018, 11, 579; doi:10.3390/en11030579.
- [8] Park H-P, Kim M, Jung J-H, "A Comprehensive Overview in Control Algorithms for High Switching-Frequency LLC Resonant Converter," *Energies* 2020, 13, 4455; doi:10.3390/en13174455.
- [9] Pajer R, Chowdhury A, Rodić M, "Control of a Multiphase Buck Converter, Based on Sliding Mode and Disturbance Estimation, Capable of Linear Large Signal Operation," *Energies* 2018, 11, 116; doi:10.3390/en11010116.
- [10] Abouchabana N, Haddadi M, Rabhi A, Grasso AD, Tina GM, "Power Efficiency Improvement of a Boost Converter Using a Coupled Inductor with a Fuzzy Logic Controller: Application to a Photovoltaic System," *Appl. Sci.* 2021, 11, 980; doi.org/10.3390/app11030980.
- [11] P. Chrin and C. Bunlaksananusorn, "Large-Signal Average Modeling and Simulation of DC-DC Converters with SIMULINK," *2007 Power Conversion Conference - Nagoya*, Nagoya, Japan, 2007, pp. 27-32, doi: 10.1109/PCCON.2007.372918.
- [12] V. S. Rajguru, S. Manjrekar and B. N. Chaudhari, "Small signal characterization of Active-Clamp Forward Converter with Full Wave Rectifier and peak current mode control," *2010 IEEE International Conference on Sustainable Energy Technologies (ICSET)*, Kandy, Sri Lanka, 2010, pp. 1-5, doi: 10.1109/ICSET.2010.5684957.
- [13] M. Veerachary, "Analysis of Fourth-Order DC-DC Converters: A Flow Graph Approach," in *IEEE Transactions on Industrial Electronics*, vol. 55, no. 1, pp. 133-141, Jan. 2008, doi: 10.1109/TIE.2007.907677.
- [14] J. Cruz, M. Castilla, J. Miret, J. Matas and J. M. Guerrero, "Averaged large-signal model of single magnetic push-pull forward converter with built-in input filter," *2004 IEEE International Symposium on Industrial Electronics*, Ajaccio, France, 2004, pp. 1023-1028 vol. 2, doi: 10.1109/ISIE.2004.1571954.



# THE IMPORTANCE OF NATURAL INSULATION BUILDING MATERIALS IN SUSTAINABLE ENERGY EFFICIENT BUILDINGS

Filiz Bal Koçyigit

Atilim University, Fac. Of Fine Art Design and Architecture, Dept. Of Arch., Ankara, Turkey,  
filiz.kocyigit@atilim.edu.tr, ORCID: 0000-0003-4191-0724

Hatice Mehtap Öz

Tarsus Üniversitesi, Lisansüstü Eğitim Enstitüsü, İmalat Mühendisliği Anabilim Dalı, 33400, Tarsus, Mersin,  
mehtap\_oz@tarsus.edu.tr, ORCID: 0000-0002-1912-9598

Gülsen Bilge Ülkü

Atilim University, Fac. of Fine Art Design and Architecture, Dept. Of Arch., Ankara, Turkey, bilge.ulku1@gmail.com  
ORCID: 0000-0002-1627-0369

Elmas Pak

Izmir Bakircay Univ. Fac. Of Architecture and Engineering, Dept. of Architecture, elmas.pakozturk@bakircay.edu.tr  
ORCID:0000-0003-0890-009X

Cahit Canberk

İzmir Bakırçay Univ., Fac. Of Architecture and Engineering, Dept. of Architecture,, cahit.canberk@bakircay.edu.tr  
ORCID:0000-0001-6224-3313

Ece Dinç

Atilim University, Fac. of Fine Art Design and Architecture, Dept. Of Arch., Ankara, Turkey,  
ece.dinc@student.atilim.edu.tr, ORCID: 0000-0002-2771-8907

Baş Koçyigit

Atilim Univ. Fac. Of Engineering, Dept. of Comp. Eng., baris.kocyigit@student.atilim.edu.tr  
ORCID: 0000-0003-3003-4976

Ercan Köse

Tarsus Üniversitesi, Mühendislik Fakültesi, Elektrik- Elektronik Mühendisliği, 33400, Tarsus, Mersin,  
ekose@tarsus.edu.tr, ORCID: 0000-0001-9814-6339

Oğuz Emrah Turgut

İzmir Bakırçay Üniversitesi, Fac. Of Architecture and Engineering, Dept. of Mech. Eng.,  
guzemrah.turgut@bakircay.edu.tr, ORCID: 0000-0003-3556-8889

**Cite this paper as:** Koçyigit FB, Oz HM., Ülkü GB., Pak E., Canberk C., Dinç E., Koçyigit B., Köse E., Turgut OE.  
*The importance of natural building materials in sustainable energy efficient buildings.*, Conf. Ren. Energy Sys. 21-23 April 2021, Istanbul, Turkey

## Abstract:

Nowadays, there is increasing interest in materials that do not harm indoor air quality and human health. Corn cobs, Sunflowers kernel hulls are left in the field and accepted as waste. Because the spaces are closed especially during the winter, therefore, not using synthetic and petroleum-based materials increases its importance in these months. In the summer, especially in the hot Köppen-Geiger climate system, Adana and its surroundings are in the hot-summer-Mediterranean region, and the extreme heat of the outdoor areas in the summer months increases the importance of thermal insulation materials and natural thermal insulation materials. It accelerates research on its subject. In

this study, recycling can be provided; theoretically, calculations such as heat transfer coefficients were made for the samples that can be obtained in approximately  $10 * 20 * 2$  cm size by mixing natural materials such as cones, walnut shells, and garlic stalks with materials such as cement and gypsum used in the construction industry.

As a result; thermal insulation is aimed to contribute to the construction sector by measuring the thermal insulation performance by using natural materials that are less harmful to human health and recyclable.

**Keywords:** *Natural materialss, , energy consumption, energy gain materials, ,engineering, architecture.*

© 2021 Published by ECRES

## 1. INTRODUCTION

Due to the increase in energy use and rising costs in recent years, the importance of energy efficiency has increased. One of the most important factors affecting energy efficiency is heat transfer losses. Heat, on the other hand, is defined as an unorganized (microscopic) and transitional (transfer) form of energy that flows between a system and its environment only due to the temperature difference, according to Greenery [1].

Heat transfer is a physical event that occurs due to temperature difference [1]. Heat transfer can be performed from one point to another in three different ways. These are stated as conduction, convection and radiation [1]. Energy efficiency stands out as a very important factor during heat transfer. Here, in order to use heat energy efficiently, it is necessary to pay attention to the thermal insulation that causes heat losses. The TS 825 standard, which is in the literature on thermal insulation and is valid in practice, is encountered [2]. The energy consumed in these structures on a global scale has a significant proportional share. As a result of the reduction of thermal losses depending on the use of suitable building materials, the energy efficiency can be increased and the amount of energy consumed can be reduced [3].

In buildings; vegetable and animal origin, (cotton-based thermal insulation material, boron-added cellulosic thermal insulation material), mineral origin, (glass wool, rock wool, perlite, aerated concrete, pumice), synthetic origin Polyurethane foam (PUR), expanded polystyrene rigid foam It is observed that materials such as (EPS), PVC – polyvinyl chloride foam are used as building materials [3]. In addition, the following studies come to the fore when the literature is researched. Eryildiz et al. saw the straw bale, a natural material used in Europe and America since the 18th century, as a material with good health and thermal performance and investigated its use in different ways. They worked on a project in which straw bales were used as filling material in the wooden carcass system. They argued that using straw as a building material instead of burning it by staying in the field every year after harvest and polluting the air with CO gas can make a great contribution to the country's economy. They found that the buildings breathe thanks to the straw bale they used in their projects, the heat permeability of the bales is high and there is no need for an additional insulation material on the walls [4].

Important in another study, Binici and friends, significant amounts of sunflower production in Turkey is carried out and 2500000 tonnes per year stated that occur as sunflower stalk waste. Because of the large amount of textile factories like that found in Turkey demonstrated that waste leads to environmental problems of waste. In their studies to determine the heat transmission coefficient of the insulation material obtained from the mixture of these wastes, they showed that a reduction in the amount of heat lost to the environment can be achieved as the insulation properties of the building elements improve, and the insulation improvements provided are realized at low cost because the additives used are waste [5]. In another study of Binici and friends, the winter heating costs in Turkey, in summer the cooling costs has been made insulation for buildings to reduce these costs because too much is consumed in about 40% of the energy consumed in Turkey, housing and heating purposes, 80% of this energy. They mentioned that it is used as. Since buildings and settlements are responsible for 40% of CO<sub>2</sub> emission, which is the main greenhouse gas that causes global warming, they stated that various insulation systems and insulation materials are used to minimize the energy required for heating buildings. For this reason, they made calculations such as unit weight, water absorption, sound permeability and heat conduction coefficient by producing thermal insulation material by mixing the corn cobs, which were ground in accordance with the standards, with epoxy (using gypsum and cement in different ratios for this). As a result, they saw that the thermal conductivity coefficient of the corn-cob-based insulation material decreased to 0.075 and this value was within acceptable limits [6].

In their study, Shastri et al. compared the strength and pressure modulus of perlite foams, which they produced as a building material from starch binder-expanded perlite material, with plaster for foam density ( $0.1-0.9 \text{ g / cm}^3$ ). They found that the higher the density, the more damaged the perlite foam. They found that when using the produced perlite foam with foamed gypsum, the compressive strength of the  $0.3 \text{ g / cm}^3$  density perlite foam was compatible with the foamed plaster with a density of  $0.7-0.9 \text{ g / cm}^3$  [7]. Ricciardi et al. Demonstrated that using effective

insulation materials can provide energy and cost savings in buildings. In this study, which was carried out to investigate the thermal and acoustic properties of 12 mm and 20 mm thick sample panels made of recycled materials, waste paper and textile fibers, it was determined that according to the test results, they displayed a good thermal behavior and their k-values varied between 0.034-0.039 W / m<sup>2</sup>.K they have done. They found that the heat conduction coefficient values of these samples were close to insulation materials such as rock wool (0.037 W / m<sup>2</sup>.K), paper wool and mineral wool (0.04 W / m<sup>2</sup>.K). They also found that the densities of these new panels (433-483 kg / m<sup>3</sup>) were higher than the densities of rock wool (90 kg / m<sup>3</sup>), paper and mineral wools (32-40 kg / m<sup>3</sup>) [8]. In our study, environmentally friendly materials such as cones, walnut shells and garlic stalk were mixed with cement and gypsum, and new thermal insulation materials were suggested to the literature, It has been demonstrated that the use of these proposed materials can be used both for the purpose of adding value to the economy and for energy efficiency of environmentally friendly waste materials.

## 2. ENERGY AND HEAT INSULATION

Due to the rapidly increasing world energy use, supply difficulties, the tendency of energy resources to be depleted and severe environmental effects (ozone depletion, global warming, climate change, etc.) have increased. The global contribution to energy consumption from buildings, both residential and commercial, has steadily increased in developed countries, reaching figures between 20% and 40%, going beyond industry and transport, which are other major sectors [9]. The energy consumption of a building is highly dependent on the properties of its exterior surface. The thermal performance of external walls is a key factor in improving the energy efficiency of the construction industry and reducing greenhouse gas emissions. Due to both winter heating and summer cooling, one of the best ways to reduce energy consumption is known as thermal insulation [10]. With the right material selection, its thickness and location provide good indoor thermal comfort conditions and sufficient energy savings. Since a single thermal insulation material cannot be used in one place, it is necessary to choose according to the characteristics of the place of use. The rates of heat loss occurring in building elements such as walls, floors, windows, roofs and thermal bridges, depending on the architecture of the building, its location, the state of heat insulation, the building features used, sound insulation, fire resistance, water vapor permeability and the impact on the environment and human health differ [10, 11]. Knowing the ways in which heat flows occur is considered an important factor in order to decide on the appropriate thermal insulation. According to the second law of thermodynamics, if there is a temperature difference between the two environments, the heat passes from the high temperature environment to the low temperature environment. Since this heat transfer depends on the difference in ambient temperatures as well as the properties of the environment and surfaces, the heat flow mechanism; heat conduction (conduction), convection, convection, heat radiation (radiation, radiation) are examined under three main headings [12]. Heat flows are given in Figure 1.

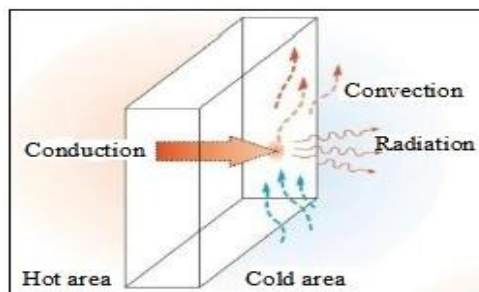


Figure 1. Heat Flows [12]

Within the framework of thermodynamic laws, heat energy passes from hot environment to cold environment in environments where the temperature is different, Heat transfer cannot be stopped but can be reduced, It is defined as large, thermal resistance that reduces the transition, The amount of heat passing through a unit area (one square meter area) is calculated by Equation 1 [13].

$$\dot{Q} = \frac{A \Delta T}{R} \quad (1)$$

$\dot{Q}$ : Heat energy per unit time	(Watt)
A: Surface area where heat passes	(m <sup>2</sup> )
$\Delta T$ : Temperature difference	(°C veya K)
R: Thermal resistance	(m <sup>2</sup> K/W)

According to Equation 1, the difference between the surface area and internal and external temperatures in a building cannot be intervened too much. Therefore, the parameter that can be changed is thermal resistance. Because the areas are determined according to the project of a building and the interior and exterior temperatures are defined in the standards for comfort conditions. For the heat loss value, the total heat transfer coefficient ( $U$ ) is mostly used instead of the thermal resistance and is calculated as in Equation 2 [13].

$$U = \frac{1}{R} \quad (2)$$

$U$ : Toplam ısı geçiş katsayısi (W/m<sup>2</sup>K)

It is known that the magnitudes contained in the total heat transfer coefficient are important factors in thermal insulation. When a wall is examined including internal and external conditions, only the thermal resistance and heat transfer coefficients of the wall are calculated with the formula in Equation 3 [13].

$$R = \frac{1}{\alpha_{iç}} + \frac{L_1}{\lambda_1} + \frac{L_2}{\lambda_2} + \frac{L_3}{\lambda_3} + \dots + \frac{1}{\alpha_{dış}} = \frac{1}{U} \quad (3)$$

### 3. MATERIAL AND METHODOLOGY

In the study, new thermal insulation materials were produced for the samples prepared by mixing environmentally friendly materials such as cones, walnut shell and garlic stalk with cement and gypsum. Heat transfer coefficient and temperature calculations were made for these produced samples. Thus, when comparing the thermal insulation performance of three different environmentally friendly waste materials, it has been revealed that it can be used both for adding value to the economy and for energy efficiency. Cone, garlic stalk and walnut shell were selected as the material. Thermal insulation material was formed by taking certain amounts from these samples. The images of the building created with the samples prepared are given in Figure 2.

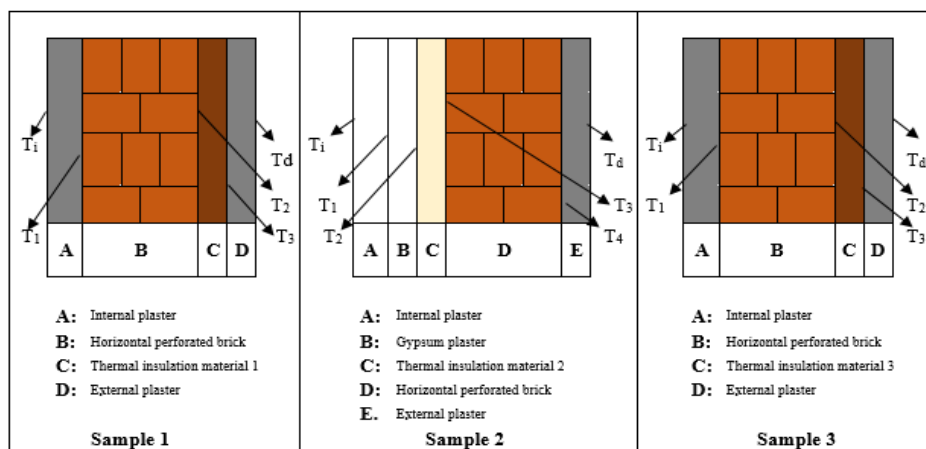


Figure 2. Images of the building prepared with samples

Table 1. Values Taken From TS 825 Standard [14]

Type of Material	TS 825 Annex E	Construction Element Thickness, d (m)	Construction Thermal Conductivity Value λh, (W / mK)	Description
Internal plaster (Lime mortar, lime-cement mortar)	4.1	0.02	1	-
Horizontal perforated brick	7.1.6	0.19	0.45	-
Thermal insulation material 1	10.5	0.05	0.04	Thermal insulation material cones
Thermal insulation material 2	10.5	0.03	0.04	Thermal insulation material garlic stalk
Thermal insulation material 3	10.5	0.06	0.04	Thermal insulation material walnut shells
Gypsum plaster (Plaster made using only gypsum (without aggregate))	4.4	0.02	0.51	-
Plaster mortar	4.3	0.04	0.70	-
External plaster (Cement mortar)	4.2	0.03	1.6	-

Regarding these samples; data taken from TS 825 Standard in calculating values such as total heat transfer coefficient, inner surface and outer surface temperature are given in Table 1 [14]. Also, in the initial calculations, according to the TS 825 Standard, the internal surface temperature ( $T_{\text{interior}}$ ) for the residences, the external surface temperature ( $T_{\text{exterior}}$ ) was taken as -10°C.

According to TS 825 Standard,  $\frac{1}{\alpha_i} = 0.13 \text{ m}^2\text{K} / \text{W}$  and  $\frac{1}{\alpha_d} = 0.04 \text{ m}^2\text{K} / \text{W}$  as seen in Equation 3. According to this; the thermal resistance (R) and heat transfer coefficient (U) of sample 1 are calculated with the help of the formula in Equation 4. According to this,

$$R = \frac{1}{\alpha_{i,c}} + \frac{L_1}{\lambda_1} + \frac{L_2}{\lambda_2} + \frac{L_3}{\lambda_3} + \dots + \frac{1}{\alpha_{d,s}} = \frac{1}{U} \quad (4)$$

$$U = \frac{1}{\frac{0,02}{0,13} + \frac{0,19}{0,45} + \frac{0,05}{0,04} + \frac{0,03}{1,6} + 0,04} \Rightarrow U = 0,53 \text{ W/m}^2\text{K}$$

Parameters such as  $T_{\text{interior}}$  surface and  $T_{\text{outer}}$  surface temperatures, surface temperatures of each material according to the type of material used in the samples with theoretical calculations are shown in Figure 3.

Accordingly, the theoretical calculations for Sample 1 are given below. The value of  $q'$  (heat flow density), which is the heat loss per unit time per hour, is calculated by Equation 5.

$$q' = U(T_i - T_d) \quad (\text{W/m}^2) \quad (5)$$

According to Equation 5;

$$q' = 0,53(20 - (-10)) \Rightarrow q' = 15,9 \text{ W/m}^2 \text{ is found as.}$$

$T_{\text{interior}}$  surface and  $T_{\text{outer}}$  surface temperatures, it can be calculated with the formula  $q'$  (heat flow density) seen in Equation 6.

$$q' = \alpha_i(T_i - T_{iy}) \quad (6)$$

According to Equation 6;

$$q' = \alpha_i(T_i - T_{iy}) \Rightarrow 15,9 = \frac{1}{0,13}(20 - T_{iy}) \Rightarrow T_{iy} = 17,93 \text{ }^\circ\text{C} \text{ is.}$$

After finding this value,  $T_1$ ,  $T_2$ ,  $T_3$ ,  $T_{dy}$  values should be calculated respectively. Equation 7 is used to calculate these values.

$$q' = \alpha_i(T_i - T_{iy}) = \frac{T_{iy} - T_1}{L_1/\lambda_1} = \frac{T_1 - T_2}{L_2/\lambda_2} = \frac{T_2 - T_3}{L_3/\lambda_3} = \frac{T_3 - T_{dy}}{L_4/\lambda_4} = \lambda_d(T_{dy} - T_d) \quad (7)$$

According to Equation 7;

$$T_1 \text{ value; } 15,9 = \frac{17,93 - T_1}{0,02/1} \Rightarrow T_1 = 17,61 \text{ }^\circ\text{C}, T_2 \text{ value; } 15,9 = \frac{17,61 - T_2}{0,19/0,45} \Rightarrow T_2 = 10,89 \text{ }^\circ\text{C},$$

$$T_3 \text{ value; } 15,9 = \frac{10,89 - T_3}{0,05/0,04} \Rightarrow T_3 = -8,98 \text{ }^\circ\text{C}, T_{dy} \text{ value; } 15,9 = \frac{-8,98 - T_{dy}}{0,03/1,6} \Rightarrow T_{dy} = -9,27 \text{ }^\circ\text{C} \text{ is.}$$

Theoretical calculations are made with the same method for sample 2 and sample 3.

#### 4. CONCLUSIONS AND RESULTS

When the studies in the literature are examined; The heat conduction coefficient is in the range of 0,034-0,039 W / m<sup>2</sup>.K for samples obtained with the mixture of waste paper and textile fibers 0,037 W/m<sup>2</sup>.K for rock wool, 0,04 W / m<sup>2</sup>.K for paper wool and mineral wool materials is seen. In the study conducted with the thermal insulation material produced with a different natural material, corn cob, it was found that the heat conduction coefficient decreased up to 0,0075.

In our study, these values were 0,53 for sample 1 (when using cones as thermal insulation material), 0,687 for sample 2 (when using garlic stalk as thermal insulation material) and 0,47 for sample 3 (when using walnut shell as thermal insulation material). has been obtained. Since the materials used in the samples are natural, it was seen that close values were obtained when the heat conduction coefficients of the samples in the studies made with natural materials in the literature were compared.

In this study, thermal insulation material was produced from natural materials using cones, garlic stalks and walnut shells. With these samples, heat flow density and heat transfer coefficients were calculated. Accordingly, the heat transfer coefficients are; 0,53 W / m<sup>2</sup>.K for sample 1, 0,687 W / m<sup>2</sup>.K for sample 2 and 0,47 W / m<sup>2</sup>.K for sample 3, heat flow density values ( $q'$ ); 15,9 W / m<sup>2</sup> for sample 1, 20,61 W / m<sup>2</sup> for sample 2 and 14,1 W / m<sup>2</sup> for sample 3. Since it is stated in the literature that the closer the heat transfer coefficient to zero, the less it will transmit heat,

the values we find are at an acceptable level according to the standards. These studies can be diversified with many natural materials that are less harmful to human health and can be recycled, contributing to the national economy.

## **REFERENCES**

- [1] Yeşilata B. Basic Heat Transfer in Engineering (Thermo-fluid systems textbooks series-2). Şanlıurfa, October 2007.
- [2] TSE Turkish Standards, TS 825 Thermal Insulation Rules in Building. ICS 91.120.10, Turkish Standards Institute, Necatibey Street No.112, Ministries/ANKARA, 2008.
- [3] Karadayı Tıkkansak T, Yüksek İ. A Research on the Selection of Thermal Insulation Materials in Buildings. Plumber Journal, Number: 242. February 2016.
- [4] Eryıldız Iraklı D, Başkaya A. Building with Straw Bale: Construction of a Prototype in Kırıkkale-Hasandede, J. Fac. Eng. Arch. Gazi Univ, Vol 15, No 2, 87-104, 2000.
- [5] Binici H, Sevinç A, H, Eken M. Isolation Material Production Using Sunflower Stalk And Textile. KSU, Journal of Engineering Sciences, 15(1), 2012.
- [6] Binici, H, Sevinç A, H, Eken M. Demirhan C. Corn on the Cob Added Heat Insulation Material Production. Çukurova University Journal of the Faculty of Engineering and Architecture, 29(2), pp 13-26, December 2014.
- [7] Shastri D, Kim S, H. A new consolidation process for expanded perlite particles. Construction and Building Materials, 60: 1–7, (2014).
- [8] Ricciardi P, Belloni E, Cotana, F. Innovative panels with recycled materials: Thermal and acoustic performance and Life Cycle Assessment. Applied Energy 134 (2014) 150–162.
- [9] Pérez-Lombard L, Ortiz J, Pout C. A review on buildings energy consumption information, Energy and Buildings. Volume 40, Issue 3, 2008, Pages 394-398.
- [10] D'Alessandro F, Schiavoni S, Bianchi F, Asdrubali F. Insulation materials for the building sector: A review and comparative analysis. Renewable and Sustainable Energy Reviews, 2016, Vol, 62, Issue C, 988-1011, 2016.
- [11] Şenkal Sezer F. Development of Thermal Insulation in Turkey and External Wall Insulation System Applied in Residential. Uludag University Faculty of Engineering and Architecture Magazine, Vol 10, No 2, 2005.
- [12] Ülker S. Effects of the Properties of Thermal Insulation Materials on the Application, Istanbul Technical University. Institute of Science, Master's Thesis, İstanbul, 2009.
- [13] Uzun İ. Thermal Insulation and Applications in the Light of the Regulations. ISBN: 978-975-978-605-2, 1st Edition 2013, Kırıkkale.
- [14] [https://www.izoder.org.tr/hesap-makinesi/ts\\_825\\_yardim.pdf](https://www.izoder.org.tr/hesap-makinesi/ts_825_yardim.pdf)



## THE PLACE OF BIOPOLYMER-BASED COMPOSITES IN ENERGY-EFFICIENCY ARCHITECTURAL DESIGN

Filiz Bal Koçyigit

Atilim University, Fac. Of Fine Art Design and Architecture, Dept. Of Arch., Ankara, Turkey,  
filiz.kocyigit@atilim.edu.tr, ORCID: 0000-0003-4191-0724

Elmas Pak

İzmir Bakırçay Univ Fac. Of Architecture and Engineering, Dept. of Architecture, elmas.pakozturk@bakircay.edu.tr  
ORCID: 0000-0003-0890-0009X

Cahit Canberk

İzmir Bakırçay Univ., Fac. Of Architecture and Engineering, Dept. of Architecture,, cahit.canberk@bakircay.edu.tr  
ORCID:0000-0001-6224-3313

Gülsen Bilge Ülkü

Atilim University, Fac. of Fine Art Design and Architecture, Dept. Of Arch., Ankara, bilge.ulku@student.atilim.edu.tr  
ORCID: 0000-0002-1627-0369

Ece Dinc

Atilim University, Fac. of Fine Art Design and Architecture, Dept. Of Arch.,ece.dinc@student.atilim.edu.tr  
ORCID: 0000-0002-2771-8907

Barış Koçyigit

Atılım Univ. Fac. Of Engineering, Dept. of Comp. Eng., baris.kocyigit@student.atilim.edu.tr  
ORCID: 0000-0003-3003-4976

Hatice Mehtap Öz

Tarsus Univ., Dept. Of manufacturing Eng., 33400, Tarsus, Mersin, mehtap\_oz@tarsus.edu.tr  
ORCID: 0000-0002-1912-9598

Oğuz Emrah Turgut

İzmir Bakırçay Üniversitesi, Fac. Of Architecture and Engineering, Dept. of Mech. Eng.,  
oguzemrah.turgut@bakircay.edu.tr, ORCID: 0000-0003-3556-8889

Ercan Köse

Tarsus Univ., Fac. Of Eng., Dept. Of Elec.and Electronic, 33400, Tarsus, Mersin, ekose@tarsus.edu.tr  
ORCID: 0000-0001-9814-6339

**Cite this paper as:** Koçyigit FB, Pak E., Canberk C., Ülkü GB., Dinç E., Koçyigit B., Oz HM., Turgut OE., Köse E. The place of biopolymer-based composites in energy-efficiency architectural design. 9th Eur. Conf. Ren. Energy Sys. 21-23 April 2021, Istanbul, Turkey

**Abstract:** University design should turn to productions that evaluate environmental data, reduce carbon emissions on a universal scale, and use endemic plants efficiently. The land should use meteorological data and local resources effectively. Developed biopolymer materials, technological material production will support the reduction of carbon emissions. As a result of the insulation materials used in building shells and their use in photovoltaic and photodetectors that can generate electricity, the use of biopolymer composites comes to the fore. For this reason, in the study to be carried out in Ankara and Izmir regions, which are sampled, the effects of solar data on the building shell at different dates and at different times were investigated and its use to increase indoor thermal comfort and air quality with the help of bio-polymer materials was investigated. It is

also planned to use organic waste materials such as almond shell, pine cone, walnut shell grown in the Ankara region. With the lamination of mono-silicon photovoltaic bio-polymer materials that can achieve heat gain, the most effective use of solar energy in the modeled buildings will be ensured, while on the other hand, it will ensure that the interior light is not compromised.

---

**Keywords:** *polymers, energy efficient architectural design, bio-polymer composites, thermodynamics*

---

© 2021 Published by ECRES

## **1. INTRODUCTION**

University buildings should develop their own building designs by using technological infrastructure in order to set an example for the society on the one hand, and to transfer their financial resources to scientific studies on the other. For this purpose, first of all, they should evaluate the data of their close environment in the best way, and on the other hand, they should turn to productions that can reduce carbon emissions at a universal scale, use energy resources efficiently and provide effective use in endemic plants in the near environment. For this purpose, it should primarily use the field data, meteorological data, and the underground and surface resources in its location effectively.

When we examine the history of polymer materials for their use as building materials; Stone and wood were the main building materials in ancient times. Over time, when he learned how to make bricks, bricks, and tiles using clay, stone and briquette took their place as the main building materials. B.C. 18th century from the construction of the pyramids in Egypt in 3000 BC. end-19. YY. Stone and briquettes, which were fragile materials up to the beginning, were the determining building materials. Although these are suitable building materials for walls and columns, they caused problems in the construction of horizontal elements due to their low tensile strength against bending. Steel and cement, which emerged at the end of the 18th century, opened a new era with their high strength against tension and compression. The use of steel has developed very rapidly. Instead of high-strength steel cables, polymeric materials (carbon fiber reinforced polymer, CFRP) reinforced with carbon fiber, which are much lighter but strong like steel cables, but because of the including carbon they have to use in controlled. CFRP is formed by embedding very fine carbon fibers with a diameter of 5-10 micrometers in polyester resin. However, CFRPs, which are 5.2 times lighter than steel, are not widely used in civil engineering due to their high price. [1]

Patented in 1824, being inexpensive, easy to manufacture, and an outstanding hydraulic binder for making concrete, Portland cement became the most popular and basic building material of the 20th century. The biggest disadvantage of this "synthetic stone" like natural stone is its low tensile strength and high brittleness. The work to improve the properties of concrete by the addition of elastic reinforcing bars, fibers, or active forces started from the end of the 19th century. In fact, the methods of using fiber to strengthen fragile materials and adding horsehair to strengthen clay-water mud date back to ancient Egyptian times. In the development of fiber-reinforced concrete obtained to increase the toughness of the material; steel fiber reinforcement began to be used in the 1960s, polymeric fibers in the 1970s, glass fiber additives in the 1980s, and carbon fiber reinforced concrete in the early 1990s and became widespread. Plastics are another group of building materials[2].

Universities' use of biological resources consisting of endemic plants in the near environment instead of chemical resources in providing polymers used in energy efficient architectural design and the production of technological materials developed from these sources will support the reduction of carbon emissions. Thus, it will contribute to the high indoor - outdoor air quality.

Different polymerized products have the tools to meet different requirements. Especially with the use of insulation materials used in building shells and photovoltaic and photodetectors where electricity can be produced, the use of biopolymer composites comes to the forefront as a result of the search for new technology.

In addition, it is known that biopolymer materials gradually increase their influence in architectural design in many aspects such as flexibility and durability. Designed smart materials will increase the efficiency of use by adapting to the environment in which they are used in different regions, as they respond to environmental warnings by changing their properties or shape instead of "fighting environmental conditions". For this reason, in the study to be carried out in the selected Ankara and Izmir regions, the sample structures will be investigated primarily at different dates (equinoxes, summer tropics, winter tropics) and at different times (morning, afternoon and evening) to investigate the effects of solar data on the building shell and drink them with the help of bio-polymer materials. its use to increase the thermal comfort and air quality of the space has been investigated. It is planned to be supported with insulation materials to be made using organic waste materials such as almond shell, pine cone, walnut shell grown in the Ankara region.

With the lamination of mono-silicon photovoltaic bio-polymer materials with which heat gains can be obtained, the most effective use of solar energy in the modeled buildings was ensured, while electrical energy was provided,

and on the other hand, architectural design studies to ensure that interior lighting was not compromised and artificial lighting was not required thanks to the use of transparent materials. Thus, it was aimed to develop energy efficient architectural design methods by using natural materials that add heat insulation to indoor air quality and high recyclable thermal insulation capacity.

Nowadays, studies on energy efficient architectural design methods are increasing due to the effects of global warming. Many parameters are taken into account in nearly zero emission building design. Parametric architectural design and parametric building design, which are among today's architectural design methods, have led to the joint studies of scientists from different scientific fields. In these works, while restitution studies are carried out, technological studies such as energy engineering (electrical, mechanical engineering joint studies) and chemical engineering are brought together on the same platform. Among these studies, polymers have a great role in providing design based on energy resources, especially in architectural design. Nowadays, the use of bio-polymer against air pollution and global warming caused by carbon emissions has an important place in the increase of livable air quality. Polymers are compounds formed by combining a large number of molecules with chemical bonds in an orderly fashion. Researchers working in this field for the first time in the middle of the 19th century started by imitating natural polymers. Since the second world war, many polymers have been produced in laboratories and started to be produced on an industrial scale. They are the most researched materials with their degradability or recyclability in nature for a better quality and sustainable life.

The aim of this study is that although it needs energy most, on the one hand, its financial resources need to be directed to research, on the other hand, the data obtained are zero in the university building located in two different climate zones according to the Köppen-Geiger climate defect classification, where the university buildings that have the highest opportunity to work integrated with architecture and engineering are sampled. is to apply close energy practices. Case building in Ankara / Turkey with Atılım University, and in Izmir / Turkey in İzmir Bakırcay University were selected. A detailed building energy simulation tool was used to determine the impact of energy-efficient retrofit scenarios. Ankara and Izmir sample university buildings model, firstly; 1) the sun angles in the morning, noon, and evening hours during the equinox of the sun, and the areas where the buildings receive the most intense sun, 2) the sun angles and the most intense sun in the morning at noon and evening in the summer tropics, and 3) in the morning afternoon and evening in the summer tropics. The angles of the sun and the regions where the buildings receive the most sunlight are simulated on the buildings. It has been calibrated by comparing the measured and simulated indoor air temperatures with the total electricity consumption. The applicability of the scenarios was evaluated with the payback period criteria.

## **2. CASE STUDY**

Today, architectural designs are required to be flexible, portable, changeable, capable of movement, and compatible with the environment and the user. This new trend leads designs to seek to adapt to the life rhythm of nature beyond the understanding that emulates nature. Thus, the natural environment, nature's material, formations, fractal geometries are the source of the origin of most designs, and the life energy of nature is transferred to the designs. Architectural designs are developed in line with approaches that establish a relationship with nature, make use of nature and its materials, transfer nature, material change, transformation, vitality, texture, rhythm, and color to designs, and share with nature, architectural applications, and material production are carried out by taking environmental data into consideration. Architectural designs are shaped on new conceptual themes with the knowledge of where and how the forms and materials in nature are formed with interdisciplinary collaboration. These searches for new forms of architecture bring new trends to architecture, the forms are organic, ecological, living, dynamic, flexible, adaptable, Istanbul Commerce University Journal of Science Fall 2011 99 changeable, portable, portable, mobile, morpho-ecological, smart architecture The development of nature and the material in nature, its geometry, the compatibility of materials and nature, and the natural life in the formation processes are sources for all these trends. [3,4,5,6,7,8,9].

Ankara is situated in Central Anatolia Region of Turkey (at 32.52 E 39.56 N) which is Dsb type climate zone under the Koppen-Geiger climate classification (World Map of Koppen-Geiger Climate Classification, 2006). The average temperature is 22.3°C and 1.4°C during summer (May-October) and winter (December-March), respectively (Turkish State Meteorological Service, 2019).

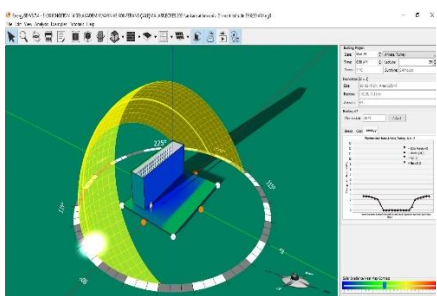


Figure 1a) Ankara / Turkey ATU building model according to sun effect in warm building. (sample simulation 21 March 06:30 latitude 39)

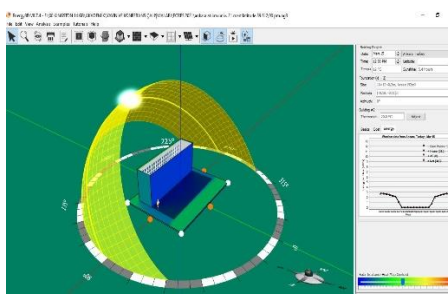


Figure 1b: Ankara / Turkey ATU building model according to sun effect in warm building. (sample simulation 21 March 12:00 latitude 39)

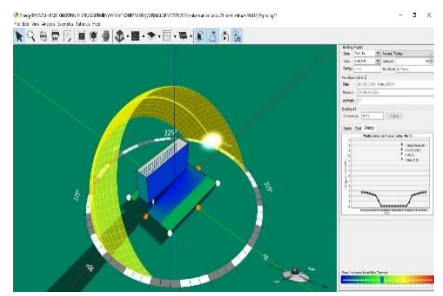


Figure 1c: Ankara / Turkey ATU building model according to sun effect in warm building. (sample simulation 21 March 17:30 latitude 39)

Figure 1aAnkara / Turkey ATU building model according to sun effect in warm building. (sample simulation 21 March 06:30, 12:00 and 17:30 latitude 39)

Izmir, according to Koppen-Geiger climate classification (Koppen-Geiger Climate Classification Map of the World, 2006) C-type climate regions, which in the Aegean region of Turkey (32.52 E 38 K) is located. The annual average temperature varies between 14-18 °C in the coastal areas. The hottest months are July (27.3 °C) and August (27.6 °C), the coldest months are January (8.6 °C) and February (9.6 °C) (Turkish State Meteorological Service, 2019).

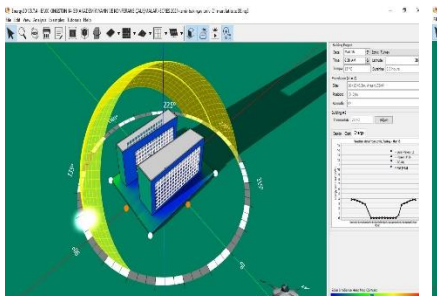


Figure 2a: Izmir / Turkey İBU building model according to sun effect in warm building. (sample simulation 21 March 06:30)

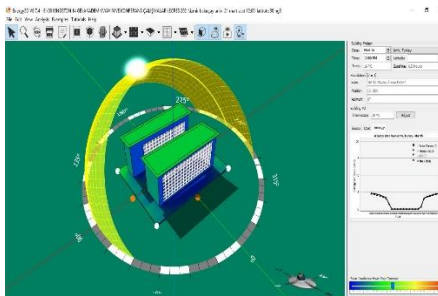


Figure 2b: Izmir / Turkey İBU building model according to sun effect in warm building. (sample simulation 21 March 12:00)

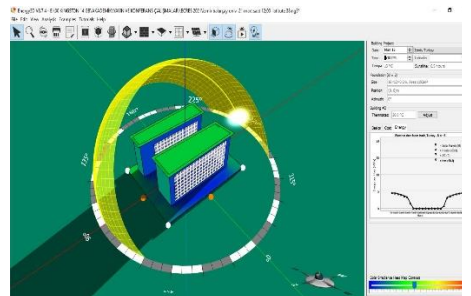


Figure 2c: Izmir / Turkey İBU building model according to sun effect in warm building. (sample simulation 21 March 17:30)

Figure 2: Izmir / Turkey ATU building model according to sun effect in warm building. (sample simulation 21 March 06:30, 12:00 and 17:30 latitude 38)

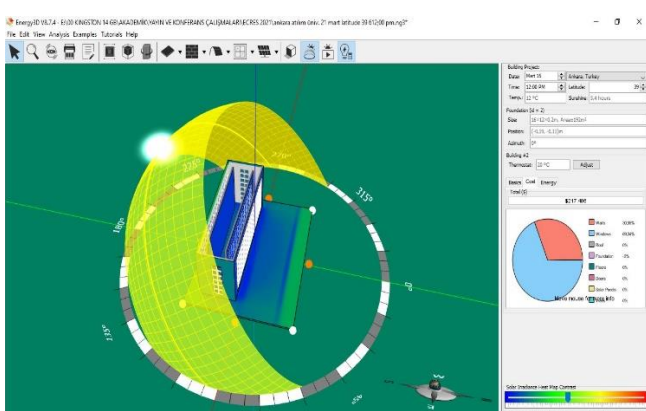


Figure 3a): Cost analysis of Ankara / Turkey ATU building model according to sun effect in warm building. (sample simulation 21 March 12:00 latitude 39)

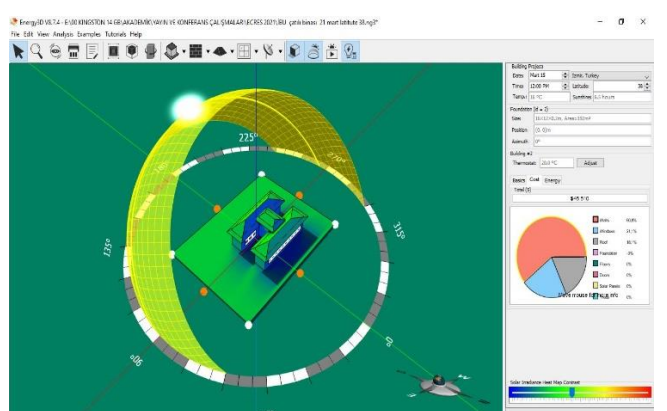


Figure 3a) : Cost analysis of Izmir / Turkey ATU building model according to sun effect in warm building. (sample simulation 21 March 12:00 latitude 38)

Figure 3a): Cost analysis of Ankara and İzmir / Turkey ATU and İBU building model according to sun affection in warm building. (Sample simulation 21 March 12:00)

## 2.1. Use of Bio Polymer Materials as Building Materials

Natural fibers obtained from annual agricultural by-products in Ankara and Izmir region offer various advantages when applied as the main component in biocomposite building materials. These fibers, such as straw and other non-wood fibers, are renewable annually and have the lowest cost worldwide compared to other natural fibers available on the industrial fiber market. In this article, the author presents three case studies of natural fiber reinforced polymers (NFRP), discussing agro-fiber densification, different architectural designs and manufacturing stages for customized applications. Natural fibers are combined with three different biopolymers: thermoplastic, thermoset and elastic thermoplastic. This allowed variations in the final designs and geometries that could be achieved, but in all cases had to change the fabrication technique accordingly. Mechanical properties and environmental evaluation were analyzed to prove the applicability of the developed products. In the design supported by the use of OPVs, electricity is generated from the windows on the building facades, while the interior remains illuminated, thus preventing the use of extra artificial lighting systems.

Common biopolymers such as cellulose [10], chitosan [11], starch [12], collagen [13], soy protein [14], which are thought to be used to protect indoor air quality while increasing energy gain on the one hand, especially in OPV and other energy gains. should be preferred to use. Melt strength, impact strength, thermal stability, permeability of biopolymers are not good enough for use in some applications, so making biopolymer composites by strengthening nanoparticles or mixing them with others are some ways to improve certain properties while keeping the original properties intact. Due to the presence of various repeating carboxyl, hydroxyl, amino functional groups, biopolymers can bind and interact with metals and organic contaminants. Non-toxicity, biodegradability and degree of functionality highlight the use of biopolymer composites in various applications such as fuel cell, battery, sensor, photovoltaic (PV) [6-10]. biomaterial-based PV and UV photo-sensing applications, but very few of these have focused on biopolymer composites and their effects on PV and UV photo-sensing. To our knowledge, there has not been a review article on PV and UV photo detection device applications of biopolymer composites to date. Therefore, this chapter will review the properties of biopolymer composites and their PV and light sensing applications [15].

## 3. CONCLUSION

In our study, it has been investigated how to re-evaluate architectural designs for the use of organic photovoltaic energy panels in order to benefit from the resources of their surroundings in order to increase the quality of indoor-outdoor kava and to be a pioneer in the designs of environmentally friendly university buildings. Due to the efficiency of environmental data and high flexibility in architectural design, it was considered to recommend biopolymers, and for this, the importance of using endemic sources came to the fore. In this study, two different shades were chosen primarily based on the Köppen Geiger climate classification. Solar data were determined for the analysis of the restoration required to make existing buildings energy efficient. In this way, the correct placement of the OPVs to be used and the evaluation of transparent areas have been prioritized.

## REFERENCES

- [1] Okay, O. Polimerik Malzemelerin Bugünü ve Yarını. İstanbul,Turkey: İTÜ, Kimya Böl., 2007.  
[www.kimya.itu.edu.tr/ookay](http://www.kimya.itu.edu.tr/ookay)
- [2] Çakmaklı B, Ateş Can S, Muraçal E. Deprem ve Mimarlıkta Kullanılan Polimer Malzemeler. In:International Burdur Earthquake & Environment Symposium; 7-9 May 2015: Mehmet Akif Ersoy University, pp.450.  
<http://ees2015.mehmetakif.edu.tr> – <http://ees2015.maku.edu.tr>
- [3] Pilar Echavarria M.. Portable Artchitecture And Unpredictabel Surrounding,. Structure Publishing Carles Broto, Barselona, 2005
- [4] Ritter A. Smart Materials In Architecture, Birkhauser, Berlin, 2007
- [5] Carbonized and Activated Non-wovens as High-Performance Acoustic Materials: Part I Noise Absorption Y. Chen1 and N. Jiang School of Human Ecology, Louisiana State University Agricultural Center, Baton Rouge, LA 70803, U.S.A.
- [6] Kronenburg R.. Flexible Architecture That Responds To Change, Laurence King Publishing, Londra.,2007
- [7] Kubo M., Salazar J. Verbs, Architecture Boogazine, Aktar, Barselona,2004
- [8] Balmond C., Smith J. Informal, Prestel Verlag, Münih, Berlin, 2002
- [9] Leach N., Turnbull D., Williams C., (2004), Digital Tectonics, Wile-Academy, Artmedia Press Ltd, Londra

- [10] M.S.A. Rani, S. Rudhzhiah, A. Ahmad, N.S. Mohamed, Biopolymer electrolyte based on derivatives of cellulose from kenaf bast fiber, *Polymers* 6 (9) (2014) 2371–2385.
- [11] M.E.I. Badawy, E.I. Rabea, A biopolymer chitosan and its derivatives as promising antimicrobial agents against plant pathogens and their applications in crop protection, *Int. J. Carbohydr. Chem.* 2011 (2011) 460381.
- [12] P. Calvert, Biopolymers: the structure of starch, *Nature* 389 (1997) 338–339.
- [13] D. Bhuiyan, M.J. Jablonsky, I. Kolesov, J. Middleton, T.M. Wick, R. Tannenbaum, Novel synthesis and characterization of a collagen-based biopolymer initiated by hydroxyapatite nanoparticles, *Acta Biomater.* 15 (2015) 181–190.
- [14] P. Kumar, K.P. Sandeep, S. Alavi, V.D. Truong, R.E. Gorga, Preparation and characterization of bio-nanocomposite films based on soy protein isolate and montmorillonite using melt extrusion, *J. Food Eng.* 100 (3) (2010) 480–489.
- [15] M. Mohiuddin, B. Kumar, S. Haque, Biopolymer Composites in Photovoltaics and Photodetectors, *Biopolymer Composites in Electronics*, 2017, Pages 1-12 DOI: 10.1016/B978-0-12-809261-3.00017-6



# SMART GRID SIMULATION BASED ON HIGH LEVEL ARCHITECTURE

Abdul Razaq

School of Design and Informatics, Abertay University, Dundee, United Kingdom, razaq@abertay.ac.uk  
ORCID: 0000-0001-7025-5381

Muhammad Majid Hussain

Department of Electrical & Electronic Engineering, University of South Wales, Cardiff, United Kingdom  
muhammad.hussain@southwales.ac.uk, ORCID: 0000-0002-6255-6966

Muhammad Siddique

Electrical Engineering Department, NFC Institute of Engineering & Technology, Multan, Pakistan,  
engr.siddique01@gmail.com, ORCID: 0000-0003-2032-0733

Cite this paper as:

Razaq, A, Hussain, MM, Siddique, M. Smart grid simulation based on high level architecture. 9th Eur. Conf. Ren. Energy Sys. 21-23 April 2021, Istanbul, Turkey.

**Abstract:** Simulation of complex systems such as Smart Grid (SG) requires intensive computing in terms of processing, network bandwidth and storage. We evaluate system architectures and technologies to implement High Level Architecture (HLA) for SG simulation system. The proposed architecture will encapsulate complexity to provide simulation as a web service. This unique design will allow users to investigate challenges related to SG without being involved in complications of co-simulation. HLA will guarantee to address reusability and interoperability of complex simulations. It will allow building custom simulations for SG without having knowledge of power and communication systems.

**Keywords:** Smart grid, distributed simulation, high level architecture

© 2021 Published by ECRES

## 1. INTRODUCTION

Increasing requirements of large scale and complex simulations (i.e., SG) require intensive computing resources. Consequently, complex, and large-scale simulations utilize distributed infrastructures. The emerging technologies in Cloud platforms present a feasible solution for processing, bandwidth and storage thriving domain of SG simulation. Implementing HLA on cloud platform guarantees the requirements of large-scale complex simulations effectively.

SG is a complex system consisting of various hardware components and software solutions. It can be visualized as "system of systems" and "service of services" given the complex nature of functions involved in four major electricity subsystems: generation, transmission, distribution, and consumption.

Simulation is an abstraction of a real system. In complex simulation such as SG, various systems share common functionality, single solution cannot fulfil the requirements of entire Modelling and Simulation (M&S). HLA is IEEE standard for M&S which consists of framework and rules. Prior to HLA, Distributed Interactive Simulation (DIS) happens to be choice of M&S architecture. The generic structure of HLA, for interoperability and reusability of components, provides structure and description for implementing the simulation application [1-2]. The basic building block of HLA simulation is federate, which represents a standalone simulation component, a set of federates within Run-Time Infrastructure (RTI) form a federation to achieve collaborative execution.

Cloud computing can be logically defined into three layers: resource, virtualization, and middleware [3]. Software as a Service (SaaS) allows aggregating the computing resources to provide a unified interface while hiding the complexity of distributed systems.

There have been various endeavors to simulate SG combined with power and communication simulators with open and commercial licenses. However, dedicated local installations and domain specific expertise are required to use these tools effectively. This deficiency has led to research into web enabled SG simulator. In [4] initiated to combine

electric power with communication components. Their work was based on ns2 which is community project with open-source license; however, the part of power simulation was performed using commercial off-the-shelf components. Electric power and communication synchronizing simulator (EPOCHS) were introduced for distributed simulation environment. They achieved interaction between these two distinct domains via development of runtime infrastructure (RTI). A federated simulation system for developed RTI was created with custom interface for easier implementation.

In [5] researched lifecycle of a cloud simulation and have proposed XML based Military Scenario Definition Language (MSDL) framework for resource delivery and scheduling mechanism. To solve the automatic resource discovery, MSDL provided discovery model which would offer model resource requirements as defined in unit's element. Such scheme should enable resource discovery before and during execution. But no resource accounting or auditing is available in their proposal. In [6] researched into structure of Simulation Service Description Framework (SSDF) with simulation services. They proposed Cloud Simulation System (CSS) as layered structure of the cloud simulation services with an ontology based layered SSDF (OLSSDF), including the layered architecture of cloud simulation service and the ontology semantics of each layer in the framework. They claim that CSS is unique representation of networked M&S lead by the requirements of application demand and background, without specifying the QoS. In [7] also researched integration of simulation resources of OS, processing, storage, and I/O devices to build a simulation environment. A virtualization-based middleware of Cloud Simulation Platform (CSP) is designed and implemented. In this approach, libvirt middleware was used to map physical resources to virtual resource pool and allocated via unified management. The work conducted by [8] and [9] termed as GridSpice is an interesting attempt in SG simulation. They have utilized Grid Lab and Mat Power as its backend for power simulation. In [10], Georg investigated HLA based co-simulation and proof of concept was implemented via Java. They integrated Dig SILENT Power Factory power system simulator with the commercial license and OPNET as network simulator. Mapping the entities between power and communication network has been claimed to form a true co-simulation.

The cross-platform communication between the power system simulator and OPNET is modelled as HLA interactions. HLA interface was implemented on both simulators. This solution lacks open-source power simulator and lack of dedicated messaging system to pass messages back and forth to and from simulators. Recently, [11] presented similar work to implement HLA interface on individual components. They proposed HLA based SG co-simulation framework based on JADE as middleware for multi-agent platform to exchange messages across federation. They have opted commercial PSCAD/EMTDC for power and open source OPNET network simulators to form a co-simulation of SG. Each component of the system has a federate ambassador interface which eventually communicates with gateway RTI. This is an interesting attempt in right direction; however, it depends on commercial power simulator. Most recently, Ciraci, have presented an interesting co-simulator termed as FNCS based on Grid LAB-D and ns-3 [12]. FNCS is implemented in C++ with interfaces for C, Java, and Fortran. It also implements limited publisher-subscriber design of HLA to provide customization and integration. However, it does not offer SIMaaS.

In [13] Liu, investigated RTI with respect to Cloud environment. The counter RTI for cloud platform is termed as Cloud-RTI (CRTI) which encapsulates traditional RTI while providing an API as Cloud service. CRTI can be visualized as a classical Remote Procedure Call (RPC) when federate requests the service a request agent delivers the request to CRTI interface. Once the request is ready to fulfil the CRTI's call-back agent prepares the response while generating the call-back event before passing the results to call-back event processor. Call-back event processor executes the relevant interface of the requesting federate. The researcher analyzed the problems associated with standard HLA in distributed simulations. It is being suggested that achieving web services-based service-oriented RTI is rather complicated in terms of development and throughput [14]. The proposed solution of Service-Distributed RTI (SDRTI), which offers several advantages, such as heterogeneous communication, load balancing, loose coupling of services, communications security, and communications optimization. Few of these deficiencies can occur in RTI as these areas are out of scope for HLA itself. A reasonable messaging engine with asynchronous I/O would be able to optimized and heterogeneous communication.

On contrary, some researchers have pointed out that HLA based solution is not the right candidate for smaller simulations. According to Ginters [15], the wide variety of HLA functionality is rarely needed, besides expenses of HLA and its implementation are rather high. SaaS is mechanism for auditing, managing and delivery a part or complete application from centralized place. Liu investigated simulation as SaaS which can be offered as SIMaaS [16]. It is being suggested that performance degradation can be further lowered with fine-tuned job scheduling algorithms. Recently, Gao, investigated deficiencies of task scheduling algorithms in cloud simulation [17]. They claim to achieve fair multidimensional QoS for resource scheduling algorithm to compute every dimensional

parameter. They propose that traditional scheduling algorithms designed for common computing architecture are not right candidates for cloud platform. Table I presents challenges in exiting SG simulation systems with possible solutions.

The paper is organized as follows. section 1 reviews the literature on various simulation techniques for SG with power and communication systems for distributed architectures. It discusses open-source solutions only which are available for further investigation. Section 2 presents our proposed HLA based scheme with distributed architecture. Section 3 provides discussions followed by future work.

*Table 1. Challenges for smart grid simulators*

Challenges	Possible solutions envisaged
Extremely complicated setup	To confine the complexity and turn to simulation as a service
Requirements of powerful computers	Cloud platform provides aggregating computing
Collaboration not possible	HLZ would allow customization and feature enhancements without core design changes
Unified simulation of co-related subsystems	Single solution for power and network applications, cyber security, and automation
Lack of core framework in SIMaaS	Open and community support CERTI with high performance distributed simulation capabilities

## 2. PROPOSED SIMULATION ARCHITECTURE

We propose a system based on HLA programming paradigm designed to be deployed on Cloud platform while providing Simulation as a service. The cloud virtualization will encapsulate complexity while providing a simulation as service to user. HLA will guarantee to address reusability and interoperability of complex simulations that are capable to perform discrete dedicated tasks or complete system simulation (Basic HLA definitions in List 1). This federate base design would allow simulating different scenarios at component and system level. CERTI will be used for HLA framework which will allow deploying the simulation on cloud platform and customizing it as SaaS. This component will play a vital role in data exchange between simulations. CERTI supports HLA 1.3 specifications (C++) and partial IEEE 1516-v2000 and IEEE 1516-v2010 (C++).

### Basic definitions of HLA components:

- a) Federate: A software that can perform independently or be coupled with Federation Document Data (FDD) functionality in a RTI.
- b) Federation: A set of federates combined, on the basis of Federation Object Model (FOM), to perform a task.
- c) Federation Object Model (FOM): How instances' attribute values will be updated within a federation.
- d) Run-Time infrastructure (RTI): An execution environment which facilitates federates in life cycle.
- e) Simulation Object Model (SOM): Specifications of a federate that can be coupled to form a federation.
- f) Object Model Template (OMT): Communication frame between simulations consisting of FOM& SOM.

CERTI is primarily developed and maintained by the Toulouse research centre of French Aerospace Labs. Its open-source version is available with GNU licence and hosted on GNU website. CERTI consist of two major components of Run-Time Infrastructure Gateway (RTIG) and Run-Time Infrastructure Ambassador (RTIA). RTIG is responsible to coordinate the HLA simulation with CERTI framework; at least one RTIG process is required for each federation.

However, a single RTIG may be used for several federations. RTIA is federate ambassador service. It is automatically launched by the federate as soon as its RTI ambassador is created. A federate ambassador consists of a fixed set of functions that can be called from the RTI. Once the RTIG process is launched a single federate can create and join the federation over TCP or UDP listening port. At this stage, another federate can join the same federation created by first federate. All federates exchange messages with RTIG via their own RTIA, and RTIG is also responsible to provide FOM file needed to create or join the existing federation.

### Conceptual system structure:

Figure 1 presents conceptual structure and workflow of proposed simulation with CERTI framework. The left side presents high level view of the system with user initiating a simulation while rendering a service from cloud without

being involved in system's complexity. The results of simulation are acquired in same manner with typical request/response custom. On the right side of the figure, three conceptual blocks present the complete functionality which is mapped to corresponding blocks. Users can access the simulation via web-browsers or via API that should communicate via RTIA. This will allow creating simulation model and receiving simulation results. Cloud entity is responsible for global management including RTIG to manage federations, channel federates, SG simulation and perform various auditing routines. Finally, Simulation unit is further divided into validation of models, execution of simulation and result reporting mechanisms. Users and Simulator do not interact directly but with service offered by SIMaaS.

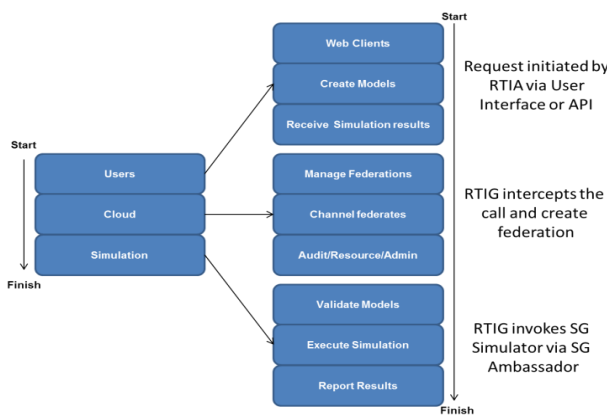


Figure 1. Conceptual system structure based on CERTI.

### 3. PROPOSED ARCHITECTURE

To provide web interface at communication layer there are multiple techniques which include Web-Enabled RTI that can provide interface for SOAP/COBRA/XML-RPC type architectures implemented on top of Blocks Extensible Exchange Protocol (BEEP). This approach can allow applications to use classical client/server type information exchange mechanism while utilizing the bidirectional facilities offered by BEEP. The disadvantage of this approach is interoperability, as every implementation should be following a common XML format and connection parameters at BEEP level should be standardized as well.

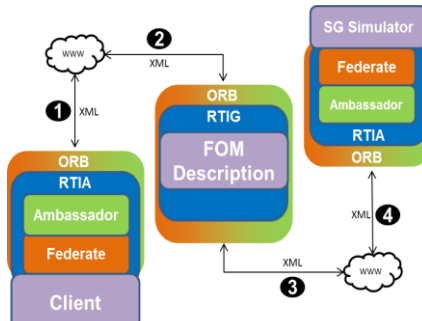


Figure 2. High level system architecture with CERTI components and communication links.

#### HLA interface layer:

This approach involves proving web interface at HLA interface level or precisely at federate level. Either web services (WS) API or Native HLA API can be implemented at federate level which can provide web services across the network. Advantage of this method is web enable services at each component level providing vast interoperability within the specific simulation and across simulations. Disadvantages of this technique include complexity and manageability of such a complex system.

#### HLA application layer:

In this method federation can provide web interface directly. This would include application specific web interface for set of federates. This federation could be accessible directly from web and RTI does not need to provide any web interface. HLA and web services should be mapped to provide specific services which would result in application dependent interfaces. Disadvantages of this approach include lack of interoperability and scalability. Another major challenge would be to modify the SG simulator itself to provide web communication channels. HLA

does not specify web interfaces as part of the standard. Although CERTI supports TCP/UDP but lacks SG specific Object Request Broker (ORB) format to exchange data between federates. Thus, proposed design suggests adopting ORB based mechanisms for SG specific format to exchange messages between federates. This can be achieved with off-shelf messaging engine (i.e., ZeroMQ). These web interfaces will further allow implementing Service-Oriented-Architecture (SOA) and will also enable separation of SG simulator from core CERTI framework. This will ensure extensibility while adding simulator nodes while updating the gateway and ambassadors for availability. The payload of exchanged XML would include connection settings, power and communication models and simulation parameters.

#### 4. PROPOSED SYSTEM DESIGN

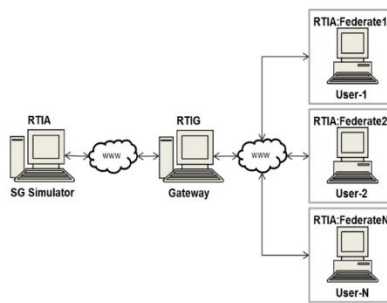


*Figure 3. System Design with SG Simulator, RTIA and RTIG*

Figure 3 presents system design based on conceptual structure and architecture illustrated in Figure 1 and Figure 2. Each ‘User-N’ in the system has a federate that talks to RTI ambassador (RTIA) to reach out to RTI Gateway (RTIG). Federate cannot directly talk to the RTIA directly except via RTIG. RTIG is responsible to provide means of connectivity to local federates to form a federation and act as bridge for subsequent message exchange between two or more federates. A single RTIG is proposed to form several federations or for complete system, this singularity will reduce the management, administration and auditing overhead of federations and resources. RTIG is also responsible to host the FOM definitions and present to each federates. This design will allow simultaneous simulations of multiple SG models as far as SG simulator does not implement any locking mechanism to force single instance execution. In such settings, all the resources including file handles, DB connections, socket etc. should offer asynchronous I/O with locking mechanism in place.

#### 5. DISCUSSIONS AND PERSPECTIVES

We propose platform independent distributed simulation for SG. The cloud virtualization will encapsulate complexity while providing a simulation as service to user. A platform independent simulator developed on open-source CERTI will simplify the design, usage, and deployment. HLA will guarantee to address reusability and interoperability of complex simulations that are capable to perform discrete dedicated tasks or complete system simulation. This federate base design would allow simulating different scenarios at component and system level. Proposed design can further provide on-demand simulation as a service and can execute parallel simulations efficiently, and reuse simulation components for cross domain research purposes. However, system would suffer slight performance degradation because of distributed nature of system, modular design, and typical overhead of web. It is also important to note that proposed approach drastically increases the complexity in terms of implementation which will result in higher development and maintenance cost. Unlike common computing platforms, distributed infrastructure requires various entities in terms of cloud software/hardware management, security policies and cost. These platforms demand different priorities for different simulation models. For example, some models require shortest processing time with high priority and greater availability. On the other hand, some models might require longer processing times with lower priority. And similar challenges exist for resource allocation to single federate or federation and reclaiming the resources back once the task is finished. All these different resource management requirements undermine the QoS and simulation results. These requirements become more challenging in cloud platform because of virtualization of dispersed resources, variety of underlying fabric and installed software. Besides resource management algorithms, RTI layer should ensure the QoS while scheduling the processing tasks, resource allocation, priority handling and load balancing within the simulation scope.

## 6. CONCLUSIONS

Work conducted by (Georg, 2010) and (Shum, 2014) is very promising, however, it lacks proven HLA framework. Both solutions have utilized custom developed HLA interfaces and integrated commercial power simulator. Our proposed scheme depends on open-source and proven HLA framework of CERTI and we target to utilize ns-2 and Grid Lab-d for SG co-simulation. HLA does not specify web interfaces as part of the standard. We will investigate to find the best design patterns to offer web services to the simulation systems. This includes web interfaces, message payload type, payload marshalling, timing requirements for different federations, communication and data collection in federations and SOA on federate level. We plan to utilize ZeroMQ in federate-to-federate communication over CERTI. ZeroMQ is an embeddable networking library which provides atomic messages across various transports like in-process, inter-process, TCP, and multicast. We will also investigate CERTI framework itself and how interoperability can be achieved at RTI level. Interoperability between federates and federations is function of deployed RTI. All federates developed for a certain RTI would be able to form various sets of federations with or without replacement for all possible combinations. However, integrating a federate in a federation executing in different RTI would pose interoperability challenges. Service-oriented resources can be reused as long as they offer services unlike federates that usually do not have re-entrant implementation.

## REFERENCES

- [1] Gagnon, F, Simon, E, Howells, P. On the development of a generic interface for HLA and DIS simulations. Proceedings 2<sup>nd</sup> International Workshop on Distributed Interactive Simulation and Real-Time Applications, 1998, pp. 52-59.
- [2] IEEE Standard for Modelling and Simulation (M & S) High Level Architecture (HLA). Framework and Rules 2000, IEEE SA Standard Board.
- [3] Armbrust, M, Joseph, AD, Katz, RH, Patterson, DA. Above the Clouds: A Berkeley view of cloud computing. University of California at Berkeley, Technical Report, 2009.
- [4] Hopkinson, K, Wang, X, Giovanini, R, Thorp, J, Fellow, L, Birman, K, Coury, D. EPOCHS : A Platform for agent-based electric power and communication simulation built from commercial off-the-shelf components. IEEE Transactions on Power Systems 2006, 21, 548-558 <10.1109/TPWRS.2006.873129>
- [5] Ying, C, Yong, P, Kedi, H, Qingyun, H. MSDL based lifecycle support of cloud simulation. Procedia Engineering 2012, pp. 1281.1285.
- [6] Li, T, Chai, X, Hou, B, Li, B. Research and application on ontology-based layered cloud simulation service description framework. Proceedings of the 1<sup>st</sup> ACM SIGSIM Conference on Principles of Advanced Discrete Simulation 2014, pp. 391-395.
- [7] Wang, Q, Ren, L, Zhang, L. Design and implementation for virtualization-based middleware of cloud simulation platform. 4th IEEE International Conference 2011.
- [8] Anderson, K, Du, J, Narayan, A, Gamal, AE. GridSpice: A distributed simulation platform for the smart grid. IEEE Transactions on Industrial Informatics 2014, 10, 1-5 <10.1109/TII.2014.2332115>
- [9] Hussain, MM, Siddique, M, Raees, A, Nouman, M, Javed, W, Razaq, A. Power management through smart grids and advance metering infrastructure. 6<sup>th</sup> IEEE International Energy Conference 2020, pp. 767-772.
- [10] Georg, H, Wietfeld, C, Muller, SC, Rehtanz, C. A HLA based simulator architecture for co-simulating ICT based power system control and protection systems. IEEE 3<sup>rd</sup> International Conference on Smart Grid Communications 2012, pp. 264-269.
- [11] Shum, C, Lau, WH, Mao, T, Chung, H, Tse, NCF, Tsang, KF, Lai, LL. HLA based co-simulation framework for multiagent-based smart grid applications. IEEE PES Asia-Pacific Power and Energy Engineering Conference 2014, pp.1-6.
- [12] Ciraci, S, Daily, J, Fuller, J, Fisher, A, Marinovici, L, Agarwal, K. FNCS: A framework for power system and communication networks co-simulation. Proceedings of the Symposium on Theory of Modeling & Simulation - DEVS Integrative 2014, p. 36.
- [13] Liu, B, Zhang, H, Yang, X. GY-RTI: An integrated distributed simulation environment. IEEE International Conference on Networking, Sensing and Control 2008, pp.232.235.
- [14] Wang, Z, Zhang, H, Zhang, R, Li, Y, Xu, B. Run-time infrastructure based on service-distributed architecture. Applied Mathematics & Information Sciences 2013, 7, 595-604 <10.12785/amis/072L32>
- [15] Ginters, E, Sakne, I, Lauberte, I, Aizstrauts, A, Dreija, G, Aquilar CRM, Merkuryev, Y, Novitsky, L, Grundspenkis, J. Simulation highway--direct access intelligent cloud simulator. 23<sup>rd</sup> European Modelling & Simulation Symposium 2011, pp. 978-988.
- [16] Liu, X, He, Q, Qiu, X, Chen, B, Huang, K. Simulation modelling practice and theory cloud-based computer simulation: Towards planting existing simulation software into the cloud. Simulation Modelling Practice and Theory 2012, pp.135-150.
- [17] Gao, FKW. Cloud simulation resources scheduling algorithm based on multi-dimension quality of service. Information Technology Journal 2012, 11, 94-101 <10.3923/itj.2012.94.101>



# CONTRIBUTION TO THE STUDY OF A DFIG WIND ENERGY GENERATION SYSTEM BASED ON A QUASI Z INVERTER

Larafa Ahcene

Department of Electrical Engineering, university Larbi Ben M'hidi oum El Baouaghi, Algeria, lar\_ahcn@yahoo.fr,  
ORCID: 0000-0003-3074-3836

Oudina Sofiane

Department of Electrical Engineering, university Mohamed Khider Biskra, Algeria, s.oudina@outlook.fr,  
ORCID: 0000-0001-7003-2452

Bahi Tahar

Department of Electrical Engineering, university Badji Mokhtar Annaba, Algeria, tbahi@hotmail.fr,  
ORCID: 0000 0001 6822 2492

*Cite this paper as:* **Larafa A., Sofiane, O., Tahar, B.** Contribution to the study of a DFIG wind energy generation system based on a quasi Z inverter. 9<sup>th</sup> Eur. Conf. Ren. Energy Sys. 21-23 April 2021, Istanbul, Turkey

**Abstract:** This article presents a study of a quasi-Z source inverter (QZSI) controlling a wind power system based on a double-fed induction generator (DFIG). This inverter recently became popular in electrical engineering journal literature due to its advantages over conventional inverter especially in the shoot-through phase of the same arm. we considered that DFIG generator is also one of the most known in the world of wind turbines, due to its many advantages, especially the use of an electric converter that absorbs a third of the total power than other generators, which gives it an advantage in terms of cost. For this reason, this study aims to control the active and reactive stator power of a DFIG generator with a minimal harmonic distortion rate using a spatial vector modulation (SVM) strategy to control this inverter, which can reduce the rotor current ripples that in its turn reduces the ripples of the electromagnetic torque and the stator current. The Matlab/Simulink program has validated this study.

**Keywords:** DFIG — QZSI — SVM — MPPT

© 2021 Published by ECRES

## Nomenclature

D	Shoot-through duty ratio Modulation index
M	Modulation index
B	Boost factor
G	Voltage gain
G	Voltage gain

## 1. INTRODUCTION

Wind power is one of the types of renewable energy that has spread for use as an alternative to fossil fuels. It is abundant and renewable energy, present in all regions, but its abundance varies from place to place. It is a clean and renewable energy which does not produce emissions such as greenhouse gases (greenhouse gases) during its operation. And its impact on the environment in general is less problematic than other energy sources [1]. Therefore, all governments and organizations are turning to this type of production in accordance with their commitments related to international climate agreements. As a result, and at first glance, researchers began to search for a more reliable and less expensive wind system model as an alternative to the traditional system. The DFIG wind power system is one of the most popular systems among manufacturers for its ability to operate at variable speeds, its small converter size compared to a synchronous machine combined with a frequency converter and its reduced losses compared to a synchronous machine associated with a frequency converter, but this does not prevent it from having disadvantages in terms of maintenance, in particular as regards the wear of the rings and brushes and

sensitization of variations in the electrical network [2]. In view of these data, this article tends to introduce a new type of electrical converter belonging to the family of Z source converters for controlling the DFIG machine and knowing its behavior and its capacity to respond to this type of converter. especially when operating the state of shoot-through to increase the DC bus voltage and triggering up and down switches the phase on the same branch and produces a desired output voltage different from the DC bus voltage available [3]. In addition, the reliability of the inverter has also been greatly improved especially in operating situations due to a locking defect between the upper and lower switch of the same branch which cannot destroy the circuit. Hence, it offers low cost, reliable efficiency and high single stage structure for Buck and Boost power conversion. The proposed QZSI incorporates all the advantages of the ZSI and has other unique features. It can achieve one-step Buck-Boost energy conversion with a wide gain range well suited for application in wind power generation systems. In addition, the proposed QZSI provides a constant input current, a lower source stress and lower component values over the conventional ZSI inverter [4], and to embody this idea, we have developed a mathematical model for the wind turbine, DFIG machine and the QZSI inverter. we put this model on Matlab/Simulink program to know the electrical output quantities and its capacity to follow its references.

## 2. COMPONENT MODELING AND SYSTEM CONTROL.

The variable-speed wind power system relies on a DFIG generator, connected to a wind turbine, and operates at a sub-synchronous regime controlled by a QZS inverter that powers the rotor windings Figure 1.

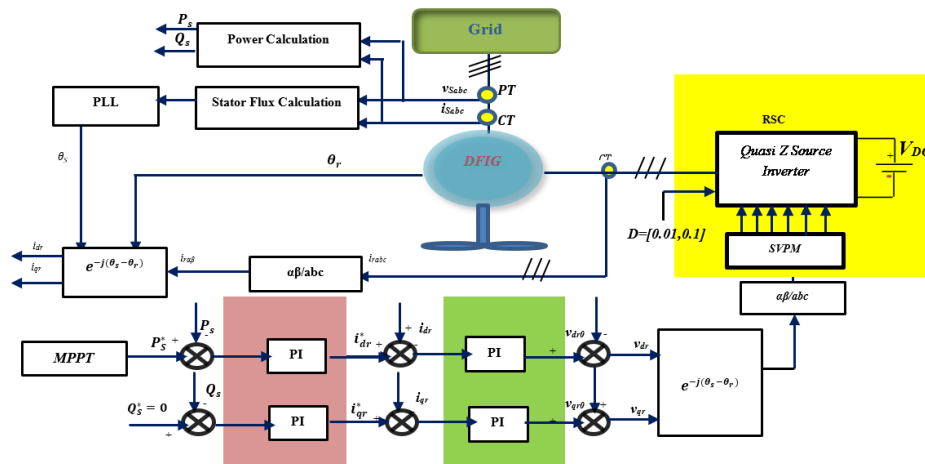


Figure 1. DFIG machine controlled by a Quasi Z source Inverter

### Wind

The wind energy captured by the wind turbine can be calculated by the following equation as follows:

$$P_m = 0.5\rho A C_p(\lambda, \beta) V_w^3 \quad (1)$$

Where:  $C_p(\lambda, \beta)$  is the power factor of the wind turbine which is a function of the specific speed ratio  $\lambda$  calculated according to equation (2) and pitch angle of the blade  $\beta$ .  $\rho$  is the density of the air,  $A$  is Swept rotor area,  $R$  is the radius of the wind turbine blade,  $V_w$  is the wind speed, and  $\omega_m$  is the speed of rotation of the wind turbine.

$$\lambda = \frac{\omega_m R}{V_w} \quad (2)$$

To get the maximum wind power, we need to maximize the power factor  $C_p(\lambda, \beta)$  through the optimization of the specific speed ratio  $\lambda$  during a given wind speed. the following mathematical equation shows the expression for the maximum wind power [5].

$$P_{max} = 0.5\rho A R^5 \frac{C_{pmax}}{\lambda_{opt}^3} \omega_m^3 \quad (3)$$

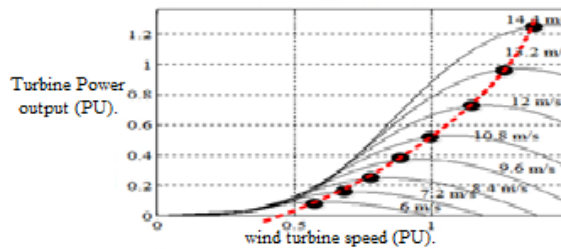


Figure 2. Power characteristic of the wind turbine (pitch angle beta = 0)

The extraction of the reference power is based on the principle of the MPPT (Maximum Power Point Tracking) algorithm, which consists of seeking an optimal operating relationship at maximum power, then tracking the maximum power based on relationship (3).

### Modelling the DFIG

A DFIG generator is mechanically connected to a wind turbine by a speed multiplier and electrically to a power grid as envisioned in this work. The DFIG machine consists of a wound rotor winding and a three-phase stator winding. The mathematical model of the DFIG is inspired by several scientific journals in this field, and it suffices to present in this article the controllable mathematical model of the DFIG machine and for more details see references [5-6]. The main objective of using vector control is to develop a simple control of the active and reactive powers of the DFIG which are respectively controlled by the rotor voltages  $V_{dr}$  and  $V_{qr}$ . This strategy is therefore based on the orientation of the stator flux according to the axis d of the rotating field with respect to the reference frame of the park, and this for the good separation between the axes d and q, see formulas [4-11], consequently the DFIG model therefore becomes simple and we can use PI controllers [7].

$$V_{sd} = -\omega_s \varphi_{qs} \quad (4)$$

$$V_{sq} = 0 \quad (5)$$

$$V_{dr} = R_{dr} I_{dr} + \sigma \frac{dI_r}{dt} - V_{dro} \quad (6)$$

$$V_{qr} = R_{qr} I_{qr} + \sigma \frac{dI_{qr}}{dt} + V_{qro} \quad (7)$$

$$\text{where } \sigma = \left( L_r - \frac{M^2}{L_s} \right)$$

$$V_{dro} = \sigma \omega_r I_{qr} \quad (8)$$

$$V_{qro} = \sigma \omega_r I_{dr} + \omega_r \frac{MV_s}{\omega_s L_s} \quad (9)$$

$$P_s = \frac{3}{2} (V_{ds} I_{ds} + V_{qs} I_{qs}) \quad (10)$$

$$Q_s = \frac{3}{2} (V_{qs} I_{ds} - V_{ds} I_{qs}) \quad (11)$$

### Modelling the QZSI

The quasi-source Z inverter (Figure. 3) appeared in the scientific literature in 2011 [8] As an alternative to the popular Z-source inverter [9], this DC-AC inverter is used to increase the voltage of the direct VDC bus by inserting shoot-through of the inverter arm into the SVPWM schematic (switches are closed up and down for the same arm simultaneously). This allows the switching of diode D (in motor mode) or of the switching of transistor TR (in reversible position) which includes the duty cycle d as a control variable. The constant height characteristic ( $V_{dc}/V_s$ ) can then be expressed by looking at the two operating sequences of the inverter, and which depend on the shoot-through state or not of the inverter. The elevation ratio of this inverter is given by:

$$V_{dc} = \frac{1}{1 - 2D} V_{in} = BV_{in} \quad (12)$$

$$B = \frac{1}{1 - 2D} \quad (13)$$

$$V_{ac} = M \cdot B \cdot \frac{V_{in}}{2} \quad (14)$$

$$G = M \cdot B$$

(15)

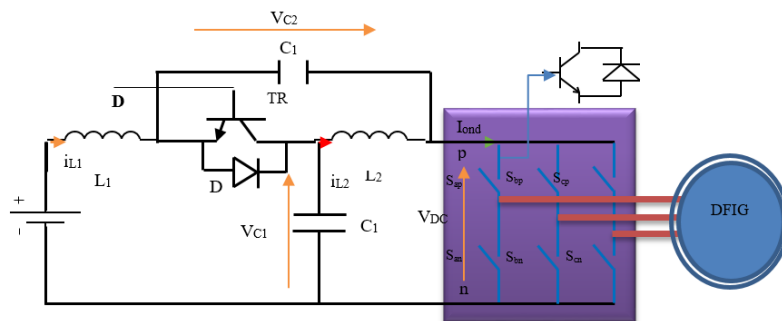


Figure 3. DFIG Machine controlled by a Quasi Z Source Inverter.

Where  $V_{C1}$  and  $V_{C2}$  are the average voltages of capacitors  $C_1$  and  $C_2$ ;  $i_{L1}$  and  $i_{L2}$  are the average currents of inductors  $L_1$  and  $L_2$ ;  $D$  is the shoot-through duty ratio,  $D = \frac{T_{sh}}{T_s}$ ;  $T_{sh}$  is the total shoot-through time interval;  $T_s$  is the switching cycle. The average voltage or pulse width  $V_{DC}$  can be easily adjusted by the duty ration of the switch conducting time ( $D$ ).

QZSI's SVM method differs from the conventional method by inserting additional short-circuit states of QZSI, and given the main objective of this article which is the control of the power extracted from the generator, we limit ourselves to setting the mathematical model of this method concerning the reference voltage vector and the switching times sequence. In the sector I, the QZSI reference voltage vector becomes [10]:

$$V_{ref} = V_1 \frac{T_1}{T_s} + V_2 \frac{T_2}{T_s} + V_0 \frac{T_0}{T_s} + V_{sh} \frac{T_{sh}}{T_s} \quad (16)$$

Where  $V_{sh}$  is the shoot through voltage vector. thus there are:

Figure 4 (a) shows the positions of the reference voltage vector of the QZSI.

$$T_s = T_0 + T_1 + T_2 + T_{sh} \quad (17)$$

The SVM switching time sequence of QZSI is shown in Figure 4 (b). The six switching times  $T_{max+}$ ,  $T_{mid+}$ ,  $T_{min+}$ ,  $T_{max-}$ ,  $T_{mid-}$ , and  $T_{min-}$  are calculated by:

$$\begin{aligned} T_{max+} &= T_{max} + \frac{T_{sh}}{12} \\ T_{max-} &= T_{max} + \frac{T_{sh}}{4} \\ T_{mid+} &= T_{mid} + \frac{T_{sh}}{12} \\ T_{mid-} &= T_{mid} + \frac{T_{sh}}{4} \\ T_{min+} &= T_{min} + \frac{T_{sh}}{12} \\ T_{min-} &= T_{min} + \frac{T_{sh}}{4} \end{aligned} \quad (18)$$

where the index + indicates the switching times of the upper switches and the index - indicates the switching times of the lower switches.

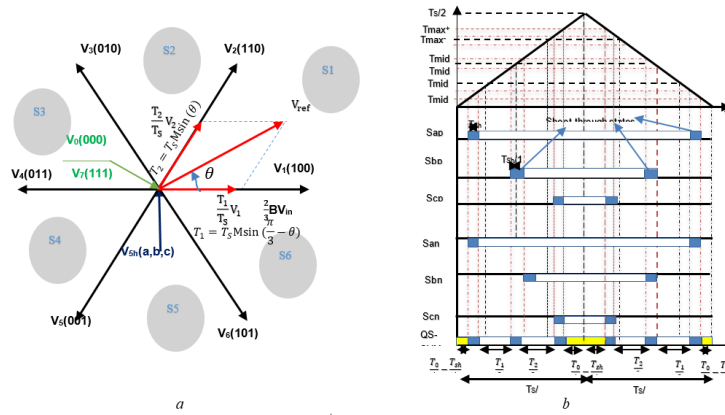


Figure 4. a) Voltage space vector b) Switching time sequences of QZSI

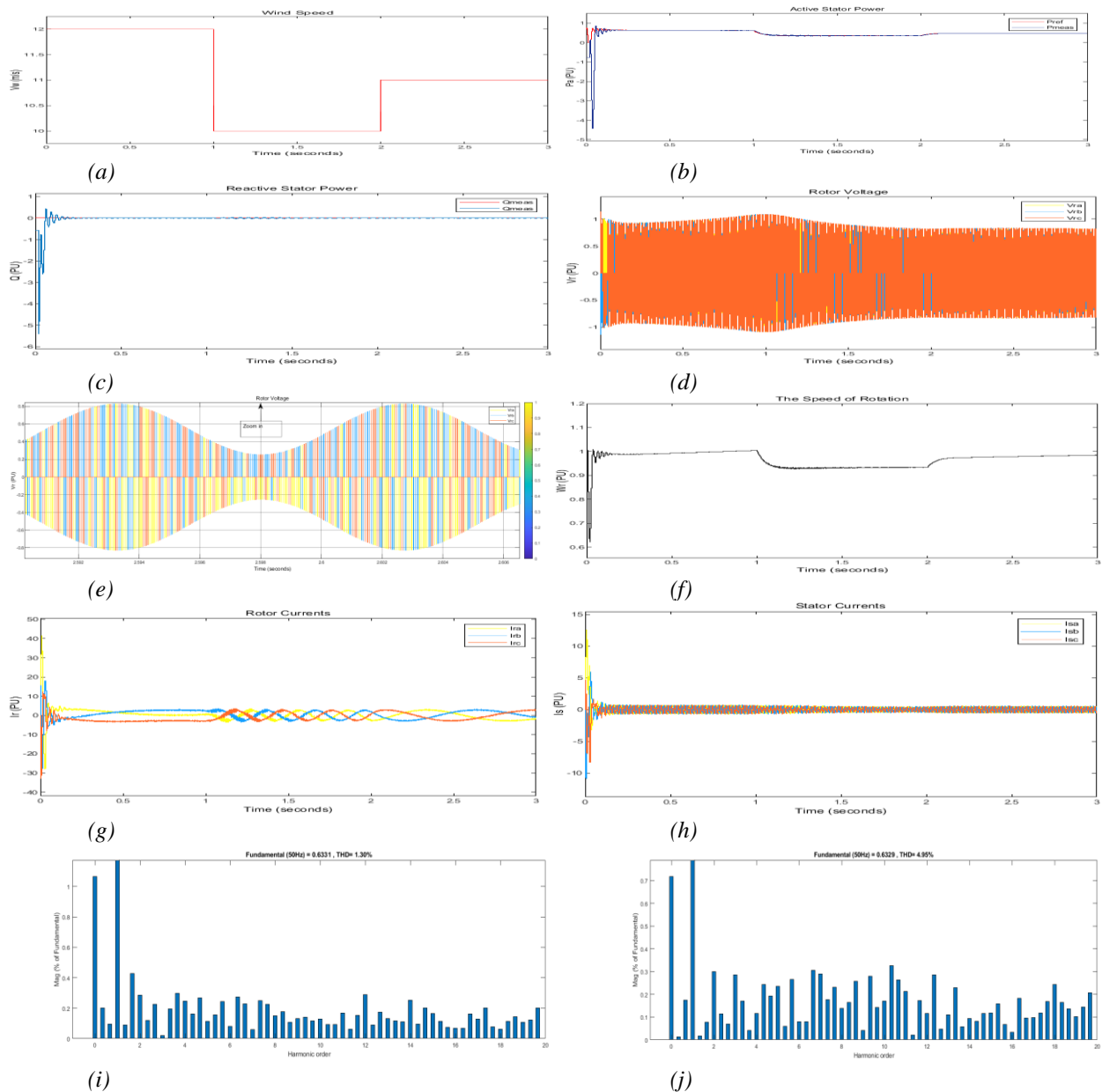


Figure 5. (a) Wind Speed (b) Active Stator Power (c) Reactive Stator Power (d) Rotor Voltages (e) Zoom of Rotor Voltages (f) The Speed of rotation (g) Rotor currents (h) Stator currents (i) The THD of the Stator Current at  $D = 0,01$  (j) The THD of the Stator Current at  $D = 0,1$

### 3. RESULTS AND DISCUSSION

The main objective is to control the DFIG electrical quantities of the generator and to ensure that these quantities follow the reference extracted from the MPPT strategy as well as the reactive power reference - which is set to zero to maintain the unit power factor. - This when operating this device in sub-synchronous mode using spatial vector pulse width modulation (SVPWM) technology applied to the inverter to optimize output quantities while reducing harmonic content (THD). therefore, this method aims to determine the modulated signals for the switches of the QZSI inverter in order to generate the desired three-phase voltages to control the DFIG generator. In this context, we used Matlab/Simulink to study this system under different wind speeds so that it takes the initial value of 12 m / s. the second speed change takes place at  $t = 1$  s, going from 12 m / s to 10 m / s. the last speed change is at  $t = 2$  s. in fact, a variation in the wind speed generates a variation in the active power of the stator which follows its reference power imposed in the 3 different operating regions of the DFIG. From the results of the simulations, it is evident that the active power follows the reference power which corresponds to the optimum rotational speed in the 3 different operating regions of the DFIG. However, we do note large variations especially at the first DFIG operating region of 0.05S before the power starts to perfectly follow its reference power, as vector control is a transient response to medium power. In addition, we can control the rate of harmonic distortion of the stator current through the transistor TR see figure (3) of QZSI by modifying the ratio D from 0.1 to 0.01 to obtain the following results THD ( $D=0.01$ ) = 1.30% & THD ( $d=0.1$ ) = 4.95%. see figure 5.

Simulation results of a DFIG-based wind power system and a quasi-z-source inverter, as shown in figures 5, were obtained using MATLAB / Simulink 2020 A, which runs on a CORE computer. i5 (2.4 GHz processor) with 6 GB of RAM. the components of the wind power system are calculated in the PU system against the actual data of the wind power plant ( $P_n = 1.5$  MW,  $V = 575$  V,  $f_n = 50$  Hz).

### ACKNOWLEDGMENT

I would also like to thank my fellow authors for their participation in this work.

### REFERENCES

- [1] Land use and electricity generation: A life-cycle analysis Vasilis Fthenakis Hyung Chul Kim
- [2] G. Abad, J. Lopez, M. Rodríguez, L. Marroyo, G. Iwanski, "Doubly Fed Induction Machine: Modeling and Control for Wind Energy Generation", John Wiley & Sons, Vol. 85, 2011.
- [3] Y. Li, J. Anderson, F. Z. Peng, and D. Liu, "Z-Source InverterTopology Improvements Review," 24th Annual IEEE Applied Power.
- [4] Dmitri Vinnikov, I. R. R. S. A., 2012. Step-Up DC/DC Converters with Cascaded Quasi-Z-Source Network. IEEE, pp. 3727-3736.
- [5] A. Tapia, G. Tapia, J. X. Ostolaza, J. R. Saens, "Modeling and control of a wind turbine driven doubly fed induction generator", IEEE Transactions on Energy Conversion, Vol. 18, No.2, pp. 194-204, 2003.
- [6] N. K. Swami Naidu and B. Singh, "Experimental Implementation of Doubly Fed Induction Generator-Based Standalone Wind Energy Conversion System," IEEE Trans. Ind. Appl., vol. 52, no. 4, pp. 3332–3339, Jul. 2016.
- [7] B. Hamane, M. L. Doumbia, M. Bouhamida, H. Chaoui, and M. Benghanem, "Modeling and control of a Wind Energy Conversion System based on DFIG driven by a Matrix Converter," 2016, pp. 1–8.
- [8] Minh-Khai Nguyen, Young-Cheol Lim, and Geum-Bae Cho. Switched-inductor quasi-z-source inverter. Power Electronics, IEEE Transactions on, 26(11) :3183 –3191, nov. 2011.
- [9] F.Z. Peng. Z-source inverter. In Industry Applications Conference, 2002. 37th IAS Annual Meeting. Conference Record of the, volume 2, pages 775 –781 vol.2, oct. 2002.
- [10] Anderson, J. and Peng, F.Z. (2008) Four Quasi-Z-Source Inverters. Proceedings of IEEE Power Electronics Specialists Conerence, Rhodes, 15-19 June 2008, 2743-2749.<http://dx.doi.org/10.1109/pesc.2008.4592360>.



# NUMERICAL INVESTIGATION OF ENERGY DESORPTION FROM MAGNESIUM NICKEL HYDRIDE BASED THERMAL ENERGY STORAGE

Sumeet Kumar Dubey

Indian Institute of Technology Delhi, New Delhi-110016, India, dubeysumeet92@gmail.com, ORCID: 0000-0002-0171-9338

K. Ravi Kumar

Indian Institute of Technology Delhi, New Delhi-110016, India, krk@ces.iitd.ac.in, ORCID: 0000-0002-8502-4321

*Dubey SK, Kumar, KR. Numerical investigation of energy desorption from Magnesium Nickel Hydride based thermal energy storage. 9<sup>th</sup> Eur. Conf. Ren. Energy Sys. 21-23 April 2021, Istanbul, Turkey*

**Abstract:** In this study, a 3-D model is developed to analyze thermal energy discharged from Magnesium Nickel hydride. Thermal energy storage (TES) system is designed with 1 kg of metal hydride in a cylindrical container with aspect ratio and porosity as 1 and 0.5, respectively. In this article, optimization of the number of heat transfer fluid tubes and effect of variation of aspect ratio on heat desorption from metal hydride bed is performed. The optimization of the number of heat transfer fluid tubes is performed with aspect ratio of 1. The study of aspect ratio variation on energy desorption characteristics is analyzed for three aspects: 0.5, 1, and 2. The different aspect ratios of geometry are analyzed for better heat transfer characteristics of the system.

**Keywords:** Thermal Energy Storage, Magnesium Nickel Metal Hydride, High Temperature Metal Hydride, Desorption,

© 2021 Published by ECRES

Nomenclature			
Abbreviation		Greek Letter	
TES	Thermal energy storage	$\Delta h$	Enthalpy of reaction (J/mol)
HTF	Heat transfer fluid	$\Delta s$	Entropy of reaction (J/mol K)
MH	Metal hydride	$\epsilon$	Porosity
TCES	Thermochemical energy storage	$\mu$	Dynamic viscosity (Pa s)
HTMH	High temperature metal hydride	$\rho$	Density (kg/m <sup>3</sup> )
LTMH	Low temperature metal hydride	K	Permeability (m <sup>2</sup> )
AR	Aspect Ratio	$\sigma$	Thermal conductivity (W/m K)
ACR	Area cross-section ratio		

## 1. INTRODUCTION

Technological advancement and rapid industrialization have led to a severe increase in energy demand. Several international agencies reported that annual energy demand increased significantly [1, 2]. The continuous and increasing burden on the conventional fuel reserves has led to increase in pollution, global warming, and the extinction of conventional fuel reservoirs. The challenges mentioned above can be addressed by utilizing renewable energy sources. Among renewable energy sources, solar energy has enormous potential to fulfill the energy demand. The challenges in solar energy technologies are diurnal variation and intermittent nature. Due to this, continuous energy generation is the major challenge. This challenge can be addressed using thermal energy storage (TES) system. Integration of the TES system with the power production and industrial process heat applications can help to overcome the challenges mentioned above.

The thermochemical energy storage (TCES) technique stores/releases energy by carrying chemical reactions. The endothermic chemical reaction stores the thermal energy while the exothermic chemical reaction discharges the

stored energy. TES using metal hydride (MH) is one of the well-known TCES techniques. The MH-based TCES technique has good reversibility, cyclic stability, wide range of temperature flexibility, and higher gravimetric and volumetric energy storage density.

The dual bed MH system is shown in Figure 1. Solar concentrator collects solar energy and converts it into thermal energy. The collected thermal energy is supplied to high temperature metal hydride (HTMH) for storage. The endothermic reaction takes place in HTMH, which is represented blue color dashed line. The hydrogen is liberated from HTMH due to endothermic reaction. The hydrogen released from HTMH is supplied to low temperature metal hydride (LTMH). Due to the absorption of hydrogen in LTMH, exothermic reaction occurs, and heat ( $Q_r$ ) is generated. When the heat stored in HTMH is required to be released, hydrogen stored in LTMH is supplied to HTMH, represented by red color dashed with a double dot line. In a dual MH bed system, HTMH acts as thermal energy storage media while LTMH acts as hydrogen storage media.

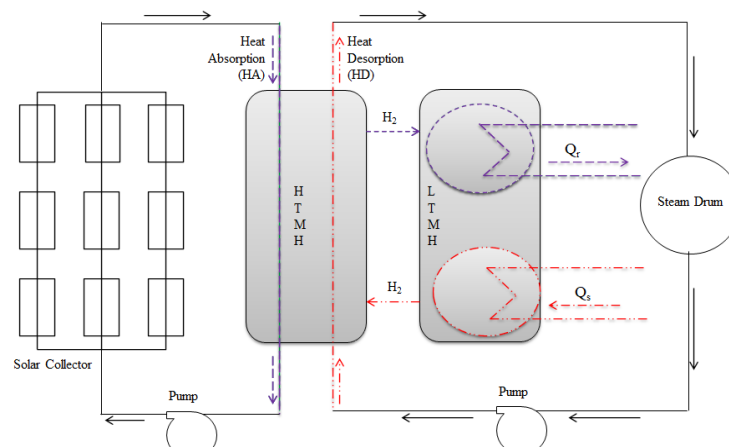


Figure 1. Schematic of dual metal hydride-based thermochemical energy storage system [3].

Magnesium (Mg) based MH attracted researchers for TES due to its high energy density and lower cost. In earlier studies, Mg-based MH were analyzed for its feasibility and different capacity models were developed for various applications [4-6]. Many numerical analyses have been performed on coupled MH-based TES system.  $\text{Mg}_2\text{FeH}_6$  and  $\text{Na}_3\text{AlH}_6$  as HTMH and LTMH, respectively, were studied for the feasibility of a dual hydride-based TES system [7]. The energy storage density of  $132 \text{ kWh/m}^3$  in the operating temperature range of  $450\text{--}500^\circ\text{C}$  is reported. Similar MH ( $\text{Mg}_2\text{FeH}_6$  and  $\text{Na}_3\text{AlH}_6$ ) pairs were studied with fins to enhance heat transfer from the MH reactor [8]. The energy storage density of  $90 \text{ kWh/m}^3$  with a storage efficiency of 96% was reported. A similar type of study with  $\text{NaMgH}_2\text{F}$  and  $\text{TiCr}_{1.6}\text{Mn}_{0.2}$  as HTMH and LTMH respectively was performed for dual MH-based TES system feasibility [9]. This study reported an energy storage density of  $226 \text{ kWh/m}^3$  with a higher temperature at  $600^\circ\text{C}$ . In another study,  $\text{Mg}_2\text{Ni}$  was used as HTMH, with  $\text{LaNi}_5$  as LTMH. The system reported a storage efficiency of 89.4% and an energy storage density of  $156 \text{ kWh/m}^3$  [10].

This work includes the analysis of energy discharge from Magnesium Nickel-based MH. A 3-D numerical model is developed in COMSOL Multiphysics 5.5. The work studies optimization of the number of HTF tubes and aspect ratio (AR) variation study on energy discharge from MH bed. Magnesium nickel hydride of 1 kg is prepared in a cylindrical container with diameter to height ratio as 1 and porosity 0.5. For an AR of 1, the number of heat transfer fluid (HTF) tubes is optimized. The optimum number of HTF tubes for AR 0.5 and 2 are calculated based on the area cross-section ratio (ACR). The three AR cases are compared based on the effective heat transfer from the MH bed.

## 2. NUMERICAL MODELING

The model geometry analyzed in this numerical work is shown in Figure 2. Magnesium nickel hydride of 1 kg is packed in cylindrical geometry, taking porosity as 0.5. One-fourth of the TES system is considered for analysis. The three AR configurations having a different number of HTF tubes are shown in Figure 2. The circle at the center of the cylindrical MH with a single circle represents the hydrogen supply tube. The concentric circles represent the axial HTF tubes distributed radially in the MH bed cross-section.

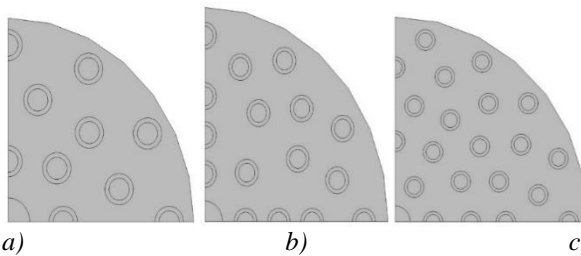


Figure 2. Computational domain for aspect ratio a) 0.5, b) 1, and c) 2.

### Governing Equations

This section includes the discussion on the governing equations of mass, momentum, and energy conservation used in the analysis.

- Mass conservation equation: The continuity equation for MH bed, hydrogen gas, and HTF are discussed below.

$$\varepsilon \frac{\partial \rho}{\partial t} + \nabla \cdot (\rho u) = -S_m \quad (1)$$

$$(1 - \varepsilon) \frac{\partial \rho}{\partial t} = S_m \quad (2)$$

$$S_m = C_a \exp \left( \frac{-E_a}{RT} \right) \ln \left( \frac{p}{p_{eq}} \right) (\rho_{ssat} - \rho_s) \quad (3)$$

$$\ln \left( \frac{p}{p_{eq}} \right) = A - \frac{B}{T} \quad (4)$$

$$\frac{\partial \rho}{\partial t} + \nabla \cdot (\rho u) = 0 \quad (5)$$

Eqs. [1, 2] represents the mass balance equation for hydrogen and MH, respectively, in the porous domain. Eq. [3] represents the rate of mass of hydrogen absorbed per unit volume. Eq. [4] is well known vant's Hoff equation that relates equilibrium pressure with temperature, enthalpy, and entropy of reaction. Eq. [5] represents mass balance for hydrogen in supply tube and HTF, respectively.

- Momentum conservation equation: The Navier stokes equation is used for free-flowing hydrogen and HTF flow, while the Brinkman equation is used for hydrogen flow in the porous domain.

$$\frac{\rho}{\varepsilon} \left( \frac{\partial u}{\partial t} + u \cdot \frac{\nabla u}{\varepsilon} \right) = -\nabla p + \nabla \cdot \left[ \frac{\mu}{\varepsilon} (\nabla u + (\nabla u)^T) - \frac{2\mu}{3\varepsilon} (\nabla \cdot u) \right] - \frac{\mu}{K} u + \frac{S_m}{\varepsilon^2} u \quad (6)$$

$$\rho \left( \frac{\partial u}{\partial t} + u \cdot \nabla u \right) = -\nabla p + \nabla \cdot \left[ \mu (\nabla u + (\nabla u)^T) - \frac{2}{3} \mu (\nabla \cdot u) \right] \quad (7)$$

Eq. [6] and [7] represent the momentum balance equation for MH and hydrogen in the supply tube and HTF, respectively. Eq [6] is the Brinkman equation, while Eq. [7] is the Navier Stokes equation.

- Energy conservation equation: As mentioned in the assumption, thermal equilibrium exists between MH and hydrogen gas flowing in the porous domain; the combined energy equation is discussed.

$$(\rho c_p)_{eff} \frac{\partial T}{\partial t} + \rho c_p (u \cdot \nabla T) = \nabla \cdot (\sigma_{eff} \nabla T) + S_T \quad (8)$$

$$(\rho c_p)_{eff} = \varepsilon \rho c_p + (1 - \varepsilon) \rho c_p \quad (9)$$

$$\sigma_{eff} = \varepsilon \sigma + (1 - \varepsilon) \sigma \quad (10)$$

$$S_T = S_m (\Delta h) \quad (11)$$

$$(\rho c_p) \left( \frac{\partial T}{\partial t} + u \cdot \nabla T \right) = \nabla \cdot (\sigma V T) \quad (12)$$

Eq. [8] and [12] represent the energy conservation equation for the MH bed and hydrogen in supply tube and HTF. Eqs. [9, 10] represents the effective heat capacity and effective thermal conductivity based on average volume calculation. Eq. [11] represents the energy generated due to the chemical reaction between hydrogen and MH.

### Assumptions Made in the Numerical Modelling

The hydrogen is treated as an ideal gas with thermal properties such as thermal conductivity and specific heat capacity constant throughout the process. MH material is homogenous, isotropic, and in thermal equilibrium with hydrogen gas.

### Initial and Boundary Conditions

The initial values at MH bed, hydrogen in supply tube, HTF, and copper tube, are listed below:

Temperature of MH bed, HTF, and copper tube	: 500 K
Pressure of MH bed, hydrogen in supply tube, and HTF	: 1 bar
Density of MH bed	: 3200 kg/m <sup>3</sup>
Temperature of hydrogen in supply tube	: 298 K

The outer surface along with the top and bottom surfaces of MH cylindrical bed, are insulated.

### Model Validation

A 2-D model is developed in COMSOL Multiphysics to validate the developed model. The temperature of MH bed is plotted with time. The temperature of the MH bed has good agreement with Jemni et al. (1999), as shown in Figure 3.

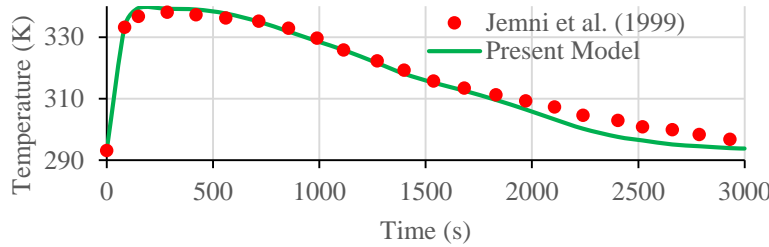


Figure 3. Model Validation [11]

## 3. RESULTS AND DISCUSSION

The results discussed in this study are divided into two different parts: a) Optimization of the number of HTF tubes for AR 1, b) Effect of variation of AR on energy desorption characteristics of Magnesium Nickel MH.

### Optimization of Number of HTF Tube

Aspect ratio terminology in this study is defined as the ratio of diameter (D) to height (H) of MH bed. To optimize the number of HTF tubes, geometry with AR 1 is considered for the analysis. The number of HTF tubes for AR 1 is increased from 36 to 54 tubes. The variation of absolute average MH bed temperature is studied as shown in Figure 4. The MH bed's temperature seems to decrease significantly when the number of HTF tubes increased from 36 to 48, but further increase in the number of HTF tubes from 48 to 54 has no significant change in MH bed temperature. Increasing the number of HTF tubes will add to the system's cost without any significant change in MH bed temperature. Therefore, 48 number of HTF tubes are decided as the optimum for the case of AR 1.

The number of HTF tubes for AR 0.5 and 2 is calculated using the term ACR. The term ACR is defined as the ratio of cross-sectional area of the MH bed to cross-sectional area of all the HTF tubes. The value of ACR calculated for AR 1 is 5.298. The same value is considered for AR 0.5 and 2 to calculate the number of HTF tubes. The number of HTF tubes calculated for AR 0.5 and 2 are 32 and 72, respectively.

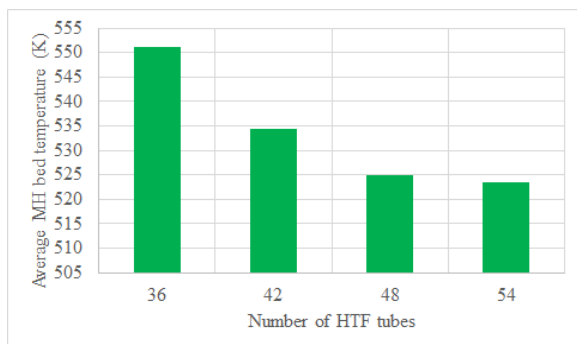


Figure 4. Variation of absolute average MH bed temperature with number of HTF tubes Model

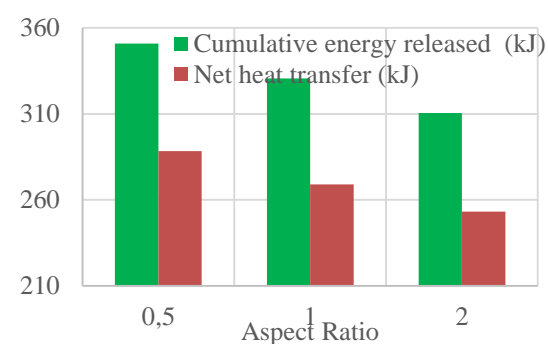


Figure 5. Variation of cumulative energy released and net heat transfer with aspect ratio

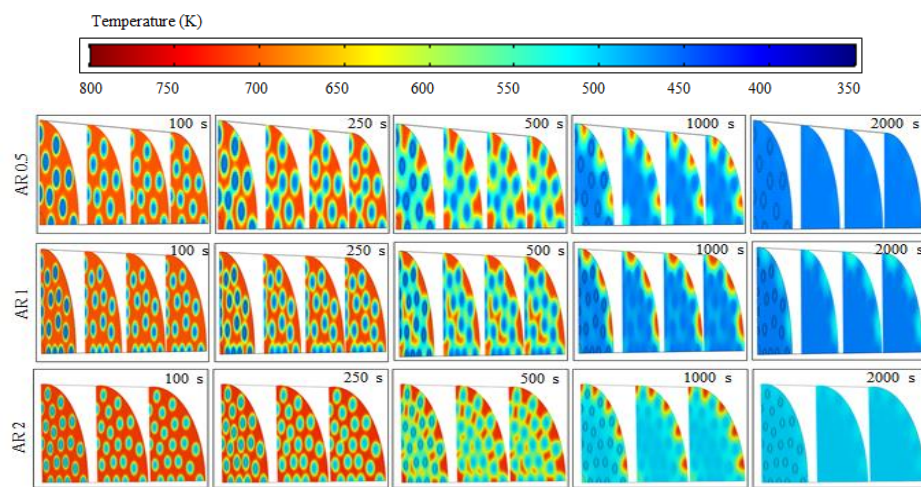


Figure 6. Temperature contour of MH bed with time for different aspect ratio

### Study of Aspect Ratio Variation on Energy Desorption Characteristics

The three configurations of AR 0.5, 1, and 2 are studied for effective heat transfer from MH bed. The effect of AR on the cumulative energy released and net heat transfer has been studied. The cumulative energy released and the net heat transfer from the MH bed for the three AR cases have been represented in Figure 5. The cumulative energy release and net heat transfer are maximum for AR 0.5, i.e., 350.94 kJ and 288.31 kJ.

The temperature contours of the MH bed cross-section at different axial lengths and different time instant for different AR have been shown in Figure 6. The contours represent the effective heat release from the MH bed, resulting in faster cooling for AR of 0.5 as compared to the other two cases. The heat resistance increases with an increase in the radial dimension of the MH bed. The radial heat transfer being dominant and it affects the heat transfer with the increase in radial dimensions.

### CONCLUSION

Magnesium Nickel MH is studied for thermal energy desorption and effective heat transfer from metal hydride bed. The optimum number of HTF tubes has been studied for three different aspect ratios. The variation of temperature of metal hydride bed and energy released is studied. The following observations are made based on the modeling of 1 kg of Magnesium Nickel MH.

- The number of optimum HTF tubes for AR 0.5, 1, and 2 are 32, 48, and 72, respectively.
- Cumulative energy released from MH bed with AR 0.5, 1, and 2 is 350.94 kJ, 330.56 kJ, and 310.42 kJ.
- The average temperature of MH bed is decreased due to effective heat transfer in lower aspect ratio geometries.
- The heat transfer from the MH bed increases with the lower radial dimension and higher axial dimensions.

### ACKNOWLEDGMENT

The authors are thankful to Science and Engineering Research Board (SERB), Department of Science and Technology (DST), Government of India, and Confederation of Indian Industry (CII) to award “Prime Minister Fellowship for Doctoral Research” to Mr. Sumeet Kumar Dubey in collaboration with Indian Oil Corporation Limited, Research and Development Centre.

## **REFERENCES**

- [1]. India 2020 Energy Policy Review, International Energy Agency Report, 2017, 1-304.
- [2]. Cozzi L, Gould T, Bouckart S, Crow D, Kim T-Y, McGlade C, et al. World Energy Outlook 2020. 2020;2050(October):1–461.
- [3]. Jain S, Dubey SK, Kumar KR, Rakshit D. Thermal Energy Storage for Solar Energy. In: Singh SN, Tiwari P, Tiwari S, editors. Fundamentals and Innovations in Solar Energy. Springer Nature Singapore Pte Ltd.; 2021.
- [4]. Bogdanovic B, Spliethoff B. The Magnesium Hydride System for Heat Storage and Cooling. Zeitschrift fur Phys Chemie. 1989;164(Part\_2):1497–508.
- [5]. Bogdanović B, Ritter A, Spliethoff B, Straßburger K. A process steam generator based on the high temperature magnesium hydride/magnesium heat storage system. Int J Hydrogen Energy. 1995;20(10):811–22.
- [6]. Paskevicius M, Sheppard DA, Williamson K, Buckley CE. Metal hydride thermal heat storage prototype for concentrating solar thermal power. Energy [Internet]. 2015;88:469–77. Available from: <http://dx.doi.org/10.1016/j.energy.2015.05.068>.
- [7]. d'Entremont A, Corgnale C, Sulic M, Hardy B, Zidan R, Motyka T. Modeling of a thermal energy storage system based on coupled metal hydrides (magnesium iron – sodium alanate) for concentrating solar power plants. Int J Hydrogen Energy. 2017;42(35):22518–29.
- [8]. Sofiene Mellouli, Askri F, Edacherian A, Alqahtani T, Algarni S, Abdelmajid J, et al. Performance analysis of a thermal energy storage based on paired metal hydrides for concentrating solar power plants. Appl Therm Eng. 2018;144:1017–29.
- [9]. d'Entremont A, Corgnale C, Hardy B, Zidan R. Simulation of high temperature thermal energy storage system based on coupled metal hydrides for solar driven steam power plants. Int J Hydrogen Energy. 2018;43(2):817–30.
- [10]. Malleswararao, K., Aswin, N., Murthy, S. S., & Dutta, P. (2020). Performance prediction of a coupled metal hydride based thermal energy storage system. International Journal of Hydrogen Energy, 45(32), 16239-16253.
- [11]. Jemni, A., Nasrallah, S. B., & Lamloumi, J. (1999). Experimental and theoretical study of a metal–hydrogen reactor. International Journal of Hydrogen Energy, 24(7), 631-644.



# A COMPARATIVE STUDY OF MELTING PERFORMANCE FOR ULTRA-HIGH TEMPERATURE LATENT STORAGE SYSTEM

Alok Kumar Ray

Centre for Energy Studies, IIT Delhi, India, qiz188618@uqidar.iitd.ac.in, ORCID: 0000-0002-4096-9997

Dibakar Rakshit

Centre for Energy Studies, IIT Delhi, India, dibakar@ces.iitd.ac.in, ORCID: 0000-0002-8469-5924

Ravi Kumar

Centre for Energy Studies, IIT Delhi, India, krk@ces.iitd.ac.in, ORCID: 0000-0002-8502-4321

Hal Gurgenci

University of Queensland, Australia, h.gurgenci@uq.edu.au, ORCID: 0000-0002-8340-0485

*Cite this paper as:* Ray, AK, Dibakar, R., Kumar, R., Gurgenci, H., A Comparative Study of Melting Performance For Ultra-High Temperature Latent Storage System. 9<sup>th</sup> Eur. Conf. Ren. Energy Sys. 21-23 April 2021, Istanbul, Turkey

---

**Abstract:**

Thermal energy storage using ultra-high temperature phase change medium (PCM) can be a potential solution to provide dispatchable solar energy from concentrated solar power (CSP) and to accumulate spillage of energy from photovoltaic and wind power. Ultra-high temperature latent heat storage (LHS) ( $>900^{\circ}\text{C}$ ) provides significant benefits of high energy storage density and efficient conversion to electric power that can be additionally augmented by cogeneration. A numerical investigation is performed to compare the melting performance of LHS of ultra-high temperature metallic PCM (silicon) with commercialized high-temperature salt ( $\text{NaNO}_3$ ) in rectangular domains of different aspect ratios (AR). The rectangular domain is subjected to uniform heat flux to capture the coupled multi-physics i.e. heat transfer, fluid dynamics, and phase change simultaneously during charging of domain. Fixed grid effective heat capacity method has been implemented using COMSOL Multiphysics to analyze the melting of silicon and  $\text{NaNO}_3$ . The influence of natural convection is observed to be different than molten  $\text{NaNO}_3$ . Circulation due to natural convection in molten silicon is clockwise and counterclockwise for molten  $\text{NaNO}_3$  and silicon respectively. Energy storage density and melting/charging rate of silicon are observed to be 40 and 3 times more than  $\text{NaNO}_3$ . The study establishes silicon as a potential PCM to design an ultra-high temperature LHS system.

---

**Keywords:**

Renewable energy, Ultra-high temperature, PCM, COMSOL Multiphysics, Melting

© 2021 Published by ECRES

## 1. INTRODUCTION

The ever-growing energy demands, declining conventional energy sources, and environmental pollution compelled us to make a transition towards renewable sources, such as solar, wind, hydropower, and biomass. Solar energy is the most attractive alternative due to its cleanliness, low cost, and abundance as compared to other renewable resources. However, the inherent intermittency of renewable sources (solar and wind) creates a mismatch between energy supply and demand. Therefore, better energy storage systems are required to effectively harness power and heat from renewable sources. In this context, thermal storage systems can have a key role to minimize the mismatch between energy supply and demand. Thermal energy storage can accumulate energy from various renewable resources and the stored energy can be retrieved later for heat and power production [1].

Storage of heat at high temperatures has higher exergy efficiency as compared to low-temperature heat storage according to 2<sup>nd</sup> law of thermodynamics. Moreover, co-generation of heat and electricity from thermal storage can be an attractive benefit at high-temperature ( $>900^{\circ}\text{C}$ )[2]. On top of that, the cost of power generation from CSP can be reduced by deploying advanced power cycles integrated with high-temperature energy storage[3].

Thermal energy can be stored in a medium by three methods:(a) sensible, (b) latent, and (c) thermo-chemical. A medium stores energy in form of sensible and latent heat by changing the thermo-physical properties of the medium. However, thermochemical storage is associated with reversible thermochemical reactions to absorb and release heat. A comparison between the three methods [4] identifies thermochemical storage as having the highest energy storage density but in an early stage of development. Sensible energy storage, though the only commercialized technology, has low energy density and high exergy loss [5].

LHS system refers to the phase transition of a PCM to store and release thermal energy at near isothermal conditions. The primary benefit is that PCM can store significant amounts of energy, both as latent and sensible heat, within a narrow temperature range[6]. However, low thermal conductivity and moderate latent heat of PCMs used in current LHS systems are the major bottlenecks for their wide-scale deployment. There are different methods to augment heat transfer rate in traditional LHS systems by using fins, cascaded PCM, and encapsulation. However, these strategies reduce the storage volume of PCM that leads to a reduction of energy density potential of LHS system and hence storage/retrieval capacity[7]. A potential alternative can be utilization of PCMs having large thermal conductivity and latent heat. Commonly, the latent heat of fusion increases with melting temperature for PCMs [8]. Hence, there is a growing interest to search for PCMs having high melting point.

In the last two decades, the investigation on high-temperature PCM mostly revolves around different inorganic salts and metallic PCM. However, metallic PCMs have the distinct merits over salts[9]:

- Salts are susceptible to subcooling but where metals generally have no or little subcooling.
- Salts change volume significantly during phase change
- Thermal conductivity below 1W/mK
- Thermal stability is below the requirement by high-efficiency power cycles

Birchenall et al. (1979) first proposed eutectic metals as potential high-temperature PCM to store thermal energy in industrial processes[10]. He and Zhang[11] developed a thermal energy storage device using a eutectic alloy of silicon and aluminum ( $\text{AlSi}_{12}$ ). Wang et al. investigated six compositions of aluminum (Al) and silicon (Si) based materials to determine their potential for high-temperature thermal storage application from medium to high temperatures (550-1200°C). Karim et al. proposed Al-Si-Ni and Mg-Si eutectic as suitable high temperature (more than 900°C) PCMs. Storage at ultra-high temperatures (> 900 °C) [12] using metallic PCMs such as Si, Al, B, can harness 20 times more energy densities than conventional molten-salt-based systems.

Non-linearity of temperature at the melting front and motion of melting interface makes it difficult to find an exact analytical solution for the phase change [13]. Experimental works are only available for low and medium-temperature PCM such as paraffin, lauric acid, n-octadecane, etc. This demands an increasing requirement for numerical models to extensively analyze the phase change of high-temperature LHS systems. Although numerical models can change widely based on the type of systems, the necessity of numerical analysis can always be attributed with reduction of cost and time. Both experimental and numerical investigation are performed by Ankit et al. [14] to analyse the melting of paraffin wax in a rectangular enclosure for different heat fluxes. Groulx et al.[15] investigated the melting of lauric acid in rectangular enclosures using COMSOL to observe the effect of mushy zone parameter. Assis et al.[16] explores experimentally and numerically the melting of paraffin wax in spherical enclosures using air on top of PCM. Veeraragavan et al.[17] investigated the solidification of silicon inside a closed truncated-cone geometry without considering the density variation between solid and molten silicon. Zeneli et al.[18] numerically investigated silicon-based latent storage system considering the effect of buoyancy-driven natural convection system.

The present article illustrates the usage of effective heat capacity formulation to mathematically model the conjugate heat transfer during melting in rectangular enclosure. Shape and position of melting interface, temperature distribution inside molten PCM have been captured for both  $\text{NaNO}_3$  and silicon. Thermal performance parameters such as energy storage density and charging rate of silicon are compared with  $\text{NaNO}_3$ .

## 2. SYSTEM DESCRIPTION

The ultra-high temperature LHS system and its charging behavior would be described by the physical and mathematical model in the following subsections. CFD simulations are performed using the commercial software COMSOL Multiphysics 5.4.

## Physical model

A rectangular enclosure is considered as the physical domain for Silicon and NaNO<sub>3</sub> melting. Figure 1 can be depicted as the two dimensional (2D) computational domain considering unit thickness of the physical domain. Hence, the computational domain is a 2D planar rectangle subjected to uniform heat flux on left wall and insulated from other sides. The 2D numerical simulation results can be considered reasonably accurate for rectangular enclosures. Three different aspect ratios (AR=L/W) are considered to analyze and compare melting of silicon with NaNO<sub>3</sub> keeping the surface area constant. Selection of  $q'' = 5000 \text{ W/m}^2$  to the left wall can be attributed to keeping the Rayleigh number below  $10^9$  during melting.

## Numerical model

Effective heat capacity method is deployed to model the phase transition of PCM, popularly known as the moving-boundary problem. Effective heat capacity, a modification of Enthalpy-porosity technique, is first implemented by Ogoh and Groulx (2012) in COMSOL without convection. Groulx and Biwole (2014) established a set of equations within COMSOL Multiphysics environment to solve the transient phase change heat transfer with natural convection. This formulation considers phase transition to take place over a fixed temperature interval ( $\Delta T$ ) which leads to an artificial mushy region during melting. This region can be treated as a pseudo-porous region where porosity varies from zero (solid phase) to 1 (liquid phase). Hence, the velocity of the molten silicon within the mushy region also varies from zero (solid phase) to the velocity generated due to natural convection in liquid phase. A momentum source term in the form of the Carman-Koseny equation is included in Navier-Stokes equation to simulate the influence of damping within mushy zone.

The schematic of computational and meshed domain of AR=1 for numerical simulation is shown in Figures 2 (a) and (b) which also remains same for other AR. The mesh is generated using quadrilateral elements with boundary layers near the active wall (left wall). The initial and boundary conditions are defined in Table 1.

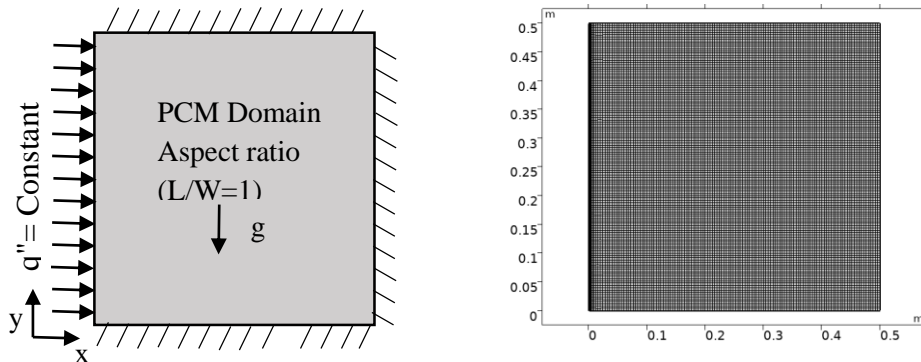


Figure 1:Numerical model of the domain. (a) Computational domain and (b) Meshed domain

Table 1:Initial and boundary conditions for the model

Initial conditions	Boundary conditions
$T(x,y,t=0) = 1680 \text{ K}$	$q''(x=0,y) = 5000 \text{ W/m}^2$
$u(x,y,t=0) = v(x,y,t=0) = 0$	$q''(y=L), q''(y=0), q''(x=W) = 0 \text{ i.e } \frac{\partial T}{\partial n} = 0$
Pressure = 1 Atm	No-slip at boundary i.e $u = v = 0$

The thermophysical properties of Silicon and NaNO<sub>3</sub> used for calculation and numerical simulation are listed in Table 2. The comparison is performed keeping operating parameters same for both cases such as  $A_{\text{mush}}$ ,  $\Delta T_{\text{subcooling}}$ , etc.

Table 2:Thermo-physical properties of silicon and NaNO<sub>3</sub> [18][19]

Properties	Density (kg/m <sup>3</sup> )	Specific heat (J/kgK)	Thermal conductivity (W/mK)	Latent heat of fusion (J/kg)	Melting temperature (K)	Viscosity (Pa.s)
Silicon	$\rho_s = 2330$ $\rho_l = 2570$	$c_{ps} = c_{pl}$ $= 1040$	$k_s = 25$ $k_l = 50$	1800000	$T_s = 1686$ $T_l = 1688$	$\mu = 0.0008$
NaNO <sub>3</sub>	$\rho_s = 2180$ $\rho_l = 1908$	$c_{ps} = 1600$ $c_{pl} = 1655$	$k_s = 0.8$ $k_l = 0.6$	1760000	$T_s = 578$ $T_l = 580$	$\mu = 0.00269$

### Governing Equations:

The mass, momentum (x and y direction), and energy conservation equations for phase change problems are solved with the help of COMSOL Multiphysics based on finite element formulation [15].

$$\text{Mass conservation: } \frac{\partial u}{\partial x} + \frac{\partial v}{\partial y} = 0 \quad (1)$$

$$\text{X momentum conservation: } \frac{\rho Du}{\partial t} = -\frac{\partial p}{\partial x} + 2\frac{\partial}{\partial x}\left[\mu\frac{\partial u}{\partial x}\right] + \frac{\partial}{\partial y}\left[\mu\left(\frac{\partial u}{\partial y} + \frac{\partial v}{\partial x}\right)\right] - S(T).u \quad (2)$$

$$\text{Y momentum conservation: } \frac{\rho Dv}{\partial t} = -\frac{\partial p}{\partial y} + 2\frac{\partial}{\partial y}\left[\mu\frac{\partial v}{\partial y}\right] + \frac{\partial}{\partial x}\left[\mu\left(\frac{\partial u}{\partial y} + \frac{\partial v}{\partial x}\right)\right] + F_B - S(T).v \quad (3)$$

The gravity ( $9.81 \text{ m/s}^2$ ) acts in vertically downward direction at the centroid of domain. Natural convection in the molten PCM due to buoyancy force is modeled through the Boussinesq approximation:

$$\vec{F}_B = \rho_o \beta \vec{g}(T - T_0) \quad (4)$$

where the operating density and temperature are taken as  $\rho_o = \rho_l$  and  $T_o = T_m$

The Carman-Kosney equation is used to define the source term  $S(T)$  in the momentum equations

$$S(T) = A_{mush} \frac{(1-\delta(T))^2}{\delta(T)^3 + \epsilon} \quad (5)$$

This is the damping term with very large values corresponds to liquid fraction zero (solid) and zero corresponds to liquid fraction 1 (liquid).

$$\text{where } \delta(T) = \text{liquid fraction} = \begin{cases} 0 & T < T_m - \frac{\Delta T}{2} \\ 0 - 1 & T_m - \frac{\Delta T}{2} \leq T \leq T_m + \frac{\Delta T}{2} \\ 1 & T \geq T_m + \frac{\Delta T}{2} \end{cases} \quad (6)$$

$\Delta T$  = Transition interval during melting of silicon (K)

$T_m$  = Melting point of silicon (K)

$A_{mush}$  = Mushy zone parameter ( $\text{kg/m}^3\text{s}$ )

$\epsilon$  = constant having very small value ( $10^{-3}$ )

The solution of the numerical model is derived considering the following assumptions:

- Silicon is considered to be homogeneous and isotropic in both the phases
- Flow in molten silicon is considered to be incompressible and laminar
- Change in volume is neglected during phase transition
- Viscous heating and loss due to radiation are considered to be negligible
- Boussinesq approximation is considered to model the density variation

Simulation is performed in COMSOL Multiphysics by using heat transfer in fluids and laminar flow physics implicitly coupled with each other. The energy equation is modelled by modifying the overall specific heat capacity ( $c_{p,\text{mod}}$ ) of PCM to account the large latent required for melting of silicon. The thermal properties such as thermal conductivity ( $k_{\text{mod}}$ ), viscosity, and density( $\rho_{\text{mod}}$ ) are modified accordingly concerning temperature. All the modified terms are finally introduced in the energy equation.

$$\rho_{\text{mod}} c_{p,\text{mod}}(T) \frac{DT}{Dt} = \nabla \cdot (k_{\text{mod}}(T) \nabla T) \quad (7)$$

## RESULTS AND DISCUSSION

A constant heat flux of  $5000 \text{ W/m}^2$  is supplied on the left wall of rectangular domain of  $AR=1/4, 1$  and  $4$  for both silicon and  $\text{NaNO}_3$ . Liquid fraction distribution and energy storage density of both mediums are compared at a particular instant. The circulation pattern inside molten PCM due to natural convection is observed for both silicon and  $\text{NaNO}_3$ . The anomalous behavior of molten silicon compared to  $\text{NaNO}_3$  is established. Figure 2 compares the average liquid fraction of silicon and  $\text{NaNO}_3$  for  $q''=5000\text{W/m}^2$  at different instants for a time duration of 2hrs. At any given instant liquid fraction is defined as the percentage of solid PCM converted to molten PCM. The melting rate of silicon is found to be significantly high than  $\text{NaNO}_3$  due to high thermal conductivity for all AR. For  $AR = 4$  the complete charging (Liquid fraction = 1) is over for silicon in 1/2hr whereas only 37%  $\text{NaNO}_3$  melts by that time. Melting rate of silicon increases with time unlike melting rate of  $\text{NaNO}_3$ . For example, after 1hr the liquid fraction of domain having  $AR=1$  is 63% and 28% for silicon and  $\text{NaNO}_3$  respectively. However, after 1.5hrs the

liquid fraction is 100% and 38% for silicon and  $\text{NaNO}_3$  respectively. Liquid fraction distribution for both PCMs is visualized using 2D surface plot in Figure 3. Figure 3 also represents the temporal variation of shape and position of the liquid front.

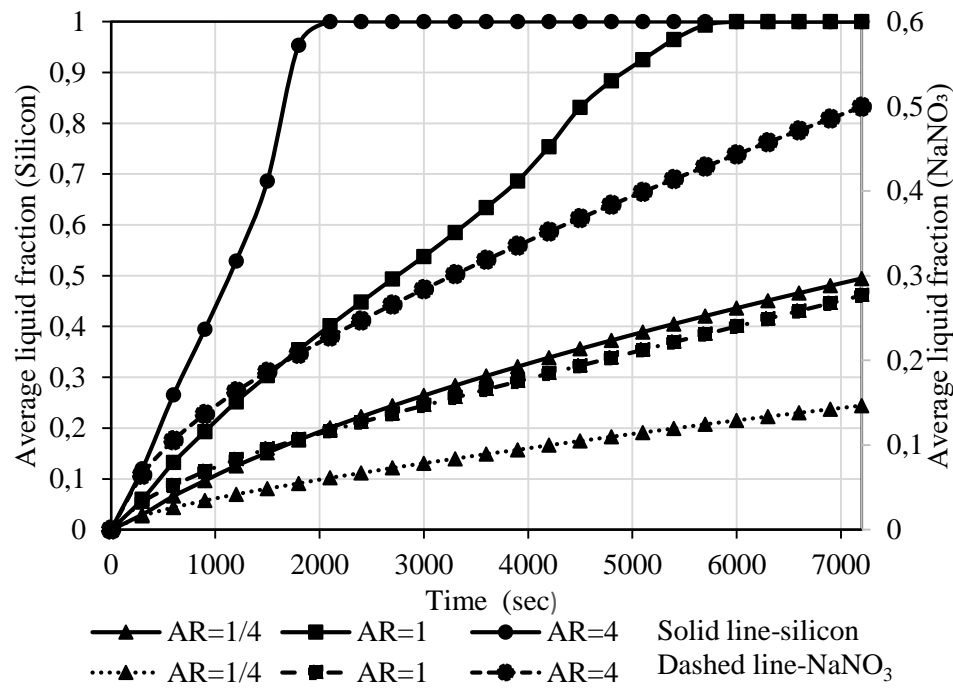


Figure 2: Comparison of temporal liquid fraction of silicon with  $\text{NaNO}_3$  domain for different AR

At the beginning of melting the shape of the melting front is flat parallel to the active wall for both PCM. As the melting progresses the shape melting front changes to a curved surface due to onset of natural convection. However, for silicon, the concavity of curved surface is towards active boundary whereas it is reverse of  $\text{NaNO}_3$ . This results faster melting at bottom portion in silicon domain and top portion in  $\text{NaNO}_3$  domain. This behavior can be attributed to different circulation patterns generated in molten silicon and  $\text{NaNO}_3$  due to the difference in density between solid and molten PCM. Silicon unlike  $\text{NaNO}_3$  has higher liquid density compared to solid.

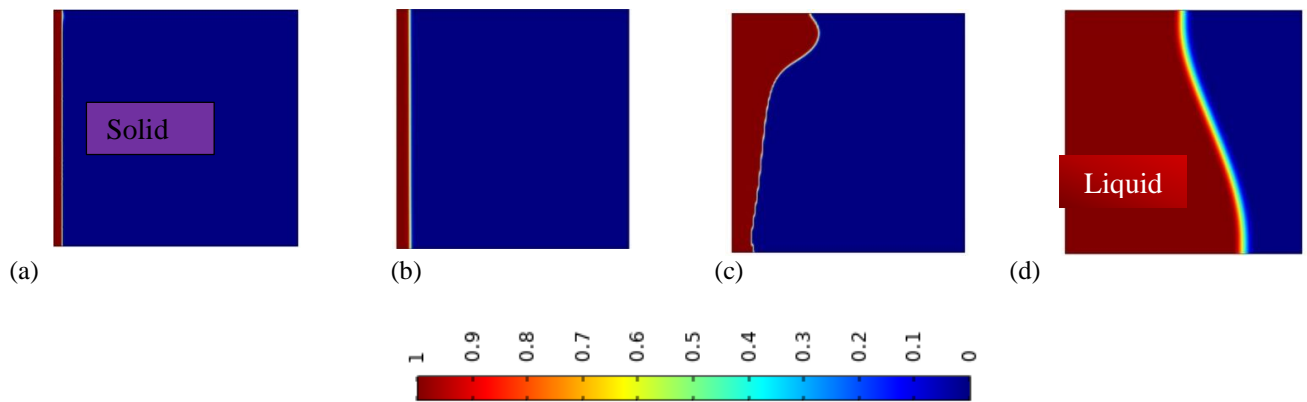


Figure 3: Comparison of liquid fraction distribution and liquid front position at different instants for domain of AR=1. (a)  $\text{NaNO}_3$  after 5mins, (b) Silicon after 5mins, (c)  $\text{NaNO}_3$  after 1hr and (d) silicon after 1 hr

Commonly molten state of a substance has a lower density than solid state. However, silicon behaves exactly like ice-water combination for a temperature range near the melting point. Hence, once silicon starts melting, it moves downwards due to higher density which results in faster melting at the bottom. Due to inertia of hot molten silicon and no penetration through left and bottom wall, the molten silicon at bottom moves to right side of domain. When the temperature of molten silicon increases above melting point to a certain value due to sensible heating, the density again decreases and molten silicon moves up to complete a circulation pattern. This results in natural convection

taking place in the opposite direction compared to  $\text{NaNO}_3$  which can be observed from the circulation pattern in Figure 4.

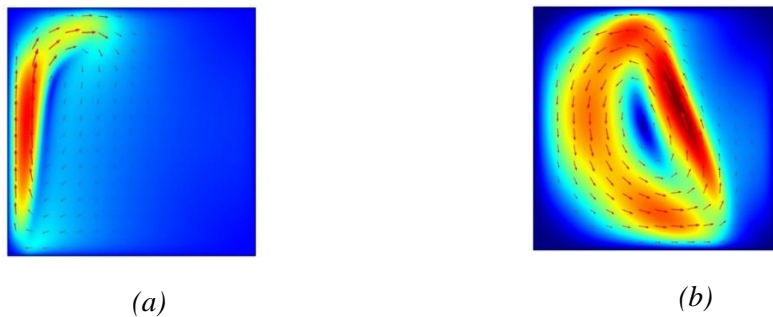


Figure 4: Comparison of circulation pattern inside molten PCM due to natural convection after 1hr of charging . (a)  $\text{NaNO}_3$  (clockwise) and (b) silicon (counterclockwise)

Figure 5 compares the latent energy storage density of silicon and  $\text{NaNO}_3$  domain during charging for three aspect ratios. Sensible storage density is not considered because it is insignificant compared to latent energy density. Latent energy storage density curves mimic the liquid fraction curves as it is a linear function of liquid fraction. The energy storage density of the domain is evaluated as follows.

$$Q_{\text{sensible}} = m \times h = m \times (c_p(T_m - T_i) + (T - T_m)) \quad (8)$$

$$Q_{\text{latent}} = m \times LF \times h_{sl} \quad (9)$$

Where  $m$  = mass of PCM in domain,  $h$  = sensible enthalpy,  $T$  = instantaneous average temperature,  $LF$  = average liquid fraction, and  $h_{sl}$  = latent heat of fusion

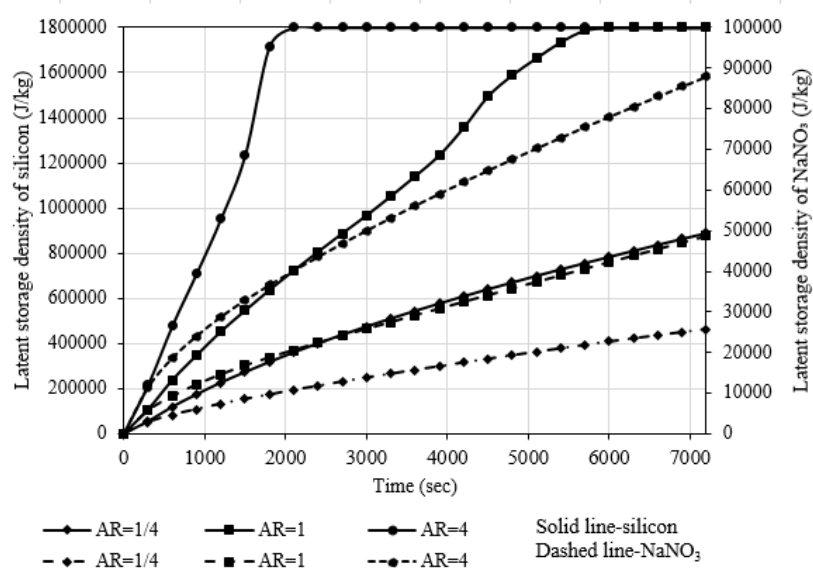


Figure 5:Comparison of latent storage density of silicon and  $\text{NaNO}_3$  for different AR

Figure 5 validates the latent storage density of silicon is significantly large compared to  $\text{NaNO}_3$  for all 3 AR. For AR=4 silicon would store reasonable amount of sensible energy in addition to latent energy after  $\frac{1}{2}$  hr till the complete charging of  $\text{NaNO}_3$ . Hence, the total energy storage density would be much higher for silicon. This behavior will remain true for any high-temperature metallic PCM compared to high-temperature inorganic salt.

## CONCLUSION

The present study demonstrated the potential benefits of a silicon-based LHS system to provide significant energy storage density and energy storage rate. Effective heat capacity method has been successfully implemented to analyze the thermo-fluidics of the non-linear solid-liquid phase transition. Thermal performance of the silicon system is compared with  $\text{NaNO}_3$  system by evaluating the melting rate and energy storage density. Silicon is found to have a significantly higher melting rate and energy storage density than  $\text{NaNO}_3$  at any instant. As these two

criteria are very critical to design cost-effective LHS, silicon can be proposed as a potential high-temperature PCM. A counterclockwise circulation pattern was observed in molten silicon unlike the traditional clockwise pattern in natural convection. The discharging process of silicon domain and reaction of silicon with containment medium for different geometrical shapes should be investigated before widespread deployment.

## REFERENCES

- [1] M. Fadl and P. C. Eames, "Numerical investigation of the influence of mushy zone parameter A mush on heat transfer characteristics in vertically and horizontally oriented thermal energy storage systems," *Appl. Therm. Eng.*, vol. 151, no. June 2018, pp. 90–99, 2019, doi: 10.1016/j.applthermaleng.2019.01.102.
- [2] W. Luft, "High-temperature solar thermal energy storage," *Int. J. Sol. Energy*, vol. 3, no. 1, pp. 25–40, 1985, doi: 10.1080/01425918408914381.
- [3] M. T. Dunham and B. D. Iverson, "High-efficiency thermodynamic power cycles for concentrated solar power systems," *Renew. Sustain. Energy Rev.*, vol. 30, pp. 758–770, 2014, doi: 10.1016/j.rser.2013.11.010.
- [4] H. Nazir, M. Batool, F. J. Bolivar Osorio, M. Isaza-Ruiz, X. Xu, K. Vignarooban, P. Phelan, Inamuddin, and A. M. Kannan, "Recent developments in phase change materials for energy storage applications: A review," *Int. J. Heat Mass Transf.*, vol. 129, pp. 491–523, 2019, doi: 10.1016/j.ijheatmasstransfer.2018.09.126.
- [5] G. Alva, Y. Lin, and G. Fang, "An overview of thermal energy storage systems," *Energy*, vol. 144, pp. 341–378, 2018, doi: 10.1016/j.energy.2017.12.037.
- [6] H. Pointner and W. D. Steinmann, "Experimental demonstration of an active latent heat storage concept," *Appl. Energy*, vol. 168, pp. 661–671, 2016, doi: 10.1016/j.apenergy.2016.01.113.
- [7] Y. Lin, Y. Jia, G. Alva, and G. Fang, "Review on thermal conductivity enhancement, thermal properties and applications of phase change materials in thermal energy storage," *Renew. Sustain. Energy Rev.*, vol. 82, no. September 2017, pp. 2730–2742, 2018, doi: 10.1016/j.rser.2017.10.002.
- [8] T. Bauer, W.-D. Steinmann, D. Laing, and R. Tamme, "Thermal Energy Storage Materials and Systems," *Annu. Rev. Heat Transf.*, vol. 15, no. 15, pp. 131–177, 2012, doi: 10.1146/annurevheattransfer.2012004651.
- [9] J. P. Kotzé, "Thermal energy storage in metallic phase change materials," no. December, 2014.
- [10] C. E. Birchenall and M. Telkes, "Thermal storage in metals," in *Sharing the Sun: Solar Technology in the Seventies*, 1976, pp. 138–154.
- [11] Q. He and W. Zhang, "A study on latent heat storage exchangers with the high-temperature phase-change material," *Int. J. Energy Res.*, vol. 25, no. 4, pp. 331–341, 2001, doi: 10.1002/er.683.
- [12] A. Robinson, "Ultra-high temperature thermal energy storage. part 1: concepts," *J. Energy Storage*, vol. 13, pp. 277–286, 2017, doi: 10.1016/j.est.2017.07.020.
- [13] K. J. Choi and J. S. Hong, "Experimental studies of melting phenomena from a constant heat flux vertical plate," *Exp. Heat Transf.*, vol. 3, no. 1, pp. 49–63, 1990, doi: 10.1080/08916159008946377.
- [14] A. Yadav and S. Samir, "Experimental and numerical investigation of spatiotemporal characteristics of thermal energy storage system in a rectangular enclosure," *J. Energy Storage*, vol. 21, no. July 2018, pp. 405–417, 2019, doi: 10.1016/j.est.2018.12.005.
- [15] A. C. Kheirabadi and D. Groulx, "the Effect of the Mushy-Zone Constant on Simulated Phase Change Heat Transfer," no. May, p. 22, 2015, doi: 10.1146/ichmt.2015.intsympadvcomputheattransf.460.
- [16] E. Assis, L. Katsman, G. Ziskind, and R. Letan, "Numerical and experimental study of melting in a spherical shell," *Int. J. Heat Mass Transf.*, vol. 50, no. 9–10, pp. 1790–1804, 2007, doi: 10.1016/j.ijheatmasstransfer.2006.10.007.
- [17] A. Veeraragavan, L. Montgomery, and A. Datas, "Night time performance of a storage integrated solar thermophotovoltaic (SISTPV) system," *Sol. Energy*, vol. 108, pp. 377–389, 2014, doi: 10.1016/j.solener.2014.07.005.
- [18] M. Zeneli, I. Malgarinos, A. Nikolopoulos, N. Nikolopoulos, P. Grammelis, S. Karella, and E. Kakaras, "Numerical simulation of a silicon-based latent heat thermal energy storage system operating at ultra-high temperatures," *Appl. Energy*, vol. 242, no. March 2018, pp. 837–853, 2019, doi: 10.1016/j.apenergy.2019.03.147.
- [19] A. Marušić and D. Lončar, "Experimental validation of high-temperature latent heat storage model using melting front propagation data," *Appl. Therm. Eng.*, vol. 164, no. April 2019, 2020, doi: 10.1016/j.applthermaleng.2019.114520.



# SINGLE-PHASE GRID-CONNECTED INVERTER WITH HIGH FREQUENCY ISOLATION FOR DC NANO-GRIDS

Ruiz Caldera, Luis Jorge

Technological Institute of Sonora, Obregón City, México, jorgeruiz.c@gmail.com, ORCID: 0000-0002-9503-5833

Beristáin Jiménez, José Antonio

Technological Institute of Sonora, Obregón City, México, jaberistain@itson.edu.mx, ORCID: 0000-0002-8371-5495

Mendivil Cuadras, Hiram

Technological Institute of Sonora, Obregón City, México, hirammendivil@gmail.com, ORCID: 0000-0003-2821-2817

Pérez Ramírez, Javier

Technological Institute of Sonora, Obregón City, México, javier.perezr@itson.edu.mx, ORCID: 0000-0003-0028-1829

*Ruiz, CLJ., Beristáin, JJA., Mendivil, CH., Pérez RJ. Single-phase grid-connected inverter with high frequency isolation for DC nano-grids. 9<sup>th</sup> Eur. Conf. Ren. Energy Sys. 21-23 April 2021, Istanbul, Turkey*

**Abstract:** Electric energy demands are growing continuously and for some communities disruptions of the main utility-grid represent an impact on its activities. Nano-grids offers a solution in terms of flexibility due to its capacity to perform in a stand-alone set-up. Renewable energies play a major role on nano-grid because it can be designed for small-scale applications. Power converters are used as an interface-means for integrating renewable energies to different applications such as interconnection to the utility-grid and nano-grids. This paper uses a single-phase low-voltage converter intended for residential applications, it focuses on a PV array as a distributed energy system connected to a DC nano-grid and interconnection to the utility-grid, the use of a High Frequency transformer is to provide the required galvanic isolation and to reduce the overall size of the system. Simulation results are presented in order to verify the circuit can be used for bidirectional power flow while maintaining a constant DC bus voltage, which make it suitable for DC nano-grid applications.

**Keywords:** Nano-grids, renewable energies, inverter, AC-AC converter, High-Frequency transformer

© 2021 Published by ECRES

## 1. INTRODUCTION

Nowadays, electrical energy is an essential requirement on a daily basis. However, for isolated rural communities that are far away from the main generation and distribution centers of energy, this is rarely accomplished. Due to this and the increasing demand of energy that also has led to concerns about the impact that centralized generator has to the environment, is needed to perform the adoption and usage of decentralized energy generators. Furthermore, it is highly desirable that these decentralized energy sources to be less pollutant which is accomplished by means of using renewable energy sources such as photovoltaic generators [1]–[3].

The use of decentralized energy generators and the continuing cost reductions of renewable energy systems have led to a new type of generation and distribution of the electric energy, this new grid type is based on the use of small-scale energy generation, small-scale energy storage devices, DC loads and/or DC loads near the site of use of electricity, and it is called nano-grid. Nano-grids can be interconnected to other nano-grids to form a micro-grid, they also can be connected to the utility-grid or operate in a standalone configuration [4], [5].

The use of micro-grids and nano-grids has the advantage that in case of disruptions of the utility-grid, nano-grids can still remain operatives in a standalone configuration due to its ability to isolate itself [6], [7].

Photovoltaic energy is considered as the fastest growing source of electricity generation [1], [8], nevertheless photovoltaic cells produce energy as a DC variable voltage and current that depends on different conditions and for

that reason the generated energy is needed to be processed and adapted to an adequate voltage level and/or an adequate frequency.

The use of galvanic isolation for interconnection to the utility-grid is required due to safety issues as mentioned by [9], high frequency transformers offer an advantage in terms of size and costs [10], and used in conjunction with power converters a solid-state transformer is developed [11], [12] which have been used on hybrid nano-grids. Also, by allowing the use of modulation techniques as SPWM it can offer an additional advantage of reducing the total harmonic distortion on the utility-grid [13].

This paper is focused on single-phase low-voltage systems with a photovoltaic (PV) array as a distributed energy source connected to a DC nano-grid, the objective of this work is to maintain the DC voltage bus at a constant level while extracting or injecting energy to the utility-grid according to the availability of the PV array.

Section 2 presents a detailed description of the proposed circuit, section 3 establishes the operating principle, and in section 4 a method proposed in [14] is followed and some considerations are taken into account in order to size the capacitor of the DC bus.

## 2. PROPOSED CIRCUIT DESCRIPTION

Figure 1 shows the proposed converter which has the following parts: a photovoltaic array, a DC load represented by  $R_b$ , which can be turned on or off, a High-Frequency (HF) inverter, a High-Frequency transformer, an AC-AC converter that converts HF AC to Grid-Frequency AC and a coupling inductor  $L$  for grid interconnection.

In figure 1,  $R_a$  represents the losses of the system

$SW_a, SW_b, SW_c$  and  $SW_d$  are ideal switches used for turning on and off the photovoltaic array or the DC load.

$SW_1, SW_2, SW_3$  and  $SW_4$  are realized by power MOSFETs and constitute the High-Frequency-Inverter. the DC bus of the inverter is attached to a photovoltaic array and a capacitor  $C_i$  to reduce voltage ripple on PV terminals, and the AC bus is connected to the primary winding of the High-Frequency Transformer, for this paper the ideal model transformer is used.

The secondary winding of the High-Frequency-Transformer is then attached to an AC-AC converter realized by switches  $SW_5, SW_6, SW_7$  and  $SW_8$  in this case each bidirectional switch can be realized by two anti-series connected MOSFETs

Figure 2 shows the switches realization.

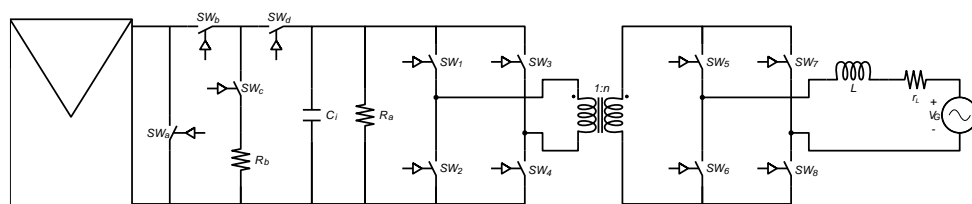


Figure 1. Proposed circuit

## 3. OPERATING PRINCIPLE

In order to simplify the analysis, a simplified version of the circuit is shown in figure 2.

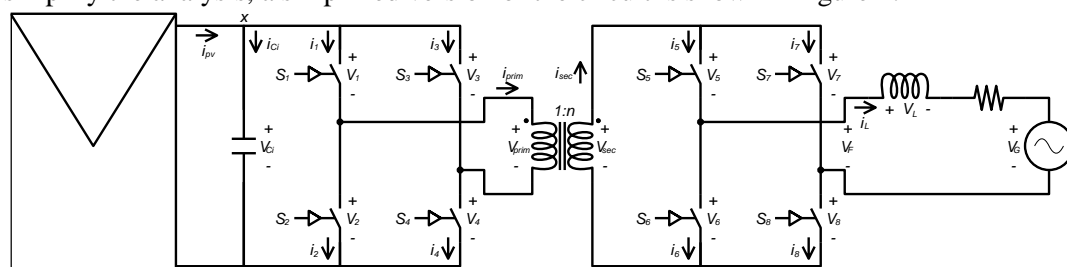


Figure 2. Simplified circuit

The output of the inverter will be a rectangular waveform with the same pulse-width on the positive and negative semi-cycles. The switching strategy for the inverter considers a signal  $S_i$  with a duty cycle of 50% as shown in table 1, where  $n$  represents the turn ratio of the transformer,  $S_1, S_2, S_3$  and  $S_4$  represents the activation signals for  $SW_1-SW_4$  respectively.

Table 1. Inverter switching strategy

$S_i$	$S_1 = S_4$	$S_2 = S_3$	$V_{prim}$	$V_{sec}$
1	1	0	$V_{ci}$	$nV_{ci}$
0	0	1	$-V_{ci}$	$-nV_{ci}$

The AC-AC converter function is to convert the HF Rectangular Voltage from the secondary winding of the transformer to a Low-Frequency Sinusoidal Pulse Width Modulated Voltage.

The switching strategy of the AC-AC converter needs to consider the following: the secondary winding voltage polarity of the transformer, which can be taken from the  $S_i$  signal is defined as follows: if  $S_i = 1$ ,  $V_{sec} > 0$ , if  $S_i = 0$ ,  $V_{sec} < 0$

The signal  $S_a$  is obtained by Pulse-Width-Modulation (PWM) of the modulating signal and the carrier signal; and the signal  $S_b$  is obtained by PWM of the modulating signal shifted by  $180^\circ$ , as shown in figure 4. The modulating signal is obtained through a controller which will be described later. The difference  $S_a - S_b$  is a Low-Frequency-Unipolar Pulse-Width-Modulated signal. Considering the description above, it is necessary to propose a switching strategy for the AC-AC converter such that at its output terminals can be obtained a unipolar SPWM Voltage, then the switching strategy is shown in tables 2 and 3.

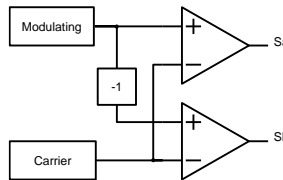


Figure 3. Pulse-Width-Modulator

Table 2. Switching strategy for the AC-AC converter

For the leg SW5-SW6					For the leg SW7-SW8				
$S_i$	$S_a$	$S_5$	$S_6$	$V_6$	$S_i$	$S_b$	$S_7$	$S_8$	$V_8$
0	0	1	0	$-nV_{ci}$	0	0	1	0	$-nV_{ci}$
0	1	0	1	$nV_{ci}$	0	1	0	1	$nV_{ci}$
1	0	0	1	$-nV_{ci}$	1	0	0	1	$-nV_{ci}$
1	1	1	0	$nV_{ci}$	1	1	1	0	$nV_{ci}$

#### 4. CIRCUIT FUNCTIONS AND CONSIDERATIONS

The capacitor will be sized in order to obtain low ripple voltage by using the following expression derived in [14] with a ripple factor defined as:  $k_{\tilde{v}_{ci}} = \frac{\Delta \tilde{v}_{ci}/2}{V_{ci}}$

$$C_i = \frac{P_{pv}}{2k_{\tilde{v}_{ci}}\omega V_{pv}^2 \cos(\beta)}$$

The goal of this paper is to validate by simulation this converter's capacity to perform the following functions when connected to a 5000 Watts PV array and a 2500 Watts DC load with different conditions:

- Extract power from the utility grid in order to keep a constant voltage at DC bus, ie.  $V_{ci}$  considering the losses of the system and PV array unavailable.
- Extract power from the utility grid in order to keep a constant voltage at DC bus, considering the losses of the system, DC load connected and PV array unavailable.
- Inject the exceeding energy when PV array is available, DC load is connected and losses of the system are considered.
- Inject the exceeding energy when PV array is available, DC load is disconnected and losses of the system are considered.

For the converter to realize the above mentioned it is proposed to use a simple PI controller as shown in figure 5.

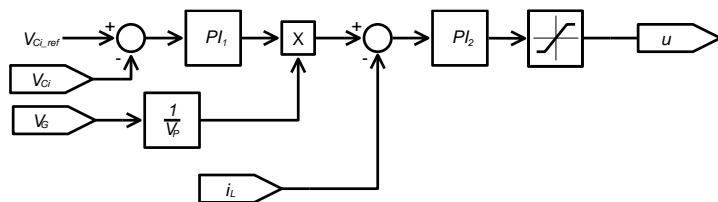


Figure 4. Proposed controller

## 5. SIMULATION RESULTS

The converter specifications are listed in table 8. The DC bus voltage proposed  $V_{C_i,ref}$  is 380 V,  $R_a$  is sized to represent the losses of the converter of 250 Watts and  $R_b$  as a DC load of 2500 Watts,  $L$  is proposed as 1 mH,  $f_{inv}$  represents the switching frequency of the inverter,  $f_{cic}$  represents the switching frequency of the AC-AC converter,  $n$  is chosen as 0.5 and represents the transformer turn ratio, and  $C_i$  is calculated in order to achieve  $k_{\tilde{v}_{C_i}} = 0.005$

Table 3. Parameters of the proposed circuit

Parameter	Value
$L$	1 mH
$R_a$	577.6 Ω
$R_b$	57.76 Ω
$f_{inv}$	5 kHz
$f_{cic}$	10 kHz
$f_{grid}$	60 Hz
$n$	0.5
$C_i$	9.185 mF

A simulation of the circuit of the figure 1 is performed for 4 seconds using the software PSIM, the switches  $SW_a, SW_b, SW_c$  and  $SW_d$  are turned on and off according to the table 9, a wattmeter was attached to the utility-grid in order to measure the extracted or injected power.

Table 4. Description of the simulation intervals

Interval	Time	$SW_a$	$SW_b$	$SW_c$	$SW_d$	PV array	DC load
I	0 – 1 sec	On	Off	Off	Off	Unavailable	Disconnected
II	1 – 2 sec	On	Off	On	On	Unavailable	Connected
III	2 – 3 sec	Off	On	On	On	Available	Connected
IV	3 – 4 sec	Off	On	Off	On	Available	Disconnected

Figure 5 shows the capacitor voltage waveform  $v_{C_i}$ , it can be seen that it reaches the DC bus voltage proposed. Figure 5 (b) shows a close up of  $v_{C_i}$  by inspection can be seen that the voltage ripple is greater during the interval IV. By using the measurement tools of PSIM it was found that the voltage ripple value was 3.62 V, which complies with the proposed  $k_{\tilde{v}_{C_i}}$ , minor differences can be attributed to numerical error due to non-optimum time-step used for simulation.

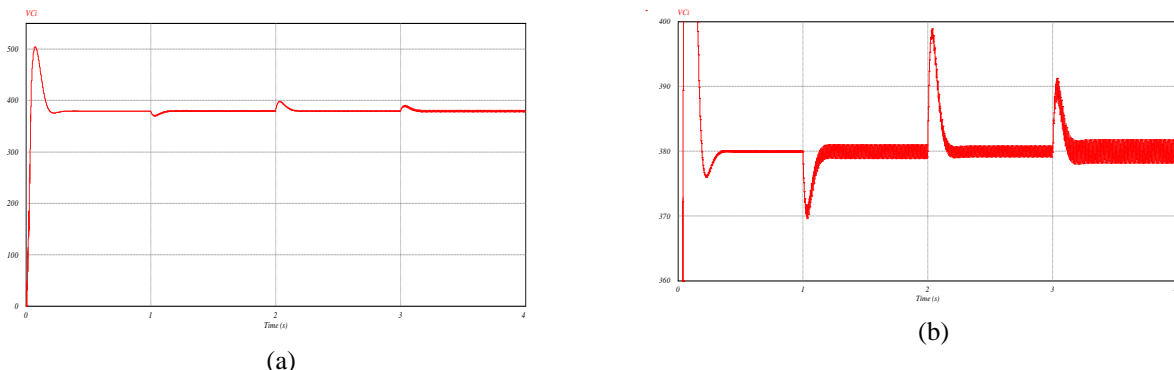
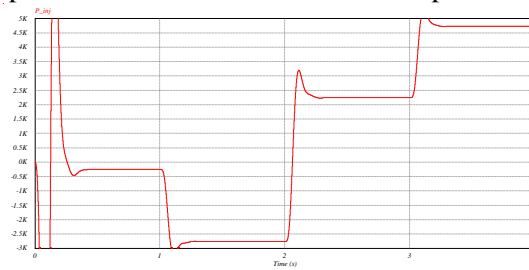

 Figure 5. Waveform of the voltage at the capacitor  $v_{C_i}$  (DC bus)

Figure 6 shows the power that is extracted or injected to the utility-grid, by using measuring tool during the steady state of each interval, the power results are shown next to the plot in figure 6.



Interval	Power measured
I	-250 W
II	-2755 W
III	2246 W
IV	4734 W

Figure 6. Plot of power vs time

The functions proposed in section 4 are fulfilled, as shown in figure 8 meaning the following:

- During interval I, the converter extracts energy from the utility-grid in order to maintain a constant DC bus voltage and supplies energy to the represented losses of the system,  $R_a$ .
- During interval II, the converter extracts energy from the utility grid and supplies energy to the DC load  $R_b$  and the energy losses.
- During interval III, the converter supplies energy to the DC load and the energy losses by using the energy available from the PV array and the exceeding energy is injected to the utility-grid.
- During interval IV, the converter supplies the energy losses of the system by using the energy from the PV array and the exceeding energy is injected to the utility-grid.

All of the above are realized while maintaining a constant DC bus voltage.

Figure 9 gives inductors current and the grid-utility voltage at the same time for the steady state of each interval, in figure 9 (a) and (b) can be seen that current and inductor are shifted by  $180^\circ$  meaning there is an extraction of energy, while in figure 9 (c) and (d) voltage and current are in phase meaning the energy is being injected to the utility.

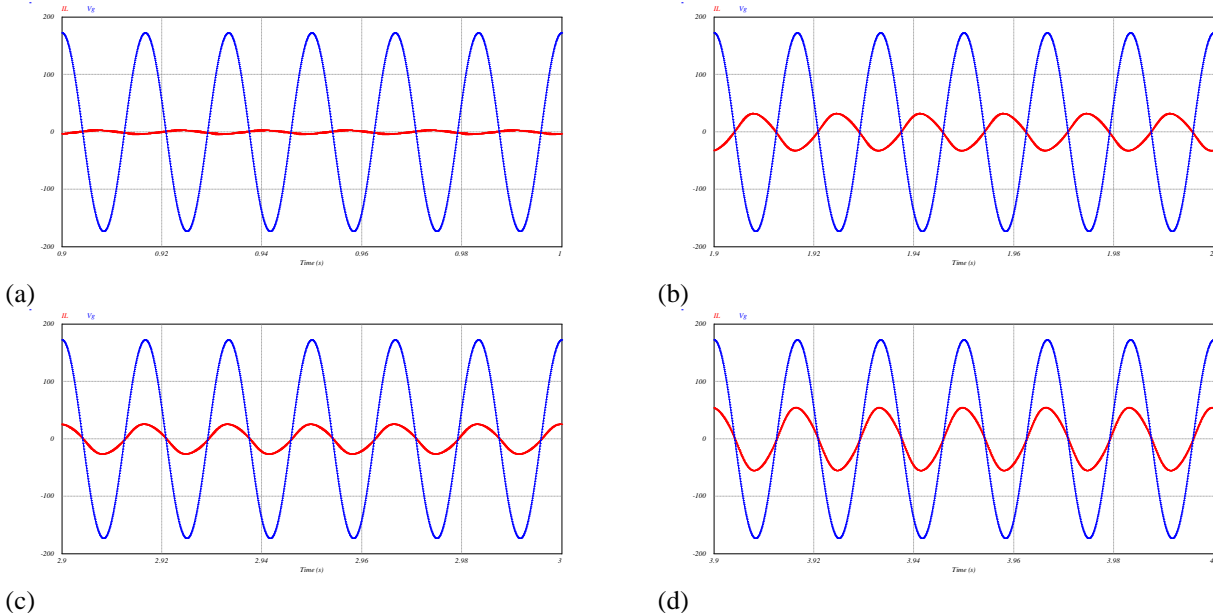


Figure 7. Inductor's current (red) and voltage utility-grid(blue) for different time intervals at steady-state.

## 6. CONCLUSIONS

In this paper, the circuit proposed is suitable for DC nano-grid applications, simulation results are provided in order to validate the proposed functions. The advantage exhibited by this converter is the reduction of the size of the transformer while maintaining the galvanic isolation required, also is useful for adequacy of voltages levels meaning the same system can be used in different voltage levels by only switching to an appropriate transformer. Figures 6 and 7 show that the DC bus voltage was maintained constant despite of the load changes and availability of the PV array, and injection or extraction of the energy from the utility-grid was also achieved. Further research can be

made by expanding the circuit's functions that were not addressed in this paper such as reactive and harmonic power compensation and the development of a robust control strategy.

## REFERENCES

- [1] A. Awasthi *et al.*, "Review on sun tracking technology in solar PV system," *Energy Reports*, vol. 6, pp. 392–405, Nov. 2020, doi: 10.1016/j.egyr.2020.02.004.
- [2] A. Hirsch, Y. Parag, and J. Guerrero, "Microgrids: A review of technologies, key drivers, and outstanding issues," *Renewable and Sustainable Energy Reviews*, vol. 90, pp. 402–411, Jul. 2018, doi: 10.1016/j.rser.2018.03.040.
- [3] R. Haroun and A. E. Aroudi, "Analysis, Design, and Simulation of a Dual Active Bridge for PV-based Residential Nanogrids," in *2020 5th International Conference on Renewable Energies for Developing Countries (REDEC)*, Marrakech, Morocco, Morocco, Jun. 2020, pp. 1–6, doi: 10.1109/REDEC49234.2020.9163840.
- [4] D. Burmester, R. Rayudu, W. Seah, and D. Akinyele, "A review of nanogrid topologies and technologies," *Renewable and Sustainable Energy Reviews*, vol. 67, pp. 760–775, Jan. 2017, doi: 10.1016/j.rser.2016.09.073.
- [5] J. Bosso, M. Llomplat, G. Oggier, and G. Garcia, "Evaluation of DC-AC Single-Phase Solid-State Transformers," *IEEE LATIN AMERICA TRANSACTIONS*, vol. 17, no. 5, p. 10, 2019.
- [6] A. F. Ebrahim and N. Elsayad, "Medium Voltage DC Testbed: A Hardware Based Tool to Integrate DC Microgrids/Nanogrids to the Utility Infrastructure," p. 7, 2018.
- [7] A. Lagrange, M. de Simón-Martín, A. González-Martínez, S. Bracco, and E. Rosales-Asensio, "Sustainable microgrids with energy storage as a means to increase power resilience in critical facilities: An application to a hospital," *International Journal of Electrical Power & Energy Systems*, vol. 119, p. 105865, Jul. 2020, doi: 10.1016/j.ijepes.2020.105865.
- [8] M. Warneryd, M. Håkansson, and K. Karlsson, "Unpacking the complexity of community microgrids: A review of institutions' roles for development of microgrids," *Renewable and Sustainable Energy Reviews*, vol. 121, p. 109690, Apr. 2020, doi: 10.1016/j.rser.2019.109690.
- [9] R. Hasan, S. Mekhilef, M. Seyedmahmoudian, and B. Horan, "Grid-connected isolated PV microinverters: A review," *Renewable and Sustainable Energy Reviews*, vol. 67, pp. 1065–1080, Jan. 2017, doi: 10.1016/j.rser.2016.09.082.
- [10] B. Zhao, Q. Song, W. Liu, and Y. Sun, "Overview of Dual-Active-Bridge Isolated Bidirectional DC–DC Converter for High-Frequency-Link Power-Conversion System," *IEEE Trans. Power Electron.*, vol. 29, no. 8, pp. 4091–4106, Aug. 2014, doi: 10.1109/TPEL.2013.2289913.
- [11] B. Zhao, Q. Song, and W. Liu, "A Practical Solution of High-Frequency-Link Bidirectional Solid-State Transformer Based on Advanced Components in Hybrid Microgrid," *IEEE Trans. Ind. Electron.*, vol. 62, no. 7, pp. 4587–4597, Jul. 2015, doi: 10.1109/TIE.2014.2350459.
- [12] J. Saha, G. N. B. Yadav, and S. K. Panda, "A Matrix-Based Solid-State-Transformer For A Hybrid Nanogrid," in *2018 IEEE International Conference on Power Electronics, Drives and Energy Systems (PEDES)*, Chennai, India, Dec. 2018, pp. 1–6, doi: 10.1109/PEDES.2018.8707623.
- [13] K. Alluhaybi, I. Batarseh, and H. Hu, "Comprehensive Review and Comparison of Single-Phase Grid-Tied Photovoltaic Microinverters," *IEEE J. Emerg. Sel. Topics Power Electron.*, vol. 8, no. 2, pp. 1310–1329, Jun. 2020, doi: 10.1109/JESTPE.2019.2900413.
- [14] J. Pérez Ramírez and J. A. Beristáin Jiménez, *Electronica de potencia: modelado y control de convertidores CD-CD*. 2016.



# THE USE OF ZnO THIN FILMS AS A FRICTION LAYER IN ENERGY HARVESTING

Yüzük Durak Gizem

Recep Tayyip Erdoğan University, Rize, Turkey, gizemyuzuak@erdogan.edu.tr, ORCID: 0000-0002-2358-8789

Özkan Seray

Recep Tayyip Erdoğan University, Rize, Turkey, serayozkan79@gmail.com, ORCID: 0000-0002-2819-4447

Yüzük Ercüment

Recep Tayyip Erdoğan University, Rize, Turkey, ercument.yuzuak@erdogan.edu.tr, ORCID: 0000-0002-2521-9362

*Cite this paper as:* Yüzük Durak, G., Özkan, S., Yüzük, E. *The use of ZnO thin films as a friction layer in energy harvesting. 9<sup>th</sup> Eur. Conf. Ren. Energy Sys. 21-23 April 2021, Istanbul, Turkey*

**Abstract:** The present study offers an environmental-, budget- and output energy-friendly triboelectric nanogenerator (TENG) based on semiconductor-based friction layers to power electronic devices with high performance systems. TENGs gather mechanical energy and convert it into electricity. Growth ZnO thin films in nano-forms as friction layers can be used to maximize the output voltages of the triboelectric nanogenerator. To raise the magnitude of triboelectric effect, the effective contact surface area, micro and nanostructure conditions of the thin film should be tuned by variations in the growing conditions such as partial O<sub>2</sub> pressures. To determine the crystal structure, surface morphology, resistance and capacitance properties of thin films XRD, SEM, AFM, ln(I)-V, and frequency dependent-capacitance measurements were done. According to the structural and electrical features was obtained both as desired and in accordance with the literature.

**Keywords:** ZnO thin films, Triboelectric nanogenerator, Energy harvesting, EIS

© 2021 Published by ECRES

## 1. INTRODUCTION

The energy crises that arise due to the increasing energy demands of human beings will continue to rise in the coming years. The most practical way to overcome the crisis caused by this lack of energy should be to reveal and develop alternative and new energy sources. When the alternative energy sources are considered renewable and waste energies arising from mechanical movement is one step ahead of those that can be obtained from other sources [1]. The basis for that is defined as the efficient recovery of wasted energy as the available resources around us. With the massive increase in portable and relatively low energy-consuming electronic devices, supplying energy crises to these devices with a pollution-free and sustainable power source is becoming a critical strategy. The solution to this problem is to turn to alternative and environmentally friendly technologies. The eco-friendly technology to this situation is that, as a new energy harvesting technology invented in 2012, it is logical to reveal that the ubiquitous and constantly available mechanical energy of the triboelectric nanogenerator (TENG) efficiently gathers and converts it into electricity. In the framework of a cheap, manageable, and effective approach, it is possible to operate small electronic devices by converting mechanical energy with low-frequency into electrical power using the friction loading process. TENG is the device that forms the layers consisting of two materials showing different triboelectric characteristics, by attaching them, growing the conductive metals that complement the structure and completing the electronic circuit [2-3].

Due to the mechanical deformation caused by friction between the two surfaces and the nano-sized surface roughness, equal but opposite sign charges are produced on both surfaces. When these opposite sign charges removed from each other, an electron flow occurs over the metal electrodes. This electron flow allows power to be generated depending on the instantaneous potential change. To raise the magnitude of this effect is necessary to increase the surface charge density and can be done by changing the effective contact surface area, micro and

nanostructure conditions of the material. In the light of basic principles, the working principle of TENG based on the coupling effect of triboelectrification and electrostatic induction and explained by Maxwell's displacement current and surface polarizations to evaluate these two fundamental effects together [4]. In addition, to evaluate the performance of TENGs from a material perspective, the FOM equation is derived and shown as a material evaluation criterion [2].

$$FOM_m = \sigma^2 \left( \frac{C^2}{m^4} \right) \quad (1)$$

where  $\sigma$  is surface charge density,  $C$  is the capacitance value,  $m$  is the repetitivity.

In many studies up to now, TENGs have tried to develop polymer surfaces as electrodes. However, although polymer structures are easy to produce, they cannot provide the desired performance because they easily deformed in long-term use. As a solution to this problem, the essential parameter that will increase efficiency is to provide long-term performance using semiconductors, which have faster electron loss than polymers TENGs.

Zinc oxides are the most known materials located at the boundary between the semiconductor and conductive material in terms of electrical properties. Although ZnO is generally known as an n-type semiconductor, it shows p-type properties under certain conditions. ZnO crystallizes in wurtzite (hexagonal symmetry) structure and are used in many areas technologically due to their high electrical conductivity and optical permeability. Therefore, inexpensive-repeatable production and technical usability of the material becomes very important.

In nanotechnology, a surface modification known as adjustment of microstructure and modify the morphology of materials are effective tools to improve structural and electrical properties. Hence, we have deposited ZnO thin films in nano-form as friction layers to develop and maximize the output voltages of the triboelectric nanogenerator and determine the resistance and capacitance properties of materials under the external applied electric field as a function of frequency is of critical importance before triboelectric characterizations.

## 2. EXPERIMENTAL

100 nm ZnO thin films were sputtered on Si (100) substrates from alloy target by RF magnetron sputtering in a high vacuum chamber with a base pressure of better than  $2 \times 10^{-7}$  mbar. The argon and O<sub>2</sub> gases (purity 6N) used at a working pressure of  $2 \times 10^{-3}$  mbar for the sputtered gases in the range of 5 - 10 and 15% partial O<sub>2</sub> pressures.

During the growing process, the substrate was rotated at 10 rpm for gaining homogeneity throughout the entire thin films. The film thickness was quantified and checked by using X-ray reflectometry (XRR) measurements. The crystallographic analysis was performed by the X-ray diffraction (XRD) method using Bragg Brentano optics with Cu  $\kappa_{\alpha}$  radiation. The morphological surface of films was performed by scanning electron microscopy (SEM). The surface microstructure measurements were performed using atomic force microscopy (AFM). The semi-logarithmic current-voltage and frequency-dependent capacitance measurements of materials under the applied electric field were conducted using an electrochemical measurement system. The variations on the partial O<sub>2</sub> pressures affect crystal and surface structure under the influence of sputtering conditions. The surface charge density characteristics were received by the influence of the variation in the partial O<sub>2</sub> pressures concerned from the frequency-dependent capacitance measurements. The maximum capacitance value at very low frequencies regarded as a further contribution for the triboelectric, which is quite close to the natural oscillation frequency due to the coupling of triboelectrification and electrostatic induction.

## 3. RESULTS AND DISCUSSION

In Fig. 1(a-b-c), the X-ray diffraction pattern, atomic force microscopy and scanning electron microscopy results are given. In X-ray diffraction patterns, two reflection peaks were observed in the whole thin films related to the ZnO wurtzite phase. However, as the pressure value was decreased, the reflection peak of the (002) was observed in the most severe and sharp way for the thin film growth at % 5 partial O<sub>2</sub> pressure.

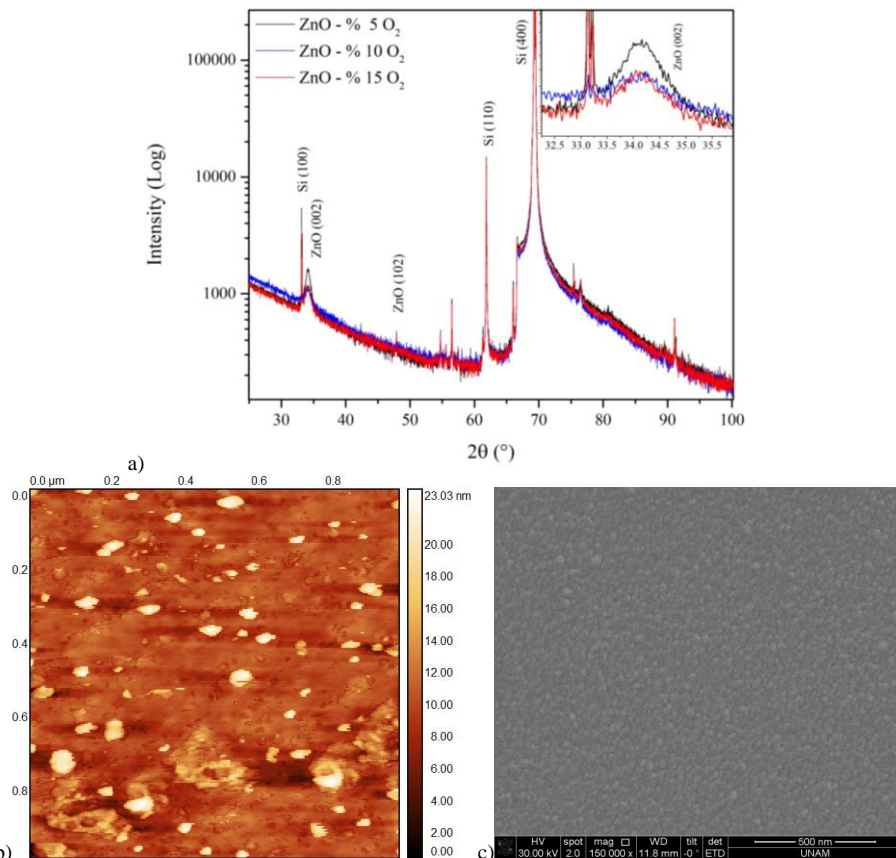


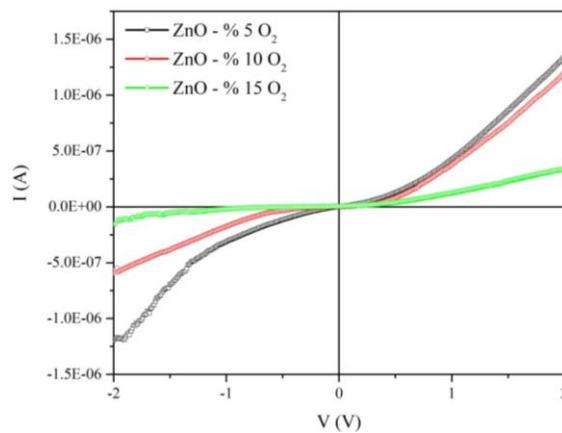
Figure 1. (a) XRD pattern of ZnO thin films with various partial O<sub>2</sub> pressures, (b) AFM and (c) SEM images of ZnO thin film with % 5 partial O<sub>2</sub> pressure

As shown in Fig. 2, current-voltage curves of thin films growth at different partial O<sub>2</sub> pressures are given. It was observed that the semiconductor performance of thin films at high partial O<sub>2</sub> pressure values increased with decreasing partial O<sub>2</sub> pressure value. The highest properties were obtained in the thin film having % 5 partial O<sub>2</sub> pressure value. The experimental value of barrier height ( $\Phi_b$ ), ideality factor (n) can be obtained from the intersection and slope between ln(I) and V graphs with the help of equations 2-3,

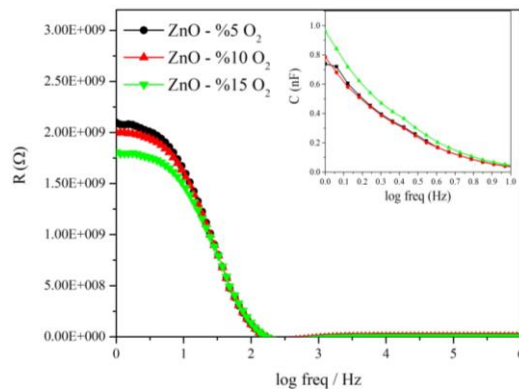
$$\Phi_b = kT/q \ln\left(\frac{AA^* T^2}{I_0}\right) \quad (2)$$

$$n = \frac{q}{kT} \left( -\frac{dV}{d(\ln I)} \right) \quad (3)$$

where q is the electronic charge, k is the Boltzmann constant, T is the absolute temperature in Kelvin, A is the effective diode field, A \* is the effective Richardson constant and I<sub>0</sub> is the saturation current value [6]. By using the Eq. (2-3), the barrier height and ideality factor were found as  $\Phi_b = 0.58$  eV, n = 3.1 for ZnO thin film grown at % 5 partial O<sub>2</sub> pressure, respectively. For diode behavior, the ideality factor is equal to 1, but experimentally it is observed to be greater than 1 for a Schottky diode [7]. It is thought that the state of currents can be caused by defects arising during production, the presence of interface conditions, the series resistance effect, and some similar effects [8-10].

Figure 2. I-V curve of ZnO thin films with various partial O<sub>2</sub> pressures

Electrochemical impedance spectroscopy (EIS) measurements of semiconductor thin film are a useful technique to investigate the electrical and dielectric properties of devices. In the Figure 3, electroimpedance (EIS) curves were taken to examine the resistance properties of ZnO thin films grown at various sputtering partial O<sub>2</sub> pressure under different bias voltage and frequencies.

Figure 3. Frequency dependent R-C curves of ZnO thin films with various partial O<sub>2</sub> pressures

From Fig. 3, it is observed that the frequency-dependent resistivity (R) values of entire films are in the low frequency region with various partial O<sub>2</sub> pressure values, and they are divided into two regions in the frequency range. In lower frequencies, it shows a rapid increase logarithmically. Afterwards, it is seen that R values below 10 Hz almost reach saturation. Another result obtained from the graphs is that the resistance decreases with the increase of the partial O<sub>2</sub> pressure as expected due to the decrease in resistivity from the scattered domains of the thin films. To calculate the FOM<sub>m</sub> of the ZnO thin films we get charge values from the electrical measurement and obtain  $8.19 \times 10^{-8}$ ,  $5.21 \times 10^{-8}$ ,  $3.38 \times 10^{-8}$  C for % 5, 10 and 15 partial O<sub>2</sub> pressure, respectively. By using the Eq. (2), FOM<sub>m</sub> parameters are calculated as  $62.72 \times 10^{-25}$ ,  $20 \times 10^{-25}$  and  $6.48 \times 10^{-25}$  for % 5, 10 and 15 partial O<sub>2</sub> pressures, respectively. Since the values found are the first results attained in the triboelectric field, there are no other material groups regarding their comparable properties, yet.

#### 4. CONCLUSION

The results of the present study advise an environmentally friendly, low-cost and increased output performance triboelectric nanogenerator based on semiconductor-based layers to power electronic devices with low energy-efficient systems. In this framework, before the layers to be revealed, the structural, electrical and material FOM<sub>m</sub> values of ZnO films as semiconductor layers according to different partial O<sub>2</sub> pressure were systematically attained and assessed. It is known that the ascertainment of electrical resistance and capacitance properties in the low-frequency region is very significant, especially below 20 Hz. The study shows the present superior triboelectric properties with the usage of the semiconductor layer to might be a preferred friction layer in the future improved triboelectric studies.

## **ACKNOWLEDGMENT**

This work was supported by the Scientific and Technological Research Council of Turkey (TÜBİTAK) under the grant number of 119M972.

## **REFERENCES**

- [1] F. Fan, Z. Tian, ZL. Wang. Flexible triboelectric generator. *Nano Energy*, 2012, 1(2), 328–34. DOI: <https://doi.org/10.1016/j.nanoen.2012.01.004>
- [2] H. Zhang, L. Yao, L. Quan, X. Zheng, Theories for triboelectric nanogenerators: A comprehensive review. *Nanotechnology Reviews*, 2020, 9:1. DOI: <https://doi.org/10.1515/ntrev-2020-0049>
- [3] S. Chand, J. Kumar. Evidence for the double distribution of barrier heights in Pd<sub>2</sub>Si/n-Si Schottky diodes from I - V - T measurements. *Semiconductor Science and Technology* 1996, 11, 1203. DOI: <https://doi.org/10.1088/0268-1242/11/8/015>
- [4] W. Deng, B. Zhang, L. Jin, Y. Chen, W. Chu, H. Zhang, M. Zhu, W. Yang. Enhanced performance of ZnO microballoon arrays for a triboelectric nanogenerator, *Nanotechnology* 2017, 28, 135401. DOI: <http://iopscience.iop.org/0957-4484/28/13/135401>
- [5] S. Goldsmith. Filtered vacuum arc deposition of un-doped and doped ZnO thin films:Electrical, optical, and structural properties. *Surface & Coatings Technology*, 2006, 201, 3993-3999. DOI: <https://doi.org/10.1016/j.surfcoat.2006.08.007>
- [6] R.T. Tung, Recent Advances in Schottky Barrier Concepts. *Materials Science and Engineering*. 2001, R35,1-38. DOI: DOI: [10.1016/S0927-796X\(01\)00037-7](https://doi.org/10.1016/S0927-796X(01)00037-7)
- [7] T. Asar, B. Korkmaz, S. Özçelik, Effect of platinum doping on the structural and electrical properties of SnO<sub>2</sub> thin films. *J. Exp. Nanosci.* 2016 11, 1285–1306. DOI: <https://doi.org/10.1080/17458080.2016.1212408>
- [8] V. L. Devi, I. Jyothi, V. R. Reddy, C-J. Choi. Schottky Barrier Parameters and Interfacial Reactions of Rapidly Annealed Au/Cu Bilayer Metal Scheme on N-type InP. *The Open Applied Physics Journal*, 2012, 5, 1-9. DOI: [10.2174/1874183501205010001](https://doi.org/10.2174/1874183501205010001)
- [9] E. Elgazzar, A. Tataroğlu, A.A. Al-Ghamdi, Y. Al-Turki, W.A. Farooq, F. El-Tantawy, F. Yakuphanoglu. Thermal sensors based on delafossite film/p-silicon diode for low-temperature measurements. *Appl. Phys. A*, 2016, 122, 617. DOI: [10.1007/s00339-016-0148-y](https://doi.org/10.1007/s00339-016-0148-y)
- [10] R. Marnadu, J. Chandrasekaran, S. Maruthamuthu, V. Balasubramani, P. Vivek, R. Suresh, Ultra-high photoresponse with superiorly sensitive metal-insulator-semiconductor (MIS) structured diodes for UV photodetector application. *Appl. Surf. Sci.* 2019, 480, 308–322. DOI: <https://doi.org/10.1016/j.apsusc.2019.02.214>



# TCAD-MODEL OF BETAVOLTAIC BATTERY STRUCTURE WITH VERTICAL MICRO TRENCHES

Konstantin Petrosyants

National Research University Higher School of Economics (Moscow Institute of Electronics and Mathematics),  
Moscow, Russia, kpetrosyants@hse.ru, ORCID: 0000-0001-7969-4786

Andrey Pugachev

National Research University Higher School of Economics (Moscow Institute of Electronics and Mathematics),  
Moscow, Russia, kpetrosyants@hse.ru, ORCID: 0000-0003-3274-9780

Igor Kharitonov

National Research University Higher School of Economics (Moscow Institute of Electronics and Mathematics),  
Moscow, Russia, ikharitonov@hse.ru, ORCID: 0000-0001-8947-8227

Dmytry Dymov

Joint Stock Company “Academician M.F. Reshetnev” Information Satellite Systems, Russia, ymovdv@mail.ru, ORCID:  
0000-0002-9873-1359

Cite this paper as:

*Petrosyants, K., Pugachev, A., Kharitonov I., Dymov D. TCAD-model of betavoltaic battery with vertical micro trenches structure. 9th Eur. Conf. Ren. Energy Sys. 21-23 April 2021, Istanbul, Turkey*

---

**Abstract:**

For effective design of Si betavoltaic structures with trenches the original TCAD-model was designed, verified and applied. The standard TCAD optical generation model “optical beam” was adopted for simulation of electron-hole generation for beta particles irradiation in element structure with 5-um width vertical micro trenches. The main parameters of betavoltaic structure with trenches were simulated in dependence of substrate doping and were compared with those of usual planar betavoltaic structure.

---

**Keywords:**

*betavoltaic battery, Nickel-63, conversion efficiency , vertical trenches, TCAD model.*

---

© 2021 Published by ECRES

## 1. INTRODUCTION

The betavoltaic silicon batteries under Nickel-63 irradiation are the very perspective for low-voltage and long-life applications. In [1] the basics of betavoltaic microbatteries TCAD model were introduced for I-V characteristics investigation and basic parameters calculation. The TCAD tools are the main tool for optimization of semiconductor devices and new device constructions creation. As for betavoltaic batteries, the optimum volume configuration of radioactive source is the basic way to reach high efficiency for it. The higher the summary effective area of isotopic source in battery, the higher is its short-circuit current density  $I_{sc}$  ( $nA/cm^2$ ) and, so, the maximum power density  $P_{max}$  ( $nW/cm^2$ ) is higher.

The shallow trench isolation is very good mastered in silicon planar technology. This is the perspective way for betavoltaic batteries too. Unfortunately the standard TCAD model for betavoltaic structure is not correct for structure with vertical trenches. The new TCAD model suitable for betavoltaic element with irradiation source in shallow trench were designed, verified and used in this work.

## 2. TCAD MODEL OF BETAVOLTAIC BATTERY STRUCTURE WITH VERTICAL TRENCHES

In our previous work the standard TCAD (Sentaurus TCAD Synopsys) optical generation model was adopted and used for simulation of electron-hole generation for beta particles irradiation. To overcome the geometrical

restrictions of this model (light flux is only vertical), we proposed the horizontal orientation of element structure, Figure 1.

The surfaces with optical sources are situated on the central axis in trench. So, the optical beam generates electron-hole pairs in two directions, Figure 2: up and down relative any trench in Figure 1. The light sources has parameters from [1].

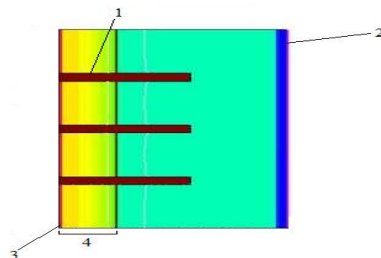


Figure 1. The prototype TCAD model of betavoltaic element structure: 1 - trench with optical source; 2-  $p^+$ -layer in  $p^-$ -substrate, 3 –  $n^+$ -layer, 4 –  $n^-$ layer

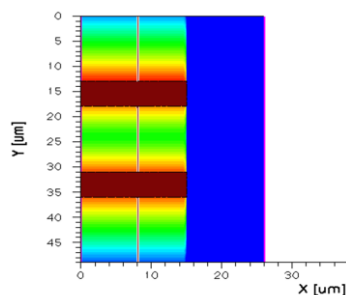


Figure 2. The optical generation rate in prototype TCAD model of betavoltaic element with trenches

### 3. SIMULATION RESULTS

For visible light source with power  $P=4.33 \cdot 10^{-7}$  W/cm<sup>2</sup> and wavelength  $\lambda=450$  nm that produces the same ionization effect for silicon as beta particle flux [1], the potential and electron current distributions were obtained, figure 3.

In the first, the optimum distance between vertical trenches was calculated by criterion of open-source voltage (short-circuit current) maximum. The obtained value of distance as 13 um is consistent with the double depth for 1000 times attenuation of electron–hole generation rate of Ni-63 beta irradiation in silicon [2].

Then, the open-source voltage and short-circuit current were calculated as function of substrate doping concentration, Figure 4. This result are in good agreement with the theoretical investigations [3].

The calculated maximum value of short-circuit current density for trench structure with  $50 \times 10$  um<sup>2</sup> area is approximately 720 pA/cm<sup>2</sup>. It was achieved with doping density  $N_{\text{sub}} = 2 \cdot 10^{16}$  cm<sup>-3</sup>. The maximum value of short-circuit current density is much greater than the current density for planar structures from [1], Figure 6(b) – approximately 22 nA/cm<sup>2</sup>.

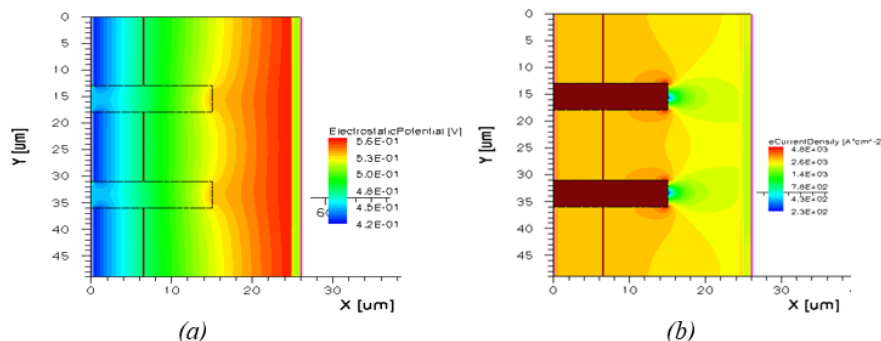


Figure 3. The potential distribution (a) and electron current density distribution (b) in prototype TCAD model of betavoltaic element with trenches

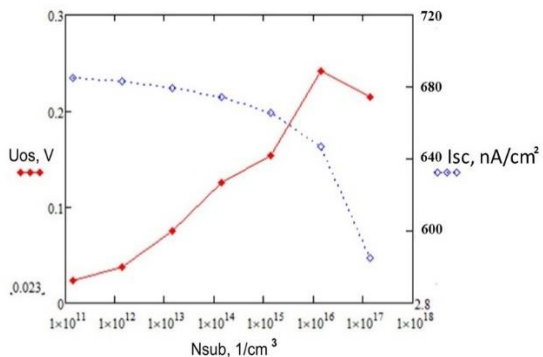


Figure 4. The open-source voltage ( $U_{os}$ ) and short-circuit current ( $I_{sc}$ ) of structure with trenches as function of substrate doping concentration

#### 4. CONCLUSION

1. The new TCAD model for enhanced betavoltaic element with vertical micro trenches was developed and verified.
2. The model was used for betavoltaic element structure investigation and optimization. Optimal doping profile of the structure was achieved.
3. The TCAD estimation of new structure parameters demonstrated its more efficiency compared with the planar structures with surface positioned irradiation sources.

#### REFERENCES

- [1] Petrosyants K O et al 2019 J. Phys.: Conf. Ser. 1353 012093
- [2] Zhang K, Gui G, Pathak P, Seo J-H, Blanchard J P and Ma Z Quantitative modeling of betavoltaic microbattery performance Sensors and Actuators A: Physical 2016; 240(2): 131–137
- [3] Savchenko A V et al Efficiency analysis of betavoltaic elements. Solid-State Electronics 2015; 111: 147-152



# TOWARDS HIGH CRYSTALLINITY AND STABLE MASNI<sub>3</sub> PEROVSKITE FILMS TREATED WITH DIFFERENT ANTISOLVENTS

Amal Bouich

Escuela Técnica Superior de Ingeniería del Diseño: Universitat Politècnica de València Camí de Vera, 46022, Valencia Spain, bouich.amal@gmail.com, ORCID:0000-0001-6745-8831

Shafi Ullah

Escuela Técnica Superior de Ingeniería del Diseño: Universitat Politècnica de València Camí de Vera, 46022 Valencia,Spain, shafi399@yahoo.com, ORCID: 0000-0003-0773-3760

Julia Mari

Escuela Técnica Superior de Ingeniería del Diseño: Universitat Politècnica de València Camí de Vera, 46022 València, Spain. juliasetze@gmail.com, ORCID: 0000-0001-6295-3091

Asmaa Bouich

Ibn Tofail University, BP 133, 14000 Kenitra, Morocco, bouich.asmaa@gmail.com, ORCID:0000-0002-0399-4595

Bernabé Marí

Escuela Técnica Superior de Ingeniería del Diseño: Universitat Politècnica de València Camí de Vera, 46022 Valencia Spain. Spain.bmari@fis.upv.es, ORCID: 0000-0003-0001-419X

Mohamed Ebn Touhami

Ibn Tofail University, BP 133, 14000 Kenitra, Morocco, mehntouhami@gmail.com, ORCID:0000-0002-5897-3652

Cite this paper as:

*Bouich,A, Ullah, S, Mari, J, Bouich, A, Marí, B, Ebn Touhami, M. Towards high crystallinity and stable masni<sub>3</sub> perovskite films treated with different antisolvents. 9<sup>th</sup> Eur. Conf. Ren. Energy Sys. 21-23 April 2021, Istanbul, Turkey*

## Abstract

Fabrication of excellence perovskite MASnI<sub>3</sub> thin films used adequate antisolvent was not investigated on any uniform platform. Here, we investigate the role of different Antisolvent diethyl ether, toluene, and chlorobenzene to illustrate their effect on the growth of the film. The obtained MASnI<sub>3</sub> thin films crystallinity, morphology, topography, and Optical properties were performed by X-ray diffraction, scanning electrons microscopy, atomic force microscopy, photoluminescence, and UV-visible spectroscopy, respectively. The effect of different antisolvent treatment was evaluate on the surface homogeneity and composition of the MASnI<sub>3</sub> thin films. The results confirmed that the use of chlorobenzene leads to a regular perovskite layer with nearly no holes and large grains size to advance the morphology of the thin films with chlorobenzene antisolvent we try to process the thermal annealing to control crystallinity and adding antisolvent in a different way to control supersaturation, the obtained results of this work could find reproducible industrial methods for perovskite device fabrication.

## Keywords:

MASnI<sub>3</sub>, Antisolvent treatment, XRD, SEM, PL and UV-Visible analysis.

© 2021 Published by ECRES

## 1. INTRODUCTION

Solar energy is considered a basis of clean and abundant energy, so it became important to take a lot more advantage of this source in the field of photovoltaic [1], recently organic and inorganic perovskite technology becomes more attractive and promising materials for researchers, especially methylammonium halides Perovskite device showed

conversion efficiency more than 23% have been reported [2], also perovskite materials have remarkable optical and electronic properties, such as broader light absorption coefficient, long charge carrier diffusion length, the small exciton binding energy and the ability to generate electrons and holes pairs [3]. Furthermore, for perovskite thin films fabrication, a variety of techniques have been used such as one-step solution deposition [4,5], two-step solution deposition [6], vapor deposition [7] and thermal deposition [8] but one step deposition by spin-coating demonstrates an excellent capability to fabricates perovskite devices. Furthermore, the efficiency is higher of the device reported by different a researcher using the spin coating technique with homogeneous and compact thin films. it has been considered that the morphology of perovskite thin films plays an important role in the device performance. Many methods and treatments have been introduced to optimize product quality by improving the surface homogeneity and crystallinity of the films.

Herein, in this study the thin films of  $\text{MASnI}_3$  treated with different antisolvents affect the supersaturation also complex interactions are happening related to physicochemical properties. Therefore, the choice of the antisolvent type is important for improving the perovskite film morphology also helpful for boosting the device performance. The antisolvent affects observed in the variation in morphology, structure, and composition with different antisolvent Toluene, chlorobenzene, and diethyl ether. The obtained  $\text{MASnI}_3$  samples were further analyzed by different available techniques such as XRD, SEM, AFM, optical and photoluminescence analysis.

## 2 Experimental Procedure

Tin (II) iodide ( $\text{SnI}_2$ ), Methylammonium iodide (MAI), n n-dimethylformamide (DMF) and Dimethyl Sulfoxide (DMSO). Various antisolvents: diethyl ether, Chlorobenzene and Toluene. The prepared solution of  $\text{MASnI}_3$  was spin coated on the FTO substrate at 2000 rpm for 20 s. During the spin-coating different amounts of different were dripped to the  $\text{MASnI}_3$  thin films, and subsequently, the as-prepared  $\text{MASnI}_3$  samples were annealed in a vacuum for 20 minutes at 250°.

## Film Characterization

The perovskite thin film's crystal structure analysis was performed by XRD RIGAKU Ultima IV diffractometer, scanning electron microscopy (SEM). The Surface morphology was investigated through Scanning (SEM) at different magnifications. The films topography was characterized using atomic force microscopy (AFM). The absorption was measured using a UV-Visible wavelength range of 300 to 850 nm and photoluminescence (PL) was performed by He-Cd laser.

## 3 Results and discussion

The influence of antisolvent onto the phase structure and microstructure of the films was studied by X-ray diffraction (XRD). Figure1 shows the X-ray diffraction patterns of  $\text{MASnI}_3$  films fabricated by spin-coating treated with different antisolvent, the strong diffraction peaks show between the angles: 14, 28, 31, 38 and 31, which to the planes (110), (220), (222), (224) and (314) it is in a good promise with the former report [9, 10] XRD results of  $\text{MASnI}_3$  films prepared shows good crystallinity and the characteristic peak (110) intensity increases enormously by using toluene like antisolvent compare to the Chlorobenzene and diethyl ether antisolvents. The decrease of intensity can be attributed to the excessive solubility of methylammonium iodide (MAI).

### **lattice parameters:**

The lattice parameters were calculated by using the equations (1) and (2) with different diffraction 2 theta angle.

$$\frac{1}{d^2} = \frac{h^2+k^2}{a^2} + \frac{l^2}{c^2} \quad (1)$$

$$\eta\lambda = d_{hkl}\sin(\theta) \quad (2)$$

Where a, b, c lattice parameters, hkl are miller indices,  $d_{hkl}$  is interplanar distance and k is the wavelength (0.154 nm).

The obtained lattice parameters of main (110) peak were  $a = b = 8 \text{ \AA}$ ,  $c = 11.9 \text{ \AA}$  corresponding to the tetragonal structure.

### **Lattice strain and dislocation density.**

The lattice strain ( $\varepsilon$ ) indicates the thin films crystals deformation calculated by the following eq (3) the obtained results is summarized between 340 nm and 400 nm (Table 1).

$$\beta\cos(\theta) = \frac{k\lambda}{D} + 4\varepsilon\sin(\theta) \quad (3)$$

Where  $\beta$  is the FWHM value, K is the constant ( $k = 0.9$ ),  $\lambda$  is the wavelength of the X-rays ( $\lambda = 0.1540$  nm),  $\theta$  is the Bragg diffraction angle, D is the crystallite size (nm). Grain size dislocation density was estimated by the equation (4) as given below.

$$\gamma = \frac{1}{D^2} \quad (4)$$

Table 1 shows that the four samples have different grain sizes from 300 nm to 400 nm with  $MASnI_3$  treated with different antisolvent, the higher grain size 400 nm for the toluene and with lower effective lattice around 0.37 that explained by a lesser of deficiencies and distortions of the grains.

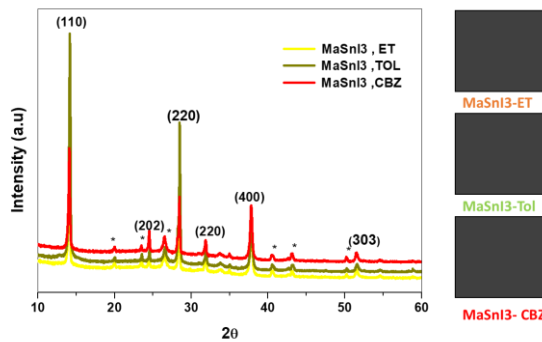


Figure 1: XRD patterns of  $MASnI_3$  Films treated with different antisolvents Toluene, Chlorobenzene, Diethyl ether

Table 1: Parameters of XRD of  $MASnI_3$  films treated with different antisolvents Toluene, Chlorobenzene, Diethyl ether.

Sample.ID	Grain size (nm)	Dislocation density ( $\text{nm}^{-1}$ )	Lattice strain ( $\epsilon$ )
MASnI3- ET	340	$1.05 \times 10^{-5}$	0.38
MASnI3- CBZ	360	$0.90 \times 10^{-5}$	0.39
MASnI3- Tol	400	$0.62 \times 10^{-5}$	0.39

Figure 2 shows (SEM) images  $MASnI_3$  treated with different Antisolvent diethyl ether. The surface morphology of  $MASnI_3$  was examined with SEM. It is found with diethyl ether that the crystals are poorly formed. even with the chlorobenzene was not changing that much in the morphology. However, the toluene has significantly altered the morphology and the largest crystal size was obtained, further, to explaining the change of the morphology of  $MASnI_3$  related to the type of antisolvent [11, 12]. Besides, the addition of antisolvent gave fine needles that agglomerate easily. This proves that supersaturation shows a vital role in a crystallization system and that then influences the size, shape, and degree of agglomeration of the crystals [13,14]. During the annealing treatment, the solvent molecules are removed from the precursors to the final stage perovskite thin film. It is found that during annealing under the  $250^\circ\text{C}$ , the conversion of forerunners to the perovskite phase is almost perfect in all cases but the way that we are introduce affect the surface.

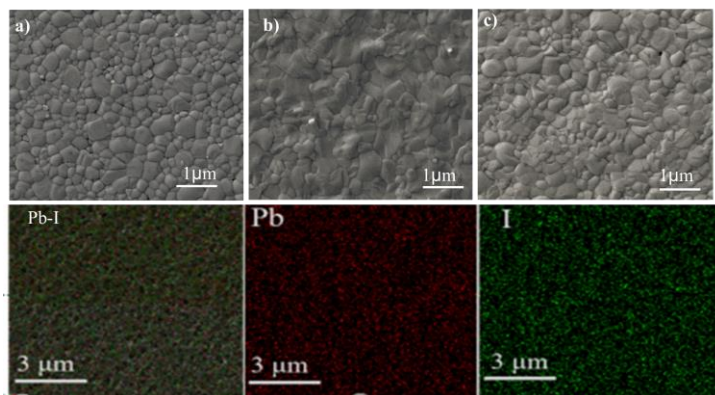


Figure 2: SEM images of  $MASnI_3$  Films treated with different antisolvents: c) Toluene, a) Chlorobenzene, a) Diethyl ether and Mapping of  $MASnI_3$ .

Figure 3 shows the AFM images of  $MASnI_3$  treated by different antisolvents where the roughness values measured for the three samples prepared and it was higher for  $MASnI_3$  with toluene. It was observed from the obtained

analysis that the surface roughness improved from 41nm, 46.73 nm and 56.99 nm corresponding to Diethyl ether, Chlorobenzene, and toluene, respectively. The AFM results are in good agreement with SEM analysis which confirmed the formation of improving surface morphology of the films.

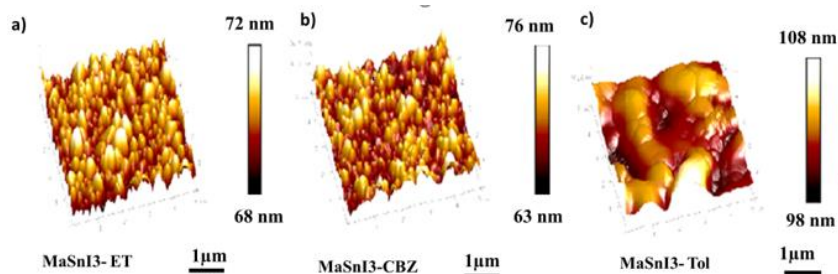


Figure 3. The topographic property of  $MASnI_3$  Films treated with various antisolvents: a) Diethyl ether b) Chlorobenzene c) Toluene,

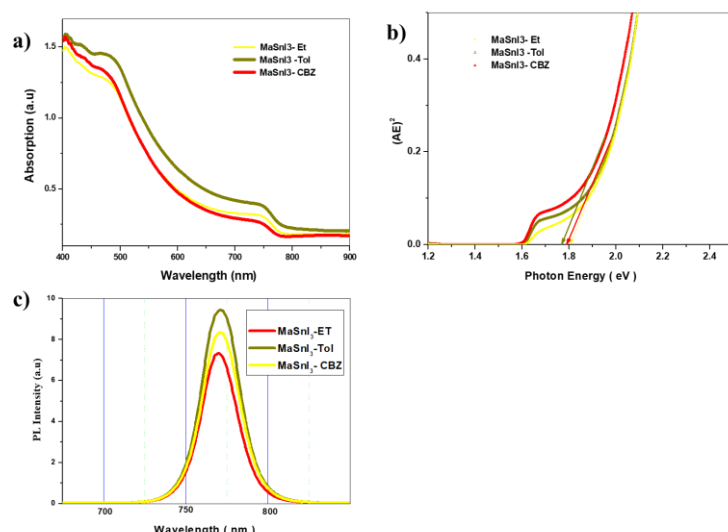


Figure 4: a) Absorption of  $MASnI_3$  films, b) band gap and c) photoluminescence (PL) treated with Toluene, Diethyl ether and Chlorobenzene.

The figure 4 shows the characteristic peak of PL for the three samples  $MASnI_3$  with different Antisolvents of diethyl ether, Toluene, Chlorobenzene in the range of 750 and 800 nm [16]. The PL peak of  $MASnI_3$  treated of toluene, shows a higher intensity compare to the  $MASnI_3$  treated with diethyl ether or chlorobenzene and also the optimum band gap around 1.75 ev. it can be related with phase transitions commonly found for halide perovskite [17,19].

Table 1: optical Band gap of the  $MASnI_3$  with treated with Toluene, Diethyl ether and Chlorobenzene.

Sample	$\lambda$ (nm)	Band Gap -PL (eV)	$\lambda$ (nm)	Band gap -UV (eV)
$MASnI_3$ -ET	779	1.59	750	1.81
$MASnI_3$ -TOL	782	1.58	759	1.77
$MASnI_3$ -CBZ	787	1.57	760	1.75

## CONCLUSION

In this work,  $MASnI_3$  thin films have been successfully prepared by one step spin coating technique. The effect of different antisolvent (Diethyl ether, Chlorobenzene, and toluene) was investigated by XRD, SEM and optical analysis.

The XRD analysis displays an extraordinary intensity of peak (110) by treating  $MASnI_3$  film with the toluene antisolvent and leading to large grains size of the  $MASnI_3$  thin film examined by SEM and AFM analysis. furthermore, the enhancement of light absorption was observed more effective using toluene antisolvent. Our results demonstrate that using toluene antisolvent is a good choice for  $MASnI_3$  thin films for efficient perovskite device.

## REFERENCE

- [1] Green, M. A., Emery, K., Hishikawa, Y., Warta, W., & Dunlop, E. D. (2015). Solar cell efficiency tables (Version 45). *Progress in photovoltaics: research and applications*, 23(1), 1-9.
- [2] Jeon, N. J., Na, H., Jung, E. H., Yang, T. Y., Lee, Y. G., Kim, G., ... & Seo, J. (2018). A fluorene-terminated hole-transporting material for highly efficient and stable perovskite solar cells. *Nature Energy*, 3(8), 682.
- [3] Quarti, C., Mosconi, E., Ball, J. M., D'Innocenzo, V., Tao, C., Pathak, S., ... & De Angelis, F. (2016). Structural and optical properties of methylammonium lead iodide across the tetragonal to cubic phase transition: implications for perovskite solar cells. *Energy & Environmental Science*, 9(1), 155-163.
- [4] Im, J. H., Kim, H. S., & Park, N. G. (2014). Morphology-photovoltaic property correlation in perovskite solar cells: One-step versus two-step deposition of  $\text{CH}_3\text{NH}_3\text{PbI}_3$ . *Apl Materials*, 2(8), 081510.
- [5] Carnie, M. J., Charbonneau, C., Davies, M. L., Troughton, J., Watson, T. M., Wojciechowski, K., ... & Worsley, D. A. (2013). A one-step low temperature processing route for organolead halide perovskite solar cells. *Chemical communications*, 49(72), 7893-7895.
- [6] Bi, D., Moon, S. J., Häggman, L., Boschloo, G., Yang, L., Johansson, E. M., ... & Hagfeldt, A. (2013). Using a two-step deposition technique to prepare perovskite ( $\text{CH}_3\text{NH}_3\text{PbI}_3$ ) for thin film solar cells based on  $\text{ZrO}_2$  and  $\text{TiO}_2$  mesostructures. *Rsc Advances*, 3(41), 18762-18766.
- [7] Chen, Q., Zhou, H., Hong, Z., Luo, S., Duan, H. S., Wang, H. H., ... & Yang, Y. (2013). Planar heterojunction perovskite solar cells via vapor-assisted solution process. *Journal of the American Chemical Society*, 136(2), 622-625.
- [8] Leyden, M. R., Ono, L. K., Raga, S. R., Kato, Y., Wang, S., & Qi, Y. (2014). High performance perovskite solar cells by hybrid chemical vapor deposition. *Journal of Materials Chemistry A*, 2(44), 18742-18745.
- [9] Kong, W., Ye, Z., Qi, Z., Zhang, B., Wang, M., Rahimi-Iman, A., & Wu, H. (2015). Characterization of an abnormal photoluminescence behavior upon crystal-phase transition of perovskite  $\text{CH}_3\text{NH}_3\text{PbI}_3$ . *Physical Chemistry Chemical Physics*, 17(25), 16405-16411.
- [10] Guo, X., McCleese, C., Kolodziej, C., Samia, A. C., Zhao, Y., & Burda, C. (2016). Identification and characterization of the intermediate phase in hybrid organic-inorganic  $\text{MAPbI}_3$  perovskites. *Dalton Transactions*, 45(9), 3806-3813.
- [11] Xiao, Z., Dong, Q., Bi, C., Shao, Y., Yuan, Y., & Huang, J. (2014). Solvent annealing of perovskite-induced crystal growth for photovoltaic-device efficiency enhancement. *Advanced Materials*, 26(37), 6503-6509.
- [12] Luo, S., & Daoud, W. A. (2016). Crystal structure formation of  $\text{CH}_3\text{NH}_3\text{PbI}_3\text{-xCl}_x$  perovskite. *Materials*, 9(3), 123.
- [13] Park, N. G. (2016). Crystal growth engineering for high efficiency perovskite solar cells. *CrystEngComm*, 18(32), 5977-5985.
- [14] Zheng, X., Chen, B., Wu, C., & Priya, S. (2015). Room temperature fabrication of  $\text{CH}_3\text{NH}_3\text{PbBr}_3$  by anti-solvent assisted crystallization approach for perovskite solar cells with fast response and small J-V hysteresis. *Nano Energy*, 17, 269-278.
- [15] Jeangros, Q., Duchamp, M., Werner, J., Kruth, M., Dunin-Borkowski, R. E., Niesen, B., & Hessler-Wyser, A. (2016). In situ TEM analysis of organic-inorganic metal-halide perovskite solar cells under electrical bias. *Nano letters*, 16(11), 7013-7018.
- [16] Liu, D., Yang, J., & Kelly, T. L. (2014). Compact layer free perovskite solar cells with 13.5% efficiency. *Journal of the American Chemical Society*, 136(49), 17116-17122.
- [17] Zhang, M., Yu, H., Lyu, M., Wang, Q., Yun, J. H., & Wang, L. (2014). Composition-dependent photoluminescence intensity and prolonged recombination lifetime of perovskite  $\text{CH}_3\text{NH}_3\text{PbBr}_{3-x}\text{Cl}_x$  films. *Chemical Communications*, 50(79), 11727-11730.
- [18] Choi, J. J., Yang, X., Norman, Z. M., Billinge, S. J., & Owen, J. S. (2013). Structure of methylammonium lead iodide within mesoporous titanium dioxide: active material in high-performance perovskite solar cells. *Nano letters*, 14(1), 127-133.
- [19] Halder, A., Chulliyil, R., Subbiah, A. S., Khan, T., Chattoraj, S., Chowdhury, A., & Sarkar, S. K. (2015). Pseudohalide ( $\text{SCN}^-$ )-doped  $\text{MAPbI}_3$  perovskites: A few surprises. *The journal of physical chemistry letters*, 6(17), 3483-3489



# EVALUATION OF THE TEMPERATURE IMPACT ON THE PRODUCTION OF PHOTOVOLTAIC ENERGY IN THE BRAZILIAN NATIONAL SCENE

Gustavo Neves Margarido

UFABC, Sao Paulo, Brazil, gnmargarido@ifsp.edu.br, ORCID: 0000-0003-1186-5694

Federico Bernardino Morante Trigoso

UFABC, Sao Paulo, Brazil, federico.trigoso@ufabc.edu.br, ORCID: 0000-0003-0343-5096

Renato Chaves Souza

IFSP, Sao Paulo, Brazil, rchaves@ifsp.edu.br, ORCID: 0000-0002-8804-2752

Wilson Carlos da Silva Junior

IFSP, Sao Paulo, Brazil, wilsoncarlos@ifsp.edu.br, ORCID: 0000-0001-8128-281X

Roberto Nunes Duarte

IFSP, Sao Paulo, Brazil, rnduarte@ifsp.edu.br, ORCID: 0000-0002-8292-1623

Fabio da Silva Bortoli

IFSP, Sao Paulo, Brazil, bortoli.fabio@gmail.com, ORCID: 0000-0001-7082-5209

Carlos Frajuba

IFSP, Sao Paulo, FURG, Rio Grande, Brazil, frajuba@gmail.com, ORCID: 0000-0001-8463-3451

Cite this paper as:

*Margarido, GN, Trigoso, FBM, Souza, RC, Silva Junior, WC, Duarte, RN, Bortoli, FS, Frajuba, C.. Evaluation of the temperature impact on the production of photovoltaic energy in the Brazilian national scene. 9<sup>th</sup> Eur. Conf. Ren. Energy Sys. 21-23 April 2021, Istanbul, Turkey.*

## Abstract:

This work presents the performance comparison of photovoltaic modules in two scenarios in which the operating temperatures are different. The operating temperature influences the maximum power achieved by the modules during their operation. The comparison was made using the average temperatures of two cities of the State of São Paulo (Brazil). The comparison shows that warmer locations have a considerable reduction in performance in photovoltaic generation. The comparison analysis indicates that it is necessary to take this problem into consideration in photovoltaic generation in hot regions.

## Keywords:

Influence of temperature, efficiency, photovoltaic modules

© 2021 Published by ECRES

## 1. INTRODUCTION

Solar energy has been gaining more and more space in the world energy matrix, not only by looking for solutions to possible depletion of the already explored traditional energy sources, but also by searching for sources that provide less environmental impacts, such as the release of pollutants or even the release of heat to the environment, since “solar energy does not disturb the Earth’s thermal balance” [1]. The direct use of solar energy can be carried out with the thermal use of energy or the electrical generation by photovoltaic effect. Only in Brazil, there was an increase in installed power, for photovoltaic generation, from 24 MW in 2016 to 935 MW in 2017 [2]. The authors have some experience in energy has the have worked with instrumentation [4-6].

Some factors influence the capacity of the modules in photovoltaic generation, such as the time of full sun exposure, presence of factors that may cause shading (in the modules), the solar incidence present in the region and the working temperature of the photovoltaic plates. The working temperature is influenced by the temperature of the environment in which the photovoltaic module is exposed, and the excess will limit the power expected in

laboratory tests, which are generally carried out at 25°C [6]. The study and knowledge of the limiting operational factors become important for the best use of photovoltaic technology.

The photovoltaic modules have, in their operation, sensitivity to the ambient working temperature. The temperature affects the functioning of the photovoltaic cells, components of the modules, with the decrease in voltage presented due to the increase in temperature. The electrical current is also affected in the cells, showing an increase in correspondence with the increase in temperature, however, this current change is very small (Figure 1). When the current change (due to the temperature change) is compared to the change in voltage, it can be considered negligible [7]

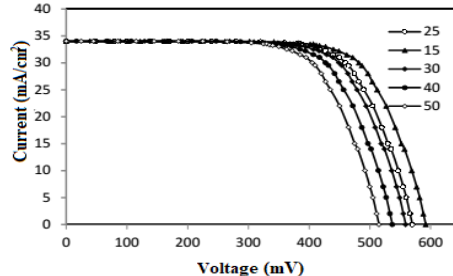


Figure 1 - Voltage and current relationship at different temperatures [8].

For the relationship between the working temperature and the voltage found in the photovoltaic cell, the coefficient  $\beta$  is established, which relates the open circuit voltage and the temperature variation Eq. [1].

$$\beta = \frac{\Delta V_{OC}}{\Delta T} \quad (1)$$

Where:

$\Delta V_{OC}$  - Open circuit voltage [V]

T - Temperature [°C]

The open circuit voltage for a given temperature can be calculated with the knowledge of  $\beta$  and the open circuit voltage informed by the module manufacturer Eq. [2].

$$V_{oc}(T) = V_{oc_{stc}} \cdot (1 + \beta \cdot (T - 25)) \quad (2)$$

Where:

$V_{oc_{stc}}$  - Open circuit voltage under standard test conditions [V].

The short-circuit current is also related to the temperature variation, establishing this relationship the  $\alpha$  coefficient Eq. [3].

$$\alpha = \frac{\Delta I_{SC}}{\Delta T} \quad (3)$$

where:

$I_{SC}$  - Short-circuit current [A].

The  $\gamma$  coefficient relates the maximum peak power to the temperature variation Eq. [4].

$$\gamma = \frac{\Delta P_{MP}}{\Delta T} \quad (4)$$

where:

$P_{MP}$  - Maximum power or peak power [W].

The temperature found in the photovoltaic module can be approximated by a simplified calculation that takes into account the solar incidence Eq. [5].

$$T_{mod} = T_{amb} + K_t \times G \quad (5)$$

Where:

$T_{amb}$  - Ambient temperature [°C].

$K_t$  - Module thermal coefficient [°C / W.m⁻²],

G - Irradiance on the module [W.m⁻²].

## 2. BRAZILIAN SCENARIO CONDITIONS

Brazil has a wide range of temperatures and intensity of solar radiation over its vast expanses. These variations are observed every year, due to the region and the time of year. Analyzing the data collection constant in climatological normals, we can obtain temperature data from some Brazilian cities and other climatological data, such as atmospheric pressure and relative humidity. The understanding of climatological normals can be achieved through the technical regulations of the World Meteorological Organization (WMO), which define normals as “average values calculated for a relatively long and uniform period, comprising at least three consecutive decades” [9]. The temperature differences in the national territory are more evident when temperature maps are observed that allow the graphical analysis of temperature levels by period. The map of average annual temperatures of a national climatological normal with data from 1981 to 2010 (Figure 2), shows the variation in the intensity of temperatures found by region or locality.

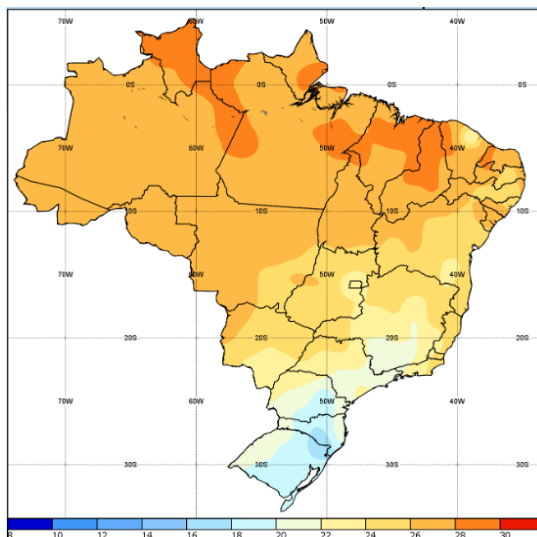


Figure 2 - Average annual temperature of climatological normal for the period 1981-2010 [9].

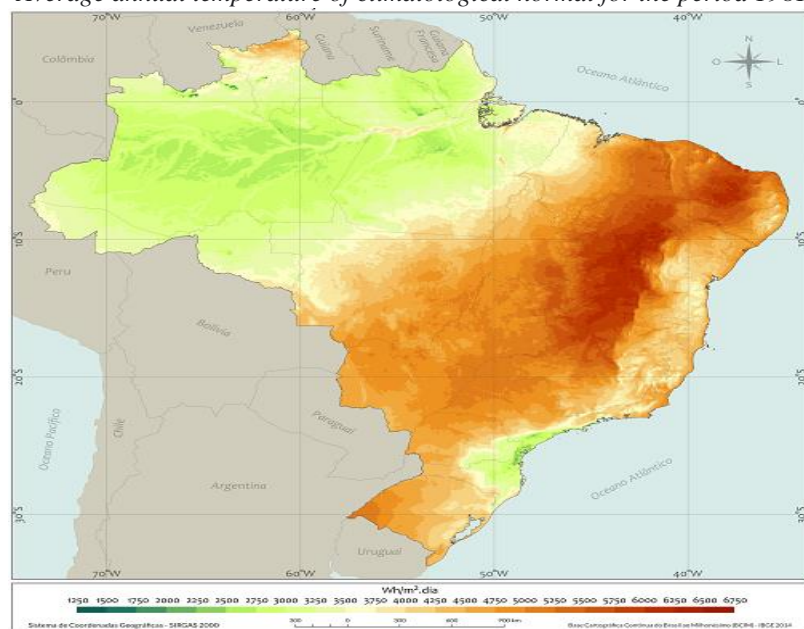


Figure 3 - Annual average of the daily total of normal direct solar irradiation [10].

As well as the temperature, the incidence of solar irradiation is also not equal and uniform throughout the entire national territory, as can be seen in the daily solar irradiation map (Figure 3).

The difference in the incidence of irradiation ends up providing a different amount of energy received in each region, as can be seen in the map of the annual total of normal direct solar irradiation (Figure 4). Some regions end up appearing as recipients of a much greater amount of annual solar energy than others. The map also shows that

the largest amount of total solar energy incident in a year is present in two limited portions of the northeast region of the national territory.

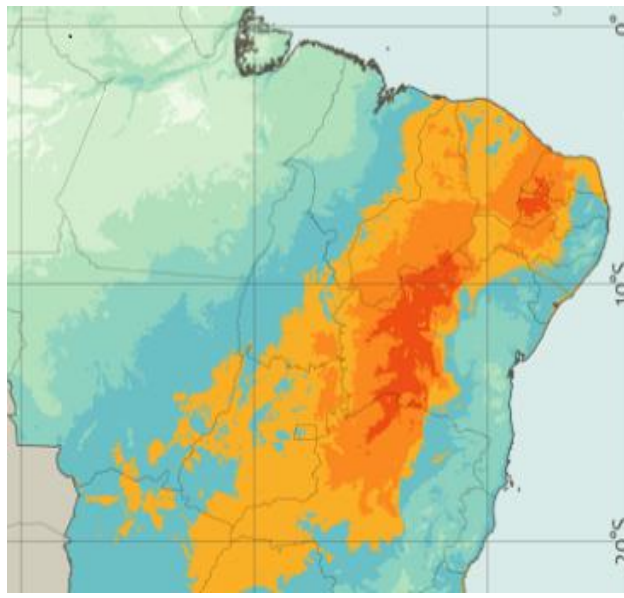


Figure 4 - Total annual direct normal solar radiation [7]).

Some regions with higher total solar irradiation also end up with higher average working temperatures, thus being able to provide a lower yield from the use of total solar irradiation in photovoltaic generation. Still in a comparison, it will be possible to observe (on the maps), regions with less total solar irradiation and also the presentation of high average temperatures, thus providing even less use. The comparisons suggest that a study of local radiation and temperature may provide a better understanding of the potential of photovoltaic generation by region.

### 3. COMPARATIVE STUDIES

A comparative study was carried out between two photovoltaic module operation scenarios, with the comparison of conditions provided by two regions with different climatic characteristics in the same political-administrative division of the national territory, in this case, the State of São Paulo. A city was selected in each of these regions to carry out the study (Figure 5).



Figure 5 - State map with indication of the study regions (adaptation of the state map presented by [11]).

The selected cities were: the city of Votuporanga as an object of study in region "1" and the city of Itapeva as an object of study in region "2". The selection took into account the availability of data for the study, such as temperature normal records (Table I).

*Table 1 - Monthly average temperature of normal climatology period between 1961-1990.*

<b>Average Temperature (°C)</b>													
	Jan	Feb	Mar	Apr	May	Jun	Jul	Aug	Sep	Oct	Nov	Dec	Average
Votuporanga	24,9	25, 1	25,0	24, 2	21,9	20, 1	20, 2	22, 5	23,2	24,8	25,4	25,0	23,5
Itapeva	22,6	23, 0	22,0	19, 7	17,1	15, 2	15, 1	16, 3	17,4	19,2	20,7	21,7	21,7

Source: Normal climatological data - [9].

Other important data for the study were the regional values of incident solar irradiation by period (Table II).

*Table 2 - Average global solar radiation period between 1995-2005*

<b>Solar Radiation (kWh/m<sup>2</sup>.day)</b>					
	Annual	Spring	Summer	Fall	Winter
Votuporanga	5,6	6,8	6,0	4,7	5,0
Itapeva	4,9	5,9	5,6	4,0	4,0

Source: São Paulo State Energy Secretary Data [12].

Using the average temperature values of each period and the solar irradiation of the respective periods, the estimated temperature values of the photovoltaic modules were calculated Eq. [5]. The difference in maximum power was calculated Eq. [4], using the calculated temperature of the module and considering the standard test temperature of 25°C and  $\gamma = -0.5\% / ^\circ C$ , and time of 07 hours of full sun. The values were gathered in a table (Table III).

Table 3 - Comparison of temperature, radiation and influence in the photovoltaic modulus per region.

<b>Região 1 -Votuporanga (SP) / Região 2 - Itapeva (SP)</b>		<b>Radiation (kWh/m<sup>2</sup>.dia)</b>		<b>Modulus Temp.(°C)</b>		<b>ΔP<sub>MP</sub>(%)</b>		
<b>Ambient Temp.(°C)</b>		<b>Reg. 1</b>	<b>Reg. 2</b>	<b>Reg. 1</b>	<b>Reg. 2</b>	<b>Reg. 1</b>	<b>Reg. 2</b>	
Jan	24,9	22,6	6,0	5,6	50,6	48,3	-12,81	-11,66
Feb	25,1	23,0	6,0	5,6	50,8	48,7	-12,91	-11,86
Mar	25,0	22,0	4,7	4,0	45,1	42,1	-10,07	-8,57
Apr	24,2	19,7	4,7	4,0	44,3	39,8	-9,67	-7,42
May	21,9	17,1	4,7	4,0	42,0	37,2	-8,52	-6,12
Jun	20,1	15,2	5,0	4,0	41,5	36,6	-8,26	-5,81
Jul	20,2	15,1	5,0	4,0	41,6	36,5	-8,31	-5,76
Aug	22,5	16,3	5,0	4,0	43,9	37,7	-9,46	-6,36
Sep	23,2	17,4	6,8	5,9	52,3	46,5	-13,67	-10,77
Oct	24,8	19,2	6,8	5,9	53,9	48,3	-14,47	-11,67
Nov	25,4	20,7	6,8	5,9	54,5	49,8	-14,77	-12,42
Dec	25,0	21,7	6,0	5,6	50,7	47,4	-12,86	-11,21

The table shows the difference in power found for the modules installed in each of the regions (1 and 2), considering the temperature of the modules in each month, thus making it possible to calculate the total accumulated power deficit in the year. It is observed that both regions exceed 100% of the monthly power during the operation in one year. Thus, at least one month of photovoltaic generation each year.

It is verified that region 1 (city of Votuporanga-SP), presents a loss of 26.15% greater than region 2 (city of Itapeva-SP), in each year, observing that the average difference in temperatures monthly averages of the two regions was 4.36 °C per year.

Despite the better yield in region 2, we did not find in that same region a yield greater than 95% throughout the

year, which yields only the losses of exploitation due to the influence of temperature, without considering other losses and module yield in the conversion of solar energy into electrical energy. A comparative graph was made, showing the ratio of percentage utilization of solar irradiation considering the loss of income due to temperature and work for each month of the year (Graph 1). In the graph it is possible to clearly observe the difference in performance of the studied regions.

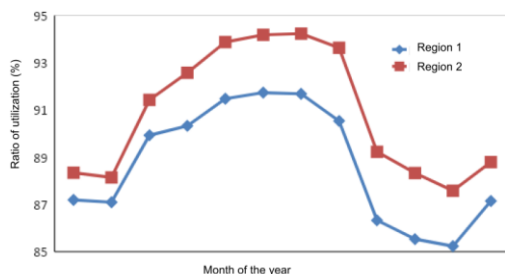


Figure 1 - Result of the study of the monthly solar power used.

#### 4. CONCLUSIONS

The comparative study between regions with different temperatures shows that this difference in ambient temperature has a strong influence on the working performance of the modules in photovoltaic generation, due to the direct influence on the module's operating temperature. Another important factor is the intensity of solar radiation present in the region, which will also influence the temperature of the module, in addition to being directly linked to the energy production capacity of the solar resource.

Regional temperature information is one of the important factors for strategic analysis of localities for the installation of photovoltaic plant plants, or even the importance of seeking solutions for a given location to minimize the loss of performance.

Greater knowledge of temperatures and incidence of solar energy in the national territory is important, with more measurement points and frequent records, thus providing a better mapping and data sharing.

#### ACKNOWLEDGMENT

Carlos Frajua acknowledges FAPESP for grant #2013/26258-4 and grant #2006/56041-3 and CNPq grant #309098/2017-3.

#### REFERENCES

- [1] PALZ, W. Energia solar e fontes alternativas. São Paulo: Hemus Editora Ltda., 1995. p.358
- [2] EPE, Empresa de Pesquisa Energética (Brasil). BEN – Balanço Energético Nacional 2018: Ano base 2017. Ministério de minas e energia. Rio de Janeiro: EPE, 2018. p 292
- [3] BORTOLI FS et al. On the Massive Antenna Suspension System in the Brazilian Gravitational Wave Detector SCHENBERG. Brazilian Journal of Physics; 2016; 46: 308. DOI: 10.1007/s13538-016-0413-8
- [4] ANDRADE LA et al. Ultra-low phase noise 10 GHz oscillator to pump the parametric transducers of the Mario Schenberg gravitational wave detector. Class. Quantum Grav; 2004; 21: 1215 DOI: 10.1088/0264-9381/21/5/122
- [5] BORTOLI FS et al. A physical criterion for validating the method used to design mechanical impedance matchers for Mario Schenberg's transducers. Journal of Physics: Conference Series 2010, 228, 012011. DOI: 10.1088/1742-6596/228/1/012011
- [6] ZAINI, N., et al. The effect of temperature on a mono-crystalline solar PV panel. Energy Conversion (CENCON), 2015 IEEE Conference on. IEEE, 2015. DOI: 10.1109/CENCON.2015.7409548
- [7] PINHO, JT, GALDINO, MA. Manual de Engenharia Para Sistemas Fotovoltaicos. Rio de Janeiro: Grupo de Trabalho de Energia Solar, GTES– CEPEL – DTE - CRESESB, Edição revisada e atualizada, Marco 2014. p 530
- [8] TOBNAGHI, DM, MADATOV, R, NADERI, D. The Effect of Temperature on Electrical Parameters of Solar Cells. IJAREEIE - International Journal of Advanced Research in Electrical, Electronics and Instrumentation Engineering 2013; 2: Issue 12:
- [9] INMET, Instituto Nacional de Meteorologia. Normais Climatológicas do Brasil, período 1982-2010. Brasília: INMET, 2018.
- [10] INPE, Instituto Nacional de Pesquisas Espaciais. Atlas brasileiro de energia solar. 2.ed. São José dos Campos: INPE, 2017.
- [11] IBGE, Instituto Brasileiro de Geografia e Estatística. Atlas geográfico escolar. 5. Ed. Rio de Janeiro: IBGE, 2009. p. 218
- [12] SAO PAULO (Estado). Energia solar paulista: levantamento do potencial. São Paulo: Secretaria de energia, 2013. p. 46



# ANALYSIS AND OPTIMIZATION OF HYBRID WIND AND SOLAR PV GENERATION SYSTEM FOR OFF-GRID SMALL VILLAGE

Nabaz Mohammedali Rasool

Cyprus International University, Nicosia, Mersin 10, Turkey, nabaz.mahamadd@gmail.com, ORCID: 0000-0003-1403-4079

Serkan Abbasoglu

Cyprus International University, Nicosia, Mersin 10, Turkey, sabbas@ciu.edu.tr, ORCID: 0000-0002-8010-9035

Mehrshad Radmehr Hashemipour

Cyprus International University, Nicosia, Mersin 10, Turkey, mradmehr@ciu.edu.tr, ORCID: 0000-0002-3822-5286

*Rasool, NM, Abbasoglu, S., Hashemipour, MR. Analysis and optimization of hybrid wind and solar PV generation system for off-grid small village. 9<sup>th</sup> Eur. Conf. Ren. Energy Sys. 21-23 April 2021, Istanbul, Turkey*

**Abstract:** As an effective means of providing power to remote and off-grid areas of developing countries, where rural electrification problems are most common, hybrid renewable energy systems are considered. HOMER simulated and configured wind turbine, photovoltaic, battery bank, and converter for the electricity demand of the Mander rural community, which has 37 families with household sizes of 7 members, as a remote village in Northern Iraq in this article. The hypothesis project was also evaluated using the parameters Net Present Value and Simple Payback Period. Daily energy consumption of 173,120kWh and peak electricity consumption of 32,14kW were measured for the outcome of the selected site. The proposed system produced 68,458 kWh/yr (13.7 percent) by the wind turbine, PV created 432,354 kWh/yr (86.3 percent), and 265 operating batteries with a total operating cost (TOC) and costs of energy (COE) of \$ 9,195 and 0.365 \$/kWh, respectively. This survey emphasized the role of solar photovoltaic and wind turbine as hybrid renewable energy systems HRESs in the sustainable supply of electricity in rural areas of northern Iraq.

**Keywords:** Hybrid power electric system, off-grid, renewable energy, remote area, load demand.

© 2021 Published by ECRES

## 1. INTRODUCTION

Throughout the previous decade, the OGPS (Off-Grid power systems) application vanished from exclusive RES (Renewable Energy System) had been growing, despite that, these resources are generally irregular [1, 2]. In either devolved or developing countries the arrangement of electrical systems is being achieved [3, 4]. It's far due to numerous factors, including the downward movement within the price of photovoltaic (PV), power systems of wind, and better storage, also micro-hydraulic and falling fees in power garage structures which includes batteries. Consequently, according to Kempener et al. [5] for the operation of those power systems of electricity in each residential and commercial operator, there's a promising horizon. Otherwise, in developing international locations there are more than one million people lacking access to this necessity power that is electricity power [5] its miles especially because of its far-flung geographical region. Consequently, as it has been mentioned above, this kind of O-GPS system will become a viable answer for offering the power of electricity in these remote areas that is problematic to get admission to the power grid.

In the northern Iraq district, as indicated by an examination [6], it was reasoned that power inclusion in rustic terrify. This study is completed ores is about 80%. As indicated by an investigation in 2014. As per a measurement government report in 2014, the age of power in the region district originating from gas and fuel assets [7]. Subsequently, provide green energy from renewable energy sources as clean energy, which include wind and solar power, for a remote area is the purpose of this study. The aim of a combined power generation of this study is to

provide continuous electricity during day and night time for small power programs with storage batteries. This could gain from solar and wind hybrid power systems (SWHES).

Hybrid power systems and frameworks, various power generators, and capacity parts are joined to fulfill the vital need of remote or provincial regions, or even an entire network. Notwithstanding photo voltage, wind, and diesel generators, little plants of hydro-power, and other wellsprings of electrical vitality could be added such as expected, to satisfy the vital need such that fits the nearby geology and different points of interest. This sort of vitality system and frameworks can tackle that issues that exist in the investigation zone that can be outlined as Oil and energy crisis in the site, contemplate; Customary power age will turn into a troublesome undertaking later on; expanding the creation of power likewise to satisfy the needs of developing populace; Toxins discharged from the traditional power age will influence nature, and the transmission generation will affect the environment, and The transmission power loss is additionally one explanation behind remote spots. By concentrating on what are the benefits of utilizing a hybrid renewable power system; how to plan diverse elective plans of the mixture vitality system? Also, contamination emanations of the system, particularly in far off.

As regards that wind and solar power are the maximum promising of the renewable power sources because of its obvious limitless ability especially for far off region. The circumstance of them emerges as exclusive from one region to any other want to be analyzed before set within the place. Thus, electricity planners have to observe the wind power, solar electricity, and other potential assets on the location of the site, similarly to the power request. The remainder of the paper is separated as pursues general data about the procedure for the demonstrated system and qualities of the chose area to study. At that point, there is another part that exhibits the system determination dependent on the computational apparatus used. After that reproduction results and exchanges are given. At last, the finishes of the present examination are displayed.

## **2. LITERATURE REVIEW**

Distinctive researches have been accomplished in solar and wind power generating technology. And the use of renewable electricity required system. The literature stands with the classification of the exceptional machine system alone as follows:

### **PV Array Modelling Solar**

PV generation is picking up an expanded significance as a sustainable power source because of its intrinsic favorable circumstances like nonattendance of fuel costs, fuel supply issue, and framework dependability with practically zero upkeep [7]. The radiation of electromagnetic of solar power can rightfully be changed into power by the impact of PV. A PV system is a connectivity of components according to the rate of equivalent of the solar panel which in opportunity is produced in either a parallel or series with a number of photovoltaic cells. The electricity generated from a lone or individual module is rarely sufficient for business usage, so that the units are connected to forming an array for weight.

The module relationship in a collection is the equal as that of the module cells [8]. The Photovoltaic panels are constructed with blended parallel or serial photovoltaic cell combinations that are commonly shown via a basic equal circuit version [8]. The Photovoltaic device simulation electricity generation model consists of different measures: radiation of Solar on the surface of the photovoltaic plate, Photovoltaic collection energy model, and Photovoltaic modules version for temperature. [9].

### **Wind turbine**

Wind power and energy are a critical part of the answer for international electricity demand and pollution troubles. With a median wind pace of 7.1m/Sec, annual wind electricity manufacturing is envisioned as nearly [10]. Wind turbines are utilized to produce electricity from wind power. In another word, providing electricity in wind turbine depending on the wind power. The generation by wind turbines relies upon the wind speed following and action upon the turbine. Wind turbines can be grouped regarding the physical highlights (measurements, axes, and the number of sharp edges), produced control, etc. Wind turbines concerning the hub structure: level rotor plane found turbines, turbines with vertical or flat turning bearings as for the wind. Turbines with cutting edge numbers: 3-blade, 2-blade, and 1-blade turbines [10].

### **Modeling of Hybrid Solar - Wind System**

Wind turbines, Photovoltaic cells, battery, controllers, inverters, and wires form part of a hybrid wind and solar system [11]. In order to satisfy load demands the PV panel and wind turbine operate together. At the point

when vitality sources (sunlight-based wind) are rich, the created influence of the sun-powered, in the daytime will keep on charging the battery bank till it is completely charged. Otherwise, when critical resources are low, the batteries discharges vitality in order to support the photovoltaic cluster and the wind turbine cover heap requires, before the capacity is exhausted [12].

The simulation of the hybrid wind and solar system primarily needs individual mechanisms to be presented. In order to predict the systemic presentation, energy sources should also be clearly designed in cooperation sources and combined to supply reliability [13]. The resulting mixture will successfully transmit control if the predictions of power generation from these individual sources are adequately correct [11]. In addition, a hybrid device might be built to be enabled through the electronic power boundary in disconnected or grid connected mode.

### 3. METHODOLOGY

The methodology of the research can be qualitative (simulation primarily based). The method of the related equations is the first step of the approach. Air temperature, radiation of solar, speed of the wind are used as inputs for the HOMER pro in the generation of wind energy, solar power and wind-solar hybrid generation. The perfect solar cell array and turbine systems are selected to provide the energy produced from such renewable assets. The next stage is to investigate the solar and wind power system combination depending on its output traits.

#### Location and population

For special regions and places, climatic conditions, along with solar irradiance, wind pace, temperature, and so forth, are constantly converting. Accordingly, there exist instability shortcomings for electric-powered power manufacturing from a wind turbine and photovoltaic modules. On the way to effectively and economically make use of renewable energy assets of wind and sun strength packages, the analyzing and foremost suit is very vital for solar-wind power technology systems with battery banks. The remote is the choice for this research is Mander village in Erbil governance, which's a small village in a high mountainous vicinity. According to the previous studies, the provinces with the Mander and some other villages are located under the lowest or non-power electricity coverage.

This study is accomplished in Mander, as it has been mentioned above, one of the sites under the non-coverage of the power of distribution of power delivery of the purpose region. Regarding to Geographical aspect, it's placed within the ( $36^{\circ}16'17.36$ ) latitude and ( $44^{\circ}32'48.32$ ) longitude. According to see level Mander is 401 meters above it. Regarding population and ratio of residence, it has a populace of around 37 houses with 222 people. The weather and climate condition are taken into consideration semi-arid, and there are four main seasons, wet and cold in winter and warm and dry in summer. As explained in Figure 1, the average temperature lays between 2 and 30 C in Figure 1b, radiation has been explain in Figure1c. Also, the average wind speed is between 4.250 and 8.280 m/2 figure1 (d) and it will be changed with height figure1 (e) also solar

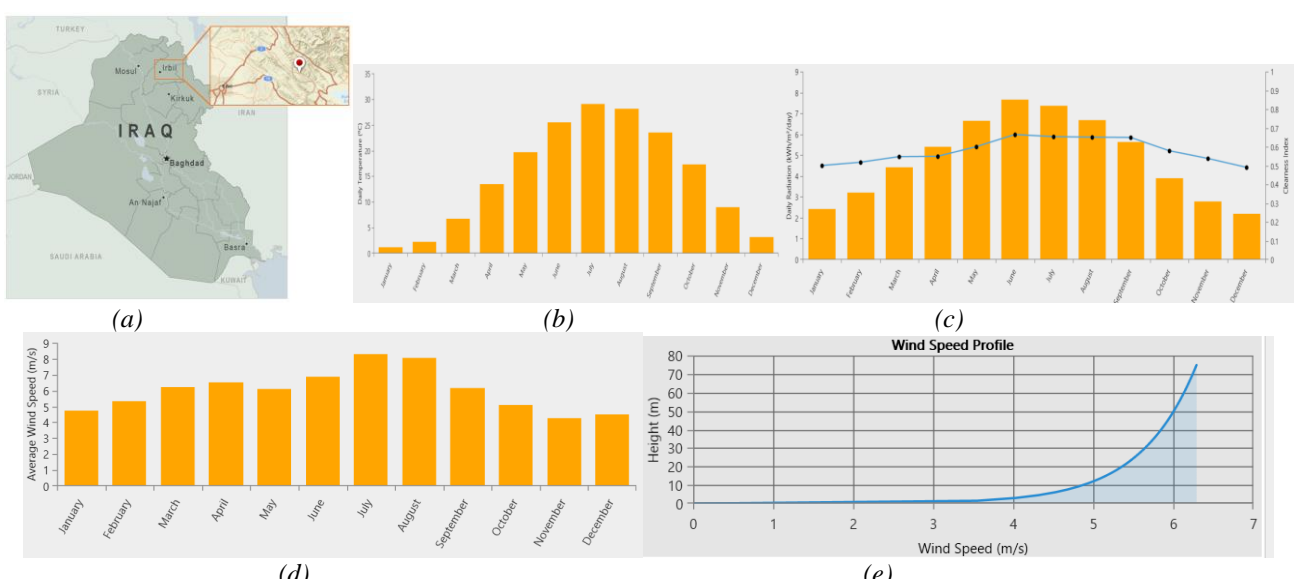


Figure 1. (a) Site study (b) The average temperature (c) Daily radiation (d) Monthly wind speed (e) wind speed with height.

### **Electricity load demand:**

The demand for electricity does not surpass urban areas in a far-off rural village. For two different seasons that they are summer (April to October) and winter (November to March), the application trends in appliances and the usage of energy in production applications have been analyzed separately.

In this research type, the power required estimation for the energy evaluation is a vital part of it. The estimation of demand for energy for one of a kind places, including Mander has been pointed out in previous research [14]. The electric load for all 37 families, which each of them composed of 7 members, in the study area is 173.12kWh is a total electricity consumption per day [14] as has been explained in Table 1. As the load factor in these places appears to be low, over the 24-hour cycle, some demand has been strategically allocated to increase the system load factor. The load of the village was split into two significant categories.

*Table1 The electric load in the Village*

Type	Appliances in Summer	Total Wh/day	Appliances in Winter	Total Wh/day	Annually kWh/day
Domestic (Wh/day/home)	CFL bulb (4* 20W* 9 h/day), TV (1* 120W* 7 h/day), Ceiling fan (3* 40W* 9 h/day)	2760	CFL bulb (12* 20W* 9 h/day), TV (7* 120W* 7 h/day), Ceiling fan (0* 40W* 9 h/day)	1800	
School	No. of homes(37)	102120	No. of homes(37)	66600	
Mosque	CFL bulb(3* 20W* 4 h/day), Ceiling fan (3* 40W*4 h/day), Computer (2* 300W* 2 h/day)	1920	CFL bulb(6* 20W* 4 h/day), Ceiling fan (0* 40W*4 h/day), Computer (2* 300W* 2 h/day)	1560	173.120
	CFL bulb (5* 20W), Ceiling fan (2* 40W)	620	CFL bulb (5* 20W), Ceiling fan (0* 40W)	300	

### **PV array model**

The ambient temperature degree is known and once the solar radiation on Photovoltaic panels, the electricity production of the photo voltage unit be able to be considered simply, and correctly. The description of fill variables can also be used to measure the maximum power generated from pv module by equation [15]. The use of HOMER as a program simulation in this research has been used to calculate and determined the maximum power output delivered by VP. Correspondingly, the Sharp NU-U245P1 PV Module's cost per watt peak was then considered to be \$2.5/Wp, including installation costs. The substitute cost for PV module is \$2.5/Wp and the lifespan of PV module is 25 years.

### **The electrical power generated by the wind turbine**

A generic 3 kW turbine, including tower and construction costs, was considered for the current study site at a cost of \$18,000, while the cost of replacing the generator is \$18,000, while the cost of maintaining the turbine is \$180,000 per year for 25 years lifetime.

### **Battery and Power converter**

The device proposed requires battery storage to supply the village with daily electricity. During the surplus generation, the battery bank should store energy and, if necessary and in the required time, supply the energy. For this analysis, generic 1kWh Lead Acid batteries have been selected. The nominal capacity is 12V and 83.4 Ah normal capacity with an estimated life of service of twelve-year expected. The battery cost estimates \$300 has been considered, while one unit costs \$300 and \$10 per year for replacement and operation, and maintenance. To connect the AC and the DC bus, it must be specified that the converter is included. For the converter, the cost of capital per kW is considered to be \$100, while the costs of the replacement shall be \$100 and maintenance and service shall be \$100.

### **Power from the hybrid**

The hybrid entire powers of this scheme, power of the hybrid is the entire generated-power with the aid of the HWSs, equal to the summation of photovoltaic-power which is the power-produced through the solar cells, and wind-power is the energy produced via the wind energy. HOMER calculate capital costs for each component to an annualized expense through a lifetime using the true discount rate.

## 4. RESULTS AND DISCUSSION

### Description of the System

Fundamentally, the proposed HES includes Solar cells, and wind turbine. There is many research in different locations international [15, 16] in which the use of the electrical generator is justified: as backup strength for the duration of height hours (peak hour); periods with few tiers of radiation of the sun and wind velocities; and to lessen the fee of electricity (COE) of the HES. However, in the referred to research, there's a fossil necessity on which products ecological and environmental influences because of the emissions of greenhouse gases. Even though from the stoichiometry factor of chemical, there's a low impact on emissions while an electric generator uses diesel as fuel and now not gas online [17, 18, 19, 20].

Figure 2 demonstrates the layout and design of HES simulation in Homer Pro software with explanation of AC and DC type for each production sources.

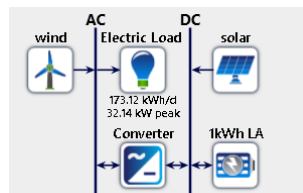


Figure 2. Use HOMER to plan and model a HRESs scheme

### Optimization system

HOMER conducts thousands of simulations repeatedly for optimal hybrid system design. The HOMER Pro program as a tool of simulation is used for the efficiency and sensitivity analysis of different groupings of power system of hybrid components. Different combinations of solar photovoltaic systems, wind turbines, batteries, and converters have been tested. Capital input sensitivity parameters were obtained based on component sizes, a total of 4809 possible device designs, and 1,143 simulations. HOMER uses the overall NPC as its principal system selection criterion. Table 2 offers the effects of categorized optimization and demonstrates the most efficient configuration for each type of system. Potential device settings are described in their overall NPC ascending order

Table2: Optimization results, in a three classification form of architecture, cost and system.

Architecture							Cost				System	
PV (kW)	wind	1kWh LA	Converter (kW)	Dispatch	COE (\$)	NPC (\$)	Operating cost (\$/yr)	Initial capital (\$)	Ren Frac (%)	Total Fuel (L/yr)		
273	13	265	33.7	CC	\$0.365	\$297,593	\$9,195	\$178,722	100	0		
378		284	53.5	CC	\$0.425	\$346,779	\$13,732	\$169,262	100	0		
111	921	62.7	CC		\$1.27	\$1.04M	\$32,613	\$615,571	100	0		

The optimal device type is the wind, PV, and battery system, according to the results of the simulation. The most viable hybrid device is composed of 265 batteries bank and a converter with 33.7 kW with 272kW PV modules and 13 wind turbines of 20 k W. In this circumstance, 100% of the renewable share is reached with a \$0.365/kWh of COE as shown in above Table that is the total optimization outcomes are presented. Initial capital investment of approximately \$178,722 is required for the project being studied, with a total NPC of \$297,593. The simple payback period is also 6.12 years.

Also, it can be seen that the individual solar cell system had also shown a 0.425 \$/kWh of COE of and an additional higher COE of 1.27 \$/kWh for the wind-alone system. From the current simulation study, it is apparent that a single, only PV or wind turbine based on the cost of renewable energy compared to the planned system of wind/PV/batteries is more expensive.

Table 3 shows that the COE (0.292 \$/kWh) of the optimized diesel hybrid system is less than 0,365 \$/kWh COE for the optimized hybrid power system for PV, Wind, and battery as stated before, according to the simulation results. It is true that the standalone hybrid electricity system proposed is significantly more costly than the hybrid and diesel generators system but the environmental perspectives are not effective as wind and PV systems.

Table3: Optimization results of hybrid and Diesel

Architecture							Cost				System		
PV (kW)	wind	Gen (kW)	1kWh LA	Converter (kW)	Dispatch	COE (\$)	NPC (\$)	Operating cost (\$/yr)	Initial capital (\$)	Ren Frac (%)	Total Fuel (L/yr)		
74.7	10	36.0	124	15.4	LF	\$0.292	\$238,330	\$10,522	\$102,313	85.7	3,221		

## Electricity production

Figure 4 displays descriptions of wind turbine-produced energy and solar photovoltaic for that system. It is clear here that the PV produces the maximum capacity. The wind turbine provided 68,458 kWh/yr (13.7 percent), the PV array created 432,354 kWh/yr of the village's total primary power needs (86.3 percent). A green hybrid energy system also benefits from replacing nonrenewable sources with renewable energy sources, which decreases the amount of GHG added to the local environment.

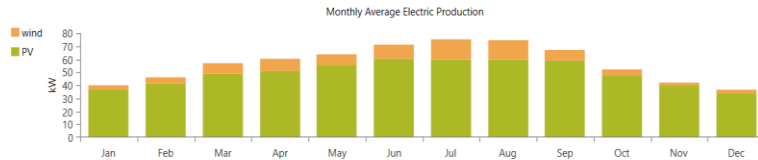


Figure 3. Power generation by PV and Wind turbine in HWS system.

## 5. CONCLUSION

Homer Pro in hybrid power system dimensioning and optimization method was used to identify the likely hybrid formations and their explanations. In the present situation, individual source of RES cannot provide full and economically will be unsustainable loads. Therefore, the most feasible alternative has been a HRE with a solar cell, wind turbine, and battery bank. This configuration comfortably satisfies the energy requirements of the considered population. The hybrid power system proposed included a 13 kW- wind turbine, 273 kW-PV panels, a 265-battery bench, and a 33.7 kW converter. There were 297, 5 93 dollars in NPC, \$0.365 per KWh in COE, and 6.12 years in the SPP. A renewable energy fraction of 100 percent could be reached by the proposed hybrid method. The proposed system would minimize greenhouse emissions by (100 percent) per year in the local environment by all these benefits if introduced. The proposed Mander hybrid system can be used for electrification with similar conditions in whichever remote rural of northern Iraq. As a movement of the steady oil price increase and a decline in capital and renewable system operating and sustaining costs, renewable energy systems are recommended to partly meet the load requirements in some areas.

## REFERENCES

- [1] Mandelli S, Barbieri J, Mereu R, Colombo E. Off-grid systems for rural electrification in developing countries: Definitions, classification and a comprehensive literature review. *Renewable and Sustainable Energy Reviews* 2016; 1;58: 1621-46 <https://ideas.repec.org/a/eee/reuns/v58y2016icp1621-1646.html>
- [2] Kumar NM, Chopra SS, Chand AA, Elavarasan RM, Shafiullah GM. Hybrid renewable energy microgrid for a residential community: A techno-economic and environmental perspective in the context of the SDG7. *Sustainability*. 2020; 12:10: 39-44<file:///C:/Users/Nabaz/Downloads/sustainability-12-03944-v2%20(1).pdf>
- [3] Mozafari SB. Design and simulation of a hybrid micro-grid for Bisheh village. *International Journal of Renewable Energy Research (IJRER)* 2016; 27;6(1):199-211.<<https://www.ijrer.com/index.php/ijrer/article/view/3328>>
- [4] Mamaghani AH, Escandon SA, Najafi B, Shirazi A, Rinaldi F. Techno-economic feasibility of photovoltaic, wind, diesel and hybrid electrification systems for off-grid rural electrification in Colombia. *Renewable Energy* 2016; 1;97:293-305. <<https://www.sciencedirect.com/science/article/pii/S0960148116304967>>
- [5] Kempener R, Lavagne O, Saygin D, Skeer J, Vinci S, Gielen D. Off-grid renewable energy systems: status and methodological issues. The International Renewable Energy Agency (IRENA) 2015.
- [6] Chilán JC, Torres SG, Machuca BI, Cordova AJ, Pérez CA, Gamez MR. Social impact of renewable energy sources in the province of Loja. *International journal of physical sciences and engineering*. 2018; 1:13-25<file:///C:/Users/Nabaz/Downloads/SocialImpactofRenewableEnergySources.pdf>
- [7] Siah S, Loka P, Polsani K, Reddy S, Skumanich A. The expansion opportunity for off-grid PV to go mainstream: Multiple case studies for village electrification and telecom power-up in India. In 2014 IEEE 40th Photovoltaic Specialist Conference (PVSC) 2014 Jun 8 pp. 2765-2766. IEEE.
- [8] Pradhan R. Development of new parameter extraction schemes and maximum power point controllers for photovoltaic power systems. PhD. National Institute of Technology Rourkela, Rourkela, India, 2014.
- [9] Ajao KR, Oladosu OA, Popoola OT. Using HOMER power optimization software for cost benefit analysis of hybrid-solar power generation relative to utility cost in Nigeria. *International Journal of Research and Reviews in Applied Sciences* 2011; 7:7(1):96-102. <<https://www.ajol.info/index.php/jast/article/view/64779>>
- [10] Zhou W. Simulation and optimum design of hybrid solar-wind and solar-wind-diesel power generation systems . PhD. Hong Kong Polytechnic University, Hong Kong, Chinese 2008.
- [11] Zhou W, Yang H, Fang Z. A novel model for photovoltaic array performance prediction. *Applied energy*. 2007; 1:84(12):1187-98.<<https://www.sciencedirect.com/science/article/pii/S0306261907000700>>

- [12] Halasa G. Wind-solar hybrid electrical power generation in Jordan JJMIE. 2010; 4(1):205-9.<  
<http://jjmie.hu.edu.jo/files/v4n1%20wrong%20header/27.pdf>>
- [13] Huang Z, Yu H, Peng Z, Zhao M. Methods and tools for community energy planning: A review. Renewable and sustainable energy reviews. 2015; 142:1335-48.<  
<https://www.sciencedirect.com/science/article/abs/pii/S1364032114009733>>
- [14] KRGMOE (2018) "Power system information". Accessed on 10 April 2019 from <http://moel.gov.krd/Paikar-EN.aspx>.
- [15] Srivastava R, Giri VK. Optimization of hybrid renewable resources using HOMER. International Journal of Renewable Energy Research (IJRER) 2016; 27;6(1):157-63<<https://www.ijrer-net.ijrer.org/index.php/ijrer/article/view/3275>>
- [16] Bekele G, Tadesse G. Feasibility study of small Hydro/PV/Wind hybrid system for off-grid rural electrification in Ethiopia. Applied Energy. 2012; 1-97:5-15<<https://www.sciencedirect.com/science/article/abs/pii/S0306261911007653>>
- [17] Barzola J. Es posible la Grid Parity en Ecuador?. Rev. Tecnológica ESPOL-RTE. 2014; 27, 1:30-9<  
<http://www.rte.espol.edu.ec/index.php/tecnologica/article/view/258/202>>
- [18] Barzola J, Espinoza M, Pavón C, Cabrera F. Solar-Wind Renewable Energy System for Off-Grid Rural Electrification in Ecuador. In 14th Latin American and Caribbean Conference for Engineering and Technology, San Juan 2016. pp. 20-22.
- [19] Barzola J, Pavón C. Estimación anual de la emisión de CO<sub>2</sub> asociada a la transportación de los docentes de la ULVR 2014; 2: 13-19 <  
[https://www.researchgate.net/publication/274899538\\_Estimacion\\_anual\\_de\\_la\\_emision\\_de\\_CO2\\_asociada\\_a\\_la\\_transportacion\\_de\\_los\\_docentes\\_de\\_la\\_ULVR](https://www.researchgate.net/publication/274899538_Estimacion_anual_de_la_emision_de_CO2_asociada_a_la_transportacion_de_los_docentes_de_la_ULVR)>
- [20] Morgan TR, Marshall RH, Brinkworth BJ. 'ARES'—A refined simulation program for the sizing and optimisation of autonomous hybrid energy systems Solar energy 1997; 1: 59: 4-6: 205-15<  
<https://www.tandfonline.com/doi/full/10.1080/23311916.2016.1189305>>



# THE POSSIBILITY OF INTEGRATING ELECTRICITY THROUGH RENEWABLE SOURCES IN SAZANI ISLAND

Driada Mitrushi

Faculty of Engineering Mathematics and Engineering Physics, Polytechnic University of Tirana, Tirana, Albania,  
driadamitrusshi@yahoo.com, ORCID: 0000-0001-8722-4231

Urim Buzra

Faculty of Engineering Mathematics and Engineering Physics, Polytechnic University of Tirana, Tirana, Albania,  
rimibuzra@yahoo.com, ORCID: 0000-0002-9240-8825

Daniela Topciu

Physics Department, Faculty of Natural Sciences "Aleksandër Xhuvani" University of Elbasan, Elbasan Albania,  
topciudaniela@yahoo.com, ORCID: 0000-0002-5740-8993

Eduart Serdari

University of Vlora, Department of Engineering and Maritime Technology, Vlore, Albania, eduartserdari@ymail.com  
ORCID: 0000-0001-7784-7398

Valbona Muda

Faculty of Engineering Mathematics and Engineering Physics, Polytechnic University of Tirana, Tirana, Albania,  
valbona\_muda@hotmail.com, ORCID: 0000-0001-7535-4856

*Mitrushi D., Buzra U., Topciu D., Serdari E., Muda V. The possibility of integrating electricity through renewable sources in Sazani island. 9th Eur. Conf. Ren. Energy Sys. 21-23 April 2021, Istanbul, Turkey*

**Abstract:** The purpose of this study is to integrate renewable energies for the electrification of an insular small area, Sazani island, in complete lack of electricity. Sazani Island in south-west of Albania (40.502, 19.282), has been a former military base and has been isolated and unreachable for many decades. In the absence of electricity from conventional sources the possibility of integrating renewable sources is very promising due to favorable climatic conditions and the tourism development of the island will be easier and applicable in the future scenarios. Wind velocity hourly data (1981-2014) are adopted from Balkan Wind Atlas and solar data from PVGIS-SARAH solar radiation database. Pallabazter model was used for wind energy output. Wind and solar shows a good complementary in seasonally basis. The levels of penetration of renewables will be discussed economically, the cost kw / euro are calculated for wind 0.039 eur/ kWh to 0037eur/ kWh. and solar 0.064 eur/ kWh respectively.

**Keywords:** Small island, lack of electricity, wind and solar complementary

© 2021 Published by ECRES

## 1. INTRODUCTION

The largest island outside Albania, with a total area of 5.7 km<sup>2</sup>, lies strategically between the Adriatic and Ionian seas, between the territorial waters of Albania and Italy. The island has long served as a military base. In 1975 the island was like a small republic. There lived an army of about 1500-2000 active soldiers and officers, equipped with heavy artillery shells, around the island sheltered in bunkers, with anti-aircraft artillery, navy, artillery, artillery, liaison, points signaling and other specialties. About 200 military families lived on the island. At that time the island was powered by a tunneled diesel-generating plant, three 250 kV, working in parallel. Also in the tunnel was the 04/6 kV transformer [1]. From there with the 6 kv airline the whole island was powered through five 6/04 kV cabins. The island was a remote area, totally isolated, and the problem was to reconstruct the entire distribution

network. . All airlines were removed because first, the strong winds on the island always caused malfunctions and power outages, but they had to be masked as well. They were replaced with 6kv land-based cable lines in 1-1.5m deep ditches open with soldiers under the technical guidance of electrical specialists of the military construction company. A major problem remained the high consumption of fuels and lubricants as well as their transportation to the island which cost the economy a great deal. Only one diesel generator consumed at that time 60 liters of diesel per hour. This fact severely limited the working hours on Sundays, including the part-time lighting of the island, 4 hours in the morning and 4-5 hours in the daytime. The shortage of 24 hours of energy caused problems for the military readiness and livelihood of the island in 1981 the island was electrified by underwater cables through a very bold project that was successfully implemented. This project actually had no life expectancy in fact at that time. After 1991 the population decreased until all the families moved to the part of the continent. The island has a very limited number of inhabitants in the military base. Today the demand to visit this island is great but it actually offers nothing but a short visit to see a very attractive island. The main problem is electricity, the demand for electricity is expected to increase continuously, and significant increases can be attributed to rapid growth of tourist development in the area. In 2015 the government for the first time briefly allowed cruise ships from the Gulf of Vlora to stop in Sazan and people could watch the hidden island and swim from its beaches. In 2016 the island was closed again from the government, but in April 2017, after the Ministry of Defense, Economy and Tourism reached an agreement, decided to reopen the island for tourist purposes from May to October. [2] Energy is the main factor of investments and tourism development of the island. In this contest will be necessary for development of sustainable strategies. The access to sustainable energy service for the area it will derive on the infrastructure of the islands.

## 2. METHODOLOGY

The purpose of wind and solar measurement in the islands was for weather forecasting in military station and therefore not a reliable one to consider it for energy studies. In this study a wind speed data measured long-term wind speed data (of the period 1981–2014) based on Balkan Wind Atlas of Sazani Island has been considered and analyzed to evaluate the potential of wind energy [3]. There is a complete lack of data on electricity consumption during the summer by tourists on the island, in recent years, and also lack of data on energy consumption in military systems throughout the year, and for the summer period during the management of simple tourist systems. The use of electricity within the necessity and in the absence of infrastructure for each period of the year on the island is intensified between the months of May-October, legally allowed to enter the area and especially frequented in June-August. In this time interval we have examined the wind potential and the potential of solar energy to reach the conclusion which of the sources is the most cost-effective. Wind speed data are for a period of 33 years based on the Balkan Wind Atlas. Long-term use of the analyzed data ensures that the evaluation of wind energy potential is within the accuracy criteria. From the data for wind speed is estimated an average variable between 5.63 to 6.94 m / s, at an altitude of 50 m [4].

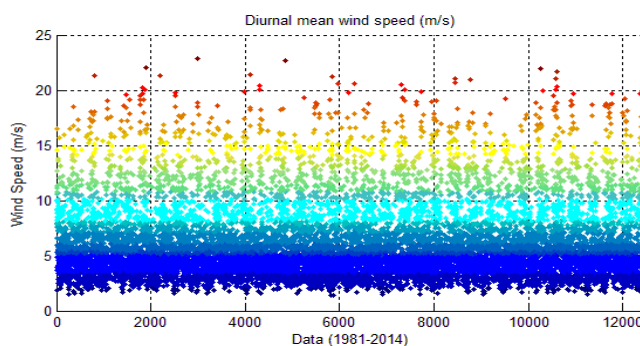


Figure 1. Thirty-four year daily mean wind speeds at height 50 m over the ground in Sazani Island.

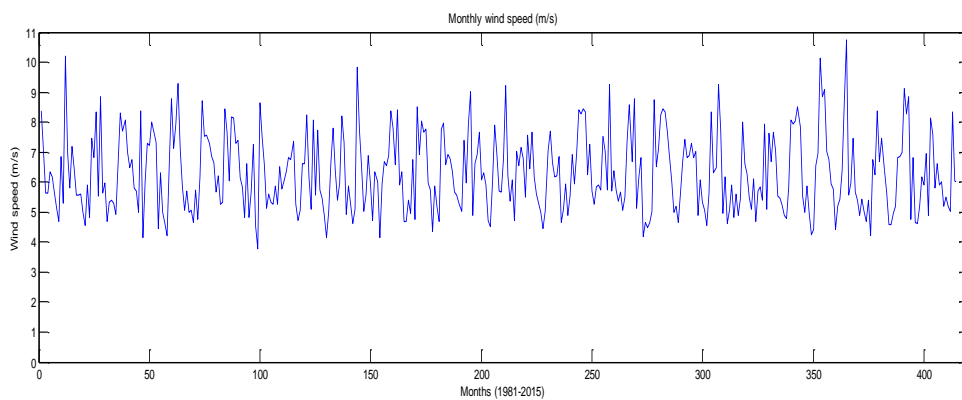


Figure 2. Variation of monthly mean wind speeds at height 50 m over the ground in Sazani Island.

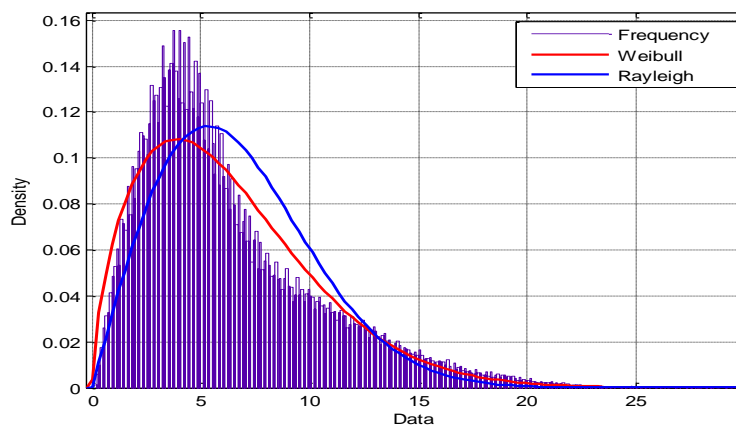


Figure 3. Probability density function

Weibull scale ( $c$  m/s) and shape ( $k$ ) parameters respectively 7.0734 m/s and 1.6221 for 34-years data for wind speed. Mean wind speed, predicted by Weibull and Rayleigh distribution 6.3341 m/s and 4.7201 m/s. Weibull statistical distribution from the measurements predict the mean wind speed profiles of the station quite adequately [5].

Table 1: Characteristics of wind turbine models, and energy output per year from measurements

Wind Turbine Model	Cutt in/ off (m/s)	Rotor diameter (m)	Hub Heights (m)	Power (kW)	Capacity Factor	Energy Output kWh/m <sup>2</sup> / year	Energy Output kWh/ year
Vestas V27	3.5-25	31.5	standart	225	24	824	471788
Vestas V 29	3.5-25	31	Standart	225	26	780	515320
Nordex N 29	4-25	50	50	250	27	894	590592
Wind World 29.2	3.5-25	41	41.5	250	24	789	528323

For the annual energy output, the chosen wind turbine capacity factor, defined by the ratio of the actual power generated to the rated power output. Cost of the project including initial costs such as transportation, installation, grid integration, are 35% of turbine cost. Fixed Operation and Maintenance costs are assumed 50eur/kW/year. Lifetime of the system will be 20 years. Annual operation and maintenance costs plus the land rent come to 5% of the turbine cost. Cost of a construction project is around (higher than in non isolated areas 1800eur/kW). The economic analysis scenario gives LCOE ranging from 0.039 eur / kWh to 0037eur/ kWh.

#### Solar Energy Potential in Island

Grounds measurements high accuracy is related with high quality sensors that should be calibrated, cleaned regularly, and the data should be available as long as 10 years. There are no meteorological stations installed in island for the purpose of accurate and reliable measurements, especially for calculating the energy obtained from these sources. The number of ground-based radiation measurements that fulfill all these criteria is relatively low in Albania and the stations are often for meteorological purposes [6]. This study use solar radiation database PVGIS-SARAH covering from 2005-2016, the data set has a high temporal (hourly, daily and monthly means)

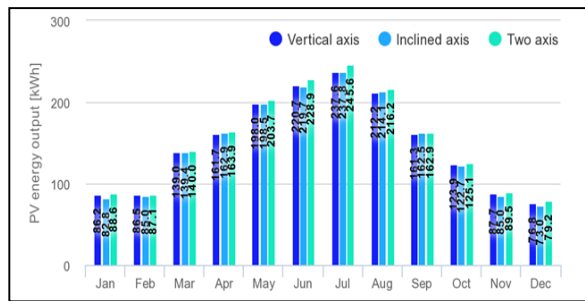


Figure 4. Monthly energy output for tracking PV system.

The calculation of the cost of electricity produced by a grid-connected PV system, and a off grid system is performed. The calculation takes into account the cost of buying and installing the PV system, the cost of maintenance, and the cost of financing. All these costs are then compared with the estimated PV energy production during the expected lifetime of the system. The calculation of PV electricity cost is done using a "Levelized Cost Of Energy" (LCOE) method [7]. In this calculation an initial loan is used to pay the whole cost of the PV system and is repaid in fixed yearly installments until the end of the lifetime of the system. For the self-repayment period in years some parameters are important, the price of electricity in the network, the investment of the systems and the predicted life of the system. For the PV system we have assumed: 97.5% inverter efficiency, 5.5% DC loss, 1.5% AC loss and 99% availability. Return on investment would vary for different clients, there is also a difference based on location, investment cost, cost of capital and electricity tariff, annual percentage of O&M maintenance and services, cost of capital 3% discount rate 5 % and annual degradation of PV production 0.5% per year. LCOE calculated is 0.064 eur/ kWh

#### Wind and Solar Complementarities

As it is suggested the most promising and most feasible application for insular areas are solar-wind hybrid systems applications. Complementary of these sources can bring a reliable system with a significant economical efficiency that is strongly dependent to the variability of the wind and solar resources. The problem that can cause the overcome of the two sources of energy can be reduced by integration optimally combination during periods of time. From the measurements more solar radiation is available during summer period and wind is significant during winter period as it is shown in the Figure 5.

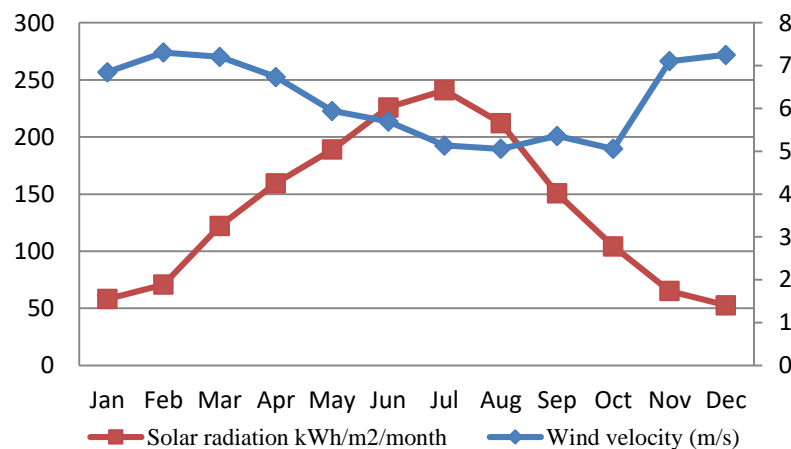


Figure 5. Annual cycle of monthly mean wind speed and solar irradiance

In the figure is presented wind and solar energy during a period of a typical year.

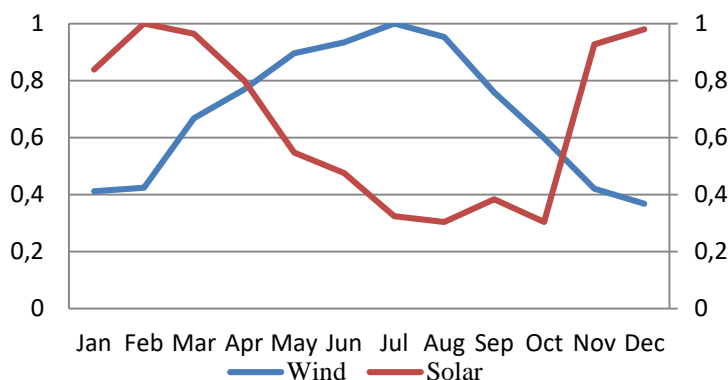


Figure 6. Energetic availabilities (solar and wind) for a typical year.

The operating thresholds for wind turbines do not vary with season, it is important to determine the wind velocity thresholds during the seasons to define “low” and “high” wind speeds using all data in the year. But it is important to note that, as seen in Figure 5, there are very few high-windy days in the summer. Similarly, the winter high-winds correspond to summer low winds that can conclude in good proportion of the available windy days, or sunny days. In reality without a real scenario it is not possible to compare strictly the outputs from wind turbine and PV systems in different season. The aim is to present the situation of energy resources on the island and to be sure that the only reliable option is the integration of wind and solar resources

## CONCLUSIONS

The possibility of integrating renewable energies in an island area, Sazani Island was discussed. The island is in complete lack of energy. Due to the distance and high cost of interconnection from the ground, renewable resources should be developed on the island. The wind potential on the island is good and considerable especially during the winter season. For the summer season where the number of tourists on the island has increased a lot in recent years, the potential of solar energy can be useful. LCOE for wind energy varies from ranging from 0.039 eur / kWh to 0037eur/ kWh. For solar energy LCOE is LCOE calculated is 0.064 eur/ kWh. Otherwise, in the scenarios of development for the island, the possibility of overlapping resources can be seen. In fact, for the complementarity of the sun and wind as well as the energy storage system would be an optimal solution.

## REFERENCES

- [1] Vives P. T.. Management Plan for Sazani Island, Albania. Pere TOMÀS-VIVES. UNDP. January 2015
- [2] Binet A.T, Ambre Diazabakana, Keurmeur N. Economic valuation of the Karaburun-Sazan Marine and Coastal Protected. UNDP September 2016
- [3] Serdari E., Berberi P., Puci I., Halili M. Potential estimation and ghg reduction of a wind power system in albanian south coast, Conf. Proc. ICE 2015, ISBN: 978-9928-4248-4-6, 622-627. 2015
- [4] Serdari E. , Berberi P., Mico S., Hasanaj A., Puci I. Wind profile characteristics and energy potential analysis in Tirana, Albania, AIP Conf. Proc. 1722, 280007, <http://dx.doi.org/10.1063/1.4944286>. 2016
- [5] Serdari E, Berberi P, Muda V, Buzra U, Mitrushi D, Halili D, Bërdufi I. A Methodology for Optimal Selection of a Wind Power Conversation System Based on Economic Analysis. Journal of Multidisciplinary Engineering Science and Technology. (JMEST) ISSN: 2458-9403.Vol. 4 Issue 3, March -2017
- [6] Mitrushi D ,Serdari E, Berberi P, Bërdufi I, Muda V, Topçiu D. Feasibility study of impact of wind energy potential in Karaburun’s area in Albania. AIP Conference Proceedings DOI: 10.1063/1.5099034. 2019
- [7 ] Pawel I. The cost of storage - how to calculate the levelized cost of stored energy (LCOE) and applications to renewable energy generation. Energy Procedia 46 ( 2014 ) 68 – 77



# ADVANCED EXERGOECONOMIC EVALUATION OF A COGENERATION SYSTEM COMBINED WITH A DRYING UNIT OF FERTILIZERS

Asmae Echeeri

Laboratory of Applied Geophysics, Geotechnics, Engineering, Geology and Environment, Mohammadia School of Engineers, Mohammed V University in Rabat, Rabat, Morocco, asmae.echeeri@gmail.com, ORCID: 0000-0001-7231-5667

Mostafa Maalmi

Department of Process Engineering, Higher National School of Mines of Rabat, Rabat, Morocco,  
Laboratory of Applied Geophysics, Geotechnics, Engineering, Geology and Environment, Mohammadia School of Engineers, Mohammed V University in Rabat, Rabat, Morocco, maalmi.mostafa@gmail.com, ORCID: 0000-0003-4913-1047

Cite this paper as:

Asmae, E., Mostafa, M. Advanced exergoeconomic evaluation of a cogeneration system combined with a drying unit offertilizers. 9<sup>th</sup> Eur. Conf. Ren. Energy Sys. 21-23 April 2021, Istanbul, Turkey.

---

**Abstract:**

The present work analyses a cogeneration plant combined with a rotary drying unit of fertilizers exergoeconomically using exergy notions and economics. The objective is to give an idea about the system's components from the costing perspective. Results show that the rotary dryer has the largest value of the total cost rate related to investment and exergy destruction (1657,54 \$/h) followed by the combustion chamber (1437,55 \$/h), the gas turbine (412,73\$/h) and the air compressor (176,29 \$/h). Hence, the rotary dryer and the combustion chamber must be given priority of improvement. The advanced exergoeconomic analysis confirms the results obtained by the conventional exergoeconomic analysis. The detailed splitting of the investment costs of each component of the unit shows that the endogenous investment cost for all components is higher than the exogenous one. Furthermore, for all elements, the avoidable endogenous investment cost is the highest.

---

**Keywords:**

Exergoeconomics, Advanced exergoeconomic analysis, Rotary drying, Cogeneration.

© 2021 Published by ECRES

---

**Nomenclature**

Ex	Exergy rate
C	Cost rate related to exergy
cu	Unit exergy cost
Z	Total cost rate related to investment expenditures
CRF	Capital investement revoverey factor
PEC	Purchased equipment cost
t	Time of work
i	Interest on capital
r	Relative cost difference
f	Factor of exergoeconomy
ε	Exergy efficiency
ϕ	Factor of maintenance and operating cost
ACR	Air compressor
CCR	Combustion chamber
GTE	Gas turbine
RDR	Rotary dryer
Exo	Exogenous
End	Endogenous
Avo	Avoidable

Una	Unavoidable
j	jth-component
F	Fuel
P	Product
D	Destruction

## 1. INTRODUCTION

The drying method necessitates a large amount of energy resources in order to provide enough energy to meet the drying target. Since energy conversion is irreversible, energy is lost as a result of this method. Therefore, determining the location and the amount of the lost energy in the overall system is essential. The main target of drying is to achieve the desired final moisture content of the product with minimal operational costs. As a result, economic research should be carried out. Exergoeconomic analyses is an approach that gives engineers valuable knowledge on how to design and operate a cost-effective system. [1]. Exergoeconomics evaluates the component's thermodynamic behavior using exergy analysis and economic concepts. The literature [2-12] presents a number of methodologies for exergoeconomics study of energy conversion systems and cogeneration plants. Tsatsaronis and Pisa [13] compared the efficiency of a regenerative gas turbine system with that of a conventional gas turbine system. Rosen and Dincer [14] assessed the exergoeconomics of different types of power plants. Kwon et al. [15] used the exergoeconomics to test the efficiency of a gas turbine cogeneration plant. The exergoeconomics of a cogeneration plant in an iron and steel factory were proposed by Mert et al. [16]. Sahoo [17] proposed an optimization for a cogeneration system using exergoeconomic principles. Li et al. [18] assessed an analysis of an industrial corn drying system using exergoeconomics. To gain a deeper understanding of the interactions between different components of the system, another concept can be introduced called the advanced exergoeconomic analysis. In this context, Tsatsaronis and Morosuk [19] analyzed the values of the investment and exergy costs using advanced exergoeconomic methods for a compression refrigeration machines components. In another work [20], authors dealed with integrated advanced exergy based evaluations. Although several works dealing with exergoeconomics in energy conversion systems have been published, few articles have been reported on the application of this concept to drying systems [18, 21-24]. As we are aware, there is no publications that have dealed with an exergoeconomic analysis of a rotary drying unit of fertilizers combined with a cogeneration system. The present work brings this novelty if the field. It carries out an exergoeconomic analysis of a rotary drying unit of fertilizers combined with a cogeneration system to determine the component's and to give an idea about the system's components from the costing perspective.

## 2. PLANT DESCRIPTION

A schematic of a cogeneration system combined with a drying unit of fertilizers is presented in the figure below. The system consists of an air compressor, a combustion chamber, a mixer, a gas turbine and a rotary dryer. The unit dries the fertilizers to a desired water content (3%). The hot gases for drying comes from the 6.75 MW gas turbine unit that covers the thermal and electrical needs of the drying unit. At the outlet of the rotary dryer, the gases charged with water vapor and dust are treated at a dust removing level. The gases removed are discharged by a fan.

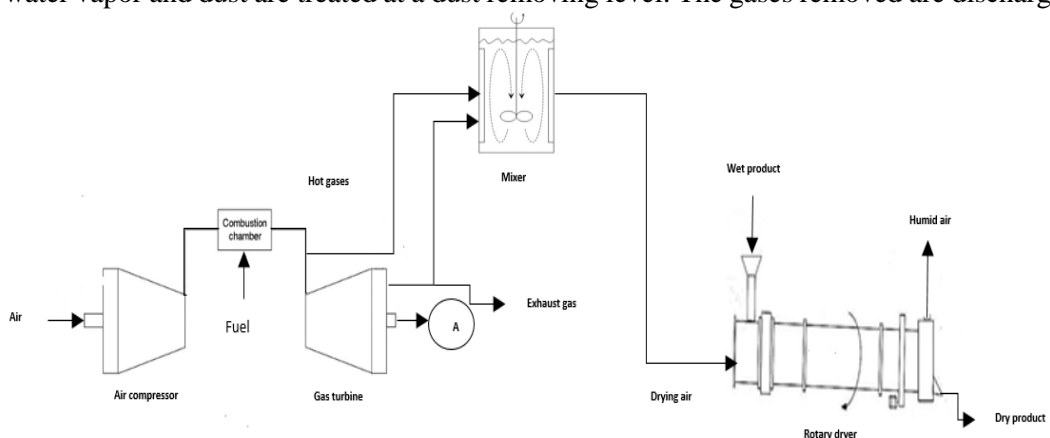


Figure 1. Simplified schema of the cogeneration system combined with the drying unit of fertilizers

### 3. METHODOLOGY

#### Exergoeconomic Analysis of the System

Exergoeconomics combine exergy analysis with economic aspects. It's the rational way to assign a monetary value to energy transport and thermodynamic inefficiencies, and it is focused on the exergy costing theory [25]. It is carried out at the component level of the system and determines the relative value in terms of cost. The exergoeconomic model is based on:

-Costs balances written for every system components: At steady state conditions, it is defined as:

$$cu_{p,j} * Ex_{p,j} = cu_{F,j} * Ex_{F,j} + Z_j \quad (1)$$

Where  $c_{p,j}$  and  $c_{F,j}$  are the unit exergy costs associated with product and fuel, respectively,  $E_{p,j}$  and  $E_{F,j}$  are the exergy rates and  $Z_k$  is the cost related to investment of expenditure of the component. It is defined by [24]:

$$Z_j = \frac{CRF}{t} * PEC * (1 + \varphi) \quad (2)$$

$$CRF = \frac{i*(1+i)^n}{(1+i)^n - 1} \quad (3)$$

Where CRF, PEC, t,  $\varphi$  represent the capital recovery factor, the purchased equipment cost, the time of work, the factor of the operating and maintenance cost and the interest on capital. The methodology for calculating the purchased equipment cost is presented in details elsewhere [1].

-Auxiliary costing equations as they are described in [1, 26-29].

The table below presents the conventional exergoeconomic model for every system's component under study:

*Table 1. Exergoeconomic model computed for the unit's components*

Component	Cost balance	Auxiliary equation
ACR	$cu_w * W_{ACR} + Z_{ACR} = cu_2 * Ex_2 - cu_1 * Ex_1$	$cu_1 = 0$
CCR	$cu_3 * Ex_3 + Z_{CCR} = cu_4 * Ex_4 - cu_2 * Ex_2$	$cu_3 = 16,45 \text{ \$/MWh}$
GTE	$cu_4 * Ex_4 - cu_5 * Ex_5 + Z_{GT} = cu_w * W_{GTE}$	$cu_4 = cu_5$
RDR	$cu_5 * Ex_5 + cu_7 * Ex_7 + Z_{RDR} = cu_6 * Ex_6 + cu_8 * Ex_8$	$cu_5 = cu_6$ $cu_7 = 0$

To analyze the unit's components exergoeconomically, other parameters are used namely:

-The exergy efficiency: is the ratio between the product exergy rate and the fuel exergy rate

$$\varepsilon_j = \frac{Ex_{p,j}}{Ex_{F,j}} \quad (4)$$

-The cost rate related to exergy destruction: displays the amount of exergy consumed during the process:

$$C_{D,j} = cu_{F,j} * Ex_{D,j} \quad (5)$$

-The relative cost difference: defined as:

$$r_j = \frac{cu_{p,j} - cu_{F,j}}{cu_{F,j}} \quad (6)$$

The factor of exergoeconomy: provides an estimate significance of the other costs than those related to the exergy destruction in comparison to the total costs of each component:

$$f_j = \frac{Z_j}{Z_j + C_{D,j}} \quad (7)$$

### Advanced Exergoeconomic Analysis of the System

It consists mainly on splitting the expenses of the investment and the exergy destruction into endogenous and exogenous and avoidable and unavoidable parts. This approach provides an excellent understanding of the relationships between the system's components, as well as the real potential for improvements and permits an improvement in the quality of conclusions based on the exergoeconomic evaluation. The cost interdependencies among the system's components are demonstrated by dividing the capital investment cost into endogenous and exogenous parts. The endogenous capital investment cost is considered when the component works in real conditions and the others components operate ideally. The exogenous part is determined as:

$$Z_j^{Exo} = Z_j - Z_j^{End} \quad (8)$$

To determine the potential of improvement in every system's components, the capital investment should be divided into avoidable and unavoidable parts. By assuming an inefficient version of a component, the component's unavoidable investment cost can be calculated [19]. The unavoidable unit exergy cost of the product  $(\frac{Z_j}{E_{p,j}})^{Una}$  should be calculated [30, 31]. The avoidable investment cost is calculated as:

$$Z_j^{Avo} = Z_j - Z_j^{Una} \quad (9)$$

The combination of the two splitting approaches permits the calculation of the avoidable endogenous investment cost (AvoEndInvC)  $Z_j^{End,Avo}$  and the cost of the avoidable endogenous exergy destruction  $C_{D,j}^{End,Avo}$ .

## 4. RESULTS AND DISCUSSIONS

The exergoeconomic analysis of the unit under study is assessed using a conventional and an advanced exergy analysis, an economic analysis and an evaluation of the results at the component level. The exergy analysis of the system's components is conducted on the basis of the methodology defined by A.Bejan [1]. It should be noted that the operating parameters of the mixer, the dust removing system and the fan will not interfere in the calculations that follow, which allows omitting the analyses in this component. The methodology presented by A.Bejan [1] is applied for the economic analysis. Furthermore, the capital investment cost is calculated for the year 2020 using cost indices. The conventional exergoeconomic analysis results's are grouped in table II.

*Table II. Results of the conventional exergoeconomic analysis*

Component	PEC <sub>j</sub> (\$/2020)	Z <sub>j</sub> (\$/h)	C <sub>D,j</sub> (\$/h)	Z <sub>j</sub> +C <sub>D,j</sub> (\$/h)	c <sub>uf,j</sub> (\$/MW)	c <sub>u,p,j</sub> (\$,MW)	r <sub>j</sub>	f <sub>j</sub> (%)
ACR	39899	139,83	36,46	176,29	36,10	48,25	0,34	79,32
CCR	134369	13,61	1423,94	1437,55	16,46	24,53	0,49	0,95
GTE	703166	249,31	163,43	412,73	25,94	29,64	0,14	60,40
RDR	108495	10,99	1646,55	1657,54	24,77	45,14	0,82	0,66

Results of the advanced exergoeconomic analysis are given in the table below:

*Table III. Results of the advanced exergoeconomic analysis*

Component	Z <sub>j,End</sub> (\$/h)	Z <sub>j,Exo</sub> (\$/h)	Z <sub>j, Avo</sub> (\$/h)	Z <sub>j,Una</sub> (\$/h)	Z <sub>j,Una,Exo</sub>	0,02
ACR	137,71	2,12	138,2	1,63	Z <sub>j,Una,Exo</sub>	0,02
CCR	124529,69	9838,92	134337,3	31,29	Z <sub>j Una,End</sub>	1,60
GTE	224,01	25,29	159,6	89,69	Z <sub>j,Una,Exo</sub>	2,29
RDR	10,19	0,80	6,0	4,99	Z <sub>j Una,End</sub>	29,00
					Z <sub>j,Una,Exo</sub>	9,10
					Z <sub>j Una,End</sub>	80,59
					Z <sub>j,Una,Exo</sub>	0,36
					Z <sub>j Una,End</sub>	4,63

The purchased equipment cost for the combustion chamber and the gas turbine are higher and impacts the cost of the overall unit. The most important components are those with a highest value of  $Z_j + C_{D,j}$ . While ranking the system's component using the sum  $Z_j + C_{D,j}$ , we notice that the rotary dryer has the highest value (1657,54 \$/h) followed by the combustion chamber (1437,55 \$/h) and the gas turbine (412,73\$/h). The air compressor has the lowest value in the order of 176,29 \$/h. The rotary dryer and the combustion chamber have the highest value of  $Z_j + C_{D,j}$  because their cost rate related to exergy is high. In the same logic, the rotary dryer has the highest value of  $r$  followed by the combustion chamber and are, respectively, 0,82 and 0,49. The air compressor comes in third place (0,34) followed by the gas turbine (0,14). The rotary dryer presents an exorbitant relative cost difference due the lowest exergy efficiency (55,04%) comparing to the other components of the system ( combustion chamber (67,29%), air compressor (93,49%) and gas turbine (94,66%)) and an exorbitant value of the cost rate related to exergy destruction. As it is seen, the air compressor and the gas turbine have the highest values of the variable  $f_k$ , 79,32% and 60,4%, respectively. As a result, they can be improving by lowering the capital investment at the expense of their efficiencies. While the combustion chamber and the rotary dryer have low values 0,95 % and 0,66% respectively because the costs related to these two components are due to exergy destruction. Therefore, the exergy efficiency of the combustion chamber and the rotary dryer must be increased by reducing the exergy destruction in order to achieve an interesting cost savings. To achieve this aim, some key variables must be identified and improved to reduce the high cost due to the exergy destruction. The temperature is one of these variables, it is a determining parameter to reach the desired moisture content of the product to be dried. At the level of the combustion chamber, an increase in the air temperature at the inlet of the combustion chamber leads to a decrease in the exergy destruction of the component and thus a reduction in the value of  $C_{D,j}$  of the combustion chamber. Considering the rotary dryer, the exergy efficiency cannot be increased if the average temperature difference between the drying air and the product to be dried is not reduced. This leads to a reduction in the value of the cost rate related to the exergy destruction. This must be reached by increasing the inlet temperature of the fertilizers. The advanced exergoeconomic analysis confirms the results obtained by the conventional one; the sum  $C_{D,j}^{\text{End,Avo}} + Z_j^{\text{End,Avo}}$  is high for the combustion chamber and the rotary dryer. Therefore, they are the most expensive components and their thermodynamic improvement is of a prior importance. The dividing of the unit's component investment costs proves that the endogenous investment cost for all components is higher than the exogenous investment cost which means that the investment cost comes from the component itself. Furthermore, the avoidable investment cost is the highest and thus there is a high potential of optimization. For all the components, the AvoEndInvC is the highest, which means that most of the avoidable investments costs for all components are caused by themselves. It seems worthwhile to reduce the investments costs within every system's component.

## 5. CONCLUSION

An exergoeconomic analysis of a cogeneration system combined to a rotary drying of fertilizers is carried out in this work. The objective was to give an idea about the system's components and their interdependencies from the costing perspective. What follows are the key conclusions:

- The rotary dryer's total cost related to investment expenses and exergy destruction accounts for 45% of the overall system's total cost, followed by the combustion chamber (39 %). Thus, these two components should be given priority of improvement;
- The rotary dryer has the highest value of the relative cost difference (0,82 )followed by the combustion chamber (0,49). The air compressor comes in the third place (0,34) followed by the gas turbine (0,14). Therefore, the exergy efficiency of the combustion chamber and the rotary dryer must be increased by reducing the exergy destruction;
- Since the air compressor and the gas turbine have the highest values of the variable  $f_k$ , they participate to the non-exergy related expense to the overall unit's total cost;
- For all the components, the endogenous part is higher than the exogenous one, indicating that the investment cost comes from the component itself;
- The AvoEndInvC for all components are the highest, implying that the majority of the avoidable investment costs are caused by the components themselves.

## REFERENCES

- [1] Bejan, A, Tsatsaronis, G, Moran, M. Thermal Design and Optimization, NEW YORK, J. Wiley, 1996.
- [2] Rosen, MA, A concise review of exergy-based economic methods, In: 3rd IASME/WSEAS. International Conference on Energy&Environment, 23-25 February 2008, University of Cambridge, UK.

- [3] Tsatsaronis, G, Winhold, M, Exergoeconomic analysis and evaluation of energy-conversion plants — I. A new general methodology, *Energy* 1985; 10: 69–80 <[https://doi.org/10.1016/0360-5442\(85\)90020-9](https://doi.org/10.1016/0360-5442(85)90020-9)>.
- [4] Frangopoulos, CA, Thermal-economic functional analysis and optimization, *Energy* 1986; 12: 563–571. <[https://doi.org/10.1016/0360-5442\(87\)90097-1](https://doi.org/10.1016/0360-5442(87)90097-1)>.
- [5] Von Spakovsky, MR, Evans, RB, The design and performance optimization of thermal systems, *J. Engrg. Gas Turbine Power* 1900, 112: 86–93.
- [6] Valero, A, Serra, L, Lozano, MA, Structural theory of thermoeconomics, *Thermodynamics and Design, Analysis and Improvement of Energy System* 1993, 30: 189–198.
- [7] Kim, S, Oh, S, Kwon, Y, Kwak, H, Exergoeconomic analysis of thermal system, *Energy* 1998, 23: 393–406. . <[https://doi.org/10.1016/S0360-5442\(97\)00096-0](https://doi.org/10.1016/S0360-5442(97)00096-0)>.
- [8] Kwak HY, Byun GT, Kwon YH, Yang H. Cost Structure of CGAM cogeneration system. *International Journal of Energy Research* 2004;28: 1145e58. <<https://doi.org/10.1115/IMECE2002-33187>>.
- [9] Balli O, Aras H, Hepbasli A. Exergetic performance evaluation of a combined heat and power (CHP) system in Turkey. *International Journal of Energy Research* 2007; 31:849-66. <<https://doi.org/10.1002/er.1270>>.
- [10] Balli O, Aras H, Hepbasli A. Exergoeconomic analysis of a combined heat and power (CHP) system. *International Journal of Energy Research* 2008; 32: 273-89.<<https://doi.org/10.1002/er.1353>>.
- [11] Reddy BV, Butcher C. Second law analysis of a natural gas-fired gas turbine cogeneration system. *International Journal of Energy Research* 2009; 33: 728-36. <<https://doi.org/10.1002/er.1510>>.
- [12] Vuckovic, GG, Stojiljkovic, MM, Vukic, MV, Stefanovic, GM, Dedeic, EM, Advanced exergy analysis and exergoeconomic performance evaluation of thermal processes in an existing industrial plant, *Energy Conversion And Management* 2014.<<https://doi.org/10.1016/j.enconman.2014.03.049>>.
- [13] Tsatsaronis G, Pisa, J, Exergoeconomic evaluation and optimization of energy systems - application to the cgam problem, *Energy* 1994, 19: 287-321.<[https://doi.org/10.1016/0360-5442\(94\)90113-9](https://doi.org/10.1016/0360-5442(94)90113-9)>.
- [14] Rosen MA, Dincer I. Exergoeconomic analysis of power plants operating on various fuels. *Applied Thermal Engineering* 2003; 23:643-58.<[https://doi.org/10.1016/S1359-4311\(02\)00244-2](https://doi.org/10.1016/S1359-4311(02)00244-2)>.
- [15] Kwon YH, Kwak HY, Oh SD. Exergoeconomic analysis of gas turbine cogeneration systems. *Exergy, an International Journal* 2001;1:31-40.<[https://doi.org/10.1016/S1164-0235\(01\)00007-3](https://doi.org/10.1016/S1164-0235(01)00007-3)>.
- [16] Mert, MS, Dilmaç, OM, Ozkan, S, Karaca, F, Bolat, E. Exergoeconomic analysis of a cogeneration plant in an iron and steel factory, *Energy* 2012; 46: 78-84.<<https://doi.org/10.1016/j.energy.2012.03.046>>.
- [17] Sahooor, PK, Exergoeconomic analysis and optimization of a cogeneration system using evolutionary programming, *Applied Thermal Engineering* 2008; 28:1580–1588.<<https://doi.org/10.1016/j.aplthermaleng.2007.10.011>>.
- [18] Li, B, Li, CH, Huang, J, Li,Ch. Exergoeconomic Analysis of Corn Drying in a Novel Industrial Drying System, *Entropy* 2020, 22, 689.<<https://doi.org/10.3390/e22060689>>.
- [19] Tsatsaronis,G, Morosuk, T, Advanced exergoeconomic evaluation and its application to compression refrigeration machines, In: Proceedings of IMECE 2007, International Mechanical Engineering Congress And Exposition, 11-15 November 2007, Seattle, Washington, USA.<<https://doi.org/10.1115/IMECE2007-41202>>.
- [20] Morosuk, T, Tsatsaronis,G, Advanced exergy-based methods used to understand and improve energyconversion systems, *Energy* 2018.<<https://doi.org/10.1016/j.energy.2018.11.123>>.
- [21] Chen, J, Han, D, Bai, G.P, Zheng, M.R, Gu, J.M. Thermodynamic analysis of a novel wood drying system based on self-heat recuperation technology. *Energy Sources Part A Recovery Util. Environ. Eff.* 2019, 41: 1–17. <<https://doi.org/10.1080/15567036.2019.1649752>>.
- [22] Atalay, H. Comparative assessment of solar and heat pump dryers with regards to exergy and exergoeconomic performance. *Energy* 2019, 189:116–180. <<https://doi.org/10.1016/j.energy.2019.116180>>.
- [23] Ozturk, M, Dincer, I. Exergoeconomic analysis of a solar assisted tea drying system. *Drying Technology* 2019, 38:1–8. <<https://doi.org/10.1080/07373937.2019.1669044>>.
- [24] Erbay, Z, Koca, N, Energetic, Exergetic and Exergoeconomic analyses of spray-drying process during white cheese powder production, *Drying Techonology: An international Journal* 2012, 30:4, 435-444. <<https://doi.org/10.1080/07373937.2011.647183>>.
- [25] Tsatsaronis, G, Morosuk, T, Understanding and improving energy conversion systems with the aid of exergy-based methods, *Int. J. Exergy* 2012, Vol. 11, No. 4.<<https://doi.org/10.1504/IJEX.2012.050261>>.
- [26] Tsatsaronis G. (1999) Design optimization using exergoeconomics. In Bejan A., Mamut E., eds. “Thermodynamic Optimization of Complex Energy Systems”, Kluwer Academic Publishers, pp. 101-117.
- [27] Lazzaretto, A, Tsatsaronis, G. SPECO: A systematic and general methodology for calculating efficiencies and costs in thermal systems, *Energy – The International Journal* 2006, 31: 1257-1289.<<https://doi.org/10.1016/j.energy.2005.03.011>>.
- [28] Colpan CO, Yesin T. Energetic, exergetic and thermoeconomic analysis of Bilkent combined cycle cogeneration plant. *International Journal of Energy Research* 2006, 30:875–894.<<https://doi.org/10.1002/er.1192>>.
- [29] Lazzaretto A, Tsatsaronis G. On calculation of efficiencies and costs in thermal systems. In: Proceedings of the ASME Advanced Energy Systems Divisions, 1999, AES-vol. 39, Nashville, Tennessee.
- [30] Morosuk T, Tsatsaronis G. Exergoeconomic Evaluation of Refrigeration Machines Based on Avoidable Endogenous and Exogenous Costs. In Mirandola A., Arnas O., Lazzaretto A., eds. Proceedings of the 20th International Conference on Efficiency, Cost, Optimization, Simulation and Environmental Impact of Energy Systems, June 25-28, 2007, Padova, Italy, Vol.1, pp. 1459-1467.
- [31] Tsatsaronis G, Park MH. On avoidable and unavoidable exergy destructions and investment costs in thermal systems. *Energy Conversion and Management* 2002, Vol.43, No.9-12, pp.1259-1270. <[https://doi.org/10.1016/S0196-8904\(02\)00012-2](https://doi.org/10.1016/S0196-8904(02)00012-2)>.



# KRIGING SURROGATE MODELS FOR OPTIMIZATION IN ENERGY-EFFICIENT BUILDING DESIGN

Salma Lahmar

Mohammadia School of Engineers, Laboratory of Applied Geophysics, Geotechnics, Engineering Geology and Environment, Mohammed V University in Rabat, Morocco, Islahmarsalma@gmail.com, ORCID: 0000-0002-9134-6925

Rachida Idchabani

Department of process engineering, Higher National School of Mines, Rabat, Morocco

Mohammadia School of Engineers, Laboratory of Applied Geophysics, Geotechnics, Engineering Geology and Environment, Mohammed V University in Rabat, Morocco, idchabani@gmail.com, ORCID: 0000-0002-6461-3629

Mostafa Maalmi

Department of process engineering, Higher National School of Mines, Rabat, Morocco

Mohammadia School of Engineers, Laboratory of Applied Geophysics, Geotechnics, Engineering Geology and Environment, Mohammed V University in Rabat, Morocco, maalmi.mostafa@gmail.com, ORCID: 0000-0003-4913-1047

Cite this paper as:

Salma, L, Rachida, I, Mostafa, M. Kriging surrogate models for optimization in energy-efficient building design. 9<sup>th</sup> Eur. Conf. Ren. Energy Sys. 21-23 April 2021, Istanbul, Turkey

**Abstract:** Over the past few years, while optimizing building efficiency, the evaluation of the objective functions are implemented using surrogate models, leading to computational cost savings in the optimization process. Different surrogate models have been used to emulate building performance assessment (BPA). This paper aims to analyze optimization studies, where the Kriging (Krgg) surrogate model is applied for optimization in energy-efficient building design. First, a review of previous research in the field is discussed. the research works are described in a summary table based on the type of building they addressed, the design variables, outputs, sampling method, hyperparameter tuning method, and simulation tool. Then, publications in the field are reviewed for particular purposes: Design problems including input, output, and target building, Sampling Strategy, and the authors' common findings are discussed. The next step is to extract key research trends that can create awareness for new researchers.

**Keywords:** Energy-efficient buildings, optimization, Kriging, surrogate modeling,

© 2021 Published by ECRES

Nomenclature	
BPA	Building Performance Assessment
BPS	Building Performance Simulation
GA	Genetic Algorithm
GP	Gaussian Process
Krgg	Kriging
LHS	Latin Hypercube Sampling
SRS	Simple Random Sampling
SSS	Sobol Sequence Sampling
MLE	Maximum Likelihood Estimation

## 1. INTRODUCTION

The use of surrogate models (or metamodels) is a rising field of research in the energy-efficient design of a building. Surrogate modeling has been shown to help with BPA by several researchers. Surrogate models are attracting a lot of attention, and they're becoming more relevant in terms of accelerating the optimization process [1]. The aim of surrogate modeling is to use mathematical models to emulate a large number of real measurements or complex

building energy simulations [2]. During the optimization process, these metamodels can be used as a less computationally costly alternative to building energy simulation tools. Among many surrogate models, the Krgg model, a particular form of a Gaussian Process (GP) model, is frequently used for BPA [3]–[8]. There are many fields of application for metamodels for building design problems, an overview is provided by Westermann et al [1]. Only optimization problems have been considered in this paper and restricted to the Krgg model. The present study deals with the energy-efficient design optimization problem where the objective functions (and sometimes constraint function) are replaced by Krgg surrogate model.

This paper first presents previous reviews in the field. Therefore, considering the increasing application of Krgg for BPA, this article provides an analysis of the most recent literature. The rescued research works are then discussed grouped by topic (Design problem, Sampling strategy, and common results). Finally, the main conclusions and practical aspects are presented.

## 2. PREVIOUS REVIEWS

Surrogate-based optimization has been the subject of several studies and attempts in the field of building to improve design objectives. The growing interest in this issue has prompted the building research community to make a review on the state of the art of building performance simulation (BPS) using surrogate-based optimization methods. The first review on the use of surrogate models for BPS is recently published by Westermann et al [1]. Early articles include sections dealing with applications of modeling for building design [9]–[11]. And comparisons between the available methods have been performed [6]–[8]. An overview of the application and characterization of metamodels based on artificial neural networks for BPS is given by Roman et al [12]. In the building design research domain, reviewers show the second most models found in the literature are GP. Moreover, it has been commonly applied for different tasks: prediction, optimization, Sensitivity or Uncertainty analysis and model calibration, etc. As was already introduced, this study focused on optimization applied using Krgg. Researches in this context are collected and introduced in the following section. A full mathematical description of Krgg is out of the scope of this paper. The interested reader is referred to [13]–[15] for more detail on Krgg surrogate modeling.

According to Westerman et al. [1] and Roman et al.[12], as they are the recent publications, seven studies used GP in combination with optimization. Google Scholar was used to conducting the literature review using the keywords “surrogate+kriging+building+energy+optimization”, “kriging+ building+energy+optimization”, and “Gaussian Process+ building +energy+optimization”. Appendix table summarized publication including: The target building, the design variables, objective functions, optimization algorithm, sampling method, hyperparameter tuning method, and simulation tool. Next section provides a discussion of this papers.

## 3. DISCUSSION OF PAPERS GROUPED BY PURPOSE

### **Design problem: Target building, input, output**

Residential [3], [4], [16], office [17], [18] and commercial buildings (retail buildings)[19], [20] are all considered as case studies. Appendix table shows which design variables (input), the objective function (output), and optimization algorithms were used for different papers under study. Energy consumption is the most common output [3], [4], [17]. Gilan et al. [18] optimize heating and cooling demand. the economic aspect is also addressed by these authors. Regarding the building design variables, the main inputs are associated with the geometry and properties of the components (windows, walls, roof, and floor), the building geometry, the internal gains, window-to-wall ratio, and orientation.

### **Sampling strategy**

According to the Appendix table, the adaptive sampling method is commonly used by all authors. Expected improvement, optimality criterion, Latin Hypercube sampling (LHS), and Monte Carlo sampling with Sobol's sequence are among the sample generation techniques used by the remaining authors. While static sampling leads to define samples in one shot before simulations, adaptive sampling identifies placement where the objective function may be optimal.

### **Common results**

- Krgg surrogate model is used as the fitness function of the optimization algorithm. It can be an alternative to simulation software for building performance. This feature can reduce calls to simulation software. Gengembre et al.[3] stated that a metamodel could help designers in exploring design space at a low simulation cost. Trisedder et al. [4] used Krgg surrogate

model to optimize building CO<sub>2</sub> emission and construction cost. They compare the results with those given by the genetic algorithm (GA) on the same design problem. They concluded that the KR model was able to find the optimum in fewer simulation calls than those of GA.

- KR surrogate model tends to reduce the simulation time effort while maintaining the accuracy of BPA. Zhang et al. [19] carried out optimization using adaptive metamodel. The method allows for more reliable results with fewer building model evaluations than are commonly required.

- The way and the best choice of the number of the initial sample are uncertain. The remaining authors did not look into the effect of the initial sample size. However, they used different strategies to generate the initial points. Hopfe et al.[17] randomly generated the first population within the variable bounds. Prada et al.[16] considered different sampling techniques to highlight the extent to which the selection of the initial sample of the energy-saving measures can affect the efficiency of the optimization process. For this reason, LHS, simple random sampling (SRS), and Sobol sequence sampling (SSS) are implemented in the optimization algorithm.

- A disadvantage of Kriging is the limitation in the number of design variables [17]. Tresidder et al. [4] noted that for the KR-based optimization problem, it is recommended that the number of design variables be limited to ten. Yang et al.[20] concluded that as the number of design variables increases, the model's accuracy decreases.

- The impact of Krgg hyperparameters tuning strategy is not checked. Maximum Likelihood Estimation (MLE) is commonly used by papers. Hopfe et al. [17] Using an MLE function to estimate the metamodel's parameters does not provide the best results which slows down the optimization process.

#### 4.CONCLUSION AND PRACTICAL ASPECTS

This paper provides a discussion of publications that use Krgg surrogate models for BPS. The publications are sorted according to the target building, the design variables, objective functions, optimization algorithm, sampling method, hyperparameter tuning method, and simulation tool. Krgg surrogate model-based optimization for building design was deduced to be efficient. The accuracy of the Krgg model was found to be acceptable at a reasonable computational cost. Based on the preceding discussion, there are still drawbacks. The following are some of the keys where future research are expected to focus:

- How many simulation runs would be needed to generate good initial surrogate models? Choose an initial sampling technique that guarantees the representativeness of the variables for generating the input sample;
- In the field of building surrogate models, a comparison of static and adaptive sampling has yet to be performed;
- Choose a Krgg Hyperparameters optimization technique to tune the variance of the model's predictions;
- Improving the speed of a surrogate model to allow for an increase in the number of parameters to be tested is a future challenge.

#### REFERENCES

- [1] P. Westermann et R. Evins, « Surrogate modelling for sustainable building design – A review », *Energy Build.*, vol. 198, p. 170-186, sept. 2019, doi: 10.1016/j.enbuild.2019.05.057.
- [2] F. Kheiri, « A review on optimization methods applied in energy-efficient building geometry and envelope design », *Renew. Sustain. Energy Rev.*, vol. 92, p. 897-920, sept. 2018, doi: 10.1016/j.rser.2018.04.080.
- [3] E. Gengembre, B. Ladevie, O. Fudym, et A. Thuillier, « A Kriging constrained efficient global optimization approach applied to low-energy building design problems », *Inverse Probl. Sci. Eng.*, vol. 20, n° 7, p. 1101-1114, oct. 2012, doi: 10.1080/17415977.2012.727084.
- [4] E. Tresidder, Y. Zhang, et A. I. J. Forrester, « ACCELERATION OF BUILDING DESIGN OPTIMISATION THROUGH THE USE OF KRIGING SURROGATE MODELS », p. 8.
- [5] N. Li, S. C. P. Cheung, X. Li, et J. Tu, « Multi-objective optimization of HVAC system using NSPSO and Kriging algorithms—A case study », *Build. Simul.*, vol. 10, n° 5, p. 769-781, oct. 2017, doi: 10.1007/s12273-017-0352-5.
- [6] L. Van Gelder, P. Das, H. Janssen, et S. Roels, « Comparative study of metamodeling techniques in building energy simulation: Guidelines for practitioners », *Simul. Model. Pract. Theory*, vol. 49, p. 245-257, déc. 2014, doi: 10.1016/j.simpat.2014.10.004.
- [7] L. Rivalin, P. Stabat, D. Marchio, M. Caciolo, et F. Hopquin, « A comparison of methods for uncertainty and sensitivity analysis applied to the energy performance of new commercial buildings », *Energy Build.*, vol. 166, p. 489-504, mai 2018, doi: 10.1016/j.enbuild.2018.02.021.
- [8] T. Østergård, R. L. Jensen, et S. E. Maagaard, « A comparison of six metamodeling techniques applied to building performance simulations », *Appl. Energy*, vol. 211, p. 89-103, févr. 2018, doi: 10.1016/j.apenergy.2017.10.102.
- [9] A. Foucquier, S. Robert, F. Suard, L. Stéphan, et A. Jay, « State of the art in building modelling and energy performances prediction: A review », *Renew. Sustain. Energy Rev.*, vol. 23, p. 272-288, juill. 2013, doi: 10.1016/j.rser.2013.03.004.
- [10] J. Zhao et X. Liu, « A hybrid method of dynamic cooling and heating load forecasting for office buildings based on artificial intelligence and regression analysis », *Energy Build.*, vol. 174, p. 293-308, sept. 2018, doi:

10.1016/j.enbuild.2018.06.050.

- [11] A.-T. Nguyen, S. Reiter, et P. Rigo, « A review on simulation-based optimization methods applied to building performance analysis », *Appl. Energy*, vol. 113, p. 1043-1058, janv. 2014, doi: 10.1016/j.apenergy.2013.08.061.
- [12] N. D. Roman, F. Bre, V. D. Fachinotti, et R. Lamberts, « Application and characterization of metamodels based on artificial neural networks for building performance simulation: A systematic review », *Energy Build.*, vol. 217, p. 109972, juin 2020, doi: 10.1016/j.enbuild.2020.109972.
- [13] T. W. Simpson, J. D. Poplinski, P. N. Koch, et J. K. Allen, « Metamodels for computer-based engineering design: survey and recommendations », *Eng. Comput.*, vol. 17, n° 2, p. 129-150, 2001.
- [14] J. N. Fuhr, A. Fau, et U. Nackenhorst, « State-of-the-Art and Comparative Review of Adaptive Sampling Methods for Kriging », *Arch. Comput. Methods Eng.*, août 2020, doi: 10.1007/s11831-020-09474-6.
- [15] C. E. Rasmussen, « Gaussian processes in machine learning », in *Summer School on Machine Learning*, 2003, p. 63-71.
- [16] A. Prada, « On the performance of meta-models in building design optimization », *Appl. Energy*, p. 13, 2018.
- [17] C. J. Hopfe, M. T. M. Emmerich, R. Marijt, et J. Hensen, « Robust multi-criteria design optimisation in building design », p. 8.
- [18] S. Safarzadegan Gilan, N. Goyal, et B. Dilkina, « Active learning in multi-objective evolutionary algorithms for sustainable building design », in *Proceedings of the Genetic and Evolutionary Computation Conference 2016*, 2016, p. 589-596.
- [19] J. Zhang, « Optimal selection of building components using sequential design via statistical surrogate models ».
- [20] D. Yang, Y. Sun, D. di Stefano, M. Turrin, et S. Sarayildiz, « Impacts of problem scale and sampling strategy on surrogate model accuracy: An application of surrogate-based optimization in building design », in *2016 IEEE Congress on Evolutionary Computation (CEC)*, Vancouver, BC, Canada, juill. 2016, p. 4199-4207, doi: 10.1109/CEC.2016.7744323.

**Appendix table: Considered paper and its properties.**

First author	Year	Target building	Design variables	Objective function	hyperparameter tuning method	Sampling method	Simulation Tools
Gengembre et al	2012	single room with a window on each vertical wall	Window-to-wall ratio for north, east, south, and west Global thermal resistance through opaque surfaces Thermal transmission through the windows Inertia Sunshade length above the south window  Glass area on two sides Size room Internal gains for People Internal gains for Lighting Internal gains for Equipment Wall layer thickness Floor layer conductivity Roof layer conductivity Infiltration rate Switch between double and single glazing	Cost of the construction  Energy consumption Cost of energy Life cycle cost assessment  Energy consumption Over- and underheating hours	MLE	Expected improvement	R5C1
Hopfe et al	2012	Office building			MLE	optimality criterion	VA114
Tressider et al	2012	simple rectangular residential building	Ten discrete variables  Wall insulation Thickness Wall insulation R-Value Roof insulation Thickness Roof insulation R-Value Infiltration Glazing Thickness Glazing Solar transmittance Glazing Front solar reflectance	Annual CO2 emissions Construction COST	Not mentioned	optimality criterion	EnergyPlus
Zhang et al	2013	Small Commercial			MLE	Expected improvement	EnergyPlus

		Glazing Back solar reflectance Glazing Visible transmittance Glazing Front visible reflectance Glazing Back visible reflectance Glazing Front infra-red hemispherical emissivity		
Gilan et al 2016	Office building	Glazing Back infra-red hemispherical emissivity Glazing Conductivity  Orientation Overhang Heating Set Point Cooling Set Point Building Fabric: Floors Building Fabric: Roof Building Fabric: Walls Glazing Ratio: Walls Glazing Coating: Walls	Heating energy Cooling energy	MLE  optimality criterion
Yang et al 2016	Retail building	Case 1 with two design variables Case 2 with forty-one design variables	Useful daylight illuminance Energy use intensity	Not mentioned  optimality criterion DAYSIM/ EnergyPlus



# DEVELOPING A REAL-TIME POWER PRICE ALGORITHM FOR AN AUTONOMOUS DEMAND SIDE MANAGEMENT IN SOLAR COMMUNITY-GRIDS WITH BATTERY STORAGE

Sebastian Finke

Bochum University of Applied Sciences, Bochum, Germany, Sebastian.finke@hs-bochum.de, ORCID: 0000-0002-4924-8096

Michele Velenderic

Green Power Brains, Munich, Germany, michele.velenderic@greenpowerbrains.de, ORCID: 0000-0002-3275-5956

Semih Severengiz

Bochum University of Applied Sciences, Bochum, Germany, semih.severengiz@hs-bochum.de, ORCID: 0000-0001-5682-0161

*Finke, S, Velenderic, M, Severengiz, S. Assessing an autonomous real-time power price algorithm for solar community-grids with battery storage. 9<sup>th</sup> Eur. Conf. Ren. Energy Sys. 21-23 April 2021, Istanbul, Turkey*

**Abstract:** A growing share of decentralized solar energy production in the electricity generation mix will put more stress on existing power transmission networks. The formation of community-grids has the potential to relieve transmission networks while at the same time bringing financial benefits to the community-grid users and granting high service security. At the same time, community-grids, or mini-grids, are an alternative to the utility grid expansion in developing countries, especially in scarcely populated areas. One way of bringing financial benefits to the community and mini-grid users is to optimize the integration of solar energy by introducing a flexible price model, where the price is determined by power demand and supply. This paper develops a real-time power price algorithm for an autonomous demand side management (DSM) in solar community-grids with battery storage. The algorithm is based on the projected energy demand and supply in a typical solar daily cycle considering the respective properties of the battery storage within the mini-grid.

**Keywords:** *community grid, power price algorithm, solar energy integration, battery storage*

© 2021 Published by ECRES

## 1. INTRODUCTION

Access to affordable, reliable and clean energy is an important goal within the framework of the Sustainable Development Goals (SDGs) [1]. To achieve this goal, usage of renewable energies must be extended. The energy transition towards renewable energy sources will put more stress on existing power transmission networks. A higher share of renewables will lead to a growingly decentralized production [2]. A central role in such a decentralized power production environment is taken by solar energy. The number of distributed solar systems is growing strongly worldwide [3]. This leads to the creation of decentralized PV based mini-grids/community grids in which users will have an important role in the stability of the grid and in the energy price shaping [4, 5].

The latter applies equally to developed and to developing countries. In the first ones, distributed power systems offer a possibility to reduce greenhouse gas emissions and to increase energy independence [6]. In developing countries decentralized PV mini-grids are a technically proven and financially feasible alternative to utility grid extension in often scarcely populated areas [7 - 9]. Here emissions also can be significantly reduced especially in rural areas, for example if they are compared to the common use of the grid or diesel generators [10].

A big challenge for the integration of solar power is the necessity for and the high cost of storage due to the high volatility of solar irradiation. Synchronizing supply and demand as much as possible reduces the need for power storage and thus the overall cost of power [11].

In order to achieve that, one of the possibilities is to apply an autonomous real-time price-based Demand Side Management (DSM) [11 - 14]. Autonomous in this regard means that the consumer can decide upfront which load to automatically reduce or shut down in case of a high electricity price. This way the consumer can experience the highest convenience without continuously having to check the current price.

In this paper, an algorithm that regulates the power price as a function of the production, the demand and the grid status is described. This price is the basis for an autonomous DSM system for a solar mini-grid. The goal of the dynamic power pricing is to incentivize the users to influence their demand to match the available power and minimize the need for storage or usage of power from the grid.

## 2. PRICE INFLUENCING FACTORS

The factors that influence the electricity price within the algorithm can be divided into three categories. Power production, power demand and grid information.

The power production includes the factors that influence the output power from the PV generators of the mini-grid. These include the solar irradiance, the weather forecast as well as parameters to model special weather influences as snowfall. The power demand is calculated using historical data for a time period similar to the one the demand is being calculated for. Finally, the grid information includes the state of charge (SoC) of the batteries in the mini-grid, the share of deferrable consumers and the share of high-priority consumers, which cannot be deferred. Furthermore, the grid information includes the real consumption data as well as the availability of the utility grid or of a diesel genset.

*Table 1: Explanation of Price Influences*

Category	Influence	Unit	Explanation
Power production	Solar irradiance on a plane (historical)	W/m <sup>2</sup>	Historical data for the mini-grid location, used as a baseline for power production prevision
	Weather forecast	W/m <sup>2</sup>	Short term forecast used for predictions of power production
	Special weather influences		Factor for special weather phenomenon that influence the power production. E.g. for European latitudes, snowfall, for Sub-Saharan Africa, the Harmattan wind.
Power demand	Daytime	Timestamp	Used together with historical data to determine the remaining power demand in a day
	Date	Timestamp	Used together with historical data of same weekdays and occurrences as holidays to determine the expected power load
	Historical load curve	-	Used for predicting short term power demand
Grid information	Battery state of charge	%	Calculation of the available power in combination with the production and consumption forecasts
	Share of deferrable consumers	%	Capacity of loads that can be deferred, i.e., switched on and off depending on the available power
	Share of high priority consumers	%	E.g., medical consumers, educational facilities that cannot be deferred
	Current load	kW	Current power demand
	Generator/Utility Grid	on/off	Availability of a generator or of the utility grid

In order to quantify the different influences for the price algorithm three main concepts for the energy supply, energy demand and battery storage have been developed as described in the sections below.

### Supply – Remaining Energy Generated Until Sunset “REGUS”

For the supply side the concept of “Remaining Energy Generated Until Sunset” (REGUS) was developed. It describes the amount of energy generated until sunset. The factors considered are visualized in Figure 1 and described below.

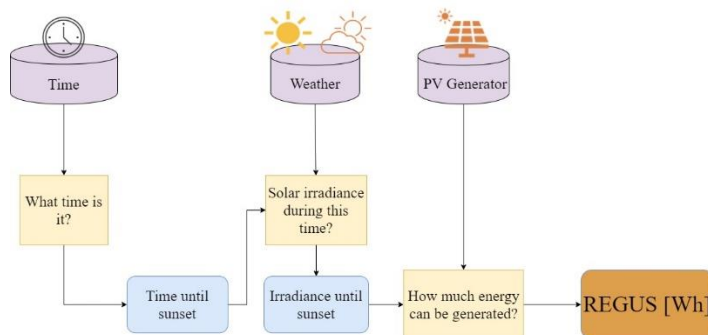


Figure 1: Flowchart for the factors to be considered for the calculation of REGUS

At any time during a day, information on weather data is used to evaluate the expected solar irradiance during the time until sunset. The REGUS for a single PV generator can be calculated as follows:

$$REGUS = P_p \cdot t_{flr} \cdot (1 - \varepsilon_c) \cdot \varepsilon_t \cdot \varepsilon_w \cdot \varepsilon_s \quad (1)$$

An overview of the parameters used for the calculation of REGUS is shown in Table 2.

Table 2: Parameters for the calculation of the REGUS

Name	Sign	Unit	Range
Panel peak power	$P_p$	Wp	$[0, \infty[$
Full load hours remaining in until sunset	$t_{flr}$	h	$[0, 12]$
Cloudiness factor	$\varepsilon_c$	%	$[0, 1]$
Temperature efficiency	$\varepsilon_t$	%	$[0, 2]$
Special weather factor	$\varepsilon_w$	%	$[0, 2]$
Overall system efficiency factor	$\varepsilon_s$	%	$[0, 1]$

$P_p$  is the peak power of a PV generator, while  $t_{flr}$  are the remaining full load hours expected until the sunset of the considered day. The upper range limit has been chosen to include all possible remaining full load hours until sunset. To better model the expected weather conditions, factors that reduce the expected output are introduced. The influences of rainy weather and clouds are accounted for with the cloudiness factor  $\varepsilon_c$ , which is 0 when no irradiation is blocked by the clouds and 1 when the irradiation is blocked completely. Short term cloud enhancements are not considered due to the low influence on the final output energy. The temperature dependence of the PV generator efficiency is taken into account in the temperature efficiency factor  $\varepsilon_t$ . To consider the influence of weather-related phenomena that affect the power output, as snow or the Harmattan wind in West-Africa, the special weather factor  $\varepsilon_w$  is introduced. The latter two factors have a range from 0 to 2, as it is possible that weather phenomena increase the power output, e.g. due to favorable reflections on the PV generator or the power output enhancement by low temperatures. The overall system efficiency  $\varepsilon_s$  includes all the system losses from the PV generator to the storage and out again to the consumers. The total REGUS for a whole mini-grid,  $REGUS_t$  is the sum of all REGUS generated by all PV generators of the mini-grid, until the next sunset, with  $n$  being the number of PV generators in the mini-grid:

$$REGUS_t = \sum_{i=0}^n REGUS_i \quad (2)$$

#### Demand – “Remaining Energy Consumed Until Sunrise” RECUS

For the demand side of the system the concept of “Remaining Energy Consumed Until Sunrise” (RECUS) is introduced. It describes the projected amount of energy needed by the consumers until energy production starts with the next sunrise. The factors that must be taken into account are visualized in Figure 2 and described below.

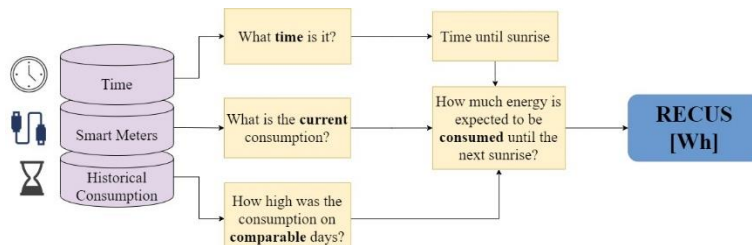


Figure 2: Flowchart for the factors to be considered for the calculation of RECUS

The parameters relevant for the calculation are summarized in Table 3.

Table 3: Parameters for the calculation of the RECUS

Name	Sign	Unit	Range
Estimated demand in time period t	$D_t$	Wh	
Real demand measured	$D_{t,true}$	Wh	
Weekday	day	int	[1, 7]
Special day	day	binary	{True, False}
Time of next sunrise	next sunrise	h, min	[0,24], [0, 60]
Time of last sunrise	last sunrise	h, min	[0,24], [0, 60]

### Battery Storage – Usable Capacity and Capacity Reserve

For the energy storage of the system, the existing concept of usable capacity is used, together with the remaining usable capacity available. Different battery types and other factors have taken into account as outlined in Figure 3.

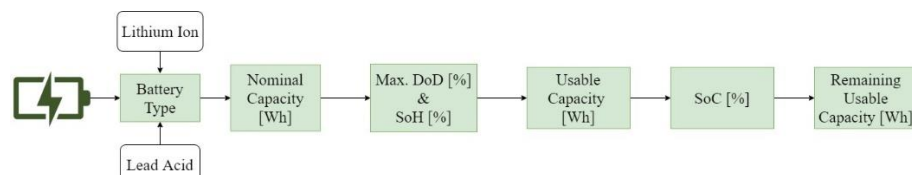


Figure 3: Flowchart for the factors to be considered for the calculation of the usable capacity.

Starting with the nominal capacity of the battery, the State of Health (SoH) as well as the maximum Depth of Discharge (DoD) of a battery have to be considered. Both reduce the nominal capacity to the usable capacity of the battery.

The overall remaining usable capacity  $C_{ur,overall}$  of the mini-grid is calculated as the sum of the remaining usable capacities stored in each battery of the mini-grid, with  $m$  being the number of batteries in the mini-grid:

$$C_{ur,overall} = \sum_{j=0}^m C_{ur,j} \quad (4)$$

Furthermore, it is reasonable to define a certain reserve capacity, per battery or for the total mini-grid, which will serve as backup to cover deviations in the power usage and power generation predictions. If considering the overall remaining usable capacity in a mini-grid,  $C_{ur,overall}$ , the reserve capacity  $C_{ur,reserve}$  can be calculated easily using a battery reserve factor  $\varepsilon_r$ , which represents the percentage of the overall remaining usable capacity to be kept as reserve:

$$C_{ur,reserve} = C_{ur,overall} \cdot \varepsilon_r \quad (5)$$

Using the factors described above, the logical foundation of the price algorithm can be outlined as shown in Figure 4.

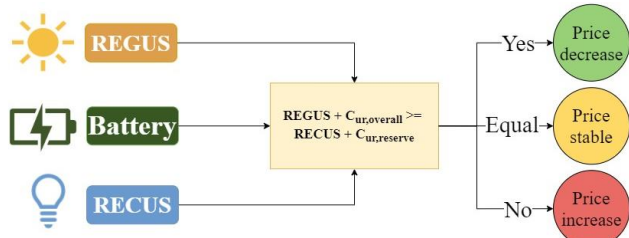


Figure 4: Flowchart for the reaction of the price algorithm.

The inputs on the left side are the factors for the supply (REGUS), demand (RECUS) and the battery. In the inequation in the middle, the available energy is on the left side, as the sum of the remaining energy generated until sunset (*REGUS*) and the overall usable capacity in all the batteries of the mini-grid  $C_{ur,overall}$ . The energy demand is on the right side, represented by the sum of the energy demanded by the consumers until the next sunrise (*RECUS*) and the reserve energy  $C_{ur,reserve}$ . If both are the same, the expected demand can be fulfilled. Therefore, the current price can remain unchanged. If the expected supply is greater than the expected demand, more consumption can be allowed, so the price can decrease. If the expected demand exceeds the available energy, the price has to increase in order to reduce the consumption.

### 3. PRICE CALCULATION

To calculate a price based on the mathematical definition of the factors described above it is necessary to calculate a quantity within specific boundaries, to ensure that the calculated price remains between desired limits. In order to reflect the logic from Figure 4 the electricity price factor  $\varepsilon_p$  is introduced:

$$\varepsilon_p = \frac{(REGUS - RECUS) + (C_{ur,overall} - C_{ur,reserve})}{\max(REGUS + C_{ur,overall}; RECUS + C_{ur,reserve})} \quad (6)$$

The denominator of the equation is used to normalize  $\varepsilon_p$  to the interval  $[-1, 1]$ . A value of 1 for  $\varepsilon_p$  results in the case of energy generation with no demand and reserve battery capacity defined, whereas a value of  $-1$  results in the case of energy demand with no energy generation and without any remaining usable battery capacity. Using  $\varepsilon_p$ , a maximal price  $P_{max}$  and introducing a price interval factor  $\alpha_{int}$ , the electricity price can be calculated as:

$$PRICE = \min[(-\varepsilon_p + \alpha_{int}) \cdot P_{max}; P_{max}] \quad (7)$$

The price interval factor is used to delimit the boundaries of the calculated price. By using a price interval factor of  $1, \alpha_{int} = 1$ , in the above eq. [6], the resulting price is contained in the interval  $[0, P_{max}]$ .  $\alpha_{int}$  can be adapted to change the price interval. E.g., by using a  $\alpha_{int} = 0.5$ , the price is in the interval  $[-0.5 \cdot P_{max}, P_{max}]$ , thus allowing negative prices.

### 4. DISCUSSION

The next step towards an autonomous demand side management (DSM) using the real-time price algorithm is an implementation in a simulation environment to test the algorithm with historical data from existing community-grids. The goal is to evaluate the behavior of the dynamic pricing in real conditions and to quantify the benefits for the consumer by quantifying the potential savings a consumer has compared to a setting without any power shift. Furthermore, the influence of the price interval factor  $\alpha_{int}$  on the long-term price development and benefits for the consumer need to be investigated. This will be used as a base for the evaluation of a suitable price calculation frequency, which must be assessed together with detailed information about deferrable loads, the switching conditions, free or constrained to certain intervals of operation, and the energy needed to fulfil an operation cycle once started.

Besides the frequency of the price calculation, the type of price level must still be determined. While it is possible to use a steady curve, allowing for all prices within the boundaries defined by eq. [6], it might be more convenient for the user of the community-grid to have a clear, pre-defined number of price levels, by transforming the price calculated with eq. [6] into a step function. Advantages and disadvantages of both approaches must be evaluated. The effectiveness of an autonomous real-time pricing heavily depends on the user acceptance within the community-grid [15]. In the course of the testing of the price algorithm, the willingness to pay and consumer behavior need to be analyzed, both in developing as well as in developed countries [16] and [17].

## **ACKNOWLEDGEMENT**

The authors would like to thank Hannes Harthan and Sebastian Schneider for their valuable contribution.

## **REFERENCES**

- [1] United Nations Department of Economic and Social Affairs 2021. The 17 Goals. Retrieved from <https://sdgs.un.org/goals>
- [2] Bauknecht, D , Funcke, S , Vogel, M . Is small beautiful? A framework for assessing decentralised electricity systems. Renewable and Sustainable Energy Reviews 2020. Volume 118. <https://doi.org/10.1016/j.rser.2019.109543>.
- [3] International Energy Agency 2020. Solar PV. Retrieved from <https://www.iea.org/reports/solar-pv>
- [4] Bhattacharyya, S C , Palit D . Mini-Grids for Rural Electrification of Developing Countries: Analysis and Case Studies from South Asia. Cham, Switzerland: Springer 2014
- [5] Rosado, S P and Khadem, S K . Development of Community Grid: Review of Technical Issues and Challenges. IEEE Transactions on Industry Applications 2019. Volume 55, no. 2, Pages 1171-1179. doi: <https://doi.org/10.1109/TIA.2018.2883010>.
- [6] Muteri, V , Cellura, M , Curto, D , Franzitta, V , Longo, S , Mistretta, M , Parisi, M L . Review on Life Cycle Assessment of Solar Photovoltaic Panels. Energies 2020.13, 252. doi:[10.3390/en13010252](https://doi.org/10.3390/en13010252)
- [7] Moner-Girona M , et al. . Electrification of Sub-Saharan Africa through PV/hybrid mini-grids: Reducing the gap between current business models and on-site experience. Renewable and Sustainable Energy Reviews 2018. Volume 91, Pages 1148-1161. <https://doi.org/10.1016/j.rser.2018.04.018>
- [8] International Renewable Energy Agency 2018. SOLAR PV IN AFRICA: COSTS AND MARKETS
- [9] Peters, J , Sievert, M , Toman, M A . Rural Electrification through Mini-Grids: Challenges Ahead, Energy Policy 2019. Volume 132, Pages 27-31. <https://doi.org/10.1016/j.enpol.2019.05.016>
- [10] Sonali Goel, Renu Sharma, Performance evaluation of stand alone, grid connected and hybrid renewable energy systems for rural application: A comparative review, Renewable and Sustainable Energy Reviews 2017. Volume 78, Pages 1378-1389. doi: <https://doi.org/10.1016/j.rser.2017.05.200>.
- [11] Hossain, A , Pota, H R , Moreno, C M . Real-time Battery Energy Management for Residential Solar Power System. IFAC-PapersOnLine 2019, Volume 52, Issue 4, Pages 407-412. <https://doi.org/10.1016/j.ifacol.2019.08.244>.
- [12] Mehra, V , Amatya, R , Ram, R J . Estimating the value of demand-side management in low-cost, solar micro-grids. Energy 2018. Volume 163, Pages 74–87. doi:[10.1016/j.energy.2018.07.204](https://doi.org/10.1016/j.energy.2018.07.204).
- [13] Jabir, H J . Teh, J , Ishak, D , Abunima, H . Impacts of Demand-Side Management on Electrical Power Systems: A Review. Energies 11 2018, Volume 1050. <https://doi.org/10.3390/en11051050>
- [14] Khouri, J , Mbayed, R , Salloum, G , Monmasson, E . Design and implementation of a real time demand side management under intermittent primary energy source conditions with a PV-Battery backup system. Energy and Buildings 2016. Volume 133, Pages 122-130. <https://doi.org/10.1016/j.enbuild.2016.09.036>.
- [15] Dutta, G , Mitra, K . A literature review on dynamic pricing of electricity. Journal of the Operational Research Society 2017. Volume 68, Pages 1131–1145. <https://doi.org/10.1057/s41274-016-0149-4>
- [16] Numminen, S , Yoon, S , Urpelainen, J , Lund, P . An Evaluation of Dynamic Electricity Pricing for Solar Micro-Grids in Rural India. Energy Strategy Reviews 2018, Available at SSRN: <https://ssrn.com/abstract=3193474>
- [17] Wei, Q et al., Adaptive Dynamic Programming-Based Optimal Control Scheme for Energy Storage Systems With Solar Renewable Energy. IEEE Transactions on Industrial Electronics 2017. Volume 64, no. 7, Pages 5468-5478. doi: [10.1109/TIE.2017.2674581](https://doi.org/10.1109/TIE.2017.2674581).



# INVESTIGATION OF GEOMETRIES FOR INCREASING THE ENERGY DENSITY IN ELECTROMECHANICAL BATTERY FLYWHEELS

Daniel Coppede

UFABC. Sao Paulo. Brazil. danielcoppede@gmail.com, ORCID: 0000-0003-2732-127X

Marco Antonio de Souza

IFSP. Sao Paulo. Brazil. marcoantonidesouza1@gmail.com, ORCID: 0000-0003-3340-5912

Renato Chaves Souza

IFSP. Sao Paulo. Brazil. rchaves@ifsp.edu.br, ORCID: 0000-0002-8804-2752

Wilson Carlos da Silva Junior

IFSP. Sao Paulo. Brazil. wilsoncarlos@ifsp.edu.br, ORCID: 0000-0001-8128-281X

Roberto Nunes Duarte

IFSP. Sao Paulo. Brazil. rnduarte@ifsp.edu.br, ORCID: 0000-0002-8292-1623

Fabio da Silva Bortoli

IFSP. Sao Paulo. Brazil. bortoli.fabio@gmail.com, ORCID: 0000-0001-7082-5209

Carlos Frajuba

IFSP. Sao Paulo. FURG. Rio Grande. Brazil. frajuba@gmail.com, ORCID: 0000-0001-8463-3451

Cite this paper as:

*Coppede, D., Souza, MA., Souza, RC., Silva Junior, WC., Duarte, RN., Bortoli, FS., Frajuba, C.*  
*Investigation of geometries and materials for increasing the energy density in electromechanical battery flywheels. 9<sup>th</sup> Eur. Conf. Ren. Energy Sys. 21-23 April 2021. Istanbul. Turkey.*

## Abstract:

This work presents a study on possible geometries and materials in flywheels through finite element modeling (FEM). Flywheels compose a fundamental part of the set of electromechanical batteries. This study aims to analyze the behavior of flywheels rotating at the highest possible rotational speed to produce the best mass–energy relation for a certain rotor geometry. For this, different flywheel models were created and simulated through successive changes in their geometry to increase the rotational speed and energy. The geometry obtained with the best performance in the form of a Gaussian solid of revolution and made entirely of the carbon fiber Hexcel UHM 12000 allows the development of a low cost and high performance flywheel in revolutions of up to  $\approx 279.000$  rpm and stored energy density of up to  $\approx 387$  Wh/kg.

**Keywords:** *Flywheel. Electromechanical Battery. Finite Element Modeling. Energy Density. High-speed rotation*

© 2021 Published by ECRES

## 1. INTRODUCTION

The working principle of an electromechanical battery is simple, as it involves basically placing a flywheel to spin in situations where it is not subject to frictional forces or significant external actions [1]. It is a simple form of energy storage, where mechanical energy is easily converted to electrical energy and vice versa, using an electric generator motor. The energy in a flywheel depends on its inertia moment and speed of rotation.

The proposal to use rotating masses to avoid variations in the speed of motors and generators is based on the fact that the energy does not change abruptly with the application of limited forces. This simple system is known as the 1st generation Flywheel [2], whose main objective is to maintain or set in motion, through the stored energy, a given rotor or mechanism at a fixed rotation speed with low variations.

The 2nd generation of Flywheels - is characterized by the path taken by the energy flow through a circuit that starts on a flywheel, passes through an AC generator, goes to a rectifier, then to an inverter and reaches the power grid. This flow can be reversed to load the flywheel. In this way, the rotating mass can vary its speed and, even so the rectifier/inverter circuit is capable of producing fixed frequency and voltage. This application is known as Flywheel Energy Storage System (FESS) and has as one of its purposes to store energy to fill gaps in the network [3].

The combination of many factors is enabling the development and implementation of 3rd generation Flywheels, which have a performance far superior to the previous generation, and whose rotation speed can reach the order of 100.000 rpm, eliminating existing usage limitations [3-5]. The search for new materials such as carbon nanotubes and silica compounds (fused silica) has provided new perspectives and possibilities for the use of flywheels, as this new generation has higher energy and power densities than batteries, as shown in Table 1.

Thus, the objective of this work is to analyze the behavior of geometries of the Flywheel as an electromechanical battery for the optimization of its kinetic energy stored per unit of mass. For this, the development of different flywheel geometries that allow greater energy storage and greater {stored energy}/mass ratio is done.

*Table 1: Comparison between different energy storage devices and promising materials for the construction of flywheels (average values). References indicated in the table.*

Energy Storage Device	Energy Density (Wh/kg)	Power Density (W/kg)
Electrochemical Batteries [6]	35	150
2nd Generation Flywheel [6]	5.5	730
3rd Generation Flywheel (Maraging steel) [6]	56	670
Carbon fiber [7]	213.8	—
Fused Silica [7]	800	—
Carbon Nanotubes [7]	2700	—

## 2. SEARCH FOR MATERIALS SUITABLE FOR FLYWHEELS

One must choose a material whose characteristics allow the flywheel to reach speeds that result in a high energy density. Important properties in the flywheel design are the yield strength and ultimate tensile strength of the material used for the rotor. The limit of rotational energy that can be stored in a rotor is often calculated with the approximation [8, 9]:

$$\frac{E}{m} = \frac{\sigma_{max}}{2\rho} \quad (1)$$

where E is the energy of the rotor, m is its mass,  $\sigma_{max}$  is the maximum allowable stress for the material and  $\rho$  is the density. Therefore eq. (1) defines the energy density of the rotor. Using this definition, Table 2 shows examples of favorable materials for flywheels and their energy densities.

*Table 2: Suitable materials for the composition of flywheels. Data obtained from Ref. [8], except Hexcel UHM Carbon Fiber 12000 which was obtained from Ref. [17] and eq. (1).*

Material	Tensile strength (MPa)	Density (kg/m <sup>3</sup> )	Energy density (Wh/kg)
Titanium Ti-15V-3Cr-3Al-3Sn ST 790 °C	1380	4760	40
Advantex E-glass (glass fiber)	~1400	2146	90
Toray T1000G composite	3040	1800	234
Toray T1000G fiber	6370	1800	491
Vapor grown carbon nanofibers	2920	2000	202
Hexcel UHM Carbon Fiber 12000	3730	1870	277

The materials presented in Table 2 are suggested by Hedlund et al. [8], except Hexcel UHM Carbon Fiber 12000. This table does not include other promising materials for this purpose, such as those consisting of carbon nanotubes [8, 10], as they involve an application technology that is currently not accessible.

The study of Coppede [11] shows a FEM analysis of different geometries for flywheels and two constituent materials: Maraging steel (AISI 18 Ni 350) and carbon fiber (Hexcel UHM 12000). The results obtained by Coppede indicate that the best configuration is the one where the flywheel consists only of Hexcel UHM 12000 carbon fiber, obtaining a speed of 171.000 rpm and stored energy of 1.200 Wh. Table 3 shows that Hexcel UHM 12000 carbon fiber is the second material with the highest storables energy density compared to the other materials

mentioned. Then this research group chose Hexcel UHM 12000 carbon fiber as the basic material FEM simulations shown in this work. The authors have experience with instrumentation [12-14], factor that help the development of this work.

### 3. RESEARCH METHODOLOGY

The present work is based on an exploratory investigation through case studies. Various flywheel geometries were simulated by FEM at different rotation speeds using SOLIDWORKS [15] software. taking as a starting point geometries proposed in previous works by Coppede [11] and Nogueira [16]. The purpose of the simulations is to find a flywheel geometry with maximum energy storage per unit of mass. avoiding reaching von Mises stresses above the ultimate tensile strength of the constituent material: Hexcel UHM 12000 carbon fiber. The general properties of the FEM simulations are shown in Table 3. The complete mechanical properties of Hexcel UHM 12000 are in Ref.[17].

The research on the geometry of the flywheel was developed in stages. and each stage was guided by the results obtained in the simulations of the previous stages. The basic geometry used in the initial model (Model A) was suggested in Refs. [11,16]. From the basic geometry we explored the influence of the geometry variation in the stress

distribution. in each of the models. keeping the external diameter of 200 mm and the height of the central cylindrical part of 100 mm. in all the models.

At each stage. the influence of the change in the geometry of the flywheel on the disc region. that is. the connecting element between the axis and the crown. is analyzed. The modifications are basically represented by the angle formed between the surface of the disc and the perpendicular to the axis of the model. with alteration of the height of the same (due to the variation of the angle. when necessary) and increase its diameter in some cases.

*Table 3: General properties of the FEM simulations.*

Analysis type	static analysis
Mesh type	solid
Friction condition	disabled
Thermal effect	activated
Load type	centrifugal
Connector/Support type	bearing

### 4. MODEL ANALYSED BY FEM

All the flywheel models analysed were simulated as solid cylindrical bodies. consisting of Hexcel UHM 12000 carbon fiber. with longitudinal and transversal symmetry. Except for model R which has a gaussian shaped part (had as initial reference the shape defined by Stodola's solution [18]), all flywheel models have a central cylindrical part with a constant diameter of 200.00 mm and a height of 100.00 mm.

### 5. FEM RESULTS FOR STRESS DISTRIBUTION

This section discusses the FEM results for the flywheel models, with emphasis on the von Mises stress distribution.

#### 5.1. Models of Stage 1

In Model **A**, stresses are observed increasing in direction of the external radius to the axis until they reach the critical point in the region where the axis meets the disc surface. The concentration of stresses in this region limited the study to a maximum rotation of 162,180 rpm.

Model **B** presents the stresses increasing in direction of the radius external to the axis in a more homogeneous way until they reach the critical point in the region of the curve applied at the base of the shaft. The expected increase in rotational speed with the introduction of the curve for connection of shaft and disc was not obtained, since the concentration of stress in this section limited the study to a maximum rotation of 153,380 rpm.

Models **C**, **D** and **E** present stresses distributed approx. homogeneously in their extension, with an accumulation of these stresses in the region where the shaft meets the disc surface. The concentration of stresses in this region limited the study of Models **C**, **D** and **E** to maximum speeds of 166,580 rpm, 192,340 rpm and 185,520 rpm, respectively (see Table 4).

The results of the five simulations performed in this stage directed the study to verify the influence of the model geometry in the stress distribution through the change of the angle formed between the surface of the disc.

*Table 4: Flywheel models and respective values of maximum rotation speed. mass. stored energy and energy density. The highest value for each property is shown in bold.*

Model	Maximum rotation speed (RPM)	Mass (kg)	Stored energy (Wh)	Energy density (Wh/kg)
A	162.180	5,893.000	1,176.79	199.69
B	153.380	6,021.000	1,053.53	175.00
C	166.580	8,234.000	1,528.64	185.65
D	192.340	8,407.000	2,042.35	242.93
E	185.520	8,546.000	1,905.67	222.99
F	187.150	7,812.000	1,803.80	230.90
G	191.980	8,151.000	1,964.55	241.02
H	194.330	8,511.000	2,086.81	245.02
I	185.070	8,923.000	1,966.80	220.42
J	185.700	9,382.000	2,064.59	220.06
K	182.130	9,914.000	2,079.99	209.80
L	187.580	10,731.000	2,328.27	216.97
M	162.920	8,545.000	1,467.64	171.75
N	175.880	8,642.000	1,715.26	198.48
O	189.900	8,825.000	2,013.91	228.20
P	195.440	9,335.000	2,145.19	229.80
Q	204.820	8,161.000	2,080.80	254.97
R	279.180	968.000	374.37	386.63

## 5.2. Models of Stage 2

In Model F, the stresses are distributed approx. homogeneously in the central region of its body with a small trend to increase towards the center; lower stresses are located in the regions of the shaft above and below the region where the shaft meets the surface of the disc, in which stress builds up. The concentration of stresses in this region limited the study to a maximum rotation of 187,150 rpm.

Models **G**, **H**, **I**, **J**, **K** and **L** present the stresses distributed in a similar way to the previous model, with an accumulation of stresses in the region where the shaft meets the disc surface. The concentration of stresses in this region limited the study of models from G to L to maximum speeds between 182,130 rpm (Model **K**) and 194,330 rpm (Model **H**).

As the results of Stages 1 and 2 indicated that the models with an angle of 30° between the surface of the disc and the perpendicular to the axis (Models **D** and **H**) are those with the most satisfactory results, the next stage was formulated based on models with adaptations in geometry involving the 30° angle.

## 5.3. Models of Stage 3

In Model **M**, the stresses are distributed approx. homogeneously in the central region of its body with a small trend to increase towards the center; lower stresses were found in the regions of the shaft above and below the region where the shaft meets the surface of the disc, in which stress builds up. This stress concentration was the critical one.

Models **N** and **O** present the stresses distributed in a similar way to the previous model, with an accumulation of stresses in the region where the shaft meets the disc surface. The concentration of stresses in this region limited the study of Models **N** and **O** to maximum rotations of 175,880 rpm and 189,900 rpm, respectively (Table 4). The models of Stage 3 produced lower rotational speed, rotational energy and energy density values than those obtained by previous models (see Table 4). Based on these results, new forms of geometry were analyzed in the next stage.

## 5.4. Models of Stage 4

Model **P** presents an approx. homogeneous distribution of intermediate stresses throughout the body and an increase in stress towards the central region. Smaller stresses occurred at the ends of the shaft and in the region between the center and the region where the model surface meets the shaft, in which the greatest stress accumulation occurs. Model **Q** presented a stress distribution behavior similar to the previous model, with a greater increase in stress towards the central region, which presented a smaller volume. The greatest accumulation of stress occurred in the

region where the shaft meets the model surface (Figure 4). The stress concentration in this region limited the study to a maximum rotation of 204,820 rpm (Table 4).

### 5.5. Models of Stage 5

Model **R**, the only one in this stage, presents stresses that gradually increase from its external radius to the geometric center of the rotor, where the maximum stress occurs (Figures 1). A worthwhile result of this model is the avoidance of stress excess on the shaft and its connections with the disc. The concentration of stresses in the central region limited the study to a maximum rotation of 279,180 rpm (Table 4). This rotation is the highest in the present work.

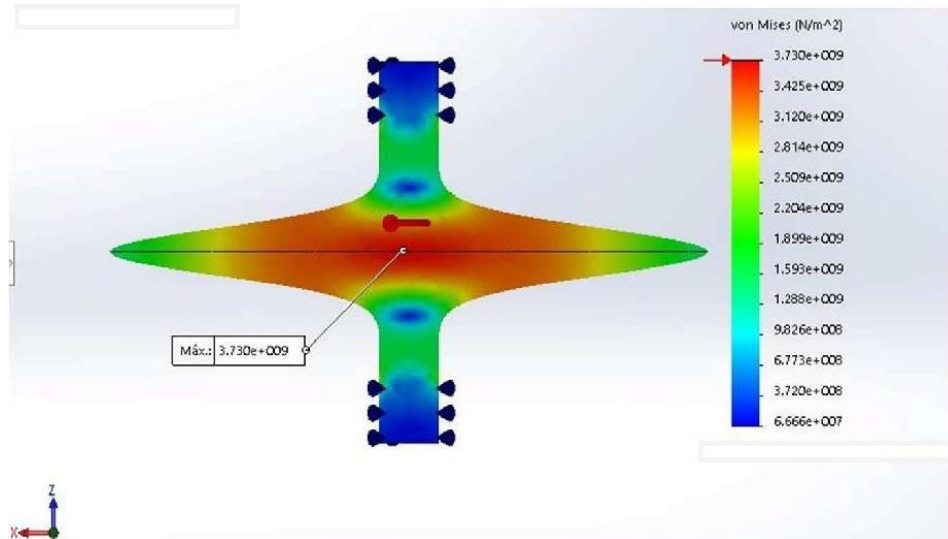


Figure 1: The von Mises stress distribution for Model R - section in xz-plane. The stress color scale is given in Pa. The blue arrows indicate the location of the connector/support of the flywheel in the FEM simulation.

## 6. DISCUSSION ON THE PERFORMANCE OF FLYWHEEL MODELS

With respect to Stage 1, the model **D** showed the best result, because it reached the highest rotational speed of 192,340 rpm and the stored energy of 2,042.35 Wh, as well as the best energy density of 242.93 Wh/kg.

Despite the gradual increase in mass of the models of Stage 2, which occurred due to the increase in the angle formed between the surface of the disc and the perpendicular to the axis, the expected increase in maximum rotational speed, rotational energy and energy density did not occur throughout the series of the stage, except in the phase from Model **F** to Model **H**. From Model **I**, there was a variation in the relation between the quantities involved: Model **H** presented the highest values of rotational speed and energy density in Stage 2, while Model **L** showed the highest rotational energy in the same stage.

The increase in the mass of each model in Stage 3 was accompanied by the corresponding increase in three quantities: rotational speed, rotational energy and energy density. However, all values achieved were lower than those obtained by the 30° angle models of the previous stages, despite having a greater amount of mass (Table 4). The Model **P** of Stage 4, with its surface formed by a sequence of inclination angles that vary gradually, presented a rotational speed above the previous ones (195,440 rpm), but the energy density in an intermediate value due to the value of its mass, the fourth largest among all models, this fact led to the Model **Q** in the form of a continuous curve.

Model **Q** of Stage 4 presented the 2nd highest rotational speed among all models (204,820 rpm), as well as the 2nd highest energy density (254.97 Wh/kg), because its mass (8.161 kg) is 12.57 % less than that of Model **P**.

Model **R** of Stage 5 was the most successful among all models, as it presented the highest rotational speed, the highest energy density, and also has a von Mises stress maximum at the central part, and not in the shaft and in its connections with the disc. Therefore, the convenience of using the Gaussian shape to achieve the best performance of the flywheel was shown.

## 7. CONCLUSIONS

Among the models with a cylindrical central part of constant radius (Models **A** to **Q**), the best result of energy density was achieved in Model **Q**. As this model has a mass 23.95 % lower than Model **L**, it presented a considerably

higher energy density, 254.97 Wh/kg. Model Q also achieved the highest rotational speed (204,820 rpm) among the models from **A** to **Q**.

However, Model **R**, with Gaussian shape, was the one that showed the best overall performance among all models, as it achieved the highest energy density (386.63 Wh/kg) and the highest rotational speed (279,180 rpm). In addition, its von Mises stress distribution shows that the connection regions of disc and shaft are not affected by high stresses which are close to the ultimate tensile strength; this is a very promising result for the final flywheel project. The energy density achieved by Model **R** is significantly higher than the value predicted by eq. (1) for the carbon fiber Hexcel UHM 12000 ( $\approx$ 277 Wh/kg), showing that the proposed Gaussian geometry offers an optimal use of the material for energy storage.

## ACKNOWLEDGEMENTS

C. Frajua thanks research grant #2013/26258-4 from Fundação de Amparo a Pesquisa do Estado de São Paulo (FAPESP) and grant 309098/2017-3 from Conselho Nacional de Desenvolvimento Científico e Tecnológico (CNPq).

## REFERENCES

- [1] Junling C, Xinjian J, Dongqi Z, Haigang W. A Novel Uninterruptible Power Supply using Flywheel Energy Storage Unit. The 4th International Power Electronics and Motion Control Conference - IPEMC 2004;3:1180–1184.
- [2] Stephan RM, Andrade Jr R, Sotelo GG. Third Generation of Flywheels: a Promising Substitute to Batteries. Revista Eletrônica de Potência 2008;13:171–176. DOI:<http://dx.doi.org/10.18618/REP.2008.3.171176>
- [3] Fiske OJ, Ricci MR. Third Generation Flywheels For High Power Electricity Storage. LaunchPoint Technologies, Inc., Goleta, California, USA; 2016.
- [4] Bankston S, Mo C. Geometry Modification of Flywheels and its Effect on Energy Storage. Energy Research Journal 2015;6(2):54–63. DOI: <https://doi.org/10.3844/erjsp.2015.54.63>
- [5] IRENA - International Renewable Energy Agency. Electricity Storage and Renewables: Costs and Markets to 2030. International Renewable Energy Agency, Abu Dhabi; 2017.
- [6] Ribeiro MR. Sistema Armazenador de Energia Cinética SAEC - Estratégia de Controle e Simulações. Rio de Janeiro: MSc thesis - COPPE/UFRJ, Brazil; 2008.
- [7] Roe G. Boeing Flywheel Energy Storage Technology. Seattle: Boeing Research & Technology, USA; 2012.
- [8] Hedlund M, Lundin J, de Santiago J, Abrahamsson J, Bernhoff H. Flywheel Energy Storage for Automotive Applications. Energies 2015;8:10636–10663. DOI: [10.3390/en81010636](https://doi.org/10.3390/en81010636)
- [9] Ashby MF. Materials Selection in Mechanical Design. Fifth edition, Elsevier Ltd., Cambridge, United States; 2017. 17
- [10] Wang B. CNT bundle material for flywheels 40 times better than batteries; 2018. Available in: <https://www.nextbigfuture.com/2018/10/cnt-bundle-material-for-flywheels-40-times-better-thanbatteries.html>
- [11] Coppede D. Análise por Simulação de Materiais Conjugados para Baterias Eletromecânicas. São Paulo: MSc thesis - IFSP, Brazil; 2018.
- [12] BORTOLI FS *et al.* On the Massive Antenna Suspension System in the Brazilian Gravitational Wave Detector SCHENBERG. *Brazilian Journal of Physics*; 2016; 46: 308. DOI: [10.1007/s13538-016-0413-8](https://doi.org/10.1007/s13538-016-0413-8)
- [13] ANDRADE LA *et al.* Ultra-low phase noise 10 GHz oscillator to pump the parametric transducers of the Mario Schenberg gravitational wave detector. *Class. Quantum Grav.*; 2004; 21: 1215 DOI: [10.1088/0264-9381/21/5/122](https://doi.org/10.1088/0264-9381/21/5/122)
- [14] BORTOLI FS *et al.* A physical criterion for validating the method used to design mechanical impedance matchers for Mario Schenberg's transducers. *Journal of Physics: Conference Series* 2010, 228, 012011. DOI: [10.1088/1742-6596/228/1/012011](https://doi.org/10.1088/1742-6596/228/1/012011)
- [15] SOLIDWORKS website: <https://www.solidworks.com/>
- [16] Nogueira PRM. Otimização de Geometria e Material para Baterias Eletromecânicas. São Paulo: MSc thesis - IFSP, Brazil; 2016.
- [17] MatWeb - The Online Materials Information Resource. Available in: <http://www.matweb.com/>
- [18] Kress GR. Shape optimization of a flywheel. *Structural and Multidisciplinary Optimization* 2000;19:74–81.



# MODELLING AND CONTROL OF A HYBRID WIND SOLAR SYSTEM OPTIMIZED BY FUZZY BASED MPPT CONTROLLER

Mennad Mebrouk

ICEPS Laboratory, Engineer Sciences Faculty, Djillali Liabès University, Sidi Bel-Abbès (22000), ALGERIA.  
Email: mabroukmenad@gmail.com (Corresponding author), ORCID: 0000-0002-8772-6984

Bentaallah Abderrahim

ICEPS Laboratory, Engineer Sciences Faculty, Djillali Liabès University, Sidi Bel-Abbès (22000), ALGERIA,  
Email: bentaallah65@yahoo.fr

Djeriri Yousef

ICEPS Laboratory, Engineer Sciences Faculty, Djillali Liabès University, Sidi Bel-Abbès (22000), ALGERIA,  
Email : djeriri\_youcef@yahoo.fr

AmeurAissa

LeDMAcScD Materials, Laboratory, Electrical Engineering Department, Laghouat University, Laghouat (03000),  
ALGERIA, Email: amaissa1@gmail.com

Bessas Aicha

LACoSERE Laboratory, Electrical Engineering Department, Amar Telidji University, Laghouat (03000),  
ALGERIA, Email : ai.bessas@lagh-univ.dz, ORCID: 0000-0002-8531-3852

*Cite this paper as:* Mennad, M, Bentaallah, A, Djeriri, y, Ameur, A, Bessas, A, Modelling and control of a hybrid wind solar system optimized by fuzzy based mppt controller. 9th Eur. Conf. Ren. Energy Sys.21-23April 2021, Istanbul, Turkey.

**Abstract:** In this paper, we study the performance and reliability of hybrid power source (HPS) system of two photovoltaic (PVG) and wind (PMSG) generators, redundant by lithium type batteries on the DC bus. In the first part, we present the mathematical model making it possible to calculate the power delivered by the module of photovoltaic generator; the efficiency of highly non-linear PV system can be improved by using the maximum power point tracking technique, such as the Perturbation-Observation (P&O) method and the Fuzzy approach. Then, we give the modeling of lithium-ion batteries because they can now claim to be storage device restoring energy to comfortable and stable power level, therefore the charge is controlled through flow converters. In the second part, we develop the mathematical model according to the design of an aero generator (PMSG) based essentially on the modeling of significant wind deposits in certain power known as the BELTZ limit Cp. In order to minimize the current harmonics of the hydride system via the two-level inverter to the grid, we propose a vector modulation control (SVPWM), from which we have implemented a passive filtering of the second order. Finally, we studied the feasibility and synchronization of the hybrid system while maintaining the performance of the electrical network, in Phase Locked Loop (PLL) which is integrated in the control blocks (VSC). The simulation results by MATLAB / Simulink present an acceptable performance of our stand-alone wind-solar hybrid system in a severe isolated and arid area.

**Keywords:** Photovoltaic generator, hybrid wind-Solar system, MPPT method, SVPWM, Fuzzy logic controller.

© 2021 Published by ECRES

Nomenclature		Nomenclature	
GPV	Photovoltaic Generator	SOC	State of Charge
PMSG	Permanent magnetic synchronous generator	NPC	Neutral point clamped
SVPWM	Space vector pulse width modulation	MPPT	Maximal Power Point Tracking
PWM	Pulse width modulation	MPP	Maximal Power Point

PLL	Phase locked loop	FLC	Fuzzy Logic Controller
DC-DC	Direct current/Direct	PI	Classic controller
DC-AC	Direct current /alternative	GA	Genetic algorithm
HPS	Hybrid power source	P&O	Perturb and observed

## 1. INTRODUCTION

The development of renewable hybrid wind-photovoltaic energy systems represents a large investment in technological research. These systems, which generate electrical energy from the wind and the sun, can constitute an economic alternative to various exhaustible energy sources, especially in isolated and arid regions [1]. Due to the non-linearity of solar and wind photo generators, we implemented the optimal technique called maximum power point (MPP) [2], in order to transfer the maximum energy supplied by Maximum Power Point Tracker (MPPT) in climatic conditions unfavorable [3].

In this article, we use the boost for hybridization of two sources solar and wind taken into consideration the point tracking of the maximum power, in the unfavorable climatic conditions (ie in excessive high temperature, insufficient radiation for solar energy and variable speed and Beltz limits for wind power). To ensure redundancy and perfect energy quality, a passive filter attached to the AC network through a two-level inverter controlled by SVM. Such ways are for ensuring synchronization of two sources in the HTA network (load).

For the improvement of the MPPT on the PVG side, we used a classic PI regulator then optimized by a fuzzy regulator in order to follow the incremental MPPT curve, including the P&O (Perturb and Observe) technique by the MPPT algorithm. However, the oscillation of the operating point of the system around its optimal position and along its transient period limits this method. On the other hand, PMSG its MPPT consists in the pursuit of the power of the turbine by the method of the gradient. This method requires the measurement of the power supplied and access to control the speed of rotation of the turbine ( $\Omega$  turbine) and the duty cycle (D) which is in direct relation with the DC / DC converter to have an output voltage. Well suited to the load. For both systems, the assembled regulators present a good solution in terms of dynamic response and better rejection of disturbances. The only drawback of the PI regulator is the determination of the range of its inputs and outputs. The range of each input or output differs from one PVG to another. To overcome this drawback, the genetic algorithm (GA) is used to calculate the optimal gains for each input and output. Such an optimal PI could provide ideal control performance and achieve the desired MPPT [3], [4].

## 2. MODELING OF A PHOTOVOLTAIC GENERATOR

In this paper, we use two-diode model to simulate the photovoltaic cell, a PVG composed of 576 cells in series and 8 columns in parallel. The electrical equation is given by:

$$I_g = I_{phg} - I_{s1g} \left[ \exp \left( q \frac{(V_g + R_{sg} I_g)}{n_s n_1 K T} \right) - 1 \right] - I_{s2g} \left[ \exp \left( q \frac{(V_g + R_{sg} I_g)}{n_s n_2 K T} \right) - 1 \right] - \frac{(V_g + R_{sg} I_g)}{R_{pg} I_g} \quad (1)$$

Figures 1 represent respectively the current and power characteristics in function of voltage, with  $T = 298K$  and  $E = 1000W/m^2$ .

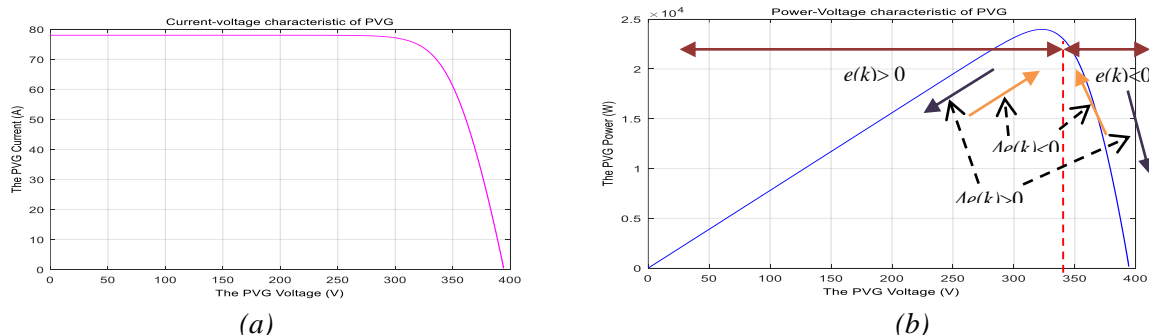


Figure 1. (a) Current-voltage characteristic of PVG, (b) Power-voltage characteristic of PVG.

## 3. BATTERY BANK MODEL

Modeling of batteries by the electrical equations below:

$$I_{MR}(t) = I_{BB}(t) - I_{GAZ}(t) \quad (2)$$

$$\begin{aligned} I_{MR} &: \text{Main battery reaction current (A)} & T_{BB} &: \text{Battery Temperature (K)} \\ I_{BB} &: \text{External battery current (A)} & V_B &: \text{Battery charging voltage (V).} \\ I_{GAZ} &: \text{Battery gassing current (A)} \end{aligned}$$

The capacity is:

$$C_B(t) = \int_{t=0}^t I_{MR}(t) * dt + C_{B,i} \quad (3)$$

With:  $C_B$ : battery capacity (Ah),  $C_{B,i}$ : Initial battery capacity (Ah).

The battery voltage as a function of SOC is given by [5]:

$$U_{bat} = U_{100\%} - \Delta U * (1 - soc) \quad (4)$$

The SOC calculation formula:

$$soc = Q_{bat} / Q_{nom.bat} \quad (5)$$

#### 4. P&O MPPT METHOD

The *P&O* algorithm, which track the MPP delivered by the PVG[3], for control PWM signal [6].

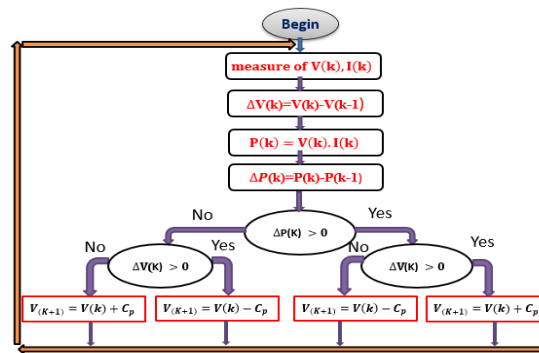


Figure 2. The *P&O* flow chart.

#### 5. DESIGN OF A FUZZY LOGIC CONTROLLER

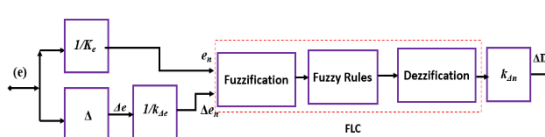


Figure 3. Block diagram of speed fuzzy logic controller.

Table 1.FLC rules base

$e \downarrow$	$\Delta e \rightarrow$	NB	NS	ZO	PS	PB
NB	ZO	ZO	PB	PB	PB	
NS	ZO	ZO	PS	PS	PS	
ZO	PS	PS	ZO	ZO	NS	
PS	NS	NS	NS	ZO	ZO	
PB	NB	NB	NB	ZO	ZO	ZO

In the case of using a *GA* method to tune the *FLC* gains in the speed control loop, the fitness function used to evaluate the individuals of each generation can be chosen to be the integral times of absolute error see [8].

#### 6. MODELING OF THE WIND CHAIN

##### THE COEFFICIENT LINKS WIND POWER TO WIND SPEED [9]:

$$Cp(\lambda, \beta) = A_{1*} \left[ \left( \frac{A_2}{\lambda_i} \right) - A_3 * \beta - A_4 \right] * e^{\frac{A_5}{\lambda_i}} + A_6 * \lambda \quad (6)$$

With:  $\frac{1}{\lambda_i} = \frac{1}{\lambda + 0.008 * \beta} - \frac{0.035}{\beta^3 - 1}$ ,  $A_1 = 0.5$ ,  $A_2 = 116$ ,  $A_3 = 0.4$ ,  $A_4 = 5$ ,  $A_5 = -21$ ,  $A_6 = 0.0068 .0777020$ .

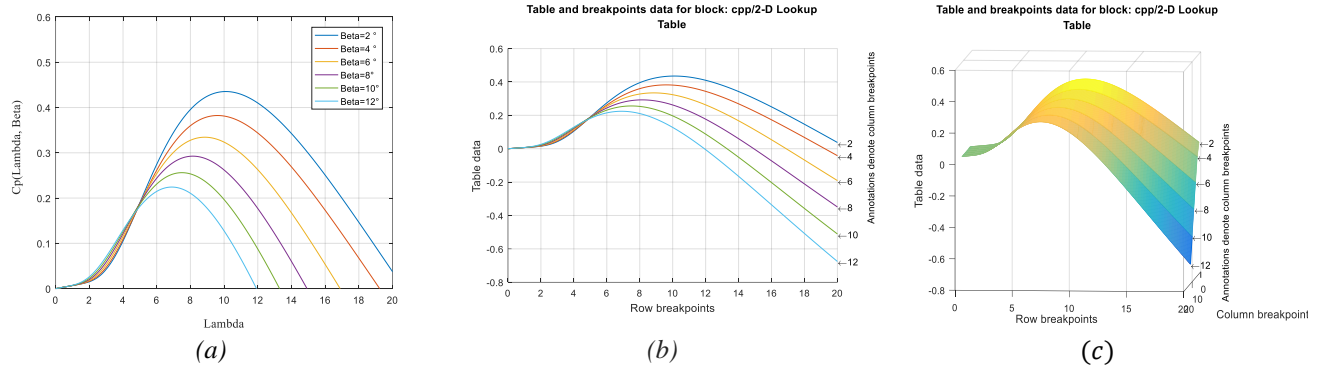


Figure 4. (a)  $C_p(\lambda, \beta)$  Model choice, (b)  $C_p(\lambda, \beta)$  model choice with lockup table graph, (c)  $C_p(\lambda, \beta)$  model choice with lockup table data.

The synchronous generator PMSG model by the following equations Park's transformation [7] :

$$\begin{aligned} \frac{d\varphi_{ds}}{dt} &= u_{ds} + R_s i_{ds} - \omega_e \varphi_{qs} \\ \frac{d\varphi_{qs}}{dt} &= u_{qs} + R_s i_{qs} + \omega_e \varphi_{ds} \\ \frac{d\varphi_0}{dt} &= u_0 - R_s i_o \\ \frac{d\varphi_r}{dt} &= u_r - R_r i_r \end{aligned} \quad (7)$$

$$\begin{aligned} \varphi_{ds} &= L_{ds} i_{ds} - \varphi_m \\ \varphi_{qs} &= L_{qs} i_{qs} \\ \omega &= \frac{d\theta}{dt} \end{aligned} \quad (8)$$

$$p(t) = \frac{3}{2} (U_d i_d + U_q i_q) + 3 U_0 i_0 - U_r i_r \quad (9)$$

$$d\omega_{mec} = \frac{3}{2} \omega (\varphi_d i_q - \varphi_q i_d) dt = T_{em} \theta dt \quad (10)$$

$$T_{em} = \frac{3}{2} P (L_d - L_q) i_d i_q + L_{ra} i_r i_q \quad (11)$$

## 7. SIMULATION RESULTS

Performances of photovoltaic generator: The figures that follow represent the performances of our photovoltaic generator using MATLAB / Simulink. All the characteristics are obtained using a fast-varying load.

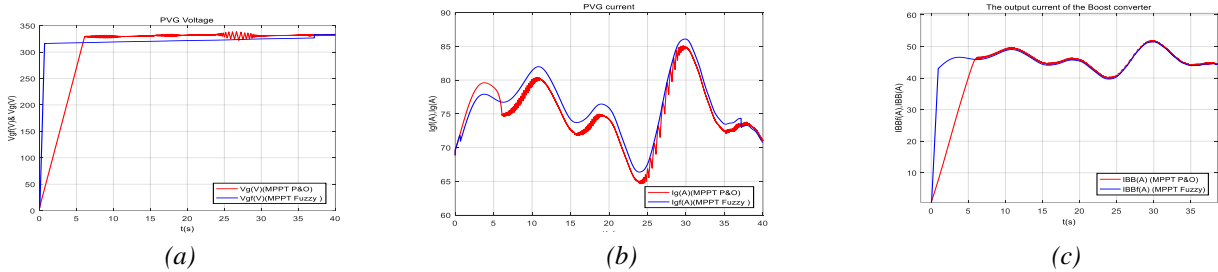


Figure 5. (a) Optimal voltage of the PVG, (b) Optimal Current of the PVG, (c) Charging current and voltage of batteries.

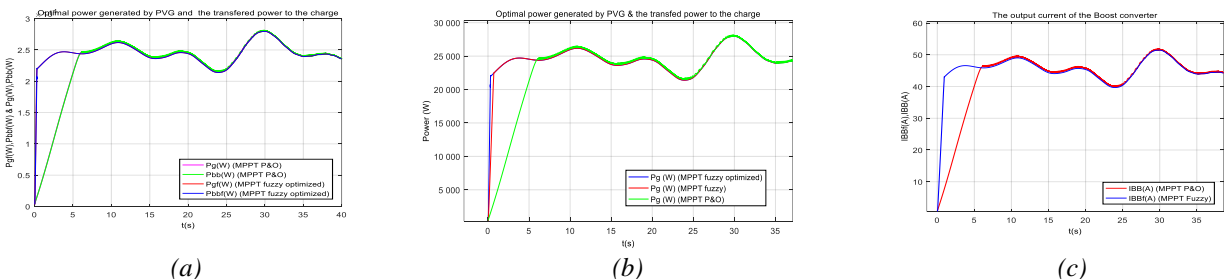


Figure 6. (a) Optimal power of PVG and the power transferred, (b) Optimal power by PVG & FLC optimized Gains, (c) Output current of the boost converter.

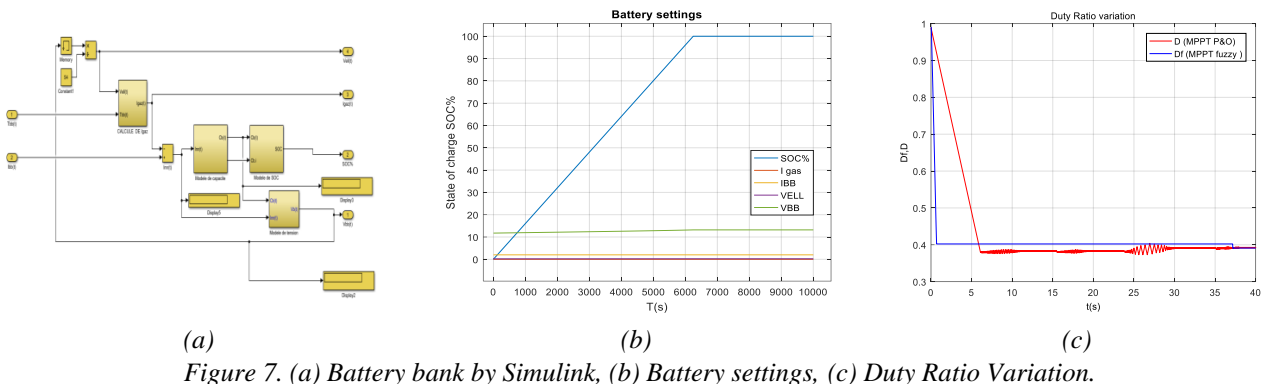


Figure 7. (a) Battery bank by Simulink, (b) Battery settings, (c) Duty Ratio Variation.

Figure 5 (a) and (b) shows the shape of two variable and stable states and the output voltage and current of the PVG. The steady state takes place after 5.3 sec in *MPPT P&O*, and 1 sec by *FLC*, knowing that we have used fast varying load to get both states. Figure 5 (c) shows the output voltage and current of the boost converter, we notice that there is no clear start-up state in the output voltage curve which comes back to the use of the batteries. Figure 7 (c) shows the variation of the Duty Ration during the start-up and steady states. It starts by an initial value (0.99) then decreases around 0.38 which meet the steady states in the case of *P&O*. The constant value of Duty Ration with *FLC* is 0.4, we observe that despite the fast variations and the sudden changes in temperature and solar radiation, our tracker (controller) has reached its goal to transfer the maximum power from the photovoltaic generator to the load. We note also that the results obtained by the fuzzy controller is better, in terms of strength the changes of meteorological parameters, and point of view of the step size increment that variable in the case of a fuzzy controller. In figure 6 (b), it can be seen that the proposed FLC-based *GAs* can improve the dynamic and steady state performance of the PV system simultaneously.

## PERFORMANCES OF THE WIND CHAIN:

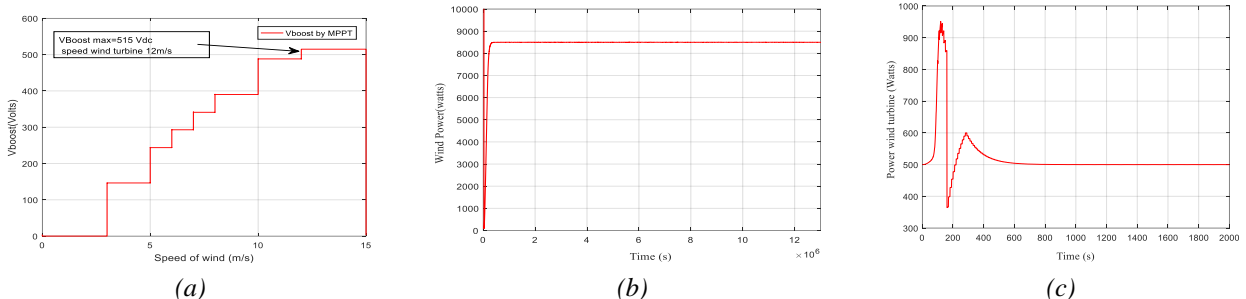


Figure 8. (a) Variation of voltage boost by speed wind turbine, (b) Variation of the wind power,(c) Variation of the power of the turbine

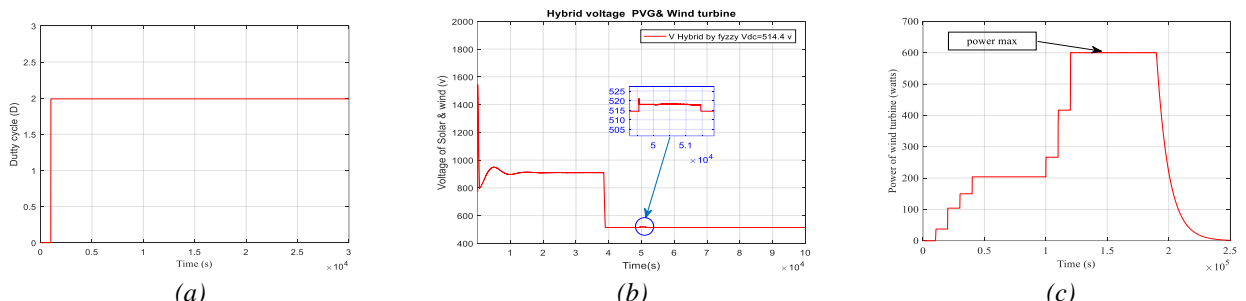


Figure 9. (a)Techniques of the MPPT of the wind turbine and its action on the duty cycle, (b) Variation of boost output voltage, (c) power of the wind turbine depending on the wind speed.

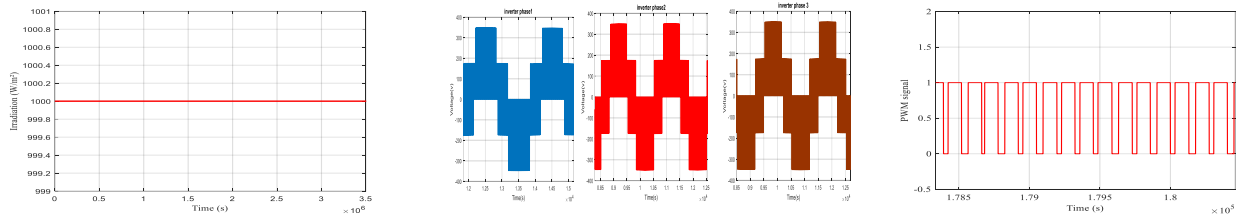


Figure 10. (a)Variation of irradiation, (b) The phase-to-neutral Voltages  $V_{abc}$  of the inverter ( $P_{pv}$ ), (c) Duty cycle of MPPT.

### Simulations of the hybrid PV-wind system:

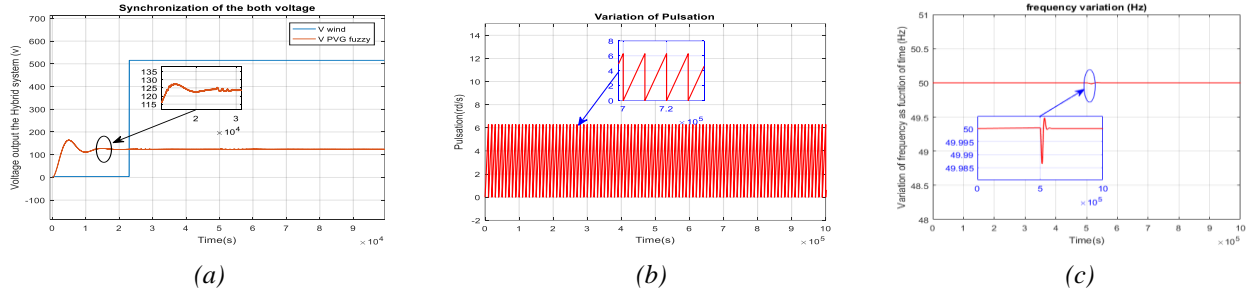


Figure 11. (a) Synchronization of the both voltage DC, (b) Variation of pulsation,(c)Variation of frequency.

### Connection of the hybrid system to the industrial network:

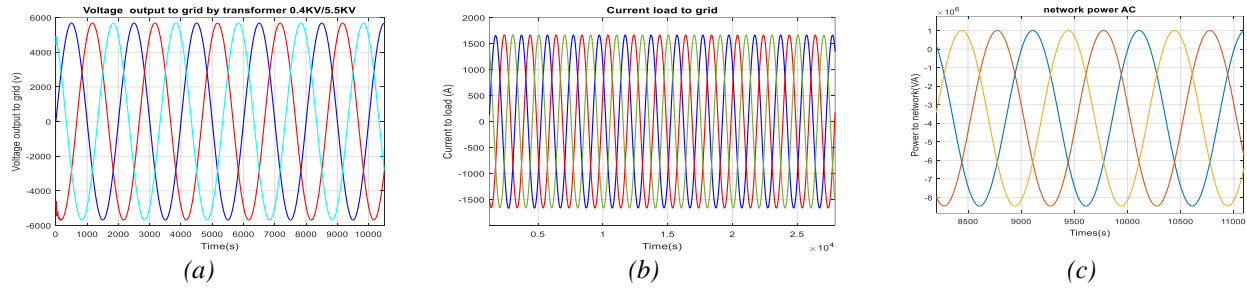


Figure 12. Three-phase voltage of the distribution network, (b) Three-phase current if distribution network, (c) Three -phases Power AC network.

**Full hybrid system model:** The complete system consisting of the solar model, the wind model, and the energy distribution network is presented below simulating the optimal power outputs of the solar and wind systems:

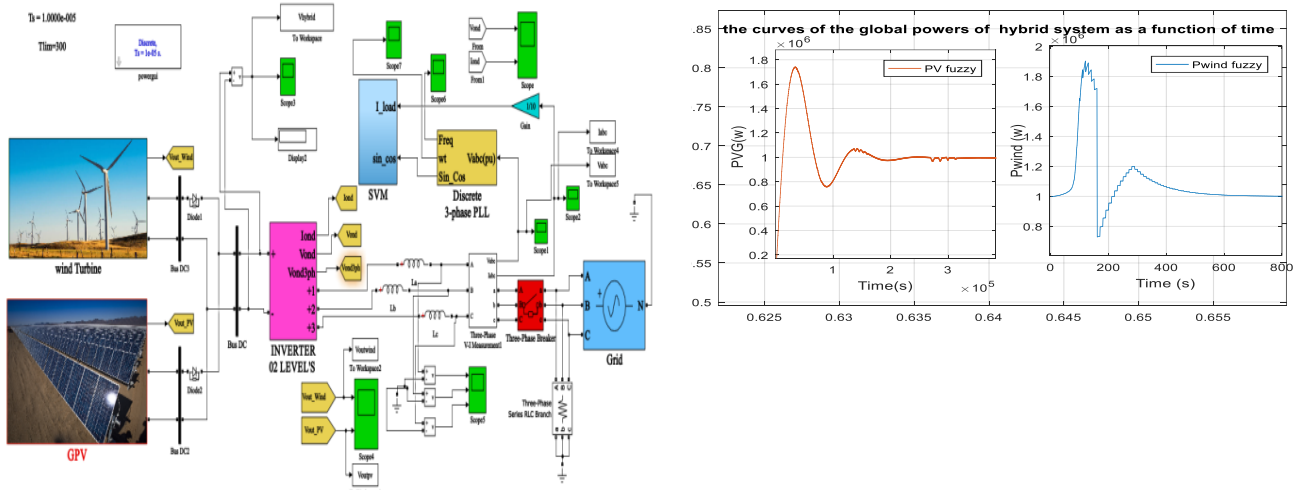


Figure 13. Scheme of the Hybrid System model connected to the distribution.

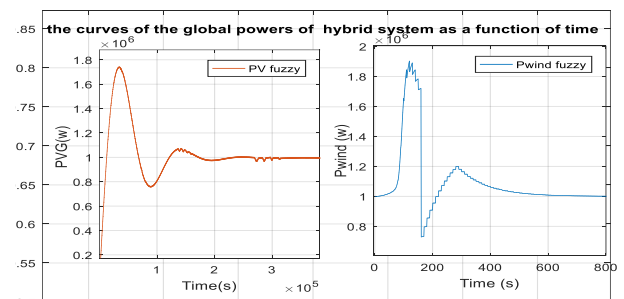


Figure 14. The curves of the global powers of the hybrid system.

From figure 28, 29 and 30 it is clear that the voltages and currents of the power system are sinusoidal with the same frequency of 50 Hz, and which are out of phase with each other. The figure 31 shows the curves of the global powers of the hybrid system. It should be noted that the photovoltaic power PV varies proportionally with the wind power  $P_{wind}$  and the resultant of two powers follow the injection power to the network. We notice a total synchronism between the power of the hybrid system and that of the network, which is explained by the command provided by the discrete SPS command which controls the connection with respect to the frequency by the PLL loop and also the voltage.

## 8. CONCLUSION

In this article, we have modelled a photovoltaic generator using the double exponential model. The characteristics of the PVG are highly dependent on the meteorological parameters, it is necessary to choose the MPP in order to achieve the maximum performance of the PVG. For this, we used the P&O method optimized by FLC based on GA proposed to ensure the robustness of classic FLC controller. Moreover, it was concluded that FLC method based on GA methods are the best among the different smart types of MPPT methods. Hence, the assured reliability as well as the economic and ecological factor.

In the second part, we proceeded to the modeling of a PMSG in order to choose the  $C_p(\lambda, \beta)$  for choice of performances and robustness of the wind turbine to reach the BELTZ limit at most 0.59. The results of the simulation shows a good behavior against hybridization..

In the last part we present the hybridization of a global renewable energy system, synchronized to the electricity grid through a step-up transformer thanks to a two-level inverter associated with a second-order passive filter by SVPWM. From these simulation results, the performance characteristics are quite acceptable from the point of view of the validation of the model.

## REFERENCES

- [1] ZhangY, Jianguo Z. Direct torque control of permanent magnet synchronous motor with reduced torque ripple and commutation frequency. In *IEEE Transactions on Power Electronics*: 26.1 (2010): 235-248.
- [2] Aït Cheikh M.S, Hadj AïssaB, MalekA, BecherifM. Mise au point d'une régulation floue pour serre agricole à énergie solaire. *Renewable Energies Review* Vol. 13 No 3 (2010) 421 - 443.
- [3] Adhikari, S, Fangxing L. Coordinated Vf and PQ control of solar photovoltaic generators with MPPT and battery storage in microgrids. In *IEEE Transactions on Smart grid* 5.3 (2014): 1270-1281.
- [4] LunardiM.M, Alvarez-Gaitan J-P, Bilbao J-I, Corkish R. A review of recycling processes for photovoltaic modules." In *A Review of Recycling Processes for Photovoltaic Modules, Solar Panels and Photovoltaic Materials*, DOI: 10.5772/intechopen.74390.
- [5] LI, Xiangjun, LI, Nan, JIA, Xuecui, et al. Fuzzy logic based smoothing control of wind/PV generation output fluctuations with battery energy storage system. In: 2011 International Conference on Electrical Machines and Systems. IEEE, 2011. p. 1-5..
- [6] Sathishkumar, S., M. ValanRajkumar, and R. Yuvaraj. "Modeling and Analysis of Soft-Switched Interleaved Boost Converter for Photovoltaic System." *International Journal for Science and Advance Research in Technology (IJSART)* 2.11 (2016): 43-48.
- [7] ElbejiO,HannachiM, BenhamedM, Sbita. Artificial neural network-based sensorless control of wind energy conversion system driving a permanent magnet synchronous generator. *Wind Engineering* (2020): 0309524X20903252.
- [8] Unai F-G, Ekaitz Z, Boyano A, Igor A, Irantzu U. Five-megawatt wind turbine power output improvements by passive flow control devices. *Energies* 10.6 (2017): 742. <http://creativecommons.org/licenses/by/4.0/>
- [9] Kokila, A., KumarV. S. Comparison of SPWM and SVPWM control techniques for diode clamped multilevel inverter with photovoltaic system. In: 2018 4th International Conference on Electrical Energy Systems (ICEES). IEEE, 2018. p. 234-241.



# ENERGY PRODUCTION USING WATER COLLECTORS SUBJECTED TO SOLAR RADIATION TO IMPROVE BUILDING INDOOR THERMAL CONDITIONS

Eusébio Conceição

FCT – Universidade do Algarve, Faro, Portugal, econcei@ualg.pt, ORCID: 0000-0001-5963-2107

João Gomes

CINTAL, Faro, Portugal, jgomes@ualg.pt, ORCID: 0000-0002-0346-6207

M Manuela Lúcio

FCT – Universidade do Algarve, Faro, Portugal, maria.manuela.lucio@gmail.com, ORCID: 0000-0003-3243-3831

André Ramos

FCT – Universidade do Algarve, Faro, Portugal, aframos@ualg.pt, ORCID: 0000-0003-2205-8142

Hazim Awbi

School of Built Environment - University of Reading, Reading, United Kingdom, h.b.awbi@reading.ac.uk, ORCID: 0000-0003-0201-3801

*Cite this paper as:* Conceição, E., Gomes, J., Lúcio, MM., Ramos, A., Awbi, H. Energy production using water collectors subjected to solar radiation to improve building indoor thermal conditions. 9th Eur. Conf. Ren. Energy Sys. 21-23 April 2021, Istanbul, Turkey

**Abstract:** This article presents a numerical study on the energy production in solar thermal collectors in a University building used to improve the internal thermal comfort conditions. This numerical study was carried out for winter conditions using a software that simulates the Building Dynamic Response with complex topology in transient conditions. The software is used to assess the human thermal comfort and indoor air quality levels, the energy consumption of the Heated Ventilation and Air-Conditioned (HVAC) system, indoor thermal variables and other parameters. The building has 107 compartments, of which 33 are for classes. The heating system is based on the use of solar energy collected by solar thermal collectors installed on the roof of the building and on the distribution of heat throughout the rooms using internal thermal convectors. The thermal comfort level, using the Predicted Mean Vote (PMV) index, and the indoor air quality, using the carbon dioxide concentration, are evaluated. The HVAC system is monitored and controlled by the PMV index. The results show that the implemented HVAC system allows to guarantee acceptable levels of thermal comfort and indoor air quality.

**Keywords:** Energy, Indoor air quality, PMV index, Solar thermal collector, Thermal comfort

© 2021 Published by ECRES

## 1. INTRODUCTION

The building sector is one of the main consumers of energy and greenhouse gas emissions in the European Union (EU), with around 40% of annual primary energy consumption and 36% of annual carbon dioxide (CO<sub>2</sub>) emissions [1]. This importance is reflected in EU directives that establish measures, reasons and procedures for the introduction of energy saving measures and the rational use of energy in buildings [2,3].

Solar energy is a renewable, effective, safe and environmentally sustainable energy resource. In recent years there has been a rapid development of technologies related to the use of solar energy and a continuous reduction in the cost of equipment associated with it. As a result, the supply of energy to buildings has been increasingly provided by solar thermal and photovoltaic energy.

The growing use of Heated Ventilation and Air Conditioning (HVAC) systems has contributed to the increase in energy consumption in buildings in Portugal. The development of HVAC systems that use renewable and sustainable energy sources, particularly solar energy, is, in this context, very relevant because it will allow to obtain acceptable levels of thermal comfort and indoor air quality with low primary energy consumption. The installation of solar thermal panels in the building, for heating its compartments in winter conditions, may be a practicable, efficient and low-consumption solution, so its development and study of its implementation is fully justified.

A solar collector is a device designed to harness the sun's energy, a particular type of heat exchanger that converts solar radiation into useful heat that can be transported. Its operation is based on the absorption of incident solar radiation, conversion to heat and transfer of that heat to a fluid (usually air, water, or a special heat transfer fluid) flowing through the collector. The energy of the circulating fluid can be used directly by a heat-demanding process or be transferred to a thermal energy storage tank [4]. In the review work done by Kalogirou et al. [5] it can be seen the several types of solar collectors, solar energy conversion processes and applications of solar thermal systems. In the review work of Suman et al. [6], it was analyzed several techniques (geometrical absorber plate changes, use of solar selective coatings and nanofluids) used to improve the performance of solar collectors. In the review work of Jamar et al. [7], it was analyzed the solar water heating systems, specially their three main components which are solar collectors (flat plate collector, evacuated tube collector, parabolic dish reflector, parabolic trough collector), storage tanks (single unit and integrated unit) and heat transfer fluids (water, glycol groups, silicon oils, hydrocarbon oils, nanofluids).

The thermal comfort of the occupants is usually assessed by the comfort indices Predicted Percentage of Dissatisfied (PPD) and Predicted Mean Vote (PMV), developed by Fanger [8], and later integrated into international standards as ASHRAE 55 [9] and ISO 7730 [10]. Three thermal comfort categories (A, B and C) for occupants in conditioned spaces are defined in ISO 7730 [10]. As example of the application of the PMV and PPD indices in the evaluation of the thermal comfort in buildings, the works of Fabbri [11] and Pourshaghaghy and Omidvari [12] can be conferred. The indoor air quality can be evaluated by CO<sub>2</sub> concentration [13,14].

The software used in this study has been developed by the authors over the years and simulates the Building Dynamic Response. It is used, among others, to evaluate the air temperature distribution, surfaces temperature distribution and energy consumption [15,16]. This software uses PMV/PPD indices to evaluate the occupants' thermal comfort [17], it has implemented the adaptive thermal comfort model [18], and temperature control model [19], and a HVAC system control methodology based on PMV index [17]. The results obtained from this software can also be used by a coupling of Computer Fluid Dynamics and Human Thermal Response numerical models to assess each occupant thermal comfort level and the airflow topology used within each space [20-24].

The aim of this numerical work is to assess the indoor air quality and occupants' thermal comfort when it is applied a new methodology of heating all occupied spaces of a university building with large dimensions. The heating process is based on the solar energy obtained from solar thermal collectors placed on the roof of the building used to heat water that will act as the transport fluid. The transported heat will be transferred to the occupied spaces through thermo-convector. The HVAC system, based on a set of thermo-convector, will be controlled by a PMV index control system in order to guarantee acceptable thermal comfort levels within category C [10].

## **2. NUMERICAL MODEL**

The numerical simulation is done by a software used to assess the Building Dynamic Response. The numerical model used in the Building Dynamic Response software was presented in [25,26]. All main equations and coefficients were introduced in these works [25,26]. Although the applications are different, the thermal response, the energy flow and the thermal comfort were analyzed in detail in these works [25,26].

This numerical model is used to calculate the temperatures of indoor spaces, opaque bodies (ceiling, floor, walls, others, transparent bodies (windows and similar) and interior bodies. The numerical model also calculates the concentration of contaminants (CO<sub>2</sub> concentration and others) and water vapor.

In this work, the level of indoor air quality is evaluated by the CO<sub>2</sub> concentration [13,27]. The level of thermal comfort is evaluated by the PMV index [10]. The PMV index takes into account environmental and personal parameters. The environmental parameters are the mean air velocity, mean air temperature, mean air relative humidity, and mean radiant temperature. The personal parameters are the activity and clothing levels. Performance monitoring and control of the HVAC system will be carried out using the PMV index.

### 3. NUMERICAL METHODOLOGY

In the simulation performed in this work, it is used a university building (Figure 1), identical to a real building, consisting essentially of classrooms, amphitheaters and a large auditorium. The building has 125 transparent surfaces, 1550 opaque surfaces and 107 compartments distributed between a ground floor and two upper floors, where teaching activities take place. The HVAC system will only be applied to the 33 occupied spaces.

This numerical simulation considers that when the spaces are occupied, it was used an airflow rate calculated according to standard [13]. When spaces are not occupied, it was used an airflow rate of one air renewal per hour. In the numerical simulation, it was considered that the classrooms are occupied, in general, by periods of 90 minutes, with breaks of 15 minutes between periods. The occupancy cycle occurs between 8:00 am and 6:45 pm. The average occupancy considered in the classrooms was 20 occupants in the medium-sized rooms (room 95) and 40 occupants in the larger rooms (rooms 94, 103 and 104). As the numerical simulation was performed for typical winter conditions, it was defined a clothing level of 1 clo [10]. The level of activity considered was 1.2 met [10].

The numerical solar heating system is constituted by 611 solar thermal collectors (with dimensions  $2 \times 1.1 \text{ m}^2$ ) installed on the roof of the building (Figure 1) to provide heat to the air conditioning system, in winter conditions. The heated water in the collectors is transported to a storage tank located in a space below the building at the level of the ground floor. From the storage tank it is distributed throughout the building by a system of thermally insulated pipes.

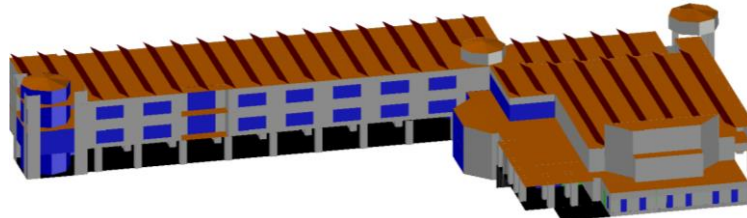


Figure 1. North-west view of the external perspective of the university building, with solar thermal collectors (dark red colour) installed on the roof.

The HVAC system considers thermo-convector installed on the ceiling of each occupied spaces. The HVAC system will be operated by a PMV index control system in order to guarantee acceptable thermal comfort levels within category C ( $-0.7 \leq \text{PMV} \leq +0.7$ ) [10]. Figure 2 shows the top view of the rooms 94, 95, 103 and 104 located on the second floor and analysed in the numerical simulation. The windows in rooms 94 and 104 face east, while the windows in rooms 95 and 103 face west. Figure 3 shows the flow diagram of the fluid used in the piping circuits. Two simulations were carried out, one using the solar thermal collector system and the other without using it.

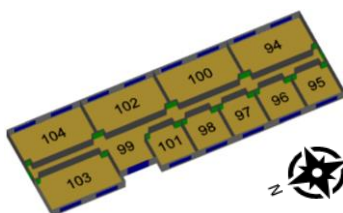


Figure 2. Top view of the rooms on the second floor.

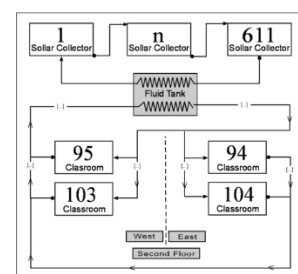


Figure 3. Flow diagram of the fluid used in the piping circuits.

### 4. RESULTS AND DISCUSSION

This section presents the results obtained of indoor air quality level (Figure 4), using CO<sub>2</sub> concentration, indoor air temperature (Figure 5), and indoor mean thermal comfort level (Figure 6), using PMV index, for four classrooms, two with east-facing windows (rooms 94 and 104) and two with west-facing windows (rooms 95 and 103). Figures 6 and 7 also shown, comparatively, the evolution of indoor air temperature and PMV index without and with the application of the solar thermal collector system.

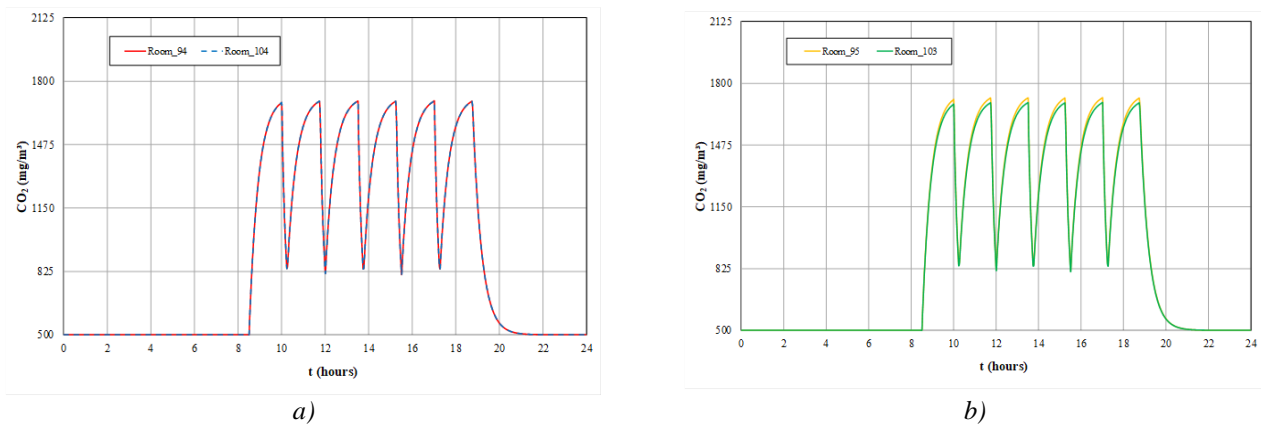


Figure 4. Evolution of CO<sub>2</sub> concentration, in winter conditions: a) classrooms 94 and 104; b) classrooms 95 and 103.

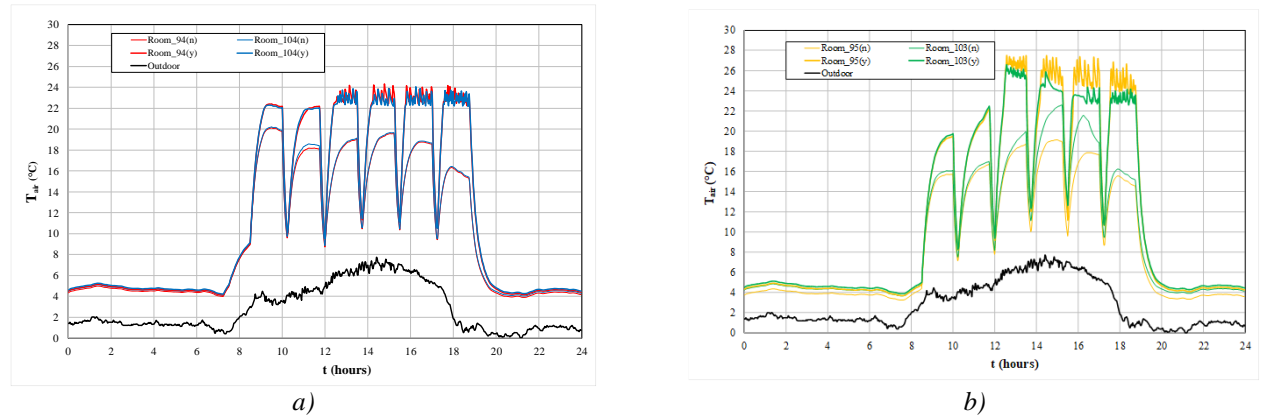


Figure 5. Evolution of indoor air temperature (T<sub>air</sub>), in winter conditions: a) classrooms 94 and 104; b) classrooms 95 and 103. The thin line is associated with no (n) solar HVAC system, while the thick line is associated with (y) solar HVAC system.

The results from the evolution of the CO<sub>2</sub> concentration show that, during occupancy, the ventilation topology used guarantees an acceptable indoor air quality level according to the standard [13], with all CO<sub>2</sub> concentration values below the accepted limit of 1800 mg/m<sup>3</sup>.

The use of the solar HVAC system makes it possible to increase the indoor air temperature between 2°C in the morning and 7°C in the late afternoon in the compartments with windows facing East. In these compartments it is possible to maintain an indoor air temperature practically constant throughout the day, with values around 22-23°C. It is noted that, during the morning, the thermal energy available that allows to increase the indoor air temperature of these compartments comes essentially from the solar radiation on their windows. In compartments with west-facing windows, the indoor air temperature increases between 4°C in the morning and 10°C in the late afternoon. In these compartments it is possible to maintain an indoor air temperature around 20°C during the morning, and between 24°C and 26°C during the afternoon. These compartments have more thermal energy available than compartments with east-facing windows because, during the afternoon, the solar radiation on their windows reinforces the thermal energy provided by the solar HVAC system. In the morning, the performance of the HVAC solar system is not very significant because it does not have enough thermal energy.

When the space is occupied and the solar HVAC system is used, the control of this system through the PMV index allows to guarantee acceptable thermal comfort levels within category C [10] (PMV between -0.7 and +0.7) by negative values of PMV index. The HVAC solar heating system is connected when the PMV value is lower than -0.7 and disconnected when the PMV value is higher than -0.7. In compartments with east-facing windows, it appears that the PMV index remains around -0.7 throughout the daily occupancy cycle, with only slightly uncomfortable values for the PMV index during the morning. In compartments with west-facing windows, it appears that the PMV index remains around -0.7 when the compartments are occupied during the afternoon. During the morning, these compartments are uncomfortable due to negative values of the PMV index, but close to the acceptable limit.

The results of the simulation, carried out for winter conditions, show that the solar HVAC system produces enough energy to provide acceptable thermal comfort level in almost all rooms throughout the occupation regime. The exception is the west-facing windows compartments in the morning. All rooms have acceptable indoor air quality level throughout the day.

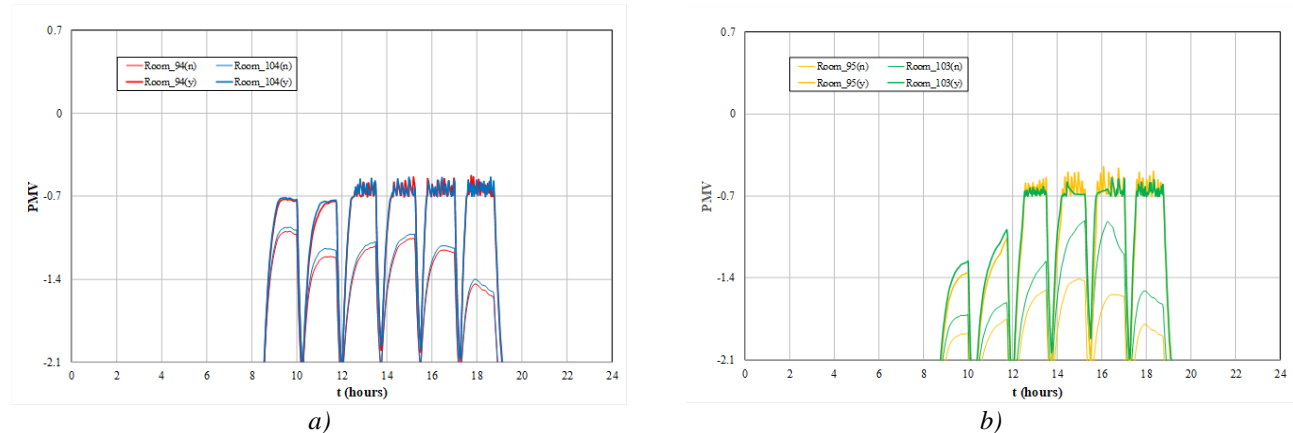


Figure 6. Evolution of PMV index, in winter conditions: a) classrooms 94 and 104; b) classrooms 95 and 103. The thin line is associated with no (n) solar HVAC system, while the thick line is associated with (y) solar HVAC system.

Table 1 shows the results obtained from the daily consumption of thermal energy in the analyzed compartments. The greatest daily thermal energy consumption is seen in the compartments with a larger area and also greater occupation. Compartment 94 is the one with the highest daily thermal energy consumption and compartment 95 is the one with the lowest daily thermal energy consumption.

Table 1. Daily thermal energy consumption

Compartment	Energy (kWh)
94	25.430
95	12.464
103	25.159
104	21.062

#### 4. CONCLUSION

In this numerical work, the energy production in solar collectors in a university building used to improve the internal thermal conditions was analyzed for winter conditions. A Building Dynamic Response software was applied in the development of this work. In this work, an HVAC system was developed based on the use of solar energy produced in solar thermal collectors and with control through the PMV index.

The use of the solar HVAC system, with control of the PMV index, guarantees acceptable thermal comfort levels within category C [10], during the afternoon, in all rooms analyzed. During the morning, the thermal comfort levels are close to the acceptable level. It also allows the indoor air temperature to rise to 22-23°C in the rooms with east-facing windows and to 24-26°C in the rooms with west-facing windows. The ventilation topology selected also guarantees acceptable indoor air quality levels in all rooms analyzed.

#### ACKNOWLEDGMENT

The authors would like to acknowledge to the project (SAICT-ALG/39586/2018) from Algarve Regional Operational Program (CRESC Algarve 2020), under the PORTUGAL 2020 Partnership Agreement, through the European Regional Development Fund (ERDF) and the National Science and Technology Foundation (FCT).

#### REFERENCES

- [1] European Commission: Buildings. <https://ec.europa.eu/energy/en/topics/energy-efficiency/buildings> (last Accessed: 21 November 2020).
- [2] Directive 2002/91/EC of the European Parliament and of the Council of 16 December 2002 on the energy performance of buildings. <http://data.europa.eu/eli/dir/2002/91/oj> (last Accessed: 21 November 2020).
- [3] Directive 2010/31/EU of the European Parliament and of the Council of 19 May 2010 on the energy performance of buildings. (last Accessed: 21 November 2020).
- [4] Kalogirou, S. Solar thermal collectors and applications. Progress in Energy and Combustion Science 2004; 30(3):231–95.
- [5] Kalogirou, S, Karella, S, Braimakis, K, Stanciu, C, Badescu, V. Exergy analysis of solar thermal collectors and processes. Progress in Energy and Combustion Science 2016; 56:106–137.

- [6] Suman, S, Khan, M, Pathak, M. Performance enhancement of solar collectors - A review. *Renewable and Sustainable Energy Reviews* 2015; 49:192-210.
- [7] Jamar, A, Majid, Z, Azmi, W, Norhafana, M, Razak, A. A review of water heating system for solar energy applications. *International Communications in Heat and Mass Transfer* 2016; 76: 178-187.
- [8] Fanger, P. *Thermal Comfort: Analysis and Applications in Environmental Engineering*. Copenhagen, Denmark: Danish Technical Press, 1970.
- [9] ANSI/ASHRAE Standard 55. *Thermal Environmental Conditions for Human Occupancy*. Atlanta, GA, USA: American Society of Heating, Refrigerating and Air-Conditioning Engineers, 2017.
- [10] ISO 7730. *Ergonomics of the Thermal Environments - Analytical Determination and Interpretation of Thermal Comfort Using Calculation of the PMV and PPD Indices and Local Thermal Comfort Criteria*. Geneva, Switzerland: International Standard Organization, 2005.
- [11] Fabbri, K. Thermal comfort evaluation in kindergarten: PMV and PPD measurement through datalogger and questionnaire. *Building and Environment* 2013; 68:202-214.
- [12] Pourshaghaghy, A, Omidvari, M. Examination of thermal comfort in a hospital using PMV-PPD model. *Applied Ergonomics* 2012; 43:1089-1095.
- [13] ANSI/ASHRAE Standard 62-1. *Ventilation for Acceptable Indoor Air Quality*. Atlanta, GA, USA: American Society of Heating, Refrigerating and Air-Conditioning Engineers, 2016.
- [14] Conceição, E, Lúcio, M, Vicente, V, Rosão, V. Evaluation of local thermal discomfort in a classroom equipped with crossed ventilation. *International Journal of Ventilation* 2008; 7(3):267–277.
- [15] Conceição, E, Lúcio, M. Numerical study of the thermal efficiency of a school building with complex topology for different orientations. *Indoor and Built Environment* 2009; 18(1):41-51.
- [16] Conceição, E, Lúcio, M. Numerical study of the influence of opaque external trees with pyramidal shape on the thermal behaviour of a school building in summer conditions. *Indoor and Built Environment* 2010; 19(6):657-667.
- [17] Conceição, E, Gomes, J, Ruano, A. Application of HVAC systems with control based on PMV index in university buildings with complex topology. *IFAC PapersOnLine* 2018; 51(10):20-25.
- [18] Conceição, E, Nunes, A, Gomes, J, Lúcio, M. Application of a school building thermal response numerical model in the evolution of the adaptive thermal comfort level in the Mediterranean environment. *International Journal of Ventilation* 2010; 9(3):287-304.
- [19] Conceição, E, Lúcio, M, Ruano, A, Crispim, E. Development of a temperature control model used in HVAC systems in school spaces in Mediterranean climate. *Building and Environment* 2009; 44(5):871-877.
- [20] Conceição, E, Lúcio, M, Awbi, H. Comfort and airflow evaluation in spaces equipped with mixing ventilation and cold radiant floor. *Building Simulation* 2013; 6:51-67.
- [21] Conceição, E, Lúcio, M. Numerical and subjective responses of human thermal sensation. In: *Proceedings of the 6<sup>th</sup> Portuguese Conference on Biomedical Engineering*, Faro, Portugal, 11-12 June 2001.
- [22] Conceição, E, Rosa, S, Custódio, A, Andrade, R, Meira, M, Lúcio, M. Study of airflow around occupants seated in desks equipped with upper and lower air terminal devices for slightly warm environments. *HVAC&R Research* 2010; 16(4):401-412.
- [23] Conceição, E.: Evaluation of thermal comfort and local discomfort conditions using the numerical modelling of the human and clothing thermal system. In: *Proceedings of 7th International Conference on Air Distribution in Rooms, ROOMVENT 2000*; 9-12 July 2000: Elsevier, Amsterdam, pp. 131-136.
- [24] Conceição, E, Lúcio, M. Numerical simulation of the application of solar radiant systems, internal airflow and occupants' presence in the improvement of comfort in winter conditions. *Buildings* 2016; 6(3):38.
- [25] Conceição, E, Silva, M, André, J, Viegas, D. Thermal behaviour simulation of the passenger compartment of vehicles. *International Journal of Vehicle Design* 2000; 24(4):372-387.
- [26] Conceição, E, Lúcio, M. Numerical simulation of passive and active solar strategies in building with complex topology. *Building Simulation* 2010; 3:245-261.
- [27] Asif, A, Zeeshan, M, Jahanzaib, M. Indoor temperature, relative humidity and CO<sub>2</sub> levels assessment in academic buildings with different heating, ventilation and air-conditioning systems. *Building and Environment* 2018; 133:83–90.



# EVALUATION OF MECHANICAL AND THERMODYNAMIC PROPERTIES OF BaZn COMPOUND BY DFT

İlknur Kars Durukan

Gazi University, Ankara, Turkey, ilknurdurukan@gazi.edu.tr, ORCID: 0000-0001-5697-0530

Yasemin Oztekin Ciftci

Gazi University, Ankara, Turkey, yasemin@gazi.edu.tr, ORCID: 0000-0001-1796-0270

*Cite this paper as:* Kars Durukan, İ, Oztekin Ciftci, Y, Evaluation of mechanical and thermodynamic properties of BaZn compound by DFT. 9th Eur. Conf. Ren. Energy Sys. 21-23 April 2021, Istanbul, Turkey

**Abstract:** The mechanical and thermodynamic properties of the BaZn compound, which crystallizes in the B2 structure, have been studied by the first principles method based on the Generalized Gradient Approach (GGA) using the VASP program. Melting temperature, Debye temperature and directional sound velocities were determined using elastic constants. Low Young's and shear modulus showed this compound to be soft materials. BaZn intermetallic compound has brittle property according to Pugh criterion and Poisson ratio calculated from elastic constants. In addition, the low value in the Debye temperature determined the softness of the material. Thermodynamic properties under different pressure and temperature such as bulk modulus, Debye temperature and Gruneisen parameter were determined using the quasi-harmonic Debye model.

**Keywords:** BaZn, intermetallic, Thermodynamic properties

© 2021 Published by ECRES

## 1. INTRODUCTION

Intermetallic materials have attracted the attention of many researchers with their unique properties and application areas in technology [1-3]. Intermetallic, which have different composition and structure, have been studied by scientists dealing with both experimental and theoretical calculations, but many of them have not yet been studied. These structures usually occur when two or more metals come together in a certain combination. The new structure formed creates a structure different from the reacting structures. The pure form of zinc has a fragile structure and its toughness is low, but its properties change greatly when mixed with another material. The phase stability and cohesive properties of 48 intermetals of the Ti - Zn system was analyzed theoretically and experimentally by Ghosh et al. [4]. Soyalp et al. [5] determined some structural and physical properties of ScZn and YZn compounds using the plane wave pseudo-potential method within the generalized gradient approximation (GGA). Jong et al. [6] reported the full elastic properties of inorganic crystalline compounds using the pseudopotential potential method. Chiotti and Kilp determined that the ZnZr compound has a simple CsCl structure [7]. Arroyave et al. calculated the free energy of the intermetallic phases of the Zn - Zr system by first principle calculations and suggested possible structures of two allotropes of Zn<sub>3</sub>Zr and the structure of Zn<sub>2</sub>Zr<sub>3</sub> was determined [8]. Yang et al. [9] determined the structural, elastic and electronic properties of seven different Ca - Zn intermetallic compounds as well as the formation temperature. Chouhan et al. [10] performed comprehensive theoretical calculations of YCu, YZn and YAg compounds using FP-LAPW method and determined that the compounds are elastically stable, B2 structure and ductile. Fatima et al. reported that ScZn, YZn and TiZn compounds were ductile in ab initio method using ab initio method [11]. Iwaoka et al. reported the elastic properties of CuZn, Cu<sub>5</sub>Zn<sub>8</sub> and CuZn<sub>4</sub> intermetallic compounds by the method of first principles [12]. In their study, CuZn<sub>4</sub> was determined to be the most suitable intermetallic compound to improve the hardness of Al-Cu-Zn alloys. There are studies on zinc-based intermetals so far. However, basic elastic, electronic and thermodynamic data are not sufficient. In order to contribute to the determination of the properties of zinc-based intermetallic compounds, the mechanical and thermodynamic properties of the BaZn intermetallic compound were analyzed using the first principles method.

## 2. CALCULATION METHOD

The mechanical and thermodynamic properties of the BaZn intermetallic compound has been investigated by DFT method [13,14] implemented in the Vienna ab initio simulation package (VASP)[15-18]. The plane-wave basis sets with an energy cut-off 700 eV and the 15x15x15 Monkhorst and Pack [19] k-points are used in the Brillouin zone for the BaZn compound. Mechanical properties were calculated from elastic constants estimated by the strain-stress method [20,21]. Thermodynamic properties of BaZn compound were evaluated by quasi-harmonic Debye model [22-25] using GIBBS code.

## 3. RESULTS AND DISCUSSION

Mechanical properties such as hardness, ductility / brittleness, stability, plasticity, anisotropy, Debye temperature, melting temperature and sound velocities were determined. Bulk modulus is a measure of how much a material resists when compressed. The bulk modulus(B) of BaZn compound is 21.3 GPa, a small value indicates that the material can be easily compressed. In the previous study [11], the bulk module of ScZn, YZn, TiZn and ZrZn compounds was 71.2 GPa, 61.8 GPa, 118.85 GPa and 109.80 GPa, respectively. The bulk modulus values of Sc, Y, Ti, and Zr were 57 GPa, 41 GPa, 110 GPa, and 91.1 GPa, respectively. This explains the different bulk modulus in compounds. The shear modulus(G) is a measure of the resistance of the atoms in the material to the motion of the atomic planes. Young's modulus(E) is the measure of the resistance of the material against elastic stress. As seen in Table 1, the values of Shear module and Young module were determined as 14.4 GPa and 35.2 GPa. The low young and shear modulus indicates that BaZn compound is a very soft material [26]. It can be seen in Table 1 that the young and shear modulus values of the compounds in the previous study [11] are greater than BaZn, but the materials are still in soft character.

Hardness is one of the criteria for evaluating the material. The hardness value (Hv) was determined as 1.6GPa. The hardness value also showed that the material is a soft material. In materials science, plasticity is defined as the irreversible deformation of a material that undergoes shape changes. It is calculated as the ratio of the Bulk modulus (B) to C<sub>44</sub>, [27] and its value was determined to be 1.33.

It is very important to know whether the structure of the material is ductile or brittle in technological applications. Pugh ratio (B/G) is one of the parameters used to estimate the brittleness or ductile behavior of the material. If the Pugh ratio is greater than 1.75, it shows ductile properties. Otherwise, it is brittleness [28]. Since the B/G ratio of BaZn compound was 1.47, it showed fragile properties. Since the Pugh value of the compounds studied in the previous study [11] is greater than 1.75, the compounds show ductile properties. The second method, Poisson ratio, provides information about ductility. The critical value is less than 0.33, it is brittle if it is large, it is ductile [29]. The Poisson ratio is 0.2241, below the critical value, and exhibits brittle properties. As seen in Table 1, other compounds show ductile properties according to Poisson ratio [11].

Cauchy pressure (C<sub>12</sub> - C<sub>44</sub>) defines the angular properties of atomic bonds in metals and compounds, when it gets a positive value, it shows a metallic character feature [30]. It shows compound metallic properties according to Cauchy pressure. The Cauchy pressure also showed metallic character traits for the three compounds of the previous study [11], as presented in Table 1. The term elastic anisotropy is important in engineering applications. It is isotropic when this value equals 1, while in other cases it is anisotropic [31]. In our work, BaZn is anisotropic with the A value 1.296 as ScZn, YZn and ZrZn [11].

Table 1. Mechanical properties of BaZn

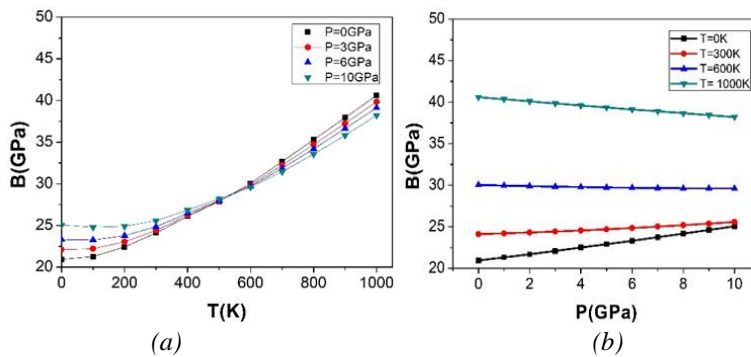
Material	B	G	E	B/G	C <sub>12</sub> -C <sub>44</sub>	B/C <sub>44</sub>	v	A	Hv
BaZn	21.3	14.4	35.2	1.47	21.8	1.33	0.2241	1.296	1.6
ScZn[11]	71.2	37.70	96.13	1.89	5.29	-	0.27	1.91	-
YZn[11]	61.8	32.27	82.47	1.91	7.2	-	0.27	1.42	-
TiZn[11]	118.85	54.83	142.57	2.16	26.5	-	0.30	1.34	-
ZrZn[11]	109.80	53.85	138.80	2.03	19.77	-	0.28	1.03	-

Debye temperature ( $\theta$ ) is one of the fundamental parameters and is related to many physical properties such as specific heat and melting temperature. The Debye(K), Melting temperature(K), average longitudinal ( $v_l(m/s)$ ) and transverse elastic wave velocities ( $v_t(m/s)$ ) and average sound velocity ( $v_m(m/s)$ ) calculated from elastic constants. The obtained results are listed in Table 2 compared previous theoretical study [11].

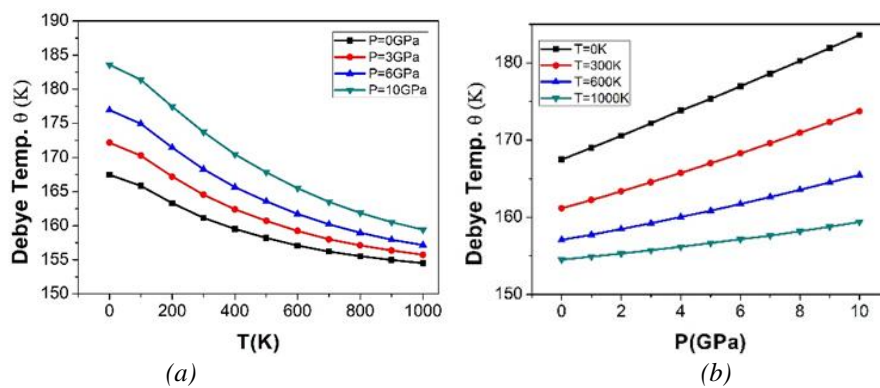
Table 2. Debye, melting temperature and sound velocities

Material	$\Theta(K)$	$T_m(\pm 300)$	$V_l(m/s)$	$V_t(m/s)$	$V_m(m/s)$
BaZn	173.9	776	2887	1721	1905
ScZn[11]	281.54	-	5043.73	2849.07	3168.88
YZn[11]	224.15	-	4342.62	2420.13	2694.74
TiZn[11]	319.87	-	5643.14	3025.76	3378.93
ZrZn[11]	275.89	-	5087.70	2772.37	3092.31

The thermodynamic properties of BaZn compound between 0-1000 K temperature and 0-10 GPa pressure range were calculated with the quasi-harmonic Debye model [22-25]. We estimate the Bulk moduli (B), Debye temperature ( $\theta$ ), and Grüneisen parameter ( $\gamma$ ). The pressure and temperature dependence of bulk modulus BaZn compound are presented in Fig. 1. The bulk modulus of the BaZn compound increases almost linearly with increasing pressure at a different temperature (Fig.1a). However, at different pressures, there is a slight increase in 0 and 300 K with the temperature increase, while a decrease close to the constant value is observed at 600K and 1000K.

Figure 1. Bulk module of BaZn as functions of (a)temperature  $T$  (in K) and (b)pressure (in GPa).

Debye temperature is an important parameter related to the heat capacity of the material. The graphs of the temperature change of the Debye temperature under constant pressure and the pressure change under constant temperature are given in the Figure 2. While the Debye temperature decreases with the temperature increase at constant pressure, the Debye temperature increases with the increasing pressure at constant temperature.

Figure 2. Debye temperature of BaZn as functions of (a)temperature  $T$  (in K) and (b)pressure (in GPa).

The Gruneisen parameter is an indication of the non-harmonic vibrations in the compound. The discrepancy in phonon frequencies depends on the sound level, and this volume dependence of the phonon is determined by the Gruneisen parameter. The graphs of the temperature change of the Gruneisen parameter under constant pressure

and the pressure change under constant temperature are given in the Figure 2. A trend similar to the Debye temperature is observed in the Gruneisen parameter.

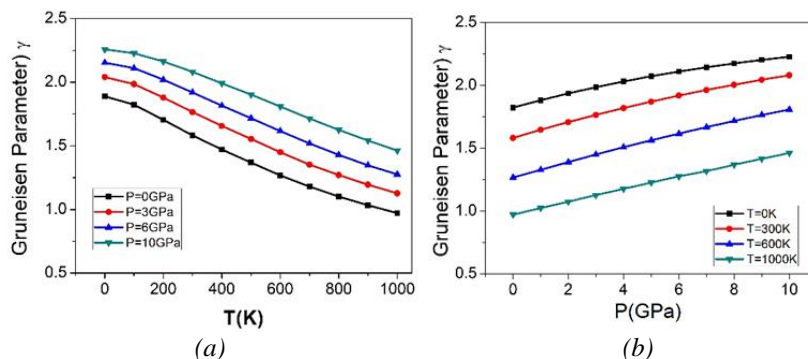


Figure 3. Gruneisen parameter of BaZn as functions of (a)temperature  $T$  (in K) and (b)pressure (in GPa).

#### 4. CONCLUSIONS

For BaZn compound crystallizing in B2 structure; mechanical, and thermodynamic properties were calculated by DFT method. This compound was a soft material according to Young module, Shear modulus, hardness and plasticity calculations. It showed brittle properties according to Pugh and Poisson ratio. According to Cauchy pressure data, it showed metallic properties. The melting temperature was determined to be  $776 \pm 300$  K. The low temperature of Debye also indicates that it is a soft material.

#### REFERENCES

- [1] Singh R P, Singh V K, Singh R K, Rajagopalan M, Elastic, Acoustical and Electronic Behaviour of the RM (R = Dy, Ho, Er; M=Cu, Zn) Compounds. Am. J. Condens. Matter. Phys. 2013; 3(5):123. <<https://doi.org/10.1016/10.5923/j.jacmp.20130305.02>>.
- [2] Fatima B, Chouhan S S, Acharya N, Sanyal S P, Density Functional study of XRh (X= Sc, Y, Ti and Zr) intermetallic compounds, Comput.Mater. Sci. 2014; 89: 205–215. DOI: <<https://doi.org/10.1016/j.commatsci.2014.03.008>>.
- [3] Chouhan S S, Pagare G, Rajagopalan M, Sanyal S P, First principles study of structural, electronic, elastic and thermal properties of YX (X = Cd, In, Au,Hg and TI) intermetallics, Solid State Sci. 2012;14:1004–1011. <<https://doi.org/10.1016/j.solidstatesciences.2012.05.005>>.
- [4] Ghosh G, Delsante S, Borzone G, Asta M, Ferro R, Phase stability and cohesive properties of Ti–Zn intermetallics: first-principles calculations and experimental results, Acta Mater. 2006; 54: 4977–4997. <https://doi.org/10.1016/j.actamat.2006.04.038>.
- [5] Soyalp F, Yavuz M, Yalcin Z, Ab initio investigations of phonons and thermodynamic properties of ScZn and YZn in the B2 structure, Comput. Mater. Sci. 2013; 77: 72–80. <<https://doi.org/10.1016/j.commatsci.2013.03.041>>.
- [6] de Jong M, Chen W, Angsten T, Jain A, Notestine R, Gamst A, Sluiter M, Ande C K, Zwaag S V D, Plata J J, Toher C, Curtarolo S, Ceder G, Persson K A, Asta M, Charting the complete elastic properties of inorganic crystalline compounds. Sci. Data 2015:1–13 <<https://www.nature.com/articles/sdata20159>>.
- [7] Chiotti P, Kilp G R, Zinc-zirconium system. Trans. Metall. Soc. AIME 1959; 215: 892–898.
- [8] Arroyave R, van de Walle A, Liu Z-K, First-principles calculations of the Zn–Zr system, Acta Mater. 2006; 54: 473–482.
- [9] Yang Z, Shi D, Wen B, Melnik R, Structural, elastic, electronic properties and heats of formation of Ca–Zn intermetallics from first principles calculations. J. Alloys Compd. 2012; 524: 53–58. <<https://doi.org/10.1016/j.jallcom.2012.02.0751>>.
- [10] Chouhan S S, Soni P, Pagare G, Sanyal S P, Rajagopalan M, Ab initio study of electronic and elastic properties of B2-type ductile YM (M = Cu, Zn and Ag) intermetallics. Physica B 2011; 406: 339–344. <https://doi.org/10.1016/j.physb.2010.10.055>
- [11] Fatima B, Sanyal S P, Ab initio study of electronic structure, elasticity, bonding features and mechanical behaviour of zinc intermetallics, Computational Condensed Matter, 2018;14: 144–152. <<https://doi.org/10.1016/j.cocom.2018.01.013>>.
- [12] Iwaoka H, Hirosawa S, First-principles calculation of elastic properties of Cu-Zn intermetallic compounds for improving the stiffness of aluminum alloys. Computational Materials Science 2020; 174: 109479. <https://doi.org/10.1016/j.commatsci.2019.109479>
- [13] Hohenberg, P., Khon, W. Inhomogeneous Electron Gas. Phys. Rev. 1964; 136: B864. <<https://journals.aps.org/pr/abstract/10.1103/PhysRev.136.B864>>.
- [14] Khon, W, Sham, L J. Self-Consistent Equations Including Exchange and Correlation Effects. Phys. Rev. 1965; 140: A1133. <<https://journals.aps.org/pr/abstract/10.1103/PhysRev.140.A1133>>.

- [15] Kresse, G and Hafner J. Ab initio molecular dynamics for liquid metals. *Phys. Rev. B.* 1993; 47: 558. <[https://doi.org/10.1016/0022-3093\(95\)00355-X](https://doi.org/10.1016/0022-3093(95)00355-X)>.
- [16] Kresse, G and Hafner, J. Ab initio molecular-dynamics simulation of the liquid-metal–amorphous-semiconductor transition in germanium. *Phys. Rev. B.* 1994; 49: 14251. <<https://journals.aps.org/prb/abstract/10.1103/PhysRevB.49.14251>>.
- [17] Kresse, G and Furthmuller, J. Efficiency of ab-initio total energy calculations for metals and semiconductors using a plane-wave basis set. *Comput. Mater. Sci.* 1996; 6: 15. <[https://doi.org/10.1016/0927-0256\(96\)00008-0](https://doi.org/10.1016/0927-0256(96)00008-0)>.
- [18] Kresse, G and Furthmuller, J. Efficient iterative schemes for ab initio total-energy calculations using a plane-wave basis set. *Phys. Rev. B.* 1996; 54: 11169. <<https://journals.aps.org/prb/abstract/10.1103/PhysRevB.54.11169>>.
- [19] Monkhorst, H J and Pack, J D. Special points for Brillouin-zone integrations. *Phys. Rev. B.* 1976; 13: 5188.<<https://journals.aps.org/prb/abstract/10.1103/PhysRevB.13.5188>>.
- [20] Page, L and Saxe P. Symmetry-general least-squares extraction of elastic data for strained materials from ab initio calculations of stress. *Phys. Rev. B.* 2002; 65: 104104.<<https://journals.aps.org/prb/abstract/10.1103/PhysRevB.65.104104>>.
- [21] Mehl, M J, Osburn, J E, Papaconstantopoulos, D A and Klein, B M. Structural properties of ordered high-melting-temperature intermetallic alloys from first-principles total-energy calculations. *Phys. Rev. B.* 1990; 41: 10311. <<https://doi.org/10.1103/physrevb.41.10311>>.
- [22] Blanco, M A, Francisco, E, Luano, V. GIBBS: isothermal-isobaric thermodynamics of solids from energy curves using a quasi-harmonic Debye model. *Comp. Phys. Commn.* 2004; 158: 57. <<https://doi.org/10.1016/j.comphy.2003.12.001>>.
- [23] Peng, F, Fu, H Z, Cheng, X L. First-principles calculations of thermodynamic properties of TiB<sub>2</sub> at high pressure. *Physica B.* 2007; 400: 83. <<https://doi.org/10.1016/j.physb.2007.06.020>>.
- [24] Peng, F, Fu, H Z, Yang, X D. Transition phase and thermodynamic properties of PtC from first-principles calculations. *Solid State Commun.* 2008; 145: 91. <<https://doi.org/10.1016/j.ssc.2007.10.030>>.
- [25] Peng, F, Fu, H Z, Yang, X D. Ab initio study of phase transition and thermodynamic properties of PtN. *Physica B.* 2008; 403: 2851. <<https://doi.org/10.1016/j.physb.2008.02.022>>.
- [26] Kars Durukan, I and Ciftci, Y O. The Effect of Pressure on Elastic Anisotropy, Vibration and Optical Properties of a AgScSi Compound. *J. Electr. Mater.* 2019; 48: 4050. <<https://doi.org/10.1007/s11664-019-07167-w>>.
- [27] Vitos, L, Korzhavyi, P A, Johansson B. Stainless steel optimization from quantum mechanical calculations. *Nat Mater.* 2003; 2: 25. <<https://doi.org/10.1038/nmat790>>.
- [28] Pugh, S F. XCII. Relations between the elastic moduli and the plastic properties of polycrystalline pure metals. *Philosophical Magazine.* 1954; 45: 823–843. <<https://doi.org/10.1080/14786440808520496>>.
- [29] Ravindran, P, Fast, L, Korzhavyi, P A, Johansson, B, Wills, J and Eriksson, O. Density Functional Theory for Calculation of Elastic Properties of Orthorhombic Crystals: Application to TiSi<sub>2</sub>. *J. Appl. Phys.* 1998; 84: 4891. <<https://doi.org/10.1063/1.368733>>.
- [30] Shinde, S M, Gupta, S D, Gupta,S K and Jha P K.Lattice dynamics and thermodynamical study of yttrium monochalcogenides. *Comput. Mater. Sci.* 2014; 92: 69. <<https://doi.org/10.1016/j.commatsci.2014.04.035>>.
- [31] Djaaafri, T, Djaaafri,A, and Saadaoui,F. First-Principles Investigation of Ferromagnetic, Thermodynamic,Elastic, and Half-Metallic Behavior of ReCrTe and RuCrTe Half-Heusler Alloys. *J. Supercond. Nov. Magn.* 31, 2449 (2018). <<https://doi.org/10.1007/s10948-017-4510-x>>.



# AB INITIO CALCULATIONS OF THE MECHANICAL, VIBRATION AND BOND NATURE OF THE CdSr COMPOUND

İlknur Kars Durukan

Gazi University, Ankara, Turkey, ilknurdurukan@gazi.edu.tr, ORCID: 0000-0001-5697-0530

Yasemin Oztekin Ciftci

Gazi University, Ankara, Turkey, yasemin@gazi.edu.tr, ORCID: 0000-0001-1796-0270

Cite this paper as:

*Kars Durukan, İ., Oztekin Ciftci, Y. Ab initio calculations of the mechanical vibration and bond nature of the CdSr compound. 9th Eur. Conf. Ren. Energy Sys. 21-23 April 2021, Istanbul, Turkey*

---

**Abstract:**

Mechanical, vibrational properties and nature of chemical bond of CdSr compound have been performed with Ab initio calculations. Several mechanical parameters such as Young's modulus, shear modulus, Pugh ratio, Caussy pressure, plasticity, Poisson ratio, anisotropy, melting temperature, velocities of sound, Debye temperature were calculated via elastic constants. After the mechanical calculations, it was determined that the material was ductile and soft. The high melting temperature showed that the material could be used in high temperature applications. Dynamic stability in the material was determined by phonon distribution curves using the super cell approach. Finally, the chemical bond natures between Cd-Sr atoms were evaluated in detail by Mulliken Atomic Populations and Charge density analysis.

---

**Keywords:**

*CdSr, Debye temperature, dynamic stability*

---

© 2021 Published by ECRES

## 1. INTRODUCTION

Different energy applications today increase the demand for high strength materials that can withstand high temperatures. In recent years, intermetallic compounds with properties between ceramics and metals have attracted attention with their high temperature resistance. Intermetallic compounds have a lot of potential for engineering applications thanks to their good oxidation resistance, low density and high strength and hardness at high temperatures [1,2]. Crystal structures of intermetallic compounds are generally different from their constituents. Intermetallics crystallize in structures such as B2, DO3, L12, L10, D019, A15, B20, C11b and C15, with ordered atomic distributions. Some intermetallics are sorted down to their melting temperature, others undergo disorganization transitions because entropy supports a less regular or random arrangement of atoms on two (or several) sub-lattices at high temperatures. Some intermetallics occur for some stoichiometric compositions, while others are observed for non-stoichiometric compositions. Intermetallic compounds with B2 structure are used especially in high temperature applications [3]. In our work aims to calculate the mechanic, vibrational, and chemical bond nature of CdSr crystallized in B2 structure. Mechanical properties including Paugh ratio(G/B), Hardness (Hv), plasticity calculations, melting temperature, velocities of sound, Debye temperature, Poisson's ratio, Cauchy pressure, and anisotropic factor (A) are predicted at ambient conditions. The ductility of the material was evaluated with different calculations. The vibrational properties of the CdSr compound are presented in detail. Moreover, the charge transfer and bonding properties of the CdSr compound were determined by the electronic charge density distribution and Mulliken atomic populations.

## 2. CALCULATION METHOD

Density functional theory (DFT) [4,5] was used to apply all theoretical calculations by the Vienna Ab-initio Simulation Package (VASP) [6-9]. Mechanical properties were calculated from elastic constants estimated by the strain-stress method [10,11]. The 2x2x2 super cell structure was used to determine the vibration properties of the

CdSr compound. The distribution of acoustic and optical phonon frequencies was determined with the PHONOPY code [12]. Mulliken atomic populations were calculated with the CASTEP code [13].

### 3. RESULTS AND DISCUSSION

Mechanical properties determined by elastic constants provide important information about the structure of solids and the character of the forces operating in solids. Young's modulus ( $E$ ; GPa) is one of the parameters that gives information about the hardness of the material. When the value of this module is high, it is understood that the material is hard. Young's modulus of CdSr is 35.8 GPa, this value indicates that the compound is soft [14]. Shear modulus is a measure of the resistance to shear stress. This module is also very low as can be seen in Table 1. Pugh ratio ( $B/G$ ) and Cauchy pressure ( $C_{12} - C_{44}$ ; GPa) are parameters that determine the brittleness or ductility of materials [15, 16]. This compound is ductile. The Pugh ratio is greater than 1.75 and the Cauchy pressure is positive (Table 1). If the Cauchy pressure is positive, it is also the determinant of the metallic property of the compound. Plasticity is the irreversible deformation of a material when pressure is applied on it [17]. Plasticity value is 1.27. The Poisson ratio of materials is accepted between 0 and 0.5. The lower and upper limits of the Poisson's ratio for the central forces in the solid and ionic crystals are given as 0.25 and 0.5, respectively. Interatomic forces for ionic crystals are central forces. In addition, these values were found to be between 0.1 and 0.25 in the previous studies for covalent materials and interatomic forces are decentralized forces [18]. In our study, the ratio of Poisson's CdSr was calculated to be 0.26. It is clear that the interatomic forces in CdSr are central forces and have ionic binding properties.  $A$  is the measure of elastic anisotropy in solid materials. For isotropic crystals, the anisotropy factor is isotropic when  $A = 1$ , while it determines the degree of anisotropy when it is smaller or greater than this value [15]. The degree of anisotropy of the CdSr compound was measured as 2.263.

Table 1. Mechanical modules of CdSr

Material	G	E	B/G	$C_{12}-C_{44}$	$B/C_{44}$	v	A
CdSr	14.2	35.8	1.78	17.2	1.27	0.2635	2.263

The Debye temperature was calculated from elastic constants as 174 K, a low Debye temperature value indicates that the material is soft. As seen in Table 2, the melting temperature was determined as  $1072 \pm 300$  K, indicating that the compound can be used in high temperature applications. Average longitudinal ( $v_l$ (m/s)) and transverse elastic wave velocities ( $v_t$ (m/s)) and average sound velocity ( $v_m$ (m/s)) calculated from elastic constants. The obtained results are listed in Table 2.

Table 2. Sound velocities, Debye and melting temperature of CdSr

Material	$v_l$	$v_t$	$v_m$	$\theta_D$	$T_m \pm 300$
CdSr	2985	1691	1880	174	1072

The graph in Figure 1 was presented to determine the vibration properties of the CdSr compound. The acoustic and optic phonon distribution curves were calculated using the PHONOPY code [12]. We used the  $2 \times 2 \times 2$  super cell approach for our phonon dispersion calculations [19]. Since there are two atoms (Cd and Sr) in the primitive unit cell of the CdSr compound, it consists of 6 branches, 3 of which are acoustic and 3 are optical. In Figure 1, the CdSr compound is dynamically stable since it does not contain a soft mode in the Brillouin region. On the right side of the plot of phonon curves in Figure 1, the total and partial density of the corresponding phonon states for this compound is presented. From total DOS, Cd atoms with 0-2 THz contribute more to the acoustic modes. The modes  $> 2$  THz are mostly detected by the vibrations of the Sr atoms.

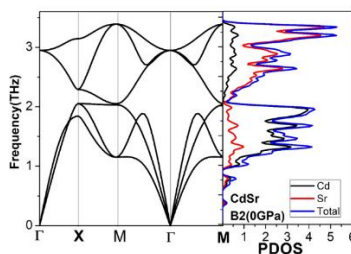


Figure 1. Phonon dispersion curves and partial density of states of the CdSr

Charge density shows the nature of the chemical bonding between different atoms. The chemical bond and charge transfer in the CdSr compound, the charge density behavior in 2D (110) plane is given in Figure 2. The electronegativities of the atoms are important in determining the bond structure of the compounds. When the difference of electronegativity between two atoms is high, the charge transfer, namely the ionic bond, when it is less, the electron sharing, covalent bond occurs [20]. Electronegativity values for Cd and Sr are 1.53 and 1, respectively. The calculated electron density is that the charge density lines in the plane structure are spherical, and this is the ionic bond property [20].

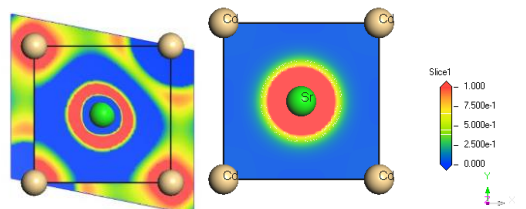


Figure 2. Electronic localized function (ELF) and Charge density map for (110) plane for CdSr

In addition to the charge density analysis, an analysis of Mulliken atom populations [21] was performed to analyze the bond structure and charge transfer of the molecules in detail, and the values obtained were listed in Table 2. According to the Mulliken population analysis, the electronic charges of the Cd and Sr atoms are -0.78e and 0.78e for the CdSr compound, respectively. This indicates that there is a charge transfer from the Sr atom to the Cd atom, an ionic bond between the two atoms.

Table 3. Population analysis of CdSr

	Atoms	s	p	D	f	Total	Charge	Bond
CdSr	Sr	2.26	5.98	0.97	0.00	9.22	0.78	Cd-Sr
	Cd	1.37	1.44	9.97	0.00	12.78	-0.78	

#### 4. CONCLUSIONS

The mechanic, vibration and chemical bond nature of the CdSr compound was analyzed in detail by DFT method. It was determined that the compound was ductile from the Young's modulus, Pugh ratio and Cauchy pressure data. The forces between bonds of the CdSr compound were central and ionic. The melting temperature was determined as  $1072 \pm 300$  K. The low Debye temperature also indicates that the material is soft. The CdSr compound, which crystallizes in the B2 structure, is dynamically stable with the absence of soft modes in the Brillouin region. The bonding nature of the CdSr compound has been shown to be ionic by electronic charge density plots and Mulliken atom populations. The ductility and high melting temperature of the CdSr compound are indicators that it can be a suitable material for engineering applications.

#### REFERENCES

- [1] Fleischer, R L and Zabala, R. Mechanical Properties of Diverse Binary High-Temperature Intermetallic Compounds. *Met. Mat. Trans.* 1990; A21: 2709. <<https://link.springer.com/content/pdf/10.1007/BF02646066.pdf>>
- [2] Stoloff, N S, Liu, C T and Deevi, S C. Emerging applications of intermetallics. *Intermetallics*. 2000; 8: 1313. <[https://doi.org/10.1016/S0966-9795\(00\)00077-7](https://doi.org/10.1016/S0966-9795(00)00077-7)>.
- [3] Hedef, F. Synthesis and disordering of B2 TM-Al (TM = Fe, Ni, Co) intermetallic alloys by high energy ball milling: A review. *Powder Technology*. 2017; 311: 556-578. <<https://doi.org/10.1016/j.powtec.2017.01.082>>.
- [4] Hohenberg, P, Khon, W. Inhomogeneous Electron Gas. *Phys. Rev.* 1964; 136: B864. <<https://journals.aps.org/pr/abstract/10.1103/PhysRev.136.B864>>.
- [5] Khon, W, Sham, L J. Self-Consistent Equations Including Exchange and Correlation Effects. *Phys. Rev.* 1965; 140: A1133. <<https://journals.aps.org/pr/abstract/10.1103/PhysRev.140.A1133>>.
- [6] Kresse, G and Hafner J. Ab initio molecular dynamics for liquid metals. *Phys. Rev. B.* 1993; 47: 558. <[https://doi.org/10.1016/0022-3093\(95\)00355-X](https://doi.org/10.1016/0022-3093(95)00355-X)>.
- [7] Kresse, G and Hafner, J. Ab initio molecular-dynamics simulation of the liquid-metal–amorphous-semiconductor transition in germanium. *Phys. Rev. B.* 1994; 49:14251. <<https://journals.aps.org/prb/abstract/10.1103/PhysRevB.49.14251>>.

- [8] Kresse, G and Furthmuller, J. Efficiency of ab-initio total energy calculations for metals and semiconductors using a plane-wave basis set. *Comput. Mater. Sci.* 1996; 6: 15. <[https://doi.org/10.1016/0927-0256\(96\)00008-0](https://doi.org/10.1016/0927-0256(96)00008-0)>.
- [9] Kresse, G and Furthmuller, J. Efficient iterative schemes for ab initio total-energy calculations using a plane-wave basis set. *Phys. Rev. B.* 1996; 54: 11169. <<https://journals.aps.org/prb/abstract/10.1103/PhysRevB.54.11169>>.
- [10] Page, L and Saxe P. Symmetry-general least-squares extraction of elastic data for strained materials from ab initio calculations of stress. *Phys. Rev. B.* 2002; 65: 104104. <<https://journals.aps.org/prb/abstract/10.1103/PhysRevB.65.104104>>.
- [11] Mehl, M J, Osburn, J E, Papaconstantopoulos, D A and Klein, B M. Structural properties of ordered high-melting-temperature intermetallic alloys from first-principles total-energy calculations. *Phys. Rev. B.* 1990; 41: 10311.
- [12] Toga, A, Oba, F, and Tanaka, I. First-principles calculations of the ferroelastic transition between rutile-type and CaCl<sub>2</sub>-type SiO<sub>2</sub> at high pressures. *Phys. Rev. B.* 2008; 78: 134106- 1-9. <<https://doi.org/10.1103/PhysRevB.78.134106>>.
- [13] Shi, D M, Wen, B, Melnik, R, Yao S, Li, T J. First-principles studies of Al–Ni intermetallic compounds. *J. Solid State Chem.* 2009; 182: 2664-2669. <<https://doi.org/10.1016/j.jssc.2009.07.026>>.
- [14] Kars Durukan, I and Ciftci, Y O. The Effect of Pressure on Elastic Anisotropy, Vibration and Optical Properties of a AgScSi Compound. *J. Electr. Mater.* 2019; 48: 4050. <<https://doi.org/10.1007/s11664-019-07167-w>>.
- [15] Pugh, S F. XCII. Relations between the elastic moduli and the plastic properties of polycrystalline pure metals. *Philosophical Magazine*. 1954; 45: 823–843. <<https://doi.org/10.1080/14786440808520496>>.
- [16] Shinde, S M, Gupta, S D, Gupta,S K and Jha P K.Lattice dynamics and thermodynamical study of yttrium monochalcogenides. *Comput. Mater. Sci.* 2014; 92: 69. <<https://doi.org/10.1016/j.commatsci.2014.04.035>>.
- [17] Vitos, L, Korzhavyi, P A, Johansson B. Stainless steel optimization from quantum mechanical calculations. *Nat Mater.* 2003; 2: 25. <<https://doi.org/10.1038/nmat790>>.
- [18] Fu, H Z, Li, D H, Peng, F. et al. Ab initio calculations of elastic constants and thermodynamic properties of NiAl under high pressures. *Comput. Mater Sci.* 2008; 44: 774–778. <<https://doi.org/10.1016/j.commatsci.2008.05.026>>.
- [19] Angsten, T, Mayeshiba, T, Wu, H & Morgan, D. Elemental vacancy diffusion database from high throughput first-principles calculations for fcc and hcp structures. *New J. Phys.* 2014; 16: 015018. <<https://iopscience.iop.org/article/10.1088/1367-2630/16/1/015018>>.
- [20] Abraham, J A, Pagare, G, and Sanyal, S P. Electronic Structure, Electronic Charge Density, and Optical Properties Analysis of GdX<sub>3</sub> (X = In, Sn, Tl, and Pb) Compounds:DFT Calculations. *Indian Journal of Materials Science.* 2015; 2015: 1-11. <<http://dx.doi.org/10.1155/2015/296095>>
- [21] Mulliken R S. Electronic Population Analysis on LCAO–MO Molecular Wave Functions. *J. Chem. Phys.* 1955; 23: 1833.



# ANALYSIS OF OPTICAL PROPERTIES OF THE CeTl INTERMETALLIC STRUCTURE

İlknur Kars Durukan

Gazi University, Ankara, Turkey, ilknurdurukan@gazi.edu.tr, ORCID: 0000-0001-5697-0530

Yasemin Oztekin Ciftci

Gazi University, Ankara, Turkey, yasemin@gazi.edu.tr, ORCID: 0000-0001-1796-0270

Cite this paper as: *Kars Durukan, İ, Oztekin Ciftci, Y Analysis of optical properties of the CeTl intermetallic structure. 9th Eur. Conf. Ren. Energy Sys. 21-23 April 2021, Istanbul, Turkey*

**Abstract:** Rare earth intermetallic structures have an important place in technology with their physical and mechanical properties. To determine the technological optical applications of the CeTl intermetallic CsCl type RM compound, the optical properties were determined using VASP program. Optical properties of intermetallic material analyzed in details. When the  $\epsilon_1$  value decreases first and then decreases to zero, it shows that it has metallic properties and the photons are completely reflected.  $\epsilon_2$  describes the absorption ability and this part has a direct relationship with band gap energy.  $\epsilon_2(0)$  zero frequency value of imaginer part of the dielectric function is zero. The imaginary part also supports the metallic nature.

**Keywords:** Rare earth intermetallic structures, CsCl type structure, optic

© 2021 Published by ECRES

## 1. INTRODUCTION

Generally, the mechanical, electrical, physical, chemical and magnetic properties of intermetallic compounds are superior to ordinary metals, but the failure to improve their high performance in engineering applications is because they can easily break at room temperature. To achieve some ductility at room temperature in intermetallic compounds, various processes such as metastable distortion or doping are applied, whereas none of these are necessary for rare earth compounds in the B2 structure [1-3]. The high ductility of RM compounds at room temperature has been studied by Gschneidner et al. [4]. CeTl shows a ductile structure due to the 4f electrons of Ce in the rare earth element class in B2 structure. The magnetic and structural properties of CeTl were analyzed experimentally, in this study, it was determined that there was a transition from the cubic phase to the tetragonal phase at CeTl, 193 K [5]. Shrivastava et al. calculated the structural, elastic, and electronic properties of the CeTl structure and determined that the CeTl compound has ductile property in the B2 structure [6]. Detailed optical evaluation of the CeTl compound was discussed using the DFT method.

## 2. CALCULATION METHOD

Density functional theory (DFT) [7,8] was used to apply optic calculations in the Vienna Ab-initio Simulation Package (VASP) [9-12]. The imaginary part of the dielectric function was determined from the electronic structure calculations made with the VASP code. then the real part is calculated by Kramers-Kronig relations [13,14]. Finally, other optical constants can be determined with the given Eqs. [1-4].

$$R(\omega) = \left| \frac{\sqrt{\epsilon(\omega)} - 1}{\sqrt{\epsilon(\omega)} + 1} \right|^2 \quad (1)$$

$$L(\omega) = \left[ \frac{\epsilon_2(\omega)}{\epsilon_1^2(\omega) + \epsilon_2^2(\omega)} \right] \quad (2)$$

$$n(\omega) = \left[ \frac{\sqrt{\epsilon_1^2(\omega) + \epsilon_2^2(\omega)} + \epsilon_1(\omega)}{2} \right]^{1/2} \quad (3)$$

$$k(\omega) = \left[ \frac{\sqrt{\varepsilon_1^2(\omega) + \varepsilon_2^2(\omega)} - \varepsilon_1(\omega)}{2} \right]^{1/2} \quad (4)$$

### 3. RESULTS AND DISCUSSION

We have examined the optical features of CeTl compound. The dielectric function plays a key role in the analysis of optical properties. Dielectric function  $\varepsilon(\omega)$  is shown as Eq. [5]

$$\varepsilon(\omega) = \varepsilon_1(\omega) + i\varepsilon_2(\omega) \quad (5)$$

$\varepsilon_1(\omega)$  and  $\varepsilon_2(\omega)$  the real and the imaginary part of the complex dielectric function, respectively. After determining the real and imaginary dielectric function, other optical constants were also evaluated in detail. The real and imaginary parts of the dielectric function are given in Fig. 1. The real part  $\varepsilon_1(\omega)$  of the dielectric function is the electronic polarization information of the material. Negative values of the  $\varepsilon_1(\omega)$  value indicate metallic properties, the photons are fully reflected, and the positive part indicates the propagation of photons in the material [15].

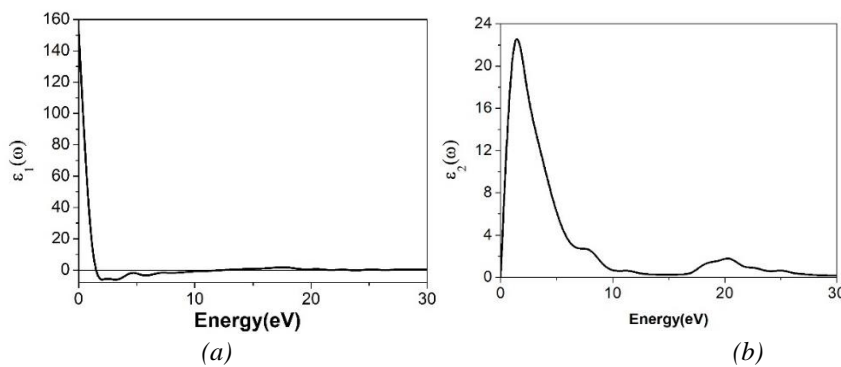


Figure 1. (a) Real part (b) Imaginert part of Dielectric function of CeTl compound.

The imaginary part  $\varepsilon_2(\omega)$  of the dielectric function provides information about the electronic band structure and the absorption activity of materials (Fig.1b).  $\varepsilon_2(0)$  zero frequency value of imaginer part of the dielectric function is zero. The imaginary part also supports the metallic nature. Since the value of the imaginary part of the  $\varepsilon_2(0)$  dielectric function at zero frequency is zero, this situation supports the metallic nature [16]. The refractive index  $n(\omega)$  and extinction coefficient  $k(E)$  are displayed in Fig. 2. Optical properties of a material are determined by knowing its refractive index. The refractive index gives information about the propagation of the electromagnetic wave in the material. The change of the refractive index with energy is similar to the trend of the change of the real part of the dielectric function with energy. The static value of  $n_0(0)$  is 12.44(Fig.2a). Refractive index value was quite high in the infrared region and gradually decreased in the visible and ultraviolet region.  $K(\omega)$  is characterized as the extinction coefficient of energy absorbed in the optical medium during the propagation of light (Fig.2b).  $K(\omega)$  value takes high values in the visible region and ultraviolet region. The largest losses in the ultraviolet region are the regions 12.9-15.51 eV and 30-40 eV.

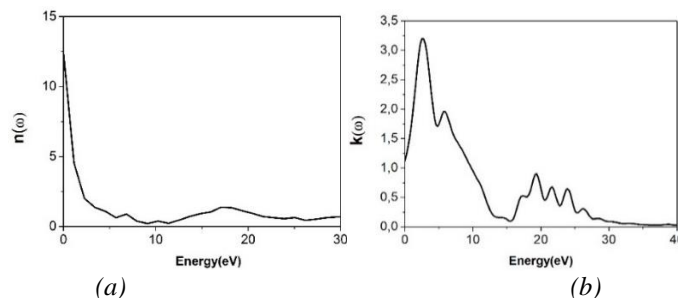


Figure 2. (a) Refractive index (b) Extinction coefficient of CeTl compound.

$L(\omega)$  describes the energy loss of an electron moving in a material(Fig.3a). The main peak is defined as the plasma frequency. This peak is located at 23.90 eV. Above this value, the material becomes transparent [16]. The

reflectivity  $R(\omega)$  is presented in Fig. 3 (b). The static value of  $R_0(0)$  is about 72 %. The region with the greatest reflection is the region between 0-15 eV. It decreased by about 7 percent in the 15-30 eV range.

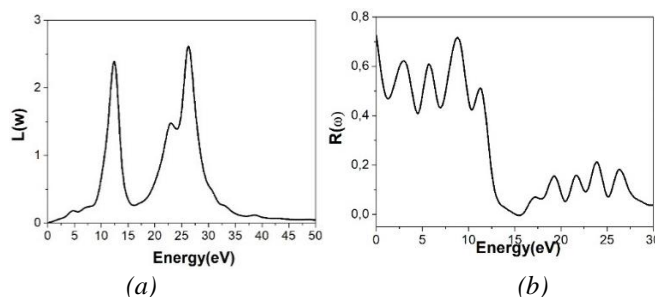


Figure 3. (a) The electron energy loss function (b) Reflectivity spectrum of CeTl compound

#### 4. CONCLUSIONS

Detailed analysis of the optical constants ( $\epsilon(\omega)$ ,  $n(\omega)$ ,  $k(\omega)$ ,  $L(\omega)$ ,  $R(\omega)$ ) of the CeTl compound was carried out by the DFT method. The static value of the real part of dielectric constant is 153.72 and its refractive index is obtained as 12.44. As a result, the CeTl compound was analyzed to contribute to the development of intermetallic compounds and to fill the lack of literature.

#### REFERENCES

- [1] Cahn, R W. Intermetallics: new physics. *Contemp. Phys.* 2001; 42: 365–375. <<https://doi.org/10.1080/00107510110084084>>.
- [2] Chen, G L & Liu, C T. Moisture induced environmental embrittlement of intermetallics. *Int. Mater. Rev.* 2001; 46: 253–270. <<https://doi.org/10.1179/095066001771048718>>.
- [3] Fleischer, R L & Zabala, R J. Mechanical properties of diverse binary high-temperature intermetallic compounds. *Met. Trans. A.* 1990; 21: 2709–2715. <<https://doi.org/10.1007/BF02646066>>.
- [4] Gschneidner Jr, K, Russell, A, Pecharsky, A, Morris, J, Zhang, Z, Lograsso, T, Hsu, D, Chester, Lo C H, Ye, Y, Slager, A, Kesse, D. A family of ductile intermetallic compounds. *Nat. Mater.* 2003; 2: 587–590. <<https://www.nature.com/articles/nmat958>>.
- [5] Kurisu, M, Tanaka, H, Kadomatsu, H, Sekizawa, K, Fujiwara, H. Magnetic and structural properties of CeTl at hydrostatic pressure. *J. Phys. soc. of Japan.* 1985; 54: 3548–3553. <<https://doi.org/10.1143/JPSJ.54.3548>>.
- [6] Shrivastava, D and Sanyal, S P. Structural, Electronic and Elastic Properties of CeTl Intermetallic Compound. *Journal of Metastable and Nanocrystalline Materials.* 2016; 28: 1–4. <<https://www.scientific.net/JMMN.28.1>>.
- [7] Hohenberg, P, Khon, W. Inhomogeneous Electron Gas. *Phys. Rev.* 1964; 136: B864. <<https://journals.aps.org/pr/abstract/10.1103/PhysRev.136.B864>>.
- [8] Khon, W, Sham, L J. Self-Consistent Equations Including Exchange and Correlation Effects. *Phys. Rev.* 1965; 140: A1133. <<https://journals.aps.org/pr/abstract/10.1103/PhysRev.140.A1133>>.
- [9] Kresse, G and Hafner J. Ab initio molecular dynamics for liquid metals. *Phys. Rev. B.* 1993; 47: 558. <[https://doi.org/10.1016/0022-3093\(95\)00355-X](https://doi.org/10.1016/0022-3093(95)00355-X)>.
- [10] Kresse, G and Hafner, J. Ab initio molecular-dynamics simulation of the liquid-metal–amorphous-semiconductor transition in germanium. *Phys. Rev. B.* 1994; 49:14251. <<https://journals.aps.org/prb/abstract/10.1103/PhysRevB.49.14251>>.
- [11] Kresse, G and Furthmüller, J. Efficiency of ab-initio total energy calculations for metals and semiconductors using a plane-wave basis set. *Comput. Mater. Sci.* 1996; 6: 15. <[https://doi.org/10.1016/0927-0256\(96\)00008-0](https://doi.org/10.1016/0927-0256(96)00008-0)>.
- [12] Kresse, G and Furthmüller, J. Efficient iterative schemes for ab initio total-energy calculations using a plane-wave basis set. *Phys. Rev. B.* 1996; 54: 11169. <<https://journals.aps.org/prb/abstract/10.1103/PhysRevB.54.11169>>.
- [13] Kronig, R. On the Theory of Dispersion of X-Rays. *J. Opt. Soc. Am.* 1926; 12: 10. <<https://www.osapublishing.org/josa/abstract.cfm?uri=josa-12-6-547>>.
- [14] Matyash, I E, Minailova, I A, Mishchuk, O N & Serdega B K. Kramers–Kronig Relations in Representation of Modulation Polarimetry by an Example of the Transmission Spectra of GaAs Crystal. *Optics and Spectroscopy.* 2017; 123: 881–888. <<https://link.springer.com/article/10.1134/S0030400X17120098>>.
- [15] Uğur, G, Kushwaha, A K, Güler, M, Charifi, Z, Uğur, S, Güler, E, Baaziz, H. Electronic structure, optical and vibrational properties of  $Ti_2FeNiSb_2$  and  $Ti_2Ni_2InSb$  double half heusler alloys. *Materials Science in Semiconductor Processing.* 2021; 123: 105531. <<https://doi.org/10.1016/j.mssp.2020.105531>>.
- [16] Kumari, M, Verma U P. Full potential study of HoMg. *Journal of Magnesium and Alloys.* 2018; 6: 189–196. <<https://doi.org/10.1016/j.jma.2018.03.002>>.



# THE PHYSICAL PROPERTIES OF NEWLY SYNTHESIZED SUPERCONDUCTOR COMPOUND LaNiGe VIA Ab-INITIO CALCULATIONS

Yasemin Oztekin Ciftci

Gazi University, Ankara, Turkey, [yasemin@gazi.edu.tr](mailto:yasemin@gazi.edu.tr), ORCID: 0000-0001-1796-0270

Ilknur Kars Durukan

Gazi University, Ankara, Turkey, [ilknurdurukan@gazi.edu.tr](mailto:ilknurdurukan@gazi.edu.tr), ORCID: 0000-0001-5697-0530

*Cite this paper as:* Oztekin Ciftci, Y, Kars Durukan, I, *The physical properties of newly synthesized superconductor compound LaNiGe via ab-initio calculations*, . 9th Eur. Conf. Ren. Energy Sys. 21-23 April 2021, Istanbul, Turkey

**Abstract:** The superconducting ternary pnictides compounds have attracted attention because of interesting physical properties. Recently, in the experimental study of LaNiGe which crystallizes LaPtSi type structure, it is found to be non-centrosymmetric compound. It has been studied pressure effects on the physical and superconductor temperature of LaNiGe using CASTEP program. Here, we have performed the structural, electronic, elastic, vibrational and superconducting properties for LaNiGe under pressure. Hardness and bonding behaviour have also been calculated for this compound. According to obtained results, LaNiGe is stable mechanically and dynamically. The calculated superconducting transition pressure is 12.4 K. From elastic properties, it can be concluded that LaNiGe has anisotropy. We have also seen from band structure that this compound has metallic behavior under pressure

**Keywords:** Superconductor, optoelectronic, pressure effect

© 2021 Published by ECRES

## 1. INTRODUCTION

In solid state physics, since the discovery of superconductivity a large of research have been made. When the materials are cooled below a critical temperature, superconductivity is physical properties which electrical resistance vanishes and magnetic fields are expelled from the materials. These materials are used for electric power and magnet applications.

The discovery of superconductivity in the noncentrosymmetric intermetallic compounds have caused a great research interest. For these materials, the absence of an inversion center along with antisymmetric spin-orbit coupling make a mixture of spin components. These unconventional superconductors show nodes in the superconducting gap and anisotropic pairing [1,2]. Early studies on non-centrosymmetric compounds for LaPtSi and LaPtGe which have LaPtSi type structure exhibit superconducting transition at 3.3 K and 3.4 K, respectively [3,4]. Experimentally, recently, LaNiGe which was synthesized from arc-melting and subsequent annealing, have been studied using experimental measurements[5].

In this study, we have investigated structural, elastic, electronic, vibrational and superconducting properties under pressure by ab-initio calculations based on density-functional theory.

## 2. CALCULATION METHOD

The first-principles calculations using Cambridge Sequential Total Energy Package (CASTEP) simulation software [6, 7] have been done to search LaNiGe. For the exchange-correlation energy, we have chosen Perdew-Burke-Ernzerhof (PBE) within the generalized gradient approximation (GGA) functional [8]. Using the Ultrasoft Vanderbilt pseudopotential the interactions were taken [9]. The electronic valence configurations were chosen as

La: 5d<sup>1</sup>6s<sup>2</sup>, Ni: 3d<sup>8</sup>4s<sup>2</sup>5s<sup>2</sup>5p<sup>6</sup>, and Ge:4s<sup>2</sup>2p<sup>2</sup>. Energy cutoff parameter is set to a 600 eV for this study. A set (12x12x12) Monkhorst-Pack [10] grid of k-points is used.

### 3. RESULTS AND DISCUSSION

LaNiGe superconductor compound crystallizes in the LaPtSi-type phase (space group *I41md*) which has tetragonal symmetry. The unit cell of LaNiGe is given in Fig.1. To access the ground state properties of the material, it should be optimized the unitcell of the compounds. Optimized lattice parameters, bulk modulus, volume and density are given in Table .1 with experimental data. It can be seen from Table 1 that obtained results for lattice parameters are good agreement with experimental values [5].

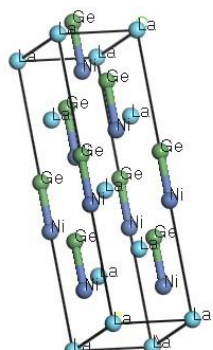


Table .1 Optimized the structural parameters such as lattice constants(*a,c*), bulk modulus(*B*), volume(*V*) and density (*d*) for LaNiGe

	<i>a</i> (Å)	<i>c</i> (Å)	<i>V</i> (Å <sup>3</sup> )	<i>B</i> (GPa)	<i>d</i> (gr/cm <sup>3</sup> )
Theory	4.2579	14.359	260.344	84.624	6.893
Exp.[5]	4.208	14.403	255.00		7.049

Fig.1 Unitcell of LaNiGe

In order to understand the electronic properties, we calculated the non-spin-polarized band structures of LaPtSi phase of LaNiGe for different symmetry points (see Fig. 2) using the optimized *a* value.

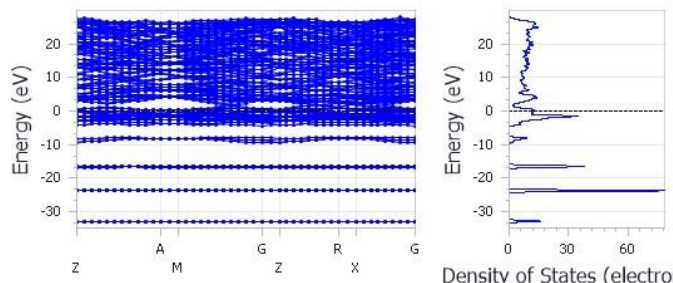


Fig.2 Electronic band structure and density of states for LaNiGe.

In Fig.2 in the zero energy level, the Fermi level is placed. The bands lines for valence band and conduction band region is mixed due to disappearing band gap. As a result of band structure graphs, the LaNiGe compound shows metallic character and it agrees well with the old study[5]. The bands near Fermi level exhibit dispersive properties. The bands along gamma- Z display non-dispersive property indicating bigger effective mass of charge carrier for this direction and anisotropy in the charge transfer.

The response of a material to the applied stress is represented by the elastic constants ( $C_{ij}$ ) which give information about mechanical stability, stiffness, type of interatomic bonding, and anisotropy of solids. For tetragonal system, a crystal should be ensured stability conditions as follows[11]

$$C_{11} > C_{12};$$

$$2C_{13}^2 < C_{33}(C_{11} + C_{12});$$

$$C_{44} > 0; C_{66} > 0$$

From the obtained values of elastic constants as given in Table 2, LaNiGe is mechanically stable .

Table 2. The calculated elastic constants(in GPa) for LaNiGe

	$C_{11}$	$C_{12}$	$C_{13}$	$C_{33}$	$C_{44}$	$C_{66}$
This study	117.07	71.032	60.85	144.57	29.58	40.45

#### 4. CONCLUSIONS

First-principles studies on superconductor LaNiGe which has synthesized newly have been performed using CASTEP program. Structural parameters given here are matching with experimental values. Calculated band structures show metallic behavior of LaNiGe. We also have calculated elastic constants and tabulated. According to obtained results for elastic constants LaNiGe is stable mechanically.

#### REFERENCES

- [1] Sigrist M. and Ueda K., Phenomenological theory of unconventional superconductivity. *Rev. Mod. Phys.* 1991; 63: 239 .< <https://doi.org/10.1103/RevModPhys.63.239>>
- [2] Yuan, H. Q., Agterberg D. F, Hayashi N., Badica P., Vandervelde D., Togano K, Sigrist M., and Salamon M. B, S-Wave Spin-Triplet Order in Superconductors without Inversion Symmetry: Li<sub>2</sub>Pd<sub>3</sub>B and Li<sub>2</sub>Pt<sub>3</sub>B, *Phys. Rev. Lett.* **97**, 2006:017006. <<https://doi.org/10.1103/PhysRevLett.97.017006>>
- [3] EVERIS J., OEHLINGER G., WEISS A., PROBST C., SOLID STATE COMMUN. SUPRACONDUCTIVITY OF LAPTSI AND LAPTGE. 1984;50: 61. <[https://doi.org/10.1016/0038-1098\(84\)90060-7](https://doi.org/10.1016/0038-1098(84)90060-7)>
- [4] PALAZZESE S., LANDAETA J. F, SUBERO D., BAUER E., BONALDE I., STRONG ANTIMETRIC SPIN-ORBIT COUPLING AND SUPERCONDUCTING PROPERTIES: THE CASE OF CONCENTROSYMMETRIC LAPTSI. *J. PHYS.: CONDENS. MATTER* 2018; 30: 255603.< DOI: 10.1088/1361-648X/AAC61D>
- [5] Nazar Z., Orest P., Ihor M., Galyna N., Pavlyuk V., Kaczorowski D, Pöttgen R.,and. Zaremba V., LaNiGe with Non-centrosymmetric LaPtSi Type Structure, *Z. Anorg. Allg. Chem.*, 2020, <DOI: 10.1002/zaac.202000317>
- [6] Segall M.D., Lindan P.J.D, Probert Pickard C.J., Hasnip P.J., Clark S.J., Payne M.C, First-principles simulation: ideas, illustrations and the CASTEP code. *J. Phys. Condens. Mater.* 2002; 14: 2717. <<https://doi.org/10.1088/0953-8984/14/11/301>>
- [7] Zhu W., Xiao H, J. Comput. Ab initio study of electronic structure and optical properties of heavy-metal azides: TiN<sub>3</sub>, AgN<sub>3</sub>, and CuN<sub>3</sub>, *Chem.* 2008; 29:176. <<https://doi.org/10.1002/jcc.20682>>
- [8] Perdew J. P. and Wang Y. Accurate and simple analytic representation of the electron-gas correlation-energy. *Phys. Rev. B* 1992; 45: 13244.. <<https://doi.org/10.1103/PhysRevB.45.13244>>
- [9] Perdew J. P., Chevary J. A., Vosko K. A., Jackson M. R., Pedersen D. J. Singh and Fiolhais C. S. H. Atoms, molecules, solids, and surfaces - applications of the generalized gradient approximation for exchange and correlation, *Phys. Rev. B* 1992;46:6671. <https://doi.org/10.1103/PhysRevB.46.6671>
- [10] [Monkhorst H. J. and Pack J. D. Special points for Brillouin-zone integrations *Phys. Rev. B* 1976;13:5188. <https://doi.org/10.1103/PhysRevB.13.5188>
- [11] Mouhat F., Coudert F, Necessary and sufficient elastic stability conditions in various crystal systems. *Phys. Rev. B*. 2014; 90: 224104. <<https://doi.org/10.1103/PhysRevB.90.224104>>



# A THEORETICAL STUDY OF PRESSURE-INDUCED EFFECTS ON CeAs COMPOUND

Yasemin Oztekin Ciftci

Gazi University, Ankara, Turkey, [yasemin@gazi.edu.tr](mailto:yasemin@gazi.edu.tr), ORCID: 0000-0001-1796-0270

İlknur Kars Durukan

Gazi University, Ankara, Turkey, [ilknurdurukan@gazi.edu.tr](mailto:ilknurdurukan@gazi.edu.tr), ORCID: 0000-0001-5697-0530

Cite this paper as: Oztekin Ciftci, Y, Kars Durukan, İ, A theoretical study of pressure-induced effects on CeAs compound, 9th Eur. Conf. Ren. Energy Sys. 21-23 April 2021, Istanbul, Turkey

---

**Abstract:**

Cerium monopnictides[1,2] attract an attention due to physical properties such as heavy-fermion, mixed-valence and Kondo insulator behaviour. CeAs compound which is rare earth compounds crystallize B1 structure at 0GPa and 0K. Due to the highly correlated f- electrons these compounds have important electronic properties. Pressure has an important effect on physical properties, since the f-electrons interact with conduction band electrons. Under high-pressure first-principles calculations have been performed to investigate structural, elastic, vibration and thermodynamic properties for CeAs. It can be concluded from enthalpy- pressures results that CeAs turns into B2 structure from B1 structure at nearly 18.6 GPa. For both structure, pressure effects on elastic constants and other elastic properties such as Young's modulus, shear modulus, Poisson's ratio, Pugh ratio, anisotropy factor have been calculated. Also electronic band strcuture and partial density of states have been investigated. From obtained phonon dispersion curves, it can be found that CeAs compound is stable dynamically for both structure

---

**Keywords:**

Rare earth intermetallic structures, CsCl type structure, optic

---

© 2021 Published by ECRES

## 1. INTRODUCTION

Lanthanides and actinides which has *f* shells partially show physical properties such as heavy-fermion behavior[1], magnetic ordering[2], unconventional superconductivity[3]. These properties are due to electronic properties like strong electronic correlation, large spin-orbital coupling and crystal field splitting. Since cerium based compounds show important electronic properties due to Ce *f* electrons, they have been considered by researchers[4]. These compounds crystallizes B1 structure at 0GPa. Pressure, which is external parameters, affects interaction of f-electrons with conduction electrons. Since pressure changes interatomic distances and this interaction varies with intetatomic distances.

The structural and electronic quatities of cerium monopnictides have been investigated using ab-initio methods by Svane et. al [5]. They have observed structural phase transition for Ce compounds under pressure. Svane et al have performed the electronic structure of rare earth chalcogenides and pnictides by first-principles methods under pressure [6]. Here, we have studied transformation from B1 structure to B2 structure, electronic band strcuture and mechanical properties under pressure for both B1 and B2 strcutures using first-principles methods.

## 2. CALCULATION METHOD

Here we have used VASP program [7-9] for calculating of all properties. This program is based on DFT method. In optimizing of the unit cell, as an exchange-correlation energy we have chosen generalized gradient approximation (GGA) based on the projector-augmented -wave (PAW) method [10, 11]. For valence-electron configurations were taken as  $4f^1$   $5d^1$   $6s^2$ ,  $5s^2$   $5p^3$ for the Ce and As respectively. To get integration in Brillouin zone we have used 14x14x14 Monkhorst and Pack [12] grid of k-points and 700 eV for the plane-wave basis as a cut-off energy in the calculations.

### 3. RESULTS AND DISCUSSION

To find optimizing structure we should find the equilibrium geometry. For this aim, the volume and atomic positions should be relaxed using ISIF= 3 in VASP. To obtain the bulk modulus (B) and first derivatives of bulk modulus (B'), for different lattice constants we have calculated total energy and obtained energies-volumes data have fitted to Murnaghan EOS for these B1 and B2 phases of CeAs. Energy-volume graphs for two phases are given in Fig. 1. Results from obtained structural optimizing are tabulated in Table I.

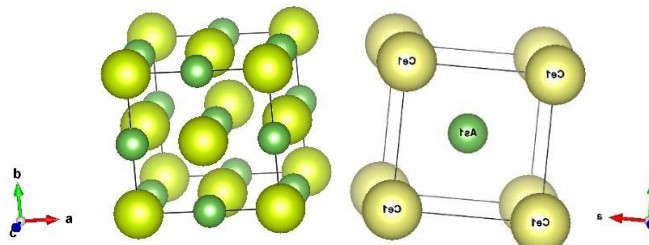


Figure 1. Unitcell of B1 and B2 phases for CeAs

Table 1. Obtained structural parameters for CeAs compound with experimental data.

Structures	a (Å)	B(GPa)	B'	V(Å <sup>3</sup> )	E <sub>tot</sub> (eV)
B1	5.949	74.2	4.12	26.33	-6.7018
Exp.	6.06 <sup>a</sup>	69.0 <sup>b</sup>			
B2	3.597	74.9	4.04	23.28	-6.3919

a: [ 14] b:[15]

From the energy-volume curves in Fig. 2, energy value of B1 phase of CeAs is more negative and lower than that B2 phase showing for this material B1 phase is stable than B2 phase. To investigate structural parameters in the high pressure, we should give phase- transition pressure for CeAs. We can conclude from Fig. 2 that the energy-volume curves show phase transformation from B1 phase to B2 phase. We can obtain phase transition pressure from enthalpy-pressure curves related to Gibbs free energy for both phases of CeAs. In the present case, the phase transition pressure from B1 to B2 phases for CeAs obtained at 18.6 GPa.

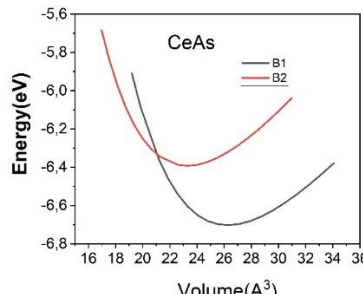


Figure 2. The energy-volume graphs for B1 and B2 crystal phases of CeAs.

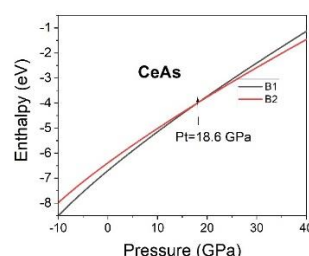


Figure 3. The enthalpies- pressures graph for estimating of phase transition pressure for B1 to B2 phases for CeAs

To search the electronic properties of both phases of CeAs, the band structure and total density of states at 0GPa for B2 and B1 phases of CeAs are calculated by CASTEP code and given in Fig. 4. In these graphs, fermi energy

level is lined at 0 eV. Our calculation shows that the B1 and B2 phases of CeAs is of metallic character due to there is no band gap near the Fermi level.

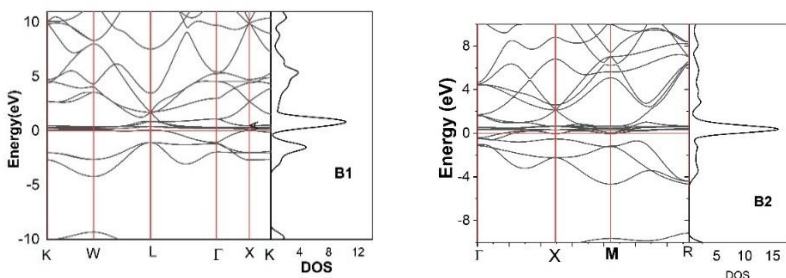


Figure 4. The graphs of band structure of B1 and B2 phases of CeAs

#### 4. CONCLUSIONS

Detailed analysis of pressure effects on the structural, electronic properties and phase transitions of CeAs compound have been performed using the first principles calculations via VASP code. The obtained lattice parameter and Bulk module of CeAs structure is in good agreement with experimental and other data. The computed band structures for both phases exhibit metallic character. The obtained pressure needed phase transformation from B1 to B2 structure for this compound is 18.6 GPa from enthalpy-pressure curves and comparable with other results.

#### REFERENCES

- [1] Stewart, G. R. Heavy-fermion systems. Rev. Mod. Phys. 1984; 5: 755. <<https://doi.org/10.1103/RevModPhys.56.755>>
- [2] Halg B.and. Furrer A, Anisotropic exchange and spin dynamics in the type-I (-IA) antiferromagnets CeAs, CeSb, and USb: A neutron study, Phys. Rev. B, 1986; 34: 6258 .< <https://doi.org/10.1103/PhysRevB.34.6258>>.
- [3] Sarrao J. L, Morales L. A., Thompson J. D., Scott B. L, Stewart G. R., Wastin F., Rebizant J., Boulet P., Colineau E., and Lander G. H., Plutonium-based superconductivity with a transition temperature above 18 K. Nature. 2002; 420: 297-299. <<https://doi.org/10.1038/nature01212>>.
- [4] Fulde P., Keller J., and Zwicknagl G., Theory of Heavy Fermion Systems. Solid State Physics, edited by H. Ehrenreich and D. Turnbull ~Academic, New York, 1988, Vol. 41, p. 1. <[https://doi.org/10.1016/S0081-1947\(08\)60378-1](https://doi.org/10.1016/S0081-1947(08)60378-1)>
- [5] Svane A. , Szotek Z., Temmermen W. M., Leagsgard, Winter H., Electronic structure of cerium monopnictides under [6] pressure, J. Phys. Condens. Matter. 1998; 10:5309-5325. <<https://doi.org/10.1088/0953-8984/10/24/009>>
- [7] Svane A. ,Temmermen W. M. Szotek Z. Theory of pressure-induced phase transitions in cerium chalcogenides
- [8] Phys. Rev. B. 1999; 59: 12, 7888. <https://doi.org/10.1103/PhysRevB.59.7888>
- [9] Kresse, G and Hafner J. Ab initio molecular dynamics for liquid metals. Phys. Rev. B. 1993; 47: 558. <[https://doi.org/10.1016/0022-3093\(95\)00355-X](https://doi.org/10.1016/0022-3093(95)00355-X)>.
- [10] Kresse, G and Hafner, J. Ab initio molecular-dynamics simulation of the liquid-metal-amorphous-semiconductor transition in germanium. Phys. Rev. B. 1994; 49:14251.< <https://journals.aps.org/prb/abstract/10.1103/PhysRevB.49.14251>>.
- [11] Kresse, G and Furthmuller, J. Efficiency of ab-initio total energy calculations for metals and semiconductors using a plane-wave basis set. Comput. Mater. Sci. 1996; 6: 15.< [https://doi.org/10.1016/0927-0256\(96\)00008-0](https://doi.org/10.1016/0927-0256(96)00008-0)>.
- [12] Perdew J. P. and Wang Y. Accurate and simple analytic representation of the electron-gas correlation-energy. Phys. Rev. B 1992; 45: 13244.. <<https://doi.org/10.1103/PhysRevB.45.13244>>
- [13] Perdew J. P., Chevary J. A., Vosko K. A., Jackson M. R., Pedersen D. J. Singh and Fiolhais C. S. H Atoms, molecules, solids, and surfaces - applications of the generalized gradient approximation for exchange and correlation, Phys. Rev. B 1992;46:6671. <https://doi.org/10.1103/PhysRevB.46.6671>
- [14] Monkhorst H. J. and Pack J. D. Special points for Brillouin-zone integrations Phys. Rev. B 1976;13:5188. <https://doi.org/10.1103/PhysRevB.13.5188>
- [15] Murnaghan F. D., The Compressibility of Media under Extreme Pressures. Proc. Natl., Acad. Sci. 1944;30:244. <https://doi.org/10.1073/pnas.30.9.244>
- [16] Wyckoff R W G 1964 *Crystal Structures* vol 1 (New York: Wiley). <<https://doi.org/10.1107/S0365110X65000361>>
- [17] WERNER A, HOCHHEIMER H D, MENG R L AND BUCHER E ABSENCE OF PRESSURE-INDUCED VALENCE CHANGE IN CEAS ; *Phys. Lett*1983. **97A** 207-209. <[https://doi.org/10.1016/0375-9601\(83\)90359-6](https://doi.org/10.1016/0375-9601(83)90359-6)>



# OPTOELECTRONIC PROPERTIES OF Zn DOPED LEAD FREE PHOTOVOLTAIC CsZnI<sub>3</sub> COMPOUND

Yasemin Oztekin Ciftci

Gazi University, Ankara, Turkey, [yasemin@gazi.edu.tr](mailto:yasemin@gazi.edu.tr), ORCID: 0000-0001-1796-0270

Cite this paper as:

Oztekin Ciftci, Y, Optoelectronic Properties of Zn doped Lead free photovoltaic CsSnI<sub>3</sub> compound. 9th Eur. Conf. Ren. Energy Sys. 21-23 April 2021, Istanbul, Turkey

**Abstract:** Due to applications in solar cells, metal halide perovskites have been studied by researchers. Since these cocompounds have remarkable performance such as controllable band gap, big optical absorption, lower carrier effective masses. Effects of Zn adding on electronic, elastic and optical properties have been performed using first principles calculations. From electronic band structure and density of states, CsZn<sub>x</sub>Sn<sub>1-x</sub>I<sub>3</sub>(x=0, 0.25, 0.5, 0.75, 1) compound are semiconductor. Also, mechanical properties show that this compound is stable according to Born's stability criteria. Obtained optical properties indicate that CsZn<sub>x</sub>Sn<sub>1-x</sub>I<sub>3</sub> have high absorption coefficient and conductivity and low reflectivity. As a result, Zn doped CsSnI<sub>3</sub> compound may has applications in optoelectronic devices.

**Keywords:** Optoelectronic, doped, CsSnI<sub>3</sub>

© 2021 Published by ECRES

## 1. INTRODUCTION

Since metal halide perovskite compounds have a adjustable bandgap, bigger optical absorption, long charge diffusion lengths, great mobility, they are used in solar cells thanks to their optoelectronic properties. These semiconductor materials are cheaper and more abundant. They have been used in a wide range of electronic devices [1-4]. Researchers have investigated the electronic, optical and mechanical properties to understand the properties of the semiconductors since it is important an understanding the characteristic of the system to improve device applications. Lead halide perovskites are promising photovoltaic material as a solar cell [2,2]

Pb free metal halide perovskite materials which have general formula ABX<sub>3</sub> have been investigated structural, optoelectronic and elastic properties by first-principle methods by Roknuzzaman et. al[5]. Here effects of Zn doping for CsSnI<sub>3</sub> on structural, elastic and optoelectronic properties have studied.

## 2. CALCULATION METHOD

In this study, ab-initio calculations have been performed by CASTEP programs which uses density-functional methods within the plane-wave pseudopotential approach[6,7]. For the exchange-correlation terms in the electron-electron interaction, we have chosen Perdew-Burke-Ernzerhof (PBE) parametrization of the generalized gradient approximation (GGA) [8]. Using the Ultrasoft Vanderbilt pseudopotential the interactions between the ions and the electrons were taken [9]. The electronic valence configurations for each atomic species were chosen as Zn: 3d<sup>10</sup>4s<sup>2</sup> Cs: 5s<sup>2</sup>5p<sup>6</sup>6s<sup>1</sup>, Sn: 5s<sup>2</sup>5p<sup>2</sup>, and I:5s<sup>2</sup>5p<sup>2</sup>. The electronic wave functions were expanded in the plane waves up to a 650 eV kinetic energy cutoff. A set (14x14x14) Monkhorst-Pack [10] grid of k-points in the irreducible Brillouin zone are used.

## 3. RESULTS AND DISCUSSION

The unitcell of CsSnI<sub>3</sub> which has space group Pm3m(no. 221)having five atoms are given in Fig.1. In the unitcell, Cs, Sn and I atoms place on the (0 0 0), (1/2 1/2 1/2) and (0 1/2 1/2) fractional coordinates for Cs, Sn and I atoms. The obtained strctural parameters like lattice parameter and volume for the optimized cel are given inn Table.1 and found to agree with the theoretical values.

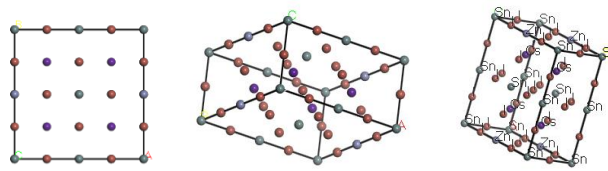


Fig.1 a) 2D unitcell b)3D unitcell and c) Zn doped( $CsZn_{0.25} Sn_{0.75} I_3$ ) unitcell of  $CsSnI_3$

Table .1 Structural parameters such as lattice constants(a), bulk modulus(B), volume(V) and density (d) for  $CsSn_{(1-x)}Zn_xI_3$

	a(A)	b(A)	c(A)	V(A <sup>3</sup> )	B (GPa)	d (gr/cm <sup>3</sup> )
$CsSnI_3$ (cubic)	6.279 6.30 <sup>a</sup>			247.603	11.274	4.240
$CsSn_{0.75}Zn_{0.25} I_3$ (Triclinic)	12.163		6.127	906.494	22.06	4.535
$CsSn_{0.5}Zn_{0.5} I_3$ (Triclinic)	12.172	11.842	6.085	877.202	19.345	4.485
$CsSn_{0.25}Zn_{0.75} I_3$ (Triclinic)	12.173	11.841	6.086	877.402		4.585
$CsZnI_3$ (Triclinic)	11.762		5.88	813.596	22.73	4.726

It can be concluded from Table 1 that lattice parameters for  $CsSnI_3$  is good agreement with other theoretical value [5]. After Zn doping on the  $CsSnI_3$ , the structure of  $CsSn_{(1-x)}Zn_xI_3$  transforms triclinic structure and has bigger volume due atomic size.

The response of a material to the applied stress is represented by the elastic constants ( $C_{ij}$ ) which give information about mechanical stability, stiffness, type of interatomic bonding, and anisotropy of solids. For cubic system, a crystal should be provided stability conditions as follows[11]

$$C_{11} - C_{12} > 0, C_{11} + 2C_{12} > 0, C_{44} > 0.$$

From the obtained values of elastic constants as given in Table 2,  $CsSnI_3$  is mechanically stable .

Table 2. The mechanic properties such as second-order elastic constants(in GPa) and shear modulus(GPa), Young's modulus (GPa) and Poisson ratio for  $CsSnI_3$

	$C_{11}$	$C_{12}$	$C_{44}$	G	E	$\nu$
This study	35.12	4.49	4.41	7.47	34.097	0.113
Theory [5]	21.34	1.22	5.74	7.55	16.18	0.07

Due to lower obtained elastic constants and bulk modulus this compound has flexibility and softness properties showing that  $CsSnI_3$  compound may be used as thin film in applications of solar cells. When the values of Poisson ratio is bigger than 0.26, the materials should be ductile character property, in other states it has brittle property. Due to obtained lower value of Poisson value  $CsSnI_3$  is brittle highly.

Using optimized lattice parameter of  $CsSnI_3$  , the electronic band structure and density of states along high symmetry points in Brilloin zone have been calculated using CASTEP code and given Fig.2. From Fig.2 it can be seen that  $CsSnI_3$  is semiconductors because of band gap of 0.445 eV in R point which is direct band gap. Here obtained band gap is compatible with other literature value (0.4 eV)[5].

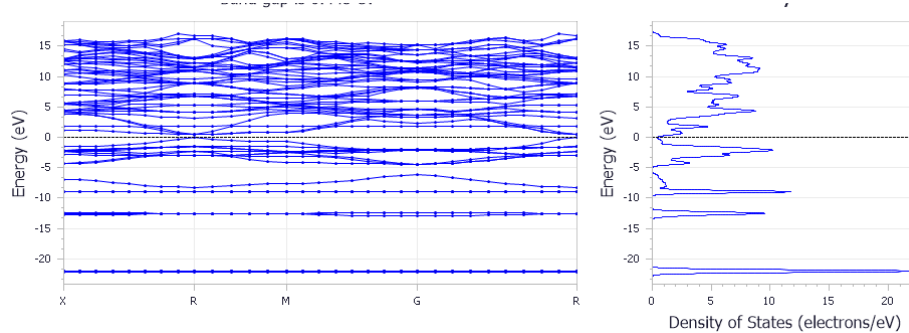


Fig.2 The obtained electronic properties for  $\text{CsSnI}_3$

#### 4. CONCLUSIONS

Here a detailed analyses of the obtained theoretical results of lead free perovskite Zn doped  $\text{CsSnI}_3$  code have been investigated using first-principles calculations by CASTEP. Obtained lattice parameter is good agreement with theoretical value. From the calculated elastic constants it can be decided as stable mechanically for  $\text{CsSnI}_3$  and has lower values. From smaller value of the Poisson ratio of  $\text{CsSnI}_3$ , it has brittle property. Also, the obtained band structure graph and band gap value is good agreement that of other study.

#### REFERENCES

- [1] Zhang, W., Eperon, G. E. & Snaith, H. J. Metal halide perovskites for energy applications. *Nature Energy* . 2016; 1: 16048. <<https://doi.org/10.1038/nenergy.2016.48>>
- [2] Swarnkar, A. *et al.* Quantum dot-induced phase stabilization of  $\alpha\text{-CsPbI}_3$  perovskite for high-efficiency photovoltaics. *Science* . 2016; 354:92–95. <DOI: 10.1126/science.aag2700>
- [3] Yin, W. J., Shi, T. & Yan, Y. Unique properties of halide perovskites as possible origins of the superior solar cell performance. *Advanced Materials*. 2014; 26:, 4653–4658. <<https://doi.org/10.1002/adma.201306281>>
- [4] Marshall, K. *et al.* Enhanced stability and efficiency in hole-transport-layer-free  $\text{CsSnI}_3$  perovskite photovoltaics. *Nature Energy* 2016; 1:16178 . <https://doi.org/10.1038/nenergy.2016.178>
- [5] Roknuzzaman M, Kostya (Ken) Ostrikov K. , Wang H., Du A. & Tesfamichael D., Towards lead-free perovskite photovoltaics and optoelectronics by *ab-initio* simulations, *Scientific Reports*, 2017; 7: 14025 .< DOI:10.1038/s41598-017-13172-y>
- [6] Segall M.D., Lindan P.J.D, Probert Pickard C.J., Hasnip P.J., Clark S.J., Payne M.C, First-principles simulation: ideas, illustrations and the CASTEP code. *J. Phys. Condens. Mater.* 2002; 14: 2717. <<https://doi.org/10.1088/0953-8984/14/11/301>>
- [7] Zhu W., Xiao H, J. Comput. *Ab initio* study of electronic structure and optical properties of heavy-metal azides:  $\text{TIN}_3$ ,  $\text{AgN}_3$ , and  $\text{CuN}_3$ , *Chem*.2008; 29:176. <<https://doi.org/10.1002/jcc.20682>>
- [8] Perdew J. P. and Wang Y. Accurate and simple analytic representation of the electron-gas correlation-energy. *Phys. Rev. B* 1992; 45: 13244,. <<https://doi.org/10.1103/PhysRevB.45.13244>>
- [9] Perdew J. P., Chevary J. A., Vosko K. A., Jackson M. R., Pedersen D. J. Singh and Fiolhais C. S. H Atoms, molecules, solids, and surfaces - applications of the generalized gradient approximation for exchange and correlation, *Phys. Rev. B* 1992;46:6671. <<https://doi.org/10.1103/PhysRevB.46.6671>>
- [10] [Monkhorst H. J. and Pack J. D. Special points for Brillouin-zone integrations *Phys. Rev. B* 1976;13:5188. <<https://doi.org/10.1103/PhysRevB.13.5188>>



## INNOVATIVE ACTIVITY OF INTEGRATED BUSINESS STRUCTURES

Vladimir Velikorossov

Plekhanov Russian University of Economics, Moscow, Russia, e-mail: velikorossov.vv@rea.ru, ORCID: 0000-0001-5845-4820

Yury Korechkov

International Academy of business and new technologies, Yaroslavl, Russia, e-mail: koryv@mail.ru, ORCID: 0000-0002-4462-3539

Maksim Maksimov

Plekhanov Russian University of Economics, Moscow, Russia, e-mail: maksimov.mi@rea.ru, ORCID: 0000-0001-9247-1819

Ona Grazyna Rakauskiene

Mykolas Romeris University, Vilnius, Lithuania, e-mail: corp.innovation@rea.ru, ORCID: 0000-0003-0007-0570

Anatoliy Kolesnikov

Plekhanov Russian University of Economics, Moscow, Russia, e-mail: kolesnokov.av@rea.ru, ORCID: 0000-0003-1776-2207

Evgeniy Genkin

Plekhanov Russian University of Economics, Moscow, Russia, e-mail: genkin.ev@rea.ru, ORCID: 0000-0002-5980-7285

Cite this paper as:

*Velikorossov, V.V., Korechkov, Yu.V., Maksimov, M.I., Rakauskiene, O.G., Kolesnikov, A.V., Genkin, E.V. Innovative activity of integrated business structures. 9<sup>th</sup> Eur. Conf. Ren. Energy Sys. 21-23 April 2021, Istanbul, Turkey*

---

**Abstract:**

The construction of a modern economic system presupposes the use of the achievements of a new technological order. Under these conditions, the role of innovative activity of business structures increases, which is most clearly manifested in the environment of integrated organizations. It is revealed that the innovative activity of integrated business structures is a set of intensive actions aimed at using progressive methods and technologies of the innovation process. Innovation activity is most clearly manifested in vertically integrated organizations connected by technological chains for the production of economic goods, which allow to unite a network of innovative interactions in different types of economic activity.

The structural and dynamic analysis of the innovation activity of an integrated organization allowed us to assess the pace and scale of innovations in production activities, and the use of technological achievements. The article reveals that the problems of effective development of an integrated company are solved by competent management of innovation activities based on strategic planning of innovations and investments. Innovative activity is manifested in the implementation of various strategies for the development of integrated business structures.

The example of Gazprom's activities shows the particular importance of implementing effective methods of innovation management.

---

**Keywords:**

*Innovation management, innovation activity, entrepreneurship, integrated organizations, investments.*

---

© 2021 Published by ECRES

## **1. INTRODUCTION**

In modern conditions of increasing competition between market entities at all levels, from the enterprise to the state, innovation is one of the decisive competitive advantages. It is obvious that innovation is unfeasible without scientific research at both levels of knowledge: fundamental and applied. Historically, the vast majority of research in our country was initiated and funded by the state. In today's environment, government support for such research is not always timely and adequate. In this regard, the authors draw attention to the innovative potential and activity of business, especially that part of it that is associated with the state (unitary enterprises, state corporations, companies built on the principle of PPP). The article examines the theoretical foundations and potential results of the company's innovative activity.

Innovation activity is a complex characteristic of the innovative activity of a company, including the degree of intensity of the actions carried out and their timeliness, the ability to mobilize the potential of the required quantity and quality.

Innovative activity is most clearly manifested in vertically integrated organizations connected by technological chains for the production of economic goods, which allow to unite a network of innovative interactions in different types of economic activity.

## **2. METHODOLOGY**

In the framework of the presented work, the authors used the following research methods: 1) at the theoretical level: study and generalization, formalization, analysis and synthesis, induction and deduction, axiomatics; 2) at the experimental-theoretical level: experiment, analysis, modeling, synthesis; 3) at an empirical level: observation, measurement, comparison.

## **3. ANALYSIS**

Research work, the expenditures on applied, fundamental research and experimental developments in Russia are carried out using different sources of funding. Research expenditures in 2019 amounted to RUB 422 billion. (less than \$ 6 billion at the exchange rate as of November 30, 2020), i.e., about 1% of GDP. This is significantly less than the task set by the President of the Russian Federation to allocate at least 2% of GDP for science. 243 billion rubles were allocated for applied research, the rest of the funds were spent for the purposes of fundamental science. In 2020, 519 billion rubles were allocated for science, and in 2021 this amount should be 486 billion rubles, which is 6% less than in 2020. Such financing of science not only threatens, but already leads to irreversible negative consequences and Russia's lagging in many high-tech spheres. For example, in the United States in 2019, \$ 118 billion was allocated from the budget for R&D (spending on science is more than 2.8% of the country's GDP), in 2020 - about \$ 134 billion, in 2021 it is planned for scientific research spend 142 billion dollars [2]. This is many times higher than the maintenance of scientific research in Russia. In many countries of the world, spending on science is above 3% of GDP (Table 1).

*Table 1 – Maintenance of scientific research, % of GDP*

Country	2018
Israel	4,8
The Republic of Korea	3,3
Sweden	3,3
Japan	3,3
Austria	3,2
Germany	3,1
Denmark	3,1
USA	2,8

The main form of spending on scientific research is investment in the non-financial sector of the economy (Fig. 1).

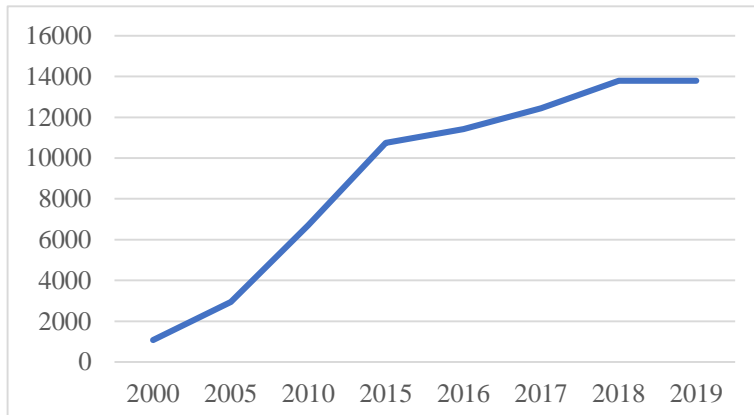


Figure 1. Investments in the non-financial sector of the economy, RUB trillion

In recent years, the growth of such investments has slowed down, which does not contribute to economic development, including the innovation spheres. Investments in fixed assets in 2010 amounted to 6,625.0 billion rubles, while investments in intellectual property - only 23.6 billion rubles. Since 2013, Rosstat has included investments in intellectual property objects in fixed assets: works of science, literature and art; software and databases for computers, inventions, utility models, industrial designs, selection achievements, non-material search costs, costs of research, development and technological work, etc. The volume of investments in fixed assets in 2019 amounted to 14,725.4 billion rubles.

The lag in research funding is unacceptable. It is necessary to significantly increase budget expenditures on science by creating mechanisms for attracting investments in scientific research from private companies. A special place in this process should be occupied by large integrated business structures, in which innovative activity should lead to an increase in their competitiveness in world markets. The analysis of organizational and managerial actions of entrepreneurial structures makes it possible to identify trends in the influence of new knowledge on the increase in the market value of integrated companies.

To identify the innovative activity of integrated business structures, it is necessary to determine its economic nature, determinants, as well as the impact of investment activity on the innovative activity of integrated organizations.

The development of the system of economic relations, the ongoing changes caused by the intensification of competition between different states and firms, lead to an intensification of the integration processes, such as combining the efforts of several organizations to achieve a common strategic goal, strengthening their competitiveness, developing and implementing innovative products and increasing the efficiency of production activities ... Integration business structures are of two types: horizontal and vertical. Innovative activity in horizontal integrated business structures is manifested in the use of intensive actions aimed at using progressive methods and technologies of the innovation process in organizations united for the implementation of certain goals. GOST R 54147-2010 "Strategic and innovative management. Terms and definitions" defines innovation activity as "a complex characteristic of the innovative activity of a firm, including the degree of intensity of the actions taken and their timeliness, the ability to mobilize the potential of the required quantity and quality."

Innovative activity is most clearly manifested in vertically integrated organizations connected by technological chains for the production of economic benefits, which allow uniting a network of innovative interactions in different types of economic activity [1].

The main purpose of the analysis of the innovative activity of an integrated entrepreneurial structure is to identify the innovative ability of the organization, as well as to find reserves that can increase the intensity of actions aimed at using progressive methods and technologies of the innovation process. To achieve this goal, it is necessary to carry out a structural and dynamic analysis of the innovative activity of an integrated organization and an analysis of organizational and managerial actions.

The assessment of the innovation activity depends on the quality and completeness of the information used by the companies. Information support for the analysis of innovative activities impacts the effectiveness of the analysis and must comply with the specific generally accepted principles of comparative analysis. The structural-dynamic analysis of the innovative activity of an integrated organization allows to assess the pace, scale of innovation in production activities, the use of the achievements of the new (6th) Technological Paradigm (TP).

In the context of the digitalization of the economy, approaches to the development of innovative activity are changing. Digital management is developing, which is based on the technology of digital platforms and digital twins in order to optimize the management process. Digital transformation leads to a change in the concept of management, when infocommunication technologies become the basis for making management decisions. A digital business model is emerging, when the architecture of value chains is associated with solving the problem of the effectiveness of technology selection while ensuring profit control [2]. Changes in the digital economy lead to an increase in the importance of using the experience and skills of employees who must constantly improve their qualifications in order to meet the ongoing changes in the surrounding digital world. The current technological changes lead to a change in the behavior of workers. Innovative strategies are the means of adaptation to an aggressive external environment. The integration into the strategy of organizing of innovative activities allows to overcome the aggressive nature of the external environment. However, this requires people to abandon opportunistic behavior and train specialists through cumulative learning, which will reduce the deficit of rationality. Problems of innovative activity and effective development of an integrated company are solved precisely through competent management of innovative activities based on strategic planning of innovations and investments. Innovative activity is manifested in the implementation of the following strategies for the development of integrated business structures.

1. "Classic" strategy. Sometimes it is called "traditional" because of the stable activity of an integrated organization in conditions when organizational and technological changes are not made to the production process, and the main efforts are directed to improving the quality of products, while adding new product properties. Innovative activity is low, in the future there may be a lag in technological, and then in financial and economic terms.

2. An "*opportunistic*" innovation strategy is also ineffective, since only a separate product is developed and produced that does not require large financial costs. This strategy can only be of a short-term nature in the context of a deep understanding of the market situation and occupation of a certain market niche.

3. Some companies use an "imitation" innovation strategy, which involves borrowing scientific knowledge and developments from other firms, for example, in the form of licenses. Small firms usually use a "dependent" innovation strategy, borrowing a new product or technology from large organizations, which does not require special financial investments.

4. The two distinct opposing innovation strategies are "defensive" and "offensive". With a defensive strategy, companies strive to keep up with competitors in the field of innovative development. As a rule, there are no own financial resources for innovative developments, or they are insufficient. With an offensive innovation strategy, a lot of money is invested in the development of a new product and qualified specialists are attracted. Of particular importance is the use of digital technologies and the development and implementation of elements of artificial intelligence. It is with an offensive strategy that innovative activity is manifested to the greatest extent.

As a rule integrated corporate structures, use a strategy of the classical type, when creating, since it is necessary to organizationally form a company and organize integrative interactions. An offensive innovation strategy is implemented when longer-term goals are achieved. This innovative strategy best meets the modern conditions of the 6th TP, representing a complex of management decisions in conditions of risk and uncertainty of the external environment.

When implementing innovative strategies, it is necessary to use project management. According to N.A. Zhdankin and M.A. Leonova, the urgency of the problem of improving the efficiency of project management in Russia is justified by the need to develop innovative approaches by generating ideas for the implementation of the most important economic tasks [3]. At the same time, in the opinion of O.A. Karpenko, a special role to technological innovations, which characterizes companies as innovation-active should be assigned [6].

The formation of a socially oriented Russian economy should take place based on innovative development methods. The export-oriented raw material approach and the possibility of obtaining rent payments are the necessary determinant of evolutionary development. The maintenance of economic growth, taking into account the achievements of the 6th TP, should rely on the use of the innovative ability of both large, medium-sized and small commercial organizations. The innovative ability is manifested as the willingness of integrated companies to create and implement innovative products using scientific and technological factors.

There are different scientific and theoretical approaches to the characterization of the concept of "innovative ability". For example, V.N. Gunin noted that the innovative ability of a company is a complex characteristic of its innovative activity, including the degree of intensity of the actions taken and their timeliness [5]. In our opinion, this definition is more suitable for the concept of "innovative activity", since the designated "ability" reflects the potential capabilities of the organization, and specific intensive actions to develop and implement innovative products reflect precisely the "activity" of activity eco-nomic structure.

The integrated development of the economy requires a systematic approach, which is based on the transition from the export of raw materials to an innovative socially oriented type of economic growth. According to S.Yu.

Glaziev, economic growth will provide "developed scientific and production potential, scientific schools, advanced technologies" [4]. It is necessary to implement methods for the development of innovative activity of organizations. Innovative activity reflects one of the most important factors of production - the entrepreneurial ability of integrated corporate structures. PJSC Gaz-prom considers the development of innovative activity as the main direction of increasing the efficiency of its production. This is reflected in the main strategic documents of the company, in particular, in the Passport of the Program of Innovative Development of PJSC Gazprom until 2025, in accordance with which the list of key performance indicators of PJSC Gazprom was approved:

- KPI<sub>1</sub> - share of R&D expenditures in revenue;
- KPI<sub>2</sub> - the effect of the introduction of innovative technologies in projects;
- KPI<sub>3</sub> - reduction in the specific consumption of fuel and energy resources for own technological needs and losses;
- KPI<sub>4</sub> - reduction of specific greenhouse gas emissions with CO<sub>2</sub> equivalent;
- KPI<sub>5</sub> - number of accidents and incidents at work;
- KPI<sub>6</sub> - increase in the number of patents used;
- KPI<sub>7</sub> - labor productivity.

The activities of PJSC Gazprom show the special importance of introducing effective methods of innovative management. The R&D program of PJSC Gazprom is developed annually and, under the conditions of contractual relations, is the basis for performing R&D work and is formed in accordance with the "Procedure for planning and organizing research, experimental design and technological developments" for PJSC Gazprom and its subsidiaries. The innovative activity of integrated business structures depends on the optimal use of possible financial instruments and directions of cash flows. In our opinion, the above KPIs of PJSC Gazprom should be supplemented with a quantitative measure for assessing the effectiveness of innovations (the criterion of expediency). This will allow to take into consideration, firstly, an increase in the level of efficiency achieved because of the development and implementation of an innovative product, and secondly, the determinants used to improve the quality of an innovative product. The criterion of the expediency of a managerial decision on the launch of an innovative product must meet the following requirements: 1) contain a quantitative assessment of the increment in the quality of an innovative product based on its intended purpose; 2) calculate the effect of the innovative activity undertaken; 3) consider all types of additional costs associated with improving the quality of products.

The peculiarity of the innovative activity of integrated business structures is also manifested in the fact that the investment support of the innovation infrastructure is carried out by companies that cover the entire cycle of innovation activities from the generation of new scientific and technical ideas, the development of an innovative product and to its implementation. Integrated entrepreneurial structures have the advantages of financial support for innovation due to a high degree of insurance and differentiation of research, the availability of products from sales channels. They realize the economies of scale of production. The process of implementing innovations in the field of economic relations takes place based on the implementation of investment projects. This leads to the satisfaction of existing market or social needs and brings a positive economic effect.

#### **4. CONCLUSIONS**

1. The current stage of development of the system of economic relations in Russia, the implementation of national projects should be based on the innovative capacities of business entities as the ability of different institutions and structures to continuously productive innovative search.
2. The most capable of manifesting innovative activity are integrated corporate entrepreneurial structures that use the latest achievements of the 6th TP and develop innovative activities due to self-organization and the formation of conditions that ensure positive synergistic effects.

#### **REFERENCES**

- [1] Korechkov, Yu.V., Dzhioev, O.V. Synergistic effect of integration processes and multiplication of investments in integrated organizations, *Online Journal of Science*, 2015. T. 7. № 2 (27). pp. 40-48
- [2] Korechkov, Yu.V. Macro Problems of Russia and Possible Ways to Solve Them, *Theoretical economics*, 2018, № 4 (46), pp. 61-67.
- [3] Zhdankin, N.A., Leonova, M.A. Improving the efficiency of project management through innovation, *Management of innovations*, 2020, № 2, pp. 106–121.
- [4] Glaziev, S.Yu. Strategy of the outstripping development of Russia in the context of the global crisis, *Selected lectures of the university*, Vol. 118, Saint-Petersburg, 2011.
- [5] Gunin, V.N. Innovative activity of enterprises: essence, content, forms, Moscow, State University of Management, 2019
- [6] Karpenko, O.A. Sources of financing for innovative activities of the enterprise, *Creative Economy*, 2014, vol.7.



# LEVEL OF MEETING THE NEEDS FOR SOLAR ENERGY FOR HOT WATER PRODUCTION IN THE IONIAN COAST OF ALBANIA

Halili Daniela

Department of physics, Faculty of Natural Science, "AleksandërXhuvani"University, Elbasan, Albania  
Daniela.Halili@uniel.edu.al, ORCID: 0000-0002-5740-8993

Serdari Eduart

Department of Engineering and Maritime Technology, University of Vlora, Albania eduartserdari@ymail.com  
ORCID: 0000-0001-7784-7389

Mitrushi Driada

Department of Engineering Physics, Faculty of Engineering Mathematics and Engineering Physics, Polytechnic University of Tirana, Tirana, Albania, d.mitrushi@fimif.edu.al, ORCID: 0000-0001-8722-4231

Buzra Urim

Department of Engineering Physics, Faculty of Engineering Mathematics and Engineering Physics, Polytechnic University of Tirana, Tirana, Albania, u.buzra@fimif.edu.al, ORCID: 0000-0002-9240-8825

*H. Daniela, S. Eduart, M. Driada, B. Urim. Level of meeting the needs for solar energy for hot water production in the Ionian coast of Albania. 9th Eur. Conf. Ren. Energy Sys. 21-23 April 2021, Istanbul, Turkey*

**Abstract:** The intensity of solar radiation in Albania is estimated approximately equal to 1300-1500 kWh/m<sup>2</sup>/year. Solar technology for the production of hot water in residential buildings today is extensively used even in our country. In coastal regions that are generally tourist areas, producing hot water by using solar collectors offers an economical alternative. Since solar energy has an uneven distribution throughout the year, another source is needed for fulfilling the insufficiency of solar energy. In this study we have calculated the amount of annual needs by using the solar energy for sanitary hot water production and the fulfill by the electrical energy. Our study is focused on the Ionian coast, specifically in the regions of Vlora, Himara and Xarrë. It results from the estimation, that December is the month with the highest value of electrical energy use for all three regions, with about 7.5kWh. June, July and August are the months when solar energy produced by solar collectors not only meets the needs for production of hot sanitary water but even exceeds them.

**Keywords:** solar collector, solar energy, electrical energy compensation

© 2021 Published by ECRES

## 1. INTRODUCTION

The use of solar technology for hot water production in residential buildings today constitutes the widest spread and the highest rate of development among renewable energy technologies, excluding hydropower.

Solar technology for producing sanitary hot water is a good economical option [1]. Albania has about 2484 sunny hours per year and a high potential of solar radiation, of about 1300 -1500 kWh / m<sup>2</sup> per year [2]. The average annual value of radiation is the main indicator that ensures economic efficiency in solar water heating panels (SWHP).

Solar Heating Systems (SHS) in residential buildings are extensively using even in Albania during last years. About 80% of such installations are located in the western part (Adriatic and Ionian coast)

According to the latest statistics of 2017, the total capacity of solar collectors for hot water production was 163MWth:158.9MWth belong to glazed flat - plate solar collectors and only 3.7 MWth to evacuated tube solar collectors. The entire area of solar collectors installed in Albania was 232,215 m<sup>2</sup>. The average area added during

2017 was 24,957 m<sup>2</sup>, with a capacity of 17.5 MW<sub>th</sub> [3]. These values are shown in Table 1. National objective for the year 2020 was to achieve 520,000 m<sup>2</sup> of total area of solar collectors [4].

*Table 1. Statistics data of the total area of solar collectors, their installed capacity and distribution by technologies used in Albania during 2017[4]*

Technology	Total area m <sup>2</sup>	Installed capacity (MW <sub>th</sub> )	Added 2017 (m <sup>2</sup> )	during	year
Glazed flat - plate solar collectors	226,969	158,9	22,471		
Evacuated tube solar collectors	5,246	3,7	2,486		

Solar energy can be used to fulfill about 60% of the needs for hot sanitary water production in the hotels [1]. The quantity of energy produced by a solar collector in a certain region is related to the quantity of solar energy potential in this region. In our country a family of four members needs about 12kWh energy per day for hot water production for sanitary use. This quantity of energy can be taken by using a solar collector with an active area of about 2m<sup>2</sup>, as if the value of solar energy potential wouldn't change throughout the year. But there is a seasonal variation of the solar radiation and a changeability of cloud cover, which strongly effect on the amount of the solar energy use.

This is why another source of energy is needed to supply the insufficiency of solar energy to assure daily needs for hot water production in certain periods of the year.

## 2. MATERIALS AND METHOD

Complete information regarding solar radiation disposability at any region is important for the design and economic estimation of a solar energy system [5]. The quantity of energy produced by a solar collector in a certain region is related to the quantity of solar energy potential in this region.

We have used data base of NASA surface meteorology and solar energy for RETScreen for estimating annual average value of solar energy for every region taken in consideration.

The price of electrical energy is 0.08 euro per kWh. The daily needed energy value for hot water production, according to SRCC conditions, is approximately 12.03 kWh [6].

In this study we have calculated the quantity of electrical energy used from the central grid as the only alternative source in Albania to fulfill the needs of hot water during all the year in an apartment house for a four member's family located in the region of Vlora, Himara and Xarrë.

The model of glazed flat plate solar collector used for producing hot water in our study is present in the Albanian market. It is set with change of inclination with horizon and has an aperture area of 2.33m<sup>2</sup>, Fr (tau alpha) 0.71 and Fr UL 4.41(W/m<sup>2</sup>)/°C.

The solar collector's price is taken 1,600 €, but it might not be the same from a year to another and it is related to a lot of factors such as manufacturers, retailers, the location, market fluctuations, etc.

In this study we have calculated the electrical energy compensated by the simple method:

$$\text{Energy compensated} = \text{Daily solar energy} - \text{Daily needed energy} \quad (1)$$

### ESTIMATION OF ENERGY COMPENSATED

Solar radiation in Albania has an uneven distribution from season to season and from a region to another. Effective use of solar energy is related to seasonal and regional variation of solar radiation. This is why we have made an estimation of amount energy compensated every month of the year. In the tables below are presented monthly average solar energy, monthly average electrical energy from the grid and the relative values for all the regions taken in consideration

Table 2. Monthly average solar energy, monthly average energy compensated from the grid and the relative values in Vlora

Month	Monthly average consumption of energy (kWh)	Monthly average solar energy (kWh)	Electrical energy compensated (kWh)	Relative value of electrical energy compensated (%)
January	372.9	179	193.9	52
February	336.8	193.6	143.2	43
March	372.9	274.4	98.5	26
April	360.9	278.9	82	23
May	372.9	361	11.9	3
June	360.9	429.3	-68.4	-19
July	372.9	470.3	-97.4	-26
August	372.9	415.9	-43	-12
September	360.9	329.5	31.4	9
October	372.9	258	114.9	31
November	360.9	169.2	191.7	53
December	372.9	140.5	232.4	62
Yearly	4391	3502.2	1099.9	25

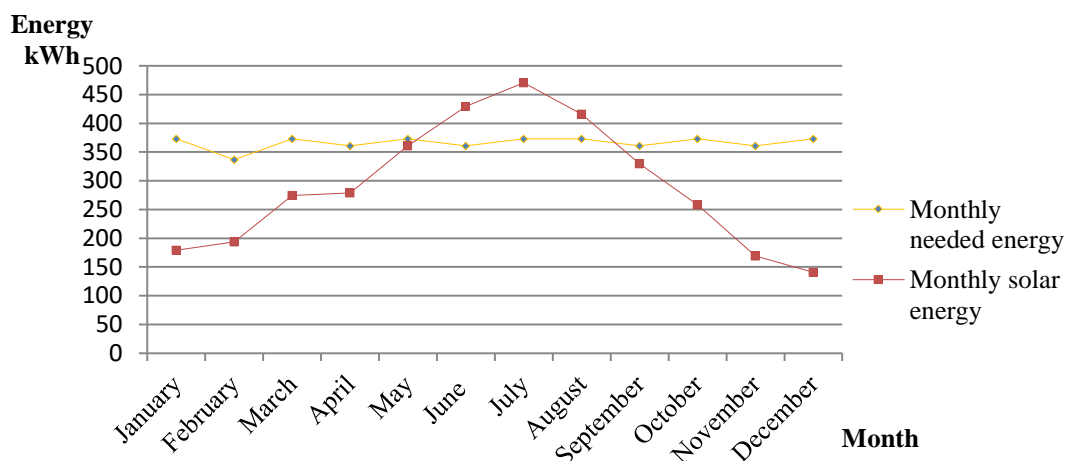


Figure 1. Monthly average solar energy provided by solar collector and the monthly needed energy for hot water production in Vlora

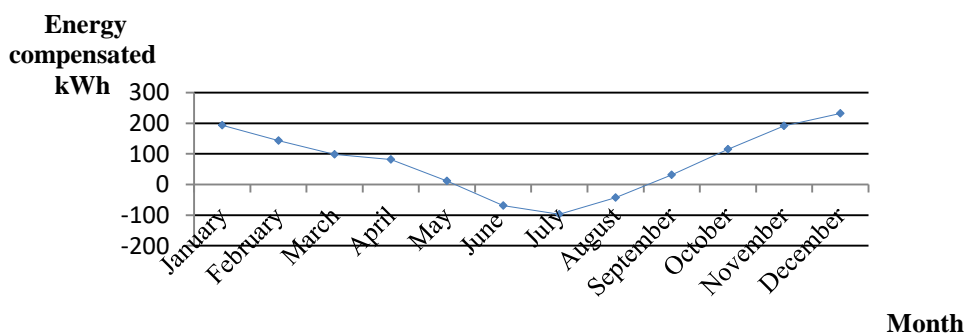


Figure 2. Variation of energy compensated from the central grid in Vlora

Table 3. Monthly average solar energy, monthly average energy compensated from the grid and the relative values in Himara

Month	Monthly average consumption of energy (kWh)	Monthly average solar energy (kWh)	Electrical energy compensated (kWh)	Relative value of electrical energy compensated (%)
January	372.9	176.9	196	53
February	336.8	191.8	145	43
March	372.9	272.3	100.6	27
April	360.9	277.9	83	23
May	372.9	359.5	13.4	4
June	360.9	428.3	-67.4	-19
July	372.9	468.7	-95.8	-26
August	372.9	414.4	-41.5	-11
September	360.9	328	32.9	9
October	372.9	255.9	117	31
November	360.9	167.2	193.7	54
December	372.9	138.5	234.4	63
Yearly	4391	3478	1116	<b>25</b>

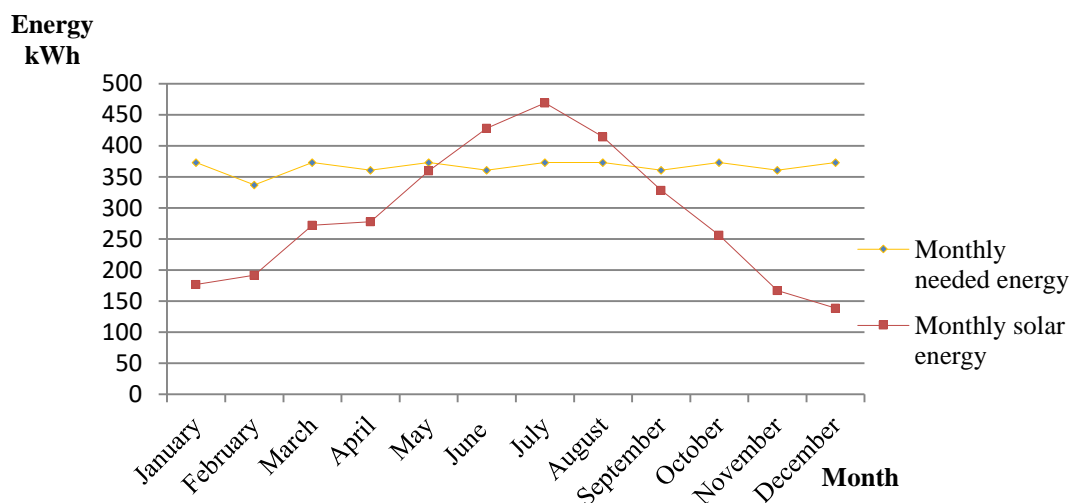


Figure 3. Monthly average solar energy provided by the solar collector and the monthly needed energy for hot water production in Himara

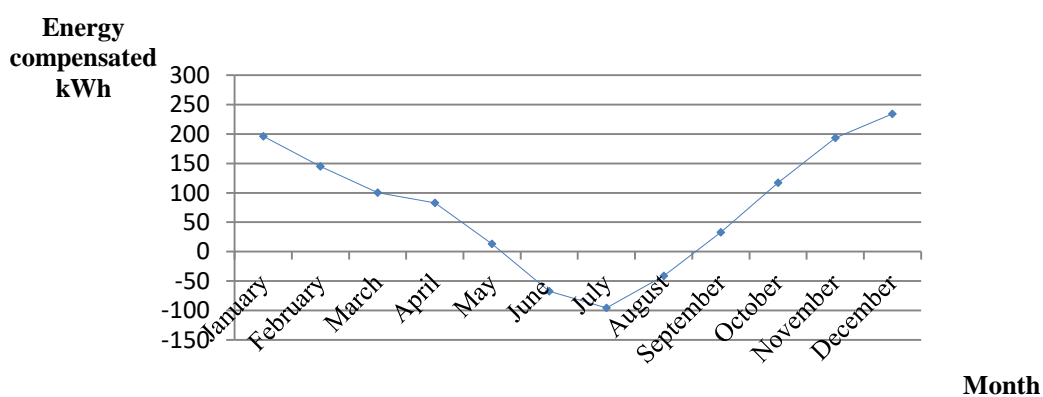


Figure 4. Variation of electrical energy compensated from the central grid in Himara

Table 4. Monthly average solar energy, monthly average energy compensated from the grid and the relative values in Xarre

Month	Monthly average consumption of energy (kWh)	Monthly average solar energy (kWh)	Electrical energy compensated (kWh)	Relative value of electrical energy compensated (%)
January	372.9	171.8	201.1	54
February	336.8	181.6	155.2	46
February	372.9	248.7	124.2	33
April	360.9	256.6	104.3	29
May	372.9	329.8	43.1	12
June	360.9	413.9	-53	-15
July	372.9	432.8	-59.9	-16
August	372.9	389.8	-16.9	-5
September	360.9	298.3	62.6	17
October	372.9	241.5	131.4	35
November	360.9	152.9	208	58
December	372.9	132.8	240.1	64
Yearly	4391	3248.5	1270	29

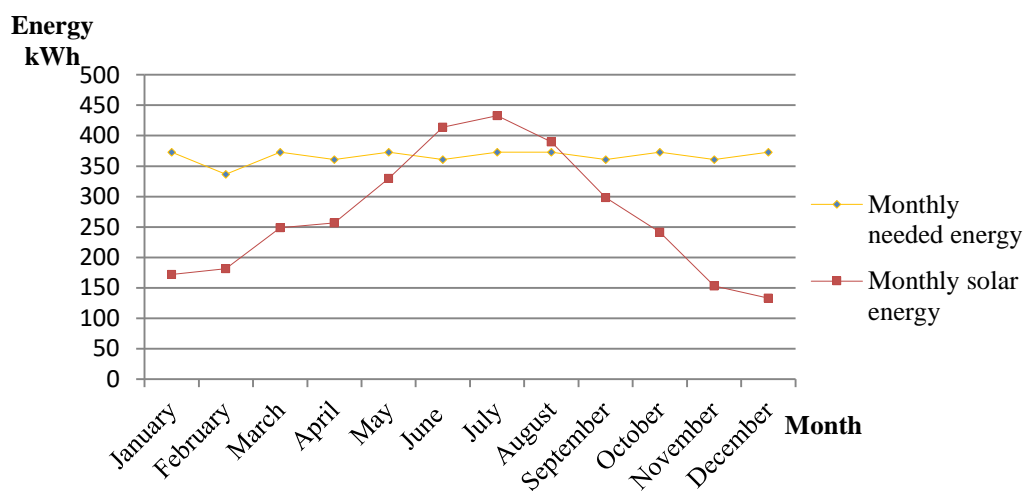


Figure 5. Monthly average solar energy provided by solar collector and the monthly needed energy for hot water production in Xarre

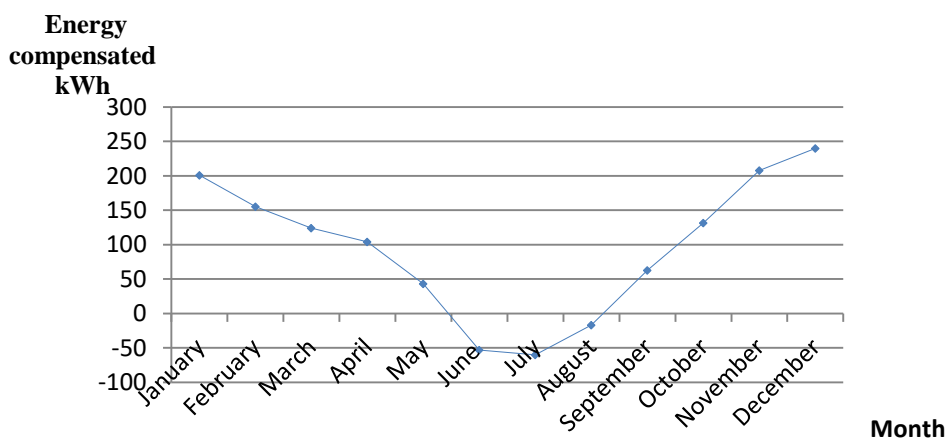


Figure 6. Variation of energy compensated from the central grid in Xarre

As it shows in the tables above, the electrical energy used from the grid, differs from one month to another, which is related to the variation of solar energy. We have sign '+' for values of electrical energy compensated from central

grid, and the sign '-' for the values of solar energy larger than the needed energy. June, July and August results the months when solar energy produced by solar collectors not only meets the needs for production of hot sanitary water but even exceeds them. For other months the values range from 11.9 kWh in 232.4 kWh for the region of Vlora, from 13.4kWh to 234.4kWh for the region of Himara, and from 43.1kWh to 240.1 kWh for the region of Xarrë. The relative values vary from 3% to 62% for the region of Vlora, from 4% to 63% for the region of Himara and from 12% to 64% for the region of Xarrë. December is the month with the highest value of electrical energy use for all three regions, with about 7.5kWh. The graphs above obviously illustrate that solar energy values vary from one day to another and consequently the requirements for the electrical energy from the grid.

## **CONCLUSIONS**

Solar technology for the production of hot water in residential buildings today is extensively used even in Albania. The intensity of solar radiation in our country is estimated approximately equal to 1300-1500 kWh/m<sup>2</sup>/year. Since solar energy has an uneven distribution throughout the year, an another source is needed for fulfilling the insufficiency of solar energy and the electrical energy is the only alternative source of energy in our country. In this study we are concentrated in the three regions of Ionion coast of Albania Vlora, Himara and Xarrë. From our estimations results that December is the month with the highest value of electrical energy use of about 7.5 kWh per day. June, July and August are the months when solar energy produced by solar collector is larger than the needed energy for production of hot sanitary water. For the other months the values range from 11.9 kWh in 232.4 kWh for the region of Vlora, from 13.4kWh to 234.4kWh for the region of Himara, and from 43.1kWh to 240.1 kWh for the region of Xarrë. The relative values vary from 3% to 62% for the region of Vlora, from 4% to 63% for the region of Himara and from 12% to 64% for the region of Xarrë.

## **REFERENCES**

- [1] Urban E. Monitoring and Modeling Hot Water Consumption In Hotels For Solar Thermal Water Heating System Optimization. MSc, University of Dayton, Dayton Ohio, U.S.A, 2011
- [2] Sanxhaku M, Lufi.A, Disa veçori të rrezatimit diellor në Shqipëri, Studime meteorologjike dhe hidrologjike 9, Tirana, ALBANIA, botim i ASHSH, 1983
- [3] Weiss W, Spörk-Dür M, Solar Heat Worldwide, E D I T I O N 2 0 1 9 , AEE - Institute for Sustainable Technologies 8200, Gleisdorf, AUSTRIA
- [4] Mauthner. F, Weiss. W. Solar Heat Worldwide, Markets and Contribution to the Energy Supply 2014, IEA SHC, 2014. <http://aee-intec.at/Uploads/dateien1016.pdf>
- [5] Goswami Yogi D, Kreith F, Energy efficiency And renewable energy Hand book, Second Edition, Oxfordshire, United Kingdom, Taylor & Francis Group, 2017
- [6] [http://www.solar-rating.org/facts/system\\_ratings.html](http://www.solar-rating.org/facts/system_ratings.html), visited on June 20, 2012.



# MORPHOLOGICAL PROPERTIES OF LOW TEMPERATURE HYDROTHERMALLY GROWN TiO<sub>2</sub> FILMS FOR DSSCS DEVICES

Atli Aycan

Department of Energy Systems Engineering, Faculty of Engineering and Natural Sciences, Ankara Yildirim Beyazit University, Ankara, Turkey, aycanathi18@gmail.com, ORCID: 0000-0003-1328-8042

Yildiz Abdullah

Department of Energy Systems Engineering, Faculty of Engineering and Natural Sciences, Ankara Yildirim Beyazit University, Ankara, Turkey, yildizab@gmail.com, ORCID: 0000-0003-4137-6971

Cite this paper as: Atli, A, Yildiz, A, *Morphological properties of low temperature hydrothermally grown TiO<sub>2</sub> films for DSSCS devices. 9<sup>th</sup> Eur. Conf. Ren. Energy Sys. 21-23 April 2021, Istanbul, Turkey*

**Abstract:** In this study, the effect of the underlying seeding layer on the morphology and structural properties of TiO<sub>2</sub> films coated with hydrothermal method was investigated. The TiO<sub>2</sub> film was grown on the FTO surface as a result of the 18-hour process at relatively low temperature. The seeding layer was obtained by chemical bath method. The presence of the seeding layer affects the surface properties of the coated film and the crystalline structure of the film. The films have an appropriate candidate for being a photoanode in dye sensitized solar cells.

**Keywords:** DSSC, TiO<sub>2</sub>, hydrothermal, seed layer

© 2021 Published by ECRES

Nomenclature	
DSSC	Dye Sensitized Solar Cell
TiO <sub>2</sub>	Titanium dioxide
XRD	X-ray diffractometer
AFM	Atomic force microscopy

## 1. INTRODUCTION

Dye sensitized solar cells are electrochemical devices which covers two rigid electrodes namely as working and counter and a liquid electrolyte between them. Photogenerated free electrons arise from excitation of dye molecules under sunlight illumination.

The working electrode generally includes wide band gap metal oxides such as TiO<sub>2</sub>, ZnO etc. This broadband material (higher than 3 eV) acts as a framework for the transmission of electrons without suppressing visible light transmission [1]. The advantage and necessity of transmitting visible light is that they require visible light at the appropriate wavelength in order to excite dye molecules and produce free electrons.

The TiO<sub>2</sub> framework also has exactly these characteristics and can only absorb UV light due to its high band gap energy. The working electrode can be obtained by many methods such as spin coating, chemical bath deposition, spray pyrolysis, electro deposition, doctor blade and hydrothermal. All these coating methods will directly affect the morphological properties of the working electrode to be obtained. Morphological features will directly affect the interface structure formed with the electrolyte, the surface roughness, the active interaction area that may occur and the amount of surface the paint can hold. Hydrothermal is the most fascinating and open way to obtain new nanostructures.

## 2. METHODOLOGY

FTO substrates were cleaned with acetone, ethanol, and deionized water using an ultrasonic bath. Seed layer of  $\text{TiO}_2$  film was obtained by chemical bath deposition of aqueous 0.1 M  $\text{TiCl}_4$  solution at 70 °C for 60 min. The film was annealed at 500 °C for 1h, immediately. It is utilized as a seed layer. Hydrochloric acid (HCl, 37 %), and DI water mixed up in volumetric ratio of 2:1 (30 ml, 15 ml) to obtain a homogenous clear solution with a magnetic stirrer. 0.2 mL of titanium isopropoxide added into the clear solution. The FTO substrates were put into a sealed autoclave for nanostructures growing.

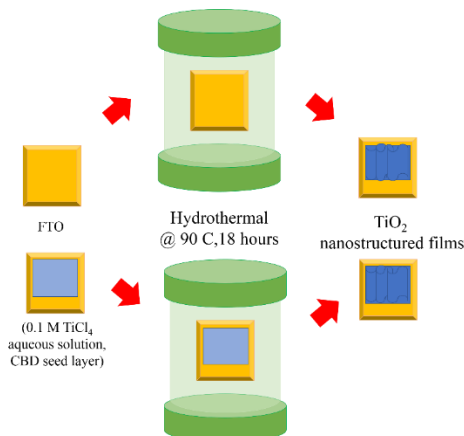


Figure 1. Illustration of  $\text{TiO}_2$  films experimental process

The morphology and microstructural characterizations of the nanostructured samples were performed using an Atomic force microscopy (AFM, Q-Scope 250, Quesant Instrument Corporation, USA). Surface morphology of films were investigated in the area of  $10 \mu\text{m} \times 10 \mu\text{m}$ . XRD pattern was obtained with  $\text{Cu K}\alpha$  radiation at  $\lambda = 0.1546 \text{ nm}$ , in the range of 20-60°.

## 3. RESULTS AND DISCUSSION

Figure 2 shows AFM images of the films. RMS value increases from 73.28 to 87.66 nm for the films without seed layer (Figure 2a) and with seed layer (Figure 2b), respectively. It might be the poor quality of the seed layer cause inhomogeneity of the surface of the FTO and this reflects to the top hydrothermal layer growth and high value of roughness.

Table 1. Surface properties of  $\text{TiO}_2$  films

Item no	Item Description	RMS (nm)
1	$\text{TiO}_2$ film without seed layer	73.28
2	$\text{TiO}_2$ film with seed layer	87.66

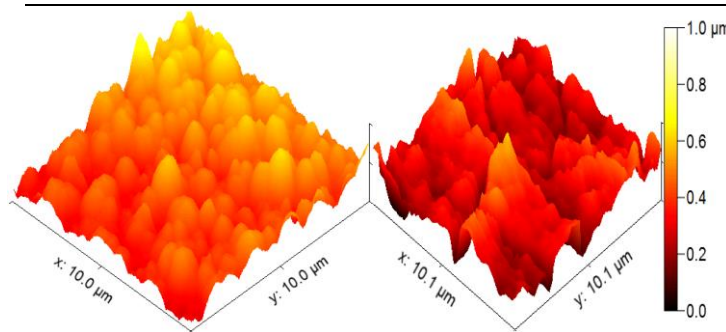


Figure 2. (a) Morphology of  $\text{TiO}_2$  films hydrothermally growth without seed layer, (b) with  $\text{TiO}_2$  seed layer.

Figure 3 shows the crystallographic information of the coated films. The peaks at  $2\theta=26.57^\circ$ ,  $33.87^\circ$ ,  $37.95^\circ$ , and  $51.75^\circ$  match with (110), (101), (200), and (211) orientations and belongs to FTO. A clear peak at  $36.68^\circ$  indicates (101) rutile of the  $\text{TiO}_2$  film (JCPDS card No. 01-073-2224) [2, 3, 4]. And the intensity of the peak is more dominant for the film obtained without seed layer. The low temperature process leads to a low energy of growth process and films have an amorphous phase of  $\text{TiO}_2$ .

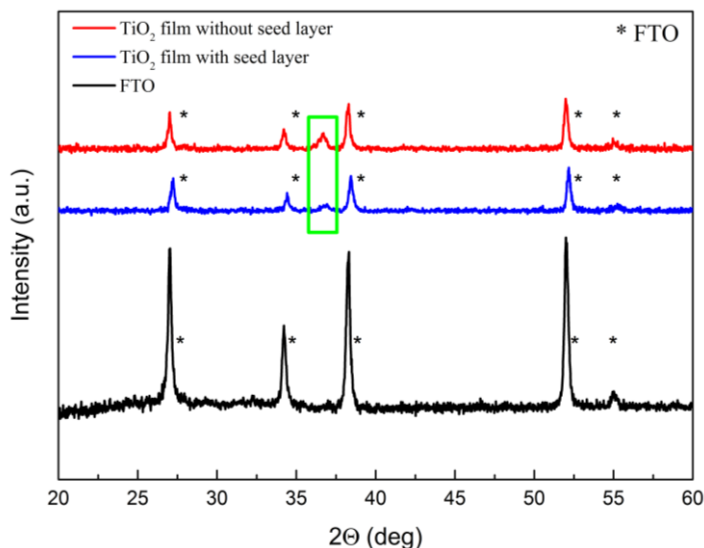


Figure 3. XRD pattern of  $\text{TiO}_2$  films hydrothermally growth without/with seed layer on FTO

#### 4. CONCLUSION

In this study  $\text{TiO}_2$  films were grown on the bare and seeded FTO substrates for 18-hour at relatively low temperature ( $90^\circ\text{C}$ ). The seeding layer was obtained by chemical bath method. The presence of the seeding layer affects the surface properties of the coated film and the crystalline structure of the film. With addition of seed layer, RMS value of the films were increased. Considering crystal structures, a peak of (101) rutile  $\text{TiO}_2$  was obtained for the film without any seed layer. The films have an appropriate candidate for being a photoanode in dye sensitized solar cells.

#### REFERENCES

- [1] D'Amato, C. A., Giovannetti, R., Zannotti, M., Rommozzi, E., Minicucci, M., Gunnella, R., & Di Cicco, A. (2018). Band gap implications on nano- $\text{TiO}_2$  surface modification with ascorbic acid for visible light-active polypropylene coated photocatalyst. 2018, 8, 599.
- [2] Haider, A. J., Jameel, Z. N., Taha, S. Y. Synthesis and characterization of  $\text{TiO}_2$  nanoparticles via sol-gel method by pulse laser ablation. 2015, 5, 761-771.
- [3] Hanaor, D. A., & Sorrell, C. C. Review of the anatase to rutile phase transformation. 2011, 4, 855-874.
- [4] Syuhada, N., Yuliarto, B. Synthesis and Characterization Hierarchical Three-Dimensional  $\text{TiO}_2$  Structure via Hydrothermal Method. In IOP Conference Series: Materials Science and Engineering 2018, May Vol. 367, No. 1, IOP Publishing, p. 012052.



# MOLARITY OF PRECURSOR DEPENDENT MORPHOLOGICAL PROPERTIES HYDROTHERMALLY GROWN TiO<sub>2</sub> FILMS

Atli Aycan

Department of Energy Systems Engineering, Faculty of Engineering and Natural Sciences, Ankara Yildirim Beyazit University, Ankara, Turkey, aycanatl18@gmail.com, ORCID: 0000-0003-1328-8042

Yildiz Abdullah

Department of Energy Systems Engineering, Faculty of Engineering and Natural Sciences, Ankara Yildirim Beyazit University, Ankara, Turkey, yildizab@gmail.com, ORCID: 0000-0003-4137-6971

Cite this paper as:

Atli, A., Yildiz, A. Molarity of precursor dependent morphological properties hydrothermally grown TiO<sub>2</sub> films. 9<sup>th</sup> Eur. Conf. Ren. Energy Sys. 21-23 April 2021, Istanbul, Turkey

**Abstract:** In the hydrothermal deposition method carried out at low temperature, the precursor molarity and structural properties of the obtained films were investigated. AFM measurement for morphological analysis and XRD measurements for crystal structure analysis were used. A distinct peak in the crystal structure was observed in the film obtained by using high molarity chemical precursor (0.1 M), and the surface roughness increased compared to the film with low molarity precursor (0.05 M).

**Keywords:** DSSC, TiO<sub>2</sub>, hydrothermal, precursor, molarity

© 2021 Published by ECRES

## Nomenclature

DSSC	Dye Sensitized Solar Cell
TiO <sub>2</sub>	Titanium dioxide
XRD	X-ray diffractometer
AFM	Atomic force microscopy

## 1. INTRODUCTION

Dye sensitive solar cells are devices that convert solar energy into electrical energy. It attracts the attention of researchers with its low costs and promising energy conversion efficiencies. TiO<sub>2</sub> photoanodes are one of the main components of these devices. Dye molecules are attached to TiO<sub>2</sub> molecules and play role on providing of photogenerated current. The light pass through this layer and exit from the circuit

Extending transmission, the path of the incident light, the fact that the light is trapped in a device will directly affect the time and amount of light energy utilization. Different TiO<sub>2</sub> nanostructures such as nanorods, nanotubes, and nanobelts can be synthesized via hydrothermal method as a particle [1, 2] to be designed to benefit more from the incoming light, as well as directly grown on the target substrate. Many parameters such as time of the growing process, temperature, and molarity of the precursors or ratio of the all chemicals.

## 2. METHODOLOGY

FTO substrates were cleaned with acetone, ethanol, and deionized water using an ultrasonic bath. 30 ml of hydrochloric acid (HCl, 37 %), and 15 mL of deionized water mixed with a magnetic stirrer at room temperature. 0.2 mL and 0.4 mL of titanium isopropoxide (TTIP) added into the clear solutions as a precursor, respectively. The FTO substrates were put into a sealed autoclave for nanostructures growing at 90 °C for 18 h. The films of TiO<sub>2</sub> grown by these solutions denoted as 0.05 M TTIP and 0.10 M TTIP for the following parts of the study.

The obtained films were characterized morphological and structural by help of atomic force microscopy (AFM, Q-Scope 250, Quesant) and X-ray diffractometry (Rigaku Miniflex 600). XRD pattern was obtained with Cu Kα radiation at  $\lambda = 0.1546$  nm, in the range of 20-60°.

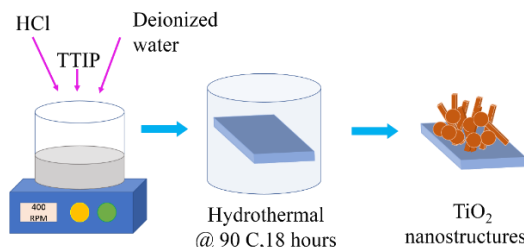
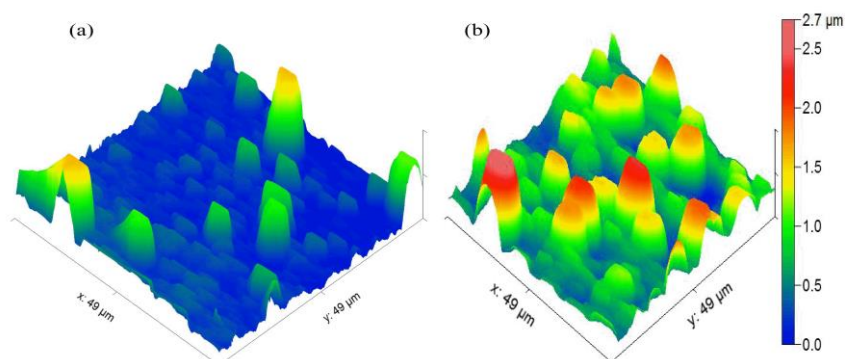


Figure 1. Illustration of the experimental process

### 3. RESULTS AND DISCUSSION

In this study, the  $\text{TiO}_2$  film prepared by using 2 different molarity starting precursors was examined in terms of morphological and structural properties. For which application the film will be used, it is very important in evaluating the surface properties. For example, a high RMS value is desirable when it is aimed to increase the interaction with dye and electrolyte, but in some cases a compact and flat surface may be desired as it affects the structure of the film to be coated on high RMS value. It is thought that the increased molarity increases the roughness on the surface and this situation will increase the optical reflections and the light path. This situation is considered suitable for DSSCs applications. The low surface roughness is an indication of how well the structure adheres to the film as known from the literature [3]. But here we might have irregular nanostructures on the surface.

Figure 2. (a) Morphology of  $\text{TiO}_2$  films hydrothermally growth with 0.05 M of TTIP, (b) with 0.10 M of TTIP precursor.

Surface property parameters such as average roughness (RMS), skewness, and kurtosis of the film surfaces were determined by detailed AFM analysis. The average roughness value appears as the arithmetic mean of the roughness on the surface compared to the accepted reference flat surface. The skewness factor is related to surface roughness symmetry and is a measure of balance between crest and trough points. The surface skewness is 2.61 and 1.26 for the films with 0.05 M and 0.10 M of TTIP. Kurtosis value reflects the sharpness of the roughness on the surface. The kurtosis values are 7.86 and 1.52 for the films with 0.05 M and 0.10 M of TTIP, respectively. Table 1 shows these stated values about surface properties of the  $\text{TiO}_2$  films. Projected area shows the geometric real area of the measured film while, surface area is the increased area due to nanostructures. Projected area values are fixed for both and the surface area values are increased for both. Due to the high value of RMS value surface area was increased more.

Table 1. Surface properties of  $\text{TiO}_2$  films

Molarity of precursor in hydrothermal sol.	RMS (nm)	Skewness	Kurtosis	Projected area ( $\mu\text{m}^2$ )	Surface Area ( $\mu\text{m}^2$ )
0.05 M TTIP	248.6 nm	2.61	7.86	2.401	2.468
0.10 M TTIP	469.4 nm	1.26	1.52	2.401	2.526

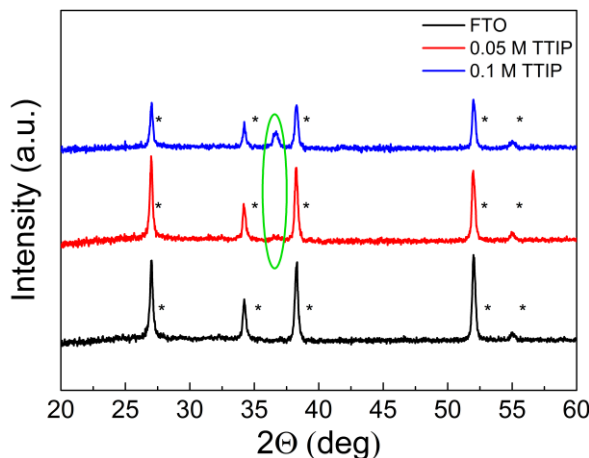


Figure 3. XRD pattern of  $TiO_2$  films hydrothermally growth under different precursor amounts.

Figure 3 shows the XRD pattern of the films with varying molarity of the precursor. The XRD image confirms that there is no clear  $TiO_2$  peak for the lower molarity. It can be related to lower amount of precursor and lower growing energy at low temperature ( $90^\circ C$ ) is not enough for the composing of  $TiO_2$  successively. Because there is no decrease or difference in the intensity of the peaks, this is similar to FTO peaks shown as a reference below. But even in the same low temperature, the increase in the precursor molarity triggers the forming of  $TiO_2$  nanostructures. There is a peak of (101) rutile phase from the  $TiO_2$  JCPDS card No. 01-073-2224 [4, 5, 6].

#### 4. CONCLUSION

This work covers a hydrothermal growing process which was handled at out at low temperature ( $90^\circ C$ ). With varying precursor molarity structural and morphological properties of the films were investigated. A distinct peak in the crystal structure was observed in the film obtained by using high molarity chemical precursor (0.1 M), and the surface roughness increased compared to the film with low molarity precursor (0.05 M). It is considered that high molarity obtained film might be suitable to be used as a direct photoanode in DSSCs or as a layer that can give reflective properties to the photoanode.

#### REFERENCES

- [1] Zhou, W., Du, G., Hu, P., Li, G., Wang, D., Liu, H., ... Jiang, H. Nanoheterostructures on  $TiO_2$  nanobelts achieved by acid hydrothermal method with enhanced photocatalytic and gas sensitive performance. 2011, 22, 7937-7945.
- [2] Suryawanshi, H., Patil, D. R. Hydrothermal Synthesis and Characterization of  $TiO_2$  Nanorod Array Grown on FTO Substrate. In Techno-Societal 2018 2020 Springer, Cham. (pp. 963-970).
- [3] Kumar, N., Wilkinson, T. M., Packard, C. E., Kumar, M. Design of low surface roughness-low residual stress-high optoelectronic merit a-IZO thin films for flexible OLEDs. 2016, 22, 225303.
- [4] Haider, A. J., Jameel, Z. N., Taha, S. Y. Synthesis and characterization of  $TiO_2$  nanoparticles via sol-gel method by pulse laser ablation. 2015, 5, 761-771.
- [5] Hanaor, D. A., & Sorrell, C. C. Review of the anatase to rutile phase transformation. 2011, 4, 855-874.
- [6] Syuhada, N., Yuliarto, B. Synthesis and Characterization Hierarchical Three-Dimensional  $TiO_2$  Structure via Hydrothermal Method. In IOP Conference Series: Materials Science and Engineering 2018, May Vol. 367, No. 1, IOP Publishing, p. 012052.

# THE FABRICATION OF $\text{SnO}_2/\text{Si}$ HETEROJUNCTION DIODE

Ozel Kenan

Ankara University, 06010 Ankara, TURKEY, nkenanozel89@gmail.com, ORCID: 0000-0002-0250-3731

Yildiz Abdullah

Department of Energy Systems Engineering, Faculty of Engineering and Natural Sciences, Ankara Yıldırım Beyazıt University, Ankara, Turkey yildizab@gmail.com, ORCID: 0000-0003-4137-6971

*Cite this paper as:*

*Ozel, K, Yildiz, A., The fabrication of  $\text{SnO}_2/\text{Si}$  heterojunction diode. 9th Eur. Conf. Ren. Energy Sys. 21-23 April 2021, Istanbul, Turkey*

**Abstract:** Herein, we report the production of  $\text{SnO}_2/\text{p-Si}$  heterojunction using sol-gel method. X-Ray diffraction (XRD) is used to analyze the orientations of  $\text{SnO}_2$  film. The current-voltage (I-V) features are recorded to determine the photoelectrical performance of  $\text{SnO}_2/\text{p-Si}$  heterostructure. The diode behavior was observed for the present device. The rectification ratio of 93 and an extremely low dark current of 33 nA indicate the formation p-n heterojunction. This work shows that n- $\text{SnO}_2/\text{p-Si}$  heterojunction is promising for diode applications.

**Keywords:** *Heterojunction, Diode,  $\text{SnO}_2$*

© 2021 Published by ECRES

## 1. INTRODUCTION

In the last decade, a great deal of research has been directed towards the production of p-n heterojunction. Some metal oxides, including  $\text{ZnO}$ ,  $\text{TiO}_2$ , and  $\text{SnO}_2$  has been captured a lot of attention owing to the enthralling optoelectrical characteristics [1-3]. Among them,  $\text{SnO}_2$  is an intriguing metal oxide with desired optoelectrical properties [4].

The deposition of metal oxides has been accomplished by a variety of methods [5]. In particular, the sol-gel spin coating is considered to be promising method, because it is inexpensive, and easy to applicable.

In this article, we report the production of  $\text{SnO}_2/\text{p-Si}$  heterojunction, which is achieved by the sol-gel method. The observed diode characteristic reveals that the fabricated structure is suitable for the diode applications

## 2. EXPERIMENTAL SECTION

After dicing and cleaning of p-Si wafer, the recipe depicted by Alsac et al. was used to synthesize  $\text{SnO}_2$  sol [5]. The  $\text{SnO}_2/\text{p-Si}$  heterojunction was obtained by two cycles of coating of the synthesized  $\text{SnO}_2$  sol. The front and back electrodes were acquired by screen printing of Ag paste. The cross-sectional view of the device is given in Figure 1.

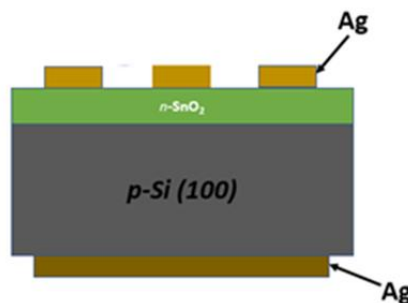


Figure 1. Cross-sectional view of n- $\text{SnO}_2/\text{p-Si}$  heterojunction diode

### 3. CHARACTERIZATIONS

XRD pattern of  $\text{SnO}_2$  are drawn in Figure 2. The pattern describes three peaks of 26.8, 34.22 and 52.28, indicating the orientations, and polycrystalline nature of  $\text{SnO}_2$ .

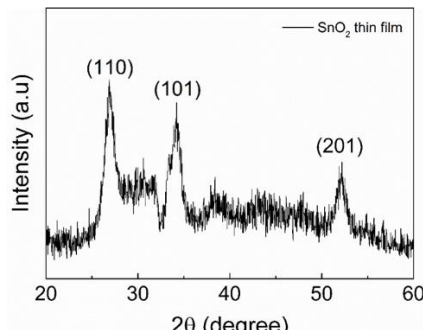


Figure 2. XRD pattern of  $\text{SnO}_2$  thin film

Figure 3 depicts the I-V curve of the device, showing a decent diode behavior. The values of ideality factor ( $n$ ), barrier height ( $\phi_{bo}$ ), and leakage current ( $I_s$ ) can be extracted by using formulas [6]

$$I = I_s \left[ \exp \left( \frac{qV}{nkT} \right) - 1 \right]$$

$$n = \frac{q}{kT} \frac{dV}{d \ln(I)}$$

$$\phi_{bo} = \frac{kT}{q} \ln \left( \frac{AA^*T^2}{I_s} \right)$$

where  $q$  is the electron charge.  $V$  refers to the applied voltage.  $k$  represents the temperature.  $A$  is the Boltzmann's constant.  $A^*$  is the Richardson constant. The values of  $n$ ,  $I_s$ , and  $\phi_{bo}$  are 6.5, 33 nA, and 0.81 eV, respectively. Generally, the non-unity value of  $n$  is resulted from some factors, including high series resistance, barrier inhomogeneity, tunneling process [7].  $RR$  ( $I_{\text{forward}}/I_{\text{reverse}}$ ) reveals the rectifying nature of diodes. Here, it is found to be 93.

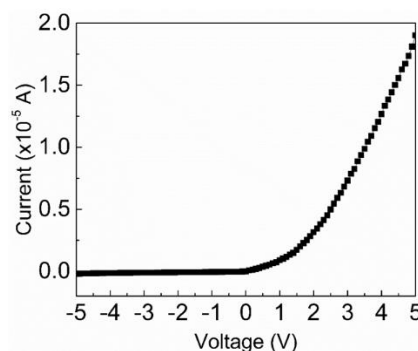


Figure 3. I-V graph of the  $\text{SnO}_2/\text{p-Si}$

### 4. CONCLUSION

In summary, the production of  $\text{SnO}_2/\text{p-Si}$  heterojunction was reported. Some figures of merits were evaluated by XRD, and I-V measurements. The results disclose that the n- $\text{SnO}_2/\text{p-Si}$  heterojunction would be suitable for the production of diodes.

### REFERENCES

- [1] Mardare, D., Yildiz, A., Girtan, M., Manole, A., Dobromir, M., Irimia, M., ... & Luca, D. Surface wettability of titania thin films with increasing Nb content. 2012, 112(7), 073502.
- [2] Serin, T., Yildiz, A., Uzun, S., Çam, E., & Serin, N. (2011). Electrical conduction properties of In-doped ZnO thin films. 2011, 84(6), 065703.
- [3] Serin, N., Yildiz, A., Alsaç, A. A., & Serin, T. Estimation of compensation ratio by identifying the presence of different hopping conduction mechanisms in  $\text{SnO}_2$  thin films. 2011, 519(7), 2302-2307.

- [4] T. Oshima, T. Okuno, and S. Fujita, UV-B Sensor Based on a SnO<sub>2</sub> Thin Film, vol. 48, no. 12, p. 120207, 2009. Doi: 10.1143/jjap.48.120207
- [5] Alsac, A. A., Yildiz, A., Serin, T., & Serin, N. Improved conductivity of Sb-doped SnO<sub>2</sub> thin films. 2013, 113(6), 063701.
- [6] Koksal, N. E., Sbeta, M., & Yildiz, A.. GZO/Si photodiodes exhibiting high photocurrent-to-dark-current ratio. 2019, 66(5), 2238-2242.
- [7] Ilican, S., Gorgun, K., Aksoy, S., Caglar, Y., & Caglar, M. Fabrication of p-Si/n-ZnO: Al heterojunction diode and determination of electrical parameters. 2018, 1156, 675-683.

# THE INVESTIGATION OF UV DETECTION PERFORMANCE OF SnO<sub>2</sub>/p-Si HETEROJUNCTION

Ozel Kenan

Ankara Yildirim Beyazit University, 06010 Ankara, TURKEY, kenanozel89@gmail.com, ORCID: 0000-0002-0250-3731

Yildiz Abdullah

Department of Energy Systems Engineering, Faculty of Engineering and Natural Sciences, Ankara Yıldırım Beyazıt University, Ankara, Turkey yildizab@gmail.com, ORCID: 0000-0003-4137-6971

*Cite this paper as:* Ozel, K, Yildiz, A. *The investigation of uv detection performance of SnO<sub>2</sub>/p-Si heterojunction. 9th Eur. Conf. Ren. Energy Sys. 21-23 April 2021, Istanbul, Turkey*

**Abstract:** In the present work, we report the fabrication of SnO<sub>2</sub>/p-Si based heterojunction photodetector. The fabricated heterojunction is excited by a UV light source of 311 nm to probe the UV sensing performance. The current-voltage curve of the device is determined in the dark and under UV illumination. The photodetector shows an outstanding photoresponsivity of 3.23 A/W.

**Keywords:** Heterojunction, Photodetector, SnO<sub>2</sub>

© 2021 Published by ECRES

## 1. INTRODUCTION

Ultraviolet (UV) photodetectors (PDs) have many application areas, including flame monitoring, territory intrusions, space exploration, and optical communication [1]. UV PDs are sensitive to light in the spectrum of 200-400 nm. Over the years, UV PDs, including the p-n homojunction, the p-n heterojunction, Schottky junction, the metal-semiconductor-metal junction, have been constructed to achieve optimal structure [2]. In particular, the p-n heterojunction-based UV PDs offer cost-effective approach to detect UV light [3]. Wide bandgap semiconductors are preferred to obtain emitter layer thanks to their advantages such as intrinsic UV sensitivity, high transparency, excellent radiation hardness [4]. Among them, SnO<sub>2</sub> has captured extensive attention owing to the absorption edge corresponding to UV spectrum, low deposition temperature and high chemical stability. To date, SnO<sub>2</sub> thin films have been coated over p-Si wafers via various deposition techniques, such as spray pyrolysis, sputtering, pulse laser deposition, sol-gel spin coating, and chemical vapor deposition. In particular, sol-gel spin coating technique offer simple and cost-effective solution to fabricate the p-n heterojunction-based devices.

## 2. EXPERIMENTAL SECTION

The structure of n-SnO<sub>2</sub>/p-Si was manufactured with sol-gel spin coating technique. Firstly, the p-type Silicon (Si) wafer was cleaned by piranha standard cleaning solution and HF. A SnO<sub>2</sub> thin film (80 nm) was coated on the polished surface of p-Si and glass substrate [5]. The Ag back and front contact was achieved by screen-printing method. The optical properties of SnO<sub>2</sub>/glass sample were determined by UV-Vis spectrometer. The current-voltage characteristics were evaluated by Keithley 2400 source meter.

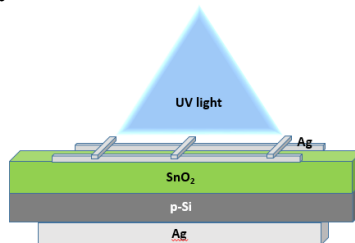


Figure 1. The schematic of n-SnO<sub>2</sub>/p-Si heterojunction diode

### 3. RESULTS AND DISCUSSION

The bandgap value of  $\text{SnO}_2$  thin film is estimated from the transmittance measurement. As seen from the Figure 3. It is found to be 3.8 eV, specifying that the fabricated device can be excited by the UV light. While the incident UV light is reached to the depletion layer, it is absorbed there to generate electron-hole pairs. Provided that the absorption process takes place, generation process continues and then the separated electron-hole pairs transforms photocurrent.

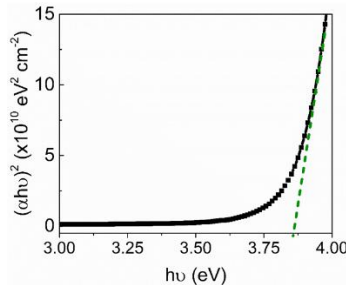


Figure 2. Tauc's plot of  $\text{SnO}_2$  thin film

The current-voltage characteristics of the device under illumination of 311 nm and in the dark is depicted in Figure 3. Notably, the n- $\text{SnO}_2$ /p-Si heterojunction exhibits a notably photoresponse to UV irradiation of 311 nm. Under the reverse bias of 5 V, there is an obvious difference in the values of photocurrent and dark current.

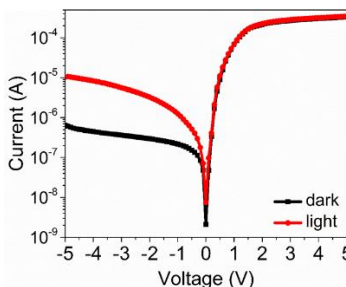


Figure 2. The I-V characteristics of the  $\text{SnO}_2/\text{p-Si}$  heterojunction

The UV detection characteristics of any photodetector are characterized by photo-responsivity ( $PR = \frac{I_{light}}{P_{in}}$ ) the ratio of photocurrent the intensity of incident light power. The value of PR is calculated to be 3.23 A/W. Note that the value of PR is directly related to the light absorption and charge transport properties of the devices.

### 4. CONCLUSION

In summary,  $\text{SnO}_2/\text{p-Si}$  based heterojunction photodetector was fabricated via sol-gel spin coating technique. The I-V characteristic of the device is recorded in the dark and under UV irradiation of 311 nm. Ultimately, it is observed that the device is very sensitive to UV irradiation of 311 nm. As a conclusion, the present design is promising for UV detection

### REFERENCES

- [1] Gao, Y., Xu, J., Shi, S., Dong, H., Cheng, Y., Wei, C., ... & Li, L. (2018). TiO<sub>2</sub> nanorod arrays based self-powered UV photodetector: heterojunction with NiO nanoflakes and enhanced UV photoresponse. 10(13), 11269-11279.
- [2] Ko, K. B., Ryu, B. D., Han, M., Hong, C. H., Doan, T. A., & Cuong, T. V. (2020). Inserting dome shape microstructure for enhancement of ultraviolet photodetector performance of n-ZnO nanorods/p-Si heterojunction. 823, 153884.
- [3] Wu, D., Jiang, Y., Zhang, Y., Li, J., Yu, Y., Zhang, Y., ... & Jie, J. (2012). Device structure-dependent field-effect and photoresponse performances of p-type ZnTe: Sb nanoribbons. 22(13), 6206-6212.
- [4] Chen, Y. C., Lu, Y. J., Liu, Q., Lin, C. N., Guo, J., Zang, J. H., ... & Shan, C. X. (2019). Ga<sub>2</sub>O<sub>3</sub> photodetector arrays for solar-blind imaging. 7(9), 2557-2562.
- [5] Ozel, K., Atilgan, A., Koksal, N. E., & Yildiz, A. (2020). A route towards enhanced UV photo-response characteristics of  $\text{SnO}_2/\text{p-Si}$  based heterostructures by hydrothermally grown nanorods. 849, 156628.



# THERMAL ANALYSIS AND PARAMETRIC STUDY ON THE INFLUENCE OF THERMO-PHYSICAL PROPERTIES ON DROPOWSE CONDENSATION HEAT TRANSFER

Mete Budakli

Ozyegin University, Faculty of Engineering, EVATEG Center, Istanbul, Turkey, [mete.budakli@ozyegin.edu.tr](mailto:mete.budakli@ozyegin.edu.tr), ORCID: 0000-0003-1721-1245

*Budakli, M., Thermal analysis and parametric study on the influence of thermo-physical properties on dropwise condensation heat transfer. 9th Eur. Conf. Ren. Energy Sys. 21-23 April 2021, Istanbul, Turkey*

**Abstract:** Fast advancement of process engineering in fields corresponding to heat exchanger design require more compact components which necessitate large heat transfer rates per unit area. In order to achieve this requirement, the transport of heat by means of dropwise condensation represents a promising mechanism for high thermal performance. Up to now, several experimental and numerical investigations on the thermo-hydrodynamic phenomena such as droplet nucleation, droplet growth and accumulation, droplet detachment, and heat transfer coefficient have been conducted. Besides the driving temperature difference between the subcooled surface and the vapor, factors like operating pressure, wall thermal conductivity, surface-liquid contact angle, and fluid thermo-physical property can affect the overall heat transfer performance during dropwise condensation. In this study, the effect of thermo-physical properties on heat transfer rates, heat transfer coefficients, and thermal resistances based on different contact angles have been evaluated by utilizing analytical modeling of a representative single droplet. Data of the low boiling fluids n-Hexane and FC-72 have been considered and the results obtained from parametric analysis have been compared with those of water. The calculations reveal that thermal conductivity and latent heat of evaporation are governing parameters for heat transfer performance during dropwise condensation.

**Keywords:** Heat Transfer, Dropwise condensation, Thermal analysis

© 2021 Published by ECRES

Nomenclature	
$A_F$	Area of droplet foot
DWC, FWC	Dropwise condensation, Filmwise condensation
$HTC$	Heat transfer coefficient
$h_V$	Latent heat of evaporation
$Q$	Heat flow rate
$R_C, R_{CV}, R_D, R_{V,D}$	Thermal resistance of Teflon coating, of droplet curvature, of droplet, of vapor-droplet interface
$R_V$	Specific vapor (gas) constant
$r, r_F$	Radius of droplet, droplet foot
$s_T$	Thickness of Teflon coating
$\Delta T_{CV}$	Temperature difference due to droplet curvature
$T_D, T_F, T_S$	Temperature at droplet surface, at droplet foot, at solid (copper) surface
$T_{sat}, T_V$	Saturation/Vapor temperature
$v_V$	Specific volume of vapor
$\alpha_{V,D}$	Heat transfer coefficient at vapor-droplet interface
$\gamma$	Contact angle at liquid-solid interface
$\epsilon$	Condensation factor
$\lambda_D, \lambda_T$	Thermal conductivity of droplet, of Teflon
$\rho_D$	Droplet density
$\sigma_D$	Surface tension of droplet

## 1. INTRODUCTION

Cost-effectiveness, compact design, long-term material-fluid compatibility, and system reliability are considered as indispensable achievements in designing heat exchangers for systems such as power electronics, petrochemical processes, thermal power plants, or concentrated solar power systems [1,2]. Besides these aspects, increased thermal capability is another major goal for heat transferring devices built in small-sizes as well as used in large-scale industrial applications [3,4]. Thereby, the thermal performance depends on several aspects like fluid inlet conditions, materials and geometries used, and the particular heat transfer mechanism. Concerning the latter, single-phase forced convection can be used as a method, but it is mostly limited by pressure drop leading to rather low thermal efficiency compared to phase-change phenomena where large amount of energy can be transported by means of latent heat. Consequently, depending on the intension of application, heat exchangers are either used for generation of process steam by boiling of a liquid or utilized to extract energy for heating/operation of other equipment or processes through condensation of a gas phase. Both methods use the phase-change mechanism which is induced by the temperature difference between the substrate and the fluid [5]. Especially on condensation, several studies have been carried out in order to determine the interrelation between complex thermo-hydrodynamic mechanisms occurring at the vapor-liquid-solid interfaces.

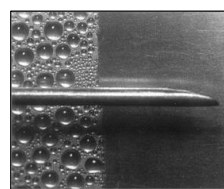


Figure 1. Dropwise and Filmwise condensation on subcooled surface [6].

This process is mainly categorized into filmwise (FWC) and dropwise (DWC) condensation mode (see Figure 1). FWC can occur on surfaces with large adhesion forces (hydrophilic) between the solid and liquid phase, while DWC happens mostly on surfaces having strong liquid repelling (hydrophobic) behavior [7,8]. From the hydrodynamic perspective, in FWC mode a thin liquid layer forms on the subcooled surface, while in DWC mode micro-/meso-size droplets partially cover the solid area. Although in both cases energy is transported by utilizing latent heat, the formation of a liquid layer during FWC leads to a large thermal resistance, hence to a much lower heat transfer coefficient (*HTC*) [9]. In contrast to this, DWC mode provides large heat transfer rates through individual droplets appearing and detaching on the surface at high-frequency. To maintain a stable DWC mode, one has to tune the free energy of the solid surface to be as low as possible to achieve a so-called superhydrophobic surface property [10]. Thus can force the droplets to grow as micro-spots and partially cover the surface, eventually coalesce and repel from the surface with concurrently sweeping adjacent droplets. In previous studies it has been reported that the *HTC* of DWC is significantly determined by the intensification of droplet frequency, their maximum sizes and numbers on unit surface area. Furthermore, the increase of the so-called three-phase contact line existing at the solid-liquid-vapor interface can be a second effect for the enhancement of heat transfer performance [11,12]. This mechanism is essentially governed by the (super)hydrophobicity of the surface which can be achieved by several approaches such as vapor deposition, laser texturing, micro-milling, sandblasting, chemical etching, and coating with Teflon, respectively [13–15]. Surfaces are defined as superhydrophobic when they exhibit a liquid-solid contact angle of larger than 150°. Up to now, large number of results on heat transfer and droplet dynamics have been published based on experiments and numerical simulations conducted for varying surface topographies and operating conditions [16–18]. Moreover, mathematical models concerning the heat transfer rate at an individual condensing droplet have been proposed by using a series of thermal resistances [19–22]. However, mainly water as working fluid has been used in most of the theoretical calculations, since it is a rather common material for heat exchangers employed in industrial applications as well as small-scale systems. When screening the literature, influences of factors such as subcooling temperature, pressure, thermal conductivity of surface coating/micro-structured surface topography on heat flow rate and *HTC* have been broadly investigated. Though, results concerning the effects of fluid thermo-physical properties are rarely discussed which represents lack of information, since the trend in replacing water by fluorocarbons (fluids with lower condensation temperature at ambient conditions) in electronics cooling increases. In the present work, a theoretical analysis and parametric study for varying fluid properties have been conducted by utilizing thermal resistance modelling of an individual droplet as representative. In terms of variation of fluid thermo-physical properties, data of the low boiling fluids n-Hexane and FC-72 have been taken into account. The resulting heat transfer rates, *HTC*, thermal resistances have been

analyzed for varying contact angles and thermal properties by focusing on an individual droplet and a comparison of the outcomes with those for water has been done.

## 2. THERMAL ANALYSIS OF A SINGLE DROPLET

For the thermal analysis, a single droplet growing on a subcooled solid surface (base material copper) has been considered as shown in Figure 2a. The heat transfer has been taken into account for saturated vapor conditions (1.01325 Bar) for the fluids water, n-Hexane, and FC-72, respectively. By applying serially connected thermal resistances caused through the droplet curvature ( $R_{CV}$ ), vapor-droplet interface ( $R_{V,D}$ ), droplet bulk liquid ( $R_D$ ), and coating layer ( $R_C$ ), the heat flow rate  $Q$ , HTC and thermal resistances have been calculated for an individual droplet at varying static contact angles  $\gamma$  (see Figure 2b). All calculations have been carried out using the subcooling temperature difference  $T_V - T_S$  between the saturated vapor phase and a copper substrate.

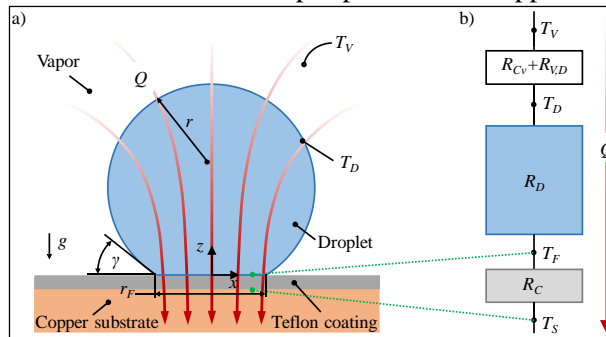


Figure 2. Theoretical model for heat transfer analysis on a single condensing droplet: a) Single droplet on coated copper substrate, b) Thermal resistance diagram.

Concerning the (super)hydrophobicity, a thin layer of Teflon ( $\lambda_T = 0.25 \text{ W/(mK)}$  from [23]) with a thickness of  $s_T = 10 \mu\text{m}$  has been assumed, since this widely-used material can result to large contact angles ( $\gamma > 120^\circ$  for water) for liquids. In terms of parametric study on the effects of thermo-physical properties, data of n-Hexane and FC-72 have been extracted from several literatures for the liquid (subscript  $D$ ) as well as for the gas phase (subscript  $V$ ) which are listed in Table 1.

Table 1. Thermo-physical properties of working fluids water, n-Hexane, and FC-72 at 1.101325 Bar, <sup>1)</sup>Data have been taken from [23], <sup>2)</sup>Data have been taken from [24,25], <sup>3)</sup>Data have been taken from [23,26].

Fluid	$T_{sat} = T_V$ [°C]	$\lambda_D$ [W/(mK)]	$\rho_D$ [kg/m³]	$\sigma_D$ [N/m]	$h_V$ [kJ/kg]	$R_V$ [J/(kgK)]	$v_V$ [m³/kg]
Water <sup>1)</sup>	100	0.679	958	0.0590	2257.0	454.2	1.6733
n-Hexane <sup>2)</sup>	68	0.113	614	0.0146	334.9	91.7	0.3095
FC-72 <sup>3)</sup>	56	0.054	1599	0.0083	94.8	23.0	0.0746

The temperature drop from the vapor to solid phase can be described with

$$\Delta T_{V,S} = T_V - T_S = \Delta T_{CV} + \Delta T_{V,D} + \Delta T_{D,F} + \Delta T_{F,S} \quad , \quad (1)$$

while the temperature difference caused by the droplet curvature and interfacial resistance was determined as follows

$$\Delta T_{CV} = \frac{2T_V\sigma_D}{rh_V\rho_D} \quad , \quad (2)$$

$$\Delta T_{V,D} = T_V - T_D = \frac{Q}{2\pi r^2(1-\cos(\gamma))\alpha_{V,D}} \quad . \quad (3)$$

The heat transfer coefficient  $\alpha_{V,D}$  for condensation at the vapor-droplet interface was calculated with [27,28]

$$\alpha_{V,D} = \frac{2\varepsilon}{2-\varepsilon} \frac{1}{\sqrt{2\pi R_V T_V}} \frac{h_V^2}{v_V T_V} \quad , \quad (4)$$

where for the condensation factor  $\varepsilon = 1.0$  was assumed for all fluids [29]. The heat transport from the droplet surface towards the droplet foot was determined using the following equation:

$$\Delta T_{D,F} = T_D - T_F = \frac{Q\gamma}{4\pi r \sin(\gamma) \lambda_D} \quad (5)$$

The contact angle in the above expression is the so-called static contact angle, which was used as one factor for parametric variation. The temperature difference resulting from the Teflon coating was attributed with

$$\Delta T_{F,S} = T_F - T_S = \frac{Q s_T}{\lambda_T r^2 \pi} \quad (6)$$

After substituting Eqs. [2,3,5,6] in Eq. [1] and rearranging the expression, the following equation for the heat flow rate has been obtained:

$$Q = \frac{T_V \left( 1 - \frac{2\sigma_D}{r h_v \rho_D} \right) - T_S}{\frac{1}{2\pi r^2 (1 - \cos(\gamma)) \alpha_{V,D}} + \frac{\gamma}{4\pi r \sin(\gamma) \lambda_D} + \frac{s_T}{\lambda_T r^2 \pi}} \quad (7)$$

The droplet radius  $r$  existing in Eq. [7] was the second factor for parametric variation. The surface temperature  $T_S$  has been supposed to be homogenously distributed at the Teflon-copper interface. All calculations have been carried out for a horizontally aligned substrate, hence the influence of gravitation was neglected. One can suppose that the droplets will tend to easily detach from a vertically oriented substrate, since the surface tension force will not be strong enough to offer resistance to gravitational force. The values for  $HTC$  have been determined through dividing  $Q$  by the area of the droplet foot  $A_F = r_F^2 \pi$  for the corresponding contact angle.

### 3. RESULTS AND DISCUSSION

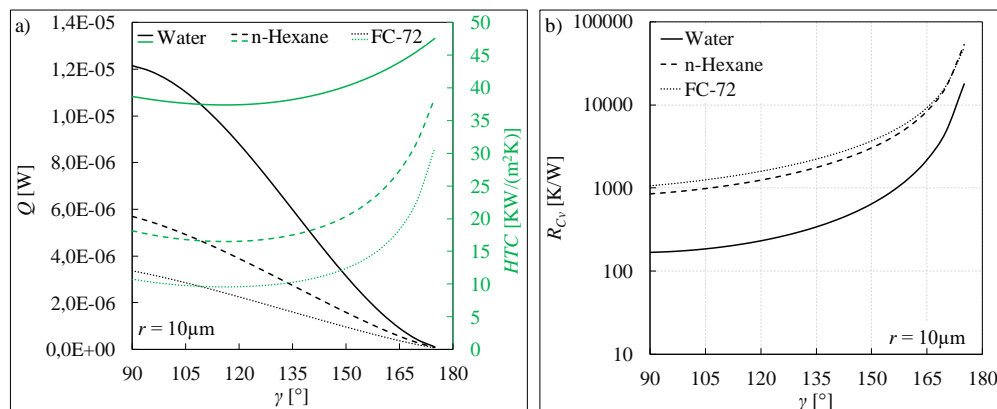


Figure 3. Exemplary results obtained for a single droplet for water, n-Hexane, and FC-72: a) Heat flow rate and heat transfer coefficient, b) Thermal resistance  $R_{Cv}$  due to droplet curvature.

In Figure 3, some exemplary results (variation of  $r$  is not shown and will be presented at the conference) on the development of heat flow rate,  $HTC$ , and thermal resistance  $R_{Cv}$  based on varying liquid contact angle are presented. The values have been determined for a single droplet with an assumed radius of  $r = 10 \mu\text{m}$  and a subcooling temperature difference of  $T_V - T_S = 1 \text{ K}$  for all three fluids. As shown in Figure 3a, when the contact angle increases,  $Q$  reduces for all fluids, while the largest heat flow rate has been predicted for water followed by n-Hexane and FC-72. The decline in heat flow rate might be caused by the effect of growth in  $R_{Cv}$ , which in turn is a result of the droplet shape due to larger contact angles (see Figure 3b). Compared to water and n-Hexane, the slope  $dQ/d\gamma$  for FC-72 seems to develop rather linear. At the maximum theoretical contact angle of  $180^\circ$ , all values tend to converge to zero, since the shape of the droplet becomes fully spherical and hypothetically it would not have a distinct interface with the solid surface. In contrast,  $HTC$  first decreases and meets a local minimum value within the spectrum  $\gamma = 115^\circ - 120^\circ$  for all fluids. However, it clearly increases for larger contact angles above  $150^\circ$  (threshold

value for definition of superhydrophobicity), where again the best heat transfer performance has been forecasted for a water droplet.

One possible reason for the subsequent increase in *HTC* can be the growth of the vapor-droplet interfacial area. Albeit  $R_{cv}$  increases, more vapor molecules can accumulate due to superior sphericity of the liquid droplet. Concurrently, larger amount of heat per unit spherical surface area released during phase-change has to be transported through a smaller liquid-solid interface ( $A_F = r_F^2\pi$ ). On the other side, the gradients of *HTC* for n-Hexane and FC-72 are much larger compared to water, which indicates that the rate in heat transfer enhancement is great for low boiling fluids. Nevertheless, it might be rather difficult to achieve large contact angles for n-Hexane and FC-72, since in liquid phase both the materials have low surface tension compared to water. The large values for *HTC* of water compared to the low boiling fluids can be attributed to the comparable better thermal conductivity and larger latent heat of evaporation, since these parameters might govern the heat transfer during phase-change on a droplet.

#### 4. CONCLUSIONS

In the present study, the influence of different fluid properties has been theoretically analyzed through thermal modelling and parametric variation by considering of a representative micron-sized droplet for dropwise condensation on a subcooled solid substrate. For this purpose, water and low boiling fluids such as n-Hexane and FC-72 have been considered. On the one hand, the results show that surface modification can lead to heat transfer enhancement, provided large contact angles can be achieved for the liquid phase of all fluids. On the other hand, it has been shown that larger thermal conductivity and latent heat of evaporation are determining factors for heat transfer performance during dropwise condensation, while the shape of the droplet can be another factor for the determination of the interfacial molecular phase-change phenomena.

#### ACKNOWLEDGMENT

The author would like to thank the Deutsche Forschungsgemeinschaft (DFG, German Research Foundation) - Funding Nr. 441193154 and the EVATEG Center of the Ozyegin University.

#### REFERENCES

- [1] Budakli, M, Salem, TK, Arik, M, Donmez, B, Menceloglu, Y. Effect of Polymer Coating on Vapor Condensation Heat Transfer. *Journal of Heat Transfer* 2020; 142, DOI: <https://doi.org/10.1115/1.4046300>.
- [2] Beér, JM. High efficiency electric power generation: The environmental role. *Progress in Energy and Combustion Science* 2007; 33: 107–134, DOI: <https://doi.org/10.1016/j.pecs.2006.08.002>.
- [3] Hu, S, Ma, X, Zhou, W. Condensation heat transfer of ethanol-water vapor in a plate heat exchanger. *Applied Thermal Engineering* 2017; 113: 1047-1055, DOI: <https://doi.org/10.1016/j.applthermaleng.2016.11.013>.
- [4] Launay, S, Sartre, V, Bonjour, J. Parametric analysis of loop heat pipe operation: a literature review. *International Journal of Thermal Sciences* 2007; 46: 621-636, DOI: <https://doi.org/10.1016/j.ijthermalsci.2006.11.007>.
- [5] Rausch, MH, Fröba, AP, Leipertz, A. Dropwise condensation heat transfer on ion implanted aluminum surfaces. *International Journal of Heat and Mass Transfer* 2008; 51:1061-1070. DOI: <https://doi.org/10.1016/j.ijheatmasstransfer.2006.05.047>.
- [6] Pandey, S. Dropwise and filmwise condensation. *International Journal of Scientific & Engineering Research* 2012; 3:320–324.
- [7] Koch, G, Zhang, DC, Leipertz, A. Condensation of steam on the surface of hard coated copper discs. *Heat and Mass Transfer* 1997; 32:149-156. DOI: <https://doi.org/10.1007/s002310050105>.
- [8] Enright, R, Miljkovic, N, Dou, N, Nam, Y, Wang, EN. Condensation on Superhydrophobic Copper Oxide Nanostructures. *Journal of Heat Transfer* 2013; 135:091304. DOI: <https://doi.org/10.1115/1.4024424>.
- [9] Nusselt, W. Die Oberflächenkondensation des Wasserdampfes. *Zeitschrift des Vereins Deutscher Ingenieure* 1916; 60:541-546.
- [10] Wilkins, DG, Bromley, LA, Read, SM. Dropwise and filmwise condensation of water vapor on gold. *American Institute of Chemical Engineers Journal* 1973; 19:119-123. DOI: <https://doi.org/10.1002/aic.690190117>.
- [11] Chiou, NR, Lu, C, Guan, J, Lee, LJ, Epstein, AJ. Growth and alignment of polyaniline nanofibres with superhydrophobic, superhydrophilic and other properties. *Nature Nanotechnology* 2007; 2:354-357. DOI:<https://doi.org/10.1038/nnano.2007.147>.
- [12] Stephan, PC, Busse, CA. Analysis of the heat transfer coefficient of grooved heat pipe evaporator walls. *International Journal of Heat and Mass Transfer* 1992; 35:383-391. DOI: [https://doi.org/10.1016/0017-9310\(92\)90276-X](https://doi.org/10.1016/0017-9310(92)90276-X).

- [13] Del Col, D, Parin, R, Bisetto, A, Bortolin, S, Martucci, A. Film condensation of steam flowing on a hydrophobic surface. International Journal of Heat and Mass Transfer 2017; 107:307-318. DOI: <https://doi.org/10.1016/j.ijheatmasstransfer.2016.10.092>.
- [14] Chen, C-H, Cai, Q, Tsai, C, Chen, C-L, Xiong, G, Yu, Y, Ren, Z. Dropwise condensation on superhydrophobic surfaces with two-tier roughness. Applied Physics Letters 2007; 90:173108. DOI: <https://doi.org/10.1063/1.2731434>.
- [15] Sharma, CS, Combe, J, Giger, M, Emmerich, T, Poulikakos, D. Growth Rates and Spontaneous Navigation of Condensate Droplets Through Randomly Structured Textures. ACS Nano 2017; 11:1673-1682. DOI: <https://doi.org/10.1021/acsnano.6b07471>.
- [16] Marto, PJ, Looney, DJ, Rose, JW, Wanniarachchi, AS. Evaluation of organic coatings for the promotion of dropwise condensation of steam. International Journal of Heat and Mass Transfer 1986; 29:1109-1117. DOI: [https://doi.org/https://doi.org/10.1016/0017-9310\(86\)90142-0](https://doi.org/https://doi.org/10.1016/0017-9310(86)90142-0).
- [17] Vemuri, S, Kim, KJ. An experimental and theoretical study on the concept of dropwise condensation. International Journal of Heat and Mass Transfer 2006; 49:649-657. DOI: <https://doi.org/10.1016/j.ijheatmasstransfer.2005.08.016>.
- [18] Mancio Reis, FM, Lavieille, P, Miscevic, M. Dropwise Condensation Enhancement Using a Wettability Gradient. Heat Transfer Engineering 2017; 38:377-385. DOI: <https://doi.org/10.1080/01457632.2016.1189277>.
- [19] Maeda, Y, Lv, F, Zhang, P, Takata, Y, Orejon, D. Condensate droplet size distribution and heat transfer on hierarchical slippery lubricant infused porous surfaces. Applied Thermal Engineering 2020; 176:115386. DOI: <https://doi.org/10.1016/j.aplthermaleng.2020.115386>.
- [20] Lee, S, Yoon, HK, Kim, KJ, Kim, S, Kennedy, M, Zhang, BJ. A dropwise condensation model using a nano-scale, pin structured surface. International Journal of Heat and Mass Transfer 2013; 60:664-671. DOI: <https://doi.org/10.1016/j.ijheatmasstransfer.2013.01.032>.
- [21] Xiao, R, Miljkovic, N, Enright, R, Wang, EN. Immersion Condensation on Oil-Infused Heterogeneous Surfaces for Enhanced Heat Transfer, Scientific Reports 2013; 3:1988. DOI: <https://doi.org/10.1038/srep01988>.
- [22] Kim, S, Kim, KJ. Dropwise Condensation Modeling Suitable for Superhydrophobic Surfaces. Journal of Heat Transfer 2011; 133:1-8. DOI: <https://doi.org/10.1115/1.4003742>.
- [23] German Engineers Society, VDI Heat Atlas, Berlin-Heidelberg, GERMANY: Springer Berlin Heidelberg, 2010.
- [24] 3M, 3M TM Fluorinert TM Electronic Liquid FC-72 Product description, 2019.
- [25] Parker, JL. Pool Boiling of Dielectric Liquids on Porous Graphite and Extended Copper Surfaces. PhD. The University of New Mexico, New Mexico, UNITED STATES OF AMERICA, 2008.
- [26] Klein, T, Yan, S, Cui, J, Magee, JW, Kroenlein, K, Rausch, MH, Koller, TM, Fröba, AP. Liquid Viscosity and Surface Tension of n-Hexane, n-Octane, n-Decane, and n-Hexadecane up to 573 K by Surface Light Scattering. Journal of Chemical and Engineering Data 2019; 64:4116-4131. DOI: <https://doi.org/10.1021/acs.jced.9b00525>.
- [27] Umur, A, Griffith, P. Mechanism of Dropwise Condensation, Journal of Heat Transfer 1965; 87:275-282. DOI: <https://doi.org/10.1115/1.3689090>.
- [28] Schrage, RW. A Theoretical Study of Interphase Mass Transfer, Columbia University Press, New York, UNITED STATES OF AMERICA, 1953.
- [29] Rohsenow, WM. Status of and Problems in Boiling and Condensation Heat Transfer, Pergamon Press 1972; DOI: <https://doi.org/10.1016/b978-0-08-017035-0.50007-0>.



# ITERATIVE EKF-BASED PARAMETER ESTIMATION ALGORITHM FOR A NONLINEAR PMSM MODEL

Artun Sel

TOBB University of Economics and Technology, Ankara, Turkey, artunsel@gmail.com, ORCID: 0000-0002-3142-3650

Cosku Kasnakoglu

TOBB University of Economics and Technology, Ankara, Turkey, kasnakoglu@gmail.com, ORCID: 0000-0002-9928-727X

*Cite this paper as:*

*Sel, A., Kasnakoglu, C. Iterative EKF-based parameter estimation algorithm for a nonlinear PMSM model. 9<sup>th</sup> Eur. Conf. Ren. Energy Sys. 21-23 April 2021, Istanbul, Turkey*

---

**Abstract:**

In this study, an extended Kalman filter based parameter estimation method is studied. In cases where only a part of the state vector is available to be measured and there is a process and measurement noise affecting the plant and measurement dynamics the estimation of the parameters becomes problematic. Depending on the nonlinearity level same estimation methods differs in terms of accuracy. Additionally, a nonlinear observability problem also becomes quite relevant in the process of determining whether or not the parameter can be estimated using the measured data points. Extended Kalman filter is a type of estimator that makes it possible to estimate the states of the nonlinear dynamical systems given they are observable in the nonlinear sense and there is enough excitation of the dynamics generated by the input signal. In this study, a EKF based parameter estimation algorithm is designed for a given nonlinear dynamical system. The design steps are detailed and the efficacies and shortcomings of the algorithm is discussed regarding the numerical simulations.

---

**Keywords:**

EKF, PMSM, nonlinear systems, parameter estimation, system identification

---

© 2021 Published by ECRES

## 1. INTRODUCTION

The question of system identification when it comes to the nonlinear dynamical systems becomes more challenging due to the immense implications that nonlinearities cause. Although it is a standard practice to determine whether or not a given LTI system is observable, this process is not standard and there is not one unique algorithm for a given nonlinear system [1]. There are some linear algebra based techniques that are available in the literature to conduct that process however those methods have certain limitations depending on the nonlinearity. In the literature, there are nonlinear observer types that are quite popular and have the ability to deal with the modelling uncertainties. Some of which can be listed as SMO (sliding mode observer) [2], HGO (high gain observer) [3], EKF (extended Kalman filter) and variations thereof [4,5]. For the mild nonlinearities EKF seems to be the prominent choice due to its straightforward design and working principle. EKF is often used to estimate the states that are not measurable and there is an available system model based on which the estimator is designed.

Another significant usage of the observer is for parameter estimation. In cases, where there are enough measured signals and some parameters are required to be estimated for the monitoring or control purposes, EKF also can be used by extending the state vectors by the parameters to be estimated. For small set of unknown parameters that technique works sufficiently accurate. However, for the cases where the number of parameters are much greater than the number of states there can be some numerical issues raise during the estimation process. To circumvent that problem it is a common practice to design 2 separate EKFs, one for the state estimation and other for the parameter estimation, and the information exchange between the two estimators is regulated by another regulation algorithm [6]. Doing so, the numerical problems mitigated to an extent. The same type of method is also used for the parameter estimation of the systems where the number of parameters are greater than the state dimension and there are enough data points to work with. In the industrial applications those requirements often arise for the system monitoring and fault detection problems [7]. In this study, a parameter estimation problem is studied for a given

PMSM model whose dynamics includes non-severe nonlinearity [8,9]. An EKF-based iterative parameter estimation algorithm is given and the efficacy of the estimation method is examined through a numerical simulation. The plant dynamics are given in section II, for the parameter estimation technique, EKF-based search algorithm is detailed in section III. To validate the performance simulation problem and the corresponding results are given in section IV. Finally, in section V the results are discussed.

## 2. PMSM MODEL

In this study, to test the parameter accuracy of the estimation algorithm that is to be presented in the next section, a PMSM model is given whose model possesses non-severe nonlinearities that is suitable to design an EKF. There are 4 states, two of which are available for measuring and 5 related system parameters to be estimated [10]. The lower and upper bounds of the parameters are considered to be known and the process and measurement noises have normal distributions.

The plant model is given as,

$$\frac{d}{dt}x_1 = p_1x_1 + p_2x_3 \sin(x_4) + p_3u_1 + w_1 \quad (1)$$

$$\frac{d}{dt}x_2 = p_1x_2 - p_2x_3 \cos(x_4) + p_3u_2 + w_2 \quad (2)$$

$$\frac{d}{dt}x_3 = p_4x_1 \sin(x_4) - p_4x_2 \cos(x_4) + p_5x_3 + w_3 \quad (3)$$

$$\frac{d}{dt}x_4 = x_3 + w_4 \quad (4)$$

With the introduced change of variables, the estimation algorithm is designed based on this model.

## 3. PARAMETER ESTIMATION ALGORITHM

In this section an EKF-based parameter estimation algorithm is presented for the system identification purposes. As stated in the previous section, there are 5 parameters and the bounds of them are known. Two of the four states are measured and the rest of the state signals are to be estimated which results in 7 variable estimation, five of them can be considered as constant signals. Instead of extending the state vector by stacking the parameters and designing an observer for a 9 dimensional system with 2 measured states, which would result in numerical difficulties, 5 separate EKFs are designed. In each EKF, whose design steps are to be presented, 4 states and 1 parameter are considered while fixing the rest of the parameters. This type of iterative parameter estimation has a considerable computational complexity, however compared to the one with larger dimensions and numerical stability issues, there may be some cases where the parameter estimation algorithm or a version thereof is desired. The overall scheme of the method is presented in the block diagram given below.

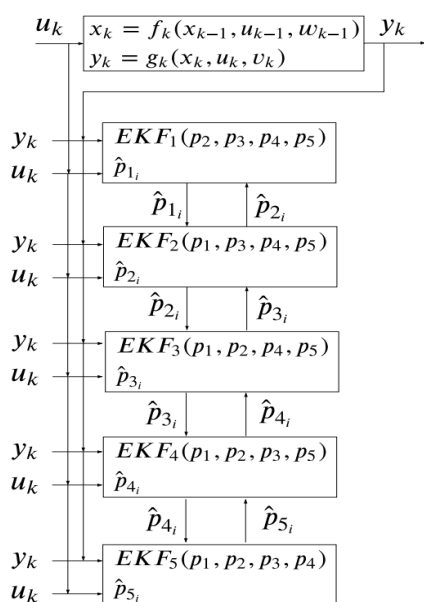


Figure 1. The parameter estimation algorithm block diagram

### General EKF Design For Parameter Estimation

For the parameter estimation, the state vector is expanded by the parameters and a new dynamic artificial system is defined. And the system is represented as,

$$x_k = f_k(x_{k-1}, u_{k-1}, w_{k-1}) \quad (5)$$

$$y_k = g_k(x_k, u_k, v_k) \quad (6)$$

For the given system, 4 jacobian matrices are defined as,

$$A_k = \frac{\partial f_k(x_{k-1}, u_{k-1}, w_{k-1})}{\partial x_{k-1}}, B_{w_k} = \frac{\partial f_k(x_{k-1}, u_{k-1}, w_{k-1})}{\partial w_{k-1}} \quad (7)$$

$$C_k = \frac{\partial g_k(x_k, u_k, v_k)}{\partial x_k}, D_{v_k} = \frac{\partial g_k(x_k, u_k, v_k)}{\partial v_k} \quad (8)$$

And the EKF steps are given below,

$$\hat{x}_{k|k-1} = f_k(\hat{x}_{k-1|k-1}, u_{k-1}) \quad (9)$$

$$\hat{y}_{k|k-1} = g_k(\hat{x}_{k-1|k-1}, u_{k-1}) \quad (10)$$

$$A_k = \left[ \frac{\partial f_k(x_{k-1}, u_{k-1}, w_{k-1})}{\partial x_{k-1}} \right] \Bigg|_{\begin{subarray}{l} x_{k-1} = \hat{x}_{k-1|k-1} \\ u_{k-1} = u_{k-1} \\ w_{k-1} = 0 \end{subarray}} \quad (11)$$

$$B_{w_k} = \left[ \frac{\partial f_k(x_{k-1}, u_{k-1}, w_{k-1})}{\partial w_{k-1}} \right] \Bigg|_{\begin{subarray}{l} x_{k-1} = \hat{x}_{k-1|k-1} \\ u_{k-1} = u_{k-1} \\ w_{k-1} = 0 \end{subarray}} \quad (12)$$

$$\Sigma_{\tilde{x}\tilde{x}|k-1} = A_k \Sigma_{\tilde{x}\tilde{x}|k-1} A_k^T + B_{w_k} Q_k B_{w_k}^T \quad (13)$$

$$C_k = \left[ \frac{\partial g_k(x_k, u_k, v_k)}{\partial x_k} \right] \Bigg|_{\begin{subarray}{l} x_k = \hat{x}_{k|k-1} \\ u_k = u_k \\ v_k = 0 \end{subarray}} \quad (14)$$

$$D_{v_k} = \left[ \frac{\partial g_k(x_k, u_k, v_k)}{\partial v_k} \right] \Bigg|_{\begin{subarray}{l} x_k = \hat{x}_{k|k-1} \\ u_k = u_k \\ v_k = 0 \end{subarray}} \quad (15)$$

$$K_k = \Sigma_{\tilde{x}\tilde{x}|k-1} C_k^T \left[ C_k \Sigma_{\tilde{x}\tilde{x}|k-1} C_k^T + D_{v_k} R_k D_{v_k}^T \right]^{-1} \quad (16)$$

$$\hat{x}_{k|k} = \hat{x}_{k|k-1} + K_k [y_k - \hat{y}_{k|k-1}] \quad (17)$$

$$\hat{y}_{k|k} = g_k(\hat{x}_{k|k}, u_k) \quad (18)$$

$$\Sigma_{\tilde{x}\tilde{x}|k} = [I - K_k C_k] \Sigma_{\tilde{x}\tilde{x}|k-1} \quad (19)$$

Where the related parameters are given in the table below,

Table I. The plant parameters and definitions

Parameter	Definition	Parameter	Definition
$\hat{x}_{k k-1}, \hat{y}_{k k-1}$	Predicted state and output	$\Sigma_{\tilde{x}\tilde{x} k-1}$	A priori state error covariance matrix
$\hat{x}_{k k}, \hat{y}_{k k}$	Predicted state and output	$\Sigma_{\tilde{x}\tilde{x} k k}$	A posteriori state error covariance matrix
$Q_k, R_k$	Process and measurement covariance matrix	$A_k, B_{w_k}, C_k, D_{v_k}$	Jacobian matrices
$K_k$	Kalman gain	$f_k, g_k$	State and output equation

## 4. SIMULATION RESULTS

To test the estimation quality of the algorithm the follow numerical simulation is constructed. The real parameters are given in the table below. For the lower bound and upper bounds of the parameters are given in the table below.

Table 2. The plant parameters and definitions

Parameter	Value	Parameter	Value
$p_1$	0.1	$p_1$	-1
$p_2$	0.1	$p_2$	10
$p_3$	1	$p_3$	10
$p_4$	1	$p_4$	-1.5
$p_5$	1	$p_5$	-1

Table 3. The plant parameters and definitions

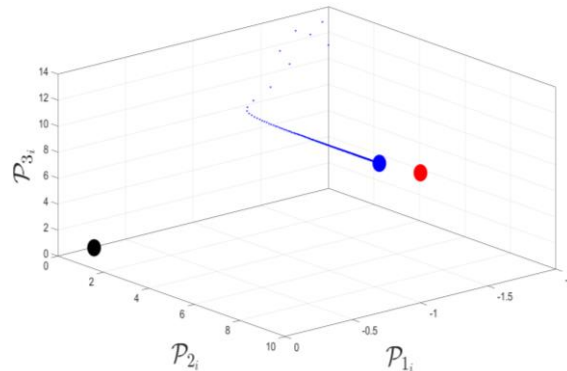
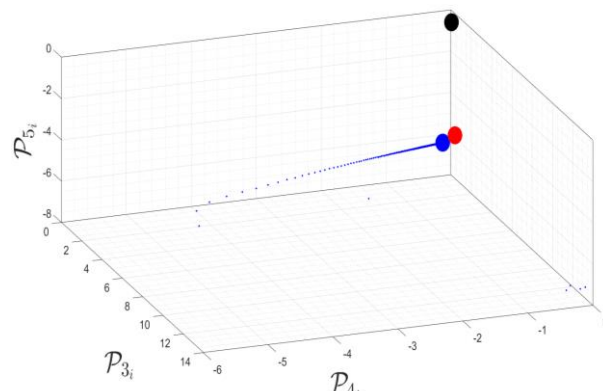
Parameter	Value	Parameter	Value
$[p_{1l}, p_{1u}]$	[0.01, 1]	$[p_{1l}, p_{1u}]$	[-100, -0.01]
$[p_{2l}, p_{2u}]$	[0.01, 1]	$[p_{2l}, p_{2u}]$	[0, 200]
$[p_{3l}, p_{3u}]$	[0.01, 2]	$[p_{3l}, p_{3u}]$	[1, 100]
$[p_{4l}, p_{4u}]$	[0.01, 2]	$[p_{4l}, p_{4u}]$	[-300, -0.0075]
$[p_{5l}, p_{5u}]$	[0.01, 2]	$[p_{5l}, p_{5u}]$	[-200, -0.005]

The EKF related selected parameters and noise variances for the real system is given in the table below.

Table 4. The plant parameters and definitions

Parameter	Value
real process noise covariance	$1 \times 10^{-1} I_4$
real measurement noise covariance	$1 \times 10^{-1} I_2$
EKF – process noise covariance	$1 \times 10^{-2} I_5$
EKF – measurement noise covariance	$1 \times 10^{-2} I_2$
real state initial value	$0.1[1 \ 1 \ 1 \ 1]^T$
EKF – state initial value	$0.2[1 \ 1 \ 1 \ 1]^T$
initial state error covariance	$0.1I_5$

It can be seen in the figure 2 and figure 3, that the parameter estimation converges to the real values of the parameters, despite of the process and measurement noise effects. In the figures, the red dots indicate the real parameters and black and large blue dots indicate first and last estimation of the related parameters, respectively.


 Figure 2. The convergence of the  $p_1, p_2, p_3$  estimations

 Figure 3. The convergence of the  $p_3, p_4, p_5$  estimations

## 5. CONCLUSION

The parameter estimation algorithm described in the section III, is tested on a given PMSM model. In the numerical simulation study it is assumed that the initial conditions regarding the state variables are not known and this information is encoded into the EKFs by defining a state error covariance matrix with large variance coefficient. As for the initial parameter estimates, they are chosen to be distant to their real values. Although the algorithm seems to converge to the real values of the parameters under the white gaussian noise effect, the computation and iteration number that is necessary to do so may not be desirable for real time systems. To increase the speed of the convergence moment based methods can be used in addition to the SVD based iteration rules that can boost the convergence speed. Another improvement that can be added to the started algorithm is related to the state vector initial values, in the process of estimating the parameters, as can be seen in the previous section, the initial values kept constant which can well be adjusted with a GLSDC based update. Another issue with the current set up is the time durations, for certain time durations seem to be more effective on some subset of the parameter set, and have small effect on the correction of other parameters. This issue is related to the system structure, depending on the system dynamics, the sensitivity of the parameters to the solution or the output varies with respect to the time. This issue is especially important for parameter or state estimation problems in system whose dynamics are given in terms of PDEs.

## REFERENCES

- [1] A. N. Zhirabok, "Observability and controllability analysis of nonlinear systems by linear methods," 2008 10th International Conference on Control, Automation, Robotics and Vision, Hanoi, Vietnam, 2008, pp. 1690-1695, doi: 10.1109/ICARCV.2008.4795781.
- [2] T. Floquet, J. A. Twiddle and S. K. Spurgeon, "Parameter estimation via second order sliding modes with application to thermal modelling in a high speed rotating machine," 2006 IEEE International Conference on Industrial Technology, Mumbai, India, 2006, pp. 2635-2639, doi: 10.1109/ICIT.2006.372710.
- [3] H. K. Khalil, "Cascade high-gain observer for high-dimensional systems," 2016 IEEE 55th Conference on Decision and Control (CDC), Las Vegas, NV, USA, 2016, pp. 7141-7146, doi: 10.1109/CDC.2016.7799370.
- [4] W. Lohmiller and J. - E. Slotine, "Contraction analysis: a practical approach to nonlinear control applications," Proceedings of the 1998 IEEE International Conference on Control Applications (Cat. No.98CH36104), Trieste, Italy, 1998, pp. 1-5 vol.1, doi: 10.1109/CCA.1998.728230.
- [5] Y. Yuan, G. Fu and W. Zhang, "Extended and unscented Kalman filters for parameter estimation of a hydrodynamic model of vessel," 2016 35th Chinese Control Conference (CCC), Chengdu, China, 2016, pp. 2051-2056, doi: 10.1109/ChiCC.2016.7553668.
- [6] Li Meng, Liu Li and S. M. Veres, "Aerodynamic parameter estimation of an Unmanned Aerial Vehicle based on extended kalman filter and its higher order approach," 2010 2nd International Conference on Advanced Computer Control, Shenyang, China, 2010, pp. 526-531, doi: 10.1109/ICACC.2010.5487116. [7] EKF fault detection param est
- [8] Ali Ahmed Adam, Kayhan Gulez & Halit Pastaci (2009) A direct torque control algorithm for permanent magnet synchronous motors with minimum torque pulsation and reduced electromagnetic interference noise, International Journal of Electronics, 96:11, 1191-1196.
- [9] Andraž Kontarček, Asst. Prof. Mitja Nemec, Primož Bajec & Prof. Vanja Ambrožič (2014) Single Open-phase Fault Detection with Fault-Tolerant Control of an Inverter-fed Permanent Magnet Synchronous Machine, Automatika, 55:4, 474-486.
- [10] Tino Jerčić, Šandor Ileš, Damir Žarko & Jadranko Matuško (2017) Constrained field-oriented control of permanent magnet synchronous machine with field-weakening utilizing a reference governor, Automatika, 58:4, 439-449.



# ALGORITHMS FOR ESS REINFORCED RES PORTFOLIO BIDDING IN TURKISH ENERGY MARKETS

Abdülhadi Çiftçi

Gebze Technical University, Kocaeli, Turkey, aciftci@gtu.edu.tr, ORCID: 0000-0001-8837-8240

Abdulkadir Balıkçı

Gebze Technical University, Kocaeli, Turkey, a.balikci@gtu.edu.tr, ORCID: 0000-0003-2621-1570

*Cite this paper as:* Çiftçi, A., Balıkçı, A. Algorithms for ESS reinforced RES portfolio bidding in Turkish Energy Markets. 9<sup>th</sup> Eur. Conf. Ren. Energy Sys. 21-23 April 2021, Istanbul, Turkey

**Abstract:** Renewable Energy Sources have challenges on penetration in power systems. Energy Storage Systems make RES more flexible and penetrating, but management of ESS is quite complex. For optimal operation of RES portfolio and ESS, there should be some rules and restrictions. In order to make ESS financially feasible, ESS and RES have to gain revenue as much as possible. RES portfolio and ESS works in this regard as “Virtual Power Plant”. The algorithm maximizes revenue of the VPP in day ahead market and balancing market. Decision variable of this problem is power input and output of ESS.

In this paper, according to Turkish Energy Market regulations, optimal algorithm for VPP is proposed. In case study, there are solar, wind, river type hydro power plants and ESS work as VPP. ESS charge and discharge rules are stated. In addition, hydro power water input has an energy storage ability, so it was considered. The problem was solved on “MS Excel” and results illustrate the success of the algorithm.

**Keywords:** VPP, renewable energy sources, energy storage, optimal bidding

© 2021 Published by ECRES

Nomenclature	
Nothing	Renewable energy sources
ESS	Energy storage system
WPP	Wind power plant
Hamilton	Hydro electrical power plant
PV	Photovoltaics
VPP	Virtual power plant
EMRE	Energy Market Regulatory Authority
TEİAŞ	Turkish Electricity Transmission Company
VRB	Vanadium redox battery
DAM	Day ahead market
DMEP	Day ahead market energy price
BEM	Balancing energy market
MEP	Marginal Energy price
DAPP	Daily approved production plan
A	Swept area
U	Wind velocity
$\rho$	Air density
RU	Ramp-up
RD	Ramp-down

## 1. INTRODUCTION

Today's energy policies of whole world are supporting higher percentage of renewable energy resources. But penetration of RES has some limits and constraints [1]. RES productions are fluctuating by natural events. A big

fluctuation on grid supply affects grid quality and may cause blackouts and instability of supply. High percentages of RES at national grid cause potential risk at grid quality and supply-demand equilibrium.

## 2. SUPPLY PROBLEMS OF RES

### Supply Problems of Wind Power

Wind energy sources which are installed widely in recent years have much debated supply-demand equilibrium problem because of having fluctuations and instability. As it is seen at Eq. [1], wind velocity affects wind power with its cube [2]. A typical power production is illustrated at Fig. [1] with 1-minute average data set. By the way, production due to the wind may decrease for national grid and energy demand is obliged to substitute with other resources.

$$P = \frac{1}{2} A \rho U^3 \quad (1)$$

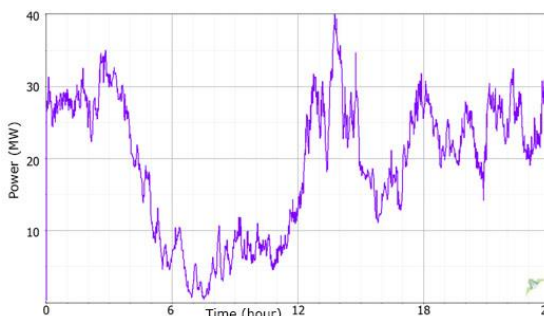


Figure 1: A typical power production of a wind farm.

### Supply Problems of Photovoltaics

Photovoltaic energy was also enormously installed recent years because of decreasing costs and ease of installation and maintenance. It uses solar radiation, so climatic events affect power production. Also, daily production profile is given at Fig. [2] is intermittent and changes day by day.

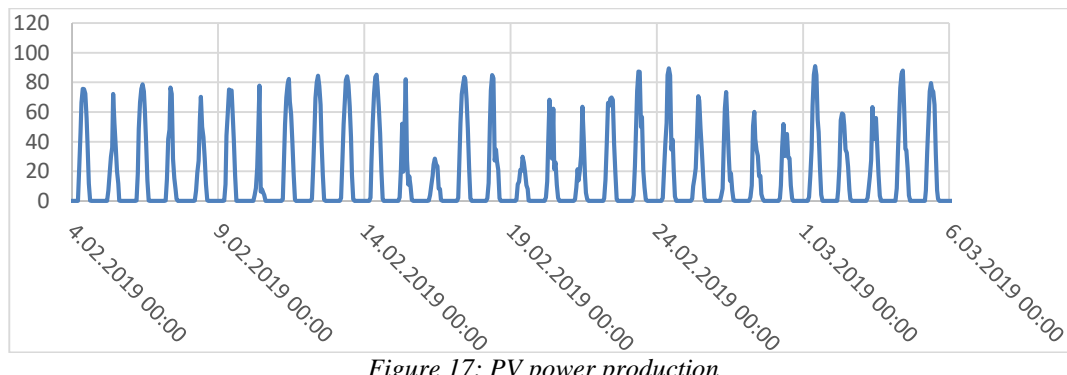


Figure 17: PV power production

## 3. ESS APPLICATIONS IN POWER PRODUCTION

ESS are highly effective in overcoming RES supply problems. There are various kind of ESS usage due to grid problems and ESS capacity. ESS types are also has different efficiency, power and energy density, power and energy price, self-discharge rate, power level. Suitable ESS type should be chosen for grid troubleshooting.

### Increasing depth of RES penetration

High percentage of total energy production will be gained from RES by using ESS. Fig. [3] shows increments of operational wind power and total installed capacity in Turkey. According to the figure, wind-solar power ratio will be higher in following years.

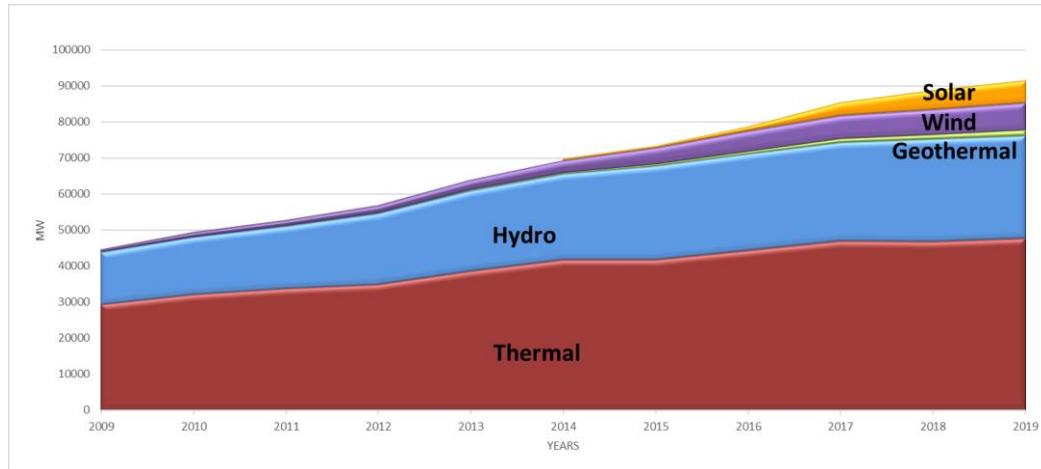


Figure 18: Increasing of installed total power in Turkey.

ESS will play important role on rising of wind-solar power percentage with power control and ancillary service support [3].

### Fluctuations Suppression

Unstable power demand causes voltage and frequency fluctuations at wind power generators. This can be reduced by a wind turbine with an ESS which coupled to DC link of the back-to-back converter [7].

ESS is the most appropriate and efficient solution for suppression of RES fluctuations, because ESS is able to damp any of oscillations efficiently by storing energy [4].

### Catching of prediction

Prediction of energy production is taken from suppliers for all market by Turkish Energy Market Regulatory Authority (EMRA). Predictions are sometimes have not good accuracy and it may cause a penalty to pay EMRA or energy price goes at low tariff. The aim is to use ESS with enough capacity to achieve maximum prediction accuracy. This will increase revenue.

### Smooth Production

ESS can be used as an active-reactive power stabilizer, so ESS control is of a great potential to provide solution to the problem of robust stabilization of power system oscillations [5]. ESS control system needs to have load profile reference [6]. Daily load profile is given from national grid operator, so production of RES can be adjusted according to the load profile. For example, 34 MW power and 245 MWh energy capacity of ESS has used for stabilization of 51 MW wind power plant and achieved to decrease oscillations to %2 [7].

Sizing of ESS is a key point for enough power stabilization. A study gives optimum values for 100 MW wind power plant as 34 MW and of power and 40 MWh of energy capacity [8].

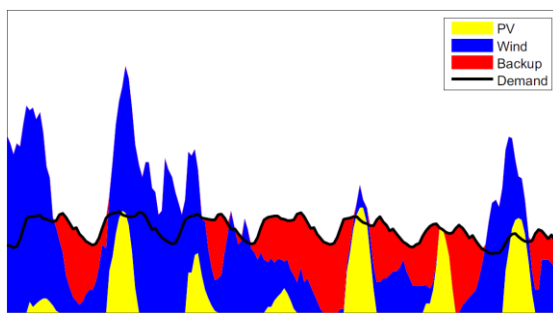


Figure 4: Example of ESS solution for supply-demand equilibrium problem [4]

### Spinning Reserve

All grid operators need to have an amount of reserve. ESS can be defined as a spinning reserve that is used for also frequency control. Spinning reserve capacity is calculated a sum of available power plant capacities which are not producing yet [9].

Turkish national grid operator (TEIAS) has tariffs as intra-day market and day-ahead market. Intra-day market values are given by TEIAS for next 24 hours; day-ahead market values are determined hourly. RES cannot bid for BEM, because of high energy production uncertainty, but they can only join BEM with using ESS. By the way, RES producer can bid to tender and play a role in determining energy market prices [10]. BEM has significant opportunities to sale energy with high tariffs. ESS should be standby fully charged in order to respond to EMRA requests immediately. Turkish national grid operator (TEİAŞ) considers having maximum power within 30-second and 15-min uninterrupted production necessary for primer frequency support [10]. ESS can easily perform these requirements.

### Time Shifting

Substitution of energy sales from cheap tariff to peak power demand periods can be easily done by ESS. So, by ESS utilization, back-up power plants is not necessary [11].

Wind turbines are producing energy continuously as long as grid quality values and blowing wind speed are within limits. If there is no enough energy demand, wind turbine has to be stopped or remaining energy from demand has to be stored. When grid needs energy again, wind turbine should continue its production coupled to ESS.

1 min average energy production of 1.5-year period data set of three wind parks in Turkey was investigated. Some samples of data are given at figure 5, 6 and 7.

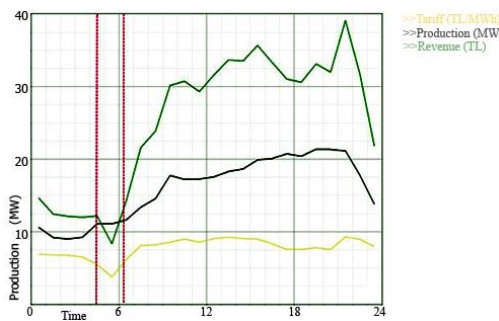


Figure 5: Low tariffs may cause revenue reduction

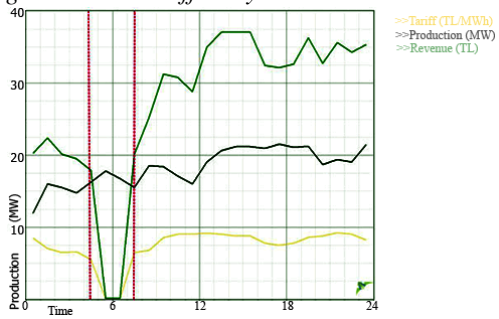


Figure 6: Another example of low tariff

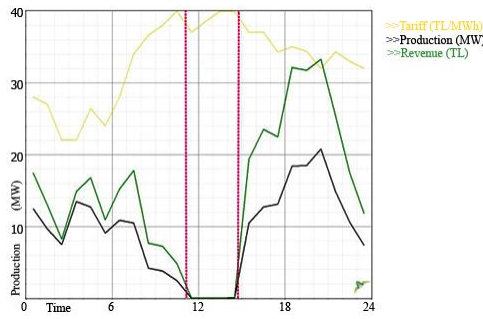


Figure 7: High tariffs might be missed without ESS

Daily profile of energy production and tariff graphical shapes are seen at Fig. [8, 9]. Multiplication of these two values gives us daily energy sales profile at Fig. [10]. ESS can boost production at high tariffs, by the way total revenue increases.

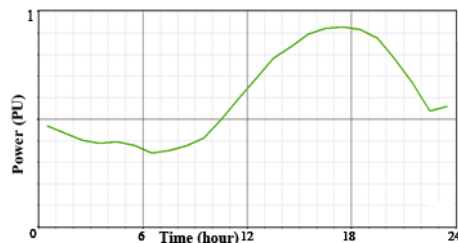


Figure 8: Daily energy production profile

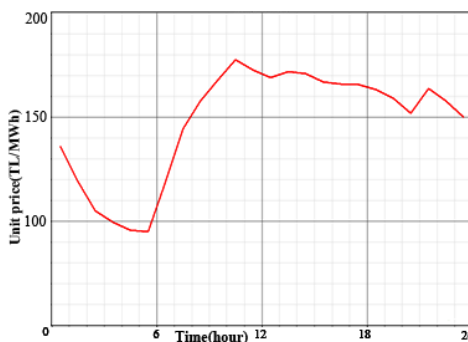


Figure 9: Daily energy tariff profile

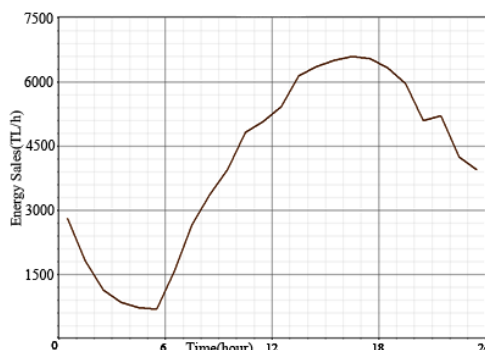


Figure 10: Daily energy sales profile

#### 4. CASE STUDY

VPP portfolio which includes 235 MW WPP, 100 MW PV and 63 MW HEPP with ESS operation is studied in case. EPIAŞ electronic auction system allows multiple power plants as one power plant. It shows that, VPP bidding is enabled by government. All portfolio units should be connected and controlled/coordinated by a central operator to get maximum efficiency.

There are some algorithms to control Battery ESS, HEPP reservoir and revenue calculation. Charge algorithm is consisted of discrete algorithms as it is illustrated as flow chart at Fig. [11] First step is choosing proper algorithm. Flow chart operations are sorted by decreasing revenue.

There are charge-discharge limits control loops are used for preventing over charge-discharge of ESS and over charge-discharge currents. If ESS has enough charge level for catching prediction of production, it will be discharged till catching prediction amount. If stored energy is lower than balance, ESS will be discharged totally for minimizing amount of penalty. Same as, if idle capacity is higher than balance, ESS will be charged with balance amount. If idle capacity is lower than balance, ESS will be charged fully. If the conditions above are not performing, ESS will not be charged or discharged.

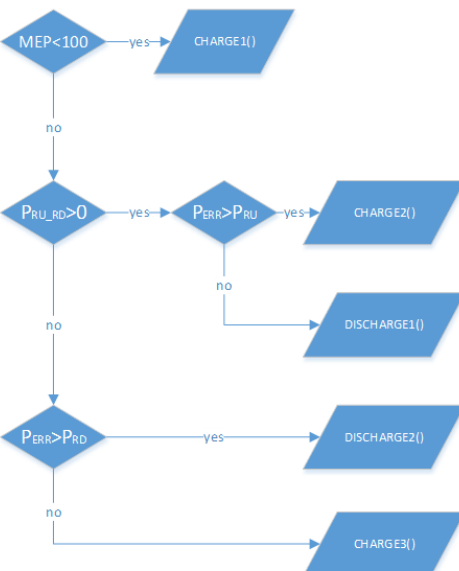


Figure 11 : ESS charge-discharge algorithm

### HEPP Charge Algorithm

ESS in question is provided by the potential energy of water that can be held in the loading pool and forced pipe in a river type HEPP. It was calculated that 70 MWh of energy can be stored in the project whose data were examined and confirmed in the realized productions. This energy was present by the calculation in Eq. [2].

$$E^{HEPP} = \emptyset_{water}^{input} K_{HEPP} \Delta t \quad (2)$$

The amount of water  $\emptyset$  is the m<sup>3</sup>/s unit water flow that can come and hold in the HEPP reservoir.  $K_{HEPP}$  is the MWh unit energy conversion coefficient obtained from unit m<sup>3</sup>.  $\Delta t$  is used for hourly conversion.

HEPP is able to bid for DAM and BEM and store energy by itself. For this reason, it is actually a structure that can operate at the maximum income on its own. If it was operated within a VPP, it will have different priorities within the VPP. Controlling the HEPP reserve from a remote center to support VPP storage is a difficult process in practice. The process will become very complicated when the details are taken into account, as well as it is likely to fail. These details can be given examples such as the necessity of opening the penstock in cases of sudden disaster, being disabled during periods when the water is very low, the regime is irregular, electrical, mechanical and construction failures. For these reasons, it is thought that the evaluation of HEPP reserve in HEPP would be more appropriate in terms of application and these problems were neglected and calculated in accordance with the VPP approach.

According to the water flow data from past years, this storage feature of HEPP, which is operating seasonally, has been evaluated as additional ESS capacity. The offer to DAM and BEM has been added to the VPP bidding on tenders, HEPP energy production is carried out in accordance with the maximum possible energy storage.

The water flow data from Excel and the DAM and BEM bid values given for HEPP in the past years have been added to the total estimate amounts, ensuring maximum energy storage instead of overproduction. With the stored energy at HEPP, the charging status of the Battery ESS is kept above 50% and in critical cases, HEPP power is supplied to the grid. This process is expressed in Eq. [3].

$$P_{ESS}^{HEPP} = IF(SOC_{ESS} < \frac{E_{max}}{2}; \frac{E_{max}}{2} - SOC_{ESS}; 0) \quad (3)$$

### Battery ESS Charging Algorithm

The VPP conditions under which ESS will be charged or discharged are decided in order of maximum revenue. First of all, each income group is run separately with ESS and revenues are calculated, and higher income is prioritized accordingly. In the first stage, charging during low-priced hours is profitable, but it is aimed to generate revenue from the BEM and DAM markets in turn.

The amount of energy produced should be accurately estimated which was given to the markets a day ahead. In case of deviation, this deviation value is  $P_{err}^{DAM}$  expressed as  $P_{ESS}$  and this amount of deviation is tried to be minimized.  $P_{ESS}$  is assumed to be positive in charging and negative in discharge.

$$P_{Prod} = P_{Est} + P_{ESS} + P_{err}^{DAM} \quad (4)$$

ESS output maximum power ( $P_{max}$ ) is considered as constant. ESS efficiency is taken into account by spending more energy at the rate of efficiency when charging.

When faced with very low market prices during the day, these prices provide an opportunity for ESS to charge. There is no large amount of penalties when the forecast is not captured at these times, and when past years are examined, there is usually no instruction to take a load in the BEM as the system direction is in the direction of "energy surplus". Therefore, charging is a priority during these hours.

$$P_{ESS} = IF(MEP < 100; Charge1); \dots \quad (5)$$

Conversely, when high prices were seen, discharge participated in the calculation and it was seen that the income did not increase. This is because in high-priced cases, higher-priced instructions come in the BEM, and larger penalties occur when these instructions are not followed.

Since BEM unit prices are generally higher than other markets, so priority is given to this market. The instruction in BEM is positive when "Ramp-up" and negative "Ramp-down". Since the charging status varies according to the direction of the instruction, the direction of the instruction is checked first.

$$\dots IF(P_{RU\_RD} > 0; \dots \quad (6)$$

If the energy generation can meet the instruction, charging, discharge control functions are called if it cannot. By controlling the lower or upper limit values of the ESS, the invoked functions calculate how much charge and discharge ESS should be.

$$\dots IF(P_{err}^{DAM} > P_{RU}; Charge2(); Discharge1()); \dots \quad (7)$$

On the contrary, if the instruction can be met, discharge, if it cannot meet, charging control functions are called. The order of operation has been changed because the instruction is negative.

$$\dots IF(P_{err}^{DAM} > P_{RD}; Discharge2(); Charge3())) \quad (8)$$

The charge control cycle of all production of DAM and BEM is given in Eq. [5], and in Eqs. [6, 7] these allow ESS energy and power limits to be controlled and the amount of charging determined.

$$Charge1(): IF(ChargeFonk > P_{Prod}; P_{Prod}; ChargeFonk) \quad (9)$$

$$Charge2(): IF(ChargeFonk > P_{err}^{DAM} - P_{RU}; P_{err}^{DAM} - P_{RU}; ChargeFonk) \quad (10)$$

$$Charge3(): IF(ChargeFonk > -(P_{err}^{DAM} - P_{RD}); -(P_{err}^{GÖP} - P_{RD}); ChargeFonk) \quad (11)$$

Eq. [8, 9] are functions that return the maximum power and energy capacity of ESS, whichever is less valuable.

$$\textbf{ChargeFonk}(): \text{IF}(E_{max} - SOC_{ESS} > P_{max}; P_{max}; E_{max} - SOC_{ESS}) \quad (12)$$

$$\textbf{DischargeFonk}(): \text{IF}(-SOC_{ESS} < -P_{max}; -P_{max}; -SOC_{ESS}) \quad (13)$$

These functions ensure that the ESS does not exceed the upper and lower limits in charging and discharge operations. Since these controls are repeated in many places, they are expressed as a separate function. Eqs. [7, 8] control the power and energy limits in the direction of charge and also Eqs. [11, 12] in the direction of discharge.

$$\textbf{Discharge1}(): \text{IF}(P_{err}^{DAM} - P_{RU} < \text{DischargeFonk}; \text{DischargeFonk}; P_{err}^{DAM} - P_{RU}) \quad (14)$$

$$\textbf{Discharge2}(): \text{IF}(-(P_{err}^{DAM} - P_{RD}) < \text{DischargeFonk}; \text{DischargeFonk}; -(P_{err}^{DAM} - P_{RD})) \quad (15)$$

## Revenue Calculation

In order to maximize revenue, ESS's charge-discharge amount is calculated for each hour and revenue is calculated according to the new situation. For this purpose, the sum of WPP, PV and HEPP productions in Eq. [13] is considered a single production value. This value is also equal to the production estimate  $P_{Est}$ ,  $P_{DAM-err}$  and ESS energy consumption total of all plants as given in Eq. [14].

$$P_{Prod} = P_{WPP} + P_{PV} + P_{HEPP} \quad (16)$$

$$P_{Prod} = P_{Est} + P_{err}^{DAM} - P_{ESS} \quad (17)$$

DAM, DIM and BEM markets are presented as 3 separate models independent of each other in terms of generating revenue independently of each other. Each has separate unit prices and separate penalties. When calculated in a unified way, they constitute the market model. It is also possible to sell at a fixed price by making a bilateral agreement. However, it is assumed that there was no bilateral agreement in this study. Sales of block offers on the market affect prices slightly. The impact of these sales has also been neglected.

In the revenue calculation, 9 different market scenarios are illustrated as given in Fig. [12] according to the status of the production, forecast and instruction values. In this graph, considering that the estimate is low or high according to the production power, and then these forecast values are taken as Daily approved production plan (DAPP), it is stated that the Ramp-up-Ramp-down instructions are added on top of this. In the 9 income accounts, it can be determined in which markets the estimate was captured or the instruction was fulfilled. Accordingly:

Ramp-down instruction cannot be met, ESS charging is required.

1. There is no instruction, ESS charging is required.
2. Ramp-up instruction was met and ESS charging is still required.
3. Ramp-down instruction cannot be met, ESS charging is required.
4. There is no instruction, the system is in balance. ESS should not work.
5. Ramp-up instruction cannot be met, ESS discharge is required.
6. Ramp-down instruction was met, ESS discharge is still required.
7. There is no instruction, ESS discharge is required.
8. Ramp-up instruction was not met, ESS Discharge Required.

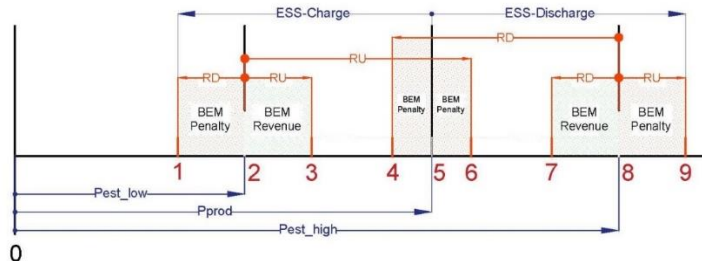


Figure 12: 9 different market scenarios

## DAM

Energy sales revenue is in section 93 of the Balancing and Reconciliation Regulation of TEİAŞ. In line with the article, the offer price given in the market before the day is calculated on the agreed basis instead. In case of non-compliance with DAPP, the amount of the loan  $\pi_{DMEP}$  multiplied by the realized portion of the offer quantity ( $P_{Est}$ ) as specified  $\pi_{DMEP}$  in Eq. [15], the amount of the offer that did not occur, and the amount  $\pi_{MEP}$  of the debt is calculated by multiplying the penalty coefficient ( $K_{DAM}$ ).  $K_{DAM}$ , as stated in section 98, the values **min(PTF, SMF)\*0.97 and max(PTF, SMF)\*1.03** in negative imbalance are taken from the positive imbalance predicted earlier in the day [12].

$$Revenue_{DAM} = P_{Est}\pi_{DMEP} - K_{DAM}P_{err}^{DAM} \quad (18)$$

## BEM

After the bids received in the BEM, instructions are sent by the system according to the situation of “energy-deficit” or “energy-surplus” by looking at the direction of the system. The reference is considered as  $\pi_{MEP}$  the price. The offer price accepted in the BEM is expected to be higher than.  $\pi_{MEP}$  is valid when Ramp-up offer is low priced or the Ramp-down offer is high priced according to section 103<sup>rd</sup> and 106<sup>th</sup> of the Balancing and Reconciliation Regulation. In BEM, the amount of income is expressed in Eqs. [16, 17, 18]. The K multipliers here are the average values that have emerged in the tender results of the past years and it is indicated how they are calculated under the heading of assumptions. The aforementioned revenues belong to the total production of VPP (i.e. WPP, PV, HEPP and ESS), and the expenses generated by the failure to capture the estimates have been added to the final part. The amount of instructions fulfilled in the Ramp-up instruction comes as much as the amount that cannot be fulfilled, and the amount that cannot be fulfilled consists of debt. The unfulfillable debt multiplier is calculated by reflecting the amount of imbalance in the market at the rate of all the cost of imbalance in the relevant time period. In the Ramp-down instruction, the reason the amount is calculated as a debt is to be retracted as much as the instruction amount of  $\pi_{DMEP}$  the production calculated through the payment with DAPP. As a result, some revenue is calculated by the system for production that does not occur with Ramp-down. When the Ramp-down instruction is not fulfilled, it is calculated by reflecting the cost of all the imbalance in the relevant time period in the market, as in Ramp-up, at the rate of the amount of imbalance here.

$$Revenue_{BEM,RU} = K_{RU}P_{bid}^{RU}\pi_{MEP} - K_{RUerr}P_{err}^{RU}\pi_{MEP} \quad (19)$$

$$Dept_{BEM,RD} = K_{RD}P_{bid}^{RD}\pi_{MEP} + K_{RDerr}P_{err}^{RD}\pi_{MEP} \quad (20)$$

$$Revenue_{BEM} = Revenue_{BEM,RU} - Dept_{BEM,RD} \quad (21)$$

## Combined Income Calculation

Since bidding together in DAM and BEM is necessary to maximize revenue, revenues must be calculated together. Eq. [19] combine these two accounts. Since the instructions Ramp-up and Ramp-down will not come to a facility at the same time, this is determined by an if function and entered into the account. The Ramp-up instruction is positive and the Ramp-down instruction is negative. Then, in case of partial fulfillment of the instructions, additional functions were removed for partial calculation. The cost of imbalance in  $P_{err}^{DAM}$  is added depending on the amount of imbalance. In cases where the BEM directive affects the imbalance, the change of the cost of DAM imbalance is found in Eqs. [20, 21]

$$\text{Revenue} = P_{DAM}\pi_{MEP} + K_{DAM}(P_{err}^{DAM} - P_{ESS}); \\ \text{IF}(P_{RU\_RD} > 0; Fonk4_{RU}; Fonk5_{RD})) \quad (22)$$

Revenue is calculated through the DAPP,  $\pi_{DMEP}$  in DAM. Although it is not possible to make any changes to DAPP, the Ramp-up and Ramp-down instructions in the BEM are applied by referencing the DAPP values. Calculation and coefficients vary according to the instruction value. Eq. [20] shows the principle of calculating the function in the way that it is calculated.

$$Fonk4, 5: IF \begin{cases} \text{Instruction was fulfilled;} \\ Prod_{excess} + Instruction_{full}; \\ Instruction_{partial} - Penalty_{BEM} \end{cases} \quad (23)$$

Up to the amount  $P_{err}^{DAM} - P_{ESS}$  of BEM instruction can be fulfilled. Therefore, this amount is compared with the volume of instructions. If this amount is incomplete from the instruction, a penalty occurs, and if it is too much than instruction, it is taken at low price.

In Eq. [21], when instruction comes, energy production must be amount of sum of DAPP and instruction. This quantity has unit price  $\pi_{MEP}$  in the  $K_{RU}$  multiplication is up to. But instructions instead part of unit price a  $K_{penalty}$  multiplier.

$$Fonk4: IF \begin{cases} P_{err}^{DAM} - P_{ESS} \geq P_{RU\_RD}; \\ -K_{DAM} * (P_{RU\_RD}) + K_{RU} * \pi_{MEP} * P_{RU\_RD}; \\ IF(P_{err}^{DAM} > 0; K_{RU} * \pi_{MEP} * (P_{err}^{DAM} - P_{ESS}) \\ -K_{PEN} * \pi_{MEP} * (P_{RU\_RD} - (P_{err}^{DAM} - P_{ESS})) \\ -K_{DAM}(P_{err}^{DAM} - P_{ESS}); \\ -K_{PEN} * \pi_{MEP} * P_{RU\_RD}) \end{cases} \quad (24)$$

In Eq. [22], when the load disposal instruction comes, it is requested to produce as little as the amount of instructions from DAPP. In this case, it  $P_{RU\_RD}$  is negatively valuable. This is usually  $K_{RU}$  a multiplier of 0.3. The amount of income is calculated by multiplying the lowest amount  $\pi_{MEP}$  of  $K_{RU}$  energy. If production is not reduced, the quantity penalty multiplier (usually  $K_{PEN}$  is 0.5) in which the instruction is not fulfilled is billed. On the other hand, the price of the production amount is paid  $K_{DMEP}$  at the unit price.

$$Fonk5: IF \begin{cases} P_{err}^{DAM} - P_{ESS} \leq P_{RU\_RD}; \\ -K_{DAM} * P_{RU\_RD} + K_{RD} * \pi_{MEP} * P_{RU\_RD}; \\ IF(P_{err}^{DAM} > 0; K_{PEN} * \pi_{MEP} * P_{RU\_RD}; \\ K_{RD} * \pi_{MEP} * (P_{err}^{DAM} - P_{ESS})) \\ +K_{PEN} * \pi_{MEP} * (P_{RU\_RD} - (P_{err}^{DAM} - P_{ESS})) \\ -K_{DAM}(P_{err}^{DAM} - P_{ESS})) \end{cases} \quad (25)$$

After checking that the instructions are fulfilled in the functions, the part of the instruction that is fulfilled and cannot be fulfilled is separated and calculated. EPIAŞ Transparency website received the instructions amounts

Ramp-up and Ramp-down in the BEM tenders in the past years, and it was assumed that these instructions were offered and a random portion of them were won. Accordingly, the BEM revenue account has been made. In this model, it will not be possible to enter all markets due to the limited amount of reserves, the revenues of each market will be calculated and the use of reserves will be divided at the rate of revenues.

## Assumptions

All coefficients have been tried to be obtained from the value of the past years in the market. In BEM, some high bids can be made from the SMF for the "Ramp-up" instruction and the tender can be won [12]. The price information for the past 2 years in the TEİAŞ TPYS system was processed and the average offer prices accepted by the system were calculated. The price for the "Ramp-up" instruction is 1.36 times that of the SMF [13]. If the instruction cannot be fulfilled, the cost of imbalance occurs. For this cost, 0.7 times the SMF has been accepted for the purpose of staying on the safe side.

For the "Ramp-down" instruction, some low bids can be made from the SMF and the tender can be won. This offer is calculated as 0.58 times SMF using TPYS data. If the instruction cannot be fulfilled, the cost price of 0.5 times the SMF has been accepted.

VRB or Lithium-ion will be used for the efficiency of ESS, and the referenced values are given in the table below [14].

ESS Type	Cycle Life	Dept of Discharge (%)	Energy Installation Cost (USD/MWh)	Cycle Efficiency (%)
<b>VRFB</b>	13000	100	119	78
<b>NMC/LMO</b>	4000	90	167	97

In order for VPP's BEM revenues to be high, this market must be offered in accordance with the available capacity. Since the offer was made before the day, it is not appropriate to consider the instant production. Bids for BEM instructions are entered according to the ESS charging status, the instruction confirmation is selected for that watch, whichever of Ramp-up and Ramp-down instructions has occurred more in the market. The approved instruction quantity is calculated as a random value between "0" and "bid quantity".

## 5. CONCLUSION

As a result of the calculations made with energy production and market data realized in 2015-19, graphs were created. ESS size selection was made through these graphs and the effect of efficiency was examined.

The number of charging-discharge cycles is important in the selection of ESS and determines battery life. When this number of cycles was calculated, it was seen that the ESS capacity decreased with the increase in Fig. [13]. In this case, when the lithium battery is selected, it will require the selection of some high capacity product for its longevity. Due to the high amount of cycles, products with high cycle life, such as VRB, may also be preferred instead of increasing ESS capacity.

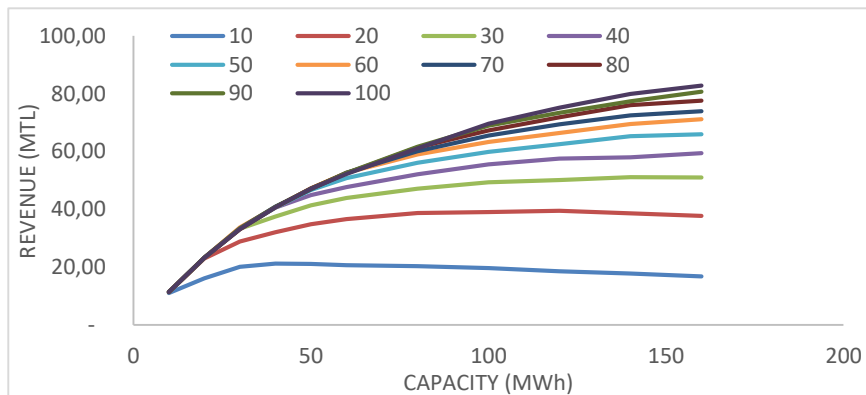


Figure 13: Change of 5-year cycle numbers by capacity

Fig. [14] from ESS power fixed by determining capacity and revenue curves. These curves are descending and increase they show. This reason ESS capacity is higher than unbalance quantity of production.

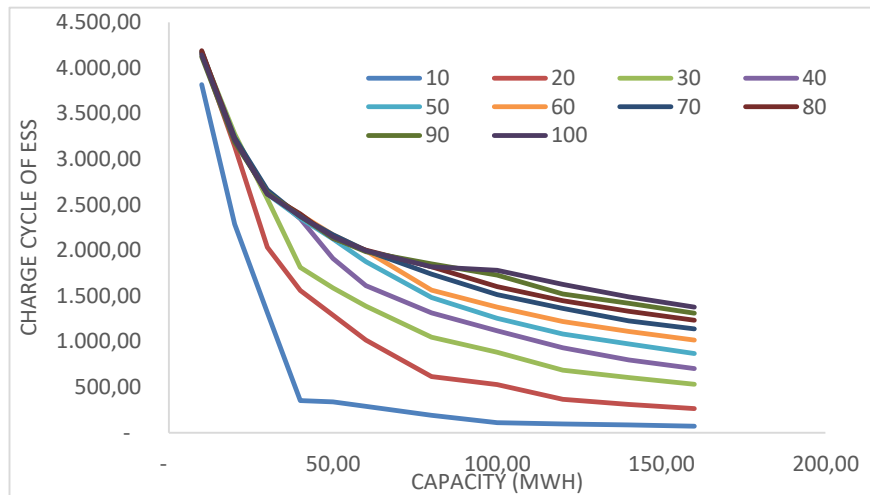


Figure 14: 5-year revenue increase by capacity

With the increase of ESS capacity, the energy needs in the market do not increase at the same rate. The revenue per MWh chart for capacity is given in Fig. [15]. Accordingly, the optimum point of ESS capacity can be removed. Figs. [14,15] were examined and calculated according to different yields on this curve, considering that the unit revenue was appropriate on the 30MW curve. Considering that the ESS efficiency will be between 60% and 90%, curves such as Fig. [16] have emerged by calculating in this range. Here the capacity of 30 MWh, which is the breaking point, was selected.

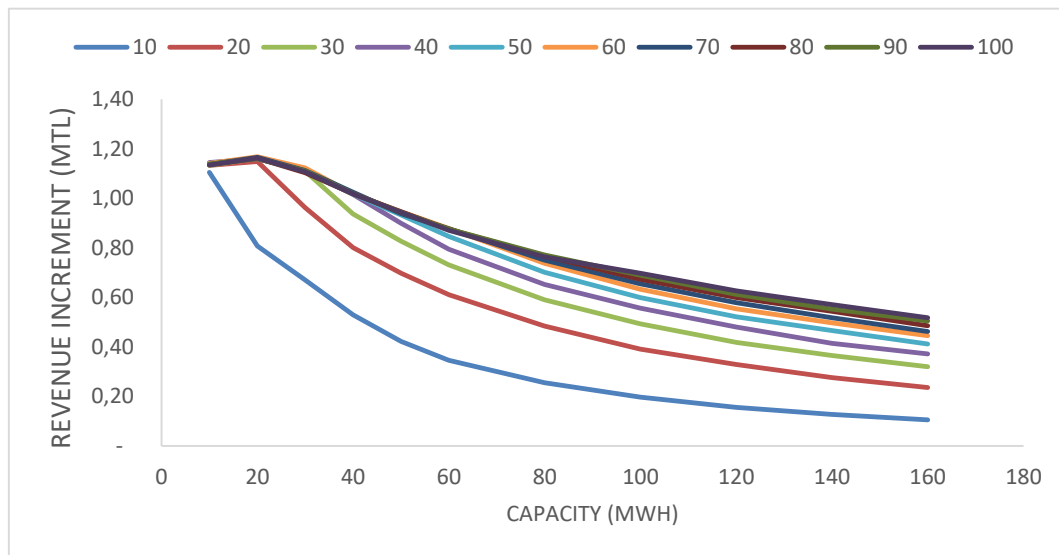


Figure 15: 5-Year EDS MWh Revenue Growth Per Unit

It was calculated that 33.1 Million TL profit would have been achieved in 5 years (between 2015-19) with ESS capacity operating with 90% efficiency of 30 MW / 30 MWh. If revenues are converted daily, it makes 9,2 M\$. It is also meaning that VPP revenues are increasing 4,5%. According to the results, ESS gets reasonably high profit by using the algorithm of this paper.

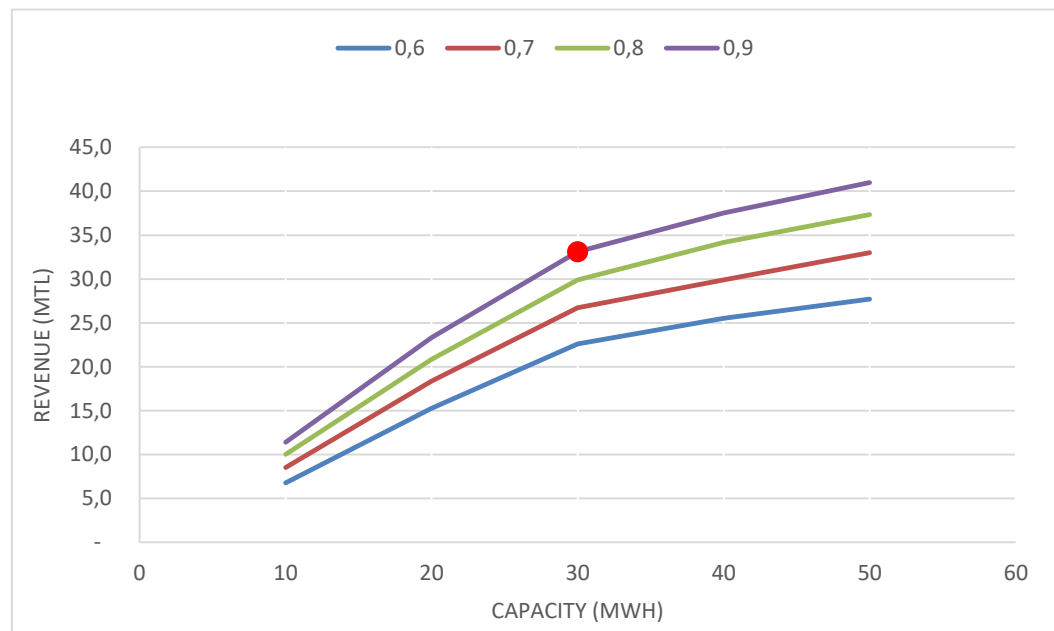


Figure 16: Impact of 30 MW EDS yield on revenue

## REFERENCES

- [1] Taneja, J., Rosenberg C. A, Comparative Study of High Renewables Penetration Electricity Grid. <[https://www.cs.cmu.edu/~smithv/docs/renewables\\_sgc\\_2013.pdf](https://www.cs.cmu.edu/~smithv/docs/renewables_sgc_2013.pdf)>
- [2] Web 1, (2011), <http://web.mit.edu/windenergy/windweek/presentations/wind %20energy%20101.pdf>, (Access date: 14/02/2021).
- [3] Díaz-González F., Sumper A., Gomis-Bellmunt O., Villafáfila-Robles R., (2012), “A review of energy storage technologies for wind power applications”, Renewable and Sustainable Energy Reviews, 5 (16), pp. 2159– 2167.
- [4] Nur Shahia H., Mohammad Y. H., Md Shah M., Hasimah A. R., (2013), “Review of storage schemes for wind energy systems”, Renewable and Sustainable Energy Reviews, 5 (21), pp. 237–247.
- [5] Du W., Wang H. F., Cheng S., Wen J. Y., Dunn R., (2011), “Robustness of damping control implemented by Energy Storage Systems installed in power systems”, Electrical Power and Energy Systems, 33 (1), 35–42.
- [6] Hida Y., Yokoyama R., Shimizukawa J., Iba K., Tanaka K., Seki T., (2010), “Load following operation of NAS battery by setting statistic margins to avoid risks”, IEEE power and energy society general meeting, 1-2, Minneapolis, USA, 25 - 29 July.
- [7] Iijima Y., Sakanaka Y., Kawakami N., Fukuhara M., Ogawa K., Bando M., Matsuda T., (2010), “Development and Field Experiences of NAS Battery Inverter for Power Stabilization of a 51 MW Wind Farm”, The 2010 International Power Electronics Conference, 1841-1842, Sapporo, Japan, 21 - 24 June.
- [8] Brekken T. K. A., Yokochi A., Jouanne A., Yen Z. Z., Hapke H. M., Halama D. A., (2011), “Optimal Energy Storage Sizing and Control for Wind Power Applications”, IEEE Transactions On Sustainable Energy, 1 (2), 76-77.
- [9] Web 2, (2005), [https://labs.ece.uw.edu/real/Library/Reports/What\\_is\\_spinning\\_reserve.pdf](https://labs.ece.uw.edu/real/Library/Reports/What_is_spinning_reserve.pdf), (Access date: 14/02/2021).
- [10] Web 3, (2009), <https://docplayer.biz.tr/272255-Turkiye-elektrik-iletim-a-s-primer-frekans-kontrol-hizmetinin-uygulanmasina-iliskin-el-kitabi.html> (Access date: 14/02/2021).
- [11] Rabiee A., Khorramdel H., Jamshid A., (2013), “A review of energy storage systems in microgrids with wind turbines”, Renewable and Sustainable Energy Reviews, 3 (18), pp. 316–326.
- [12] Web 4, (2015), <https://www.epias.com.tr/dengeleme-guc-piyasasi/smf-hesaplanmasi/>, (Access date: 14/02/2021).
- [13] Web 5, (2020), <https://tpys.teias.gov.tr/tpys/app/report.htm>, (Access date: 14/02/2021)
- [14] Web 6, (2017), <https://www.irena.org/publications/2017/Oct/Electricity-storage-and-renewables-costs-and-markets>, (Access date: 14/02/2021)



## p-n HETEROJUNCTION DIODE BASED ON TiO<sub>2</sub>/p-Si

Sekertekin Betül

KalyonPV Research and Development Center, Kalyon Güneş Teknolojileri Üretim A.Ş., 06909 Ankara, TURKEY,  
bsekertekin@kalyonpv.com, ORCID: 0000-0002-9594-9635

Ozel Kenan

Ankara Yildirim Beyazit University, 06010 Ankara, TURKEY, kenanozel89@gmail.com, ORCID: 0000-0002-0250-3731

Yildiz Abdullah

Ankara Yildirim Beyazit University, 06010 Ankara, TURKEY, yildizab@gmail.com, ORCID: 0000-0002-0250-3731  
0000-0003-4137-6971

*Cite this paper as:* Şekertekin, B., Ozel, K., Yıldız, A. P-N heterojunction diode on TiO<sub>2</sub>/p-Si. 9th Eur. Conf. Ren. Energy Sys. 21-23 April 2021, Istanbul, Turkey

**Abstract:** TiO<sub>2</sub> metal oxide layers are used for photovoltaic studies and heterojunction diode applications because of their excellent properties like chemical resistance, high refractive index, and high dielectric constant. TiO<sub>2</sub> can be operated as an anti-reflecting coating (ARC) and presents an n-type behavior because of the presence of donor-type defects, and titanium interstitials atoms. In this study, the n-TiO<sub>2</sub> film was spin-coated with different cycles of coating (x1, x2, x3) on a p-Si wafer and glass. The optical properties of the films were determined utilizing UV-Vis spectrometer. Current-voltage (I-V) characteristics of the p-n heterojunction device based on Ag/TiO<sub>2</sub>/p-Si/Ag were investigated in the dark. The results revealed that the fabricated three devices have diode behavior.

**Keywords:** Sol-gel spin coating method, Heterostructures, TiO<sub>2</sub>

© 2021 Published by ECRES

### 1. INTRODUCTION

Generally, TiO<sub>2</sub> exhibits an n-type conductivity behavior and this type conductivity is due to donor type defects, including oxygen vacancies and titanium interstitials atoms [1]. Specifically, TiO<sub>2</sub> can be employed as an antireflection coating (ARC) in solar cells for silicon surface passivation and as an emitter layer in p-n heterojunction-based devices [2]. Furthermore, one-dimensional (1-D) nanostructures such as nanowires (NWs), nanorods (NRs), nanotubes (NTs) have been demonstrated for potential technological applications due to their high surface to volume ratio and inherent quantum confinement effects [1-3]. To fabricate a solar cell or a photodiode, TiO<sub>2</sub> metal oxide layer or TiO<sub>2</sub> nanostructured layer is deposited on substrate such as FTO (Fluorine Tin Oxide)/Glass, ITO (Indium Tin Oxide)/Glass or p-Si substrates to obtain emitter layer. At this point, the effect of the number of coating of the metal oxide layer, i.e. the effect of thickness, is an important parameter to decide critical structural behaviors of the p-n heterojunction based solar cells or photodiodes. Optical and electrical characterization techniques such as UV-Vis (Transmission-Absorption Spectrophotometry) and I-V testing are conducted to specify the optoelectrical properties of the device.

### 2. EXPERIMENTAL SECTIONS

#### Theory:

TiO<sub>2</sub> is an important wide bandgap semiconductor for photovoltaic cells and photodiode applications due to its excellent properties such as chemical resistance, high refractive index, high dielectric constant. Generally, wide bandgap metal oxides such as ZnO, TiO<sub>2</sub> or SnO<sub>2</sub> are deposited on p type Si as an emitter layer to form p-n heterojunction. Many types of deposition techniques, including sol-gel spin coating, hydrothermal method, chemical vapor deposition (CVD), physical vapor deposition (PVD) have been used to coat metal oxide semiconductors on the surface of p-Si. In particular, sol-gel spin coating is widely preferred as it offers low cost manufacturing with homogeneous thin film formation [4].

#### Experimental Setup:

Prior to deposition, p-Si wafer was diced to form Si pieces of 1.5cm\*1.5cm. Then, the standard Piranha and HF cleaning procedure were applied to eliminate surface contamination. In this work, TiO<sub>2</sub> sol (0.6 M) was prepared by using the precursor

of TTIP (Titanium Isopropoxide). TiO<sub>2</sub> metal oxide thin films with three different cycles of coating (x1, x2, x3) were deposited on p-Si (100) substrate via spin coating technique. The spin-coating process was achieved at 2500 rpm, 5.0 acc, and for 30 seconds at room temperature with spin coater. The Ag paste was applied onto the back and front surface of heterojunction to form metal contacts. UV-Vis spectrometer is used to determine the optical properties of n-type layers. I-V measurement set-up (made up of a Keithley 2400, a computer and a probe station) is used to determine the electrical characteristics of the devices.

### Methodology:

The schematic of n-TiO<sub>2</sub>/p-Si heterojunction is shown in Figure 1. In the present design, the n-TiO<sub>2</sub> layer is depicted as an emitter layer, while p-Si substrate is employed as an absorber layer. In this study, the n-TiO<sub>2</sub> is deposited by sol-gel spin coating. In addition, screen printing method is used to obtain back and front metal contacts.

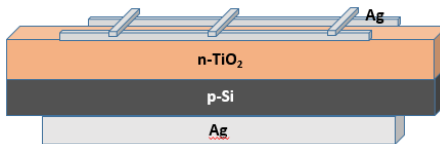


Figure 1. The schematic of n-TiO<sub>2</sub>/p-Si heterojunction

## RESULTS AND DISCUSSIONS

The optical absorbance and transmittance profiles of the device are given in Figure 2 (a) and (b). The TiO<sub>2</sub> film deposited by one cycle of coating has the highest transmittance. As the layer thickness increases, the transmittance decreases. If the n-TiO<sub>2</sub>/p-Si heterostructure is used in photodiode applications, it is obvious that the device with one cycle of coated TiO<sub>2</sub> film will be advantageous.

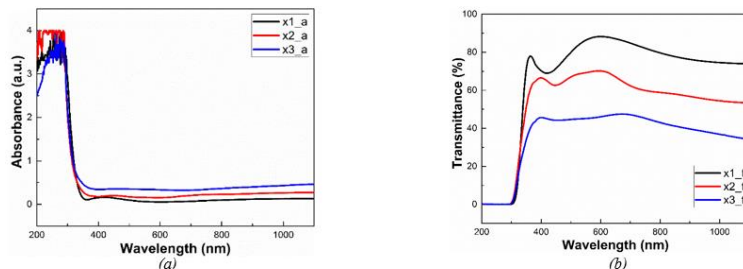


Figure 2. (a) Absorbance (b) Transmittance profiles of the samples formed by hydrothermally growth TiO<sub>2</sub> layer on three different cycles (x1, x2, x3) of coated TiO<sub>2</sub> seed layers

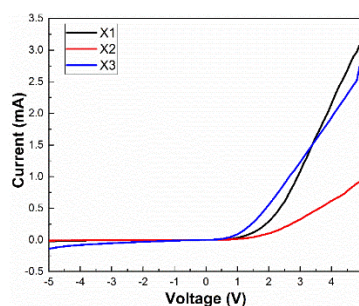


Figure 3. I-V graph of \*1-\*2-\*3 layers of TiO<sub>2</sub> coated p-Si substrates,

Figure 3 shows the dark I-V characteristics of the devices. According to I-V results, the fabricated devices exhibit diode behavior. The best diode performance is achieved for the device 1. In addition, the minimum value of leakage current belongs to this device. High optical and electrical properties make this device highly suitable for electronic and optoelectronic applications.

## 3. CONCLUSION

In summary, devices based on n-TiO<sub>2</sub> / p-Si heterojunction were produced with different cycles of n-TiO<sub>2</sub> film coated on p-Si. The optical properties of N-TiO<sub>2</sub> films were examined by UV-Vis measurement and the thinnest film was confirmed to

have the highest transmittance. In addition, the diode characteristics of the devices were determined by I-V measurement. It was found that the best performance was with the device fabricated with one cycle of coated TiO<sub>2</sub> film.

## **REFERENCES**

- [1,4] M. K. Nowotny, T. Bak, and J. Nowotny, Electrical Properties and Defect Chemistry of TiO<sub>2</sub> Single Crystal. I. Electrical Conductivity, 2006, 110, 16270-16282
- [2] Ali, K., Khan, S. A., & Jafri, M. M. Effect of double layer (SiO<sub>2</sub>/TiO<sub>2</sub>) anti-reflective coating on silicon solar cells. 2014, 9(12), 7865-7874.
- [3] Welte, A., Waldauf, C., Brabec, C., & Wellmann, P. J. Application of optical absorbance for the investigation of electronic and structural properties of sol-gel processed TiO<sub>2</sub> films. 2008, 516(20), 7256-7259.
- [4] Hinczewski, D. S., Hinczewski, M., Tepehan, F. Z., & Tepehan, G. G. Optical filters from SiO<sub>2</sub> and TiO<sub>2</sub> multi-layers using sol-gel spin coating method. 2005, 87(1-4), 181-196.



# VARIOUS RECEIPTS $TiO_2$ BASED PASTES FOR SEMI-FLEXIBLE DSSCs

Abdullah ATILGAN

Department of Energy Systems Engineering, Faculty of Engineering and Natural Sciences, Ankara Yıldırım Beyazıt University, Ankara 06760, bdlhtlgm@gmail.com, ORCID: 0000-0002-5624-3664

İrem SÜTÇÜ

Department of Energy Systems Engineering, Faculty of Engineering and Natural Sciences, Ankara Yıldırım Beyazıt University, Ankara 06760, Turkey, sutcuirem@hotmail.com, ORCID: 0000-0002-6076-6206

Abdullah YILDIZ

Department of Energy Systems Engineering, Faculty of Engineering and Natural Sciences, Ankara Yıldırım Beyazıt University, Ankara 06760, Turkey, yildizab@gmail.com, ORCID: 0000-0003-4137-6971

Cite this paper as: *Atilgan, A., Sütçü, İ., Yıldız, A., Various receipts  $TiO_2$  based pastes for semi-flexible DSSCs. 9<sup>th</sup> Eur. Conf. Ren. Energy Sys. 21-23 April 2021, Istanbul, Turkey*

**Abstract:** ITO/PET substrates of photoanodes of flexible dye-sensitized solar cells (f-DSSCs) coated with different  $TiO_2$  pastes (contain distinct  $TiO_2$  nanoparticle sizes) as a semiconductor metal oxide layer via spin coating technique and their power conversion efficiencies are investigated. Analysis of the electrical properties of the f-DSSCs was carried out using an I-V measurement system. The solar cell which coated the paste that comprises 20 nm and 100 nm  $TiO_2$  nanoparticles with a 7:3 ratio provides the best photocurrent density of  $2.48 \text{ mA cm}^{-2}$  and the best power conversion efficiency of 0.40% under 1 sun illumination. Because decreasing voids between  $TiO_2$  nanoparticles with using different particle sizes leads to increase in the interparticle connection between the particles, and this results in increasing  $J_{sc}$  value.

**Keywords:** Flexible DSSCs, paste, particle size

© 2021 Published by ECRES

Nomenclature	
DSSC	Dye-sensitized solar cells
f-DSSC	Flexible Dye-sensitized solar cells
SSCs	Silicon solar cells conduction band
CB	Conduction band

## 1. INTRODUCTION

Dye-sensitized solar cells (DSSCs) are promising alternatives to Silicon solar cells (SSCs) due to low production cost, good performances in every light condition, easy manufacturing techniques, and semitransparency [1]. From the first discovery in 1990, DSSCs are investigated intensively by research groups and until today, there are more than 9000 published papers [2].

A conventional DSSCs structure has five main components: glass substrates with conductive oxide layers, a semiconductor metal-oxide layer, a dye, catalyst, and electrolyte. Additionally, the working principle of DSSCs consists of four steps. (1) incident light comes to the dye molecule on the semiconductor layer of the photoanode and absorbed by the dye; (2) excited electrons go through the conduction band (CB) of  $TiO_2$  and then the current travel around the external circuit; (3) the dye molecules are regenerated by the electrolyte solution; (4) the electrolyte is regenerated by the counter electrode [3].

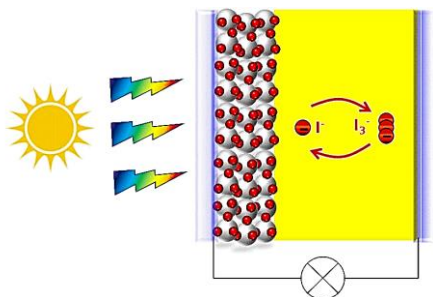


Figure 1. Schematic diagram of dye-sensitized solar cell (DSSC) assembly.

The requirement for lightweight and nonrigid solar cells in some areas causes the rising of flexible DSSCs. Generally, plastic substrates (ITO/PEN, ITO/PET) are used in f-DSSCs structures and these substrates restrict fabrication temperatures due to their low thermal stability. Hence, organic binders that need at least 450°C to leave the TiO<sub>2</sub> are not used in the low-temperature process of f-DSSCs [4]

## 2. EXPERIMENTAL DETAILS

Indium-tin-oxide (ITO) coated polyethylene terephthalate (PET) substrates for photoanode were cleaned in acetone, ethanol, and DI water, respectively in an ultrasonic bath for 10 minutes. Then, they were dried with air. Afterward, the TiO<sub>2</sub> pastes with three different recipes were prepared. First TiO<sub>2</sub> paste was included in 0.5 g of P25 (20 nm particle size), 4.25 g of ethanol, 0.07 g of DI water, 0.18 g of TTIP (it was labeled as P#1). For the second TiO<sub>2</sub> paste, anatase (100 nm particle size) and P25 (20 nm particle size) with the ratio 7:3 and 9 g of DI water are used (it was labeled as P#2). P25 (20 nm particle size) and anatase (100 nm particle size) with the ratio 7:3 and 9 g of DI water are used for the last TiO<sub>2</sub> paste (it was labeled as P#3). Samples were coated with different pastes with a spin coating method (4000 rpm, 30sec). After that, coated ITO/PET substrates annealed at 120°C for 1 hour.

Prepared photoanodes immersed 0.3 mM N719 in methanol for 18 hours in a dark place. For the counter electrode, platinum-coated FTO/GLASS was used and for the electrolyte; iodine, lithium iodide, 4-tert-butyl pyridine (TBP), 1-butyl-3-methylimidazolium iodide (BMII), guanidine thiocyanate, and acetonitrile were mixed to get a homogenous solvent. Electrolyte solution injected through the sandwich structure between the photoanode and the counter electrode.

## 3. RESULTS AND DISCUSSION

Main differences of produced pastes were particle sizes and particle phases ratio. All three pastes contain anatase and rutile phases. P25 powder consists of 85% rutile and 15% anatase phases of TiO<sub>2</sub>. Main differences of produced pastes were particle sizes and particle phases ratio. The sources of titanium oxide components for the P#1 paste are 73.5% P25 and 26.5% TTIP. Cenovar et al. was reported that at 95,6 °C the evaporation of the physically adsorbed water starts and decomposition of the organic residual precursor groups of TTIP begins at 162,8 °C and fully completed at 220,8 °C [6]. In the light of this information, it can be clearly said that TTIP is anhydrous and its particle size is below 20 nm. The components of P#2 paste are 30% anatase 100 nm, 10.5% anatase 20 nm and 59.5% rutile 20 nm. Lastly, The P#3 paste is made up of 25.5% rutile 20 nm, 4.5% anatase 20 nm and 70% anatase 100 nm.

Table 1. Components of pastes by size and phase

Label	Anatase		Rutile	Other	Rutile/Anatase Ratio	Particle Size Ratio (20/100)
	20 nm	100 nm	20 nm	<20 nm		
P#1	11.0	-	62.5	26.5	5.7	-
P#2	10.5	30.0	59.5	-	1.5	2.3
P#3	4.5	70.0	25.5	-	0.3	0.4

Changing these ratios affects the properties of the photoanode, such as:

- Rutile and anatase phases have different dye adsorption rates. P25, anatase and rutile produced under similar conditions has dye absorption rates of 70.7, 22.2, 38.9/100 nm<sup>2</sup>, respectively. These rates vary according to dye, particle size, acceptor part of dye, etc. [7].
- Larger particle sized DSSCs has lower efficiency values. The lower solar efficiency in larger particle sizes of TiO<sub>2</sub> can be attributed to a strong backscattering light and less dye adsorption. In addition, the optimal TiO<sub>2</sub> thickness for achieving the maximum efficiency depends on the particle sizes of TiO<sub>2</sub>. The larger the particle sizes of TiO<sub>2</sub>, the shorter the optimal TiO<sub>2</sub> thickness [8].
- The reflective indices of the rutile and anatase phases are 2.909, 2.488, respectively.
- For the large crystal, the electron mobility of the rutile and anatase phases is 17, 0.5 cm<sup>2</sup>V<sup>-1</sup>s<sup>-1</sup>, so electrons flow from anatase to the rutile, while for the nanocrystal it may change rotation and electron migration from rutile to anatase. This leads to controllable electron migration between rutile and anatase TiO<sub>2</sub> [9].

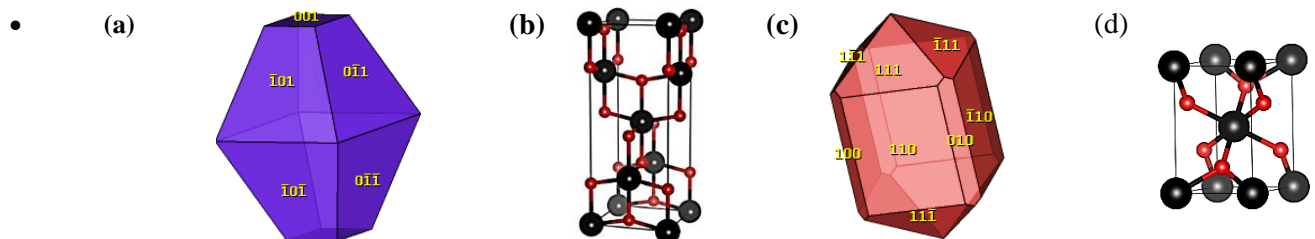


Figure 2. The equilibrium shape of a TiO<sub>2</sub> crystal in (a) anatase, (c) rutile, unit cells of (b) anatase (f) and rutile

- Equilibrium shape and unit cells of rutile and anatase phases were presented at Figure 2. As it is understood from equilibrium shapes, surfaces which adsorb the dye, have assorted density of ions. These ions have important role in anchoring dye molecule using O<sub>2</sub>Ti—O or OTiO···H—O type bonds.

As a result, with changing paste recipes, dye retention rates change the direction of electron migration, backscattering of light and reflectance properties. These factors affect all efficiency parameters, especially J<sub>sc</sub>. In Table 2, several parameters such as J<sub>sc</sub>,  $\eta$ , R<sub>s</sub> and R<sub>sh</sub> values was tabulated. Highest efficiency was obtained at P#1 whose paste involves anhydrous TTIP and highest rutile ratio and lowest average particle size. J<sub>sc</sub> value of P#1 is 2.48 mA·cm<sup>-2</sup> that is the highest among these receipts. The recipe #1 has presumably lowest reflection and scattering rates. This can be observed in both J<sub>sc</sub> and  $\eta$  values.

Table 2. Characteristics of the DSSCs fabricated using various receipt of paste.

Label	J <sub>sc</sub>	V <sub>oc</sub>	FF	$\eta$	R <sub>s</sub>	R <sub>sh</sub>
P#1	2.48	0.45	0.36	0.40	112.5	556.9
P#2	1.73	0.44	0.38	0.29	57.1	803.6
P#3	1.75	0.46	0.30	0.24	135.6	419.7

P#2 paste has got relatively moderate level R/A and particle size ratios, while P#3 paste has lowest rutile and particle size ratios. With the addition of 100 nm anatase thio2 particles to the system, a sharp decrease in current density is observed, while a fluctuation in Voc and FF is observed. For P#2 paste, fill factor (FF) sees an increasing value of 0.38V, which may indicate an improvement in optical properties, but in P#3 paste, the fill factor sees the lowest level with a value of 0.3V. The ratio of R<sub>sh</sub> / R<sub>s</sub> directly affects the FF factor, the larger the ratio, the more the cell approaches the ideal solar cell form, this ratio is ~ 5, ~ 14 and ~ 3 for P#1, P#2 and P#3 pastes, respectively. Recommendations for future studies can be listed as follows:

- Thickness optimization should be made again according to the size of the added particles.
- Coarse anatase and rutile phases should be coated on top layers to benefit from their reflective properties.

## ACKNOWLEDGMENT

We would like to thank Aycan Atli for providing illuminated I–V measurements.

## REFERENCES

- [1] Yeoh, M. E.; Chan, K. Y.; A Review on Semitransparent Solar Cells for Real-Life Applications Based on Dye-Sensitized Technology. *IEEE Journal of Photovoltaics* 2021, 11 (2), 354-361. DOI: <https://doi.org/10.1109/jphotov.2020.3047199>

- [2] Mustafa, M.N.; Sulaiman, Y.; Review on the effect of compact layers and light scattering layers on the enhancement of dye-sensitized solar cells. *Solar Energy* 2021, 215, 26-43. DOI: <https://doi.org/10.1016/j.solener.2020.12.030>
- [3] Omar, A.; Ali, M. S.; Abd Rahim, N.; Electron transport properties analysis of titanium dioxide dye-sensitized solar cells ( $TiO_2$ -DSSCs) based natural dyes using electrochemical impedance spectroscopy concept: A review. *Solar Energy* 2020, 207, 1088-1121. DOI: <https://doi.org/10.1016/j.solener.2020.07.028>
- [4] Lin, L. Y.; Lee, C. P.; Tsai, K. W.; Yeh, M. H.; Chen, C. Y.; Vittal, R.; Wu, C. G.; Ho, K. C.; Low-temperature flexible  $Ti/TiO_2$  photoanode for dye-sensitized solar cells with binder-free  $TiO_2$  paste. *Progress in Photovoltaics: Research and Applications* 2012, 20 (2), 181-190. DOI: <https://doi.org/10.1002/pip.1116>
- [5] Specification Sheet, Degussa p25 Titanium Dioxide Nanopowder, ( $TiO_2$ , Rutile:Anatase/85:15, 99.9%, 20nm), CAS: 13463-67-7 <https://www.nanoshel.com/admin/downloadPDF/download/378/spec>
- [6] Cenovar, A., Paunovic, P., Grozdanov, A., Makreski, P., & Fidanccevska, E. Preparation of nano-crystalline  $TiO_2$  by Sol-gel method using titanium tetraisopropoxide (TTIP) as a precursor. *Advances in Natural Science: Theory & Applications*. 2012, 1 (2), 133-142. <http://hdl.handle.net/20.500.12188/429>
- [7] Takahashi J, Itoh H, Motai S, Shimada S. Dye adsorption behavior of anatase-and rutile-type  $TiO_2$  nanoparticles modified by various heat-treatments. *Journal of materials science*. 2003 Apr;38(8):1695-702. <https://doi.org/10.1023/A:1023219524934>
- [8] Ming-Jer Jeng, Yi-Lun Wung, Liann-Be Chang, Lee Chow, "Particle Size Effects of  $TiO_2$  Layers on the Solar Efficiency of Dye-Sensitized Solar Cells", *International Journal of Photoenergy*, vol. 2013, Article ID 563897, 9 pages, 2013. <https://doi.org/10.1155/2013/563897>
- [9] Mi Y, Weng Y. Band alignment and controllable electron migration between rutile and anatase  $TiO_2$ . *Scientific reports*. 2015 Jul 14;5(1):1-10. <https://doi.org/10.1038/srep11482>



## EFFECT OF SUBSTRATE ROTATION SPEED ON THE OPTICAL, AND ELECTRICAL PROPERTIES OF TiO<sub>2</sub>/FTO BLOCKING LAYER FABRICATED BY SPIN-COATING

Abdullah Atilgan

Department of Energy Systems Engineering, Faculty of Engineering and Natural Sciences, Ankara Yıldırım Beyazıt University, Ankara 06760, Turkey, bdllhtlgm@gmail.com, ORCID: 0000-0002-5624-3664

Abdullah Yıldız

Department of Energy Systems Engineering, Faculty of Engineering and Natural Sciences, Ankara Yıldırım Beyazıt University, Ankara 06760, Turkey, yildizab@gmail.com, ORCID: 0000-0003-4137-6971

*Cite this paper as:* Atilgan, A., Yıldız, A. Effect of substrate rotation speed on the optical, and electrical properties of TiO<sub>2</sub>/FTO blocking layer fabricated by spin-coating. 9<sup>th</sup> Eur. Conf. Ren. Energy Sys. 21-23 April 2021, Istanbul, Turkey

**Abstract:** In this study, TiO<sub>2</sub>/FTO thin films were deposited by spin coating with various rotation speeds at room temperature. The influence of this deposition parameter on the structural, optical, and electrical properties of the fabricated films was investigated by Atomic force microscopy, UV-Vis spectroscopy, four-point probe techniques, SEM.

**Keywords:** Rotation speed, RPM, RMS, optical properties, electrical properties

© 2021 Published by ECRES

### 1. INTRODUCTION

Energy scarcity and environmental pollution have prompted governments and scientists to do research in the field of renewable energy. New generation solar cells such as dye-sensitized solar cells, perovskite solar cells, organic tandems, which have lower energy conversion value, lower cost, and higher efficiency compared to silicon solar cells, have gained interest. In 1991, O'Regan and Grätzel used Ru chelate to act as sensitizers and invented a new structure made up of solar cells, dye-sensitized solar cells (DSSCs)[1]. This was followed by perovskite-sensitive solar cells in 2009[2] and then perovskite solar cells in 2013. As of 2015, yields of perovskite tandem solar cells[3] have reached 29.5%. The blocking layer is used in all of these structures and the most commonly used structure is TiO<sub>2</sub> / FTO structure.

In this study, the TiO<sub>2</sub> / FTO structure was coated using spin-coating at various rotational speeds. It has been characterized using UV-Vis, AFM, and 4 probes. The ideal blocking layer should cover the entire surface of the FTO and TiO<sub>2</sub> to prevent recombination and should not prevent electron injection [4]. It should be in full contact with the FTO surface and be free of cracks and fractures.

### 2. EXPERIMENTAL SECTION

50 mg mL<sup>-1</sup> TiCl<sub>3</sub> was dissolved in IPA and stirred at room temperature for 3 hours. The solution was filtered. It was then coated using spin-coating 16 times by dropping 25 µL at 1600, 3200, and 6400 RPM rotation speeds, respectively. Finally, the films were annealed at 450 °C for 30 minutes.

### 2. RESULTS AND DISCUSSION

Topological SEM images are presented in figure 1. Cracks and fractures on the surface are marked with a red arrow. The surface with the lowest crack density is 3.2K, 1.6K, and 6.4K, respectively, however, the deep pits on the FTO surface draw attention. The TiO<sub>2</sub> coating has greatly reduced this. Among these surfaces, the closest to the ideal is 3.2K.

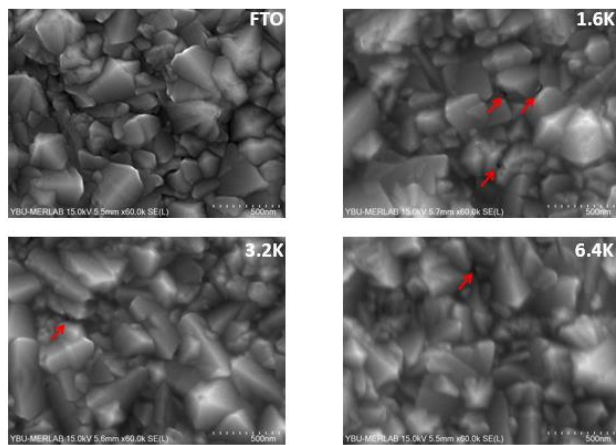


Figure 1. SEM topographies of  $TiO_2/FTO$  thin films after sintering.

The AFM 3D images and RMS values are presented in Figure 1 and Table 1, respectively. The RMS values drop in all three coatings and -27%, -16%, -9% from FTO for 1.6K, 3.2K, and 6.4K, respectively. Average transmittance data are listed in table 1. The expectation on an ideal blocking layer: It should be reflective in the UV and IR regions and very transparent in the visible region.

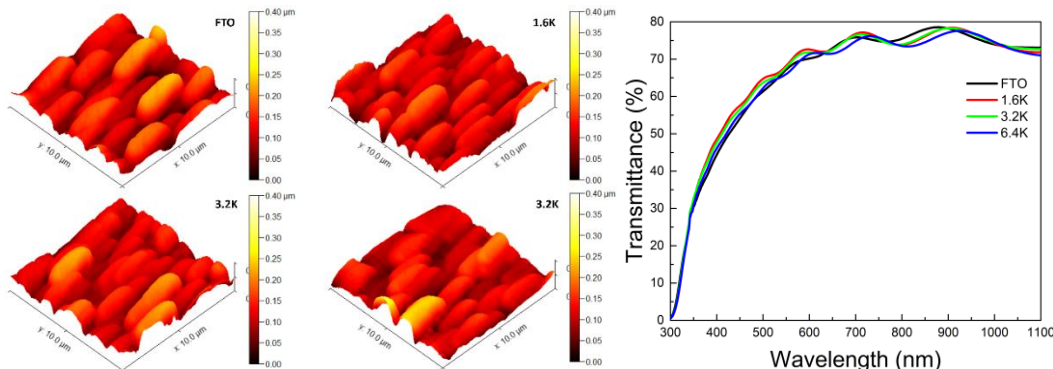


Figure 2 The AFM 3D images of coated surfaces and transmittance of thin films.

All the average transmittance values are better than FTO. Transmittance values are in the opposite trending with RMS values. In other words, as the RMS value decreases, it assigns the transmittance value. When we examine the coatings regionally, we can divide them into 3 regions, UV, vis, and IR. UV zone is disadvantageous especially for solar cells with organic components, it can damage organic components. Absorption in the IR region causes heating in the cells, which is not preferred. UV and IR regions damage the cell's stability and durability. The targeted area is the visible region and especially the green photon.

Table 1. Electrical, optical, and morphological parameters of  $TiO_2/FTO$  films

Label	UV	Vis	IR	$T_{av}$	RMS	$R_{sh}$
FTO	Rel.	Rel.	Rel.	64.46	45.20	7.55
1.6K	0.3	3.3	-0.1	66.47	33.04	8.58
3.2K	-1.5	2.2	0.3	65.85	37.89	8.33
6.4K	3.2	0.3	-0.6	64.48	41.00	7.72

For analyzing the film's electrical resistivity, the sheet resistance ( $R_{sh}$ ) is first calculated using the following equation[5]:

$$R_{sh} = \frac{\pi}{\ln(2)} \left( \frac{V}{I} \right) = 4.5324 \left( \frac{V}{I} \right) \quad (1)$$

where 4.5324 is the correction factor and I and V are the measured current and voltage, respectively. As seen in Table 1, as the RPM increases, the value of  $R_{sh}$  decreases and approaches the value of FTO. The sample coated with the highest surface resistance  $8.58 \text{ } \Omega \text{ cm}^{-2}$  at a rotational speed of 1.6K.

As a result, the effect of rotation speed on TiO<sub>2</sub> / FTO films was investigated and the closest blocking layer thickness to ideal was determined as 3.2K. Coating the layer multiple times will significantly improve the transparency for future work.

#### **ACKNOWLEDGMENT**

This work is supported by the Ankara Yıldırım Beyazıt University BAP, Turkey under project number 3746.

#### **REFERENCES**

- [1] O'regan B, Grätzel M. A low-cost, high-efficiency solar cell based on dye-sensitized colloidal TiO<sub>2</sub> films. *nature*. 1991 Oct;353(6346):737-40.
- [2] Kojima A, Teshima K, Shirai Y, Miyasaka T. Organometal halide perovskites as visible-light sensitizers for photovoltaic cells. *Journal of the American Chemical Society*. 2009 May 6;131(17):6050-1.
- [3] Bailie CD, McGehee MD. High-efficiency tandem perovskite solar cells. *Mrs Bulletin*. 2015 Aug;40(8):681-5.
- [4] Manthina V, Agrios AG. Blocking layers for nanocomposite photoanodes in dye-sensitized solar cells: comparison of atomic layer deposition and TiCl<sub>4</sub> treatment. *Thin Solid Films*. 2016 Jan 1;598:54-9.
- [5] Sbeta M, Atilgan A, Atli A, Yildiz A. Influence of the spin acceleration time on the properties of ZnO: Ga thin films deposited by sol-gel method. *Journal of Sol-Gel Science and Technology*. 2018 May;86(2):513-20.



# CONTINUOUS OCEAN DATA ANALYSIS USING ARTIFICIAL INTELLIGENCE

Kisu Kwak

MiraeOcean Corporation, Anyang-si, Korea, kksstorm@gmail.com, ORCID: 0000-0003-1838-9109

Kyu Han Kim

Catholic Kwandong University, Gangneung, Korea, khkim@cku.ac.kr, ORCID: 0000-0002-8247-225X

Chi-ok An

MiraeOcean Corporation, Anyang-si, Korea, chioki@miraeocean.com, ORCID: 0000-0003-2117-6817

Byung-sun Cho

Catholic Kwandong University, Gangneung, Korea, chobs1028@gmail.com, ORCID: 0000-0002-2465-4792

Young-eun An

MiraeOcean Corporation, Anyang-si, Korea, aye@miraeocean.com, ORCID: 0000-0002-7370-3749

Cite this paper as:

*Kwak, KS, Kim, KH, An, CO, Cho, BS, An, YE. Continuous ocean data analysis using artificial intelligence. 9<sup>th</sup> Eur. Conf. Ren. Energy Sys. 21-23 April 2021, Istanbul, Turkey*

---

**Abstract:**

Although ocean spatial data is an essential element for future marine management, Korea's marine information is coast-oriented observation data due to the nature of the ocean. As Artificial Intelligence (AI) and big data are new technologies that are still improving during this 4th industrial revolution, this study focused on using the UGIC AI model to provide insufficient ocean spatial data. For generating training data, linear interpolation (Kriging method) is performed by fitting observation point data to satellite image data and, as a result, LI showed spatial data problem which became a reason for this research. The time-series data of water temperature, salinity, sea wind, and wave are collected to train and validate the model. The model showed closer relationships to observation point data than the satellite image data, which in this research's intention of adopting observation point data to satellite image data through AI model.

---

**Keywords:**

Wave Energy, Continuous Ocean Data, GAN, Artificial Intelligence, Kriging method

---

© 2021 Published by ECRES

## 1. INTRODUCTION

The new technologies such as artificial intelligence (AI) and big data, which are the core of the 4th industrial revolution, have established themselves as catalysts to promote innovation and reorganization of existing industries, and their influence is still expanding. It is predicted that the use of AI can benefit society by improving decision-making efficiency, cost reduction, and more efficient resource allocation. This outlook is no exception in the maritime sector, and recently, the Korean Ministry of Oceans and Fisheries intends to develop and provide various and vast ocean data as continuous data and predictive data using AI. This work intends to establish a business support service for marine spatial planning and management by creating a foundation for joint use of marine and fishery informative big data and analysis of marine and fishery information. It aims to produce continuous spatial information through AI models by using coast-oriented observation data and spatially continuous but low-reliability satellite and model data as input data and intends to provide the data produced through this to users through optimal visualization.

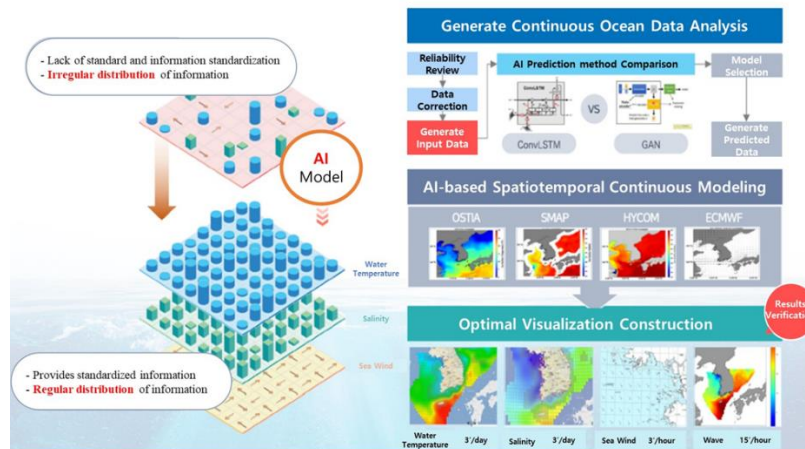


Figure 1. (Left) Generates continuous spatial information through artificial intelligence model of irregular observation vertex information. (Right-Top) The predictive AI model examines the data's reliability, generates input data, puts it into the AI model, and predicts water temperature. Using Convolutional-LSTM and GAN series models to produce water temperature prediction data and adopted a better model by comparing the performances. (Right-Middle) The model produced spatially continuous data using satellite data and numerical model data of water temperature (OSTIA), salinity (HYCOM), sea wind (ECMWF), and waves (RWW), which are existing satellite data. (Right-Bottom) A plan is to present continuously produced data using a prediction model at a glance to users.

Ocean spatial information is an essential element for future marine spatial management, and it is a crucial decision-making data in making policy decisions. However, Korea's marine spatial information is coast-oriented peak observation data due to the nature of the ocean, and this information is provided only for 17% of the number of grids and 38% of the grid area based on the MSP grid of the marine spatial plan. Also, marine satellite data have more information than observation data in terms of space due to their characteristics but are less reliable than the peak observation data accuracy. Therefore, the current marine spatial information is insufficient to be used as decision-making data. Therefore, this study aims to improve the temporal and spatial continuity using highly reliable satellite data and ocean numerical model data and produce necessary ocean information with improved reliability based on observational data.

## 2. DATA COLLECTION

In this study, all the required past data were collected to create three-minute or fifteen-minute grid data using big data to produce spatially continuous information on water temperature, salinity, and sea wind, including wave energy, essential marine elements that predict water temperature.

For the satellite image data, OSTIA data is collected from Physical Oceanography Distributed Active Archive Center (PODAAC) for water temperature, HYCOM data is collected from Hybrid Coordinate Ocean Model (HYCOM) for salinity, ECMWF data is collected from European Centre for Medium-Range Weather Forecasts (ECMWF) for sea wind, and RWW3 data is collected from Korea Meteorological Administration (KMA) for wave. For water temperature, sea wind, and wave data is collected from Korea Meteorological Administration (KMA); water temperature and salinity data is collected from National Institute of Fisheries Science (NIFS); water temperature, salinity, and sea wind data is collected from Korea Hydrographic and Oceanographic Agency (KHOA); water temperature and salinity data is collected from Korea Marine Environment Management Corporation (KOEM); water temperature, salinity, and sea wind data is collected from Ministry of Oceans and Fisheries (MOF).

## 3. METHODOLOGY

### Linear Interpolation (LI)

To this end, the point buoy or observatory data obtained by the Korea Meteorological Administration (KMA) are compared with the satellite data of sea surface temperatures based on the operational sea surface temperature and sea ice analysis (OSTIA) obtained by the Physical Oceanography Distributed Active Archive Center (PODAAC). The satellite data of sea surface temperature have a resolution of 1/20 degrees. The observation points from Gwangan (Busan) and Oryukdo (Busan) were compared with the satellite image data.

The left side of Fig. 1 shows the result of performing a time-series analysis of water temperature data obtained in 2018. The comparison of OSTIA and point data in this way verified that the results varied according to location. Fig. 2 below shows the results of the comparing satellite data with data obtained from the point observatories at Gwangan (top) and Oryukdo (bottom) and observation data obtained at the point observatories at Gwangan and Oryukdo were confirmed to be different from time-series satellite data.

The Kriging method is a solution to a fundamental problem, as it predicts values between sparse sample data from a stochastic model of spatial variation (Yoo, 2017). Thus, linear interpolation (Kriging method) was conducted to increase the low accuracy of the satellite data and point observatory data indicated on the left side of Fig. 2. On the right side of Fig. 2 shows that the accuracy of time-series data increased after linear interpolation for the data obtained at the Gwangan (top) and Oryukdo (bottom) point observatories.

It was confirmed that the accuracy of the data from each location increased through linear interpolation. The result of examining the spatial distribution in Fig. 3 shows that the low accuracy of the water temperature data in the left figure increased, as shown in the right figure, through linear interpolation. As shown in the figures, the point data were simulated with high accuracy. However, it was also confirmed that the spatial reliability decreased. In this study, an artificial intelligence (AI) model was applied to derive improved results compared to those obtained through Kriging method, although the latter were satisfactory.

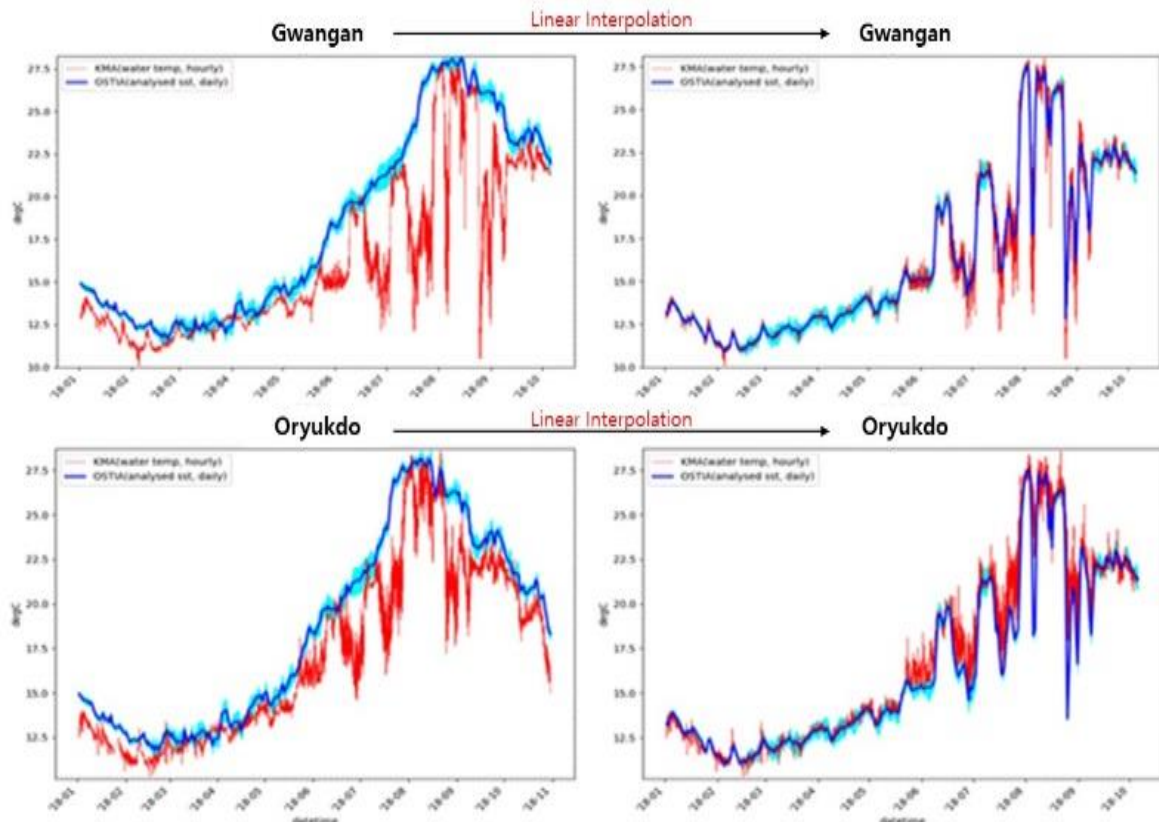


*Figure 2. Increasing the accuracy of satellite and point observatory data through linear interpolation (Kriging method) using data obtained at the Gwangan (top) and Oryukdo (bottom) point observatories*

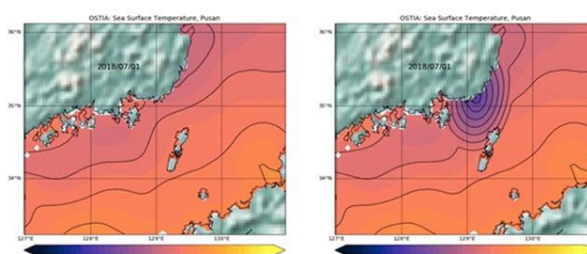


*Figure 3. Spatial simulation problems that occur due to the application of linear interpolation (Kriging method)*

## Artificial Intelligence Model Selection

An analysis was conducted based on generative adversarial networks (GAN) among various artificial intelligence models. GAN improves neural networks by making data-generation models and data performance-identification models compete through the application of individually implemented machine-learning models, such as convolutional neural networks (CNN) and recurrent neural networks (RNN). This technique has been rapidly developed and applied in various fields since it was proposed by (Goodfellow et al. 2014). Thus, a technique appropriate for this study must be selected. In this study, daily or hourly satellite model data of water temperature, salinity, sea surface wind, and waves, which were combined based on remote observation data obtained from satellites and direct observation values derived from ground observation networks, were established as background data. Accordingly, observation data obtained from adjacent sea to South Korea, which were not used in the aforementioned satellite model data, were interpolated to develop a technique which can increase data quality. The characteristics of each GAN model applied in various fields were analyzed and identified to select the most appropriate technique for the purposes of this study, which was selected to increase the level of technical development and reduce the development time.

After comparing different types of GAN models, it was decided that the user-guided image colorization (UGIC) model is the most appropriate for this study. The super-resolution GAN (SRGAN) model can derive the highest-resolution images, but it cannot be applied to ocean observation data, where ground observation data are mainly obtained from nearby coastal areas. In contrast, the real-time UGIC model allows the user to directly select information required for learning from background data, as shown in Fig. 4. In this regard, it was determined that this model can be used effectively to reflect the characteristics of the ocean observation points, which are concentrated at the coast instead of being evenly distributed. Therefore, this model was selected as the target of this study.

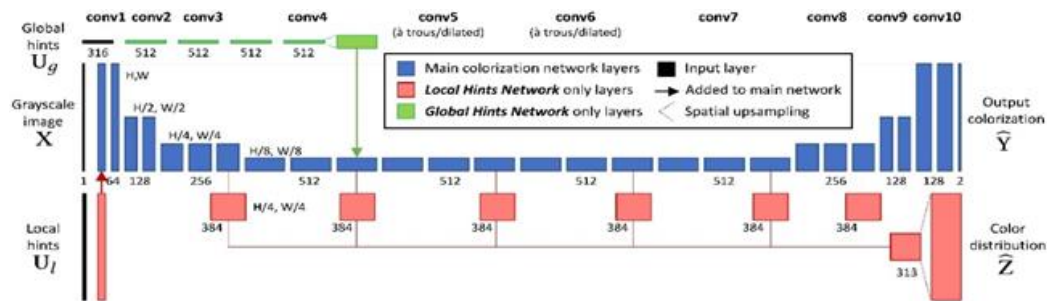


Figure 4. Learning networks of the UGIC model based on the black-and-white background and color information selected by the user, as explained by Zhang et al. (2017)

## 4. RESULTS

### 4.1 Comparison between LI and UGIC

The learning process was conducted from the 1<sup>st</sup> to 25<sup>th</sup> of each month, and the verification process was conducted from the 26<sup>th</sup> to the last day of each month. The target model trained data obtained for a year, from January 1 to December 31, 2018. The generated model through this learning process received converted input data to generate grid information. The grid was regenerated based on the 5-km and 25-km distance as continuous data. The result obtained from the UGIC model data was compared with the LI result to confirm the performance improvement. Specifically, the sea surface temperature from the point observation data and time-series salinity data were taken and compared. The left side of Fig. 5 shows the water temperature data and right side of Fig. 5 shows salinity data, indicating that the UGIC model exhibited time-series data more similar to the observation data than that from the LI method based on most observation point data. The monthly mean result of salinity data on the right side of Fig. 5 obtained through LI was compared with the monthly mean result of salinity data obtained based on daily mean values from the UGIC model, as shown in the graph below. It was verified that the salinity data produced from the UGIC model were more consistent with the observation data and that the UGIC model exhibited better performance than LI.

## 4.2 Time-series analysis and spatial distribution results obtained from the UGIC model

As mentioned above, it was confirmed that the UGIC model exhibited more excellent performance than the LI method. Subsequently, continuous data produced by the AI model and practical observation data were compared according to time-series analysis and spatial distribution to evaluate reliability of data produced by the UGIC model. A time-series analysis was conducted to compare the satellite, numerical, and analytical data used as the observation and input data produced by the AI model. The result is as follows. Fig. 6 (top-left) shows the comparison of water temperature at the Mukpo site, (top-right) shows the comparison of salinity at the Geojedo, (bottom-left) shows the comparison of wave data at the Gyeongju, and (bottom-right) shows the comparison of wind data at the Mukpo. As the values of observation data should be calibrated, directions based on the blue points were provided to implement data assimilation more smoothly. It was verified that the result of the calibration data produced followed the observation data and directions accurately. It was also confirmed that water temperature calibration data produced at different observation sites showed similar patterns to the observation data.

In addition to the above, the comparison of observation data derived from different points indicated that most calibration data obtained from these points have similar patterns to the observation data. Although the calibration data followed the satellite data patterns in few cases, the results at several sites derived from the UGIC model followed the observation data patterns. Based on these results, it was confirmed that data assimilation according to time was performed successfully by the UGIC model.

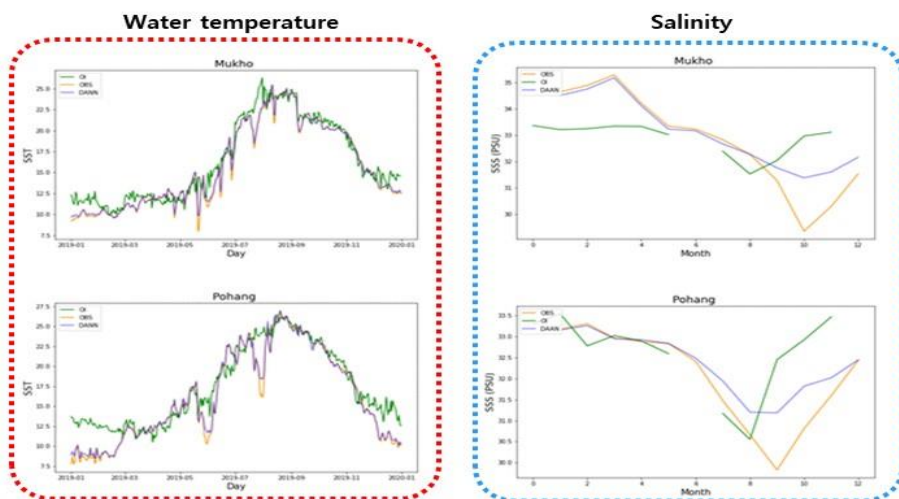


Figure 5. A difference of (left) sea surface temperature data and (right) salinity obtained at Mukho (top) and Pohang (bottom) and interpolated through application of LI and the UGIC model, respectively. The yellow, blue, and green graphs refer to point observation data, the result obtained from the UGIC model, and the result obtained from LI, respectively.

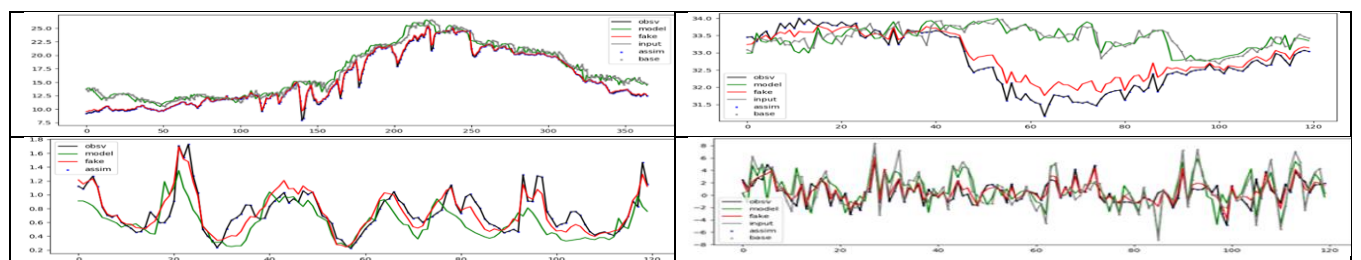


Figure 6. The result of time-series (top-left) sea surface temperature data at the Mukpo site, (top-right) salinity data at the Geojedo, (bottom-left) wave data at the Gyeongju, and (bottom-right) sea wind data at the Mukpo obtained from the UGIC model. The black line indicates values of point observation data. The green line indicates satellite, numerical, and analysis data. The red line indicates the result obtained from the UGIC model.

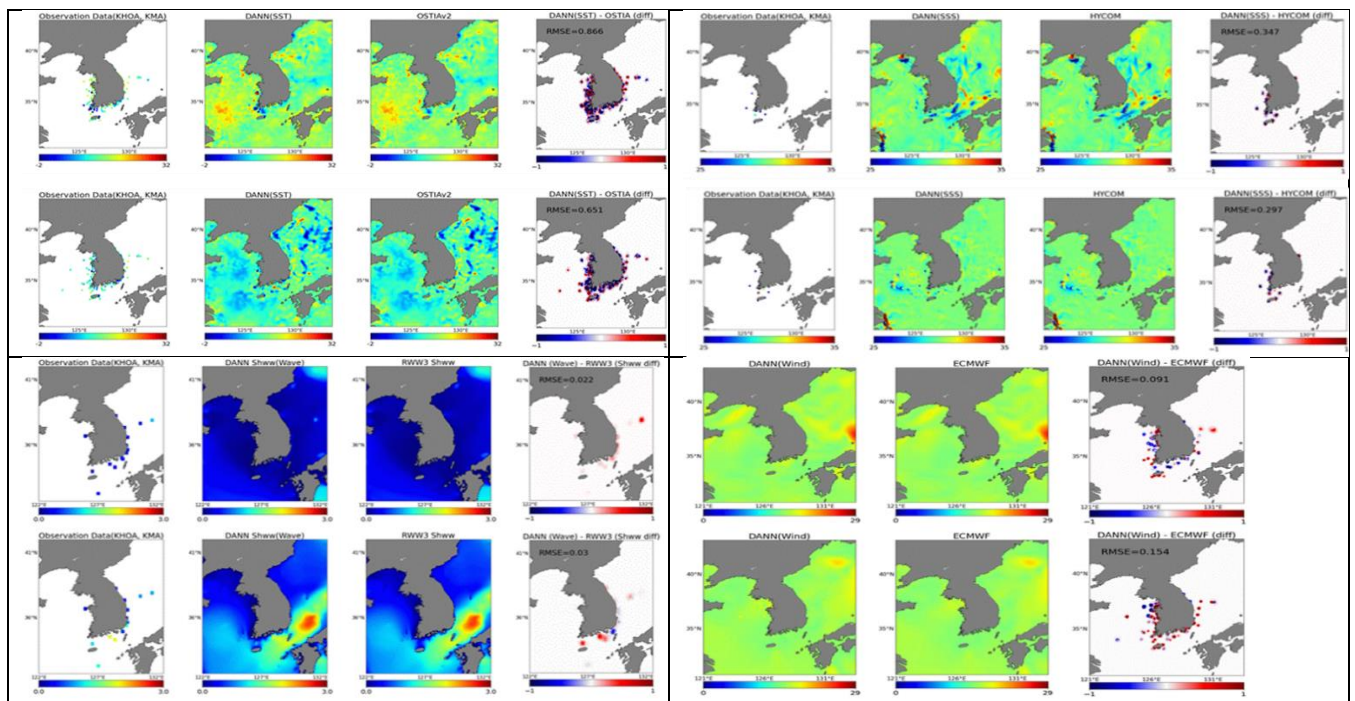


Figure 7. Spatial distribution verification images on water temperature (top-left), salinity (top-right), wave (bottom-left), and sea wind (bottom-right). Images from the left to the right indicate the point observation data, UGIC calibration data, background data, and difference in UGIC calibration data and background data, respectively

The images to verify the spatial distribution show the spatial distributions of the observation data, background data, calibration data (UGIC), and the difference between calibration data (UGIC) and background data. As the most point observation sites were located near the coast, the difference in the calibration and background data based on the UGIC model was found near the coast. Fig. 7 indicates spatial distribution verification images on sea surface temperature, salinity, wave height, and sea surface wind during summer and winter, respectively.

The result of time-series and spatial distribution analysis indicated that the AI model simulated observation data accurately. However, accuracy of simulated data was found to be low at certain points. This result was derived because of low resolution of original data and effects of quality of observation data.

## 5. CONCLUSIONS

This study focused on utilizing point observation data to calibrate satellite data of sea surface temperature, salinity, sea surface wind, and wave height, which showed low accuracy. The linear interpolation (Kriging method) methods was applied to calibrate satellite data, whereas interpolation accuracy was still low. Various AI models were examined to increase the interpolation accuracy, and the real-time UGIC model was found to be the most appropriate for the purposes of this study. Thus, the UGIC model was adopted in this study and represented higher data accuracy than the previously performed and Linear interpolation (Kriging) method. Moreover, in the future, the pix2pixGAN model will be selected to train satellite data (OSTIA) of the sea surface temperature to confirm the capability of this model to predict phenomena that will occur a day or two days from the target day. The training results will confirm the possibility of the prediction accuracy at certain observation points. In this regard, it is determined that the prediction accuracy can be enhanced by training UGIC AI model with Optimally interpolated time-series data with satellite and observation point data and future prediction possibilities will be performed using pix2pixGAN model.

## ACKNOWLEDGMENT

This study was conducted through collaboration with MiraeOcean Corporation, Catholic Kwandong University Waterfront and Coastal Research Center, Ministry of Oceans and Fisheries Korea.

## **REFERENCES**

- [1] Antipov, G., M. Baccouche, J.-L. Dugelay. Face aging with conditional generative adversarial networks 2017; <<https://arxiv.org/abs/1702.01983>>
- [2] Bin, H., C. Weihai, W. Xingming, L. Chun-Liang. High-Quality Face Image SR Using Conditional Generative Adversarial Networks 2017; <<https://arxiv.org/abs/1707.00737>>
- [3] Goodfellow, I. J., J. Pouget-Abadie, M. Mirza, B. Xu, D. Warde-Farley, S. Ozair, A. Courville, Y. Bengio. Generative Adversarial Nets 2014; <<https://arxiv.org/abs/1406.2661>>
- [4] Huang, R., S. Zhang, T. Li, R. He. Beyond Face Rotation: Global and Local Perception GAN for Photorealistic and Identity Preserving Frontal View Synthesis 2017; <<https://arxiv.org/abs/1704.04086>>.
- [5] Yoo, Eun-Hye, 1.18-Geostatistical Approach to Spatial Data Transformation 2018. <<https://www.sciencedirect.com/topics/medicine-and-dentistry/geostatistical-analysis>>
- [6] Zhang, R., J.-Y. Zhu, P. Isola, X. Geng, A. S. Lin, T. Yu, A. A. Efros. Real-Time User-Guided Image Colorization with Learned Deep Priors 2017 ; <<https://arxiv.org/abs/1705.02999>>
- [7] Zhu, J.-Y., T. Park, P. Isola, A. A. Efros. Unpaired Image-toImage Translation using Cycle-Consistent Adversarial Networks 2017; <<https://arxiv.org/abs/1703.10593>>



# STABILITY ANALYSIS OF SUNKEN VESSEL FOR ARTIFICIAL REEF USE

Hyun Dong Kim

The World Association for Waterborne Transport Infrastructure (PIANC), Seoul, Korea, [hdkim@pianckorea.org](mailto:hdkim@pianckorea.org), ORCID: 0000-0003-2599-7137

Kyu Han Kim

Catholic Kwandong University, Gangneung, Korea, [khkim@cku.ac.kr](mailto:khkim@cku.ac.kr), ORCID: 0000-0002-8247-225X

Hyumin Oh

Kanto Gakuin University, Yokohama, Japan, [ohm@pianckorea.org](mailto:ohm@pianckorea.org), ORCID: 0000-0002-8092-8823

*Cite this paper as:*

*Kim, H.D, Kim, K.H, Oh, H. Stability analysis of sunken vessel for artificial reef use. 9<sup>th</sup> Eur. Conf. Ren. Energy Sys. 21-23 April 2021, Istanbul, Turkey*

---

**Abstract:**

This study determines appropriate design waves for the planned artificial structure affected by waves at a return period of 10 years through the hydraulic model experiment and numerical simulation experiments to evaluate the stability of the scuttled ship used as an artificial reef. Based on the calculated values, experiments were carried out under the conditions of a water depth of 30 m and 40 m. In addition, the wave pressure at the side of the installed structure, scour depth at low surface, and movement phenomena during installation of the artificial reef based on the sunken vessel were examined to review the stability of the structure. Experiments were carried out under the conditions of an applied water depth of 30 m and 40 m. The experimental results indicated that the stability of the structure was greater at a water depth of 40 m than at 30 m. However, as certain movements were observed in the hydraulic model experiment, it was determined that the additional reinforcement work, such as anchoring, will be required.

---

**Keywords:**

*Artificial Reef, Scuttled Ship, Coastal Structure, Stability Analysis*

---

© 2021 Published by ECRES

## 1. INTRODUCTION

Artificial reefs are structures artificially installed in the sea, such as abandoned ships, concrete, steel, and ceramics, to establish marine environments in which various types of marine life can settle and grow. In this sense, these structures are also called apartments for fish. Moreover, they can provide places for enabling marine life to spawn and live, as well as hideouts for protecting fries and sedentary species, and are thus used as a method to develop marine and fishery resources considering the environments and characteristics of marine life (Yoon, 2018). Among various types of artificial reefs, decrepit ships are considered one of the most optimal artificial reef structures, as the environmental pollution that could occur in the process of dismantlement can be eliminated, these ships can be reused, and the cost and time of manufacturing and installing artificial reefs can be significantly reduced. In other countries, successful cases of ships used as artificial reefs have been presented (Korea Coast Guard (KCG), 2009). South Korea executed a project to establish a leisure zone in an underwater park in Gangneung, Gangwon-do. It also planned to build berth facilities, observatories, and underwater theme parks based on wrecked ships and artificial underwater structures, as well as install artificial reefs based on sunken ships. However, according to the plans established by the Korean government, artificial reefs based on sunken ships are to be installed on the pelitic and psammitic ground, except on bedrock, and located at shallow water depths significantly influenced by waves and flow. For this reason, these artificial reefs can encounter topographic changes, such as scouring and stability issues. Therefore, this study evaluates the structural stability of artificial reefs based on sunken ships by calculating the marine physical force (e.g., currents and waves) and measuring the wave pressure at the front of artificial reefs based on sunken ships based on the calculated values and a hydraulic model experiment. It also examined the causes of topographic changes and predicted

these changes in the evaluation stage to maintain the permanent functions of artificial reefs based on sunken ships and prevent problems, such as these structures becoming buried.

## 2. NUMERICAL MODEL EXPERIMENT

### Design wave experiment (SWAN model)

A design wave experiment uses the simulating waves near shore (SWAN) model to review wave changes under the conditions of the approach of deep-water design waves to target waters and calculates the marine physical force directly affecting artificial reefs based on sunken ships. The results of this experiment can be utilized as base data to evaluate the stability of such artificial reefs. As indicated in Table 1, the size of large and detailed regions is distinguished to generate grids. Moreover, deep-water design waves, as indicated in Table 2, are calculated based on data of the Report II on Deep-Water Design Waves at the Entire Seas in Korea (Korea Institute of Ocean Science & Technology, Dec. 2005).

*Table 1. An overview of the experiment*

		Experiment Content	
		Large Scale	Detailed Scale
Numerical Model		SWAN	
Model Composition	Grid Scale	50.0 km × 43.0 km 50.0 km × 29.0 km	2.0 km × 2.0 km
	Grid Size	ds = 50 m	ds = 10 m
	Grid Number	1000 × 860 1000 × 580	200 × 200
Sea Level Datum		Gangneung HHW DL.(+) 0.37m	

*Table 2. Specification of design wave*

		Wave/Wind Direction(°)	Wave Height (m)	Period (s)	Point
Incident Wave Data 10 yr Return Period	N	10.9	3.72	7.78	073100
	NNE	28.8	4.39	9.60	
	NE	48.3 (49.3)	5.13 (5.49)	10.41 (10.72)	
	ENE	66.7 (67.9)	4.59 (4.98)	9.50 (9.92)	
	E	85.1	4.04	8.98	075103
	ESE	106.8	3.16	8.28	
	SE	121.7	3.73	9.08	
	SSE	136.8	2.63	8.54	
Sea Level Datum	S	147.7	1.44	7.45	

The SWAN model used in this study was developed by Delft University of Technology in the Netherlands. This third-generation numerical wave model estimates characteristic factors of waves in adjacent seas, lakes, and estuaries based on conditions of wind, water depth, and ocean currents. In this model, an equilibrium equation applied to waves is established as a governing equation (Booij et al., 1999; Ris et al., 1999). Furthermore, this model is evaluated and found to be appropriate to calculate the marine physical forces affecting artificial reefs based on sunken ships, given that diffraction effects on islands and structures are reflected. This model considers advection in spatial coordinates during diffusion, refraction due to water depth and flow, shoaling due to water depth and flow, wave blocking, reflection, and diffraction by obstacles, wave energy dissipation by wind, wave energy dissipation by white capping, wave breaking, and bottom friction, and energy exchange by non-linear interactions.

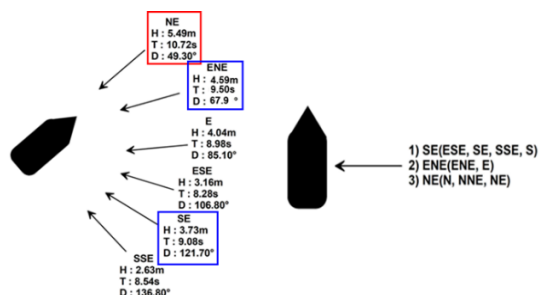


*Figure 1. Wave height and periods according to the installation direction of the artificial reef based on the scuttled ship and wave directions*

The bow direction of the decrepit ship was adjusted to W or N to select the installation direction of the artificial reef based on the sunken ship during the wave experiment. It was found that the maximum wave height and wave direction according to the installation direction of the decrepit ship did not change. When the wave direction was NE (49.3°), wave height was calculated to be 5.49 m, being the highest. When the wave direction was S (147.7°), wave height was calculated to be 1.44, being the lowest. Based on these results, the stern and stem parts of the

decrepit ship were located in the extreme NE direction to minimize wave effects. Accordingly, a numerical wave flume experiment was conducted under the conditions of a SE wave direction, wave height of 3.73 m, and cycle of 9.08 s. A cross-sectional hydraulic model experiment was applied under the same conditions; conditions of a NE wave direction, wave height of 5.49 m, and cycle of 10.72 s; and conditions of an ENE wave direction, wave height of 4.59 m, and cycle of 9.50 s.

### Numerical wave flume experiment (REEF3D)

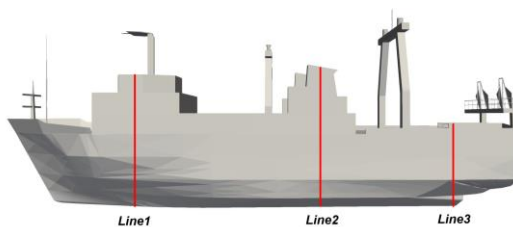
In the numerical simulation, the directions of a stern or stem section of the artificial reef based on the sunken ship, which was the least likely to be affected by waves, were established as N. Accordingly, values of a wave approaching the side of the structure, being 3.73 m and 9.08 s, in the SE wave direction were applied to the REEF3D model to conduct the numerical wave flume. The REEF3D model was discretized based on the Reynolds-averaged Navier Stoke (RANS) equation, a convective term based on the fifth weighted essentially non-oscillatory (WENO) method applying the finite difference scheme, and a time term based on the third TVD Runge-Kutta method (Shu and Osher, 1988). Free water surface displacement was analyzed based on the level set method (Osher and Sethian, 1988), which was developed to examine multi-phase flow at the boundary surface between water and air. The tidal wave and the dissipation boundary were analyzed based on the relaxation method (Larsen and Dancy, 1983). The governing equation included a continuity equation and a motion equation to solve problems of porous media in the case of pore structure included. Moreover, the shear stress equation (wall function) was applied to calculate scouring and sedimentation. It was evaluated that this equation was appropriate to review hydraulic characteristics of the artificial reef against the approaching wave in a three dimensional way. Moreover, it was estimated that effects of approaching waves would vary according to water depth due to a change in hydraulic characteristics which occur at the front part of the artificial reef during its installation and sectional sedimentation and erosion of drift sand. Thus, experiments were conducted according to water depth of 30 m and 40 m in this study. Table 3 indicates experimental details.

*Table 3. An overview of the numerical wave flume test*

		Content			
Model		REEF3D			
Composition	Domain	X	Y	Z	
		315 m	95 m	60 m	
Spacing		0.5 m – 1.0 m changeable grid			
Condition		Number			
Experiment Condition	Wave Condition	Input	Wave	Period	
			3.73 m	9.08 s	
Experiment Cases		Depth : 30 m , 40 m			

### Wave pressure

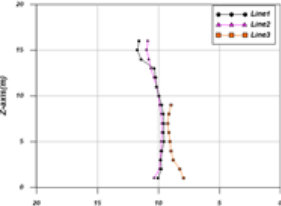
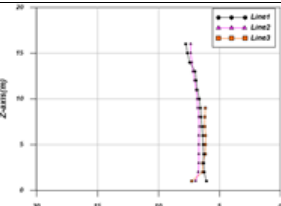
When an artificial reef based on a sunken ship is installed, a change in flow direction, change in strength, or vortex occurs according to the type of cross section due to the change in hydraulic characteristics generated at the size of the structure during its installation. To review the stability of structures that might be affected by such phenomena, the wave pressure at the front part of the artificial reef was measured in Lines 1, 2, and 3 shown in Fig. 2.



*Figure 2. Location of the wave pressure gauge on the ship*

The measurement result indicated that a maximum wave pressure of 11.75 kPa and 7.76 kPa at Line 1 was generated when the water depth was 30 m and 40 m, respectively. Based on this result, it was confirmed that the wave pressure increased as the water depth decreased. The wave pressure was greater when the water depth was 30 m in the cases of Lines 2 and 3, and this result was consistent with the results based on Line 3.

Table 4. The maximum dynamic wave pressure according to water depth

Pressure Location			Maximum Dynamic Wave Pressure Distribution
30 m	Line 1	11.75kPa	
	Line 2	10.97kPa	
	Line 3	9.27kPa	
40 m	Line 1	7.76kPa	
	Line2	7.38kPa	
	Line3	7.30kPa	

### Scour depth

Sectional erosion occurs at the bottom of a structure installed on the pelitic and psammitic ground due to hydraulic external force conditions. For this reason, scour depth and sectional scouring patterns, which would be generated on the ground of the artificial reef installed, were examined in a numerical simulation experiment. The experimental result indicated that a maximum scour depth of 0.61 m and 0.46 m was generated at a water depth of 30 m and 40 m, respectively. Based on this result, it was confirmed that the effects of external force increased as the water depth decreased.

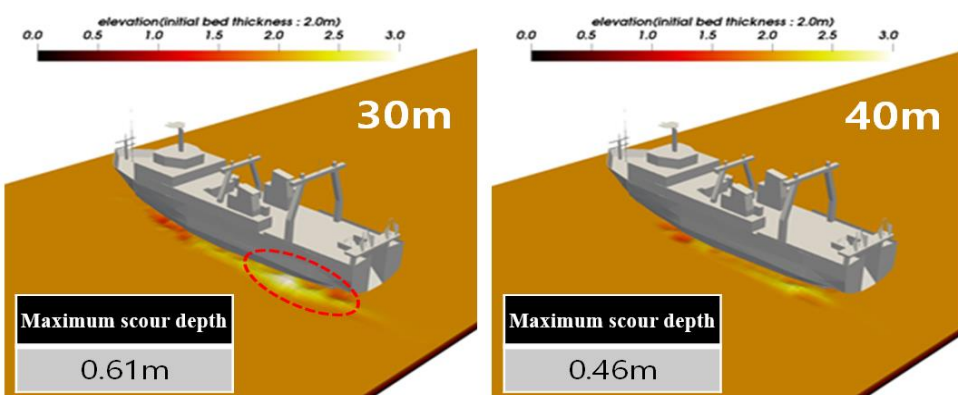


Figure 3. Sectional scouring patterns

## 4. HYDRAULIC MODEL EXPERIMENT

### Two-dimensional cross-sectional hydraulic model experiment

A hydraulic model experiment was utilized to visually confirm the scour depth and wave pressure analyzed in the numerical model experiment and review the stability of the artificial reef. The two-dimensional cross-sectional tidal wave water tank used in this experiment generated waves by using a piston which was 45 m in length, 1.0 m in width, and 1.0 m in height. The maximum cycle generated was calculated to be 0.1–3.0s, and the maximum wave height generated was 0.3 m. The artificial reef model based on the sunken ship was produced at the scale of 1/150 through 3D printing for use in the hydraulic model experiment. In addition, the weight of the structure was adjusted based on mortar and a lead sinker, in accordance with the similarity law.

Table 5. The specification of the 2D cross sectional wave flume

Division	Content
Flume Information	45m x 1.0m x 1.0m
Wave Type	Piston Type
Drive Type	Electronic
Maximum Period	0.1 – 3.0 s
Maximum Wave Height	0.3 m

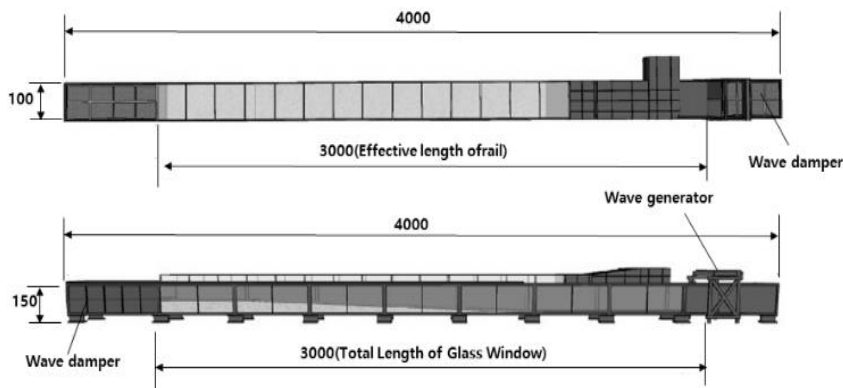
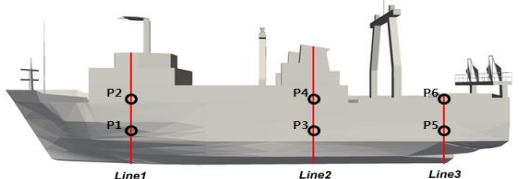


Figure 4. Wave flume wave diagram

### Wave pressure measurement

The wave pressure distribution affecting members of the artificial reef was examined to analyze the stability of the artificial reef against waves approaching from the side. The wave sign and tidal wave time were established as the approach time based on 1,000 waves in the SE wave direction, which were consistent with the conditions applied in the numerical experiment. As for wave pressure measurement, data were obtained at an interval of 1,000 Hz to analyze the maximum wave pressure affecting the artificial structure. Measurement was performed at six points, and a wave pressure gauge used in the experiment had a measurement range of 0.1 kg/cm<sup>2</sup>, which allowed this device to measure a minute pressure change. Table 6 shows experimental details.

Table 6. Details of the wave pressure measurement experiment

	Test Content			
Scale	1:150 ( $\Delta X = \Delta Y$ )			
Wave input condition	Wave Height	Wave Period		
	3.73 m	9.08 s		
Examine water depth	30 m, 40 m			
Sampling rate (Avg. data)	1000 Hz (1000Hz x 2ea)			
Obtaining data number	402,000 ea			
Wave signal	Modified Bretschneider-Mitsuyasu			

The wave pressure measurement result indicated that wave pressure strength increased as the water surface was approached more closely under the condition of a water depth of 30 m. A maximum wave pressure of 33.56 kPa was observed at P2 of Line 1. The wave pressure also increased as the water surface approached more closely under the condition of a water depth of 40 m. A wave pressure of 25.94 kPa was observed at the same point. It was observed that the wave pressure decreased by 2.5 kPa on average as the water depth changed from 30 m to 40 m. Such a decrease in wave pressure was analyzed to be affected by a change in wave depth.

Table 7. Details of the wave pressure measurement experiment

Location		Maximum Pressure		Examine Location		Maximum Pressure	
30 m	Line 1	P1	19.95kPa	Line 1	P1	18.58kPa	
		P2	33.56kPa		P2	25.94kPa	
	Line 2	P3	17.95kPa	Line 2	P3	16.47kPa	
		P4	24.93kPa		P4	23.29kPa	
	Line 3	P5	16.29kPa	Line 3	P5	14.74kPa	
		P6	21.79kPa		P6	20.16kPa	

### Movement experiments

When structures are installed at the seabed, the stability of structures affected by external force conditions should be examined. To analyze the movement of the structures, irregular waves were represented in the experiment according to the wave height and cycles in NE, ENE, and SE wave directions, which were significantly affected by such external force conditions. In addition, video recording data were utilized to examine a difference of conditions before and after tidal waves more accurately. The experiment results indicated that the artificial reef moved backward at a water depth of 30 m. The movement distance was proportional to the scale of the approaching wave and was the greatest in Case 1, with the NE wave direction. The movement of the artificial reef was also confirmed at a water depth of 40 m, whereas the movement distance was less than that at a water depth of 30 m.

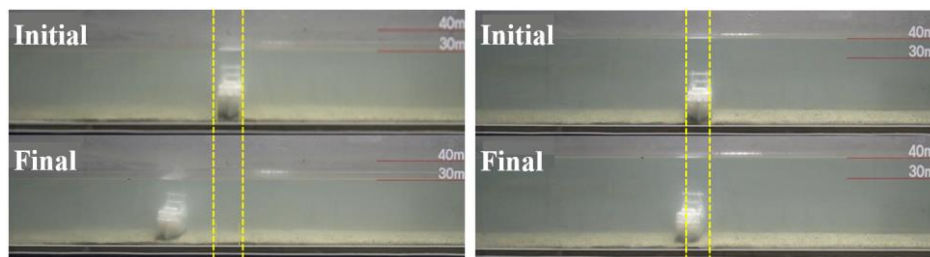


Figure 6. Experiment results at water depth of 30 m and at water depth of 40 m

## 5. CONCLUSIONS

The result of comparing the maximum wave pressure according to water depths of 30 m and 40 m in the numerical wave flume experiment indicates that the artificial reef based on the sunken ship is affected by greater wave pressures at a water depth of 30 m. For the hydraulic model experiment, 3D printed artificial reef model was connected to a wave pressure gauge to extract each wave pressure value. Regular waves were used in the REEF3D model experiment, whereas irregular waves were used in the cross section hydraulic model experiment. Thus, the results were multiplied by 1/3 to compare the maximum wave pressure distribution obtained from the hydraulic model experiment with those obtained from the numerical model (Goda, 1985). The comparison results indicated that wave pressure was greater at a water depth of 30 m than at 40 m. These results on Table 8 were consistent to those obtained from the numerical model experiment. The wave pressure according to water depth (30 m and 40 m) and the established lines were compared and analyzed based on numerical values obtained by the REEF3D model and the hydraulic model experiment. The analysis results indicated that the wave pressure was greater at water depth of 30 m than at 40 m. Moreover, the wave pressure increased as the location of wave pressure measurement approached the surface of the water for the same applied water depth. This result is consistent to the result that pressure increases closer to the water surface when pressure is measured from the surface to the bottom of water based on Stokes wave theory. Scouring and sedimentation were examined based on the shear stress equation (wall function) of the REEF3D model to evaluate stability of the artificial reef based on the sunken ship after its installation. To this end, scouring at the location of the artificial reef installed was examined according to water depth of 30 m and 40 m. The greatest score depth was calculated at water depth of 30 m where wave pressure was generally great.

Table 8. Comparison of the maximum mean wave pressure ( $H_{1/3}$ ) and the maximum scouring depth

Examined Depth	Numerical Model Result	Hydraulic Model Result	Maximum Scour Depth
30 m	11.75 kPa	20.16 kPa	0.61 m
40 m	7.76 kPa	14.32 kPa	0.46 m

The values indicated in the Table 8 were affected by a proportional relation between the wave pressure and scour depth. In other words, these values were affected by a mechanism in which greater pressure and physical force of waves result in more considerable effects of the horseshoe vortex due to the downward flow occurring after waves collide with the artificial reef upon the sunken ship. The analysis result based on the hydraulic model experiment also indicated that the movement of the artificial reef based on the sunken ship moved was greater at a water depth of 30 m accompanying greater wave pressure than at 40 m. In experiments on the design wave, numerical wave flume, and two-dimensional cross section numerical model, the installation direction of the artificial reef on the sunken ship was established according to the wave direction, wave height, and period. Accordingly, the wave pressure affecting the artificial reef was partially measured, and the scour depth and movement were calculated. Based on the analysis result, it was confirmed that the stability was proportional to water depth at a place of the artificial reef installed. The experimental result based on numerical values and the hydraulic model indicates that stability of the artificial reef based on the sunken ship depends on water depth at the area of the structure installed. The artificial reef based on the sunken decrepit ship planned by the Korean government is to be installed underwater in Gangneung, approximately 3,600 m from the land in a straight line. The water depth at this place is approximately 30 m. The experimental result based on numerical values, and the hydraulic model indicates that the stability increases at a water depth of 40 m compared to that at 30 m in terms of external force (wave pressure), submarine topography (scouring) changes, and the trend of structure movement. Thus, it is determined that additional reinforcement work will be required if the artificial reef is to be installed at the currently planned location.

## **REFERENCES**

- [1] Goda, Yoshimi, 1985, Random sea and design of marine structures, University of Tokyo Press, 1-323.
- [2] Chi-Wang Shu, Stanley Osher, 1988, Efficient implementation of essentially non-oscillatory shock-capturing schemes, Journal of Computational Physics, 77(2), 439-471.
- [3] Booij, R. C. Ris, L. H. Holthuijsen, 1999, A third-generation wave model for coastal regions: 1. Model description and validation, Journal of Geophysical Research, 104(C4), 7649-7666
- [4] R. C. Ris, L. H. Holthuijsen, N. Booij, 1999, A third-generation wave model for coastal regions: 2. Verification, Journal of Geophysical Research, 104(C4), 7667-7681.
- [5] Yoon, H, 2018, "Effect Analysis of Korean Artificial Reef", KSCOE, 21(2), 116-129.



# HIGH PERFORMANCE ION-EXCHANGE MICROPOROUS ZEOLITE MATERIAL FOR APPLICATION IN THE COLD PLASMA DEVICE

B.G. Salamov

Department of Physics, Faculty of Science, Gazi University, 06500 Teknikokullar, Ankara, Turkey, aht1911@gmail.com,  
ORCID: 0000-0002-9819-8160

H. Hilal Kurt

Department of Physics, Faculty of Science, Gazi University, 06500 Teknikokullar, Ankara, Turkey, hkurt@gazi.edu.tr,  
ORCID: 0000-0002-1277-5204

*Cite this paper as:* Salamov, BG and Kurt H.H. High performance ion-exchange microporous zeolite material for application in the cold plasma device. 9th Eur. Conf. Ren. Energy Sys. 21-23 April 2021, Istanbul, Turkey

**Abstract:** In this work the cold plasma device (ZCPD) with natural and high performance ion-exchange microporous zeolite cathode (IEZC) is examined according to the transport properties of cold non-equilibrium plasma and discharge mode. The interaction between dc cold plasma and dielectric zeolite electrode modified by different concentration of Na cations ( $\rho \sim 10^{11}$  to  $10^6 \Omega \text{ cm}$ ) and its influence on the plasma generation at different gas pressures  $p_g$  (8-760 Torr) are analyzed. Interesting experimental results show that  $\text{Na}^+$  ions are the main reason for the significant decrease of ignition voltage in ZCPDs with microporous IEZCs. The enhanced performance of the plasma emission amplification in the ZCPD with different gas-discharge gap  $d_g$  (50-250  $\mu\text{m}$ ) in ambient air as a source of stable plasma emission are presented for the first time.

**Keywords:** Cold plasma device, ion-exchange microporous zeolite cathode, Na cations, plasma emission, atmospheric pressure, enhanced performance.

© 2021 Published by ECRES

## 1. INTRODUCTION

Ion-exchange microporous zeolite material is widely used in modern technologies and is associated with the most modern and practical types of materials. Ion exchange is one of the characteristic features of zeolites to replace their own cations  $\text{Na}^+$ ,  $\text{K}^+$ ,  $\text{Ca}^{2+}$ ,  $\text{Mg}^{2+}$ ,  $\text{Sr}^{2+}$ ,  $\text{Ba}^{2+}$ , etc., located in the inner channels and cavities of the crystal lattice, with other ions from the contact solution or melt [1]. This is due to the presence of a strong covalent bond of oxygen with silicon and aluminum and a weak, predominantly ionic, bond of exchangeable cations with the aluminosilicon-oxygen framework [2]. In addition, the presence of open cavities and wide channels in their structure, in which exchange cations are located, contributes to the ease of ion exchange reactions even at low temperatures. Exchangeable ions in wide-pore zeolites exhibit significant mobility even at room temperature, comparable diffusion rates are observed in them at temperatures 400–700 °C lower than in feldspars [3].

The considered cold plasma device (ZCPD) with high performance ion-exchange microporous zeolite cathode (IEZC) [4-6] is designed to generate non-equilibrium plasma in free space by creating stable cold plasma that can use surfaces of thermally unstable materials at atmospheric pressure (AP). Due to the fact that cold plasma at AP have the following advantages: significantly low cost and simplicity of operation in comparison with low-pressure plasma, as well as the absence of the need to use a vacuum system [7, 8]. At the same time, it should be noted that the current AP cold plasma have a number of disadvantages: difficulties in maintaining the glow discharge mode, the need for higher gas breakdown voltages and difficulties in the formation of a homogeneous plasma throughout the chamber volume [9].

When using IEZC in ZCPD [10] as a source of stable plasma emission (PE) in a wide range of pressure ( $p_g$ ) up to one atmosphere for increase the plasma emission (PE) intensity, it is necessary to solve the following problems:

1) maintenance of stable atmospheric plasma on the zeolite surface; 2) controlled ion modification of the zeolite surface; 3) regeneration of already used zeolite cathode (ZC) [11]. In turn, it is known that the treatment of solids with active particles of cold plasma generated in various types of electric discharges leads to various changes in their properties [12]. The effect of cold plasma on the properties of aluminosilicates has been studied very little. Attempts have been made to use gas discharge plasma for the synthesis of calcium aluminates. Nothing is known about the modifying and regenerating effect of AP plasma on aluminosilicate stability, and it is also not clear what effect oxygen plasma causes when processing ion modification [13-17].

Recently microporous zeolite  $(\text{Ca},\text{K}_2,\text{Na}_2,\text{Mg})_4\text{Al}_8\text{Si}_{40}\text{O}_{96} \cdot 24\text{H}_2\text{O}$  has greatly applied as a perspective new dielectric materials used in technological and optoelectronic devices [18-20]. The unique surface, adsorption and transport properties make it as perspective material in the plasma light sources and energy storage devices. The number of studies in this area is relatively small [21], and therefore the continuation of work in this direction, supplemented by the determination of the plasma emission amplification and transport properties of ZCPD's based on microporous IEZC, is quite advisable. Thus, in the present work a novel results relating to the transport properties of cold non-equilibrium plasma for ZCPD with microporous ZC modified by Na cation using the AP glow discharge plasma is interpreted for the first time.

## 2. EXPERIMENTAL

Scheme of the ZCPD cell is shown in Fig.1. The unmodified dielectric electrode was manufactured from a single block of natural zeolite clinoptilolite by cutting and giving the expected shape of microporous IEZC. Further, by successive grinding on abrasive paper of various grain sizes, the surfaces of the ZC (i.e. diameter ( $D$ ) of 22 mm and a thickness of 2 mm) are prepared. A gas discharge gap  $d_g$  (3) was formed with a dielectric mica layer (4) between the IEZC plate (2) and the anode. The external surface of the microporous IEZC was covered with a Cu (1) thin film ( $\approx 40$  nm thick). The glass disc (6) coated with semi-transparent conductive  $\text{SnO}_2$  layer (5), which is an anode (30 mm), located opposite of the IEZC. The thickness of the  $d_g$  (3) is varied in the range from 45 to 250  $\mu\text{m}$ . The application of dc feeding voltage in the range 200–1400 V is enough for generation of the Townsend or Glow discharge regime at AP in ambient air. Detailed information regarding experimental system and IEZC is given in our earlier study [21].

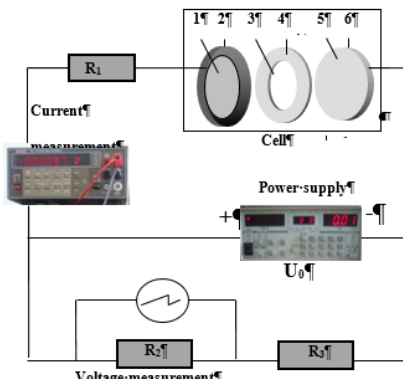


Figure 1. Scheme of the ZCPD cell

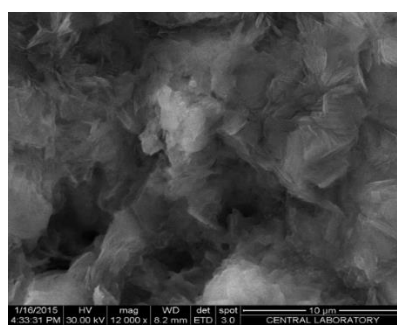


Figure 2. SEM image of the Na-modified clinoptilolite

Due to the volume of free intracrystalline space, clinoptilolite  $(\text{Ca},\text{K}_2,\text{Na}_2,\text{Mg})_4\text{Al}_8\text{Si}_{40}\text{O}_{96} \cdot 24\text{H}_2\text{O}$  [19,20,22] is referred to as medium-porous zeolites, its total porosity is on average 30%, and the specific surface area reaches about  $10^3 \text{ m}^2/\text{g}$ . The density of the mineral varies between 2.11-2.2 g/cm $^3$ . The percentage of clinoptilolite

composition was determined in the following sequence:  $\text{SiO}_2$  65 - 72%,  $\text{Al}_2\text{O}_3$  10 - 12%,  $\text{CaO}$  2.4 - 3.7%,  $\text{K}_2\text{O}$  2.5 - 3.8%,  $\text{Fe}_2\text{O}_3$  0.7 - 1.9%,  $\text{MgO}$  0.9 - 1.2%,  $\text{Na}_2\text{O}$  0.1 - 0.5%,  $\text{MnO}$  0 - 0.08%,  $\text{Cr}_2\text{O}_3$  0 - 0.01%,  $\text{P}_2\text{O}_5$  0.02 - 0.03%, loss of ignition 9 - 14%,  $\text{SiO}_2/\text{Al}_2\text{O}_3$  5.4 - 7.2%. Zeolites are aqueous aluminosilicates in which an infinite aluminosilicate frame is produced by  $[\text{SiO}_4]^{4-}$  and  $[\text{AlO}_4]^{5-}$ - tetrahedra having common vertices. The communicating cavities of these tetrahedra are occupied by large ions and water molecules [22,23]. For our study we used the clinoptilolite which contains on average 90–95% of the clinoptilolite zeolitic mineral [24]. Clinoptilolite is from the class of natural zeolites and has a clear structural topology of heulandite. Studies of the crystalline structures of clinoptilolite ( $(\rho \sim 10^{11} \Omega \cdot \text{cm})$  [21,22,25] showed that, due to the relatively high  $\text{Si}/\text{Al} > 4$  (~ 82% of tetrahedrons occupied by Si), the clinoptilolite crystalline framework is heat-resistant (in air up to 700 °C) and is also resistant to aggressive substances and ionizing radiation. It is known that  $\text{Na}^+$  and  $\text{K}^+$  ions easily enter channels and cavities in the clinoptilolite framework and, under certain conditions, can realize up to 90% of its maximum ion-exchange capacity. These cations replace the bivalent ions  $\text{Ca}^{2+}$  and  $\text{Mg}^{2+}$  during of ion exchange reactions:  $\text{Na}^+ (\text{K}^+) \rightarrow 1/2 \text{Ca}^{2+}$ ,  $\text{Na}^+ (\text{K}^+) \rightarrow 1/2 \text{Mg}^{2+}$ . The results allow us to determine the selectivity range of clinoptilolite to alkali metal cations as follows:  $\text{K} > \text{Na} > \text{Li}$ . The IEZC samples were modified using three different 0.1 M, 0.5 M and 1 M NaCl solutions for increasing the amounts of  $\text{Na}^+$ . The  $\text{Si}/\text{Al}$  ratios of the natural zeolite CL and three different Na ion-exchanged Na-CL samples were determined to be  $5.2 \pm 0.1$ ,  $5.3 \pm 0.1$ ,  $5.5 \pm 0.1$  and  $5.8 \pm 0.1$  mol, respectively. Electron microscopic studies revealed that zeolite samples mainly have a complex micro-surface relief formed by microcrystals and aggregates of various mineral phases. Mono-mineral aggregates of zeolites are represented in most cases by weakly crystallized mass or microcrystals. Micro-crystal aggregates are concentrated in microarrays and in micro-cracks fairly uniformly distributed over the surface of the sample. Clinoptilolite crystals have a lamellar shape.

### 3. RESULTS AND DISCUSSION

The transfer of electric charge in zeolites in constant an electric field can be simulated as electric transport in dispersed systems. It can be carried out due to ionic, electronic and molion conductivities. The contribution of these components is different and depends on the properties of the components included in the system. Zeolite can conditionally be considered as a system consisting of a solid phase - an alumina-silicon-oxygen framework pierced by capillaries of intracrystalline channels oriented in a certain way relative to the lines of the external electric field strength and extra-frame subsystem (exchange cations and water). It is obvious that the conductivity of the framework is negligible compared to the conductivity of the water-cationic subsystem. This is due to the high migration ability of the forming off-frame cations and water molecules.

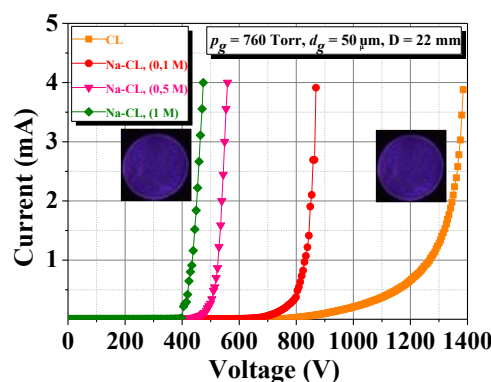


Figure 3.  $I - V$  characteristic of the ZCPD with IEZC modified by different concentration of Na cations in an ambient air.

In the ZCPD with IEZC the discharge current and PE intensity (see inset of Fig.3) are recorded simultaneously.  $I - V$  characteristics of a ZCPD with natural and Na-modified IEZC at AP are completely satisfy Ohm's law. In the feeding voltage range 200–1400 V, the current considerably increased, which occurred due to the ignition of a self-sustained Townsend discharge [26,27]. The average residual resistivity of the IEZC samples change from  $\rho \sim 10^{11}$  to  $10^6 \Omega \text{cm}$  [4,5]. Figure 3 shows that the slope of Na-modified IEZC is higher than for natural ZC, which suggests that Na modification is the main reason of the increase of transport properties. It was found that a significantly higher discharge current was observed in the ZCPD with an electrode modified by sodium cation. Since sodium cations in zeolite have a higher charge density, the anionic cascade can interact with them [28-31]. Thus,  $\text{Na}^+$  and  $\text{K}^+$  cations, having a large ionic radius, are weaker retained by the anionic framework with increasing  $p_g$ , and

therefore, they are easily released from their sites, which allows them to be more free and maneuverable, and also facilitates their conduction.

Considering the Fig.3 and Fig.4 one can note the following: (i) Breakdown voltage  $U_{ign}$  values in ZCPD with IEZC are lower compared with the  $U_{ign}$  values in the system with unmodified natural ZC, (ii) although lower  $U_0$  are used to the ZCPD with IEZC; (iii) the current in Na-modified IEZC is increased more than that for unmodified natural ZC at given values of the pressure  $p_g$ . The electrical features of the CL microporous framework ensure the amplification  $E$  between the IEZC and the gas where the dielectric constant is observed, and in this connection,  $U_{ign}$  decreases [21]. We believed that emission of the electron are observed from not only the surface but also the volume of microporous IEZC, therefore PE intensity increased when using large area IEZC with internal emission amplification. Electrons entering the discharge gap with microporous and multichannels structure of the IEZC are enhanced in the  $E$  by the amplification mechanism, so that discharge current and PE intensity increases in the ZCPD.

The different character of the I–V characteristic can be associated with an increase in the mobility of charge carriers. The hysteresis phenomenon was clearly observed (see Fig.4), which reflects the process of formation of the active surface of a Na-modified CL under the influence of Na cations and the reaction medium. It should be noted that the hysteresis phenomenon with a sharper and more distinct peak is observed at very low (8-44 Torr) pressure values. The shape of the hysteresis is determined by the type and shape of the IEZC pores. Characteristically, the presence of hysteresis indicates the simultaneous presence of both meso- and micropores [32,33]. At the same time, we suggested that observed the hysteresis phenomenon in the I – V characteristic of the ZCPD under the action of low-temperature plasma at very low pressures causes the appearance of new surface structures, which increase the transport property, selectivity, and stable operation range (see Fig.4) [5].

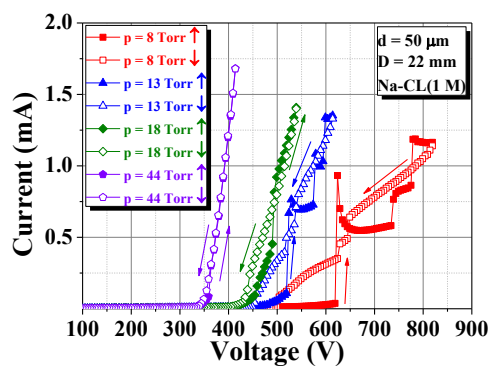


Figure 4. The hysteresis behavior of the ZCPD with IEZC in an ambient air medium.

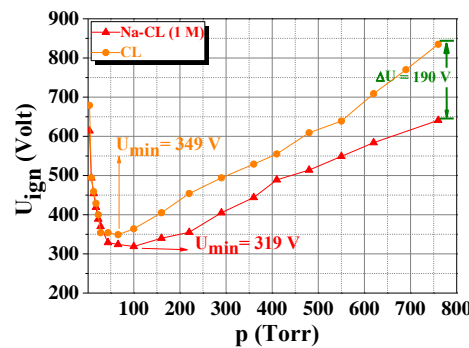


Figure 5 Measured breakdown curves for the ZCPD with unmodified and Na-modified CL materials.

The effect of the porous IEZC on the AP plasma generation is a special conduction step that requires serious consideration. Figure 5 shows the pressure dependence of  $U_{ign}$  curves of the plasma chamber with unmodified CL and Na-modified IEZC areas for  $d_g = 50 \mu\text{m}$  in air. Paschen's law demonstrates that, when  $p_g d_g$  decreases,  $U_{ign}$  diminishes, and then arrives at the Paschen minimum. The following Paschen minimum is found to be 66 Torr,  $U_{min}$  of 349 V for CL and 100 Torr,  $U_{min}$  of 319 V and  $d_g = 50 \mu\text{m}$  for Na-modified IEZC. This equals to the breakdown of electric field  $E$  of  $7.18 \times 10^6 \text{ V/m}$  for unmodified CL and  $6.61 \times 10^6 \text{ V/m}$  for Na-modified IEZC. The electric field  $E$  can be calculated as  $E = V/d_g$ . An important distinguishing feature of the difference in the threshold values of the electric field  $E$  is the peculiarities of the air environment, the surface charge, and the state of the CL surface. An increase in the value of the electric field  $E$  leads to an increase in the conduction current at constant  $p_g$ . Thus, the experimental results demonstrate that, despite the close  $E$  values, Na-modified IEZC's current transport is more effective than the CL charge transport. It follows from experimental results that the Na-modification of CL has a more effective effect than the influence of the electric field  $E$  on the transport mechanisms.

Considering the Fig.5 for the ZCPD with IEZC, one can note the following: (i)  $U_{ign}$  values in ZCPD Na-modified IEZC are lower compared with the ZCPD based on the unmodified CL; (ii) when the  $d_g$  was decreased,  $U_{ign}$  values decreased; (iii) although lower  $U_0$  are used to the ZCPD, microdischarge currents for Na-modified IEZC are substantially exceeds the corresponding value for unmodified CL at given values of the  $p_g$ ; (iv) when the  $d_g$  was increased from  $50 \mu\text{m}$  to  $250 \mu\text{m}$ ,  $U_{ign}$  values increased at AP [34]. We suggest that emission of electron is carried out both from the surface and the cross-sectional surface of the microporous IEZC framework, as a result of which large PE is obtained when using large IEZCs with internal PE amplification. The emission of electron from the nanoporous IEZC shows its usefulness for cold plasma devices.

## 4. CONCLUSION

In the current study, the transport properties in the ZCPD based on Na-modified IEZC electronic materials were investigated operating in a wide range of gas pressure  $p_g$  up to one atmosphere (8-760 Torr). From experimental results (see Fig.5), it can be stated that lower  $U_{ign}$  are required for the gas breakdown in the Na-modified IEZC (i.e.  $U_{ign}$  values are 830 V for unmodified ZC and 640 V for Na-modified IEZC at AP). Na-modified IEZC considerably enhanced the conductivity and PE intensity with respect to unmodified ZC. Moreover, it is established that Na-modified IEZC is a high performance electronic material for application in the cold plasma device. The  $\text{Na}^+$ ,  $\text{Ca}^{2+}$ ,  $\text{K}^+$ , and  $\text{Mg}^{2+}$  cations of the ZC framework are responsible for generation of the Townsend or Glow discharge regime at AP in ambient air. The enhanced performance of the plasma emission amplification in the ZCPD with different gas-discharge gap  $d_g$  (50-250  $\mu\text{m}$ ) in ambient air as a source of stable plasma emission are presented for the first time.

## REFERENCES

- [1] Yin, A, Guo, X, Dai, WL, and Fan, K. J. Phys. Chem. C 2010, 114, 8523.
- [2] Kim, HH, Teramoto, Y, Sano T, Negishi, N, and Ogata, A. Appl. Catal. B Environ. 2015, 166, 9.
- [3] Kim, HH, Teramoto, Y, Negishi, N, and Ogata, A. Catal. Today 2015, 256, 13.
- [4] Koseoglu, K, Özer, M, Salamov, BG. *Field-enhanced transport processes in the gas discharge system with porous zeolite*, IEEE Transactions on Plasma Science 2015, 43, N10, 3576-3581
- [5] Koseoglu, K., Salamov, BG. *New Approach for Charge Transport Mechanisms in the Atmospheric Pressure Cold Plasma Device with Porous Zeolite*, Plasma Process. Polym. 2016, 13, N3, 355-365.
- [6] Astrov, YuA, Portsel, LM, Lodygin, AN, Shuman VB. *Planar microdischarge device for high-speed infrared thermography: Application of selenium-doped silicon detectors*, J. Appl. Phys. 2008, 103, 114512-6
- [7] Kunhardt, EE. IEEE Trans. Plasma Sci. 2000, 28, 189.
- [8] Staack, D, Farouk, B, Gutsol, A, Fridman A. Plasma Sources Sci. Technol. 2008, 17, 025013.
- [9] Samanta, K, Jassal, M, Agrawal, AK. Indian J. Fibre Text. 2006, 31, 83.
- [10] Salamov, BG, Kurt, H Hilal. *Ar-driven gas discharge system on the basis of dielectric zeolite material*, JOM The Minerals, Metals & Materials Society, 2020, 72, 2, 644-650.
- [11] Pylinina, AI, Mikhaleenko, II, Ivanov-Shits, AK, Yagodovskaya, TV, Lunin, VV. The Influence of plasma chemical treatments on the activity of the  $\text{Li}_3\text{Fe}_2(\text{PO}_4)_3$  catalyst in butanol-2 transformations, J. Phys.Chem. 2006, 80, №6, 882-885
- [12] Lui, CJ, Yu, K, Zhang, YP. *Characterization of plasma treated Pd/HZSM-5 catalyst for methane combustion*, Appl. Catalysis B: Environmental. 2004, 47, 95-101
- [13] Koseoglu, K, Ozer, M, Ozturk, S, and Salamov, BG. Jpn. J. Appl. Phys. 2014, 53, 086203.
- [14] Alekseev, SB, Wang, L, Erofeev, MV, Liu, J, Orlovskii, VM, Tarasenko, VF, Yuan, X. Instrum. Exp. Tech. 2003, 46, 222.
- [15] Vilaseca, M, Coronas, J, Cirera, A, Cornet, A, Morante, JR, and Santamari, J. Sens. Actuat. B Chem. 2007, 124, 99.
- [16] Cerri, G, de'Gennaro, M, Bonferoni, MC, and Caramella, C. Appl. Clay. Sci. 2004, 27, 141.
- [17] Kim, H-H, Kim, J-H, and A. Ogata, A. J. Phys. D Appl. Phys. 2009, 13, 135210.
- [18] Astrov, YuA, Lodygin, AN, Portsel, LM, Beregulin, EV. *Comparative study of noise in low-current Townsend discharge in nitrogen and argon* Phys. Rev. E 2017, 95, 043206-7
- [19] Aluna, R, Bratchikova, IG, Mikhaleenko, II, and Yagodovskaya, TV. Abstracts of Papers, IV Russian Conference with the Participation of CIS Countries "Scientific Fundamentals of the Preparation and Technology of Catalysts" (Ufa, 2000), p. 93.
- [20] Gashimov, AM, Zakiyeva, IG. *Dielectric parameters of the composite based on natural zeolite treated by electrical discharge*. Tech. Phys. 2006, 51, 185.
- [21] Bunyatova, U, Orbukh, VI, Eyyazova, GM, Agamaliev, Z, Lebedeva, NN, Salamov, BG. *Peculiarities of unusual electret state in porous zeolite microstructure*, Superlattices and Microstructures 2017, 111, 1203-1210
- [22] Yagodovskaya, TV, and Lunin, VV, Zh. Fiz. Khim. 1997, 71, N5, 775 [Russ. J. Phys. Chem. 1997, 71 (5), 681]
- [23] Cai, Z, Coordrich, TL, Ziemer, KS, Warrywocla, J, and Sacco, A. J. Appl. Catal. B: Environ. 2011, 102, 323.
- [24] Gottardi, G, Galli, E, Natural Zeolites, Springer, Berlin 1985.
- [25] Gurin, VS, Petranovskii, VP, and Bogdanchikova, NE. Mater. Sci. Eng. C 2002, 19, 327.
- [26] Sadiq, Y, Aktas, K, Acar, S, and Salamov, BG. Superlattices Microstruct. 2010, 47, 648.
- [27] Sadiq, Y, Ozer, M, and Salamov, BG. J. Phys. D Appl. Phys. 2008, 41, 045204.
- [28] Rolison, DR. Chem. Rev. 1990, 90, 867.
- [29] Kim, H-H, Kim, J-H, and Ogata, A. J. Phys. D Appl. Phys. 2009, 13, 135210.
- [30] Galioglu, S, Isler, M, Demircioglu, Z, Koc, M, Vocanson, M, Destouches, N, Turan, R, and Akata, B. Microporous Mesoporous Mater. 2014, 196, 136.
- [31] Galioglu, S, Zahmakiran, M, Kalay, YE, Ozkar, S, and Akata, B. Microporous Mesoporous Mater. 2012, 159, 1.
- [32] Michot, LJ, Villieras, F. *Assessment of surface energetic heterogeneity of synthetic Nasaponites. The role of layer charge*, Clay Miner. 2002, 37, 39-57.

- [33] Neaman, A, Pelletier, M, Villieras, F. *The effects of exchanged cation, compression, heating and hydration on textural properties of bulk bentonite and its corresponding purified montmorillonite*, Applied Clay Science. 2003, 22, 153-168.
- [34] Ozturk Koç, S, Galioglu, S, Akata Kurç, B, Koç E, and Salamov, BG. New mixed conductivity mechanisms in the cold plasma device based on silver-modified-zeolite porous electronic materials, J. Electronic Materials, 2018, 47, (5), 2791-2799

# FILAMENTATION IN A PLASMA CELL WITH GAP WAFER

H. Hilal Kurt

Department of Physics, Faculty of Science, Gazi University, 06500 Teknikokullar, Ankara, Turkey, hkurt@gazi.edu.tr,  
ORCID: 0000-0002-1277-5204

B.G. Salamov,

Department of Physics, Faculty of Science, Gazi University, 06500 Teknikokullar, Ankara, Turkey,  
baht1911@gmail.com, ORCID: 0000-0002-9819-8160

Cite this paper as:

Kurt H.H., Salamov, B.G., Filamentation in a plasma cell with GaP wafer, 9th Eur. Conf. Ren. Energy. Sys. 21-23 April 2021, Istanbul, Turkey

**Abstract:** This paper reports the filamentary discharge in air media. The plasma filament is a highly ionized gas mode composed of positive ions, high energetic electrons. Discharge instabilities are investigated using dc microplasma cell with GaP cathode for a wide pressure range. It is found that the discharges in the air are inhomogeneous only at very high interelectrode distances.

**Keywords:** Filamentation, GaP, instabilities, filament, gas discharges

© 2021 Published by ECRES

## 1. INTRODUCTION

The Current filamentation has been observed in a dc gas discharge. It can be considered by a self-organization process, the result of which is a nearly planar double layer known as anode spot [1]. Accelerating electrons at higher energies can produce the ionizations. Current filaments appear after repulsive electric fields and multiplication process after secondary electron emissions near GaP cathode. Current-voltage characteristics at 44 Torr for and 525  $\mu\text{m}$  suggest a glow-like regime at 1214 V and 1241 V and also a filamentary behavior at the same conditions [2].

From the analysis of CVC characteristics, it has been found the space charges significantly dominate the plasma causing the inhomogeneity. A filamentary discharge plasma has been constructed between metal anode and GaP cathode. An Air plasma has been produced in the cell. Air plasma parameters have been recorded and the influence of the gas pressure  $p$  and interelectrode distance  $d$  has been studied. Three electron populations with different temperatures have been found. There have been two important electron emission process in the plasma. Primary avalanche cause the primary electrons and also secondary electron emissions are generated by positive ions from the walls and also cathode. Secondary electrons have enough energy to start the ionization in the plasma and discharge confinement occurs at only higher gap distance  $d$  [3]. Filamentation in an air plasma occurs at specific values of the applied voltages. The present study represents the direct current hot cathode air glow discharge plasma at different pressures in the range 28-690 Torr. The glow discharge generally is obtained by applying a high voltage between the cathode and anode to provide sustaining gas discharge following the breakdown process. DC power supply supplied the voltages for the electrodes. The results show that current filaments cause the damage on cathode. The reactive species like oxygen in air plasma can cause a negative effect like etching of the electrode surface with plasma. For this reason, argon is preferred to avoid the oxidizing of the material. It is very crucial to get the stable plasma inside the cell for controlling the plasma. Reactive oxygen species can destruct the cathode and anode by causing high energetic filaments in the discharge plasma system. For this reason, Air is used as a working gas for many plasma related applications.

## 2. RESULTS AND DISCUSSION

New plasma studies have focused on uniform discharges. But, the optimization of the plasma needs to understand the complex physical and chemical features. Non thermal plasmas are famous especially for the microelectronic systems and surface process such as etching and purification. Figure 1 shows discharge instabilities for the plasma cell with GaP electrode as a function of the time.

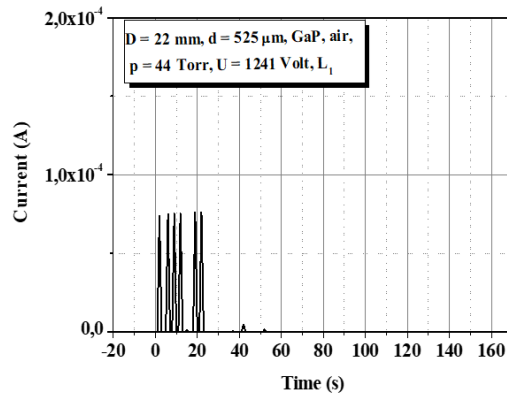


Figure 1. Filamentary CVC curves for  $p = 44$  Torr at 1241 V as a function of the time under weak illumination.

Reactive oxygen species can give damage to cathode and anode resulting in current fluctuations in the cell. Chaotic fluctuations in the time range from 0 to 60 s are experimentally demonstrated. Those low frequency instabilities that naturally-occurring disappear after a while. Figure 1 and Figure 2 are strong evidence of oscillating current. Figure 2 shows current instabilities for 44 Torr at 1214 V.

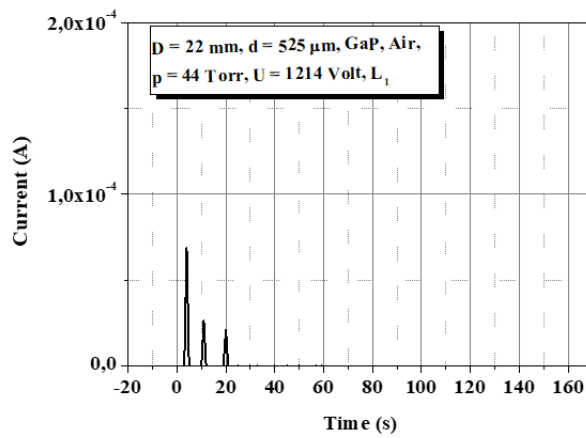


Figure 2 Filamentary discharge curve for 44 Torr at 1214 V.

Filamentary discharge or streamer discharge is a transition process that occurs at a conductive part of the GaP electrode in an air discharge. Depending on the plasma conditions, discharges makes transition from the stable mode to unstable or filamentary mode. At that time, the plasma is called as nonequilibrium. It caused to many important applications such as industrial ozone production, surface modification by plasma, excimer lasers and also large area plasma display panels [4,5].

Figure 3 shows electron flux density per unit area through gas plasma cell. It clearly shows that electrons have not reached to cathode yet and located around anode in two different energies. The total electron flux density accumulated next to anode and the max value is  $1.59 \times 10^5$  A / m<sup>2</sup>.

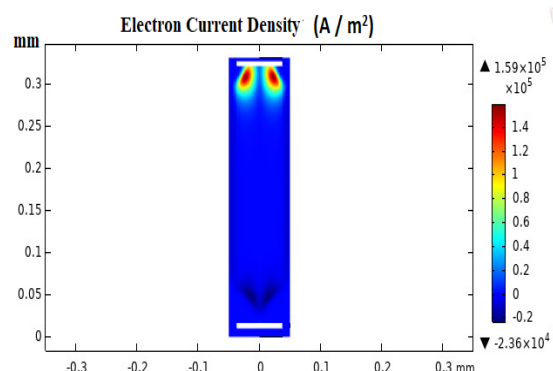


Figure 3. Electron current density as a function of the interelectrode distance  $d$ .

### **3. CONCLUSION**

Low frequency current instabilities are produced in a plasma system with GaP cathode. We recorded strong dependence of those instabilities on the applied voltage and pressure. It has been shown that the instabilities occur for a higher interelectrode distance. A parallel plate gas discharge tube has been used to carry out investigations on the current fluctuations. Electric field strength is not uniform for this gas pressure regime and it changes between cathode and anode and electric field domains move from cathode to anode. This process causes the electric current fluctuations with time [6].

### **REFERENCES**

- [1] E. Lozneanu; S. Popescu; M. Sanduloviciu, IEEE Transactions on Plasma Science .30, Issue: 1, (32) 2002.
- [2] Louis-Félix Meunier, Jacopo Profili, Sara Babaei, Andranik Sarkissian, Annie Dorris, Stephanie Beck, Nicolas Naude and Luc Stafford, “Characterization of non-thermal dielectric barrier discharges at atmospheric pressure in presence of microfibrillated cellulosic foams”, Plasma Source and Science, <https://iopscience.iop.org/article/10.1088/1361-6595/abe91c>, 2021.
- [3] J Andreu, G Sardin, J Esteve and J L Morenza, Published under licence by IOP Publishing Ltd Journal of Physics D: Applied Physics, Volume 18, 1985 (1339).
- [4] U.Kogelschatz, Filamentary, patterned, and diffuse barrier discharges, IEEE Transactions on Plasma Science..30, Issue: 4, Aug 2002)
- [5] U.Kogelschatz, Pure Appl. Chem. 62 (1990) 1667-1674
- [6] Advances in Optoelectronic Materials Editors: Ikhmayies, Shadia Jamil, Kurt, Hatice Hilal (Eds), DOI 10.1007/978-3-030-57737-7, 2021.



# MEAN ELECTRON ENERGY DISTRIBUTION IN A PLASMA SYSTEM WITH ZnSe

H. Hilal Kurt

Department of Physics, Faculty of Science, Gazi University, 06500 Teknikokullar, Ankara, Turkey, hkurt@gazi.edu.tr,  
ORCID: 0000-0002-1277-5204

Cite this paper as:

*Kurt H.H. Mean electron energy distribution in a plasma system with ZnSe, 9th Eur. Conf. Ren. Energy Sys. 21-23 April 2021, Istanbul, Turkey.*

**Abstract:** High efficiency Infrared detectors require direct band gap materials and also showing luminescent properties. The band gap energy is accepted to be one of the most important parameters in optoelectronic device applications due to strongly related to operating wavelength for those devices. Both experimental and theoretical studies are done to find optimal energy values in the system. On the other hand, electronic and optical properties of ZnSe is presented.

**Keywords:** Mean Electron energy, ZnSe, COMSOL Multiphysics plasma module

© 2021 Published by ECRES

## 1. INTRODUCTION

Gas discharges are mainly classified as a Townsend, glow and arc discharges [6]. The COMSOL software is a powerful tool for the simulation of the plasma diagnostic [1-7]. The results obtained by simulation such as electron current density and mean electron energy are in good agreement with the experimental values which was presented previously. ZnSe is a kind of photodetector operates on the principle of converting the photons that fall on them into electrons. For this reason, photon energy must be greater than the forbidden band gap energy. We should consider some parameters to choose a material as an infrared detector as follows: Spectral response, responsivity, quantum efficiency and so on. If the wavelength of the incident radiation is greater than  $\lambda_{\text{max}}$ , the absorption of the semiconductor material will decrease. ZnSe gained attention for its applications in LEDs and diodes and also detectors in Infrared region. ZnSe is a wide band gap II-VI group material and shows linear optical transmittance as an optical lenses and give good absorption spectrum in IR spectrum. It is also used as a quantum dot material when it is doped Mn [8].

## 2. RESULTS AND DISCUSSION

When the current density is increased beyond  $10^{-5}$  to  $10^{-4} \text{ A/cm}^2$ , Townsend discharge turns into Glow discharge. Now, space charge fields play an important role and the voltage required to sustain the discharge decreases. Positive charge fields and high electric fields are formed next to the cathode with cathode drop regions. A positive column of semi-neutral plasma connects the cathode region to the anode region. The complex event occurring in the transition from a Townsend discharge to a Glow discharge was recently discussed by Sijacic and Ebert (2002) [9,10].

The theory of normal Glow discharge was formulated by von Engel and Steenbeck (1934) by applying the Townsend condition to the self-feeding state to the cathode layer [9,10]. Quantum mechanical efficiency is a measure of how well a semiconductor converts carriers into photons. The quantum mechanical efficiency of direct band gap semiconductors is very high compared to indirect band gap semiconductors. Because of these features, direct band gap semiconductor detectors create an easier working area for optical devices and work faster. An example of direct band gap semiconductor detectors is ZnSe.

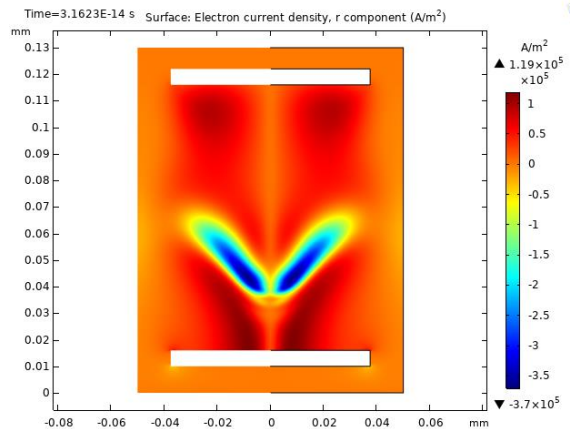


Figure 1. Electron density graph for  $p = 1000$  Torr at 2000 V.

Figure 1 shows the electron density at 1000 Torr. ZnSe operates even at higher pressures as shown in figure. ZnSe gives better plasma current at higher pressures. The maximum current density is found as  $1.19 \times 10^5$  A/cm<sup>2</sup> in the system. As a result, ZnSe is more suitable for usage as a photodetector at atmospheric pressure than low pressure values. Considering the cost of the vacuum system of photodetectors that work well at low pressures, ZnSe provides the advantage of low cost as a photodetector that works more conveniently at atmospheric pressures and beyond it. Plasma is electrically neutral to the external environment. That is, the number of positive charges in the plasma is equal to the number of negative charges. Decomposition, ionization and reconstruction (recombination) events, which are the opposite of these events, occur constantly in the plasma. These events are in a dynamic equilibrium in the plasma among themselves. Plasma is a good conductor of electricity and heat. Experiments clearly show that discharge in the air environment exhibits very different properties. In some circumstances, unstable situations have also been identified. However, it is extremely important to detect such instabilities in order to realize the stable and controllable operation of the system at atmospheric pressures.

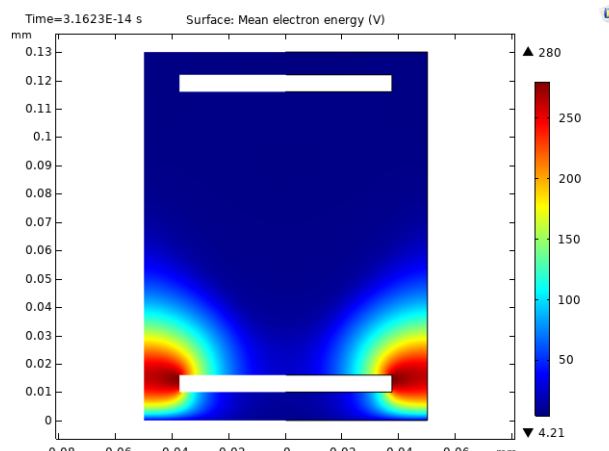


Figure 2. Mean electron energy for 1000 Torr at 2000 V.

The electron energy distribution plays an important role in plasma modeling. Because, it is essential for the electron collision reactions. In addition, electron transport process can related to this distribution. Mean electron energy is average values of the total electron energy distributions. Electrons have different energies in the plasma.

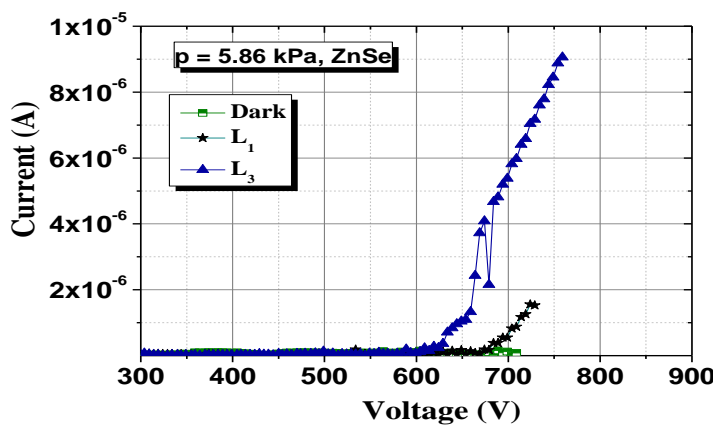


Figure 3. Current voltage graphs under different IR stimulations (dark, weak  $L_1$  and strong  $L_3$ ).  $p = 5.86$  kPa

### 3. CONCLUSION

In this work, an effort has been made to find undefined plasma parameters such as mean electron energy and electron current density by incorporating flow of gas using plasma module of COMSOL multi-physics. Model results clarified the complex behavior of the plasma and also experimental electrical CVC curve under different illumination intensities has been given to establish the optimal operating range of the plasma with ZnSe electrode in He media. By analyzing mean electron energies, electron densities also CVC graphs, the contributions of the different plasma parameters for the optimal operation range in the material and device physics. ZnSe is important photonic material that can be used for the optical lenses especially in the Infrared region.

### REFERENCES

- [1] Yu. A. Astrov, A. N. Lodygin, L. M. Portsel, and A. A. Sitnikova, Journal of Applied Physics. 124, 103303 (2018)
- [2] A. N. Lodygin, L. M. Portsel, E. V. Beregulin, and Yu. A. Astrov, Journal of Applied Physics. 126, 173302 (2019)
- [3] Yu. A. Astrov, A. N. Lodygin, L. M. Portsel, E.V. Beregulin, Phys. Rev E. 95, 043206 (2017)
- [4] Sh. S. Kasymov and L. G. Paritskii, Device for tracking images Russian Authors' Certificate 1798020/18-10, 1973
- [5] Yu.A. Astrov, A.N. Lodygin, and L.M. Portsel, J. Phys. D Appl. Phys. 49, 095202 (2016)
- [6] Advances in Optoelectronic Materials Editors: Ikhmayies, Shadia Jamil, Kurt, Hatice Hilal (Eds), 10.1007/978-3-030-57737-7, 2021.
- [7] B Hnatiuc , A Sabau and D Astanei, IOP Conf. Series: Materials Science and Engineering 591 (2019)
- [8] Kang Su 1, Yuhua Wang, Electronic structure and linear optical properties of ZnSe and ZnSe:Mn, J Nanosci Nanotechnol. 10(3):1857-9, 2010. 012050.
- [9] Danijela D. Šijačić and Ute Ebert, Phys. Rev. E 66, 066410 – Published 18 December 2002.
- [10] A. Von Engel, Max Steenbeck. J. Springer, 1934 - Electric discharges through gases



# GAS DISCHARGE SYSTEMS WITH CdSe ELECTRODE

S.UTAŞ<sup>1</sup>,

<sup>1</sup>Department of Physics, Faculty of Science, Gazi University, 06500 Teknikokullar, Ankara, Turkey,  
selcuk.utas@gmail.com,

H. Hilal Kurt<sup>1</sup>,

<sup>1</sup>Department of Physics, Faculty of Science, Gazi University, 06500 Teknikokullar, Ankara, Turkey, hkurt@gazi.edu.tr,  
ORCID: 0000-0002-1277-5204

Cite this paper as:

*Utas S, Kurt H.H. Gas discharge systems with CdSe electrode. 9<sup>th</sup> Eur. Conf. Ren. Energy Sys.  
21-23 April 2021, Istanbul, Turkey*

**Abstract:** II-VI group semiconductor CdSe has been investigated in a plasma-semiconductor structure. The interest on those materials has gained importance mainly due to their emergence of important applications over a wide range of areas such as power amplifier, light-emitting diodes, detectors, photovoltaic cells and microwave. CdSe electrode was chosen due to its high absorption coefficient and suitable band gap in gas discharge application. The paper is about the calculation of the dependence of the plasma electron density and space charge the gas pressure and interelectrode distance d.

**Keywords:** *Gas discharge systems, COMSOL Multiphysics plasma module, plasma-semiconductor structure, CdSe material, atmospheric pressure.*

© 2021 Published by ECRES

## 1. INTRODUCTION

CdSe is inorganic compound material with direct band gap and has wurtzite structure in the hexagonal modification. CdSe is an optically uniaxial semiconductor with two components of the dielectric function [1]. CdSe has many application in optoelectronic such as radiation detectors and solar cells [2]. When the photon irradiates the CdSe electrode, the photons are absorbed from the CdSe and cause the creation of the electrons so that they can make successive ionization process in the gas discharge systems. CdSe has found many application in nano sensing, laser diodes, high efficiency solar cells and biomedical imaging [3].

CdSe is a toxic material and it cannot be used in children's toys and food packaging and can cause the environment problems. [4]. But, CdSe can be used in battery technology that has growing potential for the electric vehicle power supplies and energy storage devices [4]. Cadmium selenide (CdSe) is a spherical crystallite with a wurtzite or zinc-blend structure with a diameter range of 10–100 Å. [4]. II-VI group single crystal compound wafers found applications for IR optics and THz detectors [5]. In addition, CdSe based nanocrystal-doped with phosphate glass promises a temperature fiber sensors [6]. CdSe is an optically uniaxial semiconductor.

## 2. RESULT AND DISCUSSION

We presented space charge density and electron density as a function of the interelectrode distance. The calculated max electron density was  $3.6 \times 10^{17} \text{ m}^{-3}$  and space charge density  $3.5 (\text{C} / \text{m}^3)$ . The space charge graphs indicate that space charge density increases and reaches a maximum value at 30 mm and after this distance it tends to decrease as a function of d. From Space charge map (Figure 1, Figure 2), we see that positive charges accumulated in front of the CdSe electrode. Further, it is found that they were divided in two and gathered on the coastal part of the cathode. The space charge peak indicates the majority of the accumulating positive charges next to CdSe electrode.

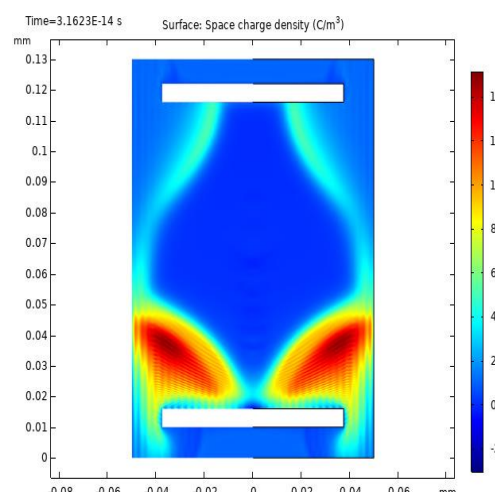


Figure 1.  $p=300$  Torr  $d=100 \mu\text{m}$   
Space charge map distribution.

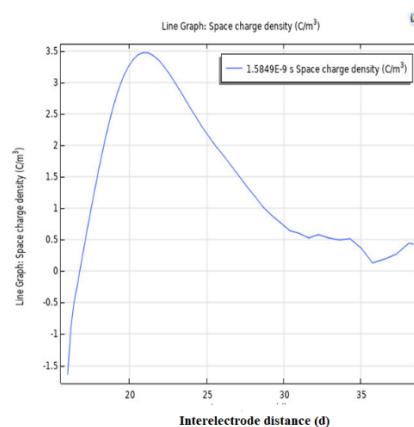


Figure 2.  $p=300$  Torr  $d=100 \mu\text{m}$   
Space charge density as a function of the  $d$ .

The electron density in accordance with the changing interelectrode distance  $d$  as shown in Figure 3. Observations from graphs evidenced that the concentration of the electrons are shifting behavior towards larger when the  $d$  is increasing and reaches the peak value at  $40 \mu\text{m}$ . Those plasma analysis with COMSOL physics were performed to learn the plasma behavior due to complex nature of the plasma systems. Because, we cannot predict those parameters from the experimental studies.

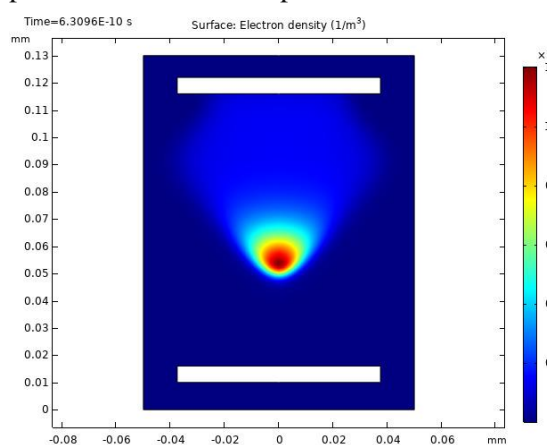


Figure 3. Electron density map.

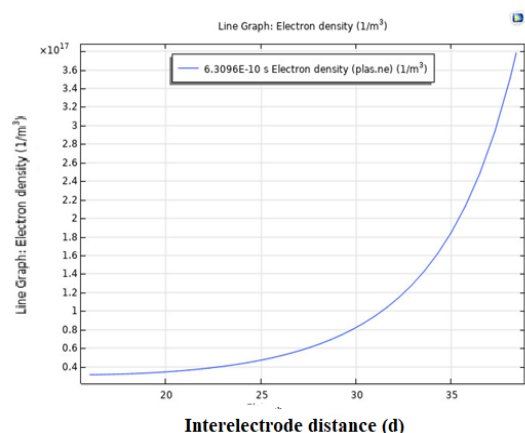


Figure 4. Electron density curve as a function of the  $d$ .

### 3. CONCLUSION

We have investigated the surface current density and electron density for the plasma cell with CdSe electrode in the pressure range 100 Torr-300 Torr by COMSOL simulation. The theoretical simulation results show that positive space charges located around CdSe cathode and the calculated max space charge density is obtained for 22 mm gap distance between the electrodes. Electron density per unit volume in the plasma is around 1020. CdSe gives good electron densities and this makes it promising candidate for the plasma based cathode material [7]. CdSe nanocrystals have very important applications ranging from LED displays to medical imaging [8]. Therefore, our simulation records are significant for understanding the properties of CdSe.

### REFERENCES

- [1] Cadmium selenide (CdSe) damaged the hepatocytes, and cell death after 8months of accumulation was noted (Ballou et al., 2004). From Dynamics of Advanced Sustainable Nanomaterials and their Related Nanocomposites at the Bio-Nano Interface, 2019
- [2] S.J. Sweeney and J. Mukherjee, Optoelectronic Devices and Materials (Springer Handbook of Electronic and photonic Material, 2017).
- [3] <https://www.azom.com/article.aspx?ArticleID=8406>
- [4] H. PILLER, in Handbook of Optical Constants of Solids, Volume 2, 1998

- [5] <https://warwick.ac.uk/fac/sci/physics/current/postgraduate/regis/mpagswarwick/ex5/intro/groupii-vi>
- [6] Fiber-optic temperature sensor based on CdSe semiconductor nanocrystal doped glass Yu. O. Barmenkov Author Affiliations+Proceedings Volume 4185, Fourteenth International Conference on Optical Fiber Sensors; 418510 (2000) <https://doi.org/10.1117/12.2302179> Event: Fourteenth International Conference on Optical Fiber Sensors, 2000, Venice, Italy
- [7] S. Mathew, Amit D. Saran, Bishwajeet Singh Bhardwaj, Santhi Ani Joseph, P. Radhakrishnan, V. P. N. Nampoori, C. P. G. Vallabhan, and Jayesh R. Bellare, Journal of Applied Physics 111, 074312 (2012).
- [8] Tamar Goldzak, Alexandra R. McIsaac & Troy Van Voorhis, “Colloidal CdSe nanocrystals are inherently defective”, Nature Communications volume 12, Article number: 890 (2021)



# THEORETICAL PLASMA SIMULATION RESULTS OF THE MICRODISCHARGE CELL WITH GaSb CATHODE

S. UTAŞ<sup>1</sup>,

<sup>1</sup>Department of Physics, Faculty of Science, Gazi University, 06500 Teknikokullar, Ankara, Turkey,  
selcuk.utas@gmail.com,

H. Hilal Kurt<sup>1</sup>

<sup>1</sup>Department of Physics, Faculty of Science, Gazi University, 06500 Teknikokullar, Ankara, Turkey, hkurt@gazi.edu.tr,  
ORCID: 0000-0002-1277-5204

Cite this paper as:

*Utas S., Kurt H.H. Theoretical plasma simulation results of the microdischarge cell with GaSb Cathode, 9th Eur. Conf. Ren. Energy Sys. 21-23 April 2021, Istanbul, Turkey*

**Abstract:** Microplasma cell with GaSb electrode has been studied by Comsol simulation programme. Space charge densities, surface electron densities, electron current densities have been obtained in a wide pressure range under certain interelectrode distance d. Our results confirm that GaSb can be used as a cathode material in plasma cell. Plasma patterns changes with respect to the time.

**Keywords:** *Microplasma cell plasma device, GaSb Cathode, plasma emission, atmospheric pressure, COMSOL Multiphysics plasma module*

© 2021 Published by ECRES

## 1. INTRODUCTION

III-V group semiconductor materials have gained growing interest especially in the microplasma systems [1]. GaSb is narrow band gap III-V group semiconducting material with direct absorption from the valence band to conduction band. It gives priority for this material because of the high speed optoelectronic response to incoming radiation when the material is used as a cathode in plasma systems. The features of the plasma is directly proportional of the quality of the cathode material and also optical properties of the material. On the other hand, the secondary electron emission mechanism play crucial role in the process. Secondary emitted electrons are associated with the positive charges or space charges that accumulated in front of the cathode. When ions hit the cathode, they cause the electron emissions from the cathode. Multiplicated electron collisions cause the ionization in the gas and thus, breakdown mechanism takes places between cathode and anode [2,3]. This process as also called as self sustained discharges.

GaSb is an important material due to its growing applications in optic, electronic and detector technology. Recent advances in fiber optic technology have promoted the suitable materials for device applications beyond 1.55  $\mu$ m. GaSb is candidate for high speed electronic and long wavelength photonic devices [4].

## 2. RESULTS AND DISCUSSION

Study of the micro gas discharge structures have important practical applications. Those plasma cells can be used as ultraviolet (UV) sources and also plays important role in industrial amplification such as purification and sterilization of the materials and also foods. As a result of many successive ionization in plasma interval, gas emits light in the visible range depending on the gas type and external conditions [5,6]. In this study we used commercial GaSb semiconductor wafer. we made our analysis with the help of Comsol simulation programme in argon media. III-V group GaSb wafer with bandgap of 0.67 eV at room temperature used as a cathode in this study. The optimal mesh with 42,000 elements was applied as seen Fig. 1.

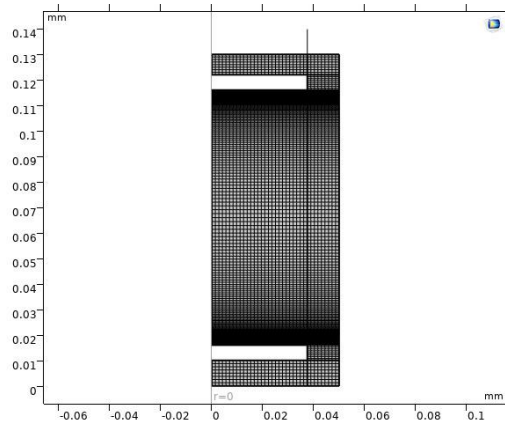


Figure 1. The mesh structure of the micro plasma system

Surface electron maps are obtained for two different time interval. According to time, surface electron density values change and the formation of the plasma is differanted. The density is  $9.34 \times 10^{18} \text{ m}^{-3}$  for  $5 \times 10^{-10}$  and for  $6.3 \times 10^{-10}$ , it is around the  $1.42 \times 10^{20} \text{ m}^{-3}$ . The formation and the distribution of the plasma depend on the time as well as the plasma conditions.

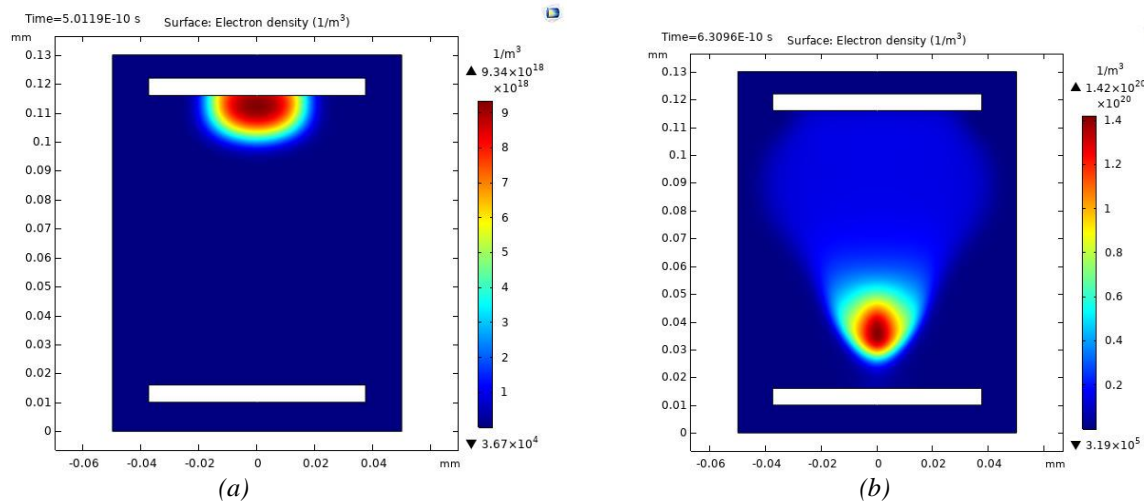


Figure 2. Electron density graphs for different time scale. a) for  $p = 100 \text{ Torr}$  b) for  $p = 760 \text{ Torr}$ .

Space charge accumulation on the cathode is the main reason of the secondary electron emission from the cathode. Those charges make the electric field unstable and cause the inhomogeneous electric field distribution along the plasma. Those charge maps found for  $p = 100 \text{ Torr}$  and  $p = 760 \text{ Torr}$ .

Space charge density maps were calculated with COMSOL multiphysics programme.

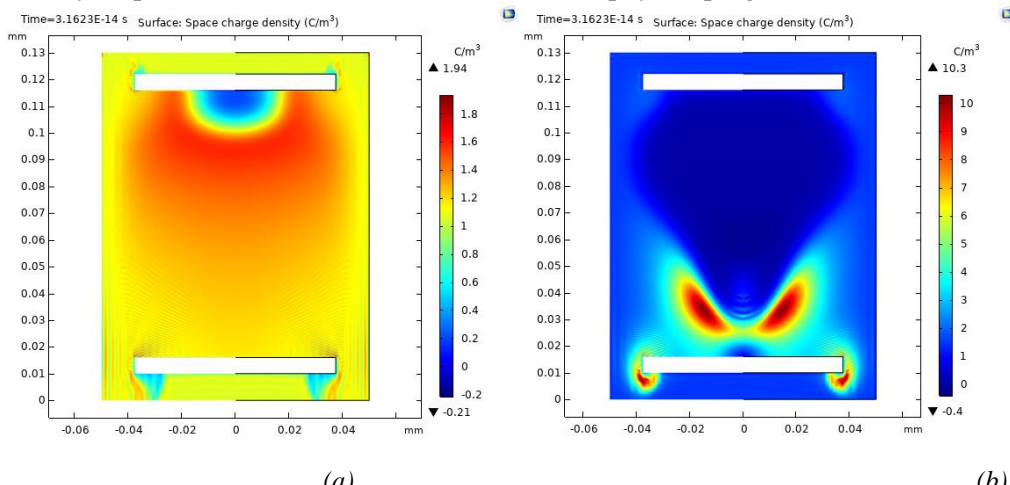


Figure 3. Space charge density maps. a) for  $p = 100 \text{ Torr}$  and b ) for  $p = 760 \text{ Torr}$ .

It is clearly seen that space charge density patterns changes with the pressure. When the pressure increased, the space charge accumulation near the cathode increases and this accumulation pattern can be seen from Figure 3b. It is around 1,94 for 100 Torr, and 10,3 for 760 Torr.

### **3. CONCLUSION**

We used the Comsol simulation programme to get the electron densities and space charge accumulation in front of the GaSb cathode. We noticed that both electron densities and space charges are directly related with the plasma pressure and their positions change with pressure. GaSb is very good material for the plasma cells when they used as cathode.

### **REFERENCES**

- [1] S.J. Sweeney and J. Mukherjee, Optoelectronic Devices and Materials (Springer Handbook of Electronic and photonic Material, 2017).
- [2] YuP Raizer, Gas Discharge Physics (Berlin: Springer, 1997).
- [3] M.C. Penache, Study of High-Pressure Glow Discharges Generated by Micro-Structured Electrode (MSE) Arrays. Dissertation zur Erlangung des Doktorgrades der Naturwissenschaften vorgelegt beim Fachbereich Physik der Johann Wolfgang Goethe Universita"t in Frankfurt am Main, 2002.
- [4] The physics and technology of gallium antimonide: An emerging optoelectronic material  
Journal of Applied Physics 81, 5821 (1997); <https://doi.org/10.1063/1.365356> P. S. Dutta and H. L. Bhat..
- [5] J.D. Freels and P.K. Jain, in COMSOL Conference Proceedings (2011).
- [6] Y. Sadiq, H. Yucel-Kurt, A.O. Albarzanji, S.D. Alekperov, and B.G. Salamov, Solid State Electron. 53, 1009 (2009).



# THE FEATURES OF THE InGaAs/InP DETECTORS IN PLASMA SYSTEMS

Selçuk Utaş,

Department of Physics, Faculty of Science, Gazi University, 06500 Teknikokullar, Ankara, Turkey,  
selcuk.utas@gmail.com,

H. Hilal Kurt

Department of Physics, Faculty of Science, Gazi University, 06500 Teknikokullar, Ankara, Turkey, hkurt@gazi.edu.tr,  
ORCID: 0000-0002-1277-5204

Cite this paper as:

*Utas, S., Kurt H.H., The features of the InGaAs/InP detectors in plasma systems. 9th Eur. Conf. Ren. Energy Sys. 21-23 April 2021, Istanbul, Turkey*

**Abstract:** The features of the plasma cell with InGaAs/InP detector are explored. The detector is composed of InGaAs and InP wafers. Surface space charges and current densities are evaluated by theoretical simulation analyses. The results helped to understand undetermined plasma parameters from experiments and also made the plasma structure more understandable. Thus, complex plasma reactions can be solved via COMSOL.

**Keywords:** *InGaAs/InP detectors, plasma emission, atmospheric pressure plasma systems, plasma cells.*

© 2021 Published by ECRES

## 1. INTRODUCTION

Studies based on plasma technology have increased very rapidly in recent years. Plasma technology has a strong application for nanotechnology tools and has attracted great attention in recent years [1,3]. Infrared transducer cells use plasma as a visualization medium in the transformation process of infrared images. Infrared radiation detection is indispensable tool for device physics and image technology. Unique designed Infrared device structures with doping control of the detector promise significant technological advances such as higher sensitivity cooled Infrared focal plane arrays. New infrared sensor technology needs to improved signal process [1-3]. Infrared related studies focused on the infrared avalanche photodiodes. The main part of the Infrared image converters is the micro discharge cell that was found in 1970 [6]. In those systems, a high resistivity semiconductor electrode is used as infrared detector that operates in near infrared region. This basic converter system has crucial importance by good sensitivity and high speed of operation [4]. InGaAs/InP detector is sensitive up to 1700 nm. It can operate in the near infrared range. It is especially used for space applications. InGaAs–InP detectors, are specifically designed for single-photon detection [5]. Infrared detectors detect infrared radiation when an infrared beam hit the sensor and even they can behave as proximity sensors and they have applications in robotic studies. Photon detection efficiency is significantly related to performance of the detector and InGaAs/InP has good absorption efficiency as a single photon detector. In that manner, InGaAs–InP single-photon detectors can be evaluated as the most sensitive tools for weak light detection [1-5].

## 2. COMSOL DATABASES

### 2.1. Geometry

It is the place where the design of the form we will use in the experiment on the Comsol screen is made. It is the part where 1D, 2D and 3D dimensional drawings can be made.

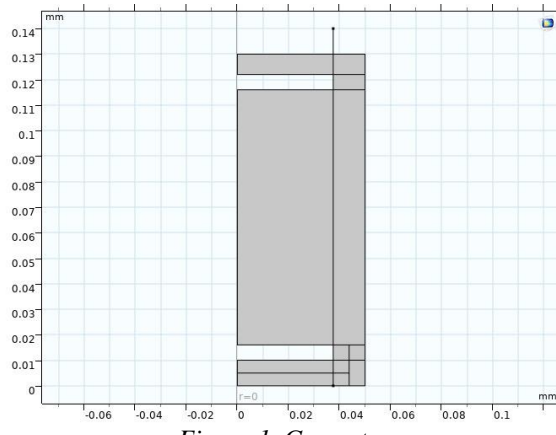


Figure 1. Geometry

## 2.2. Plasma Chemistry

According to the defined gas, all reaction stages have been shown in the table. From table, we can see that successive Argon ionizations with elastic and inelastic collisions occur and the change of the Townsend coefficient depending on its average energy depends on the change of energy of the each electron in multiplication process. In this region, the grounding values required for our system. Those are anode, cathode parts, walls of the plasma system, electrical potential values, insulating parts which are identified in the system.

REACTION	FORMULA	TYPE	$\Delta\epsilon(\text{eV})$
1	$e+Ar \rightarrow e+Ar$	Elastic	0
2	$e+Ar \rightarrow e+Ars$	Excitation	11.5
3	$e+Ars \rightarrow e+Ar$	Superelastic	-11.5
4	$e+Ar \rightarrow 2e+Ar+$	Ionization	15.8
5	$e+Ars \rightarrow 2e+Ar+$	Ionization	4.24
6	$Ars+Ars \rightarrow e+Ar+Ar+$	Penning ionization	-
7	$Ars+Ar \rightarrow Ar+Ar$	Metastable quenching	-

Figure 2. Table of collisions and reactions modeled [9,10]

### 2.2.1. Domain equations

The electron density and mean electron energy are computed by solving a pair of drift diffusion [9,10]

$$\frac{\partial}{\partial t}(n_e) + \nabla \cdot [n_e(\mu_e E) - D_e \nabla n_e] = R_e$$

$$\frac{\partial}{\partial t}(n_e) + \nabla \cdot [-n_e(\mu_e E) - D_e \nabla n_e] + E \Gamma_e = R_e$$

$$\Gamma_e = -(\mu_e E) n_e - D_e \nabla n_e$$

The electron source  $R_e$  and the energy loss due to inelastic collisions  $R_e$  are defined later. The electron diffusivity, energy mobility and energy diffusivity are computed from the electron mobility using

$$D_e = \mu_e T_e, \mu_e = \left(\frac{5}{3}\right) \mu_e, D_e = \mu_e T_e$$

### 2.2.2. Boundary conditions

Unlike RF discharges, the mechanism of sustaining the discharge depends on the emission of secondary electrons from the cathode. When an ion hits the cathode, an electron is emitted with a certain probability from the cathode surface. When these electrons then obtain enough energy to initiate ionization, they are accelerated by a strong electric field close to the cathode. Electrons can be lost due to their random movement at a few mean free path distances from the plasma wall and gain momentum due to the secondary emission mechanism, resulting in the following boundary condition. That is electron flux condition [9,10]:

$$n \cdot \Gamma_e = \left( \frac{1}{2} v_{e,th} n_e \right) - \sum_p \gamma_p (\Gamma_p \cdot n)$$

and the electron energy flux,

$$n \cdot \Gamma_e = \left( \frac{5}{6} v_{e,th} n_e \right) - \sum_p \epsilon_p \gamma_p (\Gamma_p \cdot n)$$

$$n \cdot j_k = M_w R_k + M_w c_k Z \mu_k (E \cdot n) [Z_k \mu_k (E \cdot n) > 0]$$

### 2.3. Mesh

The mesh structure of our system to be designed is of high quality. It is the section where the theoretical calculations of the mesh structure defined as finite element analysis before analysis are made in order to give results closer to experimental data.

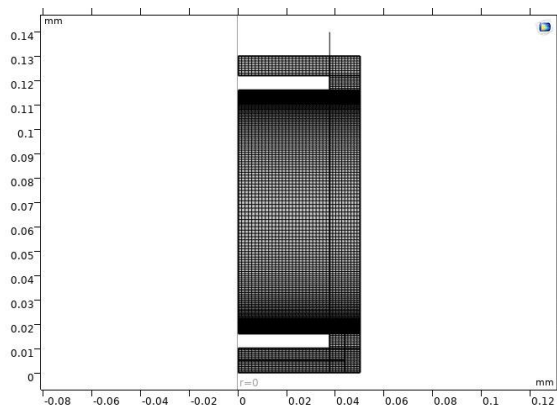


Figure 3. The mesh of the investigated structure

### 2.4. Solutions-Time

In this section, time-dependent values are entered for the formation of dc discharge zone intervals. We have entered the valid and required time values from dc glow discharge to see the plasma formation more easily and to prove the accuracy of the data. Figure 4 shows current densities forms according to various pressure regimes.

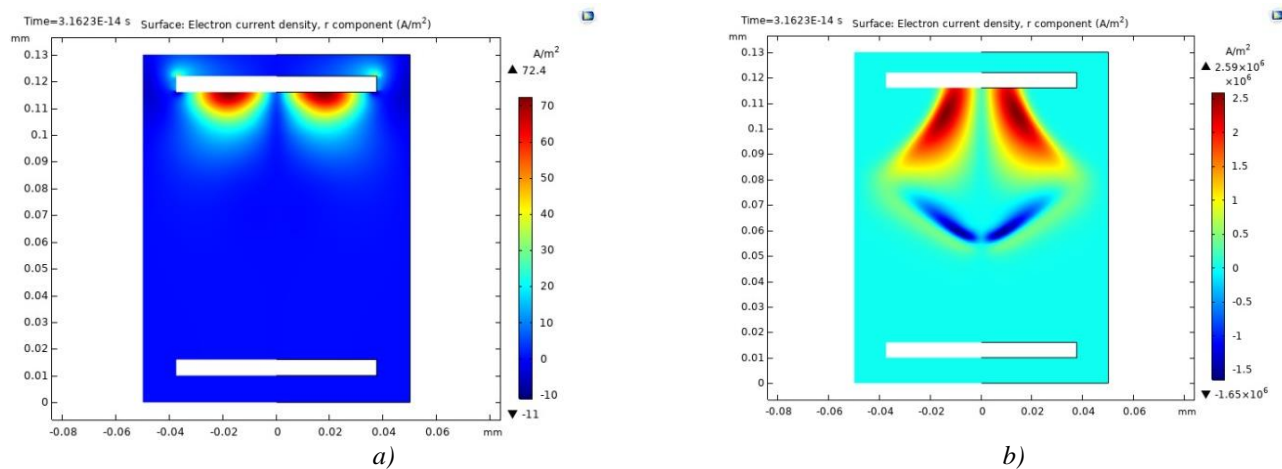


Figure 4. Electron Current Densities a) for  $p=100$  Torr b) for  $p = 220$  Torr.

As can be seen from current density maps, the pressure change made big influence on the current density values and the current density jumped from the lower ( $72.4 \text{ A/m}^2$ ) to  $2.59 \times 10^6 (\text{A/m}^2)$ .

New plasma trends are focused on stable discharges. Nevertheless, the optimization of the plasma requires to understand the complex physical and chemical process. Microdischarge systems with semiconductor electrodes promise the uniform plasma by suppressing the instabilities in the cell [8-10,11].

### 3. CONCLUSION

To demonstrate the current density maps, the advantage of the simulation programme was used at different operation pressures. As the operation pressure increases, the value of the current densities increased.

Heterostructures and devices are grown on commercially and these compound structures have strong absorption at the emission energy for device applications. In order to verify the effectiveness of binary compound materials for the plasma transport mechanism, InGaAs/InP detector was chosen as a cathode material. It has been proved that surface electron current densities were greater than other cathode materials at the same conditions. In conclusion, we have investigated the relationship between binary compound cathode material, InGaAs/InP and system performance optimization for future device applications.

## **REFERENCES**

- [1]Yu-Qiang Fang, Wei Chen, Tian-Hong Ao, Cong Liu, Li Wang, Xin-Jiang Gao, Jun Zhang, Jian-Wei Pan," InGaAs/InP single-photon detectors with 60% detection efficiency at 1550 nm", Review of Scientific Instruments 91, 083102 (2020)
- [2]<https://spie.org/OPO/conferencedetails/infrared-sensors-devices-applications>, Infrared Sensors, Devices, and Applications XI, 2021.
- [3]R. H. Hadfield, Nat. Photonics 3, 696 (2009). 2M. D. Eisaman, J. Fan, A. Migdall, and S. V. Polyakov, Rev. Sci. Instrum. 82, 071101 (2011).
- [4]A. Rogalski, Infrared Detectors, 2nd ed (Boca Raton: CRC press, 2010)
- [5]A. F. Holleman, E. Wiberg, and N. Wiberg, W. Holleman, Lehrbuch der Anorganischen Chemie, chap. Die Zinkgruppe, 101 edn. (de Gruyter, Berlin – New York, 1995), p. 1375
- [6]Sh. S. Kasymov and L. G. Paritskii, Device for tracking images Russian Authors' Certificate 1798020/18-10,1973
- [7]Yu.A. Astrov, A.N. Lodygin, and L.M. Portsel, J. Phys. D Appl. Phys. 49, 095202 (2016)
- [8] <https://arxiv.org/ftp/quant-ph/papers/0605/0605042.pdf>
- [9]I. Rafatov, E. A. Bogdanov, and A. A. Kudryavtsev, "On the accuracy and reliability of different fluid models of the direct current glow discharge," Phys. Plasmas, vol. 19, no. 3, 2012.
- [10]<https://www.comsol.com/>
- [11]Advances in Optoelectronic Materials Editors: Ikhmayies, Shadia Jamil, Kurt, Hatice Hilal (Eds),10.1007/978-3-030-57737-7, 2021.



# DEPENDENCE OF SOLUTION MOLARITY ON STRUCTURAL, OPTICAL, AND ELECTRICAL PROPERTIES OF SPIN COATED TiO<sub>2</sub>/FTO FILMS

Abdullah Atılgan

Department of Energy Systems Engineering, Faculty of Engineering and Natural Sciences, Ankara Yıldırım Beyazıt University, Ankara 06760, Turkey, bdllhtlgn@gmail.com, ORCID: 0000-0002-5624-3664

Abdullah Yıldız

Department of Energy Systems Engineering, Faculty of Engineering and Natural Sciences, Ankara Yıldırım Beyazıt University, Ankara 06760, Turkey, yildizab@gmail.com, ORCID: 0000-0003-4137-6971

*Cite this paper as:* Atilgan, A., Yıldız, A. Dependence of solution molarity on structural, optical, and electrical properties of spin coated TiO<sub>2</sub>/FTO films. 9<sup>th</sup> Eur. Conf. Ren. Energy Sys. 21-23 April 2021, Istanbul, Turkey

**Abstract:** TiO<sub>2</sub> films were deposited on FTO glass by spin-coating method. Basically, TiCl<sub>3</sub> solution was added and dissolved in IPA. The effects of TiCl<sub>3</sub> applied in various concentrations on the structural, optical, and electrical properties of films were investigated.

Morphology of TiO<sub>2</sub>/FTO films surface was studied by Atomic force microscopy (AFM). The varying concentration improved the transparency over a specific region, eg a 6.1% increase in the UV region was observed at the 25 mg / mL concentration. It was observed that, surface resistances of the films coated on FTO in the range of 8.06–8.33 Ωcm.

**Keywords:** Rotation speed, RPM, RMS, optical properties, electrical properties

© 2021 Published by ECRES

## 1. INTRODUCTION

Titanium oxide thin films have been the focus of attention in recent years due to their properties such as photocatalytic activity, availability and chemical inertness, and solar energy conversion [1,2]. Since Fujishima and Honda found out the photocatalytic water splitting, many researchers aim at applications of solar energy conversion and environmental treatment. TiO<sub>2</sub> is transparent in the visible range and has a wide optical bandwidth [2]. It is an excellent candidate for optical coatings thanks to its chemical and thermal stability. [3].

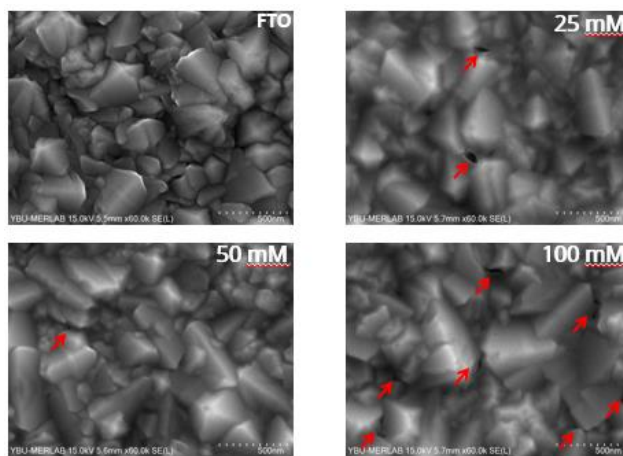
In this study, the TiO<sub>2</sub>/FTO structure was coated using spin-coating at various precursor concentrations. It has been characterized using UV-Vis, AFM, and SEM.

## 2. EXPERIMENTAL SECTION

FTO coated and 25×25×2.1 mm sized glasses were used as the substrate. 25, 50, and 100 mg mL<sup>-1</sup> TiCl<sub>3</sub> was dissolved in IPA and stirred at room temperature for 3 hours. The solution was filtered. It was then coated using spin-coating 16 times by dropping 25 μL at 3200 RPM rotation speeds, respectively. Finally, the films were annealed at 450 °C for 30 minutes.

## 2. RESULTS AND DISCUSSION

SEM images are presented in Figure 1. Cracks and fractures on the surface are marked with a red arrow. Crack formation on the surface differs with the change of concentration. There are few cracks in low concentrations, but the cracks in larger, high concentrations are small but the number is very high.

Figure 1. SEM topographies of  $TiO_2$ /FTO thin films after sintering.

The AFM 3D images, and RMS values are presented in Figure 1 and Table 1, respectively. RMS values were observed from low concentration to high as 44.99, 33.04, 39.8, respectively. In parallel with the SEM results, surface cracks are more dominant than the coated film fills the voids on the surface.

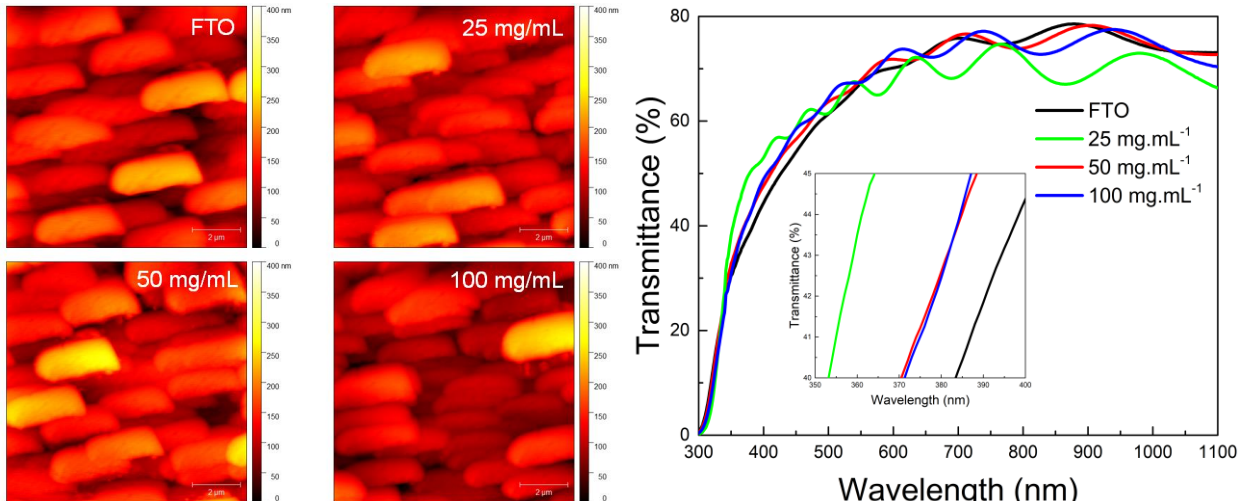


Figure 2 The AFM 2D images of coated surfaces and transmittance of thin films.

The value of average transmittance for coated films is better than FTO. As the concentration increases, transparency is decreasing. Interestingly, the film-coated with  $25 \text{ mg mL}^{-1}$  concentration solution shows a significant increase in the violet-blue area. This can be explained by the small particle size that occurs at low concentrations. However, an increase in the sample 6.1% UV region is observed. Also, the highest increase in the visible region belongs to this sample with 2.8%.

Table 1. Electrical, optical, and morphological parameters of  $TiO_2$ /FTO films

Label	UV	Vis	IR	$T_{av}$	RMS
FTO	Rel.	Rel.	Rel.	64.46	45.20
$25 \text{ mg mL}^{-1}$	6.1	2.8	-2.1	66.47	44.99
$50 \text{ mg mL}^{-1}$	-1.5	2.2	0.3	65.84	33.04
$100 \text{ mg mL}^{-1}$	2.2	1	-0.1	64.48	39.8

If there was a decrease in the IR region of 2.1%, the best average transmittance among all samples belongs to this sample again with 66.47%. The average increases in transmittance values are 2.76%, 2.16%, 0.53% from low concentration to high.

As a result, we can control the region where the transmittance value increases by changing the concentration of the solution. Increasing concentration may cause the film to be more transparent in this region, while scattering in the UV-vis region may cause reflection. The concentration selection according to the needs of the application will provide an advantage to the researchers.

## **REFERENCES**

- [1] Lv J, Shang F, Pan G, Wang F, Zhou Z, Liu C, Gong W, Zi Z, Chen X, He G, Zhang M. Effect of solution concentration on surface morphology and photocatalytic activity of ZnO thin films synthesized by hydrothermal methods. *Journal of Materials Science: Materials in Electronics*. 2014 Feb;25(2):882-7.
- [2] Barua N, Moushumi JF, Rashid AK. Effect of concentration of precursor solution on surface morphology and optical properties of titania thin film. In IOP Conference Series: Materials Science and Engineering 2018 Oct 1 (Vol. 438, No. 1, p. 012032). IOP Publishing.
- [3] Euvananont C, Junin C, Inpor K, Limthongkul P, Thanachayanont C. TiO<sub>2</sub> optical coating layers for self-cleaning applications. *Ceramics International*. 2008 May 1;34(4):1067-71.



# ELECTRIC VEHICLE ENERGY EFFICIENCY CONTRIBUTION THROUGH LABORATORY IMPLEMENTATION

Felipe A. Núñez-Donoso

Technological University of Chile INACAP, Department of Innovation, Osorno, Chile, felipe.nunez@ayn.cl, ORCID: 0000-0001-7564-5522

Jose Manuel Lopez-Guede

University of the Basque Country (UPV/EHU), Vitoria-Gasteiz, Spain, jm.lopez@ehu.eus, ORCID: 0000-0002-5310-1601

Ekaitz Zulueta

Univ. Basque Country UPV/EHU, Syst Eng & Automat Control Dept, 01006 Vitoria-Gasteiz, Spain,  
ekaitz.zulueta@ehu.es, ORCID: <https://orcid.org/0000-0001-6062-9343>

Unai Fernandez-Gamiz

University of the Basque Country (UPV/EHU), Vitoria-Gasteiz, Spain, unai.fernandez@ehu.eus, ORCID: 0000-0001-9194-2009

Jose Antonio Ramoz-Hernanz

University of the Basque Country (UPV/EHU), Vitoria-Gasteiz, Spain, josean.ramos@ehu.es, ORCID: 0000-0001-9706-4016

*Cite this paper as:* Núñez-Donoso, FA, Lopez-Gude, JM, Zulueta, E, Fernandez-Gamiz, U, Ramoz-Hernanz, JA. *Electric vehicle energy efficiency contribution through laboratory implementation. 9<sup>th</sup> Eur. Conf. Ren. Energy Sys. 21-23 April 2021, Istanbul, Turkey*

**Abstract:** A Chilean university experience serves as a case study by implementing a new laboratory for e-mobility research and career activities. Authors present the diverse contributions to an overall energy efficiency strategy from alternative use of novel university facility. In this new laboratory, energy efficiency algorithms are implemented on battery management systems of converted electric vehicles for local last-mile delivery services companies. In nineteen months, parallel laboratory activities have contributed to significant recognition of the importance of direct participation in academic and local business integration.

**Keywords:** electromobility, higher education, research grant

© 2021 Published by ECRES

## 1. INTRODUCTION

An electromobility (e-mobility) industry participation may be a good opportunity for developing countries like Chile in Latin America. It is a new worldwide market that needs human-capital training and possible side technology development. This new ground transportation paradigm is estimated to improve urban air quality and traffic, based on electrical charging and open to renewable-energy grid sources [1]. A similar disruptive phenomenon occurred in the transportation market at the beginning of the 20th century with the internal combustion automobile industry. In the last decade, the global electric vehicle stock has experienced exponential growth, as shown in Figure 1. Starting early in developed countries with the recent appearance of electric car models with similar or even better performances than conventional ones [2,3], and moving forward into the rest of the world, including Latin America

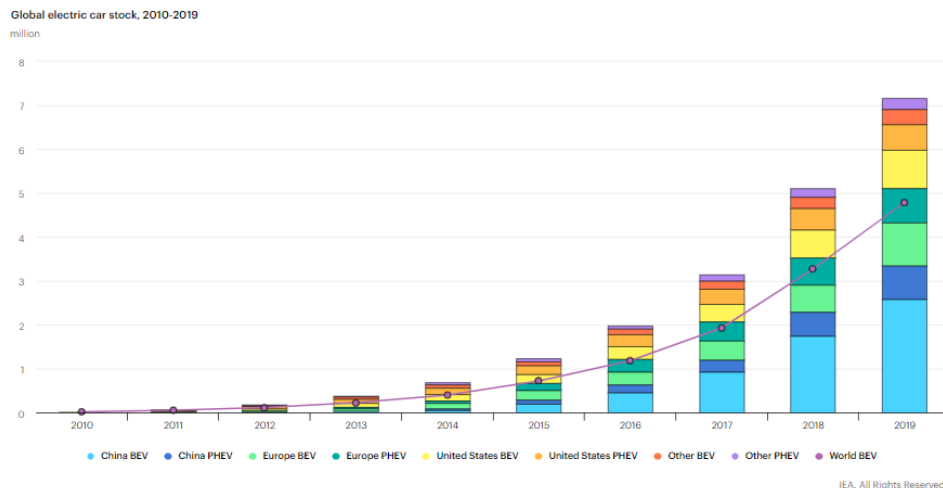


Figure 1. Global electric car stock evolution in the last decade [4].

The Chilean automotive manufacturing industry, mainly represented by North American and European brands through local assembly lines, perished a few decades ago under manufacturing globalization [5]. Since then, car imports have diminished human capital and general knowledge of automotive manufacturing. Therefore, electromobility represents a new opportunity for significant investments in newer technology and training. The Chilean government has granted research funding for electromobility projects [6]. In 2018, a research team from the Technological University of Chile (INACAP) was granted funding for developing a computer algorithm for battery optimization on electric vehicles [7]. The campus located in the southern city of Osorno holds careers related to technology, like bachelor's degree in Electrical Engineering, Computer Engineering, and Automotive Mechanics, among others.

A specialized laboratory for electric car conversion and battery management was required for the research. An existing automotive maintenance facility serves as a starting point. Local companies interested in energy efficiency programs participate in this project through a joint university and business collaboration agreement, including the University of Chile, located in Santiago. A strong collaboration is required to develop local technology with the scarce resources available to achieve the goal proposed. New instruments, facilities, and specialized personnel training are among the investment to be made in a small town that is highly polluted and needs sustainability practices to set an example of energy efficiency initiatives. Undergraduate student collaboration in this project is a complementary strategy that may be part of a future e-mobility career offering for the next decade, according to institutional strategic planning. Automotive Mechanics are present in INACAP and have more than 50 years in conventional car maintenance studies in technical and engineering careers [8]. Integration of e-mobility equipment is part of the intention for all associated academic laboratories.

## 2. MAIN OBJECTIVES AND PARALLEL CONTRIBUTIONS

In this work, the convergence of emerging technology and academic programs is pursued. Since high-end research funding is scarce in developing countries, it is of principal interest to establish a fine example of multiple positive outcomes from a single funding instance. The academic experience presented must serve the research purpose and indirectly extend to career implementation and community sustainability programs.

In this paper, a summary of the research facilities is presented, and the main activities derived from the principal research work on electric vehicle conversions and battery efficiency management. Afterward, an extended academic benefit is shown through regular career programs enhanced by direct student participation in the research laboratory.

## 3. LABORATORY IMPLEMENTATION

A new working space is needed to place the research team and equipment in the Osorno INACAP Campus. On an already crowded building, any square meter of real estate is highly demanded. Regular undergraduate classrooms and laboratories are a priority for the institution. Nevertheless, this government-funded research project, accompanied by significant investment from prominent local business companies, set enough importance to look for the best place possible. The new facility is part of the automotive academic area, already present on the campus, on regular combustion engine maintenance or car repair shop. Implementing an electromobility standard laboratory

represents a significant improvement and challenge for the conventional institution. Part of the new laboratory consists of a closed space with new electrical instrumentation for battery managing and DC systems, insulated tools, car elevator crane, among other instrumentation, as shown in Figure 2. Safety rules are implemented with delimited areas for electrical and mechanical procedures according to local standards. When working with electrical battery charging stations and elevated cars, safety procedures are a major concern when working with students.



*Figure 2. New laboratory for electromobility research.*

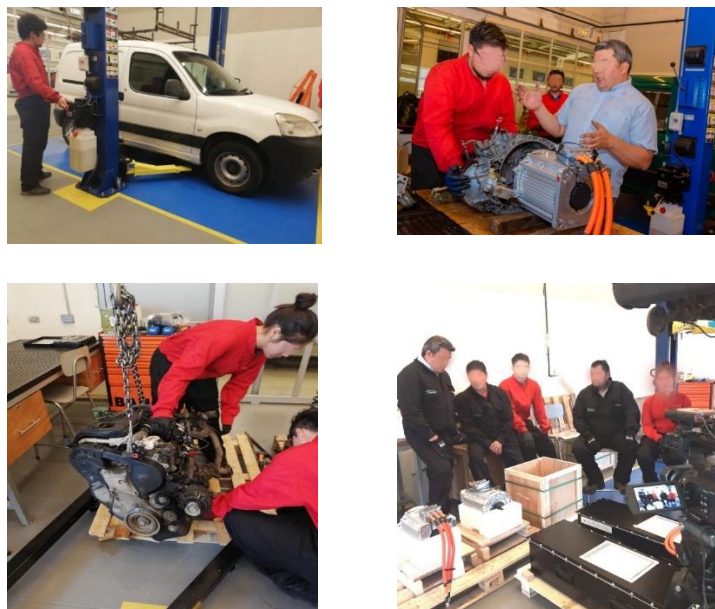


*Figure 3. Electric car conversion the electromobility laboratory.*

### **3. CAREER PROGRAM IMPACT**

Universities in Chile are implementing electric transportation topics in their undergraduate and postgraduate degree programs. Growing student interest in renewable energy sources and uses that are part of the Chilean economic strategy [9] serves as a future base for new local knowledge development on energy efficiency techniques and sustainable transportation.

This new academic research implementation strategy, determined on obtaining as many similar benefits as possible from a unique opportunity, has set up a starting point for electromobility formal studies. In this case, INACAP is starting new career courses specialized in electromobility, and this project surely helps to set a proprietary example. This project sets initial questions for possible student research topics on electric vehicle charging systems through renewable energy grid connections in other related areas. Car manufacturing techniques through combustion to electric vehicle conversion (Figure 3) and ecological strategies through e-mobility implementations are beneficial aspirations for polluted cities like Osorno.

#### **4. CONCLUSIONS AND FUTURE WORK**

The presented paper represents the work related to a local achievement of a small university campus, in the southern part of Chile, in obtaining multiple benefits from a single funding opportunity. In a centralized country where most investments take part in Santiago, Chile's capital city, the presented project contributes to set an example of energy-efficient technology practices. With an e-mobility laboratory implementation in a small city that otherwise may not have been the first choice. This implementation may be relevant to the local business and general community, which may feel closer to the benefits from future renewable energy systems associated with e-mobility projects, like solar, wind, and battery storage systems.

Complementary activities derived from a government-funded project may benefit higher education institutions. Trained faculty members who can access funding for edge technology research on energy-related topics represent a financial source for institutional investments and new specialized facilities. Continuous education in high technology fields is closer now for far-away students.

As an example of a long-term academic strategy, the new laboratory's future activities may be related to research and student thesis programs. Local businesses interested in equipment efficiency and renewable energy sources for industrial processes or vehicle transportation are now a closer reality. Extended research funding in high technology fields for small-town academic institutions is necessary for developing countries.

#### **ACKNOWLEDGMENT**

Highly appreciated support to FONDEF ID 18/10379 from the grant of the call “Concurso Idea de Investigación y Desarrollo 2018” from the Chilean National Commission of Research in Science and Technology CONICYT.

#### **REFERENCES**

- [1] Ministerio de Energía, Gobierno de Chile, “Chile ya se adapta a la Electromovilidad,” 2017. <<http://energia.gob.cl/electromovilidad>>
- [2] Z. Rezvani, J. Jansson, and J. Bodin, “Advances in consumer electric vehicle adoption research: A review and research agenda,” *Transp. Res. Part D Transp. Environ.*, vol. 34, pp. 122–136, 2015.
- [3] A. F. Jensen and S. L. Mabit, “The use of electric vehicles: A case study on adding an electric car to a household,” *Transp. Res. Part A Policy Pract.*, vol. 106, pp. 89–99, 2017.
- [4] IEA (2020), Global EV Outlook 2020, IEA, Paris <https://www.iea.org/reports/global-ev-outlook-2020>
- [5] Desrueda, «[blog.desrueda.com](http://blog.desrueda.com/),» “Sabías que en Chile se fabricaron automóviles conócelos aquí”, <<http://blog.desrueda.com/sabias-que-en-chile-se-fabricaron-automoviles-conocelos-aqui>>
- [6] Revista Electricidad, “Las cuatro tendencias en I+D para la electromovilidad en Chile”, 2019. <[http://www.revistaei.cl/2019/07/04/las-cuatro-tendencias-en-id-para-la-electromovilidad-en-chile](http://www.revistaei.cl/2019/07/04/las-cuatro-tendencias-en-id-para-la-electromovilidad-en-chile/)>
- [7] Universidad Tecnológica de Chile INACAP, “Why study at INACAP”, Dirección de Asuntos Internacionales. 2012 <<http://www.inacap.cl/tportalvp/pruebav2/extranjeros/international-exchange-students/why-study-at-inacap-2>>
- [8] Comisión Nacional de Investigación Científica y Tecnológica CONICYT, “Inauguran Primer Laboratorio de Electromovilidad en la Región de Los Lagos”, Fondo de Fomento al Desarrollo Científico y Tecnológico FONDEF <[https://www.conicyt.cl/fondef/2019/06/27/inacap-osorno-inaugura-primer-laboratorio-de-electromovilidad-en-la-region-de-los-lagos](https://www.conicyt.cl/fondef/2019/06/27/inacap-osorno-inaugura-primer-laboratorio-de-electromovilidad-en-la-region-de-los-lagos/)>
- [9] Climate-Chance “Chile An emerging key actor in the renewable energy arena” <[https://www.climate-chance.org/en/card/chile-energy-an-emerging-key-actor-in-the-renewable-energy-area](https://www.climate-chance.org/en/card/chile-energy-an-emerging-key-actor-in-the-renewable-energy-area/)/>



# COMPUTATIONAL MODELING OF A 2D VANADIUM REDOX FLOW BATTERY CELL

Iñigo Aramendia

Univ. Basque Country UPV/EHU, Nuclear Eng & Fluid Mechanics Dept, 01006 Vitoria-Gasteiz, Spain, ORCID:  
<https://orcid.org/0000-0002-4960-2729>

Joseba Martinez-Lopez

Univ. Basque Country UPV/EHU, Nuclear Eng & Fluid Mechanics Dept, 01006 Vitoria-Gasteiz, Spain, ORCID:  
<https://orcid.org/0000-0002-3268-1336>

Unai Fernandez-Gamiz

Univ. Basque Country UPV/EHU, Nuclear Eng & Fluid Mechanics Dept, 01006 Vitoria-Gasteiz, Spain, ORCID:  
<https://orcid.org/0000-0001-9194-2009>

Mirko Messaggi

Politecnico di Milano, Department of Energy, 20156 Milano, Italy, ORCID: <https://orcid.org/0000-0002-3447-7224>

Matteo Zago

Politecnico di Milano, Department of Energy, 20156 Milano, Italy, ORCID: <https://orcid.org/0000-0002-0542-1459>

Ekaitz Zulueta

Univ. Basque Country UPV/EHU, Syst Eng & Automat Control Dept, 01006 Vitoria-Gasteiz, Spain, ORCID:  
<https://orcid.org/0000-0001-6062-9343>

Jose Manuel Lopez-Guede

Univ. Basque Country UPV/EHU, Syst Eng & Automat Control Dept, 01006 Vitoria-Gasteiz, Spain, ORCID:  
<https://orcid.org/0000-0002-5310-1601>

Cite this paper as:

Aramendia, I., Martinez-Lopez, J., Fernandez-Gamiz, U., Messaggi, M., Zago, M., Zulueta, E., Lopez-Guede, JM. Computational Modeling of a 2D Vanadium Redox Flow Battery Cell. 9<sup>th</sup> Eur. Conf. Ren. Energy Sys. 21-23 April 2021, Istanbul, Turkey

## Abstract:

Nowadays the implementation of renewable energy sources has caused a change of tendency in the energy production and storage systems, forcing them to overcome the difficulties that it represents. Taking into account all of the proposed devices, vanadium redox flow batteries (VRFB) appear as a remarkable option in terms of efficiency, cyclability and scalability. In contrast, some issues like the low energy density and high costs need to be considered, making it difficult the commercial development of the VRFB. The aim of this study is to analyze the performance of a two-dimensional and steady-state cell of a vanadium redox flow battery. In order to achieve this, a 2D model consisting of an electrode, an ion exchange membrane and a flow channel was developed. Different operating conditions were tested to visualize the flow field, concentration of species and current and potential distribution.

**Keywords:** *energy storage, vanadium redox flow battery, VRFB, flow field, numerical model*

© 2021 Published by ECRES

## 1. INTRODUCTION

Over the last few years, several factors such as the increase in power demand and the environmental concern has upsurged the transition from hydrocarbon fuels to alternative renewable energy sources and the development of large-scale electrical energy storage systems [1]. In this framework, the redox flow batteries (RFB) technology has been widely researched due to the potential advantages that they offer based on their independent control of

power and energy [2,3]. In particular, the vanadium redox flow batteries (VRFB) firstly suggested in 1985 by Skyllas-Kazacos et al. [4,5] have become the most popular these last years because of their ease of operation and due to the fact that the same electrolyte is used for both the negative and positive side of the cell. The main components of a VRFB cell are the electrolyte which is stored in two separated tanks and recirculated with mechanical pumps, the carbon felt (CF) electrodes where the electrochemical reactions take place and an ion-exchange membrane to ensure that the positive and negative side are isolated [6]. The research in the field of RFBs involve the study of different type of electrolytes, electrode configurations and new materials for the ion-exchange membrane in order to improve the transport selectivity, ion conductivity and stability of the system [8–10]. However, due to the cost of large experimental facilities, the experimental studies are usually made with short stacks or small-size cells with active areas no larger than  $25\text{ cm}^2$ . Besides, they present difficulties to quantify some parameters that control the flow battery operation.

In these circumstances, Computational Fluid Dynamic (CFD) simulations have emerged as an alternative tool to design and optimize VRFB systems under different load states, distribution channels, flow rates or material properties [11]. For instance, Kumar et al. [12] studied the influence of electrode intrusion into the flow channel. To that end, numerical simulations were performed taking into account that due to the compression a portion of the electrode protruded into the flow channel. Ozgoli et al. [13] investigated the hydrodynamic and electrochemical performance with a two-dimensional model to analyze the vanadium distribution at different profiles of the electrodes and the membrane. Different classic flow channel designs have been analyzed over the years to evaluate which one is the most adequate for an efficient VRFB. The work of Messaggi et al. [14] showed that an interdigitated flow field design provided more uniform reaction rates than those obtained with a serpentine flow field design. The aim of this work is to study different flow rate conditions in a half-cell to visualize the flow field, concentration species and current and potential distribution.

## 2. NUMERICAL MODEL

### Computational domain

In this section, the model of a 2D vanadium redox flow battery is described in detail. This model is based on the one developed by Canzi [15] and it represents a half-cell modeled in *COMSOL Multiphysics®*, a commercial code commonly used for electrochemical applications. Regarding the computational domain, the half-cell is divided into three subdomains, a membrane, a positive electrode and a flow channel, as shown in Figure 1. The dimensions are listed in Table 1. The cathode and membrane are modeled as a commercial *Gas diffusion Layer GDL 10 AA* and *Nafion* material, respectively. A structured mesh with 22050 elements has been defined with quadrilateral cells with a refinement near to those interfaces where higher gradients are expected.

*Table 1. Dimensions of the 2D computational domain.*

Parameter	Value	Unit
Electrode thickness	$3.4 \cdot 10^{-4}$	m
Channel thickness	$8.0 \cdot 10^{-4}$	m
Membrane thickness	$1.25 \cdot 10^{-4}$	m
Cell height	$5.0 \cdot 10^{-2}$	m

For the simulation model, the following assumptions were taken into account:

- The model is stationary.
- Isothermal cell.
- Parasitic reactions are ignored.
- Membrane and electrode have isotropic properties.
- Incompressible fluid.
- Only  $\text{H}^+$  ions are allowed to go through the membrane.
- Electroneutrality and complete wettability of the membrane.

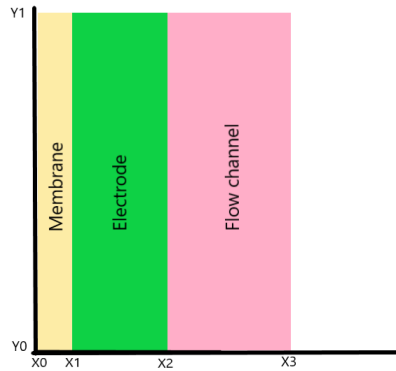
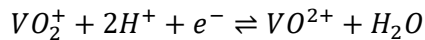


Figure 1. Scheme of the bidimensional computational domain.

In terms of electrochemistry, the reaction taking place in the surface of the positive electrode is:



The mass transport is described by the Nernst-Planck equation, which expresses the molar flux due to diffusion, migration and advection. Furthermore, the applied kinetic model is the Butler-Volmer one, and a charge balance is considered between the liquid and the solid phase. In order to simplify the model, cross contamination in the membrane is ignored, meaning that only  $H^+$  can go through it. This behavior is solved using the *Secondary Current Density Distribution*. In addition, the membrane can be considered as a liquid electrolyte when the concentration of sulphonic groups is high enough. For the fluid dynamic modeling, two domains are distinguished, the flow channel and the porous medium. The former is calculated with Navier-Stokes, and the latter is solved using the Brinkman equations, which extend Darcy's law to calculate the dissipation of kinetic energy by viscous shear, resembling the Navier-Stokes' equations.

### Boundary Conditions

As shown in Figure 1, the computational domain is divided into three subdomains and the boundaries between them need to be modeled carefully, principally for the electrochemical part. The imposed boundary conditions are reported in Table 2.

Table 2. Description of the electrochemical boundary conditions.

Boundary Condition	Equation	Position
Fluid inlet	$c_i = c_{0,i}$	$Y = 0$ for $x_1 < x < x_2$
Fluid outlet	$n \cdot D_i \nabla c_i = 0$	$Y = 1$ for $x_1 < x < x_2$
Insulation	$-n \cdot i_l = 0, -n \cdot i_s = 0$	$Y = 0$ and $Y = 1$ for $x_0 < x < x_3$
Insulation	$-n \cdot i_l = 0, -n \cdot i_s = 0$	$x = x_3$
No flux	$-n \cdot (J_i + uc_i) = 0$	$Y = 0$ and $Y = 1$ for $x_1 < x < x_2$
No flux	$-n \cdot (J_i + uc_i) = 0$	$x = x_3$
Electrolyte Potential	$\phi_l = 0$	$x = x_0$
Electric Potential	$\phi_s = \text{user defined}$	$x = x_2$
Electrolyte Current Density	$-n \cdot i_{l,mem} = i_{l,porous}$	$x = x_1$
Electrolyte Potential	$\phi_{l,mem} = \phi_{l,porous}$	$x = x_1$

For the fluid dynamic modelling, the boundary conditions include a laminar flow at the inlet of the flow channel and an atmospheric pressure at the outlet. The velocity at the inlet is calculated from each of the volumetric flow rate evaluated ( $Q = 10-30$  ml/min) and the geometrical parameters of the flow channel.

Table 3. Description of the fluid-dynamic boundary conditions.

Boundary Condition	Equation	Position
Inlet	$L_{entr} \nabla_t \left[ -pl + \mu \frac{1}{\epsilon_p} (\nabla_t u_2 + (\nabla_t u_2)^T) - \frac{2}{3} \mu \frac{1}{\epsilon_p} (\nabla \cdot u_2) I \right]$	$Y = 0$ for $x_2 < x < x_3$
Outlet	$[-pI + K]n = -\hat{p}_0 n$	$Y = 1$ for $x_2 < x < x_3$

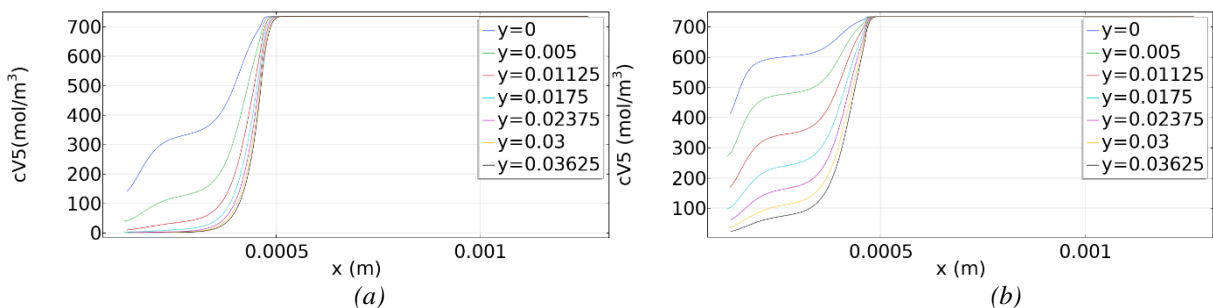
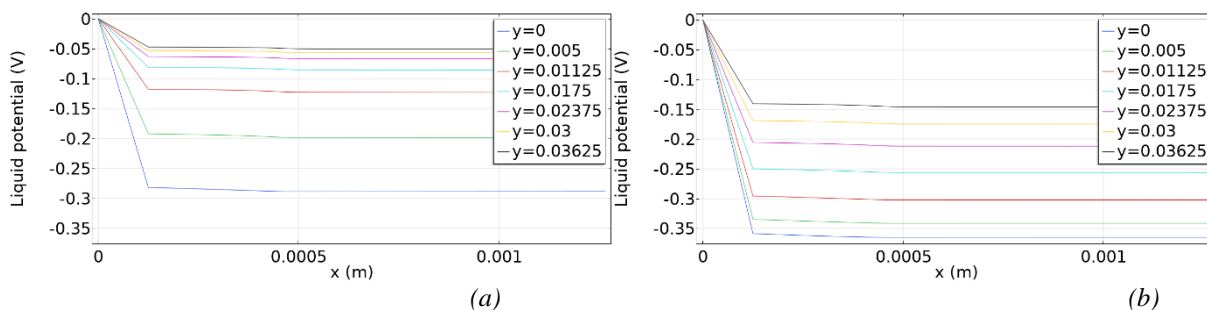
The main physical properties of the electrode and electrolyte used in the present work are summarized in Table 4.

Table 4. Parameters used to define the numerical model.

Parameter	Symbol	Value	Unit
Electrode porosity	$\epsilon$	0.8568	—
Electrode conductivity	$\sigma_s$	100	$S \cdot m^{-1}$
Channel porosity	$\epsilon_c$	1	—
Electrode permeability	$K$	$4 \cdot 10^{-10}$	$m^2$
Electrode specific area	$a$	$3.5 \cdot 10^{-4}$	$m^2 \cdot m^{-3}$
Electrolyte density	$\rho_{neg}$	1350	$kg \cdot m^{-3}$
Electrolyte viscosity	$\mu_{neg}$	0.005	$Pa \cdot s$
Cell temperature	$T$	295	$K$
Pore diameter	$r_p$	$3.2 \cdot 10^{-5}$	$m$
V(IV) diffusion coefficient	$D_{V4}$	$3.9 \cdot 10^{-10}$	$m^2 \cdot s^{-1}$
V(V) diffusion coefficient	$D_{V5}$	$3.9 \cdot 10^{-10}$	$m^2 \cdot s^{-1}$
$HSO_4^-$ diffusion coefficient	$D_{HSO_4^-}$	$1.33 \cdot 10^{-9}$	$m^2 \cdot s^{-1}$
$SO_4^{2-}$ diffusion coefficient	$D_{SO_4^{2-}}$	$1.065 \cdot 10^{-9}$	$m^2 \cdot s^{-1}$
$H^+$ diffusion coefficient	$D_{H^+}$	$9.312 \cdot 10^{-9}$	$m^2 \cdot s^{-1}$

### 3. RESULTS

The results are determined in discharge condition with a working condition of  $V = 0.75V$ , a current average of  $0.3 A \text{ cm}^{-2}$  and a state of charge of 0.77. Horizontal lines have been defined throughout the computational domain to show the results at different heights of the cell. Figure 2 illustrates the concentration trends of the V5 specie during discharge from the flow channel to the membrane, leading to a decrease as the reaction during this phase reduces this specie.

Figure 2. V5 concentration during discharge condition for (a)  $Q = 10 \text{ ml/min}$  and (b)  $Q = 30 \text{ ml/min}$ .Figure 3. Liquid potential for a flow rate of (a)  $Q = 10 \text{ ml/min}$  and (b)  $Q = 30 \text{ ml/min}$ .

Similar effect is observed in Figure 3 where the liquid potential is represented. Note that an increase in the flow rate conditions derives in an increase in the liquid potential observed.

#### 4. CONCLUSION

The current work presents a two-dimensional computational model of a half-cell of a vanadium redox flow battery with two different electrolyte flow rates ( $Q = 10\text{-}30 \text{ ml/min}$ ). V5 concentration and liquid potential parameters have been studied during discharge process. In both cases, higher values V5 concentration and liquid potential have been achieved by the larger electrolyte flow rate. As future work, more investigations are required in three-dimensional geometries to obtain a more accurate performance with respect to the flow field.

#### ACKNOWLEDGMENT

The authors appreciate the support to the government of the Basque Country through research programs Grants N. ELKARTEK 20/71 CICe2020 and ELKARTEK 20/78. The computational support provided by the Microfluidics Cluster UPV/EHU is also gratefully acknowledged.

#### REFERENCES

- [1] Gür, T.M. Review of Electrical Energy Storage Technologies, Materials and Systems: Challenges and Prospects for Large-Scale Grid Storage. *Energy Environ. Sci.* 2018, 11, 2696–2767, doi:10.1039/C8EE01419A.
- [2] Ulaganathan, M.; Aravindan, V.; Yan, Q.; Madhavi, S.; Skyllas-Kazacos, M.; Lim, T.M. Recent Advancements in All-Vanadium Redox Flow Batteries. *Adv. Mater. Interfaces* 2016, 3, 1500309, doi:10.1002/admi.201500309.
- [3] Lai, Q.; Zhang, H.; Li, X.; Zhang, L.; Cheng, Y. A Novel Single Flow Zinc–Bromine Battery with Improved Energy Density. *Journal of Power Sources* 2013, 235, 1–4, doi:10.1016/j.jpowsour.2013.01.193.
- [4] Sum, E.; Skyllas-Kazacos, M. A Study of the V(II)/V(III) Redox Couple for Redox Flow Cell Applications. *Journal of Power Sources* 1985, 15, 179–190, doi:10.1016/0378-7753(85)80071-9.
- [5] Sum, E.; Skyllas-Kazacos, M. A Study of the V(V)/V(IV) System for Use in the Positive Half-Cell of a Redox Battery. *Journal of Power Sources* 1985, 16, 85–95, doi:10.1016/0378-7753(85)80082-3.
- [6] Zhang, H.; Li, X.; Zhang, J. *Redox Flow Batteries*; CRC Press, Taylor & Francis Group: Boca Raton, Florida, USA, 2018; ISBN 978-1-4987-5394-4.
- [7] Shibata, A.; Sato, K. Development of Vanadium Redox Flow Battery for Electricity Storage. *Power Engineering Journal* 1999, 13, 130–135, doi:10.1049/pe:19990305.
- [8] Choi, C.; Kim, S.; Kim, R.; Choi, Y.; Kim, S.; Jung, H.; Yang, J.H.; Kim, H.-T. A Review of Vanadium Electrolytes for Vanadium Redox Flow Batteries. *Renewable and Sustainable Energy Reviews* 2017, 69, 263–274, doi:10.1016/j.rser.2016.11.188.
- [9] Gencten, M.; Sahin, Y. A Critical Review on Progress of the Electrode Materials of Vanadium Redox Flow Battery. *Int J Energy Res* 2020, 44, 7903–7923, doi:10.1002/er.5487.
- [10] Shi, Y.; Eze, C.; Xiong, B.; He, W.; Zhang, H.; Lim, T.M.; Ukil, A.; Zhao, J. Recent Development of Membrane for Vanadium Redox Flow Battery Applications: A Review. *Applied Energy* 2019, 238, 202–224, doi:10.1016/j.apenergy.2018.12.087.
- [11] Aramendia, I.; Fernandez-Gamiz, U.; Martinez-San-Vicente, A.; Zulueta, E.; Lopez-Gude, J.M. Vanadium Redox Flow Batteries: A Review Oriented to Fluid-Dynamic Optimization. *Energies* 2020, 14, 176, doi:10.3390/en14010176.
- [12] Kumar, S.; Jayanti, S. Effect of Electrode Intrusion on Pressure Drop and Electrochemical Performance of an All-Vanadium Redox Flow Battery. *Journal of Power Sources* 2017, 360, 548–558, doi:10.1016/j.jpowsour.2017.06.045.
- [13] Ozgoli, H.A.; Elyasi, S.; Mollazadeh, M. Hydrodynamic and Electrochemical Modeling of Vanadium Redox Flow Battery. *Mechanics & Industry* 2015, 16, 201, doi:10.1051/meca/2014071.
- [14] Messaggi, M.; Canzi, P.; Mereu, R.; Baricci, A.; Inzoli, F.; Casalegno, A.; Zago, M. Analysis of Flow Field Design on Vanadium Redox Flow Battery Performance: Development of 3D Computational Fluid Dynamic Model and Experimental Validation. *Applied Energy* 2018, 228, 1057–1070, doi:10.1016/j.apenergy.2018.06.148.
- [15] Canzi, P. Analysis of Flow Field Design for Vanadium Redox Flow Batteries through the Development and Validation of CFD Codes. PhD, Politecnico di Milano: Milan, Italy, 2017.



# AUTOMATIC IDENTIFICATION ALGORITHM OF EQUIVALENT ELECTROCHEMICAL CIRCUIT BASED ON ELECTROSCOPIC IMPEDANCE DATA FOR A LEAD ACID BATTERY

Javier Olarte

Centro de Investigación Cooperativa de Energías Alternativas (CIC energiGUNE), Basque Research and Technology Alliance (BRTA)/Bcare/University of the Basque Country, Vitoria, Spain, jolarte@cicenergigune.com, ORCID: 0000-0003-2632-9974

Jaione Martínez de Ilarduya

Bcare, Vitoria, Spain, jmartinez@bcaremb.com, ORCID: 0000-0001-8304-3388

Ekaitz Zulueta

University of the Basque Country, Vitoria, Spain, ekaitz.zulueta@ehu.eus, ORCID: 0000-0001-6062-9343

Raquel Ferret

Centro de Investigación Cooperativa de Energías Alternativas (CIC energiGUNE), Basque Research and Technology Alliance (BRTA), Vitoria, Spain, rferret@cicenergigune.com, email address, ORCID: 0000-0002-7552-6467

Unai Fernández-Gámiz

University of the Basque Country, Vitoria, Spain, unai.fernandez@ehu.eus, ORCID: 0000-0001-9194-2009

Jose Manuel Lopez-Guede

University of the Basque Country, Vitoria-Gasteiz, Spain, jm.lopez@ehu.eus, ORCID: 0000-0002-5310-1601

Cite this paper as:

*Olarte, J., Martínez de Ilarduya, J., Zulueta, E., Ferret, R., Fernández-Gámiz, U., Lopez-Gude, JM., Automatic identification algorithm of equivalent electrochemical circuit based on electroscopic impedance data for a lead acid battery. 9<sup>th</sup> Eur. Conf. Ren. Energy Sys. 21-23 April 2021, Istanbul, Turkey*

## Abstract:

The development of tools for examining and predicting battery performance represents a significant challenge for the field of monitoring. At the research level, an innovative path is marked in the development of sensors that allow monitoring at cell level and undoubtedly, Electrochemical Impedance Spectrometry (EIS), is one of the most promising tools in parallel with the development of advance multivariable models. In this article, we propose and describe an automatic identification algorithm of battery equivalent electrochemical model based in operando electroscopic impedance data. This algorithm allows in operando monitoring of the variation of the equivalent circuit parameters that will be used to further estimate the battery state of health (SOH) and state of charge (SOC) based on correlation with the experimental aging data. In the current work, authors propose a Differential Evolutions optimization based parameter identification. This optimization gives a fine parameter estimation.

## Keywords:

Automatic Identification, electrochemical model, EIS, lead acid batteries

© 2021 Published by ECRES

## Nomenclature

EIS	Electrochemical Impedance Spectroscopy
SoC	State of Charge
SoH	State of Health
RUL	Remaining Useful Lifetime
ECM	Equivalent Circuit Model
OCV	Open Circuit Voltage

CNN	Convolutional Neural Network
EEC	Electric Equivalent Circuit
CPE	Constant Phase Element
DE	Differential Evolution
ZCPE	Impedance Constant Phase Element
PSO	Particle Swarm Optimization
BMS	Battery Management System

## 1. INTRODUCTION

Batteries fulfill a critical and vital function in many stationary applications. The decrease in the remaining useful lifetime of a battery due to the destabilization of the energy storage system generated by the unidentified problems in one of its cells or modules represents a significant investment for stationary energy storage market. For instance, solutions based on manual measurements of the state of health of the energy storage systems involves high maintenance costs and when the review frequency is low the failures are not detected in time. The failures should be reduced to zero, maximizing life expectancy with the lowest total cost for the end-user. In this framework, the integration of sensors and, development and optimization of Battery Management System gain so much importance in order to create batteries that can meet these requirements. Monitoring of the battery by implementation of smart models and algorithms to the Battery Management System provides the opportunity for continuous collection historical data and the minimization of the failures of the battery [1]–[7]. Integration of smart EIS sensing and extraction of key parameters will enable monitoring of the battery in order to produce a detailed understanding and evaluation, also to develop better energy management strategies and enable smart SoC and SoH identification to improve performance.

The process of the determination of the state of charge (SoC) and state of health (SoH) of batteries is a challenging matter. Several imaginative monitoring approaches have been developed over the years, leading to numerous patents covering various sensing technologies [8]. For decades, this type of research was essentially devoted to Pb-acid technology, to make it more reliable and friendlier to customs. Many advances were made with the implementation of electrochemical impedance spectroscopy (EIS) during this period, as a tool to evaluate the evolution of cell resistance upon cycling in Pb-acid batteries, enabling estimation of their state of charge (SoC) and state of health (SoH). Overall, SoH and SoC monitoring is highly interesting, and there is currently no accurate solution. Estimation of SoC and SoH today relies on a combination of direct measurements such as EIS, resistance, current pulse quantities, coulomb counting and open circuit voltage-based approximations [9]–[12] [13] [14], [15]. Electrochemical Impedance Spectroscopy is other of the methods generally used for real time prediction by interpreting parameters from the spectra. However, in this case, the electrochemical model is difficult to be implemented and it is very specific for each technology [14], although it is expected to be very accurate. Last option, in terms of electrochemical models, is Kalman filters which can be implemented in all the battery system, although it presents high level of difficulty to be implemented.

In the present work, direct measurement based on the analysis of EIS impedance spectra is used to determine State of Health and State of Charge in combination with smart algorithm model. The main innovation of the present work consists of a new model proposed to improve the certainty of the estimation of the health status, as well as the state of charge of the battery, with special emphasis on the evaluation of the Electrochemical Impedance Spectroscopy. The process of identification and use of parameters is interactive, allowing the integration of more experimental variables in the model. As important as developing an efficient and highly accurate algorithm of battery State of Health (SoH) or Remaining Useful Life (RUL) is the ability to implement it economically in a hardware integrated into an advanced Battery Management System (BMS). This work has directed efforts to implement a computationally efficient yet robust algorithm that can be migrated into a low-cost device. With the implementation of the present algorithm, Lead-Acid batteries may position as zero maintenance reliable batteries - with adjusted predictions of the Remaining Useful Life (RuL) and historical data records that allow continuous improvement and future cost forecasts based on the need for replacement. The detailed information about SoC and SoH will improve the performance, cycling strategies, battery safety and cost reduction.

## 2. METHODOLOGY

### Ageing data and electrochemical data logs

The work is based on the aging and measurements over 4 Lead-Acid batteries models from different manufacturers. From the accelerated aged tests, suitable extraction of parameters/signals from the electrochemical system is

extracted to be integrated in the modelling for the determination of SoH of the Lead-Acid batteries. This testing protocol includes voltage, current, temperature and EIS spectra identification at different operational conditions. Figure 1 illustrates the equivalent circuit model proposed by authors.

During both tests, a data logs the electrochemical data are recorded. Specifically, from EIS spectra, electrical parameters from Electric Equivalent Circuit (EEC) are identified. Specifically, this EEC is selected with constant phase elements in order to adjust the experimental data. non-ideal capacitive behavior of an electrode (suppressed semi-circles on the Nyquist plot) are taken into account, a constant phase element (CPE) is used, see Aksal et al. [[1]]. Using the gathered data, tendencies are analyzed, and electrochemical complete models are developed for each Lead-Acid battery model.

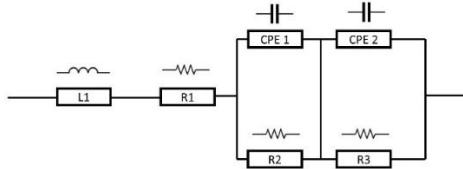


Figure 1. Equivalent EIS circuit model.

### Data processing, proposed intelligent identification algorithm and cost function

The current research proposes the so-called differential evolution (DE) algorithm first introduced in 1997 by Storn and Price [16]. Similarly, as Particle Swarm Optimization (PSO), differential evolution (DE) is a simple but powerful population-based stochastic search technique. As presented in Aramendia et al. [17], DE algorithm proposes different agents set. There are other methods like Nelder-Mead simplex method given by Lagarias et al. [19], but they need to be very near from optimal values. In Swarm optimizations, all agents follow the same procedure in order to improve the agent set, evaluation, crossing, mutation and selection. The three main vectors are described as follows:

- Target vector: It is the solution which is undergoing evolution. It is used in mutation to generate a donor vector.
- Donor vector: Undergoes recombination to obtain the trial vector.
- Trial vector. An offspring formed by recombination of the donor with the target vector.

The variables that are wanted to be optimized, in this case  $R_1, L_1, R_2, C_1, \alpha_1, R_3, C_2$  and  $\alpha_2$ , take real values, as they were codified from a vector. The length of these vectors (n) is the same as the number of variables. To define a vector the nomenclature  $X_p^g$  has been used, where p is the indicator of the individual population ( $p=1.....NP$ ), g is the corresponding generational number and NP the agent number. The candidate solutions are defined in Eq. [1]:

$$X_p^g = \{x_{p,m}^1, \dots, x_{p,m}^g\} \quad (1)$$

where  $m=1 \dots n$ .

The DE algorithm has four stages: initialization, mutation, recombination and election.

#### Initialization:

The population is generated randomly without exceeding both maximum and minimum limits as described in Eq. [2]:

$$x_{p,m}^1 = x_m^{min} + rand(0,1) \cdot (x_m^{max} - x_m^{min}) \quad (2)$$

where  $p=1 \dots NP$  and  $rand(0,1)$  represents a uniformly distributed random variable within the range [0,1]. This equation corresponds to generation 1 ( $g=1$ ).

#### Mutation:

In the mutation operation three random solutions ( $X_{r1}, X_{r2}, X_{r3}$ ) are selected from a population of solutions. These solutions must not be identical. The donor vector is achieved with the Eq. [3]:

$$V_p^g = X_{r3} + F \cdot (X_{r1} - X_{r2}) \quad (3)$$

where p=1 ... NP. The scaling factor (F) is a positive control parameter between (0,2) for scaling the difference vector. For its target  $X_{p,g}$  at the generation g, its associated donor vector  $V_p^g = \{v_{p,g}^1, \dots, v_{p,g}^m\}$  can be generated.

#### *Recombination:*

This recombination operation increases the diversity of the population. Crossover operation is applied to each pair of the target vector  $X_{p,g}$  and its corresponding donor vector  $V_p^g$  to generate a trial vector  $T_p^g = \{t_{p,g}^1, \dots, t_{p,g}^m\}$ . In the basic version, DE ploys the binomial (uniform) crossover defined in Eq. [4]:

$$t_{p,m}^g = \begin{cases} v_{p,m}^g & \text{if } \text{rand}([0,1]) < GR \\ x_{p,m}^g & \text{if any other case} \end{cases} \quad (4)$$

where p=1 ... NP, m= 1 ... n and GR is the crossover rate which is a user-specified constant within the range that controls the fraction of parameter values copied from the donor vector.  $v_{p,m}^g$  is a variable of donor vector,  $x_{p,m}^g$  is a variable of target vector and  $t_{p,m}^g$  is a variable of trial vector.

#### *Election:*

The selection operation is determined by Eq. [5]:

$$X_p^{g+1} = \begin{cases} t_p^g & \text{if } f(t_p^g) \leq f(X_p^g) \\ X_p^g & \text{otherwise} \end{cases} \quad (5)$$

The objective function value of each trial vector  $f(T_p^g)$  is compared to that of its corresponding target vector  $f(X_p^g)$  in the current population. If the trial vector has less or equal objective function value than the corresponding target vector, the trial vector will replace the target vector and enter the population of the next generation. Otherwise, the target vector will remain in the population for the next generation. The above 3 steps are repeated generation after generation until some specific termination criteria are satisfied such as number of iterations or maximum allowed error, which is defined with the cost function.

As highlighted in the study of Martinez-Rico et al. [[18]], the optimization problem covers the objective of minimizing the loss of value. To know this loss of value, the following cost function determined by Eq. [6] is proposed:

$$J = \sum_{\mu=1}^{\mu=Nsamples} ||\vec{Z}_{EISexp}(\overrightarrow{\omega_\mu}) - \vec{Z}(\vec{\rho}, \overrightarrow{\omega_\mu})||^2 \quad (6)$$

where  $\vec{\rho} = [R_1, L_1, R_2, C_1, \alpha_1, R_3, C_2, \alpha_2]$  and  $\overrightarrow{\omega_\mu}$  = angular frequency. This angular frequency vector has 121 different frequencies defined by Nsamples.

According to Eq. [6], it is possible to know the difference between the experimental values and the values of the proposed battery model. Both the real and the imaginary parts. The experimental values have been obtained as a function of different frequencies. Instead, the electrochemical impedance spectroscopy (EIS) of the model depends on several parameters, specifically the  $\vec{\rho}$  parameters. These parameters, as mentioned in the differential evolution algorithm part, are the ones that must be optimized to achieve the least possible loss of value.

#### **Test definition**

Authors have made 36 EIS experimental test for each battery model after 5 months: 6 monthly tests with 6 SoC. Tests have 121 frequencies with a logarithmic span, see Table 1.

*Table 1. Test Frequencies.*

Highest frequency	Lowest frequency	Units
10000	0.01	Hertz

## **3. RESULTS AND DISCUSSION**

### Identification process setup

Authors studied different optimization algorithms, in order to try to match a parameter set generated spectra to experimental spectrum. This issue has been explained in Eq. [9] and the corresponding frequencies are shown in Table 1. Differential Evolution algorithm options are included in Table 2.

*Table 2. Differential Evolution algorithm options*

Agents number	F option	CR option	Number of iterations <sup>1</sup>
10000	1	0.5	0.011

<sup>1</sup> Optimization options do not change much parameter identification results

In order to improve the convergence, Differential Evolution algorithms are normalized between 0 and 1. In the second step, we have made the same normalization in order to improve the convergence. Identification of parameters in order to set maximum and minimum normalized values is included in Table 3. These parameters set values have been proposed by the experience obtained from test data.

Parameters shown in Table 3 are the outputs of the proposed identification process. These parameters have to be set in order to match the experimental electrochemical impedance spectroscopy (EIS) data of tests and, usually, are identified by commercial standard software. This software needs high human expertise orientation in order to obtain reliable matches with the experimental EIS data tests.

*Table 3. Identification parameter set's maximum and minimum values applied in normalization*

Identification Parameter	Maximum value	Minimal value	Units
R1	0.01	0.001	Ohms
R2	0.02	0.002	Ohms
R3	1	0.001	Ohms
C1	12	1	F
$\alpha_1$	0.9	0.4	-
C2	300	40	F
$\alpha_2$	0.8	0.4	-
L1	$10^{-6}$	$10^{-8}$	H <sup>3</sup>

### Identified parameter sets

Figure 3 shows an EIS experiment results. This Nyquist diagram illustrates three different regions, the first one denoted by Region 1 has the contribution of the inductance and the ohmic resistance (L1 and R1 parameters, see Table 4), with high frequency samples. The second one (Region 2) is related to the first CPE element parallel to R2 identification parameter, see Table 4. It is very usual to characterize a circular EIS spectrum with these two elements. The third region is characterized as a larger circular spectrum. Due to this reason, a characterization with a second CPE element parallel to R3 has been made. In total, 36 experiments were carried out and all spectra show similar behavior with these three different regions. Consequently, the equivalent circuit schema described in Figure 1 was proposed.

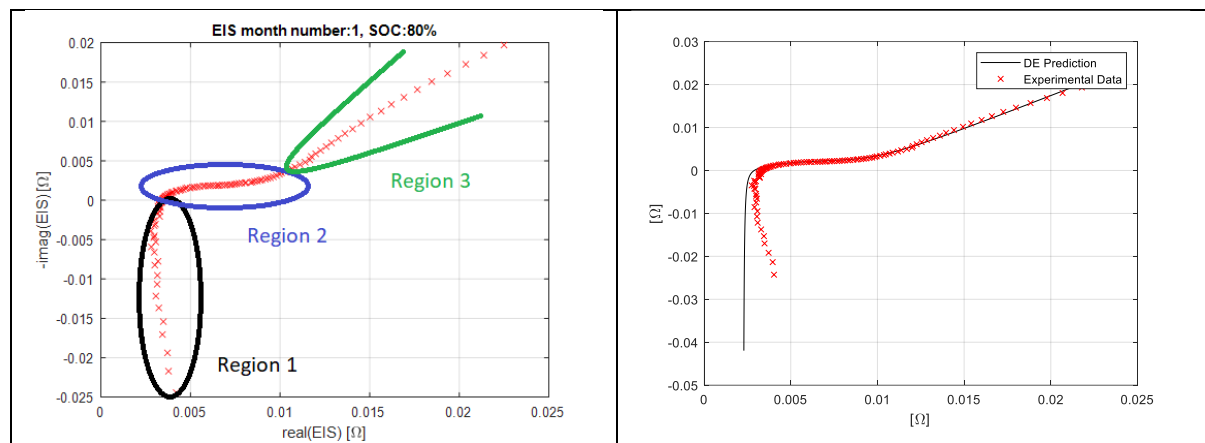


Figure 3. left side: 80% SoC EIS experiment in first iteration (Pristine Battery), right side: Comparison between DE optimization-based identification and experimental data at 80% SoC

Figure 3, right side, represents the same experiment presented in Figure 3 left side, with identification results added to the experiment samples represented by red crosses. Red line represents the DE optimization-based identification results.

#### 4. CONCLUSIONS

In summary, we propose the use of an automatic algorithm to identify in an automatic procedure. Usually, the conventional identification procedures need human expert support to guide the identification results. The proposed algorithm allows in-operando monitoring of the variation of the equivalent circuit parameters that will be used to further estimate the battery state of health (SoH) and state of charge (SoC) based on correlation with the experimental aging data. Authors have proposed a reliable alternative in order to improve the parameter identification time of an Electrochemical Impedance Spectroscopy using a swarm optimization algorithm. In that way, the best characteristics of each algorithm are applied in the identification process.

Meanwhile, by demonstrating that the proposed algorithm is robust enough there is still room for improvement with further experimental data to be further gathered as well as from post-mortem diagnosis data. The improvements will be based on the development of a complete SoH Lead-Acid battery supervisor which will gather both proposed improved algorithm and failure identification mode, manufacturer specifications and the possibility to apply preventive and corrective actions to the complete battery system. This would not only be a significant advance for the field of predicting battery performance, but also will be key to the development of remote monitoring systems.

#### ACKNOWLEDGMENT

The authors would like to express their gratitude to CIC energiGUNE for the facilities and to Bebare innovation team for their technical and scientific contributions to this work. Special thanks should also be expressed to the Torres Quevedo (PTQ) 2019 Aid from the State Research Agency, within the framework of the State Program for the Promotion of Talent and its Employability in R + D + i, Ref. PTQ2019-010787 /AEI/10.13039/501100011033.

#### REFERENCES

- [1] C. Aksakal and A. Sisman, "On the Compatibility of Electric Equivalent Circuit Models for Enhanced Flooded Lead Acid Batteries Based on Electrochemical Impedance Spectroscopy," *Energies*, vol. 11, no. 1, Art. no. 1, Jan. 2018, doi: 10.3390/en11010118.
- [2] D. Andre, C. Appel, T. Soczka-Guth, and D. U. Sauer, "Advanced mathematical methods of SOC and SOH estimation for lithium-ion batteries," *J. Power Sources*, vol. 224, pp. 20–27, Feb. 2013, doi: 10.1016/j.jpowsour.2012.10.001.
- [3] J. Badeda, M. Kwiecien, D. Schulte, and D. Sauer, "Battery State Estimation for Lead-Acid Batteries under Float Charge Conditions by Impedance: Benchmark of Common Detection Methods," *Appl. Sci.*, vol. 8, no. 8, Art. no. 8, Aug. 2018, doi: 10.3390/app8081308.
- [4] B. Culpin and D. A. J. Rand, "Failure modes of lead/acid batteries," *J. Power Sources*, vol. 36, no. 4, Art. no. 4, Dec. 1991, doi: 10.1016/0378-7753(91)80069-A.
- [5] P. Dost and C. Sourkounis, "Generalized Lead-Acid based Battery Model used for a Battery Management System," *Athens J. Technology Eng.*, vol. 3, no. 3, Art. no. 3, Aug. 2016, doi: 10.30958/ajte.3-3-4.
- [6] M. Kwiecien *et al.*, "Variation of Impedance in Lead-Acid Batteries in the Presence of Acid Stratification," *Appl. Sci.*, vol.

- 8, no. 7, Art. no. 7, Jun. 2018, doi: 10.3390/app8071018.
- [7] B. B. McKeon, J. Furukawa, and S. Fenstermacher, “Advanced Lead–Acid Batteries and the Development of Grid-Scale Energy Storage Systems,” *Proc. IEEE*, vol. 102, no. 6, Art. no. 6, Jun. 2014, doi: 10.1109/JPROC.2014.2316823.
- [8] “c\_861350-l\_1-k\_roadmap-23march.pdf.”
- [9] B. K. Chaturvedi 3 Neeta Khare 2, P. K., “Fpga Design Scheme For Battery Soc & Soh Algorithms For Advanced Bms,” Jul. 2017, doi: 10.5281/ZENODO.827494.
- [10] W.-Y. Chang, “The State of Charge Estimating Methods for Battery: A Review,” *ISRN Appl. Math.*, vol. 2013, pp. 1–7, 2013, doi: 10.1155/2013/953792.
- [11] J. Rivera-Barrera, N. Muñoz-Galeano, and H. Sarmiento-Maldonado, “SoC Estimation for Lithium-ion Batteries: Review and Future Challenges,” *Electronics*, vol. 6, no. 4, Art. no. 4, Nov. 2017, doi: 10.3390/electronics6040102.
- [12] R. Zhang *et al.*, “State of the Art of Lithium-Ion Battery SOC Estimation for Electrical Vehicles,” *Energies*, vol. 11, no. 7, Art. no. 7, Jul. 2018, doi: 10.3390/en11071820.
- [13] S. M. Lukic, Jian Cao, R. C. Bansal, F. Rodriguez, and A. Emadi, “Energy Storage Systems for Automotive Applications,” *IEEE Trans. Ind. Electron.*, vol. 55, no. 6, pp. 2258–2267, Jun. 2008, doi: 10.1109/TIE.2008.918390.
- [14] S. Piller, M. Perrin, and A. Jossen, “Methods for state-of-charge determination and their applications,” *J. Power Sources*, vol. 96, no. 1, Art. no. 1, Jun. 2001, doi: 10.1016/S0378-7753(01)00560-2.
- [15] I. Baccouche, S. Jemmali, A. Mlayah, B. Manai, and N. E. B. Amara, “Implementation of an Improved Coulomb-Counting Algorithm Based on a Piecewise SOC-OCV Relationship for SOC Estimation of Li-Ion Battery,” p. 10.
- [16] R. Storn and K. Price, “Differential Evolution: A Simple and Efficient Adaptive Scheme for Global Optimization over Continuous Spaces,” *J. Glob. Optim.*, no. Journal Article, 1995.
- [17] I. Aramendia, E. Zulueta, D. Teso-Fz-Betono, A. Saenz-Aguirre, and U. Fernandez-Gamiz, “Modeling Of Motorized Orthosis Control,” *Appl. Sci.-Basel*, vol. 9, no. 12, 2019, [Online]. Available: <https://doi.org/10.3390/app9122453>.
- [18] J. Martinez-Rico, E. Zulueta, U. Fernandez-Gamiz, I. R. de Argandona, and M. Armendia, “Forecast Error Sensitivity Analysis For Bidding In Electricity Markets With A Hybrid Renewable Plant Using A Battery Energy Storage System,” *Sustainability*, vol. 12, no. 9, 2020, [Online]. Available: <https://doi.org/10.3390/su12093577>.
- [19] J. C. Lagarias, J. A. Reeds, M. H. Wright, and P. E. Wright, “Convergence properties of the Nelder–Mead simplex method in low dimensions,” *SIAM J. Optim.*, vol. 9, no. 1, pp. 112–147, 1998.



# MULTIPURPOSE SENSOR DESIGNED TO MONITOR ELECTROCHEMICAL PARAMETERS OF 12 V LEAD ACID BATTERY BLOCKS

Javier Olarte

Centro de Investigación Cooperativa de Energías Alternativas (CIC energiGUNE), Basque Research and Technology Alliance (BRTA)/Bcare/University of the Basque Country, Vitoria, Spain, jolarte@cicenergigune.com, ORCID: 0000-0003-2632-9974

Jaione Martínez de Ilarduya

Bcare, Vitoria, Spain, jmartinez@bcaremb.com, ORCID: 0000-0001-8304-3388

Ekaitz Zulueta

University of the Basque Country, Vitoria, Spain, ekaitz.zulueta@ehu.eus, ORCID: 0000-0001-6062-9343

Raquel Ferret

Centro de Investigación Cooperativa de Energías Alternativas (CIC energiGUNE), Basque Research and Technology Alliance (BRTA), Vitoria, Spain, rferret@cicenergigune.com, email address, ORCID: 0000-0002-7552-6467

Unai Fernández-Gámiz

University of the Basque Country, Vitoria, Spain, unai.fernandez@ehu.eus, ORCID: 0000-0001-9194-2009

Jose Manuel Lopez-Guede

University of the Basque Country, Vitoria-Gasteiz, Spain, jm.lopez@ehu.eus, ORCID: 0000-0002-5310-1601

*Cite this paper as:* Olarte, J., Martínez de Ilarduya, J., Zulueta, E., Ferret, R., Fernández-Gámiz, U., Lopez-Gude, JM, Multipurpose sensor designed to monitor electrochemical parameters of 12 V lead acid battery blocks. 9<sup>th</sup> Eur. Conf. Ren. Energy Sys. 21-23 April 2021, Istanbul, Turkey

**Abstract:** This work presents the results of experimental analysis of the data correlation between an Electrochemical Impedance Spectroscopy lab testing equipment and a new design multipurpose sensor designed to monitor electrochemical parameters of a 12 V Lead-Acid battery block. The proposed sensor design integrates a basic form of impedance measurement that complementary with conventional temperature, voltage and current data allows the implementation of innovative State-of-Health strategies that can be feasibly integrated into existing energy storage solutions at reasonable cost. Additionally, the proposed sensor design allows active balancing of voltage dispersion during the charge process of Lead-Acid battery blocks. The sensor modularity and small size allows easy direct integration into different commercial cells formats and the proposed methodology could be used for other application domains from automation to stationary energy storage. Future steps will be done to perform the final adjustment of the sensor in all the range of frequencies of the impedance spectra and perform similar analysis and calibration in other electrochemical storage technologies.

**Keywords:** Multimodal sensor, Electrochemical Impedance Spectrometry, State of Charge, State of Health, Lead acid batteries

© 2021 Published by ECRES

Nomenclature	
SoH	State of Health
SoC	State of Charge
OCV	Open Circuit Voltage
EIS	Electrochemical Impedance Spectroscopy
VRLA	Valve Regulated Lead-Acid

VTZ GEIS	Name given for the multipurpose sensor Galvanostatic Electrochemical Impedance Spectroscopy
-------------	--

## 1. INTRODUCTION

Implementation of the new design multipurpose sensor in the 12 V lead-acid battery blocks will allow to apply an on-line method of measuring the State of Health (SoH) and State of Charge (SoC) that can be easily and inexpensively included in current battery systems. In parallel with the utilization of the multipurpose sensor, there should be a prior identification of State-of-Health and State-of-Charge determination algorithms based on characterization and modelling technology [1],[2]. Moreover, the device could implement voltage cell balancing that could additionally improve the life expectancy of a series strings of battery cells as suggested by Krein et Balog [3].

In the last decade, many efforts have been devoted to develop reliable and robust State-of-Health and State-of-Charge determination methods. Several authors have reported different ways to estimate this SoC and SoH variables of the batteries, which can be divided in different categories as direct measurements, electrical and electrochemical models and adaptive and machine learning methods [4],[5],[6],[7], independently of the target technology. For example, Kumar et al. [4] mentioned the problematic of SoC and SoH identification in batteries oriented to its implementation in vehicles, which is still not accurate enough, while they reviewed different SoC and SoH indication algorithms.

Electrochemical Impedance Spectroscopy is one of the methods that can be used for real time prediction by interpreting parameters from the spectra [8],[9],[10]. However, initially, the electrochemical model is difficult to be implemented and it is very specific for each technology, see the study of Piller et al. [11]; thus, it is required to develop specific protocols to extract EIS measurements for each electrochemical energy storage technology, Meddings et al. [12]. Regarding adaptive methods based on algorithms, there are some other approaches based in time series [13] or fractional analysis [14]. Another widely held approach are the genetic algorithm-based optimization developed by Ramos et al. [15] or neural networks-based approaches presented in Chun et al. [16]. From all mentioned options, it is necessary to identify those methods that are possible to be directly implemented at real operation at stationary application in order not to interfere in operating mode, as Shahriari and Farrokhi [17]. In that work, a method to measured SoC and SoH online, without the requirement of disconnect the battery from the circuit is developed. However, the battery was obliged to be continuously charging or discharging, among others drawbacks. Furthermore, Khare et al. [18] proposed an online method to estimate the SOH of hybrid electric vehicles from various battery parameters such as the internal resistance, terminal voltage and specific gravity of the battery, but differs from our target application. Sedighfar and Moniri [19] also developed an online method for the estimation of the SoC and the SoH of the Valve Regulated Lead–Acid (VRLA) batteries, although they are oriented to Electric-Vehicles application. According to Marrero et al. [20], the integration of sensors, development and optimization of Battery Management System gain much importance in order to create battery systems that can increase life expectancy or availability, and not only focused in Li-ion batteries as majority of researchers are doing, see also [21],[22].

The current study presents an experimental analysis of the data correlation between an Electrochemical Impedance Spectroscopy (EIS) lab testing equipment and a new design multipurpose sensor. That sensor is designed to monitor electrochemical parameters of a 12 V lead acid battery block and integrates a basic form of impedance measurement that allows the implementation of innovative State-of-Health strategies that can be feasibly integrated into existing energy storage solutions at reasonable cost. Therefore, the objective of this work is to present the new multipurpose sensor that allows its direct integration in each 12V block and continuous monitoring of Lead-acid battery blocks, and take the first steps towards its implementation in more electrochemical storage technologies and applications. The measurements of electrochemical parameters done by the sensor will be analyzed by means of diagnosis module also integrated in the whole energy storage system with the rectifier.

## 2. MATERIALS AND METHODS

### A 12 V multimodal sensor for a lead acid battery

The proposed VTZ sensor design integrates a basic form of impedance measurement (Z) complementary with conventional temperature (T) and, voltage (V). The sensor is easily integrated in a series of sensors associated to a battery bank or string for higher voltages that could easily be integrate with a higher-level diagnosis module controller that will monitor the battery string current. It is necessary to highlight that VTZ sensor is not a portable

measurement device, but an integrated device for battery blocks and modules to improve their maintenance and SOC and SOH prediction.

The motivation behind developing a multipurpose sensor designed to monitor electrochemical parameters of a 12 V lead acid battery block was to facilitate the real-time data monitoring for a stationary application in order to increase the battery bank life expectancy by improving the battery management strategy following the manufacturers recommendations. The sensors are installed in the complete bank of lead acid batteries together with a diagnosis module. The precise battery block voltage will allow monitoring of the voltage dispersion to optimize the frequency of equalizing charge. Monitoring not only the ambient temperature of the battery banks but every individual block will improve the floating voltage compensation and finally, a continuous monitoring of the Electrochemical Impedance Spectrometry will offer reliable information of the degradation and failures modes of the battery over its lifetime. In addition to the monitor voltage, temperature and impedance, the VTZ allows active balancing of a series of cells that allows increasing the life expectancy of the complete string as presented by Krein and Balog [3].

### Experiment setup

Different High Temperature Lead-Acid batteries (12 V battery block – 80 Ah) from the same manufacturer, oriented to back-up application, are used to develop the following experimental work. On one hand, Electrochemical Impedance Spectroscopy (EIS) measurements are recorded by means of Gamry 3000 battery tester and on the other hand, EIS spectra is done by two different types of VTZ sensors settings. The main difference between these sensors is the resistance which regulates the current pulses in the impedance measurement,  $25 \Omega$  and  $100 \Omega$ .

### 3. RESULTS AND DISCUSSION

The analysis of the EIS extracted from the sensor will be done via diagnosis module with smart electrochemical SOH model estimator integrated. Firstly, EIS spectra will be adjusted to a specific Electrical Equivalent Circuit (EEC) in order to extract independent variables. Figure 1 illustrates the equivalent circuit model proposed by authors, since all experiments show an inductive behavior at high frequencies and circular shape at medium frequencies and another larger slightly circular shape spectrum at lower frequencies. This EEC is selected with constant phase elements in order to adjust the experimental data. Non-ideal capacitive behaviors of an electrode taken into account, so a constant phase element (CPE) is used, which is a capacitor with a leakage parameter of  $\alpha$  (if this parameter is 1, the element becomes a pure capacitor) [26]. From the adjustment, independent variables as ohmic resistance,  $R_2$ ,  $R_3$ , CPE1-T, CPE1-P, CPE2-T, CPE2-P and their variations will be analyzed during the useful life of the battery. Mostly, the sensor assesses values qualitatively, not quantitatively, and the analysis is based on the variations of each of the independent variables extracted from the EIS.

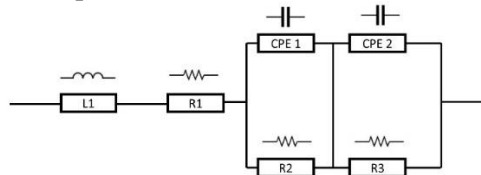


Figure 1. Equivalent proposed EIS circuit model

#### 1 kHz calibration process

Two different types of VTZ sensors have been tried in order to calibrate the impedance measurements ( $25 \Omega$  and  $100 \Omega$ ). Although the sensor provides the full range of the impedance spectrum from  $10 \text{ mHz}$  to  $7 \text{ kHz}$  for this experiment we have sought to calibrate the sensor against the measurements of the Gamry 3000 laboratory instrument, for a fixed value of  $1 \text{ kHz}$  in order to validate the calibration process based on the Rsense setting. According to Nguyen, several commercially available battery testers diagnose battery aging by measuring impedance of batteries at  $1 \text{ kHz}$  on the basis of the fact that the real part of the complex impedance of a battery at  $1 \text{ kHz}$  is almost equal to its ohmic resistance [27],[28]. In the frequency range between  $1 \text{ kHz}$  and  $10 \text{ kHz}$ , generally, only the inductance (L) and the internal resistance ( $R_i$ ) are important because the other elements of the equivalent circuit have the double-layer capacitance in parallel, which is nearly ideally conducting in this frequency range. This leads to the simplified equivalent circuit based on an inductance and ohmic resistance [29].

Regarding the  $100 \Omega$  sensor (Figure 2), the deviation in the Zreal is, approximately,  $\pm 0.0154 \Omega$ , while the deviation in the Zim is, approximately,  $\pm 0.0111 \Omega$  by observing Gamry battery tester and sensor measurements (Table 1).

The main deviation observed is at lower frequencies, in which charge transfer-diffusion stage differs in a larger stage.

*Table 1. Resistances measured at 1 kHz and voltage parameter variation before and after EIS measurements with 100 Ω sensor.*

	Sensor VTZ – 100 Ohm	Reference Gamry
1 kHz Z real (Ω)	0.0052	0.0027
1 kHz Z imaginary (Ω)	0.0026	-0.0003
Ordinate axis cut (Zimg = 0)	0.0052	0.0027
Initial voltage (V)	12.7236	12.8334
Final voltage (V)	12.6927	12.8398

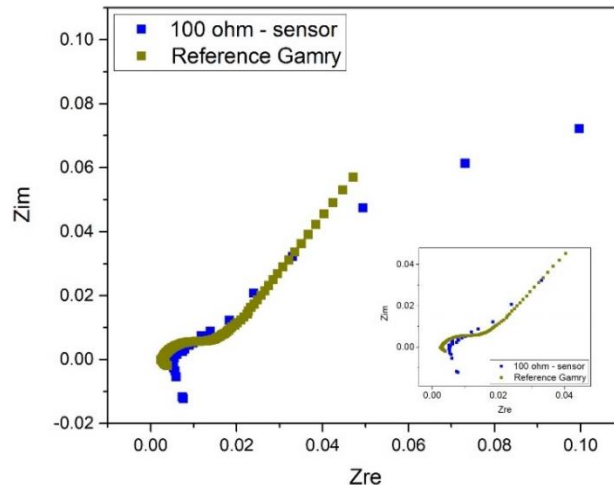


*Figure 2. Electrochemical Impedance Spectroscopy spectra from Gamry 3000 battery tester and 100 Ω sensor.*

Regarding the 25 Ω sensor (Figure 3), the deviation in the Zreal is, approximately,  $\pm 0.0111 \Omega$ , while the deviation in the Zim is, approximately,  $\pm 0.0053 \Omega$  by observing Gamry battery tester and sensor measurements (Table 2). The main deviation is observed at lower frequencies, in which charge transfer-diffusion stage differs in a larger stage.

*Table 2. Resistances measured at 1 kHz and voltage parameter variation before and after EIS measurements with 25 Ω sensor*

	Sensor VTZ – 25 Ohm	Reference Gamry
1 kHz Z real (Ω)	0.0046	0.0027
1 kHz Z imaginary (Ω)	0.0013	-0.0003
Ordinate axis cut (Zimg = 0)	0.0049	0.0027
Initial voltage (V)	12.4371	12.8334
Final voltage (V)	12.3852	12.8398

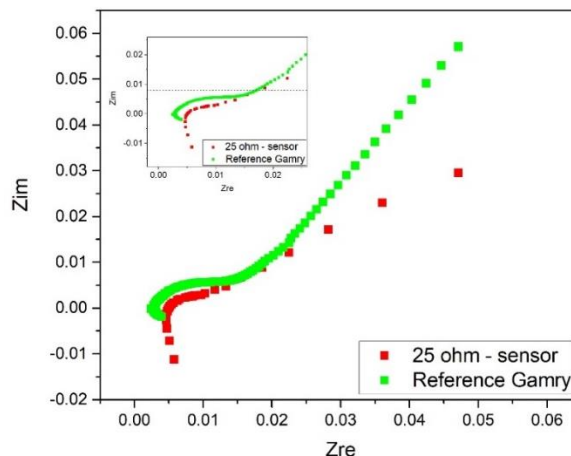


*Figure 3. Electrochemical Impedance Spectroscopy spectra from Gamry 3000 battery tester and 25 Ω sensor.*

The voltage values are included in the tables (Table 1 and Table 2) as they correspond to the starting initial voltage value before the impedance measurement and the final voltage value after the impedance measurement with both Gamry battery tester and the sensors, in order to ensure that the sensor is not drawing a large percentage of power from the battery. For all the cases, it is observed that the voltages remain stable during the measurement; thus, the functionality and adequate consumption of the sensor is assured.

Spite of having more dispersion of values at lower frequencies, it is necessary to take into account that the information given by this sensor will be evaluated in contrast with more historical data of the same setup and battery (via diagnosis module), which is going to provide information about the state of health of the battery, as presented by Kiel et al. [30].

By applying current excitation pulses of 500 mA (Figure 3), instead of 100 mA (Figure 2), the measurements have less associated noise at higher frequencies and are more appropriate. For the final version of the sensor, current pulse excitation close to 500 mA is selected.

In general, the accuracy of the VTZ is less than the one of the Gamry 3000 battery tester. However, as it has been mentioned the impedance spectrum itself will not be evaluated, but the evolution of this impedance spectrum and its independent variables.

The incorporation of these sensors, in order to measure voltage, current, temperature and EIS to further analyze the State of Health and State of Charge, will allow to minimize performing capacity test in a predictive maintenance mode. Based on the research that is being carried out in said batteries, electrochemical models are being developed that correlate the parameters extracted from the adjustment of the impedance spectrum together with the mentioned parameters and the state of charge and health parameters of the batteries. Therefore, the battery will not suffer from continuous unnecessary cycle aging and will not affect its useful life.

#### 4. CONCLUSIONS

The VTZ sensor has been designed to monitor in real time the temperature, voltage and impedance parameters of a 12V lead-acid battery. The calibration process by contrast with the Gamry laboratory instrument has allowed to adjust with good precision the impedance value at 1kHz. Subsequently, repeatability tests have been carried out with a series of 10 blocks, obtaining admissible dispersion values compared to the errors of a laboratory instrument. The sensor will allow monitoring of impedance variations throughout the life of the battery and correlating these variations with the Loss of Capacity from experimental data. Although the sensor has been calibrated for a 100 Ah capacity, it could be used for other capacities and even different battery technologies like lithium-ion, vented lead acid or NiCd following the proposed adjustment procedure. Although in the proposed set up only 1kHz was targeted, since the sensor offers the possibility of measuring entire spectrum of impedance other correlations might be investigated to monitor SoC and SoH as proposed by Meddings et al. [12], for lithium chemistries or Kiel et al. [30] for lead acid chemistries. Additionally, the proposed sensor design allows active balancing of voltage dispersion during the charge process. Regarding experimental results presented in the article, future steps will be done to perform the final adjustment of the VTZ in all the range of frequencies of the EIS spectra and perform similar analysis and calibration in other electrochemical storage technologies. In addition, the final implementation of the sensor in the lead-acid battery blocks will be developed in order to optimize the design of the final product.

#### ACKNOWLEDGMENT

The authors would like to express their gratitude to CIC energiGUNE for the facilities and to Bcare innovation team for their technical and scientific contributions to this work. In addition, special thanks should also be expressed to the Torres Quevedo (PTQ) 2019 Aid from the State Research Agency, within the framework of the State Program for the Promotion of Talent and its Employability in R + D + i, Ref. PTQ2019-010787 /AEI/10.13039/501100011033.

#### REFERENCES

- [1] J. Olarte, Ekaitz Zulueta, R. Ferret, Erol Kurt, J. Martínez de Ilarduya, J. M. Lopez-Gude, High temperature lead acid battery SOC and SOH characterization based on electrochemical impedance spectroscopy data. 8th Eur. Conf. Ren. Energy Sys. 24-25 August 2020, Istanbul, Turkey.
- [2] J. Olarte, S. Romo, J. Martínez de Ilarduya, R. Ferret, R. Pacios, E. Bekaert, E. Zulueta, F. Pazos, X. Ibarroondo, N. Alonso, VII Congreso Smart Grids, 2020.
- [3] P. T. Krein and R. S. Balog, Life extension through charge equalization of lead-acid batteries, *IEEE*, pp. 516–523, 2002.
- [4] B. Kumar, N. Khare, and P.K. Chaturvedi, Fpga Design Scheme For Battery Soc & SoH Algorithms For Advanced BMS, *IJESRT*, vol. 6.7, pp. 263–79, Jul. 2017, doi: 10.5281/ZENODO.827494.

- [5] J. Rivera-Barrera, N. Muñoz-Galeano, and H. Sarmiento-Maldonado, SoC Estimation for Lithium-ion Batteries: Review and Future Challenges, *Electronics*, vol. 6, no. 4, p. 102, Nov. 2017, doi: 10.3390/electronics6040102.
- [6] W.-Y. Chang, The State of Charge Estimating Methods for Battery: A Review, *ISRN Appl. Math.*, vol. 2013, pp. 1–7, 2013, doi: 10.1155/2013/953792.
- [7] R. Zhang *et al.*, State of the Art of Lithium-Ion Battery SOC Estimation for Electrical Vehicles, *Energies*, vol. 11, no. 7, p. 1820, Jul. 2018, doi: 10.3390/en11071820.
- [8] E. Karden, S. Buller, and R. W. D. Doncker, A method for measurement and interpretation of impedance spectra for industrial batteries, *J Power Sources*, vol. 85, pp. 72–78, 2000.
- [9] P. Keil, K. Rumpf, and A. Jossen, Thermal Impedance Spectroscopy for Li-Ion Batteries with an IR Temperature Sensor System, Barcelona, 2013, p. 11.
- [10] L. H. J. Rajmakers, D. L. Danilov, J. P. M. van Lammeren, M. J. G. Lammers, and P. H. L. Notten, Sensorless battery temperature measurements based on electrochemical impedance spectroscopy, *J. Power Sources*, vol. 247, pp. 539–544, Feb. 2014, doi: 10.1016/j.jpowsour.2013.09.005.
- [11] S. Piller, M. Perrin, and A. Jossen, Methods for state-of-charge determination and their applications, *J. Power Sources*, vol. 96, no. 1, pp. 113–120, Jun. 2001, doi: 10.1016/S0378-7753(01)00560-2.
- [12] N. Meddings *et al.*, Application of electrochemical impedance spectroscopy to commercial Li-ion cells: A review, *J. Power Sources*, vol. 480, p. 228742, Dec. 2020, doi: 10.1016/j.jpowsour.2020.228742.
- [13] S. M. M. Alavi, C. R. Birk, and D. A. Howey, Time-domain fitting of battery electrochemical impedance models, *J. Power Sources*, vol. 288, pp. 345–352, Aug. 2015, doi: 10.1016/j.jpowsour.2015.04.099.
- [14] C. Zou, L. Zhang, X. Hu, Z. Wang, T. Wik, and M. Pecht, A review of fractional-order techniques applied to lithium-ion batteries, lead-acid batteries, and supercapacitors, *J. Power Sources*, vol. 390, pp. 286–296, Jun. 2018, doi: 10.1016/j.jpowsour.2018.04.033.
- [15] P. M. Ramos and F. M. Janeiro, Gene expression programming for automatic circuit model identification in impedance spectroscopy: Performance evaluation, *Measurement*, vol. 46, no. 10, pp. 4379–4387, Dec. 2013, doi: 10.1016/j.measurement.2013.05.011.
- [16] H. Chun, J. Kim, and S. Han, Parameter identification of an electrochemical lithium-ion battery model with convolutional neural network, *IFAC-Pap.*, vol. 52, no. 4, pp. 129–134, 2019, doi: 10.1016/j.ifacol.2019.08.167.
- [17] M. Shahriari and M. Farrokhi, Online State-of-Health Estimation of VRLA Batteries Using State of Charge, *IEEE Trans. Ind. Electron.*, vol. 60, no. 1, pp. 191–202, Jan. 2013, doi: 10.1109/TIE.2012.2186771.
- [18] N. Khare, S. Chandra, and R. Govil, Statistical modeling of SoH of an automotive battery for online indication, in *INTELEC 2008 - 2008 IEEE 30th International Telecommunications Energy Conference*, San Diego, CA, Sep. 2008, pp. 1–7, doi: 10.1109/INTLEC.2008.4664086.
- [19] A. Sedighfar and M. R. Moniri, Battery state of charge and state of health estimation for VRLA batteries using Kalman filter and neural networks, in *2018 5th International Conference on Electrical and Electronic Engineering (ICEEE)*, Istanbul, May 2018, pp. 41–46, doi: 10.1109/ICEEE2.2018.8391298.
- [20] D. Marrero and A. Su, Extending the Battery Life of the ZigBee Routers and Coordinator by Modifying Their Mode of Operation, p. 22, 2020.
- [21] S. Novais *et al.*, Internal and External Temperature Monitoring of a Li-Ion Battery with Fiber Bragg Grating Sensors, *Sensors*, vol. 16, no. 9, p. 1394, Aug. 2016, doi: 10.3390/s16091394.
- [22] V. Mateev, I. Marinova, and Z. Kartunov, Gas Leakage Source Detection for Li-Ion Batteries by Distributed Sensor Array, *Sensors*, vol. 19, no. 2900, p. 14, 2019, doi: doi:10.3390/s19132900.
- [23] M. Barreiros dos Santos *et al.*, Portable sensing system based on electrochemical impedance spectroscopy for the simultaneous quantification of free and total microcystin-LR in freshwaters, *Biosens. Bioelectron.*, vol. 142, p. 111550, Oct. 2019, doi: 10.1016/j.bios.2019.111550.
- [24] T. Luo, L. Li, V. Ghorband, Y. Zhan, H. Song, and J. B. Christen, A portable impedance-based electrochemical measurement device, in *2016 IEEE International Symposium on Circuits and Systems (ISCAS)*, Montréal, QC, Canada, May 2016, pp. 2891–2894, doi: 10.1109/ISCAS.2016.7539197.
- [25] Z. Jiang *et al.*, Development of a Portable Electrochemical Impedance Spectroscopy System for Bio-Detection, *IEEE Sens. J.*, vol. 19, no. 15, p. 9, 2019.
- [26] C. Aksakal and A. Sisman, On the Compatibility of Electric Equivalent Circuit Models for Enhanced Flooded Lead Acid Batteries Based on Electrochemical Impedance Spectroscopy, *Energies*, vol. 11, no. 1, Art. no. 1, Jan. 2018, doi: 10.3390/en11010118.
- [27] Thanh-Tuan Nguyen, Van-Long Tran, and Woojin Choi, Development of the intelligent charger with battery State-Of-Health estimation using online impedance spectroscopy, in *2014 IEEE 23rd International Symposium on Industrial Electronics (ISIE)*, Istanbul, Turkey, Jun. 2014, pp. 454–458, doi: 10.1109/ISIE.2014.6864656.
- [28] J. Kischkel, VRLA white paper lead acid battery and its internal resistance, p. 11, 2008.
- [29] B. Hariprakash, S. K. Martha, and A. K. Shukla, Monitoring sealed automotive lead-acid batteries by sparse-impedance spectroscopy, *J. Chem. Sci.*, vol. 115, no. 5–6, pp. 465–472, Oct. 2003, doi: 10.1007/BF02708238.
- [30] M. Kiel, D. U. Sauer, P. Turpin, M. Naveed, and E. Favre, Validation of single frequency Z measurement for standby battery state of health determination, in *INTELEC 2008 - 2008 IEEE 30th International Telecommunications Energy Conference*, San Diego, CA, Sep. 2008, pp. 1–7, doi: 10.1109/INTLEC.2008.4664020.



# CELL-SET MODELLING OF AN ACTIVE ROTATING MICROTAB ON A DU91W(2)250 AIRFOIL

Alejandro Ballesteros-Coll

University of the Basque Country (UPV/EHU), Vitoria-Gasteiz, Spain, aballesteros013@ehu.eus, ORCID: 0000-0002-6563-2434

Koldo Portal-Porras

University of the Basque Country (UPV/EHU), Vitoria-Gasteiz, Spain, koldo.portal@ehu.eus, ORCID: 0000-0003-4747-963X

Unai Fernandez-Gamiz

University of the Basque Country (UPV/EHU), Vitoria-Gasteiz, Spain, unai.fernandez@ehu.eus, ORCID: 0000-0001-9194-2009

Iñigo Aramendia

University of the Basque Country (UPV/EHU), Vitoria-Gasteiz, Spain, iñigo.aramendia@ehu.eus, ORCID: 0000-0002-4960-2729

Ekaitz Zulueta

Univ. Basque Country UPV/EHU, Syst Eng & Automat Control Dept, 01006 Vitoria-Gasteiz, Spain, ORCID:  
<https://orcid.org/0000-0001-6062-9343>

Jose Manuel Lopez-Guede

University of the Basque Country (UPV/EHU), Vitoria-Gasteiz, Spain, jm.lopez@ehu.eus, ORCID: 0000-0002-5310-1601

*Ballesteros-Coll, Alejandro, Portal-Porras, Koldo, Fernandez-Gamiz, Unai, Aramendia, Iñigo, Lopez-Gude, J.Manuel. Cell-set modelling of an Active Rotating Microtab on a DU91W(2)250 airfoil. 9<sup>th</sup> Eur. Conf. Ren. Energy Sys. 21-23 April 2021, Istanbul, Turkey*

---

**Abstract:**

Wind turbine optimization plays a significant role on renewable energy generation. The utilization of flow control devices is a noteworthy solution for the mentioned issue. The present work offers a novel way to model these devices for Computational Fluid Dynamics (CFD) simulations, named after the Cell-set model. Basically, this method consists in reusing the cells of an already generated mesh to implement new geometries, without having to compute additional meshing. The user has to introduce the dimensional parameters of the required geometry and then all the cells around the shape are selected and split from the main fluid region. In particular, the current study approaches active rotating microtab modelling on a DU91W(2)250 airfoil. The length of the tabs has been set to 1% of the airfoil chord length, and the microtab rotations range between +5° and -5°. Two dimensional scenarios have been set, with a range of angles-of-attack that starts from 0° to 4°. Physics were based on RANS equations at  $Re = 2 \cdot 10^6$ . Cell-set model results to be an adjustable and flexible tool for active microtab modelling.

---

**Keywords:**

*flow control; aerodynamics; wind turbine; Active Microtab; Cell-set*

---

© 2021 Published by ECRES

---

**Nomenclature**

AoA	Angle-of-attack
c	Airfoil chord length
$\beta$	Microtab angle
CFD	Computational Fluid Dynamics
MT	Microtab

HAWT	Horizontal Axis Wind Turbine
$C_L$	Lift coefficient
$C_D$	Drag coefficient
RANS	Reynolds Averaged Navier Stokes
Re	Reynolds Number

## 1. INTRODUCTION

Wind energy has become an electricity generation key source for the change to a clean and sustainable energy model. Nowadays, improvement of wind turbines is required in order to compete in energy production and cost against the traditional energies. Passive flow control devices, such as microtabs (MT), are introduced in wind turbine blades with the intention of enhancing or optimizing their performance. Numerical simulations by means of Computational Fluid Dynamics (CFD) are a widely used tool to for the optimization of these devices.

This study proposes the implementation of active rotating microtabs which could be directly compared with active microflaps as they follow the same target. Numerous authors have successfully implemented both active and passive microflaps on diverse airfoils. Gerontakos and Lee [1] added an oscillating microflap on a NACA0015 airfoil, and Liu et al. [2] analyzed different active microflap configurations on a NACA0012 airfoil. Regarding the passive microflaps, Kamps et al. [3] added a flexible microflap on the trailing edge of the NACA0010 airfoil, and Friedmann et al. [4] added different microflaps on the NACA0012 airfoil, showing a slight increase on its aerodynamic performance.

Other authors have combined microtabs with other passive flow control devices. Lee and Su [5] and Bofeng et al. [6] implemented a microtab with a gurney flap on its lower surface, and Dam et al. [7] combined a microflap with a microtab. They showed a significant improvement of the lift coefficient and lift-to-drag ratio. Additionally, Bofeng et al. [6] showed a reduction of the vortexes created on the trailing edge.

This manuscript aims to study the effect of the implementation of active microtabs with different angles on a DU91W250 airfoil, using the cell-set modelling technique. The remainder of the manuscript is divided as follows: firstly, an introduction to the Cell-set model is given. Then, the numerical setup is defined. Hereafter, the obtained results are presented and explained. Finally, the main conclusions obtained from this study are provided.

## 2. SECTIONS

### Introduction to the Cell-set model

The present study presents a novel method for flow control device modelling, the Cell-set model. This method was firstly presented in Ballesteros-Coll et al. [8] and was applied and validated for a passive MT implementation on the DU91W(2)250 airfoil in [9]. This model consists in selecting cells to generate a new region, without having to carry out new meshing processes. The selection is based on a predefined geometry in which the cells that are around the mentioned geometry are selected by choosing the ID of each cell. Once a new set of cells (Cell-set) is generated, the fluid region is split and by creating two regions: the previous fluid region without the selected structured elements and the Cell-set region. A wall boundary condition is assigned to the new region. This means that the same equations are applied to the whole of the computational domain (RANS equations). For this study, an active rotating microtab was modelled by using the described method, see Figure 1.

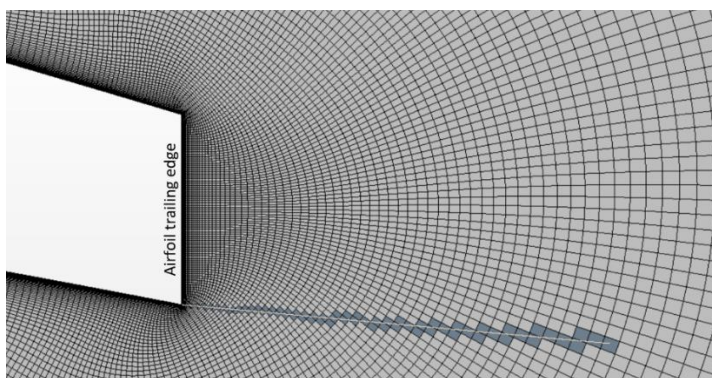


Figure 1. Active Rotating Microtab Cell-set region on the DU91W(2)250 airfoil.

## Numerical simulation setup

The current work presents the Cell-set model as a new way for modelling an active rotating microtab on the trailing edge of a DU91W(2)250 airfoil, which is extracted from one of the most referenced HAWT, the 5MW wind turbine developed by NREL, see Jonkman et al. [10]. All the simulations were launched on the STAR CCM+ commercial code [11].

An O-mesh scheme was the base for the mesh where all the simulations were run. The computational two-dimensional domain was formed by 207740 elements. As Sørensen et al. [12] propose in their study, the mesh radius was set at 32 times the chord length ( $c$ ) of the DU91W(2)250 airfoil, which is 1m (Figure 2). This mesh was compared and validated against experimental data in Fernandez-Gamiz et al. [13].

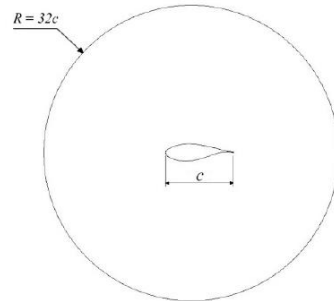


Figure 2. Computational domain, DU91W(2)250 is set in the middle.

All the numerical simulations were based on Reynolds-Averaged Navier-Stokes (RANS) equations, with a  $Re = 2 \cdot 10^6$ . The Shear Stress Transport (SST) method developed by Menter [14] has been implemented. This method is based on a combination of K-omega and K-epsilon models. A free stream velocity value of  $U_\infty = 30$  m/s was introduced. The air density value was set at  $1.204$  kg/m<sup>3</sup> and the dynamic viscosity  $\mu = 1.288 \cdot 10^{-5}$  Pa·s and kinematic viscosity  $\nu = 1.52 \cdot 10^{-5}$  m<sup>2</sup>/s respectively.

The area where the airfoil is located has been refined by applying a second order linear upwind discretization design and the first cell height was set at of  $\Delta z/c = 1.449 \cdot 10^{-6}$  which is normalized with the airfoil chord length. The surface of the profile was set as non-slipping. The refinement on the trailing edge area has been specially selected with the purpose of having an appropriate mesh resolution to implement the Cell-set model, see Ibarra et al. [15] where a dense mesh was generated in order to implement a Vortex Generator (VG) based on the Cell-set method. Figure 3 represents a layout where a detailed enlarged view shows where the MT Cell-set is located. Three different MT positions were defined: +5°, -5°, and 0° from the horizontal line (positive angles are positioned upwards). The angles-of-attack (AoAs) ranged from 0° to 4°, with a step at 2°. A tab length of 1% of  $c$  was introduced, see Table 1.

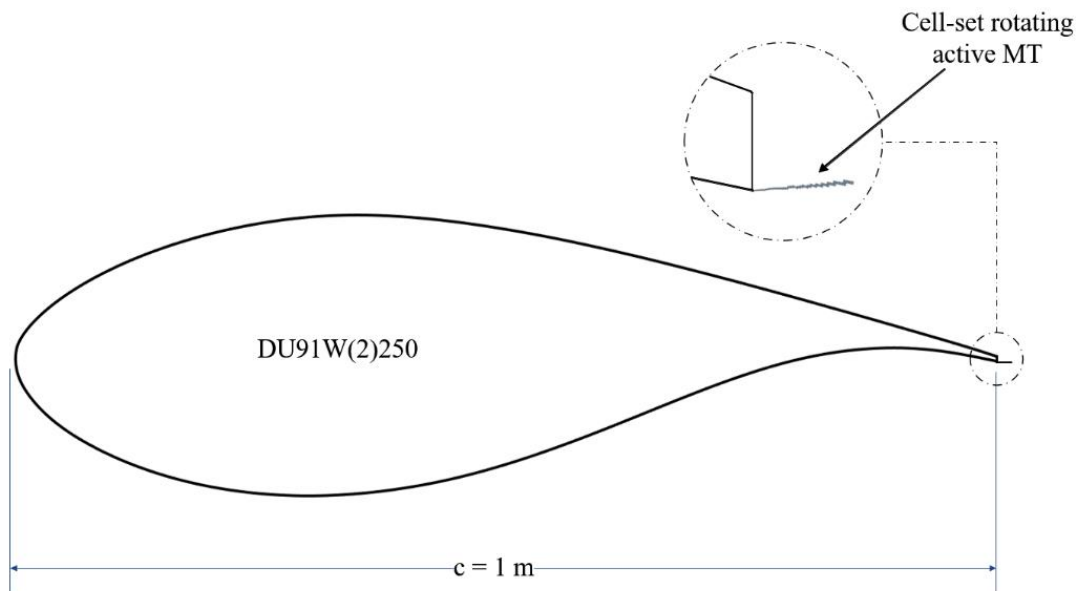


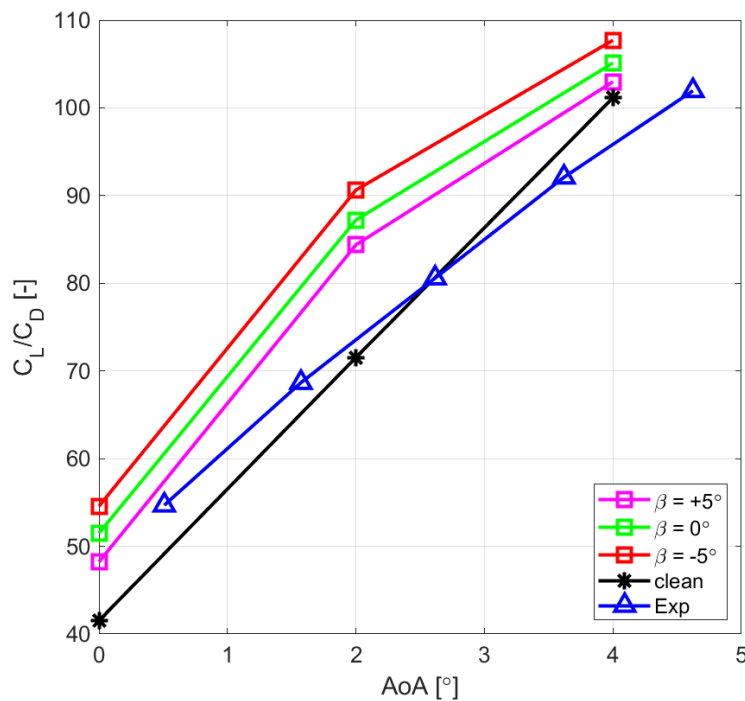
Figure 3. DU91W(2)250 layout with detailed view, Cell-set location.

Table 1. Microtab (MT) configuration cases.

Case	MT position	AoA (°)
MTCSm5_0	-5°	0
MTCSm5_2	-5°	2
MTCSm5_4	-5°	4
MTCS0_0	0°	0
MTCS0_2	0°	2
MTCS0_4	0°	4
MTCSp5_0	+5°	0
MTCSp5_2	+5°	2
MTCSp5_4	+5°	4
MTclean_0	no MT	0
MTclean_2	no MT	2
MTclean_4	no MT	4

## RESULTS

The present section aims to exhibit the results obtained from the numerical simulations on the DU91W(2)250 aerodynamic profile. All the results have been represented by means of the aerodynamic performance ( $C_L/C_D$  lift-to-drag ratio) of the airfoil. Figure 4 shows the main results: the black line with asterisks represents the values obtained for the MT clean\_0, MT\_clean\_2 and MT\_clean\_4 cases, where there is not any Cell-set model implemented, while the blue line with triangular markers shows the values extracted from Timmer et al. [16] where wind tunnel experimental results were obtained for this airfoil without any flow control device. The other three curves display the values for the three different MT Cell-set configurations (square markers): red is for -5°, green for 0°, and magenta for +5°.

Figure 4.  $C_L/C_D$  (Lift-to-drag ratio) values for the different MT configurations vs. CFD clean and experimental values.

The resulting data clearly shows that the MT modelled with the Cell-set model has an effect on the performance curves. These results reveal that negative MT angles (red lines) are the ones which generate the highest  $C_L/C_D$  ratios whereas positive MT angles have reached the lowest ratio values. 0° MT configuration results to be between positive and negative MT orientations. Despite that, all the MT implementations with the Cell-set model are over the clean profile curves (CFD and experimental). The maximum  $C_L/C_D$  ratio value of 107.71 was reached at 4° of AoA with the MTCSm5\_4 configuration.

## CONCLUSIONS

The present work is focused on the utilization of a novel method for flow control device modelling, the Cell-set model. Specifically, for this case active rotating microtabs have been modelled. The Cell-set model results to be a flexible and versatile way to implement new flow control devices on meshes that have been created for other purposes. The model reuses the elements in which the geometry would be located and splits the fluid region in order to generate a new wall region. Subsequently, mesh refinement plays a high role for the implementation of this model as the resolution of the region that is being created will be based on the mesh. Additionally, the model permits straightforward geometrical modifications and hence, meshing calculation times could be saved.

The DU91W(2)250 airfoil has been used for the numerical simulations. In order to represent the effect of an active rotating MT implementation by means of the Cell-set model, a range of AoAs has been simulated for three different microtab positions (-5°, 0°, +5°) as means to represent the movement of the tab. The tab length has been set at 1% of the airfoil chord length. Resulting data shows that the MT movements represent coherent performance curve changes, where the MT that is orientated at -5° is the one that reaches the highest  $C_L/C_D$  values. All the MT configurations perform at upper ratios than the clean cases: both experimental and CFD. However, as the positive MT angles show a tendency to reduce the aerodynamic performance, it can be considered that for MT angles >+5°, the performance curve could be resolved underneath the clean value.

Future work is being developed on the Cell-set matter. Both active and passive device implementation in three-dimensional scenarios turn out to be a source of interest in terms of wind turbine optimization.

## ACKNOWLEDGMENT

The authors are grateful to the government of the Basque Country and the University of the Basque Country UPV/EHU through the SAIOTEK (S-PE11UN112) and EHU12/26 research programs, respectively. The support of the government of the Basque Country through research programs with the Grants N. ELKARTEK 20/71 and ELKARTEK 20/78 is also acknowledged.

## REFERENCES

- [1] Gerontakos, P., Lee, T., Dynamic Stall Flow Control via a Trailing-Edge Flap. *AIAA Journal* **2006**, 44, 469–480.
- [2] Liu, L., Padthe, A.K., Friedmann, P.P., Computational Study of Microflaps with Application to Vibration Reduction in Helicopter Rotors. *AIAA Journal* **2011**, 49, 1450–1465.
- [3] Kamps, L., Brücker, C., Geyer, T.F., Sarradj, E., Airfoil Self Noise Reduction at Low Reynolds Numbers Using a Passive Flexible Trailing Edge. In Proceedings of the 23rd AIAA/CEAS Aeroacoustics Conference; American Institute of Aeronautics and Astronautics: Denver, Colorado, 2017.
- [4] Friedmann, P., Padthe, A., Liu, L., Numerical Evaluation of Microflaps for On Blade Control of Noise and Vibration. In Proceedings of the 52nd AIAA/ASME/ASCE/AHS/ASC Structures, Structural Dynamics and Materials Conference; American Institute of Aeronautics and Astronautics: Denver, Colorado, 2011.
- [5] Lee, T., Su, Y.Y., Lift enhancement and flow structure of airfoil with joint trailing-edge flap and Gurney flap. *Exp Fluids* **2011**, 50, 1671–1684.
- [6] Bofeng, X., Junheng, F., Qing, L., Chang, X., Zhenzhou, Z., Yue, Y., Aerodynamic performance analysis of a trailing-edge flap for wind turbines. *J. Phys.: Conf. Ser.* **2018**, 1037, 022020.
- [7] Dam, C.P. van, Chow, R., Zayas, J.R., Berg, D.E., Computational Investigations of Small Deploying Tabs and Flaps for Aerodynamic Load Control. *J. Phys.: Conf. Ser.* **2007**, 75, 012027.
- [8] Ballesteros-Coll, A., Fernandez-Gamiz, U., Aramendia, I., Zulueta, E., Lopez-Gude, J.M., Computational Methods for Modelling and Optimization of Flow Control Devices. **2020**, 15.
- [9] Ballesteros-Coll, A., Fernandez-Gamiz, U., Aramendia, I., Zulueta, E., Ramos-Hernanz, J.A., Cell-Set Modelling for a Microtab Implementation on a DU91W(2)250 Airfoil. *Energies* **2020**, 13, 6723.
- [10] Jonkman, J., Butterfield, S., Musial, W., Scott, G., *Definition of a 5-MW Reference Wind Turbine for Offshore System Development*; 2009; p. NREL/TP-500-38060, 947422;
- [11] Siemens Star CCM+ Version 14.02.012 Available online: <https://www.plm.automation.siemens.com/global/en/> (accessed on Feb 3, 2020).
- [12] Sørensen, N.N., Mendez, B., Munoz, A., Sieros, G., Jost, E., Lutz, T., Papadakis, G., Voutsinas, S., Barakos, G.N., Colonia, S., et al., CFD code comparison for 2D airfoil flows. *J. Phys.: Conf. Ser.* **2016**, 753, 082019.
- [13] Fernandez-Gamiz, U., Zulueta, E., Boyano, A., Ramos-Hernanz, J., Lopez-Gude, J., Microtab Design and Implementation on a 5 MW Wind Turbine. *Applied Sciences* **2017**, 7, 536.
- [14] Menter, F.R., Two-equation eddy-viscosity turbulence models for engineering applications. *AIAA Journal* **1994**, 32, 1598–1605.
- [15] Ibarra-Udaeta, I., Portal-Porras, K., Ballesteros-Coll, A., Fernandez-Gamiz, U., Sancho, J., Accuracy of the Cell-Set Model on a Single Vane-Type Vortex Generator in Negligible Streamwise Pressure Gradient Flow with RANS and LES. *JMSE* **2020**, 8, 982.
- [16] Timmer, W.A., van Rooij, R., Summary of the Delft University wind turbine dedicated airfoils. 11.



# AUTOMATIC OPTIMIZATION ALGORITHM FOR ELECTRICAL ENERGY CONTRACTS IN SPANISH MARKET

Decebal Aitor Ispas-Gil

University of the Basque Country, Vitoria-Gasteiz, Spain, dispas001@ikasle.ehu.eus, ORCID: 0000-0002-3833-7114

Asier Zulueta

University of the Basque Country, Vitoria, Spain, azulueta@arrasate.eus, ORCID: 0000-0003-0240-890X

Ekaitz Zulueta

University of the Basque Country, Vitoria, Spain, ekaitz.zulueta@ehu.eus, ORCID: 0000-0001-6062-9343

Unai Fernández-Gámiz

University of the Basque Country, Vitoria, Spain, unai.fernandez@ehu.eus, ORCID: 0000-0001-9194-2009

Jose Manuel Lopez-Guede

University of the Basque Country, Vitoria-Gasteiz, Spain, jm.lopez@ehu.eus, ORCID: 0000-0002-5310-1601

*Ispas-Gil, DA., Zulueta A., Zulueta, E., Fernandez-Gamiz, U., Lopez-Gude, J.M., Automatic optimization algorithm for electrical energy contracts in Spanish market. 9<sup>th</sup> Eur. Conf. Ren. Energy Sys. 21-23 April 2021, Istanbul, Turkey*

---

**Abstract:**

In this article authors proposes an optimization for electrical energy cost reductions. It is well known that little and medium electrical energy consumers contracts maximum power limitations too high because they are afraid to have big electrical penalties when exceed their maximum power limitations. In order to improve their electrical bill, authors proposed an optimization with the real power consumptions obtained from electrical company application of their electrical bills. Authors has applied as optimization variable the maximum power limitations, and obviously, cost function is the mean bill applied to the last few years consumptions. Authors has applied an optimization based on “brute force”, because there are no so much different standardized maximum power limitations levels, so this method is computationally affordable. There are much complex optimizations algorithms but they are much computationally much heavy and they are difficult to apply for users, see [1] and [2]. Authors has applied to Arrasate-Mondragon county-hall (in northern Spain) to 180 electrical consumption points consumption points. Authors have arrived to an annual cost reduction of 20000 euros.

---

**Keywords:**

Optimization, Electrical budget, Electrical network link power sizing

---

© 2021 Published by ECRES

Nomenclature	
$PHired_i$	Contracted power at ith period
$POptHired_i$	Contracted optimal power contract at ith period
$Pg$	Contract consumption set
$Pg_i$	Power consumptions at ith period
$PriceP_i$	Power Price at ith period
$NoPP$	Number od period for each pricinf
$i$	Period index
$c$	3.0A pricing coefficient
$PcBill_i$	Power Bill at ith period (3.0A princing only)
$DaysBilled$	Number of days of each time span

## 1. INTRODUCTION

In this article, authors propose an optimization of electrical energy contracts' power levels. The optimization is applied to Spanish electrical market. In Spanish electrical market there pricing systems. These pricing systems discriminate electrical power cost at different periods. There are different pricing models but in Spanish electrical market can be summarized to a three different models. Each pricing models are not only different on price levels, these models are different on different period kinds. The first model is a set of three pricing: 2.0A, 2.0DHA, 2.1A and 2.1DHA, the second one is the 3.0A contract model, see [3]. Finally, the third pricing model is the 3.1 and 6.X contract models. This third pricing model is the most complex contract, in computationally point of view. In this work, authors show a powerful and computationally light optimization algorithm. This domain is a very active research domain as shows the followings works[4] [5] and [6].

The cost function is the same for whole pricing models, see Eq. [1].

$$Z = \sum_{i=1}^{NoPP} (PHired_i PriceP_i) \quad (1)$$

## 2. FIRST PRINCING SET: 2.0A, 2.0DHA, 2.1A and 2.1DHA

This pricing model has these different contracts: 2.0A, 2.0DHA, 2.1A and 2.1DHA. The common characteristics of these all contracts are quantity of power periods. In this first pricing, there is only one period. If contracted power level is exceeded by user's power consumption, there is an economical penalty. Usually, if user's consumption power overcomes contracted power level, electrical supply cut off. In this case, the most usual criteria, in order to calculate the contract electrical power, it is set this contract electrical power to the historical maximum consumption level. Anyway, there is only a few contract power levels. If the maximum historical power consumption is less than minimum possible power level, this minimum level must to be set. If maximum contract level for these pricing is less than maximum historical power consumption, another user must to choose another pricing model.

The mathematical expression models the price of this contract model see Eq. [2]:

$$POptHired = \begin{cases} \max(Pg), & PRmin \leq \max(Pg) \leq PRmax \\ PRmax, & PRmax < \max(Pg) \\ PRmin, & \max(Pg) < PRmin \end{cases} \quad (2)$$

## 3. SECOND MODEL: 3.0A

The second model, the 3.0A pricing, has a very special pricing. This model is oriented to low voltage electrical supply points, but the contracted power level is bigger than 15 kW. The electrical penalties due to power consumption excesses relative to the contracted power level is the same to 3.1A model's penalties. The only restriction is to set a contract power level with a value bigger than 15 kW at least, at one of three periods of this pricing model. In Eq. [3], this restriction is modelled as follows:

$$Cardinal(PcHired_i > 15 \wedge 1 \leq i \leq 3) \geq 1 \quad (3)$$

In order to optimise the contracted power for each period, authors define a  $c$  coefficient for each period. This coefficient is a ratio between the maximum contracted power level at  $i$ th period and the maximum historical consumption power, see Eq. [4]:

$$c = \frac{\max(Pg_i)}{PcHired_i} \quad (4)$$

Spanish electrical market distinguishes the different cases. When  $c$  coefficient is less than 0.85 ( $c < 0.85$ ) the power level that must to be paid by electrical user is set to 85% of initially contracted power level, see Eq [5]:

$$PcBill_i = 0.85PcHired_i \quad (5)$$

In this case, users pay less than the contracted power level at  $i$ th period. When  $c$  coefficient is between 0.85 and 1.05 ( $0.85 \leq c \leq 1.05$ ), user must to pay as follows, see Eq. [6]:

$$PcBill_i = \max(Pg_i) \quad (6)$$

So, user must to pay the maximum power consumption at  $i$ th period. Finally, if  $c$  coefficient is bigger than  $1.05 < c$ , there is a penalty that is calculated as appears in Eq [7]:

$$PcBill_i = 3 \max(Pg_i) - 2.1Pchired_i \quad (7)$$

Authors, propose a *brute force* algorithm in order to optimize the contracted power at  $i$ th period. Authors propose this basic algorithm due to number of periods in this pricing model, and the low number of possible power levels to make a contract, it is very light computationally to verify all the possible standard power levels. Actually, the algorithm only needs to try 3 times at worse case to arrive to the best solution. The algorithm's criteria is described in Eqs. [8,9]:

$$Pchired_i = \begin{cases} 15.01, & NI_t = i \wedge \max(Pg_i) \leq 15 \\ \max(Pg_i), & NI_t \neq i \vee \max(Pg_i) > 15 \end{cases} \quad (8)$$

$$1 \leq NI_t \leq 3 \quad (9)$$

Where  $NI_t$  it is the number of algorithm's iteration. At each iteration, the algorithm calculates cost function. If the new iteration reaches the actual best case, the new one replaces the old best case.

#### 4. THIRD MODEL: 3.1A and 6.X contracts

This model fulfils 3.1A and 6.X pricings. These pricing models all are high voltage pricing models. These all pricing models must to guarantee the following restriction, see Eq. [10]:

$$Pchired_{i+1} \geq Pchired_i \quad (10)$$

In these models, also, there are some penalty criterion. This penalty criterion is equal to 3.0A pricing penalty criterion. This penalty criterion is defined in Eqs [4,5,6,7]. In 6.X pricing model, the penalty criterion is quite different. If power consumption reaches the contracted power in the  $i$ th period, during a 15 minute time span. The penalty criteria in Spanish market is defined in Eq. [11], see [7]:

$$Penalization = \sum_{i=1}^6 1.4064k_i \sqrt{\sum_{j=1}^n (Pg_i^* - PHired_i)^2} \quad (11)$$

$Pg_i^*$  are the power consumptions at  $i$ th period where the power consumptions have each the contracted power level at  $i$ th period.  $k_i$  it is a coefficient that depend on the  $i$ th period. In table I, authors show these possible values, see [8].

Table I. Spanish market $k_i$ penalty criteria coefficient values						
Period	1	2	3	4	5	6
$k_i$	1	0.5	0.37	0.37	0.37	0.17

The proposed algorithm takes into account these restrictions. The algorithms tries different contracted power levels at each  $i$ th period and verified witch it is the electrical bill. The algorithm increases gradually the contracted level for each  $i$ th period. An important question is to take into account that the second period must to have a bigger level than the second period, and so on, see Eq. [10]. It is an iterative algorithm. In 6.X pricing model, there are 6 periods.

In few words, the algorithm generates different contracted power levels at  $i$ th period. Ones, the algorithm obtain a possible contracted power set for all possible periods; the algorithm evaluates the different penalties if historical

power consumptions reach the contracted power levels at each period. After all possible contracted power level sets are evaluated, the algorithm keeps the best solution.

Therefore, the most important step in our algorithm, is contracted power level set generation. The maximum and minimum power levels at each period fixe the possible standard power levels set. The detailed contracted power levels set are founded following Eqs [12,13,14,15]:

$$uppValTmp = \begin{cases} UppBound, & i = 1 \\ PotSrchMax_{i-1}, & i > 1 \end{cases} \quad (12)$$

$$PotSrchMax_i = \min(\max(\max(Pg_i), UppValTmp), UppBound) \quad (13)$$

*UppBound* is the maximum contract power level at each period. This maximum is defined for each pricing model. *PotSrchMax<sub>i</sub>* is the upper bound at *i*th period. The lower bound fulfils the following formula, see Eq. [14].

$$LowValTmp = \begin{cases} LowBound, & i = 1 \\ PotSrchMax_{i-1}, & i > 1 \end{cases} \quad (14)$$

$$PotSrchMin_i = \max(\min(\min(Pg_i), LowValTmp), LowBound) \quad (15)$$

*LowBound* is the minimum power level that can be applied at *i*th period. *PotSrchMin<sub>i</sub>* is the lower bound at *i*th period. At each *i*th period, the proportional power increment follows Eq. [16]:

$$ChangeItera_i = \frac{PotSrchMax_i - PotSrchMin_i}{IterationDepthIndex} \quad (16)$$

*IterationDepthIndex* is an positive index that defines how many different power levels are going to be verified in our algorithm. Finally, the algorithms verifies these all power level combinations and keeps all power levels set that fulfil the restriction given in Eq. [10]. Therefore, the algorithm generates possible power levels between the contracted power level in the period before and the maximum standard power level at given period.

## 5. RESULTS & FUTURE WORKS

Authors have applied this optimization algorithm in 180 electrical consumption points at town hall of Arrasate-Mondragon, Gipuzkoa, Northern Spain. This algorithm has achieve an annual economical shaving of 20000 euros. Another important result of this work is the optimization algorithm proposal. This algorithm is going to be applied to other more complex optimization problems. For example, authors want to apply this optimization algorithm in battery-based systems in order to reduce the contracted power levels. These reductions let user to make big savings because there is important reduction not only in electrical bill payments, in electrical network connection structure savings also. A good example is the electrical transformer power size that can be reduced highly. This algorithm let user to manage in a better way its renewable energy system support also.

## ACKNOWLEDGEMENTS

Authors want to Arrasate-Mondragon local council because data support. This data is fundamental in order to test our optimization algorithms. The authors are grateful to the Government of the Basque Country and the University of the Basque Country UPV/EHU through the SAIOTEK (S-PE11UN112) and EHU12/26 research programs, respectively.

## REFERENCES

- [1] R. J. Bessa, M. A. Matos, F. J. Soares, y J. A. P. Lopes, «Optimized Bidding of a EV Aggregation Agent in the Electricity Market», *IEEE Trans. Smart Grid*, vol. 3, n.º 1, pp. 443-452, mar. 2012, doi: 10.1109/TSG.2011.2159632.
- [2] F. Garcia-Torres, C. Bordons, J. Tobajas, J. J. Marquez, J. Garrido-Zafra, y A. Moreno-Munoz, «Optimal Schedule for Networked Microgrids Under Deregulated Power Market Environment Using Model Predictive Control», *IEEE Trans. Smart Grid*, vol. 12, n.º 1, pp. 182-191, ene. 2021, doi: 10.1109/TSG.2020.3018023.
- [3] «BOE.es - BOE-A-2001-20850 Real Decreto 1164/2001, de 26 de octubre, por el que se establecen tarifas de acceso a las redes de transporte y distribución de energía eléctrica.» <https://www.boe.es/buscar/act.php?id=BOE-A-2001-20850#:~:text=el%20art%C3%ADculo%209.3.-,3.,o%20inferior%20a%20450%20kW.> (accedido mar. 15, 2021).

- [4] M. Liu y F. F. Wu, «Portfolio optimization in electricity markets», *Electr. Power Syst. Res.*, vol. 77, n.º 8, pp. 1000-1009, jun. 2007, doi: 10.1016/j.epsr.2006.08.025.
- [5] P. Faria y Z. Vale, «Demand response in electrical energy supply: An optimal real time pricing approach», *Energy*, vol. 36, n.º 8, pp. 5374-5384, ago. 2011, doi: 10.1016/j.energy.2011.06.049.
- [6] F. U. Leuthold, H. Weigt, y C. von Hirschhausen, «A Large-Scale Spatial Optimization Model of the European Electricity Market», *Netw. Spat. Econ.*, vol. 12, n.º 1, pp. 75-107, mar. 2012, doi: 10.1007/s11067-010-9148-1.
- [7] «¿Cómo se calculan los excesos de potencia en las tarifas de acceso de 3 y 6 períodos?» <https://www.respiraenergia.com/support/kb/a175/como-se-calculan-los-excesos-de-potencia-en-las-tarifas-de-acceso-de-3-y-6-periodos.aspx>.
- [8] «Todo lo que debes saber sobre la Tarifa de Acceso 3.1A.» <https://www.lumisa.es/post/90/es/todo-lo-que-debes-saber-sobre-la-tarifa-de-acceso-31a->.



# CIPHERING AND DECHIPHERING TECHNIQUE ON THE IMAGES OF ENERGY PLANTS AND NETWORKS

Erol Kurt

Gazi University, Technology Faculty, Department of Electrical and Electronics Engineering, Beşevler, TR-06500 Ankara, Turkey, E-mail: ekurt52tr@yahoo.com, ORCID: 0000-0002-3615-6926

Batuhan Arpacı

Information Systems Department, Informatics Institute, Gazi University, Ankara, Turkey, E-mail: bthnrpc@gmail.com, ORCID: 0000-0001-6607-5820

*Cite this paper as:* Kurt, E., Arpacı, B., *Ciphering and Deciphering Technique on the Images of Energy Plants and Networks, 9<sup>th</sup> Eur. Conf. Ren. Energy Sys. 21-23 April 2021, Istanbul, Turkey.*

**Abstract:** A previously proposed encryption and decryption technique [1] has been applied to the energy systems images for the secure communication facility. The technique indeed, consists of a Kurt-modified diode supported Chua's circuit (KCC) in order to generate chaotic number sequence. The Kurt-modified diode is a non-autonomous nonlinear circuit component producing quite high Lyapunov exponents in the MCC. Thus, the chaotically generated number sequences can be used for the secure communication on the energy plants and networks. In the algorithm developed for the encryption and decryption, a scrambling feature implemented at the bit level is applied to the images to be ciphered. Some required tests have been performed for the requirement of secure communication.

**Keywords:** Energy plants, networks, secure communication, ciphering

© 2021 Published by ECRES

## 1. INTRODUCTION

Achievements in information and network technologies take the image security to an important position [1-3]. The secret communication has been used especially for important industrial projects and military applications. Among the industrial projects, the information security on energy systems is a key point for the companies as well as the countries. In the secret communication concept, the cryptography has been an attractive topic. While the energy partners communicate with each other, the images related to the energy plants, networks, etc should be transferred securely. For this aim, encryption/decryption processes can be used over the images of energy systems. Meanwhile, a problem arises. Indeed, traditional encryption methods such as AES, IDEA, DES have certain security flaws since they can be decrypt by the conventional techniques as in Refs. [4-6].

Among the secure communication issues of coloured images, there exist two well-known processes called permutation and diffusion. Although they can be used for image encryption procedures, their implementation for a bit or pixel level cannot satisfy a required security. For this reason, realization of only the exchange property in the bit level would not give sufficient security, especially in permutation and diffusion [6]. Therefore a combined technique with sensitive, ergodic and random can be applied. Those features quantifies a chaotic system indeed. According to the literature, many scholars have used chaos-based encryption systems [7-10]. In the present paper, to our knowledge, for the first time, we apply this methodology with an advanced algorithm and chaotic output to the energy sector. The reason for that is increasing importance of energy plants, internet attacks to energy plants, and project-based secure communication requirements. Since energy has been a strategic concept for countries, such a secure communication technique can assist to provide the transfer of the energy-related images. For this aim, a new chaos-based algorithm has been used. The novel part comes from the topic of energy security, invented algorithm and the usage of Kurt modified Chua's circuit (KCC) in the ciphering/deciphering processes.

## 2. HYPERCHAOTIC SYSTEM DEFINITION

In this study, a KCC is used. This circuit is mainly used to get random numbers. However the generated numbers should have a chaotic character. Indeed, we use this circuit since it can generate hyperchaotic data which gives a strong randomness in the phase space of system depending on the parameters. The system equations are as follows [11]:

$$\begin{cases} \dot{x} = y - bx - \frac{1}{2}(a-b)[|x + \sin(z)| - |x - \sin(z)|], \\ \dot{y} = -\beta(y + x) + f \sin(v), \\ \dot{z} = \phi, \\ \dot{v} = \omega \end{cases} \quad (1)$$

Here,  $a, b, \phi, \beta, \omega, f$  are nothing else than the control parameters. The solutions run in MatLab environment via the well-known Runge-Kutta method as shown in Fig. 1(a,b).

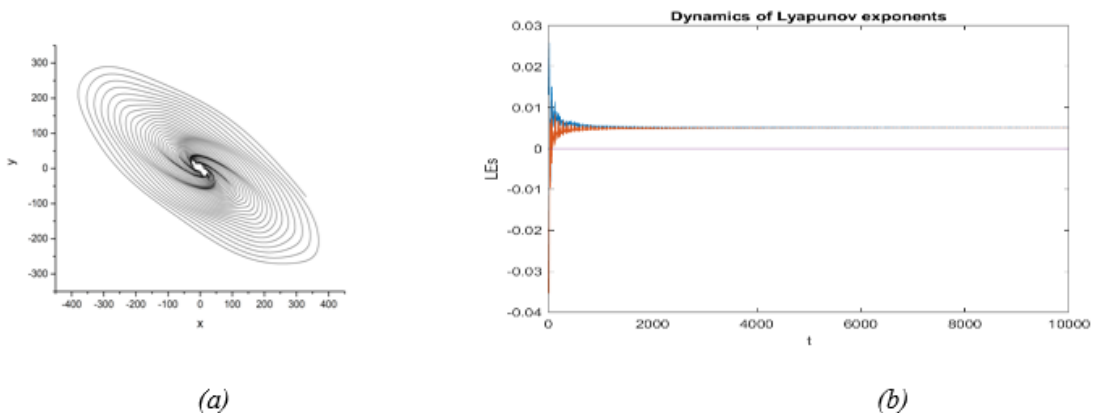


Figure 1. (a) The phase space construction for  $a = -2.91$ ,  $b = -0.56$ ,  $\beta = 0.55$ ,  $f = 12.99$ ,  $\phi = -15.1$  and  $\omega = 2.91$ . (b) corresponding Lyapunov spectrum.

In a chaotic system, at least one positive exponent should exist. If there are two positive exponents, the system is called as “hyperchaotic” as shown in Fig. 1(b). In such situation, depending on the initial conditions, two positive lyapunov exponents such as  $(0,0,+,+)$  determines the hyperchaoticity.

## 3. IMAGE ENCRYPTION SCHEME

The image encryption used in this work is defined in Refs. [1,2] in detail. Therefore, here we do not give the details. However, as a brief explanation, we explain the secret key generation, initial value definition, and algorithms.

As a cryptographic hash algorithm, SHA-256 generates a 256-bit hash value. That changes completely when there is a slight change in the input of the algorithm as expected. Indeed, a 48-bit digest output which is described as PK is obtained from the plain image for input to the SHA-256 function. Random noise (i.e. RN) is generated at the start of each encryption process. A 256-bit digest hash value SK is then generated by executing SHA-256 with the PK and RN input. Thus, the secret key produced is completely unique thanks to the SHA-256, even if there is a slight change in the plain image, or even no changes at all. The row, column, color and other information algorithms from the hash key definition can be found in Refs. [1,2].

The initial values for the functions  $x_1, y_1, z_1, v_1$  and can be derived as follows:

$$\begin{cases} x'_1 = \left( \text{hex2de}(\text{subset}(1, 10, SK)) \cdot 10^{-11} \right) \\ \quad + \left( \text{hex2de}(\text{subset}(11, 16, SK)) \cdot 10^{-14} \right) \\ y'_1 = \left( \text{hex2de}(\text{subset}(17, 26, SK)) \cdot 10^{-11} \right) \\ \quad + \left( \text{hex2de}(\text{subset}(27, 32, SK)) \cdot 10^{-14} \right) \\ z'_1 = \left( \text{hex2de}(\text{subset}(33, 42, SK)) \cdot 10^{-11} \right) \\ \quad + \left( \text{hex2de}(\text{subset}(43, 48, SK)) \cdot 10^{-14} \right) \\ v'_1 = \left( \text{hex2de}(\text{subset}(49, 58, SK)) \cdot 10^{-11} \right) \\ \quad + \left( \text{hex2de}(\text{subset}(59, 64, SK)) \cdot 10^{-14} \right) \end{cases} \quad (2)$$

Here  $\text{hex2de}()$  function converts the secret key from hexadecimal number to a decimal number,  $\text{subset}(i, j, K)$  returns elements between the  $i$ th index and  $j$ th index of the  $K$  1-D array. In Eq. (2), the multiplications are determined as  $10^{11}$  and  $10^{14}$  in order to adjust the relevant decimals of the  $x_1, y_1, z_1$  and  $v_1$ . The values of  $a_1, a_2, b_1$  and  $b_2$  are calculated according to the program schemes in Ref. [12]. The subset and hex2de functions are mentioned above. The  $\text{concat}(\cdot)$  function concatenate the values given into it. The  $\text{roundD}(\cdot)$  returns the decimal portion of the given decimal number and  $\text{sum}(\cdot)$  is aggregate function.

$$\begin{cases} x_1 = x'_1(2 - a_1) \\ y_1 = y'_1(2 - a_2) \\ z_1 = z'_1(2 - b_1) \\ v_1 = v'_1(2 - b_2) \\ f = 9.1 + a_1 \end{cases} \quad (3)$$

where, the number 9.1 denotes the lower chaotic parameter for  $f$ . Since  $a_{1,2}$  and  $b_{1,2}$  refers to the numbers lower than 1, we make the multiplication higher by using the term  $(2 - (a, b)_{1,2})$ .

Fig. 2 presents the encryption procedure. This algorithm has superiorities on the algorithms existing in the literature. Indeed, it divides the image into 2 pieces shown in Fig. 2. Here *Input* is a Plain image  $P$  and a secret key  $SK$ , whereas *Output* is a Cipher image  $C$ . For the horizontal and vertical magnitudes,  $W$  and  $H$ , the size of the image is given by  $W \times H \times 3$ .

- Step 1:** Take the initial values  $(x_1, y_1, z_1, v_1)$  and the initial parameter  $f$  of the chaotic system by using Eq. (3).  
**Step 2:** Using the iteration method, chaotic numbers with array  $CN$  and size are  $(s \times 4) + 5000$  generated by solving time-continuously chaotic system. Following the first 1000 data, one uses  $n=4s$  and  $cs=n+4000$ .  
**Step 3:**  $CN$  is produced by the chaotic generator. The key matrix  $KM$  is applied in the diffusion and scrambling stages.

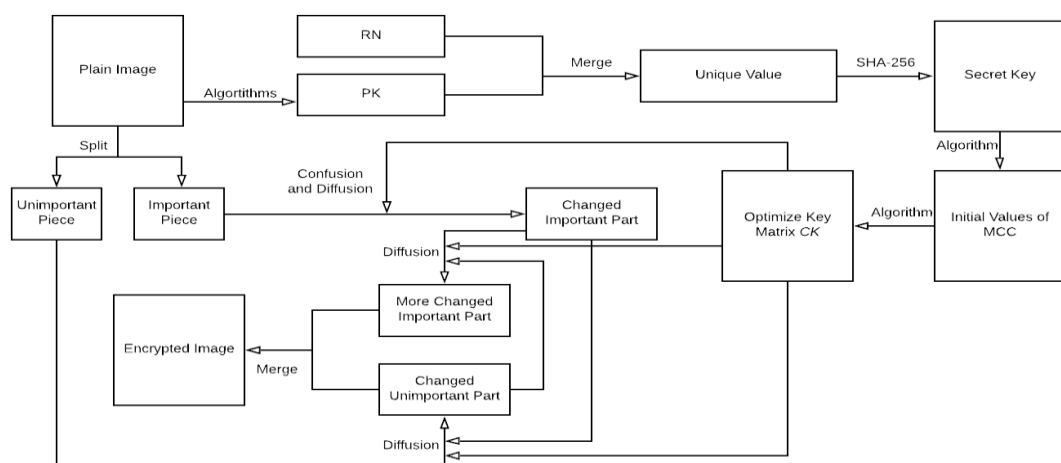


Figure 2. The flow chart of encryption process.

**Step 4:** Plain image  $P$  is resized for each pixel by beginning from component  $R$ , sequentially from upper to bottom point, then left to right with  $G$  and  $B$  components. Then each pixel is converted into 8-digit binary format.

**Step 5:** Mapping method is applied to the  $PB_2$  matrix using the  $KM$  key matrix.

**Step 6:** Diffusion method is applied to matrices  $PB_1$  and  $PB_2$  using by key matrix  $KM$ .

The vice-versa of this algorithm is used in the decryption process. The details can be found in Ref. [1,2,12].

#### 4. EXPERIMENTAL RESULTS AND RESPONSES TO THE SECURITY TESTS

The initial parameters of KCC are  $a = -2.91$ ,  $b = -0.56$ ,  $\beta = 0.55$ ,  $\phi = -0.13$ , and  $\omega = 1.29$  for the experiment. The system is hyperchaotic for  $f \geq 9.1$ . The secret key is 2A8649DDF54B044DC1A50329C54B4960010066BA8FD005D4392B536545B04ECE. The initial state variables and driving amplitude  $f$  of KCC are obtained from this secret key. We have used several images of energy plants and energy projects. Their names are 3Dnuclear, 2Dnuclear, and Plant as shown in Figs. 3(a-c), respectively.

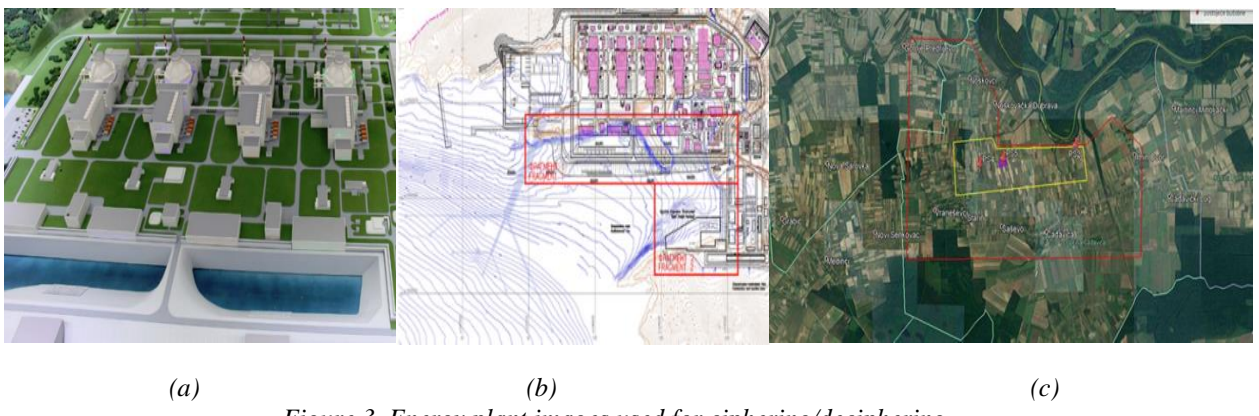


Figure 3. Energy plant images used for ciphering/deciphering

The images have been ciphered by following the algorithm in Fig. 2 and pictured as in Fig. 4(a-c).

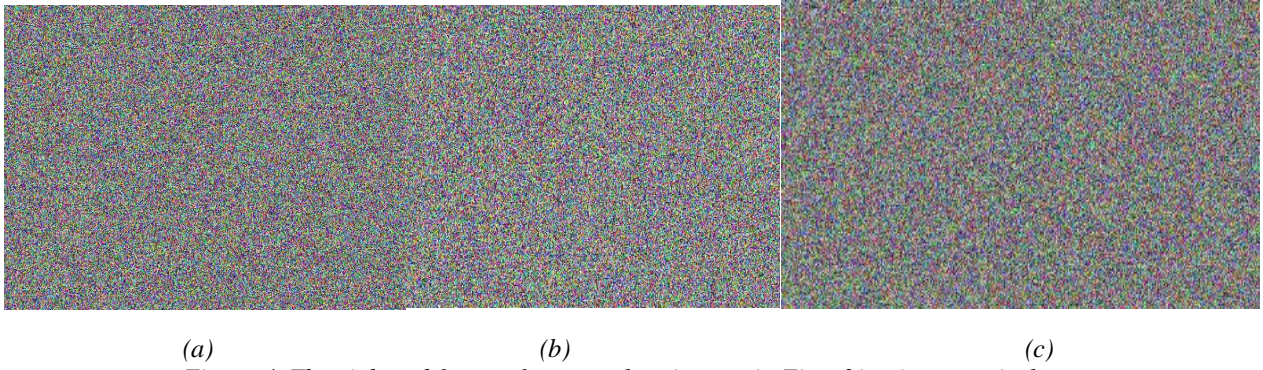


Figure 4. The ciphered forms of energy plant images in Figs. 3(a-c), respectively.

It is obvious that all the ciphered images cannot be seen truly with a naked eye. However, it is not sufficient, since the responses to the security tests should be discussed in order to be at the safe side. For this reason, we have applied several security tests including key space, key sensitivity and plain image sensitivity, resistance to known plaintext and chosen plaintext attacks, differential attacks, information entropy, correlation coefficient, histogram and resisting noise attack analyses, respectively.

For the key space analysis, the key space should be capable of neutralizing brute-force attacks. The encryption system key includes the initial values  $(x_1, y_1, z_1, v_1)$  and initial parameter of  $f$  as in previous section. For the chaotic features, the precision of the initial conditions should be as high as possible such as 14 or 15 digits after the comma [5], so that the key space can reach  $10^{70}$ . In that case, the key space is  $S = 10^{70} \approx 2^{232} > 2^{100}$  [13], so that the cryptosystem can resist to brute-force attacks.

The key of the Modified Chua crypto system is a 'nonce', based on the hash value generated by the plain image and a random sequence. So if the startup conditions of the system is modified slightly, this operation will cause to production of the diverse encrypted images. In the Chua system, considering the experimental results, it is revealed that the algorithm is very delicate to the slightest variation in the key. Figure 10(a) is a one bit modified version of the Img 1 image and its encrypted state is given in Figure 10(b). The differences between Figs. 9(b) and 10(b) is also given in Fig. 10(c). From this point of view, results of the encryptions are also divergent from each other.

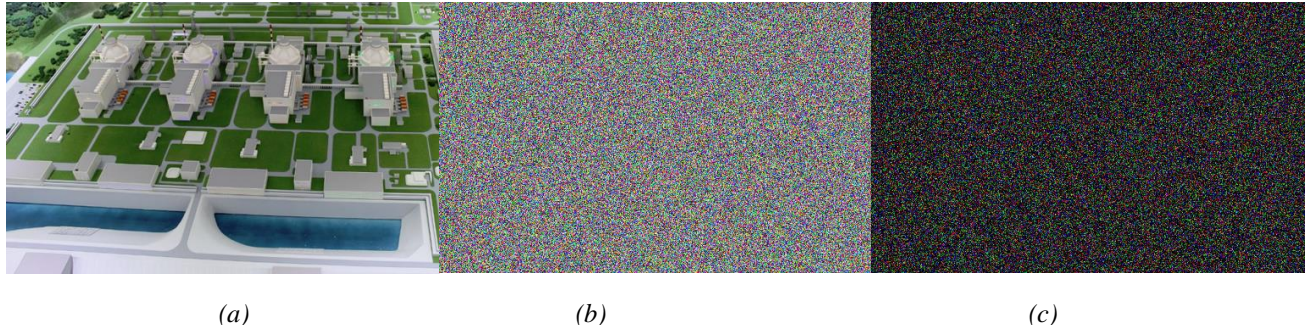


Figure 5. Key sensitivity test results: (a) One bit-modified version of Fig. 3(a), (b) its encrypted image, and (c) the difference between Figs. 4(a) and Figs. 5(b).

In the proposed algorithm, the key depends on the hash value of the original image file. Therefore, different keys will be produced for different images. The attacker cannot decipher the particular image with a key obtained from another image. As a result, the implemented software may be resistant to the known-plaintext and chosen-plaintext attacks.

In general, in the image encryption unit, it is expected that the encrypted media should be distinctive from its unencrypted version. To measure such a difference, the criteria NPCR [14] and UACI [15] are generally used. The crypto system we recommend should guarantee that the encrypted forms of the two images are dissimilar to each other when one bit modification is made in the one of them. Table I and II shows the NPCR and UACI results of 1500 randomly selected pairs and satisfactory values have been reached. As a result, the software is robust against differential attacks.

Information entropy is used for the measurement of an arbitrary distribution in a media file. The formulation of this operation is presented as follows [16]:

$$H(m) = \sum_{i=0}^{2^n-1} p(m_i) \log_2 \frac{1}{p(m_i)} \quad (4)$$

The information entropy of the encrypted image should be as high as possible and ideally it should be 8 [17]. This situation makes information difficult to disclose. Table III gives the information entropy values of the three pieces of the encrypted image using the Eq. (23) and ones can be found to be close to 8.

Table 1. The minimum, maximum and average UACI(%) values.

Image	R			G			B		
	Max	Mean	Min	Max	Mean	Min	Max	Mean	Min
3Dnuclear	31.4156	30.6879	30.3479	30.3825	28.6145	28.3108	33.2982	32.1271	31.3550
2Dnuclear	39.2922	33.6726	33.4281	38.2511	35.5371	33.4115	39.5920	33.7994	33.4635
Grid	31.4428	30.8832	30.3841	31.4087	30.3856	27.8536	33.3667	31.3421	29.4814

Table 2. The minimum, maximum and average NPCR(%) values.

Image	R			G			B		
	Max	Mean	Min	Max	Mean	Min	Max	Mean	Min
3Dnuclear	99.6106	99.5642	99.5012	99.6595	99.5556	99.5044	99.6693	99.5764	99.5123
2Dnuclear	99.1184	98.4079	98.2753	99.0128	98.9136	98.5852	99.4512	99.1001	98.9081
Grid	99.6029	99.5814	99.5516	99.6152	99.5844	99.5814	99.6649	99.5491	99.4421

Table 3. The information entropies of the ciphered images.

Image	R	G	B
3Dnuclear	7.9902	7.9897	7.9902
2Dnuclear	7.9271	7.9261	7.9362
Grid	7.9888	7.9887	7.9888

There is a relationship between neighboring pixels in an original image. To counteract statistical attacks, the correlation of neighboring pixels in the encrypted image should be minimal. The following formulation can be used to calculate the correlation between two adjacent pixels [18]:

$$r_{xy} = \frac{\text{cov}(x, y)}{\sqrt{D(x)}\sqrt{D(y)}}, \quad \text{cov}(x, y) = \frac{1}{N} \sum_{i=1}^N (x_i - E(x))(y_i - E(y)), \quad E(x) = \frac{1}{N} \sum_{i=1}^N x_i, \quad D(x) = \frac{1}{N} \sum_{i=1}^N (x_i - E(x))^2. \quad (5)$$

Fig. 6 represents the correlation distributions of two horizontally, vertically and diagonal adjacent pixels in the plain and ciphered Lena image. From here, we can understand that the correlation between neighboring pixels greatly decreases. Table 4 shows the correlation between plain images and their encrypted states. The results show that the correlation between the adjacent pixels of their encoded images is very small, whereas the correlation between the plain images is quite high, so the encryption is effective.

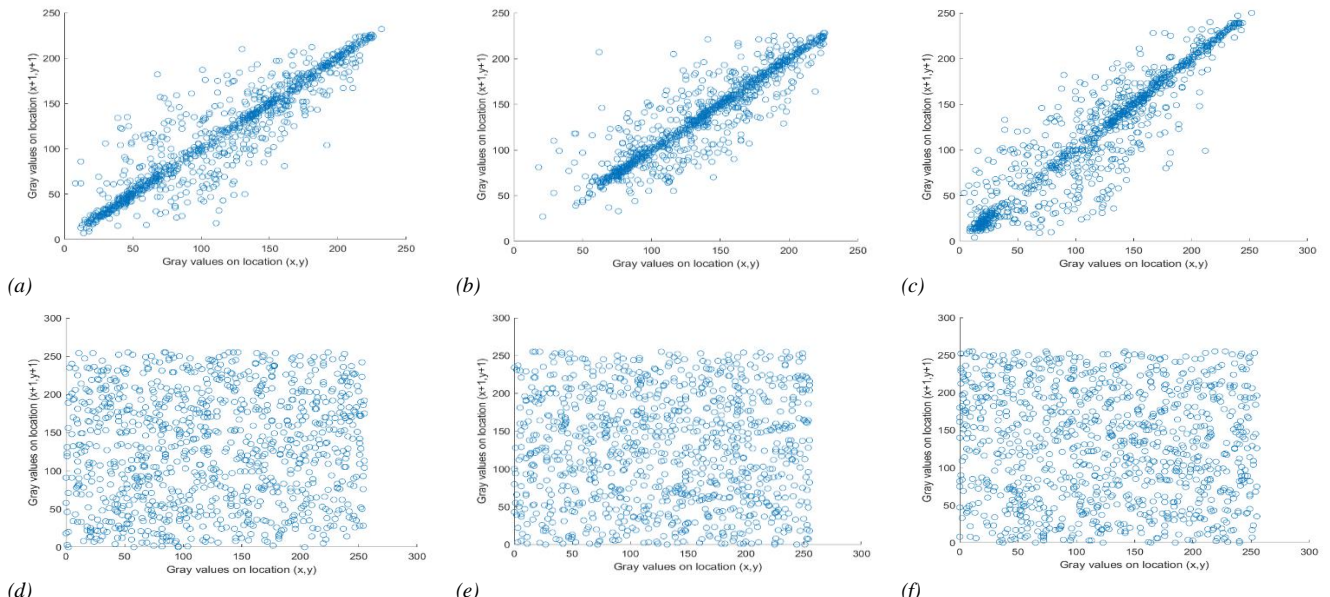


Figure 6. Distributions of the correlations between the plain and the encoded images. (a), (b), (c) are the diagonal, vertical and horizontal of 3Dnuclear, (d), (e), (f) are the diagonal, vertical and horizontal of ciphered form, respectively.

Table 4. The correlation coefficients for adjacent pixels in the original images and their ciphered forms.

Images	Directions	Original			Encrypted		
		R	G	B	R	G	B
3Dnuclear	Diagonal	0.9293	0.9133	0.9278	0.0691	0.0020	-0.0658
	Vertical	0.9534	0.9328	0.9534	0.0476	-0.0213	0.0217
	Horizontal	0.9711	0.9711	0.9762	0.0284	-0.0233	0.0623
2Dnuclear	Diagonal	0.6402	0.7254	0.6734	-0.0328	0.0635	0.0001
	Vertical	0.7477	0.7672	0.7456	0.0069	-0.0082	-0.0274
	Horizontal	0.8446	0.8736	0.8904	-0.0004	-0.0010	-0.0245
Grid	Diagonal	0.8638	0.8004	0.7974	-0.0039	-0.0052	-0.0061
	Vertical	0.9031	0.8996	0.8296	-0.0069	-0.0314	-0.0203
	Horizontal	0.9177	0.9013	0.8880	-0.0035	-0.0094	0.0201

The histogram of an image provides information about the distribution of its pixel values and represents this image. As seen in Fig. 7(a-d), the histogram of the original image has several peaks while the encrypted image has a nearly constant distribution.

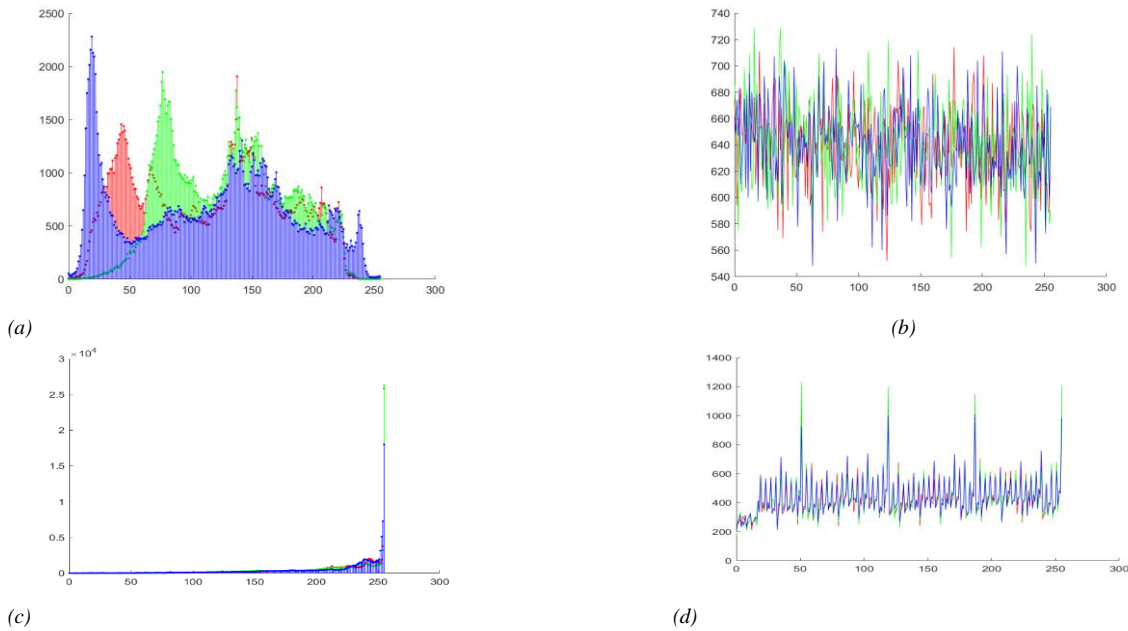


Figure 7. (a,b) Histograms of plain and encrypted images of 3Dnuclear, respectively. (c,d) Histograms of plain and encrypted images of 2Dnuclear, respectively.

The encoded image is inevitably exposed to many kinds of noise as it passes through real communication channels. This noise can cause problems during the acquisition of the original image. Therefore, the algorithm must be noise resistant so that the encryption system can be valid. The Peak Signal-to-Noise Ratio (PSNR) is used to measure the quality of the decoded image after the attack. For the components of the image, PSNR can be calculated as follows [19]:

$$PSNR = 10 \times \log_{10} \left( \frac{255 \times 255}{MSE} \right) (dB) \quad MSE = \frac{1}{mn} \sum_{i=1}^m \sum_{j=1}^n \|I_1(i, j) - I_2(i, j)\|^2 \quad (6)$$

MSE is the mean square error between the original and recovered images and is represented as  $I_1(i, j)$  and  $I_2(i, j)$  respectively, with the size of  $m \times n$ . Figs. 8(a-c) shows the encrypted images exposed to the Salt Pepper noise with different density of this and its deciphered ones. The MSE and PSNR of these decoded images are shown in Table 5. It is obvious that the original image is entirely obtained again, which is noticeable, the PSNR value is about 30 dB, and the decoded images are highly correlated (Fig. 8(d-f)). This means that the decoded images are very close to the original image. Thus, it can be said that the proposed algorithm is resistant to resisting noise attacks to some degree.

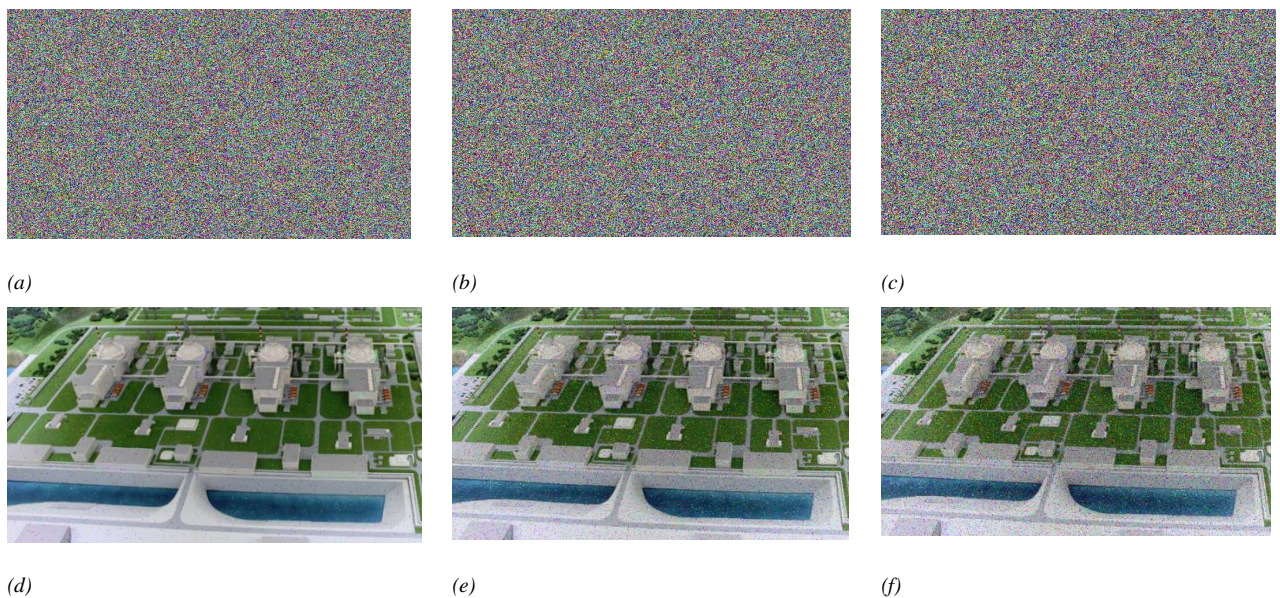


Figure 8. The ciphered images with salt & pepper noise and their deciphered forms of 3Dnuclear. The noises with (d)  $d=0.01$ , (e)  $d=0.05$  and (f)  $d=0.1$ , respectively.

Table 5. The quantitative results of resisting noise attacks.

Image	Density	MSE			PSNR			Correlation		
		R	G	B	R	G	B	R	G	B
3Dnuclear	0.01	108	109	113	27.7777	27.7514	27.6186	0.9950	0.9945	0.9944
	0.05	548	537	542	20.7406	20.8270	20.7876	0.9758	0.9755	0.9761
	0.1	1072	1067	1091	17.8274	17.8475	17.7529	0.9554	0.9471	0.9580
2Dnuclear	0.01	110	107	115	27.7324	27.8219	27.5190	0.9921	0.9950	0.9919
	0.05	557	571	558	20.6741	20.5640	20.6610	0.9633	0.9655	0.9665
	0.1	1152	1151	1082	17.5165	17.5193	17.4484	0.9240	0.9269	0.9369
Grid	0.01	106	103	113	27.8674	28.0215	27.6126	0.9911	0.9924	0.9882
	0.05	539	536	533	20.8138	20.6828	20.8599	0.9506	0.9484	0.9365
	0.1	1071	1073	1074	17.8315	17.8234	17.8210	0.9039	0.8984	0.8730

## 5. CONCLUSIONS

A original encryption/decryption algorithm has been developed for the encryption and the decryption of the energy plant images by using the modified Chua's circuit (MCC) system which exhibits hyper-chaotic behavior for a large parameter regime due to the double frequency dependent nature. The scrambling feature which is implemented at the bit level and novel diffusion system using the MCC has been applied in the algorithm. Following the encryption procedure, the encrypted colored image has been tested by a variety of tests including the secret key size and secret key sensitivity, histogram analysis, correlation analysis, differential analysis and information entropy analysis. The results of the analysis indicate that the proposed algorithm is quite effective and provide an efficient technique for the color image encryption and decryption in the area of secure communication.

## REFERENCES

- [1] Arpacı, B., Kurt, E., Çelik, K., A new algorithm for the colored image encryption via the modified Chua's circuit, *Engineering Science and Technology, an International Journal*, 23(3), 2020, 595-604, 10.1016/j.jestch.2019.09.001.
- [2] Arpacı, B., Kurt, E., Çelik, K., Cylan, B., Colored image encryption and decryption with a new algorithm and a hyperchaotic electrical circuit, *J. Electr. Eng. Technol.*, 15, 1413–1429, 2020, 10.1007/s42835-020-00393-x
- [3] Alvarez, G., Li, S. Some basic cryptographic requirements for chaos-based cryptosystems. *Int. J. Bif. Chaos*, 16(08), 2129-2151, 2006.
- [4] Kiraz, M. S., & Uzunkol, O. (2016). Efficient and verifiable algorithms for secure outsourcing of cryptographic computations. *Int. J. Information Security*, 15(5), 519-537.
- [5] Stinson, D. R. (2005). Cryptography: Theory and practice. CRC press.
- [6] Zhu, Z. L., Zhang, W., Wong, K. W., & Yu, H. (2011). A chaos-based symmetric image encryption scheme using a bit-level permutation. *Information Sci.*, 181(6), 1171-1186.
- [7] Fu, C., Lin, B. B., Miao, Y. S., Liu, X., & Chen, J. J., A novel chaos-based bit-level permutation scheme for digital image encryption. *Optics Commun.*, 284(23), 5415-5423, 2011.

- [8] Wang, Y., Wong, K. W., Liao, X., Xiang, T., Chen, G., A chaos-based image encryption algorithm with variable control parameters. *Chaos, Sol. & Fractals*, 41(4), 1773-1783, 2009.
- [9] Guan, Z. H., Huang, F., Guan, W., Chaos-based image encryption algorithm. *Phys. Let. A*, 346(1-3), 153-157, 2005.
- [10] Xiao, D., Liao, X., Wei, P., Analysis and improvement of a chaos-based image encryption algorithm. *Chaos, Sol. & Fractals*, 40(5), 2191-2199, 2009.
- [11] Kurt, E., Nonlinearities from a non-autonomous chaotic circuit with a non-autonomous model of Chua's diode. *Physica Scripta*, 74(1), 22, 2006.
- [12] Arpacı, B., Kurt, E., An Innovative Tool for the Chaotic Image Encryption, Decryption and Security Tests, *Int. Conf. Electrical, Communication, and Computer Engineering (ICECCE)*, Istanbul, Turkey, 12-13 June 2020, 10.1109/ICECCE49384.2020.9179274.
- [13] Liu, H., Wang, X., Kadir, A., Chaos-based color image encryption using one-time keys and Choquet fuzzy integral. *Int. J. Nonlinear Sci. Numerical Sim.*, 15(1), 1-10, 2014.
- [14] Zhang, Y., Xiao, D., Self-adaptive permutation and combined global diffusion for chaotic color image encryption. *AEU-Int. J. Electronics and Commun.*, 68(4), 361-368, 2014.
- [15] Seyedzadeh, S. M., Mirzakuchaki, S., A fast color image encryption algorithm based on coupled two-dimensional piecewise chaotic map. *Signal Proces.*, 92(5), 1202-1215, 2012.
- [16] Wang, X. Y., Chen, F., & Wang, T., A new compound mode of confusion and diffusion for block encryption of image based on chaos, *Commun. Nonlinear Sci. Numerical Sim.*, 15(9), 2479-2485, 2010.
- [17] Mirzaei, O., Yaghoobi, M., Irani, H., A new image encryption method: parallel sub-image encryption with hyper chaos. *Nonlinear Dyn.*, 67(1), 557-566, 2012.
- [18] Rhouma, R., Meherzi, S., & Belghith, S. OCML-based colour image encryption. *Chaos, Sol. & Fractals*, 40(1), 309-318, 2009.
- [19] Chai, X., Gan, Z., Zhang, M. A fast chaos-based image encryption scheme with a novel plain image-related swapping block permutation and block diffusion. *Multimedia Tools and Applications*, 76(14), 15561-15585, 2017.



# COMPARISON OF THE EFFICIENCY VALUES OF THE RECTIFIERS USED IN THE RF ENERGY HARVESTING SYSTEMS

Kayhan Çelik

Gazi University, Department of Electrical and Electronics Engineering, Faculty of Technology, Ankara, Turkey,  
kayhancelik1923@gmail.com, ORCID: 0000-0003-0371-0473

Erol Kurt

Gazi University, Technology Faculty, Department of Electrical and Electronics Engineering, Ankara, Turkey, E-mail:  
ekurt52tr@yahoo.com, ORCID: 0000-0002-3615-6926

Cite this paper as:

*Celik, K., Kurt, E. Comparison of the efficiency values of the rectifiers used in the RF energy harvesting systems. 9<sup>th</sup> Eur. Conf. Ren. Energy Sys. 21-23 April 2021, Istanbul, Turkey*

---

**Abstract:**

The different rectifier circuit structures are used in the in RF energy harvesting systems. The main structures used to obtain DC power from RF signals are half-wave serial rectifier, half-wave parallel rectifier, differential rectifier, Villard voltage doubler rectifier, Dickson voltage doubler rectifier and the Greinacher charge pump. In this paper, operation principles of these circuit topologies are mentioned and the efficiency values of these structures at different input power levels and at the different frequency values are examined.

---

**Keywords:**

*RF energy harvesting, Rectifier topologies, Efficiency*

---

© 2021 Published by ECRES

## 1. INTRODUCTION

The technique, which is defined as energy harvesting or recycling of energy is the process of capturing low amount of the ambient energy from the sources such as temperature, vibration, radio waves and converting it into usable electricity [1]. Energy harvesting devices detect the energy in our environment, collect it efficiently and effectively and store it for later consumption [2]. In other words, energy-harvesting devices perform all these functions to feed various sensors, low power electronic systems, wireless communication systems and control circuits. Thus, it provides an alternative solution to applications where there is no electricity grid and it is not efficient to obtain energy from great powerful energy sources such as solar or wind. As the efficiency of the systems increases with energy harvesting, it is also possible to use new technologies that require low power such as wireless sensor networks, remote sensing, body implants, radio frequency identification systems [3] [4]. In addition, it enables low power electronic devices to operate without a battery [5]. This has several benefits such as

- No need for maintenance; no need to change batteries,
- Environmental friendliness; Batteries are harmful to both the environment and human health due to their chemical substance,
- Provide as new applications; Monitoring hard-to-reach places with energy-harvesting sensors.

The fact that low-power electronic devices such as embedded systems and wireless remote sensors are fed by batteries and the life of these batteries is limited and they need to be replaced at regular intervals raises an important problem [6]. On the other hand, the energy-harvesting technologies provide an uninterrupted energy source for these systems and on the other hand, they eliminate the dangerous, impractical and costly battery replacement. Most of the energy harvesting applications are designed to be self-powered, maintenance-free for years and cost-effective [7]. In addition, since the power is obtained where the system is set up, it also eliminates cable and transmission losses. The main energy sources used for energy harvesting can be listed as light, kinetic (vibration), thermal and RF [8] [9] [10] [11].

When the literature is examined, it is seen that different rectifier circuit structures are used in the in RF energy harvesting systems. The main structures used to obtain DC power from RF signals are half-wave serial rectifier

[12], half-wave parallel rectifier [13], differential rectifier [14], Villard voltage doubler rectifier [15], Dickson voltage doubler rectifier [16] [17] and the Greinacher charge pump [18]. These circuit topologies are investigated and the efficiency values of these circuits are examined in this paper.

## 2. RECTIFIER CIRCUITS

### 2.1. Half Wave Rectifier

The most basic rectifier structure used in RF energy harvesting systems is the series half-wave rectifier which is given in Figure 1. The circuit consists of 1 diode and 1 capacitor. The operation of the circuit is as follows: At the positive cycle of the AC signal, the D1 diode is in forward biased and the input signal is transferred to the output. At the negative cycle of the AC signal, since D1 diode is reverse biased, it is in the open circuit position and the input signal is not transferred to the output. (ie the negative cycle of the signal is clipped). C1 capacitor provides smoothing of the output signal.

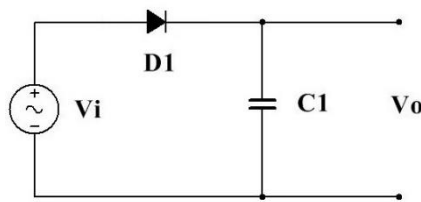


Figure 1. Half-wave series rectifier circuit

### 2.2. Villard (Cockcroft-Walton) voltage doubler rectifier

The single-stage and multi-stage version of the Villard or known as Cockcroft-Walton voltage doubler circuit is given in Figure 2 [19] [20] [21] [17]. The single-stage voltage doubler circuit consists of 2 diodes and 2 capacitors.

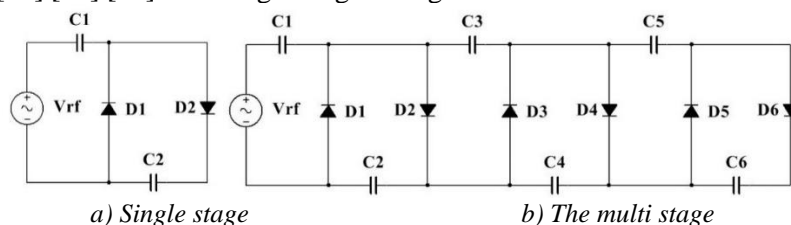


Figure 2. Villard voltage doubler circuit

The ideal state operation of the circuit is as follows: At the negative cycle of the AC signal, diode D1 is at the conduction mode and D2 diode is at the stopping mode. Thus, capacitor C1 is charged to the peak value of the input signal through the conducting diode D1. At the positive cycle of the input signal, diode D1 is at the stopping mode and D2 diode is at the conducting mode. The capacitor C2 is charged to the sum of the peak value of the input signal on the C1 capacitor and the positive peak value of the input signal from the source through the conducting D2 diode, which is twice of the input signal. The disadvantage of this circuit is that as the number of stages increases, the decrease in the output voltage increases and the output ripple voltage increases [19] [20].

### 2.3. Dickson voltage doubler circuit

Another voltage doubler circuit structure is Dickson voltage doubler rectifier which is given in Figure 3 [16] [17]. The first stage of this circuit is the same as the Villard rectifier circuit.

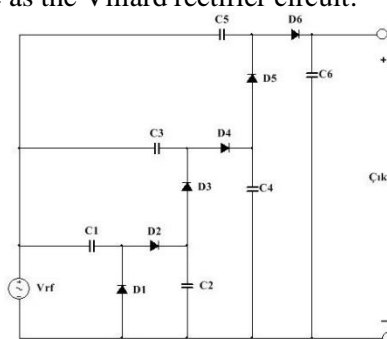


Figure 3. Dickson voltage doubler rectifier circuit

The difference between them is that at the Villard voltage doubler the new stage is connected in series to the input, while at the Dickson voltage doubler it is connected in parallel [16] [17]. Parallel connection of new stages in Dickson voltage doubler decreases the input impedance, thus facilitating impedance matching [22] [17].

#### 2.4. Greinacher voltage doubler

The general structure of the Greinacher voltage doubler rectifier circuit is given in Figure 4. When the circuit is examined, it is understood that this structure is the combined form of two voltage doublers, one positive and the other negative. The ideal state operation of the circuit is as follows: At the positive cycle of the AC signal, diode D2 is at the conduction mode and D1 diode is at the stopping mode. Thus, capacitor C2 is charged to the peak value of the input signal over the conducting diode D2. At the negative cycle of the input signal, diode D3 is at the stopping mode and D4 diode is at the conducting mode. The C4 capacitor is charged to the peak value of the input signal over the D4 diode that is in the transmission. Consequently, the output voltage is equal to twice the peak value of the input signal, which is the total voltage on capacitors C2 and C4. Since this circuit has a balanced structure, it provides a constant current and voltage to the load at the output [18] [23]. The disadvantage is that the number of elements used in the circuit is too much.

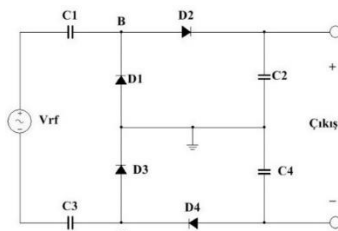


Figure 4. Greinacher voltage doubler circuit

### 3. COMPARISON OF THE RECTIFIER STRUCTURES

The above described rectifier structures are simulated using the Advanced Design System [24] package program and the efficiency values of these circuits are compared in the figures. The simulation criteria are discussed as follows.

- Selected Skyworks SMS-7630 Schottky diode is modeled with Spice parameters.
- Capacitors have been chosen as the ideal circuit element without loss, and the value has been chosen between 1pF and 1000 pF.
- Load resistance has been selected in the range of 100 Ohm to 100MOhm.
- The transmission lines connecting the circuit elements are chosen without loss.
- Impedance matching circuits have been realized with ideal lossless transmission lines as a L type and P type.
- The reverse direction voltage of the diodes are limited to be below 2 Volt, which is the breakdown voltage.

According to these criteria, the rectifier circuits are matched using the L-type and Pi-type microstrip transmission lines to the 50 Ohm source impedance which represents the typical antenna impedance at the different frequency bands such as GSM1800 (1805-1870), UMTS Band 1 (2110-2170), ISM Wi-Fi 2.4 GHz (2400–2495) and LTE Band 7 (2620–2690) [25] [26] [27]. The input power of the source representing the antenna is set to the range of -30 dBm to 0 dBm. The efficiency values obtained at different frequency bands are given in Figures 5, 6, 7 and 8.

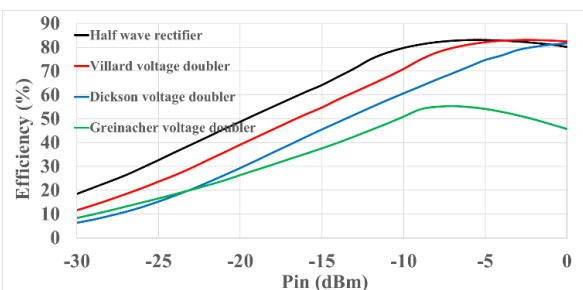


Figure 5. Efficiency values obtained for 1.85 GHz

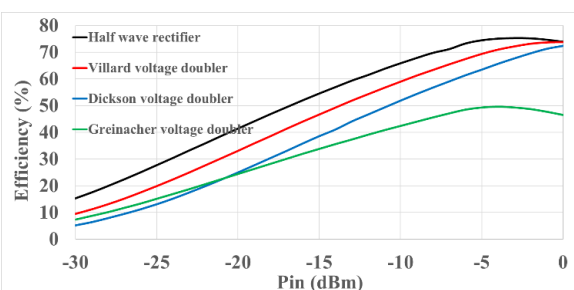


Figure 6. Efficiency values obtained for 2.15 GHz

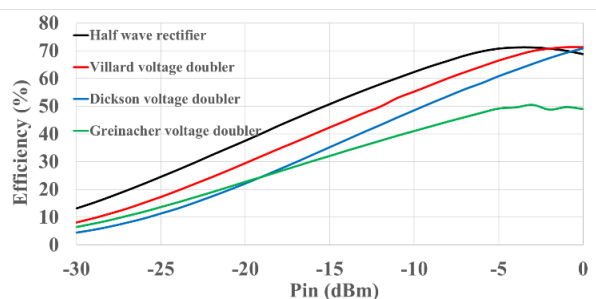


Figure 8. Efficiency values obtained for 2.45 GHz

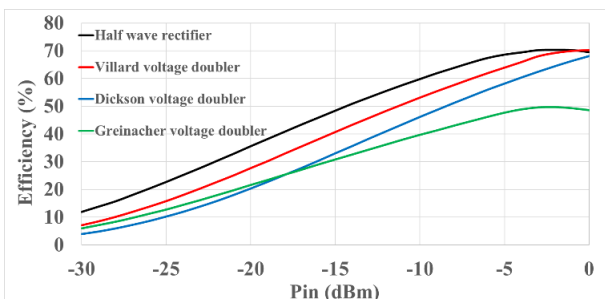


Figure 9. Efficiency values obtained for 2.65 GHz

When the figures are examined, it is seen that the efficiency of the serial half-wave rectifier is generally higher than the others between -30 dBm and -5 dBm in all frequency bands. However, between -5 dBm and 0 dBm, it is seen that the efficiency of the half-wave rectifier decreases and at some frequency values, the efficiency of the Villard voltage doubler is more than a series half-wave. Again, it is seen that the efficiency of the rectifiers decreases when the frequency value increases. In the Table 1, average efficiency values obtained from rectifiers are given. When the table is examined, it is seen that the half-wave rectifier has the highest average efficiency value which supports the above figures.

Table 1. Average efficiency values of rectifiers

	$f = 1,85 \text{ GHz}$	$f = 2,15 \text{ GHz}$	$f = 2,45 \text{ GHz}$	$f = 2,65 \text{ GHz}$
Half Wave Rectifier	59,5	51,3	47,85	45,96
Villard voltage doubler	52,95	44,96	41,82	40,04
Dickson voltage doubler	44,9	38,51	35,91	33,94
Greinacher voltage doubler	35,5	31,97	31,04	30

## 4. CONCLUSIONS

In this paper, the mostly used RF energy harvesting rectifier topologies are mentioned and the efficiency values of these structures depending on the input power and frequency is analyzed. Due to the fact that the half-wave rectifier has the highest efficiency value and the simplicity of its structure, it can be said that it is the best choice at the low power energy harvesting systems as a AC to DC converter.

## ACKNOWLEDGMENT

This study was supported by Gazi University Scientific Research Projects Unit (BAP). (Project No: 07/2020-03)

## REFERENCES

- [1] Wang, Hao, Abbas Jasim, and Xiaodan Chen. "Energy harvesting technologies in roadway and bridge for different applications—A comprehensive review." *Applied energy* 212 (2018): 1083-1094.
- [2] Elsheakh, Dalia. "Microwave antennas for energy harvesting applications." *Microwave Systems and Applications* (2017): 155.
- [3] Priya, Shashank, and Daniel J. Inman, eds. *Energy harvesting technologies*. Vol. 21. New York: Springer, 2009.
- [4] Zhou, Gongbo, et al. "Harvesting ambient environmental energy for wireless sensor networks: a survey." *Journal of Sensors* 2014 (2014).
- [5] Muncuk, Ufuk, et al. "Multiband ambient RF energy harvesting circuit design for enabling batteryless sensors and IoT." *IEEE Internet of Things Journal* 5.4 (2018): 2700-2714.
- [6] La Rosa, Roberto, et al. "Strategies and techniques for powering wireless sensor nodes through energy harvesting and wireless power transfer." *Sensors* 19.12 (2019): 2660.
- [7] Tang, Xiaoli, et al. "Energy harvesting technologies for achieving self-powered wireless sensor networks in machine condition monitoring: A review." *Sensors* 18.12 (2018): 4113.
- [8] Paradiso, J. A., & Starner, T. (2005). Energy scavenging for mobile and wireless electronics. *IEEE Pervasive computing*, 4(1), 18-27.
- [9] Chandrakasan, A., Amirtharajah, R., Cho, S., Goodman, J., Konduri, G., Kulik, J., ... & Wang, A. (1999). Design

- considerations for distributed microsensor systems. In Custom Integrated Circuits, 1999. Proceedings of the IEEE 1999 (pp. 279-286). IEEE.
- [10] Hu, Y., Sawan, M., & El-Gamal, M. N. (2005). An integrated power recovery module dedicated to implantable electronic devices. *Analog Integrated Circuits and Signal Processing*, 43(2), 171-181.
- [11] Visser, H. J., & Vullers, R. J. (2013). RF energy harvesting and transport for wireless sensor network applications: Principles and requirements. *Proceedings of the IEEE*, 101(6), 1410-1423.
- [12] Piñuela, M., Mitcheson, P. D., & Lucyszyn, S. (2013). Ambient RF energy harvesting in urban and semi-urban environments. *IEEE Transactions on microwave theory and techniques*, 61(7), 2715-2726.
- [13] Sun, H., Guo, Y. X., He, M., & Zhong, Z. (2012). Design of a high-efficiency 2.45-GHz rectenna for low-input-power energy harvesting. *IEEE Antennas and Wireless Propagation Letters*, 11, 929-932.
- [14] Lin, Quan Wei, and Xiu Yin Zhang. "Differential rectifier using resistance compression network for improving efficiency over extended input power range." *IEEE Transactions on Microwave Theory and Techniques* 64.9 (2016): 2943-2954.
- [15] Jabbar, Hamid, Young S. Song, and Taikyeong Ted Jeong. "RF energy harvesting system and circuits for charging of mobile devices." *IEEE Transactions on Consumer Electronics* 56.1 (2010): 247-253.
- [16] Nintanavongsa, P., Muncuk, U., Lewis, D. R., & Chowdhury, K. R. (2012). Design optimization and implementation for RF energy harvesting circuits. *IEEE Journal on emerging and selected topics in circuits and systems*, 2(1), 24-33.
- [17] Filiz, S. A. R. I., & Yunus, U. Z. U. N. (2019). A comparative study: voltage multipliers for rf energy harvesting system. *Communications Faculty of Sciences University of Ankara Series A2-A3 Physical Sciences and Engineering*, 61(1), 12-23.
- [18] Olgun, U., Chen, C. C., & Volakis, J. L. (2011). Investigation of rectenna array configurations for enhanced RF power harvesting. *IEEE antennas and wireless propagation letters*, 10, 262-265.
- [19] Jabbar, H., Song, Y. S., & Jeong, T. T. (2010). RF energy harvesting system and circuits for charging of mobile devices. *IEEE Transactions on Consumer Electronics*, 56(1), 247-253.
- [20] Kobougias, I. C., & Tatakis, E. C. (2010). Optimal design of a half-wave Cockcroft–Walton voltage multiplier with minimum total capacitance. *IEEE transactions on Power Electronics*, 25(9), 2460-2468.
- [21] Ali, E. M., Yahaya, N. Z., Perumal, N., & Zakariya, M. A. (2016). Development of Cockcroft-Walton voltage multiplier for RF energy harvesting applications. *Journal of Scientific Research and Development*, 3(3), 47-51.
- [22] Yuan, F. (2010). CMOS circuits for passive wireless microsystems. Springer Science & Business Media.
- [23] Al-Husseini, M., Haskou, A., Rishani, N., & Kabalan, K. Y. (2014). Textile-Based Rectennas. *WIT Transactions on State-of-the-art in Science and Engineering*, 82, 187.
- [24] <https://www.keysight.com/en/pc-1297113/advanced-design-system-ads?nid=-34346.0.00&lc=eng&cc=US>.
- [25] Selvan, Saravana, et al. "Recent advances in the design and development of radio frequency-based energy harvester for powering wireless sensors: a review." *Journal of Electromagnetic Waves and Applications* 32.16 (2018): 2110-2134.
- [26] Khemar, A., Kacha, A., Takhedmit, H., & Abib, G. (2017). Design and experiments of a dual-band rectenna for ambient RF energy harvesting in urban environments. *IET Microwaves, Antennas & Propagation*, 12(1), 49-55.
- [27] Niotaki, Kyriaki, et al. "A compact dual-band rectenna using slot-loaded dual band folded dipole antenna." *IEEE Antennas and Wireless Propagation Letters* 12 (2013): 1634-1637.



# MPPT SYSTEM IMPLEMENTATION FOR A PIEZOELECTRIC ENERGY HARVESTER

Erol Kurt

Gazi University, Technology Faculty, Department of Electrical and Electronics Engineering, TR-06500 Beşevler, Ankara, Turkey, ekurt52tr@yahoo.com,n ORCID: 0000-0002-3615-6926

Davut Özhan

Department of Electronics, Mardin Vocational High School, Mardin Artuklu University, TR-47100, Mardin, Turkey, davutozhan@artuklu.edu.tr, ORCID: 0000-0002-0400-1970

Cite this paper as:

Kurt, E, Özhan D, MPPT system implementation for a piezoelectric energy harvester. 9<sup>th</sup> Eur. Conf. Ren. Energy Sys. 21-23 April 2021, Istanbul, Turkey

---

**Abstract:**

A maximum power point tracking (MPPT) system is designed and applied to a new piezoelectric wind energy harvester (PWEH). The motivation for such an MPPT unit comes from the fact that the power scales of the piezoelectric layers are in the order of  $\mu\text{W}$  with a high total harmonic distortion (THD). Such high THD values cause a certain power loss at the output of the PWEH system and an intense motivation is given to design and implement such systems to get maximum power. The MPPT system is frequently used for many different harvesting studies, but it has been used at the first time for such a high THD output to our knowledge. It includes a rectifier unit storing the rectified energy into a capacitor with a certain voltage called VOC (i.e. the open circuit voltage of harvester), a dc-dc converter applying the one half of VOC as the critical value for control and a control circuit. It is proven that the efficiency is found as 98.41 % and power consumption is measured as low as 5.29  $\mu\text{W}$ .

---

**Keywords:**

Wind energy, piezoelectric, THD, MPPT, efficiency, power

---

© 2021 Published by ECRES

## 1. INTRODUCTION

Energy harvesting is a popular field for many systems, which are used to feed the micro- or mili- Watt energy consuming systems. Among them, wireless sensor networks are the most popular one among the harvester community. As the applications of harvesters increase, electromagnetic, electrostatic and piezoelectric types of devices flourish all over the world. According to the literature, the highest power density is obtained from piezoelectric systems when their low dimensions have been considered compared to the electrostatic and electromagnetic harvesters [1].

The most important issue for harvesters is to use them in place of batteries, since the refilling maintenances for many systems become hard due to environmental harsh conditions. In many harvester systems, maximum power transfer can be the half of the open circuit voltage (i.e.  $V_{oc}/2$ ), thereby there exist many maximum power point tracking (MPPT) systems applications by using  $V_{oc}/2$  value for the parallel connection to the energy harvester with a filtering circuit and capacitor.

According to the literature, there exist a few techniques to estimate and track the MPP point. For instance, hill-climbing (HC) [2,3] and fractional open-circuit voltage (FOCV) methods [4,5] are frequently-used ones. In the hill-climbing method, resistive matching is provided by dynamically changing the duty cycle of a dc-dc converter in discontinuous conduction mode, since it behaves like a variable resistor. Both methods can compare the power generated with a reference and thereby adjust the duty cycle of the dc-dc converter in order to keep the track of the MPP [2,3,6]. FOVC method works on the basis of the determination of  $V_{oc}$ , where the maximum power is transmitted.

According to literature, this value is obtained for  $V_{oc}/2$  for thermoelectric generators (TEGs) [7], RF antennas [7] and piezoelectric energy harvesters (PEHs) [8], whereas it stands around  $4/5 V_{oc}$  for photovoltaics [8]. Energy harvesters are transiently disconnected from the power management module to obtain their  $V_{oc}$ . Then energy

harvesters can be connected to a voltage divider formed by two resistors to determine the appropriate voltage ratio [8-10]. The resistor values are properly chosen so that the loading effect on the energy harvester and power consumption is minimized. Alternatively, the  $V_{OC}$  is sampled using a sensing capacitor [4,5]. Although FOCV implementations need low power consumption, it may not be appropriate for the PEHs every time [2,10,11], because in many applications the required  $V_{OC}$  values determined by FOCV increase to high values such as 100 V. Therefore the realization of the circuit can be expensive and possibly hindered by the voltage limitation of the fabrication technologies [10,12].

In this work, an MPPT scheme has been implemented for a PWEH having a power scale of microwatts. Although the proposed method was initially applied to a simple piezo - beam system by Chew and Zhu [13], the validity and the performance of their technique have not been tested for a high harmonic generating complicated system (i.e. PWEH). It will be proven that their MPPT scheme works well with a high efficiency for such a high harmonic device operating in triple beam system.

## 2. HARVESTER DESIGN

Fig. 1 shows the design of the proposed piezoelectric wind energy harvester (PWEH). It consists of a propeller rotating freely, a shaft transferring the mechanical rotation to the central magnet behind the white pulley, three piezoelectric layers and the filtering and storing electronic part, being responsible for the regulation and the storage of the harvested electrical signal.

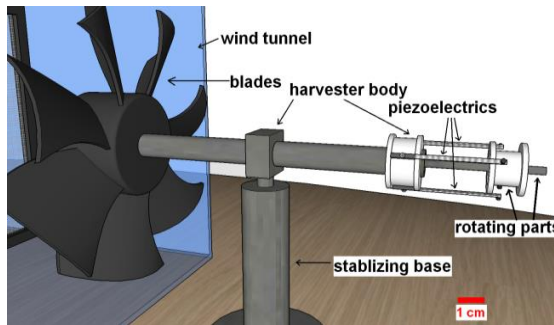


Figure 1. The piezoelectric wind energy harvester design (PWEH).

Three layers are located with 120 degrees relatively to each other on a circular geometry at the same radial distance from the center of the shaft. Each layer tip having a cylindrical permanent magnet with 1 cm diameter and 5 mm thickness. The magnet on the shaft behind the pulley is located as the same pole with the magnets located at the tips of the piezoelectric layers. Thus, they are repelled when the central magnet on the shaft come closer to the tips. The magnet numbers at the tip of the piezoelectric layers differ, thereby, the natural frequencies of the layers change because of the magnet mass. In fact, the higher mass creates lower frequency due to the buckling formation along the gravity. Note that in order to provide the security of the layers during the movement, a cylindrical polyethylene material has been put on the shaft. It prevents the damage of the piezoelectric layers especially at high wind speeds. The theory for the PWEH has been described in one of our earlier studies [14]. Therefore we will not give the details on the mathematical manipulation of the system of equations, however the equations can be summarized as follows for the clarity:

$$\frac{d\theta}{dt} = \omega, \quad (1)$$

$$m_1 \frac{d^2 r_1}{dt^2} = -k r_1 - \gamma \frac{dr_1}{dt} + \alpha v_1 + f_m \delta(\theta - \theta_1), \quad (2)$$

$$m_2 \frac{d^2 r_2}{dt^2} = -k r_2 - \gamma \frac{dr_2}{dt} + \alpha v_2 + f_m \delta(\theta - \theta_2), \quad (3)$$

$$m_3 \frac{d^2 r_3}{dt^2} = -k r_3 - \gamma \frac{dr_3}{dt} + \alpha v_3 + f_m \delta(\theta - \theta_3), \quad (4)$$

$$I_1 = \alpha \frac{dr_1}{dt} - C \frac{dv_1}{dt}, \quad (5)$$

$$I_2 = \alpha \frac{dr_2}{dt} - C \frac{dv_2}{dt}, \quad (6)$$

$$I_3 = \alpha \frac{dr_3}{dt} - C \frac{dv_3}{dt}, \quad (7)$$

Here  $\theta$ ,  $\omega$ ,  $\delta$ ,  $m$ ,  $r$ ,  $u, \alpha$ ,  $V$ ,  $fm$ ,  $\theta A$ ,  $C$ ,  $I$  and  $k$  denote angular position of the magnet, propeller speed, Kronecker delta which gives “1” for  $\theta = \theta_i$  ( $i = 1 \dots 3$ ) else “0”, mass of the layer, radial position to center of shaft, displacement of layer, force factor of piezoelectric material, piezoelectric voltage, magnetic repulsion force, angular position of layer, piezoelectric capacitance, harvested current and stiffness constant of piezoelectric, respectively. When the propeller rotates with  $\omega$ , that effect is conveyed to the radial position  $r$  for the piezoelectrics, which are denoted by 1,2 and 3. The tip mass  $m_1$   $m_2$  and  $m_3$  affects the natural frequencies of layers. When the radial distance changes via the buckling, the layers generate currents given by Eqs. (5-7). Note that the electrical current depends on the velocity and the potential change by time according to the formulation above [15].

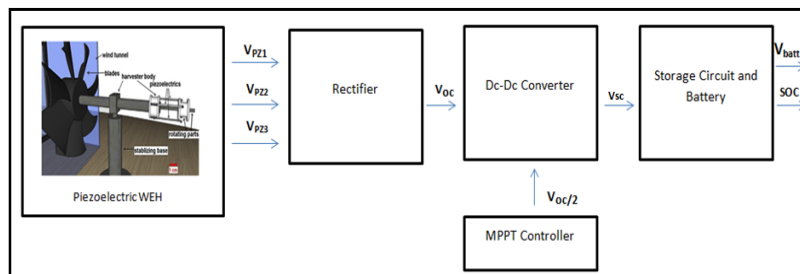


Figure 2. General circuit diagram of piezoelectric wind energy harvester (PWEH).

Fig. 2 shows the block diagram of the proposed MPPT controller added PWEH system. The harvested voltages from three piezoelectric layers are initially transferred into a rectifier circuit. Then the rectifier output is directed to a dc-dc converter as the main background for the MPPT controller. At this stage, the MPPT controller decides the power by using  $V_{oc}/2$ . Then, the output of the converter is transmitted into a storage circuit and the battery to generate the battery voltage and state of charge (SOC).

The general circuit diagram has been of 4 block units. The first block the PWEH is the piezo layers sources. A sample of the pure harvested waveforms (i.e. input waveform for the rectifier) are shown in Fig. 1. The layers have been positioned on 120 degrees angular location for each other and they produce different waveforms in amplitude and frequency. The second block of the PWEH is the rectifier. With the implementation of a full-bridge rectifier, the AC waveform of the transducer is converted to a DC waveform. The third block of the PWEH is the buck converter. Full rectified piezoelectric signal ( $V_{rect}$ ) is controlled by buck converter for MPPT. In the last block, voltage values with the battery state of charge is shown.

As mentioned before, the optimum value of the rectified signal ( $V_{oc}$ ) should be equal to half of  $V_{oc}$ . The rectifier operates as an open circuit ( $V_{oc}$ ), and then the MPPT can obtain the  $V_{oc}$  value of the rectifier. This value is stored in one capacitor and used as the reference voltage of  $V_{rect}$ . By monitoring the change of  $V_{rect}$ , the MPPT controls the DC-DC converter to regulate the output signal at the optimum value (around  $V_{oc}/2$ ).

### 3. EXPERIMENTAL

The experimental setup is shown in (Fig. 1). The harvester has been tested at different wind speeds. Each piezoelectric layer has the weight of 1.4 g and its capacitance and stiffness values are 26nF and 380 N/m, respectively. A data acquisition system with NI USB-6250 DAQ has been used during the experiments. This card can make a good precision multiple recording via its 16 analog inputs, and displacement and harvested voltages can be recorded, synchronously. A Yokogawa type oscilloscope has also been used in order to follow the outputs of the circuit. Experimental signal graph has been show Fig. 3.

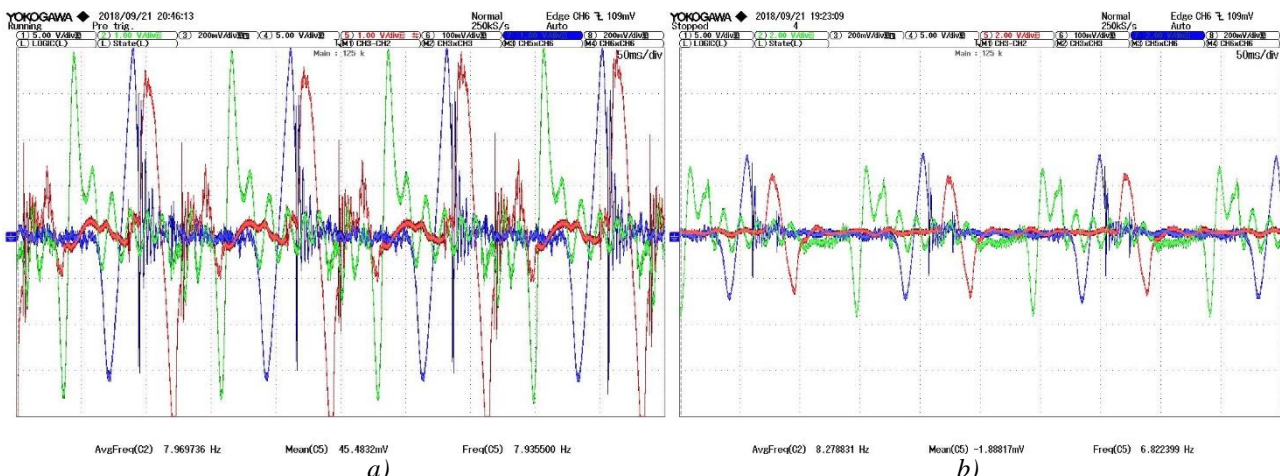


Figure 3. Real waveforms of piezoelectric layers a) wind tunnel speeds at 2.7 m/s, b) 6.1 m/s.

For a more detailed circuit scheme, we refer to Fig. 4. This simulation diagram includes an ac-dc rectifier, a dc-dc buck converter, an MPPT controller circuit and an electrochemical battery. For instance, VPZ1, VPZ2, VPZ3 denote the waveforms from the terminals of layers (PZ1,PZ2, PZ3) and VOC, VOC/2, VSC, Vbat denote the rectified voltage, output voltage of the converter, battery voltage, and state of charge of the battery, respectively.

Table 1. Simulation parameters

Item no	Item Description	Values
1	PZT layer	1.4 g
2	Output filter, $L_f$ , $C_1$	0.7mH
3	Buck converter switch, $L_c$ , $C_s$ , $R_s$	MOSFET
4	MPPT controller unit $V_{oc}$ , $V_{sc}$ , switching frequency	72 V
5	Type of battery	26nF
	Nominal voltage	380N/m
	Rated capacity,	0.12N
	Max. capacity,	275 Hz
	Full charge voltage Nominal	Lead-acid.
	discharge current Internal	12 V
	resistance	6.5Ah
		6.825Ah
		12.6 V
		0.1837 A
		0.018462 $\Omega$

Before applying the experimental work, a detailed simulation has been performed. The optimized parameters for the experimental work have been ascertained as in Table 1. Matlab signal graph has been shown Fig. 4.

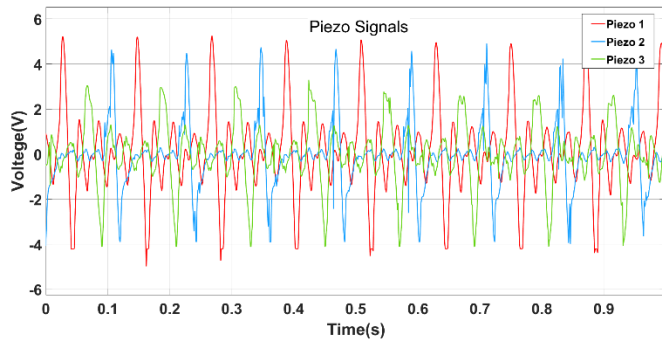


Figure 4. Matlab simulation piezoelectric signals

The experiments are performed for varying wind speeds. Initially, the blades of the PWEH have been excited by a medium speed wind flow (i.e. 3 m/s). The voltage over the buck converter increases in accordance with the wind speed  $v$ . In the PWEH system, the MPP is encountered at  $V_{oc}/2$  as mentioned before, Fig. 5 shows a measurement over the capacitor and an electrical load 100 kOhm.

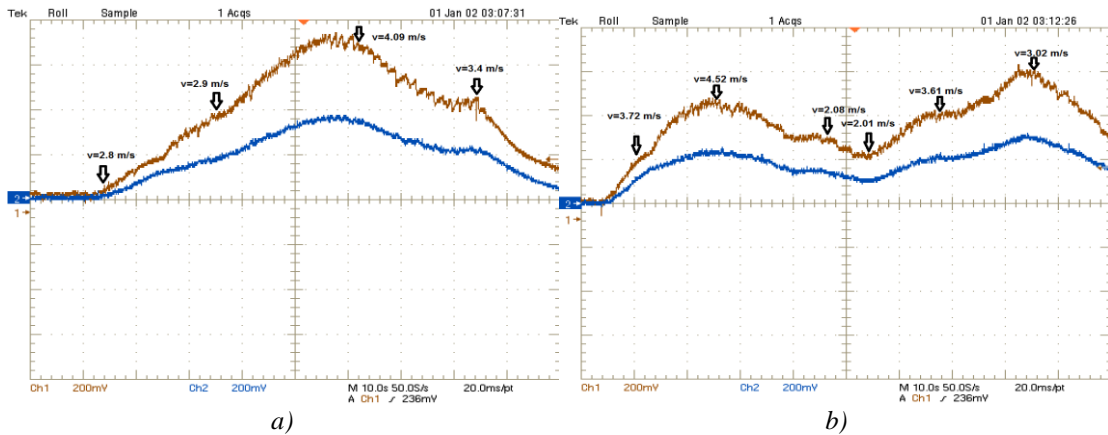


Figure 5. Real waveforms of  $V_{oc}$  and  $V_{oc}/2$  for the electrical loads (a) 100 kOhm and (b) 50 kOhm.

For the maximum power transfer efficiency, there should be an optimal load value at the output. Various electrical loads between 50 Ohm and 1.5 kOhm have been tested during the experiments. In our case, the maximum power is received at 1.2 kOhm as estimated from the simulations. The experimental harvested power values and efficiencies are depicted in Fig. 13 for various electrical loads. The maximum power is 5.6 mW when the inner impedance is equal to the load. According to the experiments, the efficiency comes closer to  $V_{oc}/2$  value between 85 and 99 %. According to experimental results, power changes between 3.82 mW and 5.49 mW in show Fig. 6.

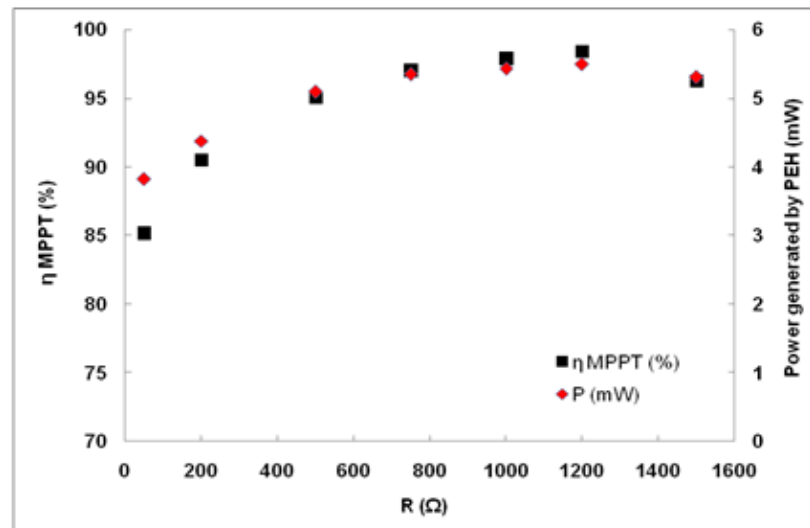


Figure 6. Experimental power and efficiency values versus resistive load.

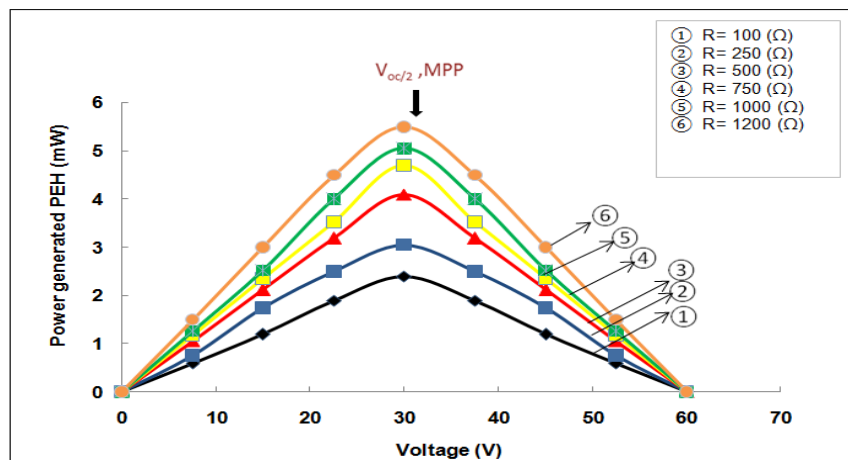


Figure 7. MPP based power generation for different resistive loads.

It is obvious that the harvested powers for various loads give different power outputs, as expected. For instance, the output power values of the lower resistances yield to 2 - 3 mW, however the loads such as 1.2 kOhm achieves 5.7 mW output power due to the contribution of the proposed MPP system. Also note that the maximum power is received for the half of the capacitor voltage in all cases, as shown in Fig. 7.

## 5. CONCLUSION

A power optimization scheme has been applied to a new developed PWEH for low power wind energy conversion tasks. The novelty of this work is that the generated voltage waveforms have high total harmonic distortion character and thereby a proper power optimization is required for such a system. The theoretical and experimental studies have been performed on the basis that  $V_{sc} = V_{OC}/2$  value. In the design and implementation, the generated signals from the harvester have been rectified via a full bridge rectifier and stored into a capacitor, where the charge voltage  $V_{oc}/2$  will then be used for the maximum power generation. In the implemented system, a very low power consumption within the order of microwatts has been obtained for the control circuit. Thus, the system is ideal for low power harvesting systems. According to the experimental tests, up to 5.7 mW power has been obtained from the output terminals. Therefore, the proposed system for the PWEH can lead to 98.41% power efficiency with very low power consumption in the control units. According to the literature, there exist many studies including very complicated control blocks and circuits, however their power consumption is the main problem for such complicated circuit morphologies.

## REFERENCES

- [1] B. Mutlu, E. Kurt, N. Bizon, and J.M. Lopez Guede, "Design and Fabrication of a New Micro-Power Scaled Electromagnetic Harvester", *J. Energy Systems*, 3(2); (2019); pp. 51-66, DOI: 10.30521/jes.554900
- [2] N. Kong, and D. S. Ha, "Low-power design of a self-powered piezoelectric energy harvesting system with maximum power point tracking," *IEEE Trans. Power Electron.*, vol. 27, no. 5, pp. 2298-2308, 2012.
- [3] H. Kim, S. Kim, C. K. Kwon, Y. J. Min, C. Kim, and S. W. Kim, "An energy-efficient fast maximum power point tracking circuit in an 800- $\mu$ W photovoltaic energy harvester," *IEEE Trans. Power Electron.*, vol. 28, no. 6, pp. 2927-2935, 2013.
- [4] M. Shim, J. Kim, J. Jeong, S. Park, and C. Kim, "Self-powered 30  $\mu$ W to 10 mW piezoelectric energy harvesting system with 9.09 ms/V maximum power point tracking time," *IEEE J. Solid-State Circuits*, vol. 50, no. 10, pp. 2367-2379, 2015.
- [5] G. Chowdary, A. Singh, and S. Chatterjee, "An 18 nA, 87% efficient solar, vibration and RF energy-harvesting power management system with a single shared inductor," *IEEE J. Solid-State Circuits*, vol. 51, no. 10, pp. 2501-2513, 2016.
- [6] A. Montecucco, and A. R. Knox, "Maximum power point tracking converter based on the open-circuit voltage method for thermoelectric generators," *IEEE Trans. Power Electron.*, vol. 30, no. 2, pp. 828-839, 2015.
- [7] K. Celik, and E. Kurt, "A novel meander line integrated E-shaped rectenna for energy harvesting applications", *Int. J. RF & Microw. Computer-Aided Engineer.*, vol. 29, no. 1, e21627, 2019.
- [8] Y. C. Shu, I. C. Lien, and W. J. Wu, "An improved analysis of the SSHI interface in piezoelectric energy harvesting," *Smart Mater. Struct.*, vol. 16, no. 6, pp. 2253-2264, 2007.
- [9] A. S. Weddell, G. V. Merrett, and B. M. Al-Hashimi, "Photovoltaic sample-and-hold circuit enabling MPPT indoors for low-power systems," *IEEE Trans. Circuits Syst. I, Reg. Papers*, vol. 59, no. 6, pp. 1196-1204, 2012.
- [10] A. Tabesh, and L. G. Fréchette, "A low-power stand-alone adaptive circuit for harvesting energy from a piezoelectric micropower generator," *IEEE Trans. Ind. Electron.*, vol. 57, no. 3, pp. 840-849, 2010.
- [11] G. K. Ottman, H. F. Hofmann, A. C. Bhatt, and G. A. Lesieutre, "Adaptive piezoelectric energy harvesting circuit for wireless remote power supply," *IEEE Trans. Power Electron.*, vol. 17, no. 5, pp. 669-676, 2002.
- [12] P. Gasnier, J. Willemin, S. Boisseau, G. Despesse, C. Condemeine, G. Gouvernet, and J. J. Chaillout, "An autonomous piezoelectric energy harvesting IC based on a synchronous multi-shot technique," *IEEE J. Solid-State Circuits*, vol. 49, no. 7, pp. 1561-1570, 2014.
- [13] Z. J. Chew, M. Zhu, "Adaptive maximum power point finding using direct VOC/2 tracking method with microwatt power consumption for energy harvesting," *IEEE Trans. Power Electr.*, vol. 33, no. 9, pp. 8164-8173, 2018.
- [14] E. Kurt, F. Cottone, Y. Uzun, F. Orfei, M. Mattarelli, D. Ozhan, "Design and implementation of a new contactless triple piezoelectrics wind energy harvester," *International Journal of Hydrogen Energy*, 42 (28), 17813-17822.
- [15] E. Kurt, Y. Uzun, "Nonlinear problems in piezoelectric harvesters under magnetic field," in: *Energy Harvesting and Energy Efficiency*, Springer, 2017.



# ANALYSIS OF ATMOSPHERIC TRANSPORTED PARTICULATE MATTER AND INVESTIGATION OF ITS EFFECTS ON SOLAR PANEL

Murat Altıntaş

Department of Electrical Engineering, Faculty of Engineering, Harran University, Turkey,  
murat@mualmuhendislik.com.tr, ORCID No. 0000-0002-2055-2801

Serdal Arslan

Department of Electrical, Harran University Organized Industrial Zone Vocational High School Sanliurfa, Turkey  
serdalarslan@harran.edu.tr, ORCID No. 0000-0002-1187-5633

Cite this paper as:

Altıntaş, M, Arslan, S. Analysis of atmospheric transported particulate matter and investigation of its effects on solar panel. 9th Eur. Conf. Ren. Energy Sys. 21-23 April 2021, Istanbul, Turkey

---

**Abstract:**

Systems that generate electricity from solar energy are exposed to dust-induced pollution depending on the geographical conditions of the regions in which they are located. It is essential to determine the effects of these pollution values on the panel on a regional basis and the characteristics of the dust. In this study, monthly data were taken of the panel located at the Solar Power Plant (SPP) in Sanliurfa, its dusty state and dust-free (cleaned) state with natural roads. In addition, dust samples collected monthly from the surface of the panel were analyzed in scanning electron microscopy. Monthly percentage distributions of elements contained in particles found in nature as oxides were obtained.

---

**Keywords:**

electron microscopy, particles, dust, solar panel, pollution

---

© 2021 Published by ECRES

## 1. INTRODUCTION

In daylight, grains of 10 microns and larger can be seen on a dark background. In dark environments without lighting, 100 microns and small particles are invisible to the eye. The rate at which a Silicon grain of  $10 \mu\text{m}$  falls to the ground is  $1 \text{ cm/sec}$ . This grain can be dragged through the air up to a distance of  $100 \text{ m}$  by air flow, while grains of 1 micron size can be moved to distances of kilometers [1]. It is known that these particles create noticeable pollution on surfaces where they fall to the ground. Although there is no review published in our country regarding dust quantity measurement, the only batch measurement report that provides bulk data flow is the data obtained from the weather monitoring and forecasting station located in 61 provinces affiliated to the Ministry of Environment and Urbanization in Turkey. These data, which include provincial-based results, give the measurement result for PM10 values in some provinces. When we select a certain date range for Sanliurfa province, we can access the data, but it shows measurement results close to the dates we choose. Achieving continuous measurement value (continuous data acquisition) for SPP in regional conditions or analyzing samples that will be taken around the clock during the day in a laboratory environment will result in a significant time loss and high cost. There are different measurement methods for surface pollution dust measurement in laboratory environment.

Weighing the total dust in a certain amount of air by separating it from the air through precipitation is a method of measuring dust by weighing. In this method, the weight of the powder is calculated as  $\text{mgr/cm}^3$ . However, in this method, the effect of large dust grains is quite high. This can also lead to an error in measurement. Experts who take into account this misleading information select dust grains larger than 5 microns before weighing begins and weighing is done with the remaining small grains. Another measurement technique used in laboratory conditions is known as counting. In the counting method, grains less than  $5 \mu\text{m}$  are collected on a glass layer and separated from large segmented powders. By counting grains less than  $5 \mu\text{m}$ , the ambient dust load is determined by calculating in  $\text{grain/cm}^3$ . In addition to these methods, the dust obtained from the field by scanning electron microscope (SEM), which allows dust analysis to take place, is placed in the dust bucket and offers us an analysis output that indicates

the amount of dust being scanned. The dust effect was investigated by obtaining monthly data by performing this measurement under regional conditions and within the Solar Power Plant.

## **2. LITERATURE REVIEW**

According to the World Health Organization (WHO) 2019 report [2], the European Union (EU) supports strong climate action, sustainable development and Environmental Protection. In industrial pollution and risk management, Turkey is said to be at an early stage for compliance with most EU directives and regulations. As of 2010, Turkey calculates the dust forecast values in 62 provinces, announces them online from the General Directorate of Meteorology (MGM) site and analyzes the dust transport values known as one of the air pollution values [2,3]. Information from the MGM site on pollination values is based on the sand and dust storm prediction method using the BSc-DREAM8b model. The system, called "Dust Transport Warning System" by MGM, has been made available to individuals and institutions by publishing point estimate values made on the basis of Provinces online over the internet. According to MGM, desert dust, known as mineral dust particles, is the most dominant type of aerosol in the atmosphere. Dust activated by meteorological effects from deserts rises to the atmospheric layers and can travel long distances, and although desert dust of large diameters succumbs to gravity near the areas where it was created, dust of smaller diameters can travel thousands of km. For this reason, there is research indicating that dust rising from large desert areas such as Sahara, Gobi, Taklamakan deserts, which are sources of desert dust, carries valuable minerals to the oceans and Amazons and has a fertilization effect [3]. Considering the average amount of dust release obtained from the combination of large desert areas and small desert areas, it was stated that it accounted for 70% of the world's dust value in a calendar year [4]. Sand and dust storms, in particular, most often affect vehicles and sectors (air, land and sea transport), as well as causing negative effects on socio-economic life. Due to its geographical location, the MGM official site on dust release values in Turkey contains online daily average surface dust concentration values. Surface dust concentration value, is expressed by microgram cube ( $\mu\text{g}/\text{m}^3$ ) that is a unit of air quality measurement. As can be seen from this unit of measurement, there is a linear relationship between the air pollution index and the surface dust concentration, and the surface dust concentration value is a factor that affects the air pollution index values. If human hair is 50-70  $\mu\text{m}$  in diameter and a fine sand grain is 90  $\mu\text{m}$  in diameter, dust, pollen, mold etc.  $<10 \mu\text{m}$  (PM10) can be accepted as particulate matter [5]. The limit value for contamination has been determined by WHO as  $50 \mu\text{g}/\text{m}^3$ . 7 factors (parameters) that play a role in determining air pollution factors are observed in Turkey. These parameters are particulate matter (PM10), ozone ( $\text{O}_3$ ), nitrogen dioxide ( $\text{NO}_2$ ), sulfur dioxide ( $\text{SO}_2$ ) and carbon monoxide ( $\text{CO}$ ) [6]. For example, according to the PM10 report dated 15.03.2020 received from the Sanliurfa province observation station, the PM10 value shows a value of  $23 \mu\text{g}/\text{m}^3$  [6]. This pollution value is known as the dust pollution value in another variation of particulate matter. These values can be obtained from City station data on an hourly daily basis. For monthly annual reports, provincial-based reporting can be done. The system allows one provincial election and one provincial station election. In terms of dust transport, there can be hourly changes based on the province, the fact that dusts are constantly in motion with the influence of the atmosphere is also a factor of regional pollination. In addition, dust particles continue to be transported in other cities in Turkey [6,7]. In addition to the fact that dust appears dirty by positioning on items, it is a known fact that electronic devices have an effective use as an obstacle to the principle of routine operation and their impact on the life of items. But if these powders are conjoined on the surface of an object, there are various cleaning methods. Dusting, which we usually do in our homes, is a rough treatment method. Photovoltaic (PV) panels, which cover a larger volume as a surface and consist of sensitive modules, have various dust treatment methods as well as rough cleaning method [8].

## **3. METHOD FOR CREATING A POLLUTION MEASUREMENT SITE AND DATA SET**

1 PV panel is located next to our unlicensed SPP site with a production capacity of 1 MW, located in Akziyaret Village, Bölgüp Location, Karaköprü district, Sanliurfa province. Figure 1 shows a general view of the solar power plant site.



Figure 1. General view of the SPP field where the panels are positioned

Technical information about the positioned PV panel, which is a data set element for dust pollution measurement, next to the area of the plant site, is as follows: It is a polycrystalline solar panel with a production power of 270 Wp (WattPeak). Each PV panel has a width ratio of 30 to 35 cm and a wall thickness of 0.5 cm, and each PV panel consists of 60 cells. Panel weight is 18 kg. PV panels are positioned at an angle of 30° in our subject plant.



Figure 2. Positioning of polycrystalline PV panel on terrain (1. day clean PV panel image)

Production values of our subject power plant were measured with digital measuring device on 15th and 30th day of each month. For 1 piece of 270 Wp PV panel that we placed in the GES plant site, the pollution and clean conditions were examined separately. In our study of the effect of dust on the panel, current and voltage measurements were made at idle and load. The measurements were recorded to be evaluated within the scope of the study. The check with eyes and cleaning of the PV panel we positioned in the Solar Power Plant was carried out on the 30th day of every month.

Since there are too many monthly dust pictures, the images of the method of obtaining the amount of dust from the panels for April are shown in Figure 3:



Figure 3. 30-day PV panel surface accumulated dust and PV panel cleaning, a-April dirty panel surface accumulated dust. b-Panel surface cleaned image.

Then, the particles that provide contamination on the panel surface were placed in a jar collected from the panel surface for analysis in the HÜBTAM Laboratory at Harran University, and the content and amount of particles that cause dust were determined by analyzing the energy scattering spectroscopy obtained from the particles contained in the laboratory. A scanning electron microscope (SEM) image of dust particles that accumulate naturally on panel glasses of particles observed in the SEM device was also studied. As can be seen from the SEM image in Figure 4 of dust particles that accumulate naturally on Panel glasses, fine dust particles are complex in shape, including spherical, ellipsoid and angled. Particles are a mixture of large and small volume particles. Random particle diameters were found to be in the range of 50 µm to 450 µm according to SEM images.

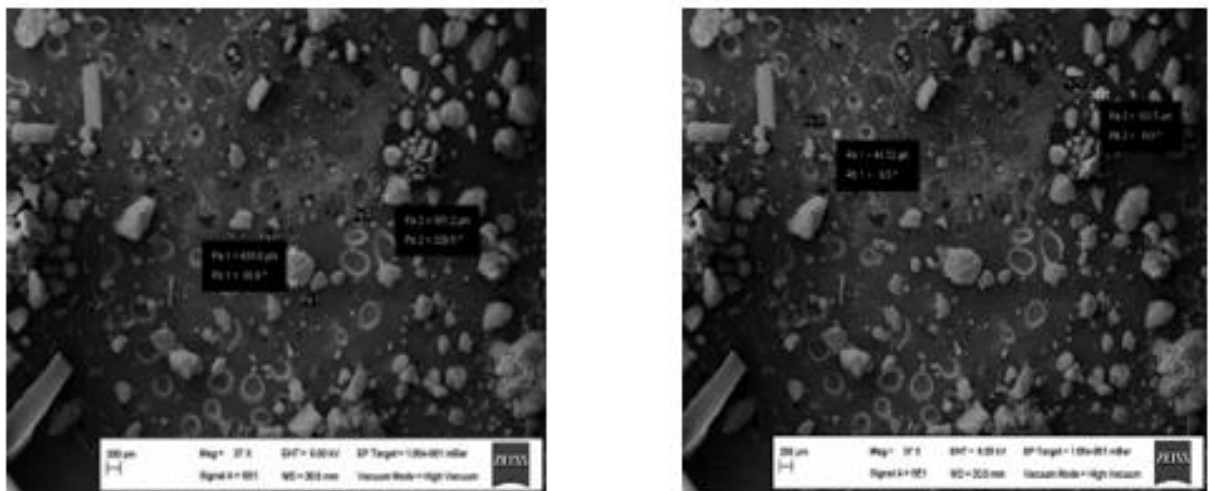


Figure 4. Appearance of microstructure of particulate matter in SEM analysis

#### 4. DISCUSSION AND EVALUATION

The panel located in SPP was analyzed monthly in terms of the impact of substances with pollution effects on electricity generation and content. First, the production value was recorded by measuring with a digital multimeter measuring device, and after this process, the panel was cleaned and the measurement was repeated. Decrease in production values due to contamination in PV panels and increase in output voltage after cleaning PV panels were observed (Table 1).

Table 1. PV shows the effect of dusting detected by a digital measuring device on panels on production measurement values comparison of dirty and clean panel production

CWT 60P 270WP SOLAR PANEL MEASUREMENTS							
CONNECTED LOAD	DATE	VOLTAGE	CURRENT	DIRTY PANEL VOLTAGE (V)	DIRTY PANEL CURRENT (A)	CLEAN PANEL VOLTAGE (V)	CLEAN PANEL CURRENT (A)
NO LOAD	30.3.2020	Voc	Isc	36.38	6,74	37.34	6,67
58Ω	30.3.2020	V	I	36.10	0.622	36.54	0.63
NO LOAD	13.4.2020	Voc	Isc	35.34	9,16	35.65	8,81
58Ω	13.4.2020	V	I	35.01	0.603	34.98	0.603
NO LOAD	27.4.2020	Voc	Isc	35.21	6,49	36.30	6,55
58Ω	27.4.2020	V	I	34.55	0.595	34.90	0.601
NO LOAD	7.5.2020	Voc	Isc	35.37	9,84	35.41	10,19
58Ω	7.5.2020	V	I	34.99	0.603	35.07	0.604
NO LOAD	21.5.2020	Voc	Isc	33.91	9,23	34.06	9,27
58Ω	21.5.2020	V	I	33.61	0.579	33.77	0.582
NO LOAD	9.6.2020	Voc	Isc	34.30	7,48	34.5	7,1

58Ω	9.6.2020	V	I	33.40	0.575	34.20	0.589
NO LOAD	24.6.2020	Voc	Isc	33.36	8.85	34.10	8.84
58Ω	24.6.2020	V	I	32.20	0.555	33.4	0.576
NO LOAD	2.7.2020	Voc	Isc	34.0	5,35	34.2	6,37
58Ω	2.7.2020	V	I	33.7	0.581	33.9	0.584
NO LOAD	21.7.2020	Voc	Isc	33.7	8,83	34.3	9,12
58Ω	21.7.2020	V	I	33.3	0.574	34.2	0.589
NO LOAD	14.8.2020	Voc	Isc	33.8	8,15	34.0	8,6
58Ω	14.8.2020	V	I	33.4	0.575	33.7	0.581
NO LOAD	29.8.2020	Voc	Isc	34.4	6,61	35.0	6,95
58Ω	29.8.2020	V	I	34.0	0.603	34.7	0.598
NO LOAD	9.9.2020	Voc	Isc	33.4	9,02	33.0	9,26
58Ω	9.9.2020	V	I	32.09	0.553	32.8	0.565
NO LOAD	30.9.2020	Voc	Isc	33.09	7,82	34.0	8,11
58Ω	30.9.2020	V	I	32.04	0.552	33.75	0.582
NO LOAD	10.10.2020	Voc	Isc	33.86	4,25	34.85	4,7
58Ω	10.10.2020	V	I	33.35	0,58	34.5	0.594
NO LOAD	28.10.2020	Voc	Isc	34.83	6,56	35.24	6,62
58Ω	28.10.2020	V	I	34.44	1,63	35.09	1,67
NO LOAD	15.11.2020	Voc	Isc	34,5V	3,05A	35,23V	2,96A
NO LOAD	8.12.2020	Voc	Isc	36,25V	1,97A	36,38V	1,46A

The particles that provide contamination on the panel surface were then placed in a jar collected from the panel surface for analysis in the HÜBTAM Laboratory and analyzed in the scanning electron microscope in the laboratory and the content and amount of particles that cause dust were determined. Figures 5, 6 and 7 show a monthly change in elements with more than 5% of the amount of elements in the powder content.

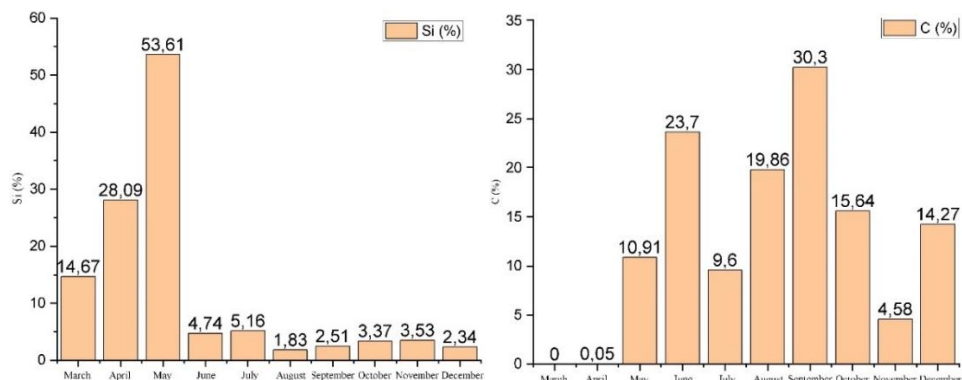


Figure 5. Monthly change of elements Si and C

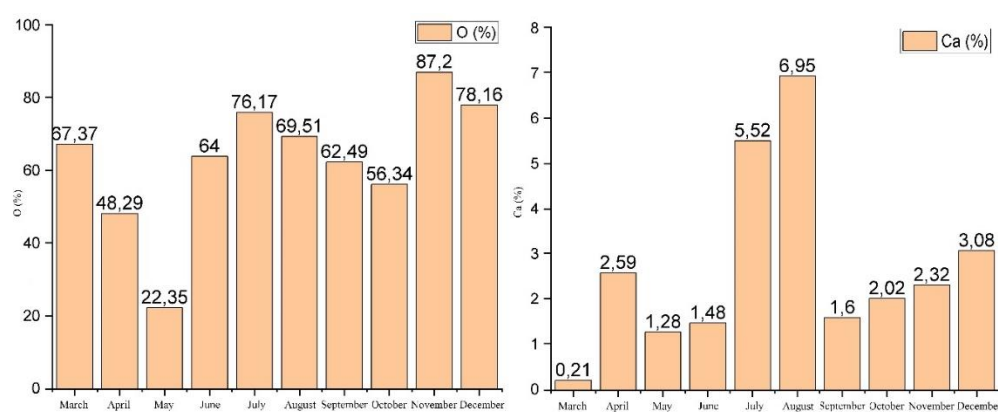


Figure 6. Monthly change of O and Ca elements

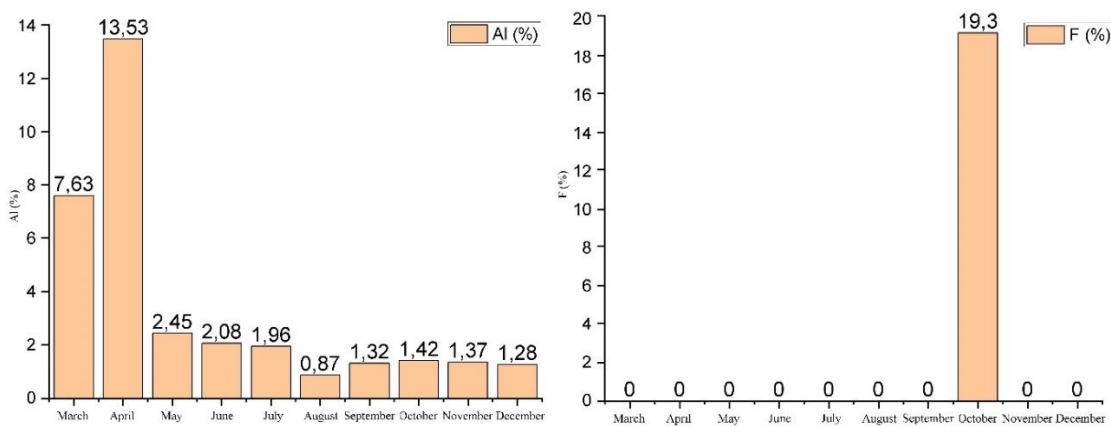


Figure 7. Monthly change of of Al and F elements

In Figure 5, Figure 6 and Figure 7, the particles contain oxide forms of elements that are found in nature, such as Si, C, Ca, O, Al and F. In particular, the height of the oxygen element given in Figure 6 shows this. Dust flying in the air, air currents, etc. can differ regionally because it is carried by meteorological events. As can be seen from the results, during the period between the end of the winter season and the transition of the spring period, the transitions of heavy elements carried by dust also increase. Due to this transition, the tendency of polluting gases to adhere to panel panel surfaces also increases. At this stage, a review of panel surface cleaning methods is considered necessary. Element change according to months below 5% is given in Table 2:

Table 2. Element distribution below %5 by month

Months	Element Name	Amount of Element (%)	Element Name	Amount of Element (%)	Element Name	Amount of Element (%)	Element Name	Amount of Element (%)	Element Name	Amount of Element (%)	Element Name	Amount of Element (%)
March	S	0	Mg	2,12	Fe	1,54	Na	1,49	In	0	K	1,09
April	S	1,19	Mg	3,6	Fe	1,3	Na	0	In	0,83	K	0,23
May	S	4,09	Mg	1,56	Fe	0,42	Na	1,93	In	1,4	K	0
June	S	0,22	Mg	1,49	Fe	0,47	Na	1,09	In	0	K	0,36
July	S	0	Mg	0,57	Fe	0,76	Na	0,01	In	0	K	0,12
August	S	0,34	Mg	0,19	Fe	0,22	Na	0,06	In	0	K	0,11
September	S	0,43	Mg	0,43	Fe	0,27	Na	0,42	In	0	K	0,2
October	S	0	Mg	1,11	Fe	0,57	Na	0,07	In	0	K	0,11
November	S	0	Mg	0,23	Fe	0,58	Na	0	In	0	K	0,16
December	S	0	Mg	0,56	Fe	0,23	Na	0	In	0	K	0,03

The other elements are found to be below %0.5 in nature, such as Nb, Cl, Ti, P, Cu, Au and Ba. It contains oxide forms of some elements found in Table 1 and Table 2. In addition, unfortunately, there are no devices in the laboratory to find the chemical formulas of these oxides. For this reason, elemental analysis was carried out. Microstructure result obtained by SEM analysis of dust particles accumulated by natural means; grain diameter change according to monthly results is given in Figure 8. Unfortunately, the size of particles cannot be determined precisely because there is no "Particle Sizer" in the laboratory. However, the diameter obtained from the microstructure according to months is preliminary data to obtain information about. About dust sizes as a result of the change. Dust sizes are high in March, April and May. It is similar in size in June, July, August, September, October and November. However, it increased in December. (Figure 8). As seen in Figure 8, as the particle size decreases, the panel output voltage decreases as given in Table 1. This situation can be expressed by the following explanation in Ertuğrul Adığüzel's work [9]: "It has been observed that the energy obtained from PV panels

increases, dust particles with small particle size prevent the radiation more, energy loss increases with the increase of dust density and marble dust blocks less radiation compared to coal dust."

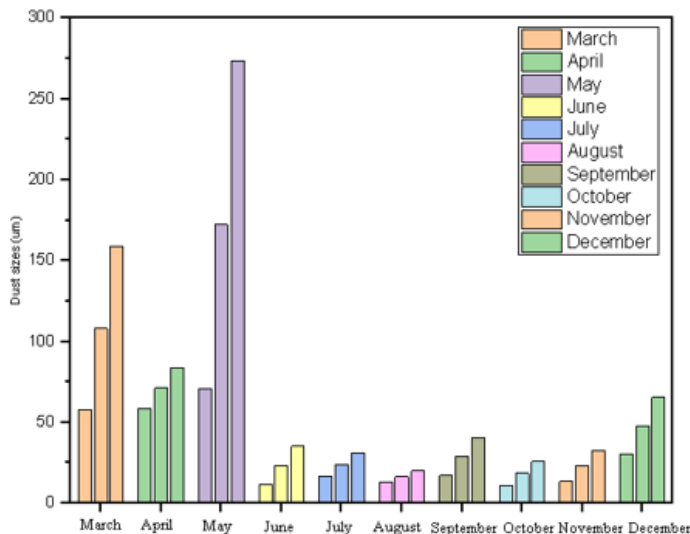


Figure 8. Change of powder diameters by month

## 5.CONCLUSION

In our previous study [10] PVsyst software was used for the solar power plant and it was shown that the increase in dust reduces the electrical energy to be obtained from the plant. In this study, the change in output voltage of the solar panel surface by natural pollination was examined. In addition, monthly research was conducted on the elements contained in the powder and the grain size of the powder. Contamination of the Panel surface is expected to reduce panel performance. But the decrease in dust-induced tension was studied with this study, as regional pollination data changed. Data on dust varies according to geographical characteristics. These values are acceptable for Sanliurfa province and vicinity. As a future study, the performance of dust cleaning with electrostatic field will be investigated in the future, as the elements contained in the dust are in an oxide state.

## REFERENCES

- [1] Simko, M., Fiedeler, U., Gazso, A., Nentwich, M. How Nanoparticles Enter the Human Body and Their Effects There. Institute of Technology Assessment of the Austrian Academy of Sciences 2010; 3:1-4 <<http://epub.oeaw.ac.at/0xc1aa5576%200x0024c7a5.pdf>>, doi: 10.1553/ITA-nt-003en
- [2] WHO Report (2019). Raises alarm about bad air in Turkish cities. p.73-97.
- [3] MGM, 2017 Yılı İklim Değerlendirmesi raporu [Climate assessment report for 2017]. Ankara: T.C. Tarım ve Orman Bakanlığı Meteoroloji Genel Müdürlüğü Yayınları, 2018.
- [4] MGM, Toz taşınımı (kum ve toz fırtınaları) tahmini bilgi notu [Dust transport (sand and dust storms) forecast information note]. Ankara: T.C. Tarım ve Orman Bakanlığı Meteoroloji Genel Müdürlüğü, Araştırma Dairesi Başkanlığı Yayınları, 2020.
- [5] Gerçekoglu, H., 2020. PM2,5 nedir? neden tehlikelidir?[What is PM2.5? why is it dangerous?]. Kalp ve Damar Cerrahi, Prof. Dr. Hakan Gerçekoglu inceleme yazısı. Retrieved at 12.05.2020. <https://drhakangercekgoglu.com/>
- [6] ÇSB Hava kirliliği izleme istasyonu [Air pollution monitoring station], T.C. Çevre ve Şehircilik Bakanlığı, Sürekli İzleme Merkezi. Erişim:12.05.2020. <https://www.havaizleme.gov.tr/>.
- [7] MGM, 2018 Yılı iklim değerlendirme raporu [Climate assessment report for 2018], Ankara:T.C. Tarım ve Orman Bakanlığı Meteoroloji Genel Müdürlüğü Yayınları. 2019.
- [8] Chanchangi, Y. N., Ghosh, A., Sundaram, S., Mallick, T.K. Dust and pv performance in Nigeria: a review. Renewable and Sustainable Energy Reviews 2020; 21:1-14.
- [9] Adigüzel E. Farklı boyutlardaki toz partiküllerinin fotovoltaik panellerin verimliliği üzerine etkisi [Effect of dust particles in different sizes on the efficiency of the photovoltaic panels], MSc, University of İstanbul, Turkey, 2018
- [10] Altıntaş M, Arslan S. 2020, PVSYST ile güneş paneli kirlilik etkilerinin incelenmesi: Şanlıurfa Güneş Enerjisi Santrali Örneği [Investigation of solar panel pollution effects with PVSYST: The Case of Şanlıurfa Solar Power Plant]. In: Hayaloğlu A, editor. Mühendislik Alanında Teori ve Araştırmalar, Turkey:Gece Kitaplığı, 2020. pp.65-84.



# DEVELOPING A LORA BASED IOT APPLICATION FOR OUTDOOR STREET LIGHTING FAULT DETECTION IN SMART CITIES

Ezgim Çelik

Kahramanmaraş Sütçüimam University, Informatics Department, Kahramanmaraş, Turkey, ezgimc@gmail.com,  
ORCID: 0000-0001-6715-1098

Mehmet Tekerek

Kahramanmaraş Sütçüimam University, Computer Education and Instructional Technology Department, Kahramanmaraş,  
Turkey, tekerek@ksu.edu.tr, ORCID: 0000-0001-6112-3651

*Cite this paper as:* Çelik, E., Tekerek, M. Developing a LoRa based IoT application for outdoor street lighting fault detection in smart cities. 9<sup>th</sup> Eur. Conf. Ren. Energy Sys. 21-23 April 2021, Istanbul, Turkey

**Abstract:** Street lighting has become a part of human life for human beings in conditions where city life is now spread over 24 hours. However, there is no IoT system that will automatically report street lighting problems. A smart system to be developed must solve the problem of energy consumption and coverage. In this study, detection of lighting faults that may occur is aimed to be achieved with LoRa technology developed with the internet of things concept. In this context, circuit boards containing end devices using LoRa technology and 2 gateway devices where radio frequency messages from these end devices are collected have been configured as LoRaWAN base station. In this context, by using various programming languages, embedded software and web software were developed and signal values were analyzed. Field tests have been carried out in and out of the city to estimate the distance between end devices and gateways and have yielded positive results. A coverage area of 11 km radius was provided, path losses were calculated. The estimation algorithm was designed from the light intensity value obtained. The results obtained have provided a great advantage for the fault detection of large numbers of lighting.

**Keywords:** IoT, LoRa, LoRaWAN, Outdoor Street Lighting, Smart city

© 2021 Published by ECRES

## 1. INTRODUCTION

Smart city refers to cities that host technologies that transform the services offered to their residents, thereby increasing operational efficiency and providing the ability to collect, analyze and distribute information to make better decisions [1]. Therefore any city in ideal world should use the knowledge gained to respond to the needs of each of its residents and become even more personalized [2]. The Internet of Things (IoT) paradigm characterizes a network of objects in which processing and storage units of devices such as sensors and / or actuators equipped with a telecommunications interface are interconnected. (3). Accessibility of end devices carrying sensors to central systems plays an important role in smart city applications. (8). When the power of the radio signal is increased to enable communication covering greater distances, this leads to higher energy consumption. These can be described as challenges that arise as the smart city and the IoT world come together [4]. These challenges are energy efficiency, coverage, low energy consumption, long distance data transmission in communication technologies [5] [6]. Low Power Wide Area Network (LPWAN) technologies have become a de facto communication standard for the LPWAN IoT, as it includes aspects such as low energy consumption, high coverage, and long-distance data transmission [4] [7] and working with the large number of low-powered end devices spread over large areas [9] [10]. Generally, in LPWAN, an end device communicates with the base station, which is the bridge in carrying data to the application server, not with the other end devices [11]. Traditional wireless communication technologies cannot achieve low power and long communication range at the same time [12] [13].

When the literature is reviewed, Various scientific studies have been carried out on LoRa in many industrial areas [14]. Lora based traffic density monitoring, smart irrigation, smart street lighting service an automatic flashing system have been established using LoRaWAN and SNR and RSSI values are examined based on the test points [2][14] [15][16].

In a wireless sensor network, among the factors of signal propagation in the wireless environment, there is path loss, known as the emitted signals getting weaker as they travel. In addition, there is a situation where signals are obstructed (also called shadowing) caused by large obstructions (mountains, buildings, etc.) and the formation of multiple copies of the same transmitted signal [17][7]. While the performance of LoRa technology is analyzed for different application types, path loss has also been examined in these analysis studies in the literature [4][18][19]. An IOT system to be built for street lighting under the smart city concept should provide coverage for kilometers. One of the problems to be solved for this application is the energy consumption of the end device to be placed on the lighting post. To sum up; the system to be installed should bring a solution to the energy consumption and coverage problem. Within the scope of the study, the number and geographical distribution of outdoor street lighting and literature studies in this field were examined. LoRa technology provides a match for us to work in terms of cost and efficiency. Street lighting offers an application and experimental work ground in order to experience LoRa technology.

In this study, it is aimed to detect fault automatically in case the outdoor lighting fails. Within the scope of the study, end devices that detect light intensity using the LoRa wireless communication protocol were designed. LoraWAN-based remote communication station was established. The data received from the end devices were transferred to the LoRAWAN server over the gateway. An application has been developed to keep, analyze and monitor the data obtained.

## 2. MATERIAL AND METHODS

### 2.1. LoRa and LoRaWAN

LoRa is a physical layer technology offered by Semtech. LoRa is a spread spectrum radio frequency modulation technique derived from chirp spread spectrum (CSS) technology [20]. Using a chirp modulation, the wireless communication link can achieve a sensitivity of -137 dBm and a link budget of up to 157 dB. The thing to achieve such a performance is to reduce the data rate to kilobits per second [21]. LoRa technology is a platform for IoT networks, where communication technology is coming, providing long-range coverage with wireless radio frequency technology, and devices operating at low power [7] [20].

The Received Signal Strength Indicator (RSSI) is the received signal strength in milliwatts, the RSSI is measured in dBm and is a negative value. The closer to 0, the better the signal. Link budget, on the other hand, is the sum of all gains and losses in a telecommunications system from the transmitter through the medium (in other words, free space) to the receiver. It is a way of measuring link performance [22].

The Signal-to-Noise Ratio (SNR) is the ratio between the received power signal and the noise floor power level. The noise floor is an area where all unwanted noise signal sources can corrupt the transmitted signal, and therefore retransmissions occur. If the SNR is greater than 0, it means that the received signal is operating above the noise floor. Typical LoRa SNR values are: -20dB to + 10dB.

LoRaWan is an open protocol developed by the LoRa Alliance. It is based on LoRa modulation technology, which corresponds to the physical layer of the OSI Model. The LoRaWAN open specification is the LPWAN protocol based on LoRa technology. LoRa uses a spectrum spreading modulation that provides secure end-to-end communication with low energy consumption and low data rates [3][23]. The specification defines the LoRa physical layer parameters and the LoRaWAN protocol to the device infrastructure and ensures seamless interoperability between devices. LoRaWAN uses only 125 kHz, 250 kHz and 500 kHz bandwidth ranges [24] [21][7].

Semtech guides the standardization and global compliance of the LoRaWAN protocol with the fast growing LoRa Alliance® technology alliance [20][25][26][27]. These channels specified in Table 1 are the minimum settings that all gateways can be listened to in Europe.

*Table 1. EU 868-870 Band Channel Frequencies [25]*

Modulation	Bandwidth [kHz]	Frequency Channel [MHz]	LoRa DR / BitRate
LoRa	125	868.10    868.30    868.50	DR0 to DR5 /0.3-5 kbps

Here, the physical protocol, LoRa, is a structure that defines the communication protocol and network system architecture while providing long-range connection. The protocol affects the determination of a node battery life, network capacity, QoS, security, and the amount of applications served by the network [9] [23].

Within the scope of the study, a private LoRaWAN server was installed. LoRaWAN-Server is open source LoRaWAN Server software that integrates both network server and application server, so it is useful for application providers or device and application developers running their own LoRaWAN networks Individual switches of the F8L10GW and the end devices have been introduced to the LoRaWAN Server. Figures 1 shows the field installation of D22 and D2A F8L10GW gateways.



Figure 1. F8L10GW D22 Field Installation

## 2.2. Log Distance Path

The formula defined in equation (1), the Log Distance Path Loss formula we will use to calculate the theoretical path loss is a general PL model used in many indoor and outdoor experiments [7]. PL is the expected path loss in decibels.  $\gamma$ , is path loss exponent and  $\sigma$  and if shadowing effect is present, the standard deviation is represented by zero mean Gaussian random variable  $X\sigma$ . In our scenario, it is considered to be 0 due to the characteristics of the test points.  $PL_0$  is the path loss of the reference point in decibels,  $d$  is the length of the path and  $d_0$  is the distance to the reference point.

$$PL = P_{Tx_{dBm}} - P_{Rx_{dBm}} = PL_0 + 10\gamma \log_{10} \frac{d}{d_0} + X_g \quad (1)$$

## 2.3. Working Structure of the System

The LoRaWAN architecture consists of end devices and gateway modules that communicate directly with the network server. The end device is designed to measure the light intensity of outdoor lighting. The sensor is connected to the Arduino-nano component. RN2483 [28] module for LoRa modulation is integrated on arduino-nano. Its main purpose is to send transceiver configuration commands that modulate the message and transmit it to the gateway. The LoRa signal detected by the gateway is converted into an ip packet. Thus, LoRa signals and gateway statuses can be monitored from lorawan-server [29] software. The data received by the LoRawan-server network server is sent to the MQTT listener designed in NodeRed [30] through the client using the MQTT communication protocol, and this flow performs the registration to the MS Sql Server database. With a transaction within the same flow, the set of corporate resource planning programs in which company processes are managed through the restful web service are transferred to the SAP (systeme, anwendungen und produkte in der Datenverarbeitung) ERP (enterprise resource planning) system.

## 3. RESULTS AND DISCUSSION

In wireless sensor networks, in packet transmission-reception experiments, path loss against logarithmic distance, received signal level profile and obtained SNR data are evaluated as performance criteria. In wireless channels, path loss refers to the loss of power along the path between transmitter and receiver. In real-world experiments, field placement and network optimization require accurate path loss (PL) modeling to estimate network coverage and performance. Within the scope of the study, various field tests were carried out and these values were examined. The situation between the theory and the real world will be examined by graphing how the signal values will change in different locations together with the field tests. When the values of luminaire light are taken at various points, it is estimated from which lux value there may be a failure. In Figure 4 below, the distribution of RSSI and SNR values according to the distance can be seen in 4 graphs.

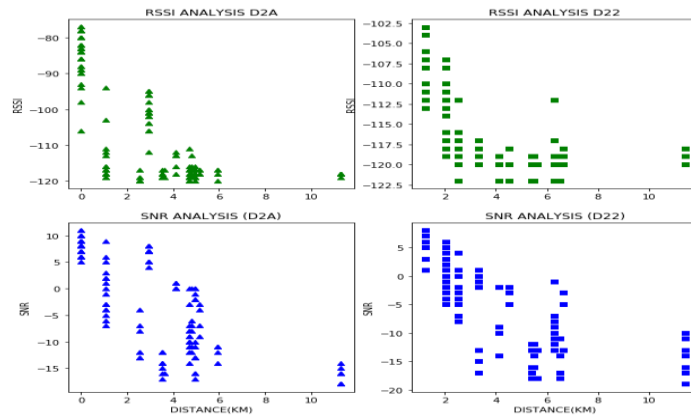


Figure. 4 RSSI and SNR Analysis.

As the distance increases, the RSSI values are affected negatively, LoRaWAN detects the signals although the signal gets weaker. For the location of D22, a region with heavy vehicle traffic was preferred. In terms of height, it is located much lower than D2A. The effect of this situation is that while D2A signal strength reaches up to -80 dbm, signals reaching D22 can have a signal strength up to -102 dbm. When the SNR values were also examined, D2A detected cleaner signals in terms of noise compared to D22. It was observed that the SNR values were affected by environmental crowds such as trees and buildings at the test point. While the distance of Test M point to D2A is approximately 4.78 km, its distance to D22 is 6.49 km. When the signal strength and signal noise are compared, it is revealed that the SNR values in the signals coming to the D2A are better than the ones coming to the D22. The reason for this has been analyzed to be due to the distance of D22 to the sender, the height of the gateway from the ground and the object density of the environment. The TEST K test point is a mountainous area with an elevation higher than both gateways, and both gateways are within sight. TEST K is 11.3 km from D2A and 11.4 km from D22, 20 signals were sent from this point and 100% data transmission rate was achieved.

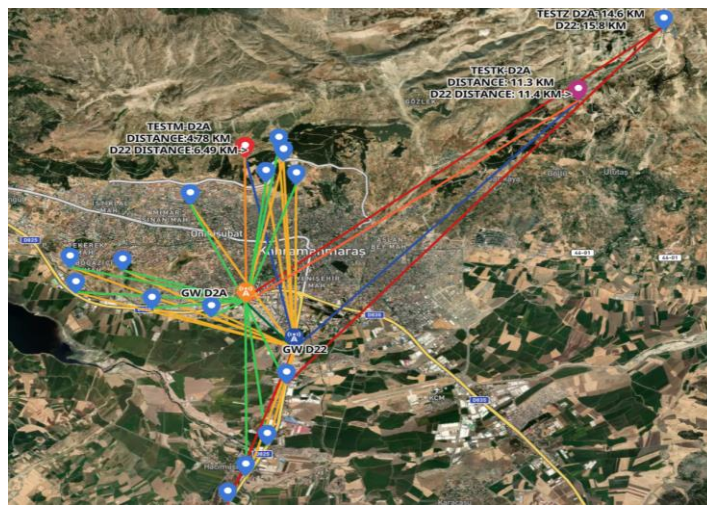


Figure 2. Test M, Test K, Test Z and other tests beds

Considering the large number of field tests (Fig. 2) and the size of the coverage area, it has contributed to the literature by presenting a serious experimental environment in this sense. Linear regression algorithm is preferred for estimation because the end device is placed close to the outer surface of the illumination and the light intensity is a linear value. Thus, the threshold value, which is an important factor for fault detection, was also determined. The linear regression fault estimation is visualized over the light intensity data obtained. The estimation made provides 88% success rate. It detects situations where the lighting is completely off or low light. While calculating the Path Loss over the values of the LoRa signal coming to the D22 gateway, the measured value and exponent 2.03 calculated expected path loss states are given in fig. 3. The reference point chosen for the formula directly affects the exponent variable.

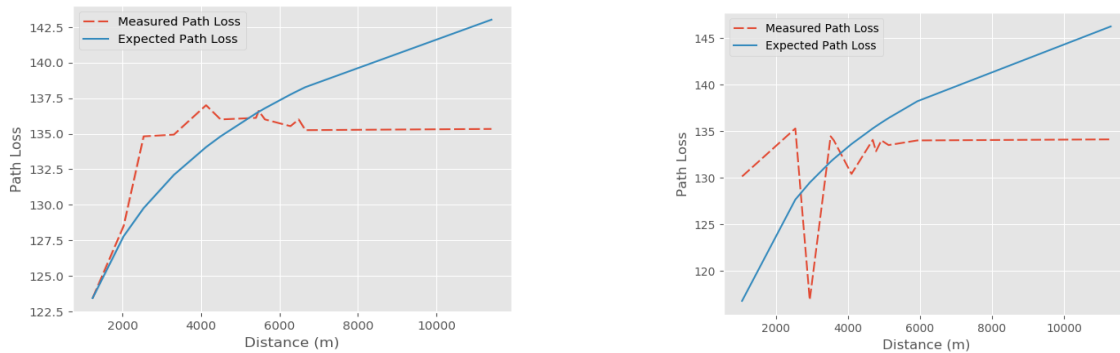


Figure 3 D22 and D2A Path Loss

D2A gateway, the exponent for D2A is calculated as 2.87 and path loss is given in Figure 3. When the Path Loss is above -136 dbm, it is seen that the data transmission also drops. According to the Lora specification, there is no transmission below -120 dbm RSSI, the link budget of our system's lora connection is 16 dbm, so -136 dbm is our maximum path loss. At the points where the expected path loss was seen above 136, it was observed that the actual path loss did not exceed -136 dbm. The theory and field measurements have matched at this point. There is no data transmission below -136 dbm values.

#### 4. CONCLUSION

As a conclusion of the field experiments, it has been observed that the RSSI values are not related to the data transmission rate. Good data transmission rates were also obtained as the distance increased and RSSI values weakened. A linear relationship between path loss values and RSSI values has been verified in a real world scenario. It has been observed that RSSI values are not affected by a factor other than path loss. With the study we have done, the traceability of the fault conditions of the street lighting has been revealed with the LoRaWAN network. It has been shown that the TSL25911 sensor can be used in the lighting fault system. It was concluded that the gateway positioning would be more accurate according to the data transmission rate, not the RSSI values. Different positioning algorithms can be designed by increasing the number of gateways.

#### ACKNOWLEDGMENT

This study was produced from the master's thesis "Development of a LoRa Based IoT Application for Outdoor Lighting Fault Notification and Estimation".

We would like to thank AKEDAŞ Electricity Distribution Corp. for their support in the realization of the research infrastructure.

#### REFERENCES

- [1] Hashem IAT, Chang V, Anuar NB, Adewole K, Yaqoob I, Gani A, et al. The role of big data in smart city. *Int J Inf Manage.* 2016;36(5):748–58.
- [2] Muthanna MSA, Muthanna MMA, Khakimov A, Muthanna A. Development of intelligent street lighting services model based on LoRa technology. *Proc 2018 IEEE Conf Russ Young Res Electr Electron Eng ElConRus 2018.* 2018;2018-Janua:90–3.
- [3] Centenaro M, Vangelista L, Zanella A, Zorzi M. Long-range communications in unlicensed bands: The rising stars in the IoT and smart city scenarios. *IEEE Wirel Commun.* 2016;23(5):60–7.
- [4] Ertürk MA, Aydin MA, Büyükkakkaşlar MT, Evirgen H. A Survey on LoRaWAN Architecture, Protocol and Technologies. *Futur Internet.* 2019;11(10):216.
- [5] Liu S, Dong B, Sun Y. Energy management system architecture based on Internet of Things. *Chinese Control Conf CCC.* 2013;11(3):8066–9.
- [6] Mehmood Y, Görg C, Muehleisen M, Timm-Giel A. Mobile M2M communication architectures, upcoming challenges, applications, and future directions. *Eurasip J Wirel Commun Netw [Internet].* 2015;2015(1):1–37. Available from: <http://dx.doi.org/10.1186/s13638-015-0479-y>
- [7] El Chall R, Lahoud S, El Helou M. LoRaWAN network: Radio propagation models and performance evaluation in various environments in Lebanon. *IEEE Internet Things J.* 2019;6(2):2366–78.
- [8] Yaqoob I, Hashem IAT, Mehmood Y, Gani A, Mokhtar S, Guizani S. Enabling communication technologies for smart cities. *IEEE Commun Mag.* 2017;55(1):112–20.

- [9] De Carvalho Silva J, Rodrigues JJPC, Alberti AM, Solic P, Aquino ALL. LoRaWAN - A low power WAN protocol for Internet of Things: A review and opportunities. 2017 2nd Int Multidiscip Conf Comput Energy Sci Split 2017. 2017;1–6.
- [10] Mekki K, Bajic E, Chaxel F, Meyer F. A comparative study of LPWAN technologies for large-scale IoT deployment. ICT Express [Internet]. 2019 Mar 1 [cited 2020 Aug 3];5(1):1–7. Available from: [www.sciencedirect.com/www.elsevier.com/locate/icte](http://www.sciencedirect.com/www.elsevier.com/locate/icte)
- [11] Mikhaylov K, Petäjäjärvi J, Hänninen T. Analysis of capacity and scalability of the LoRa low power wide area network technology. In: European Wireless Conference 2016, EW 2016. 2016. p. 119–24.
- [12] Rosmiati M, Fachru Rizal M, Susanti F, Fahreza Alfisyahrin G. Air pollution monitoring system using LoRa modul as transceiver system. TELKOMNIKA. 2019;17(2):586–92.
- [13] Afzal MK, Rehmani MH, Pescape A, Kim SW, Ejaz W. IEEE Access Special Section Editorial: The New Era of Smart Cities: Sensors, Communication Technologies, and Applications. IEEE Access. 2017;5:27836–40.
- [14] Yu F, Zhu Z, Fan Z. Study on the feasibility of LoRaWAN for smart city applications. Int Conf Wirel Mob Comput Netw Commun. 2017;2017-Octob:334–40.
- [15] Zhao W, Lin S, Han J, Xu R, Hou L. Design and Implementation of Smart Irrigation System Based on LoRa. 2017 IEEE Globecom Work GC Wkshps 2017 - Proc. 2018;2018-Janua:1–6.
- [16] Nor RFAM, Zaman FHK, Mubdi S. Smart traffic light for congestion monitoring using LoRaWAN. 2017 IEEE 8th Control Syst Grad Res Colloquium, ICSGRC 2017 - Proc. 2017;(August):132–7.
- [17] Noreen U, Bounceur A, Clavier L. A study of LoRa low power and wide area network technology. Proc - 3rd Int Conf Adv Technol Signal Image Process AT SIP 2017. 2017;
- [18] Plets D, Podevijn N, Trogh J, Martens L, Joseph W. Experimental Performance Evaluation of Outdoor TDoA and RSS Positioning in a Public LoRa Network. IPIN 2018 - 9th Int Conf Indoor Position Indoor Navig. 2018;(September):24–7.
- [19] Reda HT, Daely PT, Kharel J, Shin SY. On the Application of IoT: Meteorological Information Display System Based on LoRa Wireless Communication. IETE Tech Rev. 2018;35(3):256–65.
- [20] What is LoRa? | Semtech LoRa Technology | Semtech [Internet]. [cited 2020 Jan 1]. Available from: <https://www.semtech.com/lora/what-is-lora>
- [21] Lavric A, Popa V. LoRa™ Wide-Area Networks from an Internet of Things perspective. Proc 9th Int Conf Electron Comput Artif Intell ECAI 2017. 2017;2017-Janua:1–4.
- [22] LoRa — LoRa documentation [Internet]. [cited 2021 Feb 6]. Available from: <https://lora.readthedocs.io/en/latest/#rss>
- [23] Loriot M, Aljer A, Shahrour I. Analysis of the use of LoRaWan technology in a Large-Scale Smart City Demonstrator. 2017.
- [24] Semtech. LoRa Modulation Basics AN1200.22 [Internet]. APP NOTE. 2015. p. 1–26. Available from: <http://www.semtech.com/images/datasheet/an1200.22.pdf>
- [25] Specification L. LoRaWAN™ Specification. 2015;
- [26] Aoudia FA, Gautier M, Magno M, Gentil M Le, Berder O, Benini L. Long-short range communication network leveraging LoRa™ and wake-up receiver. Microprocess Microsyst [Internet]. 2018;56(November 2017):184–92. Available from: <https://doi.org/10.1016/j.micpro.2017.12.004>
- [27] Adelantado F, Vilajosana X, Tuset-Peiro P, Martinez B, Melia-Segui J, Watteyne T. Understanding the Limits of LoRaWAN. IEEE Commun Mag. 2017;55(9):34–40.
- [28] RN2483 LoRa ® Technology Module Command Reference User's Guide. 2015.
- [29] GitHub - gotthardp/lorawan-server: Compact server for private LoRaWAN networks [Internet]. [cited 2021 Feb 4]. Available from: <https://github.com/gotthardp/lorawan-server>
- [30] Node-RED [Internet]. [cited 2021 Feb 4]. Available from: <https://nodered.org/>

# SODIUM DOPED CADMIUM TELLURIDE (CdTe:Na) THIN FILMS PREPARED BY THE SPRAY PYROLYSIS METHOD

Shadia J. Ikhmayies

Jabal El-Hussain, Amman 11121, Jordan, shadia\_ikhmayies@yahoo.com, ORCID: 0000-0002-2684-3300

Cite this paper as:

Ikhmayies, SJ. Sodium doped Cadmium Telluride (CdTe:Na) thin films prepared by the spray pyrolysis method. 9<sup>th</sup> Eur. Conf. Ren. Energy Sys. 21-23 April 2021, Istanbul, Turkey

**Abstract:** Cadmium telluride (CdTe) is an important semiconducting material for several applications including solar cells and optoelectronic industries, where its use as an absorber layer in CdTe based solar cells is well known. In this work thin films of sodium doped cadmium telluride (CdTe:Na) are prepared on glass substrates using the spray pyrolysis method at a substrate temperature of about 300 °C. Some films remained as deposited, others were etched by potassium hydroxide (KOH), and others were etched by KOH then by ammonium hydroxide (NH4OH). The films are characterized using X-ray diffraction (XRD), UV-VIS transmittance spectroscopy, and current-voltage (I-V) plots. XRD showed that the films are polycrystalline with mixed (cubic and hexagonal) phase. The band gap energy was estimated from the first derivative of the transmittance curves. The resistivity of the films was determined from the current-voltage plots. It is found that the properties of the films are suitable for use as an absorber layer in CdS/CdTe thin film solar cells.

**Keywords:** Cadmium telluride, thin films, absorption edge, band gap energy, I-V characteristics

© 2021 Published by ECRES

## 1. INTRODUCTION

CdTe is a II-VI compound semiconductor of direct band gap of about 1.5 eV [1] at room temperature, which is close to the energy corresponding to the point of maximum intensity of the solar spectrum. It has a large absorption coefficient, where a thickness of about 2 μm can absorb most of the incident radiation. This material is important for several applications including solar cells [2], where it is used as absorber layer, and optoelectronic industries such as the detectors of x-ray and infrared radiations [3]. CdTe can be prepared by several experimental routes including rf sputtering [2,4], electrodeposition [5], thermal evaporation [6-10], closed space sublimation [11], hot wall epitaxy [3] and spray pyrolysis [12,13]. The spray pyrolysis method was chosen in this work because it is a low cost method and it enables intentional doping.

Cadmium telluride can be doped to be n-type or p-type. Variable dopants were tried by different authors to make it p-type; i.e., O, Na, Cl, Cu, Ti, As, P, Sb, Ag, and N. It was found that it is difficult to obtain high enough p-type carrier density [14] due to self compensation between the dominant defects and the dopant. In both n- and p-type CdTe, heat treatment resulted in a reduction of carrier density near the surface [15]. Group I elements (i.e. Li, Na, Cu, Ag) replace cadmium in the cation sublattice [16]. Cu is known to act as an acceptor when Cu atoms occupy a cation site such as Cd in CdTe. Group V elements (i.e. P, As, Sb) replace tellurium in the anion sublattice [16], but attempts to simply dope p-CdTe films from the vapor phase with group V acceptors have, in general, been unsuccessful [15]. Some success for P and As doping had been reported by L. Chu et al. [17] using a chemical vapor deposition (CVD) technique. Nitrogen doping to produce p-type CdTe was successfully tried by Oehling et al. [18]. Chlorine at low concentrations forms shallow acceptor complexes with native defects and due to this increases the p-type conductivity of CdTe whereas excess single substitutional chlorine acts as a donor [19]. Oxygen acts as an acceptor at low concentrations, and the formation of complexes may dominate at high oxygen concentrations [17]. In this work Na was used as a dopant for CdTe thin films, where it was introduced in the form of NaOH which was used to dissolve TeO<sub>2</sub> in distilled water. The objective of this work is to produce CdTe thin films of structural, optical, and electrical properties suitable for the use as absorber layer in thin film solar cells.

## 2. MATERIALS AND METHODS

For the production of CdTe:Na thin films by the spray pyrolysis method, the precursor solution was prepared by mixing two separate solutions; one of TeO<sub>2</sub> and the other of CdCl<sub>2</sub>. The first solution was made by dissolving 5.32×10<sup>-3</sup> mole of TeO<sub>2</sub> (Assay >95%) in 1.03×10<sup>-2</sup> mole of NaOH (minimum assay 96%) and 20 ml of distilled water where NaOH works as a doping source and helps in dissolving TeO<sub>2</sub> which is insoluble in water. The solution was stirred by a magnetic stirrer until the compounds dissolved completely. At this stage the solution was turbid white. The second solution was made by dissolving 3.42×10<sup>-3</sup> mole of CdCl<sub>2</sub>.H<sub>2</sub>O (MERECK Art. 2011) in 20 ml of distilled water. To this solution 50 ml of ammonium hydroxide NH<sub>4</sub>OH (of concentration 10%) was added. A white precipitate which is Cd(OH)<sub>2</sub> was formed when the amount of NH<sub>4</sub>OH is small, but after adding more NH<sub>4</sub>OH, the white precipitate disappeared and the solution became transparent. This is due to the formation of the complex ion Cd(NH<sub>3</sub>)<sub>4</sub><sup>2+</sup> which is the source of cadmium ions [20];



About 18 ml of hydrazine hydrate N<sub>2</sub>H<sub>4</sub>.H<sub>2</sub>O (80%) was added to this solution too, where aqueous hydrazine is a powerful reducing agent in basic solutions [21]. The second solution was added to the first one and stirring continued until the solution which was turbid white, became completely colorless. At this stage it was sprayed intermittently on the hot substrates. According to Serreze et al, [22], no complex between Cd and Te forms in the solution. This was verified by them through UV charge transfer spectroscopy. Their hypothesis was that the constituent components were first generated in the elemental state e.g.



and that these undergo a solid-state reaction at the surface of the hot plate to form CdTe in a manner similar to that observed by Yokoto et al. [22],



There is a possibility that the same thing occurs in this work, because hydrazine hydrate is a reducing agent, and that it will help in the conversion of Cd<sup>2+</sup> to Cd<sup>0</sup> and Te<sup>4+</sup> to Te<sup>0</sup> (most probably in more than one step), and then the same solid-state reaction was expected to occur on the hot plate to form CdTe.

The ratio of tellurium to cadmium in the solution was chosen to be 1.56 which was not stoichiometric. The reason for this high ratio was the removal of tellurium during the reactions on the hot substrate in the form of gases where TeH<sub>2</sub> was one of the expected evolved gases. The doping ratio of sodium to cadmium in the solution (ratio of the concentration of Na ions to that of Cd ions) was 1.94. There is no evidence that this is the best ratio, so more investigation is needed to find the best ratio which results in the smallest film resistivity and highest film quality. The produced CdTe:Na films were dark brown or gray brown, rough, and approximately opaque. The substrates which are ordinary glass microslides with dimensions 2.5×6×0.1 cm<sup>3</sup> were cleaned first by dipping in distilled water to remove the dust, and then they were ultrasonically cleaned in methanol for at least 15 min. Finally they were soaked in distilled water and polished with lens paper.

Many parameters must be controlled during the spraying process. These parameters include; the carrier gas pressure, the deposition time, the solution spray rate, the distance between the substrate and the nozzle, the time between two successive sprayings, and the substrate temperature. The spray rate was usually in the range 15-18 ml/min. The optimum carrier gas pressure for this rate of solution flow was around 5 kg/cm<sup>2</sup>. The nozzle to substrate distance was adjusted to get the largest area that was covered by the solution uniformly, and it was kept at around 30 cm. The deposition process was done intermittently, where the deposition time was chosen to be 10 seconds, and the waiting period between two successive sprayings was taken 1-3 minutes. The substrate temperature was 300 °C.

To remove the surface layer which mainly consists of different oxides, the surfaces of the films were etched with different etching solutions before making the electrical contacts. The solutions are KOH in methanol (0.11 gm in 100 ml methanol), and NH<sub>4</sub>OH. That is, KOH etching is believed to remove conducting surface oxides [23]. It is found that KOH had removed a white compound and made the color lighter, while NH<sub>4</sub>OH removed a thick white layer, changed the color to dark brown, and the films became more transparent. The thickness of the as-deposited

films is around 700 nm, and after KOH etching the thickness became around 600 nm, but when KOH-etched films were etched again with NH<sub>4</sub>OH the thickness decreased to around 400 nm.

X-ray measurements were made using a Philips PW1840 Compact x-ray diffractometer system with Cu K $\alpha$  ( $\lambda=1.5405 \text{ \AA}$ ) line. The diffraction angle  $2\theta$  was varied from  $4^\circ$  to  $60^\circ$ . The transmittance of the films was measured at room temperature as a function of wavelength in the range 400-1100 nm using a double beam Shimadzu UV 1601 (PC) spectrophotometer which was interfaced with a compatible personal computer. The transmittance of the films was recorded with respect to a piece of glass similar to the substrates, which was used as a reference.

To measure the electrical properties, copper was used as the contact material for CdTe thin films, where the contacts were deposited by thermal evaporation with thickness more than  $0.4 \mu\text{m}$ . Two strips of Cu were deposited on the surface of the film, where each strip has 1 cm length, 1 mm width, and the two strips are separated by 2-3 mm. The difficulty in the p-type CdTe is that it doesn't form ohmic contacts with the other metals, but, it always forms a Schottky contact.

The system used for measuring the I-V data consists of a Keithley 2400 Source Meter capable of measuring 10-11A, and it was interfaced by an IBM computer. To take measurements in dark, the sample in question was placed in a brass cell shielded by an aluminum box.

### 3. RESULTS AND DISCUSSION

Fig.1 shows the x-ray diffraction pattern of one of the as-deposited CdTe:Na thin films. The diffraction pattern shows both the cubic (zinc blende) and hexagonal (wurtzite) phases of CdTe with random orientations of the directions of crystal growth. The peaks are assigned by their Millar indices, where C refers to the cubic phase and H refers to the hexagonal one. Also there are unidentified peaks which may be related to other unknown oxidized phases of CdTe.

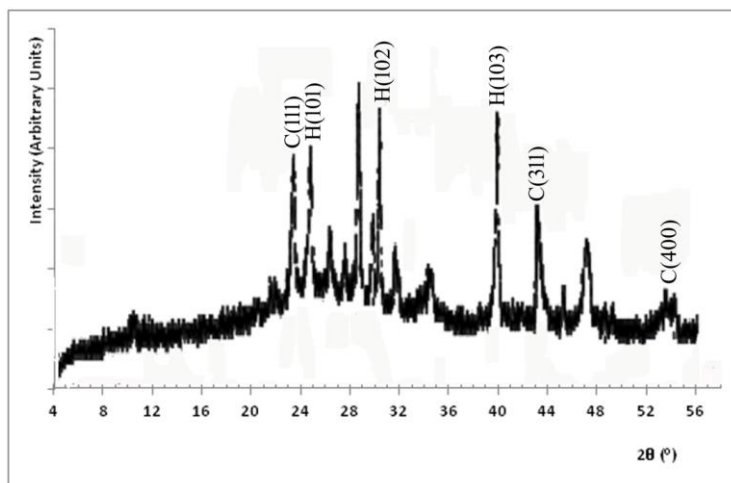


Figure 1. X-ray diffraction pattern of as-deposited CdTe:Na thin film prepared by the spray pyrolysis technique at  $T_s = 300^\circ\text{C}$ .

The transmittance curves of the as-deposited, KOH-etched, and KOH then NH<sub>4</sub>OH-etched CdTe:Na thin films are shown in Fig.2. The low transmittance of the as-deposited film is mainly due to large absorption coefficient of CdTe, where a thickness of about  $2 \mu\text{m}$  can absorb most of the incident radiation, and partially due to the roughness of the film's surface. As the figure shows, the transmittance was improved after etching due to the decrease of surface roughness and decrease of film thickness, where the highest transmittance was obtained for the film etched by KOH followed by NH<sub>4</sub>OH. It is observed that the absorption edge of as-deposited and etched films is not sharp. This may be due to the presence of other oxidized phases of CdTe, where the x-ray diffraction pattern showed a number of unidentified peaks. Similar absorption edge was observed by Cárdenas, et al. [24] in CdTe films of poor crystalline quality prepared by hot-wall-close space vapor transport system. They associated the presence of this absorption tail to states in the bandgap due to defects or complexes of cadmium vacancies with residual impurities. Gupta et al. [25] attributed the absence of the sharp absorption edge to the excess of cadmium present and attributed this to the incomplete conversion of cadmium chloride into cadmium telluride due to the escape of unreacted H<sub>2</sub>Te, hence, more than the stoichiometric amount of TeO<sub>2</sub> must be used in preparing the solution.

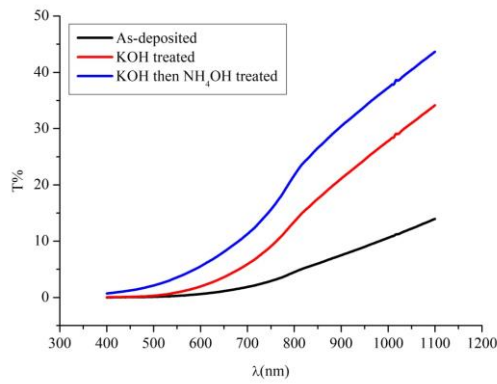


Figure 2. Transmittance curves for as-deposited and etched CdTe:Na thin films.

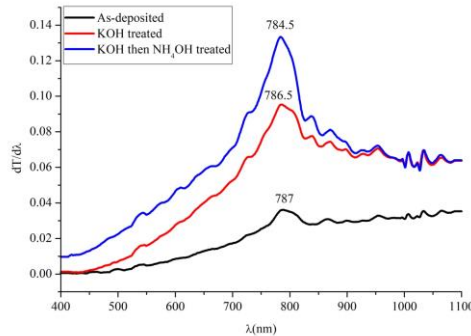


Figure 3. First derivative of the transmittance curves of CdTe:Na thin films shown in Fig.2.

To estimate the position of the absorption edges of CdTe:Na thin films, the first derivatives of the transmittance curves were deduced and displayed in Fig.3. The absorption edges can be obtained from the positions of the maxima of the curves, which are displayed on the figure. It is observed that the values of the cut-off wavelength at the absorption edges of the films are  $\lambda_c = 787$  nm, 786.5 nm, and 784.5 nm for the as-deposited, KOH-etched, and KOH then  $\text{NH}_4\text{OH}$ -etched thin films respectively, where  $\lambda_c$  refers to the cut-off wavelength at which absorption starts. From these values the approximate band gap energies ( $E_g$ ) of the films in the same order are 1.576, 1.577, and 1.580 eV. These values of band gap energy are larger than those of bulk CdTe which is 1.5 eV at room temperature [26] due to Na doping. Fig.4 displays the room temperature I-V characteristics of a set of CdTe:Na thin films. Fig. 4a shows the I-V characteristics for one of the as-deposited films in the dark, where the relationship between I and V is close to a linear one. The resistivity was estimated from this plot and found to be  $1.19 \times 10^6 \Omega\text{cm}$ . Fig.4b shows the same graphs for another film in the dark before and after KOH-etching. The I-V plot is also close to a straight line, and the resistivity was decreased after KOH etching from  $1.14 \times 10^6 \Omega\text{cm}$  for the as-deposited film to  $8.57 \times 10^5 \Omega\text{cm}$  for the KOH-etched film.

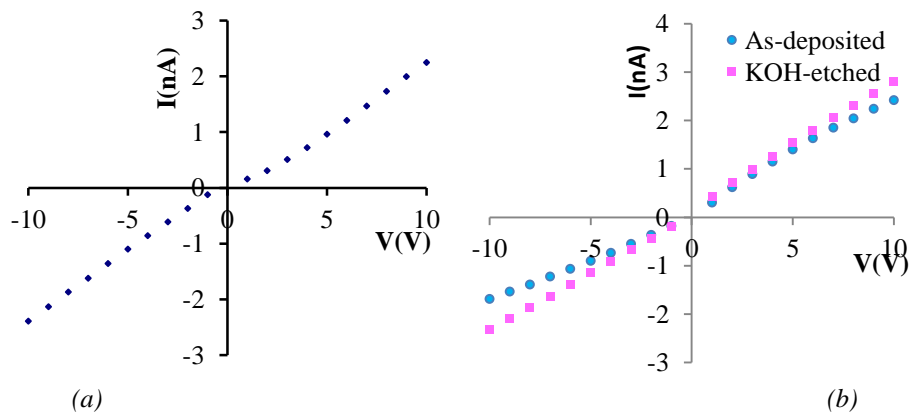


Figure 4. The I-V characteristics of the spray-deposited CdTe:Na thin films in the dark. (a) As-deposited film. (b) Before and after KOH etching.

### 3. CONCLUSIONS

Sodium doped Cadmium telluride (CdTe:Na) thin films were prepared using the spray pyrolysis method on glass substrates at substrate temperature of 300 °C. The films were characterized using X-ray diffraction (XRD), UV-VIS transmittance spectroscopy, and current-voltage (I-V) characteristics. From XRD pattern the films appeared to be polycrystalline with mixed cubic and hexagonal phase, and a set of unidentified peaks which may be related to other phases of oxidized CdTe. The films were etched using KOH and NH<sub>4</sub>OH and their transmittance was measured and found to be improved by etching. The absorption edge of the films was estimated using first derivative of the transmittance and used to estimate the band gap energies, where the band gap is slightly larger than that of bulk CdTe. The I-V plots are close to straight lines. The resistivity of the films before and after etching was deduced and found to be ~10<sup>6</sup> Ω.m. A slight decrease of resistivity occurred after etching by KOH. These properties of the films are suitable for their usage as absorber layer in CdTe thin film solar cells.

### REFERENCES

- [1] Lalitha, S, Karazhanov, SZh, Ravindran, P, Senthilarasua, S, Sathyamoorthy, R, Janabergenov, J. Electronic structure, structural and optical properties of thermally evaporated CdTe thin films. *Physica B* 2007; 387: 227-238. Doi:10.1016/j.physb.2006.04.008
- [2] Dolog, I, Mallik, RR, Malz, D, Mozynski A. Spectroscopic, topological, and electronic characterization of ultrathin a-CdTe:O tunnel barriers. *J. Appl. Phys.* 2004; 95(6): 3075. <https://doi.org/10.1063/1.1647259>.
- [3] Ferreira, SO, Leal, FF, Faria, TE, Oliveira, JE, Motisuke, P, Abramof, E. Characterization of CdTe thin films grown on glass by hot wall epitaxy. *Brazilian Journal of Physics* 2006; 36(2A): 317-319. <https://doi.org/10.1590/S0103-97332006000300022>
- [4] Gulkowski, S, Krawczak. E. RF/DC magnetron sputtering deposition of thin layers for solar cell fabrication. *Coatings* 2020; 10: 791. Doi:10.3390/coatings10080791
- [5] Basol, BM, Tseng, ES. Mercury cadmium telluride solar cell with 10.6% efficiency. *Appl. Phys. Lett.* 1986; 48: 946. <https://doi.org/10.1063/1.96667>
- [6] Ikhmayies, SJ, Abedrabbo, S, Lahlouh, B. Influence of the deposition temperature on the structure, morphology, and optical properties of thermally evaporated CdTe thin films. *Journal of Electronic Materials* 2019; 48: 6901-6909. <https://doi.org/10.1007/s11664-019-07205-7>
- [7] Ikhmayies, SJ, Ahmad-Bitar, RN. Characterization of vacuum evaporated CdTe thin films prepared at ambient temperature. *Materials Science in Semiconductor Processing* 2013; 16: 118-125. <https://doi.org/10.1016/j.mssp.2012.06.003>.
- [8] Ikhmayies, SJ, Ahmad-Bitar, RN. Optical properties of nanocrystalline CdTe thin films, *Physica B* 2010; 405: 3141-3144. <https://doi.org/10.1016/j.physb.2010.04>.
- [9] Ikhmayies, SJ, Optical parameters of thermally evaporated CdTe thin films. In: Carpenter JS, Bai C, Hwang J-Y, Ikhmayies S, Li B, Monteiro SN, Peng Z, Zhang M, (Eds.). *Characterization of Metals, Minerals and Materials* 2014. Hoboken, New Jersey: John Wiley & Sons, Inc., 2014. pp. 139-145.
- [10] Ikhmayies, SJ, Ahmad-Bitar, RN. Electrical, optical and structural properties of vacuum evaporated CdTe thin films. In: Howard S, Anyalebechi PN, Zhang L, (Eds.). *EPD Congress 2009: Extraction and Processing Division*. Warrendale, PA: Wiley-TMS. 2009. Pp. 427-434.
- [11] Mitchell KW, Eberspacher C, Cohen F, Avery J, Duran G, Bottenberg W. Progress towards high efficiency thin film CdTe solar cells. In: Proc. 18th IEEE Photovolt. Spec. Conf.: 21-25 October 1985: Las Vegas, The Institute of Electrical and Electronics Engineers, Inc., pp. 1359-1364.
- [12] Gunjal, SD, Khollam, YB, Jadkar, SR, Shripathi, T, Sathe, VG, Shelke, PN, Takwale, MG, Mohite. KC. Spray pyrolysis deposition of p-CdTe films: Structural, optical and electrical properties. *Solar Energy* 2014;106: 56-62.
- [13] Boone, JL, Doren, TPV, Berry, AK. Deposition of CdTe by spray pyrolysis. *Thin Solid Films* 1982; 87(3): 259-264.
- [14] Valdna, V, Buschmann, F, Millikov, E. Conductivity conversion in CdTe layers. *Journal of Crystal Growth* 1996; 161: 164-167.
- [15] Bube, H. Richard. Materials for photovoltaics. *Annu. Rev.Mater. Sci.* 1990; 20: 19-50.
- [16] Babentsov, VN, Rashkovetskii, LV, Sal'kov, EA, and Tarbaev, NI. Luminescence profiling investigation of the transformation of defects in CdTe crystals by brief annealing. *Sov. Phys. Semicond.* 1992; 26 (6): 608-612.
- [17] Chu, TL, Chu, SS, Firszt, F, Naseem, HA, Stawski, R. Deposition and characterization of p-type cadmium telluride films. *J. Appl. Phys.* 1985; 58(3): 1349-1355.
- [18] Oehling, S, Lugauer, HJ, Schmitt, M, Heinke, H, Zehnder, U, Waag, A, Becker, CR, Landwehr, G. p-type doping of CdTe with a nitrogen plasma source. *J. Appl. Phys.* 1996; 79(5): 2343-2346.
- [19] Valdna V. Complex defects in Cl doped ZnTe and CdTe. In: Materials Research Society symposia proceedings series, 442: Materials Research Society symposia, 1997. ACA, USA: 585-591.
- [20] Sahu, SN. Chemical deposition of CdS films: structure, RBS, PIXI, optical and photoelectrochemical solar cell studies. *Journal of Materials Science: Materials in Electronics* 1995; 6: 43-51.

- [21] Albert Cotton F, Geoffrey Wilkinson, FRS. Advanced Inorganic Chemistry, 3rd edition. New York, USA, Interscience Publishers, a division of John Wiley and Sons, 1972.
- [22] Serreze, HB, Lis, S, Squillante, MR, Turcotte, R, Talbot, M, Entine, G. Spray pyrolysis prepared CdTe solar cells. In: Photovoltaic Specialists Conference, 15<sup>th</sup>. May 12-15, 1981, Institute of Electrical and Electronics Engineers, Inc.: Kissimmee, FL: pp. 1068-1072.
- [23] Fulop, G, Doty, M, Meyers, P, Betz, J, Liu, CH. High efficiency electrodeposited cadmium telluride solar cells. *Appl. Phys. Lett.* 1982; 40(4): 327-328.
- [24] Cárdenas, M, Mendoza-Alvarez, JG, Sánchez-Sinencio, F, Zelaya, O, and Menezes, C. Photoluminescent properties of films of CdTe on glass grown by a hot-wall-close space vapor transport method. *J. Appl. Phys.* 1984; 56 (10): 2977-2980.
- [25] Gupta, BK, Agnihotri, OP. Effect of cation-anion ratio on crystallinity and optical properties of cadmium sulphide films prepared by chemical spray deposition. *Solid State Communications* 1977; 23: 295-300.
- [26] Fonthal, G, Tirado-Mejía, L, Marín-Hurtado, JI, Ariza-Calderón, H, Mendoza-Alvarez, JG. Temperature dependence of the band gap energy of crystalline CdTe. *J. Phys. Chem. Solids.* 2000; 61(4): 579-583. Doi:10.1016/s0022-3697(99)00254-1.

## COUNTRIES AND PRESENTERS LIST

ID	TITLE	COUNTRY	PRESENTER
2	Towards integration of carbon capture and storage approaches in waste processing technologies	Latvia	Maris Klavins
5	Establishing reduced thermal mathematical model (RTMM) for a space equipment	Turkey	Mustafa Akbulut
12	Design the superconducting magnet power supply for medical proton accelerator	China	Shengmin Pan
23	Renewable energy supply chain network design	Egypt	Marwa Mekky Mohamed Abdallah
24	Power loss calculation of photovoltaics using python	Iraq	Kerry Sado
29	Techno-economic feasibility analysis of PV potential with passive cooling in the desert climate	Kingdom of Saudi Arabia	Ghida AlZohbi
30	Promissing HDR project in the North Caucasus	Russia	Alan Lolaev
31	Application of power spectral density and the support vector machine to fault diagnosis for permanent magnet synchronous motor	Morocco	Sara Zerdani
32	The impact of radiant heating on the performance of sustainable constructional component under elevated temperature: Part 2	Jordan	Wail N. Al-Rifaie
34	System integration and data models to support smart grids energy trading	Ireland	Silva Fábio
35	Power control strategy of a photovoltaic system	Algeria	Bedoud Khouloud
36	Artificial neural network forecasting models for wind and photovoltaic energy prediction utilizing time-series input data with different resolutions	Hungary	Mutaz AlShafeey
37	Performance assessment of the windows glazing system for the office building	Turkey	Pinar Usta
39	Wireless charging systems for electric vehicles: review article	Iraq	Kerry Sado
40	Exergy assessment of the energy efficiency of the clean room air treatment system	Russia	Nikolay Romanovich Kharlamov
41	Deep-learning approach to the iron concentration evaluation in silicon solar cell	Russia	Oleg Olikh
42	Determining of optimal tilt angle of solar panels in three cities in Albania	Albania	Buzra Urim
43	Effect of Estonian woody biomass gasification temperature on the composition of the producer gas	Estonia	Alejandro Lyons Cerón
44	The increasing importance of smart home applications as a major trend for the future value creation of German energy companies	Germany	Andreas Ensinger
45	Energy harvesting through landscape design	Turkey	İşıl Kaymaz
46	Thermal energy grid simulation (TEGSim) for smart urban regions	Austria	David Huber
47	A two-step metal-assisted chemical etching process for formation of silicon nanowires based black silicon	Kingdom of Saudi Arabia	Hazem ElGhonimy
48	Performance investigation of an integrated solar-powered RO/Adsorption cooling trigeneration system	Egypt	Ahmed A. Hassan
50	Development of energy saving system based on microcontroller for boiler manufacturer	Turkey	Halit Cetiner
51	Energetic analysis of a PVT-based solar-driven hybrid adsorption-compression refrigeration system	Egypt	Mohamed G. Gado

52	Testing the Abrasion resistance of broadband anti-reflection coatings for solar modules	Turkey	Sibel Yilmaz
54	Design of 2S2L based buck - boost converter with wide conversion range	India	Prasanna Chunduru
55	Hybrid dedicated outdoor air system in buildings	Thailand	Dararat Tongdee
56	Energy analysis of vapor compression refrigeration cycle using a new generation refrigerants with low global warming	Algeria	Rabah Touaibi
59	Estimating of the output voltage parameters for T-type Inverter with ANN	Turkey	Tugba Atar
60	Estimating of the leakage inductance value for single-phase isolation transformer with ANFIS	Turkey	Busra Aslan
61	Technological forecasting for electric battery technology in the electric vehicle industry	Turkey	Koten Hasan
62	New concepts and technologies for electrical machines and mechanical engineering	Kazakhstan	Amangeldy M. Zhunusbekov
63	Analysis of positive output buck-boost topology with extended conversion ratio	India	Sahithi Priya Kosika
65	Recycling of Waste Tires by Thermal Dissolution (Pyrolysis) and Thermochemical Degradation (Gasification)	Turkey	Yayalik İbrahim
66	Review of Thomson heat	Mexico	Igor Lashkevych
70	Development of an adaptive control system for a hot water supply using solar power plant	Russia	Yury Koshlich
71	Comparison of different regression algorithms for estimating energy consumption	Turkey	Halit Cetiner
74	Data extraction of perovskite solar cells materials by using natural language processing tools	Colombia	Mary Zuleika Jiménez Díaz
76	Performance of a solar based combined power and cooling system under solar, solar storage and storage mode of operations	India	Tapan Kumar Gogoi
77	Enhancing the flexibility of electricity generation and heating for Kızıldere II geothermal power plant by demonstrating heat storage systems	Turkey	Hakan Alp Sahiller
80	Selection of the suitable greenhouse orientation on the basis of energy saving	Morocco	Laila Ouazzani Chahidi
83	Supercritical CO <sub>2</sub> binary mixtures for brayton power cycles complex configurations coupled to solar thermal energy plants	Spain	Paul Tafur-Escanta
84	A Review of the life cycle assessments of Brazilian biodiesel	Brazil	Marina Weyl Costa
86	Ageing effect evaluation of PV installation after 10 years continuous operation	Bulgaria	Nikolay Tyutyundzhiev
87	Upscaling of perovskite solar cell technology by a semi-automatic blade-coating technique at ambient condition	Italy	Luigi Vesce
88	Clean power generation: environmentally friendly lubrication products and pollution prevention	Brazil	Kethlyn G. Moscon
89	Distance protection based on the synchrophasor data in control room	Croatia	Igor Ivanković
92	Torrefaction and carbonization of water hyacinth stems and leaves: impact on energy	Egypt	Amr Moataz Sanad
93	Energetic and financial evaluation of a solar-powered absorption chiller integration into a CO <sub>2</sub> commercial refrigeration system	Greece	Evangelos Syngounas
94	Determination of wind energy potential and evaluation of the feasibility analysis of a wind turbine via RETScreen for Çerkezköy, Turkey	Turkey	Aytac Perihan Akan
95	Technological ecovillages: auto sustainable urban pilots in the community of Llucanayacu in Chazuta, San Martin, Peru	Peru	Nerida del Carmen Pastrana
96	Computational thermal-fluid coupling analysis of a variable nozzle turbine for solar power generation	Algeria	Abdelmadjid Chehhat
97	Optimization of an offshore wind jackets manufacturing project through an investment analysis using 3D discrete-event simulation	Spain	Santiago José Tutor Roca

99	On Minimization of the group variability of intermittent renewable generators	Croatia	Dubravko Sabolić
103	Assessments of global warming potential of Brazilian biodiesel	Brazil	Marina Weyl Costa
104	Solar collector with increased heat transfer efficiency	Russia	Andrey Batukhtin
105	Effect of position of heat flux profile on the absorber surface of parabolic trough solar collector for direct steam generation	India	Ram Kumar Pal
113	Modal excitation energy	Turkey	Tarik Tufan
114	Economic aspects of market formation reactive power in electric power industry	Russia	Sergey Filin
116	A innovative methodology for visual impact assessment of wind power plants	Italy	Blois Luciano
119	Characteristics of beach erosion at Kkotji Beach in Korea	Korea	Jinwoo Jeong
121	Issues of renewable energy sources with grid-tied inverter connected to an off-grid system	Lithuania	Mantas Zelba
122	Improving the fatigue of newly designed mechanical system subjected to repeated food loading	Ethiopia	Seongwoo Woo
123	Geothermal projections in Colombia from Oil & Gas industry	Colombia	Eduardo López-Ramos
124	Hybrid state of charge estimation of lithium- ion batteries; improvements on electric vehicle battery management system	USA	Odera Ohazurike
126	Energy efficiency improvement for the mobile air conditioning systems	Turkey	Serkan Erdem
128	The magnetic saturation effect on fault diagnosis in squirrel cage induction motor using current park's vector pattern	Algeria	Chaouch Abdellah
129	Effect of the three main directions of an external magnetic field on the free convection in $Fe_3O_4$ - water nanofluid filled cubic enclosure	Algeria	Maache Mouna Battira
131	Bio-energy characteristics of black pine ( <i>Pinus nigra Arn.</i> ) hydrodistillation waste products	Bulgaria	Hafize Fidan
133	Electric energy load forecasting with ARIMA vs XGBoost for Australia VIC state	Turkey	Muhammed Can Özdemir
136	Predicting cost of farm-based biogas plants	Canada	Arash Samizadeh Mashhadi
137	Use of synthesis gas as fuel for a solid oxide fuel cell	Mexico	Jesus Antonio. Alvarez-Cedillo
138	An averaged large-signal model method of DC-DC isolated forward resonant reset converter based on solar cells battery charger for IoT application	Thailand	Pattarapongsathit Wachiravit
142	The importance of natural insulation building materials in sustainable energy efficient buildings	Turkey	Hatice Mehtap Öz
144	The place of biopolymer-based composites in energy-efficiency architectural design	Turkey	Barış Koçyiğit
146	ESS influence investigation on the operation of critical network nodes	Lithuania	Virginijus Vasylus
148	Smart grid simulation based on high level architecture	United Kingdom	Muhammad Majid Hussain
149	Contribution to the study of a DFIG wind energy generation system based on a quasi Z inverter	Algeria	Larafa Ahcene
151	Numerical investigation of energy desorption from magnesium nickel hydride based thermal energy storage	India	Sumeet Kumar Dubey
152	A comparative study of melting performance for ultra-high temperature latent storage system	India	Alok Kumar Ray
153	Application of PEMFC electrical fluctuation for in-situ diagnostics	Russia	Evgenii Denisov
154	Single-phase grid-connected inverter with high frequency isolation for DC nano-grids	México	Luis J Ruiz Caldera
155	High strength and lightweight steel profiles used in the installation of photovoltaic systems	Turkey	Celal Erkal Kahraman
156	The use of ZnO thin films as a friction layer in energy harvesting	Turkey	Yüzyük Durak Gizem

157	Assessment of energy saving possibilities in construction with the use of solutions based on renewable energy sources	Poland	Elżbieta Szafranko
158	An attempt to assess the correctness of assembly and geometry of solar panels using laser scanning	Poland	Elżbieta Szafranko
162	TCAD-model of betavoltaic battery structure with vertical micro trenches	Russia	Konstantin Petrosyants
164	Towards high crystallinity and stable $\text{MASnI}_3$ perovskite films treated with different antisolvents	Spain	Amal Bouich
166	Bioinspired polymer materials for thermal management of heating and cooling in buildings	Romania	Stiubianu George
167	Evaluation of the temperature impact on the production of photovoltaic energy in the Brazilian national scene	Brazil	Carlos Frajua
168	Analysis and Optimizes of Hybrid wind and solar PV Generation system for off-grid Small Village	Turkey	Nabaz Mohammedali Rasool
169	The possibility of integrating electricity through renewable sources in Sazani Island	Albania	Driada Mitrushi
170	Advanced exergoeconomic evaluation of a cogeneration system combined with a drying unit of fertilizers	Morocco	Asmae Echeeri
171	Kriging surrogate models for optimization in energy-efficient building design	Morocco	Salma Lahmar
172	Developing a real-time power price algorithm for an autonomous demand side management in solar community-grids with battery storage	Germany	Sebastian Finke
173	Investigation of geometries for increasing the energy density in electromechanical battery flywheels	Brazil	Carlos Frajua
175	Modelling and control of a hybrid wind solar system optimized by Fuzzy Based MPPT controller	Algeria	Mennad Mebrouk
176	Energy production using water collectors subjected to solar radiation to improve building indoor thermal conditions	Portugal	Eusébio Conceição
177	Evaluation of mechanical and thermodynamic properties of $\text{BaZn}$ compound by DFT	Turkey	İlknur Kars Durukan
178	Ab initio calculations of the mechanical, vibration and bond nature of the $\text{CdSr}$ compound	Turkey	İlknur Kars Durukan
179	Analysis of optical properties of the $\text{CeTl}$ intermetallic structure	Turkey	İlknur Kars Durukan
180	The physical properties of newly synthesized superconductor compound $\text{LaNiGe}$ via Ab-initio calculatios	Turkey	Yasemin Oztekin Ciftci
181	A theoretical study of pressure-induced effects on $\text{CeAs}$ compound	Turkey	Yasemin Oztekin Ciftci
182	Optoelectronic properties of Zn doped Lead free photovoltaic $\text{CsSnI}_3$ compound	Turkey	Yasemin Oztekin Ciftci
183	The impact of the external environment on energy consumption in residential ventilation and air-conditioning systems on the example of north-eastern Poland	Poland	Aldona Skotnicka-Siepsiak
184	Innovative activity of integrated business structures	Russia	Evgeniy Genkin
185	Analysis of the actual and standard consumption of thermal energy in buildings	Poland	Bogacz Piotr
186	Differential settlement of pile foundation for wind turbine tower on multilayered subsoil	Poland	Dyka Ireneusz
189	Level of meeting the needs for solar energy for hot water production in the Ionian coast of Albania	Albania	Daniela Halili
192	Morphological properties of low temperature hydrothermally grown $\text{TiO}_2$ films for DSSCs devices	Turkey	Aycan Athi
193	Molarity of precursor dependent morphological properties hydrothermally grown $\text{TiO}_2$ films	Turkey	Atli Aycan
195	The fabrication of $\text{SnO}_2/\text{Si}$ heterojunction diode	Turkey	Ozel Kenan
196	The investigation of UV detection performance of $\text{SnO}_2/\text{p-Si}$ heterojunction	Turkey	Ozel Kenan

197	Thermal analysis and parametric study on the influence of thermo-physical properties on dropwise condensation heat transfer	Turkey	Mete Budakli
198	Iterative ekf-based parameter estimation algorithm for a nonlinear PMSM model	Turkey	Artun Sel
199	Algorithms for ESS reinforced RES portfolio bidding in Turkish Energy Markets	Turkey	Abdülhadi Çiftçi
200	p-n heterojunction diode based on TiO <sub>2</sub> /p-Si	Turkey	Sekertekin Betül
201	Various receipts TiO <sub>2</sub> based pastes for semi-flexible DSSCs	Turkey	Abdullah Atılgan
202	Effect of substrate rotation speed on the optical, and electrical properties of TiO <sub>2</sub> /FTO blocking layer fabricated by Spin-Coating	Turkey	Abdullah Atılgan
203	Continuous ocean data analysis using artificial intelligence	Korea	Chi-ok An
204	Stability analysis of sunken vessel for artificial reef use	Korea	Hyun Dong Kim
205	High performance ion-exchange microporous zeolite material for application in the cold plasma device	Turkey	H. Hilal Kurt
206	Filamentation in a plasma cell with GaP wafer	Turkey	H. Hilal Kurt
207	Mean Electron energy Distribution in a Plasma System with ZnSe	Turkey	Selçuk Utaş
209	Gas discharge systems with CdSe electrode	Turkey	Selçuk Utaş
210	Theoretical plasma simulation results of the microdischarge cell with GaSb cathode	Turkey	Selçuk Utaş
211	The Features of the InGaAs/InP detectors in plasma systems	Turkey	Selçuk Utaş
212	Dependence of solution molarity on structural, optical, and electrical properties of spin coated TiO <sub>2</sub> /FTO films	Turkey	Abdullah Atılgan
213	Electric vehicle energy efficiency contribution through laboratory implementation	Spain	Felipe A. Núñez-Donoso
214	Computational modeling of a 2D vanadium redox flow battery cell	Spain	Joseba Martinez-Lopez
215	Automatic identification algorithm of equivalent electrochemical circuit based on electroscopic impedance data for a lead acid battery	Spain	Jose Manuel Lopez-Gude
216	Multipurpose sensor designed to monitor electrochemical parameters of 12 V lead acid battery blocks	Spain	Jose Manuel Lopez-Gude
217	Cell-set modelling of an active rotating microtab on a DU91W(2)250 airfoil	Spain	Alejandro Ballesteros-Coll
218	Automatic optimization algorithm for electrical energy contracts in Spanish market	Spain	Ekaitz Zulueta
219	Ciphering and deciphering technique on the images of energy plants and networks	Turkey	Batuhan Arpacı
220	Comparison of the efficiency values of the rectifiers used in the RF energy harvesting systems	Turkey	Kayhan Çelik
221	MPPT system implementation for a piezoelectric energy harvester	Turkey	Davut Özhan
222	Analysis of atmospheric transported particulate matter and investigation of its effects on solar panel	Turkey	Serdar Arslan
223	State-of-The-Art: DC-to-DC converters for fuel cell vehicular power train – power electronics in fuel cell technology	Denmark	Sanjeevikumar Padmanaban
224	The co-simulation studies of the power electronic circuits with FEA software	Turkey	Selami Balci
225	Is exergy destruction minimization is the same thing with energy efficiency maximization?	Turkey	Birol Kılıkış
226	Next-generation smart grids: power electronics dominated power systems	Qatar	Sertac Bayhan
227	IoT with green energy	India	Sudan Jha
228	Developing a LoRa based IoT application for outdoor street lighting fault detection in smart cities	Turkey	Ezgim Çelik
229	Sodium doped cadmium telluride (CdTe:Na) thin films prepared by the Spray pyrolysis method	Jordan	Shadia J. Ikhmayies

**HOPE TO SEE YOU IN OUR NEXT EVENT**  
**[www.icmece.org](http://www.icmece.org)**